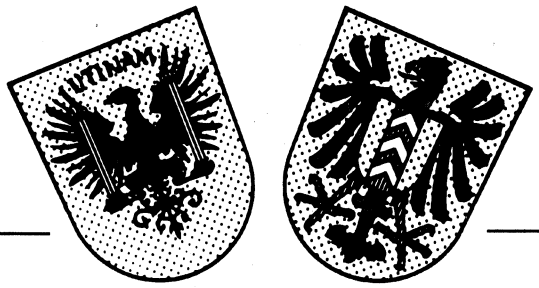

EFTF 2001

15th European Frequency and Time Forum
15ème Forum Européen Fréquence et Temps

March 6-8, 2001
Neuchâtel, Switzerland

PROCEEDINGS

ADDITIONAL COPIES OF THESE PROCEEDINGS CAN BE PURCHASED FROM THE

Permanent EFTF Secretariat

c/o FSRM
Swiss Foundation for Research in Microtechnology
Rue Jaquet-Droz 1 / Case postale 20
CH-2007 Neuchâtel, Switzerland

☎ +41 32 720 09 00 / 🖷 : +41 32 720 09 90
E-mail: eftf@fsrm.ch

15th European Frequency and Time Forum

15ème Forum Européen Fréquence et Temps
Neuchâtel, Switzerland – March 6-8, 2001

PROCEEDINGS

Conference organizer and proceedings publisher:

FSRM
Swiss Foundation for Research in Microtechnology
Rue Jaquet-Droz 1 / Case postale 20
CH - 2007 Neuchâtel, Switzerland

Table of contents

INTRODUCTION

OPENING SESSION

✏ = abstract only

MATERIALS

ATOMIC FOUNTAINS

SENSORS

ATOMIC FREQUENCY STANDARDS

QUARTZ OSCILLATORS

OPTICAL FREQUENCY STANDARDS

GPS CARRIER PHASE

CRYO FREQUENCY GENERATION

SAW

INSTRUMENTATION & TELECOMMUNICATIONS

GALILEO & ACES

POSTERS

MATERIALS

SENSORS

SAW

QUARTZ OSCILLATORS & RESONATORS

ATOMIC, OPTICAL & FOUNTAIN FREQUENCY STANDARDS

INSTRUMENTATION & TELECOMMUNICATIONS

GPS, GALILEO & CARRIER-PHASE

REPORTS

LISTS

Organisation '01

EFTF LOCAL ORGANIZATION

Marcel Ecabert	FSRM, Neuchâtel
Bernard Schlueter	FSRM, Neuchâtel
Nathalie Schor	FSRM, Neuchâtel
Stéphanie Montandon	FSRM, Neuchâtel

TECHNICAL PROGRAMME CHAIRMAN

Léon Prost, METAS - Office Fédéral de Métrologie et d'Accréditation, Berne

Executive committee

Audoin Claude		Chatenay-Malabry, France
Besson Raymond	SFMC c/o ENSMM - LCEP	Besançon, France
Ecabert Marcel	FSRM	Neuchâtel, Switzerland
Hauden Daniel	LPMO - CNRS	Besançon, France
Leschiutta Sigfrido	Istituto Elettrotecnico Nazionale «Galileo Ferraris»	Torino, Italy
Riehle Fritz	Physikalisch-Technische Bundesanstalt	Braunschweig, Germany
Schlueter Bernard		Villers-le-Lac, France
Thomann Pierre	Observatoire Cantonal	Neuchâtel, Switzerland
Underhill Mike	University of Surrey	Guildford, United Kingdom

Scientific committee EFTF '01

Aubry Jean-Pierre	Oscilloquartz SA	Neuchâtel, SWITZERLAND
Audoin Claude		Châtenay-Malabry, FRANCE
Bauch Andreas	PTB - Physikalisch-Technische Bundesanstalt	Braunschweig, GERMANY
Bava Elio	Politecnico di Milano	Milano, ITALY
Besson Raymond	LCEP / ENSMM	Besançon, FRANCE
Bigler Emannuel	LCEP / ENSMM	Besançon, FRANCE
Boulanger J.-Simon	National Research Council of Canada	Ottawa, CANADA
Brunet Michel	CNES	Toulouse, FRANCE
Busca Giovanni	Observatoire Cantonal de Neuchâtel	Neuchâtel, SWITZERLAND
Clairon André	BNM / LPTF	Paris, FRANCE
De Jong Gerrit	NMi Van Swinden Lab.	Delft, THE NETHERLANDS
De Marchi Andrea	Politecnico di Torino	Torino, ITALY
Deyzac François	ONERA	Châtillon, FRANCE
Dimarcq Noël	Observatoire de Paris	Paris, FRANCE
Eskelinen Pekka	Helsinki University of Technology	Helsinki, FINLAND
Feltham Steve	ESA - ESTEC	Noordwijk, THE NETHERLANDS
Garvey Mickael	Datum,	Beverly, USA
Gill Patrick	NPL - National Physical Laboratory	Teddington, UNITED KINGDOM
Giordano Vincent	LPMO / CNRS	Besançon, FRANCE
Godone Aldo	Istituto Elettrotecnico Nazionale	Torino, ITALY
Granveaud Michel	BNM - LPTF	Paris, FRANCE
Gulyaev Yury	Russian Academy of Sciences	Moscow, RUSSIA
Hahn Jörg	ESA - ESTEC	Noordwijk, THE NETHERLANDS
Hauden Daniel	LPMO / CNRS	Besançon, FRANCE
Hilty Kurt	METAS - Swiss Federal Office of Metrology & Accreditation	Berne, SWITZERLAND
Hruska Carl	York University	North York, CANADA
Kalliomäki Kalevi	University of Oulu	Oulu, FINLAND
Kihara Masami	NTT Network Innovation Lab.	Yokosuka, JAPAN
Kirchner Dieter	Technische Universität Graz	Graz, AUSTRIA
Krempl Peter	AVL List GmbH	Graz, AUSTRIA
Kulakov Sergei	State University of Aerospace Instrumentation	St-Petersburg, RUSSIA
Leschiutta Sigfrido	Istituto Elettrotecnico Nazionale	Torino, ITALY
Maleki Lute	NASA Jet Propulsion Lab.	Pasadena, USA
Matsakis Demetrios	U.S. Naval Observatory	Washington, USA
Neubig Bernd	Tele Quartz GmbH	Neckarbischofsheim, GERMANY
Prost Léon	Chairman 2001, METAS - Swiss Federal Office of Metrology & Accreditation	Berne, SWITZERLAND
Salomon Christophe	Ecole Nationale Supérieure	Paris, FRANCE
Santarelli Giorgio	BNM - LPTF	Paris, FRANCE
Schlüter Wolfgang	Institut für Angewandte Geodäsie	Kötzting, GERMANY
Stenger Jörn	PTB - Physikalisch-Technische Bundesanstalt	Braunschweig, GERMANY
Sullivan Donald	NIST	Boulder, USA
Tavella Patrizia	Istituto Elettrotecnico Nazionale	Torino, ITALY
Thomann Pierre	Observatoire Cantonal de Neuchâtel	Neuchâtel, SWITZERLAND
Uhrich Pierre	BNM / LPTF	Paris, FRANCE
Uljanov Adolph	Kvarz Institute of Electonic Measurements	Nizhny Novgorod, RUSSIA
Underhill Mike	University of Surrey	Guildford, UNITED KINGDOM
Unverdross Rainer	Unverdross Technik	Wörthsee, GERMANY
Vanier Jacques		Quebec, CANADA
Zingg Walter	Montres Rolex SA	Genève, SWITZERLAND

OPENING SESSION

Chairman: Léon Prost

GALILEO
Design Baseline and Importance of accurate Time-keeping

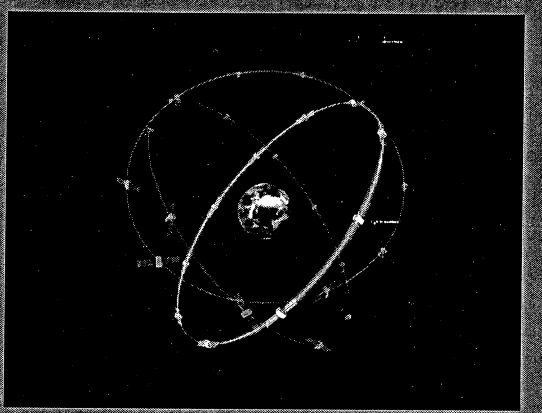

Jörg Hahn
Hans-Hermann Fromm

European Space Agency
GALILEO Programme Office

15th EFTF, Neuchatel
6 - 8 March 2001

European Commission

www.galileo-pgm.org
www.esa.int/navigation

esa

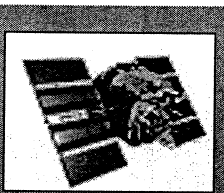

GPS/SBAS and GALILEO together

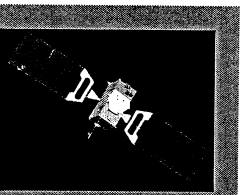

- greatly enhance signal availability
- cater for an alternative in case of system failure

... and require (time) co-ordination

European Commission

esa

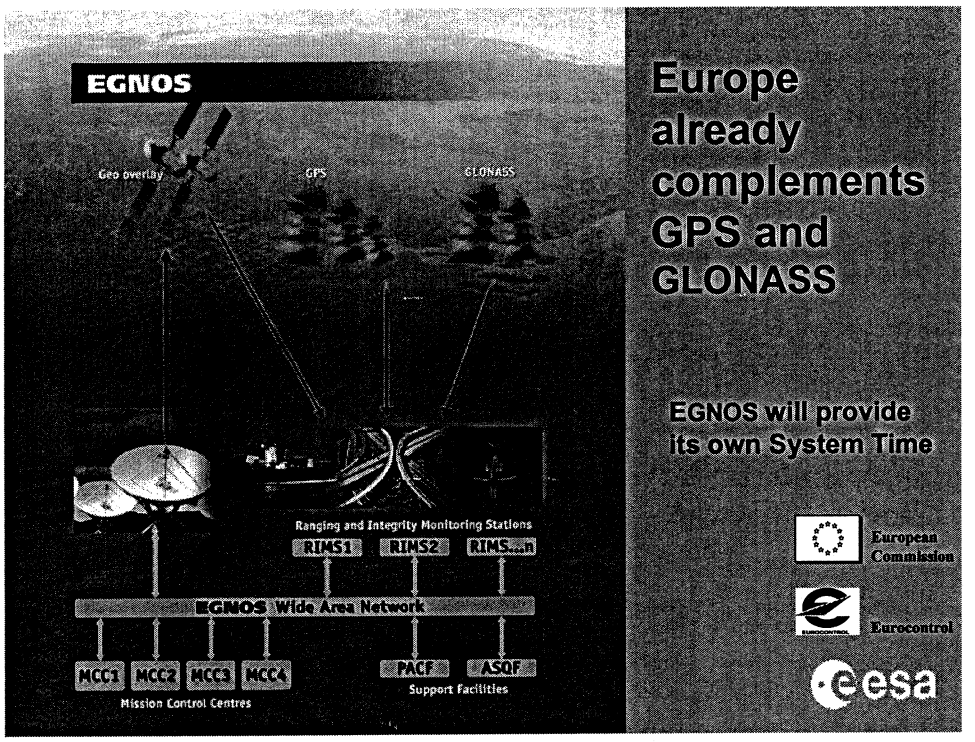
EGNOS
Geo overlay
GPS
GLONASS
Ranging and Integrity Monitoring Stations
RIMS1
RIMS2
RIMS...n
EGNOS Wide Area Network
MCC1
MCC2
MCC3
MCC4
Mission Control Centres
PACF
ASQF
Support Facilities
Europe already complements GPS and GLONASS
EGNOS will provide its own System Time
European Commission
Eurocontrol
esa

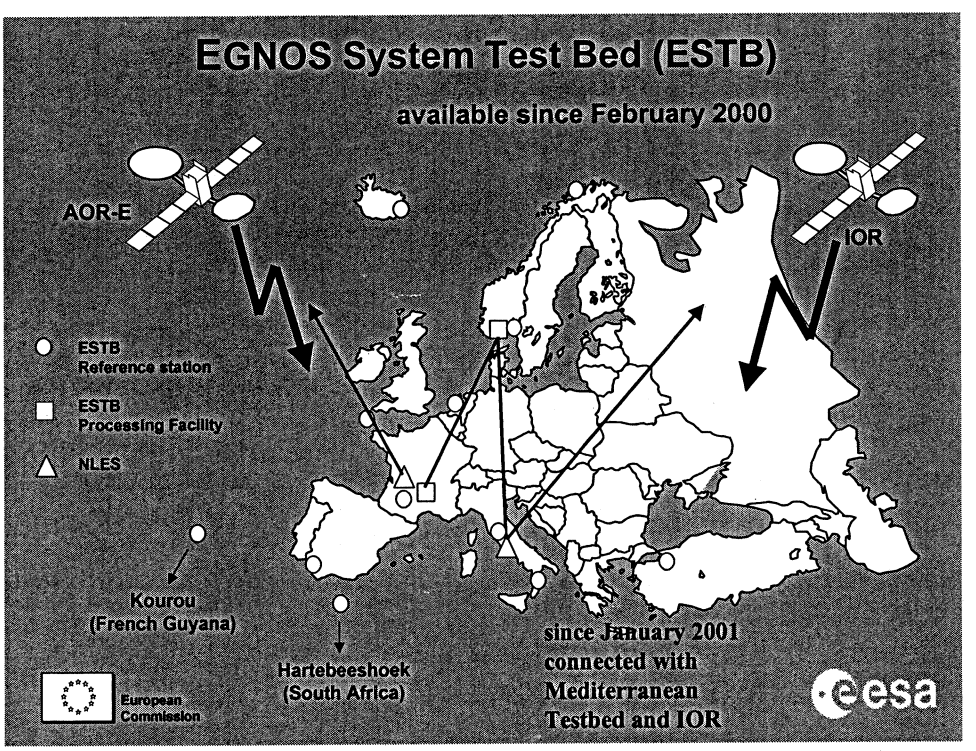
EGNOS System Test Bed (ESTB)
available since February 2000
AOR-E
IOR
ESTB Reference station
ESTB Processing Facility
NLES
Kourou (French Guyana)
Hartebeeshoek (South Africa)
since January 2001 connected with Mediterranean Testbed and IOR
European Commission
esa

GALILEO Service Offerings

	General Purpose (Open) Service	Commercial Service		Public Utility Service	
Coverage	global	global	local	global	local
Accuracy	15 – 20 m (single freq.) 5 – 10 m (dual freq.)	5 – 10 m (dual freq.)	< 10 cm – 1 m	4 – 6 m (dual freq.)	1 m (local augment.)
Time	Less than 50 nano seconds relative to TAI				
Access control	Free access	Controlled access of value added data	Controlled access of local correction data	Controlled access of navigation code and/or value added data	Controlled access of local correction data
Service Guarantees	None	Guaranteed services possible		Build for certification, guarantee of service possible	

European Commission

esa

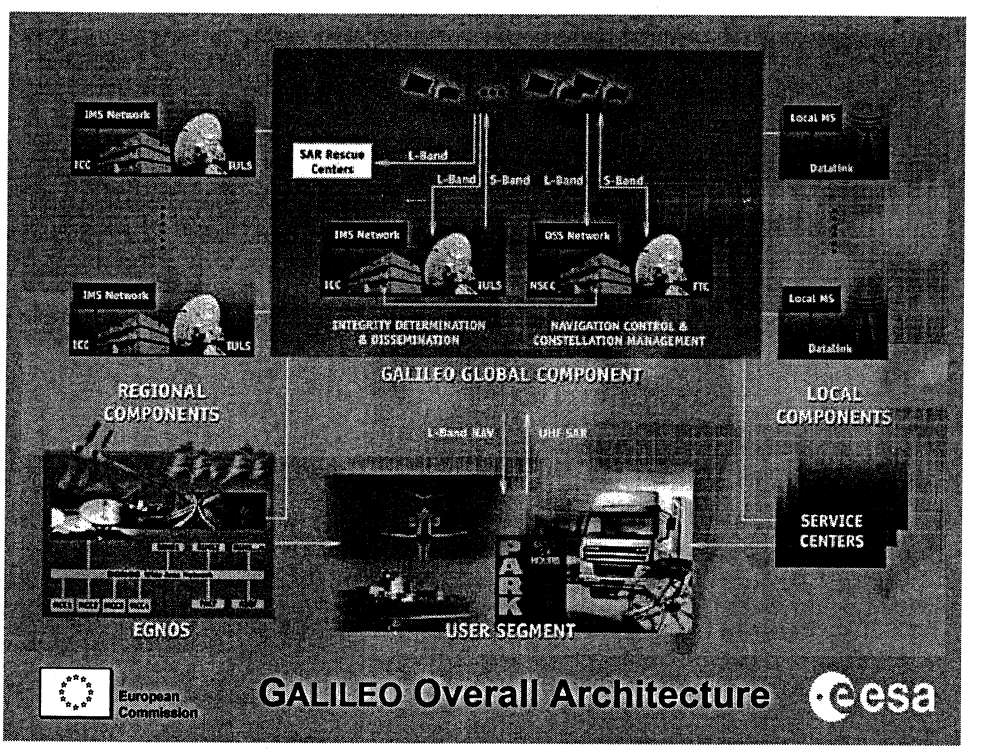

European Commission

GALILEO Overall Architecture

esa

GALILEO
Constellation Design Drivers

	Mass Market Applications	Safety Related Applications
User Masking Angle	25 °	5 °
Accuracy (95 %)	10 m horizontal	4 m vertical
Coverage	global	
Availability	better than 70 %	better than 99 %
Integrity	not generally required	mandatory

European Commission

esa

GALILEO
Constellation Optimisation

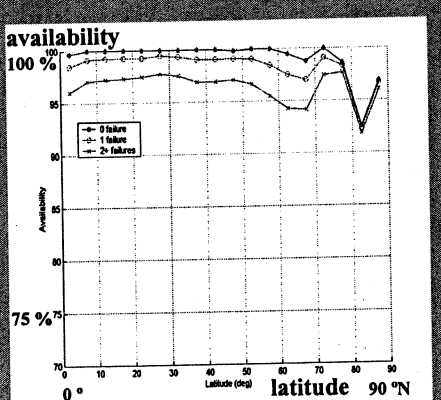

Availability
mass-market applications
30 MEO

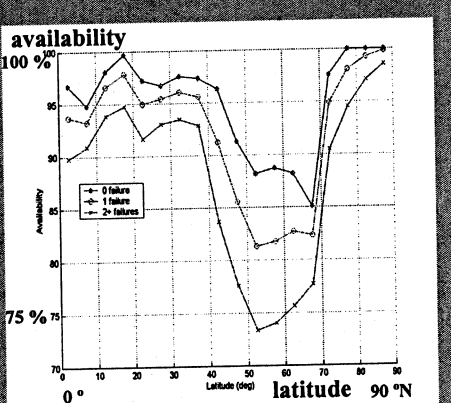

Availability
mass-market applications
24 MEO + 8 GEO, 1 GEO failed

European Commission

esa

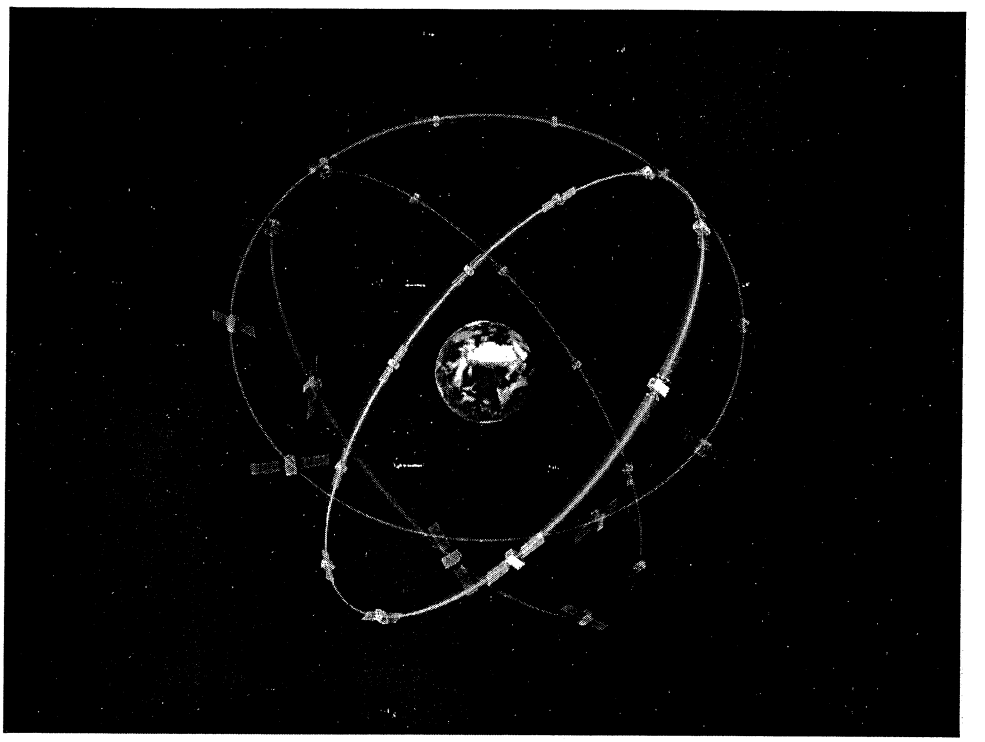

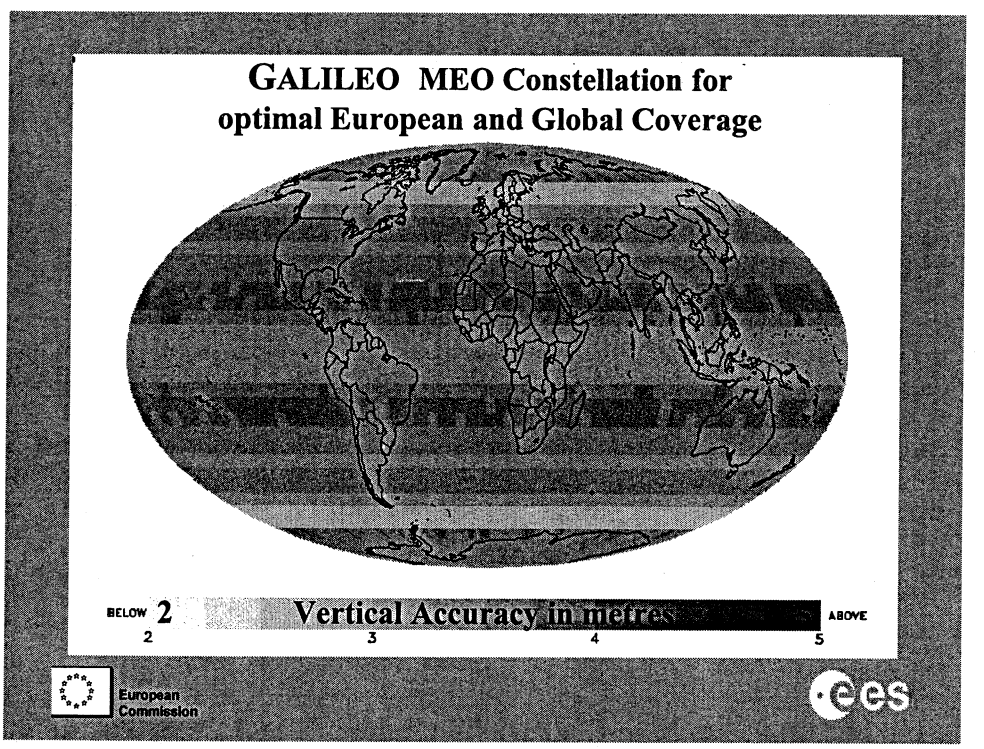
GALILEO MEO Constellation for
optimal European and Global Coverage
BELOW 2
2
Vertical Accuracy in metres
3
4
ABOVE
5
European
Commission
ees

GALILEO in Flight Configuration

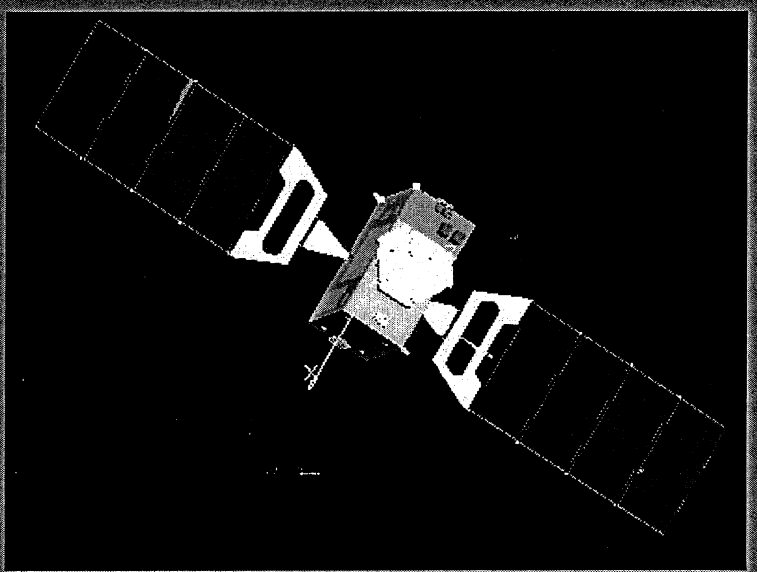

European Commission

esa

GALILEO/EGNOS Implementation Schedule

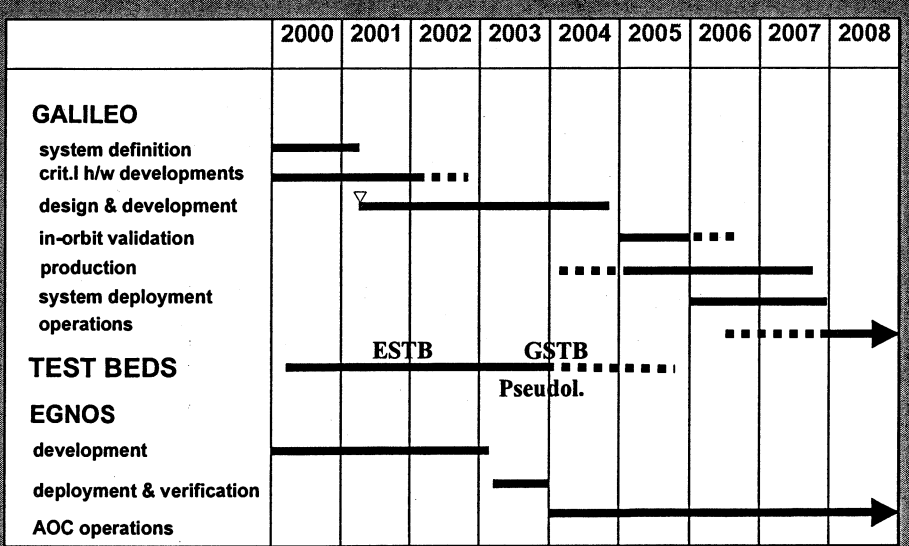

European Commission

esa

GALILEO Orbit Determination and Time Synchronisation

Objectives:

Determine orbit parameters of all satellites, all clock corrections and the Galileo System Time.

Input:

One-way pseudo-ranging measurements collected by a global network of stations.

Processing:

centralised at the Orbitography and Synchronization Processing Facility

European Commission

esa

GALILEO
It is all about keeping clocks under control

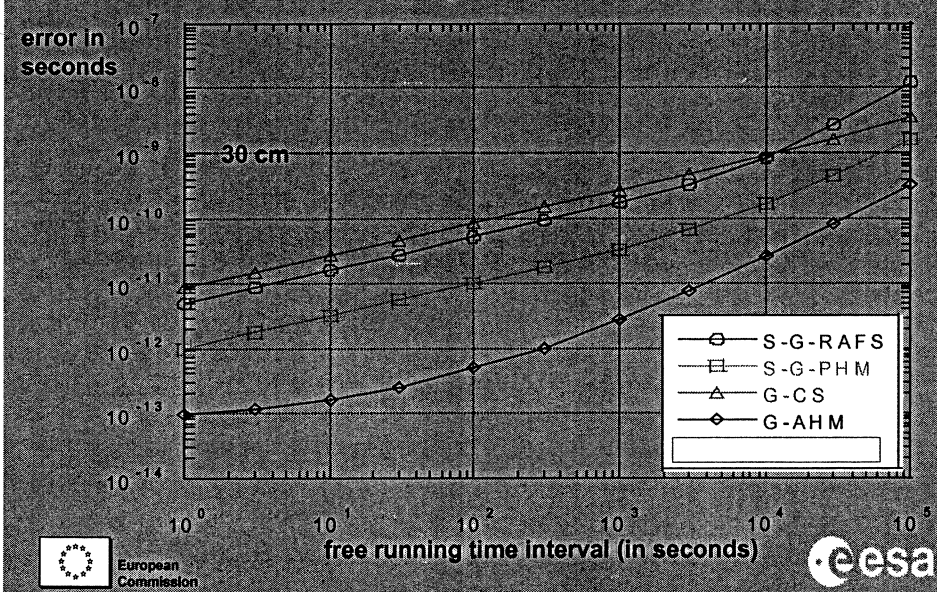

European Commission

esa

GALILEO: The Time Contributors

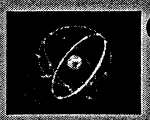

Constellation

30 MEO satellites, per satellite two passive Hydrogen masers and two Rubidium clocks

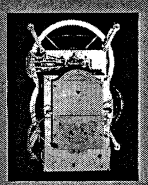

Two Precision Timing Stations (PTS)

each equipped with some 12 Caesium clocks and two active Hydrogen masers

Orbitography & Synchronisation Stations (OSS)

all equipped with redundant ground Rubidium clocks

European Commission

esa

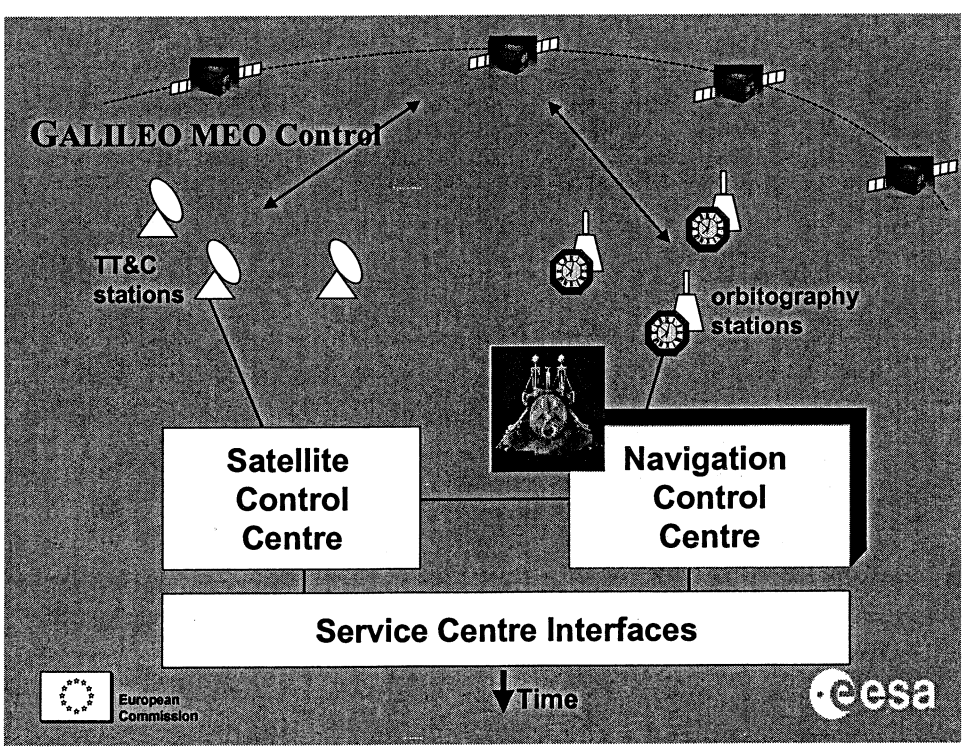

GALILEO Space Clocks

Passive Hydrogen Maser

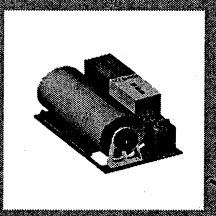

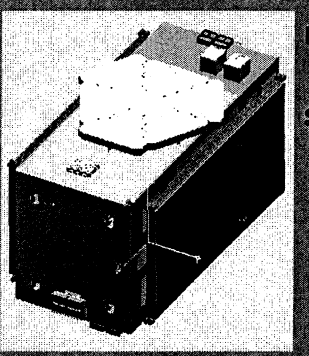

Navigation payload:
70-80 Kg / 850 W
SAR transponder:
appr. 20 kg

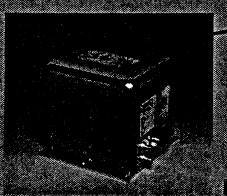

Rubidium Frequency Standard

European Commission

esa

Architecture of Precise Time Station (PTS)

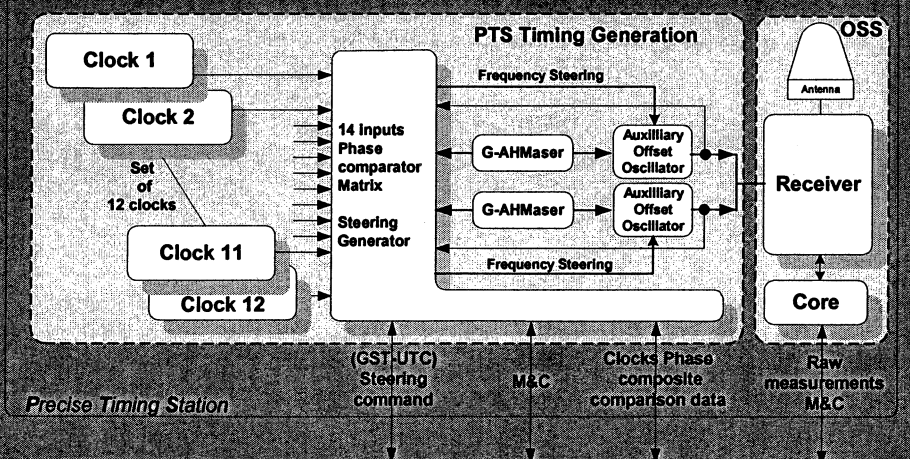

European Commission

esa

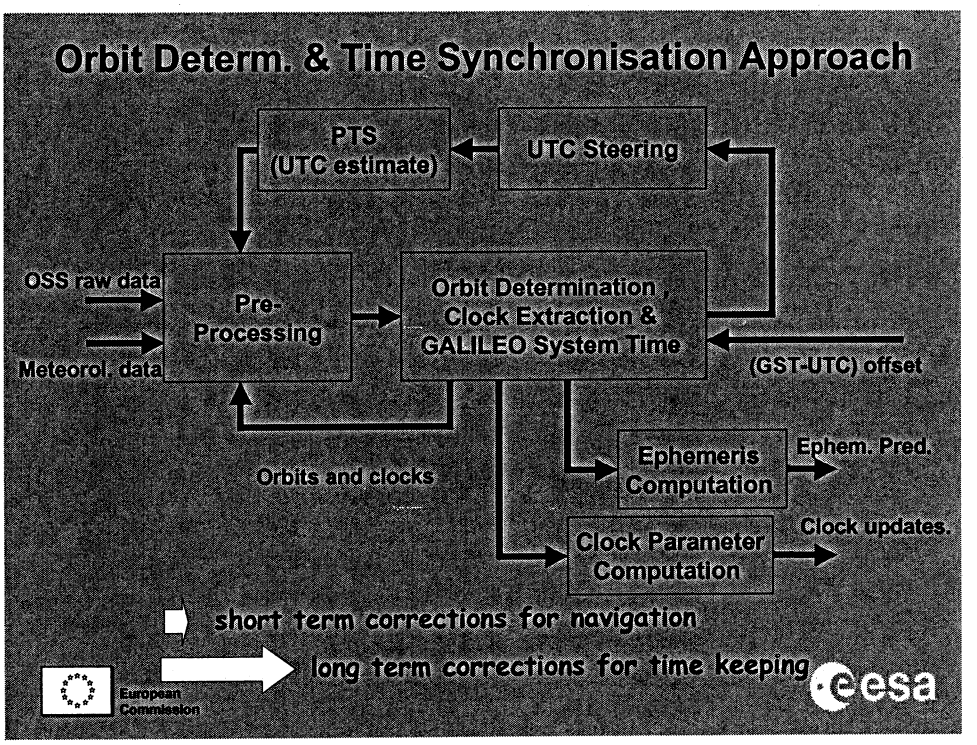
Orbit Determ. & Time Synchronisation Approach
PTS
(UTC estimate)
UTC Steering
OSS raw data
Meteorol. data
Pre-
Processing
Orbit Determination,
Clock Extraction &
GALILEO System Time
(GST-UTC) offset
Orbits and clocks
Ephemeris
Computation
Ephem. Pred.
Clock Parameter
Computation
Clock updates.
short term corrections for navigation
long term corrections for time keeping
European
Commission
esa

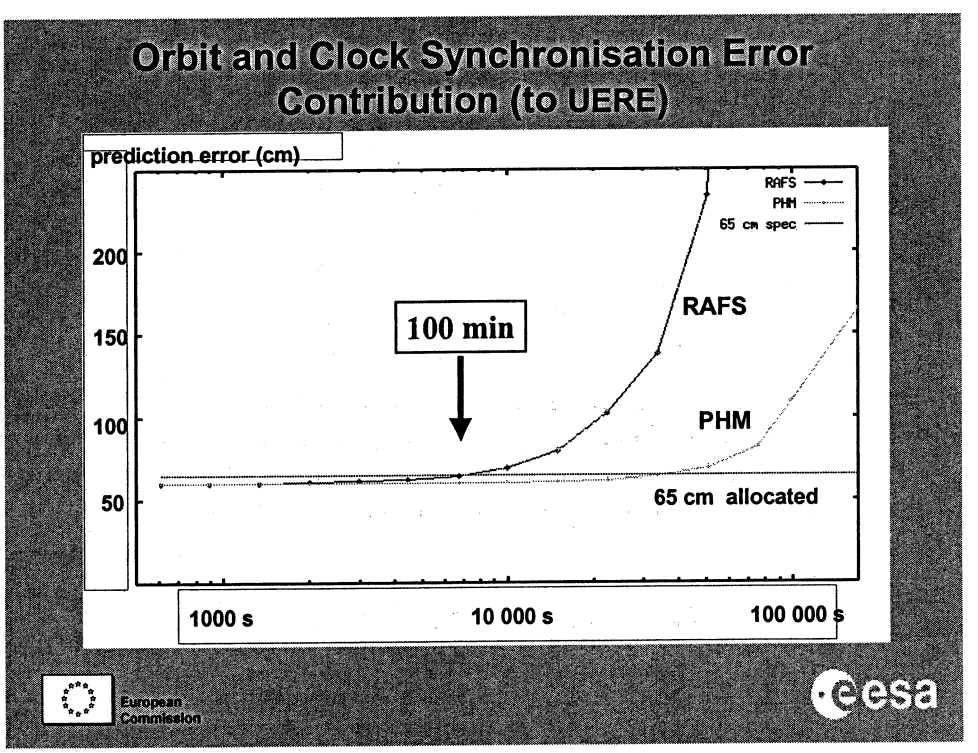
Orbit and Clock Synchronisation Error
Contribution (to UERE)
prediction error (cm)
200
150
100
50
RAFS
PHM
65 cm spec
100 min
RAFS
PHM
65 cm allocated
1000 s
10 000 s
100 000 s
European
Commission
esa

GALILEO System Time (GST)

... is a weighted ensemble of all space and ground clocks

- a continuous, co-ordinated time scale synchronised to TAI
- |TAI - GST| < 50 ns (95% confidence level).
- |TAI - GST| known in real-time with an uncertainty of 33 ns, 95% confidence
- Difference between UTC and TAI (leap seconds)will be broadcasted
- GST frequency stability, in terms of the Allan-Deviation, better than 5.5×10^{-14} over 1 day and better than 1.0×10^{-14} over 30 days

European Commission

esa

GST Synchronisation with TAI/UTC

GALILEO needs the expertise of the Timing community ....

GST could be synchronised to TAI/UTC through one or several European laboratories realising a UTC(*k*) real-time representation of UTC

GALILEO could establish its own real-time estimation of UTC (and this is probably mandatory to cope with the 33 ns uncertainty specification)

.... and GALILEO offers new service opportunities for the Timing community

European Commission

esa

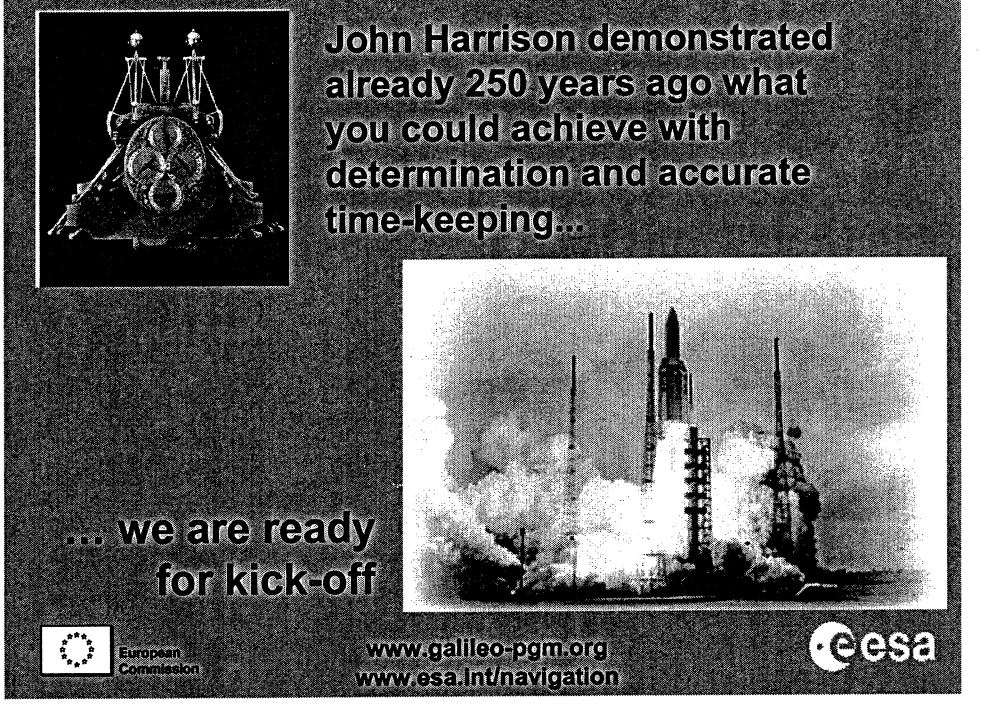
John Harrison demonstrated already 250 years ago what you could achieve with determination and accurate time-keeping...
... we are ready for kick-off
European Commission
www.galileo-pgm.org
www.esa.int/navigation
esa

Measuring the Frequency of Light with Ultrashort Pulses

T. W. Hänsch, R. Holzwarth, J. Reichert, M. Zimmermann, and Th. Udem.
Max-Planck-Institut für Quantenoptik,

Hans-Kopfermann-Straße 1, D-85748 Garching, Germany
http://www.mpq.mpg.de/~haensch/chain/chain.html

Abstract. Femtosecond laser frequency comb techniques are vastly simplifying the art of measuring the frequency of light. A single mode-locked femtosecond laser is now sufficient to synthesize hundreds of thousands of evenly spaced spectral lines, spanning much of the visible and near infrared region. The mode frequencies are absolutely known in terms of the pulse repetition rate and the carrier-envelope phase slippage rate, which are both accessible to radiofrequency counters. Such a universal optical frequency comb synthesizer can serve as clockwork for future atomic clocks, based on atoms, ions or molecules oscillating at optical frequencies.

1. Introduction

For more than a century, precise optical spectroscopy of atoms and molecules has played a central role in the discovery of the laws of quantum physics, in the determination of fundamental constants, and in the realization of standards for time, frequency, and length. The advent of highly monochromatic tunable lasers and techniques for nonlinear Doppler-free spectroscopy in the early seventies had a dramatic impact on the field of precision spectroscopy [1, 2]. Today, we are able to observe extremely narrow optical resonances in cold atoms or single trapped ions, with resolutions ranging from 10^{-13} to 10^{-15}, so that it might ultimately become possible to measure the line center of such a resonance to a few parts in 10^{18}. Laboratory experiments searching for slow changes of fundamental constants would then reach unprecedented sensitivity. A laser locked to a narrow optical resonance could serve as a highly stable oscillator for a future all-optical atomic clock that can satisfy the growing demands of optical frequency metrology, fiber optical telecommunication, or navigation.

However, until recently there was no reliable optical „clockwork" available that could count optical frequencies of hundreds of THz. Most spectroscopic experiments still rely on a measurement of optical wavelengths rather than frequencies. Unavoidable geometric wavefront distortions have so far made it impossible to exceed an accuracy of a few parts in 10^{10} with a laboratory-sized wavelength interferometer.

To measure optical frequencies, only a few harmonic laser frequency chains have been built during the past 25 years which start with a cesium atomic clock and generate higher and higher harmonics in nonlinear diode mixers, crystals, and other nonlinear devices [3, 4, 5, 6]. Phase-locked transfer oscillators are needed after each step, so that such a chain traversing a vast region of the electromagnetic spectrum becomes highly complex, large, and delicate, and requires substantial resources and heroic efforts to build and operate. Most harmonic laser frequency chains are designed to measure just one single optical frequency.

In 1998, our laboratory has introduced a revolutionary new approach that vastly simplifies optical frequency measurements. We could demonstrate that the broad comb of modes of a mode-locked femtosecond laser can be used as a precise ruler in frequency space [7, 8]. This work has now culminated in a compact and reliable all-solid-state frequency „chain" which is actually not really a chain any more and requires just a single mode-locked laser [9,10,11,12]. As a universal optical frequency comb synthesizer it provides the long missing simple link between optical and microwave frequencies. For the first time, small scale spectroscopy laboratories have now access to the ability to measure or synthesize any optical frequency with extreme precision. Femtosecond frequency comb techniques have since begun to rapidly gain widespread use, with precision measurements in Cs [7], Ca [13,14], CH_4 [15], H [15], Hg^+ [13], I_2 [10,16] and In^+ [17] already completed or underway.

The same femtosecond frequency comb techniques are also opening new frontiers in ultrafast physics. Control of the phase evolution of few cycle light pulses, as recently demonstrated [11, 18], provides a powerful new tool for the study of highly nonlinear phenomena that should depend on the phase of the carrier wave relative to the pulse envelope, such as above threshold ionization, strong field photoemission, or the generation of soft x-ray attosecond pulses by high harmonic generation.

In the first experiment of its kind, we have applied the frequency comb of a mode-locked femtosecond laser to measure the frequency of the cesium D_1 line [7]. This frequency provides an important link for a new determination of the fine structure constant α. More recently, we have measured the absolute frequency of the hydrogen 1S-2S two-photon resonance in a direct comparison with a cesium atomic fountain clock to within 1.9 parts in 10^{14}, thus realizing one of the most accurate measurement of an optical frequency to date [15]. During the past few years, precision spectroscopy of hydrogen has yielded a value for the Rydberg constant that is now one of the most accurately known fundamental constant [31]. Nonetheless, after more than a century of spectroscopic experiments, the hydrogen atom still holds substantial challenges and opportunities for further dramatic advances.

2. Optical frequency differences

While it has been extremely difficult in the past to measure an absolute optical frequency, a small frequency difference or gap between two laser frequencies can be measured rather simply by superimposing the two laser beams on a photodetector and monitoring a beat signal. The first experiments of this kind date back to the advent of cw He-Ne-lasers in the early 1960's. Modern commercial fast photodiodes and microwave frequency counters make it possible to directly count frequency differences up to the order of 100 GHz. Since the gap between the high frequency endpoint of a traditional harmonic laser frequency chain and an unknown optical frequency to be measured can easily amount to tens or hundreds of THz, there has long been a strong interest in methods for measuring much larger optical frequency differences.

Motivated by such problems in precision spectroscopy of atomic hydrogen, we have previously introduced a general, although perhaps not very elegant solution for the measurement of large optical frequency gaps with the invention of the optical frequency interval divider (OFID) which can divide an arbitrarily large frequency difference by a factor of precisely two [19]. An OFID receives two input laser frequencies f_1 and f_2. The sum frequency $f_1 + f_2$ and the second harmonic of a third laser $2f_3$ are created in nonlinear crystals. The radio frequency beat signal between them at $2f_3 - (f_1 + f_2)$ is used to phase-lock the third laser at the exact midpoint $f_3 = (f_1 + f_2)/2$. Phase-locking of two optical frequencies is achieved electronically by locking the phase of their beat signal to zero or, to reduce $1/f$ noise, to a given offset radio frequency, provided by a local oscillator. Techniques of conventional radio frequency phase-locked loops can be applied. With a divider chain of n cascaded OFIDs, the original frequency gap can be divided by a factor 2^n.

Frequency intervals up to several THz can also be measured with passive optical frequency comb generators [20]. These are electro optical modulators that create side bands very efficiently. Beat signals can then be observed with sidebands on different sides of the carrier and frequency gaps on the order of a few THz can be bridged. To measure larger gaps, a chain of OFIDs can be followed by an OFCG.

3. Femtosecond light pulses

It has long been recognized that the periodic pulse train of a mode-locked laser can be described in the frequency domain as a comb of equidistant modes, so that such a laser can serve as an active OFCG. More than twenty years ago, the frequency comb of a mode-locked picosecond dye laser has first been used as an optical ruler to measure transition frequencies in sodium [21]. This route was further pursued in the seventies and eighties [22, 23, 24], but the attainable bandwidths were never sufficiently large to make it a widespread technique for optical frequency metrology. Broadband femtosecond Ti:sapphire

lasers have existed since the beginning of the nineties, but only our recent experiments at Garching have shown conclusively, that such lasers can play a crucial role in this field [8, 12].

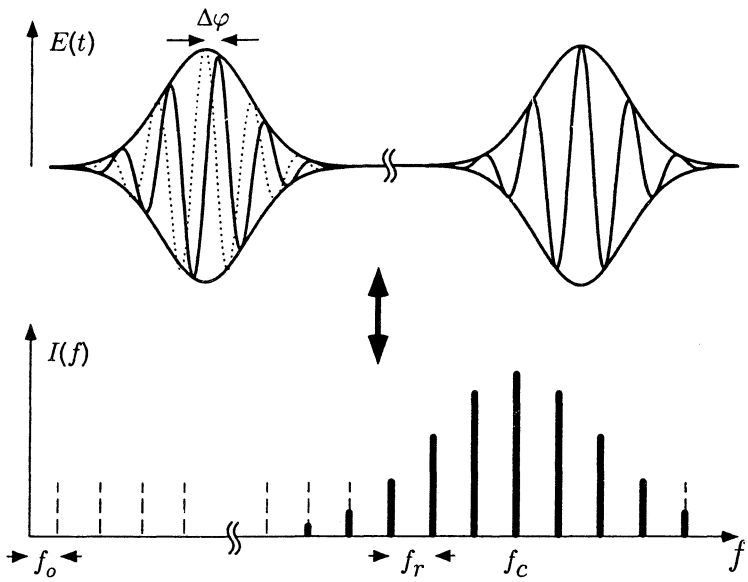

Fig. 1: Two consecutive pulses of the pulse train emitted by a mode locked laser and the corresponding spectrum. The pulse to pulse phase shift $\Delta\varphi$ results in a offset frequency $f_0 = \Delta\varphi / 2\pi T$ because the carrier wave at f_c moves with the phase velocity v_p while the envelope moves with the group velocity v_g.

To understand the mode structure of a fs frequency comb and the techniques applied for its stabilization one can look at the idealized case of a pulse circulating in a laser cavity with length L as a carrier wave at f_c that is subject to strong amplitude modulation described by an envelope function $A(t)$. This function defines the pulse repetition time $T = f_r^{-1}$ by demanding $A(t) = A(t - T)$ where T is calculated from the cavity mean group velocity: $T = 2L / v_g$. Because of the periodicity of the envelope function the electric field at a given place (e.g. at the output coupler) can be written as

$$E(t) = \mathrm{Re}(A(t)e^{-2\pi i f_c}) = \mathrm{Re}(\sum_q A_q e^{-2\pi i (f_c + q f_r)t})$$

where A_q are Fourier components of $A(t)$. This equation shows that the resulting spectrum consists of a comb of laser modes that are separated by the pulse repetition frequency. Since f_c is not necessarily an integer multiple of f_r the modes are shifted from being exact harmonics of the pulse repetition frequency by an offset $f_0 < f_r$:

$$f_n = n f_r + f_0 \qquad n = \text{a large integer}$$

This equation maps two radio frequencies f_r and f_0 onto the optical frequencies f_n. While f_r is readily measurable, f_0 is not easy to access unless the frequency comb contains more than an optical octave [25]. In the time domain the frequency offset is obvious because the group velocity differs from the phase velocity inside the cavity and therefore the carrier wave does not repeat itself after one round trip but appears phase shifted by $\Delta\varphi$ as shown in Fig. 1. The offset frequency is then calculated from

$f_0 = \Delta\varphi / 2\pi T$ [22, 25, 26]. Note that such a fs frequency comb has two free parameters which are the repetition frequency f_r and the offset frequency $f_0 < f_r$. Depending on the application one or both parameters have to be stabilized.

4. Femtosecond combs as frequency rulers

At the high peak intensities of femtosecond laser pulses nonlinear effects due to the $\chi^{(3)}$ nonlinear susceptibility are considerable even in standard silica fibers. The output spectrum of a femtosecond laser can be broadened significantly via self phase modulation in an optical fiber therefore increasing its useful width even further beyond the time-bandwidth limit of the laser.

Now the question arises whether or not this broad frequency comb is equally spaced and can therefore be used as a ruler to measure frequency differences. To test this we have compared the fs comb with an optical frequency interval divider as illustrated in Fig. 2. We have found that the frequency comb is equally spaced even after spectral broadening in a standard single mode fiber at the level of a few parts in 10^{18} [39]. Note that the coherence between the pulses is obviously preserved.

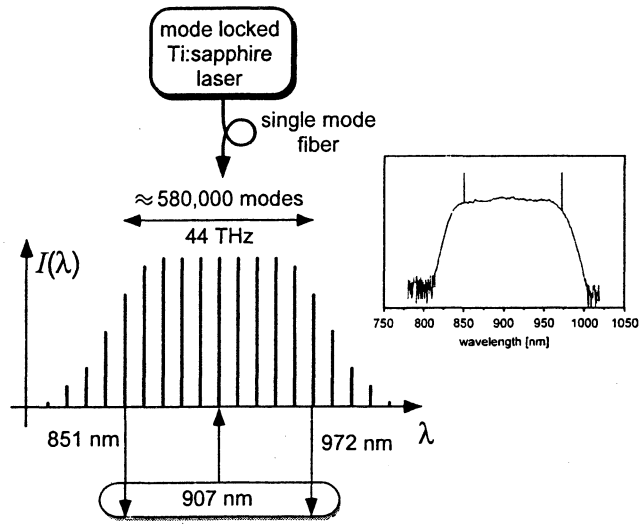

Fig. 2: Comparison of the broadened fs comb and an optical interval divider (oval symbol). The inset shows the observed spectrum on a logarithmic intensity scale. The peaks mark the position of the 972 nm and 851 nm laser diodes and the comb was generated with a Mira 900 system (Coherent Inc.) delivering 73 fs pulses at a 75 MHz repetition rate.

Previously we have also shown that the easily accessible repetition rate of such a laser equals the mode spacing within the experimental uncertainty of a few parts in 10^{16} [8]. Following the rapid advances in ultrafast technology recently a 104 THz gap has been bridged with such a broadened comb [28].

To phase-lock the pulse repetition rate to a signal provided by a synthesizer one faces the problem of noise multiplication. It is well known that the total noise intensity grows as N^2 when a radio frequency is multiplied by a factor of N [29]. Fortunately the laser cavity acts as a filter and prevents the high frequency noise components from propagating through the frequency comb [25].

For most applications it is desirable to fix one of the modes in frequency space and phase-lock the pulse repetition rate simultaneously. For this purpose it is necessary to control the phase velocity (more precisely the round trip phase delay) of that particular mode and the group velocity (more precisely the round trip group delay) independently. A piezo driven folding mirror changes the cavity length and leaves $\Delta\varphi$ approximately constant as the additional path in air has a negligible dispersion. A mode-locked laser that uses two intracavity prisms to produce the negative group velocity dispersion

($\partial^2\omega/\partial k^2 < 0$) necessary for Kerr-lens mode-locking provides us with a means for independently controlling the pulse repetition rate. We use a second piezo-transducer to slightly tilt the mirror at the dispersive end of the cavity about a vertical pivot that ideally corresponds to the mode f_n [25]. We thus introduce an additional phase shift $\Delta\Phi$ proportional to the frequency distance from f_n, which displaces the pulse in time and thus changes the round trip group delay [25]. In the frequency domain one could argue that the length of the cavity stays constant for the mode f_n while higher (lower) frequency modes experience a longer (shorter) cavity (or vice versa, depending on the sign of $\Delta\Phi$). In the case where only dispersion compensation mirrors are used to produce the negative group velocity dispersion one can modulate the pump power or manipulate the Kerr lens by slightly tilting the pump beam [12]. Although the two controls (i.e. cavity length and pump power) are not independent they affect the round trip group delay T and the round trip phase delay differently and this is which allows us to control both, f_0 and f_r.

5. Absolute optical frequencies

For the absolute measurement of optical frequencies one has to determine frequencies of several 100 THz in terms of the definition of the SI second represented by the cesium ground state hyperfine splitting of 9.2 GHz.

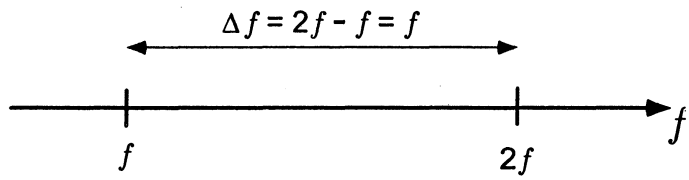

Fig. 3: The new principle of absolute optical frequency measurements. The interval Δf between f and $2f$ is just equal to the frequency f itself.

Extending our principle of determining large frequency differences to the intervals between harmonics or subharmonics of an optical frequency leads naturally to the absolute measurement of optical frequencies. In the most simple case this is the interval between an optical frequency f and its second harmonic $2f$ as illustrated in Fig. 3. But of course other intervals can be used as well.

Such an optical frequency synthesizer directly relates a radio frequency to an optical frequency f simply by multiplying the known mode spacing f_r (i.e. a radio frequency) with the number of modes between the harmonics (e.g. between f and $2f$).

6. Hydrogen 1S-2S transition

The first frequency chain following this principle has been used in a recent determination of the hydrogen 1S-2S transition and measured the interval between $3.5f$ and $4f$ where f is the frequency of a HeNe laser at 3.4 μm (88 THz) [9]. Fig. 4 gives a simplified sketch: The He-Ne laser is operated at the 28th subharmonic of the hydrogen transition frequency which is driven by the forth harmonic of a dye laser at $7f$. The femtosecond laser, whose spectrum is broadened in a single mode optical fiber, measures the frequency difference between the output of the optical frequency interval divider at $4f$ and the subharmonic of the dye laser at $3.5f$. This frequency difference of $0.5f \approx 44.2$ THz equals one half of the absolute frequency of the He-Ne laser. Its frequency is therefore directly determined by the Cs clock that controls the mode spacing of the mode-locked. Here the 10 MHz output from the Cs clock is multiplied in one step to 44.2 THz. Because our 3.39 μm He-Ne laser could not be tuned far enough to reach the 28th subharmonic of the 1S-2S transition we used an additional laser (not shown in Fig. 4) at around $4f$ that was displaced by about 1 THz. The displacement was simultaneously measured with the frequency comb. A more detailed description of the frequency chain is found in Ref. [9].

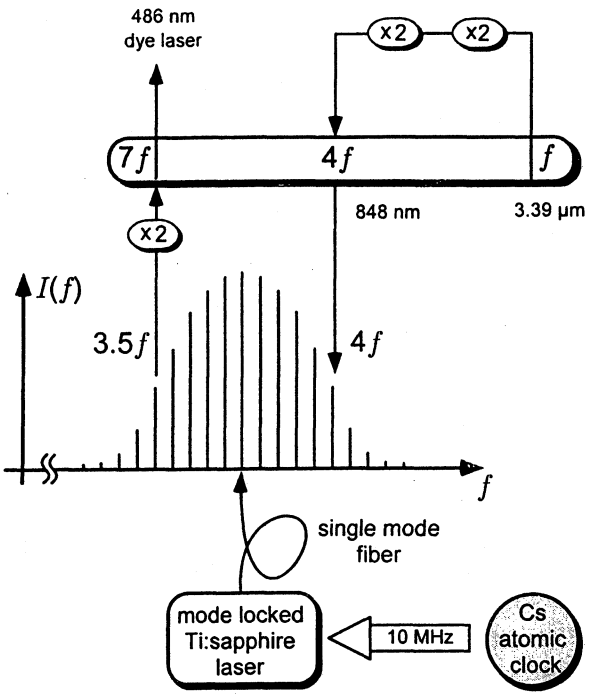

Fig. 4: Frequency chain used for the frequency determination of the hydrogen 1S-2S transition (simplified). The oval symbol represents on optical frequency interval divider as discussed earlier, except that it does now receive the input frequencies $7f$ and $4f$ and delivers the frequency f.

The hydrogen 1S-2S transition is excited by Doppler-free two-photon spectroscopy with a standing laser wave near 243 nm in a cold atomic beam. The hydrogen spectrometer is operated by the hydrogen team in our group (M. Niering, M. Fischer, M. Weitz) and has been described before in detail [34].

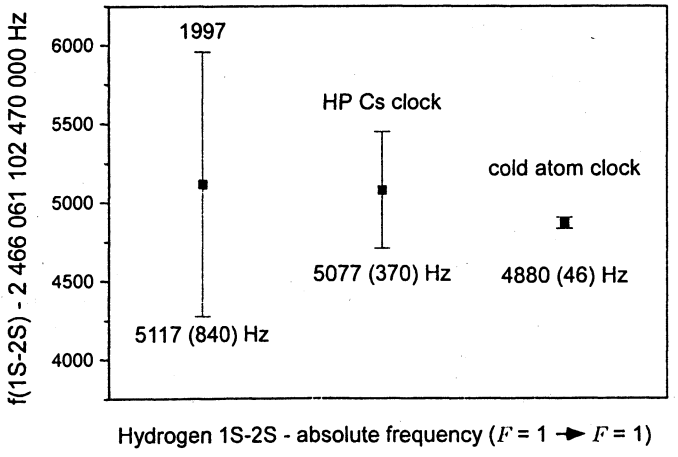

Fig. 5: Recent measurements of the hydrogen 1S-2S ($F = 1 \rightarrow F = 1$) transition.

Fig. 5 visualizes the recent advances in the measurement of the 1S-2S transition in hydrogen. The 1997 value has been obtained by shuttling a methane stabilized Helium Neon laser back and forth between the PTB (Braunschweig/Germany) where it was calibrated with a traditional harmonic frequency chain and our laboratory near Munich/Germany where the hydrogen measurements have been carried out by

comparision with the 28th harmonic of that laser [3]. After completion of the $3.5f:4f$ frequency chain described above in March 1999 we have been able to reproduce the old value within a few measurement sessions using a commercial GPS disciplined cesium clock (HP 5071A) as a reference [9]. This at the same time represents a test of our frequency comb technique on the 3×10^{-13} level. And finally in collaboration with the Paris cesium fountain clock group at LPTF (P. Lemonde, G. Santarelli, M. Abgrall, P. Laurent, C. Salomon, and A. Clairon) we have used the currently most precise cesium frequency standard in the radio-frequency domain as a reference [35]. Together with a sophisticated line shape model [34] we have reached an accuracy for the 1S-2S transition of 1.9×10^{-14}. This represents by now the most precise measurement of an optical frequency [15]. Our new chain is providing the first phase coherent link from the vacuum UV (121 nm) to the radio frequency domain.

7. Frequency combs spanning more than an octave

The first absolute measurement of an optical frequency with a fs frequency comb has inspired further rapid advances in the art of frequency metrology. In collaboration with P. St. Russell, J. Knight and W. Wadsworth from the University of Bath (UK) we have used novel microstructured photonic crystal fibers (PCF) [36] to achieve further spectral broadening of femtosecond frequency combs. In the fiber used here light is guided in a pure silica core with a diameter of approximately 1.5 μm by surrounding it with an array of air holes. The remarkable dispersion characteristics attainable with the large effective index step (including zero group velocity dispersion well below 800 nm) and the high peak intensities associated with the short pulses and the small core size, enables one to observe a range of unusual nonlinear optical effects [37], including very effective spectral broadening to more than an optical octave even with the moderate output power from the laser oscillator. Similar experiments have been reported by S. Cundiff, J. Hall and coworkers in Boulder using a fiber fabricated at Bell Laboratories [10, 11].

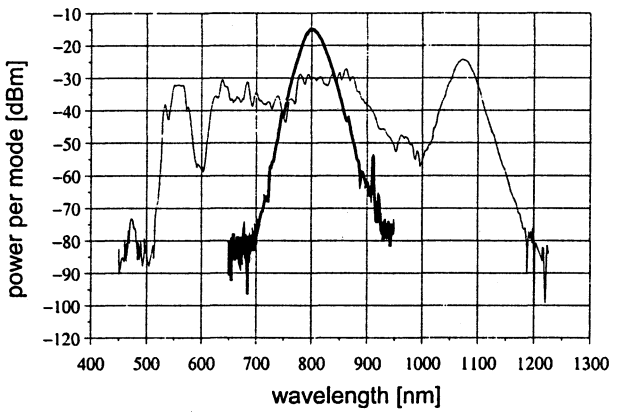

Fig. 6: Spectral broadening of fs pulses in a photonic crystal fiber. The narrow peaked curve in the middle (bold) denotes the initial pulse directly from the fs laser (25 fs, 625 MHz repetition rate). The broadened spectrum stretches from 520 nm to 1100 nm (-10 dB width) and results from coupling 170 mW average power through 35 cm photonic crystal fiber. We achieve reliable phase locking to modes above –44 dBm.

With such a broad spectrum as shown in Fig. 6 we can directly access the interval between an optical frequency f and its second harmonic $2f$. Such a frequency chain [9, 10, 11, 12] allows the direct comparison of radio and optical frequencies without the need of any optical frequency interval dividers or further nonlinear steps.

Although self phase modulation is likely to be the dominant mechanism of spectral broadening there are other processes like stimulated Raman and Brillouin scattering, modulation instability or shock wave formation that might spoil the usefulness of these broadened frequency combs. And indeed in an experiment using 8 cm of PCF and 73 fs pulses at 75 MHz repetition rate from a Mira 900 system

(Coherent Inc.) we have seen an exceptionally broad spectrum from 450 to 1400 nm but with excessive broadband noise. We did not observe these problems with the 25 fs pulses at 625 MHz or 1GHz repetition rate resulting in the spectrum shown in Fig. 6 and used for the $f:2f$ frequency chain reported below.

8. The $f:2f$ optical frequency synthesizer

The $f:2f$ interval frequency snthesizer [12] sketched in figure 7 is based on a Ti:sapphire 25 fs high repetition rate ring laser (GigaOptics, model GigaJet). While the ring design makes it almost immune to feedback from the fiber, the high repetition rate increases the available power per mode. It has been operated with repetiton frequencies of 625 MHz, 750 MHz (double folded) and 950 MHz (single folded). The original setup has been modified as depicted in the right part of Fig. 7. Piezo tranducer (PZT) and translation stage (TS) have been added for coarse adjustment and locking of the repetiton rate f_r fused silica wedge (W) and an electro optic intensity modulator (EOM) have been incorporated for coarse adjustment and locking of the offset frequency f_0. The highly efficient spectral broadening of the PCF compensates for the decrease of available peak power connected with a high repetition rate. To generate an octave spanning comb we have coupled 190 mW average power through 35 cm PCF. The pump beam at 532 nm (Verdi, Coherent Inc.) is modulated by an EOM (LM 0202, Gsänger). With 7 W of pump power we achieve above 650 mW average power from the fs laser. In our setup a Nd:YAG laser (Prometheus, Innolight) serves to pick and amplify one of the modes by phase locking it to that mode. The Nd:YAG laser is then frequency doubled in a periodically poled KTP crystal and a beat signal in the green with another mode of the comb is observed. This beat signal gives direct access to the offset frequency f_0 introduced earlier as shown in Fig. 7. The offset frequency f_0 is phase locked with the help of an EOM in the pump beam while the repetition rate f_r is phase locked with a PZT mounted folding mirror. Both are referenced to our cesium atomic clock. By this means the absolute frequency of each of the modes is phase coherently linked to the rf reference and known with the same relative precision.

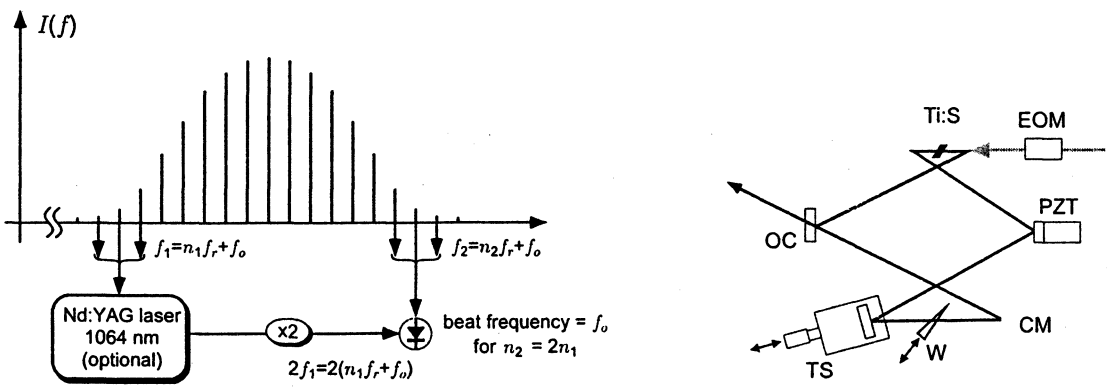

Fig. 7: Left: Principle of the $f:2f$ frequency chain with photonic crystal fiber. Right: The high repetition rate laser. Piezo tranducer (PZT) and translation stage (TS) are used for coarse adjustment and locking of the repetiton rate f_r fused silica wedge (W) and an electro optic intensity modulator (EOM) are used for coarse adjustment and locking of the offset frequency f_0. All mirrors except the output coupler (OC) are chirped.

9. Single laser optical frequency synthesizer

The Nd:YAG laser can be omitted [10,11,12], as first demonstrated by J. Hall's group at JILA in Boulder (USA), if one does not take a single mode of the comb but several modes and generates the sum and second harmonic frequencies directly from the infrared part of the fiber output.

As sketched in Fig. 8 sum and second harmonic frequencies of the modes in the infrared are generated in a 7 mm long KTP crystal. The beat signal between this frequency doubled pulse and the green part of the spectrum directly gives access to the offset frequency. A grating serves as a bandpass filter. The delay line in one of the arms is used to overlap the pulses in time on the detector.

We have now arrived at an optical frequency synthesizer that consists of one fs laser only and nevertheless links a 10 MHz rf reference phase coherently in one step with the optical region. It occupies only 1 square meter on an optical table with the potential for further miniaturization. At the same time it supplies us with a reference frequency grid across much of the visible and infrared spectrum with comb lines that are separated by 625 MHz and can be distinguished with a wavemeter. This makes it an ideal laboratory tool for precision spectroscopy and a compact solid state system that is ready to serve as a clockwork in future optical clocks. In the reverse direction we expect this clockwork to transfer not only the accuracy but also the superior stability of optical oscillators to the rf domain.

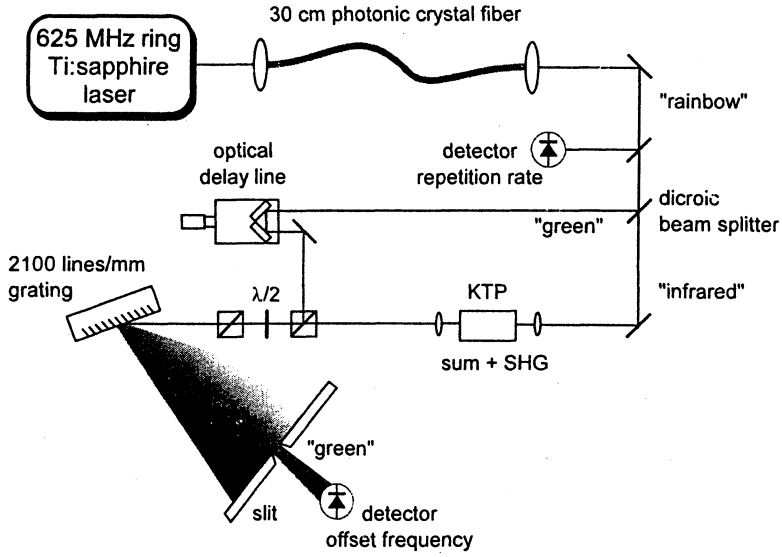

Fig. 8: Frequency chain consisting of one single laser (and pump).

12. Validation of the $f:2f$ optical frequency synthesizer

To check the integrity of the broad frequency comb and evaluate the overall performance of the $f:2f$ optical synthesizer we have compared it with the $3.5f:4f$ frequency chain used for the measurement of the hydrogen 1S-2S transition frequency as described above.

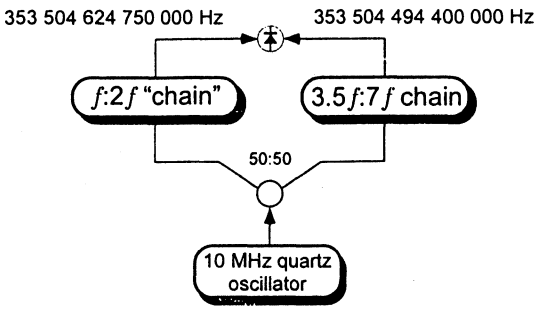

Fig. 9: Comparision of two frequency chains.

The fs comb used here is only 44.2 THz wide and has been thoroughly tested [8]. This chain was modified to replace the dye laser by a frequency doubled diode laser/tapered amplifier combination at 969 nm [38]. The additional frequency gap of 1 THz in the previous setup [9] has been removed by operating the diode laser at exactly $3.5f$ [12].

To compare the two frequency chains we use the 848 nm laser diode and a second 848 nm laser diode locked to the frequency comb of the $f:2f$ chain. The setup is schematically shown in Fig. 9. After averaging all data we obtained a mean deviation from the expected beat frequency of 71 ± 179 mHz at 353 THz. This corresponds to a relative uncertainty of 5.1×10^{-16}. No systematic effect is visible at this level of accuracy [12]. Some details of the measurement data are shown in Fig. 10.

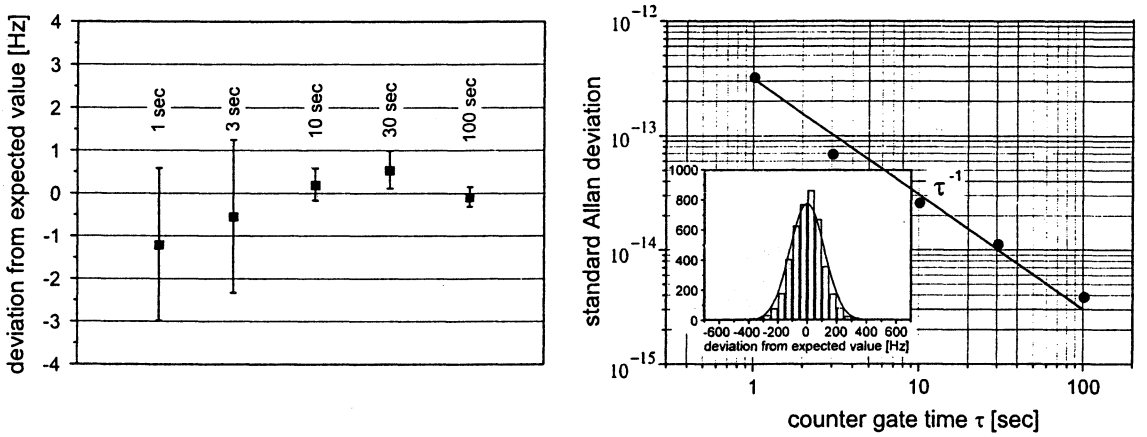

Fig. 10: Left: summary of results for different counter gate times. The weighted mean yields 71 +/- 179 mHz. Right: the measured Allan standard deviation for different gate times. Note that the Allan standard deviation decreases approximately as the inverse of the counter gate time as expected for phase locked signals. Inset: The histogram (bin size 40 Hz) shows the distribution of measured data points with the counter gate time set to 1 sec. The plotted normal distribution as derived from the data shows that the data scatter is nearly Gaussian.

13. Conclusion

We have developed a new concept to measure optical frequencies. This new technique has been applied to the measurement of the Cesium D_1 line which is a cornerstone for a new determination of the fine structure constant α and the hydrogen 1S-2S transition needed for the determination of the Rydberg constant and the 1S Lamb shift. The development culminates in the fully phase locked single laser optical frequency synthesizer. It uses a single fs laser and is nevertheless capable of phase coherently linking the rf and the optical domain.

Other important applications of this frequency domain technique in the time domain where the carrier offset slippage frequency is an important parameter and needs to be controlled for the next generation of ultrafast experiments. In collaboration with F. Krausz (Vienna technical university) we have applied fs comb techniques to control the phase evolution of ultra-short pulses lasting for only a few optical cycles [18].

Future applications of precise optical frequency measurements also include the search for variations in the fundamental constants and the test of CPT invariance with anti-hydrogen now underway at CERN.

We believe that the development of accurate optical frequency synthesis marks only the beginning of an exciting new period of ultra-precise physics.

Finally we would like to thank our collaborators, without their help the work presented here would not have been possible.

References

[1] „Nonlinear Spectroscopy", N. Bloembergen, ed., Proceeedings of the International School of Physics „Enrico Fermi", North Holland Publ. Co., (1977)

[2] „Frontiers in Laser Spectroscopy", T.W. Hänsch and M. Inguscio, eds., Proceeedings of the International School of Physics „Enrico Fermi", North Holland Publ. Co., (1994)

[3] Th. Udem et al., *Phys. Rev. Lett.* **79**, 2646 (1997).

[4] H. Schnatz et al., *Phys. Rev. Lett.* **76**, 18, (1996).

[5] C. Schwob et al., *Phys. Rev. Lett.* **82**, 4960 (1999).

[6] J. E. Bernard et at., *Phys. Rev. Lett.* **82**, 3238 (1999).

[7] Th. Udem et al., *Phys. Rev. Lett.* **82**, 3568 (1999).

[8] Th. Udem et al., *Opt. Lett.* **24**, 881 (1999).

[9] J. Reichert et al., *Phys. Rev. Lett.* **84**, 3232 (2000).

[10] S. A. Diddams et al., *Phys. Rev. Lett.* **84**, 5102 (2000).

[11] D. Jones et al., *Science* **288**, 635 (2000).

[12] R. Holzwarth et al., *Phys. Rev. Lett.* **85**, 2264 (2000).

[13] Th. Udem et al., to be published.

[14] J. Stenger et al., *Phys Rev. A* **53**, 021802(R) (2001).

[15] M. Niering et al., *Phys. Rev. Lett.* **84**, 5456 (2000).

[16] R. Holzwarth et al., to be published.

[17] J. von Zanthier et al., *Opt. Lett.* **25**, 1729 (2000).

[18] A. Apolonski et al., *Phys. Rev. Lett.* **85**, 740 (2000).

[19] T.W. Hänsch, Proceedings of *The Hydrogen Atom*, edited by T. W. Hänsch, Berlin: Springer 1989. H. R. Telle, D. Meschede, and T. W. Hänsch, *Opt. Lett.* **15**, 532 (1990).

[20] M. Kourogi et al., *IEEE J. Quantum Electron.* **31**, 2120 (1995) and L. Brothers, D. Lee and N. Wong, *Opt. Lett.* **19**, 245 (1994) .

[21] J. N. Eckstein, A. I. Ferguson, and T. W. Hänsch, *Phys. Rev. Lett.* **40**, 847 (1978).

[22] A. I. Ferguson, J. N. Eckstein, and T. W. Hänsch, *Appl. Phys.* **18**, 257 (1979).

[23] Y. V. Baklanov and V. P. Chebotayev, *Appl. Phys.* **12**, 97 (1977).

[24] D. M. Kane, S. R. Bramwell and A. I. Ferguson, *Appl. Phys. B* **39**, 171 (1986).

[25] J. Reichert et al., *Opt. Commun.* **172**, 59 (1999).

[26] D. J. Wineland et al., Proceedings of *The Hydrogen Atom*, edited by T. W. Hänsch, Berlin: Springer 1989.

[27] R. Holzwarth et al., *Phys. Rev. Lett.* **85**, 2264 (2000).

[28] S.A. Diddams et al., *Opt. Lett.* **25**, 186 (2000).

[29] F. L. Walls et al., *IEEE Trans. Instrum. Meas.* **24**, 210 (1975).

[30] Kinoshita T., *Rep. Prog. Phys.* **59**, 1459 (1996), and references therein.

[31] P. J. Mohr and B. N. Taylor, *Rev. Mod. Phys.* **72**, 351 (2000).

[32] D. L. Farnham et al., *Phys. Rev. Lett.* **75**, 3598 (1995).

[33] M. P. Bradley et al., *Phys. Rev. Lett.* **83**, 4510 (1999).

[34] A. Huber et al., *Phys. Rev. A* **59**, 1844 (1999).

[35] G. Santarelli et al., *Phys. Rev. Lett.* **82**, 4619 (1999).

[36] J. C. Knight et al., *Opt. Lett.* **21**, 1547 (1996).

[37] J. Wadsworth et al., *Electron. Lett.* **36**, 53 (2000).

[38] C. Zimmermann et al., *Appl. Phys. Lett.* **66**, 2318 (1995).

[39] R. Holzwarth, *PhD thesis*, Ludwig-Maximilians-Universität, Munich, Germany (2000).

Global Transmission Services
New Radio Signals from Space

Felix Huber
Steinbeis Transferzentrum Raumfahrt
Rötestr. 15
D-71126 Gäufelden

Abstract

Global Transmission Services (GTS) is a new system for transferring radio signals from the International Space Station (ISS).

Starting in the year 2001 it will be tested in the framework of a pilot project. GTS is the first experiment on the new space station and at the same time the possibilities of future commercial uses of the space station as a space-born platform will be investigated. The experiment is being supported by Daimler-Chrysler, Fortis Swiss Watches as well as the German Aerospace Center (DLR) and the European Space Agency (ESA).

Two areas of applications will be investigated during the first phase of the experiment: the worldwide synchronization of watches and the deactivation of stolen vehicles. In this paper, an additional capability of the GTS hardware will also be presented: precision orbit determination.

Functional Overview:

The GTS hardware consists of an external antenna located on the nadir side of the Russian service module „Zvesda" (SM) and an electronics unit inside the pressurized area. GTS takes advantage of the ISS orbital parameters, which are as follows

- In comparison to other satellites, the ISS has a very low altitude of 400 km with a high inclination of 51.6°. Therefore any ground point between ±70° latitude can be reached 5-7 times per day via the radio link. Figure 1 shows the typical coverage during a 24h period.
- The combination of low orbit height and the high orbital velocity creates signal properties (Doppler shift, high angular rate) that can be used for coarse navigation of the ground receivers and proof of signal authenticity.
- The ISS, the biggest space project of all time, is available on this advantageous orbit for the next 15-20 years (independent of any special service) and at the same time offers the possibility for the astronauts to exchange and maintain devices, as well as convenient transport possibilities approximately every three months.

However, there is the disadvantage of the ISS that contrary to the mobile radio satellite constellations like Iridium, Globalstar and ICO, a real time operation is not possible. This means that a time critical operation can not be supported at this time.

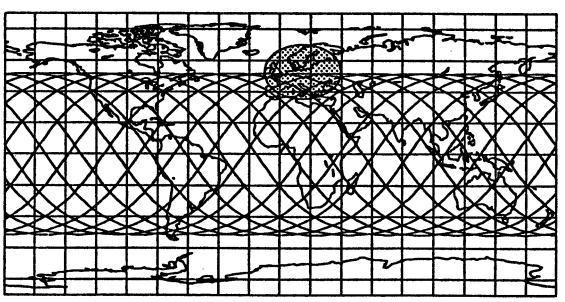

Fig. 1: ISS ground tracks with a typical reception area

In the near future, GTS shall transmit commercial data packets to miniaturized mobile receivers worldwide including applications such as

- Global time dissemination
- Paging services
- Data transfer into smart cards with polymer displays
- Theft protection for cars, credit cards, mobile phones etc.
- Car safety recalls / breakdown emergency calls
- Remote controlling
- Tracking of containers and other objects
- Fleet management

By means of miniaturization of the receiver even small objects such as wrist watches mobile phones, electronic car keys and chips cards can be protected against illegal use. The experiment shall also show whether the position of large expensive stolen objects (containers, construction machines) can at least be tracked down to some square kilometers in range. This can be realized using a small uplink transmitter of some 100 mW located also in the receiver.

The start of the experimental operation is foreseen to start in the middle of 2001. After a two year testing phase, the new services will be offered by a newly founded operating company. For redundancy reasons, two independent systems will then have to be installed on board the ISS.

Operating principle

Radio controlled wrist watches have been around for several years in various countries. They remove the need from their users to adjust the clock regularly. However, all of these time transmitters operate with proprietary signal format and are incompatible to each other which results in a malfunction of the receiver when brought to a different country. An alternative would be the use of the „Global Positioning System" which allows the coordinated universal time (UTC) to be received on every point of the Earth's surface, but this system lacks the availability of local time zone information and the switching of the daylight saving time. Currently available systems are using a database that needs to be updated when changes of time zones occur.

All systems established so far also lack the possibility of transmitting short messages (emergency calls, paging) to a certain receiver or to locate the receiver.

The new system uses an antenna and a transmitter on board the ISS and sends out a specially encoded signal that can be received by a miniature receiver within almost the whole habited surface area of the Earth. One of the major applications is the synchronization of clocks by using a certain signal structure that allows for the transmission of the current local time.

The system is therefore capable of compensating the time offset that is caused by geography, political time zones or daylight saving without user intervention. By decoding the information in the signal, the receiver can perform a simple navigation, removing the need from the user to manually set the current geographical position. The low orbit height of the ISS allows for an extreme miniaturization of the receiving electronics,

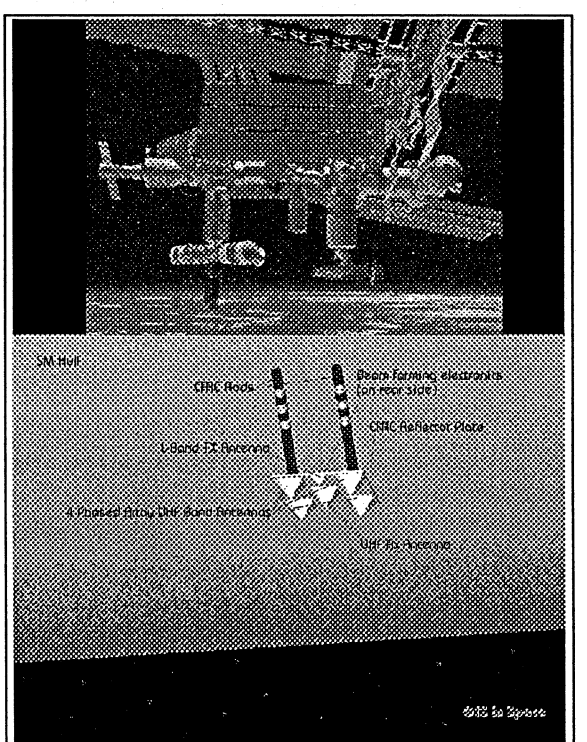

Fig 2: Location of the external antenna

such that it can be located within a wrist watch or a car key housing.

Signal generation

In addition to the external antenna located on the nadir side of the Russian service module, there is an electronic unit containing an ultra-stable quartz crystal oscillator, radio transmitters and a control computer. In order to have a secure and spoofing-proof signal link, a new spread spectrum system was developed that allows for both a fast signal acquisition and secure encoding by using a combination of linear and non-linear pseudo random numbers (PN). Linear PN-codes are well known in communication systems as they have mathematical properties that have been intensively investigated. By analyzing the received signal, one can therefore easily recalculate the generating functions of the PN codes. This renders the system unusable for application such as theft protection. The linear code is therefore only used for a rapid signal acquisition and helps as a guide to lock onto the highly encrypted non-linear code. This code is non-repetitive and by using certain mathematical properties of the generating function, a receiver can easily detect whether a received code sequence has already been received. This is needed in order to prevent the recording and replaying of a certain code fragment which might otherwise be used to imitate the signal on the ground.

The data modulated onto the signal can only be decoded when certain parameters have been programmed into the receiving chip during the licensing process in order to prevent the manufacturing of illegal replicates. In the case of a deactivation of a stolen object such as an automobile, these parameters are irreversibly deleted to prevent the reactivation of stolen objects.

Receiver navigation

Terrestrial radio watches usually only synchronize once per day to save battery power. For a space born signal this method cannot be used, as the transmitter must reside within the ground reception area when the synchronization takes place. To compensate for this, in addition to the plain time information, orbital information for the next passages are transmitted to the ground receivers allowing them to know in advance the times of the next contacts.

The reception area on the ground can cover several time zones. The receiver must therefore check the distance between its own position and the subsatellite point for which the time data was calculated. By measuring the Doppler shift of the received frequency generated during a fly-by, the time and distance of the closest approach can be calculated.

In a second step, the ambiguity of a left or right hand passage must be resolved. To simplify this process, the signal is not transmitted uniformly but rotates in the form of a beacon. This rotation, created electronically by means of a phased array antenna, causes a swelling of the signal on the ground. Angular information contained in the data stream and correlated to the current transmitting direction is then used to define a left or right hand passage during the closest approach.

Object tracking

In addition to the theft protection mechanism that is activated upon reception of spoofing-proof signal, an optional tracking of individual receivers on the ground is provided by the system. They locate a ground receiver, the system transmits a tracking sequence and measures the time delay of a short response pulse generated by the ground receiver. Due to the low orbit height of the ISS, only a very low power signal must be created by the

receiver. The control computer evaluates the delays of several measurements at various positions caused by the fast orbital motion of the ISS and can then determine the position of the object on the ground. For security reasons, the receiver answers every request only once. After that a new signal sequence must be received before an additional response is generated. This helps to save power but also to prevent the discovery of the receiver by a „non-cooperative" user through the means of RF test receivers. A typical application would be the protection of construction machines, where the receiver can operate hidden for several years and can be located world wide when needed.

Precision orbit determination

The transmitters of the GTS electronics operate in the 400 MHz and 1.4 GHz range both using PN codes. This gives a frequency ratio of 3.5 which allows for ionospheric correction with both absolute and Group vs. Phase (DRVID) measurements roughly four times better than GPS.

The main hardware limiting factors of the GTS electronics are a relative accuracy of the local oscillator better than 10^{-13} in the 30s range and the 1 Mchip/s PN Code in the L-Band. Currently no PN-code is used in the uplink. Therefore, when using short chunks of 10-second measurements, GTS allows better orbit dermination models to be delevloped. These sigificantly outperform the current ISS precision orbit determination limits of 2.7m that are due to the constraints of the physics and models used. Figure 3 shows the signal path used for the orbit determination.

There are several advantages of GTS compared to other systems:

- GTS transmits from space to ground: No local RF licences needed
- Low cost (<20 KEuro) receivers can be used
- Receivers can be accomodated indoors, no special tracking antennas are needed
- A global network of estimated 50 receivers can be established via Internet connections with immediate remote data readout, that is GTS allows for almost real time high precision orbit determination.

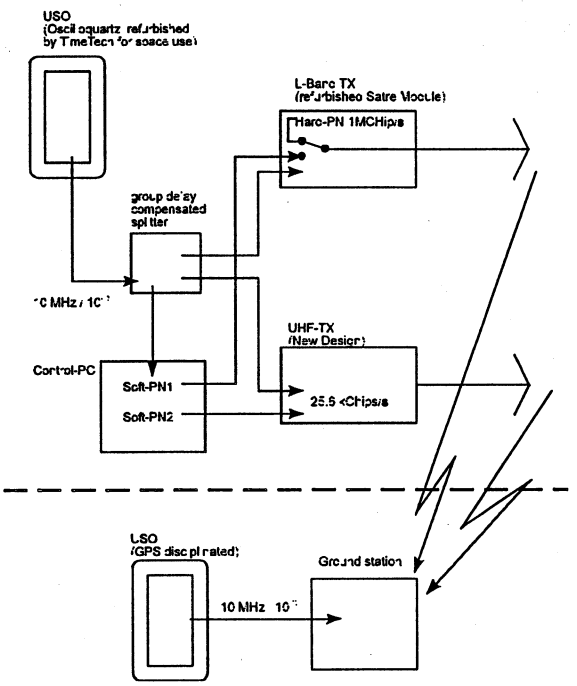

Fig. 3: Hardware setup for the precision orbit determination measurements

Aknowledgements

The GTS Experiment is support by the European Space Agency ESA and Deutsches Zentrum für Luft und Raumfahrt DLR contract 98069.

MATERIALS

Chairman: Peter Krempl

PRESENT STATE OF THE DEVELOPMENT OF THE PIEZOELECTRIC MATERIALS

E. PHILIPPOT, YU. V. PISAREVSKY[+], B. CAPELLE[°*], J. DÉTAINT[°]

LPMC, Université de Montpellier II, Place E. Bataillon, cc 003, F-34095 Montpellier cedex 5.
[+]Institute of Crystallography RAS, Leninskii prospect 59, Moscow Russia 117333
° LMCP, case 115, 4 Place Jussieu, F-75252 Paris cedex
*LURE, Université Paris-Sud, F-91405 Orsay Cedex

1. INTRODUCTION

In the last decades, many efforts were developed to obtain crystals with more intense piezoelectric properties than quartz, allowing to realize stable resonators with time and temperature. The most apparent interest of these new materials is the possibility to obtain much larger bandwidth for the filters or larger frequency shifts for the oscillators than those possible with quartz.
These materials can be divided in three classes:

- the well known compounds such as first the quartz itself and, the lithium tantalate and niobate which are the most frequently used materials for the present applications.
- the very promising materials of which the crystal growth is going well such as the quartz homeotypes, aluminium and gallium phosphates, the crystals of the very large langasite family and the lithium tetraborate. These materials seem to be very well adapted to several important forthcoming applications.
- the last part is constituted by crystals of which the crystal growth process exhibits difficulties: such as zinc oxide, ZnO or recently investigated crystals with theoretically very large coupling coefficients, such as perovskite crystals (PZN-PT, PZT-PT, etc...).

In this short paper, a special attention will be devoted to the second groups of materials: langasite (and related materials) and quartz homeotypes which were first investigated in the beginning of the eighties and then much perfected. These crystals exhibit a rather high coupling coefficient, high Q-factors and compensated cuts for SAW and BAW applications. They seem to be very well adapted to several new applications related to the implementation of the Information Society such as the future radiocommunication systems. Several among them allow also to find much better solutions to the increasing need of transducers to monitor many processes of our environment. We will discuss the technological problems which are pending in view of a mass production and how is possible to solve them in due time.
In the first table, we have summarized some of the more important characteristics of some well known piezoelectric materials: the coupling coefficient and the corresponding Q-factor, the limiting transition or melting temperature and the crystal growth method.
We can observe that langasite and gallium phosphate exhibit some interesting and analog physical properties and, then, we will try to give a critical and comparative analysis of the situation for quartz homeotypes and langasite family crystals: the crystal growth methods, the present crystal quality and the main properties of these crystals.

2. QUARTZ HOMEOTYPES

Quartz homeotype material composition is given by the general formula MXO_4 where M^{III} = B, Al, Ga, Fe, Mn and X^V = P, As and, also, the germanium oxide GeO_2. The only structural difference between MXO_4 and SiO_2/GeO_2 crystals is the c-parameter value, twice for MXO_4 materials, with alternately M and X atoms shifted by c/2. All these compounds exhibit structural transitions before melting or a simultaneous melting/decomposition. Then, the hydrothermal synthesis at temperature less than transition temperature is the only way to obtain such crystals. After preliminary investigations in the seventies, Ref. 1, the first crystal growth study of a quartz-like material was berlinite, $AlPO_4$, in the beginning of the eighties, Refs 2-5.

Table 1 – Some piezoelectric and thermal characteristic of piezoelectric materials and their growth process.

Crystals	k (%)	Q.f 10^{12}	stability (°C)	crystal growth
α-quartz	8	>10	573	hydrothermal
$AlPO_4$ (berlinite)	11	>5	586	hydrothermal
$GaPO_4$	16	>5	933	hydrothermal
$Li_2B_4O_7$	23	>0.5	300	Czochra+hydro.
$LiTaO_3$	45	>0.05	600	Czochralski
$LiNbO_3$	70	>0.05	1200	Czochralski
$La_3Ga_5SiO_{14}$	13	>10	1500	Czochralski
$La_3Ga_{5.5}Nb_{0.5}O_{14}$	15	>10	1500	Czochralski
$La_3Ga_{5.5}Ta_{0.5}O_{14}$	18	>10	1500	Czochralski

2. QUARTZ HOMEOTYPES

Quartz homeotype material composition is given by the general formula MXO_4 where M^{III} = B, Al, Ga, Fe, Mn and X^V = P, As and, also, the germanium oxide GeO_2. The only structural difference between MXO_4 and SiO_2/GeO_2 crystals is the c-parameter value, twice for MXO_4 materials, with alternately M and X atoms shifted forward c/2. All these compounds exhibit structural transitions before melting or a simultaneous melting/decomposition, then, the hydrothermal synthesis at temperature less than transition temperature is the only way to obtain such crystals. After preliminary investigations in the fifties, Ref. 1, the first crystal growth study of a quartz-like material was berlinite, $AlPO_4$, in the end of the seventies, Refs 2-5.

2.1 Berlinite, $AlPO_4$

As the other MXO_4 compounds, berlinite shows, for temperature less than 300°C and pressure less than 5 MPa, a retrograde solubility in the most well known acids: phosphoric, sulfuric, hydrochloric acids and their mixtures. Several teams in the United States and in France and, more recently, in Russia succeeded to develop large (more than 10 cm and very good crystals of this material, figures 1.

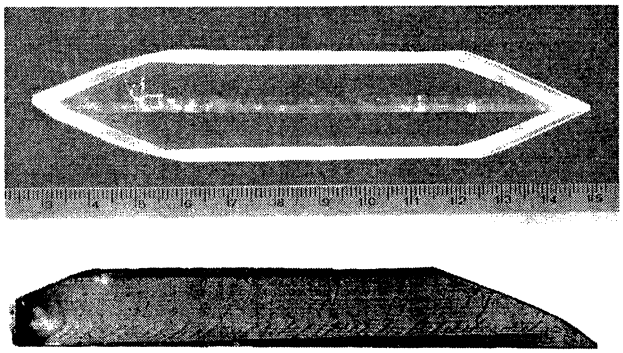

Figures 1 – $AlPO_4$ crystal from VNIISIMS, Alexandrov, Russia and X-ray topography from French crystal.

The best crystals, Ref 6, are obtained in sulfuric acid medium for a growth temperature of 240°C and a growth rate of 0.2 mm/day. Their [OH] content, computed from infrared spectra with the relation proposed by Steinberg, Ref. 7, gives a value close to 0.2 cm^{-1} and corresponding AT-cut resonators have a coupling coefficient, k=0.11, with a very good Q-factor=10^6 at 5 MHz.Unfortunately, for berlinite, first results about gallium phosphate and langasite showed that these materials also exhibited temperature compensated cuts with higher coupling coefficient and wider stability range of temperature. Then, its industrial production was not developed.

2.2 Gallium phosphate, $GaPO_4$

During the course of the fundamental research about MXO_4 compounds, some similarities and some drastic differences among the members of this series have become apparent. For example, the continuous solid solution $Al_{(1-x)}Ga_xPO_4$ for $0 \leq x \leq 1$, Ref. 8, for which the cell volume is constant ($V=230 \pm 1 Å^3$), suggests that a very similar structural packing scheme characterizes the end member compounds $AlPO_4$ (berlinite) and $GaPO_4$. From this analogy, it was possible to synthesize, by hydrothermal way, the first large as-grown crystals of $GaPO_4$ from berlinite seeds in acidic medium, Ref. 9, figure 2.

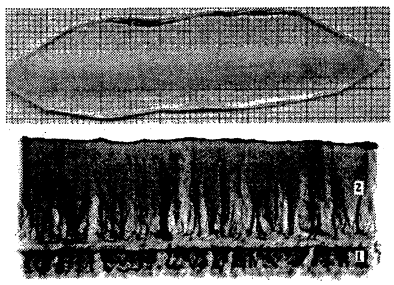

Figures 2 – Example of flat $GaPO_4$ crystal obtained from epitaxy on Z-berlinite seed and corresponding X-ray topography.

Unfortunately, the berlinite seeds are not so frequent and another way had to be found to develop this crystal growth.
The first one is the epitaxy on quartz seeds, Ref. 10. The problem is often the appearance of twins in the as-grown part, twins which have to be eliminated in the further crystal growth experiments.
Another way, by similarity with berlinite, is the splicing method which consists to accurately line up some small seeds in the Y-direction where Vy≈0.0 mm/day, Ref. 11. The problem is a high density of defects (chiefly dislocations) stemming from the edge sharing. These dislocations can be strongly reduced by two successive crossed crystal growth experiments, figures 3.

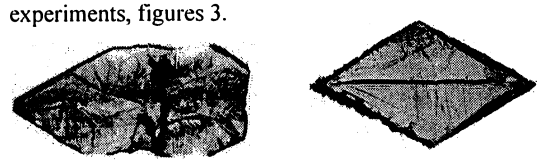

Figures 3 – X-ray topographies: left - after splicing; right – after two consecutive crossed crystal growths.

Whatever the chosen process, good crystals are allowing to obtain AT-cut resonators with already high Q-factor, greater than 10^6 at 5 MHz. This result is all the more encouraging since the corresponding α-value computed from infrared spectra is close to 0.8-0.9 cm^{-1}. If we consider that for similar Q-factor values, α is close to 0.1 and 0.2 cm^{-1} for quartz and berlinite respectively, very high Q-factors can be expected for gallium phosphate.
As summarized in the first Table, another advantage of $GaPO_4$ is its high thermal stability range, more than 900°C accompanied by a very weak sensitivity to the temperature. In the figures 4 are reported the evolutions of a basic structural characteristic, the delta angle value, of quartz and different quartz-like materials in terms of temperature.
As observed, from 200°C, this δ value decreases more and more quickly to δ=0 for the α quartz/β quartz transition. Conversely, this evolution becomes less and less sensitive and linearly related to temperature when the initial delta value increases, i.e. when the structural packing distortion increases. This structural evolution being related to physical properties, Ref. 12, the sensitivity of $GaPO_4$ to temperature will be weaker than that of quartz and, then, the $GaPO_4$ devices will exhibit a very good stability in a wide range of temperature.

Figures 4 – **a** : Delta, δ, is the MO_4 (or XO_4) tetrahedron rotation between α and β quartz positions.
b : Evolution of the δ angle for different quartz-like materials versus temperature.

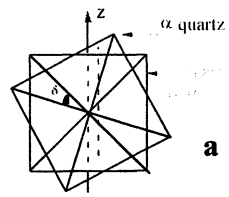

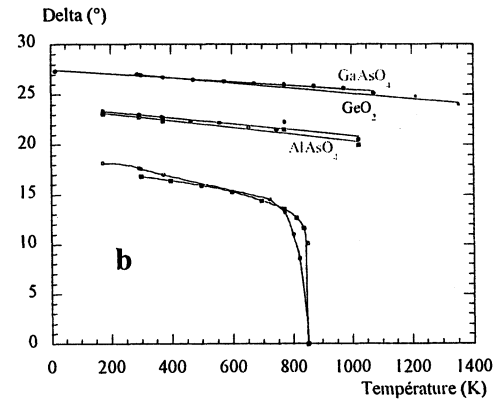

With all these better piezoelectric properties than quartz, what slows down the industrial development of this material?

Unfortunately, conversely to berlinite, the best crystal growth process is much more difficult to optimize. Two main factors are responsible of this difficulty:

- the weak solubility of gallium phosphate in acidic medium (≈ 3 times less than berlinite in the same conditions), accompanied by a slow decrease of this

solubility versus temperature, leads to a very weak solubility variation, $\Delta S/\Delta T$, and then a poor supply of $GaPO_4$ at the interface solid/solution during the crystal growth process;

- the very strong anisotropy of the growth rates whatever the crystals growth conditions: $V_y \approx 0.0$; $V_x \geq 0.2$ and $V_z \approx 0.02$mm/day.

The result of these two preceding behaviors is, in the present state of the investigations, for Z-seeds, to lead to quite long growth cycles for large crystals. This is the result on the fact the mechanism of hydrothermal transport in concentrated liquid and/or the kinetic of complex decomposition at the interface limit the supply of the nutrient for the crystal growth. Although it was already shown that good crystal growth conditions are obtained using this low supply that limits the growth rate to a small value (Vz=0.02 mm/day), figure 5, it will be very interesting to find mechanisms that allows to increase this supply in a significant manner whereas keeping the quality of growth

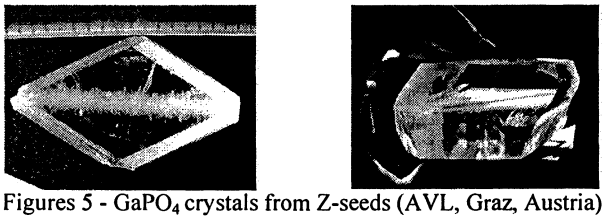

Figures 5 - $GaPO_4$ crystals from Z-seeds (AVL, Graz, Austria)

Conversely, if X-seeds are used, the $GaPO_4$ supply at the crystal growth interface becomes too weak for $V_x \geq 0.2$ mm/day and leads to a very disturbed and unusable crystal growth process, figure 6.

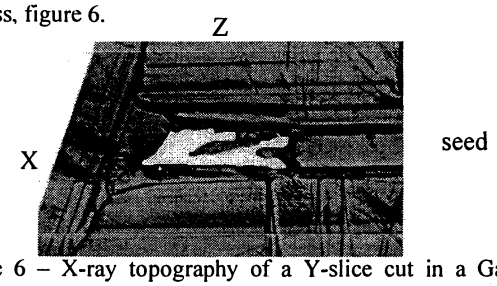

Figure 6 – X-ray topography of a Y-slice cut in a $GaPO_4$ crystal obtained from Z-seed.

Then, the success of the further $GaPO_4$ mass production depends on the possibility to increase the $GaPO_4$ supply to the crystal interface. The chemical solution being limited by the solubility itself, a mechanical solution has to be found to increase the circulation in the autoclaves: either by stirring directly inside the autoclave or by using oscillating autoclave. This last possibility succeeded, Ref.13 & figure 7, but, for the moment, only at the laboratory scale.

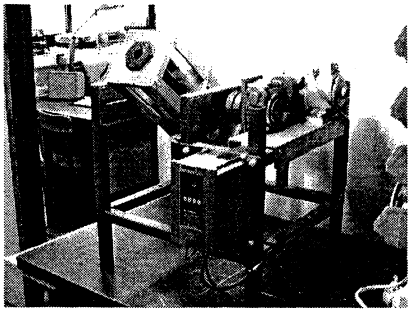

Figure 7 – Oscillating horizontal autoclave

2.3 Other quartz homeotypes

In conclusion for this part, what can be said about the other members of the quartz-like family? As experimentally observed, structural and piezoelectric properties being closely related for the three known crystals (SiO_2, $AlPO_4$ and $GaPO_4$), those of the other members can be extrapolated, figure 8.

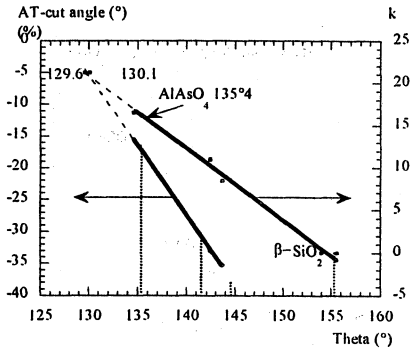

Figure 8 – Coupling coefficient andAT-cut angle in terms of the bridging angle M-O-X.

Then, for example, the AT-cut characteristics (k and angle) of the three known crystals are linearly related to another structural parameter, theta (the Si-O-Si or M-O-X bridging angle), Ref. 12. From this relation, $GaAsO_4$ and GeO_2 should be the most promising materials with a coupling coefficient greater than 20% and an AT-cut angle close to zero. In the same way, and from figure 4, these materials should exhibit the best thermal behavior. On this basis, first experiments are now developed in Russia to grow GeO_2, Ref. 14.
Let us try, now, to compare the state of the art of these quartz-like materials to that of the langasite family which presents

3. LANGASITE FAMILY

This family was discovered in late 70's by Professor Mill and his team of the Russian Academy of Sciences, Ref. 15. This is a very wide family comprising to day more than 100 compounds with similar structure that were synthesized. It could be divided into the following groups:

1. $Ln_3Ga_5M^{4+}O_{14}$ (Ln = La, Pr, Nd and M= Si, Ge, Ti, Sn, Zr, Hf);
2. $Ln_3Ga_{5.5}M^{5+}_{0.5}O_{14}$ (Ln = La, Pr, Nd and M=Nb,Ta,Sb);
3. $La_3Ga_{5.67}M^{6+}_{0.33}O_{14}$ (M=Mo,W);
4. $A^{2+}Ln_3Ga_5SbO_{14}$ (Ln = La, Pr, Nd and A=Ba, Sr and Ca;
5. $La_2Ga_4SrSi_2O_{14}$
6. $Ln_3Al_{3+x}Si_{3-x}O_{12+x}N_{2-x}$ (Ln=La, Ce, Nd, Sm, Gd, Dy, Y ; $0 \leq x \leq 1$);
7. $La_2Zn_3Sb\ C^{4+}O_{14}$(C=Si,Ge)
8. $A^{+2}{}_3B^{3+}{}_2Ge_4O_{14}$ (A=Ca,Sr,Ba,Pb and B=Ga,Al,Fe,Cr,In);
9. $NaA^{+2}{}_2B^{3+}Ge_4O_{14}$(A=Ca,Sr,Pb and B=Ga,Al, Fe,Sc,In);
10. $Na_2A^{+2}Ge_6O_{14}$(A=Ca,Sr);
11. $SrA^{+2}Ge_5O_{14}$ (A=Mg,Zn,Ni,Co,Fe,Mn);
12. $A^{+2}B^{3+}{}_3C^{4+}M^{+5}O_{14}$ (A=Ca,Sr,Ba,Pb; B=Ga,Al,Fe,In; C=Si,Ge and M=Sb,Nb,Ta)

Most of compounds are mixed gallates (groups 1-5), germanates (groups 8-11) or silicates. The synthesis of aluminates and oxinitrides reveal additional possibilities of new compounds.
Most above compounds melt incongruently and therefore are not suitable for conventional Czochralsky crystal growth method. About 20 congruently melting compounds were

grown up to-day as single crystals by the conventional Czochralsky melt pulling technique similar to $LiTaO_3$. The three most commonly cited compounds: $La_3Ga_5SiO_{14}$ (LGS), $La_3Ga_{5.5}Nb_{0.5}O_{14}$ (LGN), and $La_3Ga_{5.5}Ta_{0.5}O_{14}$ (LGT) are grown in 3" diameter crystals at several places, figure 9.

Figure 9 – LGS crystal from Mitsubishi, Japon.

Even though the basic growth process seems straightforward, the actual growth is much more complicated and, despite the promises, the results of the different growth experiments conducted by several teams have often shown visible differences.

3.1 Growth of langasite family compounds

Different problems have to be solved such as:

- evaporation during growth, so the melt has to be compensated;
- distribution ratios may not be equal to unity for all the growth components in all cases;

Depending on the specific crystal, a specific melt composition has to be used in order to maintain high quality growth and with high material yield. Finally, the crystal can form a number of defects such as twinning, domain structure and inhomogeneity.

The melting temperature is always rather high, close to 1500°C. Therefore, it is possible to use either platinum or iridium crucible with either resistant or induction heating for growth. To start the growth, the chemicals are carefully weighed and mixed before loading. The melt composition is adjusted depending on the specific crystal. Single crystal were pulled directly from the melt, using a rotating seed with a specific orientation, with a melt conversion into crystal close to 80%. Compared to $GaPO_4$, typical growth cycles are much shorter, depending on size of the charge, but always expressed in days.

It is known that the color of langasite crystals is sensitive to the oxidation state during growth: from a deep reddish orange color under ambient oxygen condition to colorless or light yellow under nitrogen environment. *Although everybody claims that the color of the crystal has no effect on the piezoelectric performance, there is no controlled test to prove one way or the other.*

In addition to the large contrast in color, crystals also show distinctive overall shape, some of them are round while other crystals exhibit a strong facet development.

3.2 Defects in langasite crystals

The difficulty to grow langasite crystals seems to increase with increasing the crystal diameter. The reason is that the material intake by the crystal is much faster for large boules and diffusion rate at the crystal-melt interface becomes more critical. In other words, defects are very easy to be formed. These more frequent defects are inhomogeneity, twinning and structural defects.

3.2.1 – Inhomogeneity field

The inhomogeneity is partly due to the lack of knowledge on congruent-melting composition, then, most of the crystals are grown from the stoichiometric composition. As the result, the composition of the crystal shifts not only along the growth direction but also the radial direction and the composition of both crystal and residual melt is different and opaque white inclusions are generally found in the bottom portion of the crystals. A recent systematic growth investigation around the stoichiometric composition confirms that the composition La_2O_3 = 30.10±0.05 mol%, Ga_2O_3 = 50.60±0.05 mol% and SiO_2 = 19.30±0.05 mol% showed no shift in the compositions of both the crystal and the residual melt, thus is concluded to be the congruent-melting composition of langasite, Ref. 17, figure 10. The homogeneity of the crystals seems considerably improved by the application of this congruent-melting composition.

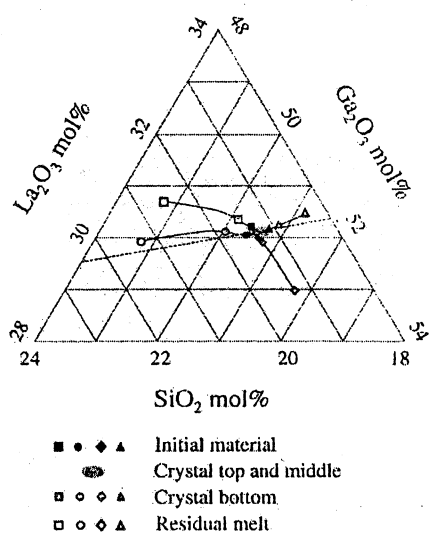

Figure 10 – Compositions of initial material, crystal and residual melt.

The inhomogeneity of the crystals is also related to the dissociation of some of the components (Ga_2O_3 in Ga_2O + 2O or GeO_2 in GeO + O) at lower oxygen pressure. This dissociation results in complication of phase relation, Pt or Ir appearance in the melt and crystal. Nevertheless, recently, Ref. 16, LGS, LGN and LGT near colorless crystals were obtained in pure nitrogen atmosphere. These results seem to suggest that nitrogen, in oxygen absence, plays oxygen part and enter in the crystal structure (remember oxinitrides), Ref. 18. So the crystal composition will be different from initial (e.g. $La_3Ga_{5-x}Si_{1+x}O_{14-x}N_x$). Under argon, the mechanism will be different because Ar cannot enter into the crystal. In this condition, the first colorless crystal was obtained recently, Ref. 19, but nothing is specified about its homogeneity.

3.2.2 Twinning

Twinning is expected in langasite crystal because of the symmetry. The distribution of twins looks nearly identical to that of the quartz crystals. This kind of twin seems more developed in LGN and LGT crystals than in LGS crystals. This difference can be related to the ordering of the octahedral site due to 50/50 occupation by Nb^{5+} (or Ta^{5+}) and Ga^{3+} ions. Partial ordering of the two ions may be the cause of twinning. On the other hand, in LGS, the octahedral site is occupied by Ga^{3+} ion only. This subtle difference may be the reason for the difference in twin appearance.
Related to the twinning is the low angle domain structure. In many occasions, the crystal starts with a smooth growth and then all of a sudden a small domain is formed at the rim of the crystal in contact with the melt. Once the domain is formed, it will grow along with the crystal quite persistently until the end of the run. These domains are very thin, but, unfortunately, because its orientation is different from the original crystal, the differential thermal expansion will force the region to crack into small pieces.
The formation of the domain structure is quite random, at any stage during the growth period, although if it is most frequently formed during the growth of the cone section. Since the domain region has an orientation quite different, it is certainly due to a local supersaturation giving nucleus formation which grows continuously to the end of the run. This kind of defect is quite unique for langasite. The easiness of formation of stable nuclei indicates that the melt can tolerate very little supersaturation, perhaps, because of the complex ternary melt composition. From different approaches to overcome this problem, it seems that is due to the temperature control system itself. To eliminate the domain problem, it needs a very stable growth control domain to minimize the power fluctuation, such as a two-loop cascade adaptive control system which seems to succeed for 2" diameter crystals, Ref. 16.

3.2.3 Structural defects

Langasite family has higher symmetry (P321) than quartz-like materials ($P3_121$ or $P3_221$). On the other hand, since all crystals are trigonal in symmetry, all the calculations developed for quartz can be used directly for langasite.
Finally, there is another point, seldom tackled, related to the crystal structure itself. All the langasite crystals, excepted $Ca_3NbGa_3Si_2O_{14}$, exhibit a disordered structure because at least two kinds of atoms are in one of the same site. For example, in LGS, a part of Ga^{3+} and Si^{4+} are in the same tetrahedral site 2d. What can be the repercussion of this situation on the crystal packing when the Si-O and Ga-O bond lengths are quite different (close to 1.6 and 1.82 Å for Si-O and Ga-O respectively? Certainly, a strong increase of thz strains in the macroscopic crystal.

4. CONCLUSION

If langasite and gallium phosphate crystals exhibit some very interesting and analog physical properties, from this comparative analysis, it results that some pending problem shave to be overcome in view of a reproducible mass production.
For $GaPO_4$ crystals, if the lengthening of the seeds seems in good way to be solved, the remaining drastic difficulty is related to the too slow growth process or the insufficiently controlled one for growth in the X-direction.
For langasite crystals, there is no growth rate problem, but the homogeneity (related to partial component dissociation and congruent-melting composition knowledge) remains the most important difficulties to overcome.
On the whole, it appears that both families of materials have the requested properties for important applications in the next generation of mobile communications systems but the recent results have shown that further studies are required to improve several points of the presently known growth processes. Recently also, it was shown that several new crystals of both families may have even greater performances so that their elaboration should be studied.
It appear necessary to emphasized again the importance to use accurate characterization methods as early as possible to assess the crystal quality and the reproducibility of the characteristics of the devices.

REFERENCES

1 – Y.P. Chang and G.R. Barsch, IEEE Trans. Sonics Ultrasonics SU-23 (1976) 127.
2 – B.H.T. Chai, M.L. Shand, E. Buehler and M.A. Gilleo, Proc. IEEE Ultrasonics Symp., (1979) 577.
3 – K. Nagai, T. Ogawa, J. Okuda, J. Asahara and S. Taki, Proc. 1st Intern. Symp. On Hydrothermal Reactions, (1982) 496.
4 – J. Détaint, H. Poignant and Y. Toudic, Proc. 34th Frequency Control Sump., (1980) 93.
5 – J.C. Jumas, A. Goiffon, B. Capelle, A. Zarka, J.C. Doukhan, J. Schwartzel, J. Détaint and E. Philippot, J. Cryst. Growth, 80 (1987) 133.
6 – E. Philippot, J.C. Jumas, A. Goiffon, M. Cochez, A. Zarka, B. Capelle, J. Schwartzel and J. Détaint, J. Crystal Growth, 104 (1990) 713.
7 – R.F. Steinberg, M.K. Roy, A.K. Estes, B.H.T. Chai and R.C. Morris, Proc. IEEE Ultras. Symp., 1984, 279.
8 – D. Cachau, J. Bennazha, A. Goiffon, A. Ibanez and E. Philippot, Eur. J. Solid State Inorg. Chem., 29 (1992) 1295.
9 – E. Philippot, A. Ibanez, A. Goiffon, M. Cochez, A. Zarka, B. Capelle, J. Schwartzel and J. Détaint, J. Cryst. Growth, 130 (1993) 195.
10 – P.W. Krempl, F. Krispel and W. Wallnöfer, Ann. Chim. Sci. Mat., 22 (1997) 623.
11 – P. Yot, O. Cambon, D. Balitsky, A. Goiffon, E. Philippot, B. Capelle and J. Détaint, J. Cryst Growth, in press.
12 – E. Philippot, D. Palmier, M. Pintard and A. Goiffon, J. Solid State Chem., 123 (1996) 1.
13 – P. Yot, O. Cambon, D. Balitsky, A. Goiffon and E. Philippot, Proc. 4th Inter. Conf. Crystals: Growth, real structure, properties, applications, 308-322 (1999).
14– D. Balitsky, V. Balitsky, D. Pushccharosky, G. Bondarenco, and A. Kosenko, J. Cryst. Growth, 180 (1997) 212.
15 – B.V. Mill, A.V. Buashin, G.G. Khodzhabagyan, E.L. Belokoneva and N.V. Belov, Sov. Phys. Dokl., 27 (1982) 434.
16 – B. Chai, H. Qiu, Y.Y. Ji and J.L. Lefaucheur, Proc 1999 Joint Meeting EFTF – IEEE IFCS, (1999) 821.
17 – S.Q. Wang, J. Harada and S. Uda, J. Cryst. Growth, 219 (2000) 263.
18 – B.V. Mill, Yu. V. Pisarevsky and E.L. Belokoneva, Proc. 1999 Joint Meeting EFTF-IEEE IFCS, (1999) 829.
19 – H. Kawanaka, H. Takeda, K. Shimamura and T. Fukuda, J. Cryst. Growth, 183 (1998) 274.

CHARACTERISATION OF PIEZOELECTRIC PROPERTIES OF AlN AND GaN THIN FILMS DEPOSITED ON Si (111) AND SAPPHIRE BY MBE AND MOCVD TECHNIQUES

T. Pastureaud, A. Soufyane, S. Camou, V. Laude, S. Ballandras,
D. Schenck* and F. Semond*
LPMO/CNRS, 32 avenue de l'Observatoire, 25044 Besançon cedex, France
*CRHEA/CNRS, rue Bernard Grégory, Sophia–Antipolis, 06560 Valbonne, France

Abstract – In order to adapt surface acoustic waves (SAW) properties to high frequency range applications, stratified substrates are considered in this paper. This multilayered medium includes a "high velocity" substrate (Sapphire, (111) Silicon) and a piezoelectric layer (AlN, GaN) deposited on the substrate top surface to generate / detect acoutic wave by interdigital transducers (IDT). Comparaison between numerical simulations and experiments performed on such material combinations are reported in this paper.

I. Introduction

During the passed 10 years, many efforts have been done to improve the characteristics of SAW devices for High Frequency (HF) filtering application. Frequency filtering above 1 GHz for cellular phones particularly benefits of materials like $LiTaO_3$ or $LiNbO_3$ on which SAW can propagate which a relatively high velocity ($V > 4000\ ms^{-1}$) exhibiting a large electromechanical coupling. This allows wide band filtering (up to 20% of the fundamental frequency *Fo*) with very small Insertion Losses (close to or less than 1 dB).

Nevertheless, materials like Diamond, Sapphire, Silicon–carbide or simply Silicon exhibit very attractive elastic properties, allowing the propagation of very high velocity surface waves ($6000 < V < 18000\ ms^{-1}$). Since these materials do not exhibit any piezoelectric properties, it is necessary to deposit thin layers at their surface to use standard interdigital transducers well suited to excite and detect SAW propagation. Different materials have been identified and tested for such application, particularly ZnO or AlN [1] deposited by sputtering techniques.

In the proposed paper, a study of AlN or GaN thin films deposited on Sapphire and on Si (111) using MBE and MOCVD techniques is reported. If AlN is one of the most used piezoelectric material for thin film deposition, GaN appears as a very attractive material due to its numerous notable physical properties (very large gap semiconductor, optical wave–guide, and piezoelectricity) [2,3].

A brief description of theoretical tools used to predict elastic wave properties in multilayered structures is presented. Experiments performed on various combinaisons of AlN, GaN and even ALGaN deposited on C oriented sapphire or Si (111) are then exposed. The measured propagation characteristics are compared to theoretical predictions, showing a rather good agreement.

II. Model

In this section, only a brief recall of the basic equations used to address the problem of SAW propagation atop a stratified structure with periodic IDT is given. More details can be found in Ref. [4]. The general configuration of Fig. 1 is considered. Propagation occurs along the x_1 axis, and all quantities are assumed to be independent of the x_3 coordinate, although a general polarization is considered.

A spectral Green's function for the stratified structure is first obtained as follows. Using a procedure first proposed by Fahmy and Adler in 1973 [5], and assuming plane wave propagation in the structure, the generalized displacement distribution in each layer is obtained in the spectral domain as a decomposition over a set of 8 eigenvalues and associated eigenvectors. Assuming perfectly plane interfaces, these distributions are linked by continuity, for instance based on the so–called transfer matrix approach [6,7].

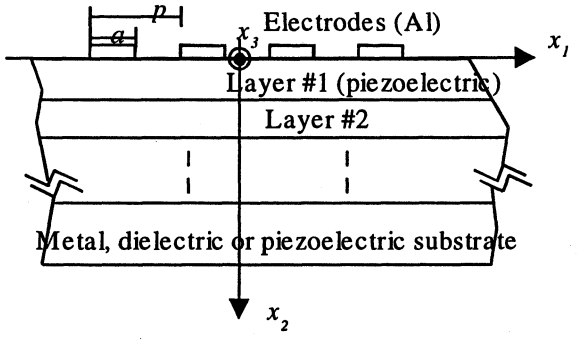

Figure 1: Stratified structure.

We alternatively use a method based on the decomposition of incident and reflected partial waves at the different interfaces [8], which avoids numerical instabilities arising when the layer thickness' increase. Whatever the approach used, the Green's function appears as usual as a 4x4 matrix relating the mechanical displacements and the electrical potential to the mechanical stresses and the charge density. Going back to the space domain, and in the case of an infinite periodic IDT, this relation becomes

$$\begin{Bmatrix} u_i(x_1) \\ \phi(x_1) \end{Bmatrix} = \frac{1}{p} \int_{-\frac{p}{2}}^{\frac{p}{2}} \left[G_{ij}^{p}(\omega, x_1 - x'_1) \right] \begin{Bmatrix} T_{i2}(x_1) \\ Q(x_1) \end{Bmatrix} dx'_1 \quad (1)$$

This problem can be solved by considering proper assumptions about the charge density, in a mixed FEA/BIM analysis [9]; furthermore, the P–matrix or coupling of modes (COM) parameters can be estimated from the harmonic admittance thus obtained. However, insight can be gained from the Green's function of the stratified structure alone, especially to identify the existence of guided modes and to try and estimate some of their characteristics. For instance, Fig. 2 shows some estimations of the wave velocity and the coupling coefficient versus the frequency–thickness product of a single layer of AlN or GaN deposited on Si(111) or C–oriented sapphire substrates; these are obtained from the G_{44} term relative to purely electrical effects. The combinations AlN/Sa and GaN/Si(111) appear the most promising in terms of electromechanical coupling and phase velocity. Although the coupling is not high enough for large bandwidth filtering applications, it is still twice or three times larger than that of Rayleigh waves on quartz. Moreover, with AlN/Sa and GaN/Si(111), it is found that both coupling and mode velocity are stable around some value of the frequency–thickness product. This is generally not the case for an arbitrary combination of materials and will help in case of industrial implementation.

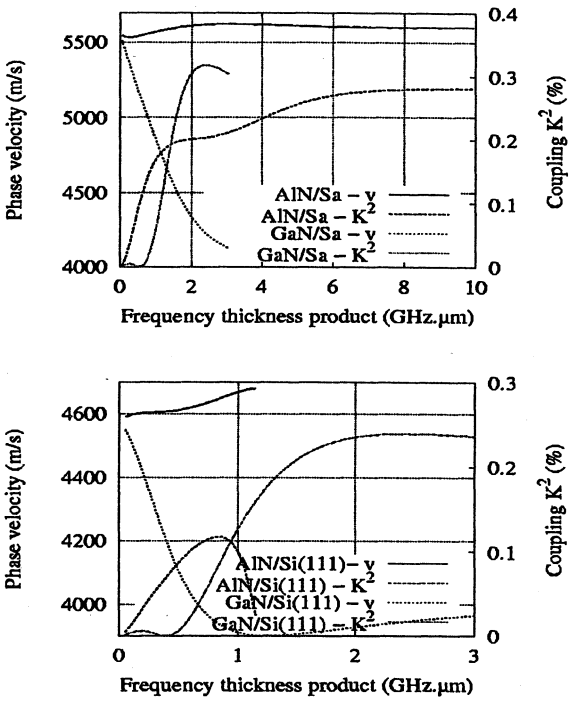

Figure 2: Theoretical prediction of phase velocity and coupling factor for single layers of C–oriented AlN and GaN deposited on Si(111) or C–oriented Sa substrates.

All the substrates measured were processed by the CRHEA to deposit a piezolayer. The technological deposition methods are discussed in details in [10,11], but due to MOCVD and MBE processes, the crystal quality of layers is rather good compared to bulk materials.

III. GaN over sapphire

In a first set of experiments, a two–port synchronous resonator was fabricated over a 10 µm single layer of GaN deposited over a C–oriented sapphire substrate. The resonator parameters were p=5µm, a/p=0.5 and $h/2p$=4%. Fig. 3 shows the modulus of the measured S_{12} as a function of frequency, together with the computed admittance for an infinite resonator with the same parameters. Although the two curves are not plotted in the same units, the different propagation modes are clearly visible. The modes numbered 1 and 2 on Fig. 3 propagate without attenuation at about 3900 m/s and 5300 m/s respectively. For frequencies higher than about 575 MHz, label 3 on Fig. 3, bulk waves are radiated into the substrate; this value is directly connected to the slow shear velocity which is approximately 5740 m/s for the cut of sapphire used.

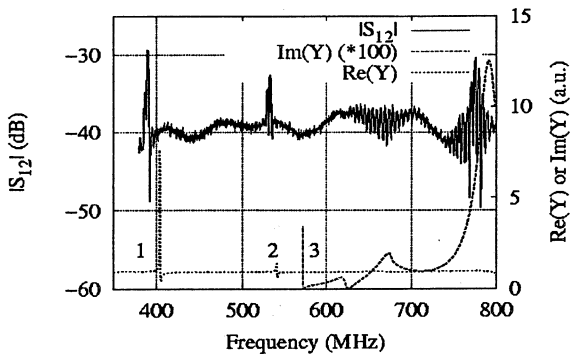

Figure 3: Measured $|S_{12}|$ for a two–port synchronous resonator on GaN/Sa, together with the computed admittance.

IV. AlN / GaN over Si (111)

In a third set of experiments, a single–port resonator was fabricated on a bilayer structure over a silicon (111) substrate. The two layers are respectively 100 nm thick AlN and 900 nm thick GaN (the latter deposited on the substrate). The resonator parameters were p=24μm, a/p=0.5 and $h/2p$=0.83%.

Fig. 5 shows the modulus of the measured $|S_{11}|$ as a function of frequency, together with the simulated harmonic admittance for an infinite resonator with the same parameters. Three modes can be seen on the HA, but the second is not apparent on the measurement, which we cannot presently explain. We tried and fit the first and third modes to a P–matrix model [12]. A comparison between the experimental third mode and the P–matrix simulation is plotted in Fig. 6. It can be seen that some oscillations in the admittance could not be accounted for. The results of the fit are shown in Tab. 1. The predictions of the FEA/BIM model are also shown for mode one, and are found to be in relatively good agreement with the experimental data, considering that precise material data are not available for the deposited layers. We were not able to extract the parameters from the FEA/BIM simulation for the third mode.

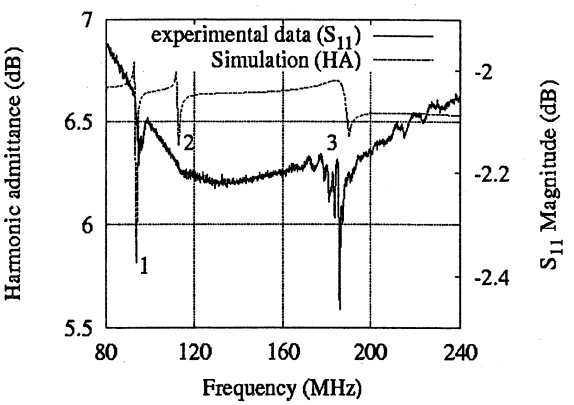

Figure 5: Signature of propagating modes on the AlN/GaN/Si(111) sample.

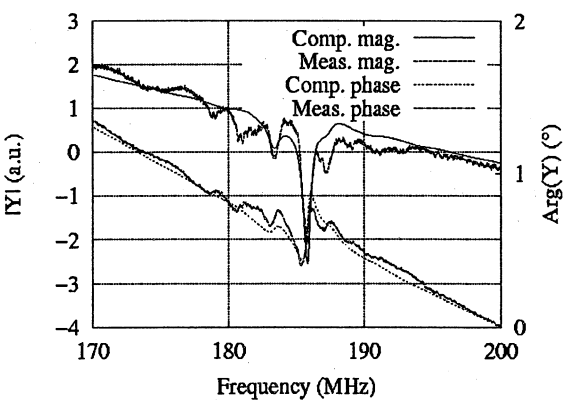

Figure 6: Fit of mode 3 in Fig. 5 using a P–matrix model.

Table 1: Waves parameter estimation for the AlN/GaN/Si(111) sample.

	Velocity (m/s)	**Coupling (%)**	**Refl. coef. (%)**	**Ref. phase (°)**
Mode 1 meas.	4471	0.33	1.28	0
Mode 1 FEA/BIM	4421	0.39	0.74	0
Mode 3 meas.	8922	0.26	0.75	90

The same estimation procedure was repeated for several other resonators with different periods fabricated on the same sample. The phase velocity of the first mode is shown in Fig. 7 for some values of the frequency thickness product.

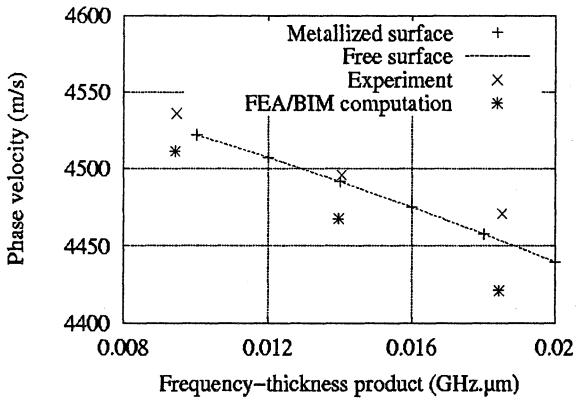

Figure 7: Velocity as a function of the frequency thickness product for the AlN/GaN/Si(111) sample.

V. Conclusion

First results of a study of AlN and GaN thin films deposited on Si (111) and sapphire for the excitation of guided elastic waves were reported. A general model has been developed for stratified media, and is used to identify propagating modes and their parameters. The electromechanical coupling was found to remain smaller than 1% in all tested cases. However, large phase velocities were observed, as high as 5600 m/s in the case of AlN/Sa with a good stability versus the layer thickness. Although these results are already known, the potential application of such structures to filtering applications have not been generally discussed. Actually, with a coupling of 0.25% and a phase velocity of 5600 m/s, a narrow band DART filter can be designed for operation around 500 MHz, whereas DART filters on standard single crystals are usually restricted to operating frequencies below 300 MHz by the usual technology limitations linked to the small finger width that has to be patterned. In the long run, it would be interesting to combine the piezoelectricity of (Al,Ga)N layers with their other properties (semiconductor, optical waveguide, laser diode) to imagine new classes of components for high frequency signal processing.

Acknowledgment – This work was supported by the Centre National de la Recherche Scientifique under grant FINARCOS.

VI. References

[1] K. Dovidenko, S. Oktyabrsky, J. Narayan and M. Razeghi, J. Appl. Phys., Vol. 79, 249, 1996.

[2] R. B. Schwarz and K. Khachaturyan, Appl. Phy. Lett., vol. 70, 1122–1124, 1997.

[3] F. Bernardini, V. Fiorentini and D. Vanderbilt, Phys. Rev. B, vol. 56, R10024–R10027, 1997.

[4] S. Camou, S. Ballandras and Th. Pastureaud, in Proc. of the IEEE Ultrasonics Symp., pp. 143–146, 1999.

[5] A. H. Fahmy and E. L. Adler, Appl. Phys. Lett., vol. 22, pp. 495–497, 1973.

[6] E. L. Adler, Ferroelectrics, and Frequency Control, vol. 37, pp. 485–490, 1990.

[7] P. M. Smith, Proc. of the IEEE Ultrasonics Symp., pp. 137–141, 1999.

[8] L. Boyer, Ph.D. Dissertation (in French), Université Paris 7, 1994.

[9] P. Ventura, M. Solal and J.–M. Hodé, Proc. of the IEEE Ultrasonics Symp., pp. 263–268, 1995.

[10]F. Semond, B. Damilano, S. Vezian, N. Grandjean, M. Leroux and J. Massies, Appl. Phys. Lett., vol. 74, 82, 1999.

[11]T. Pastureaud, A. Soufyane, S. Camou, V. Laude, S. Ballandras, D. Schenck , F. Semond, J. Desbois , Proc. of the IEEE Ultrasonics Symp. 2001

[12]J.–M. Hodé, J. Desbois, P. Dufilié, M.Solal and P. Ventura, Proc. of the IEEE Ultrasonics Symp., pp. 39–50, 1995.

LIQUID PHASE EPITAXY OF $LA_3GA_5SiO_{14}$

Christine Klemenz

Institute of Micro- and Optoelectronics, Department of Physics
Swiss Federal Institute of Technology EPFL
CH-1015 Lausanne, Switzerland

ABSTRACT

This paper reports on the first successful growth of single-crystalline $La_3Ga_5SiO_{14}$ films by liquid phase epitaxy (LPE) for bulk (BAW) and surface acoustic wave (SAW) devices. The films were grown from a high-temperature solution (flux) on X- and Y-oriented langasite substrates (homoepitaxy), after establishment of basic substrate, solvent, and growth parameters. These films were characterized by XRD, AFM, SEM/EDX, and Nomarski microscopy. Whereas the X-oriented films show rather an undulating surface, the Y-oriented LPE films show a clear tendency to step/facet formation, with macrosteps propagating over the whole surface of about $1x1cm^2$. This indicates that at least the surface of Y-oriented LPE LGS films can evoluate to the formation of a facet. These films have a a thickness of a few μm, a high structural perfection with a FWHM of 0.2°, no secondary phases, and are crack-free due to perfect lattice match.

Keywords : langasite, liquid phase epitaxy, BAW, SAW.

1. INTRODUCTION

Langasite-type crystals $La_3Ga_5SiO_{14}$ (LGS), $La_3Ga_{5.5}Nb_{0.5}SiO_{14}$ (LGN), and $La_3Ga_{5.5}Ta_{0.5}SiO_{14}$ (LGT) are considered as superior piezoelectric materials for bulk (BAW) and surface acoustic wave (SAW) applications. They belong to the same trigonal crystal class 32 than quartz and can be grown by Czochralski already to relatively large diameters of 3-inch for LGS [1]. However, bulk growth of large LGS-type crystals is faced with several difficulties, and the crystals often present a defect structure (precipitates, inclusions, striations, dislocations, etc.) which limit their performance in devices.

SAW are very sensitive to the quality of the substrate surface [2,3]. During SAW propagation, substrate surface displacements are of the order of (typically) few Å, and 90 to 95% of the energy is concentrated within one acoustic wavelength of the surface. Thus, fundamental requirements for reproducibility and precision of BAW and SAW devices are defect-free substrate crystals and highly perfect surfaces, since it is the only way to have an undisturbed propagation of acoustic waves.

High-temperature solution (or flux) growth is a growth method which has the potential yield highly perfect crystals (lowest dislocation and defect densities). Films grown by LPE may show a high structural and surface perfection, when growth and substrate parameters are sufficiently met. This has been demonstrated for several materials (ex. : GaAs, GaP, garnets, high-T_C superconductors). Another advantage of near-equilibrium growth is that dopants and impurities will be incorporated in a more homogeneous way than in melt growth. This might be important for reduced acoustic losses for higher Q, as it was shown for quartz.

In LPE, growth occurs near thermodynamic equilibrium, and it is therefore a technique which is very sensitive to substrate parameters. In the case of heteroepitaxy, the lattice mismatch (misfit) between film and substrate lead to the formation of misfit dilocations at the growth interface during growth, and different thermal expansion coefficients may lead to cracking of the LPE films during cooling [4]. The availability of LGS, LGN and LGT substrates to be used for homoepitaxial deposition represents therefore a serious advantage.

In case of homoepitaxy (LPE), the supersaturation required to initiate nucleation is extremely small, and inhomogeneities, scratches, as well as residual strain of the polished substrate surface will strongly affect the initial stages of the growth process. Chemical etching is necessary and efficient to remove the damaged surface layer prior to LPE. The substrate misorientation as well as supersaturation should be as small as possible to allow the Frank- van der Merwe (or layer-by-layer) growth mode [5], for reduced step densities and possibly step bunching [6]. A very low supersaturation (<<1°C) is difficult to adjust over the whole substrate surface. Thus, etching and regrowth may occur, which will also depend on substrate surface inhomogeneities, defects, hydrodynamics, and temperature gradients in the solution. When all parameters are well fitted, the LPE surface may evoluate to the the development of an equilibrium crystal facet. Such surface is perfectly oriented towards defined crystallographic axes, which may cancel problems due to surface misalignment in devices. However, which surface will develop as equilibrium face depends mainly on the "nature" of the solvent and impurities. Finding a suitable solvent/solvent system for such complex compounds, fulfilling all conditions, may therefore represent a real challenge. The aim of this work was to study basic requirements for the achievement of high-quality LGS LPE films for improved SAW and BAW devices.

2. EXPERIMENTAL

2.1 Substrates for LPE

Due to the high sensitivity of the LPE process, the quality of the substrate surface to be used for LPE is a critical parameter. Chemical etching is

needed to remove the surface-layers of polished substrates which may have residual strain. Polishing and etching of LGS has already been investigated [7,8], and good results were achieved by polishing with colloidal silica and etching with HCl:HF:H_2O [7]. Various acids, HF, HCl, HNO_3, H_2SO_4, CH_3COOH, and methods proven to be successful in quartz technology were tested. However, LGS, LGN and LGT have more crystal-chemical similarities with perovskite-type compounds and garnets for which hot orthophosphoric acid is generally used.

X- and Y-oriented (YZ, XZ, in-plane axis, respectively) LGS and LGT substrates were etched in hot orthophosphoric acid at 130°C for 2-3 hours. Formation of the white deposit on the substrate surface could be avoided by mixing. The typical resulting surface morphology of Y-oriented substrates is shown in fig. 1.

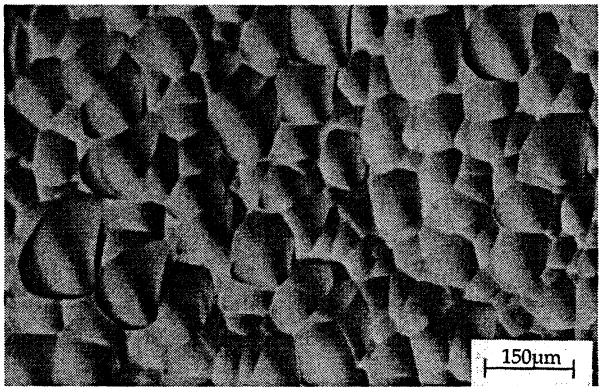

Fig.1. Typical surface morphology of Y-LGS substrates after etching in hot H_3PO_4.

Interpretation of Nomarski microphotographs requires careful consideration, since it is often difficult to distinguish between hillocks and hollows. Thus, the structures of fig.1 appear rather as bulging to the eye, whereas in reality they are concave. Randomly oriented crystal faces could not be well etched, which shows a certain selectivity of this etchant.

Best results were obtained for X-oriented substrates. Due to the polarity of the X-axis in LGS-type crystals, both X-cut substrate faces are not equivalent, e.g. they have not the same "termination" and behave therefore differently upon etching. Striations became visible, as shown in the Nomarski microphotography of fig.2, top, and by AFM a periodicity of about 5µm and height of about 10nm were respectively found for these growth strae, fig 2. bottom.

Striations might be due to solid-solubility of Si/Ga (tetrahedral site, CN IV) in LGS, Nb/Ga in LGN and Ta/Ga in LGT (octahedral site CN VI), associated with temperature fluctuations at the growth interface. These striations cause periodic (3D) variations of lattice parameters [9] (e.g. density) and thus thermal expansion coefficients. Furthermore, they lead to inhomogeneous dopant incorporation. Striations may be eliminated if temperature oscillations at the growth interface during Czochralski growth can be suppressed [10].

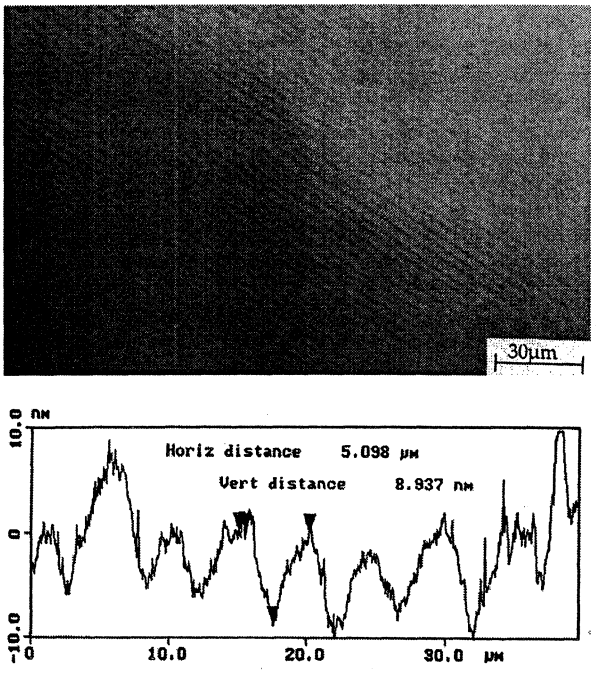

Fig.2. Striations on X-cut LGT substrates after chemical etching in hot H_3PO_4. Top : Nomarski microphotography, bottom : AFM profile.

When a film is grown by LPE on a striated substrate of same composition (homoepitaxy), the first monolayers of the film will try to adapt their composition to minimize the misfit strain. This phenomenon is called lattice pulling effect. The resulting film may then show a variation of composition in function of its thickness, and therefore also, the substrates used for LPE should be sufficiently characterized.

2.2 Solvent system

Potential solvent systems for LGS, LGN and LGT were searched through systematic studies of the already available respective or related phase diagrams. A first selection of possible fluxes was done according to chemical and structural aspects. Ideally, the solvent should be chemically similar (in the type of bonding) to the solute, but with sufficient crystal-chemical differences between solvent and solute constituents to avoid incorporation of solvent species into the crystal.

Alkali vandates, molybdates and tungstates were widely used as fluxes for crystal growth of silicates and germanates. Li_2MoO_4:MoO_3 dissolves readily many oxides, and was used for the growth of BeO, GeO_2, SiO_2, TiO_2, Be_2SiO_4, Y_2SiO_5, as well as for emerald ($Be_3Al_2Si_6O_{18}$). In this study, however, the langasite phase could not be crystallized in the investigated temperature/concentration range by using a Li_2MoO_4:MoO_3 flux.

Another common solvent for oxides is PbO. PbO-B_2O_3 fluxes as well as BaO-BaF_2-B_2O_3 ternary solvent systems were successfully used in flux growth of perovskites and LPE of garnets [11]. Bi_2O_3-based fluxes have similarities with PbO fluxes, and are often used to replace the toxic PbO. However, when large RE ions are present, e.g. in LGX, they are not suitable due to

possible substitution.

PbO-based solvent systems with various solute ions ratios and concentrations were tested by flux-growth experiments. Lanthanum gallate was often obtained as secondary phase, and the use of B_2O_3 lead to crystallization of $LaBO_3$ and was therefore avoided. LPE films of LGS could successfully be grown from a PbO-flux containing 1% PbO_2, and a solute concentration between 15 to 20wt% of stoichiometric LGS. Future work is needed to understand the phase relations and establish the solubility curve, and these results will be reported in a separate paper.

2.3 Growth procedure

The LGS LPE experiments were performed in a vertical tube furnace with 3 heating zones, as described earlier [12]. The starting oxides were hand-mixed and introduced into a cylindrical Pt/Au5% crucible of about 45cm^3. The crucible was closed with a Pt lid to prevent PbO evaporation, and placed in suitable location (for optimized temperature gradients) in the furnace. The temperature was raised to 800°C in 3 hours, and then to 1150°C in 4 hours, followed by 5h soaking at this temperature. The temperature was then lowered to about 950°C and hold at this temperature for about 24hours for equilibration. The Pt lid was then removed, and search of the liquidus temperature was performed by dipping LGS substrates and crystal pieces in the solution while cooling the solution, and X-ray analysis of the phases which crystallize on them [13]. The substrates were fixed with Pt wires on an alumina holder. The films were grown by vertical dipping, with a substrate rotation of typically 15 to 35rpm, in a temperature range of about 950 to 870°C, depending on solvent/solute parameters. After the growth, the films were cleaned in diluted nitric acid at room temperature, and rinsed with distilled water and ethanol.

3. RESULTS

Fig. 3 is a Nomarski microphotograph of a LGS LPE film grown on X-cut LGS substrates.

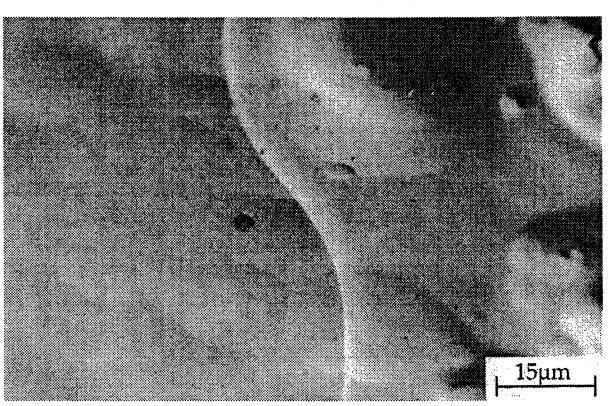

Fig.3. Microphotography of a LGS LPE film grown on X-cut LGS substrate.

These X-oriented films appear as undulating surface with no clear habit, e.g. no development of steps or/and facets with preferential orientation(s). However, this does not exclude the possibility to faceting transition for X-oriented films.

The morphology of a LGS films grown on a Y-oriented LGS substrate (fig.1) is shown in Fig. 4, top. The clear tendency to step/facet formation is an indication that this surface (at least) can develop to an equilibrium facet. Fig. 4 bottom is an AFM profile of the train of macrosteps.

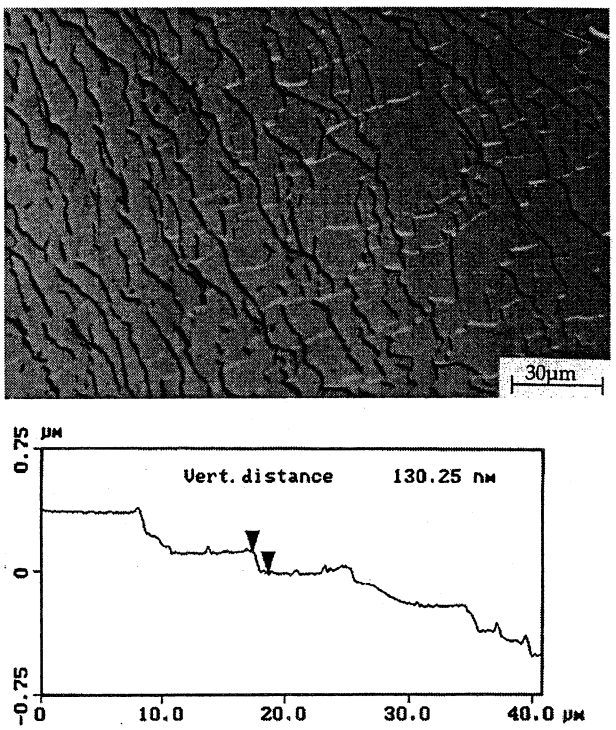

Fig.4. Top : Nomarski micropohotography of macrosteps which propagate on a Y-oriented LGS LPE film. Bottom : AFM profile.

On this LPE film, propagation of macrosteps (step bunches) was observed over the whole surface of about 1cm^2, with some variations in step heights and interstep distances, and with development of larger steps and growth hillocks. As can be recognized in fig. 4, the terraces between macrosteps are very flat.

Step bunching can be described by the kinematic wave theory [14], which was developed to explain water flow movements and traffic jam on crowded roads.

The mechanisms governing step bunching are not well known, but it is assumed that in solution growth interface kinetics as well as bulk transport are important. Unequal rate of incorporation of growth units in the upper and lower steps, and non-linear dependence of the rate of advance of steps on supersaturation which might be caused by impurities (intermittent pinning or stoppers) belong to possible mechanisms. In liquid phase epitaxy, substrate misorientation and hydrodynamics are important aspects to be considered to avoid (or reduce) step bunching. The misorientation of the substrates used in these experiments was typically < 0.5 degrees. The use of substrates with lower misorientation and improved surface preparation, together with optimization of

hydrodynamic conditions and growth parameters (supersaturation), will allow to reduce step bunching and to further improve the surface flatness of the LPE films.

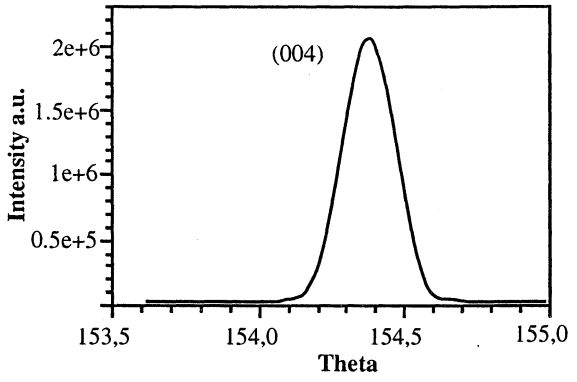

Fig.5. Rocking curve of LGS LPE film, (004) peak with a FWHM of about 0.2 degrees.

The X-ray diffraction analysis show that these films have already a good structural perfection, with a FWHM of about 0.2° for the (004) peak, as shown in fig. 5. No secondary phase(s) could by found by XRD and EDX analysis. In the case of oxides grown from PbO fluxes, Pb incorporation/contamination represents often a problem, and occurs in the form of solvent inclusions or/and by substitution of a lattice ion by Pb. Whereas solvent inclusions can usually be prevented by adjusting the growth rate below a limiting value to avoid growth instability, substitutions mainly depend on crystal-chemical aspects of the system, and cannot (usually) be controlled. In these LGS films, no Pb-contamination could be found by EDX at a detection limit of about 0.1%.

The film thickness was estimated at about 3-4μm by SEM, which gives a mean growth rate of about 23Å/s for the film shown in fig.4. In comparison with LPE of other oxides, this growth rate is about 10 times less than the maximum growth rate observed for $YBa_2Cu_3O_7$ films on $NdGaO_3$ [12] and about 5-20 times less the growth rate of magnetic garnet films (depending on rotation velocity and supersaturation) [15,16].

4. CONCLUSIONS

After establishment of basic requirements, single-crystalline LPE films of LGS could be grown for the first time on X- and Y-oriented LGS substrates.

These films show a very promising surface morphology : step-flow mode on Y-LGS, no cracks, no residual flux, which can be easily removed, and no detected secondary phase(s).

Several aspects have to be further investigated. This includes phase diagram studies, solubility determination for improved supersatiration control, substrates with lower misorientation and improved surface pretreatment, and hydrodynamics/growth parameters optimization.

ACKNOWLEDGMENT

The author express her thanks to Steven Tidrow and Chris Fazi for stimulating discussions, and to Kevin Kirchner and Matt Erwin for the XRD and EDX/SEM analysis. Financial support by the European Research Office of the US Army under Contract No. N68171-99-M-6663 is gratefully acknowledged.

REFERENCES

[1] S. Uda, A. Bungo, C. Jian, Jpn. J. Appl. Phys. 38 (1999) 5516.

[2] H. Matthews, Surface Wave filters, Wiley, New York, 1977.

[3] S. Kelling et al. J. Chem. Phys. 107 (1997) 5609.

[4] C. Klemenz, I. Utke, H.J. Scheel, J. Crystal Growth 207 (1999) 62.

[5] C. Klemenz, I. Utke, H.J. Scheel, J. Crystal Growth 204 (1999) 62.

[6] C. Klemenz, J. Crystal Growth 187 (1998) 221.

[7] S. Laffey, M. Hendrickson, and J.R. Vig, IEEE Frequency Control Symposium (1994) 245.

[8] A.N. Gotalskaya, D. Dresin, S.N. Schegolkova, N. Saveleva, V. Bezdelkin, G. Cherpoukhina, IEEE Frequency Control Symposium (1995) 657.

[9] S.A Sakharov, Yu Pisarevsky, A.V. Medvedev, P.A. Senushencov, V. Lider, IEEE Frequency Control Symposium (1995) 642.

[10] D. Elwell and H. J. Scheel, in : Crystal Growth from High-Temperature Solutions, Academic Press, London, 1975.

[11] S.L. Blank, in : Crystal Growth : Magnetic Garnets by Liquid Phase Epitaxy, JEMMSE, The Pennsylvania State University, 1979.

[12] C. Klemenz, Liquid-Phase Epitaxy of YBCO and NdBCO High-Tc Superconductors, Ph. D thesis Nr. 14645, The University of Tokyo, 2000.

[13] C. Klemenz, H. J. Scheel, J. Crystal Growth 200 (1999) 435.

[14] M.J. Lighthill, G.B. Whitham, Proc. Roy. Soc. 229 (1955) 218 and 317.

[15] R. Ghez and E.A. Giess, Mat. Res. Bull. 8 (1973) 31.

[16] M.H. Randles, in : Crystals : Growth, Properties, and Applications, Vol.1 : Crystals for Magnetic Applications, ed. C.J.M. Rooijmans, Springer, Berlin-Heidelberg-New York, 1978, p. 71-96.

PIEZOELECTRIC ALUMINUM NITRIDE THIN FILM FOR ULTRASONIC TRANSDUCERS

L. Sevely, L. Valbin, S. Spirkovitch

Groupe ESIEE Paris – Noisy-le Grand – France

ABSTRACT

Piezoelectric aluminum nitride (AlN) thin films have been developed to realize ultrasonic transducers.

AlN up to 1.5µm is deposited at low temperature (140°C) by reactive DC magnetron sputtering of an Al target in argon and nitrogen on Si, $Si/SiO_2/Al$, and Si/Al substrates, and is wet etched (rates from 0.1 µm/min to 0.2 µm/min and selectivity of 1:10 with Al, and no etching with Si).

SiO_2/Al/AlN/Al, Al/AlN/Al and Si/AlN/Al square and circular membranes, from 10µm to 1.5mm size are fabricated using silicon deep reactive ion etching (DRIE), which gives etch profiles about 90°, which allows larger integration density than wet anisotropic etching for ultrasonic transducers arrays.
By varying size and thickness of membranes, resonance frequencies from 10kHz to 20MHz are expected, acoustic and electrical measurements are in progress.

Ultrasonic transducers using this technology will be used to measure flows velocity by Doppler method. Other potential applications for ultrasonic transducers include medical ultrasounds and sonar.
Other structures are also in progress such as Thin Film Bulk Acoustic Resonator (TFBAR), and Lamb wave devices using this technology.

Aluminum Nitride, Piezoelectric thin film, Micromachined ultrasonic transducer.

1 INTRODUCTION

This paper reports the use of AlN deposited by reactive DC magnetron sputtering with micromachining technology to realize micromachined ultrasonic transducers.
Micromachined ultrasonic transducers have been built using PZT and wet etch silicon, Ref. 1.
Because silicon wet etch is anisotropic, low density integration is expected. Using silicon deep reactive ion etching, high density integration is possible.
Because AlN is deposited at low temperature, electronic can be integrated on same wafer.
Micromachined ultrasonic transducer integrated with electronic on same wafer will allow high performance system.

2 EXPERIMENT

AlN thin films were deposited on different substrates by reactive DC magnetron sputtering of a high purity (99,999%) aluminum target in a gas mixtures of argon (99,9997%) and nitrogen (99,9991%)
Sputtering process parameters for AlN thin film deposition are listed in Table 1

Substrate	$Si/SiO_2/Al$, Si(100)/Al	Si(100)
Power (W)	700	700
Substrate temperature (°C)	140	220
Pressure deposition (mbar)	$0.66\ 10^{-2}$	$0.53\ 10^{-2}$
N_2 / Ar + N_2 (%)	65	65

Table 1: sputtering process parameters.

The vacuum chamber is evacuated by a turbo molecular pump to a pressure below $4\ 10^{-7}$ mbar, then the substrate is heated up to deposition temperature.
The target is pre-sputtered in a pure argon atmosphere for about 5 minutes to remove native oxide layer on Al target.
Nitrogen gas is admitted and AlN deposition begins.
Deposition rate is about 1.4µm/h and AlN thickness uniformity is about 10% on 100 mm diameter wafers.

3 AlN CARACTERIZATION

2.1 Thin film crystallography

To improve the electromechanical coupling factor, crystallographic c-axis orientation perpendicular to substrate must be obtained.
The X-ray diffraction θ–2θ was performed on AlN thin film samples. Figs 2.1 and 2.2 show XRD measurement of AlN thin films on various substrates.
AlN is deposited with c-axis orientation perpendicular to substrate.

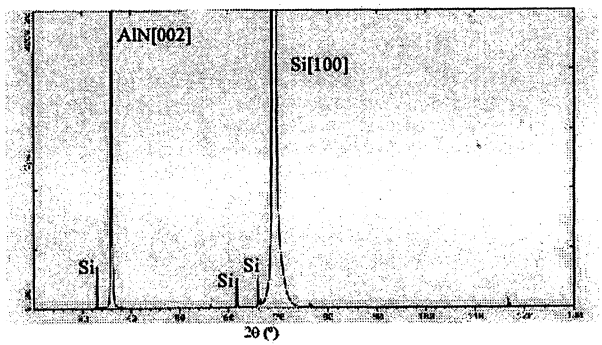

Fig. 2.1: Si(100)/AlN(0.7 µm)
(Sputtering process parameters, see Table 1)

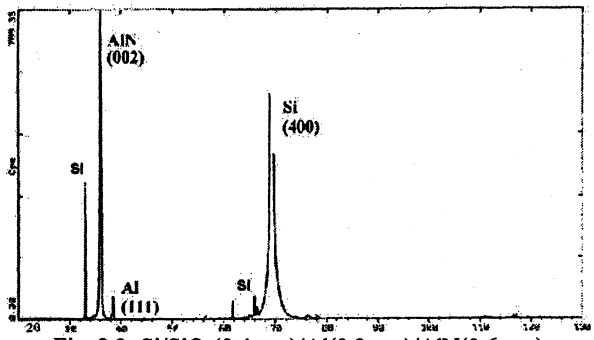

Fig. 2.2: Si/SiO_2(0.4 µm)/Al(0.2 µm)/AlN(0.6 µm)
(Sputtering process parameters, 750 W, 160 °C, 0.42 10^{-2} mbar, 64 % N_2)

2.2 Surface observation of AlN thin film

Atomic force microscopy (AFM) was used to measure AlN roughness.
AlN surface was observed at the end of the process, after deposition and etching of top aluminum to realize top electrode.
Figs 2.3 and 2.4 show AFM measurements

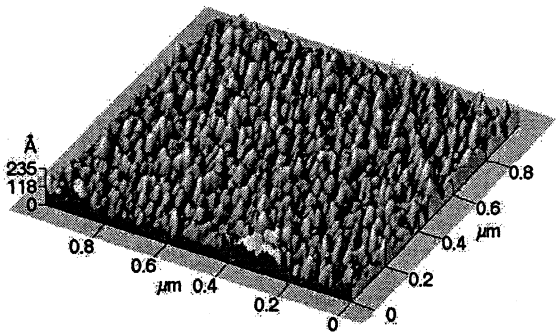

Fig. 2.3: Si(100)AlN(0.7 µm)
(Sputtering process parameters, see Table 1)

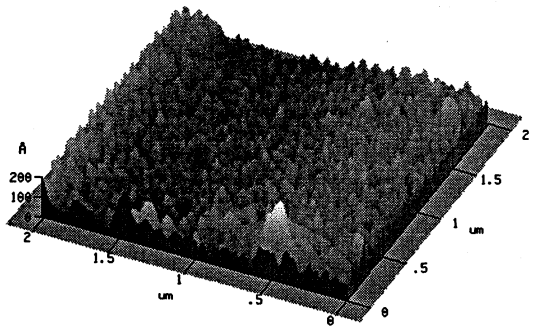

Fig. 2.4: Si(100)/ Al(0.2 µm)/AlN(0.9 µm)
(Sputtering process parameters, see Table 1)

Many crystal grains of AlN on Si and AlN on Si/al have a 40nm in diameter, and AlN roughness is about 3.5nm on Si and 4.4nm on Si/Al.

According to Ref. 2, great quality surface acoustic wave (SAW) is expected.

2.3 Film stress

Film stress is given by Stoney formula (1) by measuring pre- and post- AlN deposition wafer curvatures using surface profilometry.

$$\sigma = \left(\frac{1}{R_{post}} - \frac{1}{R_{pre}}\right)\frac{E_s}{6.(1-\nu_s)}\frac{t_S^2}{t_f} \quad (1)$$

where Es and vs are substrate Young modulus and Poisson ratio, ts and tf are substrate and film thickness and R_{post} and R_{pre} wafer curvature after and before film deposition.

Substrate	Si(100)	Si(100)/Al
Stress	0	100 MPa

Table 2: (Sputtering process parameters, see Table 1)

New sputtering process parameters are expected to decrease tensile stress by changing pressure deposition Ref. 2.
Al deposited on AlN to perform top electrode doesn't modify the stress.
Al/AlN/Al or Si/AlN/Al membrane can be fabricated.

2.4 Electrical measurement

Relative permittivity was measured by capacitance extraction (2) with a Multi-Frequency LCR meter HP4275A, the voltage and frequency were respectively $1V_{pp}$ and 40kHz.

$$\varepsilon_{33}^{T} = \frac{t_{AlN}}{\varepsilon_0 A}C \quad (2)$$

Resistivity was measured by capacitance leakage current (3), the leakage current was 1µA, electrical field was about 150 MV/cm and electrical field breakdown with a Curve Trace Tektronix 477.

$$\rho(E) = \frac{A}{t_{AlN}}\frac{V}{I(E)} \quad (3)$$

Density current is exponential (4) with electric field Ref. 3.

$$J(E) \sim J_0 e^{E/E_0} \Rightarrow \rho(E) = \frac{E}{J(E)} \approx e^{-E/E_0} \quad (4)$$

Results are shown in Table 2.

Substrate	Si(100)	Si(100)/Al	Si/SiO2/Al
ε_{33}^{T}	10.7	10	11
ρ(E) (GΩ.cm)	15	2.1	3.2
E_{br} (MV/cm)	2.5	4.2	2.5

Table 3: (Sputtering process parameters, see Table 1)

4 APPLICATIONS

3.1 Transducer fabrication

A cross section of a complete device is shown in Fig. 3.1

Double-side polished, 100 mm diameter by 500 µm thick wafers are used.
Wafers are oxidized and back side oxide is removed. Bottom metal (0.2 µm Al) is deposited and patterned by photolithography. Piezoelectric layer (1 µm AlN) is deposited and patterned by photolithography. Top metal (0.2-1 µm Al) is deposited and patterned by photolithography. Al is deposited on back side and patterned by photolithography then silicon back side is etched by deep reactive ion etching (Bosch process, etch rate: 7.5 µm/min).Then oxide can be etched by RIE.
Circular and square membranes were realized with central and ring top electrode.
Optical top view of ultrasonic transducers, 800 µm diameter, with central electrode (200 µm diameter) and ring electrode (600 µm internal diameter) are shown in Figs 3.2 and 3.3.
For each devices, thickness of each layer is:
SiO_2: 0.4 µm
Bottom Al: 0.2 µm
AlN: 1 µm
Al: 0.8 µm

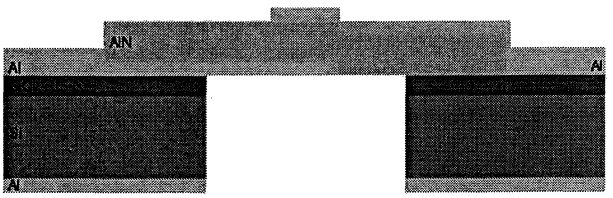

Fig. 3.1: Cross-section of ultrasonic transducer

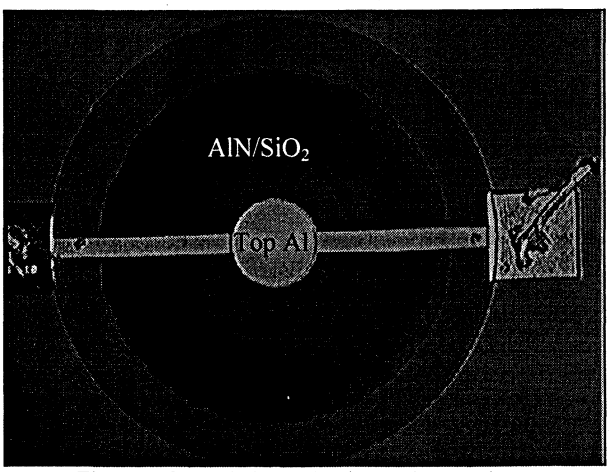

Fig. 3.2: Central electrode ultrasonic transducer

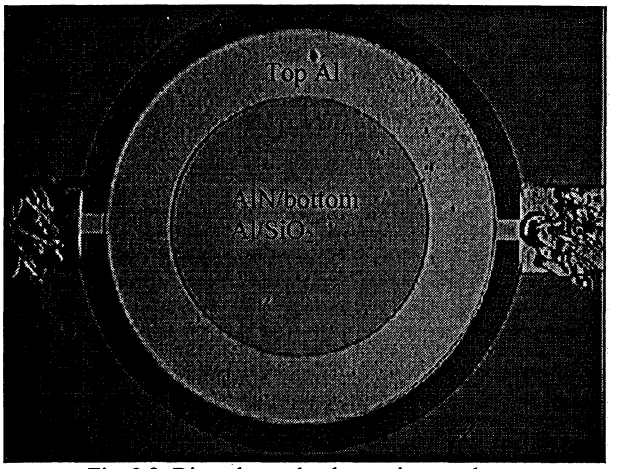

Fig. 3.3: Ring electrode ultrasonic transducer

3.2 First experimental results

Sensitivity test was realized in air. Generated electrical charges were measured (Table 4).

electrode	central	ring
sensitivity	No signal	1 pC/mbar

Table 4: (frequency < 50 kHz)

Because electrical measurement is not enough sensitive, we can't detected generated charge.
In addition, there is too much stress in membrane and thickness ratio between layers is not optimum , so sensitivity decreases.

4 CONCLUSIONS

This paper has presented Aluminum Nitride piezoelectric thin film to realize ultrasonic transducers.
Al/AlN/Al membrane with a better process to realize no stress membrane is expected.
Because there is no stress in AlN deposited on Si, membrane using SOI wafer will be realized.
To improve electrical measurement new electrical measurement circuit will be developed.
First results show that using AlN and silicon deep reactive ion etching is a good way to realize high density micromachined ultrasonic transducers.

5. ACKNOWLEDGEMENTS

The authors acknowledge P. bassoul (ESPCI) for XRD measurements, U. Rabibisoa (IOTA) for AFM measurement and SMM for his help for using silicon deep reactive ion etching.

5 REFERENCES

Ref 1: J. Bernstein, K. Houston, L. Niles, S. Finberg, H. Chen, L. E. Cross, K. li, K. Udayakumar, "Micromachined ferroelectric transducers for acoustic imaging"
Proceeding of transducers 97
Ref 2: H.M. Liaw, F.S. Hickernell, "The characterization of sputtered polycristalline aluminum nitride on silicon by surface acoustic wave measurements", IEEE Transactions on

ultrasonics, ferroelectrics, and frequency control **42**, pp. 404-409, 1995

Ref. 3: L. Valbin, L. Sevely, S. Spirkovitch, "Low temperature piezoelectric Aluminum Nitride thin film"
Proceeding of Micromachining and Microfabrication SPIE 2000

ELASTIC CONSTANTS AND TEMPERATURE-COMPENSATED ORIENTATIONS OF $GaPO_4$

C. Reiter, H. Thanner, W. Wallnöfer, P. M. Worsch and P. W. Krempl

AVL List GmbH, Hans-List-Platz 1, A-8020 Graz, Austria

ABSTRACT

$GaPO_4$ is of interest for bulk and surface acoustic wave applications due to its outstanding temperature stability and relatively high coupling. An evaluation of elastic constants using the frequency measurements of thickness shear and extensional resonators between –50 °C and 700 °C was undertaken. For singly rotated Y-cuts, two angles with temperature compensation exist for any temperature. The equivalent circuit parameters C_0, C_1 and R_1 which are typically achieved for both groups of orientations are given. The properties of interesting surface acoustic wave orientations were calculated using the new data set. An overview of multiply rotated orientations is given.

Keywords: gallium orthophosphate, $GaPO_4$, temperature compensation, BAW, SAW, high temperature

1. INTRODUCTION

$GaPO_4$ is a quartz-homeotypic piezoelectric crystal. It possesses temperature compensated cuts for piezoelectric BAW and SAW resonators and filters, high electric resistivity and no pyroelectricity (Ref. 1). These properties are similar to quartz, but $GaPO_4$ shows higher electromechanical coupling and a high thermal stability of its physical properties up to an irreversible transition into the cristobalite-phase at 970 °C.

2. ELASTIC CONSTANTS

The first measurements of the elastic constants were done by Brillouin scattering (Ref. 2) and by the method of pulse-echo (Ref. 3), with good agreement in most constants at room temperature. Brillouin scattering measurements were done up to 327 °C. Due to the excellent high temperature properties of $GaPO_4$ a new evaluation of elastic constants between –50 °C and 700 °C was performed.
The determination was done by measuring the resonances of thickness shear and extensional resonators (Ref. 4). The elastic constants and the temperature coefficients were calculated by a least squares algorithm. Resonator samples were bevelled only outside the electrodes. This bevelling was done to determine the thickness of the resonators accurately and to have energy trapping too. The theoretical model for the determination of the elastic constants was the infinite extended plane plate. In this model the energy trapping effect is not taken into consideration and so the elastic constants are sometimes too high. Thus the agreement between experimental and theoretical frequency temperature behaviour of BAW and SAW resonators was not very good and a new determination with the same measurement data was performed.

2.1 Model for plano-convex resonators

In this evaluation the energy trapping is approximated by an expression of Stevens and Tiersten (Ref. 5). This expression is developed for the frequency wavenumber dispersion relation for doubly rotated plano-convex quartz plates.

$$\omega_{nmp}^2 = \frac{n^2\pi^2\hat{c}}{4h_0^2\rho}\left[1+\frac{1}{n\pi}\left(\frac{2h_0}{R}\right)^{1/2}\left(\sqrt{\frac{M'_n}{\hat{c}}}(2m+1)+\sqrt{\frac{P'_n}{\hat{c}}}(2p+1)\right)\right] \qquad (1)$$

nmp *vibration mode; $n = 1,3,\ldots$; $m, p = 0,2,4,\ldots$*
n00 : harmonic overtone
nmp : anharmonic overtone $m \neq 0, p \neq 0$
R *curvature radius*
$2h_0$ *resonator thickness*
M', P' *linear combination of elastic constants*

$$\hat{c} = \bar{c}\left(1-\frac{8k^2}{n^2\pi^2}-2\hat{R}\right) \qquad (2)$$

$\bar{c}$ *effective elastic constant (piezoelectric stiffened)*
k *coupling coefficient*
$\hat{R}$ *electrode massloading*

2.2 Experimental determination

The least squares algorithm used for calculation in (Ref. 4) was modified with equation (1) for the new determination. The new determination was done for the temperature coefficients only, because calculations done with elastic constants from Brillouin scattering measurements at room temperature show good agreement with experimental results. So the elastic constants at room temperature given in (Ref. 2) are used as room temperature values in the new determination too.
The temperature coefficients were determined only by using the change in resonant frequency of the resonators related to resonant frequency at room temperature to minimise the error due to the error of thickness and curvature of the contoured resonators.
The anharmonic frequency spacing and the resonant frequency depend on the curvature of the contoured resonator. To take the curvature into consideration the anharmonic frequency spacing of the different resonators were used to determine an "equivalent" radius of the curvature. The determination was only possible for the singly rotated thickness shear Y-cut resonators, but not for the singly rotated thickness extensional X-cut resonators, because the admittance frequency spectra do not show any anharmonic frequencies.
But considering that this expression is correct for plano-convex resonators only, the use of the model of Stevens and Tiersten for these samples is only an approximation.
A typical admittance frequency spectrum for a singly rotated Y-25 ° BAW[1] resonator is shown in Figure 1.

[1] According to standard IEEE 176-1978

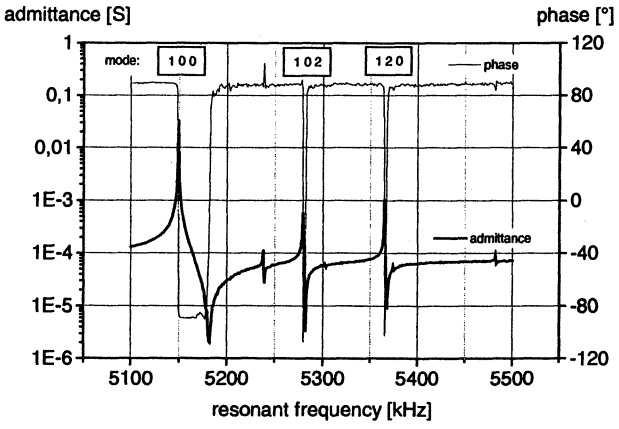

Figure 1: Admittance frequency spectrum of a singly rotated Y-25 ° BAW resonator

The determination of the temperature coefficients were done up to the 3rd order. The results are shown in Table 1.

Table 1: Elastic constants and temperature coefficients

	c^E @ RT [10^9 Nm^{-2}]	$Tc^{(1)}$ [10^{-6} K^{-1}]	$Tc^{(2)}$ [10^{-9} K^{-2}]	$Tc^{(3)}$ [10^{-12} K^{-3}]
c^E_{11}	66.58±0.37	-44.1	-28.5	-59.4
c^E_{12}	21.81±0.70	-226.7	-70.8	-205.7
c^E_{13}	24.87±0.60	-57.6	41.3	-109.9
c^E_{14}	3.91±0.33	507.2	280.6	-99.9
c^E_{33}	102.13±0.55	-127.5	-18.3	-134.8
c^E_{44}	37.66±0.27	-0.4	-43.8	-37.1
c^E_{66}	22.38±0.32	44.9	-7.9	11.9

3. TEMPERATURE COMPENSATED SINGLY ROTATED Y-CUTS

There are two ranges of rotation angles for thickness shear BAW resonators with temperature compensation of resonant frequency. The difference between the two ranges is the strength of electromechanical coupling.
The dependence of the electromechanical coupling from rotation angle is shown in Figure 2. This Figure also shows that for applications with no need for temperature compensation electromechanical coupling up to 20 % for resonators near Y-cut is possible.

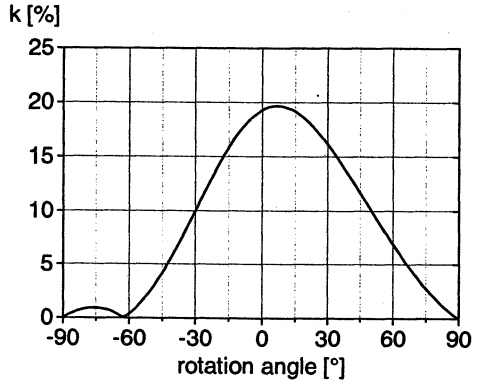

Figure 2: Electromechanical coupling versus rotation angle of singly rotated BAW resonators

3.1 Resonators with high electromechanical coupling

The electromechanical coupling is between 15 % and 17 %, which is about two times the coupling of quartz AT-cut. The range of rotation angles is between Y-17 ° and Y-11.5 °. For an inversion temperature up to 400 °C these cuts are showing a parabolic frequency temperature dependence with a 2nd order temperature coefficient (2nd TCF) ranging from 18 10^{-9} to 6 10^{-9} $°C^{-2}$ which is flatter than quartz BT-cut with 40 10^{-9} $°C^{-2}$.
The dependencies of 2nd TCF and T_0 versus rotation angle are shown in Figure 3.

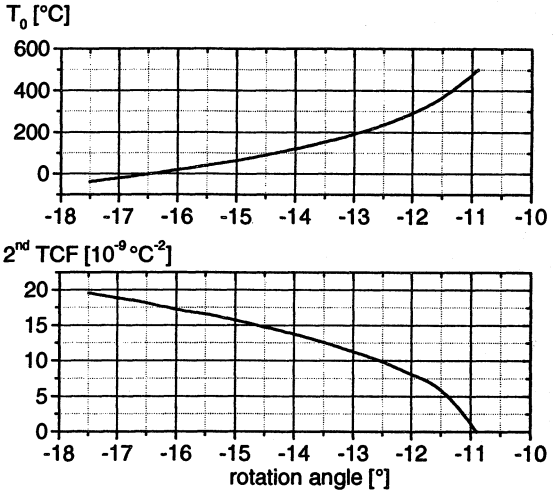

Figure 3: Dependence of inversion temperature T_0 and 2nd temperature coefficient 2nd TCF from rotation angle for singly rotated BAW resonators (calculated)

The resonant frequency temperature behaviour of a Y-16.5 ° resonator with an inversion temperature at 18 °C is shown in Figure 4.

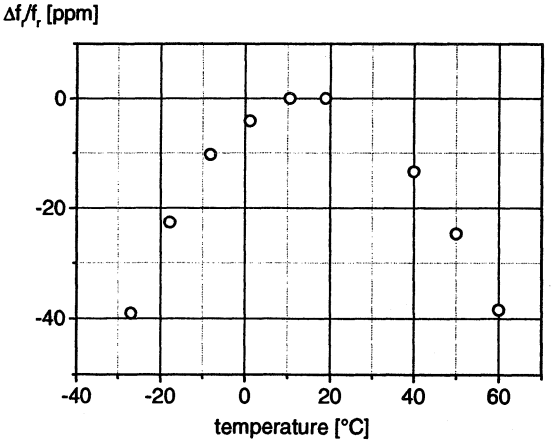

Figure 4: Experimental data for a Y-16.5 ° BAW resonator

Resonators with a rotation angle of Y-10.8 ° are showing cubic frequency temperature behaviour with a point of inflection near 500 °C, depending on the curvature of the contoured resonator, as seen in Figure 5.

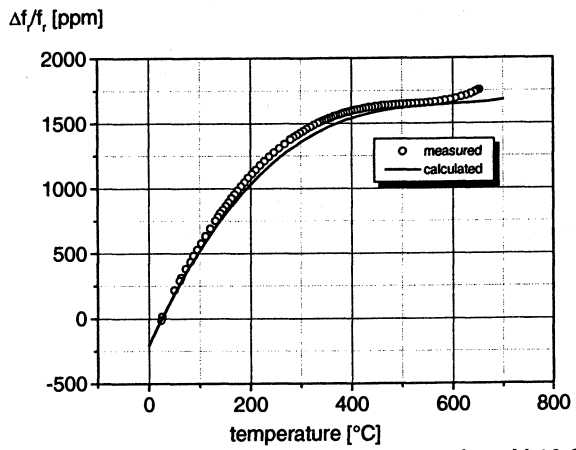

Figure 5: Experimental and calculated data for a Y-10.8 ° singly rotated BAW resonator

Resonators with a rotation angle near Y-10.8 ° are showing in the temperature range between 350 °C and 650 °C a change in resonant frequency lower than ±30 ppm.

3.2 Resonators with low electromechanical coupling

Temperature compensated low coupling resonators are near a rotation angle of Y-84 °. A Y-84 ° resonator is showing an inversion temperature of 87 °C – Figure 6. The coupling is lower than predicted at about 0.3 % ... 0.4 %.

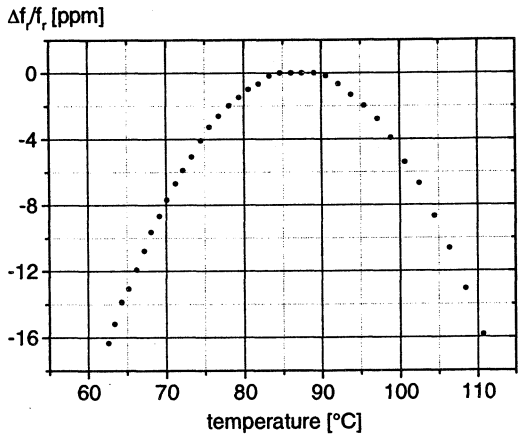

Figure 6: Frequency temperature behaviour of a low coupling singly rotated BAW resonator with rotation angle of Y-84 °

4. RESONATOR PROPERTIES

The simple linear equivalent circuit of a single resonance mode of a BAW resonator is shown in Figure 7. The most important parts of this circuit are R_1, C_1 and C_0.

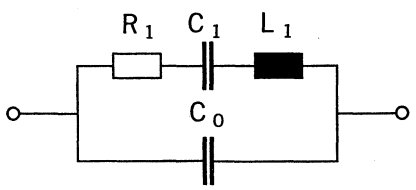

Figure 7: Simple crystal equivalent circuit

Typical data for $GaPO_4$ resonators with a crystal diameter of 7.4 mm, an electrode diameter of 3.6 mm and a fundamental resonant frequency of about 6 MHz are given in Table 2.

Table 2: Typical resonator data

	$GaPO_4$ Y-16.5 °	$GaPO_4$ Y-84.0 °	Quartz AT-Cut
	at ambient pressure		
R_1 [Ω]	5-10	4000	7-50
C_1 [fF]	40-60	(30-60) 10^{-3}	8-12
C_0 [pF]	2-3	2.5	1.6-2.6
k [%]	15-17	0.3-0.4	9
Q [1000]	100-200	200	10-100
	at high vacuum		
Q[1000]	1200	**8.000**	900

In Table 2 electromechanical coupling factor k and the quality factor Q are also given. These parameters are showing for low coupling resonators very high motional resistances and on the other hand the motional capacity is very low. Thus the quality factor at ambient pressure is as high as resonators show with high coupling.

Low coupling $GaPO_4$ resonators under vacuum at about 0.1 mbar show an increase of the quality factor up to 8.000.000. This increase is due to the fact that the resonators were heated up to 500 °C after deposition of the electrodes. Maybe this heating procedure leads to a decrease of stress between electrodes and crystal in conjunction with the measured increase of quality factor.

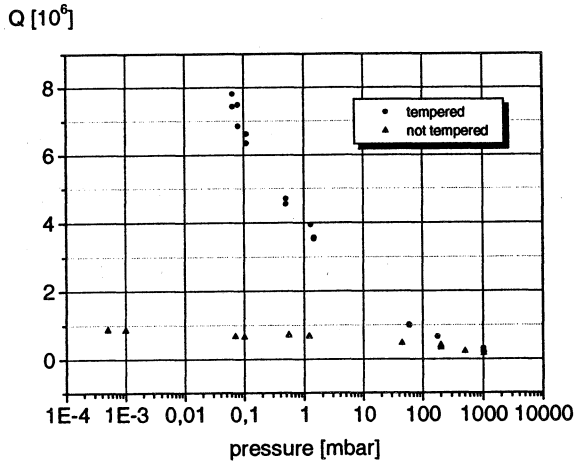

Figure 8: Influence of pressure on quality factor of tempered and not tempered $GaPO_4$ resonators (Y-84 °)

Figure 8 shows that only tempered $GaPO_4$ resonators are showing such a strong increase of quality factor under low pressure. This increase of quality factor is due to a decrease of motional capacity C_1 and motional resistance R_1 which is shown in Figure 9.

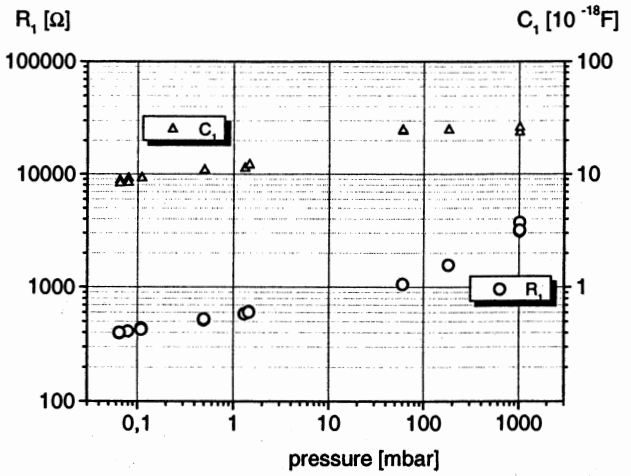

Figure 9: Pressure dependence of C_1 and R_1 of low coupling $GaPO_4$ resonators (Y-84 °)

These properties makes this cut suitable for OCXO applications.

5. SAW RESONATORS

An other type of acoustic applications, for which $GaPO_4$ is of interest due to its high electromechanical coupling and its temperature compensated cuts, are those which use surface acoustic waves (SAWs). Results of calculations of SAW properties done with earlier sets of material constants were published (Ref. 6, 7, 8). With the new set of elastic constants, new calculations were performed. Velocities are between 2300 m/s and 2900 m/s, which means that the elements for a given frequency are smaller than in quartz.

The orientations with propagation along the x axis are especially interesting because they show no beam steering. For most of these orientations, an inversion temperature is predicted. The properties for temperature compensation are shown in Figure 10. Angles are given starting from a z plate. For room temperature, a coupling k^2 of 0.30 % and a second temperature coefficient 2^{nd} TCF of $-19\ 10^{-9}\ K^{-2}$ are both significantly better than the values for the quartz ST cut. For higher inversion temperatures they improve further, up to 0.41 %, 3.5 times the value of the quartz ST cut, and $-18\ 10^{-9}\ K^{-2}$ for the x-propagation cut compensated at 275 °C which is the highest predicted inversion temperature. Experimental results (Ref. 7, 9) show inversion temperatures which are below the calculated values, the reasons for this deviation are not yet clear.

There exist many other temperature compensated orientations with 2 or 3 angles. Figure 11 shows contour plots of 1^{st} temperature coefficients of frequency for different values of the first Euler angle. For the whole studied range up to 700 °C, temperature compensation is possible.
Two important SAW applications for which $GaPO_4$ is of interest are:

- Intermediate frequency filters, which need a combination of high coupling and good temperature compensation; the low SAW velocities in $GaPO_4$ further allow a miniaturisation of the filter (Ref. 10);

SAW sensors. especially if the operating temperature is so high that other materials do not work reliably or stable. The possibility of passive sensor elements with wireless transmission allows precise measurements even in extreme environments or on moving parts.

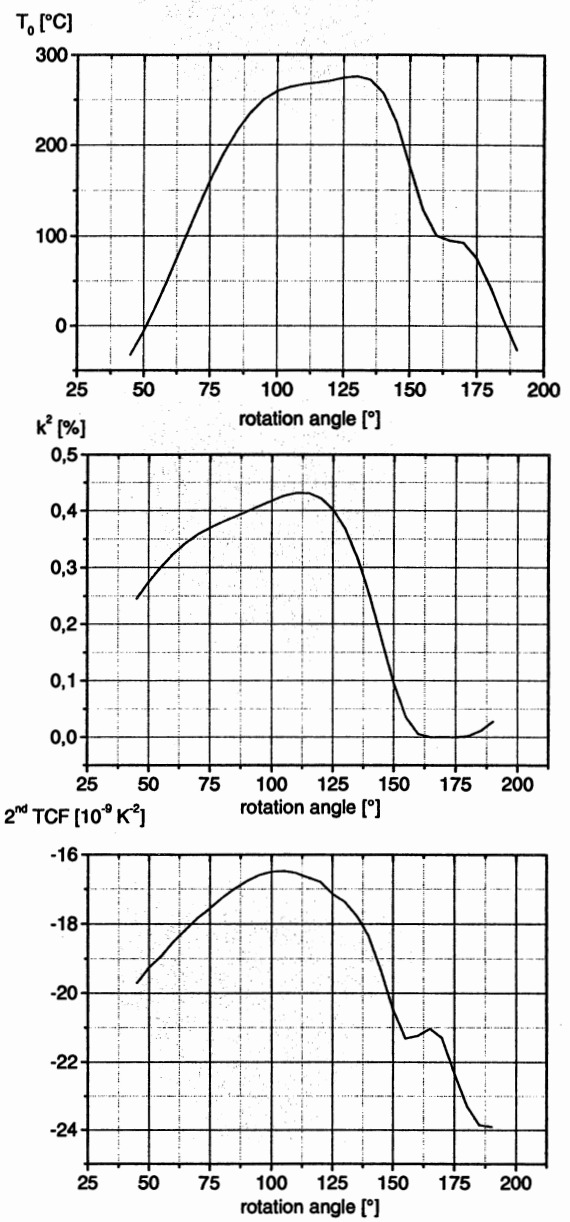

Fig. 10: top: Inversion temperatures for singly rotated X-propagation SAW orientations of $GaPO_4$ (angle starting from z plate); centre: coupling k at T_0; below: 2^{nd} temperature coefficient of resonant frequency at T_0

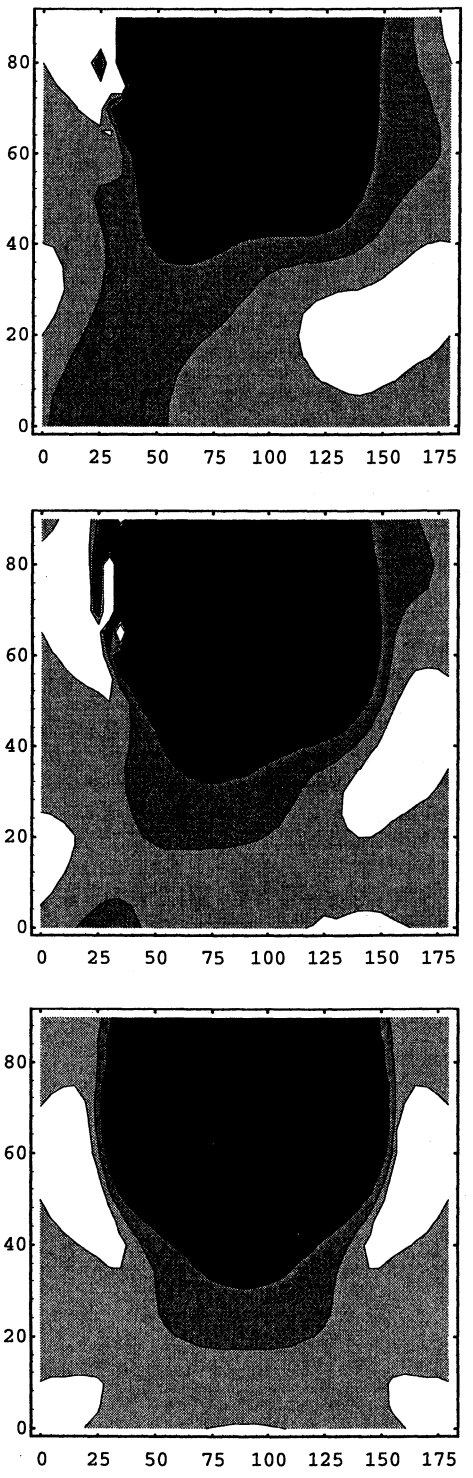

Fig. 11: Contour plots of 1st temperature coefficient of frequency at 25 °C for orientations (λ, μ, θ). top: λ=0 °, centre: λ=15 °, below: λ=30 °; horizontal axis: μ, vertical axis: θ; contours for –10 ppm/K, 0 ppm/K and 10 ppm/K are given

6. CONCLUSIONS

The elastic constants are now determined in the temperature range between –50 °C and 700 °C. This data set allows a prediction of BAW and SAW resonator properties. One prediction was done for low coupling BAW resonators with a following experimental confirmation.
For singly rotated Y cut resonators two ranges of rotation angles for temperature compensated BAW resonators are existing, for high and low coupling resonators respectively.
High coupling resonators are compensated up to 650 °C with a coupling between 15 % and 17 %.
Low coupling resonators are showing a coupling of about 0.3...0.4 %.
Under vacuum the quality factor is increasing up to 8.000.000 for tempered resonators which were heated up to 500 °C. These properties makes this cut suitable for OCXO applications.

SAW resonators are showing high coupling and good temperature compensation, these properties are needed for intermediate frequency filters. The low SAW velocities allow miniaturisation of the filters too.
Another application of $GaPO_4$ are high temperature devices where other materials do not work reliable or stable.

ACKNOWLEDGEMENT

This work was supported in part by the European Communities under the Brite-Euram project BE96-3105.

7. REFERENCES

1. C. Reiter, P. W. Krempl, H. Thanner, W. Wallnöfer and P. M. Worsch. Proc. 3. European workshop on piezoelectric materials. Montpellier. 5-6. 10. 2000. to be published.
2. W. Wallnöfer, P. W. Krempl, A. Asenbaum. The American Physical Society. third series. vol. 49. number 15. (1994), 10075-10080.
3. D. Palmier. Thèse Université Montpellier II. Nov. 1996.
4. C. Reiter. Diplomarbeit. Technische Universität Graz. 1998.
5. D. S. Stevens and H. F. Tiersten. J. Acoust. Soc. Am. vol 79 (6). (1986), 1811-1826.
6. W. Wallnöfer, J. Stadler and P.W. Krempl. Proc. 7th Eur. Time and Frequency Forum. Neuchatel. 16-18.3. 1993, 653-657.
7. E. Henry Briot, E. Bigler, W. Daniau, G. Marianneau. First joint meeting EFTF/IFCS-Besancon. 12.-16. 4. 1999.
8. M.P. da Cunha and S. A. Fagundes. IEEE Trans. UFFC 46 (6). (1999), 1583-1590.
9. E. Bigler, S. Ballandras, C. Bonjour, D. Palmier and E. Philippot. Proc. 1994 IEEE Ultrasonics Symp.. Cannes. 1.-4. 11. 1994, 385-389.
10. M. Solal. Proc. 3. European workshop on piezoelectric materials. Montpellier. 5-6. 10. 2000. to be published.

ATOMIC FOUNTAINS

Chairman: André Clairon

FIRST COMPARISON OF REMOTE CESIUM FOUNTAINS

T. Parker*, P. Hetzel#, S. Jefferts*, S. Weyers#, L. Nelson*, A. Bauch#, J. Levine*

*National Institute of Standards and Technology
325 Broadway, Boulder, CO 80305, USA
#Physikalisch-Technische Bundesanstalt,
POB 3345, D-38023 Braunschweig, GERMANY

1. ABSTRACT

The frequencies of the cesium fountain primary frequency standards at the National Institute of Standards and Technology and the Physikalisch-Technische Bundesanstalt have been compared. Two-way satellite time and frequency transfer and GPS carrier-phase were the principal frequency-transfer techniques used to make the comparison. For the 15-day interval in which both fountains were in operation the frequencies were compared with an additional uncertainty due to the comparison process of only 5.8×10^{-16}. The two standards agree within their stated one-sigma uncertainties of ~ 1.7×10^{-15}.

Key Words: atomic frequency standard, cesium fountain, comparison.

2. INTRODUCTION

During the months of August and September, 2000 the new cesium fountains at the National Institute of Standards and Technology (NIST) and the Physikalisch-Technische Bundesanstalt (PTB) were operated at nearly the same time. The NIST fountain, NIST-F1, was in operation during the period MJD (Modified Julian Date) 51764 to 51794, and the PTB fountain, CSF1, was operated over the period MJD 51764 to 51779. Two additional periods of operation for the PTB standard (MJD 51799 to 51814 and 51824 to 51839) are also included in this comparison. In the first PTB run there is a 15-day overlap with the NIST run. These evaluations have all been reported to the Bureau International des Poids et Mesures (BIPM) and details of the frequency standards have been presented in other papers at this conference [1, 2]. The PTB-CSF1 was operated at constant operational parameters and the real measurement time comprised about 94% of the nominal total measurement time of 1080 hours. During the operation of NIST-F1 a range of atom densities was used so it is not practical to shorten the comparison period to coincide exactly with that of the first interval for CSF1. Therefore, the comparison must be made by extending the PTB interval with a stable (but not necessarily accurate) frequency reference. This can be done with either EAL, which is a free atomic scale calculated by the Bureau International des Poids et Measures (BIPM), or the post processed NIST maser ensemble, AT1E. The fact that the overlap of the two fountain runs is not exact means that the stability of the frequency reference contributes to the uncertainty of the comparison.

Long-distance techniques for frequency comparison must be used since the two primary frequency standards are separated by thousands of kilometers, and this also adds an additional uncertainty to the comparison. An evaluation of the extrapolation and frequency transfer-uncertainties is presented in this paper, and overall comparison uncertainties are calculated.

3. FREQUENCY TRANSFER

Three techniques for time and frequency transfer were used for the fountain comparison in order to minimize the chance of a statistical aberration. These techniques are Two-Way Satellite Time and Frequency Transfer (TWSTFT) [3], GPS carrier-phase [4], and GPS common-view [5]. The GPS common-view comparison was made with data from the BIPM publication Circular T, where corrections are made using precise orbits and measured ionospheric data. The TWSTFT measurements followed the standard three days per week (Monday, Wednesday and Friday) BIPM schedule and were made at Ku-band using a commercial communications satellite. The two-way data used for the fountain comparison were the same as that reported to the BIPM, except that data comparing UTC(NIST) to the maser H2 at PTB was extracted. The GPS carrier-phase data comes from two dual-frequency, geodetic-quality receivers located at NIST and PTB [6]. The TWSTFT and carrier-phase data both give the time difference between UTC(NIST) (which is derived from a maser ensemble) and the maser H2. The fountain frequencies can be related to these two standards via internal measurements. At PTB the fountain directly measures the frequency of H2. At NIST an internal measurement system is used to relate the frequency of the specific maser used as the fountain reference to UTC(NIST). The uncertainty of the NIST internal measurement is well under 1×10^{-16} at 15 days. The common-view GPS data relate the fountain frequencies to International Atomic Time (TAI) via the reference clocks for each standard.

Figure 1 shows time-difference data for UTC(NIST) - H2 via the TWSTFT link for a 200 day period that includes the intervals of the fountain comparison. Frequency offset and drift have been removed. It is evident in Fig. 1 that the day-to-day

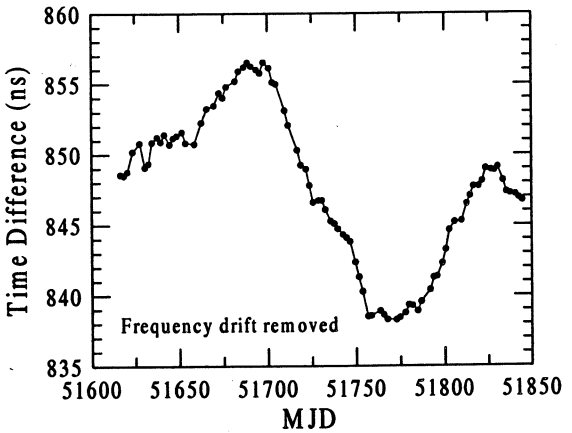

Figure 1. Time difference between UTC(NIST) and H2 via two-way.

variations are typically less than 1 ns. The long-term variations are due to clock instabilities. Figure 2 shows that the time deviation, $\sigma_x(\tau)$, for this data is about 300 ps at a few days. It is very likely that even at a few days the time deviation values are also influenced to some extent by clock noise. $\sigma_x(\tau)$ was calculated for both the unevenly spaced two-way data (solid circles) and for data interpolated to an even spacing (diamonds). If the time difference data were taken with an even spacing $\sigma_x(\tau)$ would fall between the two curves. Measurements between UTC(NIST) and H2 with GPS carrier-phase give time-deviation values at two days of about 200 ps, indicating that carrier-phase may be slightly quieter than two-way in the short term. By differencing the data from both transfer techniques the clock noise can be removed and this gives a clearer picture of the stability of the frequency-transfer processes, particularly in the long term.

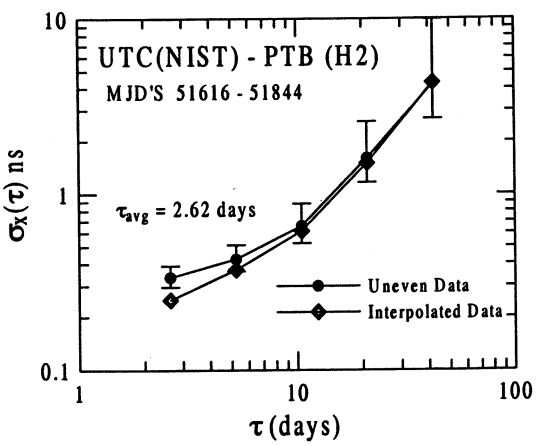

Figure 2. Time deviation of UTC(NIST) minus H2

Figure 3 shows the time difference between the TWSTFT and carrier-phase data for the UTC(NIST) - H2 link over a 100-day period that includes the fountain

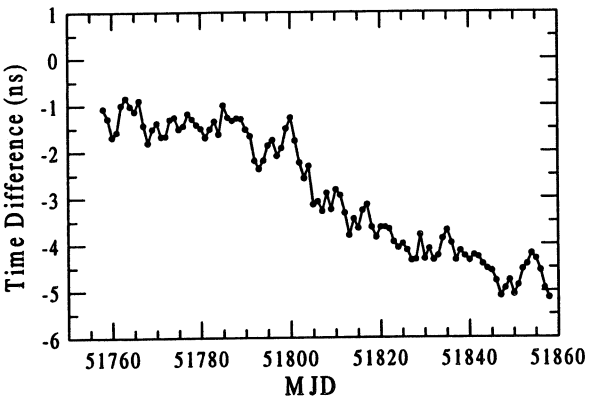

Figure 3. TWSTFT minus GPS carrier-phase for UTC(NIST) – H2

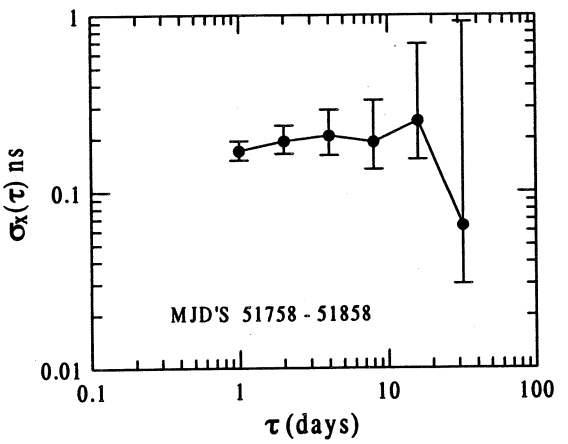

Figure 4. Time deviation of TWSTFT minus carrier-phase for UTC(NIST) – H2

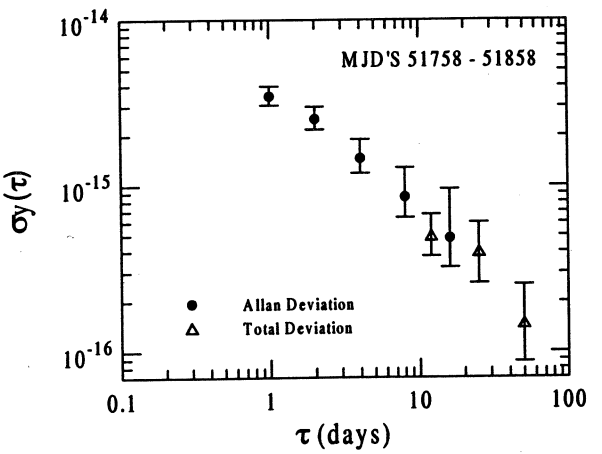

Figure 5. Allan deviation of TWSTFT minus carrier-phase for UTC(NIST)-H2.

comparison intervals. The data interval is one day and the two-way data have been interpolated to match this interval. The long-term stability of this data is better than that in Fig. 1, but there is still some drift in the time difference. It is not clear whether this drift comes

from two-way, carrier-phase, or both, but in any case, it would constitute a real systematic error (rate offset) on the order of $5x10^{-16}$ in the frequency measurement if attributed to either one of the methods. It is important to note that the final carrier-phase solution is a combination of 3.5 day analysis periods with half-day overlaps. Therefore the solution is sensitive to the overlapping offsets of the consecutive data series as well as corrections for jumps and gaps in the data.

Figure 4 shows the time deviation for this data and Fig. 5 shows the Allan deviation. The $\sigma_x(\tau)$ and Allan deviation values at one day are both biased low because of the interpolation of the two-way data, but in general the time deviation is flicker-phase in nature at a level of about 200 ps. The Allan deviation plot indicates that the combined frequency uncertainty of TWSTFT and carrier phase is about $5x10^{-16}$ at 15 days. However, this may be optimistic because both the Allan deviation and time deviation statistics are based on the second difference of a time series, which is insensitive to a rate (or frequency) offset.

A slightly larger uncertainty of $6x10^{-16}$ at 15 days is obtained using a first-difference statistic that is the RMS fractional frequency of the time-series data in Fig. 3 [7]. This is more consistent with the observed slope in the data. For the purposes of this comparison we will assume that the instabilities of TWSTFT and carrier phase are independent and that they contribute equally to the combined instability. Taking $6x10^{-16}$ as the combined uncertainty of the two transfer techniques gives a frequency-transfer uncertainty of $4.2x10^{-16}$ at 15 days for each of the two techniques.

For the uncertainty in GPS common-view we will use the BIPM estimate of $2x10^{-15}$ at 15 days, as stated in Circular T.

4. EXTRAPOLATION

A stable frequency reference must be used as a transfer standard since none of the fountain evaluations overlap perfectly. To estimate the uncertainty of comparisons with dead time we have used the method of Douglas and Boulanger [8]. The comparisons have been made with both AT1E [9], a post-processed scale based on a maser ensemble at NIST, and EAL, the free atomic scale calculated at the BIPM. The stability characteristics of these scales are shown in Table 1 for τ in units of 1 day.

Table 1. Frequency Stability Characteristics of AT1E and EAL

Scale	White FM	Flicker FM	RW FM
AT1E	$4x10^{-16}$ ($\tau^{-1/2}$)	$4x10^{-16}$	$1.3x10^{-16}$ ($\tau^{1/2}$)
EAL	$60x10^{-16}$ ($\tau^{-1/2}$)	$6x10^{-16}$	$1.6x10^{-16}$ ($\tau^{1/2}$)

The white FM and flicker FM noise characteristics of AT1E were estimated from internal measurements made at NIST, and the random-walk FM noise level was estimated from measurements against EAL and CS2 (a thermal-beam primary frequency standard at PTB). The stability characteristics of EAL are those published by the BIPM in Circular T. The main advantage of AT1E is its much lower white FM noise. This is expected since EAL is affected by noise from GPS common-view.

5. COMPARISON RESULTS

The results of the various comparison methods are summarized in Tables 2 a-d. The stated uncertainties for the one NIST-F1 run are ub = $1.5x10^{-15}$ and ua = $0.8x10^{-15}$, where ub is the systematic uncertainty and ua is the statistical uncertainty. The combined uncertainty for the NIST-F1 run is $1.7x10^{-15}$. Since the uncertainties for the various PTB-CSF1 runs were not all the same they are listed individually in the tables. All uncertainties that are statistical in nature will be identified as "ua". The frequency uncertainty due to the time-transfer process is identified as ua(TT) and ranges from $0.42x10^{-15}$ for TWSTFT and carrier-phase to $2.0x10^{-15}$ for common-view GPS. The uncertainties due to dead time are identified as ua(dead) and range from $0.4x10^{-15}$ to $2.9x10^{-15}$. The total uncertainty due to the comparison process is ua(comp.), which is obtained from ua(TT) and ua(dead) combined in quadrature. Finally, the uncertainty of the remote standard, u(remote), is calculated from the quadrature combination of ua(standard), ub(standard), and ua(comp.). In this discussion PTB-CSF1 will be treated as the remote standard as seen from NIST, although the roles could be reversed.

The four tables compare data for: (a) TWSTFT with AT1E used as a transfer standard, (b) GPS carrier-phase with AT1E used as a transfer standard, (c) GPS common-view with AT1E used as a transfer standard, and (d) GPS common-view with EAL used as a transfer standard. All uncertainties are one sigma. The first row of data in each table is for the first PTB run, which overlapped the NIST run by 15 days. In Tables 2 a-c, the uncertainty ua(dead) is small (but not zero) because the two runs overlapped, but were not the same length. Note that ua(dead) is considerably larger with EAL used as the frequency reference (Table 2d) since EAL has a much larger white FM noise level. The observed values for the frequency difference of the two standards, y(F1-CSF1), are $-0.36x10^{-15}$ for comparison by two-way, and $-0.24x10^{-15}$ for comparison by carrier-phase. ua(comp.) is $0.58x10^{-15}$ for both methods and u(remote), the uncertainty of PTB-CSF1 as seen from NIST, is $1.9x10^{-15}$. This is only slightly larger than the stated combined uncertainty of CSF1, which is $1.8x10^{-15}$ for that run. The two standards are in excellent agreement in the first run. The comparison results using common-view GPS with AT1E and EAL are given in the first

data rows of Tables 2c and 2d. Note that ua(comp.) is much larger. The agreement between the two standards is not as good as with two-way and carrier phase, but it is still within u(remote) for these comparisons.

The second and third runs of PTB-CSF1 can also be compared to the NIST-F1 run, as shown in the second and third rows of the tables. However, ua(dead) gets larger because the runs don't overlap at all. In general, the agreement in the second run is not as good as in the first. In the second run the frequency differences for the comparisons using AT1E with two-way and AT1E with common-view are large enough that the error bars of the two standards don't overlap. For AT1E with carrier-phase and EAL with common-view they do overlap. The agreement in the third run is much better, even though u(remote) is getting rather large, particularly when EAL and common-view are used.

Table 2. Comparison of NIST-F1 with PTB-CSF1

Table 2a Referenced to AT1E via two-way (units of 10^{-15}) ua(TT) = 0.42

PTB Runs	y(F1-CSF1)	ub CSF1	ua CSF1	u CSF1	ua (dead)	ua (comp.)	u (remote)	y(F1-CSF1) (w. avg.)	uw (remote)
First	-0.36	1.5	1.0	1.8	0.4	0.58	1.9	-0.36	1.9 (1 run)
Second	4.23	1.4	1.0	1.7	1.2	1.3	2.1	1.19	1.7 (2 runs)
Third	2.13	1.4	1.0	1.7	1.7	1.8	2.5	1.36 (?)	1.7 (3 runs)

Table 2b Referenced to AT1E via GPS carrier phase (units of 10^{-15}) ua(TT) = 0.42

PTB Runs	y(F1-CSF1)	ub CSF1	ua CSF1	u CSF1	ua (dead)	ua (comp.)	u (remote)	y(F1-CSF1) (w. avg.)	uw (remote)
First	-0.24	1.5	1.0	1.8	0.4	0.58	1.9	-0.24	1.9 (1 run)
Second	2.72	1.4	1.0	1.7	1.2	1.3	2.1	0.76	1.7 (2 runs)
Third	1.99	1.4	1.0	1.7	1.7	1.8	2.5	0.98 (?)	1.7 (3 runs)

Table 2c Referenced to AT1E via common-view GPS from Circular T (units of 10^{-15}) ua(TT) = 2.0

PTB Runs	y(F1-CSF1)	ub CSF1	ua CSF1	u CSF1	ua (dead)	ua (comp.)	u (remote)	y(F1-CSF1) (w. avg.)	uw (remote)
First	-1.63	1.5	1.0	1.8	0.4	2.0	2.7	-1.63	2.7 (1 run)
Second	5.20	1.4	1.0	1.7	1.2	2.3	2.9	1.41	2.2 (2 runs)
Third	2.20	1.4	1.0	1.7	1.7	2.6	3.1	1.62 (?)	2.0 (3 runs)

Table 2d Referenced to EAL via common-view GPS from Circular T (units of 10^{-15}) ua(TT) = 2.0

PTB Runs	y(F1-CSF1)	ub CSF1	ua CSF1	u CSF1	ua (dead)	ua (comp.)	u (remote)	y(F1-CSF1) (w. avg.)	uw (remote)
First	2.5	1.5	1.0	1.8	1.2	2.3	2.9	2.5	2.9 (1 run)
Second	4.3	1.4	1.0	1.7	2.5	3.2	3.6	3.16	2.5 (2 runs)
Third	0.2	1.4	1.0	1.7	2.9	3.5	3.9	2.46 (?)	2.3 (3 runs)

A weighted average of the various runs can also be calculated. The last two columns in rows 2 and 3 show the weighted averages for y(F1-CSF1) and the corresponding uncertainties, uw(remote), for the first two runs, and all three runs, respectively. (Results for the first run are repeated for clarity in the first row of these columns even though there is no averaging.) The weighting was based on the combined statistical uncertainties for each case. It is questionable how meaningful the weighted average is for all three runs because it is very likely that the errors due to the dead time are correlated between the second and third run;

thus the question marks in the tables. However, the weighted average of the first two runs should be meaningful and it also shows very good agreement between the two fountains. Note that uw(remote) for the weighted average of the first and second runs using either TWSTFT or carrier phase is essentially at the level of the stated uncertainty of the PTB-CSF1.

In principle, one could average the TWSTFT and carrier-phase comparisons together to further reduce ua(TT) by another factor of $1/\sqrt{2}$. However, this would have only a small impact, and may not be justified until the assumption of independence between TWSTFT and carrier-phase can be verified.

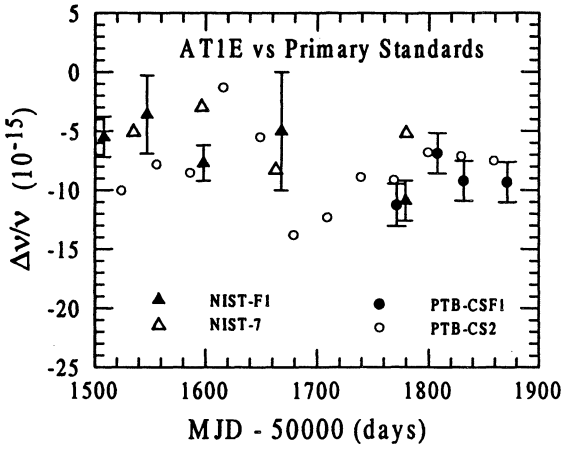

Figure 6. Frequency of AT1E versus four primary frequency standards.

Figure 6 shows the frequency of AT1E relative to the two fountains and two thermal-beam standards, NIST-7 and PTB-CS2, for about the last 400 days. The combined uncertainty for CS2 is typically 12×10^{-15} and for NIST-7 ranges from 5 to 10×10^{-15}. Individual uncertainties are shown for the fountains. The figure provides a qualitative view of the relative frequencies of the four primary frequency standards and also contains a forth CSF1 run that was not included in the tables above. The overall agreement among the four standards is quite good. The slight downward frequency drift is a characteristic of AT1E.

6. CONCLUSION

The cesium fountain primary frequency standards at PTB and NIST have been compared by three different frequency transfer techniques and with two different stable frequency references. This variety of comparison techniques was used in order to minimize the chance that a statistical fluctuation in one technique might give an unusually good or bad result. It has been demonstrated that the uncertainties of the comparison process can be reduced to a nearly negligible level with the use of TWSTFT or GPS carrier-phase if the duration of the comparison is 15 days or longer. Only two cases out of the twelve individual comparisons and the four weighted averages exhibit a frequency difference large enough that the uncertainty limits of the two standards don't overlap. This is entirely consistent with one-sigma uncertainties. In most cases the observed frequency differences were well within the uncertainties of a single standard.

The best estimate of the frequency difference of the two standards is given by the weighted average of the first two PTB runs using either two-way or GPS carrier-phase. The frequency difference is less than 1.2×10^{-15}, which is within the stated uncertainties of either of the two standards. As more fountain evaluations are carried out an even better assessment of the agreement between the two fountains will be obtained.

7. REFERENCES

1 S. Weyers, R. Schröder , and A. Bauch, "Recent Results from PTB's Caesium Fountain CSF1," in Proc. this conference.

2 S. Jefferts, D.M. Meekhof, T.P. Heavner, T.E. Parker, "Latest Results from NIST-F1, a Laser-Cooled Cesium Fountain Primary Frequency Standard," in Proc. this conference.

3 D. Kirchner, "Two-Way Time Transfer Via Communication Satellites," in *Proc. of the IEEE*, vol. 79, pp. 983-990, 1991.

4 K.M. Larson and J. Levine, "Carrier-Phase Time Transfer," in *IEEE Trans. on Ultrason., Ferroelect., and Freq. Contr.*, vol. 46, no. 4, pp. 1001-1012, 1999.

5 W. Lewandowski and C. Thomas, "GPS Time Transfer," in *Proc. of the IEEE*, vol. 79, pp. 991-1000, 1991.

6 L. Nelson, J. Levine and P Hetzel, "Comparing Primary Frequency Standards at NIST and PTB," in *Proc. 2000 IEEE International Freq. Control Symp.*, pp. 622-628, 2000.

7 T.E. Parker, D.A. Howe and M. Weiss, "Accurate Frequency Comparisons at the 1×10^{-15} Level," in *Proc. 1998 IEEE International Freq. Control Symp.*, pp. 265-272, 1998.

8 R.J. Douglas and J.S Boulanger, "Standard Uncertainty for Average Frequency Traceability," in *Proc. 11th European Frequency and Time Forum*, pp. 345-349, 1997.

9 T.E. Parker, "Hydrogen Maser Ensemble Performance and Characterization of Frequency Standards," in *Proc. 1999 Joint Meeting of the European Frequency and Time Forum and the IEEE International Frequency Control Symp.*, pp. 173-176, 1999.

RECENT RESULTS FROM PTB'S CAESIUM FOUNTAIN CSF1

S. Weyers, R. Schröder, A. Bauch

Physikalisch-Technische Bundesanstalt, Bundesallee 100, D-38116 Braunschweig (Germany)

1. ABSTRACT

At the Physikalisch-Technische Bundesanstalt (PTB) a new primary frequency standard, the atomic caesium fountain CSF1, has been put into operation. The first uncertainty evaluation yielded a relative 1σ frequency uncertainty of $1.4 \cdot 10^{-15}$. The short-term relative frequency instability is typically $3.5 \cdot 10^{-13} \cdot (\tau/\mathrm{s})^{-1/2}$, dictated by the available quartz oscillator as the local frequency source. Some details of the uncertainty evaluation are given in this contribution. Between August 2000 and November 2000 first data of CSF1 for the steering of the free atomic time scale EAL were reported covering four periods, each of 15 days duration.

Keywords: atomic frequency standard, caesium fountain, TAI

2. INTRODUCTION

In CSF1, laser cooled caesium atoms are collected in a magneto-optical trap (MOT) and launched after a 100 ms molasses phase into a magnetically shielded titanium vacuum chamber. The atoms are launched to a height of 83 cm above the cooling region. During the ballistic flight, a TE011 microwave cavity mounted 44 cm above the MOT is passed twice and the atomic state is subsequently analyzed in a detection region located between the cavity and the MOT. Ramsey fringes with a full width at half maximum of 0.88 Hz are obtained. A detailed description of the CSF1 setup was given elsewhere [Refs. 1, 2]. A preliminary evaluation of the individual CSF1 uncertainty components was previously performed [Ref. 3]. After a reconstruction during spring 2000, this evaluation was confirmed and extended [Ref. 4]. Some details are given in section 3.

For the realization of International Atomic Time TAI, a linear function of time is added to the time scale EAL (Echelle atomique libre) with the slope adjusted in order to generate TAI as an international time reference which conforms to the definition of the SI second [Ref. 5]. This so-called steering of TAI is based on comparisons between TAI and a few primary frequency standards which are operated in national metrology institutes and which realize the SI second with a specified uncertainty.

During 1999 and 2000, data were available from the primary frequency standards NIST-7 (USA), CRL-01 and NRLM-4 (Japan), and JPO (France), which use optical pumping both for state selection and detection, and from CS1, CS2, and CS3 of Physikalisch-Technische Bundesanstalt (PTB), which use magnetic state selection. In all these standards thermal atomic beams are used. In 1999 first data were reported to the BIPM from the atomic caesium fountain NIST-F1 [Ref. 6] of the National Institute of Standards and Technology (USA), covering a period in November and December. Between August 2000 and November 2000 first data of the fountain CSF1 were reported covering four periods, each of 15 days duration. These data were obtained by frequency comparisons using two active hydrogen masers H1 and H2 as local references. These masers in turn are compared with the primary clocks of PTB and with UTC(PTB), and the results are reported to the BIPM. That way the maser frequencies are known with respect to TAI for standard 5-day intervals. CSF1 was compared with the masers following the same time schedule. Thus the TAI scale unit could be measured with respect to the SI second as realized with CSF1.

3. UNCERTAINTY OF CSF1

The main frequency corrections and uncertainty contributions of CSF1 are listed in Tab. 1. The evaluation should be considered as valid only in the CSF1 routine operation mode (explained below) used in particular for the measurement of the TAI scale unit.

Tab. 1: Current uncertainty budget of CSF1 in the routine operation mode.

Effect	Correction $[10^{-15}]$	Uncertainty $[10^{-15}]$
C-field	− 46.4	< 0.1
Collisional shift	8.0	1
Black body shift	16.7	0.2
Majorana transitions, Rabi-pulling, Ramsey-pulling, microwave leakage	–	0.5
First order Doppler effect	–	0.5
Microwave spectral impurities, Electronics	–	0.2
Light shift	–	0.2
Background gas collisions	–	< 0.5
Total 1σ uncertainty		1.4

The main contributions to the CSF1 uncertainty are of the order of $1 \cdot 10^{-15}$ or less and are considered to be linearly independent. Therefore the resulting standard uncertainty is the square root of the sum of squares of the individual components which are listed in Tab. 1, and amounts to $1.4 \cdot 10^{-15}$ (1σ). This evaluation is valid in the case of operating CSF1 without state selection cavity. Its use promises a further reduction of uncertainty and instability in the near future. In this section only some details of the evaluation are given. The complete evaluation was described in [Ref. 4].

3.1 Uncertainty due to cold collisions

In CSF1, the collisional shift [Ref. 7] is determined by measuring the frequency in dependence on relative atomic densities. If the experimental conditions such as detection efficiency, launching height, and atomic temperature are kept constant, the signal N_4 of detected atoms in the state $F = 4$ is proportional to the mean atomic density during the ballistic flight above the cavity $\bar{n}$. Thus, a linear dependence of the fountain frequency on N_4 is expected, and the unperturbed frequency can be obtained by extrapolation to signal $N_4 = 0$.

In a first series of measurements, N_4 was varied using different MOT loading times (0.2 s to 1.6 s). The results of frequency measurements between CSF1 and the masers confirmed the expected linear dependence on N_4 [Refs. 3, 4]. The slope has been later on determined periodically by measuring relative frequency differences y (CSF1-H maser) alternating for low and high atomic density during several days. Further six slope determinations were performed up to now. The individual measurement results are depicted in Fig. 1. The scatter of the last six values around the mean is within $\pm 0.1 \cdot 10^{-15}$. It is only the result of the earliest slope determination which significantly deviates from this mean.

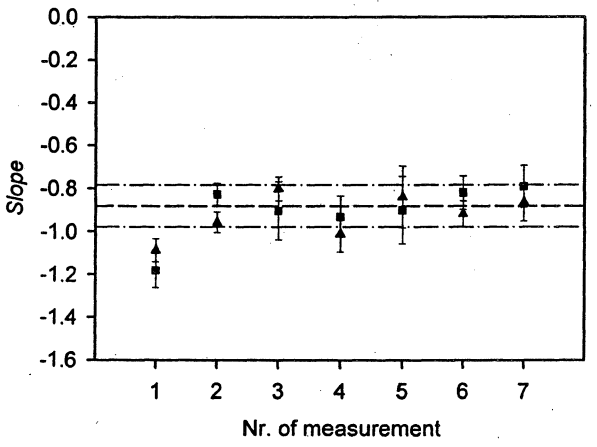

Fig. 1: Results of the available slope determinations of the linear dependence of the fountain frequency on N_4. Triangles: using H1 as reference; squares: using H2 as reference. In total, seven slope determinations were performed, each lasting about two weeks. The vertical error bars reflect the statistical uncertainty of the slopes due to the noise of CSF1 and of the hydrogen masers. The dashed line and the dashed-dotted lines indicate the mean of the last six determinations and deviations of ±10%, respectively.

This is supposed to be due to the fact that at the time of the first measurement the final residual gas partial pressure in the cavity region was not yet reached. An increased rate of collisions of the falling atom cloud with background gas molecules in the cavity region and below will cause fewer atoms to be detected from a cloud of the same mean density $\bar{n}$. This would explain a larger collisional shift at a certain number N_4 of detected atoms and thus explain the larger slope of the first measurement.

When data are collected for contributing to TAI, CSF1 is operated in a so-called routine operation mode at $N_4 \approx 9$. This represents a compromise between low instability and low uncertainty due to the collisional frequency shift [Ref. 3]. During the measurement, N_4 is recorded and the relative frequency correction is afterwards calculated based on the average $\langle N_4 \rangle$ and the average slope determined before and after a routine measurement. Typically a relative frequency correction $F_{coll} = 8.0 \cdot 10^{-15}$ is applied.

The uncertainty of the correction F_{coll} is made up by two components. The first one reflects a hypothetical undetected change of the proportionality factor between N_4 and $\bar{n}$ of as much as 10% during the 15-day measurement interval. The results obtained so far indicate that for unchanged experimental parameters this is a conservative estimate. The second one is due to the statistical uncertainty of the slope determination, mainly caused by the long-term instability of the masers. Typically the square root of the quadratic sum of both components yields a relative frequency uncertainty contribution of $1 \cdot 10^{-15}$. This uncertainty contribution is larger, if CSF1 is not in routine operation. In the future, it might be reduced by use of the state selection cavity. A more stable reference in the long-term, e.g. a second fountain frequency standard, could reduce the statistical uncertainty of the slope determination.

3.2 Potential frequency shift at increased microwave power

In microwave frequency standards, it is a powerful tool to increase the microwave power with respect to the optimum excitation power (π pulse of the clock transition) and to look for simultaneous frequency shifts. These may be due to microwave leakage, Ramsey-pulling, Rabi-pulling and/or cavity pulling [Ref. 8].

In a series of frequency measurements CSF1 was operated alternating at optimum excitation power and at increased power (+9.5 dB). The results are depicted in Fig. 2. Using H1 as reference, the frequency difference between the two operation modes is $(0.47 \pm 1.48) \cdot 10^{-15}$. With H2 as reference we obtain $(1.90 \pm 2.31) \cdot 10^{-15}$. The measurement uncertainties are determined by the long-term instability of the reference maser frequencies during several days of measurement. The current estimate for the frequency shifting effect of Rabi- and Ramsey-pulling, Majorana transitions, and microwave leakage in normal operation is $0.5 \cdot 10^{-15}$ [Refs. 3, 4]. Further studies are planned when individual m_F levels are populated by the use of the state selection cavity.

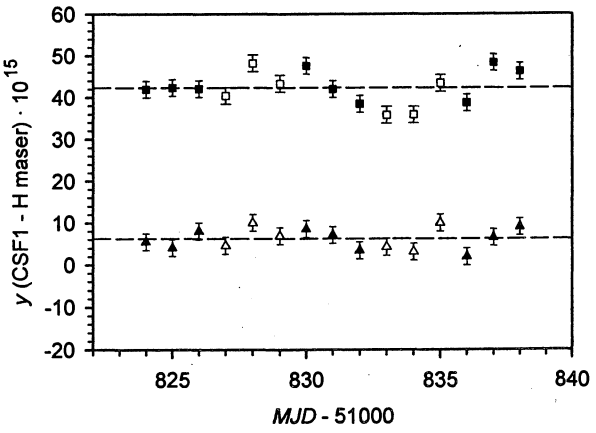

Fig. 2: Relative frequency differences y (CSF1-H maser) between CSF1 and the hydrogen masers H1(triangles) and H2(squares). Full symbols: optimum microwave excitation power; open symbols: increased microwave excitation power (+ 9.5 dB). MJD designates the Modified Julian Date; MJD 51825 corresponds to 2000-10-08. The vertical error bars reflect the statistical uncertainty due to the noise of CSF1 and of the hydrogen masers. Dashed lines indicate the mean of the respective set of data. Maser drifts obtained from linear least-squares fits to the original data points were subtracted.

3.3 Residual first-order Doppler effect

A general advantage of an atomic fountain microwave frequency standard is that the atoms cross the same microwave cavity twice. If the atomic trajectories were perfectly vertical, frequency shifts due to axial and radial cavity phase variations would be perfectly cancelled as each atom would interact with the field once with velocity v (upwards) and once later with $-v$ (downwards). It is the transversal residual thermal velocity and a possible misalignment of the launching direction, which cause a spread of the trajectories between the first and the second passage through the cavity. In this case, a non-vanishing transverse phase variation of the cavity field can give rise to a residual first-order Doppler effect frequency shift, unless the trajectories are distributed around the vertical symmetry axis in a proper way.

The microwave field in the cavity can be described as a superposition of various field modes which are excited with different amplitudes and phases. In the CSF1 cavity design a single microwave feed excites two symmetrically arranged vertical coupling slits [Ref. 2]. For exactly symmetric coupling, transverse electrical field modes TEn11 with $n = 0,2,4,...$ can be excited in the cavity, but the field modes TEn11 with $n = 1,3,...$ are suppressed. Hence the predominant first-order Doppler shift contribution results from the TE211 mode: If one assumes in a worst case estimate that all atoms ascend in a negligibly small cloud through the cavity center and descend next to one of the coupling slits (still in a negligibly small cloud on one side of the cut-off bore), the residual relative first-order Doppler effect frequency shift is calculated to be less than $0.5 \cdot 10^{-15}$.

For asymmetric coupling, further first-order Doppler shift contributions are due to the TE111 mode and the TE311 mode. For a coupling asymmetry of 10%, which is much larger than the asymmetry expected from mechanical tolerances, one calculates a residual relative first-order Doppler effect frequency shift of less than $0.2 \cdot 10^{-15}$. This is another worst-case estimate, where it is assumed that all atoms ascend through the cavity aperture next to one coupling slit and descend again next to the other slit (again in a negligibly small cloud on one side of the cut-off bore upwards, on the opposite side downwards).

Both cases considered here are improbable, if the non-horizontal molasses laser beams are vertically well aligned and centered to the microwave cavity axis and all laser beam intensities are balanced. Furthermore the extension of the atomic cloud is non-negligible, so that all remaining effects are averaged to a large extend. Presently, a maximum relative frequency uncertainty of $0.5 \cdot 10^{-15}$ is estimated.

3.4 Light shift due to residual laserlight

The interaction of atoms with laser light during the ballistic flight in and above the microwave cavity entails a frequency shift through the AC Stark effect (light shift) [Ref. 8]. In the optical setup of CSF1, a high power laser diode provides the six cooling laser beams. The diode is injection locked to a narrow-linewidth master laser diode. The frequency of the cooling laser light is tuned by acousto-optical modulators (AOMs). To prevent any interaction of the atoms with the laser light during their ballistic flight above the cavity, the rf supply of the AOMs is switched off and residual laser light is blocked by mechanical shutters in front of each

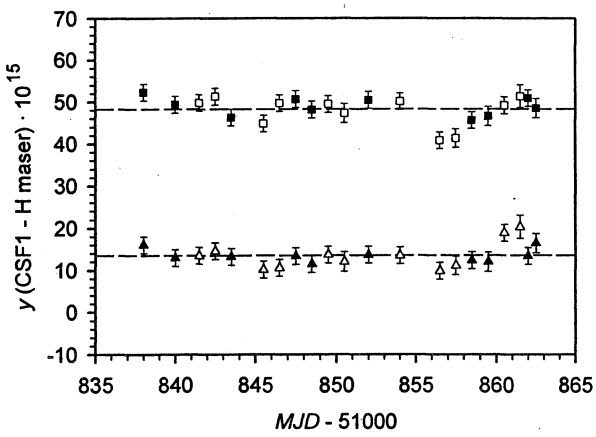

Fig. 3: Relative frequency differences y (CSF1-H maser) between CSF1 and the hydrogen masers H1(triangles) and H2(squares). Full symbols: master laser light blocked; open symbols: master laser light not blocked. MJD designates the Modified Julian Date; MJD 51835 corresponds to 2000-10-18. The vertical error bars reflect the statistical uncertainty due to the noise of CSF1 and of the hydrogen masers. Dashed lines indicate the mean of the respective set of data. Maser drifts obtained from linear least-squares fits to the original data points were subtracted.

optical fiber connecting the optical table and the fountain setup. Furthermore, the injection locking of the slave laser is interrupted by using a mechanical shutter to block the master laser light.

A series of frequency measurements was performed alternately blocking or not blocking the master laser light for injection locking (Fig. 3). The measured frequency differences between these two operation modes were $(0.01 \pm 1.15)\cdot10^{-15}$ and $(1.14 \pm 1.34)\cdot10^{-15}$ using H1 and H2 as references, respectively. Again the measurement uncertainties are determined by the long-term instability of the reference maser frequencies. From these results we estimate that a potential light shift does not exceed $0.2\cdot10^{-15}$, if the injection locking is interrupted by the shutter as is the case during normal operation.

4. CONTRIBUTIONS OF CSF1 TO TAI

Between August 2000 and November 2000 four measurement series were performed during which CSF1 contributed to the realization of TAI, each for a period of three standard 5-day intervals: MJD 51764–51778, MJD 51799–51813, MJD 51824–51838, MJD 51864–51878. In Fig. 4 the corresponding relative frequency differences y(CSF1-H1) between CSF1 and the maser H1 are depicted, which were communicated to the BIPM. The linear least squares fit to the data points in Fig. 4 indicates a frequency drift of the maser H1 of $(0.137 \pm 0.009)\cdot10^{-15}$/day during this period. A similar result is obtained when comparing the H1 maser to the primary clock CS2, however with a considerably larger measurement uncertainty.

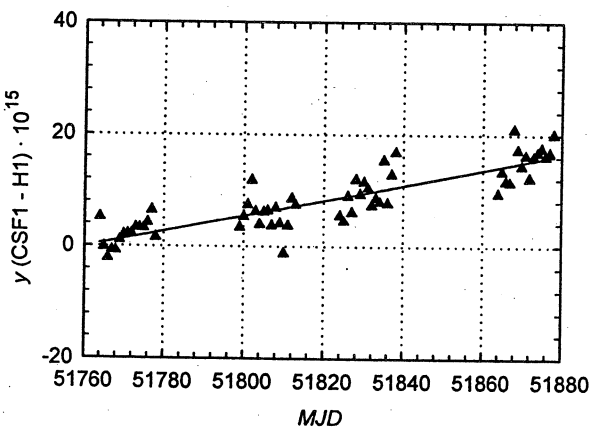

Fig. 4: Relative frequency differences y(CSF1-H1) between CSF1 and the maser H1 corresponding to four measurement cycles (each of a period of 15 days), subsequently communicated to the BIPM. MJD designates the Modified Julian Date; MJD 51760 corresponds to 2000-08-04. The line is a linear least-squares fit to the data and yields a drift of $(0.137 \pm 0.009)\cdot10^{-15}$/day.

Measurement of the TAI scale unit with respect to the SI second as realized with CSF1 has been possible with a combined uncertainty of $2.6\cdot10^{-15}$, as documented in the Section 5 of the CircularT of the BIPM Time Section [Ref. 9].

Fig. 5 shows the data of all primary frequency standards having contributed to TAI during the recent 14 months period. The deviation found with CSF1, NIST-F1 and NIST-7 is significant with respect to the comparison uncertainty, and steering of TAI has already been affected [Ref. 9]. With the availability of fountain data the steering of TAI can obviously be based on more accurate data than before.

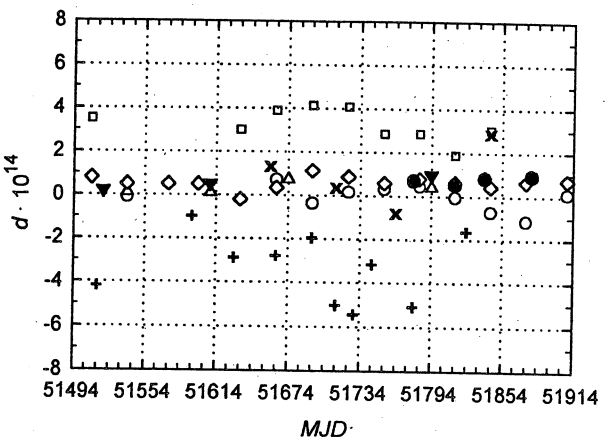

Fig. 5: Fractional deviation d of the duration of the TAI scale interval from the SI second as realized by the individual primary frequency standards CSF1 (•), CS1 (○), CS2 (◇) and CS3 (□) of PTB, NIST-7 (△) and NIST-F1 (▼) (USA), NRLM-4 (+) and CRL-01 (×) (Japan), during the period MJD 51494–51914. MJD designates the Modified Julian Date; MJD 51494 corresponds to 1999-11-12.

5. CONCLUSION

In the routine operation mode the new PTB primary frequency standard CSF1 currently realizes the SI unit "second" with an uncertainty of $1.4\cdot10^{-15}$. Several frequency shifting effects were investigated in detail. At the same time, the relative frequency instability is $\sigma_y(\tau) = 3.5\cdot10^{-13}\,\tau^{-1/2}$. These results are obtained without preselection of atoms in the substate $m_F = 0$. First experiments with the state selection cavity let expect a further reduction of uncertainty and instability in the near future.

Up to now CSF1 contributed to TAI during 60 days in total. In the future, it is intended to continue to operate CSF1 intermittently in the routine operation mode and to continue measurements of the TAI scale unit during these intervals.

References

[1] Weyers S., Bauch A., Griebsch D., Hübner U., Schröder R., Tamm Chr., *Proc. Joint Mtg. Europ. Freq. Time Forum (EFTF) and the IEEE Int. Freq. Contr. Symp. (FCS)*, 1999, 16–19; Weyers S., Bauch A., Hübner U., Schröder R., Tamm Chr., *IEEE Trans. Ultrason., Ferroelect., Freq. Contr.*, 2000, 47(2), 432–437.

[2] Schröder R., Hübner U., *Proc. 14th Europ. Freq. Time Forum (EFTF)*, 2000, 480–484.
[3] Weyers S., Hübner U., Fischer B., Schröder R., Tamm Chr., Bauch A., *Proc. 14th Europ. Freq. Time Forum (EFTF)*, 2000, 53–57.
[4] Weyers S., Hübner U., Schröder R., Tamm Chr., Bauch A., to be published in: *Metrologia*, 2001, **38**(4).
[5] Thomas C., Wolf P., Tavella P., *Time Scales*, 1994, BIPM Monographie 94/1.
[6] Jefferts S. R., Meekhof D. M., Shirley J. H., Parker T. E., Levi F., *Proc. Joint Mtg. Europ. Freq. Time Forum (EFTF) and the IEEE Int. Freq. Contr. Symp.(FCS)*, 1999, 12–15.
[7] Ghezali S., Laurent Ph., Lea S. N., Clairon A., *Europhys. Lett.*, 1996, **36**(1), 25–30.
[8] Vanier J., Audoin C., *The Quantum Physics of Atomic Frequency Standards*, Bristol and Philadelphia, Adam Hilger, 1989.
[9] BIPM Time Section, CircularT, 2000–2001, issues 152–156, Sections 4 and 5.

INITIAL CHARACTERIZATION OF THE USNO CESIUM FOUTAIN

Eric A. Burt, Christopher R. Ekstrom and Thomas B. Swanson

U. S. Naval Observatory
3450 Massachusetts Ave. NW
Washington, D. C. 20392 U.S.A.

ABSTRACT

We have performed an initial characterization of the stability of the U.S. Naval Observatory (USNO) cesium fountain atomic clock. This device has a short-term fractional frequency stability of $1.5 \times 10^{-13}\tau^{-1/2}$. This short-term performance enables us to measure hydrogen maser behavior over the short to medium term. When measured against a maser co-located in the same lab with the fountain, we observe a flicker floor of 1.5×10^{-15} that is statistically consistent with that maser's performance. Measurements of our detection noise give an upper bound on Dick-effect noise of $1.4 \times 10^{-13}\tau^{-1/2}$. Improvements in our laser servo systems have resulted in continuous data sets from this fountain of up to 7 days.

1. INTRODUCTION

Working atomic fountain clocks have now become ubiquitous in the high-performance frequency standard community [1]. This success is generally due to both the excellent stability and accuracy that this device can achieve. At USNO we have undertaken a program to integrate atomic fountain clocks into the USNO timing ensemble. The mission of the Observatory does not require that any of our standards be accurate realizations of the second, only that they be stable and run continuously.

The first USNO fountain based on cesium and described in this paper has essentially two goals. First, we would like to demonstrate a short-term stability of $1–2 \times 10^{-13}\tau^{-1/2}$ and a systematic floor of $1–3 \times 10^{-16}$. A consequence of this stability is that it will allow us to determine what hydrogen masers are doing in the medium to long-term far more precisely than previously possible. Second, this fountain is a research device that will enable us to learn how best to optimize this technology for the specific goals of the observatory, in particular, long term continuous operation.

In this paper we will describe an initial characterization of the stability of this first USNO fountain

2. EXPERIMENTAL LAYOUT

The physical layout of our fountain has been described previously [2] so we will only give a brief overview here.

We collect atoms in either a MOT or molasses and launch them in a (1,1,1) geometry. The laser light for the upward and downward directed laser beams are generated by two injection seeded tapered amplifiers. The light is then transported to the vacuum chamber with optical fibers. The light exiting these fibers (and the detection light optical fiber) have power servos closed around the fiber path to reduce amplitude noise at the atoms.

The atoms are launched in two phases, the first optimized for violent acceleration and the second for final cooling. Immediately after launch, the atoms are pumped into the F=4 hyperfine levels with a repumping beam tuned to the $F=3\rightarrow F'=4$ transition. The atoms are state selected at the detection zone by exposure to 9.2 GHz microwaves (tuned to the $|F=4,m_f=0\rangle\rightarrow|F'=3,m_f'=0\rangle$ transition) from an axial loop antenna inside the vacuum chamber and a subsequent transit of a light sheet that removes remaining F=4 atoms.

The microwave cavity and the drift region are enclosed in a high-performance magnetic shield set providing an axial shielding effectiveness of better than 35,000 [3]. An axial solenoid provides a 225 nT magnetic field for the cavity and free precession regions.

The entire outer shield and the part of the vacuum chamber that it encloses is held at 44.5±0.1°C. As a result, everything inside the shields, including the microwave cavity, the drift region and the C-field solenoid is temperature stabilized and gradients are minimized. Making the entire outer shield an isotherm instead of temperature stabilizing individual components contained therein greatly reduces the sensitivity of this fountain to ambient temperature fluctuations and enhances its robustness for continuous operation. The small fields generated by the resistive heaters are kept far away from the sensitive drift region. Tests indicate no detectable perturbation to the atoms due to these fields.

After making two transits of the microwave cavity the atoms return to the detection region. Both F=3 and F=4 atoms are detected allowing us to calculate a signal normalized to the total atom number. We run the fountain with a typical cycle time of 1.35 seconds.

Since our last report on this fountain we have made significant changes to enhance its performance. We have optimized the phase-locked loop (PLL) between the hydrogen maser and the quartz crystal in the microwave frequency chain, located and plugged several microwave leaks, improved the detection quantization axis to stabilize the detection process, and closed several servo loops, including the repump laser intensity and the temperature servo on the outer magnetic shield.

In addition we have made changes in the way we perform frequency modulation of our interrogation microwaves. Previously we used square wave modulation of the interrogation frequency. Our Ramsey fringes are about 1 Hz wide so the frequency modulation used was ±0.5 Hz. This was accomplished by frequency modulating a digital synthesizer whose output is mixed in with the frequency chain to produce the final interrogation frequency. We found that if we instead modulate the phase of this synthesizer, leaving its frequency constant, we improve the fountain's stability. The phase is changed by ±90° between the two microwave pulses that are part of each interrogation cycle. This approach is insensitive to fluctuations in launch height and is very similar to a scheme being considered for space-borne cold atom clocks to reduce their sensitivity to vibrations [5].

Another important change is an improvement to our laser frequency locks. Our diode lasers are locked to a saturation cell in the conventional way using an analog integrator to control the diode PZT voltage. We found that this method was stable for up to a day, but not longer. To address this deficiency we have added a digital integrator that periodically polls the laser for its PZT voltage and compares this to the servo control voltage. If the difference is outside a threshold, the digital integrator adjusts the bias PZT voltage bringing the control voltage back towards zero. This essentially gives the loop infinite gain at DC and keeps our lasers in lock for months at a time.

Finally we devised a new microwave frequency chain that has resulted in a 25% improvement in short term stability. At the heart of the new chain, which is displayed in Figure 1, is a small commercial component containing a Step Recovery Diode (SRD) and a Dielectric Resonant Oscillator (DRO).

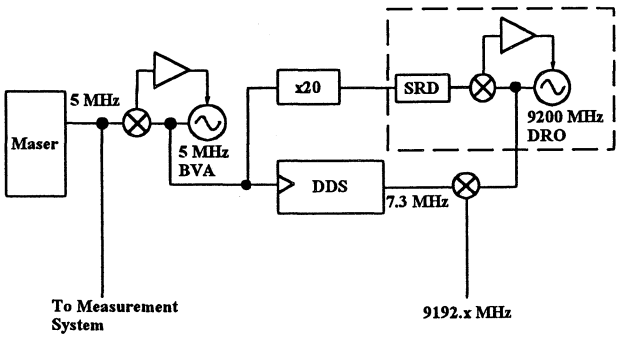

Fig. 1. The new microwave frequency chain. The dashed section is a DRO-based unit that provides the phase-coherent multiplication from 100 MHz to 9.2 GHz.

The 9.2 GHz of the DRO is phase-locked to the 92nd harmonic of the 100 MHz reference input. This output is mixed with the output of the previously mentioned digital synthesizer to produce the required interrogation frequency. The various sidebands are not suppressed but the 300 kHz linewidth of our high-Q cavity rejects these with extreme efficiency. This chain is simple, robust and built entirely from commercially available components. In addition, the new topology allows us to insert the digital synthesizer at the top of the chain (instead of at approximately 500 MHz as was done previously) removing a multiplicative factor of its contributed noise. While we have not fully characterized this chain yet, it has improved the short-term stability of our fountain and reduced the upper bound on our Dick-effect [4] noise.

3. RESULTS

Figure 2 shows the Allan deviation of frequency differences between the fountain and hydrogen maser N17, over a 7-day period. There are four features to note in this graph. First, the short-term stability is $1.7 \times 10^{-13}\tau^{-1/2}$. Further optimizations in the operation of our frequency chain have brought this number consistently down to $1.5 \times 10^{-13}\tau^{-1/2}$ as will be shown later. Second, there is a small but statistically significant deviation from white FM noise at about 5 seconds. Third, there is another deviation that begins at just under 1000 seconds. And fourth, the data appears to have a floor at around $1.5 \times 10^{-13}\tau^{-1/2}$.

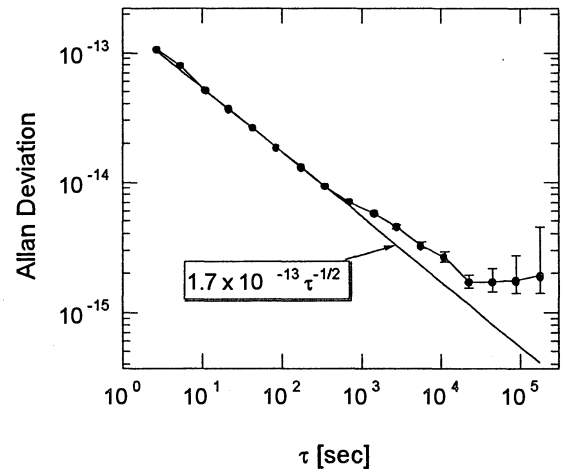

Fig. 2. Allan deviation of frequency differences between the fountain and hydrogen maser N17.

To get a better understanding of the deviations from white noise we measured the behavior of the underlying detection process. The microwave power is adjusted to give a total $\pi/2$ pulse after two transits of the microwave cavity (instead of the usual π), resulting in an even superposition of F=3 and F=4 states when the microwaves are on resonance. This produces a signal that is maximally frequency-insensitive [6] and does not include Dick-effect noise [4] and is therefore a good measure of detection noise. This $\pi/4$ data is shown in Figure 3 where a short-term stability of $6 \times 10^{-14}\tau^{-1/2}$ with no indicated floor into the mid-10^{-16}'s is observed.

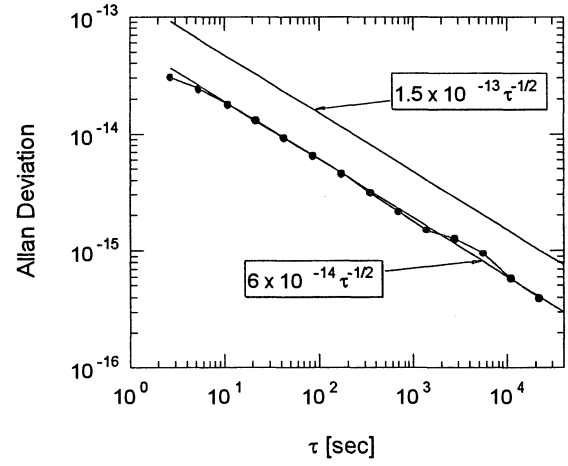

Fig. 3. Allan deviation for frequency-insensitive $\pi/4$ data taken on resonance. The result is largely detection noise which is shown to be much smaller than, and therefore not contributing significantly to, the total fountain noise.

This demonstrates that the detection noise does not contribute appreciably to the overall noise of the device over the indicated time scale. By comparing this to our current total short-term stability of $1.5 \times 10^{-13}\tau^{-1/2}$ we get an upper bound on Dick-effect noise of $1.1\text{–}1.4 \times 10^{-13}\tau^{-1/2}$. This compares to an upper bound of $1.7\text{–}1.9 \times 10^{-13}\tau^{-1/2}$ for our previous frequency chain and

agrees well with the level of Dick-effect noise that can be predicted from the phase noise of our quartz crystal.

Next, we suspected that the non-statistical characteristic at 1000 seconds in Figure 2 is due to the well-known behavior of cavity-tuned masers which exhibit a similar deviation from white noise in their Allan deviation at about this averaging time. To test this we turned the cavity tuner off for N17. We expected that this would dramatically increase the drift rate, but that the deviation from white noise at 1000 seconds would disappear. The results are shown in Figure 4.

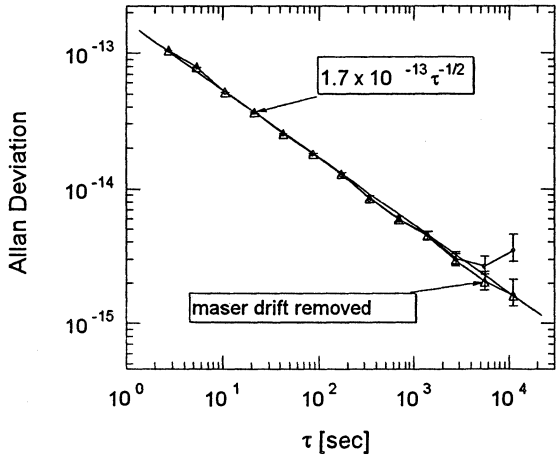

Fig. 4. Allan deviation for frequency differences between the fountain and N17 with N17's cavity tuner off. The non-statistical deviation is gone at the expense of a much larger drift as expected. The closed circles show the raw data and the open triangles show that data with the drift removed.

Indeed, the noise is completely white until it becomes dominated by the drift now estimated at about 2 x 10^{-14}/day (with the cavity tuner on, the drift for this maser is about 4 x 10^{-16}/day). When this drift is removed, the fountain minus N17 Allan deviation is consistent with white noise.

To further verify that the 1000 second deviation in figure 2 belongs to the maser and not to the fountain, we have been able to estimate N17's behavior by performing a three-cornered hat analysis between 3 masers, including N17 (Figure 5). The data for this analysis was collected over the same time period as frequency differences were monitored between N17 and the fountain. Note that the measurement system used for this comparison contributes white phase noise that has been measured to be $8x10^{-13}/\tau$ and dominates the short-term noise of these solutions.

Figure 6 shows the fountain minus N17 data taken at the same time as the data for the three-cornered hat analysis shown in Figure 5. This is the first data to incorporate all of the changes indicated in the previous section. The short-term stability is now 1.5 x $10^{-13}\tau^{-1/2}$ and the deviation at 5 seconds is gone (most likely due to optimization of the maser-crystal PLL).

Superimposed on this graph we have added the N17 three-cornered hat solution with measurement system noise removed and the known short-term fountain noise contribution of 1.5 x $10^{-13}\tau^{-1/2}$ added in. The latter value is justified by the fact that the maser is known to have performance significantly below $1.5x10^{-13}\tau^{-1/2}$ for time periods of 1 to several hundred seconds. Thus over this time period at least, the noise is determined by the fountain.

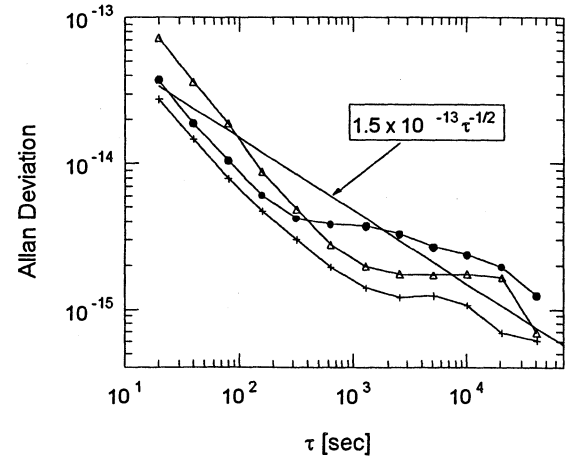

Fig. 5. A three-cornered hat solution for masers N17 (closed circles), MC3 (open triangles) and N18 (crosses). The short term out to between 200 and 500 seconds is dominated by measurement system noise ($8x10^{-13}/\tau$).

The agreement in Figure 6 between synthesized fountain minus N17 data (using the three-cornered hat solution) and the real fountain minus N17 data is striking and supports the hypothesis that the 1000 second deviation is due to the maser's cavity tuner. In addition, the data is statistically consistent with the statement that the floor is due to N17.

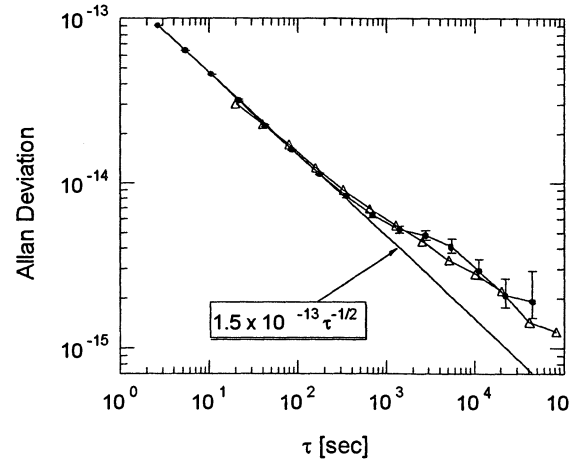

Fig. 6. Allan deviation for fountain vs. N17 (solid circles) and a synthesized estimation that assumes an entirely white FM noise contribution from the fountain (open triangles) – see text.

This type of calculation could be turned around to steer out the maser effects on paper. In the future, to gain further understanding into fountain behavior, we plan to physically steer the maser to the fountain via a synthesizer. The synthesizer would be inserted either between the maser and crystal oscillator or between the maser and the measurement system (see Figure 1). We then plan to compare the steered maser to USNO time scales. While our current data suggests that our observed noise floor may be due to the maser, proof will have to await steered operation.

4. CONCLUSIONS

In conclusion, we have performed an initial stability analysis of the USNO cesium fountain. We have demonstrated a short term stability of $1.5 \times 10^{-13}\tau^{-1/2}$ and have shown data demonstrating that deviations from statistical behavior at around 1000 seconds are due to the maser local oscillator's cavity tuner. In the longer term we are able to establish an upper bound for the fountain "flicker floor" of 1.5×10^{-15}, and have shown data that is consistent with the hypothesis that this floor is due to the maser. We have also demonstrated continuous operation of the fountain for 7 days and see no limitations to running the maser/fountain combination in steered mode for one month or more. Thus we have reached the short and medium term stability goals for this device as well as the goal of being able to measure short to medium term maser performance and continue to analyze long term behavior. In addition we have laid the basis for future continuously operating USNO fountains already under construction.

5. REFERENCES

[1] A. Clairon, et al., "Preliminary Accuracy Evaluation of a Cesium Fountain Frequency Standard" in Proceedings of the Fifth Symposium on Frequency Standards and Metrology, 1995, pp. 49-59; S. Bize, et. al. "Interrogation Oscillator Noise Rejection in the Comparison of Atomic Fountains", pp. 9-11; S. R. Jefferts, et. al., "Preliminary Accuracy Evaluation of a Cesium fountain Primary Frequency Standard at NIST", pp. 12-15; S. Weyers, et. al., "First Results of PTB's Atomic Caesium Fountain," pp. 16-19; P. B. Whibberly, "Development of a Caesium Fountain Primary Frequency Standard at the NPL," pp. 24-26, all in Proceedings of the conference EFTF and IEEE FCS, 1999. T. Swanson, et al., "Preliminary Results from the USNO Cesium Fountain," in Proceedings of the 2000 IEEE/EIA International Frequency Control Symposium, p. 672. F. Levi et al., "Preliminary Accuracy Evaluation of the IEN Cesium Fountain" and G. Mileti et al., "Recent Developments on the ON/OFMET Continuous Cs Fountain Standard" both in this proceedings.

[2] C. Ekstrom, et al., "The USNO Cesium Fountain," in Proceedings of the 14th EFTF, p. 502 (2000).

[3] T. Swanson, et al., "Preliminary Results from the USNO Cesium Fountain," in Proceedings of the 2000 IEEE/EIA International Frequency Control Symposium, p. 672.

[4] G. J. Dick, "Local oscillator induced instabilities in trapped ion frequency standards," in the Proceedings of the 19th PTTI Applications and Planning Meeting, p. 133 (1987).

[5] W.M. Klipstein, et al., "Phase Modulation for Reduced Vibration Sensitivity in Laser-Cooled Clocks in Space", this proceedings.

[6] G. Santarelli et al., "Quantum Projection Noise in an Atomic Fountain: A High Stability Cesium Frequency Standard", Phys. Rev. Lett. **82**, 4619 (1999).

LATEST RESULT FROM NIST-F1 A LASER-COOLED CESIUM FOUNTAIN PRIMARY FREQUENCY STANDARD

S.R. JEFFERTS, D.M. MEEKHOF, T.P. HEAVNER, T.E. PARKER
NIST – Time and Frequency Division
Boulder, Colorado, U.S.A.

We will present the latest results from NIST-F1, the US primary frequency standard. This work includes a density extrapolation for evaluation of the spin-exchange shift. We find that, within the experimental uncertainties, the density extrapolation technique agrees with our previously estimated spin-exchange correction. We will also discuss the use of the NIST time scale, with 5 hydrogen masers, as a long-term flywheel in the frequency evaluation. In particular we show that measurements of F1 with respect to that time scale demonstrate the run-to-run stability of the fountain and that continuous operation to measure the Allan variance is not necessary to demonstrate stability.

RECENT DEVELOPMENTS ON THE ON/METAS CONTINUOUS CS FOUNTAIN STANDARD

Alain JOYET, Gaetano MILETI, and Pierre THOMANN
Observatoire cantonal, 58 Rue de l'Observatoire, CH-2000 Neuchâtel, Switzerland

Gregor DUDLE
Swiss Federal Office of Metrology and Accreditation, CH-3003 Bern-Wabern, Switzerland

Abstract

We report on recent progress with the ON/METAS primary frequency standard based on a continuous beam of laser cooled cesium atoms. The resonator is briefly described and preliminary measurements with the resonator are presented. 1 Hz Ramsey fringes have been recorded on the clock transition with and without transverse cooling. Based on a signal-to-noise measurement we estimate the available atomic flux and deduce the achievable short-term stability. In the present configuration the short-term stability is limited to $2.5 \cdot 10^{-13}\tau^{-1/2}$ by the atomic shot-noise. This value has been experimentally verified in first stability measurements. Finally, we discuss the current theoretical investigations and results on the Dick effect in a continuous fountain and compare the results to the case of pulsed fountains.

1 INTRODUCTION

Most prototypes of Cs fountain frequency standards rely on a pulsed mode of operation. The principle of continuous operation of the Ramsey resonator overcomes two limitations encountered in the pulsed operation mode: the short-term stability limitation due to the Dick effect is essentially removed, and the trade-off between stability and accuracy imposed by the collisional shift is relaxed by more than one order of magnitude.

Based on the experimental demonstration of a continuous beam of $2 \cdot 10^8$ atoms/s [1], the Allan deviation of a continuous fountain standard using the same initial atomic flux is expected to be $7 \cdot 10^{-14}\tau^{-1/2}$ and the potential for accuracy below 10^{-15} [1].

The design of the fountain has already been presented in details previously [2, 3]. The assembly of the resonator is now completed and first measurements have been performed. We recall briefly the main parts of the continuous fountain in section 2. Section 3 of the paper will concentrate on preliminary stability measurements and first attempts to estimate the light shift. In the last part (section 4) the current status on the theoretical work on the Dick effect is exposed.

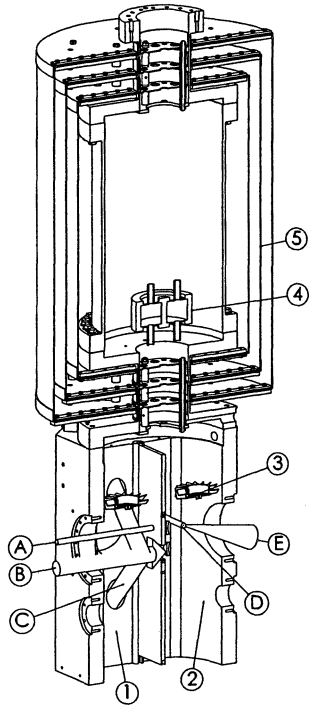

Figure 1: Cut through the resonator of the continuous Cs fountain. 1) Source chamber 2) Detection chamber 3) Light trap (light shields not shown for clarity) 4) Microwave cavity 5) Magnetic shielding. A) Transverse cooling B) & C) Main cooling and launching D) Detection beam E) Fluorescence.

2 FOUNTAIN DESCRIPTION

Figure 1 shows the main parts of the ON/METAS continuous Cs fountain. The whole vacuum chamber is machined out of aluminium. Indium seals are used on the metallic transitions and on the optical openings. The atoms are prepared in the lower part (left chamber on figure 1, labeled 1), launched upwards

and detected after their parabolic flight in the right chamber (labeled 2). For the cooling and launching 4 laser beams at 45° with respect to the vertical are used. A fifth beam propagates in the horizontal plane and is retroreflected inside the vacuum chamber. The upper part of the installation is surrounded by three layers of magnetic shields. A fourth layer envelopes the whole installation, including the source and detection part.

The overall height of the resonator is about 160 cm. The distance from the continuous source of atoms to the apogee of the parabola is of the order of 75 cm of which 31 cm are above the microwave cavity. The two microwave pulses of the Ramsey interrogation are thus separated by 0.5 s yielding 1 Hz Ramsey fringes.

More details about the optics, the trajectory of the atoms and the microwave cavity can be found in [3].

3 EXPERIMENTAL RESULTS

Transverse cooling The aimed short term stability of $7 \cdot 10^{-14}\tau^{-1/2}$ is based on the assumption that $5 \cdot 10^5$ atoms are detected per second in the probe region. To optimize the atomic flux, 2 dimensional transverse cooling has been installed at the exit of the continuous source. While this technique increases the longitudinal temperature of the beam, the transverse temperature of the atoms is significantly reduced. The longitudinal temperature of the atomic beam will affect the contrast of the off-resonance Ramsey fringes but to first order not the detected number of atoms. A lower transverse temperature on the other side prevents atoms from spreading to wide and contributes thereby to an increase of the detected flux. In the present configuration the flux of $m_F = 0$ atoms measured in the probe region is 200'000 at/s which corresponds to an increase by a factor of at least 20 with respect to the situation without transverse cooling. From this increase we infer that the transverse temperature of the atomic beam is reduced from 55 μK to 5 μK.

Ramsey fringes Figure 2 shows a typical scan of the microwave frequency over the clock transition. The central fringe has a width of 1 Hz corresponding to a time between the two microwave pulses of 0.5 s. From a fit to the experimental values the mean launching velocity can be deduced. The obtained value, (3.81 m s^{-1}) is in agreement with the frequency detuning of the optical molasses. A major difference to most pulsed fountains is the decreasing contrast of the fringes for increasing microwave frequency detuning. This decrease is due to a larger velocity distribution in the continuous fountain and can be used to estimate the longitudinal temperature

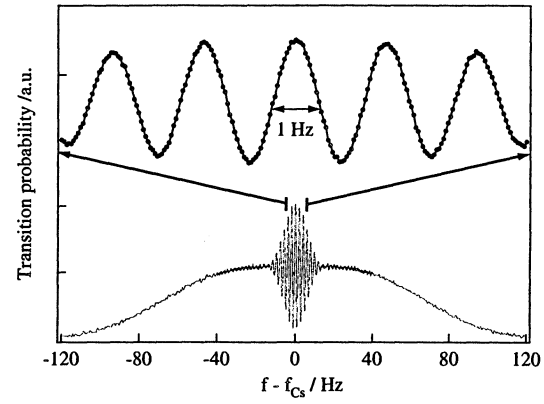

Figure 2: Ramsey fringes on the clock transition. The width of the central fringe is 1 Hz. The shape is fully explained by a launching velocity of 3.81 m s^{-1} (width of Rabi pedestal) and a longitudinal temperature of the beam of 120 μK (lost of contrast off-resonance)

of the beam. A fit to the experimental values indicate a temperature of 120 μK. This confirms that the reduction of the transverse temperature goes together with an increase of the longitudinal temperature.

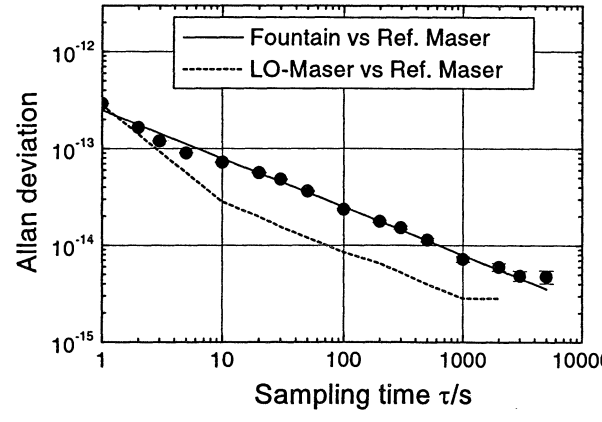

Figure 3: Stability of a LO locked to the continuous fountain measured against a hydrogen maser. The full circles represent the experimental values, the plain line indicates a short term stability of $2.5 \cdot 10^{-13}\tau^{-1/2}$. The stability of the maser against which the LO is compared is also shown on the graph.

Stability With the bright atomic beam of 200'000 useful atoms per second the noise of the signal is dominated by atomic shot noise and no longer by thermal noise from the detection system. As a result, stability measurements become possible with the current flux. For these measurements we use a quartz oscillator FTS 1000B locked to a hydrogen maser as local oscillator (LO). Its 10 MHz output

is fed into the RF-synthesizer of a commercial frequency standard. We use square wave phase modulation (PM) and square demodulation at 1 Hz in the locking loop. For the stability measurement the 5 MHz of the locked LO is compared to the output of a second hydrogen maser.

A stability measurement obtained with the continuous fountain is shown in Figure 3. It is clear that for all displayed sampling times $\tau > 10$ s the comparing maser does not affect the stability. The Allan deviation between 10 s and 10'000 s corresponds therefore to the stability achieved with the continuous fountain and is of $2.5 \cdot 10^{-13}\tau^{-1/2}$. As will be shown in section 4 this result is already beyond the stability that would be reached with the same LO locked to a pulsed fountain.

Light shift As the operation of the fountain is continuous, all lasers are switched on at all times. Special care must therefore be taken to overcome the light shift. A light trap has been deviced and has already been presented earlier. Such a light trap is in its final stage of assembly but has not yet been implemented into the fountain. As the atoms are not protected against the light scattered from the source, their frequency is shifted. It is, nevertheless, possible to verify to what extent the observed shift can be attributed to the effect of the light scattered by the source. In Figure 4 we represent the relative frequency offset versus the 2nd harmonic of the locking signal. This signal is used as an indicator of the detected flux. To vary the detected signal the repumping power has been changed. Under the assumption that the repumping power does not affect the temperature of the atomic beam the detected signal is thus a measure of the brightness of the source.

The obtained value of $+1.3 \cdot 10^{-12}$ at maximum flux is in agreement with a rough theoretical estimate of the light shift. The dependence of the shift on the second harmonic strongly suggests that the light shift is the main contribution to the total shift of 10^{-12}. Implementation of the light trap whose attenuation factor for scattered light is larger than 10^4 will reduce the total bias due to the light shift to below 10^{-16}.

4 DICK EFFECT

The degradation of the frequency stability due to the Dick effect in pulsed fountains has been described several times already [4, 5, 6] and references therein.

In continuously operated frequency standards, a similar degradation of the frequency stability may also arise. This effect, known as intermodulation effect [7], depends on the scheme of modulation-demodulation and on the modulation frequency. To evaluate to what extent aliasing or intermodulation

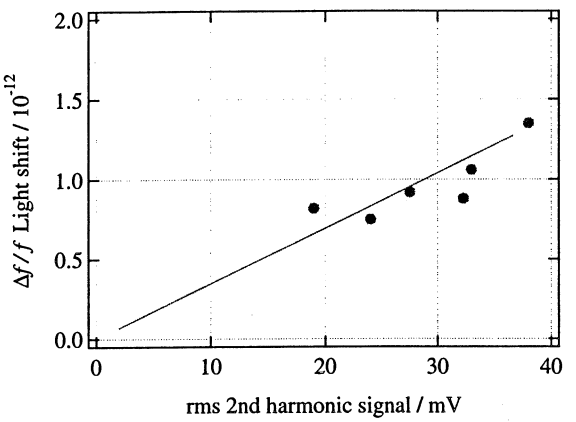

Figure 4: Relative frequency offset versus the second harmonic of the locking signal. The second harmonic is used as an indicator of the flux of the atomic beam and thus of the brightness of the source.

will affect the frequency stability of a continuous fountain we have developed a simple model which applies to a Ramsey type interrogation [6]. For a monokinetic beam the model predicts that no frequency instability due to aliasing will be added to the locked LO if the condition $T_M = 2T$ is fulfilled (T_M being the modulation period, T the transit time of the atoms above the cavity).

With an atomic beam of finite temperature this optimum condition can obviously not be met by all atoms and as a result a residual aliasing may appear. The model has therefore been extended to take into account a velocity distribution of atoms in the beam.

It is interesting to compare the added instability for a given LO in both cases, the pulsed and the continuous fountain. For this purpose we measure the spectral density of phase fluctuations $S_\phi^{\mathrm{LO}}(f)$ of the FTS 1000B locked to a hydrogen maser (Fig. 5). Based on $S_\phi^{\mathrm{LO}}(f)$ and on a typical longitudinal temperature of 100 μK we first compute the total contribution to the frequency instability in the continuous case.

If square PM and square demodulation is used respecting the condition $T_M = 2T$ (where the mean transit time is used as T in the case of a velocity distribution) the total effect remains below $1 \cdot 10^{-15}\tau^{-1/2}$ and is therefore clearly negligible.

The same computation can been performed for a pulsed fountain with the same transit time. The calculation has been made for a period of modulation $T_M = 2T_c$ (T_c being the cycle time) and a duty cycle of 0.5 which is a typical value for most pulsed fountains. With the chosen LO the degradation amounts to $5 \cdot 10^{-13}\tau^{-1/2}$, more than 2 orders of magnitude above the value of the continuous case.

These results are summarized in figure 6. The dotted line corresponds to the case of the pulsed fountain

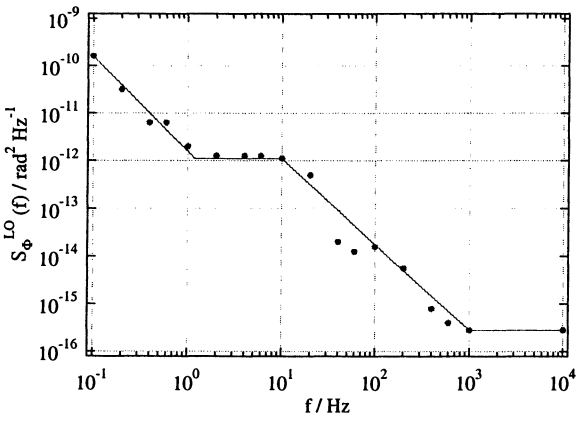

Figure 5: Power spectral density of phase fluctuations of the quartz oscillator FTS 1000B locked to the maser. The circles are the measured points and the full line is the fit used in the calculations.

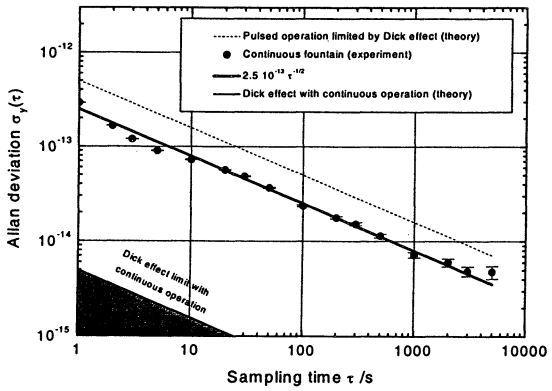

Figure 6: Contribution of the Dick effect to the Allan deviation. The dotted line corresponds to the case of the pulsed fountain and the plaine line is the fit of the experimental points of the continuous fountain

and the plain line is the fit of the experimental points of the continuous fountain. The shadowed area represents the level at which the Dick effect limits stability in the continuous fountain with this particular LO.

One can see that the stability would already be limited in pulsed operation by the Dick effect whereas in the continuous operation its estimated contribution is almost two orders of magnitude below the present, atomic shot-noise limited stability.

Let's also compare the contribution of the Dick effect to the frequency instability for a pulsed and a continuous fountain as a function of the ratio $2T/T_M$, i.e. of the frequency of modulation.

For a pulsed fountain, if the transit time is kept constant, varying the period of modulation is equivalent to vary the cycle time and therefore the duty cycle. In the continuous case we compute again with

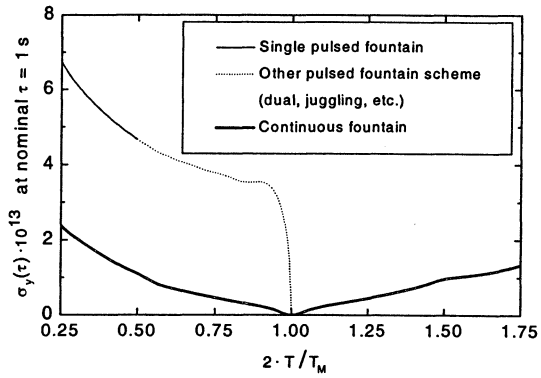

Figure 7: Contribution of the Dick effect to the Allan deviation at $\tau = 1$ s in function of the ratio $2T/T_M$.

the square PM and square demodulation. Fig. 7 summarizes the results. The thin line represents the case of a single pulsed fountain. Values above $2T/T_M = 0.5$ corresponding to a duty cycle higher than 0.5 are not accessible to this type of device. The dotted line refers to proposed schemes of operation of pulsed fountains such as dual or juggling fountains [8, 9]. The thick line corresponds to the continuous case.

It is readily seen that any pulsed operation is very sensitive to the value of the duty cycle (or of the cycle time). This is especially true for values close to $2T/T_M = 1$ as it has been pointed out in Dick's original paper [4]. The contribution from the Dick effect for the continuous fountain shows also a dependance on the period of modulation. However, the values are very small in a wide range around the optimal period of modulation. From Fig. 7 it becomes clear that the total contribution in a continuous fountain is negligible even though the optimum condition $2T = T_M$ can not be met by all atoms.

5 CONCLUSION

The assembly of a continuous fountain resonator is completed and first measurements have been performed. The flux of atoms has been optimized and reaches now 200'000 $m_F = 0$ atoms per second in the detection region. A key point for this improvement is the transverse cooling which increased by at least a factor of 20 the detected flux with respect to the situation without transverse cooling. With this flux stability measurements are possible. In the present situation, measured with a quartz oscillator the continuous fountain has a short term stability of $2.5 \cdot 10^{-13}\tau^{-1/2}$. This value is limited by the atomic shot noise and will decrease further if the flux is increased. A calculation for the pulsed case has shown that with the same local oscillator the short term sta-

bility would already be limited by Dick effect. Preliminary measurements of the light shift indicate a maximum shift of the order of 10^{-12} at maximum flux. Taking into account that the light trap has already shown an attenuation factor larger than 10^4 in a separate experiment this bias can safely be reduced below 10^{-16}.

On the theoretical side, the model describing aliasing effects has been developed further to take into account the finite temperature of the atomic beam. It has been shown that for square phase modulation and square demodulation the total contribution to the frequency instability arising from aliasing effects is negligible even though the optimum modulation condition ($2T = T_M$) can not be fulfilled by all atoms.

References

[1] P. Berthoud, E. Fretel, A. Joyet, G. Dudle, and P. Thomann. Toward a primary frequency standard based on a continuous fountain of laser-cooled cesium atoms. *IEEE Trans. Instrum. Meas.*, 48(2), pp. 516 – 519, 1999.

[2] G. Mileti, A. Joyet, P. Berthoud, P. Thomann, and G. Dudle. Development of the ON/OFMET continuous Cs fountain standard: A progress report. In *Proc. 14th EFTF, 14–16 March 2000, Torino, Italy*, pp. 58 – 62.

[3] G. Dudle, G. Mileti, A. Joyet, E. Fretel, P. Berthoud, P. Thomann. An alternative cold cesium frequency standard: The continuous fountain. *IEEE Trans. Ultrason., Ferroelect., Freq. Contr.*, 47(2), pp. 438 – 442, 2000.

[4] G. J. Dick. Local oscillator induced instabilities in trapped ion frequency standards. In *Proc. 19th PTTI, 1 – 3 December 1987, Redondo Beach, California*, pp. 133 – 140, 1987.

[5] G. Santarelli, C. Audoin, A. Makdissi, P. Laurent, G. J. Dick, and A. Clairon. Frequency stability degradation of an oscillator slaved to a periodically interrogated atomic resonator. *IEEE Trans. Ultrason., Ferroelect., and Freq. Contr.*, 45(4), pp. 887 – 894, 1998.

[6] A. Joyet, G. Mileti, G. Dudle, and, P. Thomann. Theoretical study of the Dick effect in a continuously operated Ramsey resonator. *IEEE Trans. Instrum. Meas.*, 50(1), pp. 150 – 156, 2001.

[7] C. Audoin, V. Candelier, and N. Dimarcq. A limit to the frequency stability of passive frequency standards due to an intermodulation effect. *IEEE Trans. Instrum. Meas.*, 40, pp. 121–125, 1991.

[8] S. Ohshima, T. Kurosu, T. Ikegami, and Y. Nakadan. Cesium atomic fountain with two-dimensional moving molasses. *Jpn. J. Appl. Phys.*, 34(9A), pp. L1170–L1173, 1995.

[9] C. Fertig and K. Gibble. Laser-cooled Rb87 clock. *IEEE Trans. Instrum. Meas.*, 48, pp. 520 – 523, 1999.

SENSORS

Chairman: Raymond Bessond

INVESTIGATION OF ACTIVITY-DIPS IN THERMO-SENSITIVE QUARTZ RESONATORS AT CRYOGENIC TEMPERATURE

°B. Dulmet, °R. Bourquin, *L. Spassov, *V. Georgiev, *R. Velcheva

°LCEP/ENSMM, 26 Chemin de l'Epitaphe , 25000 Besançon, France
*ISSP-BAS, 72 Tzarigradsko Chaussee Blvd, 1784 Sofia, Bulgaria

Bernard.Dulmet@ens2m.fr Tel: 33 (0)3 81 40 28 25 Fax: 33 (0)3 81 88 57 14

Abstract

Thermo-sensitive quartz resonators (TSQRs) can be used as temperature sensors over a wide temperature range.
TSQRs operating at 26.5 MHz on third overtone of C-mode have been made and tested at ISSP-BAS, in a doubly rotated cut which combines good sensitivity and reduced non linearity of the temperature frequency characteristics over an extended rage, but some samples exhibit various kinds of activity dips in the vicinity of 130 K. This paper presents the results of the first investigations undertaken for the modelling of thermo-dependent couplings which may provoke such disturbances. Simulations were made with LCEP's proprietary 3D finite elements program built upon a combination of Lagrange's formulation and cubic interpolating functions. Predicted occurence of couplings depends on the refinement of FEM mesh. Although precise measurements of the mode patterns are still needed, the performed analyses clearly indicate an influence on electrodes tabs orientation on the location of predicted activity dips.

1 Introduction

The Acoustoelectronics Laboratory of ISSP-BAS has since long investigated the use of TSQR for thermometers, especially at low temperatures. The currently adopted design operates on third overtone of thickness shear C–modes in flat parallel quartz plates, in the cut defined by $\varphi = -10°54'$ and $\theta = 11°06'$. These features provide with quite a linear behavior in the temperature range $70 \div 450$ K, with a rather convenient temperature sensitivity about 1000 Hz/K when the resonant mode is settled around 26.5 MHz, as mentionned in Ref. [1]. Despite of a reduced sensitivity at extremely low temperature, only 2 Hz/K at 4.2 K quickly increasing up to 600 Hz/K near 70 K, the very correct time stability of this design of TSQR permits to achieve accuracy better than 0.002 K above 20 K. Nevertheless, various disturbances on temperature behavior of some TSQRs may appear on some samples in dedicated temperature ranges, and particularly in the ranges $90 \div 110$ K and $120 \div 135$ K. One suggested cause of this is attributed to possible excitation of other modes at given temperatures, as a consequence of the various thermal sensitivities of the many kinds of resonant modes that may exist in a piezoelectric resonator. This is the main phenomenon which is generally understood by the generic term of "activity dip", although it is unclear whether this term should encompass disturbances of other origin as well.
Such thermo-dependent couplings between two different kinds of thickness shear modes could be isolated and consistently modelled in a case-study on 7^{th} overtone C mode of contoured quartz resonator proposed at Ref. [2]. This kind of coupling is absolutely linear and can be explained by the fact that the well-established representation of a resonant mode issued from the general theory of guided waves in thin plates cannot be restricted to a single dispersion curve whenever resonant modes belonging to different branches of the dispersion curves occur at the same frequency. After this first step, it was possible to extend the perturbation model to describe any thermo-dependent coupling arising from a coincidence of two (or more) quasi-thickness modes [3]. This possibility existed because one of the basic ideas of this model consisted in considering all modes as sums of closed–form temperature–dependent functions :

$$\hat{\mathbf{u}}(T) = \sum_{\lambda} C_{\lambda}(T)\, \hat{\mathbf{u}}^{\lambda}(T) \qquad (1)$$

where the dependence of the coefficients C_λ with respect to temperature is actually more important than the thermal dependence of the functions $\hat{\mathbf{u}}^\lambda$ themselves. A typical behavior of the sum is repesented on Fig. 1. The coupling at crossing point acts to separate the modes which progressively "exchange" their nature around the crossing point. In this manner, a spurious mode which is otherwise piezoelectrically inactive is excited by the regular mode in a limited temperature region, and the oscillator carries out a frequency jump according to the basic behavior schematically represented on Fig. 2. This framework still can be extended to model activity dips between thickness-shear modes and spurious modes from a completely different nature, but, indeed, a case-by-case analysis is then required. At this point, it can be preferred to perform the modelling with a fully numerical approach such as FEM [4, 5, 6, 7], since this method is expected to strongly minimize the prerequisite knowledge about spurious modes suceptible to couple with

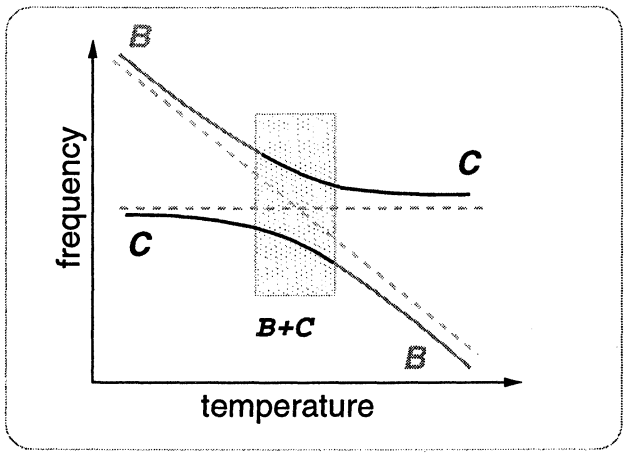

Figure 1: A typical thermo-dependent coupling near crossing point

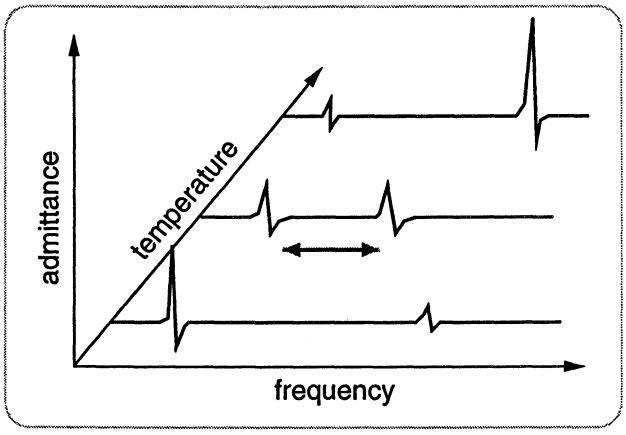

Figure 2: Electrical output of two thermally coupled modes near crossing point

the regular ones in an arbitrary temperature range. Instead of representing the vibration as a sum of 3D functions well-defined in the whole resonator with some physical significance related to dispersion branches, FEM describes the vibration as a big number of separate sums of simple spatial 3D-functions, according to the discretization into finite domains :

$$\hat{\mathbf{u}}(\mathbf{x}) = \sum_{e} \langle \hat{\mathbf{F}}_n^e(\mathbf{x}) \rangle \{\hat{\mathbf{u}}_n^e\} \qquad (2)$$

where the subscript e symbolically denotes a finite (elementary) domain, $\hat{\mathbf{F}}_n^e(\mathbf{x})$ denotes the so-called shape functions [8, 9] for element e, $\{\hat{\mathbf{u}}_n^e\}$ denotes a vector holding the values of the field variables at the nodes of the element e. The dot product indicated by the notation $\langle \cdots \rangle \left\{ \vdots \right\}$ is performed over the $n = 1 \ldots N$ nodes of element e. The ability of this approach to model thermo–dependent couplings automatically comes out from the variation of both coefficients and shape functions in the local sums.

2 Main features of FEM model

Previous works have demonstrated that linear and quadratic interpolations are not best suited to model the oscillating behavior of TS modes along the thickness of plate. Initial attempts of using trigonometric interpolations along thickness [10] were soon followed by the achievement of new elements based upon cubic interpolations along the thickness [4]. Then, it was found that, to model one half wavelength of TS, prismatic elements such as given on Fig. 3b–e), which pile up four layers of nodes in equal number give better results than elements built on incomplete cubic basis along all directions, *eg* as represented on Fig. 3a).

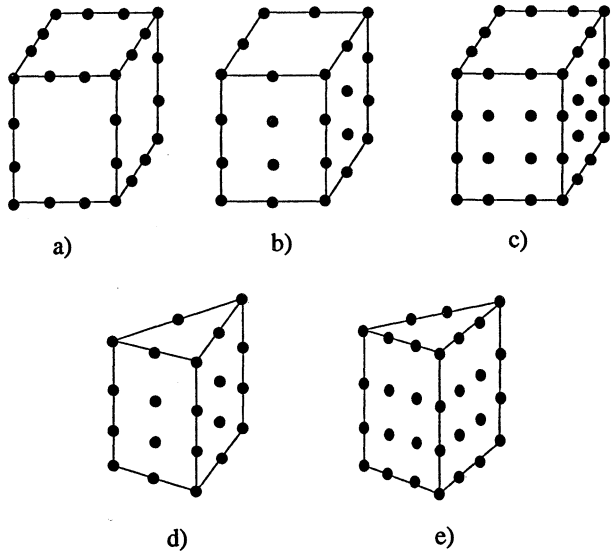

Figure 3: finite elements of interest

Finite elements like 3b) and 3d) provide with cubic interpolation along the thickness and incomplete parabolic ones along in–plane axes of plate, whereas elements represented on Figs. 3c) and 3e) provide complete interpolation along the thickness and incomplete cubic interpolation along in–plane axes. Here-presented analyses were performed with types 3b) and 3c) only. As detailed in Refs. [4] and [13], LCEP's FEM program systematically uses the so-called Lagrangian formulation, *ie* all equations are mapped onto the coordinates of the body in a fixed state, so-called reference state, thereby avoiding recomputation of resonator's shape along temperature variations. This implies the use of appropriately defined temperature coefficients of material constants whose numerical values were proposed in [12] and [11]. Details on the shape functions used in the program can be found at Refs. [4] and [13].
The modelled TSQRs are disks with $\phi = 8$ mm and $\phi_e = 4$ mm for electrodes,whereas the current path to electrodes is 2 mm wide. It was difficult to accurately mesh this design without avoiding the use of very distorted bases from the ideal rectangle. So, we chose the models presented on Figs. 4 (32-nodes elements) and 5 (48-nodes elements), previously employed in Ref. [4]), where three layers of el-

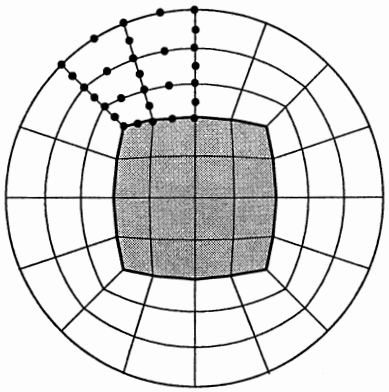

Figure 4: model with parabolic in-plane interpolations

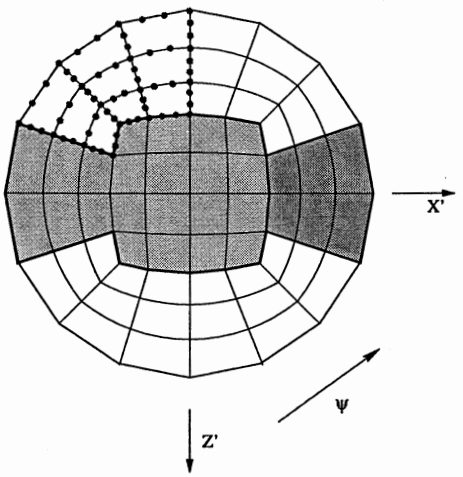

Figure 5: model with cubic in-plane interpolations

ements are piled up along the thickness of plate to account for 3^{rd} overtone amplitude distribution. Models complying with Fig. 5 were achieved with and without electrodes tabs. Under those conditions, Fig. 4–type models typically required 177 Mb of RAM, and 45 minutes per temperature point, and Fig. 5–type models typically required 405 Mb of RAM and roughly 4 hours per temperature point, on a not so expensive 550 MHz PC equipped with 1 Mb of RAM, and running Linux. Since the eigenvalues problem is solved by iterative method (variant of so-called subspace method [9]), the number of iterations needed for stabilization of results is indeed not know in advance. It was found typically between 30 and 80 for a subspace consisting of 38 modes from which 30 solutions are retained.

3 Results

Since our program is currently limited to the search of undamped eigenmodes, we only simulated $f(T)$ characteristics with associated mode patterns, which may be a de-

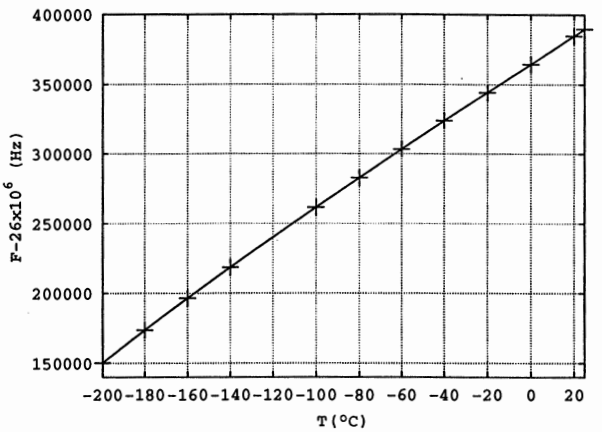

Figure 6: computed FTC with rougher model

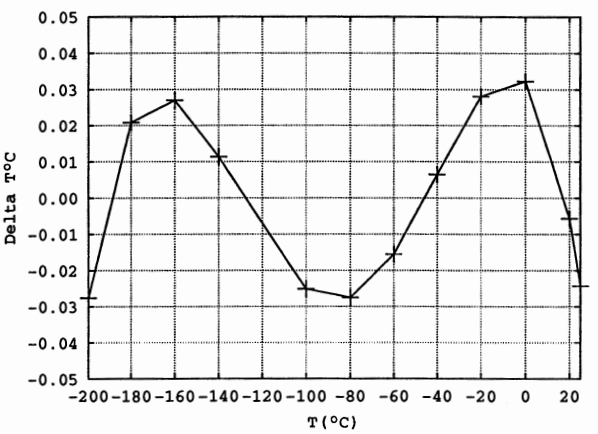

Figure 7: residue of cubic fit of FTC (rougher model)

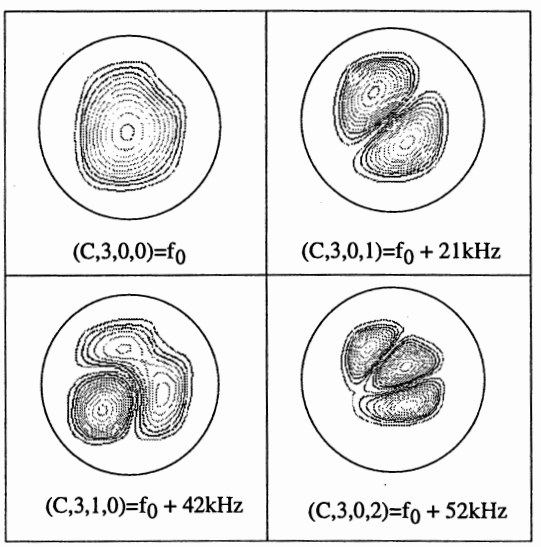

Figure 8: pred. patterns of first TS modes (rougher model)

manding task according to the time required to compute a single temperature point. We started comparing results obained with 32-nodes and 48-nodes elements. The 32-nodes elements mesh provided with a rather smooth frequency temperature curve of regular $(C, 3, 0, 0)$ mode given at Fig. 6, whereas the predicted pattern remained unchanged along the full temperature range $73 \div 293$ K.

A least square fit of the computed FTC by a cubic function in terms of temperature provided a first order coefficient equal to 1011.39 Hz/K. Fig. 7 plots the residue of this fit. Nevertheless, the computed mode patterns, given on Fig. 8 appear rather distorted, independently from temperature effect. This was interpreted as a proof of unsufficient accuracy of this model, inasmuch as the finer model made with 48–nodes elements (Fig. 5) provided with much more symmetrical patterns as shown on Fig. 9 (without electrodes tabs), even for relatively high order anharmonic modes such as $(C, 3, 1, 0)$ or $(C, 3, 5, 0)$. This indicates a much better convergency of the FEM model with 48-nodes elements. The oblong shape of $(C, 3, 0, 0)$ pattern is interpreted as coming from the compromise between inner symmetry of dispersion properties of guided waves propagation in this cut (Tiersten's angle -36.8^o for this overtone), and the "squared" shape of simulated electrodes due to the use of elements with a quadrangular base.

Thus, a new FTC was simulated in the same range as before, and provided with a very close value of linear coefficient 1011.39 Hz/K of $(C, 3, 0, 0)$ mode, but this time, the residue of least square fit with a cubic function showed a discontinuity near 193 K, as shown of Fig. 10, corresponding to occurence of irregularities of the mode pattern. This behavior remained unchanged after electrodes tabs were included in the FEM model. Distribution pattern of $|\hat{\mathbf{u}}|$ in the perturbated case is shown of Fig. 11, whereas outside this region, the simulated mode pattern is perfectly smooth, as shown on Fig. 12. Simulations performed after rotating the material constants around the plat normal by -45^o and -90^o showed a strong influence on the occurence of perturbation, since in the $\psi = -45^o$ case, perturbations of the predicted mode pattern disappeared from the 193 K in the $\psi = -90^o$ case, nothing was observed in the limited range $173 \div 213$ K investigated at the time the conference. In addition, reducing the theoretical thickness from 0.1919 mm down to 0.1912 mm moved the firstly observed perturbation from 193 K down to 183 K and a new one was observed at 85 K. This can be explained by the fact that a slight decrease of thickness has not the same impact on the regular and on the spurious modes, since they are from different nature. The spurious modes involved in those couplings appear as combined (u_2, u_3) waves obliquely propagating along in-plane axes of plate. A closer look on invoved patterns shows that perfectly modelling would still require an even denser mesh.

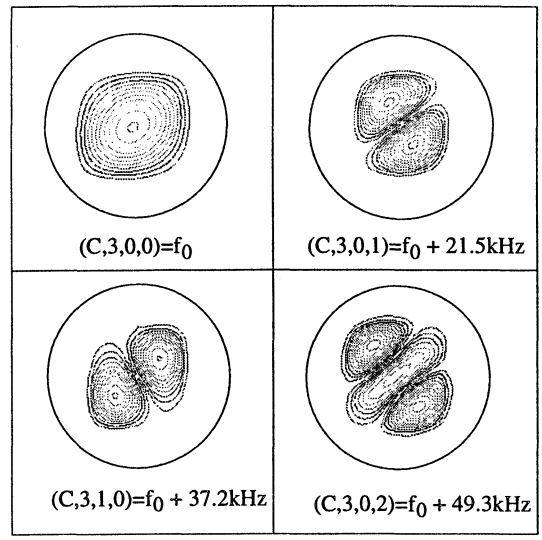

Figure 9: pred. patterns of first TS modes (finer model)

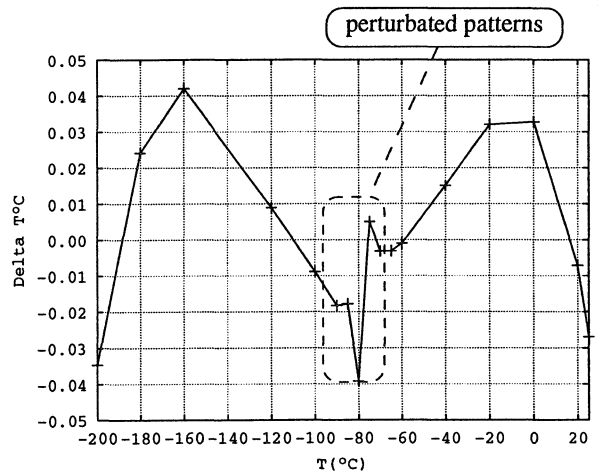

Figure 10: residue of cubic fit of FTC (finer model)

Conclusion

Analyses of 3^{rd} overtone modes performed with prismatic elements with a quadrangular base clearly predict thermodependent couplings affected by orientation of the metallizations system, and by the thickness of resonator. Those couplings affect the predicted mode pattern as well as the frequency *vs.* temperature characteristics, but accessing them requires with refined FEM models, implying the need of cubic–interpolating elements and leading to analyses in the Gigabyte–of–RAM range, which can be run on nowadays PC computers, but convergence of the patterns of involved spurious modes in terms of mesh refinement does not seem fully attained in already perfomed analyses, but it seems rather correct for main modes far from the coupling region. Although further designing new prismatic elements with a

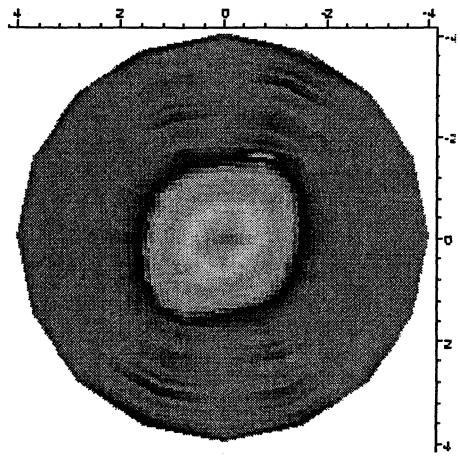

Figure 11: perturbated mode pattern ($-80°C$)

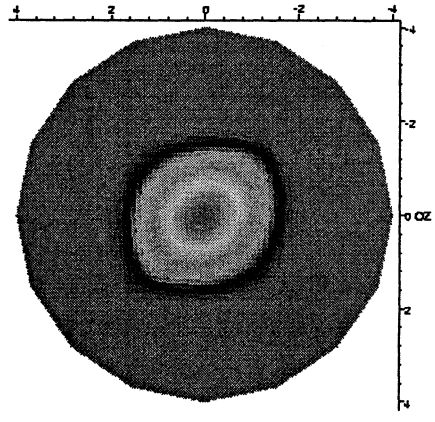

Figure 12: smooth mode pattern ($-60°C$)

triangular base will permit a more realistic modelling of the electrodes system, already obtained results suggest that a precise design of electrode shape and orientation is a key issue for controlling the occurence of activity dips in here-studied TSQRs.

Acknowledgements

Since year 2000, this study is jointly supported by CNRS (Direction Relations Internationales) and BAS under bilateral cooperation number 8686. Authors wish to thank both organisms for this precious help.

References

[1] V. Georgiev, L. Spassov, L. Vergov, R. Velcheva, "Some Investigations of thermosensitive quartz resonators at cryogenic temperatures", *Proc.* 14^{th} *Europ. Freq. and Time Forum*, Torino, pp. 273–275, 2000.

[2] R. Bouquin, B. Dulmet, G. Genestier "Jumps in Frequency Temperature Response of Contoured Resonators: an Analysis Performed with a Perturbation Model and X-Rays Patterns", *Proc. IEEE Ultrasonics Symposium*, pp 388–392, Dallas, November 1984.

[3] B. Dulmet, "A general model for quasi thickness vibrations in contoured plates", *Proc.* 5^{th} *Europ. Freq. and Time Forum*, pp 164–172, Besançon, March 1991.

[4] F. Raoelijaona and B. Dulmet, "FEM Modeling of Spectrum and High Order Thermal Sensitivities of Flat Plates Resonators Operating in Fundamental Modes of Essentially Thickness Shear", *Proc.* 11^{th} *Europ. Freq. and Time Forum*, pp 24–28, 1997.

[5] K. Trümpy, W. Zingg, "Finite Element Analysis of AT Strip Quartz Resonators", *Proc.* 7^{th} *Europ. Freq. and Time Forum*, pp45–50, 1993

[6] K. Trümpy, "Analysis of Quartz Resonator Activity Dips with High–degree FEM", *Proc.* 11^{th} *Europ. Freq. and Time Forum*, pp 29–34, 1997.

[7] K. Weiss, W. Szulc, E. Żuchowski, M. Tupaj, B. Dumet, "A new miniature quartz Y+5 temperature sensor", *Proc.* 12^{th}*Europ. Freq. and Time Forum*, Warsaw, 1998.

[8] D.C. Zienkiewicz, "The Finite element method", *Ed. Mac Graw Hill*, 1977.

[9] G. Dhatt, G. Touzot, "A presentation of finite element method", *Ed. Maloine S.A.*, Paris, 1984.

[10] F. Raoelijaona and B. Dulmet, "Finite Elements Analysis using Trigonometric Interpolations for high overtones thickness modes resonators", *Proc.* 4^{th} *Europ. Freq. and Time Forum*, pp. 121–126, 1995.

[11] B. Dulmet, R. Bourquin, S. Ballandras and E. Bigler, "On the Thermal Derivatives of Effective Material Constants for the Modelling of Higher Order Thermal Behavior of both SAW and BAW Propagations in Quartz", 9^{th} *Piezoelectric Conference, Piezo'96, ITR, Warsaw*, pp 31–36, 1996.

[12] B. Dulmet, R. Bourquin, "Influence of the definition of material constants in the study of crystal plates thermal behavior", *Proc.* 3^{rd} *Europ. Freq. and Time Forum*, pp 305–312, 1989.

[13] B. Dulmet, "Current Trends of finite elements methods applied to piezoelectric resonators", *Proc. of ISSWAS-4, pp 36–44, St Petersburg*, June 1998.

AUTODYNE MICROWAVE SENSOR OF COMBUSTION PROCESS: BEHAVIOUR UNDER FAST HEATING

Safonova E.V. and Boloznev V.V. Kazan State Technical University, e-mail: kate@cg.ru, **tel:+7(8432)637687, fax:+7(8432)764307**

1. ABSTRACT

Microwave methods of an electron density diagnostics in flames were considered as not efficient up to our present researches. The reason is: fast erosion in flame of equipment components (antenna especially). Flush- mounted antennas and autodyne's methods of diagnostics have been not used for combustion processes investigations, despite the wide usage of microwave diagnostics for other purposes We were able to depress this disadvantage by using those two technical solutions. Flush-mounted antenna is a good technical decision and of course the electromagnetic waves don't burn.

But the problem of antenna, resonator and Gunn diode heating is occurred. Part of it was solved in [1,2,5]. In this work we are interested in effects, during the switching the device on and it passage into operating mode.

Purpose: the search of an analytical dependence between chamber temperature and measuring signal frequency during the switching the transport thermal engine devices on and it passage into operating mode. First stage of the work is to build physics and mathematical models of the heating process.

In offered physics model the temperature influence at the frequency passes through five "channels". They map contribution of an antenna (1); resonator (its elongation) (2); permittivity growth in longitudinal (3) and transversal (4) directions; and a diode (5).Where 1,2,3,4,5- are the channels of the physics model. Spectrum of the temperature process $T(\Omega,t,x)$ is wide (sometimes up to tens kHz) in a start mode. Propagation of different length temperature waves in a sensor's body happens with a different velocities.

Most complicated part of a mathematical model falls on the resonator ("channel" (2) and (3)). Triple integration of an initial process $T(\Omega,t,x)$ on frequency Ω, time t and area among axis x is necessary here. In generally case it iscarried out with a special functions (Frenel functions). The numerical integration is more preferable. For many special cases it is possible to receive more simple expressions after decomposition of the problem.

Analysis, the received results and compensation methods of high temperature influence will be presented in this paper.

Conclusions: The held analysis has shown, that the process of the sensor's heating at TED-start essentially lags from the temperature growth of the operating body. Measuring error in comparison with a quasi-static condition increases several times, especially during the first seconds after TED passage into operating mode. Spectrum of an autodyne response is much more narrow-band than an initial temperature process. High-frequency components in it are stipulated by the contribution of an antenna. Taking into consideration of the design measures (2) it gives a hope for realization of a rather simple (not too high-frequency or in " sense narrow-band ") system of a measuring signal correction.

2. INTRODUCTION

Temperature influence of the controlled operating body as an origin of the sensor error, was being considered by us for two situations: frequency bias under the quasistatic heating till the nominal operating temperature [1] and frequency fluctuations during the diagnosing process [2]. The third situation is: fast heating of the sensor under the well known law of operating body temperature growth. By well known we consider the knowledge of start and final temperatures near the flame surface of the sensor, rise time and roughly the form of the growth curve. An attempt of this process study, undertaken in [2], was not successful.

Sensor's heating and corresponding variations of its frequency obviously don't keep pace with operating body heating. The dynamics of the temperature distribution in the sensor's volume and under the heating is quiet complicated.

Influence on the frequency has a multifactor character. Mathematical manipulations are very difficult. But an opportunity of receiving an experimental results is much more problematic.

The expected results are necessary for short technological combustion processes research: explosion, shot, impulse switch on of rocket engine, and also the start switch on and emergency state. This work is a direct continuation of the Kansas paper [2], that is why we tried to refrain from repetition below.

3. STATEMENT OF PROBLEM

In the microwave diagnostics of combustion processes in TPE, for example in rocket engines, antenna is exposed to an intensive heating. Under the start heating rate runs up to hundreds degrees per second. Antenna elements deformation, temperature changes of the dielectric properties lead to mismatch (reflectivity variations) and measurement error growth. At the same time, reflectivity contains also an information about the diagnostic parameter – flame permittivity. The difficulty in diagnostics of current error value is, that even if we make a float mounted antenna as a slit in thin plate or strap, the process of its heating is inertial. The time for achieving the stationary temperature is much more, than the start time, the interconnection law with a growing flame temperature is unknown. Temperature and pressure behavior in chamber under the operating duties changes for the different rocket engines is well presented in reference.

4. PURPOSE OF INVESTIGATION

We are trying :

- To determine analytically sensor's frequency variations character under the fast (seconds and split seconds) and significant growth of the temperature on its firing surface;
- To find out the difference between the dynamic and quasi-static frequency magnitudes for each moment of time; to estimate the extent of delay;
- To reveal the main origin of the dynamic error.

We would like to use the received relations for the computer correction of results of combustion process diagnostics, and also for the possible variations of the scheme and/or constructions of the sensors.

5. MODEL

Process (1) activates the "five-channel" mechanism of frequency destabilization: antenna (a), length(L), permittivity (ε), wave resistance(ρ), diode (d).The first to respond to the temperature variation is the antenna.

Further in accordance with a temperature an antenna wave's propagation in the resonator there is a heating (or cooling) of segments, that are more and more remote from an antenna. Correspondingly three more destabilizing channels are switched on: linear extension and an electrical sizes change because of the temperature dependence of permittivity. The last one creates two effects: not only an electrical length change, but wave resistance also.

At last, the diminished temperature wave reaches the diode (the fifth channel is switches on). Thus, we obtain an opportunity to construct a generalized electro-thermal model of a sensor. It represents a quadripole with a five-channel inner structure, with known transfer functions of all nodes and with the signals $T_1(t)$ - on input and $\omega(t)$ - on output. Now we have to establish the functional interconnection of an original temperature process with frequency variations of the sensor. By an explicit mathematical analogies we consider the heat propagation as an impulse electrical signal advancing in transmission line.

It is necessary to find an impulse function of electric chain and an output signal (to be more exact in the cross-sectional x).

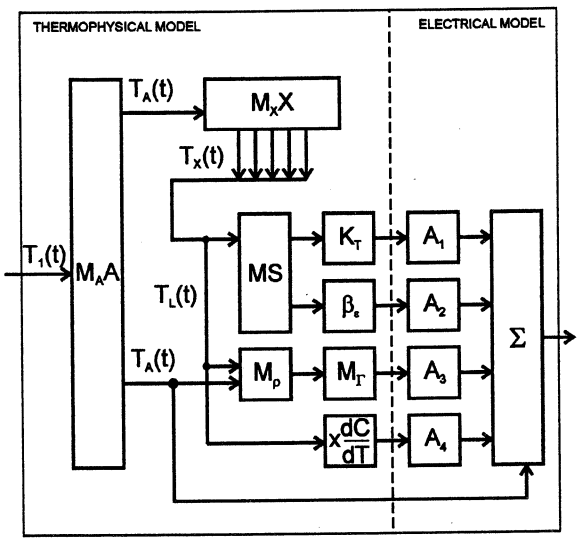

Figure 1. Joint thermophysical and electrical models of the sensor

As distinct from [2] five-channel structure response (fig.1) on the input action $T(t)$ we consider taking into account phase relations. In consequence of evident analogies we use an accepted in radioelectronics technique :

1. Impulse function searching :

$$h(t)=\int_0^{\infty} F(\Omega,x)\cdot\exp(j\Omega t)d\Omega$$

where for antenna $F(\Omega,x)=F_1(\Omega)$

$$F(\Omega,x)=F_1(\Omega)\cdot F_2(x,\Omega)\cdot F_3(x)$$

$$\varphi_A=arcctg(1+H/q)$$

$$F_1(\Omega)=\left(1/\sqrt{1+2q/H}\right)\cdot\exp(j\varphi_A)$$

$$F_2(x,\Omega,t)=\exp(-qx)\cdot\cos(\Omega t-qx)$$

$$F_3\approx 2\exp(-mx)\cdot[1-\exp 2m(x-L)]$$

[see2,4].

Functions $F_{1,2,3}$ show an amplitude and phase changes in the antenna (F_1) and in resonator during an internal heat exchange (F_2) and in the case of heat emission into an environment (F_3). $q=\sqrt{\Omega/2a}$ - per unit length damping, Ω - frequency of a Fourier -component, a - thermalphysic thermal diffusivity, H,m - thermal constants, describing heat exchange with an environment.

2.Convolution of impulse function and input action $T(t)$:

$$\int_0^{\infty} h(t)\cdot T(t-\tau)dt=\int_0^{\infty}\int_0^{\infty} F(\Omega,x)\cdot T(t-\tau)\cdot \cdot\exp(i\omega t)d\Omega dt=T_N(\tau,x) \quad (2)$$

where $N=A,L,\varepsilon,D,T_L(t)=T_\varepsilon(t)$, (by wave resistance we neglect as earlier in[]).

3. Relative frequency variation by each channel influence is:

$$\Delta_A=\frac{\Delta\omega_A}{\omega}=\frac{1}{\omega}\cdot\frac{\partial\omega}{\partial\Gamma}\cdot\frac{\partial\Gamma}{\partial T}\cdot T_A(t,x=0)$$

$$\Delta_L=\frac{1}{\omega L}\cdot\frac{\partial\omega}{\partial L}\cdot\frac{\partial L}{\partial T}\cdot\int_0^L T_L(t,x)dx \quad (3)$$

$$\Delta_\varepsilon=\frac{1}{\omega L}\cdot\frac{\partial\omega}{\partial\varepsilon}\cdot\frac{\partial\varepsilon}{\partial T}\cdot\int_0^L T_\varepsilon(t,x)dx$$

$$\Delta_D=\frac{1}{\omega C_D}\cdot\frac{\partial\omega}{\partial C_D}\cdot\frac{\partial C_D}{\partial T}\cdot T_L(t,L).$$

Here, by virtue of electric processes (in comparative with thermal) corresponding derivatives have the same values, that in quasistatics [1]. Because the processes (3) are quasideterministic, their total frequency variation in time is defined as an algebraic sum (3). Note also, that

$$\int T_L(t,x)dx=\int T_\varepsilon(t,x)dx$$

6. ANALYSIS

Lets do it in parts, beginning from the impulse function $h_A(t)$ and antenna's temperature $T_0+\Delta T_A(t)$, also corresponding frequency bias $\Delta_A(t)$. After reduction to one argument we have:

$$h_A(t)=4a\int_{-\infty}^{\infty} q\left(1+\frac{2q}{H}\right)^{-\frac{1}{2}}\cdot \quad (4)$$

$$\cdot\exp\left[-jarcctg\left(1+\frac{H}{q}\right)-j2aq^2t\right]dq$$

The result of integration is not possible to present neither using elementary functions, nor special functions. In order to receive the approximate result, keep in mind, that $q << H$ in an energy-significant area of spectrum of the process $T_f(t)$. After Taylor linearization and correspondingly restricting the limits of integration by requirement $q < H/2$ and acting according to complex variable function rules, we receive:

$$h_A(t) \approx \frac{1}{t} \cdot \{[1 - \frac{1}{16bt}] \cdot \sin bt + \\ + \frac{1}{16t} \cos bt\} \approx \frac{1}{t} \sin bt \qquad (5)$$

here, this value is connected with limit of integration $\Pi = H/2$.

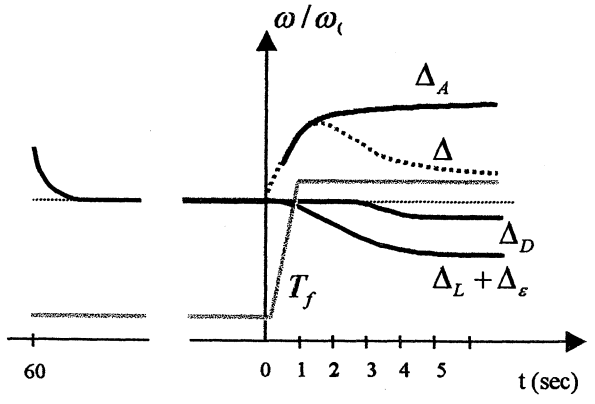

Figure 2. Frequency error stipulated by each channel contribution.

For the better result clearness lets consider the linear approximation of the flame temperature (fig.2) as:

$$T_f(t) = \left\{ \begin{matrix} T_0(1+\gamma_f t) \\ (T_0 + \Delta T_f) = T_0(1+\Delta_f) \end{matrix} \right\} \begin{matrix} , t \in (0, \theta_f) \\ , t > \theta_f \end{matrix} \qquad (6)$$

Now we make a convolution. Casting out secondary by influence terms of series we receive:

$$T_A(t) \approx \left\{ \begin{matrix} T_0(1+\gamma_A t) \\ T_0 + \Delta T_A \end{matrix} \right\} \begin{matrix} , t = 0, \theta_A \\ , t > \theta_A \end{matrix} \qquad (7)$$

where $\gamma_A \approx \gamma_f \cdot Si(b\theta)$,

$$\Delta T_A \approx \Delta T_f \cdot \left[Si(b\psi) - Si(b\theta) - \frac{b}{\gamma_f} \cdot \cos(b\theta) \right]$$

and point of time θ_A, as the end of antenna's heating, is easily calculating from (fig.2).

$$\theta_A = \Delta T_A / \gamma_A T_0$$

On the figure 3 two dependencies are presented: one- for the titanium antenna another one –for copper antenna. On the starting part (line dotted) our results are rough. Integration by time ψ was chosen taking into account the properties of integral sine $\lim_{x \to \infty} Si(x) \to \pi/2$ and is sensibly equal to limit when $x > 5$. We hope, that this may increase the process of numerical integration in future. For the preliminary rough estimations $Si(b\psi) = \pi/2$.

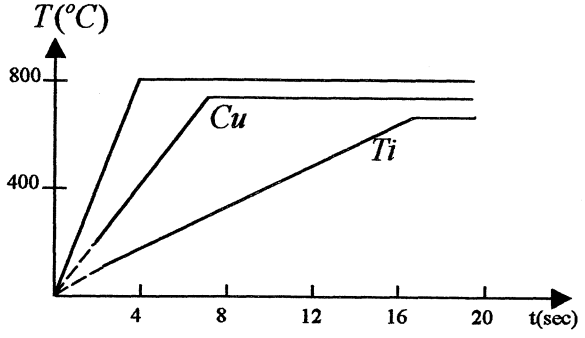

Figure 3. The process of heating for copper and titanium antennas.

The result of (7), is good under the analysis of other "channels" we use (7) as an input noise action.

7. DISCUSSION

Duration of the investigating process and comparative contribution of "channels" into resultant frequency variation is determined by sensor's construction and combination of three thermal physics magnitudes: speed of heat-wave propagation $v = \sqrt{2a\Omega}$; this wave length $\Lambda = 2\pi\sqrt{2a/\Omega}$; $q = \sqrt{\Omega/2a}$ - per unit length damping. All this magnitudes connected with each other through a - thermal diffusivity and appear in subintegral expressions 2,3 in an implicit

way[4]. As a result of this interconnection on the length, equal to the proper length $x = L$, wave amplitude decay in $e^{2\pi} = 540 times$; (when $x = \Lambda/2$ it decays in $e^{\pi} = 22 times$).

In the dielectrics, used by us, $a \sim 10^{-4} (m^2 Hz)$. The corresponding waves-lengths $\Lambda = 11;35;100 mm$ (when $\nu = \Omega/2\pi = 10;1;0.1 (Hz)$ and $q = 542;175;55 (1/m)$. By the terms of Gunn diode heat-reflection the sensor's length should be not less than $60...100 mm$. That is why only antenna and the part, closely set to it, are subjected to the fast heating.

Sequence of above-stated is an excessive duration of heating and establishment of stationary temperature distribution in sensor. During all this time measuring error will be severe. At the same time big parameter spread in a different moments of inflammation hamper the realization of correction on the preregistered program. We also can't suggest the new construction of the sensor, that would be able to ensure an analog error compensation, as was made for the fluctuation error in [5]. We are going to continue our research in this direction. It is not easy to do, because we have laid down the requirements to materials for antenna and resonator, specifically on temperature conductivity they have to differ as much as possible (actually more than in 100 times). Trend of heating processes for copper and titanium antennas is shown on figure 3. Impulse function for resonator in the arbitrary cross-section x is:

$$h_x(t) = 4a \int_{-\infty}^{\infty} q \exp\left[-qx - j\left(aq^2 t + xq\right)\right] dq \quad (8)$$

this integral is reduced to standard integrals. Making the convolution with (7) and then integrating by resonator length we receive desired results. They are presented graphically (fig. 2).

8. CONCLUSTIONS

The sensor heat time until the stationary temperature distribution in its body in many times exceeds the start time. Sensors with antennas for this and others constructions were developed for fuel-propellant rocket engines diagnostics. The experiments were run on the test benches, where electron density in flame was registered on all stages of duty cycle.

The results of the present work convince, that estimations and conclusions from this experiments applied to inflammation and process of burning evaluation (but not to the stationary mode) in most cases are faulty. At that time sensor heating process was observed but not the density growth. For the start processes of fuel-propellant rocket engines research we need the sensors with a different circuit and design solution.

Nevertheless, the sensor usage for the other processes diagnostics with a different time characteristics is perspective

- air-feed jet engine transition into cruising regime. Sensor heating $q << H$ is close to the quasistatic
- Shot, explosion, solid-fuel rocket engine switch on. Here $q >> H$ on the most part of the spectrum- sensor just doesn't have time to heat up.

In both cases it is simple to correct the error. We are going to continue our investigations of this regimes in more details in near future.

9. REFERENCE

1) V.Boloznev, E.Safonova, "Microwave oscillator as a sensor of electrophysics flow parameters", Proc. 13th EFTF , April 1999pp.1062-1066, Besancon, France

2) V.Boloznev, E.Safonova, "Determination of the frequency of oscillations in the autodyne's sensor under the regular and casual temperature mode variations" , Proc. 2000 IEEE/EIA international frequency control symposium and exhibition, Kansas city, USA

3)A.Angot "A l'usage des ingenieurs de l'elektronique et des telecommunications", Paris,1957

4) A.V. Luikov " Heat conduction theory"[in Russian], Moscow: High school, 1967, p.600

5) E.Safonova "Minimization of an autodyne sensor's error, stipulated by the antenna's heating", Proc. EFTF 14th Italy

IMPROVEMENT OF HUMIDITY SENSITIVITY OF QUARTZ RESONATORS USING FULLERENE LAYER AS A SORBENT

Tsvetan Angelov[a)], Zdravka Raicheva[a)], Lozan Spassov[a)], Bernard Dulmet[b)]

a) Institute of Solid State Physics, Bulgarian Academy of Sciences
72, Tzarigradsko Chaussee Blvd., 1784 Sofia, Bulgaria
Tel. : (+359-2)77 25 10, Fax : (+359-2)975 36 32, E-mail : lspassov@issp.bas .bg

b) Laboratoire de Chronométrie, Electronique et Piézoélectricité, ENSMM,
26 Chemin de l'Epitaphe, 25000 Besançon cedex, France.

Abstract

In an earlier work, we have investigated the sensitivity of quartz resonators with thin fullerene (C60) layer deposited on them for the measurement of relative humidity [1].

This paper deals with further investigations of such resonators aimed to increase their sensitivity. One of the possibilities to improve it would be to increase the effective (active) surface of sorption and obtaining more loading mass with the same (electrode) configuration of the quartz resonator.

Quartz resonators with different grades of final lapping, and consequently with different roughness and effective surfaces have been made and investigated after depositing a fullerene layer. In this way, a strong relationship has been first established between measured roughness, equivalent resistance and humidity sensitivity. We have shown that up to some grade of roughness, the dynamic parameters of quartz resonators are not significantly degraded while effective surface of the system increases over 30% in the same time. Directly computing the influence of roughness on effective surface by simple interpolating methods, we can in turn evaluate the impact of surface enlargement due to roughness upon the humidity sensitivity.

1. Introduction

AT cut quartz resonators are characterized with high temperature stability. At the same time strong dependence of frequency while loading additional mass over their surface [2].

Their high degree of mass sensitivity opens new opportunities for their usage as humidity or toxic gases sorption sensors [3,4]. As a rule the surfaces of the resonator are overlaid with sorption substances (sorbents) which often possess selective properties as well.

Still the issue of the resonator relief influence on the sorbent relief and therefore - its mass sensitivity has not been investigated in details. There is no doubt that the relief of the resonator surface would have a substantial impact on the sorption effectiveness of the sorbent due (at the very least) to the enlarged surface. On the other hand increase of the surface roughness results in increase of the acoustic losses of the resonator. In this case we face the logical question - to what extent the surface of the relief can be enlarged without causing substantial acoustic losses.

This current paper studies the influence of the surface relief on the acoustic characteristics of quartz resonators and their humidity sorption effectiveness.

The aim of the study is optimization of the surface relief of resonators that are used as mass sensitivity sensors, while preserving their acoustic parameters.

Subject to investigation are AT cut quartz resonators with a plate diameter 8mm and electrode diameter - 4 mm. The metalization of the exciting electrodes is achieved through vacuum thermal evaporation of gold. The thickness of each electrode is 1000Å. Additionally on both sides of the resonator structure a 0.02 μm thick fullerene layer is deposited so that higher sorption effectiveness is achieved.

2. Experiment

Individual samples differ in their final mechanical processing done with abrasive materials with different size of the grain. Thus processed, the resonator's surfaces are characterized by different relief. For the sake of simplicity the samples are grouped in four groups - P (polished), M3, M7 and M14. The final processing of resonators from the first (P) group represents polishing with cerium oxide with size of the grains 0.1 μm. Samples from the M3 group are treated with abrasive micropowder of silicone carbide whose size of grains are predominantly 3 μm. Respectively resonators from the M7 group are processed with abrasive grains of 7 μm and resonators from M14 type - with size of the grains 14 μm.

In order to determine the influence of the size of abrasive grains on the quartz plate's relief we measured the roughness of treated surface of each of the four groups. The analysis of the surface was carried out with a mechanical inductive appliance "TELYSTEP" of the company Taylor – Hobson. It allows measurements of thresholds of 20Å with sensitivity 5 Å. The usage of this appliance makes possible the scanning of the whole surface of the resonator, without any limitations in respect with the type and structure of the surface layer. It also gives opportunity for scanning of one and the same surface after different processing. The precision of measurement is ±3%.

3. Results

3.1. *Influence of the size of abrasive micropowder grains on the relief of the treated surface*

After being mechanically processed all quartz plates underwent standard chemical processing and vacuum metalization. In order to be determined the influence of the chemical etching and the additionally deposited thin layers of gold and fullerene, control measurements of the relief of the surface were made after each technological operation.

Results show that after a chemical etching (1 μm), followed by metalization (0,1 μm) and deposition of a fullerene layer (0.02 μm) there are no changes in the roughness of the quartz plate.

Measurement of roughness of the surface of each group has been accomplished. On the basis of these measurements an evaluation was made of the surface relief of the plates from each group. Obtained results are summarized in Table 1.

Table 1

No	group	h μm	N /mm^2	S avg. mm^2	K= S_{avg}/S
I	P	0	0	25,12	1
II	M3	1.25	1400	27,356	1,089
III	M7	2.3	1600	28,737	1,144
IV	M14	3.5	3457	33,234	1,323

where:

H - average arithmetic value of the height of deviations from the polished surface, μm

N - number of deviations from the polished surface in an area of 1 mm^2.

S_{avg} - average spread out surface of resonator electrodes, mm^2.

K - the relation of the spread surface to the surface of electrodes of a polished resonator.

Results show that by increasing the size of the abrasive micropowder the spread(effective) underelectrode surface could be enlarged up to 30% (in M14) compared to that of a polished resonator.

3.2 *Influence of the relief of the processed surface on the acoustic losses of the resonator*

For evaluation of the acoustic losses of resonators we measured the equivalent dynamic resistance R_s. The measurements data is systematized in Table 2.

Table 2

No. of group	After metallization		After fullerene deposition		Thick ness of fullerene
	f [Hz]	R_s [Ω]	f [Hz]	R_s [Ω]	h_{full} [μm]
P	13913240	18.1	13911400	16	0.019
M3	14118420	13.4	14118400	14.5	0.017
M7	14132260	13.7	14130200	8.6	0.017
M14	14126550	19	14123200	13	0.02

The thickness of the fullerene layer h_{full} is calculated by the frequency change of the resonator before and after it was deposited. It is evident that the fullerene layer with thickness less 0.02 μm does not lead to increase of acoustic losses. On the contrary, for groups with a "higher" relief, R_s even improves (M7 and M14 groups).

The obtained data proves that the acoustic parameters of resonators are not substantially influenced when the quartz plate is finally treated with micropowders, whose abrasive beans are of 3 μm, 7 μm and 14 μm.

3.3 *Influence of the relief of the surface on the sorption effectiveness of the resonator structure*

For the task of evaluation of the surface relief influence on its sorption effectiveness we measured the humidity sorption capability of resonator structures from different groups with deposited thin fullerene layer. Climatic chamber „Mytron-KPW" and standard frequency measuring devices were used.

Resonators were enclosed in a chamber with fixed degree of relative humidity (RH). Resonance frequencies have been measured within the interval 30% - 99% RH. Temperature of 25°C± 0,5°C was constantly maintained.

Measurement results, presented in Table 3, show that with the increase of the size of micropowder's grains from 3μm to 14μm effective surface (S_{avr}) increase with about one third. In its turn humidity sensitivity ($C_\varphi=df/d\varphi$) raise ten times.

Table 3

No.	group	$K=S_{avr}/S$	$C_\varphi=df/d\varphi$
I	P	1	1
II	M3	1,09	1,404
III	M7	1,14	2,312
IV	M14	1,32	9,364

Graphics present of figure 1 demonstrate frequency dependence on the relative humidity in interval 30% to 99% RH. It represents a polynomial of third degree with coefficients depending on the surface relief of the resonator. Polished samples demonstrated a very low degree of humidity sensitivity and for that reason were not included in the graphics.

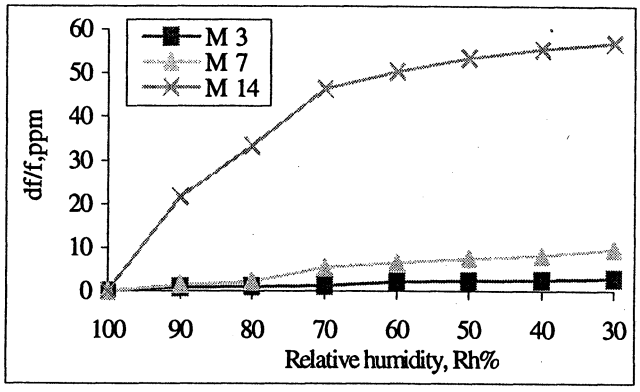

Figure 1

4. Conclusions

Obtained results show that acoustic parameters of resonators do not change significantly when the final processing has been done with abrasive materials, whose grinding beans increase size from 3 μm, to 14 μm. At the same time effective surface of the resonance structure increase over 30% and

humidity sensitivity intensifies about ten times.

It is possible to increase the sorption effectiveness of quartz resonators as a result of enlarged unfolded surface.

Reference

[1] E. Radeva, V. Georgiev, L. Vergov, L. Spassov, N. Koprinarov, St. Kanev, *Sens. & Act.*, B42, pp 11-13, 1997.

[2] R. Lucklum, B.Henning, P.Hauptmann, K.D.Schierbaum, S.Vaihinger, W.Gopel, *Sens.&Actuators*, A, Vol 25-27, pp705-7010, 1991

[3] W.King, *Anal. Chem.*, Vol.36, pp1735-1739, 1964

[4] E.Benes, M. Groschl, F. Seifert, A. Pohl, *IEEE Trans. of UFFC*, Vol.45, No.5, pp 1314-1330,1998

$GaPO_4$ USED FOR HIGH TEMPERATURE MICROBALANCES

H. Thanner, P.W. Krempl, F. Krispel, C. Reiter and R. Selic

AVL List GmbH, Hans-List-Platz 1, A-8020 Graz, Austria

ABSTRACT

Quartz-homeotypic gallium (ortho-) phosphate, $GaPO_4$, is of special interest for resonator applications asking for temperature compensated cuts with higher electro-mechanical coupling than quartz and operational temperatures up to 970 °C. The crystal microbalance technique, well known for quartz which can be used only at moderate temperatures, can now be extended to much higher temperatures using $GaPO_4$ crystals, benefiting from all three advantages mentioned above.
Two different experiments were done to demonstrate the principle function of a microbalance based on $GaPO_4$ thickness shear resonators. First, the $GaPO_4$ resonator was mounted in a standard microbalance holder for monitoring the film thickness during a sputter process. The measured shift in the resonant frequency was related to the film thickness and compared with the so called „Z-match theory".
Second, a $GaPO_4$ thickness shear resonator was mounted in a new microbalance holder developed for very high temperature operation and lube oil was applied on one resonator surface. Heating up the resonator to 750 °C causes the lube oil to evaporate from the crystal surface and thus the resonator became completely clean.

Keywords:

gallium(ortho)phospate, $GaPO_4$, microbalance, BAW resonators, high temperature;

1. INTRODUCTION

Because of its excellent thermal stability up to 970 °C, a coupling coefficient twice as high as in quartz for the most favourable cuts and very low acoustic losses, $GaPO_4$ offers a large field of resonator applications, in particular at high temperatures (Ref. 1). During the last years, a lot of experimental and theoretical work in basic material property research has been done in both, BAW (Refs. 2-3) and SAW (Refs. 4-5) resonators. For thickness shear resonators, temperature compensated cuts near room temperature were found with a flatter frequency-temperature curve as in BT-cut quartz and other piezoelectric materials.
For rotated Y-cut $GaPO_4$ resonators, the inversion temperature (T_0) depends on the orientation of the crystal plate whereby the cut angle sensitivity of the inversion temperature is much lower as in quartz which opens the way for very high stability applications. The inversion temperature (T_0) of the resonant frequency increases by rotating the cut angle whereby the frequency temperature curve becomes flatter. Near 500 °C the 2nd order temperature coefficient vanishes and the frequency temperature behaviour becomes cubic where the resonant frequency shifts only ±30 ppm in the temperature range from 350 °C to 650 °C (Ref. 2).

2. $GaPO_4$ MICROBALANCE FOR FILM THICKNESS MONITORING

2.1 Film thickness monitoring

Quartz crystal microbalances (QCM) are commercially used for thin film thickness determination in particular for in-situ monitoring and control of the deposition rate in vacuum coating systems (Ref. 7). With a QCM, the thickness of metallic or dielectric films e.g. in the semiconductor and optical industry can be determined with a resolution less than 0.1 nm.
To show the principle function of a $GaPO_4$ crystal microbalance (GCM) for film thickness monitoring, gold was sputtered on both, a $GaPO_4$ thickness shear resonator 6.2 MHz (fundamental mode), temperature compensated near 50 °C and on a 6 MHz AT-cut quartz standard microbalance simultaneously.
Figure 1 shows a $GaPO_4$ thickness shear resonator with 10 mm diameter, plan convex design and with gold electrodes on both surfaces. The cutting angle is chosen near
Y-15.5 ° (Ref. 9) to achieve temperature compensation between room temperature and 100 °C.

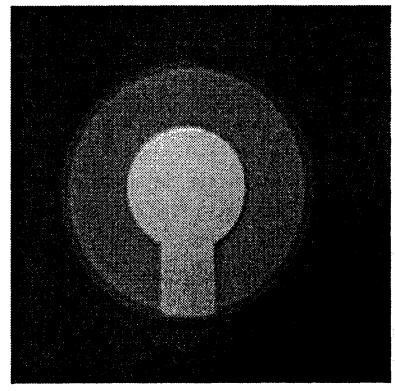

Figure 1: $GaPO_4$ thickness shear resonator with gold electrodes (10 mm diameter)

The shift in the resonant frequencies of both Q(G)CM, caused through the mass accumulations during the sputter process were measured, monitored and stored in frequency and film thickness units. Figure 1 shows the measured and calculated values for the GCM.

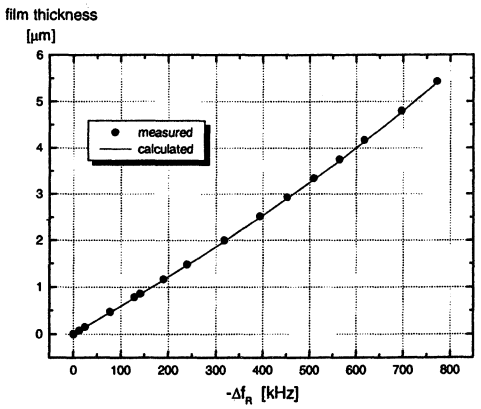

Figure 2: Film thickness determination by using a $GaPO_4$ microbalance (GCM)

Figure 2 shows the excellent validity of the so called "Z-match theory" (Ref. 8) for thin film thickness monitoring by using a GCM, too. In addition, the very favourable temperature compensated behaviour of the resonant frequency suppresses the thermal influence caused by the sputter process. The use of commercially available deposition monitors in combination with $GaPO_4$ sensor elements is possible simply by modifying the acoustic impedance ratio Z, depending on the density and shear modulus of the piezoelectric sensor material.

2.2 Q-value in high vacuum

The initial sensitivity of a crystal microbalance is given by the resonant frequency of the "unloaded" resonator. The fundamental mode resonant frequency of the most commercial available quartz resonators for QCM applications is in the range 6 MHz to 10 MHz where the upper limit is given by the fragility of the very thin resonator plates.
The maximum resolution of a microbalance measuring system (e.g. film thickness resolution) is limited by the used oscillator electronic and the Q-value of the piezoelectric resonator. While the resolution of the oscillator electronic remains essentially constant, the resonator becomes more damped with increased mass loading. For that reason, the resolution of the microbalance system decreases during the mass loading process (e.g. film-thickness monitoring). This limits the measuring range of the microbalance system.

The Q-value is defined by:

$$Q = \frac{f_R}{\Delta f} \qquad (1)$$

where f_R... resonant frequency
Δf....3 dB bandwidth

and can be determined from the resonance behaviour of the resonator.
Figure 3 shows the resonance curve of a $GaPO_4$ thickness shear resonator, which was measured with a HP network analyser. The resonator was mounted in a standard microbalance holder for measuring the resonance behaviour in high vacuum.

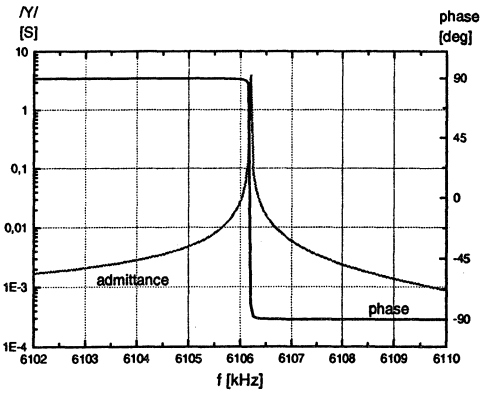

Figure 3: Resonance behaviour of a $GaPO_4$ thickness shear resonator in high vacuum (fundamental mode)

With a center frequency around 6.1 MHz and a 3 dB bandwidth near 5 Hz follows a Q-value of about 1.2 million by using equation 1.

The performance of a piezoelectric resonator, which is influenced by the resonator design and limited by the crystal quality can be defined as:

$$Q * k^2 = const. \qquad (2)$$

where k...coupling coefficient

For a 14 mm diameter AT-cut quartz resonator with silver electrodes (6.0 MHz fundamental mode), measured in high vacuum, follows by using equation 2:

$$0.944*10^6 * (8.8\ \%)^2 = 7300 \qquad (3)$$

and for the $GaPO_4$ resonator, measured under comparable conditions:

$$1.2*10^6 * (15\ \%)^2 = 27000 \qquad (4)$$

The comparison of equation 3 and 4 shows the very high performance of the $GaPO_4$ resonator and this indicates the excellent crystal quality, too.

2.3 Motional resistance R_1

Another definition of the Q-value of a piezoelectric resonator is given by:

$$Q = \frac{1}{2\pi f_R R_1 C_1} \qquad (5)$$

where: R_1...motional resistance
C_1...dynamic capacity

The dynamic capacity C_1 is mainly determined by the properties of the used piezoelectric material, the thickness of the resonator plate and the diameter of the electrode. For that reason, C_1 remains essentially constant during thin film deposition onto the resonator surface.
The motional resistance R_1 represents the acoustic losses in the resonator. For that reason, R_1 increases with increasing mass loading. Figure 4 shows the measured values of R_1 of the GCM and the QCM during thin film deposition.

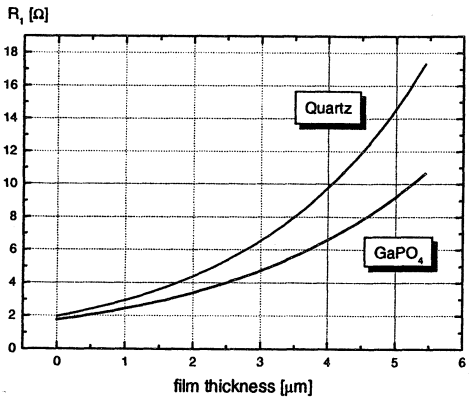

Figure 4: Motional resistance of a $GaPO_4$- and a quartz thickness shear resonator during thin film deposition

In Figure 4 one can see, that the motional resistances R_1 for the $GaPO_4$- and the quartz resonator started at nearly the same value. But during the film deposition, R_1 of the quartz resonator increased much more as the R_1 of the $GaPO_4$ resonator. This indicated clearly a larger possible measuring range for the $GaPO_4$ resonator for microbalance applications as it is possible with the AT-cut quartz resonator.
The physical reason for this very attractive behaviour is given by the higher coupling coefficient k of the $GaPO_4$ resonator which is twice as high as the coupling coefficient of the common used AT-cut quartz resonator.

3. HIGH TEMPERATURE MICROBALANCE APPLICATION

3.1 High temperature crystal holder

The maximum specified temperature limit of the most commercially available microbalance holder is near 120 °C. In addition there are some bakeable microbalance holders on the market with a maximum temperature limit at 400 °C.

Several reasons which limit the maximum operating temperatures have been found:

- the used materials are not useful for high temperature operation
- electrical contacting forces are not stable enough
- thermal influenced mechanical expansions cause mechanical stress in the sensor element

For that reason, a new concept of resonator mounting for very high temperature microbalance applications has been developed. The new microbalance holder, shown in Figure 5, is based on a single ceramic plate.

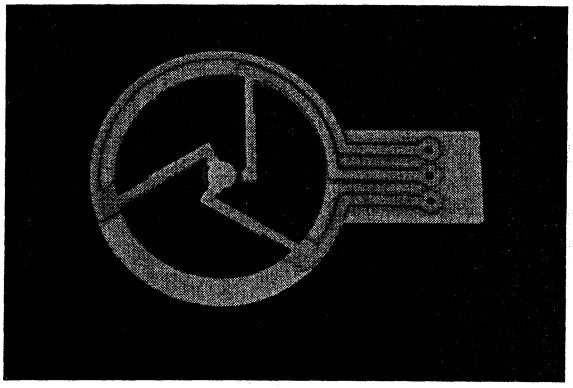

Figure 5: New „radial" forced high temperature microbalance holder (Ref. 10)

The basic principle of this sensor holder is to apply only radial mounting- and electrical contacting-forces on the lateral surface of the sensor element. For this the electrodes of the resonator plate have to be extended to the lateral surface.

3.2 High temperature microbalance demonstration

To show the high- temperature performance of the GCM, lube oil was applied on one resonator surface and after this, the crystal was heated up to 720 °C. Figure 6 shows the measuring procedure schematically.

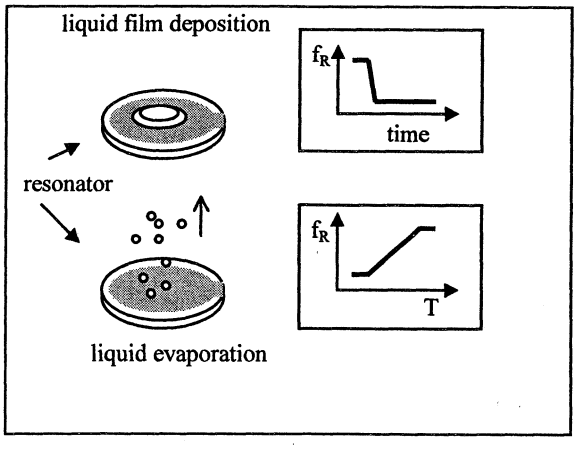

Figure 6: Measuring procedure for high temperature microbalance demon-stration based on $GaPO_4$ resonators

For this measurement, a single rotated Y-11 ° cut (Ref. 9) $GaPO_4$ resonator with 7.4 mm diameter and a resonant frequency near 6.2 MHz (fundamental mode) was used. The frequency temperature

behaviour of this resonator is very flat in the temperature range between 350 °C and 650 °C as reported in (Ref. 2)

The resonator was mounted in the new high temperature microbalance holder which is shown in Figure 5. Than lube oil was applied on one resonator surface. During this procedure, the resonant frequency was measured and is shown in Figure 7.

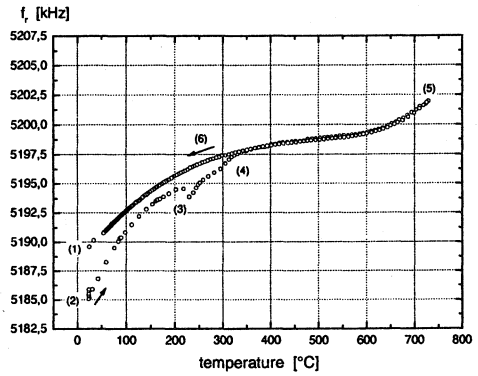

Figure 7: Thermogravimetry and crystal cleaning by heat up to 720 °C

Description of Figure 7: The shift in the resonant frequency Δf_R caused by the added liquid film was approximately 4.2 kHz (1) → (2). Than the resonator was heated up and the resonant frequency increased rapidly because of the thermal influenced lowering of the viscosity and density of the liquid. Near 200 °C, the properties of the liquid film changed and became more elastic (3), which lowered the resonant frequency. With further increased temperatures, the liquid film evaporated from the resonator surface and near 350 °C the resonant frequency approached the „unloaded" frequency temperature behaviour of the resonator (4). During the following heating procedure, up to 720 °C (5), the resonant frequency approximated more and more the „unload" behaviour. Finally the heater was switched off and the resonant frequency decreased like the well known cubic behaviour (6) which indicated a completely cleaned resonator surface.

4. CONCLUSION

The experiments demonstrated the very favourable function of $GaPO_4$ resonators for microbalance applications in particular at very high temperatures.

The mass accumulation, e.g. during thin film deposition, caused a much less damping in $GaPO_4$- than in quartz AT-resonators. Therefore, with $GaPO_4$ resonators the maximum measuring range can be extended and the resolution can be increased respectively for both thin film deposition monitors and (high-) viscose liquid measurement applications.

Also the function of the new high temperature microbalance holder has been demonstrated up to 720 °C successfully. This opens the way to combine the high sensitive microbalance method with thermogravimetric analysis in an extended temperature range.

Acknowledgement:

This work was supported in part by the European Communities by the Brite-EuRam project BE96-3105.

5. REFERENCES

[1] P.W. Krempl, F. Krispel, W. Wallnöfer, Industrial development and prospects of $GaPO_4$, Ann. Chim. Sci. Mat. 22 (1997) 623-626

[2] C. Reiter, H. Thanner, W. Wallnöfer, P.W. Krempl, Properties of $GaPO_4$ thickness shear resonators, Ann. Chim. Sci. Mat. 22 (1997) 633-636

[3] J. Detaint, B. Capelle, O. Cambon and E. Philippot, Properties of AT cut gallium phosphate resonators, 2000 Frequency Control Symposium, Kansas City, Missouri, USA, June 7-9 (2000)

[4] E. Henry Briot, E. Bigler, W. Daniau, G. Marianneau, A comprehensive mapping of Surface Acoustic Wave properties on gallium orthophosphate ($GaPO_4$), First joint meeting EFTF/IFCS-Besancon, IEEE cat no 99CH36313, p. 811 – 815, 12-16 April (1999)

[5] E. Bigler, J.B. Briot, A comparison of surface transverse wave propagation on quartz and gallium orthophosphate, Joint-meeting ASA/EEA „Forum Acusticum", Technical University Berlin, 13-16 March (1999), proceedings on CD-ROM, paper no 2AEA_9, file 1AEA_9.pdf

[7] C. Lu, A.W. Czanderna, Methods and Phenomena 7; Applications of piezoelectric quartz crystal microbalance, ELSEVIER (1984)

[8] Leybold Inficon, XTM/2 Deposition Monitor, Manual, September (1992)

[9] Sign according to standard IEEE 176-1987

[10] patent pending

ATOMIC FREQUENCY STANDARDS

Chairman: Pierre Thomann

PHASE MODULATION FOR REDUCED VIBRATION SENSTIVITY IN LASER-COOLED CLOCKS IN SPACE*

W.M. Klipstein[1], G.J. Dick[1], S.R. Jefferts[2], F.L. Walls[2]

[1]Jet Propulsion Laboratory, Pasadena, California, U.S.A.
[2]National Institute of Standards and Technology, Boulder, Colorado, U.S.A.

ABSTRACT

The standard interrogation technique in atomic beam clocks is square-wave frequency modulation(SWFM), which suffers a first-order sensitivity to vibrations as changes in the transit time of the atoms translates to perceived frequency errors. Square-wave phase modulation (SWPM) interrogation eliminates sensitivity to this noise. We present a particular scheme utilizing independent phase control of the two cavities. The technique is being considered for use with the Primary Atomic Reference Clock in Space (PARCS), a laser-cooled cesium clock scheduled to fly aboard the International Space Station in 2005. In addition to eliminating first-order sensitivity to vibrations, the minimum attack time now in this scheme is the Rabi pulse time (t), rather than the Ramsey time (T). This helps minimize dead time and the degradation of stability due to aliasing.

INTRODUCTION

The vibration spectrum on the International Space Station (ISS) is expected to be sufficiently severe that it can cause serious problems for atomic clocks using laser-cooled atoms and traditional (SWFM) techniques. As a result, we propose as a solution for the PARCS [1]clock, an old idea, dating back to Ramsey[2], of using phase modulation. SWPM is relatively easily realized in many modern frequency synthesizers which depend on direct digital synthesizers(DDS)[3,4] as a part of the synthesis chain. SWPM has several distinct advantages over SWFM, most importantly for PARCS, the vibration sensitivity is reduced by orders of magnitude. The actual implementation of SWPM for PARCS will use two independent frequency synthesizers, one driving each of the Ramsey interaction zones. With this topology, the duty cycle of the clock is significantly enhanced for the case of a multiple launch per "lineside" (or phase). Lastly, a whole class of systematic frequency shifts is greatly suppressed as will be discussed in a later paper[5].

While the focus of the present paper is towards laser-cooled atomic clocks in space, with two separated Ramsey interaction zones, many of the advantages apply equally well to other clock geometries, including traditional thermal beam clocks, pulsed fountain clocks and continuous fountain clocks[6]. We have tested SWPM in October 1999 on NIST-F1, the NIST primary frequency standard (a pulsed cesium fountain) and found no significant frequency offset relative to SWFM at the 10^{-15} level. SWPM has also recently been implemented on the USNO cesium fountain with success[7].

LINE SHAPE and MODULATION

PARCS, as shown schematically in Fig. 1, has two Ramsey interaction zones separated by 75 cm. In the vicinity of the central Ramsey fringe the fringe can be described by

$$P_4 = \frac{1}{2}[1+\cos(\Omega_o T_R+\phi)]\sin^2 b\tau \qquad (1)$$

where P_4 is the probability of transition from the $|3,0\rangle$ to the $|4,0\rangle$ level, Ω_o is the offset from the resonance frequency, $\Omega_o=\omega-\omega_o$, T_R is the Ramsey time, and ϕ is the phase angle between the microwave fields in the two Ramsey interaction zones[8].

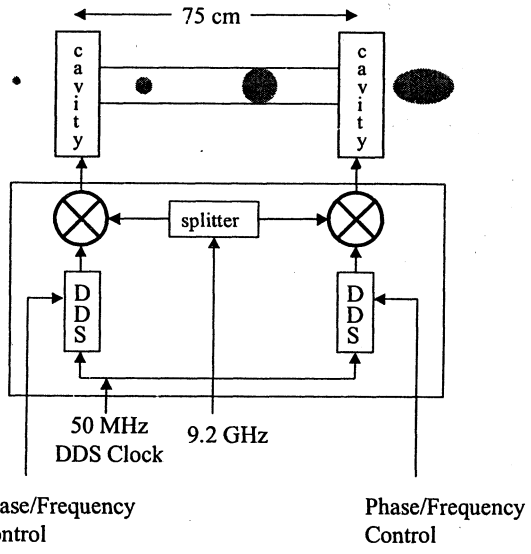

Figure 1 - The PARCS Ramsey zone (shown schematically) with independent phase control of the two cavities.

In the usual Ramsey interrogation technique, ϕ is set equal to zero and the interrogation frequency is modulated between the points a and b in Fig.2. The frequency at point a (or b) is adjusted to be higher (lower) by an amount $\delta\omega$ such that the phase of the microwave field in the second Ramsey interaction leads (lags) the phase of the atomic superposition by $\pi/2$ at a given Ramsey time of T_R. If $P_4(a)$ is larger (smaller) than $P_4(b)$, the synthesizer frequency is lowered (raised) by an appropriate amount so that $P_4(a)=P_4(b)$. The relative phase between the atomic superposition and the microwave field in the second Ramsey zone therefore depends on the Ramsey time. Vibrations of the atomic clock along the atomic trajectory

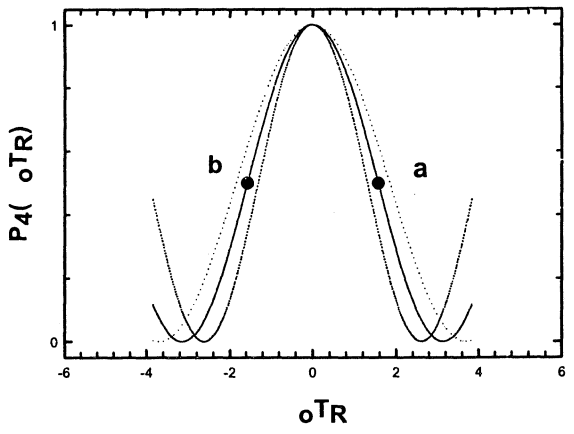

Figure 2 - The central Ramsey fringe with no vibration is shown solid while the effects of vibration are shown as dotted fringes. The points a and b are the FWHM of the fringe, which is the normal modulation using SWFM.

will change the Ramsey time resulting in Ramsey resonances depicted by the dotted lines in Fig2. These vibrations cause noise in the clock as a result of this "breathing" of the width of the Ramsey fringe[9].

If ϕ in equation 1 is set to $\pm\pi/2$ instead of 0 then the resulting Ramsey curve has either a rising or falling dispersion shape as shown in Fig 3. The $\pi/2$ phase difference between the two Ramsey interactions causes the $P_4(a)=P_4(b)$ point to occur at the resonance frequency of the atom. The frequency servo now works by first measuring P_4 for $+\pi/2$ relative phase between the Ramsey zones and then $-\pi/2$. The frequency is adjusted so that $P_4(\pi/2)=P_4(-\pi/2)$. Because the phase of the microwave field is advancing at the same rate as the phase of the atomic superposition, changes in the Ramsey time do not affect the relative phase between the atomic superposition and the microwave field in the second Ramsey interaction zone. Changes in the Ramsey time cause the slope of the dispersion curve to change, as is

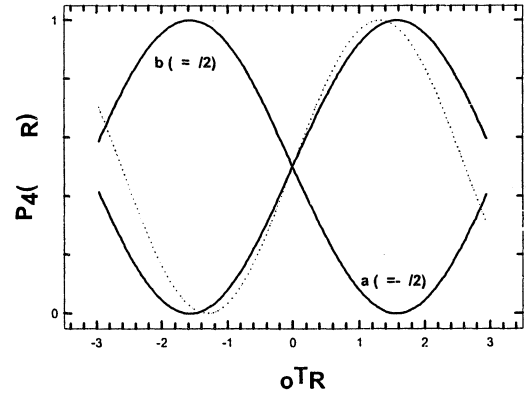

Figure 3 - The central Ramsey fringe under $\pm\pi/2$ phase modulation conditions. The servo steers the frequency to the fringe crossing point. The effect of vibration is illustrated by the dotted fringe.

illustrated by the dotted lines in Fig. 3, but the crossing point (i.e. the point $P_4(\pi/2)=P_4(-\pi/2)$) is unchanged. This insensitivity to Ramsey time greatly reduces the vibration sensitivity of the atomic clock as will be shown below.

An additional advantage of the independent phase modulation technique is realized in the PARCS clock which launches many (of order 10) balls of atoms at either $\pi/2$ of phase lag or lead. In a traditional SWFM modulation scheme the servo must be blanked for a time on the order of the transit time of the atoms through the clock $\approx T_R$ between frequencies above and below the resonance. This blanking time contributes to the dead time and therefore increases aliasing of the local oscillator noise (Dick Effect)[10]. When using SWPM, however, the servo blanking time is reduced to the atom transit time through the second Ramsey cavity$\approx\tau$ and the dead time fraction therefore reduced, thus reducing the aliasing effect. The reduction in dead time fraction also reduces the total number of atoms which must be launched in order to support a given short term frequency stability, thus reducing the magnitude of the spin-exchange frequency shift as well as relaxing the short term stability requirements on the local oscillator through the aforementioned reduction in aliasing. This technique (SWPM) has significant terrestrial applications as well[11].

Impact of Random Accelerations on Frequency Stability

Interrogation errors due to unwanted accelerations of the waveguide structures used to distribute microwave signals to two physically separated interrogation sites can substantially degrade the performance of a laser-cooled frequency standard. In such a standard, slow-moving laser-cooled bunches of atoms are sequentially interrogated as they arrive at one and then the other of the two interrogation regions. Errors arise if the phase of the microwave signal is systematically varied with respect to the atomic phase itself.

F M Effects

Here, an error arises because physical acceleration of the beam tube causes microwave interrogations to take place too soon or too late, giving rise to an unwanted phase difference between atoms and L.O. due to the FM frequency offset.

The effect of random motions of the beam tube $x(t)$ have been properly analyzed in terms of an aliasing effect, where motions at frequencies near $f=1/2T_c$ are aliased to near zero frequency[9]. We rewrite eq. 2.26+ of [9], in terms of a dependence on interrogation (or drift) time t_i, and assuming the usual $\pi/2$ phase progression during the interrogation as:

$$y_{fm}(f) = \frac{x(f)}{4t_i\nu_o L} \qquad (2)$$

where $y=\delta\nu/\nu$ and x(f) is a time dependent motion along the axis of the drift space.

Because the frequency error induced by a (e.g.) motion-delayed measurement shows periodic sign reversals due to frequency modulation, slow variations will show an aliasing effect, with the lowest frequencies effectively eliminated, and other frequencies aliased to near zero frequency. Actual aliasing amplitudes will depend on

details of the interrogation strategy; dead time, etc.

We calculate the effect for a model of SWFM with no dead time. This will give aliased responses at odd harmonics of the modulation frequency, with amplitudes given by the harmonic content of a square wave with unit amplitude. This methodology is similar to that developed in Ref[9], except we include a missing amplitude for the aliasing effect itself of $2/\pi$ for SWFM and also include the higher (odd) harmonics.

Because the characteristics of the ISS are given in terms of accelerations as $S_a(f)$ we rewrite the previous equation as:

$$s_y^{fm}(f) = \frac{S_a(f)}{(2\pi f)^4} \frac{1}{(4t_i \nu_o L)^2} \qquad (3)$$

If the frequency standard is interrogated with a half-cycle (frequency measurement) time of T_c, its operation will show aliased frequency fluctuations $S_y^a(0)$ as:

$$s_y^a(0) = (\frac{2}{\pi})^2 \sum_{n=1,3,..}^{\infty} [s_y^{fm}(\frac{n}{2t_c})\frac{1}{n^2}] \qquad (4)$$

This spectral density gives rise to an Allan deviation limit to the performance of the frequency standard of:

$$\sigma_y^a(\tau) = \sqrt{\frac{CS_y(0)}{\tau}} \qquad (5)$$

where C=1/2.

Figure 4 shows a smoothed plot of the acceleration spectrum expected on the ISS together with a conversion from the 1/3 octave plot to a more conventional spectral density of acceleration. This allows us to calculate an expected limitation to the $1/\sqrt{\tau}$ performance as given by the previous equations. The result of this calculation is shown in Fig.5.

It is clear from Fig. 5 that any problems due to FM interrogation are strongly dependent on the operating conditions of the frequency standard. For a short interrogation and a half cycle time of 1 second, as is planned for PHARAO, the aliasing effect is small.

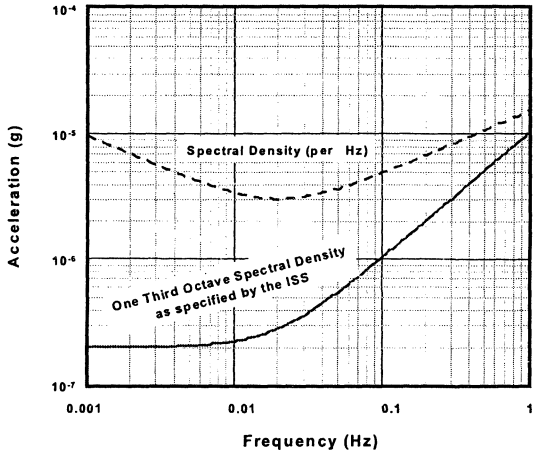

Figure 4 Smoothed approximation to ISS vibration specification. Shown are both the 1/3 octave form as specified by the ISS and the more traditional $Hz^{-1/2}$ form used in our calculations.

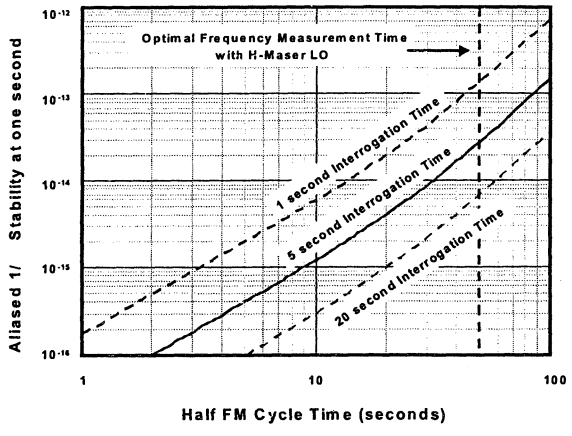

Figure 5. Vibration-induced limitation to white frequency noise performance due to aliasing with FM interrogation. Nominal PARCS conditions are a 5 second interrogation (drift) time and a 50 second frequency measurement time to match performance of the H-maser L.O.

PARCS, is expected to operate with multiple balls of atoms per "lineside", long Ramsey times, a high-performance hydrogen maser local oscillator(LO). and half cycle times of typically 50 s, a process that involves hundreds of balls of atoms. For this case, aliased noise is clearly an issue because the performance is marginal. In particular PARCS is expected to operate before ISS construction is complete, during which time microgravity conditions are not obtained and frequency stability would be substantially degraded.

Other Effects

The linear phase progression as the atoms drift down the beam tube can be eliminated by the use of interrogation schemes using SWPM instead of frequency modulation. This eliminates the large frequency sensitivity discussed above.

However, there remain several smaller effects which are discussed here. It is worth mentioning that the signs of these remaining smaller effects do **not** reverse during the course of either phase or frequency modulation, and so the sensitivity to very low frequency physical acceleration is not reduced by averaging over many interrogation cycles.

Phase Delay

Even if the microwave interrogation structures move rigidly, any motion will give rise to phase shifts between the two interrogating cavities due to the fact that the microwave photons are not dragged with the waveguide structure that feeds the interrogating microwave signals to the cavities. Here we assume that the waveguides are empty and not filled with a dielectric. For this effect we write:

$$y_{pd}(f) = \dot{x}(f)\frac{L}{c^2 t_i} = 2\pi x(f)\frac{L}{c^2 t_i}. \qquad (6)$$

Mechanical Compression

A phase error can also result from mechanical compression of the waveguide structure under acceleration. Linear compression under a uniform acceleration $a(f)$ where

$f \approx 0$ is given by:

$$\delta L(f) = a(f)\frac{\rho L^2}{2Y} = a(f)\frac{L^2}{2v_s^2} = (2\pi)^2 f^2 \delta x(f)\frac{L^2}{2v_s^2} \quad (7)$$

where ρ is the material density and Y is the stiffness which combine to give the speed of sound as $v_s = \sqrt{Y/\rho}$. A change in waveguide length changes the rf phase to give rise to an imputed frequency error as:

$$y_{mc}(f) = \frac{\delta\phi(f)}{\phi} = \frac{\delta L(f)/\lambda}{v_o t_i} = \frac{\delta L(f)}{c t_i} \quad (8)$$

and so

$$\frac{y_{mc}(f)}{\delta x(f)} = \frac{2\pi^2 f^2 L}{v_s^2 c t_i} . \quad (9)$$

Comparison

We can compare the phase delay and mechanical-compression frequency tunings with that due to FM interrogation, irrespective of aliasing, and a comparison that is valid at frequencies higher than $f=1/(2T_c)$. Plugging in values of $v_o = 10^{10}$, $v_s = 10^4$ m/s, L = 1m, f = 1 Hz, and t_i = 10s gives a frequency sensitivity of

$$\frac{y_{fm}(f)}{a(f)} \approx 2.5\times 10^{-12}\,(\frac{1Hz}{f})^2\,/g \quad (10)$$

for FM, while the smaller underlying electromagnetic and electromechanical effects described by Eq. 6,9 combine to give a sensitivity remaining with SWPM of

$$\frac{y_{pm}(f)}{a(f)} \approx 2.5\times 10^{-18}(1 + \frac{0.1Hz}{f})/g . \quad (11)$$

Note that while the FM term is a true position dependence, the two terms in the PM expression are actually velocity and acceleration dependencies, respectively. Thus while the PM terms do not show the nominally zero sensitivity at the lowest frequencies that characterize FM modulation, the terms are smaller by a power of f or f^2 at these low frequencies. Additionally they will not show the aliasing of relatively larger accelerations in the mid-frequency range to zero frequency, as does the FM sensitivity.

INDEPENDENT PHASE CONTROL

The main operational difficulty in implementing independent phase control of the two cavities is in evaluating and maintaining the end-to-end cavity phase shift. In traditional beam tubes this shift results from differing electrical path lengths to the two cavities, a quantity which is typically extremely stable as it results from the mechanical properties of the waveguide only. This typically is evaluated by reversing the direction of the beam through the cavities and comparing the results.

In the cesium instrument of PARCS beam reversal is not practical, but several additional handles are available. Specifically, laser cooling provides extremely narrow velocity distributions and the ability to vary the launch velocity, which remains constant in the absence of gravity. Since the end-to-end shift is truly a phase offset, the apparent frequency error of interest can be related to the phase offset from Eqn. 1 as:

$$\delta\Omega_{end} = \frac{\phi_{end}}{T_R} . \quad (12)$$

For separation, L, between the two microwave cavities, the frequency error can be expressed in terms of the launch velocity as

$$\delta\Omega_{end} = \frac{\phi_{end}\, v_{launch}}{L} . \quad (13)$$

Eqn. 13 makes explicit the utility of varying the launch velocity as a technique for extracting the phase error, ϕ_{end}. Measuring the clock frequency over a range of velocities allows a determination of the phase-offset as shown in Figure 6. The phase error could then be corrected by the synthesizer controlling the second cavity.

The performance goals of PARCS include accuracy of 5×10^{-17}, which for a 5 s Ramsey time means that phase offsets must be known to 14 μrad. Just as long Ramsey times mitigate the effect of phase errors on the fractional frequency performance of the clock, so too can higher launch velocities make the phase errors measurable. Launch velocities of 10s of meters per second are attainable, with 15 m/s representing a 100-fold increase over the standard operation of PARCS, using 15 cm/s launches. Varying the launch velocity obviously impacts more than just the end-to-end shift, requiring some care in order to separate out the piece linear in velocity. First, one might worry that operating at high velocities would compromise the stability of the clock, since the line Q degrades linearly with velocity. However, since most launched atoms are never detected due to thermal expansion of the cloud, the immediate result of increasing the launch velocity is to increase the number of detected atoms getting through the final aperture, roughly

$$N_{det} \propto v_{launch}^2 . \quad (14)$$

The net result of increasing the launch velocity is that the stability improves as:

$$\sigma_y(\tau) \propto \sqrt{v_{launch}} . \quad (15)$$

This improvement holds up to the point at which most launched atoms are detected, which occurs at roughly 2 m/s, above which the stability would begin to degrade. Even out to launch velocities of 20 m/s, the stability would remain better than that obtained from the operating condition of 15

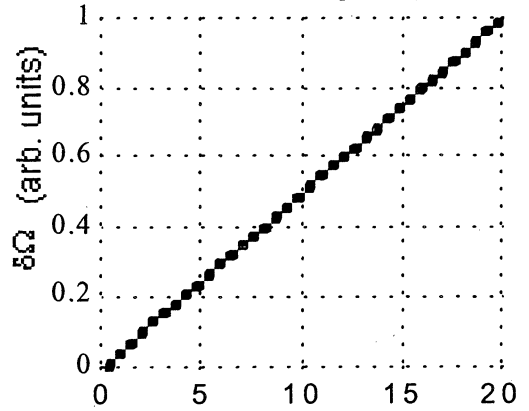

Figure 6 Apparent frequency error is linearly proportional to velocity. Launching at high velocities gives over 100-fold increase on the measurement of the phase offset.

cm/s. This comparison assumes only one ball is launched at a time, which is how the end-to-end evaluation will likely be performed, but during normal operation multiple launching will improve the stability by roughly a factor of 3. The design stability for PARCS is $5 \times 10^{-14} t^{-1/2}$, so launches at 15 m/s would be expected to run at a stability of $1 \times 10^{-13} t^{-1/2}$ taking these different factors into account. With a lever of 100 on the relative size of the phase error, this suggests that ongoing evaluation of this error term would take 4% of the time spent in normal clock operation. The extent to which this shift is stable will have to be empirically determined, and based on this a proper protocol for making these measurements will be developed.

Comparison of measurements made with 15m/s launches to those with 15cm/s launches is problematic since too many other factors could vary. The cold-collision shift which typically dominates cold-atom cesium clocks is of particular concern here. With a five second Ramsey time, the density will drop three orders of magnitude from one end of the clock to the other, while with a 0.05 second Ramsey time the density change is roughly 4%. The collision shift during the end-to-end evaluation will be roughly 35 times larger than in the operational mode, but with a lever of 100 on the phase error, variations in the density during fast launches will not be a limitation.

Of equal importance to the density is the collision energy involved in interatomic collisions, as the frequency shift is a strong function of energy as calculated by Williams and co-workers at NIST (submitted to Phys. Rev. A, 2000), growing in magnitude and even changing sign. Initially, the collision energy is roughly the thermal energy until the cloud has expanded an amount comparable to its initial size. Then the collision energy is dominated by phase space considerations: atoms at the same point in space must be traveling at nearly the same velocity, so the collision energy is reduced. Under normal operating conditions PARCS will strongly be in this latter condition, crossing into an intermediate condition at around 1 m/s, and significantly above that the thermal energy dominates. Comparing measurements using several fast launch velocities between 5m/s and 20m/s satisfies the requirement that collisional frequency offsets are stable.

The relative phase between the cavities will be affected by changes in the temperature and microwave power incident on the mixers.We have measured the temperature dependence of a mixer to determine this sensitivity, and find that in order to maintain an uncertainty of a few parts in 10^{17} the temperature must be stable to 10 mK. Note that this is not an absolute temperature, but the time scale over which this temperature stability holds could well set the limit on how often we must measure the end-to-end shift.

In order to realize a factor of 100 lever on the velocity, while maintaining $\pi/2$ excitation, we require 40 dB changes in the RF power. Matched attenuators can be quite stable over such a broad range, but not at the performance level we need. A more likely approach is to maintain the power level on the mixers at the highest level, but playing one of several tricks to maintain the p/2 condition. In order to determine the power stability requirement, we have directly measured the power sensitivity of a mixer and conclude that the power must be stable to 0.1% to keep phase errors to the low 10^{-17} level. One way to realize this would be to adjust the phase of the DDS output by pi on a time scale fast compared to the cavity ring time, spending a bit more time with the "plus" phase than the "minus" phase. The power in the microwave cavity will rapidly advance for a short time, then retreat, taking 100 steps forward and 99 back over and over again so that the net power in the cavity gives p/2 to the atoms. Other approaches similar in principle would involve using a variable amount of on-frequency RF with white noise added, or a mixture of on-resonant RF with an off-resonant frequency to make up the power budget without affecting the atomic spins.

One requirement of all these tricks, satisfied by the phase switching solution, is that the excitation must be spread over the entire transit time so the Rabi pedestal is not broadened artificially. This phase adjustment involves a single bit in the DDS, and seems to be the most elegant solution.

Acknowledgments

The authors have benefitted from discussions with the entire PARCS team. Andrea DeMarchi has previously suggested the benefits of phase modulation.

REFERENCES

1. Heavner, T.P. et al, "Characterization of a Cold Cesium Source for PARCS: Primary Atomic Reference Clock in Space", *Proc of the 2000 IEEE Freq. Control Symposium*, 2000, 656-658.
2. Ramsey, N.F., *Molecular Beams,* Oxford at the Calrendon Press, 1956. Ch. V.§4.
3. SenGupta, A., Popovic, D., Walls, F.L., "Cs Frequency Synthesis: A New Approach", *Proc of the 1999 Joint Meeting of the E.F.T.F and the IEEE F.C. S*, 1999, 615.
4. Rovera, G.D., Santarelli, G., Clairon, A., "Frequency Synthesis Chain for the Atomic Fountain Primary Standard", *IEEE Trans. Ultran., Ferroelect., Freq. Contr.*, **43**, 354-358 (1996).
5. Klipstein, W., et. al. to be submitted to the *IEEE Trans. Ultran., Ferroelect., Freq. Contr.*
6. Thomann, P, et.al. *These proceedings.*
7. Burt, E, et. al. *These proceedings.*
8. Vanier J., Audoin, C., *The Quantum Physics of Atomic Frequency Standards*, Adam Hilger, 1989, pg. 634.
9. Lemonde, P., "Pharao: Etude D'une Horologe Spatiale Utilisant des Atomes Refroids Par Laser; Relisation d'un Prototype", These De Doctorate de L'Universite Paris iV, 1997.
10. See for example the collection of articles in *IEEE Trans. Ultran., Ferroelect., Freq. Contr.*, **45**, 1998, 876-905 and the references contained therein.
11. Kujundzic, D., Heavner, T.P., Jefferts, S.R., "Design Studies for a high-Stability Laser-Cooled Rubidium Local-Oscillator at NIST" *to be presented at the 2001 IEEE Frequency Control Symposium.*

PRELIMINARY ACCURACY EVALUATION OF THE IEN CESIUM FOUNTAIN IEN-CSF1

Filippo Levi[†] Aldo Godone[†] Luca Lorini[†], Davide Calonico[‡] and Giorgio Brida[†]
[†]Istituto Elettrotecnico Nazionale " Galileo Ferraris", Torino, Italy
[‡]Politecnico di Torino, Torino Italy

1 ABSTRACT

In this paper we present a very preliminary accuracy evaluation of the Italian new primary frequency standard, the IEN cesium fountain IEN-CSF1. A brief overview of the frequency standard is given, together with the evaluation of several shifts.

Keywords: *Primary frequency standard, Atomic fountain, Laser cooling, Cesium*

2 INTRODUCTION

The IEN Cs fountain (optical structure, physical package, and control system) was previously described in detail [1]. We recall here only the principal working parameters.
IEN-CSF1 is build in a x-y-z geometry and the launch of the atomic clouds is performed along the z axis using the moving molasses technique, similarly to other fountain primary frequency standard [2-3-4] (figure 1).
The optical system consists of a DBR master laser, frequency locked with a Pound technique, amplified by two 150 mW slaves lasers that generate the cooling beams; in addition a second DBR laser, 1f locked, is used as a repumper. Light from the master and the repumper lasers is used as well in the detection region.
A loading time of 700 ms in a MOT is followed by 80 ms of expansion in Doppler molasses; the atoms are then transferred in the moving frame and after 1 ms the post cooling process starts with a simultaneous amplitude and frequency ramp on the trapping beams that lasts less then 2 ms. The achieved atomic temperature is around 2 μK.
The launched atoms travel above the detection region entering the magnetically shielded region and first interact with the state selection cavity, where a π pulse at 9.192 GHz moves the F=4 m=0 atoms in F=3, m=0 state. After that a 5 ms vertical intense light pulse blasts away the remaining F=4 atoms.
After this pulse the light is switched off by the AO modulators and by mechanical shutters; at the same time also the microwave power in the state selection cavity is attenuated by nearly 100 dB.
The atoms then enter the Ramsey cavity and proceeds in the drift tube; the apogee height can obviously be chosen by changing the launching speed.
The Ramsey cavity is a OFHC copper cylindrical TE_{011} with four coupling loop fed from two external rectangular cavities; the cavity and the drift tube are part of the vacuum structure. A detailed description of the cavities can be found in [5].
On the way down after exiting the Ramsey cavity and the shielded region the atoms enter in the detection region where a differential detection of the atoms in F=4 and of those in F=3 is performed, allowing a direct measurement of the transition probability and a normalization of the total number of launched atoms in each cloud.
The total duty cycle for a transition probability measurement is of the order of 1.5 s; to allow a frequency measurement of the value of the central fringe a square wave modulation is applied and at least two probability measurement have to be done one on each side of the central fringe. The computer then calculates the central frequency value and set the synthesizer frequency for the next measurement.
The various function of the fountain operation are driven by the control PC trough three different boards: a pattern generator, a GPIB and a A/D converter.

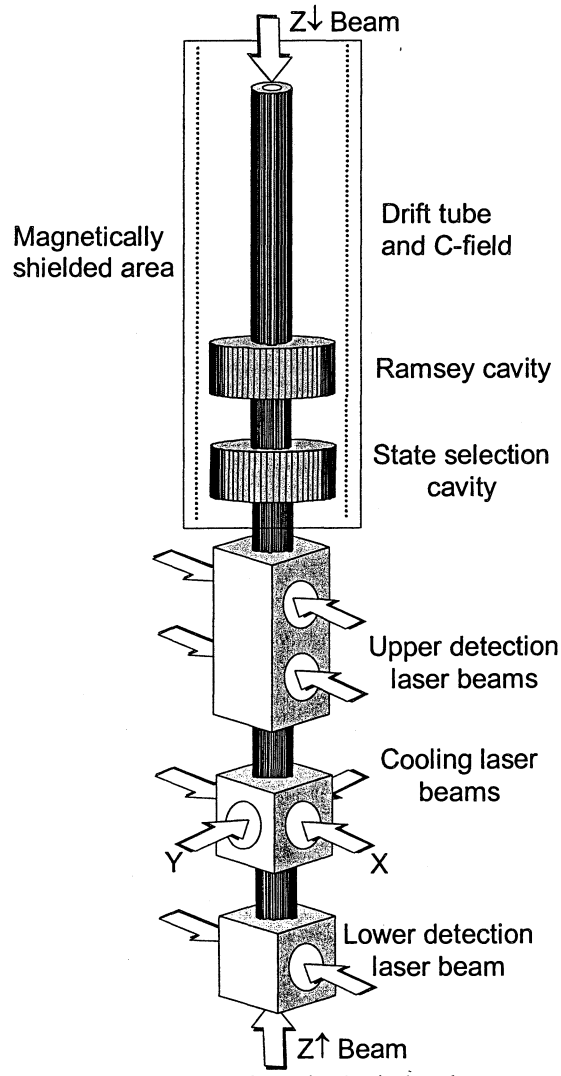

Figure 1:IEN Cs fountain physical package

As it will be discussed later on in the following sections, the IEN CSF1 wasn't yet used as primary frequency standard for two reason: first the atomic loss rate have to be improved by fixing some problems in the vacuum pumping system and second because the IEN time scale is not stable enough to support a fountain frequency measurement in a reasonable time: the master clock of UTC(IEN) is currently a HP 5071, two maser oscillators are expected to be delivered in the next year allowing a dramatic improvement of the short term stability of UTC(IEN).
However most of the main frequency biases have been analyzed and characterized (with the relevant exception of the atomic density) in our fountain frequency standard.
A Ramsey fringe pattern of the 0-0 transition is shown in figure 2

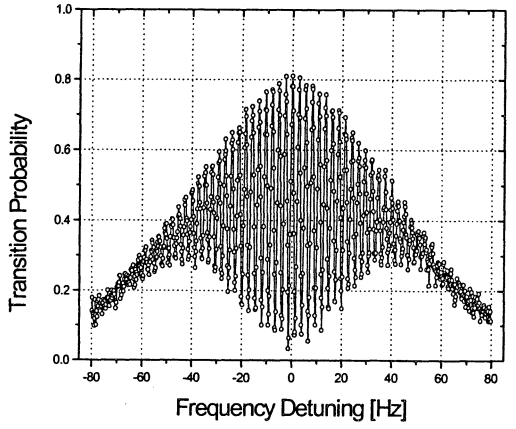

Figure 2 Ramsey fringes pattern of the 0-0 transition

3 MAIN UNCERTAINTY EVALUATION

We will discuss in the present section some of the frequency shifts that affect our frequency standard.

3.1 Second order Zeeman shift

To perform an evaluation of the magnetic field a mapping of the quantization magnetic field "C" has been carried on.
To measure locally the value of the field, Majorana transitions between the state F=3 m=0 and F=3 m=±1 are excited when the atoms reach their apogee [6].
A couple of long coils are placed along the whole drift region, starting 10 cm above the Ramsey cavity for construction reasons.
On the way up the state selection is applied as in normal fountain operation: a π microwave pulse move the atoms in F=4, m=0 into F=3, m=0, then the atoms left in F=4 are optically removed from the cloud.
When the atoms reach apogee, at a given height, a 70 ms long low frequency pulse is applied with the coils, exciting the transition between the magnetic lines; on the way down in the state selection cavity a second π pulse moves the atoms left in F=3, m=0 in F=4 m=0, allowing a simple differential measurement of the transition probability (figure 3).

In this way it is straightforward to map the magnetic field along the whole drift tube. The value of the field in the Ramsey cavity is evaluated by a simple Rabi transition between the F=4,m=-1, F=3 m=-1 states. In figure 4 is reported the map of the magnetic field obtained with the above described technique with a nominal applied C field of $.99\times10^{-7}$T.
The lack of knowledge of the magnetic field in the space between the Ramsey cavity and the starting of the coils is not dramatic, in fact the value of the Zeeman shift is given by a time average over the atomic trajectory and the time spent in this region is lower the higher is the apogee.

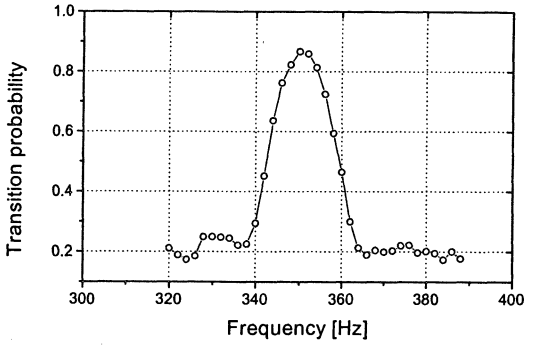

Figure 3 Low frequency transition between the F=3, m=0 and F=3, m=±1 states: the applied field is nominally .99 mG

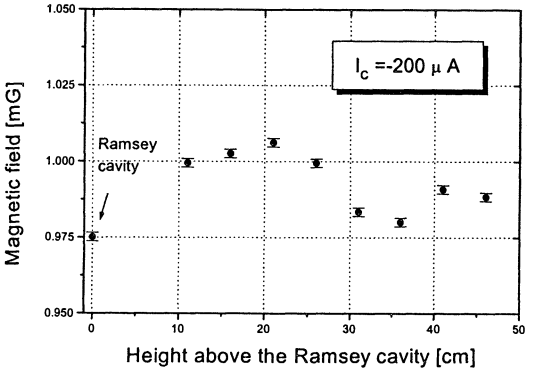

Figure 4 Map of the magnetic field above the Ramsey cavity

To evaluate the real shift on the 1-1 transition we have used a linear and a quadratic interpolation of the measured points. With the exception of the first 25 cm where the lack of information lead to a maximum discrepancy between the two calculation of 2.5 Hz, the agreement of the evaluated shift is well within a fringe width (figure 5), allowing to identify with high confidence the magnetic central fringe; however a more detailed mapping of the field in the drift region can easily be done, and will consequently improve the knowledge of B(t).
However even a misassignment of a whole fringe will lead to a relative error in the second order Zeeman shift of 2.6×10^{-16}.
The inhomogeneity of the magnetic field is of the order of ±1.3 nT the difference between $\langle B\rangle^2$ and $\langle B^2\rangle$ according to our field mapping can be estimated as:

$$\left| < B^2 > - < B >^2 \right| \approx 2B^2 \times 10^{-3}$$

the relative uncertainty is then below 10^{-16}.

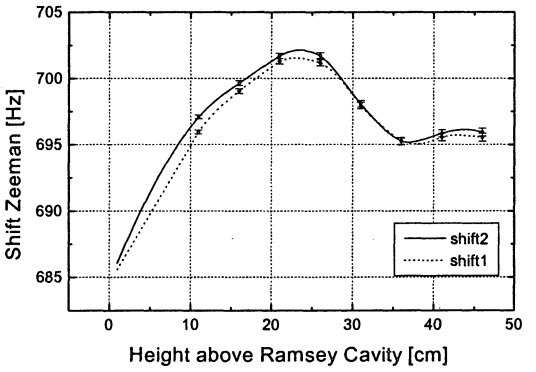

Figure 5 The evaluated shift on the 1-1 line, with linear and quadratic interpolation of the mapped point (shift 1 and 2). The frequency difference is below a fringe width for launches of 20 cm above the Ramsey cavity or higher.

3.2 Black body radiation

The temperature of the cavity and of the drift tube is monitored by several high quality thermocouples, the maximum measured temperature difference in the flight region is below .5 K. The temperature of the flight zone is set at 68 °C. If we use the relation [7,8]

$$\delta(\nu_0) = -1.573 \times 10^{-4} \left(\frac{T}{300K} \right)^4 Hz$$

we obtain a relative shift of

$$\delta(\nu_0)/\nu_0 = -(2.856 \pm .02) \times 10^{-14}$$

3.3 Cavity pulling and phase shift

The relatively high temperature set in the cavity and drift tube is chosen for cavity tuning purpose; the four coupling loop of our cavities allows in fact the observation in transmission of the resonance frequency and consequently a fine tuning of the cavity resonance. Assuming a conservative detuning of the cavity of a full linewidth, the resulting shift is $<.5\times10^{-16}$ and is then negligible.
The feeding of the cavities [5] is done through two distinct coupling rectangular cavities placed on the side of the main cavity. To minimize the phase shift is necessary to set the phase and the amplitude of the two feeding circuits equals; this can be done by tuning separately the four independent parameters and measuring the atomic response changing the feeding side on the way up and on the way down.

3.4 Light shift

Mechanical shutters are used to stop the during atomic interrogation. In absence of shutters, attenuating the laser beams only by means of acousto-optics modulators, a shift of the order of units of 10^{-13} is measured, depending strongly on the optical alignment of the AO cat-eye systems. The mechanical shutters allow an attenuation of the laser beams of more than four order of magnitude, making the light shift due to straight light negligible. The shutters are placed in such a way to minimize the possibility that scattered radiation could accidentally enter in the fountain structure.

3.5 Gravitational shift

IEN building has a geodetic point on the building roof, its elevation above the geoid surface is [9]:

$$h_{IEN} = (305.701 \pm .043)\,\mathrm{m}$$

the fountain is located 13.7 meters below that point, the gravitational shift with respect to the geoid is then

$$\delta(\nu_0)/\nu_0 = -(318 \pm 1) \times 10^{-16}$$

3.6 Atomic density

The atomic density frequency shift has not been evaluated yet, in fact in our system the atomic losses due to scattering with background gases are still too high because of inadequate vacuum level that will be fixed in the near future. This problem causes an atomic loss observed between the atomic signal on the way up and on the way down nearly a factor 100 higher than expected from thermal expansion considerations. We are therefore forced to operate the system with a very long loading time. The detected signal at contrary is relatively small impairing partially the S/N ratio currently available; according to the measurement reported in figure 6 of the central fringe of the Ramsey pattern, the signal to noise ratio of a single measurement is more than 50.

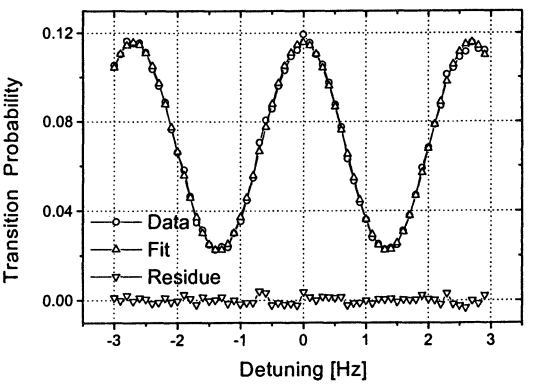

Figure 6 Central fringe of the Ramsey pattern, the S/N is calculated on the residuals after the sinusoidal subtraction.

3.7 Synthesis chain and reference

The synthesis chain is done by direct frequency multiplication of a high quality 5 MHz quartz oscillator up to 90 MHz, then the step recovery diode that generates the higher harmonics is mixed with a 12.6 MHz, reaching the Cs hyperfine frequency. The 12.6 MHz is obtained by a DDS synthesizer whose frequency is set by the control PC via GPIB.
Since the 5 MHz oscillator is locked against UTC(IEN) the DDS synthesized frequency is used also as frequency counter.
The spectral phase noise level of the synthesis chain, measured at the 90 MHz intermediate frequency is shown in figure 7. 50 Hz harmonics are more than 50 dB below the carrier.

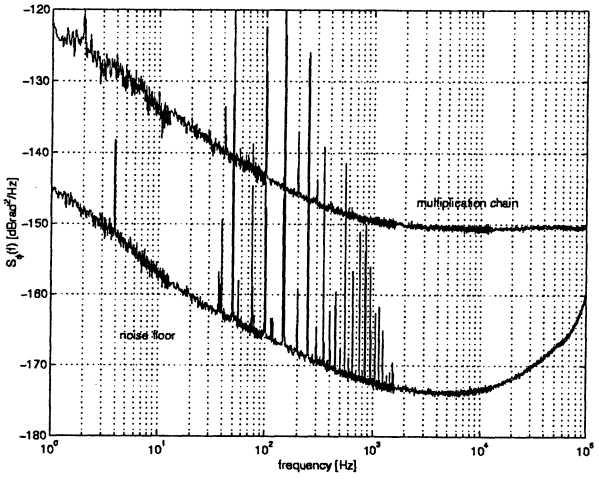

Figure 7 Phase noise of the synthesis chain

The actual synthesis chain could in principle support a fountain short term stability better than $10^{-13}\ \tau^{-1/2}$; but the reference time scale of UTC(IEN) is currently generated only by commercial Agilent 5071 units that have a short term stability of $8\times10^{-12}\ \tau^{-1/2}$, impairing strongly our sensitivity.
The improvement of the Italian time scale with the introduction of H-masers is planned for the next year.

3.8 Other effects

IEN fountain is highly insensitive to Majorana transition; state selection happens after the atoms are entered inside the magnetically shielded regions, while the clock transition detection is sensitive only to F=4 and F=3 population.
Doppler effect (classic and relativistic) are strongly reduced by the fountain geometry and atomic slow speed, and are estimated to contribute below the 10^{-16} to the relative error budget of our fountain.

4 CONCLUSIONS

We have reported a very preliminary evaluation of IEN-CSF1, a fountain primary frequency standard developed at IEN. In particular we have considered most of the main shifting effects present in a fountain frequency standard. Our accuracy evaluation is not completed yet because of two principal reasons, inadequate S/N level and quality of the reference UTC(IEN); all the other biases considered here are under control at the level of 10^{-15} relative uncertainty.
No shift have been observed at the 10^{-13} level with respect to UTC(IEN).

5 AKNOWLEDGMENTS

The realization of the IEN fountain is performed in the frame of a scientific agreement between IEN, NIST and the Politecnico di Torino.
We would like to thanks S.R. Jefferts for his invaluable help in the realization of the IEN fountain

6 REFERENCES

[1] F. Levi A. Godone, L. Lorini and D. Calonico Proceedings of the 14th EFTF Torino 14-16 march 2000 pg 450
[2] A.Clairon *et al* Proceedings of 5th Symposium on frequency Standard and Metrology, Woods Hole, MA, Ed. World Scientific Publishing, (1997)
[3] S. Jefferts *et al* Proceedings of the Joint meeting EFTF-IEEE FCS, Besancon 1999
[4] S. Weyers *et al.* Proceedings of the 14th EFTF Torino 14-16 march 2000 pg5 3
[5] S. Jefferts, B. Drullinger, A. De Marchi, Proceedings of IEEE-FCS (1998)
[6] G.A. Costanzo D.M. Meekhof, S.R. Jeffetrs and A. De Marchi Proceedings of the 14th EFTF Torino 14-16 march 2000 pg 494
[7] A. Bauch R. Schroeder, PRL Vol 78 n°4 (1997) p 622
[8] E.Simon, P. Laurent and A. Clairon, PRA Vol 57n°1 (1998) p 436
[9] A. Banni L. Mureddu, Internal Report Cagliari Astronomical station

INTERACTIONS BLACKBODY RADIATION WITH Cs AND Rb ATOMS: APPLICATIONS TO ATOMIC FREQUENCY STANDARDS

Yu.S. Domnin, A.V. Novoselov and V. G. Pal'chikov

Institute of Metrology for Time and Space at National Research Institute for Physical-Technical and Radiotechnical Measurements, Mendeleevo, Moscow Region, 141570 Russia. Fax: 007095 5350609,
E-mail: vitpal@mail.ru

ABSTRACT

A general method is presented for calculating the higher-order terms of series in powers of the blackbody radiation field for the Stark-state wave functions, dipole transition matrix elements and corresponding frequency shifts of hyperfine splitting on the ground states for Cs and Rb atoms. A precise method of calculating the hyperfine Stark shifts is described, which is based on the Green's function method for summation over all intermediate states and exact Dirac-Hartree-Fock wave functions in the relativistic single-double approximation for the resonant transitions to the first excited p-states.

1. INTRODUCTION

It is well known that the blackbody radiation (BR) shifts are most important for atoms in highly excited Rydberg states, because these states have low-frequency ($\omega << kT$) transitions as well as the huge electric dipole matrix elements Ref.1. Nevertheless, BR shifts are present even in the ground-state systems and this effect is large enough to be significant in the atomic frequency standards employing laser-cooling techniques for Cs and Rb atoms. These effects have drawn steady attention in the recent years. This interest has been caused both by the development of experimental techniques Ref.2-3 and by new theoretical approaches for describing of hyperfine Stark shifts due to BR field. The level of experimental accuracy in this field of study is sufficiently high to enable the unequivocal determination of the corresponding numerical values for frequency shifts and for straightforward comparison between the experimental and theoretical data.

The main goal of this paper is to analyze the higher-order Stark effect on hyperfine-structure components of Rb and Cs atoms due to the BR effect as well as the temperature-dependent shift on transition probability 7s-6s in Cs atom.

In the first part of the paper, we estimate theoretically the BR shift on hyperfine splitting for Cs and Rb atoms in the ground states. We introduce few separate differential susceptibilities (polarizabilities and hyperpolarizabilities) to describe of the calculating approaches based on the sum of oscillator strengths and on the Green's function method in the framework of the Fues' model potential approximation Ref.4.

The second part contains the accurate results for the temperature-dependent shift in Cs on 7s-6s transition probability. The corresponding expression for the transition probability is given by the sum of the differential spontaneous transition rates, which correspond to anti-Stokes scattering contribution and to two-photon transition contribution. The T-dependence of the total decay rate is analyzed.

2. HIGHER-ORDER STARK EFFECT ON HYPERFINE STRUCTURE COMPONENTS OF ALKALI ATOMS

The induced dipole moment d_e of an atom by a uniform static electric field F is given by

$$d_e = \alpha F + \frac{1}{6}\gamma F^3 + \ldots, \qquad (1)$$

where α is the electric dipole polarizability, and the γ represents the electric dipole hyperpolarizability. The corresponding expression for the energy shift is given by

$$E - E_0 = \Delta E = -\alpha F^2/2! - \gamma F^4/4! - \ldots, \qquad (2)$$

where E_0 is the field-zero energy. These quantities can be written in terms of the scalar (s) and tensor (t) parts

$$\alpha_{nLJM} = 2 < nLJM | D G_{nLJ} D | nLJM >, \qquad (3)$$

$$\alpha_{nLJM} = \alpha^s_{nLJM} + \alpha^t_{nLJM} \frac{3M^2 - J(J+1)}{J(2J-1)}. \qquad (4)$$

Here

$$G_{nLJ} = \sum_{|m> \neq |nLJ>} \frac{|m><m|}{E_m - E_{nLJ}} \qquad (5)$$

is the reduced Green function of the atom with excluded the state |nLJ> from the sum over the complete set of $|m>$. D is the z-component of the electric dipole moment of the atom.

The corresponding expression for hyperpolarizability has the similar form Ref.4:

$$\gamma_{nLJM} = \gamma_0(nLJ) + \gamma_2(nLJ)\frac{3M^2 - J(J+1)}{J(2J-1)}$$
$$+\gamma_4(nLJ)\frac{3(5M^2 - J^2 - 2J)(5M^2 + 1 - J^2)}{J(2J-1)(2J-2)(2J-3)}$$
$$-\gamma_4(nLJ)\frac{10M^2(4M^2-1)}{J(2J-1)(2J-2)(2J-3)}. \quad (6)$$

In the lowest order the total shift of the state |a> due to BR effect can be calculated by using second order perturbation theory Ref.5:

$$\Delta E_a = \frac{1}{4}\sum_b |<a|r|b>|^2$$
$$\times \int_0^\infty F^2(\omega)\left(\frac{1}{\omega_a - \omega_b - \omega} + \frac{1}{\omega_a - \omega_b + \omega}\right)d\omega \quad (7)$$

Here $F(\omega)$ is the frequency dependent electric field of blackbody radiation:

$$\frac{1}{8\pi}F^2(\omega) = \frac{1}{3}u(\omega, T), \quad (8)$$

where $u(\omega, T)$ is the spectral energy density

$$u(\omega, T) = \frac{\alpha^3}{\pi^2}\frac{\omega^3}{e^{\omega/kT} - 1}. \quad (9)$$

Therefore we can express (7) in the following form

$$\Delta E_a = \frac{2\alpha^3}{3\pi}\sum_b |<a|r|b>|^2 \int_0^\infty \omega^3 (e^{\omega/kT} - 1)^{-1}$$
$$\times\left(\frac{1}{\omega_a - \omega_b - \omega} + \frac{1}{\omega_a - \omega_b + \omega}\right)d\omega \quad (10)$$

There are 4 main limiting cases in the calculations of (10) Ref.5:

1. *Quasistatic perturbation.* In that case the frequency ω is much less than the natural linewidth of atomic transition . The static approximation works well and the energy shift is given by

$$\Delta E_a = \frac{2\pi^3}{15}\alpha^3\alpha(0)(kT)^4 \quad (11)$$

2. *Slowly varying perturbation.* In the such a case the frequency ω is bigger than the natural linewidth, but much less than the energy separation. In that case it is necessary to take into account the average (rms) value of the electric field:

$$<F^2(\omega)> = \frac{1}{2}\int_0^\infty F^2(\omega)d\omega = \frac{4\pi^3}{15}\alpha^3(kT)^4$$
$$= (8.319V/cm)^2\left[T(K)/300\right]^4 \quad (12)$$

3. *Rapidly varying nonresonant perturbation.* When the frequency of the perturbation is much bigger than the linewidth and the perturbation frequency ω is far from resonance, the corresponding Stark shift is given by formula (7) without integration operation (dynamic Stark effect)
4. *Resonant perturbation.* When the perturbation is approximately resonant with atomic transitions.

The Stark effect on atomic hyperfine structure leads to a shift of sublevels with different momenta $f = I + J$ (I is the nuclear spin, J is the total electron momenta), and to a splitting along the projection of the total momentum in the direction of the external field. The general expressions for the energy shift have different representations for $f = I \pm 1/2$ and , for example, for $f = I + 1/2$ can be written as Ref.6:

$$\Delta E(f = I + 1/2, m_f) = -CF^2$$
$$\times\left\{\alpha^s(f) + \alpha^t(f)\frac{3m_f^2 - (I+1/2)(I+3/2)}{I(2I+1)} + \frac{F^2}{12}\right.$$
$$\times\left[\gamma^s(f) + \gamma^{t1}(f)\frac{3m_f^2 - (I+1/2)(I+3/2)}{I(2I+1)} - \right.$$
$$+\gamma^{t2}(f)\frac{3(5m_f^2 - f^2 - 2f)(5m_f^2 + 1 - f^2)}{f(2f-1)(2f-2)(2f-3)}$$
$$\left.\left.-\gamma^{t2}(f)\frac{10m_f^2(4m_f^2-1)}{f(2f-1)(2f-2)(2f-3)}\right\}\right], \quad (13)$$

Here C is the constant dependent from the g-factor of the nucleus with spin I.

3. ANALYTICAL BASIS SET

We used the Green's function method and have investigated further the analytical Laguerre polinomial series expansion. This method, in principle, is similar to an analytical Sturmian basis set representation. All possible intermediate states are incorporated into the Green's function sum over all bound states and all positive continuum electron states in the framework of the Fues' model potential Ref.4.

The radial part of the Green's function has an analytical form Ref.4

$$g_l(E;r,r') = -\frac{4Z}{\nu}(xx')^l \exp\left(-\frac{x+x'}{2}\right) \times \sum_{k=0}^{\infty} \frac{k!\, L_k^{2\lambda_l+1}(x)\, L_k^{2\lambda_l+1}(x')}{\Gamma(k+2\lambda_l+2)(k+\lambda_l+1-\nu)} \qquad (14)$$

and $x = 2Zr/\nu$, $\nu = Z/(-2E)^{1/2}$, $L_m^l(x)$ is the Laguerre polynomial, $\Gamma(x)$ is the gamma-function. An exact Dirac-Hartree-Fock wave functions in the relativistic single-double approximation Ref.7 have been used in the calculation of the resonant transitions to the first excited p-states.

4. NUMERICAL RESULTS

In this paper, we estimate the temperature-dependent shift induced by an BR electric field $\langle E^2 \rangle = (831.9V/m)^2 [T(K)/300]^4$ on the $\nu = 6S_{1/2}(f=3, M_f=0) - (f=4, M_f=0)$ clock transition.

The frequency shift is given by

$$\frac{\delta\nu}{\nu_0} = -17.2 \times 10^{-15}(T/300K)^4 \times [1 + 0.014(T/300K)^2 - 1.65 \times 10^{-4}(T/300K)^2].$$

The second term is a correction due to separation in the frequency for D1 and D2 lines Ref.8. The last connected with higher-order Stark effect (hyperpolarizability).

The preliminary result for Rb atom is the next

$$\delta\nu = -8.451 \times 10^{-5} Hz$$

The present results are in good agreement with precise measurements based on the use the atomic frequency standards []. In have also estimated the second order temperature-dependent shift on transition $7s_{1/2}$-$6s_{1/2}$ in Cs due to BR effects based on the method, presented above. The corresponding BR correction induced depopulation rate for the $7s_{1/2}$ state at 300 K is 1.25 s^{-1}.

5. ACKNOWLEDGEMENTS

The authors thank Prof. W. R. Johnson (Notre Dame University, USA) for his interest in the work and for kindly sending us his unpublished data of reduced dipole matrix elements for Cs.

6. REFERENCES

[1] T.F. Gallagher and W.E.Cooke, Phys. Rev. Lett.Vol. 42, pp. 835-839, 1979.

[2] A.Bauch and R.Schroder, Phys. Rev. Lett. Vol. 78, pp. 622-625, 1997.

[3] E. Simon, P.Laurent and A.Clairon, Phys. Rev. Vol. 57A, pp. 436-439, 1998.

[4] A.Derevianko, W. R. Johnson, V. D. Ovsiannikov, V. G. Pal'chikov, D. R. Plante, G. Von Oppen, Phys. Rev. Vol. 60A, pp. 858-864, 1999.

[5] J. W. Farley and W.H. Wing, Phys. Rev. Vol. 23A, pp. 2397-2424, 1981.

[6] V.G. Pal'chikov, Hyperfine Interaction, Vol.127, pp.287-292, 2000

[7] M. S. Safronova, W.R.Johnson and A.Derevianko, Phys. Rev. Vol. 60A, pp. 5675-5689, 1999.

[8] W. M. Itano, L. L. Lewis and D. J. Wineland, Phys. Rev. Vol. 25A, pp. 1233-1236, 1982.

A SEARCH OF A TIME VARIATION OF THE FINE STRUCTURE CONSTANT USING COLD ATOM CLOCKS

Y. SORTAIS[1], S. BIZE[1], M. ABGRALL[1], S. ZHANG[1], C. MANDACHE[2], P. LEMONDE[1], G. SANTARELLI[1], P. LAURENT[1], C. SALOMON[3] AND A. CLAIRON[1]

[1] BNM-LPTF, 61 Av. de l'Observatoire, 75014 Paris, France,

[2] Institutul National de Fizica Laserilor, Plasmei si Radiatiei, P.O.Box-MG36, Bucuresti, Magurele, Romania,

[3] Laboratoire Kastler Brossel, Ecole Normale Supérieure, 24 rue Lhomond, F-75231 Paris Cedex 05, France

Corresponding author: Y. Sortais, Fax: 33 01 43 25 55 42, E-mail:yvan.sortais@obspm.fr

The question of the stability of fundamental constants has recently gained a broad interest. On one hand, several theoretical models attempting to unify gravity and the other fundamental interactions predict a dependence of physical constants with space and time [4]. On the other hand, a number of experiments testing the time variation of the fine structure constant α have been performed recently [1, 2, 3]. The most stringent tests so far rely on measurements performed at the cosmological scale.

We have built an experiment to perform a new test of the stability of α at the laboratory scale. The principle of the method is to compare at various times the hyperfine energies of ^{87}Rb and ^{133}Cs [5]. We have compared a a Rb fountain and two Cs fountains during two years, leading to a test of $\dot{\alpha}/\alpha$ at the level of 8×10^{-15} per year.

We present a new system to improve this result by more than one order of magnitude. It is a dual fountain operating with both Cs and Rb simultaneously. This dual operation in the same vacuum tube will allow a large reduction of several systematic frequency shifts affecting the comparison. If both fountains reach a frequency stability set by the fundamental quantum noise, the relative frequency stability in the comparison will be $\sim 1 \times 10^{-16}$/day. Finally the sensitivity of this test will also be improved by extending this frequency comparison method to other microwave frequency standards such as trapped ion clocks and to optical clocks.

References

[1] See for instance, F. Dyson, in *Current trends in the theory of fields*, ed. J. Lannutti and P. Williams, Am. Inst. of Physics, New York, (1978).

[2] Damour T. and Dyson F., Nucl. Phys. B **480**, 37 (1996).

[3] J. Webb, V. Flambaum, C. Churchill, M. Drinkwater, and J. Barrow, Phys. Rev. Lett. **82**, 884 (1999).

[4] T. Damour and A. Polyakov, Nucl. Phys. B **423**, 532 (1994).

[5] J. Prestage, R. Tjoelker, L. Maleki, Phys. Rev. Lett. **74**, 3511 (1995).

USE OF NEW DATA TO DETERMINE THE RELATIVISTIC RED SHIFT TO 3×10^{-17} AT NIST, BOULDER [1]

Nikolaos K. Pavlis[1], Marc A. Weiss[2]

[1]Raytheon ITSS Corporation, 4400 Forbes Blvd., Lanham, MD 20706, email: npavlis@terra.stx.com
[2]NIST Time and Frequency Division, MS 847.5, 325 Broadway, Boulder, CO 80303, email: mweiss@boulder.nist.gov

ABSTRACT

We have estimated the relativistic red shift correction due to gravity at the National Institute of Standards and Technology (NIST) in Boulder, Colorado, USA, using a new survey and the new U.S. detailed geoid model, G99SSS. We have computed the frequency offset that a standard at NIST would suffer in several ways. We referenced the frequency offsets computed from the different methods to the same geoid surface, one defined with respect to the current best estimate of an ideal mean-Earth ellipsoid. The new results are: (1) -1797.61×10^{-16}, based on the global gravitational model EGM96, (2a) -1798.72×10^{-16}, based on the regional, high-resolution geoid model G96SSS, (2b) -1798.49×10^{-16}, based on the regional, high-resolution geoid model G99SSS, and (3) -1798.91×10^{-16}, based on the value provided in the National Geodetic Survey's data sheet for the NIST reference marker. The minus sign implies that clocks run faster in the laboratory in Boulder than a standard clock located on the geoid. The values from (2b) and (3) are expected to be the most accurate and are also *independent*. Based on these results, we estimate the frequency shift at the reference point at NIST to be -1798.7×10^{-16}, with an estimated standard uncertainty of $\pm 0.3 \times 10^{-16}$.

Keywords: geoid, geodetic leveling, geopotential, mean-Earth ellipsoid, relativistic red shift, vertical datum

1. THEORETICAL BACKGROUND

This is a continuation of previous work [1]. Whereas previously we used coordinates accurate to about 1 m, using a recent GPS survey we now have coordinates that should be accurate to 20 cm or better. In addition, there is now available a new regional model of the geoid for the continental U.S., which we also used in our computations.

With the advent of new primary frequency standards with uncertainties approaching 1 part in 10^{15}, there is a need for improved estimates of the relativistic red shift. This is an effect predicted by relativity theory as the sum of a special and a general relativistic effect. In general relativity, a clock at a higher gravitational potential runs faster relative to a clock at a lower potential. In relativity, *"higher"* potential means less negative, since the convention used is such that potential has (in general) negative value, approaching zero as a particle moves towards infinity away from an attracting body. Thus the effect of the geopotential on a clock would cause it to run faster as it moves away from the Earth, or in our case, higher above the geoid. Note that geodesy uses the *opposite* sign convention for geopotentials than that used in relativity theory. In geodesy, all potentials are positive, so that a higher potential would generally be closer to the Earth. In this paper we will use the geodetic convention, in which all geopotentials are positive.

A second relativistic effect enters, the so-called second-order Doppler shift of special relativity, in which a standard clock runs slower as it moves faster, relative to a clock at rest. The rotation of the Earth, therefore, gives rise to a centripetal potential that also changes the clock's frequency. We differentiate between the potential due to *gravitation* and that due to *gravity*: the former arises from the presence of attracting masses *only*, the latter contains in addition the centripetal potential due to the Earth's rotation [2, section 2-1]. It is the gravity potential that we need to consider here, therefore the term "gravitational red shift" is somewhat misleading and has been avoided herein.

A primary frequency standard that contributes to International Atomic Time (TAI) must be corrected to run at the rate clocks would run on the Earth's geoid. It is therefore necessary to determine the difference in gravity potential $(W_0 - W_P)$, between the geoid (0) and the location of a primary frequency standard (P), in order to correct for this frequency offset, according to [3]

$$(f_0 - f_P)/f = \Delta f/f = (W_P - W_0)/c^2, \qquad (1)$$

where $f = (f_0 + f_P)/2$, and c denotes the speed of light. Note that if the point P is above the geoid, we generally have $W_P < W_0$, using the convention in which potentials are positive. Hence, Δf is negative in this case, since this clock correction would make the clock in Boulder run slower to match the rate of a standard clock on the geoid.

The *geopotential number* $C = W_0 - W_P$ [2, page 56] is given by:

$$C = W_0 - W_P = \int_{H=0}^{H=H_P} g\,dH\ , \qquad (2)$$

where g is the magnitude of the gravity acceleration vector, and dH is the length increment along the positive upward plumb line. The path-independent line integral in equation (2) starts from a reference equipotential surface whose gravity potential is W_0 (on which every point has *orthometric* height equal to zero) and ends at the station location where $W = W_P$ and $H = H_P$.

The Earth's geoid is a unique equipotential surface that closely approximates in some prescribed fashion the Mean Sea

[1] Contribution of U.S. Government not subject to copyright

Surface (MSS). The geoid has to be defined and realized through the operational development of models [4,5]. The presence of a quasi-stationary (i.e., non-vanishing through averaging over long time periods) component within the Dynamic Ocean Topography (DOT) results in departures of MSS from an equipotential surface ranging, geographically, between -2.1 m and +1.3 m approximately. Due to these departures (and in some cases due to additional considerations related to mapping applications), different vertical datums refer to different equipotential surfaces. Therefore, given a datum-dependent C value, the determination of $\Delta f/f$ with respect to a unique equipotential surface requires the estimation of that datum's offset from that unique equipotential surface.

There exist global geoid models, developed through the combination of satellite tracking data, surface gravimetry, and satellite altimetry. EGM96 is a state-of-the-art such model, complete to degree and order 360, corresponding to a half-wavelength resolution of ~55 km at the equator [6]. The resolution of such global models is limited primarily by the available surface gravimetric data used in their development. Detailed (i.e., higher-resolution) local or regional geoid models are developed by incorporating the information contained within dense gravity and topography data into a global geoid model. This adds high (spatial) frequency details to the broader geoid features represented within a global model. G99SSS [7] is such a regional geoid model for the United States. Global and regional geoid models can also be used to estimate the geopotential number C, given the geocentric coordinates of the point *P*.

We distinguish therefore two general approaches for the computation of C (and hence $\Delta f/f$): one based on spirit leveling and gravity observations, and another based on the use of geoid models (either global or regional/local). It is important to recognize that each computational method or model used may yield a result that refers to a different equipotential surface. Since the various reference surfaces may be offset by several decimeters, estimation of their relative offsets becomes important if one desires to compare the various results at the level of a decimeter or less.

It is useful to recall the correspondence between the approximate magnitude changes of *H*, *C*, and $\Delta f/f$. Near the Earth's surface $g \approx 9.8 ms^{-2}$ and since $c = 2997924.58\ ms^{-2}$, a change in H by one meter implies roughly a 9.8 m^2s^{-2} change in C, and therefore a change in $\Delta f/f$ of -1.1×10^{-16}. Our present requirement is that $\Delta f/f$ be computed with an error not exceeding $\pm1\times10^{-16}$. Therefore, the total error in an absolute determination of the geopotential number C, consisting of the error in W_0 (absolute) and the error in $W_0 - W_P$ (relative), should not exceed ~ 9.8 m^2s^{-2} (equivalently, the absolute orthometric height H_P of our station should be determined to better than 1.0 *m*).

2. COMPUTATIONAL ASPECTS

In the following paragraphs we discuss the specific computations involved in the estimation of $\Delta f/f$, according to three methods. The first two methods are based on geoid model information (global and regional respectively), while the third method is based on spirit leveling and gravity observations. The first two methods share some (long-wavelength) errors, but the third method is *independent* of the other two.

2.1 Mean-Earth Ellipsoid

The concept of a *mean-Earth ellipsoid* [2, section 2-21] is of central importance in gravimetric geodesy (and in our specific application). This purely mathematical construct is a rotating ellipsoid of revolution (i.e., bi-axial), whose surface is also an equipotential surface of its gravity field. The gravity potential on its surface is pre-supposed to equal the gravity potential on the geoid. Four parameters are necessary and sufficient to define uniquely its size, shape, rotation, and gravity field. One may assume that these parameters are numerically equal to the corresponding parameters of the real Earth. Then, the departures of the geoid from such an "ideal" ellipsoid, called *geoid undulations* and denoted *N*, have vanishing zero-degree term (i.e., their average over the whole Earth equals zero). Therefore, by suppressing the zero-degree term in the spherical harmonic expansion of *N*, we "automatically" obtain geoid undulations that refer to this "ideal" mean-Earth ellipsoid, *without* the need to know the specific scale (semi-major axis) of this ellipsoid. Specification of the scale and the gravity field of this "ideal" ellipsoid require numerical specification of its defining parameters. These values can be determined only from analyses of various geodetic observations and therefore contain random (and possibly systematic) errors. Here we will define this "ideal" mean-Earth ellipsoid, in a *tide-free* system [8], by adopting the current best estimates for the values of the following parameters [9]:

Equatorial radius: $a = 6378136.46\ m$
Flattening: = 1/298.25765
Geocentric gravitational constant: (3)
$GM = 3.986004418\text{x}10^{14}\ m^3s^{-2}$
Mean rotational speed:
$\omega = 7292115\text{x}10^{-11}\ rad\ s^{-1}$

We should emphasize here that the mean-Earth ellipsoid defined by the above four values is only as "ideal" as the current accuracy of these values allows. The adopted defining values of equation (3) imply a value of the gravity potential on the geoid equal to:

$$W_0 = 62636856.88\ m^2s^{-2}\ , \qquad (4)$$

with an estimated error of $\pm1.0\ m^2s^{-2}$ [9].

2.2 Reference Point

For this work we compare gravity potential based on models with potential based on spirit leveling and gravity measurements. To accomplish this we used two different markers at NIST. The U.S. National Geodetic Survey surveyed three points on the NIST campus in September, 2000 [10]. One of these, identified as DMA (it was first surveyed by the Defense Mapping Agency in 1977 using the Transit system), was used to obtain geocentric Cartesian coordinates for use in evaluating models. This point is located on the flat roof above the fourth floor at NIST, Boulder. There is also a point on the side of the second floor of the building designated Q407. This point is part of the North American Vertical Datum 1988 (NAVD88), network of spirit leveling and gravity measurements. Since most of the frequency standards at NIST are on the second or third floors, it is more convenient to

evaluate the relativistic red shift at an elevation equal to that of point Q407 rather than that of the DMA point.

Q407 is approximately 18.6 m distant horizontally from a point directly below the DMA point. We measured the Q407 point as 9.903 m below the DMA point. For evaluating the global and regional models, we used the coordinates of a point 9.903 m below the DMA point. This rather fictitious point is the point P we refer to in what follows. The change in gravity potential from point P to Q407 should be small in that it is due to a horizontal shift of only about 18.6 m. The relativistic red shift at P should agree with the value at the Q407 point to better than 10^{-18}, or 1 cm in terms of orthometric height.

2.3 Method 1

For method 1 we evaluated the EGM96 global model for the *gravitational* potential, i.e. the potential due to the Earth's attracting mass. To this we added the centripetal potential. For details on our evaluation of EGM96 see [1]. The EGM96 model is realized in the form of coefficients, $\overline{C}_{nm}$, for an expansion in terms of fully-normalized associated Legendre functions of the first kind [2, sections 1-11, 1-14], of degree n and order m. EGM96 [6] currently provides the most accurate estimate of a set of $\overline{C}_{nm}$, complete to degree and order 360.

The geocentric Cartesian coordinates of our reference point (P) 9.903 m below the DMA point, at the level of the Q407 marker for NIST, Boulder in ITRF97 are:

$$\begin{aligned} X_P &= -1288394.075 \\ Y_P &= -4721673.869 \\ Z_P &= 4078630.782 \end{aligned} \qquad (5)$$

These coordinates are expected to be accurate to 20 cm or better.

We converted these coordinates to spherical coordinates $(r_P, \theta_P, \lambda_P)$ and evaluated the EGM96 gravitational model plus the centripetal potential. We obtained:

$$W_P = 62620700.75\ m^2 s^{-2}, \qquad (6)$$

which, implies due to equations (1) and (4):

$$\Delta f/f = -1797.61 \times 10^{-16}\,. \qquad (7)$$

There are two types of error associated with the use of EGM96: (a) error of commission due to the fact that the coefficients $\overline{C}_{nm}$ are imperfectly known, and, (b) error of omission due to the truncation at degree 360. The commission error of EGM96 has two components. The first one (long wavelength) can be computed rigorously from the error covariance matrix that accompanies the part of the model up to degree and order 70. The second component, corresponding to degrees 71 to 360, can be computed only in terms of a global root mean square (RMS) estimate that does not account for the specific geographic location of our station. This estimate can be computed from the standard deviations of the EGM96 coefficients above degree 70. The omission error of EGM96 can also be estimated based on some theoretical model describing the decay of the gravitational spectrum of the Earth *globally*. Based on the EGM96 geoid error assessment in [6, sections 7.3.3.1 and 10.3.2], we estimate the total (commission plus omission) geoid undulation error of EGM96 at our reference point (P) to be approximately $\pm 0.6m$. Details of this error estimate are available in [1]. Combining this with an estimated error in ellipsoidal height of 0.2 m yields an error of the $\Delta f/f$ value given in (7) of 0.7×10^{-16}.

2.4 Method 2

A significant reduction of the omission error encountered with EGM96 can be effected through the use of a detailed regional geoid model. We have used the coordinates obtained from the new survey both with the 2'x2' gravimetric geoid model G96SSS [11] (which we also used in [1] along with the old survey coordinates), and the updated G99SSS [7] model. We estimated the geoid undulations at P, N_{GxxSSS}, (xx=96 or 99) using a bicubic spline to interpolate the grid on which each GxxSSS values is given (2'x2' for 96 and 1'x1' for 99). We computed the offset required to reference the N_{GxxSS} to an ideal mean-Earth ellipsoid. For both xx=96 and 99, this gave us (see [1] for details)

$$N_{GxxSSS}(ideal) = N_{GxxSSS} + 0.40\,m\,. \qquad (8)$$

We used the geodetic coordinates of P,

$$\begin{aligned} \varphi_P &= 39°59'42.86105" \\ \lambda_P &= 254°44'14.54111" \\ h_P &= 1634.421m \end{aligned} \qquad (9)$$

in particular the ellipsoidal height h_P, to determine the orthometric height, H_P, from

$$H_P(ideal) = h_P - N_{GxxSSS}(ideal) \qquad (10)$$

We then determined the geopotential number, C, using Helmert's equation as in [2, equation 4-26, and 12].

2.4.1 Method 2a

Using G96SSS, the model we used previously in [1], we now obtained with the new coordinates:

$$C = 16166.08\,m^2 s^{-2}\,, \qquad (11a)$$

which yields, from equation (1):

$$\Delta f/f = -1798.72 \times 10^{-16}\,. \qquad (12a)$$

Unlike EGM96, the GxxSSS regional geoid models are not accompanied by propagated error estimates. Their accuracy has been assessed only through comparisons with *independent* geoid undulation estimates obtained from GPS positioning and leveling observations [11,7]. Based on this uncertainty assessment, we estimate the error in N_{G96SSS} to be approximately 0.20 m. Considering also a 0.20 m error in the ellipsoidal height h_P, this implies an error for the $\Delta f/f$ value given in (12a) of 0.31×10^{-16}.

2.4.2 Method 2b

Using the new geoid model G99SSS, we now obtained with the new coordinates:

$$C = 16164.01\ m^2 s^{-2}\ , \qquad (11b)$$

which yields, from equation (1):

$$\Delta f/f = -1798.49 \times 10^{-16}\ . \qquad (12b)$$

From comparisons with *independent* geoid undulation estimates obtained from GPS positioning and leveling observations [11] we estimate the error in N_{G99SSS} to be approximately 0.18 *m*. Considering the 0.20 *m* error in the ellipsoidal height h_P, this implies an error for the $\Delta f/f$ value given in (12b) of 0.30×10^{-16}.

2.5 Method 3

The $\Delta f/f$ values given in equations (7) and (12a, 12b) were computed based on a global and two regional geoid models, respectively. We turn now to the $\Delta f/f$ computation from spirit leveling and gravity measurements, as shown in equation (2). We performed this computation as documented in [1] and found

$$C_{NAVD88} = 16170.76 m^2 s^{-2}\ , \qquad (13)$$

where the subscript "*NAVD88*" emphasizes the fact that this value refers to the equipotential surface that passes through the origin point (Father Point/Rimouski located in Quebec) of the North American Vertical Datum 1988 [12].

We adopted the value $\bar{d} = -0.30\ m$ as our current "best" estimate of the offset between the NAVD88 reference equipotential surface and the geoid surface. The minus sign implies that the equipotential surface passing through the origin of NAVD88 is *below* the geoid surface that is realized through the EGM96 model, when the latter is referenced to our current best estimate of a mean-Earth ellipsoid. We should also mention that in the above analysis the permanent tide effect was consistently accounted for. The offset value is expressed in the tide-free system.

Applying the offset $\bar{d}$ to estimate the correction dC necessary to convert C_{NAVD88} to C_{ideal} we find:

$$dC = -2.94\ m^2 s^{-2} \Rightarrow C(ideal) = 16167.82\ m^2 s^{-2} \qquad (14)$$

which implies:

$$\Delta f/f = -1798.91 \times 10^{-16}\ . \qquad (15)$$

Errors in the estimate of $\Delta f/f$ given in (15) arise from errors in the NAVD88 dynamic height value provided in the NGS data sheet for our reference marker, and errors in our estimation of the NAVD88 datum offset. The NGS data sheet for our reference marker contained no error estimates, other than the designation that "First order, Class II" leveling was performed to determine our station's height. Zilkoski et al. [12] discuss a comparison of NAVD88 heights with corresponding *independent* estimates from Canadian leveling observations over the USA-Canada border. Over 14 points the maximum difference found was 0.11 m. This value does not necessarily apply to our station; nevertheless (and in lieu of more precise information) a reasonable estimate of our station's dynamic height error may be about $\pm 0.15 m$. Considering an error of 0.20 *m* in our estimate of the NAVD88 datum's offset, we conclude that the $\Delta f/f$ value given in (15) is probably accurate to 0.28×10^{-16}.

3. COMBINED RED SHIFT ESTIMATE

The results from the three methods are summarized below in Table 1.

Table 1

Method	Red Shift parts in 10^{-16}	Uncertainty parts in 10^{-16}
1. EGM96	-1797.61	0.70
2a. G96SSS	-1798.72	0.31
2b. G99SSS	-1798.49	0.30
3. Leveling/Gravity	-1798.91	0.28

Method 3 is *independent* from the others. We accept G99SSS as an update to G96SSS and use only the results from methods 2b. and 3. to determine our final result. These differ by 0.42×10^{-16}, while our estimated errors from Table 1 imply a 0.41×10^{-16} uncertainty (1 sigma) for this difference.

Averaging methods 2b. and 3. to evaluate $\Delta f/f$, we estimate its value and uncertainty for our reference marker to be

$$(-1798.70 \pm 0.3) \times 10^{-16}. \qquad (16)$$

We note that the uncertainty here is larger than our previous estimate of 0.2×10^{-16}. We consider this uncertainty estimate to be perhaps more realistic.

We should mention that we have not accounted here for luni-solar tidal effects. At this level of accuracy the effects of (at least) the semi-diurnal lunar tide M_2 (and possibly of other constituents) must be considered. One should therefore interpret our $\Delta f/f$ result as an average value over multiples of the main tidal constituents' periods.

4. SUMMARY AND FUTURE PROSPECTS

Based on our work, it appears that the existing measurements and models of the Earth's gravity field may not support estimates of the relativistic red-shift correction to better than the 10^{-17} level for frequency standards on the Earth. Since this number contributes to the error budget of a primary frequency standard in an RMS sense, this implies that a primary frequency standard in an Earth-bound laboratory will have difficulty contributing to TAI at better than the 10^{-16} level. In the next decade it seems reasonable to expect frequency standards to reach accuracies challenging our current accuracy in the determination of the red-shift correction.

Currently two geopotential mapping missions are in preparation, which are expected to support a significant advance in the present application: NASA's Gravity Recovery And Climate Experiment (GRACE), and ESA's Gravity Field and Steady-State Ocean Circulation (GOCE) missions. GRACE is scheduled for launch in 2001, and promises to

deliver centimeter-level geoid undulation accuracy with half-wavelength resolution of 200 to 300 km. GOCE (scheduled for launch in 2005) is expected to improve even further the resolution, allowing cm-level geoid undulation accuracy down to ~80 km resolution [13]. The global geopotential models expected from these missions, in combination with locally available detailed surface gravity and topography data, may permit point geoid undulation determination approaching centimeter-level accuracy. In addition, radar altimeter data from satellites such as TOPEX/Poseidon and its follow-on Jason-1, in combination with the global geopotential models from GRACE and GOCE, should permit improvements in the determination of the equatorial radius of the mean-Earth ellipsoid, which directly affects the accuracy of W_0. These advances may permit determination of $\Delta f/f$ accurate to a few parts in 10^{18}.

On the opposite side, development of frequency standards accurate to 10^{-17} or better may provide one possibility for the verification and error calibration of geopotential differences estimated from data acquired in part from the GRACE and GOCE missions. This could be attempted following ideas such as those proposed originally by Bjerhammar [3]. In addition, frequency standards of such high accuracy, located on different continents, provide an alternative technique well recognized among geodesists for connecting different vertical datums. While there is promise for standards of such accuracies, methods for transferring such time and frequency measurements appear to be lacking. The current best time transfer methods appear to be at the level of 200 ps stability, or about 2×10^{-15} frequency transfer over 1 day [14]. In conclusion, it appears that technological advances in the development of frequency standards and advances in determination of the gravity field over the upcoming years are expected to benefit both disciplines in complementary ways.

5. REFERENCES

[1] Pavlis, N.K., M.A. Weiss, The Relativistic Red Shift with $2x10^{-17}$ Uncertainty at NIST, Boulder, Colorado, U.S.A., *Proceeds International Frequency Control Symposium*, June 2000, pp. 642-650.

[2] Heiskanen, W.A. and H. Moritz, *Physical Geodesy*, W.H. Freeman and Co., San Francisco, 1967.

[3] Bjerhammar, A., On a relativistic geodesy, *Bull. Géodésique, 59*, 207-220, 1985.

[4] Heck, B. and R. Rummel, Strategies for Solving the Vertical Datum Problem Using Terrestrial and Satellite Geodetic Data, IAG Symposia, Vol. 104, *Sea Surface Topography and the Geoid*, H. Sünkel and T. Baker (Eds.), Springer-Verlag, New York, 1990.

[5] Jekeli, C., The world of gravity according to Rapp, IAG Symposia, Vol. 119, *Geodesy on the Move*, R. Forsberg, M. Feissel, and R. Dietrich (Eds.), Springer-Verlag, Berlin, 1998.

[6] Lemoine, F.G., S.C. Kenyon, J.K. Factor, R.G. Trimmer, N.K. Pavlis, D.S. Chinn, C.M. Cox, S.M. Klosko, S.B. Luthcke, M.H. Torrence, Y.M. Wang, R.G. Williamson, E.C. Pavlis, R.H. Rapp, and T.R. Olson, The Development of the Joint NASA GSFC and the National Imagery and Mapping Agency (NIMA) Geopotential Model EGM96, *NASA/TP-1998-206861*, Goddard Space Flight Center, Greenbelt, MD, July, 1998.

[7] NGS page on the internet for G99SSS is: http://www.ngs.noaa.gov/GEOID/G99SSS/g99sss.html

[8] Rapp, R.H., R.S. Nerem, C.K. Shum, S.M. Klosko, and R.G. Williamson, Consideration of permanent tidal deformation in the orbit determination and data analysis for the TOPEX/Poseidon mission, *NASA Tech. Memo. 100775*, Goddard Space Flight Center, Greenbelt, MD, January, 1991.

[9] Bursa, M., Report of Special Commission SC3, Fundamental Constants (SCFC), Travaux de l' Association Internationale de Géodésie, Tome 30, Rapports Généraux et Rapports Techniques, IAG, 140 rue de Grenelle, 75700 Paris, France, 1995.

[10] NGS Data Sheets available on the internet by Permanent Identifier (PID) at: http://www.ngs.noaa.gov/datasheet.html
PID's for points DMA and Q407 are: AI7564 and KK1350, respectively.

[11] Smith, D.A. and D.G. Milbert, The GEOID96 high-resolution geoid height model for the United States, *J. Geod.*, *73*, 219-236, 1999.

[12] Zilkoski, D.B., J.H. Richards, and G.M. Young, Results of the General Adjustment of the North American Vertical Datum of 1988, *Surv. and Land Info. Systems, 52(3)*, 133-149, 1992.

[13] ESA SP-1233(1), The Four Candidate Earth Explorer Core Missions, Gravity Field and Steady-State Ocean Circulation Mission, European Space Agency, 1999.

[14] Nelson, L.M., J. Levine, K.M. Larson, P. Hetzel, Comparing Primary Frequency Standards at NIST and PTB, *Proceeds International Frequency Control Symposium*, June 2000, pp 622-636.

Notes

See page 121 for Quartz Oscillators


11th European Frequency and Time Forum
MARCH 6 - 8, 2001
NEUCHATEL
BIENVENUE
WELCOME
WILLKOMMEN
ORGANIZATION
Transat corp.
patum
Quartzlock
Lambe
Zyfer


Posters A & B
Auditorium
Exhibition

Notes

QUARTZ OSCILLATORS

Chairman: Jean-Pierre Aubry

OSCILLATOR NOISE SIMULATION BY USING NONLINEAR DIPOLAR METHOD

R. Brendel, D. Gillet, N. Ratier, M. Addouche, J. Delporte*

Laboratoire de Physique et Métrologie des Oscillateurs du CNRS associé à l'Université de Franche-Comté-Besançon
32, Avenue de l'Observatoire – 25044 Besançon Cedex – France

* Centre National d'Études Spatiales
18, Avenue E. Belin – 31055 Toulouse Cedex – France

ABSTRACT

Nonlinear dipolar analysis has been successfully used to quickly and accurately obtain both steady state oscillation frequency and signal amplitude of quartz crystal oscillators. Furthermore, by using slowly varying function method it is possible to obtain oscillation frequency and amplitude transients without having to perform long simulation runs. It is shown in this paper that a perturbation method applied in the vicinity of the steady state oscillation can be used to describe the effect of an additive noise source located in the oscillation loop. The perturbation source results in both amplitude and frequency modulations of the oscillation signal. By reducing all noise sources of the amplifier to a single equivalent current noise source, it is possible to obtain both AM and FM perturbation as a function of the Fourier frequencies close to the carrier. Amplitude and phase noise spectra are then easily derived. Eventually, it is shown that the phase noise spectrum obtained by using this time domain analysis fully agrees with the Leeson's model.

1. – INTRODUCTION

Dipolar modelling of crystal oscillators consists in characterising separately the behaviour of the resonator that is strongly varying with frequency but weakly varying with the current amplitude and the amplifier regarded as a nonlinear dipole whose impedance strongly varies with the current amplitude but weakly varying with frequency. The nonlinear behaviour of the dipolar amplifier is obtained by performing SPICE's transient analyses. Because the time constant of the amplifier alone is usually much shorter than the one of the whole crystal oscillator, the amplifier nonlinear characterisation does not need too long transient runs.

By looking for the amplifier current amplitude for which the amplifier impedance matches exactly the crystal impedance it is possible to obtain both steady state amplitude and oscillation frequency of the crystal oscillator.

Since the amplifier nonlinear impedance is known, it is possible to derive the oscillation condition under the form of a second order nonlinear differential equation controlling the oscillator loop current. Because of the high Q-factor of the crystal oscillators, the loop current is quasi sinusoidal and asymptotic method, such as slowly varying function method [Refs 1, 2], can be used to solve the nonlinear differential equation leading to both oscillator amplitude and frequency transients [Ref. 3].

All the additive noise sources of the amplifier can be reduced to a unique equivalent current noise source in parallel with the amplifier dipole so that it can be considered as a small amplitude current source in the oscillator loop, that acts as a time varying perturbation term in the nonlinear differential equation describing the oscillator behaviour. The effect of the small current source can be analysed by using a perturbation method in the vicinity of the steady state solution and results in a FM and AM modulation of the oscillation signal. By varying the frequency of the perturbation term around the oscillation frequency, both amplitude and phase spectra of the current source can be obtained. It is shown that the magnitude and shape of these spectra depends on the nonlinear characteristics of the amplifier dipole. By using the appropriate transfer function, amplitude and phase noise spectra at any location in the oscillator circuit can be derived from the reduced noise current source spectra.

Using these principles, an analysis program dedicated to quartz crystal oscillator is being completed to help the designer in the development of oscillator circuits.

2. – NOISE SOURCES

Noise sources can be categorized into two main groups according to their origin and/or their effect:

- Additive noise sources such as thermal noise associated with resistive components or shot noise associated with active components. These sources act as random voltage or current generators whose perturbing signal adds to the oscillation signal. Because of the selectivity of the resonator, only Fourier components close to the carrier will have a significant effect on the oscillation signal.
- Parametric noise comes from perturbation that affects the value of some components in the oscillating loop. Most often, they come from variation of the circuit environment like temperature, magnetic field, pressure, etc.

The variation of a component usually induces amplitude and frequency modulation so that only low frequency components of the perturbation that are close to the carrier will affect the oscillator performance.

In this paper, only additive noise sources will be considered.

3. – DIPOLAR METHOD PRINCIPLE

As described in a previous paper [Ref. 4], a quartz crystal oscillator can be represented by a resonator Z_Q connected across a two port amplifier circuit Z_D acting as a nonlinear dipole as shown in Fig. 1.

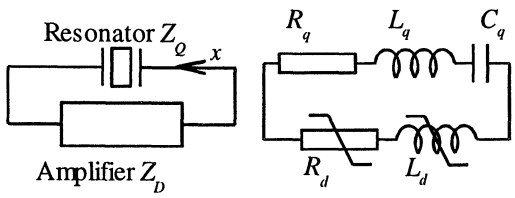

Fig. 1

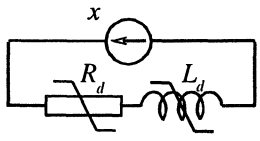

Fig. 2

The real and imaginary parts of the amplifier nonlinear resistances R_d and inductance L_d are obtained by replacing the resonator with a sinusoidal current source x (Fig. 2) the frequency of which is close from the oscillation frequency ω_0 and by performing a set of SPICE transient analyses of various current amplitudes. A Fourier analysis of the voltage across the dipolar amplifier is performed for each current amplitude y so as to obtain both real and imaginary parts $R_d(y)$ and $L_d(y)$ of the amplifier dipolar impedance.

The oscillation condition, readily obtained by inspection of the circuit in Fig. 1 is quite simple

$$\left(Z_D+Z_Q\right)x=0 \tag{1}$$

where Z_Q is the impedance of the series branch (L_q, C_q, R_q) of the quartz resonator equivalent circuit

$$Z_Q=\frac{L_q}{s}\left(s^2+\frac{R_q}{L_q}s+\omega_q^2\right) \text{ with } \omega_q^2=\frac{1}{L_qC_q} \tag{2}$$

and Z_D the amplifier nonlinear dipolar impedance

$$Z_D=R_d(y)+sL_d(y) \tag{3}$$

Replacing (2) and (3) in (1) gives the oscillation equation

$$s^2+\frac{1}{L_q}\left(R_q+R_d(y)\right)s+\omega_q^2\left(1-\frac{L_d(y)}{L_q}\right)=0 \tag{4}$$

where s is the Laplace's operator.

In the frequency domain, equation (4) splits into two equations corresponding to the real and imaginary parts. The steady state oscillation characteristics are then obtained by searching for the amplitude y_0 and the frequency ω_0 satisfying both real and imaginary parts.

In the time domain, equation (4) becomes the nonlinear second order differential equation (5) that can be used to describe the oscillation transient and, as we shall see, to perform noise analysis.

$$\frac{d^2x}{dt^2}+\frac{1}{L_q}\left(R_q+R_d\right)\frac{dx}{dt}+\omega_q^2\left(1-\frac{L_d}{L_q}\right)x=0 \tag{5}$$

4. – NOISE SOURCE REDUCTION

It is well known that all additive noise sources spread out in a circuit can be reduced to a single voltage or current noise source having the same effect at a given node of the circuit. The noise spectrum of the equivalent source can be obtained by using SPICE models and noise analyses [Ref. 5]. Thus, assuming that all noise sources of the amplifier have been reduced to a single equivalent noise current source x_d. The oscillator equivalent circuit can be completed as shown in Fig. 3 where x_q is the thermal noise current source associated with the resonator motional resistance R_q.

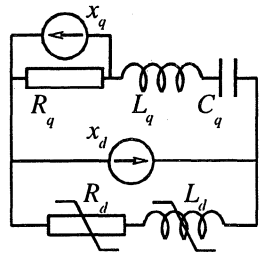

Fig. 3

5. – NOISE EQUATIONS

In order to analyze in the time domain how additive noise sources located in the oscillation loop perturb the output signal it is convenient to take into account some important features peculiar to quartz crystal oscillators:

- because of the high Q–factor of the motional series branch of the resonator, the loop current is quasi sinusoidal so that asymptotic resolution methods like slowly varying function method can be used,
- noise sources act as very small amplitude sources that slightly modify the oscillation signal, therefore their effect can be analyzed by using perturbation method,
- it is possible to get amplitude and phase noise spectra without having to consider noise sources as random processes. In fact, because any time domain signal can be expanded into Fourier series, noise sources can be replaced by sinusoidal sources having the same power spectral density.

The basic noise equation is obtained by inspection of Fig. 3 in which noise sources act as perturbation terms modifying the oscillation condition (1)

$$\left(Z_D+Z_Q\right)x=Z_Dx_d+R_qx_q \tag{6}$$

Substituting Z_D and Z_Q by their expression (2) and (3) gives the perturbed equation (7)

$$\left[s^2+\frac{R_q+R_d}{L_q}s+\omega_q^2\left(1-\frac{L_d}{L_q}\right)\right]x=\left(\frac{L_d}{L_q}s^2+\frac{R_d}{L_q}s\right)x_d(t)+\frac{R_q}{L_q}sx_q(t) \tag{7}$$

In the time domain, equation (7) can be expressed as a nonlinear differential equation. In the present case, because the loop current is known to be a quasi sinusoidal function and x_d and x_q are very small perturbation terms, the perturbed equation (7) can be

considered as a linear second order differential equation with a small nonlinear perturbation term in the right hand side

$$\frac{d^2x}{dt^2}+\omega_q^2 x = \frac{-(R_q+R_d)}{L_q}\frac{dx}{dt}+\frac{\omega_q^2 L_d}{L_q}x+\frac{L_d}{L_q}\frac{d^2x_d}{dt^2}+\frac{R_d}{L_q}\frac{dx_d}{dt}+\frac{R_q}{L_q}\frac{dx_q}{dt} \quad (8)$$

It should be noted that the right hand side can be split into an autonomous part in which time does not appear explicitly and that governs the unperturbed oscillation and frequency through the nonlinear functions $R_d(y)$ and $L_d(y)$, and a non autonomous part corresponding to external excitation terms $x_d(t)$ and $x_q(t)$ that are explicit functions of time.

To analyze the effect of the small perturbation terms, the steady state of the unperturbed autonomous equation is first obtained by using slowly varying function method [Ref. 4] that gives the unperturbed amplitude y_0 and frequency ω_0 of the signal. Then, by using perturbation method, it is possible to obtain both amplitude and frequency perturbation in the vicinity of the steady state.

6. – SLOWLY VARYING FUNCTION METHOD

Slowly varying function method consists in transforming the initial unperturbed autonomous equation (5) rewritten under the form

$$\frac{d^2x}{dt^2}+\omega_q^2 x = \frac{1}{L_q}\left(-(R_q+R_d)\frac{dx}{dt}+\omega_q^2 L_d x\right) \quad (9)$$

By using the variable change

$$x = y\cos(\omega_q t+\varphi) \quad (10)$$

Where y and φ are considered as slowly time varying functions. Equation (9) is then transformed into a nonlinear first order differential system in the variables y and φ

$$\frac{dy}{dt} = \frac{-y}{2L_q}\left(R_q+R_d(y)\right)$$
$$\nu = \frac{d\varphi}{dt} = \frac{-\omega_q L_d(y)}{2L_q} \quad (11)$$

where $R_d(y)$ and $L_d(y)$ are the dipolar resistance and inductance described in section 3. Solving system (11) by using numerical method will give steady state amplitude y_0 and frequency shift ν_0 that leads to the steady state unperturbed oscillation frequency

$$\omega_0 = \omega_q+\nu_0 \quad (12)$$

As assumed in section 5, noise sources have a small amplitude compared with the oscillation amplitude and, as explained in section 2, only Fourier components close from the carrier have to be considered. Furthermore, because the sources x_d and x_q are not correlated, their effect can be obtained by square summing their individual contributions.

The effect of the equivalent noise source current x_d can then be obtained by assuming that it has the form

$$x_d = \hat{x}_d\cos\omega_q t \quad (13)$$

where $\hat{x}_d$ is the amplitude of the noise source at the Fourier frequency ω (usually $\hat{x}_d$ depends on ω), so that

$$x_d \ll y_0 \quad (14)$$

and $\omega = \omega_q+\Omega$ with $|\Omega| \ll \omega_q$ (Ω can be either positive or negative).

It can be shown that applying the slowly varying function method to the perturbed equation (8) for the excitation term x_d leads to the associated system (15)

$$\frac{dy}{dt} = \frac{-y}{2L_q}(R_d+R_q)+\frac{\alpha}{2}\cos(\Omega t-\varphi)-\frac{\beta}{2}\sin(\Omega t-\varphi)$$
$$y\frac{d\varphi}{dt} = \frac{-y\omega_q L_d}{2L_q}+\frac{\alpha}{2}\cos(\Omega t-\varphi)+\frac{\beta}{2}\sin(\Omega t-\varphi) \quad (15)$$

where

$$\alpha = \frac{R_d\omega}{L_q\omega_q}\hat{x}_d$$
$$\beta = \frac{L_d\omega^2}{L_q\omega_q}\hat{x}_d \quad (16)$$

Note that if there is no perturbation term ($x_d = 0$) α and β vanish and the system (15) reduces the unperturbed system (11).

7. – PERTURBATION METHOD

When the steady oscillation is established, the small excitation terms will slightly perturb both amplitude and frequency so that they can be written under the form

$$y = y_0+z \qquad (z \ll y_0)$$
$$\nu = \frac{d\varphi}{dt} = \nu_0+\eta \qquad (\eta \ll \omega_q) \quad (17)$$

Furthermore, it can be shown that the solution of the perturbed system (15) appears under the form of a signal modulated both in amplitude and frequency at a modulation frequency Ω_m that is the difference between the excitation frequency ω and the unperturbed oscillation frequency ω_0

$$\Omega_m = \omega-\omega_0 = \Omega-\nu_0 \quad (18)$$

so that in first approximation, time varying terms of equation (15) can be expressed as

$$\cos(\Omega t-\varphi) \approx \cos(\Omega_m t-\varphi_0)$$
$$\sin(\Omega t-\varphi) \approx \sin(\Omega_m t-\varphi_0) \quad (19)$$

where φ_0 is an arbitrary constant phase shift.

By putting expressions (17) and (19) into the system (15) and keeping only the first order terms leads to the perturbation system (20)

$$\frac{dz}{dt}+\Omega_R z = \frac{\alpha}{2}\cos(\Omega_m t-\varphi_0)-\frac{\beta}{2}\sin(\Omega_m t-\varphi_0)$$
$$\eta = \frac{-\Omega_L z}{y_0}+\frac{\alpha}{2y_0}\sin(\Omega_m t-\varphi_0)+\frac{\beta}{2y_0}\cos(\Omega_m t-\varphi_0) \quad (20)$$

where

$$\Omega_R = \frac{y_0\vartheta_R}{2L_q} \qquad \vartheta_R = \left(\frac{\partial R_d}{\partial y}\right)_{y_0}$$
$$\Omega_L = \frac{y_0\omega_q\vartheta_L}{2L_q} \qquad \vartheta_L = \left(\frac{\partial L_d}{\partial y}\right)_{y_0} \quad (21)$$

θ_R and θ_L are respectively the slope of the nonlinear dipolar resistance and inductance at the steady state amplitude y_0 as shown in Fig. 4.

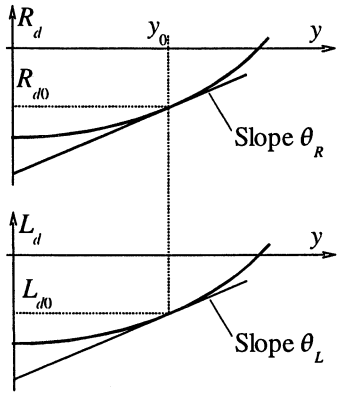

Fig. 4

8. – CURRENT NOISE SPECTRA

The system (20) consists in a linear first order differential equation with a forcing term giving the amplitude modulation term and a simple algebraic relation giving the frequency modulation term. Thus, the solution of the system (20) is searched under the form

$$\eta = \hat{\eta}\cos\Omega_m t \qquad z = \hat{z}\cos(\Omega_m t + \varphi_a) \tag{22}$$

where $\hat{\eta}_d$ and $\hat{z}_d$ are respectively the FM and AM amplitudes and φ_a is the phase shift between FM and AM. It is straightforward that

$$\hat{z}^2 = \frac{\gamma^2}{4(\Omega_m^2+\Omega_R^2)} \qquad \hat{\eta}^2 = \frac{\gamma^2\left[\Omega_R^2+(\Omega_m-\Omega_L)^2\right]}{4\,y_0^2(\Omega_m^2+\Omega_R^2)} \tag{23}$$

$$\text{and } \tan\varphi_a = \frac{\Omega_R}{\Omega_m-\Omega_L} \tag{24}$$

$$\text{where } \gamma^2 = \alpha^2+\beta^2 \text{ (cf. Eq. 16)} \tag{25}$$

Amplitude and phase noise spectra can then be readily obtained by using relations (24) and (25).

$$S_z(\Omega_m) = \frac{\hat{z}^2}{2} = \frac{\gamma^2}{8(\Omega_m^2+\Omega_R^2)} \tag{26}$$

$$S_\varphi(\Omega_m) = \frac{\hat{\eta}^2}{2\Omega_m^2} = S_z(\Omega_m)\frac{\Omega_R^2+(\Omega_m-\Omega_L)^2}{2\,y_0^2\Omega_m^2} \tag{27}$$

It should be recalled here that γ usually depends on the modulation frequency Ω_m. By using the same procedure as for the amplifier noise, the contribution of the resonator noise source has the same expression as given by the system (23), here the term γ has the following expression $\gamma = \frac{R_q\omega}{L_q\omega_q}\hat{x}_q$ (28)

By calling $\hat{z}_d$, $\hat{\eta}_d$ and $\hat{z}_q$, $\hat{\eta}_q$ the contributions of the noise sources x_d and x_q, the resulting AM and FM takes the simple form

$$\hat{z}^2 = \hat{z}_d^{\,2}+\hat{z}_q^{\,2} \qquad \hat{\eta}^2 = \hat{\eta}_d^{\,2}+\hat{\eta}_q^{\,2} \tag{29}$$

The amplitude and phase noise spectra have the same form as above

$$S_z(\Omega_m) = \frac{\hat{z}^2}{2} \qquad S_\varphi(\Omega_m) = \frac{\hat{\eta}^2}{2\Omega_m^2} \tag{30}$$

9. – VOLTAGE NOISE SPECTRA

In the previous section, we have shown how to calculate the current noise spectra, that is the amplitude and phase noise spectra of the current flowing through the motional branch of the resonator. These spectra can then be used to obtain noise spectra of any current or voltage in any location in the circuit as soon as the transfer function between the loop current and the desired variable is known.

Remember that if a variable X having a noise spectrum $S_X(\omega)$ feeds a linear system of transfer function $H(j\omega)$, the noise spectrum of the output variable Y is given by

$$S_Y(\omega) = |H(j\omega)|^2 S_X(\omega) \tag{31}$$

For example, the noise spectrum of the voltage v across the resonator given by (see Fig. 1 and equation (2))

$$v = Z_Q(j\omega)x \tag{32}$$

$$\text{is } S_v(\omega) = |Z_Q(j\omega)|^2 S_x(\omega) \tag{33}$$

$$\text{with } |Z_Q(j\omega)|^2 = R_q^2+\frac{L_q^2(\omega^2-\omega_q^2)^2}{\omega^2} \tag{34}$$

Here $S_x(\omega)$ is either the amplitude or the phase noise spectrum of the current x.

Most often, it is not possible to obtain an analytical expression of the transfer function between the resonator's current x and a given variable in the oscillator circuit. Nevertheless, it is possible to obtain this transfer function by using SPICE's time domain simulation. For example, assume that the output v where the noise spectra are to be calculated is located somewhere in the amplifier circuit as shown in Fig. 5

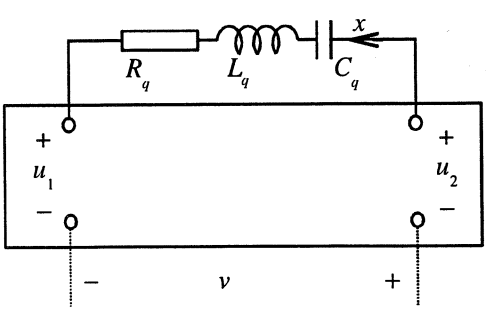

Fig. 5

The voltage v is related to the loop current x by the relation $v = u_1-u_2+Z_Q(j\omega)x$ (35)

In the general case, intermediates voltages u_1 and u_2 depends on both frequency and loop current amplitude, but because the noise spectra are calculated in the vicinity of the steady state, only the relationships

between u_1, u_2 and x for the steady state amplitude y_0 are required.

These relationships can be taken under the form

$$u_1 = Z_1(y, j\omega)x \qquad Z_1 = R_1 + jX_1$$
$$u_2 = Z_2(y, j\omega)x \qquad Z_2 = R_2 + jX_2 \tag{36}$$

Z_1 and Z_2 can be obtained by replacing the resonator with a sinusoidal current generator of amplitude y_0 and by performing a set of SPICE transient analysis in the desired frequency range close to the oscillation frequency. Real and imaginary parts of the impedances Z_1 and Z_2 are then calculated by performing a Fourier expansion of the waveforms u_1 and u_2 for each simulated frequency. Substituting (36) and (34) into (35) gives the desired transfer function

$$v = Z_t(j\omega)x \qquad Z_t = R_t + jX_t \tag{37}$$

with

$$R_t = R_1 - R_2 + R_q$$
$$X_t = X_1 - X_2 + \frac{L_q(\omega^2 - \omega_q^2)}{\omega} \tag{38}$$

Amplitude and phase noise spectra of the output voltage v are then calculated by using general expression (31)

$$S_v(\omega) = \frac{|Z_t(j\omega)|^2}{|Z_t(j\omega_0)|^2} S_x(\omega) \tag{39}$$

10. – VAN DER POL'S OSCILLATOR

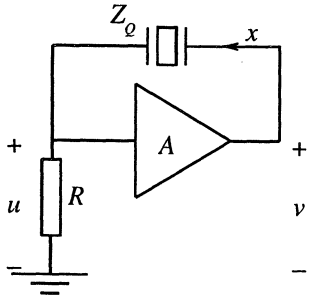

Fig. 6

Let us demonstrate the noise analysis principles on the simple behavioural example represented in Fig. 6, that can be calculated analytically. The amplifier output is a nonlinear function of the input voltage

$$v = Au(1 - \epsilon u^2) \tag{40}$$

It can be shown [Ref. 4] that the dipolar impedance Z_D can be expressed as

$$Z_D = (1 - A)R + \frac{3A\epsilon R^3}{4} y^2 \tag{41}$$

And that the loop current steady state amplitude is given by

$$y_0^2 = \frac{4R_M}{3A\epsilon R^3} \qquad R_M = (A-1)R - R_q \tag{42}$$

The equivalent amplifier noise source x_d can be calculated by inspection of Fig. 7

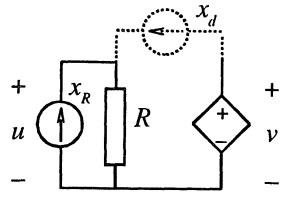

Fig. 7

In which the amplifier is represented by a voltage controlled voltage source. In this simple case, the only current noise source is associated with the resistor R and has a magnitude given by

$$\hat{x}_R^2 = \frac{4kT}{R}\Delta f \tag{43}$$

It is easy to show that the equivalent source x_d has the same expression

$$\hat{x}_d^2 = \frac{4kT}{R}\Delta f \tag{44}$$

Besides, the current noise source associated with the resonator is

$$\hat{x}_q^2 = \frac{4kT}{R_q}\Delta f \tag{45}$$

The amplitude and phase noise spectra of the loop current are obtained by means of relations (26) and (27) in which

$$\gamma^2 = \frac{\omega^2}{L_q^2\omega_q^2}(R_d^2\hat{x}_d^2 + R_q^2\hat{x}_q^2) \tag{46}$$

and

$$\Omega_R = \frac{R_M}{L_q} \qquad \Omega_L = 0 \tag{47}$$

Replacing $\hat{x}_d^2$ and $\hat{x}_q^2$ by their expressions (44) and (45) and taking into account the fact that when the steady state is reached $R_d^2 = R_q^2$, (46) becomes

$$\gamma^2 = \frac{4kTR_q^2\omega^2}{L_q^2\omega_q^2}\left(\frac{1}{R} + \frac{1}{R_q}\right) \tag{48}$$

Amplitude and phase noise spectra of the loop current are represented in Fig. 8(a) and (b).

The output voltage v in Fig. 6 can be readily expressed as a function of the loop current x

$$v = (Z_Q(j\omega) + R)x \tag{49}$$

The noise spectra of the output voltage are then given by

$$S_v(\omega) = \frac{|Z_Q(j\omega) + R|^2}{(R + R_q)^2} S_x(\omega) \tag{50}$$

where

$$|Z_Q(j\omega) + R|^2 = (R_q + R)^2 + \frac{L_q^2(\omega^2 - \omega_q^2)^2}{\omega^2} \tag{51}$$

Amplitude and phase noise spectra of the output voltage are also shown in Fig. 8(a) and (b).

The phase noise spectrum and the amplitude noise as well, present a cut off frequency Ω_c that can be analytically obtained from Eq. (51)

$$\Omega_c = \frac{R_q + R}{2L_q} \tag{52}$$

Ω_c is related to the loaded Q–factor Q_c by the relation

$$Q_c = \frac{\omega_q}{2\Omega_c} = \frac{L_q\omega_q}{R_q + R} \tag{53}$$

This example can be considered as a formal proof of the Leeson's phase noise model by using time-domain analysis.

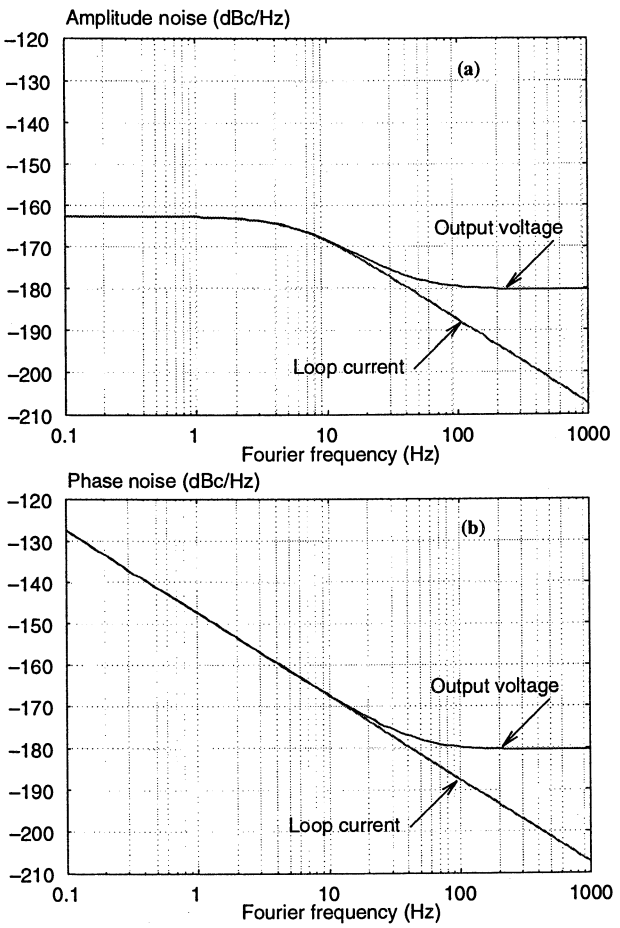

Fig. 8

8. – CONCLUSION

Because of the increasing performance of hardware and software, the nonlinear dipolar analysis of quartz crystal oscillators, that extensively uses SPICE transient analyses to characterize the amplifier behaviour, becomes an accurate, powerful and easy to use method to obtain oscillation characteristics and sensitivity of high–Q resonator circuits.

By using the well suited slowly varying function method combined with a perturbation method, a time domain analysis of noise is possible that allows to quickly obtain both amplitude and phase noise spectra for the additive noise sources. It should be recalled that noise analysis is performed here by using SPICE noise reduction principle. In this method, the operating point is first calculated and the circuit is linearized so as to obtain the appropriate transfer function. Although this method is useful to obtain an order of magnitude of the noise spectra, a more rigorous approach would need to consider a full nonlinear time domain analysis of the noise source effects [Ref. 6]. In any case, the method used still apply to $1/f$ additive noise source as far as the SPICE $1/f$ noise model parameters are known.

Noise spectra calculation based on this method are currently being implemented to complete ADOQ that is a CAD software dedicated to quartz crystal oscillator circuit design.

ACKNOWLEDGEMENTS

This work has been supported by CNES under contract # 714/CNES/99/7671/00.

REFERENCES

[1] N. Kryloff and N.N. Bogoliuboff, Introduction to Nonlinear Mechanics, Princeton University Press, 1943.

[2] A. A. Andronov, A. A. Vitt and S. E. Khaikin, Theory of Oscillators, New-York, Pergamon Press, 1966.

[3] R. Brendel, N. Ratier, L. Couteleau, G. Marianneau and P. Guillemot, "Slowly Varying function Method applied to Quartz Crystal Oscillator Transient Calculation", IEEE trans. on UFFC, Vol. 45, N° 2, March 1998.

[4] R. Brendel, D. Gillet, N. Ratier, F. Lardet-Vieudrin, J. Delporte, "Nonlinear Dipolar Modelling of quartz crystal oscillators", Proc. of the 14th EFTF, Torino, Italy, March 2000.

[5] L.W. Nagel, SPICE2: "A Computer Program to Simulate Semiconductor Circuits", Memorandum N° ERL-M520, University of California, Berkeley, May 1975.

[6] P. Bolcato, R. Poujois, "A New Approach for Noise Simulation in Transient Analysis", CEA-CONF 10958, 1992.

NEURAL NETWORK BASED PREDICTION OF CHUA'S CHAOTIC CIRCUIT FREQUENCY - POSSIBLE EXTENSION TO QUARTZ OSCILLATORS

O. Teytaud*, J.-M. Friedt**, M. Planat**
* ISC, Bron Cedex, France
** LPMO/CNRS, Besançon Cedex, France

Abstract

This paper theoretically and practically discusses the prediction of chaotic time series. Different articles having put into relief the efficiency of Support Vector Machines, we give theoretical tools explaining the role of hyperparameters, and explain some recent improvements of learning theory for the treatment of noise. We work on real world data and discuss the extension of prediction in three directions:
- Prediction without knowledge of the internal state of the chaotic system.
- Extension from prediction to stabilization
- amplitude-based frequency prediction

Keywords: Chaotic Time Series, Chua's circuit, Stabilization, Statistical Learning Theory, Learning theory with noise.

1. INTRODUCTION

We consider a chaotic time series verifying Takens' theorem. This means that a sequence $(x_n)_{n\in\mathbb{N}}$ of reals verifies $x_{n+1} = f(L, x_{n-\mathcal{D}+1}, x_{n-\mathcal{D}+2}, \ldots, x_n)$, with $L \in \mathbb{R}^{\mathcal{D}_L}$ the parameter of the chaotic oscillator. For the sake of sample complexity, $\mathcal{D}$ has to be chosen as small as possible. The smallest value ensuring optimal prediction is usually called *minimal embedding dimension* or *order* of the system. One could believe that using a larger value of $\mathcal{D}$ would ensure a regression more robust to noise; this was not verified in our experiments, what can be attributed to the fact that old points are made useless by sensitivity to initial conditions.

Lots of works study the prediction of chaotic oscillators: refs. [18, 15, 13, 11]...Refs. [13, 15] use Radial-Basis-Functions, leading to models with high number of parameters. These models are efficient, meanwhile they do not allow human intuitive understanding of the regression function. Ref. [18] reports good results even with a low number of parameters and discusses the relevance of learning theory in chaotic time series. The first part of our work, following ref. [11], is prediction on real world data, including justifications come from learning theory. The second part of our work is the study of the prediction of the subsequent values of the sequence *including L as a parameter*, ie allowing L to vary. The third part of our work is the study of the possibility of stabilizing chaotic oscillators, using efficient prediction of subsequent values of the sequence. Our data come from a Chua's oscillator. The circuit is fully described in ref. [11]. Links between Chua's circuit and the Colpitts oscillator are studied in refs. [20, 17].

2. DISCUSSIONS

2.1 Models and kernels

Refs. [18, 11] both conclude to the efficiency of support vector machines (SVM) for predicting chaotic time series. The problem of the choice of the kernel remains. The kernel was originally required in SVMs to verify Mercer's condition, in the spirit of embedding data in reproducing kernel Hilbert spaces. Some specialized kernels might lead to better results, but we prefer polynomials, for their fast computability, their understandability, and the easiness of computing derivatives (this will be of some use below). Degree 3 or 4 was enough for predictions with fixed values of L, but not for prediction with variable values of L. A simple solution would be increasing the degree of the polynomial, but this would be damageable to *clarity*, *speed*, and *sample complexity*. The notion of *sample complexity*, classical in Valiant's theory of learning, is the number of examples required to ensure optimal choice in a class of models, within a precision ϵ of the optimal model, with confidence $1-\delta$; worst case-sample complexity is roughly linear in the VC-dimension[1] - and VC-dimension of the polynomial kernel $K(x,y) = (1+ < x|y >)^d$ [2] is (in short) $O(d \times (dim + dim_L)^d)$. This leads to exponential increase of sample complexity as d increases. Another solution would be considering an original kernel, verifying Mercer's condition, thanks to Schur's theorem [3] proving that the product of two positive definite kernels is a positive definite kernels: $K(< x, L_x >, < y, L_y >) = (< x|y > +1)^d \times (< L_x|L_y > +1)^{d_L}$. This kernel (called A in the sequel) has VC-dimension $O(d \times \mathcal{D}^d \times d_L \times \mathcal{D}_L^{d_L})$. This allows a high dimension in L with a linear increase of sample complexity (as in our case $\mathcal{D}_L = 1$). Yet another solution, called B, is using the product of a polynomial kernel on x and y, and a Gaussian kernel for L_x and L_y. This completely fails to provide a model with a low number of parameters, making the learning local in L; moreover, sample complexity becomes very large and difficult to study. Whenever some global models as these

[1] An important point must be put into relief. Sample complexity is the number of samples required for ensuring nearly optimal parameters in the case of algorithms approximatively minimizing the empirical risk (or some related paradigms). Meanwhile, many algorithms minimize other related criterion, and sample complexity is then an approximation which should be justified.

[2] $< x|y >$ denotes the usual scalar product.

[3] See ref. [6] for more details about Mercer's condition and Schur's theorem.

are studied, the best solution was *local learning in L*: the domain of L was cut in 40 small parts, and linear interpolation was done between local models. This has computational cost linear in the number of parts during the learning phase, and logarithmic cost during experimentations themselves. For more sophisticated local learnings, the interested reader can read ref. [4]. Fixing the second layer of weights in SVM can be very time-consuming. We decided to replace this costly step by a naive algorithm based upon the same kernel representation: pseudo-inversion of the kernel matrix by singular value decomposition. This algorithm has the advantages of being old, fast, well known, and freely available. Bounding the coefficients as in SVM make this algorithm closer to the initial SVM.

2.2 Direct and iterated algorithms

If $x_{n+1} = f(L, x_{n-\mathcal{D}+1}, x_{n-\mathcal{D}+2}, \ldots, x_n)$, then $x_{n+2} = f(L, x_{n-\mathcal{D}+2}, x_{n-\mathcal{D}+3}, \ldots, x_n, f(L, x_{n-\mathcal{D}+1}, ..., x_n)))$, and so on for x_{n+k}. Developing this expression unfortunately leads to the apparition of an exponential number of f's (increasing as Fibonacci numbers if $\mathcal{D} = 2$), so an exponential addition of errors, provided that $\mathcal{D} > 1$. Experiments of ref. [11] illustrate this point: with $\mathcal{D} = 1$, this iterated algorithm works, whereas with $\mathcal{D} > 1$, the direct regression of x_{n+k} from $(x_{n-\mathcal{D}+1}, x_{n-\mathcal{D}+2}, \ldots, x_n)$ was more efficient, at least in our experiments. Another more subtle argument can explain the bad behavior of the iterated algorithm. This is detailed in part 2.5.

2.3 Hyperparameters of SVMs

Ref. [18] experimentally chooses the values of hyperparameters ϵ and C in SVM, arguing that the behavior of these parameters, respectively the parameter of insensitivity (the loss function is the $max(0, \delta - \epsilon)$ for a difference of δ between the predicted value and the observed value) and the parameter of penalization of errors, is still theoretically unclear. The sequel tries to explain how these parameters can be predicted. Meanwhile we admit that this solution is only theoretical as theoretical algorithms are not computationally faster, as detailed below. We recall the following theorem (*structural risk minimization*), which is the theoretical foundation of SVM in classification. Many versions of this theorem have been studied by many authors. A detailed study can be found in ref. [9].

Theorem 1 (Structural Risk Minimization) *Let C^1, C^2, C^3, ... be a sequence of families of classifiers with increasing finite VC-dimension V^1, V^2, V^3, ... Define $V(f) = \min\{k / f \in V^k\}$.*

Assume that the union $C = \cup_{i \in \mathbb{N}} C^i$ can approximate arbitrarily well any function for any distribution. Then with $f_m = \arg\min_f \frac{1}{m} \sum_{i=1}^{M} \chi_{f(X_i) \neq Y_i} + \sqrt{\frac{32 \times V(f)}{m} \log(e \times m)}$, with $\{(X_1, Y_1), \ldots, (X_m, Y_m)\}$ independent draws, and χ characteristic function (ie equal to 1 whenever $f(X_i) \neq Y_i$ and 0 otherwise else), has the following properties:

- The error rate decreases with probability 1 to the Bayes error.

- If the Bayesian classifier belongs to C, then the expectation of the error rate of classifier f_m decreases towards the Bayes'error at asymptotic rate $O(1/\sqrt{m})$.

Bounds on the VC-dimension of large margin classifiers justify the following expression 1 of the term to be minimized in SVM, in the case of f linear (at least in a given embedding reproducing kernel Hilbert space through Mercer's condition (so-called "kernel trick") - this allows infinite-dimension linear classifiers, with infinite VC-dimension).

$$\frac{1}{m} \sum_{i=1}^{m} \chi_{f(X_i) \neq Y_i} + A \sqrt{\frac{\log(m)}{m}} \parallel f^R \parallel \quad (1)$$

$$\frac{1}{m} \sum_{i=1}^{m} max(0, Y_i \times f^R(X_i) - 1) + \parallel f^R \parallel^2 \quad (2)$$

$$C \frac{1}{m} \sum_{i=1}^{m} max(0, Y_i \times f^R(X_i) - 1) + \parallel f^R \parallel^2 \quad (3)$$

$$C \frac{1}{m} \sum_{i=1}^{m} max(0, |Y_i - f^R(X_i)| - \epsilon) + \parallel f^R \parallel^2 \quad (4)$$

$$\frac{1}{m} \sum_{i=1}^{m} \chi_{|Y_i - f^R(X_i)| > \gamma} + \theta\left(\sqrt{\frac{\parallel f^R \parallel^2}{m \gamma^2}}\right) \quad (5)$$

where f^R denotes the linear function associated to the classifier f, which norm is the opposite of the margin (ie $f(x) = 1$ if $f^R(x) \geq 1$, -1 if $f^R(x) \leq -1$, and 0 otherwise else, with $Y_i \in \{-1, 1\}$). The NP-complete nature of this problem in many cases justifies the replacement of eq. 1 by eq. 2. Equation 1 was (in most cases of reproducing kernel Hilbert spaces) the compromise between two terms, structural risk and empirical error, ensuring results of theorem 1, and is no more justified in eq. 2. This explains the introduction of C in eq. 3. The adaptation to regression has been done as in eq. 4. Assuming that the noise is bounded by ϵ, this leads to a better sample complexity, as the zero error case is known faster than the non-zero case (for models of finite VC-dimension). Further justification of SVM, both in regression and classification, is due to the notion of *fat-shattering dimension*. Whereas VC-dimension appears relevant for classification, ref. [2] proves the decisive advantage of fat-shattering dimension for regression. Ref. [5] reports lots of properties of fat-shattering dimension. Equation 5 has to be minimized in regression, according to fat-shattering dimension theory. An adaptation of this to the problem of choosing C and ϵ would be the choice minimizing the above bound with $\gamma = \epsilon$. Unfortunately and as far as we know, there's for the moment no better algorithm for such a minimization than minimizing eq. 4 for many values of ϵ and C and choosing the best one. Moreover, lots of different bounds exist, all of them leading to too large constants for many practical cases; can one really consider that minimizing a bound larger than the

size of the interval is reasonable ? However, there are some cases, especially in the case of *a priori* knowledge, of reasonable and interesting bounds even with small samples. The interested reader is reported to ref. [14]. Note that similar results are possible even with non-linear mappings, even without Mercer's condition for ensuring that the mapping is a linear application in an embedding Hilbert space (even though bounds are larger).

2.4 The handling of noise

Lots of scientists have studied the possibility of regression or classification from a mathematical point of view (see refs. [9, 22]). A drawback is the lack of models including a proportion of noisy examples. Refs. [7, 3, 8, 16, 12] study the dependency of the asymptotic error rate and of the sample complexity in the noise rate. Results include optimal robustness to "malicious" noise and sample complexity in $O(1/\epsilon)$ in some cases[4], instead of the classical $O(1/\epsilon^2)$; moreover, some of the adaptations from PAC-learning to the noise case have polynomial-time complexity, with low degree. Some models (ref. [7]) make too many unreasonable assumptions on the distribution of noise (classification with constant misclassification rate of the oracle), some other (ref. [16]) allow too "malicious" errors (worst case of misclassification except in the independently distributed nature of occurrences of noise). However, ref. [8] shows good behavior of algorithms resulting from these theories in intermediate noise models (noise rate constant on a finite number of areas, ie CPCN model, or mixtures of malicious/constant-rate noise), and most of the algorithms of this area of learning theory are based upon similar tools. This suggests that the solutions might be very general, under the assumtion of a fixed proportion of occurences of output noise. Moreover, extension from classification to regression is (partially, mainly in the case of malicious errors) straightforward.

We now explain the principles of an algorithm of ref. [16], studied and improved in ref. [7, p101]. The principle is cutting the learning set of size m in $O(\sqrt[3]{m})$ subsets of equal size, using a PAC-algorithm on each subset except one, and choosing among all the hypothesis computed by comparison on the last subset. Ref. [16] proves that this polynomial-time algorithm[5], tolerates the optimal rate of "malicious" errors (within a constant factor), linear in ϵ achieved in the noise-free case. Ref. [7, 8] explains that similar (within a constant factor) robustness and smaller sample complexity can be achieved by fixing the number of subsets. This will be compared to the algorithm consisting in learning on each subset of the learning sample, and averaging the result. Learning directly on the whole dataset is impossible because of bounded computational resources.

2.5 Relevance of statistical learning

The assumption of independent identically distributed data is often tacitly admitted, even in learning theory articles applied to chaotic time series. Of course, consecutive points generated by chaotic systems are not independent and identically distributed. However, ref. [1, 19, 10] have shown extensions in a more adapted framework (notice, however, that the extension to such distributions of examples is not achieved). Note that these results imply that learning is possible, but this *only* leads to a satisfactory L^p error minimization, and not to coherent trajectories. Learning theory provides lots of tools for learning with low L^p error or classification error rate. Unfortunately and as we verified it in our experiments, there's no reason for an algorithm minimizing efficiently the error to have the same behavior than the initial chaotic oscillator. Experiments show that learning efficiently within a few steps is possible. But even a very small error lead to points out of the admissible trajectories. Then, there's no reason for the algorithm to predict efficiently: this area of the input space *was empty during the learning phase.* In practical experiments, even with very precise predictions, after a few steps the model predicted absurd values and was no more relevant. We consider that this can explain the failure of iterated algorithms, too. We underline that we do not only conclude that iterated algorithms are not efficient for p-steps prediction with p large, but that they do not have the same statistical properties as the original oscillator, too.

2.6 Stabilization

As explained in [22], control theory is a wide research area, and for the moment it is not established that results come from learning theory could be of some use in such an area. This section is to be considered as prospective.

A main originality of this paper is the hope of translating *prediction* into *stabilization.* The purpose of this part is describing the method. The principle lies in small alterations of the parameters in order to decrease the variance of the sequence. More precisely, define $X_{n,s} = \frac{1}{s}(x_n + x_{n+1} + x_{n+2} + \ldots + x_{n+s-1})$ and consider E, *energy* to be minimized, equal to the variance of $(X_{n\times s,s})_{n\geq 0}$. Now the parameter L is indexed by discretized time[6], and we will assume that for small variations of L, the relaxation time is negligible and we assume that equality 6 is nearly verified. The required functions $f_{k,s}$ are fixed by a preliminary regression as detailed above. The solution we propose is a gradient descent with regard to L_n: we increment L_n of dL_n defined in eq. 7. M is the expectation of $(x_n)_{n\geq 0}$ and $\hat{X}_{n,s}$ being the estimated value for $X_{n,s}$ if the parameter was fixed. The development of this term is

[4] In all the paper, logarithmic factors in $1/\epsilon$ are often neglected.

[5] This algorithm is polynomial-time provided that the initial learning algorithm, in the case of no noise, is polynomial.

[6] One can notice that as successive measures of frequencies are value dependent, the discretized steps are not linearly distributed on $\mathbb{R}^+$.

complicated by the fact that the modification of L, in practical cases, is not necessarily immediate. So, eq. 6 must be written as illustrated by eqs. 8 and 9. This allows a computation of dL_{n-m} at step $n-k$. Equation 9 leads to eq. 10. M being unknown at step $n-m$, it has been replaced by an estimation $\hat{M}$. Other solutions than gradient descent have been experimented, like predicting with a few values close to L and choosing the best one.

$$X_{n,s} = f_{k,s}(L_{n-k}, X_{n-k,\mathcal{D}}) \quad (6)$$

$$dL_n = \eta \frac{M - \hat{X}_{n,s}}{\frac{\partial \hat{X}_{n,s}}{\partial L_n}(L_n, X_{n,s})} \quad (7)$$

$$\hat{X}_{n,s} = f_{m,s}(L_{n-m}, \hat{X}_{n-m,\mathcal{D}}) \quad (8)$$

$$\hat{X}_{n,s} = f_{m,s}(L_{n-m}, f_{k-m,\mathcal{D}}(L_{n-k}, X_{n-k,\mathcal{D}})) \quad (9)$$

$$dL_{n-m} = \eta \frac{\hat{M} - f_{m,s}(L_{n-m}, f_{k-m,\mathcal{D}}(L_{n-k}, X_{n-k,\mathcal{D}}))}{\frac{\partial f_{m,s}}{\partial L}(L_{n-k}, f_{k-m,\mathcal{D}}(L_{n-k}, X_{n-k,\mathcal{D}}))} \quad (10)$$

As explained below, these has led to disappointing results. A modification is the replacement of $\hat{M}$ by constant values. In our experiments with such an arbitrary value, we observe a significant improvement of the synchronization of two series. Further work should include a value of M dependent of the previous $\mathcal{D}$ values of the frequency and of the parameter.

3. PRACTICAL RESULTS

3.1 Prediction: varying parameter

The following results have been got *without learning specifically points with this value of L.* Indeed, examples with values of L equal to the ones of the test set have been *removed* of the learning set. The algorithm is local in the sense that the interval of values of L has been cut in 40 parts and learnt independently on each part. Notice that 20 parts were indeed sufficient for a similar precision. Moreover, L could be predicted from the sequence without prior knowledge.

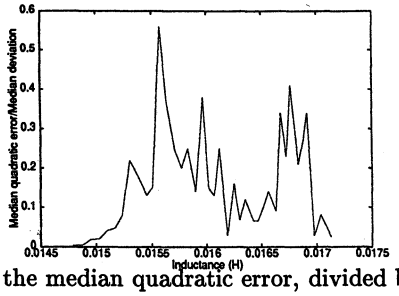

This is the median quadratic error, divided by the median quadratic deviation from mean (mean evaluated for this value of the parameter - the local algorithm is so compared to a trivial algorithm choosing the mean value corresponding to this parameter and succeeds significantly better), for different values of the parameter. 1500 points were used for learning and 500 for testing and parameters used for testing were disjoint from the ones used for learning. $\mathcal{D} = 3$ and the model is polynomial of degree 4. The abscissa is $L \times 10^3$ (inductor, mH). 6 experiments among these have been restarted with algorithms modified as suggested in 2.4 with segmentation in 9 subsets. Results were not significantly different (meanwhile a bit better) but much faster. An important point is that learning on the 3 last *amplitudes* instead of the 3 last *frequencies*, for predicting the following *frequency*, leads to very similar result.

The following results hold in the case of learning in *one* global model, without local segmentation. The best parameters have been chosen, and then tested again with new points. The learning and testing sets are both made of 3200 points. $\mathcal{D} = 3$, and the parameter lies in the same interval than previous experiments. Inputs and outputs have been normalized (mean 0, variance 1).

Kernel	Polynomial kernel	Kernel *A*	Kernel *B*
Parameters	Deg 2	Degs $d = d_L = 2$	Var 10 Deg 2
Mean quadratic error / Variance	0.84	0.74	0.76

3.2 Stabilization

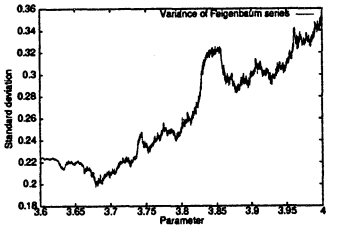

Variance of Feigenbaum series ($x_n = A \times x_{n-1} \times (1 - x_{n-1})$) depending upon the parameter A. Our experiments with the gradient descent detailed in part 2.6 succeeded in the case of Feigenbaum series in the sense that small variations lead to a significantly smaller variance than the initial oscillator. Meanwhile, studying the behavior of the parameter shows that the algorithms slowly evolves toward a fixed value, for which variance is lower. So, simulating another such oscillator with this value of the parameter leads to similar results. The algorithm only succeeds in finding a "good" value of the parameter, close to the initial one. Experiments on the Chua oscillator was possible only with $m = k \geq 5$ because of technical constraints. No significant improvement has been shown. We hope that a decrease of m and k, with better devices, would lead to better results. A strong drawback of this technique is that prediction-based stabilization would require previous frequencies, what requires a reference oscillator. This implies that we do not *stabilize*, but that we *synchronize*. Meanwhile, our experiments above show that prediction of frequency can be done from amplitudes as well as from frequencies.

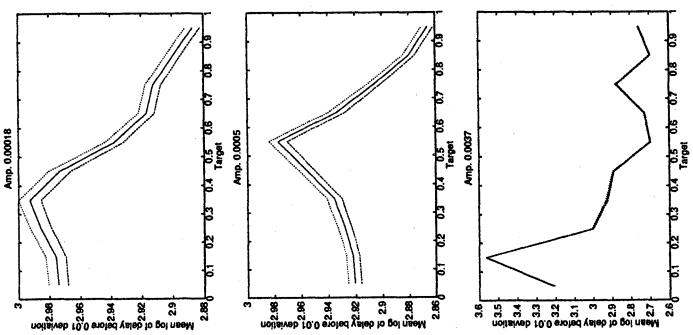

Different logs of delays (with confidence intervals) before deviation for different amplitudes of η in eq. 10, depending

upon the choice of M. We expect significant improvement by optimizing the choice of M and η taking into account the current state. Without correction, the log is 2.90. The two first graphs show the average time before deviation *averaged* on different values on the initialization of the Feigenbaum serie, whereas the third one considers the same initial value (arbitrary value: 0.64). In the third case, the average logarithm of time before deviation without correction was 3.16. These results show that:

- Stabilization *is* possible, with small variations of the parameter A.
- The optimal choice of M depends upon η and is not simply the mean.
- The optimal choice of M depends upon the current value of the sequence. Specializing on an initial value improved very significantly the results.

This suggests that these results, coming from fixed value of M and based upon small variations of A, could be much improved by optimized values of $M(x_n)$ and $\eta(x_n)$.

4. CONCLUSION

One can be interested in prediction for one of the following applications:
- Stabilization. Unfortunately, our results on Chua are far from being positive. The feasibility of stabilization by prediction/correction remains an open question, as far as we know. However, we show on theoretical series that such stabilization seems to be possible, and we show on Chua that future frequency can be deduced from previous amplitudes. This suggests algorithm for stabilizing chaotic oscillators. Future experiments on Chua require faster electronic devices, and extension to quartz oscillators will be still more difficult. Other further work could include optimization of the retroaction by multiple attempts and corrections: our "temporal" gradient descent could be considered as the initial point of a trajectory in the space of parameters of a retroaction devoted to stabilize the sequence. - Modelization. Some algorithms are indeed much better for this than regression tools. As underlined in part 2.5, minimizing the error in prediction is not sufficient for ensuring a good modelization by iterations.
- Prediction itself. This paper (and others) show that prediction is possible. Our article has the particularity of showing that this is possible even with unknown parameter. Our best results have been got with local models, but some experiments with original kernels suggest that improvements are possible.
- Interpretability. In as many cases as possible, we tried to keep a low number of parameters, and to avoid local models. In the case of prediction with fixed value of L, a polynom of degree 3 or 4 was enough (meanwhile some better results could be achieved with restrictionless kernels). Global modelization by polynomials was not possible by usual kernels, but our modified kernels A and B lead to improved results, whenever A is completely polynomial, and has linear dependency of sample complexity in the degree wrt L. It is interesting to notice that as local models have large sample complexity, in the case of a restricted number of examples the best results have been got with kernel A. Such manipulations on kernels based upon Schur's theorem seem to be promising for regression with parameters of different natures.

References

[1] D. ALDOUS, U. VAZIRANI, *A Markovian extension of Valiant's learning model, Proc 31st Annual IEEE Symp. on the Foundations of Comp. Sci., p392-396, 1990.*

[2] N. ALON, S. BEN-DAVID, N. CESA-BIANCI, D. HAUSSLER, *Scale-sensitive dimensions, uniform convergence and learnability. Journal of the ACM, 44(4):615-631,1997.*

[3] J.-A. ASLAM, S.-E. DECATUR, *On the sample complexity of noise tolerant learning, information processing letters, 1996.*

[4] C.-G. ATKESON, A.-W. MOORE, S. SCHAAL, *Locally Weighted Learning. Artificial Intelligence Review. 1996 .*

[5] P.-L. BARTLETT, *The sample complexity of pattern classification with neural networks: the size of the weights is more important than the size of the network, IEEE transactions on Information Theory, 44:525-536, 1998.*

[6] C. BERG, J.-P.-R. CHRISTENSEN, P. RESSEL, *Harmonic Analysis on Semigroups, Theory of Positive Definite and Related Functions, Springer, 1984.*

[7] S.-E. DECATUR, *Efficient learning from faulty data, Thesis, 1995.*

[8] S.-E. DECATUR, *PAC learning with Constant-Partition Classification Noise and Applications to Decision Tree induction, Proceedings of ICML 1997.*

[9] L. DEVROYE, L. GYORFI, G. LUGOSI, *A Probabilistic Theory of Pattern Recognition, Springer, 1996.*

[10] L. DEVROYE, L. GYORFI, *Nonparametric density estimation: An L_1 view, Wiley, New York, 1985.*

[11] J.-M. FRIEDT, O. TEYTAUD, D. GILLET, M. PLANAT, *Simultaneous amplitude and frequency noise analysis in Chua's circuit - neural network based prediction and analysis, VIII Van Der Ziel Symposium on Quantum 1/f Noise and Other Low Frequency Fluctuations in Electronic Devices, 2000.*

[12] C. GENTILE, D.-P. HAMBOLD, *Improved Lower Bounds for Learning from Noisy Examples: an information-theoretic approach, Proceedings of the 11th Annual Conference on Computational Learning Theory, ACM Press, 1998.*

[13] S. HAYKIN, J.PRINCIPLE, *Using Neural Networks to Dynamically model Chaotic events such as sea clutter; making sense of a complex world, IEEE Signal Processing Magazine 66:81, 1998.*

[14] R. HERBRICH, T. GRAEPEL, J. SHAWE-TAYLOR, *Sparsity vs. Large Margins for Linear Classifiers. . In Proceedings of the Thirteenth Annual Conference on Computational Learning Theory, pages 304-308, 2000.*

[15] W. HONG, *The application of Radial Basis Function Networks to the prediction of Chaotic Time Series, Term Project, Course 2.160, Intelligent Control and Sensing, 1993.*

[16] M. KEARNS, M. LI, *Learning with malicious errors, SIAM Journal on Computing, 22, 807-837, 1993.*

[17] M.-P. KENNEDY, *On the relationship between the chaotic Colpitts oscillator and Chua's oscillator, IEEE transaction on Circuits and Systems 42 (6), 1995.*

[18] S. MUKHERJEE, E. OSUNA, F. GIROSI, *Non-linear Prediction of Chaotic Time Series Using Support Vector Machines, Proc. of IEEE NNSP'97, Amelia Island, FL, 1997.*

[19] A. NOBEL, *On uniform laws of Averages, Ph. D. Thesis, Dept of Statistics, Stanford University, 1992.*

[20] G. SARAFIAN, B.-Z. KAPLAN, *Is the Colpitts a relative of Chua's circuit ? IEEE Transaction on Circuits and Systems 42 (6) 1995.*

[21] V. VAPNIK, *Estimation of Dependencies Based on empirical data. Springer-Verlag, New York, 1982.*

[22] M. VIDYASAGAR, *A theory of learning and generalization, Springer 1997.*

STATISTICAL MODEL OF A MODULATED OSCILLATOR WITH AN ADDITIONAL RESONANT FEEDBACK

yuriy shmaliy, anatoliy marienko*, stanislav nedorezov*, miguel torres-cisneros, oscar ibarra-manzano,

guanajuato university, fimee, salamanca, 36730, mexico, shmaliy@salamanca.ugto.mx
* "sichron" center, 4 skrypnyka str., kharkiv, 310057, ukraine

Abstract – In this paper we discuss a generalized statistical model of modulated oscillator with an additional resonant feedback produced by an anharmonic of a crystal resonator. It is also considered this feedback as a sensor of environment. The signal model is presented for a far carrier range of a sensor operation as a mixture of a deterministic signal and a white Gaussian noise (phase noise floor). General moments of a sensor response in an oscillator signal are studied within a gap of a sensor bandwidth for an arbitrary signal-to-noise ratio (SNR) with respect to modulation by both the internal noise (1 ≈ SNR) and intended signal (1 < SNR).

Crystal oscillator, Modulation, Anharmonic sensor

1. INTRODUCTION

A novel technique of self-contained frequency control of precision crystal oscillators is based on use of the resonator spurious (anharmonic) resonances as sensors of environment (Ref. 1). Such approach was first used to compensate temperature dependence of oscillator frequency, employing a temperature sensitive crystal resonator "B"-mode in dual-mode oscillator (Ref. 2). Practice showed to the limited compensation accuracy due to a high drive level of a sensor necessary to obtain stability of the dual-mode operation. The recently described modulational method (Ref. 3) inherently provides a small excitation level for the sensor (Ref. 4).

In a modulated oscillator an external signal brings to AM-FM with modulation frequency $\Omega \cong \omega_i - \omega_0$, where ω_i and ω_0 are frequencies of an additional feedback and oscillator carrier, respectively. An upper spectral line of oscillator signal with the frequency $\omega_0 + \Omega$ excites a sensor for the drive level dependent on amplitude of a modulating signal. While changing this amplitude, the sensor drive level is optimized for a small interaction with the fundamental mode and for the signal-to-noise ratio (SNR) enough to estimate a sensor frequency in real time with required accuracy. Moreover, the concept, by extension, holds true for another kinds of oscillators (Refs 5-8). In each case, an oscillator model is readily reduced to the closed feedback of the fundamental mode, in parallel to which an additional resonant feedback is included (Refs 1, 2, 9-11).

In this paper we discuss the statistical steady-state model of generalized modulated oscillator (crystal oscillator) with an additional resonant feedback. We focus attention on both the cases of modulation by either a noise (1 ≈ SNR) or intended signal (1 < SNR). We assume the signal to be a Gaussian random process formed by a mixture of a deterministic signal and a white Gaussian noise (Refs 11, 12). We learn statistical properties of a sensor through the modulation amplitude-frequency and phase-frequency characteristics (AFC) and (PFC) of oscillator (Refs 1, 9). While studying, we consider AFC and PFC as a sensor responses in an oscillator signal (Ref. 10), discussing their major statistical moments for an arbitrary SNR. In this way we answer the following major questions: what is a steady-state statistical model of generalized modulated oscillator with an additional resonant feedback (sensor) in a far carrier range, and what are the statistics of an additional feedback (sensor) signal for an arbitrary SNR?

2. FLUCTUATING MODEL OF AN OSCILLATOR

Let us be based on the Leeson's oscillator model (Ref. 13) formed by an active part with a gain G and a general resonant feedback response $H_g(j\omega)$ of the fundamental mode (Refs 5-8). Add the other feedback with response $H_i(j\omega)$ produced by an anharmonic. Figure 1 shows the model, where $u_{out}(t)$, $u_g(t)$, and $u_i(t)$ are deterministic outputs of an active part, general and additional feedbacks, respectively; $\varepsilon_a(t)$, $\varepsilon_g(t)$, and $\varepsilon_i(t)$ are noise signals of an active part, general and additional feedbacks, respectively; $e_{in}(t)$, $e_{out}(t)$, $e_g(t)$, and $e_i(t)$ are total signals of an active part input, oscillator output, and outputs of general and additional feedbacks, respectively.

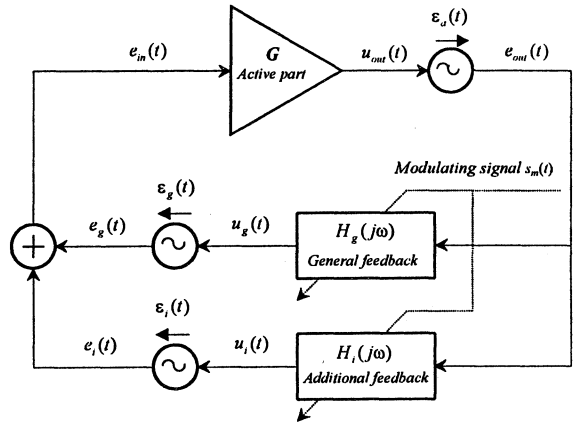

Figure 1. The oscillator model

In this oscillator both the necessary and sufficient operation conditions are satisfied for the general feedback only. Then at the frequency of the anharmonic sensor the general feedback seems to be opened and the exciting signal in the additional feedback is caused only by the noise floor $\varepsilon_{NF}(t)$ of the oscillator spectrum. Figure 2 illustrates this case.

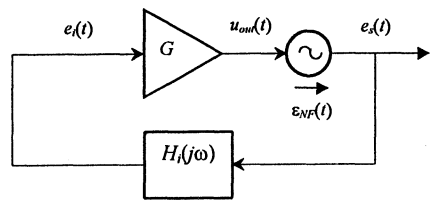

Figure 2. Oscillator model for the sensor frequency

Here $e_s(t)$ is a sensor signal. It follows straightforward from the model (Fig. 2) that the sensor signal is defined as $e_s = \frac{H_i(j\omega)}{1-GH_i(j\omega)}\varepsilon_{NF}$. Then, since for an anharmonic we get $|GH_i| < 1$ and $|H_i| < 1$, a SNR of a sensor signal is around one. For example, assume that $|GH_i| = 0.8$ and $|H_i| = 0.2$, then get $e_s/\varepsilon_{NF} = 1$. We then suppose that an internal noise $\varepsilon_{NF}(t)$ yields $1 \approx$ SNR and that intended modulation brings to $1 <$ SNR or even to $1 <<$ SNR.

3. THE MODEL OF AN OSCILLATOR SIGNAL

To describe the signals, first, decompose a total input $e_{in}(t)$ into a deterministic voltage $u_{in}(t)$ and a white Gaussian noise $\varepsilon_{in}(t)$ with zero mean and known covariance

$$e_{in}(t) = u_{in}(t) + \varepsilon_{in}(t). \quad (1)$$

Generally, we deal with both AM and FM then, dropping harmonics of modulating frequency, present the deterministic part $u_{in}(t)$ as (Ref. 9)

$$u_{in}(t) = U_{in0}\left[1 + m_A\cos(\Omega t - \varphi_A)\right], \times\cos\left[\omega_0 t + m_\varphi \sin(\Omega t - \varphi_\omega) + \varphi_0\right] \quad (2)$$

where $\Omega = 2\pi F$; $\omega_0 = 2\pi f_0$ and f_0 and φ_0 are an oscillator carrier and initial phase, respectively; U_{in0} is average amplitude of a signal, $m_A(\Omega) = k_A H_A(\Omega)$; $m_\varphi(\Omega) = \frac{\omega_0}{\Omega} m_\omega(\Omega)$; $m_\omega(\Omega) = k_\omega H_\omega(\Omega)$; k_A and k_ω are coefficients of static AM and FM, respectively; $H_A(\Omega)$ and $\varphi_A(\Omega)$ are AFC and PFC of AM, respectively, and $H_\omega(\Omega)$ and $\varphi_\omega(\Omega)$ are AFC and PFC of FM, respectively. For a small modulation ($m_A << 1$ and $m_\varphi << 1$) enough to excite a sensor (Ref. 3), we may represent (2) with respect to an additional resonant feedback as follows

$$u_{in}(t) = U_{in0}\left[1 + m_{Ai}\cos(\Omega t - \varphi_{Ai})\right] \times\cos\left\{\omega_0 \int\left[1 - m_{\omega i}\cos(\Omega t - \varphi_{\omega i})\right]dt + \varphi_0\right. \quad (3)$$

where $m_{Ai}(\Omega) = k_{Ai}H_{Ai}(\Omega)$ and $m_{\omega i}(\Omega) = k_{\omega i}H_{\omega i}(\Omega)$ are AFC of AM and FM, respectively, and φ_{Ai} and $\varphi_{\omega i}$ are PFC of AM and FM, respectively, of an additional feedback in an oscillator signal. This allows writing all the aforementioned DMC in the forms given in Ref. 9 as

$$m_{Ai} = \sqrt{m_{A0}^2 + 2m_{A0}k_i\cos(\varphi_{A0} - \phi_i) + k_i^2}, \quad (4)$$

$$\varphi_{Ai} = \operatorname{arctg}\frac{m_{A0}\sin\varphi_{A0} + k_i\sin\phi_i}{m_{A0}\cos\varphi_{A0} + k_i\cos\phi_i}, \quad (5)$$

$$m_{\omega i} = \sqrt{m_{\omega 0}^2 - 2m_{\omega 0}k_i g\cos(\varphi_{\omega 0} - \phi_i) + k_i^2 g^2}, \quad (6)$$

$$\varphi_{\omega i} = \operatorname{arctg}\frac{m_{\varphi 0}\sin\varphi_{\omega 0} - k_i\sin\phi_i}{m_{\varphi 0}\cos\varphi_{\omega 0} - k_i\cos\phi_i}, \quad (7)$$

where $g = \Omega/\omega_0$; m_{A0}, $m_{\omega 0}$, φ_{A0}, and $\varphi_{\omega 0}$ are DMC values beyond a sensor bandwidth; $k_i(\Omega)$ and $\phi_i(\Omega)$ are gain and phase, respectively, of a sensor at an arbitrary frequency Ω.

Before giving a statistical analysis, we observe that m_A, φ_A and m_ω, φ_ω are, in fact, amplitude and frequency responses, respectively, of a sensor in an oscillator signal. When considered a sum of a deterministic signal (1) we had shown early in (Ref. 10) that the noisy DMC may be presented for an arbitrary modulation frequency Ω as narrowband random functions

$$m_{Ai}(\Omega,t) = \sqrt{(b_1 + X_1)^2 + (b_2 + X_2)^2}, \quad (8)$$

$$\varphi_{Ai}(\Omega,t) = \operatorname{arctg}\frac{b_1 + X_1}{b_2 + X_2}, \quad (9)$$

$$m_{\omega i}(\Omega,t) = \sqrt{(d_1 + X_1)^2 + (d_2 + X_2)^2}, \quad (10)$$

$$\varphi_{\omega i}(\Omega,t) = \operatorname{arctg}\frac{d_1 + X_1}{d_2 + X_2}, \quad (11)$$

where $b_1(\Omega) = V_{is} + U_{+\Omega}m_{A0}\sin\varphi_{A0}$, $b_2(\Omega) = V_{ic} + U_{+\Omega}m_{A0}\cos\varphi_{A0}$, $d_1(\Omega) = V_{is} - U_{+\Omega}m_{\varphi 0}\sin\varphi_{\omega 0}$, and $d_2(\Omega) = V_{ic} - U_{+\Omega}m_{\varphi 0}\cos\varphi_{\omega 0}$; $X_1 = A\sin\Psi$ and $X_2 = A\cos\Psi$ are independent centered Gaussian processes with equal variances $\sigma_{x1}^2 = \sigma_{x2}^2 = \sigma^2$. When further introduced for (8)—(11) the orthogonal components $U(t)\sin\phi(t) = y_1(t) + X_1(t)$ and $U(t)\cos\phi(t) = y_2(t) + X_2(t)$, and a correspondent analytical signal $U(t)\exp[j\phi(t)]$, where $y_{1,2}(t)$ equals either $b_{1,2}(t)$ or $d_{1,2}(t)$, $U(t) \geq 0$, and $-\pi \leq \phi(t) \leq \pi$, we had also proved in (Ref. 10) the following principal relationships

$$(m_\omega, m_A) \equiv U(t),$$
$$(\varphi_\omega, \varphi_A) \equiv \begin{cases} \phi(t), & if \quad y_2 + X_2 \geq 0 \\ \phi(t) \pm \pi, & if \quad y_2 + X_2 < 0, \end{cases} \begin{cases} y_1 + X_1 \geq 0 \\ y_1 + X_1 < 0 \end{cases} \quad (12)$$

Hence, aiming to learn the stochastic model special features, instead of (4)—(7) we can study DMC (8)—(11), pointing that statistical properties of oscillator with an anharmonic sensor may be exhaustively learned through those of an envelope and phase $U(t)$ and $\phi(t)$ of an introduced analytic signal.

4. STATISTICAL PROPERTIES OF A SENSOR

To investigate the statistical properties of a sensor, we now substitute for (8)—(11) the forms of $y_1(\omega) = \frac{y_0}{1+\varsigma^2}$, $y_2(\omega) = -\frac{y_0\varsigma}{1+\varsigma^2}$, and $y(\omega) = \frac{y_0}{\sqrt{1+\varsigma^2}}$, where y_0 corresponds to ω_i, $\varsigma(\omega) = Q_i\left(\frac{\omega}{\omega_i} - \frac{\omega_i}{\omega}\right)$ is generalized detuning, and Q_i is Q-factor of an additional feedback. Employing the Gaussian theory, we study below the statistical properties of DMC (8)—(11) in a far-carrier range through the probability distributions of X_1 and X_2. On this way, once an oscillator process exhibits both the stationary and the non-stationary nature, we examine the four major distributions of $m_{A,\omega}(t)$, $\varphi_{A,\omega}(t)$, $\frac{dm_{A,\omega}(t)}{dt}$, and $\frac{d\varphi_{A,\omega}(t)}{dt}$. Noting that the functions X_1, X_2, $X_1' = \frac{dX_1}{dt}$, and $X_2' = \frac{dX_2}{dt}$ are jointly Gaussian uncorrelated random processes (Ref. 14), we have obtained in (Refs 10, 11, 17) the probability distributions for all aforementioned functions:

$$p_1(U) = \frac{U}{\sigma_\varepsilon^2}\exp\left(-\frac{U^2 + y^2}{2\sigma_\varepsilon^2}\right)\mathbf{I}_0\left(\frac{Uy}{\sigma_\varepsilon^2}\right), \quad (13)$$

$$p_1(U') = \frac{1}{\sigma_1\sqrt{2\pi}}\exp\left(-\frac{U'^2}{2\sigma_1^2}\right), \quad (14)$$

$$p_1(\phi) = \frac{1}{2\pi}\exp\left(-\frac{y^2}{2\sigma_\varepsilon^2}\right)\left\{1+\sqrt{2\pi}\frac{y}{\sigma_\varepsilon}\exp\left[\frac{y^2}{2\sigma_\varepsilon^2}\cos^2(\phi-\beta)\right]\right. \quad (15)$$
$$\left.\Phi\left[\frac{y}{\sigma_\varepsilon}\cos(\phi-\beta)\right]\cos(\phi-\beta)\right\}$$

$$p_1(\phi') = \frac{\sigma_\varepsilon}{2\sigma_1}\exp\left(-\frac{y^2}{2\sigma_\varepsilon^2}\right)\left(1+\phi'^2\frac{\sigma_\varepsilon^2}{\sigma_1^2}\right)^{-3/2} \quad (16)$$
$$\times {}_1F_1\left[\frac{3}{2},1;\frac{y^2}{2\sigma_\varepsilon^2}\left(1+\phi'^2\frac{\sigma_\varepsilon^2}{\sigma_1^2}\right)^{-1}\right]$$

where $\beta = \arctan(y_1/y_2)$, $\mathbf{I}_0(x)$ is the Bessel function of zero-order, and ${}_1F_1(a, c; z)$ is the degenerate hypergeometric function. Now we would like to examine the major moments of those distributions, namely mean and variance, aiming to study in this way the properties of a sensor.

4.1 Amplitude response of a sensor

It follows from (13) that $p_1(U)$ is the Rayleigh-Rice's law (Ref. 16) with the *k*-order moment

$$m_{U(k)} = \int_0^\infty U^k p_1(U)dU = \sqrt{2^k\sigma_\varepsilon^{2k}}\,\Gamma\left(\frac{k}{2}+1\right){}_1F_1\left(-\frac{k}{2},1;-\frac{y^2}{2\sigma_\varepsilon^2}\right), \quad (17)$$

where $\Gamma(x)$ is the Gamma function. It is easily to show that (17) yields the mean and the variance in the forms of

$$\overline{U} = \sigma_\varepsilon\sqrt{\frac{\pi}{2}}\,{}_1F_1\left(-\frac{1}{2},1;-\frac{y^2}{2\sigma_\varepsilon^2}\right), \quad (18)$$

$$\sigma_U^2 = 2\sigma_\varepsilon^2\left(1+\frac{y^2}{2\sigma_\varepsilon^2}\right)-\overline{U}^2. \quad (19)$$

Figure 3 shows the mean (18) and the variance (19) as functions on SNR determined as $a = y(\varsigma = 0)/\sigma_z$.

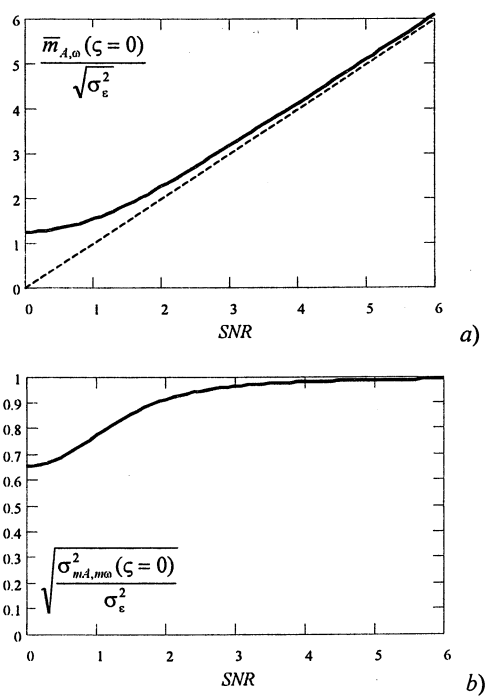

Figure 3. Mean and variance of the amplitude response

It follows from Fig. 3 straightforwardly that with SNR = 1 the mean changes poorly and slightly exceeds the noise variance (SNR = 0), obeying $\overline{m}_{A,\omega}(\varsigma=0) \cong \sqrt{\frac{\pi}{2}}\left(1+\frac{a^2}{4}\right)$ (Ref. 15). With 3 < SNR, the mean depends on SNR rather linearly, so that $\overline{m}_{A,\omega}(\varsigma=0) \cong y(\varsigma=0)$. With this, the variance does not exceed the noise variance for all SNR, obeying the approximation $\sigma_{mA,m\omega}(\varsigma=0) \cong \sqrt{2-\frac{\pi}{2}\left(1+\frac{a^2}{4}\right)}$ for 0 < SNR < 1, and $\sigma_{mA,m\omega}(\varsigma=0) \cong \sigma_\varepsilon$ for 3 < SNR (Ref. 15). Figure 4 gives dependencies on ζ of the same mean and variance for some SNR in a gap of an additional feedback bandwidth (Ref. 10).

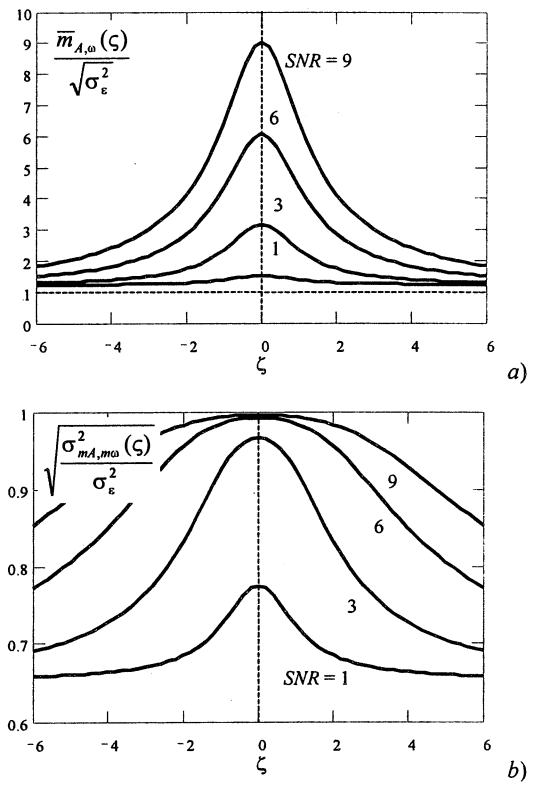

Figure 4. Mean and variance of the amplitude response as functions on modulation frequency

One may conclude here that SNR rise gains the brightly pronounced splash of AFC mean and that frequency range of this splash remains with this rather the same (Fig. 4a). In contrast, the splash of variance tends to be diffused and gained with SNR rise.

4.2 Time derivative of amplitude response

Observe that distribution of time derivative of the amplitude response $p_1(U')$ (14) does not depend on SNR and is just a normal law with mean zero $\overline{U}' = 0$ and variance $\sigma_{U'}^2 = \sigma_1^2$.

4.3 Phase response of a sensor

Distribution (25) has the mean

$$\overline{\phi} = \arctan\frac{y_1}{y_2} \quad (20)$$

and the variance

$$\sigma_\phi^2 = \frac{\pi^2}{3} + 4\pi\sum_{n=1}^{\infty}\frac{(-1)^n}{\pi n! n^2 2^{n/2}}\left(\frac{y}{\sigma_\varepsilon}\right)^n \Gamma\left(1+\frac{n}{2}\right){}_1F_1\left(\frac{n}{2}, n+1; -\frac{y^2}{2\sigma_\varepsilon^2}\right) \quad (21)$$

Figure 5 illustrates both (20) and (21) for several SNR and typical shape of a phase response of a sensor in an oscillator signal (Ref. 3).

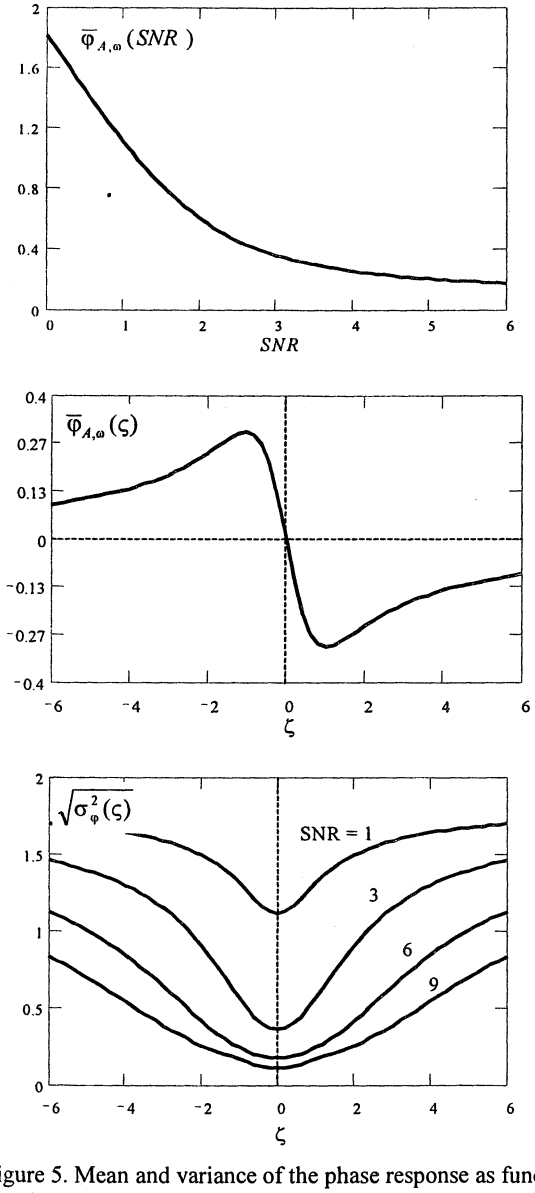

Figure 5. Mean and variance of the phase response as functions on *SNR* (a) and modulation frequency (*b*), (*c*)

Analyzing Fig. 5, we conclude that phase mean (20) does not depend on SNR and that variance (21) reaches a minimum at the frequency $\varsigma = 0$, being decreasing monotonously with SNR rise for an arbitrary ζ. Under the same conditions, crevasse of a function (Fig.5b) tends to be deepened and diffused. Here the following approximations may be useful:

$$\sigma_\phi(\varsigma=0) \cong \frac{\pi}{\sqrt{3}}\left[1 - 0.398a + 0.0132a^2\right] \text{ for } 0 \le \text{SNR} \le 1,$$

$$\sigma_\phi(\varsigma=0) \cong \frac{\pi\cdot 1.042}{\sqrt{3}}\left[1 - 0.42a + 0.07a^2\right] \text{ for } 1 < \text{SNR} \le 3, \text{ and}$$

$$\sigma_\phi(\varsigma=0) \cong 869.57\left[1 - \frac{2}{\pi}\arctan(521.5a)\right] \text{ for } 3 < \text{SNR}.$$

It seems important to note that, in contrast to AFC (Fig.4b), since SNR tends infinity then variance of PFC drops to zero. It means that distribution $p_1(\phi)$ inherently exhibits a splendid property to transfer to a delta-function with SNR rise. In other words, an oscillator noise does not influence a sensor phase response with an extremely big SNR.

4.4 Time derivative of a phase response

Distribution (16) is symmetric with mean zero $\overline{\phi'} = 0$. To calculate variance we observe that the integral $\int_{-\infty}^{\infty}\phi'^2 p_1(\phi')d\phi'$ in (16) diverges, so the best way to estimate the dissipation power is to consider mean of the absolute values $\overline{|\phi'|} = \int_{-\infty}^{\infty}|\phi'|p_1(\varepsilon')d\phi' = 2\int_{-\infty}^{\infty}\phi' p_1(\phi')d\phi'$. Integrate that and get

$$\overline{|\phi'|} = \frac{\sigma_1}{\sigma_\varepsilon}\exp\left(-\frac{y^2}{4\sigma_\varepsilon^2}\right)\mathrm{I}_0\left(\frac{y^2}{4\sigma_\varepsilon^2}\right), \quad (22)$$

Figure 6 scratches function (22) in a range of small SNR and in a gap of a sensor resonance.

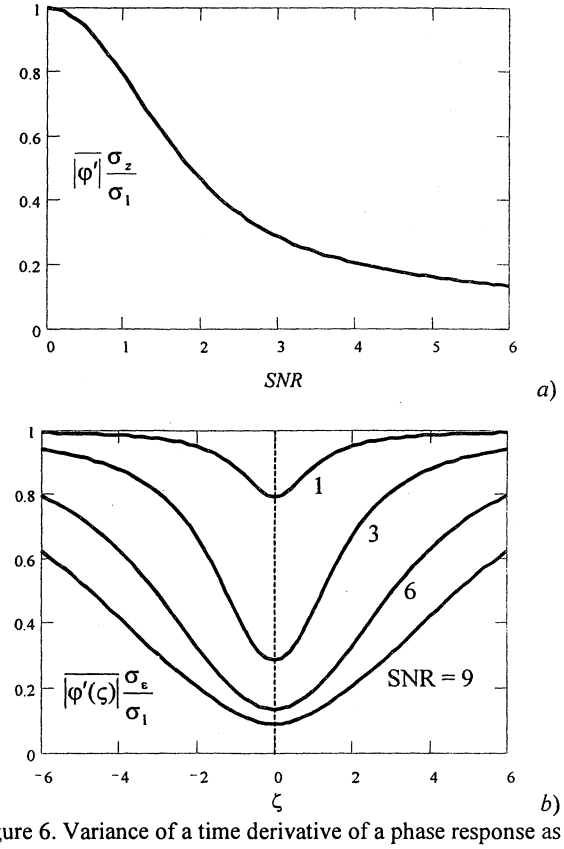

Figure 6. Variance of a time derivative of a phase response as functions on SNR (a) and modulation frequency (b)

Qualitatively, we watch here for the same but more smoothed law of the phase response illustrated by Fig. 5*a*. As well as in the case of the phase variance in the bandwidth gap of sensor the function ϕ' exhibits crevasse at the resonance frequency and big variance with SNR < 1, demonstrating ability to be reduced to zero since SNR rises to infinity (Fig. 6*b*). Again, noise influence small the time derivative of phase response with big SNR.

V. CONCLUSION

We have presented a generalized statistical model of modulated oscillator with a sensor feedback inherently produced by an anharmonic of a crystal resonator. The background was the present view on such kind of resonant feedbacks as on the environmental sensors for precision oscillators and that the best operation mode for those sensors assumes a drive level closed to a noise floor. The main point that had been made is the possibility to exhaustively describe the stochastic model through the oscillator DMC (AFC and PFC) since those accumulate the oscillator noise properties and, moreover, represent a sensor response in an oscillator signal. This was the principal reason to provide a probability analysis of DMC and their particular values, namely, amplitude and phase, time derivatives, and gain for the oscillator far carrier range of the sensor operation within its bandwidth gap.

Both "mechanisms" of the sensor excitation had been accounted, namely, modulation by an internal noise, in which case we basically assume $1 \approx$ SNR, and intended modulation by an external signal that yields $1 <$ SNR. We show that, once $1 \approx$ SNR, both AFC and PFC exhibit big variances that requires appreciable time to estimate a sensor frequency in real time with enough accuracy. This is the reason perhaps why this mode has not gained currency yet. In contrast, even with SNR = 3, all DMC reduce their variances significantly so that with a relatively small external modulation signal an accurate estimate is available through rather the same operation time as that related to the dual-mode (multimode) oscillator. It apparently speaks in favor of an external signal if to recall as well the splendid property of a sensor phase characteristic (PFC), this is its ability to yield negligibly small variance at an operation frequency with big SNR independently on variance of an oscillator noise. However, SNR, strictly, must be restricted to avoid interaction of both the sensor and fundamental modes.

Yet, let us note that the presented model holds true for various types of oscillator with a multimode resonator (Refs 5-8), once statistics in a far carrier range of an additional feedback are of a special interest and both feedbacks have disjoint bandwidths and are uncorrelated. In the opposite case, one should obviously be based on the theory of multi-dimensional random processes (Refs 14, 15) applied to the theory of DMC (Ref. 9), in which case the results can readily be extended as well on the more than one additional feedback.

6. REFERENCES

1. Yu. S. Shmaliy, "Toward resonator anharmonic sensors for precision crystal oscillators: a Gaussian model," *IEEE Trans. on Ultrason., Ferroel. And Frequency Control,* vol.47, pp.379-389, March 2000.
2. E. K. Miguel. "A temperature compensated SC-cut quartz crystal oscillator," *Proc. IEEE Annual Freq. Contr. Symp.*, 1982, pp.576-585.
3. Yu. S. Shmaliy, "The Modulation Method of Quartz Crystal Oscillator Frequency Stabilization", *IEEE Trans. on Ultrason., Ferroel. And Frequency Control,* vol.45, pp.1476-1484, Nov.1998.
4. Yu. S. Shmaliy, A. Ph. Kurotchka, E. G. Sokolinskiy, and A. V. Marienko. "Quartz crystal oscillator with an effective aging rate compensation". *Proc. 12th European Frequency and Time Forum*, Warsaw, Poland, pp.234-239, 1998.
5. T. E. Parker, "Characteristics and Sources of Phase Noise in Stable Oscillators", *Proc. IEEE Annual Freq. Contr. Symp.*, pp.99-110, 1987.
6. W. R. Shreve and P. S. Cross, "Surface Acoustic Waves and Resonators", *Precision Frequency Control: Acoustic Resonators and Filters,* Vol. 1, E. A. Gerber and A. Ballato, Eds., New York: Academic Press, pp.118-145, 1985.
7. E. N. Ivanov, M. E. Tobar, and R. A. Woode, "Ultra-low-noise microwave oscillator with advanced phase noise suppression system", *IEEE Microwave Guided Lett.*, vol. 6, no. 9, pp.312-314, 1996.
8. L. L. Lewis. Introduction to frequency standards. *Proc. IEEE*, vol.79, no.7, pp.922-935, 1991.
9. Yu. S. Shmaliy, "Dynamic Distortions in FM Oscillatory Systems", *Izv. VUZov. Radioelectronika,* pp.40-44, 1986.
10. V.N.Romanko and Yu.S.Shmaliy, "Probability Properties of Dynamic Modulation Characteristics of Crystal Oscillator," *Izv. VUZov. Radioelectronika,* 1992, pp.37-44.
11. Yu.S. Shmaliy, "Probability distributions of the envelope and phase, and their derivatives in time of the sum of a non-stationary sine signal and narrow-band Gaussian noise," *Journal of the Franklin Institute*, Vol.336, No.6, pp.1013-1022, 1999.
12. F. X. Kaertner, "Analysis of white and $f^{-\alpha}$ noise in oscillators", *Int. Journal of Circuit Theory and Appl,* pp.485-519, 1990.
13. D. B. Leeson. "A simple model of feedback oscillator noise spectrum", Proc. IEEE, Vol.64, no.2, pp.329-330, 1966.
14. A. Papoulis, *Probability, Random Variables, and Stochastic processes*, 2nd ed., New-York: McGraw-Hill Book Co., 1984, 584p.
15. V. I. Tikhonov, *Non-linear transformations of random processes*, Moscow: Radio I Zvias, 1986, 296p.
16. S. O. Rice, "Statistical Properties of a Sine Wave Plus Random Nise," in *BSTJ,* Vol.27, No.1, 1948, pp.109-157.
17. Yu. Shmaliy and R. Besson. "Probability properties of an anharmonic sensors for precision crystal oscillators", *Proc. 14th European Frequency and Time Forum*, Turin, Italy, 2000.

Digital OCXOs using Dual-mode Excitation

Y. WATANABE, K. OZAKI, S. GOKA, T. SATO and H. SEKIMOTO
Graduate School of Engineering, Tokyo Metropolitan University
Hachioji, Tokyo 192-0397, JAPAN

Abstract - **A high-stability oven-controlled crystal oscillator (OCXO) (frequency stability; +/- 10 ppb from –30 to 70 oC) has been developed using a dual-mode SC-cut quartz crystal oscillator. The oscillator's frequency stability includes a frequency-temperature hysteresis over the range of operational temperatures, and repeatability of frequencies after power is switched off then back on. In this OCXO a conventional oven-control system is used for coarse compensation and a digital correction system is used for fine compensation. The digital correction system uses B and C mode signals. The combination of these forms of compensation greatly improves the c-mode frequency stability and expands the operational temperature range with a very small additional requirement for electric power.**

Experimental results indicate that the frequency-temperature stability of the OCXO was 10 times better, and its operational temperature range 30 degrees wider, than the conventional OCXOs.

I. Introduction

Recent advancements in mobile communications technology requires that frequency sources be highly stable and have good spectrum purity. Because of its cost and reliability, oven controlled crystal oscillators (OCXOs) are widely used frequency sources that are ideally suited for base stations in mobile communication systems. However, with the development of synchronous network systems and high-speed mobile communication systems, higher performance OCXOs must be developed [1].

We have already developed a low-phase-noise dual-mode SC-cut oscillator that simultaneously excited C and B modes in a 3rd overtone resonator [2]. We showed the phase noise level in this dual-mode oscillator was only 3-6 dB higher than that in a single-mode oscillation [3,4]. We also reported the static-temperature characteristics of the OCXO using a dual-mode oscillator excites the C and B-modes in the same SC-cut crystal resonator. We showed that the developed OCXO structure provides very good frequency-temperature characteristics with a very small additional requirement for electric power [5]. The frequency stability of the OCXO was within ± 0.5 ppb in the temperature range from -10 to 50 °C. However, its characteristics were static and the thermal hysteresis and retrace characteristics were not measured.

In the current work, we have therefore measured the thermal hysteresis and the frequency retrace, and expanded the operational temperature range of the dual-mode OCXO. Experimental results indicate that the dynamic frequency-temperature stability of the OCXO is 10 times better, and its operational temperature range 30 degrees wider, than that of conventional OCXOs.

II. Dual-mode SC-cut oscillator

Figure 1 illustrates the dual-mode oscillator we presented at the 1997 Frequency Control Symposium [3]. This oscillator uses two narrow-band active circuits with different negative-resistance bands; the circuits are connected in parallel at a common resonator terminal. It can excite any mode in the common resonator even if the resonant frequencies are close to each other. Under the experimental

condition [3], the frequency deviation of the B mode was ± 70 ppm even when the resonator was placed in an oven. We therefore used a ceramic resonator filter that produced a wide gain-band in a B-mode driving circuit.

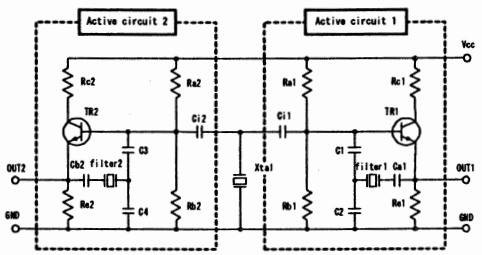

Fig.1. Dual-mode transistor Colpitts oscillator.

III. Temperature Detection and Frequency Compensation

The developed OCXO is shown as a block diagram in Fig. 2. It uses a B-mode signal as a temperature sensor and a C-mode signal as the frequency reference of the B-mode counting. The B-mode frequency was measured with a frequency counter and the output of the counter was inputted to a D/A converter via a control circuit. The D/A converter output controls the inverse bias voltage of a varactor diode connected in series to the SC-cut resonator. The SC-cut resonator was placed in an oven typically used for OCXOs. The temperature in the oven was kept at 70 ± 1°C even if the external temperature changes from – 10 °C to 50 °C. This temperature range is the operational range of the original OCXO.

The temperature compensation data that stabilize the C-mode frequency are determined by using the following procedure [4];

(1) Change ambient temperature.
(2) Measure C-mode frequency with an external frequency counter using the Cesium frequency standard.
(3) Generate voltage data that matches the C-mode frequency with the nominal frequency.
(4) Measure B-mode frequency with an internal counter governed by the C-mode frequency.
(5) Record the voltage value and the B-mode frequency.
(6) Repeat (1) to (5) at ten-degree intervals.

In this procedure, the measured B-mode frequency contains errors because the C-mode frequency is slightly changed by the control voltage. However, the temperature sensitivity of the B-mode frequency is over 100 times larger than that of the C-mode one, making the errors negligible. Because the B-mode frequency and control voltage were measured at ten-degree intervals, we used the Lagrangian form to interpolate the frequency-voltage relation.

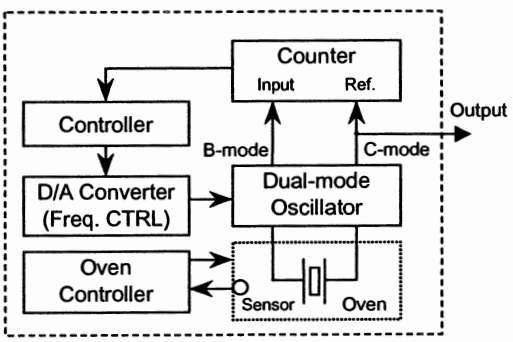

Fig. 2. Block diagram of dual-mode OCXO.

IV. Results

A Cesium frequency standard that has stability of 10^{-13}/day was used as the reference frequency when the temperature compensation data and the frequency stability of the dual-mode SC-cut oscillator were measured. The compensation data was taken at ten-degree intervals from -30 to 70 °C, and the frequency stability of the OCXO was measured for the same temperature range and intervals. We used a third degree

Lagrangian function to interpolate the data for the temperature compensation table. The oscillation frequency was measured every 10°C from –30°C to 70 °C, and back to –30°C with the same interval, and the preheating time was set at 90 minutes at each temperature.

4.1 Thermal hysteresis

Before measuring the new OCXO's hysteresis, we measured the intrinsic hysteresis of the original OCXO. Figure 3 shows frequency drift of the OCXO in the free-running mode (without temperature compensation). In this experiment, we repeated the frequency-temperature measurement two times. The ordinate was normalized by the measured frequency at 20 °C on the first measurement. Hysteresis is defined as the difference between frequency vs. temperature characteristics of the up-cycle and the down-cycle, and is quantified by the difference at the temperature where it is maximum. This figure shows that the frequency stability of the OCXO in free-running mode is ± 100 ppb in the experimental temperature range, and that the thermal hysteresis is about ± 10ppb. These values are within the specification of typical OCXOs.

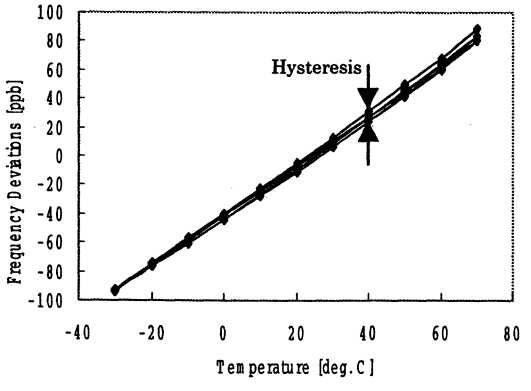

Fig. 3. Frequency-temperature characteristics of an OCXO without temperature compensation.

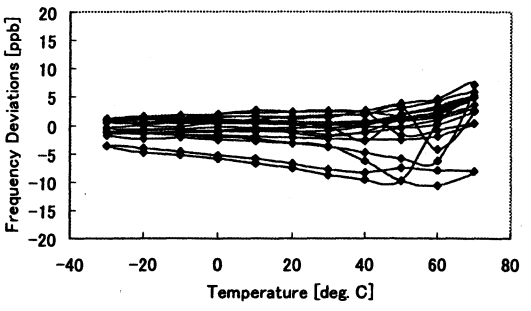

Fig. 4. Frequency-temperature characteristics of an OCXO with digital temperature compensation.

Figure 4 shows the frequency drift of the OCXO in the temperature-compensation mode. In this experiment, the frequency-temperature measurement was repeated ten times. This figure shows that the frequency stability (including thermal hysteresis) of the proposed OCXO is ± 10 ppb. Although this stability is considerably larger than that of the static stability [4], this stability is equivalent to the hysteresis of the original OCXO. The measurement of frequency drift took about ten days, so the results are affected by the aging of the SC-cut resonator.

4.2 Frequency retrace

Retrace is defined as the non-repeatability of the frequency-vs.-temperature characteristic at a fixed temperature during on-off cycling of an oscillator under specified conditions. To measure frequency retrace, the OCXO was placed in an external oven. The oven temperature was maintained at 40 ± 1 °C. The retraces are obtained by the following procedure;

(1) Measure the oscillation frequency continuously during a specific period.
(2) Turn-off the OCXO and cease measurement undone during a specific period.
(3) Turn-on OCXO again.
(4) Repeat (1) to (3).

Figure 5 shows measured frequency deviation vs. time (24 hours operation and 1-hour off-period). The frequency deviation is about 0.3 ppb lower than that just before turn-off at the end of the first period. However, the frequency quickly returns to what it was just before turn-off (± 0.1 ppb).

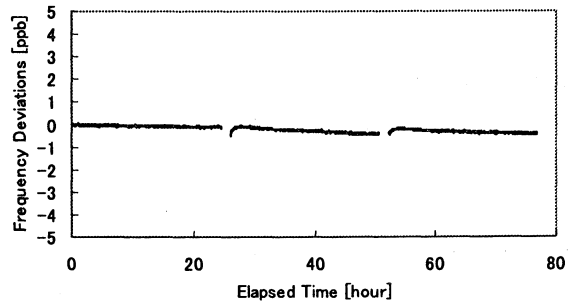

Fig. 5. Frequency retrace of the dual-mode OCXO. (driving 24 hours and 1-hour off-period)

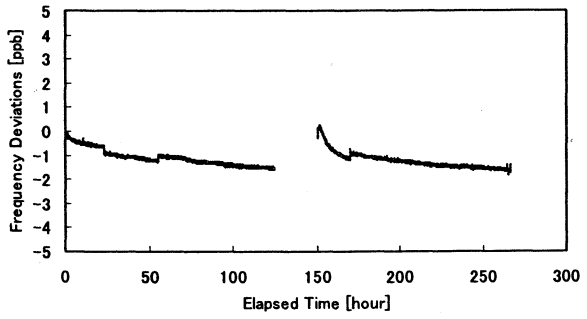

Fig. 6. Frequency retrace of the dual-mode OCXO. (driving 5 days and 1 day off-period)

Figure 6 shows the frequency deviations upon restarting the oscillator after a day off-period. The frequency deviation is about 2 ppb higher than that just before turn-off. However, after ten hours the frequency deviation returns to what it was just before turn-off (± 0.2 ppb). These results indicate that the new OCXO has very good retraceability. Note that the positive trend observed in Fig. 5 and 7 is caused by the aging of the SC-cut resonator.

V. Conclusion

The developed dual-mode digital OCXO's dynamic frequency stability, including hysteresis, is 10 times better than that of free-running mode, and it has very good frequency-retrace characteristics. Moreover , its operation temperature range was expanded to – 30°C to + 70°C.

Although the compensation circuitry for this OCXO in not yet complete (not integrated), we have shown a highly stable OCXO with low power consumption can be produced without using a double oven.

Acknowledgement

The authors would like to thank for Takeshi Uchida, NDK co. ltd. for supplying OCXO units.

References

[1] H. Ujiie, K. Maruo, Y. Watanabe, S. Goka and H. Sekimoto, Proceedings of Joint Meeting of The 13th European Frequency and Time Forum and 1999 IEEE International Frequency Control Symposium.

[2] I. Niimi, Y. Watanabe, H. Sekimoto and S. Goka, , IEICE Transactions on Electronics, Vol.E81-C, No.2 ,pp.284-289 (Feb., 1998, in Japanese)

[3] Y. Watanabe, T. Okabayashi, S. Goka, and H. Sekimoto, , Trans. UFFC, Vol. 47 Number 2, pp.374

[4] Y. Watanabe, H. Sekimoto, S. Goka, and I. Niini, , Proceedings of 1997 IEEE International Frequency Control Symposium, pp.932-937.

[5] Y. Watanabe, K. Ozaki, S. Goka and H. Sekimoto, Proceedings of 1997 IEEE International Frequency Control Symposium,, pp. 459-462

OPTICAL FREQUENCY STANDARDS

Chairman: David Knight

TWO-PHOTON RAMSEY FRINGES AT 10 MICRONS WITH A 50 CM INTERZONE DISTANCE

A. Shelkovnikov*, C. Grain, R.J. Butcher♣, C.T. Nguyen, A. Amy-Klein§ and Ch. Chardonnet

Laboratoire de Physique des Lasers (UMR 7538 CNRS), Université Paris 13, 99 av. J.B. Clément, F-93430 Villetaneuse, France
* Permanent address : Lebedev Physical Institute, Russian Academy of Sciences, Leninskii pr. 53, Moscow, 117924 Russia
♣ Permanent address : The Cavendish Laboratory, Madingley Road, Cambridge, CB3 OHE, UK
§ Corresponding author : amy@lpl.univ-paris13.fr

1. ABSTRACT

We report observation of Ramsey fringes on a 10.6 μm two-photon transition of SF_6. We used two interaction zones separated by 20 or 50 cm and fringes of periodicity down to 500 Hz were recorded. The signal to noise ratio is presently limited by the technical noise and might be increased with high frequency detection. Concerning the metrological features, the ultimate accuracy is at least two orders of magnitude better than the present secondary standard at 10 μm based on the CO_2 laser locked onto a saturated absorption resonance of OsO_4.

Infrared standard, Ramsey fringes, molecular spectroscopy

2. INTRODUCTION

The development of optical frequency standards and ultra-high resolution spectroscopy has become very rapid in recent years mainly because of the possibility of laser cooling and trapping atoms [1-3] and ions [4]. In addition, the new development of femtosecond comb [5] which permits a precise and easy link between any frequencies from the radiofrequency to the UV domain (see, for example, [6]) opens fascinating applications.

Molecules, with their dense spectra, cannot be cooled in the same manner and the new method of trapping with static electric fields [7] is only applicable to highly polar molecules, up to now. For most of the molecules alternative methods need to be developed for reaching the highest resolution.

For this reason, our group has explored during the last few years high resolution spectroscopy with a molecular beam, since it allows the use of the method of separated fields or Ramsey fringes. The basic idea is to replace the single interaction zone by two spatially separated zones, with a fixed relative optical phase. Then the signal linewidth is no longer limited by the transit time through the laser beam, and the absorption exhibits fringes with a periodicity given by the transit time between the zones.

In the optical domain, this method must be associated with a sub-Doppler technique in order to avoid scrambling of the fringe pattern due to the velocity dispersion of the beam. It has been first suggested to use saturated absorption and a three- or four-zone configuration [8, 9]. But this imposes severe conditions on parallelism and equidistances between zones and this limits, in practice, the distance between zones and, finally, the ultimate resolution.

By contrast, in the case of two-photon spectroscopy only two zones are required [10], each comprising a standing wave, and the Doppler shift is compensated in each one. Thus the setup is quite simple. There is no condition concerning any zones parallelism. The only constraint is that the relative phase between the laser fields in the two zones vanishes. This can be easily fulfilled by generating both standing waves inside the same Fabry-Perot cavity.

The fringes periodicity is then given by half the inverse of the mean transit time between two zones for the mean velocity.

A simple expression for the lineshape can be derived at low power and for a small velocity dispersion of the beam. It is proportional to :

$$\left[1+C\cos\left(\left(\omega-\omega_{eg}/2\right)/\Delta v\right)\exp\left(-\left(\frac{\omega-\omega_{eg}/2}{4\,(u/\Delta u)\cdot\Delta v}\right)^2\right)\right] \times \exp\left(-\left(\frac{\omega-\omega_{eg}/2}{u/w}\right)^2\right) \quad (1)$$

where ω is the laser angular frequency and ω_{eg} the two-photon transition angular frequency, $\Delta v=u/2D$ is the fringe periodicity, u is the mean velocity of the molecules and Δu the velocity dispersion, w is the beam radius.

The cosine term which gives the fringes is multiplied by an exponential term which describes the attenuation of the side fringes due to the longitudinal velocity dispersion. The entire pattern is superimposed on the broader two-photon signal arising from the absorption in one single zone and whose linewidth is given by the transit time w/u of the molecule through one laser beam. The factor C is the contrast and corresponds to the ratio of the fringes to the absorption signal. It is less than unity due to the molecular beam divergence. This formula was used to analyse our experimental data.

In a more general approach, this set up can be analysed as a matter wave interferometer. An extensive study of the line shape was recently reviewed by Ch.J. Bordé [11] using a complete treatment of energy and momentum conservation. The fringes must then be interpreted as arising from the change of momentum of the molecules perpendicular to the laser beam. In this framework, it might be noted that the area between the paths corresponding to the two excitation channels is negligible. This makes this interferometer highly insensitive to external fields such as those due to rotation or gravity. This is a main advantage compared to the Ramsey-

Bordé interferometer in the context of the frequency metrology.

3. EXPERIMENTAL APPARATUS

The experiment has been presented in details elsewhere [12]. It was performed on a rovibrational transition of SF_6 : the P(4) transition of the $2\nu_3$ band. The two-photon resonance is composed of 4 main hyperfine components spanning around 40 kHz.

The set-up is composed of three parts (Figure 1) : the frequency-controlled laser system, the Fabry-Perot cavity, and the molecular beam apparatus.

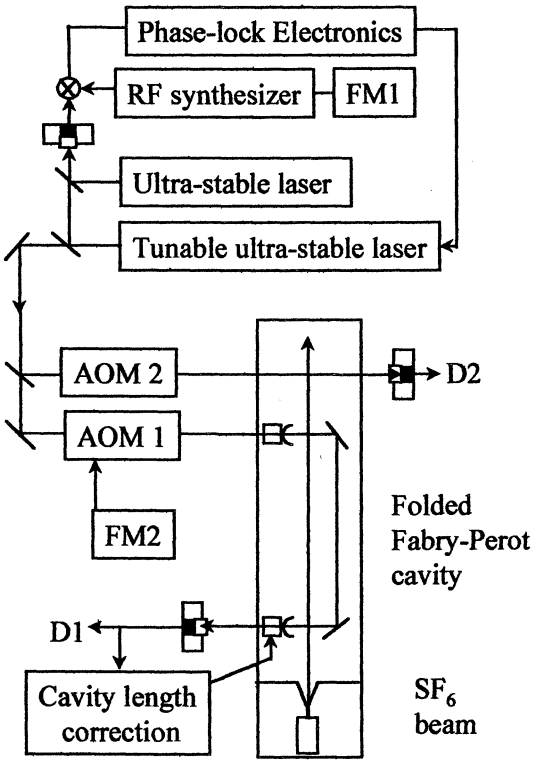

Figure 1 : experimental apparatus (AOM : acousto-optic modulator, FM : frequency modulation)

A reference CO_2 laser is locked on a saturation line of OsO_4 [13], resulting in a typical linewidth of 10 Hz and a long-term stability of 0.1 Hz for an averaging time of 100 s. This performance is transferred through a phase-lock loop to a second laser, which can be tuned with a RF synthesizer around each emission line of CO_2. The laser frequency is then shifted by two acousto-optic modulators to reach either the two-photon resonance or the upper one-photon resonance.

A key point of the experiment is the generation of the two phase-coherent standing waves forming the two interaction zones for the Ramsey spectroscopy. They are realized within a symmetric four-mirror folded Fabry-Perot cavity. The mirrors are mounted on an independent structure which is lying on an isolating padding inside the vacuum chamber. This structure was recently reconstructed and is now in invar. The distance between zones can be adjusted to 10, 20 or 50 cm, and the laser beam diameter is around 6 mm. The finesse is about 500. The whole cavity is surrounded by a magnetic shielding to avoid any fringes scrambling due to Zeeman effect.

The molecular beam apparatus was designed for a supersonic expansion of SF_6. This allows a rotational cooling of the beam and then a strong enhancement of the population in the J=4 starting level. We use either a pure SF_6 or an He-seeded beam, with a nozzle pressure of 5×10^5 Pa and we measured a total flux in the J=4 level of a few $\times10^{12}$ molecules/s. With the pure SF_6 beam, the velocity is slower (400 m/s) so the transit time is longer, and the resolution better. But the rotational cooling is less efficient than with an He-seeded beam, and then the useful population in the J=4 level is reduced.

Fringes can be recorded on the transmission of the cavity, detection channel D1 on figure 1. This has the advantage that the signal contrast is enhanced by a factor proportional to the cavity finesse. Alternatively, the signal can be recorded by probing the molecular beam absorption on the upper 1-photon transition. For that purpose, we are using an auxiliary beam, detection channel D2 in conditions similar to the rapid adiabatic passage.

4. EXPERIMENTAL RESULTS

4.1 20 cm-interzone distance

Figure 2 displays a two-photon spectrum for 3.3% SF_6 in He and a 20 cm distance between zones. Since we are using first harmonic detection this is in fact the derivative of the lineshape. The central part exhibits Ramsey fringes with more than 30 oscillations, which are superimposed on a broader signal arising from the two-photon absorption in a single zone. The background signal fits very well with the derivative of a Gaussian, peak-to-peak width 76 kHz, which indicates that the interaction time is limited by the transit time. The fringe periodicity is 2.9 kHz which corresponds to the 20 cm distance and a velocity of 1200 m/s. The fit with the theoretical lineshape (1) allows a determination of the central frequency with an uncertainty of ± 4 Hz. This is limited by the signal to noise ratio (S/N) which is 15 for 1s. The contrast was fitted to 1/15.

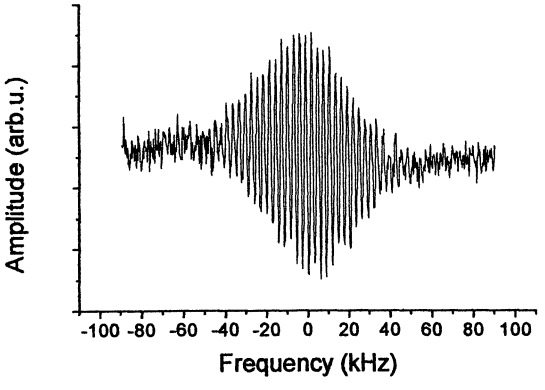

Figure 2 : Two-photon absorption signal detected on the cavity transmission beam. Experimental conditions are : 3.3% SF_6 in He, nozzle pressure 4.8×10^5 Pa, FM 467 Hz, modulation depth 500 Hz, 32 mW inside cavity, 2 s/point.

4.2 50 cm-interzone distance

As a second step, to increase the resolution, we increased the distance between zones to 50 cm, and reduced the proportion of He in the beam to slow down the SF_6 molecules.
Figure 3 presents the Ramsey fringes corresponding to the central hyperfine component for a 50-cm interzone.
The upper spectrum corresponds to the better resolution we achieved, with 50 % SF_6 in He. The fringe periodicity is 500 Hz. The S/N is about 5 for 1 s integration time and the central frequency was fitted within ± 4 Hz.
The second spectrum was recorded with a reduced proportion of SF_6 : this is now 20 %. The velocity is then increased and the periodicity is 690 Hz. But, the better rotational cooling associated with the tunnelling of the heavier SF_6 molecules inside the He beam enhances the partial flux in the beam center and results in a signal increasing. The S/N is now 14 for 1 s and the line center was fitted within ± 2 Hz.

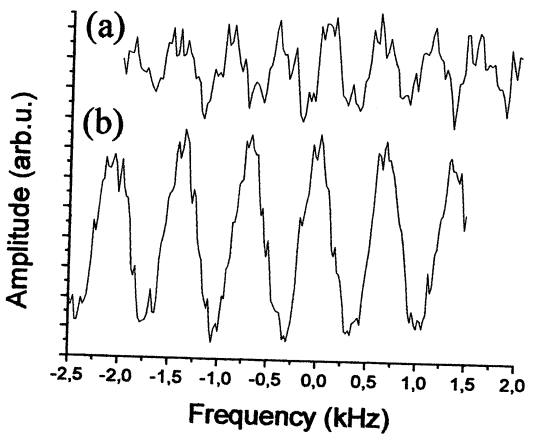

Figure 3 : Two-photon Ramsey fringes detected on the cavity transmission beam. (a) 50% SF_6 in He, period 490 Hz (b) 20% SF_6 in He, period 690 Hz. Experimental conditions : nozzle pressure $4.5x10^5$ Pa, FM 467 Hz, modulation depth 300 Hz, 28 mW inside cavity, 2 s/point.

These results demonstrate the capability of our set-up for ultrahigh resolution. Concerning the metrological features, the main advantage is that it is now possible to resolve the hyperfine structure. Figure 4 displays a spectrum spanning around 30 kHz which exhibits the different sets of fringes for 4 hyperfine components. The periodicity is 600 Hz.

4.3 Systematic shifts

With such a high resolution we were able to do some first measurements of the light shift, which amounts about 10 Hz for a $\pi/2$ power and a 50 cm-interzone. This is quite small and consistent with previous estimation [14]. Note that the most important shift is given by the second-order Doppler effect which is estimated to be 36 Hz for 50 % SF_6 in He. The other systematic shifts are either null or negligible.

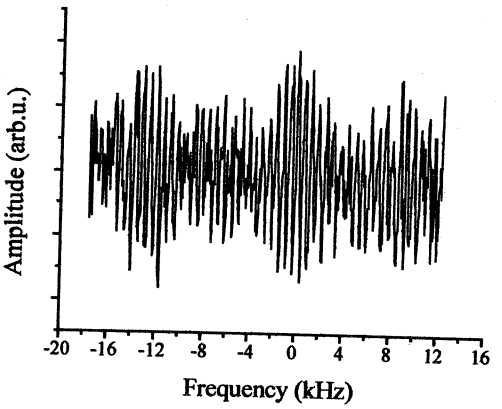

Figure 4 : Two-photon Ramsey fringes detected on the cavity transmission beam with 33 % SF_6 in He, period 600 Hz. Experimental conditions: nozzle pressure $4.5x10^5$ Pa, FM 465 Hz, modulation depth 300 Hz, 28 mW inside cavity, 4 s/point.

5. CONCLUSION AND PERSPECTIVES

These results are very promising : the period of 500 Hz corresponds to a HWHM of 125 Hz which is the best resolution ever recorded at 10 μm. This is improving by a factor 20 the previous fringes periodicity obtained with a saturated absorption resonance of SF_6 [15]. This is two times better, and the S/N is much better, than the resolution achieved in a cell experiment with the same two-photon line and the method of slow molecules detection [16].
This signal strength is quite significant and corresponds to an absorption of a few nW i.e. by about 10^{10} molecules per second.
The experimental contrast is 1/15 or 1/20, when the prediction for a 50 cm distance is around 1/10 due to the beam divergence and the hyperfine structure. This small discrepancy can be related to the drift of the reference laser, non-optimal modulation parameters, imperfect alignment of the molecular beam relative to the laser zones...

There are still some limitations in our experimental set-up. First the rotational cooling is not very efficient with a pure SF_6 beam, and the beam has to be seeded with He to enhance the signal.
Then the S/N is limited to less than 20 for 1 Hz bandwidth. We are using modulation at low frequencies, and are thus sensitive to all the technical noise.
We want now to improve the signal detection by using the other detection channel with the auxiliary beam. A Fabry-Perot cavity can be used to increase the transmitted absorption signal, and it will be possible to use high frequency modulation. This should allow to reach the shot noise limit.

The OsO_4 standard exhibits still one order of magnitude better spectral purity and stability performance than the one we could obtain when using the present fringe signal as a reference signal for locking the CO_2 laser. However for the two-photon Ramsey fringes systematic frequency shifts are

smaller than for the OsO_4 standard [14, 17], and they can already be controlled within a few Hz. Then we can estimate that the long-term stability is still comparable. In the future, when improving the fringe detection, we can estimate that the stability performance will become much better and that the shifts could be controlled with an uncertainty less than 1 %. The accuracy would reach the range of 10^{-14}-10^{-15} and compare with the new visible standards using cold particles.

6. ACKNOWLEDGMENTS

This work has been supported by the Bureau National de Métrologie and the European Union through two HCM programs. A.S. acknowledges support of CNRS and R.J.B. support of Gonville & Caius College and Université Paris 13.

7. REFERENCES

1. F. Riehle, H. Schnatz, B. Lipphardt, G. Zinner, T. Trebst, and J. Helmcke, IEEE Transactions on Instrumentation and Measurement **48**, 613-617 (1999);
2. M. Niering, *et al.*, Phys. Rev. Lett. **84**, 5496-5499 (2000);
3. C.W. Oates, E.A. Curtis, and L. Hollberg, Opt. Lett. **25**, 1603-1605 (2000);
4. R.J. Rafac, B.C. Young, J.A. Beall, W.M. Itano, D.J. Wineland, and J.C. Bergquist, Phys. Rev. Lett. **85**, 2462-2465 (2000);
5. T. Udem, J. Reichert, R. Holzwarth, and T.W. Hänsch, Phys. Rev. Lett. **82**, 3568-3571 (1999);
6. K.R. Vogel, *et al.*, Opt. Lett. **26**, 102-104 (2001);
7. H.L. Bethlem, G. Berden, A.J.A. van Roij, F.M.H. Crompvoets, and G. Meijer, Phys. Rev. Lett. **84**, 5744-5747 (2000);
8. E.V. Baklanov, B.Y. Dubetsky, and V.P. Chebotayev, App. Phys. **9**, 171-173 (1976);
9. Ch.J. Bordé, C. R. Acad. Sc. Paris **284B**, 101-104 (1977);
10. Y.V. Baklanov, V.P. Chebotayev, and B.Y. Dubetsky, Appl. Phys. **11**, 201-202 (1976);
11. Ch.J. Bordé, "Matter-wave interferometers: a synthetic approach", in *Atom interferometry*, P.R. Berman, Editor, 257-292 (1997);
12. A. Amy-Klein, L.F. Constantin, R.J. Butcher, G. Charton, and C. Chardonnet, Phys. Rev. A **63**, 013404-1-8 (2000);
13. V. Bernard, C. Daussy, G. Nogues, L. Constantin, P.E. Durand, A. Amy-Klein, A. van Lerberghe, and C. Chardonnet, IEEE J. of Quant. Electron. **QE-33**, 1282-1287 (1997);
14. A. Amy-Klein, L.F. Constantin, R.J. Butcher, C. Daussy, P.E. Durand, G. Nogues, and C. Chardonnet, Opt. Expr. **4**, 67-76 (1999);
15. Ch.J. Bordé, C. Salomon, S. Avrillier, A.V. Lerberghe, C. Bréant, D. Bassi, and G. Scoles, Phys. Rev. A **30**, 1836-1848 (1984);
16. P.E. Durand, G. Nogues, V. Bernard, A. Amy-Klein, and C. Chardonnet, Europhys. Lett. **37**, 103-108 (1997);
17. O. Acef, Opt. Comm. 134, 479-486 (1997).

OPTICAL FREQUENCY STANDARD AT 1.5 μm BASED ON SATURATED ACETYLENE AND Er-Yb BULK LASERS

G. Galzerano, C. Svelto, A. Onae*, and E. Bava

Dipartimento di Elettronica e Informazione – Politecnico di Milano, INFM, and CNR - CSTS
Piazza Leonardo da Vinci 32, 20133 Milano, Italy
E-mail: Cesare.Svelto@PoliMI.IT Phone: +39 02 2399 3610 Fax: +39 02 2399 3413

*National Research Laboratory of Metrology, 1-1-4 Umezono, Tsukuba, Ibaraki 305, Japan
E-mail: onae@nrlm.go.jp Phone: +81 298 54.4045 Fax: +81 298 54.4135

ABSTRACT

A novel Er-Yb:glass quasi-monolithic diode-pumped laser has been developed to realize a high-accuracy frequency standard at 1.54 μm based on saturated absorption of isotopic acetylene. This compact oscillator shows low amplitude- and frequency- noise, wide wavelength tunability (~20 nm), and continuous output power in excess of 20 mW with excellent linear polarization (~30 dB extinction ratio). Employing this laser source sub-Doppler spectroscopy of the acetylene around 1.54 μm has been performed. To obtain the necessary saturation intensity (~3.5 W/mm^2), the absorbing sample is placed inside a Fabry-Perot cavity with a Finesse of ~150. By dithering the Fabry-Perot piezo and employing a lock-in detection scheme the dispersion signal of the sub-Doppler resonance, useful to stabilize the laser frequency, has been obtained.

1. INTRODUCTION

Laser systems based on the ytterbium co-doped erbium phosphate glass medium [1] are very promising optical sources due to their wide wavelength tunability range [2] around a central emission wavelength of 1.54 μm thus corresponding to the third transmission window of optical fibers. In addition, diode-pumping further increases the interest devoted to this class of laser since with this pumping configuration both the amplitude and frequency noises are intrinsically limited [3]. Diode-pumped Er-Yb:glass lasers are therefore attractive sources for high-density wavelength division multiplexing communication systems [4], high-resolution spectroscopy [5], metrology [6], and high-sensitivity optical sensors [7].
An end fiber-pumped Er-Yb:glass laser with improved performance has been realized in a quasi-monolithic configuration which reduces the influence from acoustic vibrations and permits a more agile transportability.

Non-linear spectroscopy of the acetylene molecule has been performed in the wavelength range from 1532 nm to 1549 nm, by means of a novel diode-pumped Er-Yb:glass laser with single frequency emission and narrow linewidth (<50 kHz over 1 ms). In order to saturate the acetylene lines, the gas sample was placed within an external high finesse resonator.

2. THE NOVEL Er-Yb LASER

The novel fiber-pumped Er-Yb:glass laser is shown in Fig. 1. For the first time a Brewster plate has been successfully inserted in the low-gain laser cavity

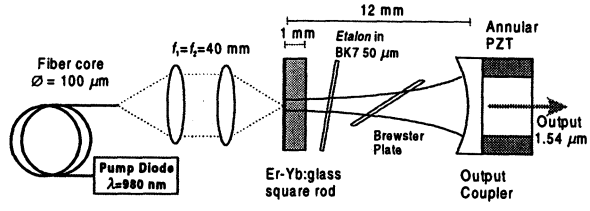

Figure 1. The erbium-ytterbium microlaser.

still allowing for several milliwatt of 1.5 μm output power. Due to the insertion of the Brewster plate within the optical cavity, excellent linear polarization has been achieved. A linear polarization purity of 632:1 (~28 dB) was measured using a polarizer/analyzer made of a polarizing cube beam splitter (PBS) with a 30 dB extinction ratio. This means that the laser beam has itself a ~30 dB polarization extinction ratio, which is quite a record for these 1.5 μm optical sources.

A very wide continuous wavelength tunability of ~1 THz or 7 nm (from 1532 nm to 1549 nm) was measured when tilting the intracavity etalon. Figure 3 shows a typical spectrum of the laser beam showing a single line at an operating wavelength of ~1532 nm. The typical output power in this wavelength range is in excess of 20 mW with an oscillation linewidth below

50 kHz over an observation time of 1 ms. Fine frequency tuning of the oscillation frequency is achieved by means of an annular piezoelectric transducer used to vary the optical cavity length with a sub-micrometric resolution.
Serious thermal problems limit the maximum pump power to ≈[300-500] mW in this double pass scheme. New strengthened glasses withstanding tree times this power allow using all the available pump power. In our experiments, to work on the safe side, the maximum pump power was limited to the value of 300 mW when the laser operates in single longitudinal mode.

3. FREQUENCY NOISE MEASUREMENTS

In order to characterize the laser frequency noise a Pound-Drever discriminating technique has been employed [8, 9]. The adopted experimental setup is shown in Fig. 2.

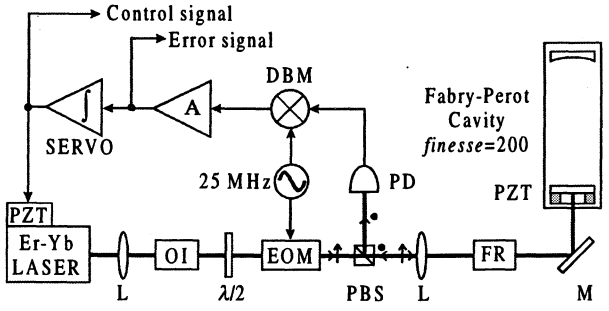

Figure 2. Experimental setup for the characterization of Er-Yb:glass frequency noise. OI: optical isolator, L: lens, $\lambda/2$: half wave plate, M: mirror.

The laser frequency is phase modulated by means of an electro-optic modulator (EOM) and then is coupled to a Fabry-Perot cavity. The cavity reflection is selected by means of a faraday rotator (FR) and a polarizing beam splitter (PBS), and it is impinged on a fast photodetector (PD). By using a synchronous detection of the generated photocurrent at the modulation frequency it is possible to observe the dispersion-like signal of the cavity resonance. This signal can therefore be used as a frequency discriminator to convert laser frequency fluctuations, with respect to the resonance frequency, into voltage fluctuations at the output of the doubled-balanced-mixer (DBM). About 80% of the 10 mW laser power was coupled into the Fabry-Perot cavity (a plano-spherical resonator of length 30 cm) which showed a linewidth of 2.5 MHz and a finesse of 200. With a modulation frequency of 25 MHz and a phase modulation index of 1.07 rad a frequency discrimination coefficient of 10 V/MHz was achieved at the amplifier (A) output with a *SNR* of ~60 dB in a measurement bandwidth of 1 MHz. These values set a frequency noise sensitivity for the discriminating system at a level of 0.1 Hz^2/Hz. In order to keep the laser frequency locked to the center of the cavity resonance, the low frequency component of the error signal was integrated and fed back to the laser PZT. The control bandwidth was set approximately to 10 Hz. In this way the spectrum of the error signal contains the converted laser frequency noise for Fourier components above 10 Hz whereas the loop actuator (PZT) signal represents the laser frequency noise below 10 Hz. The measured spectral density of the laser frequency noise, obtained by the FFT analysis of the error signal, is reported in the diagram of Fig. 3.

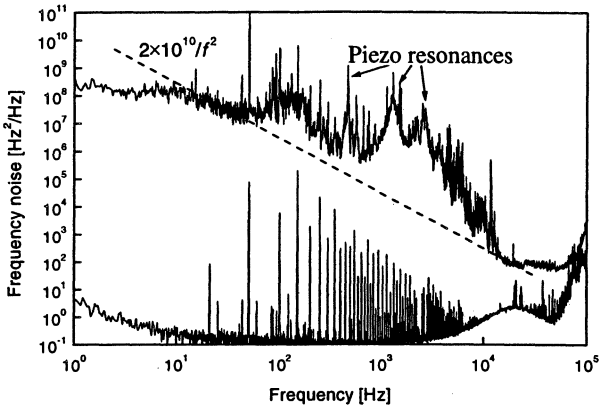

Figure 3. Frequency noise spectral density for the Er-Yb microlaser.

The power spectral density of the laser frequency noise can be assumed as: $S_{\Delta\nu}(f)=k_{-2}f^{-2}+k_0=(2\times10^{10}f^{-2}+100)\ Hz^2/Hz$ having supposed the noise exceeding the dashed line in Fig. 3 is due to technical origin. According to Joss *et al.* [10], after defining the oscillator bandwidth, $B_{-2}=\pi(0.5k_{-2}T_{obs})^{1/2}$ where T_{obs} is the observation time, it follows that the power spectrum lineshape, in the case $B_{-2}T_{obs}>>1$, is approximately Gaussian with a Full Width at Half Maximum linewidth given by $\Delta\nu_{-2}\cong4(\ln2)^{1/2}B_{-2}=4\pi[(\ln2)/2]^{1/2}(k_{-2}T_{obs})^{1/2}\cong 10^6\ (T_{obs})^{1/2}$ Hz. For observation time in the order of 1 ms, this laser shows a typical linewidth of ~30 kHz.

4. THE $^{13}C_2H_2$ SATURATION SPECTROSCOPY

In order to achieve narrow reference lines at 1.5 μm, saturated acetylene lines have proved [5] to be a useful candidate. This gas, in fact, is stable and does not show a permanent electric dipole moment allowing for good reproducibility of the absorption frequencies. An accurate optical frequency atlas of the C_2H_2 and $^{13}C_2H_2$ lines at 1.5 μm was recently measured with an accuracy level better than 10^{-9} [5]. Unfortunately, the saturation intensity for the acetylene transitions in this spectral region is quite high, ~1 W/mm^2, and hence a power enhancement is needed. In order to obtain a saturated absorption signal, a Brewster-window quartz cell filled with $^{13}C_2H_2$ at a pressure of 4 Pa is placed inside the

Fabry-Perot cavity used in the frequency noise characterization setup [11].
The observed finesse when the laser frequency was on the acetylene resonance it decreased to ≈140 (observed linewidth of 3.5 MHz). To keep the resonance condition between the laser frequency and the cavity, the Pound-Drever-Hall locking set-up reported in Fig. 2 has been adopted. Using a modulation frequency of 25 MHz and a phase modulation index of ≈0.2, the laser frequency was locked to the resonance of the cavity by means of an electronic servo system closed on the laser PZT (see Fig. 4) with a control bandwidth of 1 kHz (limited by the piezo resonances). The incident optical power in front of the cavity was 9 mW and about 75% of this power was coupled into the resonator fundamental mode.
With the laser frequency locked to the cavity resonance, by scanning the resonator length it was possible to observe the saturated absorption profile of the $^{13}C_2H_2$ rovibrational line by means of the cavity transmission signal (see Fig. 4).

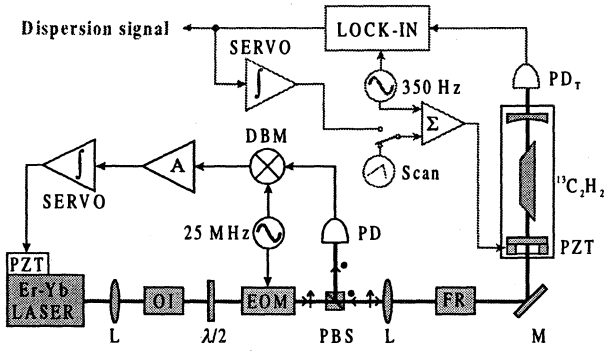

Figure 4. Experimental set-up for saturation spectroscopy of the $^{13}C_2H_2$.

Several rovibrational lines of $^{13}C_2H_2$ (from P(10) to P(16)) have been observed and an example of the recording of the transmission profile for the P(16) line, at a wavelength of 1542.38 nm, is shown in Fig. 5. In this diagram a Lamb-dip of relative contrast of 3% with respect to the linear absorption (linewidth of ≈500 MHz) appears just at the line center with a full width linewidth of ≈1 MHz [5]. In our setup, taking into account the cavity finesse, the coupling factor, the beam profile inside the cavity, and the phase modulation index, the saturating intensity inside the cavity was found to be in the order of 3.5 W/mm^2.
In addition, we measured the first derivative of the signal corresponding to this saturated line using wavelength-modulation spectroscopy and synchronous detection. A sinusoidal frequency modulation was superimposed to the laser frequency by applying to the PZT of the Fabry-Perot cavity a sinusoidal signal with frequency equal to 350 Hz and amplitude 250 mV, providing for a modulation frequency deviation of 2 MHz. In order to retrieve the first derivative signal,

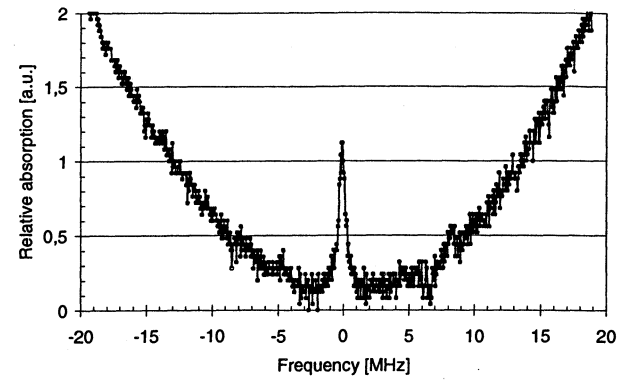

Figure 5. Saturation spectroscopy of the $^{13}C_2H_2$ P(16) line at λ=1542.384 nm. The saturation line contrast is ~3%.

the output voltage from the photodiode detecting the Fabry-Perot transmission was sent to a lock-in amplifier, set with a sensitivity of 50 mV and a time constant of 30 ms. The obtained first derivative is shown in Fig. 6: this signal shows an odd symmetry with respect to the resonant frequency and therefore could be used to lock the laser frequency to the central frequency of the saturated line. The slope of this derivative signal was 0.4 V/MHz.

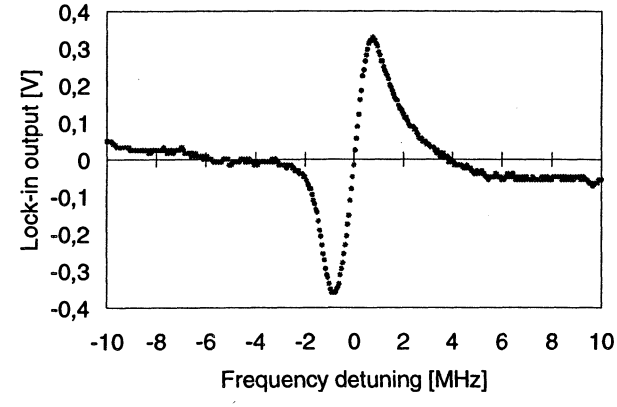

Figure 6. First derivative of the saturated absorption line P(16) of the $^{13}C_2H_2$ at λ=1542.384 nm.

When the Er-Yb:glass laser was locked against the saturated $^{13}C_2H_2$ line the estimated relative frequency stability, limited by the obtained SNR, should be at the level of $5\times10^{-12}\ \tau^{-1/2}$.

5. CONCLUSIONS

The developed fiber-pumped Er-Yb microlaser finds important applications as a high power oscillator with low intensity and frequency noise for cable television transmission, high-density wavelength division multiplexing and for coherent optical communication in the whole 1530-1565 nm spectral range, in near-infrared frequency metrology, and high-resolution spectroscopy.

Frequency noise characterization of the novel Er-Yb:glass microlaser was performed using a frequency discriminator based on a Fabry-Perot cavity and the Pound-Drever technique. The realized discriminator system reached a frequency noise sensitivity of 0.1 Hz^2/Hz. The measured power spectral density of the laser frequency noise has shown a random walk noise contribution which determine a laser linewidth of 30 kHz for 1 ms observation time.

Using this powerful and narrow-linewidth laser source at 1.5 μm, saturation spectroscopy of the acetylene molecule was performed using non-linear wavelength-modulation spectroscopy.

Frequency locking of the erbium laser to acetylene Doppler-free absorptions is saturated is in progress and the obtained frequency stability will be experimentally evaluated by means of beat frequency analisys in order to establish a new optical frequency standard in this spectral region.

REFERENCES

1. Laporta P., Taccheo S., Longhi S., Svelto O., and Svelto C., "Erbium-ytterbium microlaser: optical properties and lasing characteristics", *Optical Materials* **11**, pp. 269-288, 1999.
2. Taccheo S., Laporta P., and Svelto C., "Widely tunable single-frequency erbium-ytterbium phosphate glass laser", *Appl. Phys. Letters* **28**, pp. 2621-2623, 1996.
3. Fan T. Y. and Byer R.L., "Diode-laser-pumped solid-state lasers", *IEEE J. Quantum Electron.* **QE-24**, pp. 895-904, 1988.
4. ITU-T Recommendation G.962, "Optical interfaces for multichannel systems with optical amplifiers", Oct. 1998.
5. De Labachelerie M., Nakagawa K., Awaji Y., and Ohtsu M., "High-frequency-stability laser at 1.5 μm using Doppler-free molecular lines", *Opt. Lett.* **20**, pp. 572-574, 1995.
6. Breton M., Tremblay P., Julien C., Cyr N., Têtu M., and Latrasse C., "Optically pumped rubidium as a frequency standard at 196 THz", *IEEE Trans. IM* **44**, pp. 162-165, 1995.
7. Arie A., Lissak B., and Tur M., "Static fiber-Bragg grating strain sensing using frequency-locked lasers", *J. Lightwave Technol.* **17**, pp. 1849-1855, 1999.
8. Drever R.W.P., Hall J.L., Kowalsky F.V., Hough J., Ford G.M., Munley A. J., and Ward H., "Laser Phase and frequency stabilization using an optical resonator", *Appl. Phys. B* **31**, pp. 97-105, 1983.
9. Cheng Y.J., Mussche P.L., Siegman A.E., "Measurement of Laser Quantum Frequency Fluctuations Using a Pound-Drever Stabilization System", *IEEE J. Quantum Electron.* **QE-30**, pp.1498-1504, 1994.
10. Joss B., Bernier L. G., and Gardiol F., "", *Proceedings of the 40th Annual Frequency Control Symposium*, Philadelphia, pp. 300-305, 1986.
11. Onae A., Okumura K., Yoda J., Nakagawa K., Yamaguchi A., Kourogi M., Imai K., and Widiyatomoko B., "Toward an accurate frequency standard at 1.5 μm based on acetylene overtone band transition", *IEEE Trans. Instrum. Meas.* **48**, pp. 563-566, 1999.

DEVELOPMENT OF AN OPTICAL FREQUENCY MEASUREMENT SYSTEM USING CW OPTICAL PARAMETRIC OSCILLATORS

Takeshi Ikegami, Sergey Slyusarev and Shin-ichi Ohshima
National Research Laboratory of Metrology,
1-1-4, Umezono, Tsukuba-Shi, Ibaraki-Ken 305-8563, Japan
E-mail : ikegami@nrlm.go.jp

ABSTRACT

A 532nm pumped, ultra-wideband, and stable monolithic cw-OPO tunable over 1 octave from 777nm to 1687nm was developed. By the phase-coherent optical frequency division of 532nm using cw-OPOs, we obtained 532nm, 798nm, 912nm, 1064nm, 1277nm, and 1596nm, which were phase-locked to each other. By measuring the frequency-difference of any pairs of these light, the absolute frequency of light can be determined as a nature of cw-OPO. This optical frequency interval bisection system can be used to evaluate the accuracy of the mode-locked fs comb and the self-phase modulation inside the optical fiber.

Keywords: contnuous-wave optical parametric scillator, optical frequency measurement, optical frequency division

1. INTRODUCTION

We have been developing an optical frequency measurement system using continuous-wave (cw) optical parametric oscillators (OPOs) and optical frequency comb generators (OFCGs) [1,2] to deterimne the absolute frequency of light by measuring the frequency-difference between the fundamental light and its second harmonics of an Iodine stabilized Nd :YAG laser as a first target. This frequency difference is equal to the laser light frequency and is 282THz. To reduce this frequency difference, we achieved optical frequency division by 3 using a cw-OPO, and the optical frequency interval bisection. The finally obtained frequency difference was 47THz, which is small enough to be measured with a recent fs Ti:S mode-locked laser. The current status of our frequency measurement experiments is described.

2. CONTINUOUS-WAVE OPTICAL PARAMETRIC OSCILLATORS AS PRACTICAL LIGHT SOURCES

The cw-OPO was assumed to be a scientific toy for a long time due to the difficulty of the frequency tuning and the instability of the operation. However, owing to the development of recent good nonlinear crystals and solid state light sources, the cw-OPOs are revivaling as practical light sources. Different from the lasers which oscillate only at atomic or molecular transition wavelength, the OPOs have no restriction for the oscillating wavelength. Denoting the frequencies of the pump light, the signal light, and the idler light as ν_p,ν_s, and ν_i, respectively, the equation $\nu_p=\nu_s+\nu_i$ is satisfied considering the energy conservation of photons. Thus, the cw-OPO is considered to be an arbitrary wavelength light source.

As a widely tunable light sources for the optical frequency measurement, we developed a monolithic cw-OPO using 5% MgO doped $LiNbO_3$ crystal as nonlinear optical crystal. The OPO was pumped by a 532nm, frequency-doubled Nd:YAG laser. The details are described in Ref. 3. As shown in Fig.1, we obtained the oscillaion over 1 octave of the wavelength range from 777nm to 1687nm. Also, we confirmed, (1) arbitraly longitudinal mode selectivity, (2) stable single-mode-pair operation of signal and idler without any mode-hopping over 1 day, (3) moderate output power of several milliwatts, (4) continuous frequency-tuning of 500MHz, which satisfied the the requirements for our frequency measurement system.

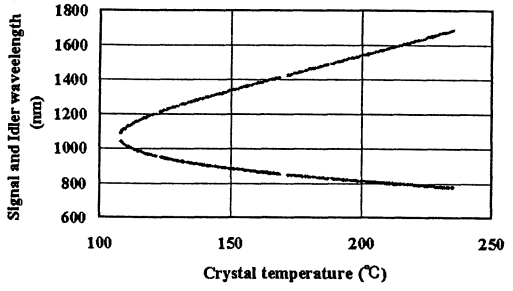

Fig. 1. The experimentally obtained, temperature-tuning curve of the monolithic cw-OPO.

3. OPTICAL FREQUENCY DIVISION BY 3 OF 532NM LASER LIGHT

By controlling the output frequencies from the cw-OPO so as to keep the relation $\nu_s=(N-1)\nu_i$ where N is an integer, the equation $\nu_i=\nu_p/N$ holds and the OPO works as a phase-coherent optical frequency divider by N. The details are described in Ref.4. We adjusted the temperature of the OPO crystal to produce the signal and idler wavelength of 798nm and 1596nm (=3 × 532nm), respectvely. The approximate temperature was 218°C. The idler light was frequency-doubled to produce 798nm light using a periodically poled $LiNbO_3$ as a nonlinear crystal (0.5mm×5mm×20mm), and the generated second-harmonic (SH) light was spatially overlapped with the signal light. Both light was detected with a high-speed photodetector and the beat signal was mixed with the signal from the microwave synthesizer by a double-balanced mixer (DBM). The error signal was fed-back to the EO tuning voltage for the nonlinear crystal. As shown in Fig.2, the successful phase-locking between the signal light and the SH of the idler light was acheived. The spectral linewidth of the beat signal was less than 10kHz even under the free running condition, which verified the good spectral characteristics of the cw-OPO..

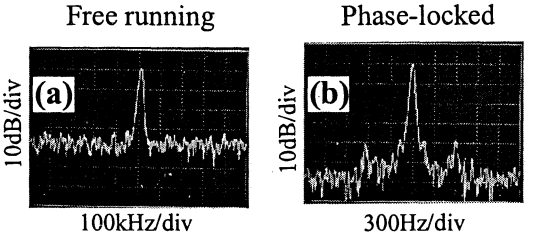

Fig. 2. The spectrum of the beat signal between the signal light and the SH of the idler light. (a) Free running condition, Resolution bandwidth (RBW) = 10kHz (b) phase-locked condition, RBW=30Hz.

4. OPTICAL FREQUENCY INTERVAL BISECTION OF 798NM AND 1064NM

After the optical frequency division by 3 of 532nm light, we could obtain 798nm and 1596nm light which were phase-coherent to 532nm pump light. Also, we already have 1064nm fundamental light from the Nd:YAG laser which is also phase-coherent to these light. Because the frequency interval between 798nm and 1064nm is still 94THz, we constructed a optical frequency interval bisector [5] to divide this frequency interval by 2 further. The details of this divider is described in Ref.6. The 912nm light, which was the average frequency light of 798nm light and 1064nm light, was produced by a cw-OPO using $RbTiOAsO_4$ as a nonlinear crystal. The second harmonics of the 912nm light was obtained by a nonlinear crystal $KNbO_3$ (a-cut, 3mm×3mm×5mm). The noncritical phase-matching (NCPM) was obtained at the temperature of 135°C. The sum-frequency (SF) generation between 798nm light and 1064nm light was achived with a-cut $KNbO_3$ crystal at the NCPM temperatre of 149°C. The beat signal between the SH of 912nm and the SF of 798nm and 1064nm was detected by a fast photodetector, mixed with the signal from the microwave synthesizer by a DBM, and fed-back to the electrode of the nonlinear crystal used for electrooptic tuning of the phase. The beat signal was successfully phase-locked to the synthesiezer signal as shown in Fig.3.

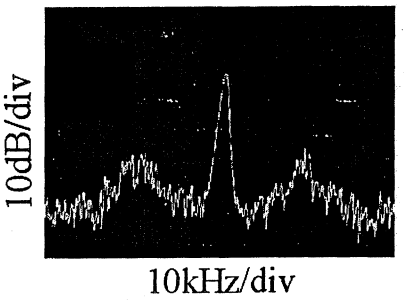

Fig. 3. The spectrum of the beat signal between the SH of 912nm light and the SF of 798nm light and 1064nm light. Resolution bandwidth was 300Hz.

5. SUMMARY AND DISCUSSION

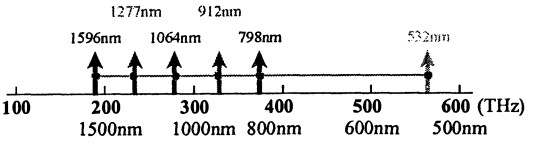

Fig. 4. The obtained light which are phase-coherent to each other.

After the 2 stage divider, we could obtain 532nm, 798nm, 912nm, 1064nm, 1277nm, and 1596nm, which were produced by cw-OPOs and were phase-locked to each other, as shown in Fig.4. The frequency interval between these light is 47THz. By measuring any pair of the above light, the absolute frequency of light can be determined from the nature of cw-OPO. Recently, the frequency span of the OFCG was extended to 50THz by using the self-phase-modulation (SPM) inside an optical fiber [7]. Also, the mode-locked Ti :S femtosecond laser was proved to be useful as an 'active' optical frequency comb generator and its performance was demonstrated [8, 9]. We also succeeded to obtain the frequency span over 1 octave using a fs comb [10]. By combining these tools, we are now in position to measure the absolute frequency of light. In addition, our optical frequency interval

bisection system can be used to check the accuracy of the comb generation inside the optical fiber used for the extension of the comb of the OFCG and the mode-locked femtosecond Ti :S laser. Also, our widely tunable cw-OPO over 1 octave can be used to investigate the noise characteristics of the fs comb. We plan to investigate these characteristics further.

REFERENCES

[1] N.C.Wong, Opt.Lett. 17, 1155 (1992).

[2] T.Ikegami and S.Slyusarev, Proc. 11th European Frequency and Time Forum. (1997) p.104.

[3] T.Ikegami, S.Slyusarev, and S.Ohshima, To be published in Proc. SPIE Vol.4269, "Laser Frequency Stabilization, Standards, and Applications", Photonics West 2001, San-Jose.

[4] S.Slyusarev, T.Ikegami, and S.Ohshima, Opt.Lett. 24, 156 (1999).

[5] H.R.Telle, D.Meschede, and T.W.Hänsch, Opt.Lett. 15, 532 (1990).

[6] S.Slyusarev, T.Ikegami, and S.Ohshima, Jpn. J. Appl. Phys. 40, 134 (2001).

[7] K.Imai, B.Widiyatmoko, M.Kourogi, M.Ohtsu, IEEE JOURNAL OF QUANTUM ELECTRON. 35, 559 (1999).

[8] R.Holzwarth, Th.Udem, T.W.Hänsch, J.C.Knight, W.J.Wadsworth, and P.St.J.Russel, Phys.Rev.Lett. 85, 2264 (2000).

[9] D.J.Jones, S.A.Diddams, J.K.Ranka, A.Stentz, R.S.Windeler, J.L.Hall, and S.T.Cundiff, Science 288, 635 (2000).

[10] K.Sugiyama, A.Onae, T.Ikegami, S.Slyusarev, F.Hong, K.Minoshima, H.Matsumoto, To be published in Proc. SPIE Vol.4269, "Laser Frequency Stabilization, Standards, and Applications", Photonics West 2001, San-Jose.

Phase-coherent frequency measurement of optical reference transitions with a femtosecond frequency comb

Jörn Stenger, Nils Haverkamp, Harald Schnatz, Christian Tamm, Harald R. Telle

Physikalisch-Technische Bundesanstalt, Bundesallee 100, 38116 Braunschweig, Germany

ABSTRACT

A frequency comb, generated by a Kerr-lens mode-locked femtosecond laser, was used to phase-coherently link the frequencies of both the 657 nm intercombination transition of ^{40}Ca and the 435.5 nm electric-quadrupole transition of $^{171}Yb^{+}$ to a cesium fountain controlled hydrogen maser. We discuss the frequency comb technique and frequency fluctuations due to optical fiber links.

1. INTRODUCTION

The development of frequency comb generators based on Kerr-lens mode-locked femtosecond lasers [1,2] during the last few years led to substantial progresses in frequency metrology. Frequency combs allow a phase-coherent link between optical and microwave reference frequencies. The technique has been applied for the measurement of several optical clock transition frequencies in samples of cold atoms or single trapped ions, such as the hydrogen Lyman-α transition [3], the 657 nm intercombination transition in Ca [4,5], or the mercury ion transition at 282 nm [5]. Recently, the indium ion clock transition at 237 nm was measured with respect to a cesium-fountain calibrated He-Ne standard [6]. In this paper we investigate the performance of the femtosecond frequency comb as obtained with the measurement of the Ca transition [4] and with the recent, first absolute frequency measurement of the electric-quadrupole transition of $^{171}Yb^{+}$ at 435.5 nm (688 THz) [7].

2. FREQUENCY COMBS

A frequency comb was generated by a Kerr-lens mode-locked femtosecond laser. The emitted periodic pulse train corresponds in the frequency domain to a comb-like frequency spectrum of equidistant lines. The spectral span of this comb reflects the duration of an individual pulse while the spacing between the lines equals the pulse repetition frequency. It has been shown, that the fast, spectrally far-reaching Kerr-lens mode-locking mechanism enforces a tight coupling [1] of the optical phases of the individual lines. As a result, the frequency of any of these lines is given by an integer multiple of the pulse repetition frequency f_{rep} and a frequency ν_{ceo} which accounts for the offset of the entire comb with respect to the frequency origin. Thus, any external optical frequency ν_{ext} to be measured can be written

$$\nu_{ext} = \nu_{ceo} + m f_{rep} + \Delta x \,, \qquad (1)$$

where Δx is the beat frequency of the external optical signal with the mth comb mode. In our experiment the radiofrequencies ν_{ceo}, f_{rep}, and Δx are referenced to a hydrogen maser, which in turn is compared with a cesium fountain.

The experimental setup as used for the measurement of the $^{171}Yb^{+}$ transition frequency and similar for the calcium transition frequency is schematically shown in Fig. 1. The frequency comb was generated by a 10 fs Kerr-lens mode-locked Ti:Sapphire laser with optical power of 150 mW, repetition rate of 100 MHz and a 200 nm wide spectrum centered at 800 nm. The spectrum was externally broadened in a microstructure fiber [8] by self-phase modulation. By coupling approximately 30 mW of the laser output into a 10 cm long piece of fiber we achieved a spectrum ranging from 500 nm to 1200 nm [4]. The light from the $^{171}Yb^{+}$ standard and from the calcium standard was guided to the frequency comb generator via approximately 200 m long single-mode polarization preserving fibers. About 1 mW of either light was combined with light from the femtosecond laser. After spectral filtering in 10 nm (FWHM) interference filters and spatial filtering in a short piece of single mode fiber the beat note Δx was detected by a fast Si PIN photodiode (PD 1, S/N ratio 30 dB, BW 100 kHz). The electronic signal was filtered in a phase-locked loop (PLL) and counted. To keep the beat signal frequency within the hold-in range of the PLL tracking oscillator the cavity length of the femtosecond laser was controlled by a servo loop using the frequency-to-voltage converted beat frequency.

According to Eqn. (1) the repetition rate f_{rep} enters the optical frequency measurement with a large multiplication factor m. Thus we detected the 103rd harmonic of f_{rep} at 10 GHz with a fast InGaAs PIN photodiode (PD 2) after spectral filtering in a fused-silica etalon with free spectral range of 10 GHz in order

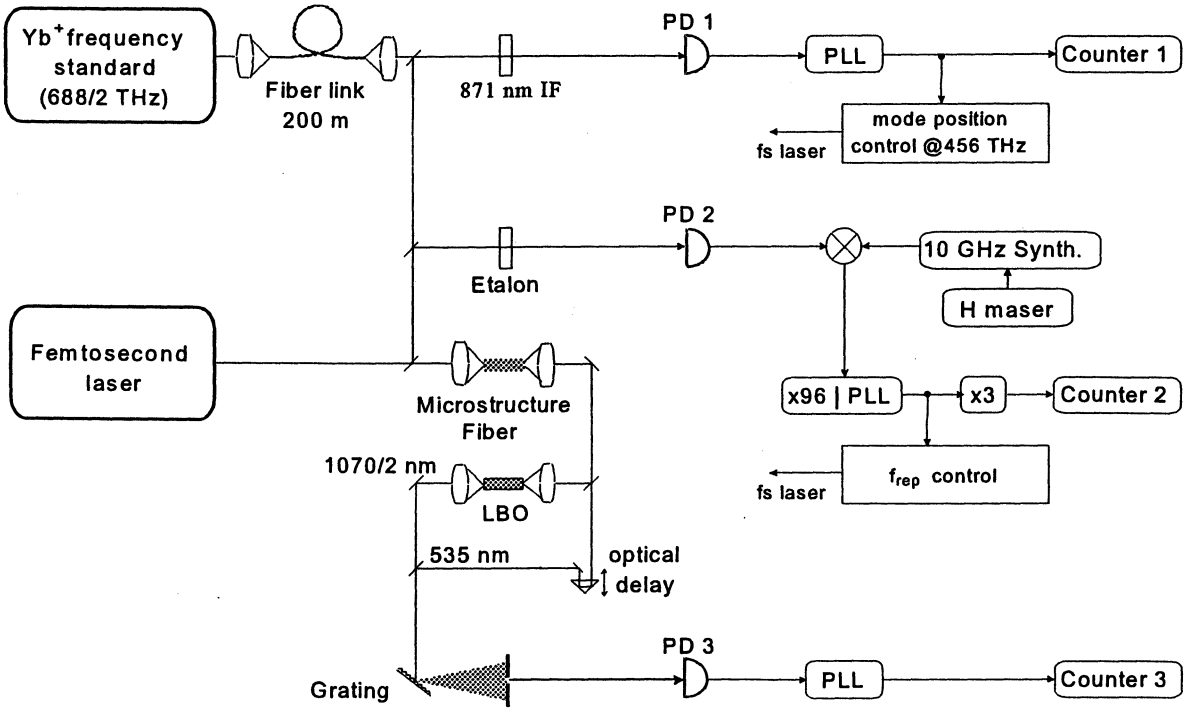

Figure 1: Schematic of the setup for the frequency measurement of the $^{171}Yb^{+}$ clock transition. The scheme shows the optical part of the setup on the left hand side of the photo detectors PD 1-3, and the electronic part on the right hand side. LBO denotes the LiB_3O_5–frequency doubling crystal, IF interference filter, and PLL phase-locked loop, respectively. Details are described in the text. Two servo loops were used for a slow stabilization of f_{rep} and Δx in order to keep the beat signals within the hold-in range of the PLL tracking oscillators.

to make use of the full dynamical range of the photodiode. This microwave signal was downconverted by mixing with a 10 GHz signal from an dielectric-resonator oscillator, which in turn was controlled by a 10 GHz signal derived from the 100 MHz signal from the hydrogen maser. The downconverted signal was filtered, frequency-multiplied by 288 and counted. Owing to the resulting large overall multiplication factor of 29 664 the digitization error of the counting process was reduced below the instability of the hydrogen maser. Another servo loop stabilized the repetition rate of the femtosecond laser. The wavelength of the 871 nm signal was pre-measured by a lambdameter with absolute accuracy corresponding to 1.5 MHz, thus determining the longitudinal mode order m.

The measurement of the offset frequency ν_{ceo} requires at least one nonlinear optical process [9]. In the simplest case ν_{ceo} can be measured by detecting the beat note between frequency-doubled comb modes of the low frequency part of the spectrum and modes of the high frequency part. Whereas the frequencies of the fundamental comb modes are shifted by ν_{ceo}, the harmonics are shifted by $2\nu_{ceo}$. We used a non-critically phase-matched, 10 mm long LiB_3O_5 (LBO) crystal, which was heated to about 140 °C in order to fulfill the type-I phase-matching condition for a wavelength of around 1070 nm. The resulting beat note ν_{ceo} was detected by a photo multiplier (PD 3) after spatial and spectral filtering both fields at 535 nm in a single mode fiber and a 600 l/mm grating, respectively. The signal was tracked with a third PLL and finally counted.

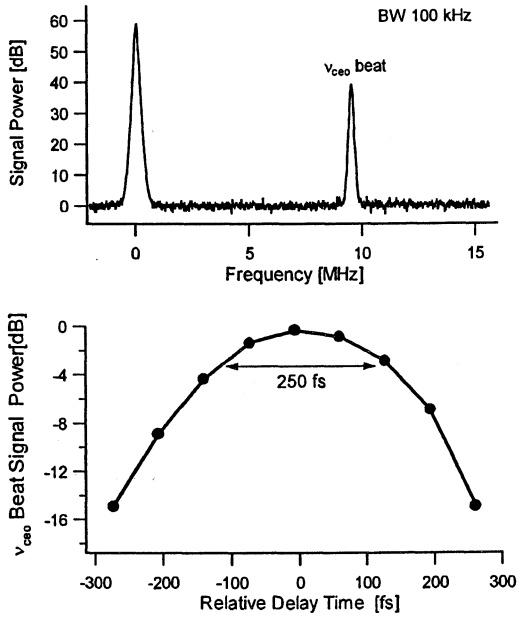

Figure 2: The ν_{ceo}-beat note arising from frequency-doubled modes near 1070 nm and fundamental modes near 535 nm, and the beat note power as a function of the relative delay time.

Fig. 2 shows the ν_{ceo}-beat note and its power as a function of relative delay time between the frequency-doubled and fundamental modes near 535 nm. The beat note power is reduced by 3 dB for a relative delay time as short as 125 fs. Thus one concludes from this field cross correlation function that as many as about 40 000 modes within a bandwidth of 4 THz contribute to the beat. The detection of the ν_{ceo} beat demonstrates the coherence of the comb spectrum across one octave. Since the radiation both at 535 nm and at 1070 nm is generated in the optical fiber, the ν_{ceo} beat in particular demonstrates the preservation of coherence and comb structure of the spectrum in the fiber. For given pulse parameters, the spectral width after the fiber is a function of fiber length. The most stable beat notes were achieved for the shortest possible fiber ($\approx$ 10 cm) for the generation of an octave wide spectrum.

The $^{171}Yb^+$ reference frequency was derived from a single ion that was laser cooled and confined in a spherical radiofrequency Paul trap. The clock transition at 435.5 nm (688 THz) was alternately probed on both sides of the resonance line with the frequency-doubled output of an extended-cavity diode laser emitting at 871.0 nm (344 THz). The frequency of the probe laser was stabilized to the line center with an effective time constant of 30 s through a second-order integrating servo algorithm. Short-term fluctuations were reduced by stabilization to an environmentally isolated high-finesse cavity. More details are given in Ref. [10].

Data of the frequency of the $6s\ ^2S_{1/2}(F=0) - 5d\ ^2D_{3/2}(F=2)$ electric-quadrupole clock transition of the $^{171}Yb^+$ ion were taken on several days. By averaging we derive the following value:

$$\nu_{Yb} = 688\ 358\ 979\ 309\ 312\ \text{Hz} \pm 6\ \text{Hz}\ . \qquad (2)$$

Fig. 3 shows the Allan standard deviation of one day's data. The typical instability of the hydrogen maser (open circles in Fig 3) is approached. This result and the sources of uncertainty are discussed in more detail in Ref. [7]. The frequency of the intercombination transition in atomic calcium was measured using a setup similar to that shown in Fig. 1. The cold-atom based calcium frequency standard and the results of the Ca-frequency measurement are described in more details in Refs. [11,12] and in Ref. [4], respectively.

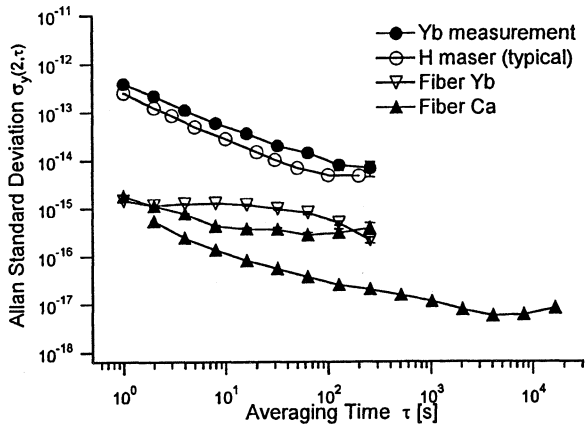

Figure 3: The Allan standard deviations of the $^{171}Yb^+$ clock frequency measurement, that of the hydrogen maser and that of frequency fluctuations due to thermally and acoustically induced fiber length fluctuations.

Here, we investigate another possible contribution to the uncertainty due to the 200 m long fiber link from the $^{171}Yb^+$ standard to the femtosecond comb generator and due to the 250 m long fiber link from the calcium standard. The thermally and acoustically induced fluctuations of fiber length and of index of refraction lead to frequency fluctuations of the transmitted signal. These frequency fluctuations were analyzed by an interferometric measurement of the fiber length.

The corresponding Allan standard deviations for the frequency fluctuations at the fiber output for a perfect input signal are shown in Fig. 3. Measurements were taken with a double-heterodyne technique at different times during the day both for the $^{171}Yb^{+}$ fiber and the calcium fiber. Different acoustic and thermal conditions led to fluctuations differing by up to almost two orders of magnitude. However, we never observed systematic frequency offsets larger than 2×10^{-15} for averaging times $\tau > 100$ s. Thus, frequency fluctuations due to fiber length fluctuations can be neglected for our frequency measurement in the uncertainty range of 10^{-14}. For future measurements with uncertainties substantially better than that the double-heterodyne technique can be used to compensate the fiber fluctuations.

In conclusion, we demonstrated the capability of a femtosecond comb generator of measuring optical frequencies with Cs clock accuracy. A future application can be the direct frequency comparison of the $^{171}Yb^{+}$ standard with calcium standard, aiming to surpass the short-term frequency instability of the hydrogen maser.

We gratefully acknowledge financial support from the Deutsche Forschungsgemeinschaft through SFB 407 and contributions of Andreas Bauch, Thomas Binnewies, Ursula Keller, Burghard Lipphardt, Fritz Riehle, Günter Steinmeyer, Uwe Sterr, Stefan Weyers and Guido Wilpers in several stages of the experiment. We are also indebted to Robert Windeler of Lucent Technologies for providing the microstructure fiber.

3. REFERENCES

[1] T. Udem, J. Reichert, R. Holzwarth, and T. W. Hänsch; Opt. Lett. **24** 881 (1999).

[2] S. A. Diddams, D. J. Jones, J. Ye, S. T. Cundiff, J. L. Hall, J. K. Ranka, R. S. Windeler, R. Holtzwarth, T. Udem, and T. W. Hänsch; Phys. Rev. Lett. **84** 5102 (2000).

[3] M. Niering *et al.*; Phys. Rev. Lett. **84** 5496 (2000).

[4] J. Stenger, T. Binnewies, G. Wilpers, F. Riehle, H. R. Telle, J. K. Ranka, R. S. Windeler, A. J. Stentz; Phys. Rev. A. **63** 021802(R) (2001).

[5] T. Udem, S. A. Diddams, K. R. Vogel, C. W. Oates, E. A. Curtis, W. D. Lee, W. M. Itano, R. E. Drullinger, J. C. Bergquist, and L. Hollberg; submitted (eprint arXiv:physics/0101029) (2001).

[6] J. von Zanthier et al.; Opt. Lett. **25** 1729 (2000).

[7] J. Stenger, Ch. Tamm, N. Haverkamp, S. Weyers, and H. R. Telle; submitted (eprint arXiv:physics/0103040) (2001).

[8] J. K. Ranka, R. S. Windeler, and A. J. Stentz; Opt. Lett. **25** 25 (2000).

[9] H. R. Telle, G. Steinmeyer, A. E. Dunlop, J. Stenger, D. H. Sutter, U. Keller; Appl. Phys. **B 69** 327 (1999).

[10] Ch. Tamm, D. Engelke, V. Bühner; Phys. Rev. **A61** 053405 (2000).

[11] F. Riehle, H. Schnatz, B. Lipphardt, G. Zinner, T. Trebst, J. Helmcke; IEEE Trans. Instrum. Meas. **IM 48**, 613 (1999).

[12] F. Riehle *et al.*; in *Proceedings of the 1999 Joint Meeting of the European Frequency and Time Forum and The IEEE International Frequency Control Symposium* (EFTF co/Société Francaise des Microtechiques et de Chronométrie (SFMC), Besancon, France) p. 700 (1999).

GPS CARRIER PHASE

Chairwoman: Felicitas Arias

THE GETT CAMPAIGN: FINAL RESULTS FROM THE TRANSATLANTIC MEASUREMENTS AND CALIBRATION OF THE STATIONS

Gregor Dudle, Léon Prost
Swiss Federal Office of Metrology, Lindenweg 50, CH-3003 Berne-Wabern

Rolf Dach, Urs Hugentobler, Thomas Schildknecht
Astronomical Institute of the University of Berne, Sidlerstrasse 5, CH-3012 Berne

In Summer 1998 a terminal for for time and frequency transfer by GPS Carrier Phase (CP) has been installed at the Physikalisch Technische Bundesanstalt (PTB) in Braunschweig and one at the US Naval Observatory (USNO) in Washington. The purpose of this experiment was to study time and frequency transfer over a long baseline. These stations were referred to as Geodetic Time Transfer (GeTT) Terminals and have been operated almost without interruption since their installation. After more than two years of service the campaign has now been discontinued.

Over the long period of the campaign, it was possible to study the capabilities of GPS CP and to compare its performance with other, well established techniques. Partial results have already been presented at former EFTFs. The latest update will include comparisons over the whole campaign.

The two terminals have not be differentially calibrated before their deployement. However, they have been operated under stable conditions on both sides, allowing to address the time transfer accuracy issue even without calibration constant. Different analysis strategies will be studied to emphasis the importance of this component in the technique.

In parallel, a third GeTT station has been assembled and can be used for calibration purposes. We report on the progress of the calibration work of the GeTT terminals.

Beyond the time and frequency data, the transatlantic campaign has also generated a lot of information on GPS CP as time and frequency transfer method. The paper looks back on the encountered problems and draws the conclusions for future applications.

PROGRESSES IN THE CALIBRATION OF "GEODETIC LIKE" GPS RECEIVERS FOR ACCURATE TIME COMPARISONS

Gérard Petit[1], Zhiheng Jiang[1], Philippe Moussay[1], Joe White[2], Ed Powers[3], Gregor Dudle[4], Pierre Uhrich[5]

[1]BIPM, Pavillon de Breteuil, 92312 Sèvres CEDEX, France

[2]US Naval Research Laboratory, Washington DC, USA

[3]US Naval Observatory, Washington DC, USA

[4]METAS, Wabern, Switzerland

[5]BNM-LPTF, Paris, France

ABSTRACT

Dual frequency carrier-phase and code measurements from geodetic like GPS receivers are a promising tool for frequency and time transfer. To use them for time transfer, one must be able to report their measurement to an external reference and to calibrate all electrical delays. After having carried out the calibration of one such receiver of Ashtech Z12-T type, we plan to differentially calibrate all similar receivers located in time and frequency metrology laboratories. The procedure for the differential calibration is presented and preliminary results of the first calibration trip are presented.

Keywords: GPS receiver, calibration, time comparisons

1. INTRODUCTION

Time comparisons are usually carried out with GPS time receivers using C/A code measurements. A few number of these receivers have had their electrical delays absolutely calibrated with an uncertainty of a few nanoseconds. By differential measurements of receivers operated side by side, it has been possible to calibrate over the years most of the receivers operating in time laboratories worldwide so that time comparisons used e.g. for TAI are expected to be accurate to within a few nanoseconds. Such an exercise of differential calibration is also being carried out for multi-channel code receivers. Recently the use of dual frequency carrier-phase and code measurements from geodetic like receivers has emerged as an outstanding tool for frequency comparisons [Refs 1,2]. In order to be used also for time comparisons, such receivers should be calibrated to obtain the absolute values of the electrical delays.

The outline of the paper is the following: First we define in section 2 what we consider the internal time reference of the Ashtech Z12-T receiver and we recall the results of the absolute calibration of the BIPM unit. Then we present in section 3 the procedure to perform the differential calibration of two such receivers by operating them side by side. We finally show in section 4 the preliminary results of the first measurements of a calibration trip initiated by the BIPM.

2. CALIBRATION OF THE BIPM's ASHTECH Z12-T RECEIVER

The Ashtech Z12-T receiver performs pseudo-range and carrier phase measurements which are referred to an "internal reference". This reference is derived from an externally provided 20 MHz signal. An important modification of the Z12-T version with respect to the Z12 is that an externally provided 1-PPS signal allows the receiver to unambiguously choose one particular cycle of the 20 MHz to form the internal reference, therefore providing repeatability of this reference in case of any interruption of the tracking or operation of the receiver. According to the Ashtech documentation, we define the internal clock as the input 20 MHz inverted and delayed by 15.8 ns. For receivers equipped with a 20 MHz output, the internal clock should coincide with this signal, advanced by 2.4 ns. The internal reference is then defined as the first positive zero crossing of the internal clock following the 1-PPS in signal [Ref. 3].

The offset between the internal reference and the 1-PPS signal entering the receiver is here denoted X_0 and is to be measured at each change in the set-up of the receiver. To do so, we direct the 1-PPS and the 20 MHz signals on two channels of a digital oscilloscope where the 1-PPS signal triggers the data acquisition. By direct measurement on the oscilloscope display (Figure 1), it is possible to determine the relative phase of the two signals with an uncertainty of a few hundred ps. It is reminded that, for proper operation of the receiver, X_0 may not be arbitrary fixed but must take a defined value (within a range of about +/- 5 ns). The oscilloscope display also allows to check the proper configuration of the signals (see an example in Figure 1).

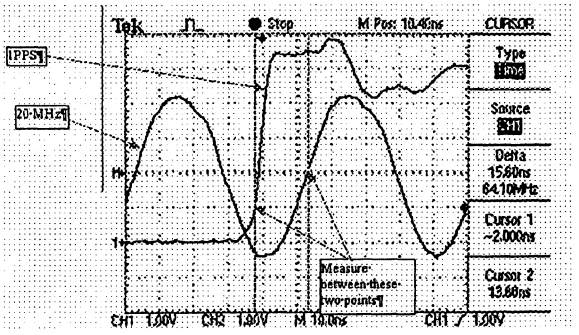

Figure 1: Oscilloscope display of the measurement of the relative phase of the rising zero-crossing of the 20 MHz (after inversion), and of the 1-PPS (at 1 V) input signals. The delay X_0 is obtained by adding 15.8 ns to this measurement.

Having defined the internal reference, it is possible to define the receiver delays, noted here X_{Ri} for frequency i, that are to be determined by absolute calibration, as described in [Ref. 4]. Other delays to be determined are the antenna internal delays, noted here X_{Si} for frequency i, and those of the cables between the antenna and the receiver. When necessary, we distinguish the antenna cable itself, which delay is noted here X_C, from the set of splitter and short cable linking the splitter to the receiver, which delay is noted here X_D. Figure 2 provides a description of the different delays in the typical set-up. The values that have been determined for the BIPM Ashtech Z12-T and its TSA antenna [see details in Ref. 4] are shown in Table 1.

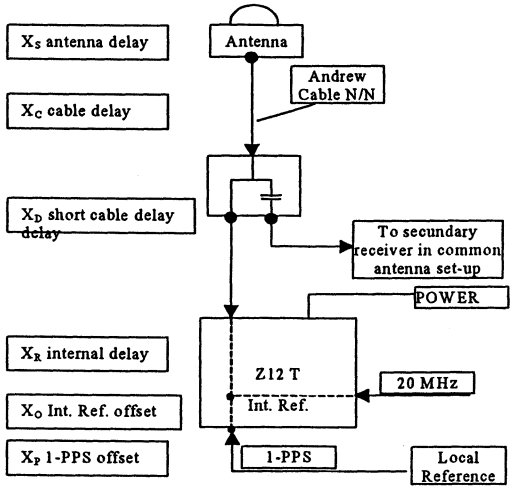

Figure 2: Definition of the different delays used in the typical set-up of the BIPM Ashtech Z12-T.

Delay	L1 value / ns	L2 delay / ns
Receiver internal X_R	281.1 ± 0.6	295.4 ± 0.7
Short cable X_C	5.1	Id.
Antenna cable X_D	200.6	Id.
TSA antenna X_S	30.7 ± 2.0	23.7 ± 2.0
Ashtech antenna X_S	23.6 ± 2.0	25.1 ± 2.0

Table 1: Summary of the delay values for elements of the BIPM Ashtech Z12-T (from [Ref. 4] except for the Ashtech antenna). Total cabling uncertainty is estimated to be 0.5 ns.

In addition to this complete absolute calibration, a number of partial and differential calibrations have been performed. First, two differential methods have been used to provide the value of X_{R1} - X_{R2} : one is by using a GPS simulator, though an uncalibrated one; another is by using a GPS receiver from the USNO for which the difference between the L1 and L2 delays had been previously determined. Both results are consistent with the results in Table 1. Then the total system had been differentially calibrated at the L1 frequency with respect to a classical time receiver [Ref. 5], also yielding a value for $X_{R1} + X_{S1}$ consistent with those in Table 1. In addition, the original Ashtech antenna has been differentially calibrated at the BIPM with respect to the TSA antenna, the values of the delays are also indicated in Table 1. The uncertainties in Table 1 are from [Ref. 4], where a detailed discussion of the uncertainty sources may be found. It concludes that the one-sigma uncertainty of the delay of the total system is 2.5 ns.

3. A PROCEDURE FOR THE DIFFERENTIAL CALIBRATION OF Z12-T RECEIVERS

Having laid out the definitions in the preceding section, it is straightforward to define a procedure to carry out the differential calibration of all components of a receiver like the Z12-T, of the same type. It consists of three steps

a) Relating the internal reference to the laboratory reference: The procedure is that described in section 2. It should be carried out at the beginning and the end of the experiment for the two Z12-T systems. An uncertainty of a few hundred ps should be attained, after checking that the result is independent of the settings of the oscilloscope used.
b) Measure the difference between the total delays (internal + antenna) of the two systems: For that measurement, the two systems are set-up independently ('short-baseline' configuration), with the 20-MHz in and 1-PPS in for the two systems derived from the same reference. The difference in the measured pseudo-ranges at frequency i yields, after taking into account the geometric term due to the different positions of the two antennas, the difference in $X_{Ri} + X_{Si} + X_C + X_D - X_O - X_P$ between the two receivers. Thus the values of $X_{Ri} + X_{Si}$ for the receiver under calibration are determined.
c) Measure the difference between the internal delays of the two systems: For that measurement, the two systems are fed by the same antenna ('zero-baseline' configuration), with the 20-MHz in and 1-PPS in for the two systems derived from the same reference. The difference in the measured pseudo-ranges at frequency i directly yields the difference in $X_{Ri} + X_C + X_D - X_O - X_P$ between the two receivers, and therefore the value of X_{Ri} for the receiver under calibration. The values of its antenna delays X_{Si} are then obtained by simple difference.

With one day of data, the differential calibration may easily be performed with an uncertainty of 100 ps. The dominant uncertainty is likely to be the sensitivity of the equipment (the travelling receiver as well as the receiver under calibration) to the temperature. It is advised to maintain these equipment in a temperature controlled room and to avoid temperature variations larger than one degree.

4. A FIRST INTERNATIONAL CALIBRATION CAMPAIGN

An international calibration campaign aiming at calibrating Ashtech type receivers in metrology time and frequency laboratories has been initiated by the BIPM. The first trip concerns the METAS (Bern, Switzerland), the BNM-LPTF (Paris, France), the USNO (Washington DC, USA), the NPL (Teddington, UK), the ORB (Brussels, Belgium), the CNES (Toulouse, France), the CRL (Koganei,

Japan). As often as is practicable during the trip, the travelling Z12-T receiver (noted BIPC) is installed at the BIPM where it is checked against another "geodetic like" receiver which also provides access to its internal reference, and which is kept in stable conditions. A number of classical time transfer receivers are also available at the BIPM for cross-check. Preliminary results from the first two stages, conducted in February 2001 at METAS and in March 2001 at the BNM-LPTF are presented here.

As examples let us consider the calibration of the systems WAB1 at METAS and LPTF at the BNM-LPTF. Figure 3 shows the variations in the differenced delay WAB1-BIPC for the total systems (short-baseline configuration) for one day of measurements, after removing the mean values indicated in the figure. The data has been processed with the Bernese software [Ref. 6] to account for the geometrical effect of the short baseline. The mean value for each frequency i is just the differences in $X_{Ri} + X_{Si} + X_C + X_D - X_O - X_P$ between the two receivers, from which one determines the values of $X_{Ri} + X_{Si}$ for the receiver under calibration. The variations of order 200 ps amplitude are thought to be due to the travelling receiver because the local receiver is kept in a temperature-controlled chamber. Figure 4 shows similar data for LPTF-BIPC; the variations are again consistent with expected environmental effects.

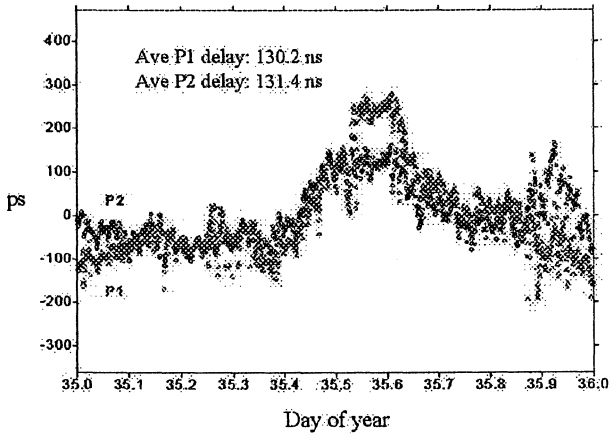

Figure 3: Differenced delay between the two systems WAB1-BIPC (short-baseline configuration), after removing the indicated mean values.

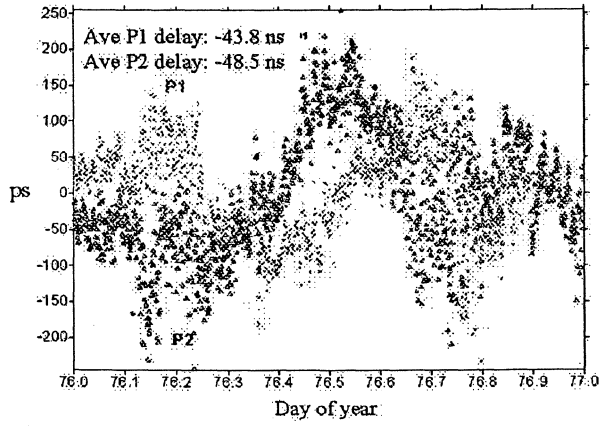

Figure 4: Differenced delay between the two systems LPTF–BIPC (short-baseline configuration), after removing the indicated mean values.

From the analysis of the differenced data, we determine that the uncertainty in the differenced delay is of order a few hundred ps and is dominated by environmental effects. We therefore conclude that the uncertainty in the delays of the system under calibration is of order that of the calibrating system, i.e. 1 ns for the internal delay, 2 ns for the antenna and 2.5 ns for the total system (one sigma). It is to be noted, however, that impedance mismatch between the antenna preamplifier and the receiver is a potential source of error which could have a non negligible effect [Ref. 4].

5. CONCLUSION

Having performed the absolute calibration of an Ashtech Z12-T GPS receiver for the two frequencies, we define a procedure to carry out the differential calibration of similar equipment in metrology laboratories. We started a first calibration trip in which seven laboratories will be visited. Preliminary results from the first two stages indicate that the procedure should provide an uncertainty in line with that of the absolute calibration i.e. of order 1 ns for the internal delay of the receiver and 2.5 ns for the delay of the total system.

REFERENCES

1. G. Petit, C. Thomas, Z. Jiang, P. Uhrich, F. Taris, "Use of GPS Ashtech Z12T receivers for accurate time and frequency comparisons", *IEEE Trans. On Ultrason., Ferroelectr., and Freq. Control*, Vol. 46, No. 4, pp. 941-949, July 1999.
2. Schildknecht T. and Dudle G., "Time and Frequency Transfer: high precision using GPS phase measurements", *GPS World*, Feb. 2000, pp. 48-52.
3. G. Petit, Z. Jiang, J. White, R. Beard, E. Powers, "Absolute calibration of an Ashtech Z12-T GPS receiver", *GPS Solutions* 4-4, pp. 41-46, 2001.
4. J. White, R. Beard, G. Landis, G. Petit, E. Powers, "Dual frequency absolute calibration of a geodetic GPS receiver for time transfer", these proceedings.
5. Petit G., Jiang Z., Uhrich P., Taris F., "Differential calibration of Ashtech Z12T receivers for accurate time comparisons", *Proc. 14th EFTF*, pp.40-44, 2000.
6. Astronomical Institute University of Bern, "Bernese GPS software version 4.0", Rothacher M. and L. Mervart Ed., 1996.

DUAL FREQUENCY ABSOLUTE CALIBRATION OF A GEODETIC GPS RECEIVER FOR TIME TRANSFER

J. White*, R. Beard*, G. Landis#, G. Petit**, E. Powers+

*U.S. Naval Research Laboratory, Washington, DC, USA
#SFA Inc/NRL, Washington, DC, USA
**BIPM, Pavillon de Breteuil, 92312 Sèvres CEDEX, France
+U.S. Naval Observatory, Washington, DC, USA

1. ABSTRACT / KEYWORDS

The use of geodetic quality Global Positioning System (GPS) receivers for time transfer offers the possibility of excellent low noise measurements. This paper describes an approach to making high accuracy, low noise, independent calibrations of the internal delays in such receivers. Typical noise levels are around one nanosecond with comparable bias uncertainties. Calibration results for several current receivers are presented and compared with results from other calibrations of the same receivers.

GPS Receiver, Calibration, Geodetic Simulator

2. INTRODUCTION

As the GPS system and GPS receivers continue to improve, the need to be able to make accurate and repeatable calibrations of timing receivers is also growing. The most widely used approach to calibration of receivers is co-locating the receiver to be calibrated with a reference receiver. Time transfer data are collected with both receivers for several days and processed. The difference between the test receiver and the reference receiver is used as the calibration. This method has been shown to produce very good results (ref 1). However, there are several potential disadvantages. First, there is no absolute standard. For consistency, there has to be single "golden" receiver to which all others are compared. There is always the question of how stable the "golden" receiver's calibration is. Secondly, as the available precision improves, the need to periodically recalibrate occurs at an increasing frequency. This necessitates a continuous flow of receivers among the timing centers. As the number of high accuracy users increases, the method will tend to become unwieldy.

On the other hand, if an independent means of absolute calibration can be demonstrated, user's receivers can be calibrated at multiple sites without reliance on the stability or availability of any particular receiver. This paper describes a method used by the U.S. Naval Research Laboratory and the U.S. Naval Observatory. A GPS signal simulator is calibrated using standard laboratory test equipment. That simulator is then used to calibrate GPS receivers without the need for a reference receiver (refs 2-4). We demonstrate the use of the GPS signal simulator to calibrate a C/A code timing receiver and two dual frequency geodetic receivers.

3. APPROACH

The key to using a GPS simulator to calibrate a receiver's internal timing delays is calibrating the simulator itself. That calibration must be traceable to widely available standards. The calibration method must be reasonably simple to perform and must be repeatable. The amplifiers, filters and cables needed to connect the receiver to the simulator can be done by standard delay measuring techniques. For this effort, a vector network analyzer was used to provide calibrations at the GPS frequencies of 1227.6 MHz and 1575.42 MHz.

3.1 Simulator Calibration

Calibration of a GPS signal simulator for timing is done by determining the relationship between the GPS code epoch and the 1 pulse per second (PPS) output signal provided by the simulator. A feature of the GPS signal structure makes this practical. The GPS pseudorandom code bi-phase modulates the carrier at the code rate. Bi-phase modulation is a 180-degree shift in the carrier phase. When this shift occurs, there is a dip in the amplitude envelope of the signal that can be observed on a fast digital oscilloscope, figure 1. The calibration of the simulator is simply the time difference between the dip and the rising edge of the one pulse per second.

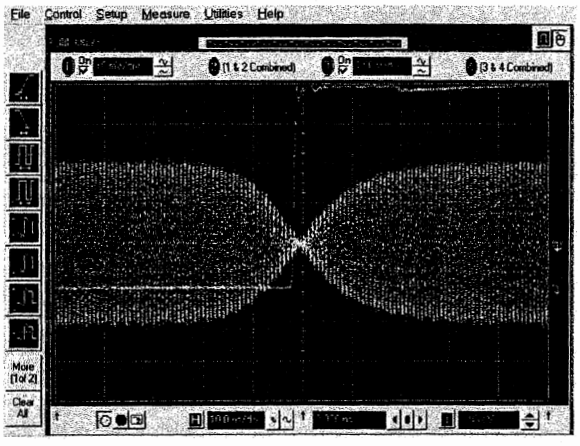

Figure 1. Simulator Amplitude Envelope

The cause of the observed amplitude dip can be thought of as a combination of a sine wave signal whose amplitude begins to decay at the point of the code epoch and a second sine wave 180 degrees out of phase with the original signal whose amplitude begins a rise at the epoch. The time constants of the rise and fall result from the finite bandwidth of the simulator. The simulator bandwidths are comparable to those in the GPS satellites. It can be seen that the dip in the amplitude of the summed signal does not fall at the code epoch. It trails the code epoch by a significant delay on the order of the time constant of the decay. This delay at first seems to lead to a calibration error since the signal observed in figure 1 is based on the location of the dip as opposed to the true code epoch. However, the receiver utilizing this signal also sees the dip as the true code epoch, canceling out the apparent error. The cancellation is effective to the

extent that the simulator's bandwidth approximates that of a GPS satellite.

The simulator signals for C/A and P code can all be measured for both L1 and L2 by this method. This allows a precise knowledge of the offsets inherent in the simulator signal providing the same kind of information gathered on the live GPS signals for geodetic use. The availability of a precisely measured difference between the L1 and L2 signals allows calibration of the test receiver's internal L1 to L2 bias and thus calibration of the receiver's perception of ionospheric effects.

3.2 Configuration

Calibrations were done in two different configurations. The first was a receiver-only method where the receiver is directly connected to the simulator. For system level calibrations, it is also necessary to measure the user's antenna, feedline, and other circuit elements used with the receiver.

3.2.1 Direct connection

Configuration for Receiver Only

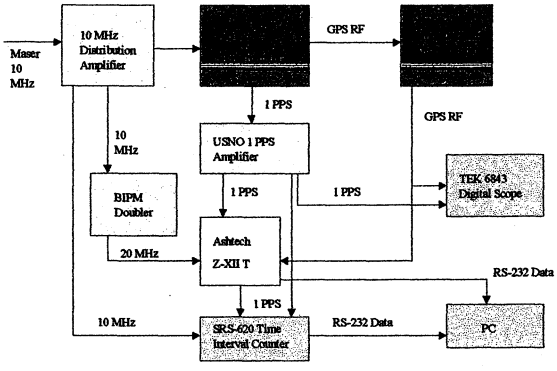

Figure 2

Direct connection, as shown in figure 2, is the simplest method and has the advantage of having very high signal to noise and no multipath or other interference. This configuration is essentially the simulator calibration setup with attenuators added to reduce the signal level. This simplifies the receiver calibration process since the only corrections needed are the simulator to 1 PPS offset and the delay in the attenuators. The cable from the amplifiers connected to the oscilloscope during the simulator calibration and to the receiver for receiver calibration with suitable attenuators is added to achieve the correct signal level.

Results with the direct connection method are usually very good. One problem that has been observed is the effect of impedance mismatches between the simulator output and the receiver input. This effect has been previously documented by NIST for GPS receivers (ref 5). When there are standing waves in the line to the receiver, the receiver correlator may be upset by the presence of a second signal very similar to the desired signal but delayed in time by about twice the length of cable. The net effect is that the correlator locks on the composite signal and has an offset. As will be discussed in section 3.2.3, the effect is more pronounced in dual frequency applications

In order to apply the results of the direct calibration to a receiver in a real working environment, the user must provide delay values for the antenna, amplifiers, feedline and any other elements in the signal path. This can be done very accurately for elements such as amplifiers and cables. It is more difficult for antennas. The method used for these tests was to measure the delay of the antenna in a shielded environment using a network analyzer. The uncertainty of that measurement is one of the largest sources of error in the experiments. In the results section 5, data are presented for calibration of a dual frequency, temperature controlled antenna.

3.2.2 Coupled through an antenna

It is often desirable to calibrate a receiver with it's own antenna, preamplifier, feedline, and other associated electronics. This approach provides a complete measurement of the receiver as the user intends to deploy it. All delays in the system are present at the time of the measurement and are imbedded in the calibration results.

Configuration for Receiver and Antenna

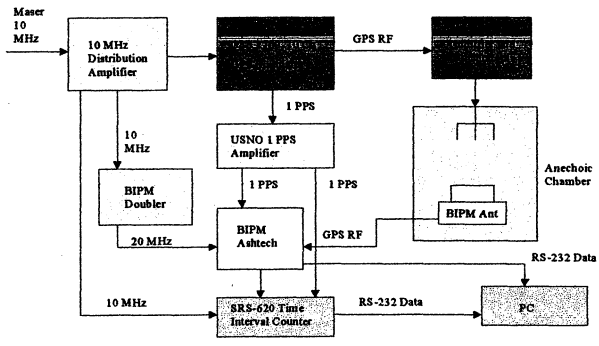

Figure 3

The receiver's antenna is placed in an anechoic box using the cable and preamplifier to be used in normal operation. A calibrated antenna is built into to the top of the anechoic box and the distance between the reference antenna and the test antenna is measured so the path delay can be removed from the calibration.

In this configuration, the simulator is calibrated in the same manner as the direct connection package, the amplifier output connected to a digital oscilloscope for calibration and then reconnected to the input to the anechoic box for receiver calibration. Alternatively, the box and path delays can be included in the calibration by replacing the test antenna with another reference antenna and amplifier. In either case, the delay of the reference antenna(s) must be accurately known.

3.3 Dual frequency considerations

Geodetic quality receivers use both GPS frequencies to compensate the effects of the ionosphere. The difference in measured range between the L1 and L2 frequencies is

used to determine the delay caused by the ionosphere. To get an accurate ionospheric correction, the frequency sensitive bias in the receiver, antenna, feedline, and electronics must be known. The simulator calibration method can be used to measure the response at each frequency.

Errors in the L1 to L2 bias calibration have a stronger effect than simple delay errors in the L1 signal. Since the L2 – L1 difference is used to determine the ionospheric delay, a bias error there will be multiplied.

In this series of experiments it was noted that a major factor in L1-L2 bias errors was impedance mismatch between the antenna/preamplifier and the receiver. These errors are frequency dependent, thus giving greater possible magnitude to the L1-L2 difference. In some cases, the insertion of a short piece of coaxial cable in the antenna line could result in 10's of nanoseconds of calibration error.

There are two possible solutions for L1-L2 calibration errors caused by mismatch. The first is simply to provide sufficient impedance matching to eliminate the standing waves. If the receiver itself is not well matched this can be done using attenuators at the ends of the cable. The other solution is to make the cable long enough that the code phase of the reflected wave is delayed by more than a code chip, thus reducing it as a source of error.

3.4 Simulated scenarios

The scenario used for this test was a simple, fixed site with no simulated satellite errors. For the receivers whose ionospheric and tropospheric corrections could be turned off, the simulation did not include ionospheric or tropospheric effects. This step eliminated possible calibration errors in modeling between the receiver and simulator. For dual frequency receivers, the output data was observed to determine the residual L1 to L2 bias with no ionosphere present. Nominal GPS almanac with all satellites enabled was used. No GPS systematic errors, Selective Availability, or Anti-spoofing are included in the scenarios.

For each scenario generated, the simulator provides a truth file that provides the generated range for each GPS satellite in view. This data can be used with a geodetic receiver, such as the Ashtech, to determine the time difference between the receiver's measured ranges and truth.

A calibration consisted of several simulator runs of identical scenarios. This provides sufficient data for good statistics and also allowed separation of random effects, systematic effects, and receiver specific phenomena. Power cycling the receiver within a test is also done to determine the repeatability of the receiver's response.

4. TEST HARDWARE

4.1 Simulator.

These tests were conducted using a Global Simulation Systems model 2760 GPS satellite signal simulator. The simulator produces ten simultaneous satellite signals with L1 C/A, L1P and L2P code modulations. The frequency reference for the simulator was the NRL house reference hydrogen maser.

4.2 Receivers.

Three receivers were tested. The first was an Ashtech Model Z12 "T", the timing version of the Z12 geodetic receiver. This receiver is owned by BIPM. Two U.S. Naval Observatory receivers were also calibrated. The first was an Allan Osborne Associates (AOA) Model TTR-12P, which is a derivative of the TurboRogue geodetic receiver. The other was a C/A code, single frequency Motorola Encore.

5. RESULTS

5.1 Internal Biases.

Each receiver was calibrated using the direct method. The dual frequency receivers have delay numbers for both the L1 and L2 frequencies.

Bias (Rcvr only)	L1 / 1-σ (ns)	L2 – L1 / 1-σ (ns)
Z12 T	281.1 / 0.6	143.0 / 0.3
TTR-12P	-144.9 / 0.2	10.6 / 0.3
Encore	168.1 / *	NA

* - Not available

Table 1. Internal Delays

The numbers shown in Table 1 are the residual internal delays after compensation of measured systematic delays and frequency biases in the simulator and cabling.

5.2 Calibration of antennas, amplifiers, cabling

The BIPM Ashtech receiver antenna and cables were calibrated using the network analyzer, with a receiver in a system configuration, and as a system at the U.S. Naval Observatory in a live calibration. The most difficult measurement was the antenna. Using the network analyzer with the anechoic box, delay values of 30.7 ns for L1 and 23.7 ns for L2 were measured. Applying those values to the data collected with the receiver operating as a system in the anechoic box produced no measurable bias change to within the noise level. An independent measurement of the antenna in operation of the same receiver system at USNO resulted in bias estimates of 31.7 ns for L1 and 25.3 ns for L2.

Adding the delays to the receiver internal delay calibration as shown in table 2, provides the system level calibration.

Receiver Component	Delay (ns)
Receiver Internal Delay	253.5
DC Block & Short Cable	5.1
Antenna Cable	200.6
Antenna	30.7
Ashtech Reference Delay	27.6
Total	**517.5**

Table 2. BIPM Receiver Calibration

The L1 to L2 bias determined in the calculation is used in the pseudorange processing as an adjustment to the ionospheric correction.

5.3 Error Budget

Table 3 shows the calibration error budget for the BIPM receiver.

Calibration	Error (ns 1-σ)
Simulator	1.0
Cabling	0.5
Antenna	2.0
Ashtech Reference	0.3
Mismatch Error	1.0
Total (RSS)	**2.5**

Table 3. Error Budget

5.4 Live Calibration Comparison.

Table 4 summarizes the comparisons between the simulator data and calibrations made at BIPM and USNO of the same units against reference receivers. The Z12 data is referenced to a BIPM test with a NIST receiver. The TTR-12 is referenced to the USNO reference receiver. The Encore data is referenced to the TTR-12 at USNO. The resulting 3 ns residual bias is after correction for the known offsets between C/A code and P/Y code in the GPS satellites.

Receiver	Live Test Bias (ns)
Z12 T (ref 4)	1.5 ± 3
TTR-12P	2 ± 3
Encore (Bias to TTR-12)	3 ± 3

Table 4. Live Data Comparison

5.5 Limitations of the Method

The simulator method provides repeatable data with direct connections and very good impedance matching. The system operating with an antenna against the simulator has the advantage of combining the hard to measure items with the basic calibration, but provides a wider distribution of errors due to multipath in the anechoic box. The impedance mis-match induced biases will be problems in any calibration approach. More investigation on the effects of band limiting elements in the calibration scenarios is needed.

6. CONCLUSIONS

GPS signal simulators offer unique capabilities for precision calibration of GPS receivers for timing purposes. They allow detailed examination of bias and time dependent delays in the hardware in an environment that can be carefully controlled and repeated. These results indicate closure at the level of a few nanoseconds with traditional live calibrations.

7. ACKNOWLEDGEMENTS

Dr. Ken Senior of the U.S. Naval Observatory provided data processing and analysis support for the live calibration testing at USNO. Mr. Alick Frank of SFA Inc at NRL provided valuable assistance in the network analyzer aspects of the system calibrations.

8. REFERENCES

1. Petit G., Jiang Z., Uhrich P., Taris F., 2000: "Differential calibration of Ashtech Z12T receivers for accurate time comparisons", *Proc. 14th EFTF.*
2. Brad, J.,Landis, G.,Powers, E., White, J., 1995:"Receiver Time Delay Calibration Using a GPS Signal Simulator", Proceedings 17th Biennial Guidance Test Symposium.
3. Beard, R.,Brad, J.,White, J.,Oaks, O.,1998:"Calibration Considerations for the IGS/BIPM Pilot Time Transfer Project Using Carrier Phase", Proceedings 30th Annual Precise Time and Time Interval (PTTI) Meeting.
4. Petit, G., Jiang, Z., White, J., Beard, R. & Powers, E., 2000:"Absolute calibration of an Ashtech Z12-T GPS receiver", IGS Analysis Center Workshop.
5. Ascarrunz, F.G., Parker, T.E., Jefferts, S.R., 1998: "Pseudo-Random Code Correlator Timing Errors due to Multiple Reflections in Transmission Lines", Proceedings 30th Annual Precise Time and Time Interval (PTTI) Meeting.

CRYO FREQUENCY GENERATION

Chairman: Daniel Hauden

A MECHANICALLY COMPENSATED SAPPHIRE OSCILLATOR OPTIMIZED FOR OPERATION AT 40 KELVIN

G. John Dick and Rabi T. Wang
Jet Propulsion Laboratory, California Institute of Technology
Pasadena, CA 91109-8099, U.S.A.

Abstract

We present preliminary design features for a second generation thermomechanically compensated sapphire resonator. Developed a few years ago, the 77 K compensated sapphire oscillator (CSO) resonator showed a quality factor $Q = 2\times10^6$ at an operating temperature of 85 K, enabling a frequency stability of $\delta f/f < 1\times10^{-13}$. The new design promises a frequency stability of parts in 10^{15} with cooling provided by a cryocooler consuming several hundred watts or less. Optimization of the resonator design for a temperature of 40 K results in a mechanical tuning rate requirement (MHz/mm) reduced by a factor of 8, allowing for reduced EM fields at the surface of the sapphire and reduced losses compared to the previously used WGH mode. The lower tuning rate also contributes to higher frequency stability by significantly reducing the sensitivity to mechanical deformation. The optimized electromagnetic design is implemented in a self-assembling mechanical configuration that allows easy disassembly for cleaning, together with first-order cancellation for expected mechanisms of physical creep. The new design shares the short internal thermal time constants characteristic of previous CSO resonators, and so achieves high frequency stability by effectively compensating temperature fluctuations over a wide range of time scales.

1. Introduction

An important new ultra-stable oscillator technology is promised by the very high inherent quality factor of whispering gallery sapphire resonators at temperatures achievable by the use of single-stage cryocoolers [1-4]. With quality factors $Q \geq 10^8$ at temperatures above 35 K, such a resonator could support an oscillator with frequency stability better than $\delta f/f \leq 3\times10^{-15}$ with cooling provided by a small single-stage Stirling or pulse-tube cryocooler. However, thermal fluctuations, together with a very substantial variation of sapphire's dielectric constant with temperature limit stability to much lower levels. If the thermal variations could be effectively cancelled or compensated, the inherent promise of the sapphire resonators could be realized. The technical challenge is to provide a relatively quick compensation process without impairing the quality factor of the resonator, and without otherwise limiting its stability.

The 10 K CSO is presently the only available continuously operating short-term frequency source with ultra-high stability [5,6,7]. A smaller cryocooled oscillator with short-term stability of 1×10^{-14} or better ($1\text{ s} \leq \tau \leq 1000\text{ s}$) at easily reached cryogenic temperatures represents a break-through technology. Mated with JPL's LITS trapped ion standards, a 40 K CSO would offer inexpensive long-term operation and replacement of hydrogen masers in NASA's Deep Space Network (DSN) [8]. It also offers the local oscillator (LO) performance required by the new generation of laser-cooled frequency standards. With a cryocooler drawing 100-300 W, a 40 K CSO can provide a needed performance with much lower cost and power than previously available for both ground and flight capabilities. This compares to 5kW required by the 10 K CSO cryocooler [5].

A short-term oscillator with 10^{-14} stability offers the DSN nearly all of the performance advantages of the 10 K CSO with much cost and upkeep. In particular, short term performance is 10 times better than the present hydrogen masers, and 5 times better than near-term spacecraft USO performance. Additionally, this performance is an ideal mate as LO to the JPL LITS and linear ion trap extended (LITE) ion standards, allowing their inherent performance to be realized.

2. Background

Figure 1 shows frequency stabilities and operating temperatures for previously demonstrated short-term frequency standard technologies with stabilities of 1×10^{-13} or better. The figure shows a very large gap between the ultra-high stability available from very low temperature ($T \leq 10$ K), oscillators and the approximately 1×10^{-13} stability available at more easily reached temperatures. It also outlines a region of presently needed capability with stability better than 1×10^{-14} while using the cooling available from single stage cryocoolers. Of the capabilities shown, those at 10 K and higher represent continuously operable frequency standards, with cooling provided by available cryocoolers.

While the short thermal time constants of sapphire and other materials in this temperature range give rise to a host of possible compensating methodologies, a primary difficulty so far

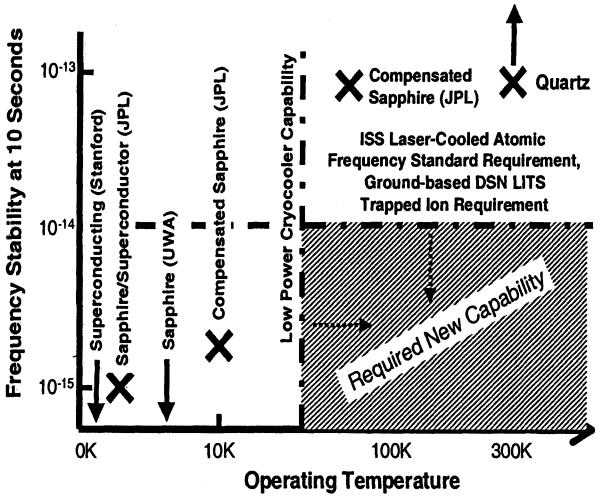

Figure 1. Scatter plot of short-term frequency standard capabilities below 10^{-13}. Parameters for a new capability, meeting the requirements of laser-cooled atomic frequency standards now being developed are also indicated

has proven to be in finding a mechanism with sufficiently low loss that sapphire's quality factor is not degraded. This problem becomes progressively more severe with increasing temperature due to a T^4 dependence for sapphire's dielectric constant. Additionally, severe constraints are placed on any mechanical motion, such as those that might be due to external vibrations or internal creep and on internal thermal time constants.

A number of promising compensated sapphire resonator technologies have already been demonstrated. These include the following:

1) Thermomechanical, for a $Q \approx 2\times10^6$ at 85 K and a frequency stability of 8×10^{-14} [1,2].
2) Dielectrics, such as Rutile, showing compensated Q's up to 10^7 at 65 K [3,4].
3) Paramagnetic impurities;
   a) Incidental impurity compensation for $Q > 10^9$, $T \leq 6K$ and stability better than 10^{-15} [9].
   b) External ruby compensation with $Q > 10^9$ below 10 K and stability of 2×10^{-15} [10].

So far, these efforts fall short of reaching the needed capability in one way or another. For example, cryocoolers for the 10 K CSO frequency standards with external ruby compensation dissipate 5kW of line power, and substantially add to the size and expense of operation. On the other hand, oscillators with compensation by thermal expansion have so far showed a relatively low quality factor of 2×10^6, and large frequency drift of $\delta f/f = 10^{-8}$/day, precluding long-term frequency locking to an external source.

Figure 2 illustrates two methods for bridging the gap between the capabilities of two previously developed JPL-developed technologies--the 10 K CSO and the 77 K CSO. The 10 K CSO, presently being implemented in the DSN for the Cassini Ka-band experiment, represents the first cryogenic oscillator to provide ultra-high short term stability together with long-term cryocooled operation. It provides a frequency stability of 2—4 parts in 10^{15} at measuring times ($1\ s \leq \tau \leq 1000\ s$) without the use of liquid helium and the frequent maintenance required by previous technologies. With a short term stability 25 times better than the hydrogen maser, the 10K CSO is making possible a significant upgrade of DSN frequency stability as required by the Cassini Ka-band experiment. The technology of the 10 K CSO was based on our previously developed 77 K CSO, which showed a stability of 8×10^{-14} with a Q of 2 million. We now propose to infuse what has been learned during the 10K development into a second generation thermomechanically compensated CSO.

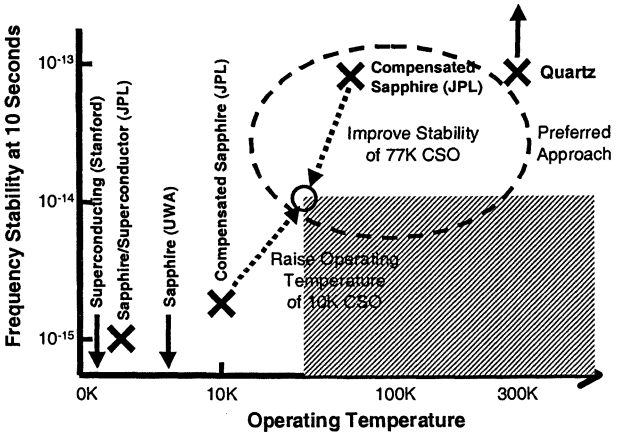

Figure 2. Approaches to the needed capability based on demonstrated compensated sapphire technologies

3. Resonator Design

We identify general design requirements for a compensated sapphire resonator to achieve parts in 10^{-15} stability as:

1) A quality factor of 4×10^7 or greater
2) A Drift rate of 1×10^{-16}/s or less
3) Internal thermal time constants of 3 s or less coupled with an appropriate external time constant
4) An acceleration sensitivity of 10^{-9}/g or less.

Table 1 shows a comparison of these requirements with capabilities actually achieved in the previous design. It is clear the primary challenge for a new design is to increase resonator quality factor and reduce frequency drift rate and that a strength of the previous design was the low thermal time constant.

Table 1 New requirements vs 77 K CSO capability

77K CSO	Need Now	How to accomplish
$Q=2\times10^6$	$Q=4\times10^7$	♦ Post-polish anneal of sapphire parts decreases surface losses by 4 times or more ♦ Optimize design for 40 K – allows 8 times less energy at surface ♦ Self assembly for cleaning ease
Drift = 1×10^{-13}/sec	Drift = 1×10^{-16}/sec	♦ Motion-canceling design ♦ Lower stress ♦ Symmetric transverse stress ♦ Lower temperature
Thermal τ = 5 sec	Thermal τ = 3 sec	♦ Utilize same general design—metal to sapphire joint inside inner caustic where RF fields are small ♦ Lower temperature gives improved thermal conductivity, reduced heat capacity
$\delta f/f = 1\times10^8$/g	$\delta f/f = 1\times10^{-9}$/g	♦ Center—mount resonator design

An intermediate figure of merit of considerable import is the required mechanical tuning rate for the electromagnetic resonator, typically measured in MHz/mm. A challenge for the original design was to achieve a large 660MHz/mm tuning rate required for compensation at temperatures above 77K, while using only materials (copper, sapphire) with excellent

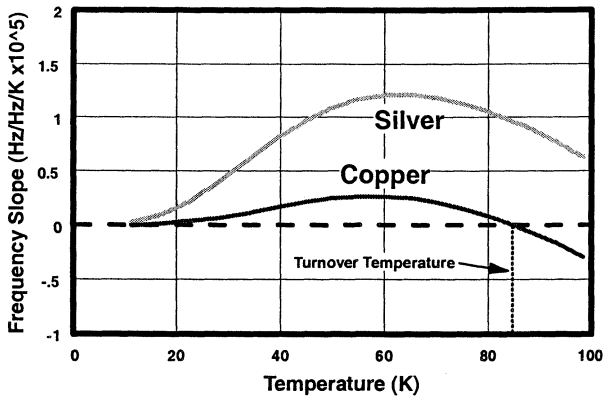

Figure 3. A high tuning rate of 660 MHz/mm enabled a turnover of 85K with a copper spacer and WGH mode orientation in the 77 K CSO

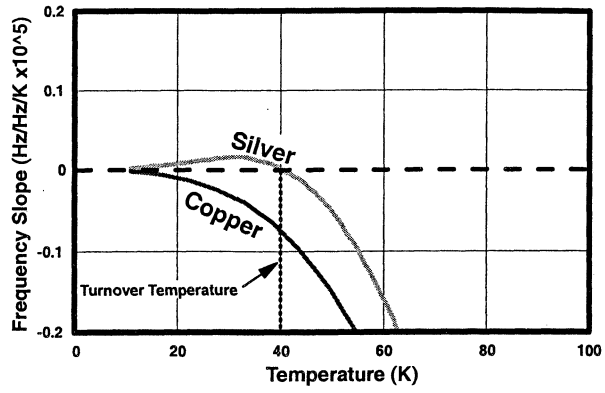

Figure 5. A turnover at 40K with a silver spacer and WGE mode is achieved by reducing the tuning rate by 8.33 times. Such a resonator with a copper spacer would be under-compensated at all temperatures.

thermal properties in this temperature range (see Fig. 3). This requirement is considerably relaxed in the new design. Lower values for the mechanical tuning rate allow smaller surface electrical fields in the resonator for reduced surface losses, a more open resonator design, and reduced sensitivity to all types of mechanical deformation.

Figures 3-5 show calculated frequency slopes for the thermomechanically compensated oscillator for progressively smaller values of mechanical tuning sensitivity. The model is based on Debye temperatures of 900 K, 550 K, 330 K, and 225 K for sapphire expansion, the sapphire dielectric constants, and copper and silver expansion, respectively. The slopes for the resonator configuration previously used are shown in Fig. 3. Figure 4 demonstrates the effectiveness of reducing the operating temperature to 40 K—use of a higher-Q WGE mode is enabled, and the mechanical tuning rate can be substantially reduced, still using a copper center post. Trading copper for silver allows a further reduction of the mechanical tuning rate as shown in Fig. 5. At the lowest temperatures, all the curves scale as T^3.

Figure 6 shows frequency dependencies for several examples of whispering gallery transverse magnetic (WGH) and transverse electric (WGE) modes. The slope of the dashed line

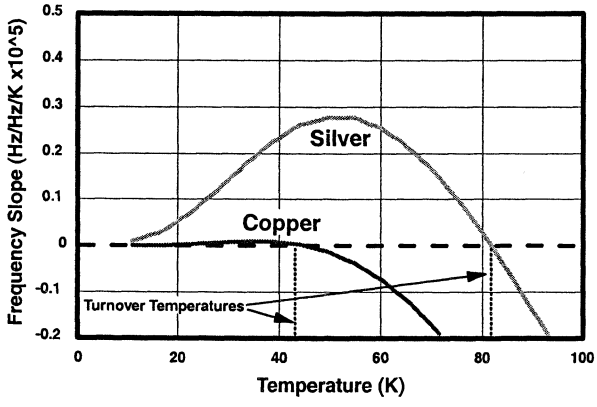

Figure 4. Use of WGE mode and a 2.84 times lower tuning rate gives a turnover of 45 K for the copper spacer, together with nearly complete compensation at lower temperatures; a silver spacer would give an 82 K turnover.

corresponds to the 77 K CSO tuning rate, as used in Fig. 3. Reduced slopes, as specified in Figs. 4 and 5, can be achieved by increasing the gap spacing and/or choosing a different mode.

Details of these curves and their first derivative are shown in results of more detailed finite element calculations displayed in Figs. 7 and 8. The mechanical tuning rate of 1.32 MHz/MHz/(cm/cm) is characteristic of the previous resonator as shown in Fig. 7. Figure 8 shows that a reduction by 8.33 times to a value of 0.159 MHz/MHz/(cm/cm) can be obtained by using a WGE mode with a gap of 9%. Such a resonator with a silver center post would show a turnover at 40 K as shown by Fig. 5.

On the basis of these calculations we have identified technical approaches to meet the requirements given in Table 1 as follows:

1) Operation at 40 K instead of 85 K:
   a) Lower temperature operation alone allows a reduction of the required mechanical tuning rate by a factor of 1.69 times.

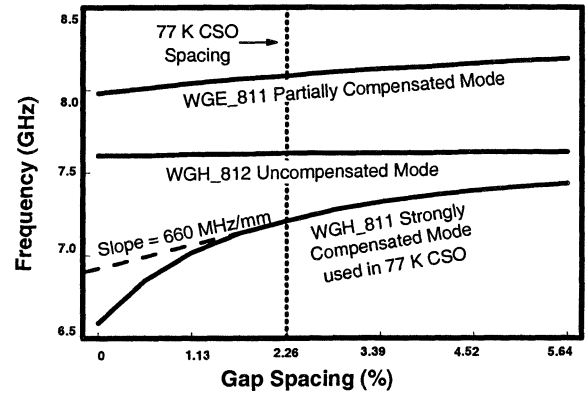

Figure 6. Finite element calculation of frequency dependence on the gap between sapphire elements for 77 K CSO resonator. Lower slope requirement now allows use of WGE mode with its higher Q, and lower temperature coefficient for epsilon.

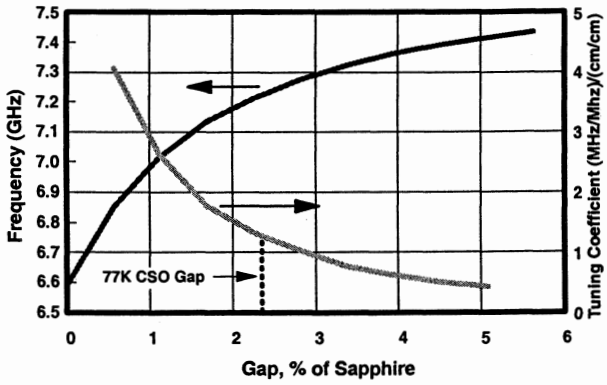

Figure 7. Finite element calculation of frequency and mechanical tuning coefficient for WGH "Fully Compensated" mode as a function of the gap between the two sapphire halves. A 2.26% gap gave a tuning coefficient of 1.32 for a turnover temperature of 85 K.

   b) Lower temperature also reduces creep rates—experience with 10K CSO showed > 100 times reduction.

2) Further optimization of resonator design for 40 K:
   a) Metal spacer made of silver with its Debye temperature of 225 K gives larger thermal expansion rate at low temperatures compared to copper at 330K—reduces tuning rate by 2.93 times.
   b) Use of WGE mode with its reduced sapphire dielectric thermal sensitivity further reduces tuning rate by 1.68 times.
   c) Overall reduction of tuning rate requirement is 8.33 times. This contributes to higher Q and reduced mechanical sensitivities by this same factor.
3) Post-polish anneal of sapphire parts:
   a) Experience with 10 K CSO indicates that annealing reduces overall losses by 4 times or more. Surface losses important to tunable resonator design may be reduced even more.
4) Self-assembling mechanical design:
   a) Use transverse (radial) joining by differential thermal contraction on cool-down.
      i) Join metal spacer to the 2 sapphire end parts.
      ii) Also join spacer to internal support .
   b) Use gravity alignment at room temperature; the parts support each other but then pull away after the grips take hold.
   c) High hardness and precision of sapphire parts prevents groove formation and allows re-assembly.
   d) Makes for easy re-cleaning of parts.
   e) A low temperature anneal after first assembly may reduce subsequent mechanical creep.
   f) Reduce material stress by control of mechanical clearances--0.3 mil tolerance is required.
   g) Use very short metallic contact regions to reduce sensitivity to angular misalignment upon cool-down.
      i) A very long contact region would be required to prevent binding due to misalignment.
      ii) A short region eliminates negative consequence of slight misalignment.
5) Advanced mechanical design to give first order cancellation of axial motion due to relaxation of radial stress:
   a) Three axial/radial motion transfer coefficients impact frequency creep:
      i) Radial relaxation of center grip of metal spacer onto sapphire post can change spacer length.
      ii) Radial relaxation of end grips of metal spacer onto sapphire parts can change spacer length.
      iii) Radial relaxation of end grips of metal spacer onto sapphire parts can bend sapphire.
   b) Advanced mechanical design can adjust each of these to give nominally zero axial motion due to radial relaxation of grip stress.
6) Center support of the 3-part compensated resonator for reduced g-sensitivity:

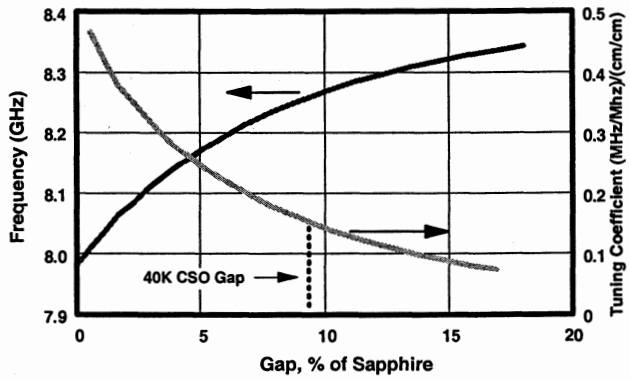

Figure 8. Frequency and mechanical tuning coefficient for WGE "Partially Compensated" mode as a function of the gap. A 9% gap gives a tuning coefficient of 0.159, a value reduced by 8.33 times from Fig. 7 as required for a turnover temperature of 40 K.

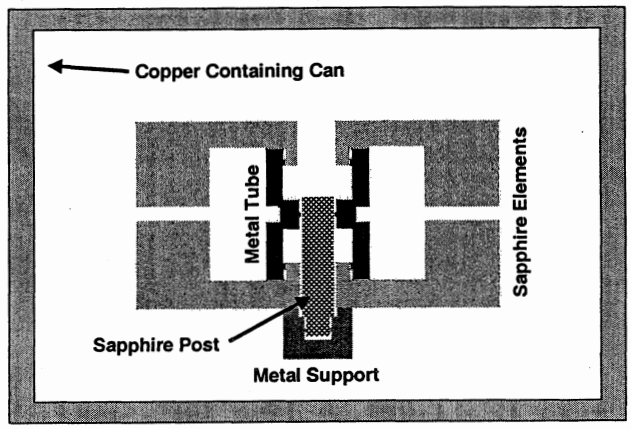

Figure 9. Cylindrical cross section of self-assembling resonator design. Upon cool-down, thermal contraction causes metal spacer and support to grip sapphire parts and then retract from other contacts.

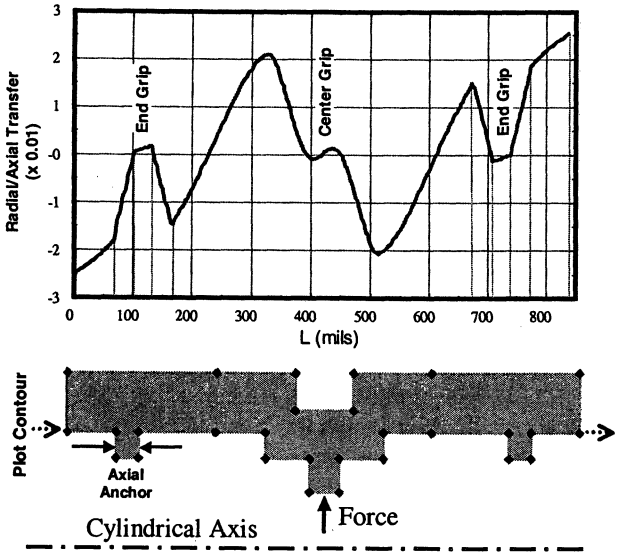

Figure 10. Motion-canceling designs eliminate axial motion and associated frequency creep when force at either center grip or end grips relaxes with time. This example shows nominally zero motion of end grips due to force on center grip of metal spacer.

   a) Accurate center support should reduce acceleration sensitivity by 100 times or more.
   b) The previous design used an end support.
7) Thermal contact between elements by metal to sapphire joint in low RF field region of resonator:
   a) Region inside inner caustic has very low RF fields, allows use of metallic parts
   b) Use of soft metals, possible gold-plating on metal spacer improves improve thermal contact
   c) Previous designs used indium-sapphire joint to achieve 5 s thermal time constant at 77 K, 1 s at 10 K. However, ultra-soft indium seems a likely candidate as source for mechanical creep and is not being considered here.

Figure 9 shows a cross section view of the mechanical resonator design. Figure 10 shows the results of finite element calculation of axial motion in response to radial force at the center grip for a preliminary design candidate. One half of the cylindrical cross section is shown, rotated 90 degrees from Fig. 7. A similar finite element calculation is used to adjust end grip positions so as to eliminate any axial motion induced by radial creep at the end grips.

4. Conclusions/Acknowledgment

We have presented preliminary design features for a second-generation thermomechanically compensated sapphire resonator optimized for operation near 40 K. This development builds on JPL capabilities demonstrated in the successful development of the 10 K and 77 K CSO's, short term frequency standards which achieve stability in the 10^{-14}'s and 10^{-15}'s without the use of liquid helium. This work was carried out at the Jet Propulsion Laboratory, California Institute of Technology under a contract with the National Aeronautics and Space Administration.

References

1. Santiago, D. G., R. T. Wang and G. J. Dick (1995), "Improved Performance of a Temperature-Compensated LN2 Cooled Sapphire Oscillator", *Proceedings of the 1995 IEEE International Frequency Control Symposium* pp. 397-400.
2. Kersale, Y, V. Giordano, F. Lardet Vieudrin, I Lajoie, M. Chaubet (1999), "Thermal Stabilization of Microwave Sapphire Resonator References", *Proceedings, 13th EFTF and 1999 IEEE Frequency Control Symposium, Besancon, France, April 1999*, pp. 585-588.
3. Tobar, M. E., J. Krupka, J. G. Hartnett, R. G. Geyer, and E. N. Ivanov (1999), "Measurement of Low-Loss Crystalline Materials for High–Q Temperature Stable Resonator Application", *Proceedings, 13th EFTF and 1999 IEEE Frequency Control Symposium, Besancon, France, April 1999*, pp. 573-580.
4. Tobar, M. E., J. Krupka, J. G. Hartnett, E. N. Ivanov, and R. A. Woode (1997), "Sapphire-Rutile Frequency Temperature Compensated Whispering Gallery Microwave Resonators", *Proceedings of the 1997 IEEE International Frequency Control Symposium* pp. 1000-1008.
5. Wang, R. and G. J. Dick (1998), "Cryocooled Sapphire Oscillator with Ultrahigh Stability", *Proceedings of the 1998 IEEE International Frequency Control Symposium* pp. 528-533.
6. Dick, G. J. and R. T. Wang (1999), "Stability and Phase Noise Tests of Two Cryo-cooled Sapphire Oscillators", *Proceedings, 13th EFTF and 1999 IEEE Frequency Control Symposium, Besancon, France, April 1999*, pp. 548-551.
7. Wang, R. T. and G J Dick (2000), "Stability Tests of Three Cryo-cooled Sapphire Oscillators," *Proceedings, Conference on Precision Electromagnetic Measurements, Sydney, Australia, May 2000* pp. 191-192.
8. Prestage, J. D., R. L. Tjoelker, and L. Maleki (1999), "Higher Pole Linear Traps For Atomic Clock Applications", *Proceedings, 13th EFTF and 1999 IEEE Frequency Control Symposium, Besancon, France, April 1999*, pp. 121-124.
9. Mann, A G, C. Sheng, and A. N. Luiten (2000), "Cryogenic Sapphire Oscillator with Exceptionally High Frequency Stability," *Proceedings, Conference on Precision Electromagnetic Measurements, Sydney, Australia, May 2000* pp. 188-189.
10. Wang, R. T. and G. J. Dick (1990) "Improved Performance of the Superconducting Cavity Maser At Short Measuring Times", *Proceedings of the 44th Annual Frequency Control Symposium* pp.89-93.

FURTHER DEVELOPMENTS OF A SAPPHIRE/RUTILE COMPENSATED DIELECTRIC RESONATOR FREQUENCY STANDARD

John Gallop and Ling Hao

National Physical Laboratory,
Teddington TW11 0LW, UK

1. ABSTRACT

Further work has been carried out on the secondary microwave frequency standard which we first proposed and demonstrated some four years ago – Refs. 1-2, with the aim of providing a self-contained, miniaturised cryogen-free microwave flywheel frequency standard for applications in support of primary standards and for navigation and positioning.

Microwave frequency standard, dielectric resonator

2. INTRODUCTION

The principle of using a composite dielectric resonator composed of at least two different low-loss dielectrics with opposite signs for the temperature dependence of their permittivities has been shown to allow high frequency stability with only moderate temperature control requirements – Refs 1-4. The long term aim of this work is to build an oscillator based on a whispering gallery (WG) mode resonance in such a composite resonator with a fractional frequency stability of better than $10^{-13}\ \tau^{-1/2}$, suitable as a flywheel standard for *Cs* primary clocks. We report below progress towards this goal. Future improvements required to achieve this figure are suggested and outlined.

Recent work has concentrated on improved stability at all timescales, brought about by radical changes to the methods of mechanical vibration isolation, between the resonator and the Giffard-McMahon closed cycle cooler, which are described below. In addition improved thermal design has led to reduced thermal gradients within the system. The modelling of the dynamic changes in temperature, following fluctuations in dissipated microwave power levels has led to an appreciation that oscillator power level control is essential. This has been implemented, together with improved Pound stabilisation techniques. Further improvements in room temperature electronics, including band pass filtering and electronic phase shifters have also had a significant impact.

2.1. Construction of Resonator

The construction of the composite resonator is as follows: a stack consisting of a quartz disc (radius = 10.5 mm and height =12 mm), a thin (radius = 10.5 mm and height=0.4 mm), rutile disk and a sapphire puck (radius = 16 mm and height = 15 mm), enclosed in a cylindrical housing machined from OFHC-copper. The quartz plate is glued to this copper housing and then the composite resonator is glued to the quartz. Coupling to the WG mode is provided by semi-rigid coaxial loops. (see Fig. 1).

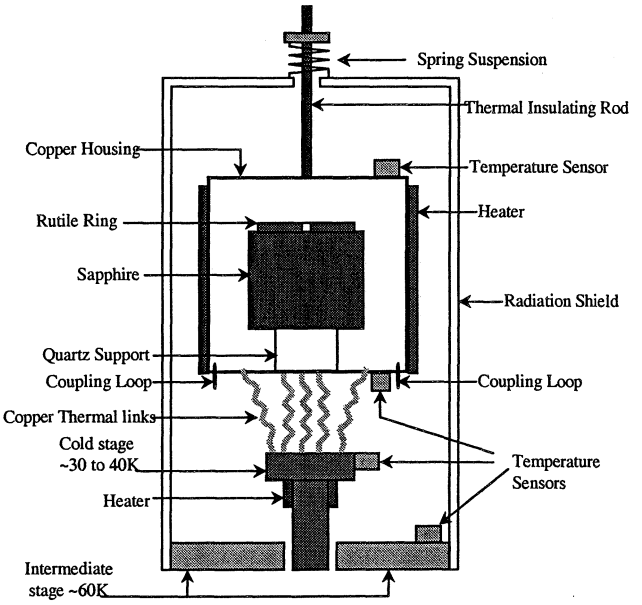

Fig. 1. Schematic of resonator construction, showing details of measures for cooler vibration isolation.

2.2. Electromagnetic design

The ratio of stored energy in the rutile component, compared to that in sapphire, is the filling factor Γ which determines the frequency f versus temperature T behaviour of the resonator and the turning point temperature T^*, at which $df/dT = 0$. In order to achieve the required value of Γ, and thus of T^*, with a rutile plate thickness > 100μm (required for robustness) the diameter of the plate has to be smaller than the diameter of the sapphire disk. The plate diameter was optimised with respect to azimuthal mode number of the WG mode ($7 < n < 12$) using MAFIA software. Note that the original dimensions were chosen to yield a whispering gallery mode at or close to the *Cs* hyperfine frequency (since an anticipated application of this device is as an ultra-low phase noise flywheel oscillator in support of *Cs* fountain or beam standards). In practice the

frequency of the selected mode is 9.2984 GHz, with a difference between model and experimental frequency which amounts to ~1% in this case. We have demonstrated with other designs that agreement should be attainable at least to a factor of 10 greater than this. These calculations show that the loss contributions from the quartz support and copper shielding cavity may be made negligible by suitable choice of dimensions.

3. KEY RECENT IMPROVEMENTS.

3.1. Vibration isolation

At present the high Q oscillator is installed in a two-stage Giffard McMahon (GM) cooler. The limiting component in this system is a piston oscillating at 1.5Hz, carrying high pressure ^{4}He gas between cold and warm regions. The relatively high mass of the piston means that the cold head of the refrigerator, a flat Cu plate to which the resonator housing has to be thermally attached, vibrates with an amplitude of several μm at low frequency. The key step in reducing the effects of mechanical vibration consisted of suspending the resonator housing from the outer radiation shield of the refrigerator, using a low thermal conductivity suspension, with additional mechanical isolation being provided by a spring (see Fig. 1). Cooling, from the cold head to the resonator housing situated ~ 3 cm. above it, is provided by a bundle of copper braids which appear to be sufficiently flexible, even when cold, to provide mechanical vibration isolation. One should avoid attaching the coaxial lines connected to the resonator housing to the second stage of the cooler cold finger (the component most liable to suffer vibration) but instead heat sink them to the first stage which provides cooling for the radiation shield. This is much less subject to mechanical vibration from the displacer movement than is the cold finger itself.

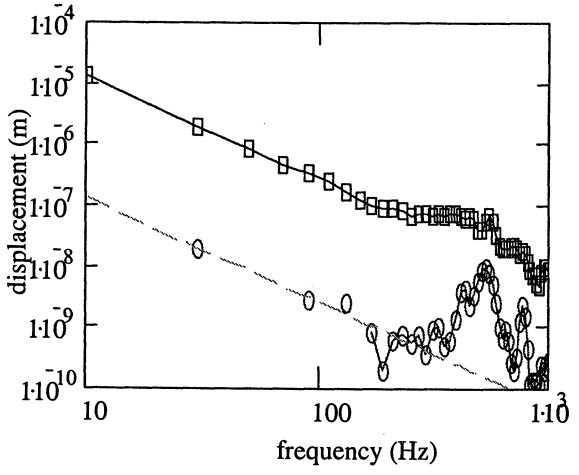

Fig. 2 Demonstration of the reduction in vibrational displacement achieved in the present system. The upper curve represents the vibrational level at the cold finger whereas the lower shows the vibration levels at the resonator housing.

Measurements of the vibration amplitude spectrum were made at various points in the cryostat volume at room temperature and it has been shown that over most of the frequency range the vibration amplitude is reduced by greater than a factor of 100 between the cold finger and the resonator housing for frequencies up to 300Hz (shown in Fig. 2). A relatively strong resonance at around 800Hz is still apparent in the vibrational level at the housing, which originates in the motor which drives the piston. It is also suspected that residual vibration is transmitted along the flexible microwave cables which link the resonator to the room temperature environment. Further improvements to reduce these effects, as well as the general level are being investigated.

3.2 Temperature control

Recently two-stage temperature control has been introduced into the GM closed cycle cooler cold stage (see Fig. 1). Thus the cooler cold finger has a Si diode temperature sensor and 30 Ω heater which is controlled by a Lakeshore *93C* temperature controller at a temperature a few K below the turning point of the resonator. The resonator housing has two resistance temperature sensors attached, together with a non-inductively wound phosphor bronze wire heater wrapped around its curved surface, with a resistance of around 30 Ω. A second temperature controller (Lakeshore model 340) is used to control the housing temperature close to the resonator turning point. This controller has a set point resolution of 1mK and the short term noise at a temperature of around 45 K is also ~ ±1 mK. Temperature measurements made over a long period of the housing Pt sensor deviations from the control point have been analysed using the two-sample variance concept similar to that used for frequency fluctuation analysis. A representative example of the square root two-sample variance of the temperature $\sigma_T(t)$ as a function of sampling time t is shown in Fig. 3. Note that the long term temperature stability is better than 100 μK, representing frequency stability better than 10^{-15} (well beyond the design specifications for this project) if the resonator can be stabilised within 1 mK of the $f(T)$ turning point temperature.

The above temperature measurements indicate the stability of the resonator housing temperature. It is legitimate to question whether this indicates the true stability of the internal, frequency determining components. Although the resonator represents an effectively isothermal enclosure, given the thickness of its wall and the high thermal conductivity of the copper from which they are constructed, the puck is subject to internal temperature differentials, due to microwave power dissipation within its separate components. We

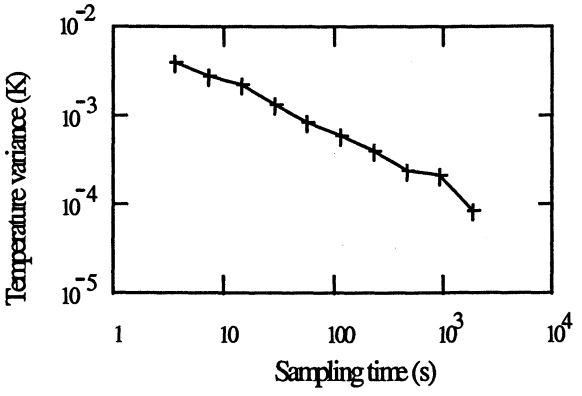

Fig. 3 Two sample variance of the housing temperature as a function of sampling time.

discuss the thermal properties at greater length in another paper within this conference proceedings – Ref. 5, but here we simply note that a discrete temperature differential ΔT exists between rutile and sapphire pucks, given by

$$\Delta T = \frac{P_{Ru}}{K_{Ru}}$$

where P_{Ru} is the power dissipated in the rutile puck component and K_{Ru} is the thermal conductance between sapphire and rutile component. For the value of K_{Ru} = 4.2×10^{-5} W/K, as derived by experiment, and assuming that $P_{Ru} \sim 10^{-5}$ W, a value derived from determining the insertion loss of the resonator itself, including the loss in the microwave cables between room temperature and the cryogenic environment we find

$$\Delta T = 0.24\ K$$

a very substantial temperature difference. Note that a temperature differential between the puck components is not in itself a source of instability since, for any small given temperature differential ΔT there will always be a mean temperature T^* at which $f(T^*)$ will exhibit a turning point.

3.3. Microwave power level control

In view of the evidence presented in the previous section it is important to ensure that the temperature differential ΔT should remain constant. If the heat sink temperature T_0 for the pucks remains fixed the only other source which could result in a variation of ΔT is due to changes in the input microwave power. Thus it becomes essential to stabilise the level of microwave power in the pucks. This need is amplified by the fact that the observed thermal time constants for the two dielectric puck components are different by more than an order of magnitude. This difference means that a sudden increase in power induces an initial increase in frequency (since the thermal time constant for the rutile component (with *+ve df/dT* behaviour) is shorter than for the more massive sapphire puck, with *–ve* coefficient) followed by a slower decrease in frequency as the sapphire component temperature follows this change.

The power level in the pucks cannot be directly measured with our present system. Instead we measure the power using one of two detector diodes, one attached to the third port of the cryo-cooled circulator (see fig. 4) detects the reflected power from the resonator. A second diode at room temperature measures the power fed into the input port of the resonator. The voltage from the selected diode is inverted, with added variable offset, amplified by 100x and low pass filtered (using a Stanford *SR560* low noise amplifier) before being fed to a voltage controlled attenuator (ACA Inc. Type A121) with an attenuation factor of 10 dB/V. The loop gain of this system is around 110. Without stabilisation the power level has been observed to fluctuate by as much as 1 dB over the long term but with the loop power stabilisation in operation the level is stable within the limits of the power level measurement uncertainty (standard deviation of a single measurement $\sigma \sim 0.012$ dB)

To minimise the effect of power fluctuations on the time dependent frequency of the oscillator at least two straightforward approaches could be adopted: either the thermal resistance between the puck components or the absolute power level within the resonator could be reduced. We have proposals for the first which we outline in the section 5, whereas the second has been addressed by minimising the power in the resonator but maintaining constant the oscillation amplitude at the amplifier output by using a –20 dB directional coupler between this output and the input to the resonator.

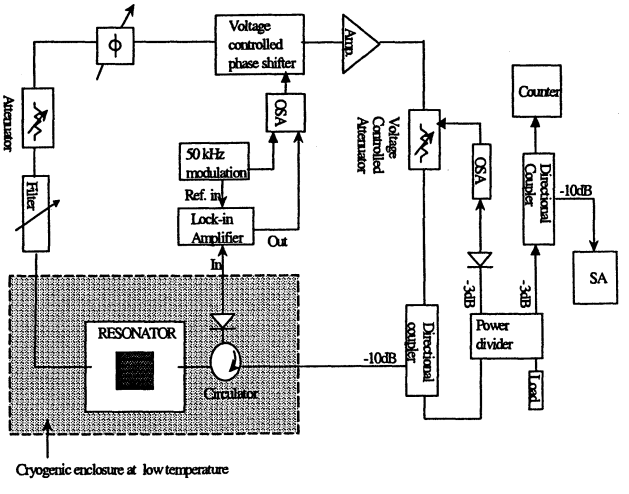

* OSA: Offset & Summing Amplifier

Fig. 4. Schematic of experimental set up of composite puck oscillator.

For optimum unstabilised power the output level of the final amplifier should be adjusted (by means of the mechanical attenuator) to be a few dB below the level at which gain saturation becomes detectable. This measure causes the power dissipated in the rutile element to be reduced to ~ $2x10^{-7}$ W, allowing the temperature differential between puck components to be reduced to ~ 4 mK, even for the low thermal conductance value reported above.

3.4 Ageing and long term stability

A challenging issue for high Q dielectric resonators is the question of their long-term frequency stability. For oscillators without temperature compensation the issue of temperature stability would dominate but for the composite dielectric resonator operated near its turning point other sources of ageing may be investigated. We have previously demonstrated that for our original design of resonator (which used a spring-loaded copper clamp to hold the rutile and sapphire components in good contact) the frequency of the loop oscillator (when maintained close to the turning point temperature) drifted steadily over time, showing an exponential time dependence with a half life of some 30 hours. The most likely source of this drift was creep due to stress relaxation arising from differential thermal contraction following the relatively rapid cool down (2 hours) from room temperature. We have introduced a modification to the present resonator construction in which the rutile and sapphire components are held together with a low microwave loss polymer adhesive and the composite puck is supported on a quartz single crystal spacer. Although the loaded Q seems to have been reduced by a factor of ~ 2 due to the losses in the adhesive this measure appears to have completely eliminated the exponential drift.

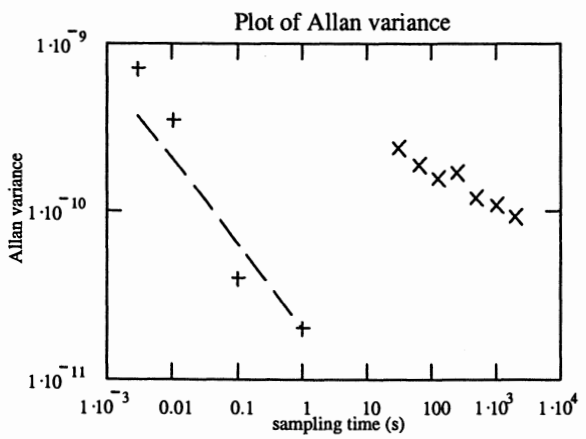

Fig. 5 Allan variance for the oscillator, measured using two different counters, to demonstrate white noise dominated performance for short times and also no long term drift out to 2.10^3 s

4. PRESENT PERFORMANCE

At present we have only a single oscillator based on the design described above. To begin testing its present and potential future stability we have measured the Allan variance of the oscillator against two different reference oscillators. In the first case we have measured the beat frequency (for short sampling times) between the sapphire-rutile referenced oscillator and a synthesised CW source (Anritsu-Wiltron 68037B). A Stanford SR620 counter measured the jitter on the beat frequency for gate times out to 1s. For longer averaging times the oscillator frequency was counted directly with a microwave counter (Marconi 2440) with a fixed gate time of 1s. A Labview program has been written to acquire data over prolonged periods, allowing analysis of the Allan variance subsequently. The combined results of these two measurements are summarised in Fig. 5. Note that the poor performance of the oscillator as measured by this second method is dominated by the jitter of the microwave counter. The purpose in showing this relatively poor data is to demonstrate that the oscillator does not show drift out to sample times of at least 2000 s and probably much longer. The ageing processes which have been detectable in previous designs have been apparently considerably reduced.

5. FUTURE DEVELOPMENTS AND CONCLUSIONS

The next major step to improve the performance of this oscillator involves the replacement of the GM cooler with a modern pulse tube type. In this form the mechanical oscillation of a piston is replaced by an oscillating column of gas, with a resulting major reduction in vibration levels. The specified rms displacement of the cold head is less than 1 μm, less than the level achieved with the present system, after the application of vibration isolation measures.

It should prove possible, for well characterised dielectric puck components, to adjust the thermal time constant of each component to be approximately the same. Thus if the thermal resistance between the rutile and sapphire component can be made greater than that between sapphire puck and the heat sink by the ratio of the heat capacities of sapphire and rutile, the sharply differentiated time constant problem would be removed to first order. This would further improve the limitation set by power level fluctuations.

The thermal conductivity of the adhesive used in this work has been measured to be $1.2x10^{-6}$ W/m.K. This is not far from measured values of similar materials (– Ref. 6) in the temperature range from 30-70 K. The problem of slow variations in power can be minimised if the thermal time constant of the pucks were reduced to be much less than the typical time constant of these fluctuations and this would also serve to lessen the

temperature gradient across the puck components. In future we plan to investigate a number of other methods of joining together the puck components including fusion bonding, 'wringing' together of optically flat components and the use of low melting point crystalline compounds – Ref. 7. When all these measures have been implemented we estimate that the design target for frequency stability of $10^{-13}\ \tau^{-1/2}$ should be attainable, although it must be expected that further unexpected problems remain to be solved.

This work was supported under the UK Department of Trade Industry NMS Foundation Programme (project PF9834) and under the European Commission Framework 5 *CSG* Programme (FOAMS project).

REFERENCES

[1] F Abbas, J. C. Gallop & L.Hao, 'Microwave dielectric composite puck resonators' Applied Superconductivity (IOP Conference Publication 158) pp. 315-8, 1997.

[2] J. C. Gallop, C. D. Langham, L. Hao and F. Abbas, "Dielectric loaded HTS resonators as frequency standards and low phase noise oscillators," *IEEE Trans. Instrum. Meas.*, vol. 46, pp. 122-125, April, 1997.

[3] M E Tobar, J Krupka, J G Hartnett E N Ivanov & R A Woode, "High Q sapphire-rutile frequency temperature compensated microwave dielectric resonators", IEEE Trans. Ultrasonics vol. 45 pp.830-5, May, 1998

[4] L Hao, N Klein, J C Gallop, W J Radcliffe & I S Ghosh, "Temperature compensated cryogenic whispering gallery mode resonator for microwave frequency standard applications," *IEEE Trans. Instrum. Meas.*, vol. 48, pp. 524-527, April, 1999.

[5] L Hao & J C Gallop, "Measurement of thermal conductance of interfaces using microwave resonant composite dielectric structures", presented at 15th EFTF (March 2001)

[6] F. Pobell "Matter & methods at low temperatures", Springer (Berlin) 1996

[7] Mark Oxborrow (NPL) – private communication.

MEASUREMENT AT MICROWAVE FREQUENCIES OF DIELECTRIC PROPERTIES OF $La_3Ga_5SiO_{14}$ BETWEEN 10K AND 400K

Vincent GIORDANO*, Yann KERSALÉ* and Jean Jacques BOY◇

* LPMO CNRS, 32 av. de l'Observatoire, F-25044 Besançon, France
fx +33.381.666998, e-mail giordano@lpmo.edu

◇ Laboratoire de Chronométrie, Électronique et Piezoélectricité.
ENSMM 26, chemin de l'Épitaphe, 25000 Besançon FRANCE.

Abstract

Single crystals as sapphire, rutile, quartz, $LaAlO_3$ or MgO are currently used in the design of microwave resonators, filters or subtrats. These materials show a high temperature sensitivity of permittivity leading to frequency variations with temperature. Langasite has been extentively studied as ultrasonic waves propagation medium. Preceeding measurements at low frequencies show that LGS has two permittivity components of opposite sign [1]. As it is demonstrated in this paper, such an unique characteristic can exploited to realize a self–compensated microwave resonator.

We report measurements of dielectric permittivity and dielectric losses at microwave frequencies of Lanthanum Gallium Silicate single crystal as a function of the temperature. The dielectric rod resonator method was used to evaluate the two relative permittivity tensor components ϵ_t and ϵ_z of this uniaxial dielectric crystal.

Between 10 K to 400 K, ϵ_t varies from 18.92 to 19.65 whereas ϵ_z ranges from 60.75 to 46.66. Around 300 K, the temperature coefficients of ϵ_t and ϵ_z are equal to 130 ppm/K and -720 ppm/K respectively. These temperature coefficients enable to design microvave LGS resonators presenting a low temperature sensitivity. Preliminary measurements of LGS dielectric losses are also presented.

1 Introduction

Telecommunication, space and metrological applications need significant improvements in the performances of microwave devices such as oscillators and filters. These high technology applications can benefit from the availability of high purity single crystal dielectrics combined with reliable cryocoolers achieving temperature as low as 10K. Sapphire (Al_2O_3) exhibits ultra low losses in X-band and thus is the most efficient material to build high Q-resonators.[1,2] Quartz has been proposed for Ku-band and millimeter wave resonators.[3,4] Compact resonators with high performances have been designed with high permittivity dielectrics as Rutile (TiO_2).[5] $LaAlO_3$ and MgO are currently used as substrata for HTS films deposition.[6] Nevertheless, the relative permittivity ϵ_r of these materials, presents a high temperature sensitivity which transforms temperature fluctuations into frequency fluctuations.[7,8] High frequency stability can only be achieved with a sapphire resonator at ultra low temperature near 4K limiting thus their range of applications.[9,10] At upper temperatures, some other solutions as mechanical compensated structures or composite resonators have been studied. These structures are difficult to design and to construct and suffer from mechanical sensitivity.[11–14]. Thus, there is a great interest in the measurement of other dielectric crystals to extend the range of available materials for the microwave resonator designer.

In this letter, we report measurements of relative permittivity components and dielectric losses of Lanthanum Gallium Silicate ($La_3Ga_5SiO_{14}$, Langasite or LGS) between 400K and 10K. LGS is an uniaxial crystal which has been firstly developed for laser applications.[15] It is now extensively used for its good piezoelectric and thermal properties enabling the design of efficient ultrasonic resonators and filters operating in RF and VHF frequency ranges.[16,17,18] Nevertheless, the thermal behavior of LGS dielectric properties at microwave frequencies has never been published up to now.

2 Permittivity measurements

Our permittivity measurement procedure is based on the dielectric rod resonator method.[19] A cylindrical dielectric rod sample of diameter ϕ, length l and unknown relative permittivity ϵ_r is inserted between the two parallel conducting plates of a Courtney-type cavity similar to that described by Krupka et al.[8] For such a microwave structure, resonant mode frequencies can be computed with a great accuracy. Therefore, ϵ_r can be determined from the measured reso-

nant frequency of one particular mode of the Courtney cavity and by solving its characteristic equation. It is a common use to choose the TE_{011} mode which is easily recognizable and weakly affected by the resonant structure imperfections. For an anisotropic sample, the crystal c-axis has to be aligned with the rod axis. We define ϵ_t and ϵ_z as the relative permittivity perpendicular and parallel to the c-axis respectively. In the cylindrical coordinate of the resonant structure, the relative permittivity tensor $[\epsilon_r]$ is

$$[\epsilon_r] = \begin{bmatrix} \epsilon_t & 0 & 0 \\ 0 & \epsilon_t & 0 \\ 0 & 0 & \epsilon_z \end{bmatrix} \quad (1)$$

For this class of materials, ϵ_t is computed as previously from the resonant frequency of the TE_{011} mode. Then, the measurement of the hybrid HE_{111} frequency enables to collect additional data required to determine ϵ_z. We had at our disposal a large LGS crystal of russian origin grown a few years ago. We prepared a first cylindrical sample whose diameter is $\phi = 9.66 \pm 0.01$ mm and length is $l_1 = 11.82 \pm 0.01$ mm. The rod axis and the crystal c–axis are aligned within 1°. The Courtney cavity has an internal diameter of 60 mm and is made entirely in gold plated OFHC cooper. Frequency and Q-factor measurements were performed with a network analyzer. At 300K, TE_{011} and HE_{111} resonance frequencies are 6.66 GHz and 4.41 GHz respectively. The cavity containing the sample was placed on the cold finger of a closed-cycle cryocooler (see fig 1).

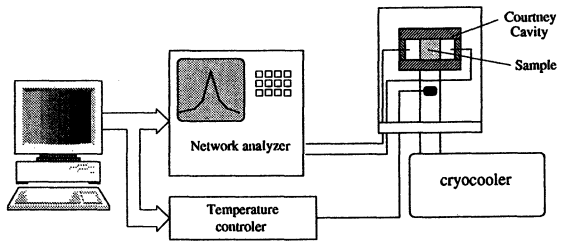

Figure 1: *Experimental set-up for the measurement of relative permittivity*

Temperature regulation within 0.01K is performed thanks to a PID temperature controler connected with resistive heaters and a silicon diode sensor both placed on the cold finger. After cooling down to 10K the cavity temperature was slowly increased step by step and measurements taken every 10K. Sample dimensions have been computed taking into account the thermal expansion coefficients of LGS found in the litterature.[20] Then by solving the characteristic equations of TE_{011} and HE_{111} modes, we extracted ϵ_t and ϵ_z as a function of temperature. Obtained data are given in figures 1 and 2. The accuracy in the values of ϵ_t and ϵ_z is better than 1% mainly limited by the uncertainty in the sample dimensions.

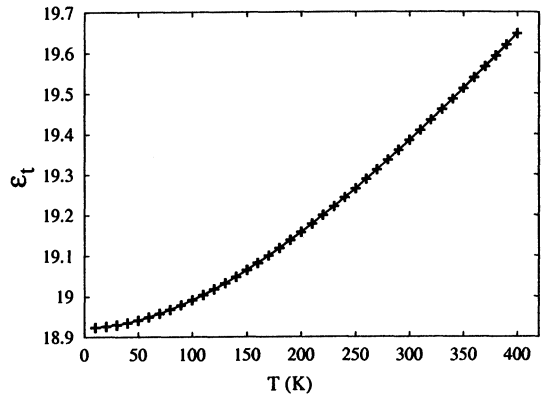

Figure 2: *Variation of the relative permittivity component ϵ_t perpendicular to the c–axis of Langasite crystal with temperature*

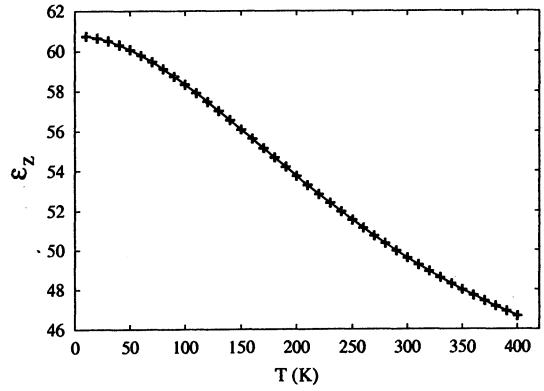

Figure 3: *Variation of the relative permittivity component ϵ_z parallel to the c–axis of Langasite crystal with temperature*

In order to give a useful approximation of the thermal behavior of LGS, we fitted preceeding data with forth-order polynomial laws assuming that:

$$\epsilon(T) \approx a_4 T^4 + a_3 T^3 + a_2 T^2 + a_1 T + a_0 \quad (2)$$

Where coefficients a_i are given in Table I for ϵ_t and ϵ_z.

3 Temperature coefficients of mode frequencies

Compared with other crystals, LGS features a high anisotropy ratio, i.e. $\epsilon_z/\epsilon_t \approx 3$. Moreover ϵ_t and ϵ_z show temperature coefficient of opposite sign. At ambient temperature:

$$\frac{1}{\epsilon_t}\frac{\partial \epsilon_t}{\partial T} = 131 \times 10^{-6}/K \quad \frac{1}{\epsilon_z}\frac{\partial \epsilon_z}{\partial T} = -720 \times 10^{-6}/K \quad (3)$$

This unique characteristic can be exploited to design a self-compensated resonator as shown in figure 3.

Table 1: Coefficients of polynomial approximation for LGS relative permittivity components

a_i (K^{-i})	ϵ_t	ϵ_z
a_4	6.49×10^{-12}	-7.49×10^{-10}
a_3	-1.06×10^{-8}	8.73×10^{-7}
a_2	7.71×10^{-6}	-3.15×10^{-4}
a_1	2.39×10^{-6}	-1.32×10^{-3}
a_0	18.923	60.811

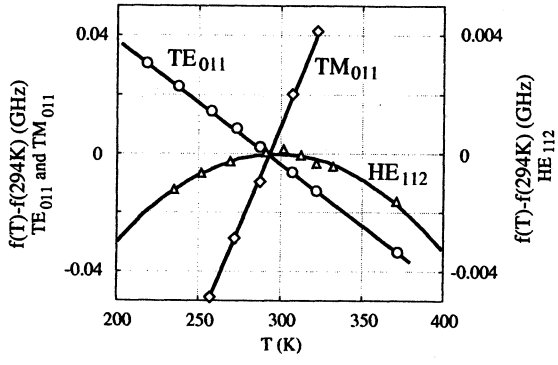

Figure 4: *Variation of the resonant frequencies with temperature of three modes TE_{011} mode (circles and left scale), TM_{011} mode (squares and left scale) and HE_{112} mode (triangles and right scale)*

This figure reports the frequency variation of three modes of the Courtney cavity, i.e. TE_{011}, TM_{011} and HE_{112}, when temperature is raised from 200 K to 400 K. Note the different scale for HE_{112} which is ten times smaller than the other one. TE_{011} and TM_{011} modes have a quasi-linear frequency variation with temperature, whereas HE_{112} mode presents a turnover temperature, i.e. $T_0 = 294K$. At T_0 the temperature sensitivity of HE_{112} is canceled at first order. These behaviors can be easily understood by neglecting the contribution of thermal expansion which leads to a second order effect. In these conditions, the frequency temperature dependance of any resonant mode of the structure can be written as:

$$\frac{1}{f}\frac{\partial f}{\partial T} \approx -\frac{1}{2}\ p_t\left[\frac{1}{\epsilon_t}\frac{\partial \epsilon_t}{\partial T}\right] - \frac{1}{2}\ p_z\left[\frac{1}{\epsilon_z}\frac{\partial \epsilon_z}{\partial T}\right] \quad (4)$$

where p_t and p_z are the electric energy filling factors in the dielectric sample perpendicular and parallel to the z-axis respectively. p_t and p_z are obviously positive or null functions on the resonator geometry and permittivity. For TE_{011} mode, the electric field is transverse, i.e $p_z = 0$ and $p_t \approx 1$. The resonant frequency depends only on ϵ_t and decreases with temperature. For TM_{011} mode, the electric field is essentially axial: $p_z \approx 0.73$ and $p_t \approx 0.23$. The temperature coefficient of frequency is then positive. At $T_0 = 294$K and for HE_{112} mode, the two right terms in equation (4) balance themselves leading to a minimum in frequency temperature sensitivity. We computed the turnover temperature for HE_{112} as a function of the dielectric rod aspect ratio l/ϕ (see figure 4).

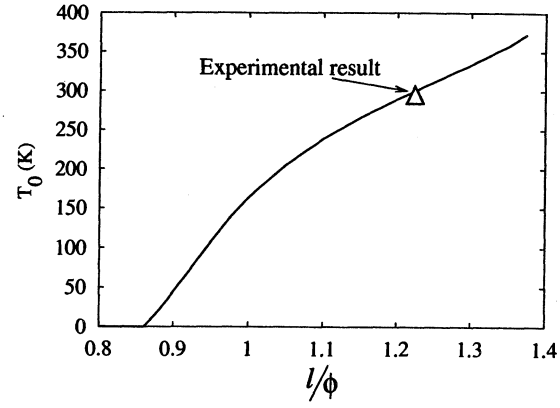

Figure 5: *Calculated turnover temperature T_0 as a function of l/ϕ for HE_{112} mode of a Courtney cavity loaded with a LGS rod ϕ diameter and l length.*

This calculation is based on the preceeding measured permittivities and takes into account the thermal expansions of LGS and copper. The experimental turnover temperature agrees quite well with the theoretical model strengthening our confidence in the measured values of LGS permittivity components. The small departure from - 4 K can be attribued to residual uncertainties in sample dimensions and in thermal expansion coefficients of LGS. Although Courtney cavity HE_{112} mode has no real interest for direct applications, it proves the feasibility of a self-compensated resonator. This compensation mechanism can be extented to more useful structures consisting of an isolated resonator or a dielectric resonator mounted on a microstrip.

4 Dielectric losses

In a first attempt to evaluate LGS dielectric losses, we implemented the method described by Kobayashi .[21] Another LGS rod of length $l_2 = l_1/2 = 5.91$ mm has been cut from the same crystal. Sample 1 (11.82 mm length) and sample 2 (5.91 mm length) have been successively inserted in the measurement apparatus and excited respectively on TE_{012} and TE_{011} modes. Prodived that l_2 equals exactly $l_1/2$, these modes have the same resonance frequency. Experimentally we observed a departure from 2 MHz for a mean frequency of 8.8 GHz. Moreover the contribution of the surface resistance of the cavity copper plates on Q-factor is the same for the two resonators.

In these conditions, the loss tangent tanδ of the material can be expressed as:

$$\tan\delta = A\left[\frac{2}{Q_1} - \frac{1}{Q_2}\right] \quad (5)$$

where Q_1 and Q_2 are the unloaded Q-factors of resonator 1 and 2 respectively. A is a parameter nearly equal to unity and depends on the resonator geometry and permittivity. In our case $A = 1.02$. The evaluation of the resonator unloaded Q-factor needs an accurate calibration of the measurement set-up at the resonator ports. Such a calibration has been only achieved at ambient temperature before closing the cryocooler vaccum can and thus it was not possible to ensure a uncertainty better than 5.10^{-6} on the entire temperature range. Obtained values of tanδ as a function of temperature are shown in figure 5. At low temperature, the evolution of LGS tanδ can be approximated as:

$$\tan\delta \approx 5.6 \times 10^{-8} T^{1.55} \quad (6)$$

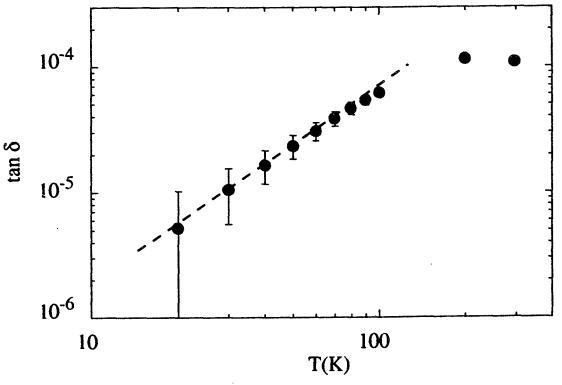

Figure 6: *Dielectric losses* tanδ *of langasite. Measured values (dots) and power law approximation at low temperature (dashed line)*

5 Conclusion

Dielectric losses of our LGS sample appear relatively high compared to other more usual dielectric crystals. It should be noted that our sample does not represent the state of the art of LGS crystal quality. Growth techniques of LGS monocrystals are currently studied and improved.[22] Supplemantary measurements on new materials are needed to conclude on the ability of LGS to be used for the design of high-Q microwave resonators. Nevertheless, around 80K which is a temperature easily achievable with low cost cryocooler, LGS offers the possibility to built microwave resonators presenting Q–factor of the order of 50,000 and low frequency sensitivity on temperature fluctuations.

6 References

[1] A.N. Luiten, A.G. Mann and D.G. Blair, Electronics Letters, **29**,(10), 879 (1993).

[2] J. Krupka, D. Cros, A. Luiten and M.E. Tobar, Electronics Letters, **32**, (7), 670 (1996).

[3] I. Lajoie, R. Barhaila, Y. Kersalé, D. Cros, D. Duchiron and V. Giordano,
Electronics Letters, **36**,(2), 150 (2000).

[4] J. Krupka, D. Cros, M. Aubourg and P. Guillon, IEEE Trans. on MTT, **42**, (1), 56 (1994).

[5] N. Klein, C. Zuccaro, U. Dähne, H. Schutz and N. Tellman, J. Appl. Phys., **78**,(11), 6683 (1995)

[6] M.Reppel and J.C. Mage, IEEE MGW Letters, **10**,(5), 180 (2000).

[7] J. Krupka, K. Derzakowski, M.E. Tobar, J. Harnett and R.G. Geyer, Meas. Sci. Technol., **10**,387 (1999).

[8] J. Krupka, R.G. Geyer, D. Kuhn and J.H. Hinken, IEEE Trans. on MTT, **42**,(10), 1886 (1994).

[9] A.N. Luiten, A.G. Mann, M.E. Costa and D.G. Blair, IEEE Trans on IM, **44**, (2), 132 (1995).

[10] R.T. Wang and G.J. Dick, IEEE Trans. on IM, **48**,(2), 528(1999).

[11] GJ. Dick, D.G. Santiago and R.T. Wang, in Proceedings of the 10^{th} European Frequency and Time Forum (Brighton UK 1996) published by the Institute of Electrical Engineers London UK., ISSN 0537–9989, pp. 262-265.

[12] V. Giordano, Y. Kersalé, O. Di Monaco and M. Chaubet, European Physical Journal AP, **8**, (3), 269 (1999).

[13] M.E. Tobar, J.G. Harnett, E.N. Ivanov, D. Cros, P. Blondy and P. Guillon, IEEE Trans. on MTT, **48**, (7), 1265 (2000).

[14] L. Hao, N. Klein, J.C. Gallop, W.J. Radcliffe and I.S. Ghosh, IEEE Trans. on IM, **48**, (2), 524 (1999).

[15] A.A. Kaminskii, I.M. Silvestrova, S.E. Sarkisov and G.A. Denisenko, Phys. Stat. Sol (a), **80**, 607 (1983).

[16] R.C. Smythe, R.C. Helmbold, G.E. Hague and K.A. Snow, IEEE Trans. on UFFC, **47** , (2), 355 (2000).

[17] N.F. Naumeko and L.P. Solie, in Proceedings of the 1999 IEEE Ultrasonics Symposium (Caesars Tahoe, Nevada USA, 1999), published by the Institute of Electrical and Electronic Engineers New-York USA, ISSN 1051–0117, pp. 243–248

[18] G.D. Mansfeld in Proceedings of the 12^{th} European Frequency and Time Forum, (Warsaw, Poland 1998), published by Tele and Radio Research Institute Warsaw Poland, pp. 61–65.

[19] W.E. Courtney, IEEE Trans. on MTT, **18**,(8), 476 (1970).

[20] I.M. Silvestrova, Y.V. Pisarevskii, P.A. Senyushchenkov and A.I. Krupnyl, Sov. Phys. Solid State, **28**, (9), 1613 (1986).

[21] Y. Kobayashi and M. Katoh, IEEE Trans. on MTT, **33**,(7), 586 (1985).

[22] A.N. Gotalskaja, D.I. Dresin, S.N. Schegolkova, N.I. Savela, V.V. Bezdelkin and G.N. Cherpoukhina, in Proccedings of the 1995 IEEE International Frequency Control Symposium, (San Francisco, CA USA, 1995), published by the Institute of Electrical and Electronic Engineers New–York USA, ISBN 0–7803–25001, pp. 657–666.

TEMPERATURE STABILIZATION OF A SOLID-NITROGEN-COOLED SECONDARY FREQUENCY STANDARD

J.G. Hartnett, P. Bilski, M.E. Tobar, E.N. Ivanov

Department of Physics, University of Western Australia, 35 Stirling Hwy, Crawley WA 6009 Australia
Email: john@physics.uwa.edu.au

Abstract : We report on the frequency stability, expected in a cryogenic solid-nitrogen-cooled temperature-stabilised oscillator. The temperature fluctuations of both a liquid and a solid nitrogen bath, at 77 K and 52 K, respectively, were directly measured. Using a free runnning loop oscillator at 12.03 GHz, based on a temperature compensated composite rutile-sapphire resonator, the temperature fluctuations in the resonator were also measured. The results indicated that solid nitrogen, due to its large thermal heat capacity, has an order of magnitude lower temperature instability than liquid nitrogen. The temperature fluctuations at the cavity resonator were estimated to be of the order of 100 nK at 1s when immersed in the solid nitrogen bath.

Keywords: Temperature stabilisation, Allan deviation, fraction frequency fluctuations, thermometer

1. INTRODUCTION

To construct low noise and high stability oscillators, the high Q-factor of sapphire is essential. This ensures good short-term frequency stability resulting from a high sensitivity of the control electronics to frequency fluctuations. However, to improve the long-term frequency stability of the oscillator the temperature induced frequency fluctuations should be suppressed.

At liquid helium temperatures, frequency-temperature compensation of monolithic sapphire resonators has been achieved by the residual paramagnetic impurities of the order of a few parts per million [1-2]. Intentionally doped sapphire with a larger concentration of Ti^{3+} ions was used to raise the temperature of compensation above 50 K [3]. Another technique achieved compensation at about 10 K, in a composite ruby-sapphire structure [4].

A mechanical compensation technique [5] involves a coupled mode resonator to cancel the resonator's temperature dependence above 77 K. Another technique utilizes composite dielectric structures consisting of more than one low loss monocrystal. For example, two very thin slices of monocrystalline rutile were clamped tightly against the ends of a cylinder of sapphire monocrystal [6-8]. The temperature coefficient of permittivity of sapphire and rutile are of opposite sign and thus the temperature coefficient of the composite resonator was annulled at temperatures above 50 K. Such a resonator was used in the oscillator reported in this paper.

In order to take full advantage of the reduced sensitivity to temperature fluctuations in the resonator, and understand the contribution temperature makes to an oscillator's frequency stability, it is necessary to measure and control the temperature fluctuations in the resonator under operating conditions.

2. THERMOMETERS

Any temperature control system for a highly stable oscillator or any temperature measurement system will have a temperature sensitive element at its heart. In order to determine which one would be the most suitable for our application at temperatures accessible with liquid or solid nitrogen, it was necessary to characterize the temperature dependence of the commercially available resistance-thermometers. The sensitivity of a resistance-thermometer is defined as

$$\theta(T) = \frac{T}{R_{Th}} \frac{\partial R_{Th}}{\partial T} \qquad (1)$$

where T is the temperature (in kelvin) and R_{Th} the resistance (in Ohms) across the thermometer at temperature T. A number of thermometers were investigated and their dimensionless coefficient or sensitivity compared (see fig. 1). Over the desired temperature range (50 K – 77 K), the platinum resistance thermometer (PRT) (curve 1) had the highest sensitivity, and, as a result for this experiment, was chosen as the best choice.

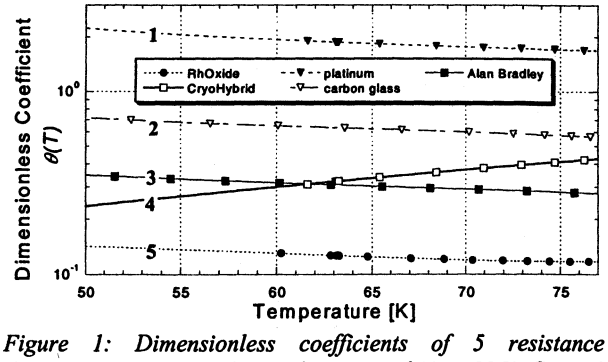

Figure 1: Dimensionless coefficients of 5 resistance thermometers measured over the range of 50 to 77 K. Curve 1 was a standard platinum strip (PRT), curve 2 a carbon-glass Lakeshore CGR-1-2000 type, curve 3 an Alan Bradley resistor, curve 4 a Neocera CryoHybrid, and curve 5 was a Scientific Instruments (USA) ruthenium oxide RO105 type thermometer.

3. AC-BRIDGE READ-OUT

The measurement system implemented was a bridge with ac excitation (see fig 2). The ac-bridge circuit was part of a temperature controller supplied by Poseidon Scientific Instruments P/L, Fremantle, Western Australia. The bridge driving voltage (u_0) was supplied by an on-board (150mV, 238 Hz) signal oscillator. The bridge was balanced using the variable resistor (R_B). The 2 kΩ and 10 Ω resistors were high-precision low-temperature coefficient type resistors. Only the

PRT and its leads were in the cryogenic environment. The bridge error voltage was amplified by an ac-coupled amplifier, then demodulated and read out on a DVM and recorded by computer.

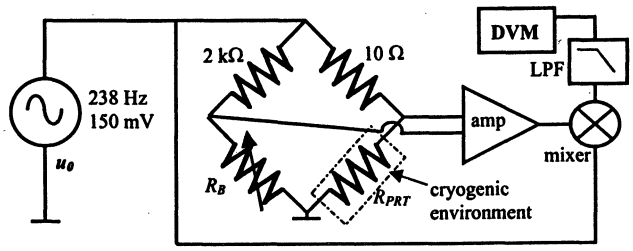

Figure 2: The ac bridge used to measure voltage fluctuations in a Platinum resistance thermometer (labelled R_{PRT}).

The bridge error voltage fluctuations at the output of the mixer in fig. 4 (δu_{mix}) are related to the temperature fluctuations of the PRT by

$$\delta u_{mix} \approx R_{PRT} \frac{\partial u}{\partial R_{PRT}} \theta(T_0) \frac{\delta T}{T_0}. \qquad (2)$$

where $\partial u/\partial R_{PRT}$ is a parameter that characterises the measurement system sensitivity, δT is the ambient temperature fluctuations, R_{PRT} is the resistance of the PRT at some mean temperature T_0.

If the bridge stays balanced, the noise from the source is rejected. (There was some systematic drift from this balance, which was subtracted from the raw data). After taking the statistical Allan variance [9] of fractional fluctuations of temperature and voltage, the square root Allan variance or Allan deviation of fractional temperature fluctuations (σ_T) was calculated. From (2), the Allan deviation of fractional temperature fluctuations (σ_T) is related to the Allan deviation of fractional voltage fluctuations (σ_u), by,

$$\sigma_T \approx \frac{\sigma_u}{\frac{\partial u}{\partial R_{PRT}} R_{PRT}(T_0)\theta(T_0)}. \qquad (3)$$

4. TEMPERATURE FLUCTUATIONS OF THE NITROGEN BATH

Using the circuit of fig. 2, the voltage fluctuations out of the bridge were recorded with the PRT positioned in the cryogenic fluid just above the brass vacuum can (see fig. 3). The results are plotted in fig. 4 for the liquid nitrogen bath (curve 1) and solid nitrogen bath (curve 2). The nitrogen was solidified by pumping constantly on the fluid at a pressure below 10^{-1} torr. The temperature was maintained at around 52 K. The measurement system noise floor (curve 3) was measured with a temperature-insensitive resistor. The solid nitrogen data were very close to the noise floor at short integration times, and should only be considered as an upper limit.

A temperature control circuit was designed with the control PRT situated very close to a small 30 W foil heater, which was attached to the copper post supporting the cavity (see fig. 3). The copper post was connected to the brass vacuum can by a stainless-steel post and 3 mounting bolts. When the vacuum was sustained, the stainless-steel post provided good thermal impedance, and allowed the temperature to be stabilised at a chosen set point, above the bath temperature.

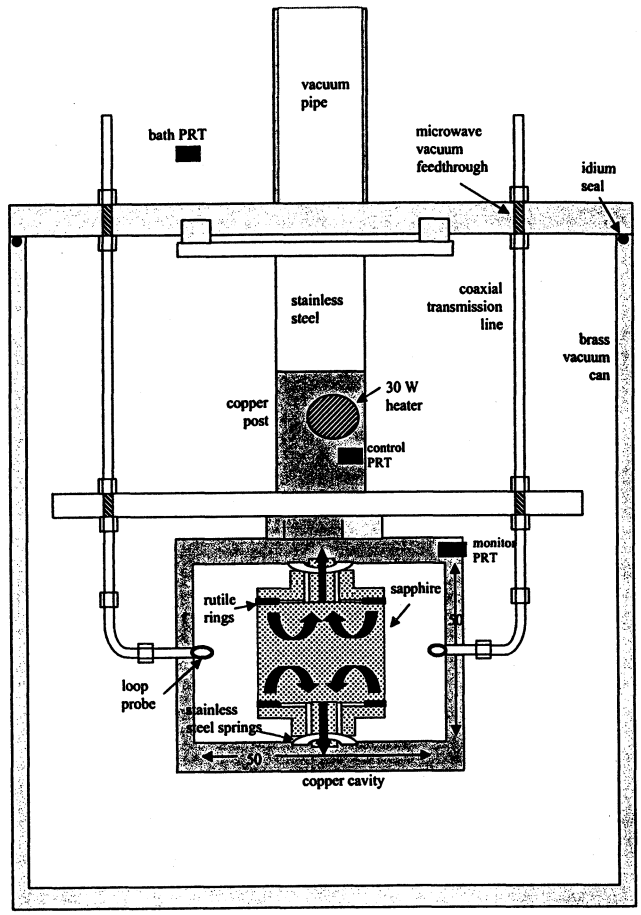

Figure 3: Simplified design of the cryostat insert showing brass vacuum can and composite rutile/sapphire resonator loaded copper cavity. Black arrows indicate path of heat flow.

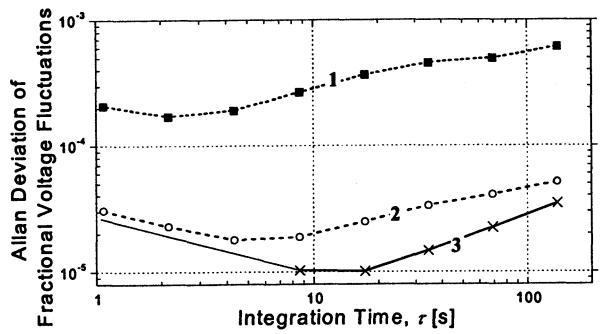

Figure 4: The Allan deviation of voltage fluctuations out of the bridge (normalised by the bridge sensitivity). Curve 1 is for the liquid nitrogen bath, curve 2 for the solid nitrogen bath and curve 3 is the measurement system noise floor.

The voltage fluctuations (σ_u) at the cavity (see control PRT in fig. 3) for various set points between 58.5 K and 80 K were measured. These voltage fluctuation measurements were not significantly distinguishable from the noise floor (curve 3). However, the results for the liquid nitrogen (curve 1) and solid

nitrogen above 10 s of integration time (curve 2) were sufficiently above the noise floor to be significant.

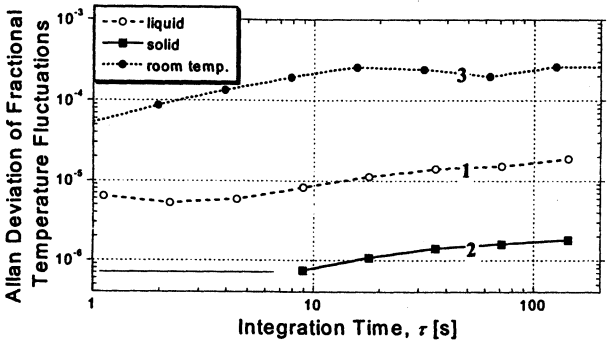

Figure 5: The Allan deviation of fractional temperature fluctuations of a liquid nitrogen bath (curve 1) and a solid nitrogen bath (curve 2) measured with the ac-bridge. Curve 3 are the measured room temperature fractional fluctuations.

Using (3), the data in fig. 4 was converted into Allan deviation of fractional temperature fluctuations (σ_T) (see fig. 5). A comparison is made between room temperature (curve 3) and liquid nitrogen (curve 1) and solid nitrogen (curve 2).

5. THERMAL TIME CONSTANTS

The temperature controller stabilises the temperature at the point where the PRT is located very close to the heater (see fig. 3). The level at which we were able to control the temperature at the cavity depends on the bath and temperature control system but the temperature stability at the sapphire resonator depends on the thermal resistance and heat capacity of the sapphire dielectric itself. Using data taken from [10] for the thermal conductivity and the specific heat of sapphire and rutile, the thermal time constants were calculated for a composite rutile/sapphire resonator [11, 12]. Because the mass of the rutile is small with respect to sapphire, over the temperature range, 50 K – 77 K, the thermal time constant for the rutile rings (of 0.4 mm thickness) is 5 ...18 times less than for the sapphire resonator alone. Therefore, provided the surface contact zones of the rutile annuli and the sapphire do not introduce large thermal resistance, the rutile rings do not limit the time constant of the resonator. Surface roughness will have the effect of increasing the time for the different pieces to come into equilibrium with each other. Also it is worth noting that in the sapphire dielectric the thermal time constant is 4 ms and 72 ms at 50 K and 77 K, respectively. This indicates that the thermal time constant associated with heat path shown in black arrows in fig. 3 will come from the interfaces between sapphire and the copper cavity lids and between the gaps in the structure, which haven't been considered.

6. LOOP OSCILLATOR

With the temperature servo running, the temperature fluctuations could not be measured using the ac-bridge because of the measurement system noise floor. For this reason, a free running loop oscillator (fig. 6) was used to get an estimate of the effects of temperature fluctuations on oscillator frequency stability.

The loop oscillator incorporated a 11-14 GHz amplifier, a custom-made band-pass filter, a mechanical phase shifter and a mechanical attenuator in die-cast aluminium box anchored to a 16-mm thick aluminum plate, with stainless screws. The amplifier was thermally grounded to the base-plate. The resonator coupling on both probes was approximately 0.005, set previously to measure the Q-factor as a function of temperature. This resulted in a resonator insertion loss of 44 dB. As a result, no Pound frequency discriminator and electronic-noise-reduction servo was implemented. The oscillator frequency was down-converted by beating it with a HP8673G synthesizer locked to an Oscilloquartz 5 MHz reference, and counted on a HP53131A frequency counter.

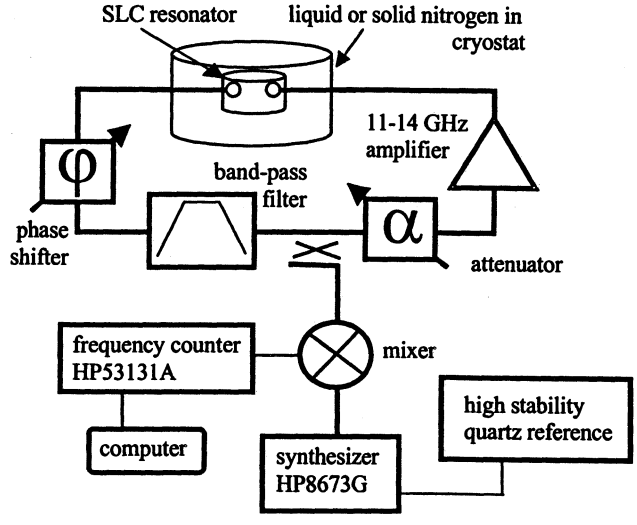

Figure 6: Schematic of loop oscillator used. Temperature control servo is not shown.

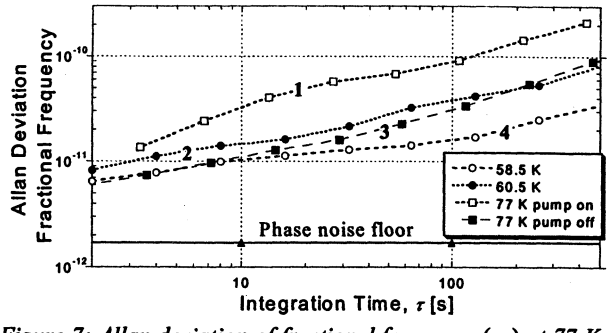

Figure 7: Allan deviation of fractional frequency (σ_y) at 77 K without the temperature servo running with the vacuum pump on (curve 1); σ_y at 60.5 K with the temperature servo and the vacuum pump on (curve 2); σ_y at 77 K without the temperature servo and vacuum pump off (curve 3); σ_y at 58.5 K with the temperature servo and the vacuum pump on (curve 4). The phase noise floor is the Allan deviation of fractional frequency calculated from a phase noise measurement of the active components of the loop oscillator under the same power conditions and bandwidth as the 77 K oscillator.

To determine the stability of the HP synthesizer, we used a similar synthesizer with both referenced by there own internal quartz 10 MHz quartz oscillators, and recorded the beat frequency of the two 12.03 GHz signals separated by about 65 kHz. The Allan deviation of fractional frequency fluctuations for the synthesizer was calculated to be 1.1×10^{-12} at 1 s rising to 2.5×10^{-12} at 100 s. The Oscilloquartz reference oscillator has been measured to have $\sim 3 \times 10^{-13}$ stability, and as a result

the HP8673G synthesizer, referenced to this oscillator, would have this stability too.

The Allan deviation of fractional frequency fluctuations was plotted, in fig. 7, for the free running oscillator at 77 K (without the temperature servo operating), but with the vacuum pump running (curve 1). The 77 K measurement was repeated without the vacuum pump running (curve 3). There were no isolators installed in the long microwave coaxial transmission lines leading to the cryogenic resonator (see fig. 3). Therefore, we would expect significant vibration sensitivity due to frequency pulling effects of the probes. Also changes in the bath level would result in temperature induced frequency fluctuations from changes in the coaxial line dielectric permittivity. This is observed with curve 1 significantly higher than curve 3.

Secondly, the Allan deviation of fractional frequency fluctuations was plotted for various operating set points (60.5 K - curve 2, 58.5 K - curve 4). In both cases the vacuum pump was running constantly keeping the nitrogen solid, while the 30 W foil heater raised the cavity temperature to the set point. The fractional frequency stability of the oscillator appears to reach a measurement noise floor (curves 3 and 4 run into each other).

7. TEMPERATURE FLUCTUATIONS IN RESONATOR

Provided temperature fluctuations are the dominant noise mechanism, the fractional frequency fluctuations of an oscillator may be related to the fractional temperature fluctuations of the resonator by

$$\frac{\delta f}{f_0} = \left(\frac{T_0}{f_0}\frac{\partial f}{\partial T}\right)\frac{\delta T}{T_0}. \qquad (4)$$

After calculating the Allan deviation of both frequency and temperature fluctuations, after re-arranging, (4) becomes

$$\sigma_T = \sigma_y \Big/ \left(\frac{T_0}{f_0}\frac{\partial f}{\partial T}\right). \qquad (5)$$

The dimensionless temperature coefficient of frequency (TCF) $(T_0/f_0)df/dT$ for both compensated and pure sapphire was calculated from measured frequency-temperature data and is shown in fig. 8.

Knowing the oscillator's fractional frequency stability (σ_y), the fractional temperature stability (σ_T) can be calculated from (5). From three measurements of oscillator frequency at 77 K, 60.5 K and 58.5 K σ_T was calculated. It has been assumed here that the frequency stability is solely due to temperature fluctuations. This assumption was not completely valid for the latter two temperature set points, as those measurements were closer to the turning point temperature (T_{TP}) of 53.8 K. For these data the value of TCF is considerably reduced as compared with the 77 K measurements. The 60.5 K and 58.5 K data were at least partially affected by other noise sources. These include amplifier phase noise resulting in an oscillator frequency instability at the 1.7×10^{-12} level and length variations of the coaxial microwave transmission lines coupled to the resonator due to fluctuations of the ambient temperature.

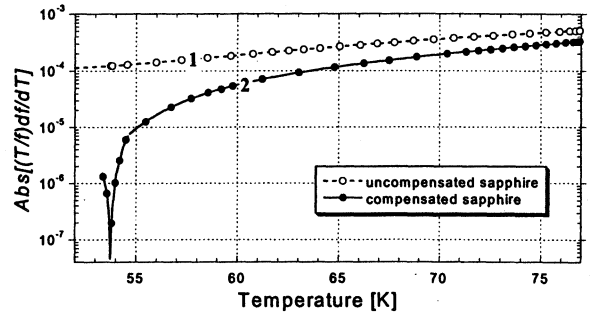

Figure 8: The absolute value of the dimensionless sensitivity parameter (T/f)df/dT for the 12.03 GHz $H_{8,1,\delta}$ mode in the sapphire-rutile compensated resonator (curve 2) calculated from the measured data, compared with the dimensionless sensitivity of the 11.88 GHz $H_{14,1,\delta}$ mode in pure sapphire (curve 1).

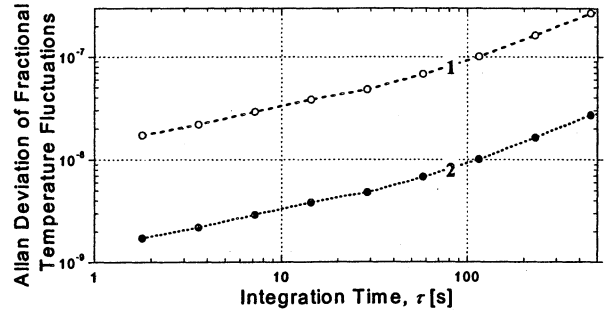

Figure 9: Allan deviation of fractional temperature fluctuations estimated from fractional frequency fluctuations (fig. 7) using the gradient of the frequency-temperature dependence derived from the data in fig. 8. Curve 1 was calculated from curve 3 in fig. 7. Curve 2 is inferred from the order of magnitude lower Allan deviation of fractional temperature fluctuations of the solid nitrogen bath over that of the liquid bath.

Therefore, by making sure that the frequency stability measurement was dominated by temperature fluctuations, by operating at a temperature where df/dT is large, we determined the temperature stability at the cavity to be about 1 μK at 1 s rising to 10 μK at 100 s (at $T_0 = 77$ K).

From a comparison of the liquid and solid nitrogen temperature fluctuations in fig. 5, the temperature fluctuations at the cavity in a solid nitrogen bath (curve 2 in fig. 9) are inferred to be an order of magnitude less than at the cavity in a liquid nitrogen bath (curve 1). This means that fluctuations of the sapphire loaded cavity (SLC) temperature at 52 K can be estimated to be 100 nK at 1 s rising to 500 nK at 100 s.

To measure the temperature fluctuations more precisely using the frequency data, the oscillator must be tightly locked to the SLC resonance (making use of a Pound technique). This will be implemented in the next phase of the development of the temperature compensated-resonator oscillator.

8. DISCUSSION

The fractional frequency of a frequency-temperature compensated resonator sufficiently close to the turning point (T_{TP}) can be expressed as a quadratic function in (T–T_{TP}). When operating an oscillator with such a resonator, (4) must

be replaced by an equation in the second derivative. From this we can derive

$$\sigma_y = T_{TP} \cdot \left(\frac{1}{f_0} \frac{\partial^2 f}{\partial T^2} \right) \cdot \sigma_T \cdot \Delta T \qquad (6)$$

where $\Delta T = |T - T_{TP}|$, which represents the operating temperature offset from the turning point.

The Allan deviation of fractional frequency fluctuations due to temperature fluctuations was calculated from (6) based on the estimate of temperature fluctuations (σ_T) at the cavity in a solid nitrogen bath (curve 2 from fig. 9). It was assumed that ΔT = 1 mK and $1/f_0(\partial f/\partial T^2)$, the fractional curvature was measured in the $H_{8,1,\delta}$ mode at the T_{TP} = 53.8 K to be 8×10^{-8} K^{-2}. The result is $\sigma_y = 6.4 \times 10^{-18}$ at 1 s rising to 4×10^{-17} at 100 s. Therefore the temperature control requirements are considerably relaxed, even increasing ΔT by 100 times the temperature induced noise floor is still less than the target of 1×10^{-14} at 1 s.

9. CONCLUSION

The temperature fluctuations of both a liquid and a solid nitrogen bath, at 77 K and 52 K, respectively, were directly measured. A solid nitrogen bath was found to have an order of magnitude lower temperature instability than liquid nitrogen. The temperature fluctuations in a resonator, filtered by a high thermal impedence, were also measured. This yielded a value of 100 nK at 1 s of averaging time. Calculations based on solid nitrogen bath fluctuations, passively filtered at the cavity, indicate that an oscillator with sub-10^{-14} fractional frequency stability at 1 s, due to temperature control, is a modest expectation provided a temperature compensated resonator is used.

ACKNOWLEDGEMENT

The authors wish to acknowledge the contributions of the Australian Research Council (ARC) and Poseidon Scientific Instruments Pty Ltd.

REFERENCES

[1] S. K. Jones, D. G. Blair, and M. J. Buckingham, "The effects of paramagnetic impurities on the frequency of sapphire loading superconducting resonators," *Electron. Lett.*, vol. 24, pp. 346-347, 1988.

[2] A. N. Luiten, A. G. Mann, and D. G. Blair, "High resolution measurement of the temperature-dependence of the Q, coupling and resonant frequency of a microwave resonator," *IOP Meas. Sci. Technol.*, vol. 7, pp. 949-953, 1996.

[3] J. G. Hartnett, M. E. Tobar, A. G. Mann, E. N. Ivanov, and J. Krupka, "Frequency-temperature compensation in Ti3+ and Ti4+ doped sapphire whispering gallery mode resonators," *Proc. IEEE Int. Freq. Contr. Symp.*, pp. 512-517, 1998.

[4] G. J. Dick and R. T. Wang, "Cryo-cooled sapphire oscillator for the Cassini Ka-band experiment," *Proc. IEEE Int. Freq. Cont. Symp.*, pp. 1009-1014, 1997.

[5] G. J. Dick, D. G. Santiago, and R. T. Wang, "Temperature compensated sapphire resonator for ultra-stable oscillator capability at temperatures above 77 Kelvin," *Proc. IEEE Frequency Control Symp.*, pp. 421-432, 1994.

[6] J. G. Hartnett, M. E. Tobar, E. N. Ivanov, and D. Cros, "High-Q frequency-temperature compensated sapphire/rutile resonator," *Electron. Lett.*, vol. 36, pp. 726-727, 2000.

[7] M. E. Tobar, J. Krupka, J. G. Hartnett, E. N. Ivanov, and R. A. Woode, "Sapphire-rutile frequency-temperature compensated whispering gallery microwave resonators," *Proc. IEEE Int. Freq. Cont. Symp.*, pp. 1000-1008, 1997.

[8] M. E. Tobar, J. Krupka, J. G. Hartnett, E. N. Ivanov, and R. A. Woode, "High-Q sapphire-rutile frequency-temperature compensated microwave dielectric resonators," *IEEE Trans. on UFFC*, vol. 45, pp. 830-836, 1998.

[9] D. W. Allan, "Time and frequency (time domain) characterization, estimation, and prediction of precision clocks and oscillators," *IEEE Transactions on Ultrasonics, Ferroelectrics and Frequency Control*, vol. 34, pp. 647-654, 1987.

[10] Y. S. Touloukian, *Thermophysical properties of matter*, vol. 2, 4. New York: IFI/Plenum, 1970.

[11] M. E. Tobar, J. Krupka, E. N. Ivanov, and R. A. Woode, "Dielectric frequency-temperature-compensated microwave whispering-gallery-mode resonators," *J. Phys. D: Appl. Phys.*, vol. 30, pp. 2770-2775, 1997.

[12] M. E. Tobar, J. G. Hartnett, D. Cros, P. Blondy, J. Krupka, E. N. Ivanov, and P. Guillon, "Design of high-Q frequency-temperature compensated dielectric resonators," *Electron. Letters*, vol. 35, pp. 303-304, 1999.

SAW

Chairman: Emmanuel Bigler

EXPERIMENTAL CHARACTERIZATION OF RAYLEIGH WAVE PROPERTIES ON A NEW DOUBLY ROTATED QUARTZ CUT

S. Ballandras*, W. Steichen, E. Henry-Briot, M.Solal, M. Doisy
*LPMO-CNRS associé à l'Université de Franche-Comté, 32 Ave. de l'observatoire, 25044 Besançon Cedex
THALES MICROSONICS (TMX),399 Rte des Crêtes,06904 Sophia Antipolis Cedex

Abstract : The analysis of the Quartz properties has shown the existence of unexplored angular domains for which Rayleigh waves exhibit physical characteristics better than the ones of the (ST,X) cut. This paper presents new results in the experimental characterization of effective properties of a new family of quartz cuts. Significant improvements of SAW devices on Quartz are accessible using this new cut.

I. Introduction

The reduction of the thermal sensitivity of SAW devices built on Quartz has been addressed by Schultz, Matzinger and Holland as soon as 1970 [1]. The first order Temperature Coefficient of Frequency (TCF1) was then calculated for all singly rotated cuts of quartz according to Campbell and Jones procedure [2]. The existence of at least one crystal orientation exhibiting a TCF1 close to zero was pointed out and called (*ST, X*) cut. It is defined by the IEEE std 176 notation [3] (*YXl*)/42,75°. The (*ST, X*) cut also exhibits attractive properties like its robustness to technological implementation. Consequently, this cut has been adopted by the SAW device designers as an industry standard and billions of SAW devices have been produced on (*ST, X*) cut substrates.

Nevertheless, the evolution of industrial requirements of Intermediate Frequency (IF) filtering (ranging from 50 to 500 MHz) pushes the designers to use the (*ST, X*) cut at its very limits with always smaller package size. An investigation of Rayleigh wave properties on quartz has allowed to determine a new family of quartz cuts exhibiting better characteristics than those of (ST, X) cut [4]. According to the results of this theoretical systematic investigation, this new crystal orientation has been selected to check the considered properties experimentally (phase velocity, thermal sensitivity, reflection coefficient). It is very close to an already tested orientation and correspond to cut angle $\phi = -20°$, $\theta = -35°$ and propagation direction $\psi = +20°$ [5]. One of the most interesting properties of this new cut is its negative reflection coefficient on a single aluminum strip found equal to $-1{,}5.h/\lambda$ ($0{,}5\ h/\lambda$ for (ST, X) cut) using Datta-Hunsinger's model [6]. It is also theoretically more coupled than the SAW industry standard cut ($K_s^2 = 1{,}36$ ‰ to compare to the usual value of 1,16 ‰) [4].

These results have been checked using the FEM/BEM model developed by Ventura *& al* [7]. Also, experimental measurements have been performed to validate the theoretical calculations. The wave velocity has been measured, but also temperature sensitivity for different metal thickness and compared to theory. The reflection coefficient has been also measured, showing the good agreement between theoretical and experimental results. Particularly in the present work, the measurement of the phase of the reflection coefficient has been performed using different experimental approaches (delay lines, synchronous one-port resonators,...). The most precise measurement compared to FEM/BEM calculation is based on the observation of resonance at the beginning and the end of the frequency stop band of single port resonators. Such devices are used to fit the actual parameters of the SAW on the new cut which are compared to the theoretical predictions. Finally, these data are used to optimize the devices and to cancel this phase. An example of a 71 MHz filter is presented to validate this approach.

II. Theoretical computation results

The theoretical analysis of Rayleigh waves on piezoelectric substrates is mainly based on the standard linear harmonic models proposed in the late sixties (see for instance [2]). However, more precise modeling tools have to be used to correctly determine the electromechanical characteristics of the SAW under periodic gratings used to excite, detect or reflect the surface wave in almost any SAW device. Such a theoretical model [7] has been used in the present study to provide a comprehensive description of the Rayleigh wave properties for the different quartz cuts considered here. A particular focus is proposed for a doubly rotated quartz cut with non zero propagation angle found to be temperature and stress compensated, with a beam steering angle close to zero and a coupling coefficient k_s^2 slightly larger than the one of the (*ST, X*) cut [4]. This crystal orientation, first proposed in [5], is defined according to the IEEE Std-176 by the notation (*YXwlt*)/∓ 20°, - 35.5°, ± 20° and is identified in the following as "the new cut". It was shown in [4] that the new cut provides better coupling as mentioned above, but also an improved reflection coefficient on a single aluminum electrode, computed first according to Datta and Hunsinger approach [6].

This result is particularly important because it allows to intend the reduction of the size of reflective grating, yielding a significant compaction gain when considering the same spectral function on the (*ST, X*) cut. However, the Datta-Hunsinger calculation method is only an approximation of the SAW reflection on shallow obstacles and it is now well known that more advanced models give a better understanding of the phenomenon (see for instance [7]). Consequently, this coefficient has been computed again using such a model assuming Rayleigh propagation under infinite periodic Aluminum grating for precisely determining the reflection properties of the new cut. Figure 1 shows the general geometry of the problem. The results have shown an effective gain in reflection coefficient of 2.25 to 2.5 when using the new cut [4]. This is clearly sufficient to offer attractive opportunities in the development of improved IF SAW filters compared to those built on the standard *ST* cut.

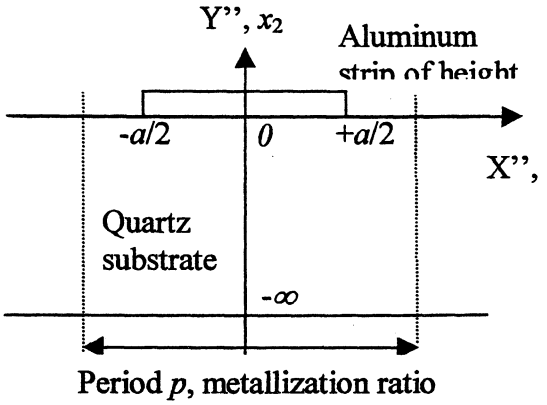

Fig. 1 Geometry and definition of a single cell of periodic gratings on quartz for excitation and propagation of Rayleigh waves

On the other hand, the phase of this reflection coefficient is equal to 170° when computed with the Datta-Hunsinger approach, which means that this cut exhibit small directivity properties as in the case of the NSPUDT quartz cut [8]. This result can also be checked using the FEM/BEM approach which gives access to a directivity factor [9] corresponding to the half of the reflection coefficient phase. However, the calculation proposed in [9] does not allow to definitely identify the sign of this phase. This point will be addressed again later. Computation have been then performed for different values of *h/2p* and *a/p*, yielding the following maps of the amplitude and phase of the reflection coefficient.

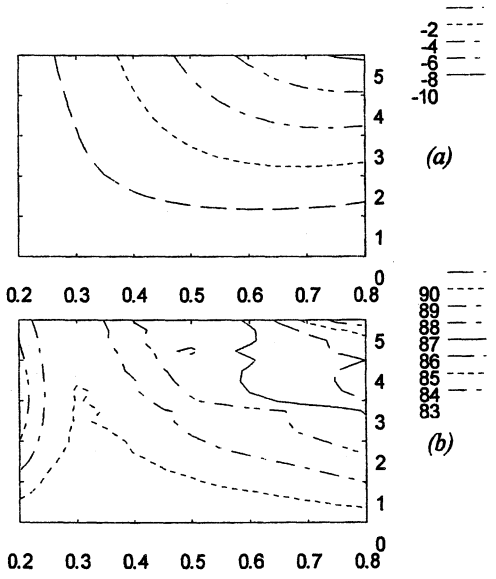

Fig. 2 Map of the amplitude of the reflection coefficient (a) and the directivity factor (b) of the new cut (a/p varies from 0.2 to 0.8, h/2p from 0 to 5)

These maps confirm of course the large values of reflection coefficient accessible using the new cut but they also show that the directivity factor is affected by the mass loading (*a/p* and *h/2p*). One can explain this dependence by considering that only the complex amplitude of the mechanical displacements are affected by this effect and not the potential one, yielding the observed shift in the directivity property.

Whatever the explanation, this directivity property has to be taken into account when using the new cut. The first step consists then in verifying experimentally the existence of these directivity properties and then to check its influence on an industrial filter. It is then interesting to check the dependence of this parameter versus the propagation direction to find corrected cuts exhibiting no directivity properties.

III. Experimental measurements

A simple and efficient method to characterize the properties of SAW under periodic grating on a given substrate consists in fitting the experimental admittance of a single port synchronous resonator using a mixed-matrix model [7, 9]. This model requires the following information :

- v_{cc} - propagation velocity of the wave
- r_{cc} - magnitude of the reflection coefficient
- φ_{rcc} - phase of the reflection coefficient
- α - attenuation coefficient of the wave
- k^2 - piezoelectric coupling factor
- ε - substrate permittivity

Experimental devices have been fabricated on 3" wafers of the new cut. Single port synchronous resonators have been built with 100 pairs of finger in the transducer part, surrounded by mirror gratings composed of 20 electrodes, the acoustic aperture being set to 20 wavelengths. The devices have been designed to operate at 200 MHz (λ = 17.342 µm), the electrode thickness being fixed to 380 nm. Different metallization ratio (0.525, 0.6, 0.71 and 0.78) have been also tested. Also 3 propagation directions have been tested (ψ= 10°, 15°, 20°). Figure 3 shows an example of S_{11} parameter of an experimental device used to perform the above mentioned fit.

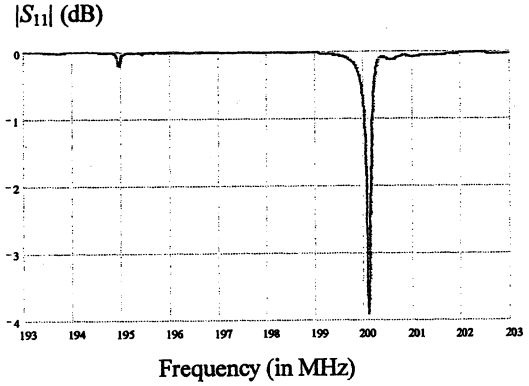

Fig.3 S11 parameter of one of the tested resonator

For single port resonators on directive substrate, 2 resonant peaks are expected, respectively at the beginning and at the end of the frequency stopband. In the present case (φ_{rcc} close to 180°), the maximum amplitude of the resonance is found at the end of the frequency stop band while only a small contribution is found at its beginning. In comparison, only one resonance occurs at the beginning of the stopband for such resonators on ST cut.

Starting from the data provided by the computation, one can efficiently fit the actual values of the mixed-matrix model parameters along the following procedure :

a - r_{cc} is first adjusted to respect the spread of the frequency stopband

b $-v_{cc}$ is then fitted to well predict the absolute frequency value of both responses
c $-\varepsilon$ is changed (if necessary) to exhibit the correct capacitance value
d $-\alpha$ is determined to well represent the quality factor of the peaks (α is frequency dependent)
e $-\varphi_{rcc}$ is then modified to have the correct magnitude ratio between the 2 contributions
f – finally, k2 is determined to fit the effective peak magnitudes

The quality of the fit procedure is illustrated in fig.4 for the 2 contributions to S11 for one of the tested device.

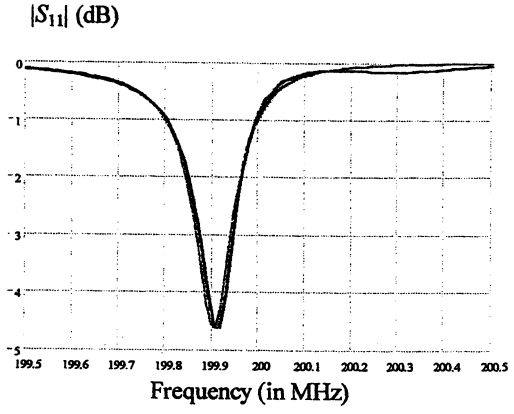

(1st)

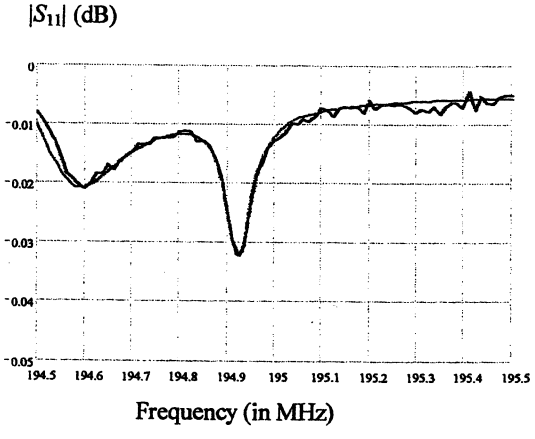

(2nd)

Fig.4 Results of the fit procedure, comparison between experimental and fitted S11 parameter: end (1st) and beginning (2nd) of the stopband, a/p =0.6, h/2p=2.2%, ψ = 15°, dashed line exp., solid line fit

It was then possible to verify the theoretically predicted tendency concerning the evolution of the parameters versus the metallization ratio. The following curves compare experimental and theoretical predictions for the propagation direction $\psi = 20°$ and give a good illustration of the capability of advanced models to faithfully predict the effective properties of SAW under periodic gratings. The quasi perfect agreement between experiments and predictions is obtained by slightly reducing the parameter h/2p in the theoretical computations, within the possible technology fluctuations (+/- 1%).

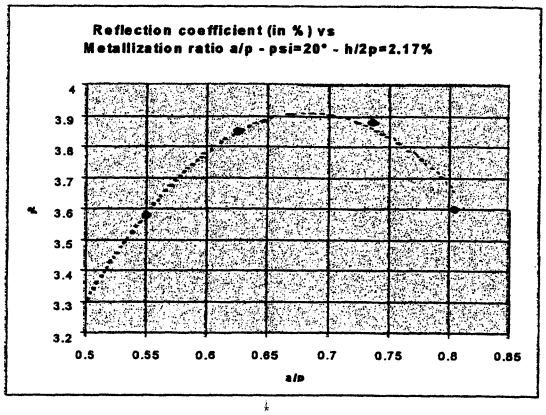

(a)

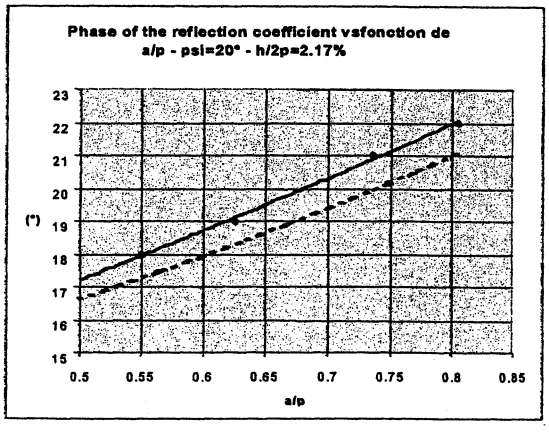

(b)

Fig.5 Comparison between theory and experiments for propagation along ψ = 20°, amplitude (a) and phase (b) of the reflection coefficient

IV. IF Filter design and fabrication

Using the above theoretical and measured electro-acoustics characteristics of this new Quartz cut and taking advantage of the high reflection coefficient, a very compact IF GSM Filter has been designed and manufactured. The measured transfer function is shown on figure and is comparable with the result obtained with a GSM filter design on ST-cut Quartz. The filter fits in a 10x6 mm^2, the die dimension is 7.4x4mm^2 and the aluminum electrodes thickness is 8000A (compared to 10000A for 13.3x6.5 mm^2 package filter on ST-Cut QZ). This lower thickness makes the filter center frequency less sensitive to manufacturing thickness and metallic ratio variations.

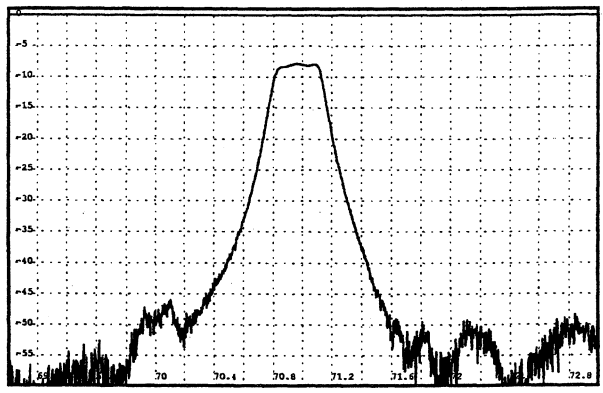

Fig6. an example of GSM filter built on the new cut (5 dB/div vertical scale, 200kHz/div horizontal)

It was necessary to take precisely into account the influence of the phase of the reflection coefficient to avoid unwanted side lobes capable to reduce the rejection of the filter.

One can see that the filter response corresponds to specifications required for this application. The filter is found temperature compensated at 10°C and the IL exhibit a total variation of less than 1 dB for the whole temperature range.

V. Conclusion

A new triply rotated quartz cut has been theoretically and experimentally found to exhibit better physical properties than the standard (*ST*, *X*) cut for IF SAW filter applications. Large reflection coefficients have been experimentally measured, allowing a significant reduction of aluminum thickness or chip size compared to what is available on (*ST*, *X*) quartz. The phase of the reflection coefficient has been particularly studied to perfectly control its influence on the filter responses. It appears consequently that in many applications, the new cut can advantageously replace the (*ST*, *X*) cut.

References :

[1] M.B Schultz , B. J. Matzinger , M .G. Holland, "Temperature dependence of surface acoustic wave velocity of quartz" , J. Appl. Phys. , vol.41 , n°7 , pp. 2755 - 2765 , 1970 .

[2] J.J. Campbell, W.R. Jones, "A method for estimating crystals cuts and propagation direction for excitation of piezoelectric surface waves", IEEE Trans. On Sonics and Ultrasonics, Vol. 15, pp. 209-217, 1968

[3] IEEE Standard an piezoelectricity 176 - 1949 , Proc. of the IRE , vol. 37 , pp1978 - 1995 , 1949

[4] S. Ballandras, E. Henry-Briot, M.Solal, W. Steichen, M. Doisy, F. Bourrit, D. Bellon, J.-M. Hodé, "a new triply rotated quartz cut for the fabrication of low loss SAW filters", Proc. of the IEEE Ultrasonics Symp.2000 (In Press)

[5] S. Ballandras, E. Bigler, "Doubly rotated SAW quartz cuts with low sensitivity to stress and temperature effects exhibiting a power flaw angle close to zero", J.A.S.A., Vol. 95 n°3, pp. 1390-1395, 1994.

[6] S. Datta, B. Hunsinger, "First order reflection coefficient of surface acoustic waves from thin strip overlays", J. Appl. Phys., 50, 9, pp. 5661-5665, 1979.

[7] P. Ventura, J.M. Hodé, M. Solal, J. Desbois, J. Ribbe, "Numerical methods for SAW propagation charaterization", Proc. Of the IEEE Ultrasonics Symp., IEEE cat #98CH 36102, pp. 175-186, 1998.

[8] P.V. Wright, "The natural single phase unidirectionnal transducer : anew low loss transducer", Proc. of the IEEE Ultrasonics Symp., pp. 58-63, 1985

[9] P. Ventura, J.M. Hodé, "A new accurate analysis of periodic IDTs built on unconventional orientation on quartz", Proc. of the IEEE Ultrasonics Symp., pp. 139-142, 1997

MODELING OF TRANSVERSE PLATE MODE RESONATORS BY PURE FINITE ELEMENT AND MIXED FINITE ELEMENT/BOUNDARY INTEGRAL TECHNIQUES

*S. Ballandras, *T. Pastureaud, Y. Fusero*
LPMO-CNRS associé à l'Université de Franche-Comté, 32 Ave. de l'observatoire, 25044 Besançon Cedex
**THALES MICROSONICS (TMX),399 Rte des Crêtes,06904 Sophia Antipolis Cedex*

Abstract : Two approaches are developed allowing to accurately model the physical characteristics of plate mode devices and more particularly resonators. They are respectively based on mixing boundary integral methods and finite element analysis (BIM/FEA) and on pure finite element computation. Considering infinite periodic structure and using the harmonic admittance allow to determine the main parameters of the wave propagation (velocity, coupling factor, reflection, and so on) and is inserted in a mixed matrix model. Comparison between theory and experiments is reported.

I. Introduction

A lot of work has been devoted to Acoustic Plate Mode (AMP) devices for the development of sensors used in gravimetry or for the measurement of pressure or viscoelasticity and so on [1, 2]. The pure shear APMs are particularly attractive because compatible with immersed applications for which the smallest acoustic radiation from the plate to the fluid medium is wanted. Moreover, the capability of the so-called transverse plates mode to exhibit high quality coefficients when propagating under metal strip gratings [3] allows one to expect the measurement of fine phenomena (improvement of the sensitivity and of the resolution). Finally, it is possible to fabricate transverse plate mode resonators exhibiting quality factor time's frequency product larger than 10^{13} at frequency higher than 100 MHz using mixed strip and groove gratings [4]. The later point allows to investigate the interest of transverse plate mode resonators used as high spectral purity sources.
Even if some theoretical efforts have been performed to understand the way these resonators work, particularly the capability of the resonator to present resonance at the beginning and at the end of the frequency stop band of each mode (especially on AT cut, propagation along Z'), no model has been developed to simulate the electrical response of these devices to the best of our knowledge. The existence of such a model would allow to better understand the working principles of these resonators, allowing to optimize their electrical characteristics more efficiently than using experimental measurements in a blind fold test behavior.

In the proposed paper, two different approaches are presented allowing to predict the electrical harmonic admittance of transverse plate mode structures taking into account the influence of the electrodes for both excitation and mechanical loading of the plate. The first approach is based on pure Finite Element Analysis (FEA) calculations, the second one is based on the combination of a Boundary Integral Method (BIM) to simulate the electroacoustic properties of the plate and FEA to describe the influence of the metal strip on the propagation characteristics of the wave. In this later case, the admittance of a standard one-port resonator can be predicted assuming long transducer structure. This approach is the most efficient to simply characterize the properties of the different excited modes provided above-mentioned alternate excitation conditions. The pure FE approach is more timing consuming, the results are mesh dependent but it is possible to simulate complete devices, provided the number of electrodes is not too large in regard with theoretical standard computer capacities. Comparison between experiments and predictions is reported and discussed.

II. Theoretical developments

Previous work has been devoted to understand the trapping mechanism of pure transverse wave in fine quartz plate [3, 4] but with simplified electrical boundary conditions. In this work, considering the geometry of fig.1, real electrical excitation conditions are considered.

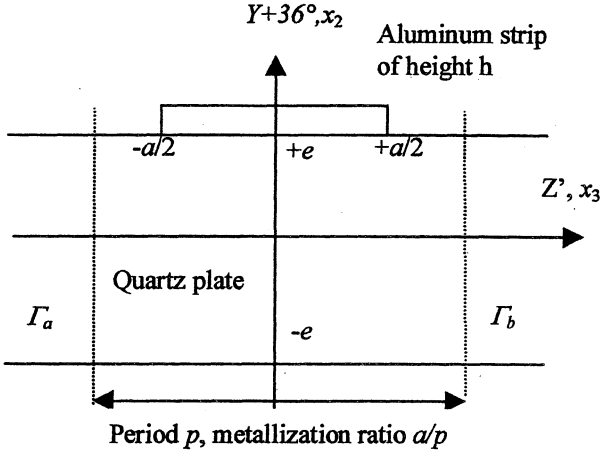

Fig. 1 Geometry of the problem

II.1. FEA/BIM approach

This approach was first developed by Ventura & al for the characterization of Rayleigh wave properties under electrodes of general shape [5]. The idea consists in computing the behavior of the substrate via a Green's function formalism and the contribution of the electrode by FEA. Since the equations of the model are fully developed, only the important parts the analysis are recalled here. First, we consider a periodic problem allowing to take into account only one period of the grating. The model consists then in relating the generalized displacements to the generalized surface stresses via the following convolution equation :

$$u_i(\omega,x) = \int G_{ij}^{p}(\omega,x-x')t_{i2}(\omega,x')dx' \qquad (1)$$

where G_{ij}^{p} represents the periodic Green's function. Since this equation cannot be solved directly, a Chebychev expansion of the stresses and displacements is used as in [5], assuming also the dependence of the generalized stress in $\sqrt{(1-x^2)}$:

$$u_i(x) = \sum C_{ui}^n T_n(x)$$
$$t_{i2}(x) = \left(\sum C_{ti}^n T_n(x) \right) / \sqrt{1 - x^2} \quad (2)$$

The main difference between [5] and the present calculation consists in the dispersive behavior of the Green's function due to the finite thickness of the plate. Fortunately, one can demonstrate that the asymptotic behavior proposed in [5] remains valid for the case of the plate. The contribution of the electrode is performed exactly like in [5] and is not recalled here. Finally, one has to solve a linear algebraic problem to identify the weights of the stress development (2), allowing the calculation of the charge under the electrode as follows :

$$Y = j\omega Q = j\omega \int_{-a/2}^{+a/2} t_{42}(x)dx = j\omega \frac{\pi}{2} C_{t4}^0 V_0 \quad (3)$$

where V_0 is the potential excitation applied on the 0^{th} electrode of the grating, according to the assumption of harmonic excitation.

II.2. Pure FEA calculations

In the pure FEA approach, the calculation of the whole mechanical and electrical distribution is performed assuming the very usual FEA principles. Such an approach has already been implemented for Rayleigh waves [6] but not for other polarization (to the best of our knowledge). Two elements have been specially developed to allow the computation of the most general polarization and pure shear phenomena respectively. These elements exhibit respectively 4 and 2 degrees of freedom (dof), i.e. u_1, u_2 (the displacements in the sagittal plane), u_3 and ϕ. Only the results corresponding to the 2 dof element are reported here since rigorously identical to those provided by the 4 dof one (in quartz YZ, sagittal field are not coupled). The theory is simply based on the resolution of the system :

$$[K - \omega^2 M]\{u\} = \{f\} \quad (4)$$

where K and M are the stiffness and mass matrices respectively, and u the generalized solution vector (in our problem, the right hand side of eq. (4) is left free). This problem is solved assuming periodic boundary conditions (see fig.1) given by :

$$\{u\}_{\Gamma_a} = \{u\} e^{j2\pi\gamma}\Big|_{\Gamma_b} \quad (5)$$

where γ is the same excitation parameter as the one used in [5]. Once eq.(4) is solved taking (5) into account, the admittance is then simply obtained by the sum of the charge under the electrode times the angular frequency as follows :

$$Y = j\omega Q = j\omega \sum_{n=1}^{N} Q^n \quad (6)$$

where Q^n represents the nodal charge under the electrode. It is important to underline that nothing else is required to make this calculation but these equations and a well prepared mesh, i.e. respecting a regular distribution of elements without stretched or compressed anomalous geometry. From 500 elements and 2^{nd} degree interpolation, results were found stable.

II.3. Comparison between theoretical results

In this section, we compare the information delivered by both models using a fit procedure based on the following isomorphic representation of the mode contribution to the harmonic admittance:

$$\tilde{Y}(\gamma) = R(\gamma) + jY_p \frac{1-\eta}{\hat{\eta} - \eta} \quad (7)$$

η is equal to $cos^2(\pi\gamma)$ and $R(\gamma)$ represents the residual behavior of the harmonic admittance. Assuming an alternated excitation +V/-V (i.e. γ=0.5), the different frequency stopbands of the wave guide are scanned using both theoretical approaches as reported in fig. 2. The agreement between the two proposed model is found excellent concerning the spread of the stopband. The corresponding frequency values are slightly shifted ($5^0/_{00}$) because the influence of vacuum was neglected in the pure FEA calculation. Table I compares the results provided by the two approaches in terms of reflection coefficient for a device according to the experimental one (described in the next section).

Mode order vs Reflection coefficient	R (module and phase) (FEA/BIM)	|R| (pure FEA)
Mode 1	.18 / 86.4°	.18
Mode 2	.265 / 86°	.27
Mode 3	.255 / 72°	.26
Mode 4	.244 / 26.5°	.25

Table I Comparison between reflection coefficient obtained using the two implemented models

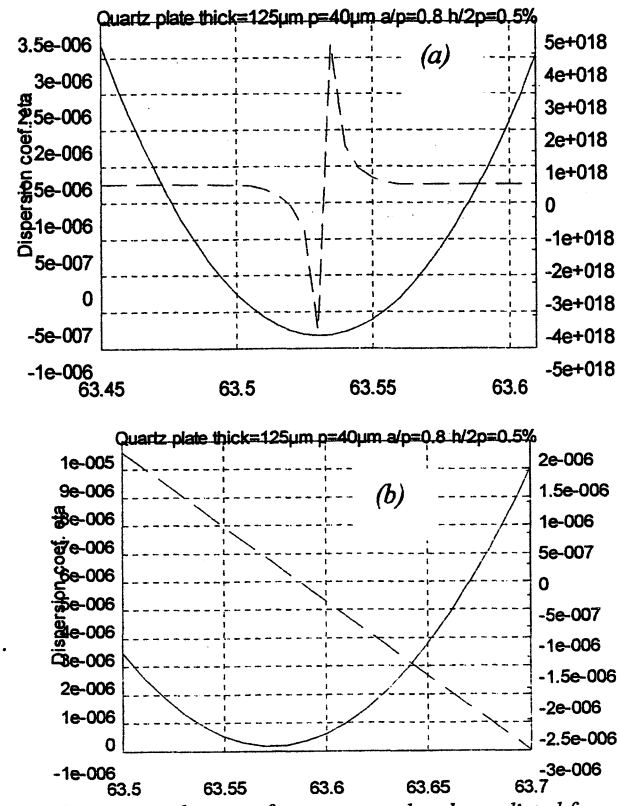

Fig. 2 Comparison between frequency stopbands predicted for the first mode using the two proposed theoretical approaches

(a): pure FEA (b): FEA/BIM (the corresponding model parameters are those of the experimental setup)

One can note that the two first modes are very directive, the other ones exhibiting less directivity (the 5th mode is found non directive, higher modes too). Although the pure FEA analysis seems to provide identical information about the phase of the reflection coefficient (the sign of Y_p changes in the middle of the frequency stopband), the form of the pole amplitude is so different than the usual one that we prefer not discuss it.

II.4. P-Matrix for APM devices

Once the parameters of any given mode have been identified accurately, it is possible to insert them in a P-matrix like model to compute the electrical response of given synchronous devices like resonators or delay lines. In that matter, one has to identify the beginning and the end of the frequency stopband which directly provides the phase velocity φ and the reflection coefficient $sin(\Delta)$. The magnitude of the mode contribution at these two frequency locations are also needed to identify the coupling strength G and the directivity δ. All these terms are computed using the rules given in [7].

III. Experimental assessment

An experimental device working at low frequencies has been fabricated to allow a better separation of the different modes and particularly of their electrical admittance. Single port resonators have been manufactured on (YX*l*) 36°,90° quartz plate of thickness 125µm. The number of periods of the interdigital transducer was 200, and 200 electrodes were used in the mirror gratings. The grating period was 40 µm ($\lambda \approx 80$ µm), the electrode height was set to 400 nm (h/λ=0,5%) and the metallization ratio a/p = 0.8. Figure 3 shows the admittance of the device measured using an network analyzer in reflection mode. In comparison, the harmonic admittance at γ=0.5 provided by the proposed models is reported, showing the good prediction of the mode distribution in both cases. Another result is reported in fig.5 showing the 4th mode and the P-matrix model. Although the exact form of the admittance is not given by the model, one can well identify the major acousto-electric contributions of the considered plate mode. This result proves that simulating accurately any plate mode using the P-matrix approach can be efficiently performed and the electrical response can therefore be optimized using standard design tools.

IV. Conclusion

Two theoretical approaches have been developed and numerically implemented to predict the electrical response of transverse plate mode resonators. Particularly, it was shown that NSPUDT phenomena are predicted and measured for the first modes of the plate, the other being excited conventionally. These theoretical models provide trustful information about the mode properties which can be used in a standard design procedure for optimization purpose, as demonstrated here. Furthermore, their capability to take into account complicated non homogeneous surface conditions allows one to imagine new kind of structure for the excitation and propagation of elastic waves on dispersive media. Finally, the possibility to model finite length devices using pure FEA will be explored.

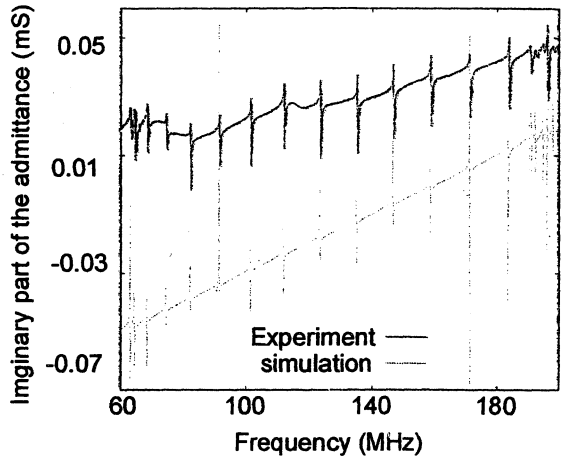

Fig. 3 Experimental admittance of the test device, comparison with theoretical harmonic admittance

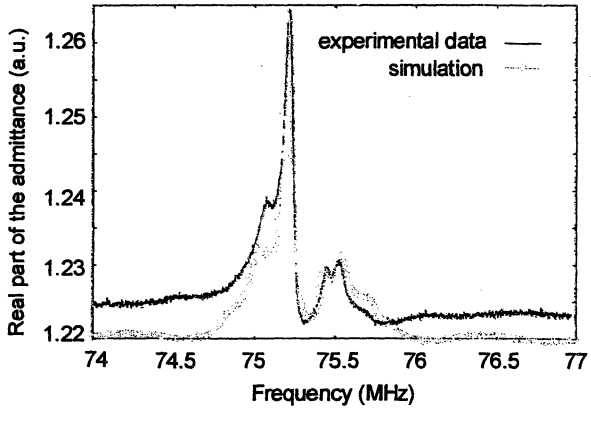

(a)

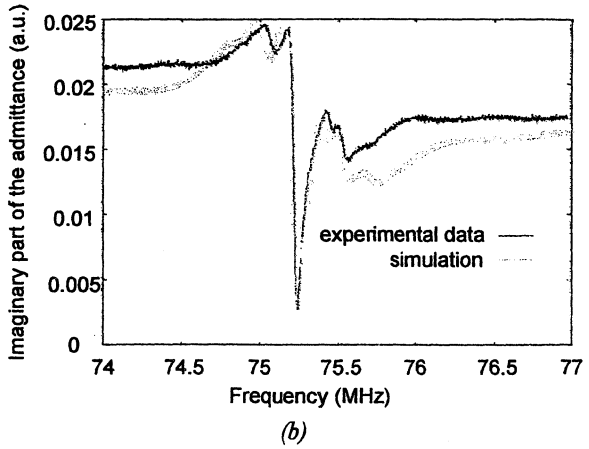

(b)

Fig.4 Experimental and P-matrix model responses of the 4th mode approaches
(a): real part of the admittance Y_{11}
(b): Imaginary part of the admittance Y_{11}

Acknowledgements : The authors thank P. Ventura and J. Desbois for their help in the theoretical developments and to J.B. Briot for his contribution to the first prospective developments.

References :

[1] M.F. Lewis, "High frequency acoustic plate mode device employing interdigital transducers", El. Lett., Vol. 17, n°21, pp. 819-821, 1981

[2] S.J. Martin, A. Ricco, T.M. Niemczyk, G.C. Frye, "Characterization of SH-APM Liquid sensors", Sensors & Actuators, n°20, pp. 253-268, 1989

[3] S. Ballandras, E. Gavignet, E. Bigler, G. Martin, "Experimental measurements of STW properties on quartz plates of finite thickness", El. Lett., Vol. 32, n°4, pp. 413-414, 1996

[4] J. B. Briot, S. Ballandras, "Transverse plate mode resonators exhibiting very high quality factors and small insertion losses", Proc. of the IEEE Ultr. Symp., pp. 7-10, 1999

[5] P.Ventura, J.M. Hodé, M. Solal, "A new efficient FEM and periodic Green's function formalism for the annalysis of periodic SAW structures," Proc. of the IEEE Ultr. Symp., pp. 263-268, 1995.

[6]P. Bauerschmidt, R. Lerch, J. Machui, W. Ruile, G. Visintini, "Reflection and Transmission coefficient of SAW in a periodic grating computed by finite element analysis", Proc. of the IEEE Ultr. Symp., pp. 421-423, 1990

[7] J.M. Hodé, J. Desbois, P. Dufilié, M. Solal, P. Ventura, "SPUDT-based filters : design, principle and optimization", Proc. of the IEEE Ultr. Symp., pp. 39-50, 1995

Interface Waves characteristics using Effective Permittivity and Harmonic Admittance approaches on common crystal cuts

S. Camou, S. Ballandras, V. Laude
LPMO UPR 3203 CNRS - 32, Avenue de l'Observatoire, 25044 Besançon, France

Abstract : An analytical method assuming infinitily thin excitation electrodes is presented in this paper to modellize Interface Waves properties. This theoretical analysis is then applied for standard crystal cuts often used in acoustic wave devices. A comparaison between Interface Waves and Surface Acoustic Waves (without any mechanical effect of the metal strips) is performed, pointing out the dependance of different acoustic wave properties in terms of reflection coefficient, phase velocity, attenuation and electromechanical coupling factor on the studied configuration compared to SAW' ones.

1 Introduction

Acoustic waves propagating along a plane interface between two semi-infinite solids were theoretically predicted by Stoneley in 1924 [1]. They were partially studied for many years, but have received a particular attention since the development of elastic wave devices for signal processing applications (delay lines, filters, resonators, etc.). Interface waves exhibit totally different properties than surface acoustic waves and much work has been done to identify optimal configuration for efficient excitation and propagation of such waves using piezoelectric coupling.

In this paper, the harmonic admittance according to the Blötekjaer approach is computed using a boundary effective permittivity at the interface between two piezoelectric semi-infinite materials in order to compare propagation parameters of interface waves propagating at the interface with SAW' ones. No mechanical contributions are taken into account in this model to allow analytical calculations, so electrodes are assumed infinitely thin and just introduce a charge distribution at the excitative interface.

Depending on the material combination and crystal cuts, a modal selectivity is first pointed out with excitation of different kind of waves from elliptically polarized ones to longitudinal leaky modes. The phase velocity, propagation losses and electromechanical coupling are extracted from the harmonic admittance, and the electric reflection coefficient is also calculated. Calculation of the thermal sensitivity of acoustic wave devices is done by using the method developped in [2]. Computations are performed for standard materials like $Quartz$, $LiNbO_3$, $LiTaO_3$.

2 Principle of the numerical analysis

The bimorph substrate response to an electric charge distribution along the excitation interface is modellized by computation of the effective permittivity ε_{eff} (fig. 1).

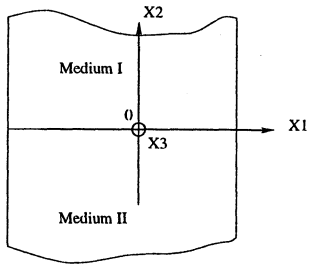

Figure 1: *Definition of the studied geometry*

Penetration coefficient n_2^r are obtained by solving the Christoffel equation in the Fourier domain, and four of them are selected according to some physic principles (evanescent waves toward the bulk of semi-infinite material). Thus, the mechanical displacements, electric potential, normal stresses and electric displacement's discontinuity are written as the combination of four partial waves with weighting coefficients. Assuming that the experimental devices are infinite in the x_3 direction, expressions (x_3 coordinate independant) are obtained as follows in each medium :

$$\overline{u}_i(\gamma, x_2, \omega) = \sum_{n=0}^{4} A_r \overline{u}_i^{(r)} e^{-j\frac{\omega}{v} n_2^r x_2} \quad (1)$$

Then, equations of continuity conditions at the interface between the two media give a complete system in terms of coefficients A_r^I and $A_{r'}^{II}$. To solve this problem with no more hypothesis about the charge density at the plan $x_2 = 0$, the Kramer's method yields the following expression of ε_{eff} [3] :

$$\varepsilon_{eff} = \frac{\overline{Q}(\gamma, \omega)}{\mid \gamma \mid \overline{\phi}(x_2 = 0)} = \frac{\Delta \overline{D}_2(x_2 = 0)}{\mid \gamma \mid \overline{\phi}(x_2 = 0)} \quad (2)$$

where $\overline{Q}$ is the electrical load representing the electric charge distribution introduced by interdigital transducer.
This scalar parameter takes into account all piezoelectric coupled acoustic waves propagating on a multilayer substrate. To include a periodicity condition in the charge distribution (according to the fact that generation and detection at interdigital transducers generate a charge density under metal strips (fig. 2)), the harmonic admittance defined according to [4] is now considered, neglecting metal fingers thickness so that no mechanical effects are taken into account in the model.

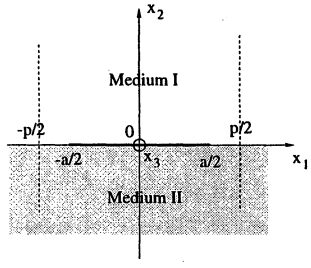

Figure 2: *Geometry of one period p of infinite periodic metal strips (a : metal finger's width)*

According to Floquet's theorem and Fourier transform theory, the parallel electric field and the normal electric displacement are developped over one period. Then all the continuity equations are solved using Legendre polynoms P_n and mathematical identities mentionned in [5], in order to determine a set of coefficients α_n :

$$\Upsilon(\omega, s) = j\omega\varepsilon_\infty \sin(\pi s) \frac{\sum_{n=N_1}^{N_2+1} \alpha_n P_{n-1+s}(\cos(\Delta))}{\sum_{n=N_1}^{N_2+1} (-1)^n \alpha_m P_{n-1+s}(-\cos(\Delta))} \quad (3)$$

with $s = \gamma p$, $\Delta = \pi a/p$ and this normalized $\Upsilon(\omega, s)$ including all harmonics (even those with orders out of the range defined by $[N_1, N_2]$).

Around a pole corresponding to an acoustic wave close to $s = 0.5$, the $\Upsilon(\omega, s)$ variation can be locally fitted with a function defined in the mixed matrix approach as follows :

$$\Upsilon(\omega, s) = \left(j\Upsilon_o + \frac{j\Upsilon_p}{\cos(2\pi\gamma_{cc}) - \cos(2\pi\gamma)} \right) \sin^2(2\pi\gamma) \quad (4)$$

where the pole coordinate is denoted γ_{cc} and the first and second terms are proportional to the capacitive coupling and the acoustical coupling respectively. The Υ_p and $S_p = \cos^2(\pi\gamma_{cc})$ evaluation in an analytic manner enable one to precisely caracterize the stopband edges f_{in} and f_{out} : in the stopband, $\cos^2(\pi\gamma_{cc})$ is negative whatever the wave considered (SAW or Leaky wave). These two parameters contain a lot of information but limited here around the reflexion coefficient $\mid r \mid$ (purely electric) fixed as:

$$\mid r \mid = \sin\left(\pi \frac{f_{out} - f_{in}}{f_{out} + f_{in}} \right) \quad (5)$$

The thermal sensitivity is also calculated using the classic Campbell & Jones approach. To describe the relative frequency shift versus the temperature, an effective set of constants are computed for each temperature: the phase velocity extracted from the effective permittivity, coupled with the thermal expansion yields the synchronism frequency of acoustic devices for each temperature. A fit by a parabolic function gives two coefficients:

$$\frac{\Delta f}{f}(\Delta T) = CTF1 \,.\, \Delta T + CTF2 \,.\, (\Delta T)^2 \quad (6)$$

The second order $CTF2$ become important when the first order coefficient is close to zero. This method was tested on surface acoustic wave devices and gave some accurate results for $CTF1$. But close to compensated crystal cuts, the model isn't able to predict very precisely the two coefficients due to basic hypothesis. Thus, results about the $CTF2$ aren't accurate, but $CTF1$ is sufficient to detect approximatively the cuts exhibiting a frequency stability versus the temperature.
These numerical models are applied to study materials such as quartz, lithium niobate and tantalate in order to compare the propagation parameters of surface acoustic waves propagating along a metallized surface on a semi-infinite substrate, with those of interface waves using twice the same material on both side of the excitation interface.

3 $LiNbO_3$, $LiTaO_3$ and *Quartz* substrates

Three standards materials often used in acoustical devices are studied. First at all, the modal selectivity phenomenon is pointed out considering the case of a *ST Quartz* substrate (fig. 3).

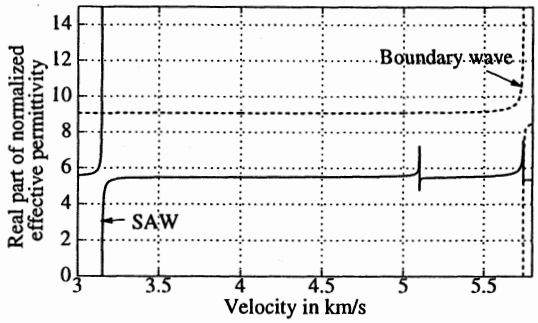

Figure 3: *Comparaison of effective permittivities versus velocity for SAW and IW on ST Quartz*

First, the Rayleigh wave , with an elliptic polarisation in the sagittal plane and a metallized phase velocity about 3.15575 km/s, disappears in the IW configuration. Second, the longitudinal bulk wave becomes a real interface wave (Leaky Interface Wave), mostly polarized along the propagation axis.

The waves considered are different, consequently modifying the thermal sensitivity of acoustic waves (fig. 4).

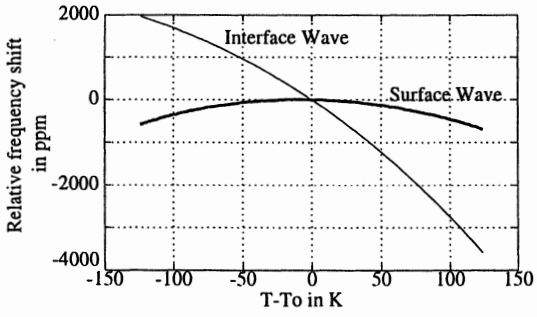

Figure 4: *Synchronism relative frequency shift versus temperature for SAW and IW on ST Quartz*

Considering the case of the 64 YX $LiNbO_3$ substrate, the two shear bulk waves are transformed into transversaly polarized interface waves (fig. 5) with different coupling factor (proportionnal to the pole amplitude).

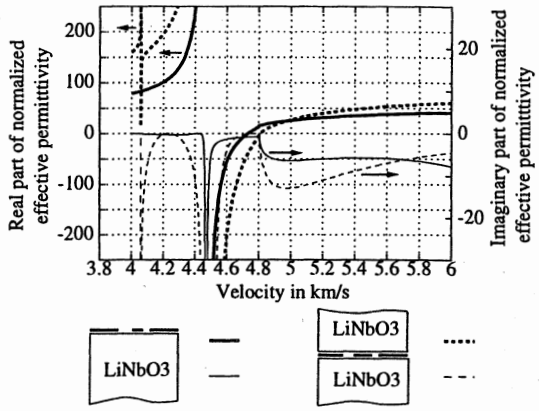

Figure 5: *Comparaison of effective permittivities versus velocity for SAW and IW on* 64 $LiNbO_3$

Thus, the first IW, which is guided by the interface wihout any losses, is not coupled enought to be of any use. The second one, with a phase velocity around 4.49065 km/s, exhibits an important attenuation coefficient $\alpha = 30\ 10^{-2}$ dB/λ, approximatively twenty times the attenuation coefficient for SAW on the same substrate (tab. 1). In figure (6) appear the dispersion curves obtained with this cut of lithium niobate: the stopband widhts, so the coefficient $\mid r \mid$ are similar in both configurations.

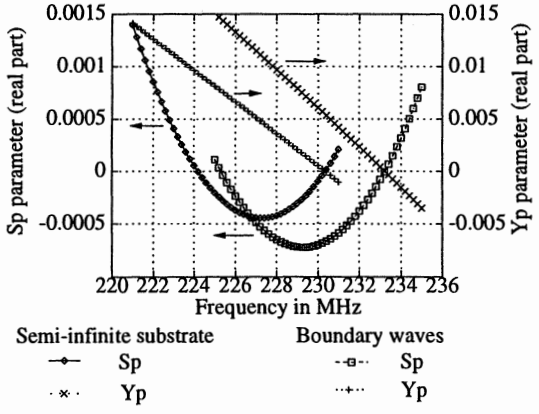

Figure 6: *Comparaison between the dispersion curves of Interface Waves and Surface Acoustique Waves with a* 64 YX $LiNbO_3$ *substrate*

Table 1 contains data for these three materials (*ST Quartz*, 36 YX $LiTaO_3$ and 64 YX $LiNbO_3$) including the results obtained for surface waves and interface waves applying the same method.

	v in km/s	α in mdB/λ	k^2 in %	$\mid r \mid$ in %	$CTF1$ ppm/K
ST Quartz SAW	3.15575	0.	0.11	0.04	0.6
ST Quartz IW	5.74403	0.08	0.02	0.007	−22.1
36 YX SAW $LiTaO_3$	4.11296	0.7	6.1	2.16	−27
36 YX IW $LiTaO_3$	4.11378	6.6	6.1	2.18	−25
64 YX SAW $LiNbO_3$	4.47171	1.5	12.5	4.26	−75
64 YX IW $LiNbO_3$	4.49065	30.	16.6	5.42	−75.3

Table 1 :*Results obtained by coupling two similar substrates*

Generally, the waves parameters are different between the two configurations, but they change in different manners. The three combinations studied in this paper and correponding to an optimization of propagation parameters for SAW devices, aren't appropriate for IW configuration.

4 Conclusion

It has been shown that Interface Waves' properties are different from that of SAW. When IW exists, their velocities can be easily deduced from the slowness curve of materials (when two materials are symetrically combined together), but the efficiency of the coupling and the reflexion coefficient per period need a numerical analysis. Since it modifies the acoustic wave polarization, the IW configuration can be used to obtain improved parameters with the same material ($LiTaO_3$,...) and the same technology to generate and detect acoustic waves (interdigital transducers).

The analytical model presented in this article is still available to study combination of two differents materials [6]. As shown in previous work, particular couples of materials and angular orientations allow to significantly reduce the propagation losses corresponding to wave partially radiated toward the bulk of the substrates from both side of the interface [7] [8].

References :

[1] R. Stoneley, *Elastic waves at the surface of separation of two solids*, Proc. Royal Society (London), A106, pp. 416-428, 1924

[2] J.J. Campbell & W.R. Jones, *A method for estimating optimal crystal cuts and propagation direction for excitation of piezoelectric surface waves*,IEEE Trans. on Sonics and Ultrason., SU-15,pp. 209-217, 1968

[3] D.P. Morgan, *Surface-wave devices for signal processing*, vol. 19, Elsevier, 1985

[4] K. Blötekjaer, K.A. Ingebrigtsen, H. Skeie, *A method for analyzing waves in structures consisting of metal strips on dispersive media*, proc. of IEEE Trans. on Elec. Devices, vol. 20, no 12, decembre 1973

[5] A. Erdélyi, *Higher transcendental functions*, vol. 1, New-York : McGraw-Hill Book Company, 1953

[6] S. Camou, *Étude de nouveaux guides d'ondes lastiques pour les applications de filtrage haute frquence et les sources de haute qualit spectrale*, pH-D thesis of University of Franche-Comté, # 833, 2000, France (in french)

[7] M. Yamaguchi, T. Yamashita, K. Hashimoto, T. Omori, *Highly piezoelectric boundary waves in $Si/LiNBO_3$ and $Si/SiO_2/LiNbO_3$ structures*, unpublished

[8] S. Camou, S. Ballandras, V. Laude and P. Tournois *Theoretical Calculations of BOUNDARY WAVES using Effective Permittivity and Harmonic Admittance approaches on various combination of materials*, proc. of IEEE Ultrasonics Symposium 2000, to be published

THE USE OF SYNCHRONEOUS SAW RESONATORS FOR A STUDY OF NEW PSEUDO-SAW MODES

valeri grigorievski *), victor plessky **), and laurent kopp**)

*) institute of radioengineering and electronics, ras, moscow region, fryazino, russia.
**) thomson microsonics, saw design bureau, neuchatel, switzerland
**) thomson microsonics, sophia antipolis, france

1. ABSTRACT

A new fast quasi-longitudinal leaky mode exists on the ordinary YZ cut of lithium niobate. The wave corresponds to a complex valued singular point of the effective permittivity function. Due to the trapping effect under large mass and stress periodical loading the new mode effectively resonates in long interdigital transducers. The admittance characteristics of a synchronous SAW resonator exhibit a typical resonance behavior in the frequency region slightly below the frequency of skimming longitudinal bulk wave. The measured Q-factors at resonant and anti-resonant frequencies are equal to 32 and 30 respectively. The fractional bandwidth equals 3 percent. The effective wave velocity of the mode approximates the value of 6000 m/s.
Keywords: leaky surface acoustic wave, pseudo-SAW mode, resonators.

2. INTRODUCTION

The pseudo-surface acoustic waves (SAW) otherwise referred to as the leaky SAW find expanding applications in low loss SAW filters for mobile communication systems. These waves have a higher propagation velocity and electromechanical coupling constant than Rayleigh SAW in piezoelectric crystals, that makes possible increasing the operating frequencies and bandwidths of SAW filters required in modern systems.

The fast leaky surface acoustics waves with low intrinsic attenuation have been reported in lithium tetraborate and some other crystals [Ref. 1-2]. The propagation velocity of these waves approximates the velocity of longitudinal bulk wave that makes possible significant increase in operating frequencies of SAW filters [Ref. 3].

It has been shown recently in [Ref. 4] that the admittance of a long interdigital transducer (IDT) with thick aluminum electrodes on several cuts of lithium niobate (LN) and lithium tantalate (LT) exhibits the excellent resonance behavior. The authors of [Ref. 4] refer to longitudinal leaky SAW grating modes propagating in periodic systems of thick metal electrodes.

The leaky SAWs are usually associated with singularities of effective permittivity function (EPF) analytically continued from the real axis of slowness into the complex plane [Ref. 5]. The singular points for known FLSAW are located in "sub-sonic" region that is slightly higher on slowness axis than the branch point of longitudinal bulk wave skimming along the crystal surface. However, for many cuts of LN and LT the effective permittivity function does not show singularities near the longitudinal branch point. It has been recently shown in [Ref. 6] that in LN and LT the singular points of effective permittivity function can be located in "super-sonic" region. The characteristic feature of the new high velocity pseudo SAW is that the singularities of effective permittivity can be located far enough from the real axis of slowness. This means that the intrinsic attenuation of these waves reaches the value of the order of one dB per wavelength. The calculations of [Ref. 4, 6] show that the attenuation can be significantly reduced when the waves propagate in periodic systems of thick metal electrodes.

The measurements of admittance characteristics of synchronous SAW resonators confirm the existence of the new mode and agree satisfactorily with theoretical calculations.

3. EFFECTIVE PERMITTIVITY

The effective permittivity function (EPF) is known to be the ratio of surface charge to electric potential harmonics for a piezoelectric half space, and it is a basic tool in investigations of SAW propagation and excitation phenomena [Ref. 7].

In calculations of real space fields of surface excitation sources, the EPF is continued from the real axis of slowness into the complex plane. The continuation procedure assumes the localization of branch points and drawing appropriate cut lines. As a result a single valued analytic function of effective permittivity is determined [Ref. 5]. The singularities of EPF located at complex values of slowness correspond to leaky SAW modes.

In numerical calculations, the cuts are drawn vertically up as a most convenient way, and the singular points of known FLSAW are usually occur in subsonic region that is slightly higher on slowness axis than the longitudinal branch point.

To illustrate location of singularities, figure 1 shows the real and imaginary parts of EPF for LN A-orientation as it mentioned in [Ref.4]. The Euler angles are equal to (60°, 9°, 0°) referenced to YZ cut. The complex plane is shown schematically by the right axis of imaginary part of slowness. The resonance like behavior after the branch point at 0.2312 is associated with the quasi shear leaky SAW. A numerical procedure to position poles based on drawing the vertical cuts gives the complex slowness s_m=0.23943+i·0.002222. However the same procedure fails to find out a pole near the branch point at s_b=0.14630. The pole location can be determined when the continuation procedure starts from a real valued slowness located slightly higher than the branch point and reaches the complex values of

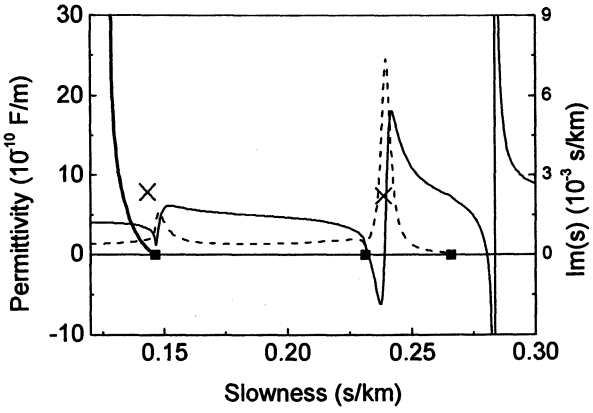

Figure 1: EPF for LN-A. The solid and dashed lines refer to real and imaginary part respectively. The solid squares show branch points, and the crosses represent poles.

slowness with real part less than the branch point. Such continuation corresponds to the curved cut shown in the figure by bold solid line. The pole is located at s_m=0.14621+i·0.0023612, the real part of which is slightly lower than the branch point.

The new pseudo SAW wave exists on the ordinary YZ cut of LN. Fig.2 shows the EPF for this cut. The electrically coupled waves have only two elastic components, and only two branch points are shown as solid rectangles. The pole is located at s_m=0.13932+i·0.0038327, that is slightly higher than the longitudinal branch point s_b=0.13846. The characteristic feature of the quasi-longitudinal leaky wave is a rather high intrinsic attenuation, that on metallized surface of YZ–LN can be estimated as $2\pi \times 8.68 \times \mathrm{Im}(s_m)/\mathrm{Re}(s_m)$=1.5 dB/λ. The numerical values were obtained using the material constants of LN taken from [Ref. 8].

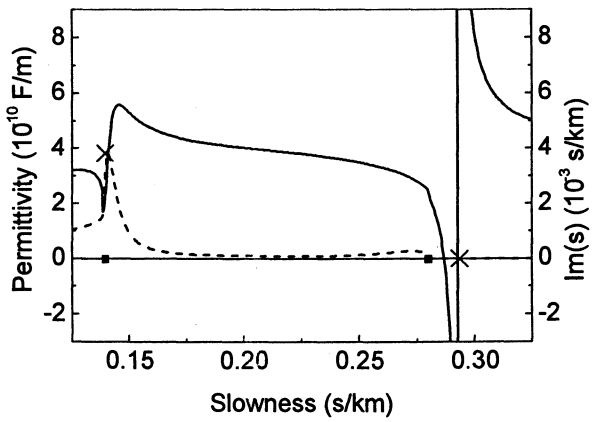

Figure 2: EPF for YZ LN.

It should be noted that the pole in YZ-LN is very close to the branch point. The calculated position of the pole relative to the longitudinal branch point can be dependent on small variations of material constants. When the total set of material constants for LN is taken from [Ref. 9], the pole s_m= 0.13518+i·0.0044577 is located in supersonic region that is slightly lower than the branch point s_b=0.13617 [Ref. 10].

4. CALCULATION OF INFINETLY LONG IDT

The method of EPF assumes that the interface between vacuum and a piezoelectric half space is free of mechanical stresses. Therefore, the method is well suited for investigations of eigen modes or wave excitation by pure electrical sources. However, in low loss SAW filters periodic structures of rather thick electrodes are widely used to obtain desired performances. Long transducer-type resonators with Al electrodes as thick as 8% or even 10% of wavelength are widely used as building blocks for ladder type filters, also known as impedance element filters (IEFs) [Ref. 11]. Because of strong reflectivity and coupling, the interaction of the LSAW with the electrode system is fairly local with the characteristic length of 10 fingers or so, while the transducer structure typically includes a few hundreds fingers. In many aspects, such a structure behaves as infinite, the finite length being manifested only in small ripples in the passband and in some secondary effects. In practice, the dependence of the admittance on frequency is all that is required to be known to use the resonators as "building blocks" for IEF design.

As an alternative to the method of effective permittivity the approach of harmonic admittance [Ref. 11] is known as a powerful tool for analyzing SAW excitation and propagation in periodic arrays of heavy metal electrodes.

In our calculations we used a particular case of the harmonic admittance method, when the excitation phases are opposite between adjacent electrodes. This case directly describes an infinitely long IDT. The calculation method is similar to that of [Ref.12], and uses the periodic Green's function to represent waves in a substrate and the finite element method (FEM) to describe elastic motion in electrodes. The periodicity of IDT, thickness of aluminum electrodes and mettalization ratio are assumed to be λ, h and 0.5 respectively.

Figure 3 shows the calculation results of the transducer admittance referenced to one electrode pair as a function of frequency. The curves in this figure show the admittance for various values of h/λ. It is seen that there is an optimum value of h/λ=0.08 at which the admittance exhibits rather high resonance behavior. The fractional bandwidth is determined as (fa-fr)/fa and equals 3.8% at the optimum value of h/λ=0.08. The velocity of the supersonic FLSAW on YZ LN near resonant frequency approximates the value 6200 m/s

It was shown in [Ref.12], that heavy periodical loading can significantly reduce the attenuation due to the leakage of the quasi shear pseudo mode in YX+64° LN. The energy radiation into the bulk wave disappears when the leaky SAW velocity makes less than that of the slow shear bulk wave, and the leaky SAW behaves as a pure SAW. A similar trapping effect occurs for high velocity leaky modes on YZ-LN.

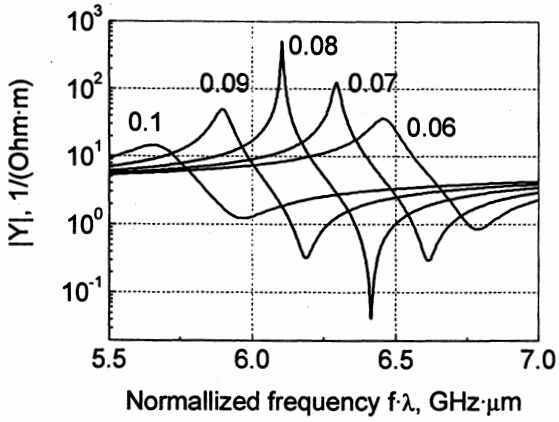

Figure 3: Calculated admittance characteristics of a long IDT on the surface of YZ LN.

As an additional evidence of quasi-longitudinal nature of the new mode, figure 4 shows particle displacements at the electrode – substrate interface at resonant frequency. It is seen that the longitudinal particle displacements are predominant as compared to shear vertical displacements.

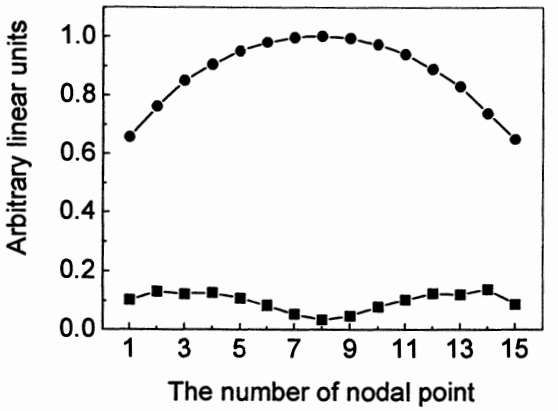

Figure 4. The particle displacements at the interface between electrode and substrate. The circles refer to longitudinal displacements. The rectangles show shear vertical particle displacements.

5. EXPERIMENT

To check the existence of high velocity leaky mode on YZ-LN and evaluate the predicted results for infinitely long IDTs the admittance characteristics of synchronous one-port SAW resonators with the periodicity of electrode structure of 4 μm were measured. The thickness of electrodes was equal to 0.32 μm, that exactly corresponded to the optimum value of h/λ=0.08. The number of electrodes in IDTs was 100, and the aperture length was 12λ. Short-circuited reflectors of 67 electrodes were used to exclude the energy dissipation at the ends of IDTs
A network analyzer HP8753D was used to measure the scattering parameter S11 that then re-calculated into the admittance responses.

Figure 5 shows the measured real and imaginary parts of admittance on YZ-LN. The admittance exhibits a typical resonance behavior of inductive type in the restricted region between resonant and anti resonant frequencies.

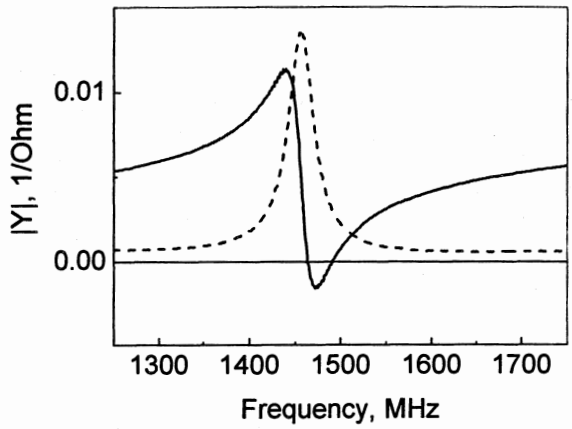

Figure 5. The measured admittance response of a synchronous one-port SAW resonator. Solid and dashed curves refer to imaginary and real part respectively

The fractional bandwidth estimated as (fa-fr)/fa is equal to 3%, and an effective propagation velocity approximates the value 6000 m/s, that is 1.7 times larger than the velocity of Rayleigh SAW on YZ-LN.
As a comparison between theory and experiment figure 6 shows the absolute value of admittance along with calculated data. The results agree satisfactorily.

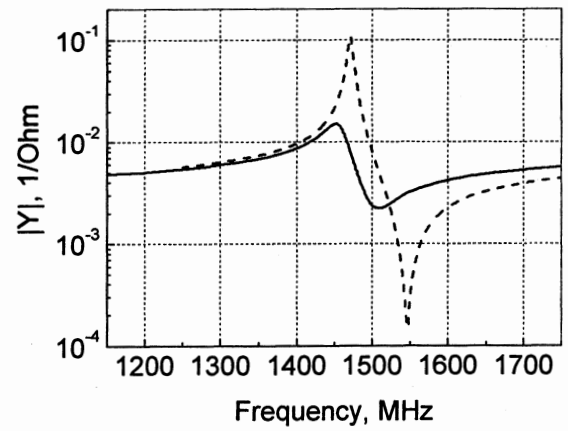

Figure 6. Comparison between theory and experiment. The solid curve shows the absolute value of admittance response. The dashed curve refers to calculated data.

The quality factors at resonant and anti resonant frequencies were calculated as [Ref.4]

$$Q_r=\omega/\mathrm{Re}(Z)\times\partial\mathrm{Im}(Z)/\partial\omega|_{\omega=\omega r}$$

$$Q_a=\omega/\mathrm{Re}(Y)\times\partial\mathrm{Im}(Y)/\partial\omega|_{\omega=\omega a}$$

and found to equal 32 and 30 respectively. While the

calculated data of quality factors were Qr=200 and Qa=1200. The discrepancy might be attributed to the intrinsic attenuation at high frequencies in the substrate material as well as in rather thick electrodes.

6. CONCLUSION

The new high velocity pseudo SAW mode exists on the ordinary YZ cut of LN. Due to the trapping effect of strong mechanical loading, the admittance response of a synchronous one port SAW resonator YZ LN exhibits a typical resonant behavior. The mode due to its high propagation velocity is promising for application in high frequency resonator filters. Additional investigations of loss mechanisms are to be done.

7. ACKNOWLEDGMENT

The authors would like to thank many colleagues from TMX for helpful discussions. One of the authors (VG) is grateful to TMX for partial support of this work.

8. REFERENCES

[1] N.F.Naumenko " Leaky surface acoustic waves with quasilongitudinal polarization in the crystal of lithium tetraborate," Sov. phys. Crystallogr., vol. 35, no.4, pp.520-522, 1992.

[2] T.Sato and H.Abe "Propagation Properties of Longitudinal Leaky Surface Waves on Lithium Tetraborate," in Proc. IEEE Ultrason. Symp., 1994, pp. 287-292.

[3] T.Sato and H.Abe "Longitudinal leaky surface waves for high frequency SAW device applications," in Proc. IEEE Ultrason. Symp., 1995, pp. 305-315.

[4] A.Isobe, M.Hikita and K.Asai "Propagation characteristics of longitudinal leaky SAW in Al-grating structure", IEEE Trans. on UFFC, Vol. 46, No.4, July 1999, pp. 849-855.

[5] S.V.Biryukov and M.Weihnacht "Real space field of surface sources and the problem of fast leaky wave generation in a piezoelectric half-space" J. Appl. Phys., Vol. 83, No. 6, March 1998, pp.3276-3287.

[6] V.I.Grigorievski "Fast leaky surface acoustic waves on lithium niobate and lithium tantalate," to be published in Proc. IEEE Ultrason. Symp., 2000.

[7] D.P.Morgan "Surface wave devices for signal processing," Elsevier, 1985.

[8] G.Kovacs, M.Anhorn, H.E.Engan, G.Visintini, and C.C.W.Ruppel "Improved material constants for $LiNbO_3$ and $LiTaO_3$," in Proc. IEEE Ultrason. Symp., 1990, pp. 435-438.

[9] R.T.Smith and F.S.Welsh "Temperature dependence of the elastic, piezoelectric and dielectric constants of lithium tantalate and lithium niobate," J. Appl. Phys., vol.42, no. 6, pp. 2219-2230, 1971.

[10] V.I.Grigorievski "Fast leaky surface acoustic waves on YZ cut of lithium niobate," in Abstr. of the 5th Int. Forum on Wave Electronics, 2000, pp. 36-37.

[11] V.P.Plessky, S.V.Biryukov, and J.Koskela, " Harmonic admittance and dispersion equations – The theorem," to be published in Proc. IEEE Ultrason. Symp., 2000.

[12] J.Koskella, V.P.Plessky, and M.MSalomaa "Suppression of the leaky SAW attenuation with heavy mechanical loading, " IEEE Trans. on UFFC, Vol. 45, No.2, March 1998, pp. 439-449.

SECOND HARMONIC REFLECTORS

S. Lehtonen[1], J. Koskela[1], V. P. Plessky[2], and M. M. Salomaa[1]
[1]*Materials Physics Laboratory, P.O. Box 2200, FIN-02015 HUT, Finland*
[2]*Thomson Microsonics, SAW Design Bureau, Fahys 9, CH-2000 Neuchâtel, Switzerland*

Abstract—**In this work, we study theoretically the operation of surface-acoustic wave (SAW) reflectors on the second harmonic. There is a renewed interest on second harmonic reflectors for high-frequency devices and for sensor and tag applications. Here, we demonstrate that the reflectivity of the 2nd harmonic reflectors can be very high, *e.g.*, on 128°-$LiNbO_3$. We have simulated performances of a few typical SAW devices with such reflectors. For 128°-$LiNbO_3$, rigorous simulations for test structures tailored to extract losses due to bulk scattering suggest total losses, inside the stopband, for the second harmonic to be on the same order as those for fundamental harmonic operation.**

I. Introduction

The frequency range 3-5 GHz holds great potential for several SAW applications (*e.g.* tags and UMTS and WLAN filters). However, the required linewidths being at or beyond the limits of current lithographic mass-production techniques, the production yield remains poor. One possible approach to facilitate the fabrication is to employ reflectors operating at the second or higher harmonic stopband.

Another motivation for studying higher harmonic reflectors is that considerable reflectivities may be obtained on substrates such as 128°YX-$LiNbO_3$, where the reflectivity at the fundamental harmonic is low. The combination of the low spurious level of 128°YX-$LiNbO_3$ with high reflectivity would be very attractive for SAW sensor and tag applications.

The properties of reflectors at harmonic frequencies are not very well known, although first studies [1] have shown that the reflectivity can be rather strong. Experimental work towards this direction has been done, e.g., by Campbell and Edmonson [2], who studied the properties of a harmonic one-port resonator on 64°YX-cut $LiNbO_3$. In this work we attempt to characterize the reflectors by theoretical means.

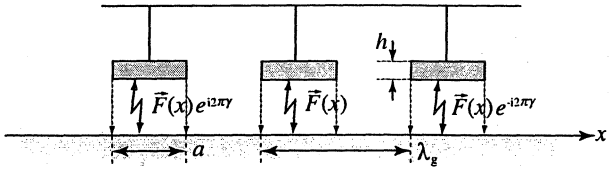

Fig. 1. Numerical experiment where an infinite periodic grating is driven by mechanical forces acting at the interface between the electrodes and the substrate.

II. Methods

As our method of investigation, a two-step procedure is applied. First, the velocities v and the reflectivities in the gratings are initially characterized using a FEM/BEM simulator for infinite periodic electrode arrays [3]. The most promising structures are then subject to considerably slower but more realistic FEM/BEM simulations of finite structures [4].

There are methodological difficulties related to the numerical characterization of infinite periodic electrode arrays operating at the second harmonic. For even-order harmonics $f_{2n} = nv/p$, where p denotes the pitch of the array, the electromechanical coupling coefficient of the SAW eigenmodes tends to vanish. To circumvent the problems with electric sources, we follow the general idea of mechanical excitation, a possibility mentioned by Ventura *et al.* [5]. Mechanical sources, *i.e.*, oscillating stress forces $\vec{T}(x)$ acting at the electrode-substrate interface, are employed to drive the grating in the harmonic configuration with the excitation wavenumber γ close to zero, see Fig. 1. The resulting resonances in such a numerical experiment enable one to detect the edges of the stopband and, hence, the center frequency and reflectivity.

The complete dispersion relation–especially the attenuation due to the scattering into bulk waves–remains difficult to evaluate from simulations of the infinite arrays. Further complication are the potentially significant losses due to SAW-BAW scattering at the discontinuities between the reflectors and the

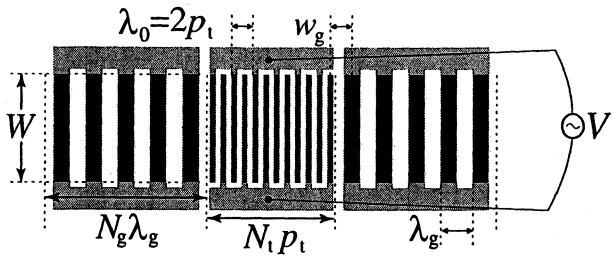

Fig. 2. Resonator with second harmonic reflectors.

IDT, not taken into account by periodic simulations. Hence, rigorous FEM/BEM simulations of finite structures [4] are carried out for the most interesting cases. The asynchronous one-port resonator in Fig. 2 is used as the test structure. The coupling-of-modes (COM) model is employed to analyze the results of the simulations and to compare them with those of the periodic FEM/BEM simulator.

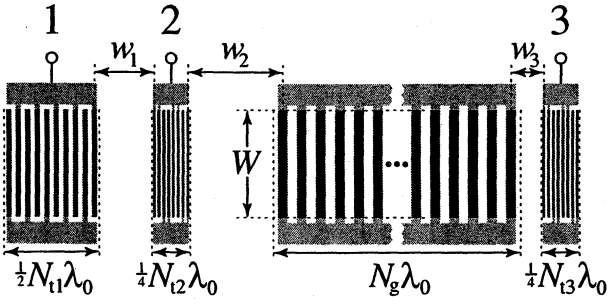

Fig. 3. Test structure for evaluation of attenuation. In the simulation for 128°$LiNbO_3$, values N_{t1} = 10, N_{t2} = N_{t3} = 8, N_g = 80, λ_0 = 4 μm, W = 32 μm, w_1 = 100 μm, w_2 = 170 μm, and w_3 = 30 μm were used.

By introducing proper test structures, rigorous simulations also offer a means to estimate losses due to bulk scattering. In this work, a structure consisting of a transmitting transducer, two receiving split-finger transducers, a reflector placed between the receiving transducers, and gaps with different widths between the test structure building blocks (see Fig. 3), was used to address the scattering losses. The responses in the receiving transducers (ports 2 and 3), calculated in terms of Y-parameters, contain contributions attributed to multiple reflections from the reflector and the transmitting (port 1) transducer. However, the reflections from the receiving transducers are negligible due to the split-finger geometry. Through time gating the direct signal, transmitted from the source transducer and received at the first split-finger transducer, can be separated from the contribution of the signal reflected back from the grating. Correspondingly, the direct signal received in the second split-finger transducer can be identified.

The source being in port 1, it is justified to assume that the admittances observed in ports 2 and 3 are proportional to the corresponding acoustic wave amplitudes. Thus, energy comparison serves as evaluating the losses:

$$|Y_{21}^d|^2 \geq |Y_{21}^r|^2 + |Y_{31}^d|^2, \qquad (1)$$

where the superscripts d and r refer to the direct and reflected signals, respectively.

III. Results

The periodic structure simulator with mechanical sources was used to determine the velocity and reflectivity on the 128°YX-cut $LiNbO_3$, supporting a Rayleigh wave, and on 64°YX-cut $LiNbO_3$ and 42°YX-cut $LiTaO_3$, supporting leaky surface-acoustic waves, as functions of the metallization ratio a/λ_0 and the relative electrode thickness h/λ_0. The materials parameters by Kovacs *et al.* [6] were used for $LiNbO_3$ and $LiTaO_3$. The aluminum electrodes were assumed rectangular and isotropic.

Some characteristics are typical for all cases. The velocities obtained are slightly or considerably higher than those for fundamental harmonic frequencies. The effect is probably due to reduced screening of the electric fields by the electrodes. The velocities tend to be quite sensitive to the metallization ratio.

A. 128°YX-cut $LiNbO_3$

The obtained velocities and reflectivities are illustrated in Fig. 4. The velocities are notably (almost 50 m/s) higher than when operating at the fundamental frequency. The reflectivity increases strongly with electrode thickness, reaching a value as high as 20% for $h/\lambda_0 = 8\%$. Such an excellent reflectivity is somewhat unexpected result, especially when compared to the rather poor reflectivity for the fundamental harmonic. For all studied thicknesses, the maximum reflectivity is achieved for a/λ_0 close to 0.4.

The simulation of a finite one-port resonator with $h/\lambda_0 = 5\%$ and $a/p = 0.5$ is displayed in Fig. 5. Also shown is the admittance obtained from COM with the parameters determined from the periodic FEM/BEM simulations. The agreement is reasonable. No significant attenuation is predicted in the simulations, suggesting that the second harmonic reflectors on 128°-cut $LiNbO_3$ indeed are promising for applications demanding high reflectivity.

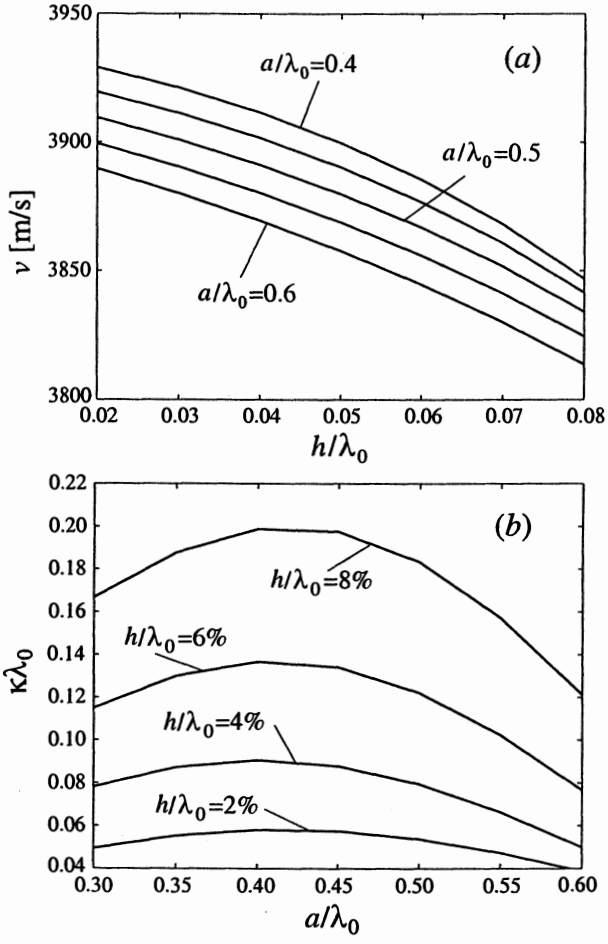

Fig. 4. (*a*) Velocities and (*b*) reflectivities for second harmonic reflectors on 128°YX-cut $LiNbO_3$, determined from simulations of infinite periodic gratings.

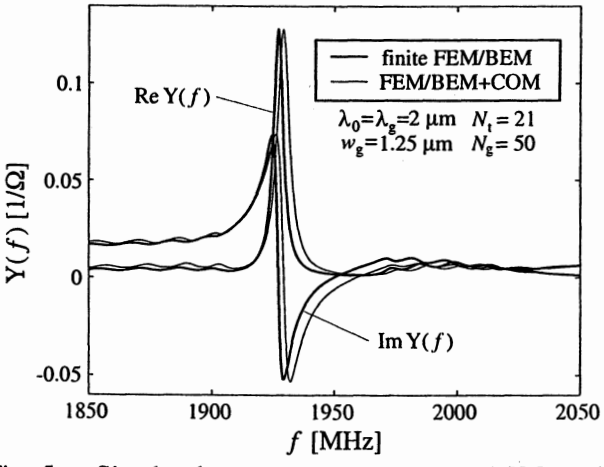

Fig. 5. Simulated resonator response vs. COM model on 128°YX-$LiNbO_3$ with h/λ_0=5% and metallization ratio 0.5. The structure is of the type shown in Fig. 2.

The simulation result for the attenuation test structure (Fig. 3) for $h/\lambda_0 = 5\% \hat{=} 1000$Å and $a/p = 0.5$ is shown in Figure 6. It can be readily seen that in the reflector passband regions close to the stopband, the total losses vary from 5 to 7 dB, which correspond to $\gamma_{att}\lambda_0 = 0.007 \ldots 0.01$. The value is about one order of magnitude higher than that estimated for fundamental mode operation, 0.7...1.2 dB $\hat{=} \gamma_{att}\lambda_0 = 0.001 \ldots 0.002$.

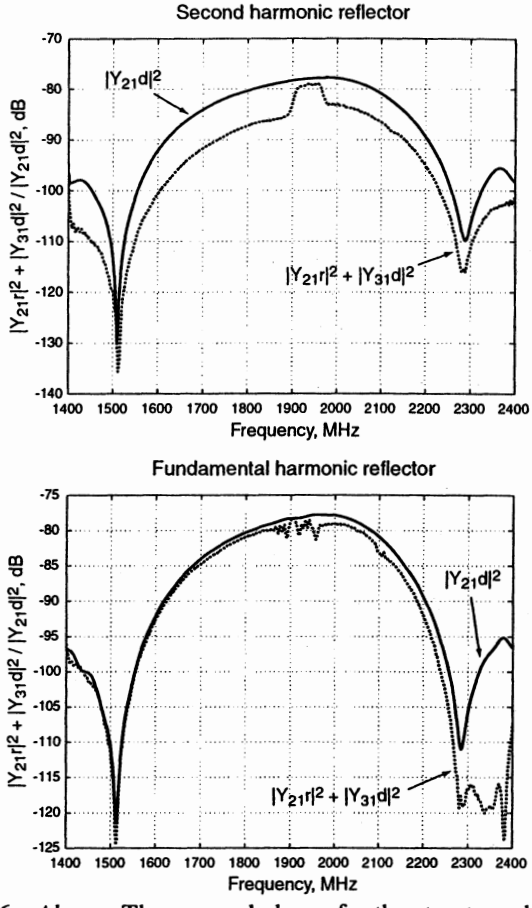

Fig. 6. *Above:* The energy balance for the structure shown in Fig. 3. *Below:* The energy balance for an equivalent test structure with the reflector operating at the fundamental frequency ($N_g^{fund} = 2N_g^{2harm}$). The substrate is 128°YX-$LiNbO_3$ with h/λ_0=5% and metallization ratio 0.5.

However, in the reflector stopband region, the attenuation is significantly reduced for the second harmonic mode of operation while no systematic change is seen (Fig. 6) for the fundamental mode reflector. Actually, we see little if any increase in losses in the stopband compared to the case of fundamental harmonic reflector. This is likely to be the result of the small penetration depth of the wave into the reflector due to the high reflectivity. Thus, the losses attributed to scattering, present in the whole frequency range, are limited in the stopband. Note also that the resistive losses are practically absent in the second harmonic reflector, while they are essential in fundamental harmonic operation.

The reflectivity per strip $\kappa\lambda_0$ can be estimated from

Y_{31} as

$$\mathbf{T} = \frac{1}{\cosh(\kappa\lambda_0 N_g)}, \qquad (2)$$

where $\mathbf{T}$ is the grating transmission coefficient at the stopband. The resulting value for the test structure with $N_g = 80$, $h/\lambda_0 = 5\%$, and $a/\lambda_0 = 0.5$ is found to be about 6.5%, less than the 10% calculated for an infinite periodic structure.

B. 64°YX-cut $LiNbO_3$

The results from infinite grating simulations for 64°YX-cut $LiNbO_3$ are shown in Fig. 7. The obtained velocities are visibly higher than those for operation at the fundamental frequency. The velocities depend strongly on the metallization ratio, indicating that, depending on the application, precise control over a/λ_0 may be required in the fabrication. For $a/\lambda_0 = 0.4 \ldots 0.6$ and with the aluminum thicknesses varying from h/λ_0=2 to 8%, reflectivies ranging from 2 to 15% are predicted. This is somewhat lower than for the fundamental harmonic operation.

The attenuation at the first edge of the stopband was estimated from the Q-factor of the infinite array simulations. Towards the second edge of the stopband the simulations display strong increase in the losses.

Figure 8 illustrates a simulation of a one-port resonator with second harmonic reflectors on 64°YX-$LiNbO_3$ with thickness h/λ_0=6% and metallization ratio 0.55. Different pitch was used in the IDT and the reflectors to match the reflector stopbands with the maximum radiation conductance of the short IDT.

It is interesting to compare the theoretical results with the experiments conducted by Campbell and Edmonson [2]. The predicted first edge of the stopband agrees with experiment up to a few MHz (about 20 m/s). The difference fits within the numerical error or, noting the strong sensitivity of the velocity and reflectivity to the electrode profile, it might be due to a non-controllable difference in the materials or the electrode geometry between the experiment and our simulations. On the other hand, about twice as high a reflectivity is predicted here than that deduced by Campbell and Edmonson. However, we note that, due to the strong BAW scattering at high frequencies, the location of the upper edge of the stopband is rather difficult to determine experimentally.

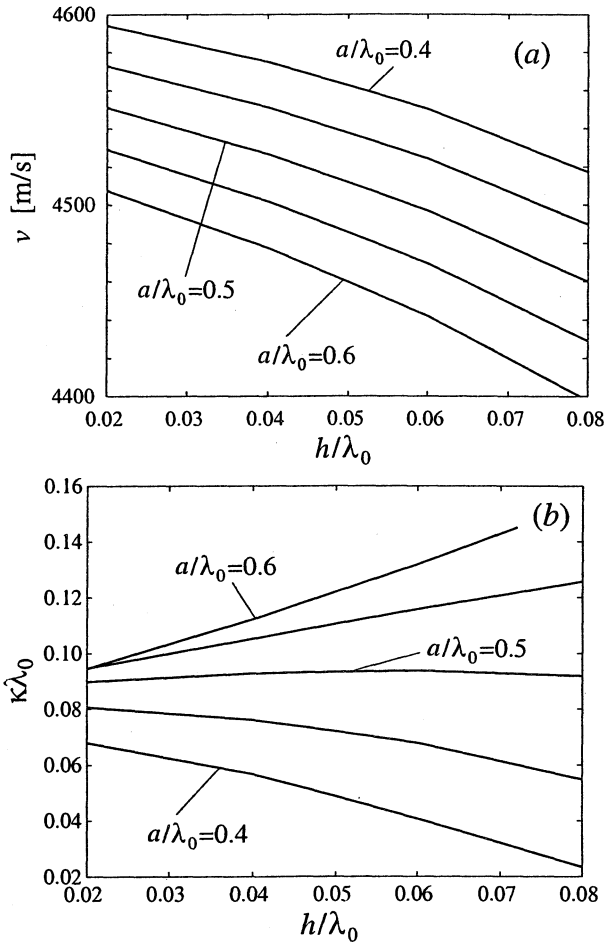

Fig. 7. (*a*) Velocities and (*b*) reflectivities for second harmonic reflectors on 64°YX-cut $LiNbO_3$. The values were determined from simulations of infinite periodic gratings.

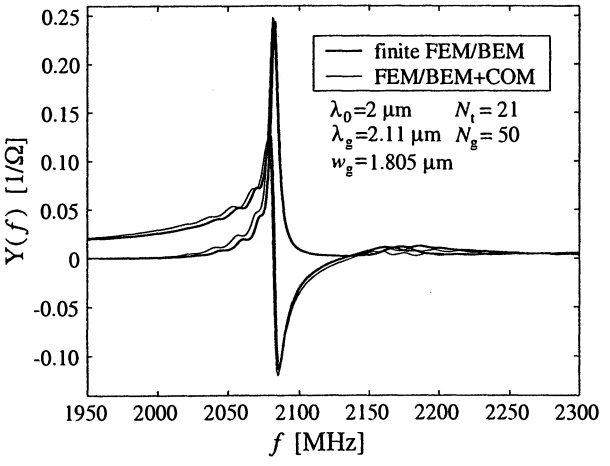

Fig. 8. Simulated resonator response vs. COM model on 64°YX-$LiNbO_3$ with h/λ_0=6% and metallization ratio 0.55. The structure is of the type shown in Fig. 2.

C. 42°YX-cut $LiTaO_3$

The velocities and reflectivities determined from simulations of infinite periodic arrays on 42°YX-cut

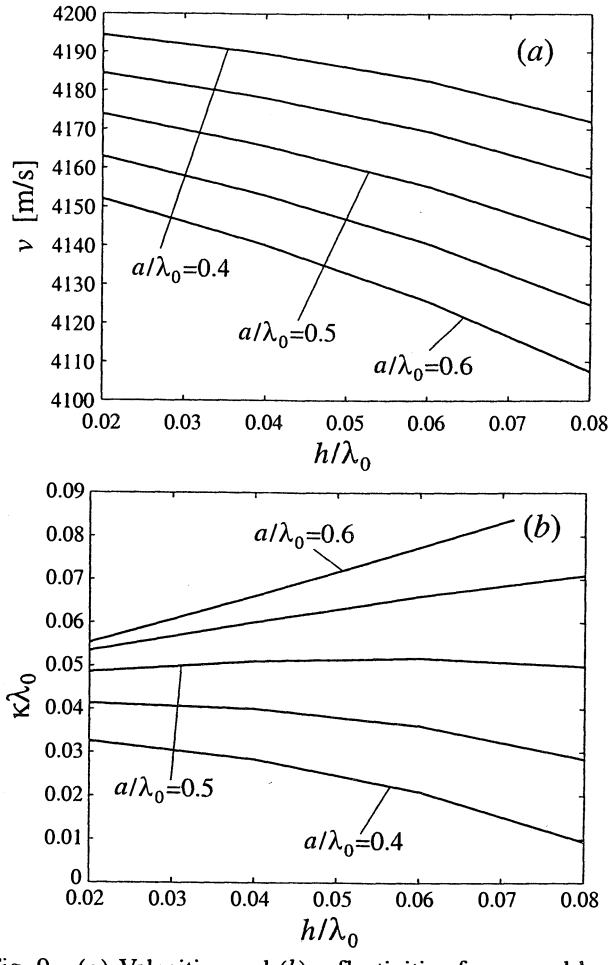

Fig. 9. (*a*) Velocities and (*b*) reflectivities for second harmonic reflectors on 42°YX-cut $LiTaO_3$, determined for infinite periodic gratings.

$LiTaO_3$ are illustrated in Fig. 9. With the relative electrode thicknesses h/λ_0 from 2 to 8%, reflectivities per period within 1-10% are achieved. The velocities are again a few dozens of meters per second higher than those for the fundamental harmonic operation. Due to the radiation of BAWs, the attenuation per period $\gamma_{att}\lambda_0$, simulated with the periodic FEM/BEM simulator for infinite arrays, increases to about $0.5\text{-}1.5\cdot10^{-3}$. Although the attenuation is one order of magnitude higher than the theoretical values in simulations for the fundamental frequency, the values are, nevertheless, comparable to the experimentally observed attenuation at the fundamental frequency and, hence, appear quite acceptable.

Interestingly, for leaky SAWs on both 42°-$LiTaO_3$ and 64°-$LiNbO_3$ the dependence of reflectivity on the thickness of the aluminum electrodes is different from that for Rayleigh waves on 128°-$LiNbO_3$ (compare Figs. 7, 9 with Fig. 4). For LSAWs and a/λ_0 about 0.5, the reflectivity is almost independent of h/λ_0. For $a/\lambda_0 < 0.5$ the reflectivity decreases and for $a/\lambda_0 > 0.5$ it increases with the electrode thickness.

IV. Discussion

We have investigated second harmonic reflectors numerically. Reflectivities varying from modest to high seem achievable with reasonable electrode thicknesses. The technique appears particularly interesting for 128°YX-$LiNbO_3$. Special attention must be paid on the phase, velocity, and reflectivity shifts between reflectors and IDTs. Rigorous simulations for 128°YX-$LiNbO_3$suggest that the losses due to BAW scattering inside the grating and at the discontinuities are about one order of magnitude higher in passband and, in stopband, practically equal to those for operation at the fundamental harmonic.

Acknowledgments

The first two authors acknowledge the Academy of Finland for fellowships within the Graduate School in Technical Physics and the NOKIA Foundation for research grants.

References

[1] R. C. M. Li and J. Melngailis, "The influence of stored energy at step discontinuities on the behaviour of surface-wave gratings," *IEEE Trans. Sonics Ultrason.*, vol. 22, pp. 189-198, May 1975.

[2] C. K. Campbell and P. J. Edmonson, "Conductance measurements on a leaky SAW harmonic one-port resonator," *IEEE Trans. on Ultrason., Ferroelect., and Freq. Control*, vol. 47, pp. 111-116, Jan. 2000.

[3] J. Koskela, V. P. Plessky, and M. M. Salomaa, "SAW/LSAW COM parameter extraction from computer experiments with harmonic admittance of a periodic array of electrodes," *IEEE Trans. Ultrason., Ferroelectr., and Freq. Control*, vol. 46, pp. 806-816, July 1999.

[4] P. Ventura, J. M. Hodé, M. Solal, J. Desbois, and J. Ribbe, "Numerical methods for SAW propagation characterization," *Proc. 1998 IEEE Ultrasonics Symp.*, pp. 175-186.

[5] P. Ventura, J. Desbois, and L. Boyer, "A mixed FEM/analytical model of the electrode mechanical perturbation for SAW and PSAW propagation," *Proc. 1993 IEEE Ultrasonics Symp.*, pp. 205-208.

[6] G. Kovacs, M. Anhorn, H. E. Engan, G. Visintini, and C. C. W. Ruppel, "Improved material constants for $LiNbO_3$ and $LiTaO_3$," *Proc. 1990 IEEE Ultrasonics Symposium*, pp. 435-438.

INSTRUMENTATION & TELECOMMUNICATIONS

Chairman: Pekka Eskelinen

TIME SYNCHRONIZATION NETWORK FOR WDM-SDH-BASED ATM SERVICE SYSTEM

Masami Kihara, Taichi Hiramatsu*, Shu-ichi Maruyama*, Kenji Hisadome
NTT Network Innovation Laboratories
*NTT Communications

ABSTRACT

NTT will introduce a time synchronization network in a new system that provides ATM(Asynchronous Transfer Mode) services. The system transfers ATM cells via SDH(Synchronous Digital Hierarchy) frames which are transmitted over WDM(Wavelength Division Multiplexing) networks. The SDH frames can transfer time information, and can realize a time synchronization function. The SDH network and ATM systems will utilize the reference time supplied by the time function for network operation and management. This paper describes the new ATM network configuration, reference signal networks to support time synchronization, time keeping systems, and some initial measurement results on time synchronization in practical systems.

Keywords: time transfer, time synchronization, WDM and SDH

1. INTRODUCTION

Telecommunication networks are moving toward terabit transmission capacity. This is undoubtedly the result of the demand for Internet services. Two important technologies are required; WDM(Wavelength Division Multiplexing) to achieve enormous transmission capacity, and advanced network management to control the data stream traffic and QoS(quality of Service).

NTT is introducing a WDM-SDH based ATM network. The network provides a broadband ATM service that supports conventional interfaces and IP system services. ATM allows highly developed management functions for the network for itself and for individual channels. One of the keys to these ATM features is time. ATM systems can utilize the reference time synchronized throughout the network to achieve multiple services as ATM connections can be set and released at specified times.

Reference time is transferred to each ATM node as well

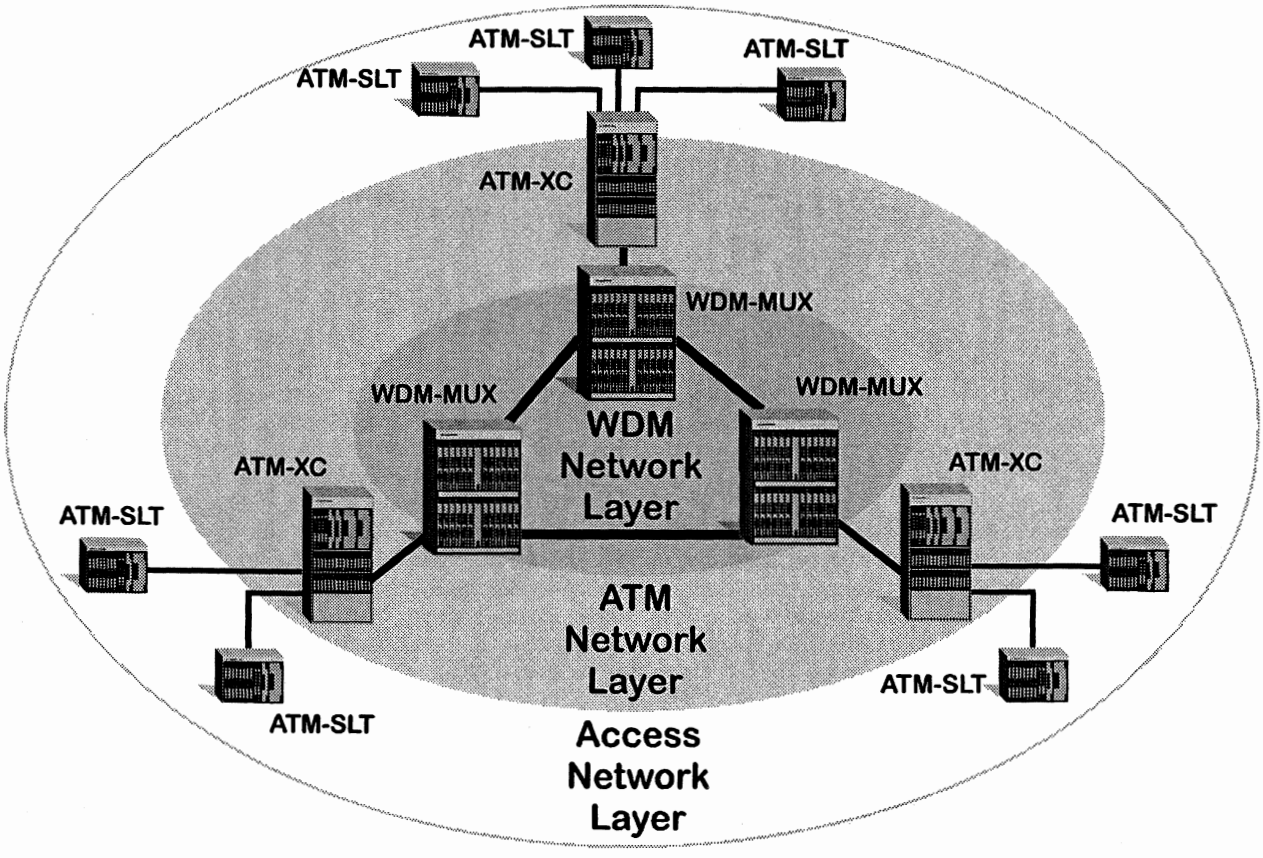

Fig.1-Network configuration for the new service

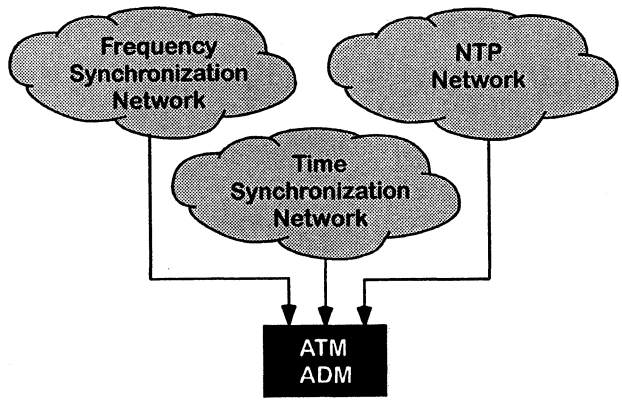

Fig.2 – Reference signal networks for ATM-XC

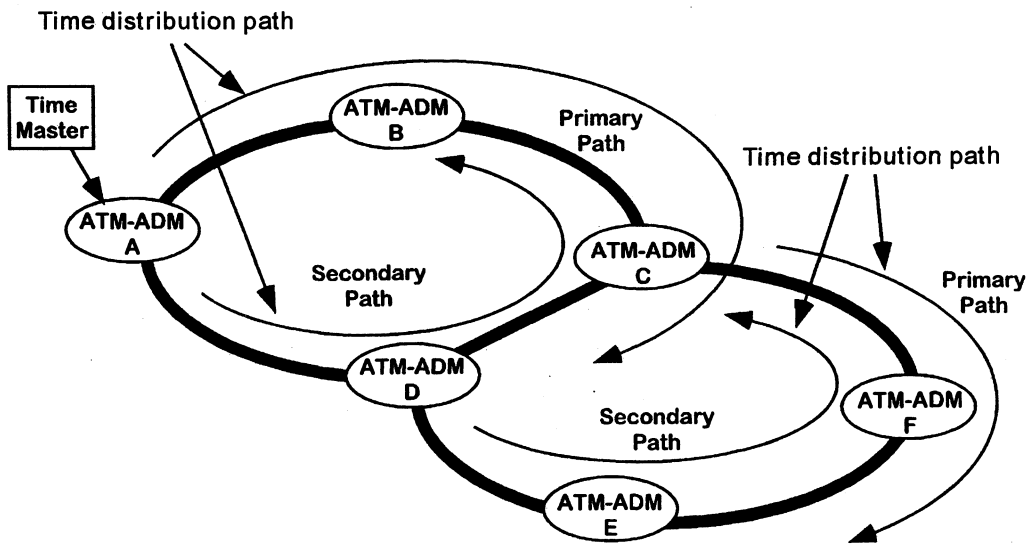

Fig.3 – Time distribution paths

as reference frequency, and is kept and maintained by ATM systems. The kept time is distributed to each function block, so reference time is shared by every function.

This paper describes a network that provides ATM services based on WDM-SDH, and a reference time system together with a time synchronization method, time transfer network, time keeping and management and some initial measurement results of time transfer characteristics.

2. NETWORK CONFIGURATION

The new ATM network consists of three layers: WDM network layer, ATM network layer, and access network layer. Figure 1 shows the total network configuration for the new NTT service. The WDM network layer is a long-haul transmission network based on WDM techniques. The WDM termination points have 2.5Gb/s channel multiplexing and demultiplexing functions. The ATM network layer is composed of ATM cross-connect systems. Each ATM cross-connect system has a 2.5Gb/s channel interface and an access network interface. The Access network layer includes ATM-SLT among the premises equipment. General information is translated into ATM cells using the CLAD function of each ATM-SLT. In this configuration, reference time is maintained in the ATM cross-connect system. Reference time can be transferred by the WDM network layer over long distances.

3. REFERENCE SIGNAL SYSTEM

The ATM cross connect system keeps reference time using its internal management function. The system receives reference signals from three networks as shown in Fig.2: the frequency synchronization network, the time synchronization network, and the NTP network.

Reference frequency, which is used as the time clock, is

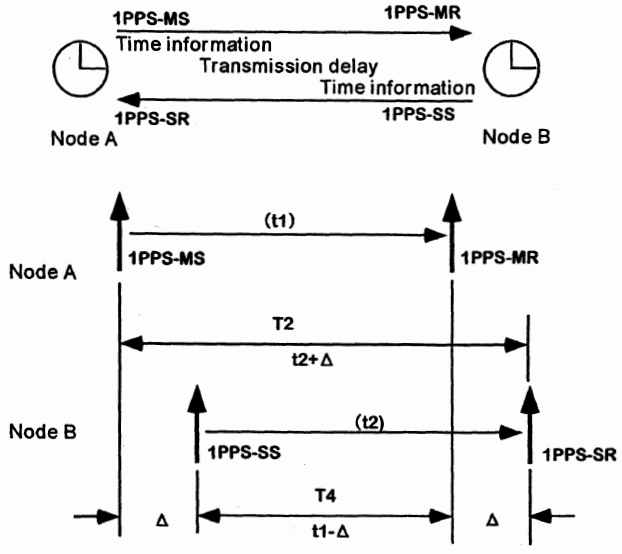

Fig.4 – Two-way time transfer

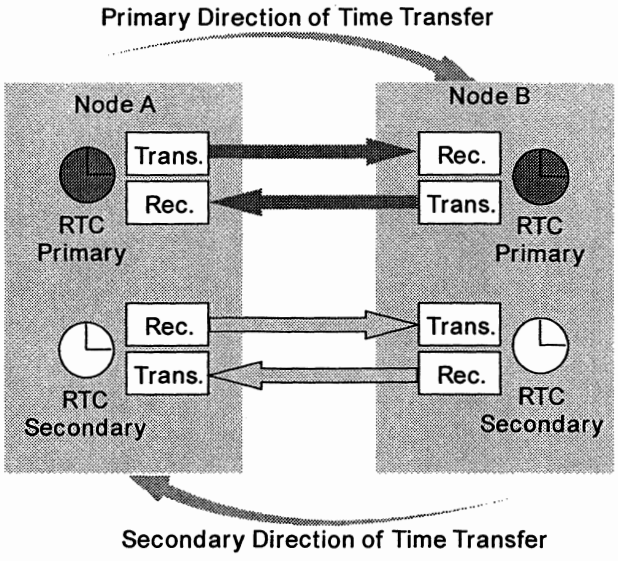

Fig.5 – Bi-directional time transfer

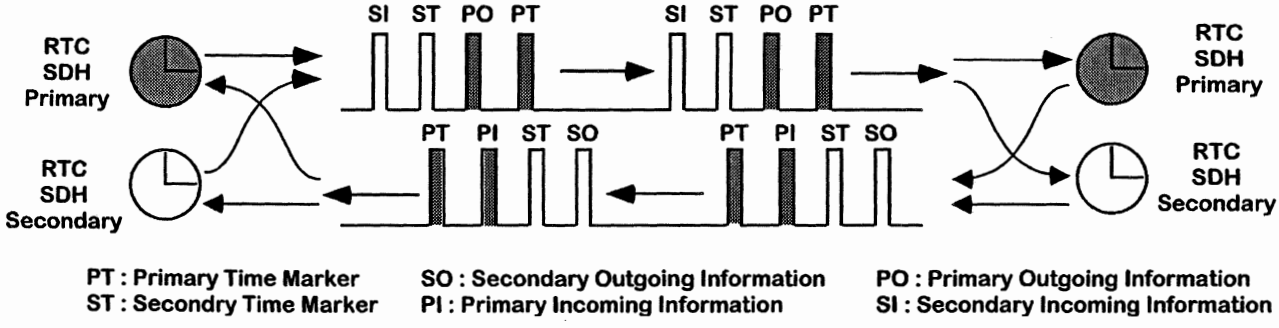

Fig.6 – Time information transfer mechanism

kept in the external equipment, generally called BITS. BITS can hold reference frequency to better than 10^{-12}, even if the reference frequency network fails. This highly reliable and stable network clock is supplied to the ATM cross connect systems. Even if the time synchronization network fails, time in the ATM cross connect system is kept to the nano second level by the network clocks.

NTP is used to back up the reference time network. The NTP network is modified to make the transmission delay constant. This enables NTP to maximize the time accuracy.

The NTP time input is single, while other reference inputs are redundant. They have primary and secondary inputs.

4. TIME SYNCHRONIZATION NETWORK

4.1 Network configuration

The new time synchronization network is a ring network. A ring consists of several ATM cross connect systems, one of which becomes a master node as shown in Fig.3. ATM cross connect A is the master in Fig.3. Reference time of the master node is transferred from node to node both clockwise and counterclockwise. Adjacent rings contact and share some ATM cross connect systems. ATM cross connects C and D are shared by two rings in Fig.3. Every node is connected in this manner. The total network is composed of multiple rings.

4.2 Time master

Reference time is first generated in a time master.
We intend to use the LF standard radio signal receiver as the time master. Time accuracy of the LF standard radio signal is several hundreds of micro seconds. This is definitely much lower than that offered by GPS. The LF standard radio signal is, however, guaranteed as an administrative service, and we can get traceability of Japanese standard time.

The network configuration we adopt does not restrict the

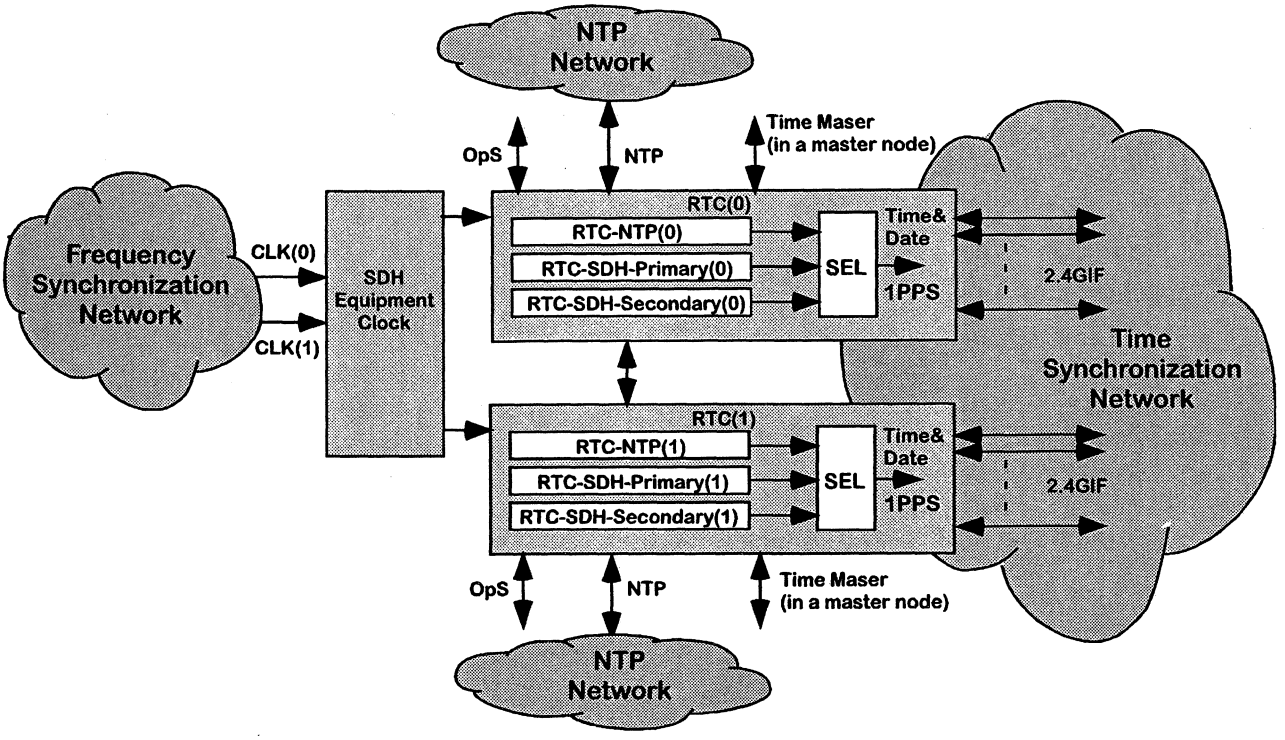

Fig.7 – Time keeping and management system in ATM-XC

number of master nodes. We can set any node as a master node if it has an LF standard radio receiver. Cost determines how many master nodes should be installed. However, 1 or 2 master nodes is sufficient if we focus on the relative time difference between nodes.

4.3 Time transfer method

Time transfer of the new system is based on the two-way time transfer method shown in Fig.4. Each node measures the time difference between its own time and the transferred time. If B node is synchronized to A node in Fig.4, the two-way time transfer measurement results acquired in A node are sent to B node. This is achieved over a data communication channel between the nodes. This allows B node to adjust its own time. This process is repeated to propagate the reference time throughout the network.

4.4 Redundancy in time transfer

Figure 5 represents a practical network configuration. Reference time is transferred over primary and secondary paths. One ring has two paths for time transfer without exception to ensure time transfer reliability. Bi-directional paths mean clockwise and counterclockwise time transfer routes. This configuration requires 4 time transfer paths, that is, 4 optical fibers appear necessary. While a 4-fiber ring network configuration is possible, it is not used in practice due to its cost. We developed a new bi-directional two-way time transfer method to allow the use of a 2-fiber ring network configuration.

In our method, time transfer signals are multiplexed and demultiplexed to and from the data communication channels in SDH frames as shown in Fig.6. This method allows bi-directional time transfer to be realized over a 2-fiber ring network.

5.TIME KEEPING AND MANAGEMENT SYSTEM

ATM cross connect systems can receive time information from primary and secondary paths in ring networks, and from the NTP network. Each time is held internal clocks called RTC(Real Time Clock) in the ATM cross connect systems as shown in Fig.7. This enables the three kinds of time to be independent and to independently managed. In this configuration, the failure of one kind of time does not influence the others, and fault location and system switching can be achieved without interruption.

6. CONCLUSION

Time is becoming an important element in telecommunication networks. Its current role is just time stamping; however, time will become an essential part of the basic network functions.

While there is still some way to go to achieve a complete time system, the new time synchronization network is definitely a promising start to the use of synchronized time given its excellent accuracy, stability, and low system costs.

Acknowledgement

The authors wish to thank Mr. Imae of CRL for his suggestions concerning the LF radio standard signal.

The Readout of Time: Calendars and Superheterodyning

Michel Planat*, Jean-Philippe Marillet* and Jacky Cresson**

* Laboratoire de Physique et Métrologie du CNRS,
associé à l'Université de Franche-Comté,
32 avenue de l'Observatoire, 25044 Besançon Cedex, France
e-mail: planat@lpmo.edu

** Equipe de Mathématiques de Besançon,
Université de Franche-Comté,
16 Route de Gray, 25030 Besançon Cedex, France
e-mail: cresson@math.univ-fcomte.fr

Abstract

Time and frequency measurements of a high frequency oscillator need the comparison to a reference oscillator: the physical units of the measurement are the integers and the relevant approach is analytical number theory. We show this in the context of the moon-sun calendar discovered in ancient Greece and in the context of a communication receiver. It is shown that the resets in time measurements are governed by continued fraction expansions and that their low frequency statistics connects to prime number theory. A link between Riemann hypothesis and $1/F$ noise arises in this context.

1 The Time and Noise in Oscillators

Over the last years it has been observed that low frequency noise of electronic oscillators carries a strong arithmetical structure [1],[2]. Such a structure was implicitely discovered by the Greeks when establishing their moon-sun calendars. Time and noise go hand by hand in the astronomical calendar and in the superheterodyne receiver discovered by E.H. Armstrong at the dawn of the electronic age.

In the Greek calendar one divides the tropical year by the moon year in units of the earth day and one gets 12 (the number of months in a sun year), plus $\frac{1}{2}$, or $\frac{1}{3}$ or $\frac{3}{8}$ depending on the approximation of the ratio by rational numbers: this can be taken into account by adding one month every two years, or one month every three years or three months every eight years respectively.

The random reset of a time period takes place automatically in Armstrong's superheterodyne detection which is based on mixing of two input oscillators and baseband filtering [2]. This principle has wide applicability in most communication receivers. We found that as a result the mean period fluctuates with $1/F$ power spectral density. The mathematical structure underlying the resets in the Greek calendar and in Armstrong's receiver is continued fraction expansions of the period ratio between the oscillators. This also resorts to the general theory of primes.

In Sect. 2 we remind some properties of continued fractions for the pedestrian in the context of the moon-sun calendar. The arithmetical structure of the mixer+filter set-up is described in Sect. 3. Finally Sect. 4 is an attempt to connect the observed randomness of frequency resets to prime number theory.

2 The Moon-Sun calendar

Most early calendars have been devised from the motion of moon and sun as observed from the earth. In the astronomical calendar one finds 365.242191 days for the tropical year (equinox to equinox) and 29.530589 days for the moon year (new moon to new moon). The ratio is $\nu = 12.4952 \simeq 12$ months $\frac{1}{2}$. Moon-sun calendars are all based on a principle which was recognized in the 18^{th} century by Laplace: continued fractions. The continued fraction expansion of the ratio ν between the sun year and the moon year is

$$\nu = \frac{365.242191}{29.530589} = 12 + \cfrac{1}{2 + \cfrac{1}{1 + \cfrac{1}{2 + \cfrac{1}{1 + \cfrac{1}{1 + \cfrac{1}{17 + \ddots}}}}}} \quad (1)$$

The rule is quite simple [4]: one takes the integer part $a_0 = [\nu] = 12$ of the real number ν and its fractional part $\nu_1 = \nu - [\nu] \simeq 0.368$; then one takes the inverse $1/\nu_1 \simeq 2.715$, its integer part $a_1 = [1/\nu_1] = 2$ and its fractional part $\nu_2 = 1/\nu_1 - a_1 \simeq 0.715$; one takes the inverse of the new number $1/\nu_2 \simeq 1.398$, its integer part is $a_2 = [1/\nu_2] = 1$ and its fractional part is $\nu_3 = 1/\nu_2 - a_2 \simeq 0.398$; and so on : $1/\nu_3 \simeq 2.514$, $a_3 = [1/\nu_3] = 2$, $\nu_4 = 1/\nu_3 - a_3 \simeq 0.514$. Formally

$$\nu = \{a_0; a_1, a_2, \cdots, a_i, a_{i+1}, \cdots\} \tag{2}$$

where the series of integer parts (the so-called partial quotients) is set on the same line to simplify the writing.

A moon-sun calendar is implicitely based on the use of the continued fraction (1): one chooses a year with 12 months and one corrects by taking into account new terms in the expansion. The first approximation is not precise since 12 moon months lead to $12 \times 29.53 \simeq 354$ days for the sun year. If one corrects to first order one adds $\frac{1}{2}$ to 12, that is one month every two years: the year now has $12.5 \times 29.53 \simeq 369$ days. To second order the correction is $\frac{1}{2+1/1} = \frac{1}{3}$, that is one adds one month every 3 years, the year now has $12.333 \times 29.53 \simeq 364$ days. To third order the correction is $\frac{1}{2+1/(1+1/2)} = \frac{1}{2+2/3} = \frac{3}{8}$, that is one adds 3 months every 8 years leading to a year with $12.375 \times 29.53 \simeq 365$ days. This last correction was finally taken by the Greeks as the octaeterid. The metonic cycle which adds two new terms in the continued fraction was also found but not implemented by the Greeks

$$\nu = \{12; 2, 1, 2, 1, 1\} = 12 + \frac{7}{19} = \frac{235}{19} \tag{3}$$

It adds 7 months every 19 years and the year now has 365.246 days which is close to the exact value 365.242 days.

Continued fractions find applications in many fields. The ratio

$$\nu_{\text{gold}} = \frac{1+\sqrt{5}}{2} = \{1; 1, 1, 1, \ldots\} = \{1, \overline{1}\} \tag{4}$$

was recognized in many civilisations and used by the architect Le Corbusier. Similarly the number

$$\nu_{\text{silver}} = 1 + \sqrt{2} = \{1, \overline{2}\} \tag{5}$$

is approximately the size ratio for the $A4$ format, that is $\frac{29.7}{21} \simeq \frac{99}{70} = \{1; 2, 2, 2, 2, 2\}$.

Examples can be found in transcendental numbers, that is numbers which are not solutions of an algebraic equation (a polynomial with integer coefficients), such as

$$\pi = \{3; 7, 15, 1, 292, 1, 1, 1, 2, 1, 3, 1, 14, 2, 1, 1 \ldots\} \tag{6}$$

for which the approximation $\pi \simeq \{3; 7\} = \frac{22}{7}$ is well known. Lagrange proved that the necessary and sufficient condition for a continued fraction to be periodic is for ν to be a quadratic irrational number. But the transcendance of π (and the impossibility of circle quadrature) was only proved in 1881 by Lindemann.

3 The Superheterodyne Calendar

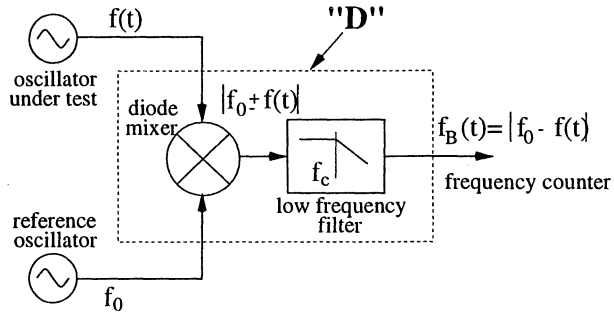

Figure 1: Schematic of the detector "**D**".

In Armstrong's receiver a reference oscillator, of frequency f_0, is compared to a test oscillator of frequency $f(t)$ thanks to a nonlinear element. In our measurements the mixer element is a balanced phase bridge with four Schottky diodes [2]. A low frequency filter of cut-off frequency f_C is used to remove high frequencies so that only frequencies close to baseband remain. They are defined from

$$f_B = |pf_0 - qf(t)| \leq f_c \tag{7}$$

In the application to demodulation in a communication receiver, the frequency of one channel is f. However due to intermodulation frequencies as given in (7), there are many channel frequencies $f = (pf_0 \pm f_B)/q$ for a given intermediate frequency f_B instead of one. The unwanted signals have to be rejected using sophisticated architectures or highly selective filters [3].

Equation (7) may be rewritten by using the ratio $\nu = \frac{f(t)}{f_0}$ between the two oscillators at the input of "**D**"

$$\left|\nu - \frac{p}{q}\right| \leq \frac{f_c}{qf_0} \tag{8}$$

or by using the relative error $\mu = \frac{f_B}{f_0}$

$$\mu = \frac{f_B}{f_0} \leq \frac{f_c}{f_0} \tag{9}$$

Equation (9) implies that the result of the measurement is located below the dotted line at $\mu = \frac{f_c}{f_0}$, but it still doesn't explain the observed basins.

From now we postulate that the detector "**D**" operates like a moon-sun calendar by truncating the continued fraction (2) according to the cut-off frequency

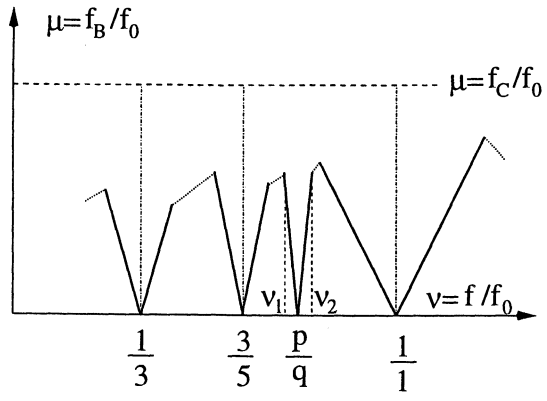

Figure 2: Intermodulation spectrum in detector "D".

f_c. Like the calendar it performs jumps to correct the errors. These jumps are the underlying structure of $1/F$ noise, which is the universal feature of all rythmic systems [2]. Let us compare relation (8) to the following well known property of continued fractions expansions [1],[4]

$$|\nu - \frac{p_i}{q_i}| \leq \frac{1}{a_{i+1}q_i^2} \tag{10}$$

Fraction $\frac{p_i}{q_i} = \{a_0; a_1, a_2, \ldots a_i\}$, which is a so-called convergent, means that the continued fraction expansion is truncated at level i and a_{i+1} is the first neglected partial quotient. The relation (10) is the resulting error. The shift is different in decimal approximations $\frac{a_i}{b_i}$ for which one gets

$$|\nu - \frac{a_i}{b_i}| \leq \frac{1}{b_i} \tag{11}$$

As an example for $\pi \simeq 3.14159$, $\frac{a_1}{b_1} = 3$, $\frac{a_2}{b_2} = \frac{31}{10}$, $\frac{a_3}{b_3} = \frac{314}{100}\ldots$ satisfy (11), while the first diophantine approximations of π are $\frac{p_1}{q_1} = 3$, $\frac{p_2}{q_2} = \frac{22}{7}$, $\frac{p_3}{q_3} = \frac{333}{106}, \ldots$ and satisfy (10). Diophantine approximation is better than decimal approximation for π since there are large terms in the continued fraction expansion; this is in contrast to numbers ν_{gold} et ν_{silver} in (4) and (5) where the continued fraction expansion only shows small partial quotients 1 and 2.

From the filtering condition (8) and the diophantine condition (10) we expect that the detector "D" will truncate at

$$a_{i+1} = a_{\max} = \left[\frac{f_0}{f_c q_i}\right] \tag{12}$$

where [ ] means the integer part. Eq. (12) can be proved rigorously and is in very good agreement with all experiments on receiver "D" [2],[5]. In addition, since $a_{\max} > 1$, we get $q_i \leq q_{\max} = \frac{f_0}{f_c}$. For example if one chooses $f_0 = 10$ MHz and $f_c = 300$ kHz, $q_{\max} = 33$, the fundamental basin $\frac{p_i}{q_i} = \frac{1}{1}$ where $q_i = 1$ will be truncated at $a_{\max} = \left[\frac{10}{0.30}\right] = 33$, and the basin of $\frac{p_i}{q_i} = \frac{3}{5}$ will be truncated at $a_{max} = \left[\frac{10}{0.30\times 5}\right] = 6$. The frequency structure of "D" now condensates into a single equation which collects (8), (10) and (12)

$$|\nu - \frac{p_i}{q_i}| \leq \frac{f_c}{f_0 q_i} \tag{13}$$

where we remind that the $\frac{p_i}{q_i}$ are the convergents, that is the truncations of the continued fraction expansions of ν. This is illustrated in Fig. 3.

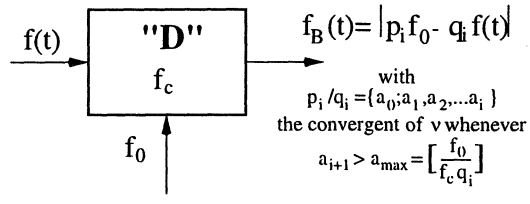

Figure 3: Detector "D" is a diophantine approximator.

We expect the spectrum in Fig. 2 to be built with straight lines of slope q_i emanating from the points $\frac{p_i}{q_i}$. It is easy to show [2] that the edges of the basins are located at

$$\begin{aligned} \nu_1 &= \{a_0; a_1, a_2, \ldots a_i, a_{\max}\} \\ \nu_2 &= \{a_0; a_1, a_2, \ldots a_i - 1, 1, a_{\max}\} \end{aligned} \tag{14}$$

where the partial quotients before $a_{\max}$ corresponds to the two possible expansions of the rational number $\frac{p_i}{q_i}$. The basin of number $\nu = \frac{3}{5} = \{0; 1, 1, 2\}$ extends to $\nu_1 = \{0; 1, 1, 2, a_{\max}\}$, $\nu_2 = \{0; 1, 1, 1, 1, a_{\max}\}$. With $a_{\max} = 6$ as above one finds $\nu_1 = \frac{19}{32} \simeq 0.594$ et $\nu_2 = \frac{21}{34} \simeq 0.618$. For a reference oscillator with $f_0 = 10\ MHz$, this corresponds to a frequency bandwidth $(0.618 - 0.594) \times 10^7\ MHz = 240\ kHz$.

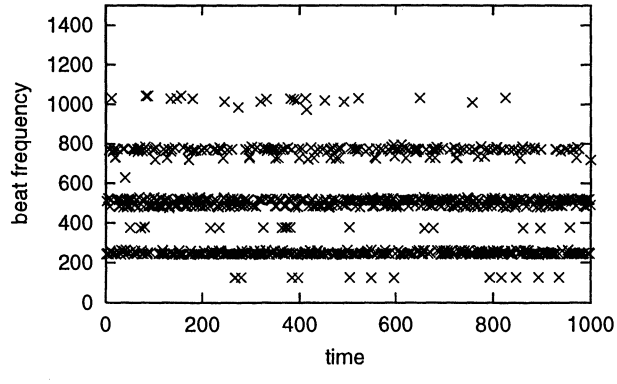

Figure 4: Frequency jumps (in Hz) in the superheterodyne detector. Input frequencies are $f_0 = 1.000\ 000\ 07$ MHz and $f = 0.599\ 975$ MHz. The unit of time is the integration time 1 msec.

Let us remind that our first goal is to characterize the oscillator under test of fluctuating frequency $f(t)$. So the working point slightly fluctuates in the selected basin. In our experiment of Fig. 4 we chose $\frac{p_i}{q_i} = \frac{3}{5}$, with the input reference frequency $f_0 = 1.000\ 000\ 07$ MHz and oscillator under test frequency $f = 0.599\ 975$ MHz. This corresponds to the ratio $\nu = \frac{f}{f_0} = 0.599\ 974\ 958\ldots = \{0; 1, 1, 2, 1596, 1, 10\ldots\}$. This is very close to a resonance such as

$$\nu(a) = \{a_0; a_1, a_2, \cdots a_i, a\} = \frac{p(a)}{q(a)} \quad , a > a_{\max} \quad (15)$$

It is found on Fig. 4 that the observed frequencies are those predicted from the following relation

$$f_B = |p(a)\ f_0 - q(a)\ f| \quad \text{with} \quad 1589 \leq a \leq 1605 \quad (16)$$

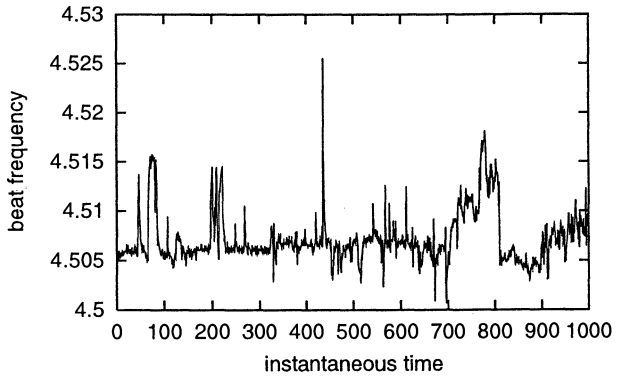

Figure 5: Instantaneous beat frequency (in Hz) for beat frequency close to baseband. Input frequencies are $f \sim f_0 \sim 5.0206$ MHz. The unit of time is the period.

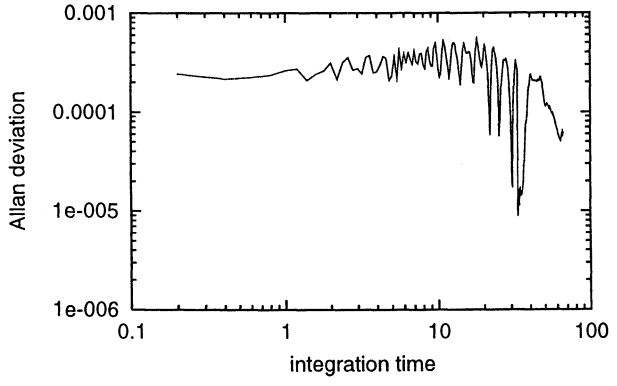

Figure 6: Allan deviation for the file plotted in Fig. 5 (beat frequency close to baseband). The integration time is in sec.

The detector jumps randomly from one value to the other. For example for $a = 1598$, 1599, 1600 we have $f_B = 135$ Hz, 261 Hz and 386 Hz respectively and for $a = 1593$, 1594, 1595 we have $f_B = 490$ Hz, 365 Hz,and 240 Hz. The range of observed values of f_B is restricted to the bandwidth of counting measurement: it is defined as the inverse of the integration time τ. Here we used $\tau = 1$ ms so that $f_B \leq 1$ kHz.

As in the moon-sun calendar these jumps have the aim to correct the errors that the detector encounters in its read-out of time.

For experiments performed very close to baseband $f_B \simeq 0$ there are many allowed values of index a and it is difficult to identify which basin is occupied at a given time. An exemple is given in Fig. 5. Here we used input oscillators at frequencies $f \sim f_0 \sim 5.0206$ MHz and a beat frequency $f_B \sim 4.5$ Hz. The statistics may be defined from the Allan deviation $\sigma_y(\tau)$, where $y^l(\tau) = \frac{f_B^{(l)}(\tau)}{f_B}$ is the relative beat frequency for the measurement l over the integration time τ, the index $l = (1, 2, \ldots, N)$ stands for the N measurements and $\langle\ \rangle$ means the averaging.

The observed Allan deviation in Fig. 6 is almost constant and this corresponds to a $1/F$ frequency noise.

4 The Statistics of Frequency Jumps and Prime Number Theory

We found in Sect. 3 that the measurement of time in an oscillator involves continued fractions, but we still didn't discover which statistics governs random frequency jumps in time. One tentative arithmetical program for the phase of jumps is the von Mangoldt function

$$\Lambda(n) = \begin{cases} \ln p & \text{if } n = p^k \text{ and } p \text{ prime} \\ 0 & \text{otherwise} \end{cases} \quad (17)$$

For example $\Lambda(2) = \ln 2$, $\Lambda(2^2) = \ln(2)$, $\Lambda(5) = \ln(5)$, $\Lambda(6) = 0, \ldots$. At time t the cumulative phase jump is

$$\psi(t) = \sum_{n=1}^{n=t} \Lambda(n) = t + \varepsilon(t) \quad (18)$$

It is most remarkable that the last term can be expressed analytically as [6]

$$\varepsilon(t) = -\ln(2\pi) - \frac{1}{2}\ln(1 - t^2) - \sum_{\varrho} \frac{t^{\varrho}}{\varrho} \quad (19)$$

In (19) the three contributions correspond to singularities of the Riemann zeta function $\zeta(s)$, a function of the complex variable s introduced by Riemann in his famous paper on prime number theory [6]. Fig. 7 shows the mean frequency deviation $\frac{\varepsilon(t)}{t} = \frac{\psi(t)}{t} - 1$ versus time t.

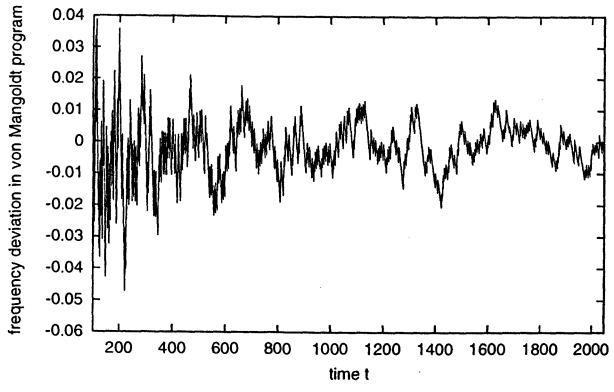

Figure 7: Mean frequency deviation for the von Mangoldt jumps

Riemann zeta function $\zeta(s)$ is defined from the Euler product

$$\zeta(s) = \sum_{n=1}^{\infty} \frac{1}{n^s} = \prod_{p \text{ prime}} \frac{1}{1 - \frac{1}{p^s}} \quad \text{where } \Re(s) > 1 \quad (20)$$

Riemann great achievement in 1859 was his ability to complete the formula to the whole complex plane of the variable s. Von Mangoldt function $\Lambda(n)$ connect to $\zeta(s)$ thanks to the expressions

$$\zeta_\Lambda(s) = \sum_{n=1}^{\infty} \frac{\Lambda(n)}{n^s} = -\frac{\zeta'(s)}{\zeta(s)} \quad (21)$$

The zeros of $\zeta(s)$ lead to poles in the inverse zeta function and its logarithmic derivative, and thus play a major role in the sum (18). From the completed zeta function [6] it is easy to find that they are (trivial) zeros on the negative real axis located at $s = -2l$ (l integer): they are responsible for the second term at the right hand side of (19). The remaining zeros of $\zeta(s)$ (billions of them have been computed) are located on the critical line $s = \frac{1}{2}$. Riemann hypothesis is the conjecture that all non trivial zeros are located on the critical line. These zeros are responsible for the third (random) term at the right hand side of (19).

One understands from now that randomness of the prime number distribution is reflected into the randomness of the position of zeros of $\zeta(s)$ on the critical line $s = \frac{1}{2}$.

We now want to emphasize the link to $1/F$ noise. We calculated numerically the power spectral density FFT of frequency fluctuations in von Mangoldt program

$$S(F) = \mathrm{FFT}(\frac{\varepsilon(t)}{t}) \quad (22)$$

As shown in Fig. 8 we observe that the fluctuations follow the condition

$$S(F) \times F \leq A \quad (23)$$

where A is constant and F is the Fourier frequency. This condition is typical of $1/F$ noise.

The connexion between prime number theory and physics is an emerging and fascinating field. A review of some theoretical links can be seen at the adress www.maths.ex.ac.uk/ mwatkins/zeta/physics.htm

In the present paper it is suggested from number theory that the randomness of time resets in the communication receiver "D" may resort to primes. However the connexion still needs to be refined before $1/F$ frequency noise in oscillators may be considered as a solved problem.

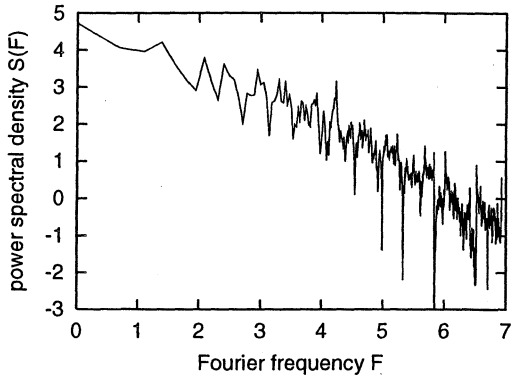

Figure 8: Power spectral density of frequency fluctuations in von Mangoldt program.

References

[1] M. Planat, *Noise, Oscillators and Algebraic Randomness: from Noise in Communication Systems to Number Theory, Lecture Notes in Physics* **550**, Springer, Berlin (2000).

[2] M. Planat and C. Eckert, *On the Frequency and Amplitude Spectrum and the Fluctuations at the Output of a Communication Receiver, IEEE Trans. on Ultrason. Ferroel. and Freq. Cont.* **47** (2000) 1173–1182.

[3] J.R. Smith, *Modern Communication Circuits, Second Edition.* McGraw-Hill, Boston (1997)

[4] M.R. Schroeder, *Number Theory in Science and Communication, Third Edition*, Springer, Berlin (1999).

[5] J. Cresson and M. Planat, *Number Theory and Oscillators*, submitted to *Communication in Mathematical Physics.*

[6] H.M. Edwards, *Riemann's zeta function.* Academic Press, New York (1974).

Backward Noise at the Input of Electronic Amplifiers

E. Rubiola$^{\diamond}$ and V. Giordano*

$\diamond$ ESSTIN and LPMI, Université Henri Poincaré
2 av. Jean Lamour, F-54519 Vandoeuvre Lès Nancy, France
fx +33.383.542173, e-mail rubiola@esstin.uhp-nancy.fr

$\star$ LPMO CNRS, 32 av. de l'Observatoire, F-25044 Besançon, France
fx +33.381.666998, e-mail giordano@lpmo.edu

Abstract

Any scientist who has experimented on the old super-regenerative receiver scheme finds sound that an electronic circuit may radiate backwards from the input. Solid state physics suggests that the random current fluctuations in the semicondutors of the input stage of an amplifier act as a source of noise directed backwards. This unwanted phenomenon can limit the sensitivity of the noise measurement instruments based on correlation, impact on the performance of precision circuits, and be responsible for stability degradation in dual-mode oscillators. Measurement methods and some preliminary results are presented.

1 Introduction

The noise behaviour of amplifiers is generally described in terms of the equivalent noise temperature T or in terms of the noise figure F. A more sophisticated approach, known as the Rothe-Dahlke model [1], makes use of two noise generators — voltage and current — in order to account for the general case of an arbitrary impedance connected the device input. Whatever the chosen model is, the generator identification relies upon the noise measurement at the device *output*. Hence, one may question if the noise generators are actual devices that can deliver power backwards at the input of the amplifier — and therefore disturb other circuits — or if they are virtual generators that can only describe the amplifier output. The answer is not trivial because the amplifier is an active device.

In the domain of $T\&f$ metrology, applications may be found in the design of amplifiers and auxiliary circuits for ultrastable oscillators, and in the design of isolation amplifiers; the two active devices of a dual mode oscillator may disturb one another via the input circuit; moreover, we are aware that the residual noise floor of the phase noise measurement instruments based on correlation [2] may be limited by the combined effect of backward noise of the two amplifiers and non-perfect isolation of the power splitter in between. New spectrum analyzers based on correlation, whose sensitivity is therefore not limited by the thermal energy k_BT at room temperature [3], and shortly recalled in Section 3, give some indications.

2 Background

This work starts from some simple observations. Firstly, FET operational amplifiers exhibit incredible noise performances. The noise temperature $T = 2\sqrt{S_v S_i}/k_B$ — where S_v and S_i are the power spectrum densities of noise voltage and current, $k_B = 1.38\times10^{-23}$ J/K is the Boltzmann constant, and the factor 2 is due to the equal contribution of the two noise generators — can be of the order of 10 K, although difficult to exploit because of the high noise impedance $R_b = 2\sqrt{S_v/S_i}$. Secondly, all low noise microwave amplifiers are based on FET-type devices, but their noise temperature is significantly higher than that of operational amplifiers. Table 1 gives a summary of some amplifiers considered as a useful reference.

In this preliminary analysis we restrict our attention to white noise.

Noise theory for semiconductors is a well developped science that describes precisely the noise behaviour of devices [4, 5, 6, 7], at least in small-signal conditions. But engineers work with modules, whose internal parameters are hardly accessible or secret, hence the device level knowkedge often fails to be useful. Thus we just recall some simple facts.

When the noise current is measured as the difference of the noise in grounded input condition and with a sufficiently high resistance connected to the input, the result turns out to be correlated if two device inputs are connected in parallel. On the other hand, the measurement of the noise voltage with the amplifier input grounded might hide the correlation between current and voltage.

Noise in bipolar transistors is mainly due to the shot noise of the base current, to thermal noise of the distributed base resistance $r_{bb'}$, and to the thermal noise of the dynamical emitter resistance $r_e = V_T/I_E$, or a fraction of the latter. The corresponding noise generators can deliver power from the base circuit.

The noise of field-effect devices at high frequencies

Table 1: Relevant data of some reference amplifiers.

ampifier type	feature & tecnol.	noise volt. ... /$\sqrt{\text{Hz}}$	noise curr. ... /$\sqrt{\text{Hz}}$	R_b best	noise temperat.	noise figure
OP-177	precision BJT	10 nV	0.5 pA	20 kΩ	725 K	5.4 dB
OP-27 / 37	fast BJT	3 nV	0.4 pA	7.5 kΩ	174 K	2 dB
LT-1028	fast BJT	0.9 nV	1 pA	900 Ω	130 K	1.6 dB
CLC-425	1.7 GHz BJT	1.4 nV	1.2 pA	1.2 kΩ	244 K	2.6 dB
SSM-2016	audio BJT	0.8 nV	2.5 pA	320 Ω	290 K	3 dB
SSM-2131	audio FET	13 nV	7 fA	1.9 MΩ	13 K	0.19 dB
OP-42	FET	12 nV	7 fA	1.7 MΩ	12 K	0.18 dB
AD-745	FET	2.9 nV	7 fA	415 kΩ	2.9 K	0.043 dB
OPA-111	low I_b FET	6 nV	0.5 fA	12 MΩ	0.43 K	0.0064 dB
general purpose wideband low-noise amplifier (10 GHz)					170 K	2 dB
front-end amplifier of a satellite television receiver (12 GHz)					43 K	0.6 dB

is more complex. The channel noise — due thermal and diffusion processes — is injected at the input via the gate-channel capacitance c_{gc} and amplified, which occurrs beyond a cutoff frequency related to c_{gc} and to the channel resistance. Fortunately, the same parameters also impact on the cutoff frequency of the gain. In fact, the noise performances of microwave MESFET devices are well known by radiamateurs [8] for use at some lower frequencies, where the equivalent temperature of the sky is particularly low.

Additional noise contribution is due to the input network that matches the resistive 50 Ω input of the amplifier to the capacitive input the FET. This network results from a difficult trade-off between noise, gain and bandwidth. Often, the best noise impedance is far from the highest gain impedance, and the input network required for the lowest noise figure exhibits reactive losses that may exceed 10 dB; obviously, narrowband amplifiers are expected to work better than the wideband ones. It seems that the noise generator accounting for the channel noise can hardly deliver noise power at the amplifier input, particularly if an odd matching network is present.

3 Basics of the measurement method

The principle of the correlation spectrum analyzer is shown in Fig. 1 (top), in which the hybrid is a purely reactive device, hence loss free.

Let $n_1(t)$ and $n_2(t)$ be two independent random signals with power spectrum density (PSD) $N_1(f)$ and $N_2(f)$. The cross correlation function $\mathcal{R}_{ab}(\tau)$ of the sum and the difference

$$a(t) = \frac{1}{\sqrt{2}}\Big[n_1(t) - n_2(t)\Big] \qquad (1)$$

$$b(t) = \frac{1}{\sqrt{2}}\Big[n_1(t) + n_2(t)\Big] \qquad (2)$$

results in the difference of the two indivindual auto-correlation functions, and therefore the cross PSD is

$$S_{ab}(f) = \frac{1}{2}\Big[N_1(f) - N_2(f)\Big] \ . \qquad (3)$$

Let us assume that that $n_2(t)$ is a pure thermal process, thus $N_2(f) = k_B T$, and that $n_1(t)$ can be divided in thermal and extra noise, thus $N_1(f) = k_B T + N^{\text{ex}}(f)$; this is consistent with Fig. 1. Hence it holds

$$S_{ab}(f) = \frac{1}{2} N^{\text{ex}}(f) \ . \qquad (4)$$

This means that, under the assumption of temperature

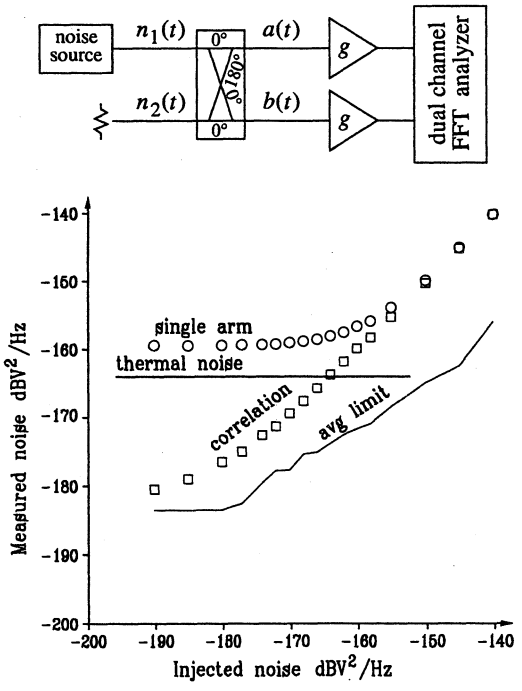

Figure 1: Top: basic scheme of the correlation spectrum analyzer. Bottom: the instrument is tested injecting a reference noise N^{ex} ($R = 10$ kΩ).

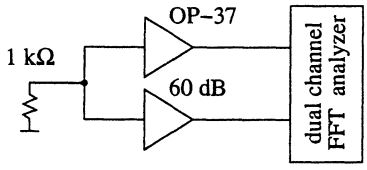

Figure 2: Measurement of the correlated noise of two operational amplifiers with the inputs connected in parallel.

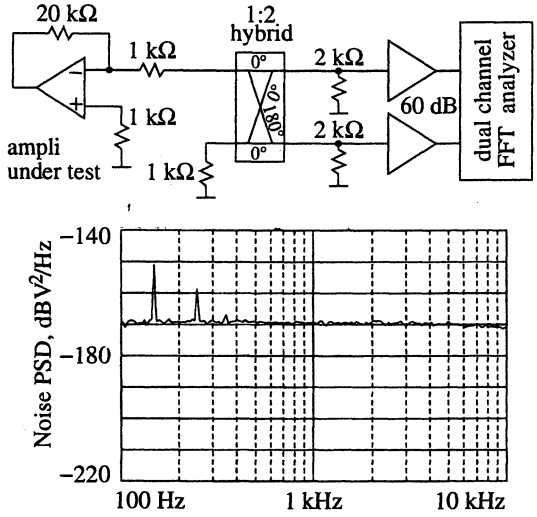

Figure 3: Measurement of the noise at the input of an operational amplifier.

homogeneity, the instrument compensates for thermal noise and measures the extra noise $N^{\mathrm{ex}}(f)$ only.

The scheme of Fig. 1 is similar to the early correlation radioastronomy receivers [9, 10] and to the correlation radiometers [11].

Figure 1 (bottom) shows the result of an experiment in which a variable amount of extra noise is injected at the input, in addition to thermal noise. Decreasing N^{ex}, the single arm noise S_0 approaches $\sqrt{2Fk_BT/\ell_h}$, where ℓ_h is the dissipative loss of the hybrid, and the factor 2 accounts for the power splitting inside the hybrid. Yet, the correlated noise is equal to the injected extra noise, and this holds up to several dB below the thermal floor k_BT. In the absence of N^{ex}, the residual noise is $S_0/\sqrt{2m}$, where m is the number of averaged acquisitions. For each measurement point, m is set to the appropriate value up to the maximum $m_{\max} = 2^{15}$ of the available FFT analyzer.

The microwave version of the correlation spectrum analyzer differs from the scheme of Fig. 1 by the presence of a down conveter in each arm (Fig. 4 top). The phase γ must be set for the two mixer to detect the same phase of the input signal. Obviously, due the conversion mechanism, the instrument can only detect the noise component in quadrature to the mixer pump signal. This is not a problem because the device under test is not driven by the pump signal.

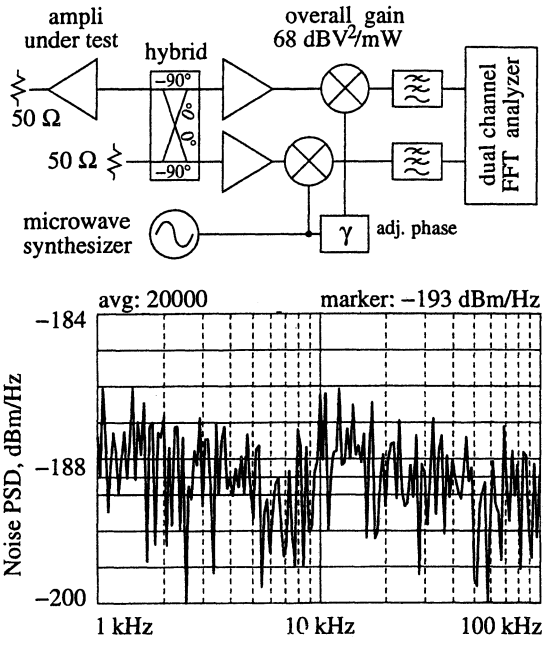

Figure 4: Measurement of the noise at the input of a microwave amplifier.

4 Experiments and results

The first experiment (Fig. 2) is the noise measurement of two paralleled amplifiers. This is similar to the scheme of Fig. 1, but the hybrid is removed, thus the two amplifier inputs are no longer isolated. Each amplifier consists of three equal stages based on an OP-37 in noninverting configuration, and shows an overall gain of 60 dB. The input resistor is 1 kΩ, significantly smaller than the $R_b = 7.5$ kΩ of the OP-37, whereat the noise voltage dominates. The measured noise is 5.6 nV/$\sqrt{\mathrm{Hz}}$ single-arm, and 4.4 nV/$\sqrt{\mathrm{Hz}}$ correlated. Accounting for the thermal noise of the 1 kΩ resistor, there results a correlated noise of 1.7 nV/$\sqrt{\mathrm{Hz}}$ of non-thermal origin. This is a factor almost 3 higher than the effect of the current noise of the two amplifiers, which reveals the presence of other types of correlated noise, probably due to the noise voltage of the amplifier.

The second experiment (Fig. 3) is the measurement of the backward noise at the input of an OP-37. The isolation of the hybrid — in the 30–40 dB range, depending on the frequency — is sufficient to prevent any correlation effect from the two 60 dB amplifiers. The effect of the current noise crossing the two 1 kΩ resistors is 0.8 nV/$\sqrt{\mathrm{Hz}}$, while the measured noise is 3.2 nV/$\sqrt{\mathrm{Hz}}$. This confirms the presence of correlated noise other than the noise current.

Then, a microwave amplifier (Menlo) is measured with the configuration of Fig. 4, operated at the carrier frequency $\nu_c = 11$ GHz, while the first stages following the hybrid are Miteq amplifiers. A summary of the amplifier parameters is given in Table 2.

The instrument is first calibtrated by injecting a

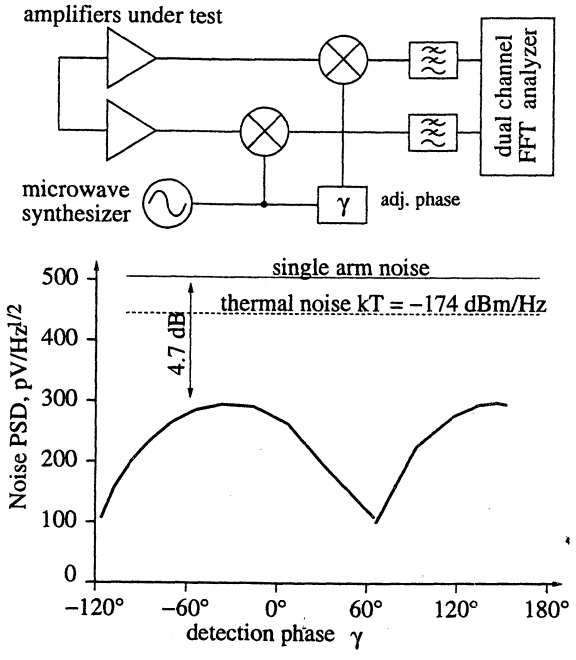

Figure 5: Paralleled microwave amplifiers.

Table 2: Microwave GaAs MESFET amplifiers.

manuf. & model	F dB	pow. dBm	gain dB	freq. GHz
Menlo MLA-60120	2.7	18	25	6–12
Miteq GS3-08001200-11-8P	1.1	10	15	8–12

sideband of frequency $\nu_c + f_b$ at the hybrid input — thus temporarily removing the amplifier under test — and adjusting γ to null the imaginary part of the cross spectrum at the frequency f_b; in this condition the two arms detect the same phase of the input signal. The sideband is also used to measure the instrument gain.

The cross PSD is lower than the value of −193 dBm/Hz highlighted by the marker in Fig. 4, and still limited by the number m of averaged acquisitions. In fact, the single arm noise S_0 is −168 dBm/Hz in our case; hence the expected instrument floor $S_0/\sqrt{2m}$ is −191 dBm/Hz with $m = 20000$, which is in the spread of the observed PSD. As a result, the amplifier under test is in thermal equilibrium with the 50 Ω termination, and therefore it does not deliver extra noise from the input.

Finally, the hybrid is removed and the inputs of the two Miteq amplifiers are connected in parallel according to the scheme of Fig. 5. The phase adjustment procedure based on the $\nu_c + f_b$ sideband is no longer possible, and therefore γ must be adjusted for the maximum of the cross PSD in the actual measurement condition, as shown in Fig. 5. The residual cross PSD is relatively high, some 4.7 below the single arm noise, which makes one think to an odd behaviour of the input matching network of the amplifiers, rather than to a noise at the gate of the first stage. It should be remarked that the Miteq amplifiers are optimized for noise, while the Menlo is not, then all noise phenomena are expected to be lower. But the correlated noise is as high as 4.7 dB below he single arm noise. This seems to indicate an odd behaviour of the input network of the amplifiers in the unusual operating conditions.

Acknowledgments

We wish to acknowledge Fabrizio Bonani of the Politecnico di Torino, Olivier Llopis and Laurent Escotte of the LAAS, Toulouse, and Giorgio Brida of the IEN, Torino, for useful discussions.

References

[1] H. Rothe and W. Dahlke, "Theory of noisy fourpoles," *Proc. IRE*, vol. 44, pp. 811–818, Jun 1956.

[2] E. Rubiola and V. Giordano, "Correlation-based phase noise measurements," *Review of Scientific Instruments*, vol. 71, pp. 3085–3091, August 2000.

[3] E. Rubiola and V. Giordano, "A correlation-based noise measurement scheme showing a sensitivity below the thermal floor," in *Proc. 15th International Conference on Noise in Physical Systems and 1/f Fluctuations*, (Hong Kong, Federal Republic of China), pp. 483–486, 23–26 August 1999.

[4] A. van der Ziel, *Noise in solid state devices and circuits*. John Wiley, 1986.

[5] Y. Netzer, "The design of low-noise amplifiers," *Proc. IEEE*, vol. 69, pp. 728–742, Jun 1981.

[6] H. Fukui, "Optimal noise figure of microwave GaAs MESFETs," *IEEE Trans. on Electron Devices*, vol. ED-26, pp. 1032–1037, July 1979.

[7] R. A. Purcel, D. J. Massé, and C. F. Krumm, "Noise performance of gallium arsenide field effect transistors," *IEEE J. Solid-State Circuits*, vol. SC-11, pp. 243–255, April 1976.

[8] R. Bertelseimer DJ9BV, "Low noise preamp for 1.3 GHz," *Dubus*, no. 4, pp. 37–50, 1991.

[9] R. Hanbury Brown, R. C. Jennison, and M. K. Das Gupta, "Apparent angular sizes of discrete radio sources," *Nature*, vol. 170, pp. 1061–1063, 20 December 1952.

[10] E. J. Blum, "Sensibilité des radiotelescopes et recepteurs à correlation," *Annales d'Astrophysique*, vol. 22, no. 2, pp. 140–163, 1959.

[11] C. M. Allred, "A precision noise spectral density comparator," *J. Res. NBS*, vol. 66C, pp. 323–330, October-December 1962.

DETERMINATION OF THE CAPTURE RANGE AND LOCKING RANGE OF INJECTION LOCKED OSCILLATORS

MICHAEL J. UNDERHILL, NIPAPON SIRIPON AND NICOS CHRISTOFOROU

School of Electronics, Computing and Mathematics,University of Surrey, UK

ABSTRACT

Any oscillator can be treated as a positive feedback system that multiplies the Q (Quality Factor) of a tuned circuit many millions of the times. The closed loop transfer function of the feedback system amplifies and filters the natural thermal noise in the system (by this Q multiplication factor) to give a 'pure' carrier with a minimum of residual phase noise. This is the 'Leeson' model of an oscillator and it can be used to predict the fundamental phase noise of any oscillator.

The purpose of this paper is to show how the Leeson oscillator model can also be used to predict the locking range and capture-range of an injection locked oscillator as the power level of the injection locking signal is varied relative to the oscillator power. Some experimental results are presented to confirm the theoretically predicted equations.

The Leeson model is also used to explain the characteristic spectrum observed when an oscillator is not quite locked

Keywords:- Injection-locking, oscillators, capture, lock range.

1. INTRODUCTION

Injection locked oscillators are particularly suited to the selection of a high harmonic of a fixed lower frequency injection source of low phase noise and high spectral purity. Very little, if any, additional circuitry is needed other than the oscillators themselves. At most a harmonic generator is needed to maximise (and equalise) the powers of the high harmonic components of the low frequency injection locked signal. With such simple circuitry it is important to establish performance limitations of the overall injection locked oscillator system.

In 1989 it was proposed [1] that the Leeson model [2] could also be used to predict the capture range and locking range of any oscillator for a given level of injected locking signal. (Note that lock range, lock-in range and locking range have identical meanings in this paper). Formulas for these ranges were derived in terms of the power, the injection power and the oscillator resonator (loaded) Q factor. An estimate was also made of the suppression achievable for harmonics adjacent to the harmonic of the injection locked signal to which the oscillator is synchronised and locked. This paper provides confirmation of the basic injection locking formulas by measurements at 2GHz and 10MHz. On this basis the prediction of adjacent harmonic suppression can be regarded with a higher degree of confidence. Further measurements are planned to confirm the degree of adjacent harmonic suppression achievable in practice.

2. OSCILLATOR MODEL

Any oscillator can be treated as a positive feedback system that multiplies the natural loaded Q (Quality factor) of some form of resonator many millions of times. The closed loop transfer function (CLTF) of the feedback system amplifies and filters the phase noise component of the natural thermal noise of the system by the Q multiplication factor (M_Q) to give what appears as a "pure" carrier with residual noise sidebands. This model predictts that the entire output of the oscillator is phase noise albeit with a highly filtered spectrum. This is the basis of the Leeson oscillator model. The model applies to all oscillators whether electronic or mechanical and over the entire frequency range covering from x-ray lasers to (grand-father) pendulum clocks.

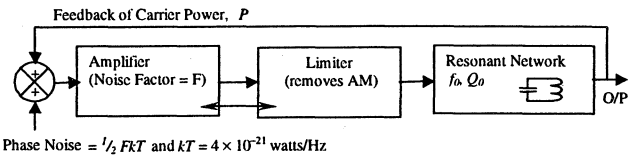

Fig1 Fundamental Model of any Oscillator – D.B.Leeson

Figure 1 shows the essential parts of the Leeson oscillator model. The total system thermal noise is FkT per unit bandwidth when referred back to the input of the amplifier. F is the amplifier noise factor. k is Boltzmann's constant and T the ambient temperature. Half of the thermal noise is assumed to be phase noise. It is therefore ½FkT per Hz and it has a uniform (flat) power spectral density (PSD).

The amplitude noise, also with PSD of ½FkT, is suppressed by the amplitude limiting function required in any oscillator to prevent infinite amplitude of oscillation and prevent oscillator self-destruction. All functioning oscillators have some form of amplitude limitation. Note that narrow band AGC (automatic gain control) can leave AM noise unsuppressed at higher sideband frequencies and this can be undesirable.

The amplifier ensures that the closed loop gain of the oscillator as a feedback system is positive in sense and initially sufficiently greater than unity. A high feedback gain ensures faster "start-up" of the oscillator when the DC power supply is first applied. It also ensures good amplitude limiting and good suppression of AM noise when the oscillator has reached a steady state condition. When the steady slate is reached the amplitude limiting process causes the loop gain to become a very small amount less than unity.

The positive feedback amplifies the natural thermal phase noise by the Q multiplication factor M_Q. The peak power spectral density of the resulting phase noise spectrum is increased by M_Q^2. The width of the spectrum is decreased by M_Q. The output power of the oscillator is the total phase noise power and this is the integral of the PSD of the oscillator spectrum. Thus the output power of the oscillator is proportional to $M_Q^2/M_Q = M_Q$. The level to which the output power is limited automatically sets the value of the Q multiplication M_Q.

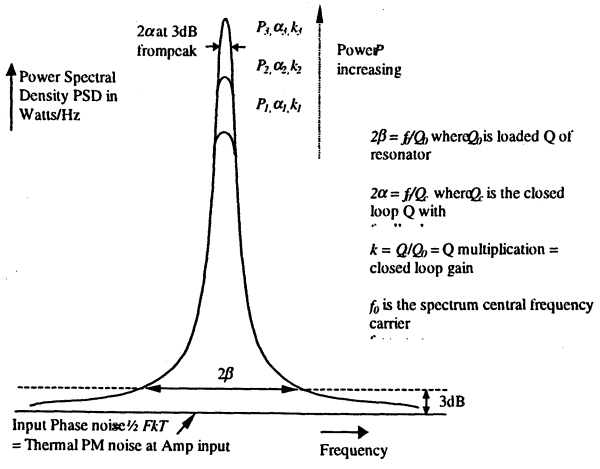

Fig 2 Spectrum of any Oscillator

We do not need to know the Q multiplication factor in order to derive the oscillator noise spectrum. The Power Transfer Function (PTF) of any tuned circuit normalised to be unity at the resonant frequency ω_o is given by

$$|G(j\omega)|^2 = 1/(1 + 4\omega_m^2 Q^2/\omega_o^2) \quad (1)$$

where ω_m is the sideband frequency $|\omega - \omega_o|$ and $\omega_m = 2\pi f_m$.

If Q_o is the resonator loaded Q with no feedback gain then when feedback is applied the Q increases from Q_o to $Q_m = M_Q Q_o$ and the gain at resonant frequency increases by M_Q. The Power Transfer Function of the oscillator regarded as a filter is then

$$|G(f_m)|^2 = M_Q^2/(1 + 4 M_Q^2 Q_o^2 f_m^2/f_o^2) \quad (2)$$

Except at the peak the phase noise is given by

$$N(f_m) = ½FkT f_o^2/4Q_o^2 f_m^2 \quad (3)$$

But by definition

$$L(f) = N(f_m)/P = ½FkT (F_o/f_m)^2/4PQ_o^2 \quad (4)$$

where P is the oscillator power

Note that P is actually the power presented back at the input where the original phase noise was ½FkT. This power may or may not be absorbed and dissipated in the input of the amplifier. Slightly higher power efficiency may be obtained if the input can be deliberately mismatched without raising the noise factor F.

Equation (4) represents the fundamental phase noise spectrum of any oscillator. Because neither Q_o nor P can be infinite, nor can T be zero, all oscillators have a finite phase noise spectrum. No oscillator can be noise free.

3. TOTAL PHASE NOISE

The total phase noise power of an oscillator is the integral over all frequencies f_m from $-\infty$ to $+\infty$ of $N(f_m)$, as given by equation (2). This is equal to the oscillator power P. According to this definition $L(f)$ integrated over all frequencies is always unity. Using the convenient substitution

$$\tan\theta = 2M_Q Q_o f_m/f_o \quad (5)$$

or otherwise, we find

$$P = \pi FkT M_Q f_o/4Q_o \quad (6)$$

This equation allows the Q multiplication factor M_Q to be found, although it is rarely if ever necessary to do so.

The conventional (IEEE) definition of baseband phase noise is

$$L(f) = ½ S_\phi(f) \quad (7)$$

The integral of $L(f)$ is unity, and the total baseband phase noise of any oscillator is thus 1 in units of radians squared.

But if the rms modulation index of a sideband component is $m(f_m)$ for the phase deviation of this component, the modulation sideband power that appears at RF is $(1/2m)^2 \times P$. This results in the relationship

$$L(f) = ½ S_\phi(f) = ¼ m^2(f_m) \quad (8)$$

The RMS modulation index of the total of the baseband phase noise $S_f(f)$ can be seen to be $\sqrt{2}$ for any oscillator. (The mean square modulation index is 2).

The modulation index for a sideband component $m(f_m)$ can be directly related to time jitter $\tau(f_m)$ by

$$\tau(f_m) = m(f_m)/\omega_o \quad (9)$$

where $\omega_o = 2\pi f_o = 2\pi/T_o$ is the carrier frequency in radians per second.

4. THE INJECTION LOCKING PROCESS

A signal of power P_l inserted at the input of an oscillator of power P at a frequency f_m away from the oscillator natural frequency f_o can "capture" and lock the oscillator frequency over frequency range defined as the capture range. We can define f_c to be the maximum value of f_c over which capture of the oscillator frequency can be achieved, and f_l the maximum value at which the oscillator becomes unlocked starting from the locked condition. Assuming the oscillator spectra to be symmetrical the "capture" range is therefore $2f_c$ and the "locking" range is $2f_l$.

It has been proposed that injection locking can be analysed on the basis of the "capture" process that occurs when two RF signals are presented to an amplitude limiter [1]. An oscillator always has to have a limiter of some form. For the purpose of analysis it is assumed that the limiter in the oscillator is a "hard limiter" with a reasonably abrupt limiting characteristic.

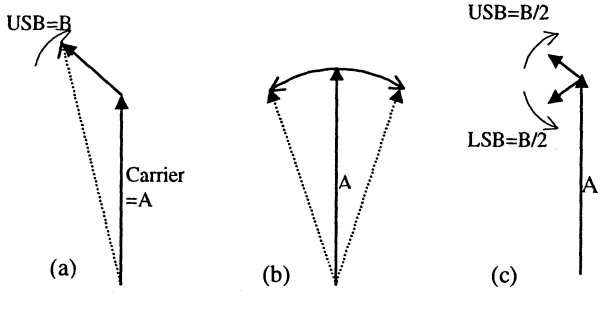

Fig 3 Phasor Diagram of Limiter Action on 2 Signals A>B:
(a) before limiting, (b) phasor trajectory after limiting,
(c) sidebands formed by limiter USB=LSB=B/2.

Fig 3 shows the combination of two unequal amplitude signals of slightly different frequencies on a phasor diagram. The stronger signal is shown as the vertical reference vector, Fig

3(a) represents the two signals with no amplitude limiting action taking place. Fig 3(b) shows the combined phasor trajectory after amplitude limiting has been applied. Fig 3(c) shows that the limited signal can be resolved into a carrier component at the original frequency f_a of the strongest component and two sideband components, one at the original frequency f_b and the other at a frequency $2f_a - f_b$ equally spaced from the carrier. The limiting process splits the original injection locking component into two sideband components (USB and LSB) of half original amplitude, or each 6dB lower relative to the carrier.

Again we can treat the oscillator circuit as an amplifying filter with a power transfer function given by equation 2. An injection signal of power P_I that is not exactly on the oscillator free running frequency and which is at too low a power to cause locking suffers a loss of 6dB, or 0.25 times with respect to the power transfer function of equation 2. When the oscillator is locked this factor of 0.25 is not present for the locking signal.

When the amplitude of the amplified locking signal exceeds the power of the oscillator P, locking will occur or be maintained. But because the filter gain is 6dB less for the injection lock, on the basis of this simple model one can predict that the injection power level for locking will be 6dB higher than the injection power level for unlocking. Because any tuned circuit has a spectrum shape of 6dB per octave of f_m the sideband frequencies, then the capture bandwidth should be half the lock-in bandwidth.

The amplified locking signal is $P_I \mid G(f_m)\mid^2$ in the locked state, and $\frac{1}{4}P_i \mid G(f_m)\mid^2$ in the unlocked state. $\mid G(f_m)\mid^2$ is given by equations 2 or 3.

If $P_i \mid G(f_m)\mid^2 > P$ (10)
then lock will be retained.

If $\frac{1}{4}P_I \mid G(f_m)\mid^2 > P$ (11)
then capture will occur.

We can therefore define the *lock-in range* from equations 10 and 3 as

$$2f_l = 2 f_o P_i^{1/2}/2Q_o P^{1/2} = f_o P_i^{1/2}/Q_o P^{1/2} \quad (12)$$

The *capture range* from equations 11 and 3 becomes

$$2f_c = f_o P_i^{1/2}/2Q_o P^{1/2} \quad (13)$$

(where f_o is the (unlocked) carrier frequency)

We also have the resonator (natural) bandwidth defined as $f_{BW}=f_o/Q_o$ and so

$$Lock\ in\ range = f_{BW}(P_i/P)^{1/2} \quad (14)$$
$$Capture\ range = \tfrac{1}{2}f_{BW}(P_i/P)^{1/2} \quad (15)$$

Note that this analysis has been based on the assumption that the thermal noise and injection locking signals are combined in a "hard" limiter. Particularly in a class A oscillator the limiter may have a very "soft" characteristic. Then there will be no "capture effect" in the limiter causing a gain reduction of the smaller signal One can then expect that the capture range will be increased to become equal to the lock in range. There is then no hysteresis in the process.

5. 2GHZ OSCILLATOR

A balanced oscillator, using two Siemens CFY30 GaAs FETs in the circuit as shown in Fig 4, was constructed. on FR4 printed circuit board with the layout as shown in Fig 5 .The completed circuit is shown in Fig 6. The oscillator design is essentially the same as was reported at the 2000 EFTF [3] but with transmission line resonators of lengths suitable for 2GHz operation. Then the Ka and Ku band frequencies were stabilised with additional resonators, with lengths of many wavelengths, attached at one of the load positions R_l. The quarter wave lines in the sources are essential to ensure the degeneration required for oscillation. The injection signal is applied at the balance point at the centre of the horizontal half-wave resonator.

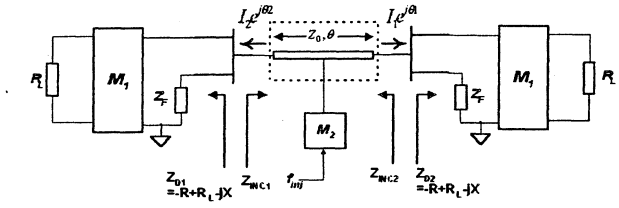

Fig 4 Circuit Schematic of 2GHz Oscillator

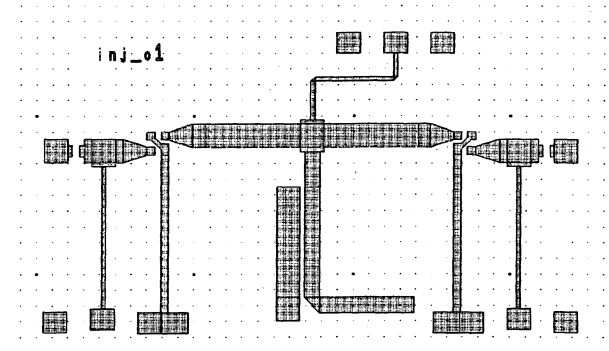

Fig 5 Printed Circuit Layout of 2GHz Oscillator

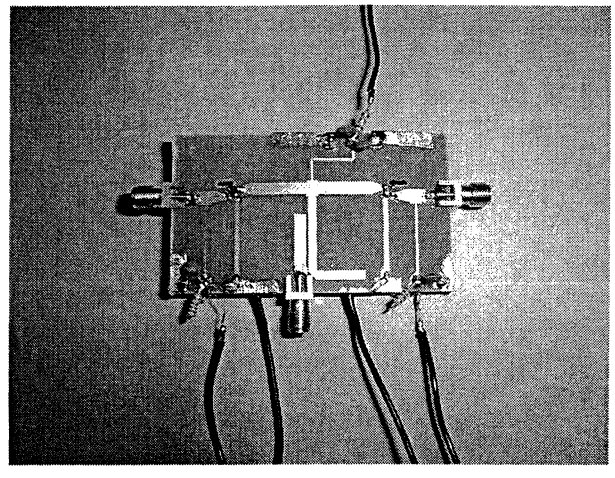

Fig 6 2GHz Oscillator Printed Circuit (populated).

Fig 7 shows the measurement set-up. The HP8563E spectrum analyser on the right is used to observe when the oscillator is, or is not, in lock. The HP signal generator on the left provides the injection signal. To measure the locking range the injection frequency is slowly moved manually away from the centre locked frequency successively in both directions ,up and down, until a change in the spectrum shape indicates that lock has been broken. The locking range is the difference between the upper and lower frequencies at which lock is broken.

To find the capture range the frequency is moved inwards from the upper and lower out-of-lock regions and the difference in the frequencies at which lock is captured gives the capture range

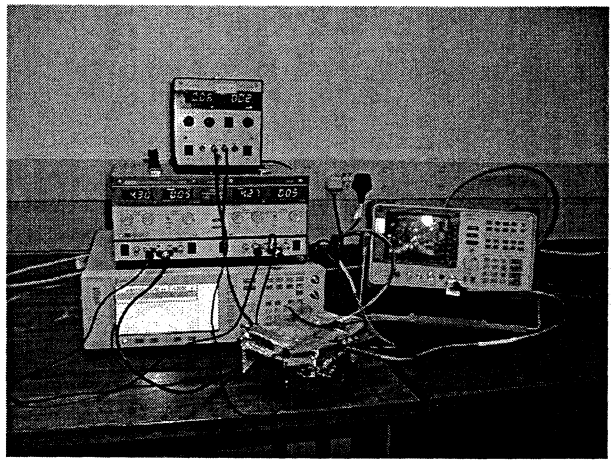

Fig 7 Measurement set-up for 2GHz Oscillator

Table 1 shows the first results for the 2GHz oscillator for different injection power levels The additional aluminium screening was not present for these results. Note that the theoretical prediction the two-to-one ratio of the locking and capture ranges, is followed quite closely. The range variation with power level also follows the prediction within the apparent experimental error.
The oscillator output power was 6.33dBm and the frequency of operation was 2.006 GHz.

Injection power (dBm)	locking range (kHz)	capture range (kHz)
-10	282.25	153.08
-15	119.98	58.04
-20	75.908	46.538
-25	56.91	34.44

Table 1 2GHz Oscillator Results – example 1

Table 2 shows the second set of results after the transistors had been replaced and the aluminium screening added as shown in Fig 7. Note that the bandwidths are much lower even though the oscillator power was reduced to5.0 dBm Thus changing the transistors gave a substantial increase in the apparent Q. The frequency was 2.012GHz Again the theoretical predictions are followed quite closely although the agreement with the power level prediction is slightly less good.

Injection power (dBm)	Locking range (kHz)	Capture range (kHz)
-10	99.999	54.163
-15	43.468	24.752
-20	21.808	11.906
-25	10.41	5.318

Table 2 2GHz Oscillator Results – example 2

6. 10MHZ OSCILLATOR

A 10MHz Clapp single transistor oscillator [5] was made with a circuit as shown in Fig 8 and construction shown in Fig 9..

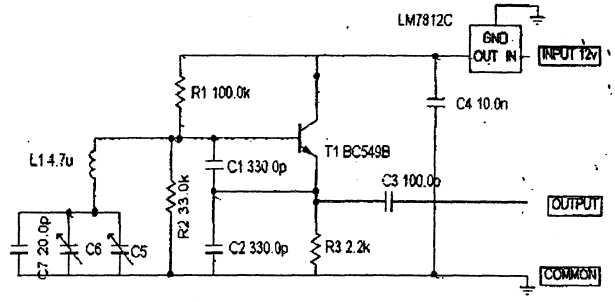

Fig 8 10MHz Clapp Oscillator Circuit

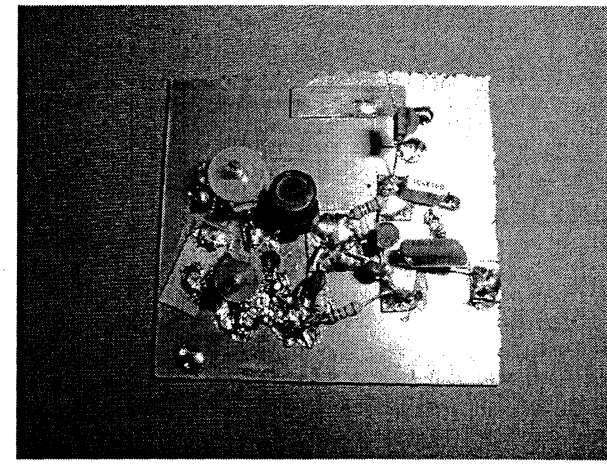

Fig 9 Construction of 10 MHz Clapp Oscillator

Table 3 shows that the 10MHz oscillator has a very soft limiting action, because there essentially no difference between the capture and locking ranges.

The agreement with the prediction of variation of locking range with injection power is excellent. Note that relative, not absolute, power (in dB) is used in this case.

Injection level	Locking range	Capture range
(dB)	(kHz)	(kHz)
-20	71.79	71.79
-25	41.19	41.19
-30	21.37	21.37
-35	8.78	8.78
-45	5.07	5.07
-50	2.79	2.79
-55	1.64	1.64

Table 3 results of 10MHz Oscillator

7. INJECTION LOCKING SPECTRUM SHAPE

In the "not quite locked" situation a very characteristic spectrum shape was observed, as shown in Fig 10. The shape appears to be the same as recently reported by.Banai and Farzaneh [6]. Note that the envelope on the resonator natural frequency side is almost a straight line on the log-amplitude linear-frequency plot

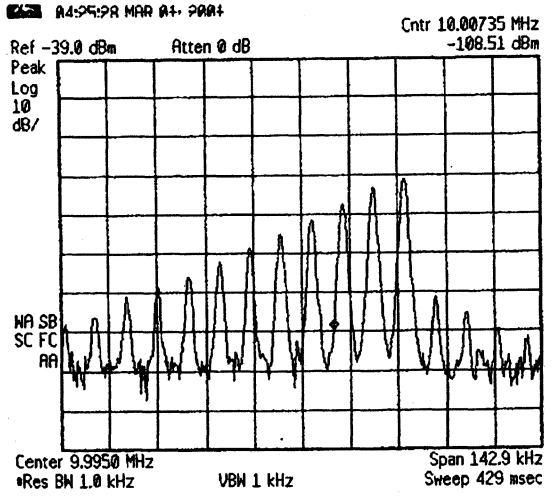

Fig 10 "Not quite locked" Spectrum Shape

The characteristic spectrum can be explained using the Leeson type of oscillator model. We assume that the limiter creates intermodulation products of the oscillator signal and the injection signal. Certainly for the higher order products the relative component amplitudes are then proportional to the ratio of the powers of the two signals raised to the power of n. 2n-1 is the order of the intermodulation product and n is also the number of an intermodulation product counting from the original signals. The intermodulation products are all equally spaced in frequency. On a log scale the component amplitudes are of the form $\text{Log}\,[(1/n)(A_1A_2)^n] = n\,\text{Log}\,A_1A_2 - \text{Log}\,n$. The first term dominates and it has a slope proportional to n. Thus the envelope containing these products will be a straight line and this is what is observed.

The signals on the oscillator side of the spectrum see a closed loop gain within the locking range that is only a little less than unity, and so the straight line spectrum shape is retained in this region. However on the locking signal side the closed loop gain drops rapidly and the intermodulation components are therefore heavily attenuated.

8. CONCLUSIONS

A theory for injection locking of an oscillator, based on the Leeson oscillator model, has been presented.

It predicts that the locking range is the 3dB (loaded Q) bandwidth of the oscillator resonator on its own (with no feed-back) multiplied by the square root of the ratio of injection power to the oscillator power.

If the limiter in the oscillator is operating as a hard limiter the capture range is predicted to be half the locking range. When a soft limiter is used the two ranges are predicted to be equal.

Two oscillators were constructed to test these predictions, one at 2GHz and one at 10MHz. Both oscillators confirmed the predicted relationship for the locking range

The 2GHz oscillator was a two transistor balanced push-pull type with a transmission line resonator. This oscillator showed a capture range equal to half the locking range for two sets of results at slightly different oscillator power levels and different transistors of nominally the same type.

The 10MHz Clapp oscillator was found to have ha a capture range that was essentially the same as the locking range. This indicated that the loop gain was not sufficiently high to ensure a hard limiter action of any significance.

The characteristic spectrum of a nearly locked oscillator was observed from the 10MHz oscillator. An explanation based on the Leeson simple model of an oscillator has been put forward.

Chaotic frequency jumping was observed occasionally on both oscillators but the chaotic region appeared to be quite small and difficult to maintain.

9. REFERENCES

[1] M.J. Underhill, "Fundamental limitations of oscillator performance", IEE Conf. Publ. 303, Frequency control and synthesis, 1989, pp 18-3.

[2] D.B. Leeson, "A Simple model of feedback oscillator noise spectrum", Proc IEEE, 54, No. 2, 1966, pp 329-330.

[3] K.S. Ang, M.J. Underhill and I.D. Robertson, "Transmission Line Stabilised Monolithic Oscillators", 14th EFTF, Torino, Italy, 2000, pp 88-92.

[4] N. Siripon, M. Chongcheawchamnan, K.S. Ang and I.D. Robertson, "Injection-locked balanced oscillator", Electronics Letters, 26th October 2000, vol 36 No. 22, pp 1854-55.

[5] M.J. Underhill, "Reduction of Phase Noise in single transistor oscillators", 10th EFTF, Brighton, UK, 5-7 March 1996, IEE Conference Pulication No. 418, pp 476-490.

[6] A.Banai and F.Farzaneh, "Locked and unlocked behaviour of mutually coupled microwave oscillators" IEE Proc.-Microw. Antennas Propag., Vol. 147, No. 1, February 2000, pp. 13-18.

THE MOMENT CONDITION: AN EQUIVALENCE PRINCIPLE BETWEEN DRIFT INSENSITIVITY AND LOW FREQUENCY CONVERGENCE

François Vernotte
Laboratoire d'Astrophysique de l'Observatoire de Besançon, UMR CNRS 6091
41 bis, avenue de l'Observatoire, 25010 Besançon Cedex, FRANCE - E-mail: francois@obs-besancon.fr

Abstract—**It is well known that the low frequency noises (flicker FM and random walk FM) yield convergence problems unless a low cut-off frequency is introduced, the physical meaning of which is not clear. As an example, in the case of random walk FM, the mean frequency of an oscillator does not converge if the low cut-off frequency tends toward zero. On the other hand, linear drifts appear if a phase sequence of random walk FM is observed over a duration smaller than the inverse of its low cut-off frequency. Moreover, the estimators which are insensitive to linear frequency drifts (i.e. the Hadamard variance) converge for lower frequency noises (f^{-4} FM).**

The moment condition explains the link between the insensitivity to drifts and the convergence for low frequency noises. This condition may be summarized by the following consideration : the divergence effect of a low frequency noise for the lowest frequencies induces a false drift with random drift coefficients; the lower the low cut-off frequency, the higher the variance of the coefficients of this drift. These variances may be known by theoretical calculations. The order of the drift is directly linked to the power law of the noise.

The moment condition will be demonstrated and applied for creating new estimators (new variances) and for simulating low frequency noises with a very low cut-off frequency.

1. Introduction

In many cases, a time deviation sequence may be modelized by a quadratic drift mixed with random fluctuations:

$$x(t) = C_0 + C_1 t + C_2 t^2 + \epsilon(t), \qquad (1)$$

where C_0, C_1 and C_2 are the drift parameters and $\epsilon(t)$ is the noise, i.e. the purely random behavior of $x(t)$.

However, this drift may be a deterministic one but the very long term random fluctuations of the low frequency noises (f^{-2}, f^{-3}, f^{-4} PM) may also induce a "false drift".

On the other hand, the estimation of the noise levels is generally performed by a variance (Allan variance, Hadamard variance, etc.). The choice of the estimator, i. e. of the variance, must be carried out by taking into account its sensitivity to quadratic drifts (the estimation should not be influenced by this drift) and its convergence for low frequency noises (the estimate must be finite with a random walk FM without taking into account a low cut-off frequency).

Concerning the "false drifts", i. e. the drifts induced by the long term random fluctuations, it is well known that the variance of the parameters C_0, C_1 and C_2 converges for a white PM noise without taking into account a low cut-off frequency. On the other hand, for a white FM, the variance of the parameter C_0 doesn't converge anymore, and for a random walk FM, the variance of neither C_0 nor C_1 converges.

The question is then, what is the link between:

- the drift sensitivity of an estimator (variance),
- the convergence for low frequency noises,
- the variance of the "false drifts" parameters,
- the low cut-off frequency ?

The answer to this question, called the **"moment condition"**, was briefly given 19 years ago by Deeter and Boynton, in a paper dealing with millisecond pulsar analysis (Ref. 1). Unfortunately, this important principle remained unknown in the time and frequency field.

Thus, in this paper, after recalling the basics of estimation in both time and spectral domains, the moment condition will be demonstrated and illustrated by two applications: the selection of estimators (variances) and the noise simulation.

2. Estimation

An estimator may be defined by its sampling function $h(t)$. The estimate θ is obtained by integrating the product of the time deviations $x(t)$ by the sampling function over the whole sequence:

$$\theta = \int_{-\infty}^{+\infty} h(t)x(t)dt. \qquad (2)$$

Actually, the sampling function $h(t)$ is discrete:

$$h(t) = \sum_{i=0}^{N-1} h_i \delta(t - t_i), \qquad (3)$$

and the estimate is then obtained by:

$$\theta = \sum_{i=0}^{N-1} h_i x(t_i). \qquad (4)$$

The variance of this estimate is:

$$\langle \theta^2 \rangle = \left\langle \left[\sum_{i=0}^{N-1} h_i x(t_i) \right]^2 \right\rangle. \qquad (5)$$

Such estimators may be, for example, the Allan variance, drift parameter estimators, etc.

2.1 Example 1: the Allan variance

The Allan variance is defined by:

$$\sigma_y^2(\tau) = \left\langle \left[\sum_{i=0}^{2} h_i x(t_i) \right]^2 \right\rangle \tag{6}$$

with the following sampling function:

$$\begin{cases} h_0 = 1 \\ h_1 = -2 \\ h_2 = 1, \end{cases} \tag{7}$$

and $t_i = i\tau_0$ (τ_0 is the sampling period).

2.2 Example 2: drift parameter estimation

The linear drift parameter may be estimated by using the second Tchebytchev polynomials (see section 6):

$$C_1 = \sum_{i=0}^{N-1} h_i x(t_i) \tag{8}$$

where the sampling coefficients (see figure 1) are given by $h_i = \Phi_1(i\tau_0)$ ($\Phi_1(t)$ is defined in (17) and τ_0 is the sampling period). The variance of the linear drift parameter estimate is then:

$$\sigma_{C_1}^2 = \left\langle \left[\sum_{i=0}^{N-1} h_i x(t_i) \right]^2 \right\rangle. \tag{9}$$

3. Estimation in the spectral domain

From Parceval-Plancherel, (5) may be written in the spectral domain (Ref. 2):

$$\langle \theta^2 \rangle = \int_0^{\infty} |H(f)|^2 S_x(f) df \tag{10}$$

where $S_x(f)$ is the power spectral density of $x(t)$ and $H(f)$ is the Fourier transform of $h(t)$.

We must verify that this estimator converges for $S_x(f) \propto f^{\alpha}$ with $\alpha = -1, -2, -3, -4$. In other words, $H(f)$ must go to zero for small f more rapidly than $f^{(-\alpha-1)/2}$ (see figure 2).

The MacLaurin expansion of $H(f)$ near zero exhibits explicitly the dependence of $H(f)$ versus the power laws of f:

$$H(f) = H(0) + f\left(\frac{dH}{df}\right)_{(f=0)} + \frac{f^2}{2}\left(\frac{d^2H}{df^2}\right)_{(f=0)} + \ldots + \frac{f^q}{q!}\left(\frac{d^qH}{df^q}\right)_{(f=0)} + R_q. \tag{11}$$

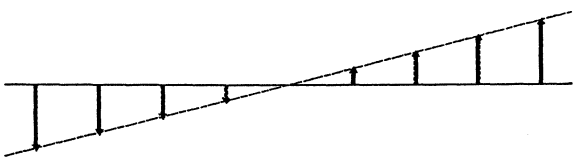

Figure 1. Sampling function of the Tchebytchev linear drift parameter.

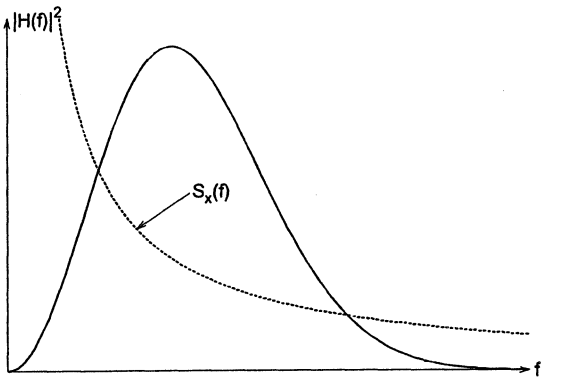

Figure 2. Graph of $|H(f)|^2$ (solid line) and $S_x(f)$ (dashed line) modelized by a f^{α} law. In order to insure the convergence of the variance of the estimate, $H(f)$ must go to zero for small f more rapidly than $f^{(-\alpha-1)/2}$.

Therefore, the convergence is verified if the leading $(-\alpha+1)/2$ terms of (11) vanish (Refs 1, 2).

On the other hand, these terms may be written by using the inverse Fourier transform:

$$\begin{cases} H(0) = \int_{-\infty}^{+\infty} h(t)dt, \\ \left(\frac{dH}{df}\right)_{(f=0)} = \int_{-\infty}^{+\infty} (-j2\pi t)h(t)dt, \\ \vdots \\ \left(\frac{d^qH}{df^q}\right)_{(f=0)} = \int_{-\infty}^{+\infty} (-j2\pi t)^q h(t)dt. \end{cases} \tag{12}$$

Consequently, the condition $H(0) = 0$ is equivalent to the insensitivity of $h(t)$ for a constant, $\left(\frac{dH}{df}\right)_{(f=0)} = 0$ is equivalent to the insensitivity of $h(t)$ for a linear drift, etc.

4. The moment condition

This leads us to the **moment condition** (Refs 1, 2, 3): **"the convergence for low frequency noises is equivalent to the insensitivity to drifts"** according to the following condition

$$\int_{-\infty}^{+\infty} |H(f)|^2 f^{\alpha} df \quad \text{converges} \quad \Leftrightarrow \quad \int_{-\infty}^{+\infty} h(t) t^q dt = 0 \quad \text{for} \quad 0 \le q \le \frac{-\alpha-1}{2}. \tag{13}$$

By using (3), the moment condition (13) may be written for a discrete sampling function:

$$\int_{-\infty}^{+\infty} |H(f)|^2 f^{\alpha} df \quad \text{converges} \quad \Leftrightarrow \quad \sum_{i=0}^{N-1} h_i t_i^q = 0 \quad \text{for} \quad 0 \le q \le \frac{-\alpha-1}{2}. \tag{14}$$

Conver. for: Insensit. to:	f^{-1}	f^{-2}	f^{-3}	f^{-4}	f^{-5}
constant	⋆	⋆	⋆	⋆	⋆
t drift			⋆	⋆	⋆
t^2 drift					⋆

TABLE I

CORRESPONDENCE BETWEEN LOW FREQUENCY NOISE CONVERGENCE AND DRIFT INSENSITIVITY: IF AN ESTIMATOR CONVERGES FOR A f^{-1} NOISE **THEREFORE** IT IS INSENSITIVE TO A CONSTANT, IF AN ESTIMATOR CONVERGES FOR A f^{-3} NOISE **THEREFORE** IT IS INSENSITIVE TO BOTH A CONSTANT AND A LINEAR DRIFT, ETC.

Insensitive to: Convergence for:	constant	t drift	t^2 drift
f^{-1}	⋆	⋆	⋆
f^{-2}	⋆	⋆	⋆
f^{-3}		⋆	⋆
f^{-4}		⋆	⋆
f^{-5}			⋆

TABLE II

CORRESPONDENCE BETWEEN DRIFT INSENSITIVITY AND LOW FREQUENCY NOISE CONVERGENCE: IF AN ESTIMATOR IS INSENSITIVE TO A CONSTANT **THEREFORE** IT CONVERGES UP TO A f^{-2} NOISE, IF AN ESTIMATOR IS INSENSITIVE TO A LINEAR FREQUENCY DRIFT **THEREFORE** IT CONVERGES UP TO A f^{-4} NOISE, ETC.

5. APPLICATION TO VARIANCES

Tables I and II shows the translation of the moment condition in the usual cases of the time and frequency field. The interest for selecting a variance, or more generally a structure function (Ref. 4), concerns the knowledge of both convergence for low frequency noises and drift insensitivity.

If we define a variance in the spectral domain, by its transfer function (high-pass variance, band-pass variance, etc., see Ref. 5), it is very easy to know the convergence properties of this estimator from its slope for small frequencies. These convergence properties may be directly converted into drift insensitivity properties with table I.

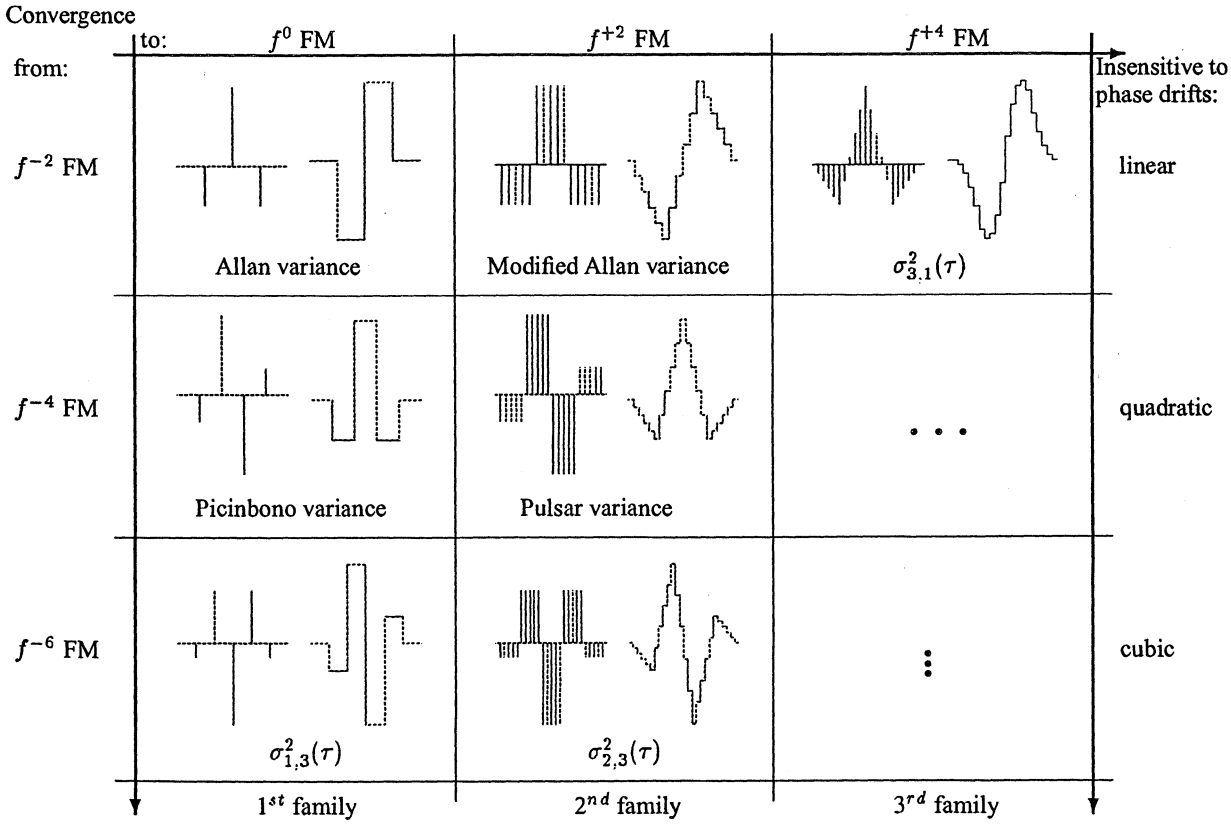

Figure 3. The different classes of structure functions (Refs 4, 6). The left drawings represent the calculation sequences for time error data and the right ones represent the calculation sequences for frequency deviation samples. From top to bottom, the order of difference increases: it yields convergence for lower frequency noises and insensitivity to higher order polynomial drifts. From left to right, the different families yield convergence for higher frequency noises.

On the other hand, if we define a variance in the time domain, by its sampling function, it is very easy to know its drift insensitivity properties: if it is a first order difference (first derivative), it is insensitive to constants, if it is a second order difference, it is insensitive to linear drifts, etc. (see figure 3). These drift insensitivity properties may be directly converted into convergence properties by using table II.

Thus, thanks to the moment condition, it is possible to define new variances in the time domain as well as in the spectral domain, from given special properties, in terms of drift insensitivity or low frequency noise convergence.

6. Application to noise simulation

Another application of the moment condition concerns the simulation of noise. The difficulty of the low frequency noise generation is due to the low cut-off frequency.

Such a generation is generally performed by filtering a white noise with a f^α slope. Let us denote N the number of samples and τ_0 the sampling period, the low cut-off frequency is:

$$f_l \approx \frac{1}{N\tau_0}. \tag{15}$$

Therefore, if f_l is very small, N must be huge. As an example, if we want a set of 1000 samples with a low cut-off frequency equal to $10^{-6}/\tau_0$, we have to generate one million samples, to keep one thousand of them, and to waist the 999000 other ones.

However, the moment condition proves that the effects of the low cut-off frequency consists in "false drifts" added to the noise. Thus, the generation of a low frequency noise with a very low cut-off frequency may be achieved by generating a smaller sequence and adding a drift. **The lower the low cut-off frequency, the higher the "false drift".**

We calculated the theoretical variance of the drift parameters versus the noise levels and the low cut-off frequency (see table III and Ref. 2 for calculation details).

The Tchebytchev drift parameters P_0 and P_1 are uncorrelated, contrary to the classical drift coefficient C_0 and C_1 of relationship (1). It is then important to consider the Tchebytchev parameters rather than the classical coefficient. Using this approach, equation (1) may be written as a linear combination of the Tchebytchev polynomials (Ref. 2):

$$x(t) = P_0\Phi_0(t) + P_1\Phi_1(t) + \epsilon(t), \tag{16}$$

with

$$\begin{cases} \Phi_0(t) = \frac{1}{\sqrt{N}} \\ \Phi_1(t) = \sqrt{\frac{3}{(N-1)N(N+1)}}\left[2\frac{t}{\tau_0} - (N-1)\right]. \end{cases} \tag{17}$$

The classical parameters C_0 and C_1 may be easily deduced from the Tchebytchev parameters P_0 and P_1:

$$\begin{cases} C_0 = \frac{1}{\sqrt{N}}P_0 - \sqrt{\frac{3(N-1)}{N(N+1)}}P_1 \\ C_1 = \frac{2}{\tau_0}\sqrt{\frac{3}{(N-1)N(N+1)}}P_1 \end{cases} \tag{18}$$

$S_x(f)$	$\sigma^2_{P_0}$	$\sigma^2_{P_1}$
f^{-4} PM	$\frac{4Nk_{-4}}{3f_l^3}$	$\frac{\pi^2N^3\tau_0^2k_{-4}}{3f_l}$
f^{-3} PM	$\frac{3Nk_{-3}}{2f_l^2}$	$[7-4\ln(2\pi N\tau_0 f_l) - 4C]\frac{\pi^2N^3\tau_0^2k_{-3}}{12}$
f^{-2} PM	$\frac{2Nk_{-2}}{f_l}$	$\frac{\pi^2N^2\tau_0k_{-2}}{5}$
f^{-1} PM	$[-2\ln(2\pi N\tau_0 f_l) + 3]\frac{Nk_{-1}}{2}$	$\frac{3Nk_{-1}}{4}$
f^0 PM	k_0f_h	k_0f_h

TABLE III
THEORETICAL VARIANCE OF THE TCHEBYTCHEV DRIFT PARAMETERS VERSUS THE NOISE LEVELS AND THE LOW CUT-OFF FREQUENCY. THE LOW CUT-OFF FREQUENCY f_l IS ASSUMED TO BE MUCH LOWER THAN $\frac{1}{N\tau_0}$. C IS THE EULER CONSTANT: $C \approx 0,5772$. ASSUMING A SAMPLING SATISFYING THE SHANNON RULE, THE HIGH CUT-OFF FREQUENCY IS $f_h = \frac{1}{2\tau_0}$.

The drift parameters must be randomly chosen in such a way that their variance is equal to the theoretical variance of table III.

The simulation process consists then in:

1. generating a white noise sequence
2. filtering this sequence with a f^α slope
3. removing the drift of the sequence
4. choosing randomly the P_0 and P_1 parameters according to table III
5. adding the "false drift" to the sequence.

7. Conclusion

The moment condition is then a principle of equivalence between the drift insensitivity of an estimator and its convergence properties for low frequency noises. We have applied this principle to the definition of variances adapted to special conditions, and to noise simulation with a given low cut-off frequency. However, the moment condition may also be useful in many other topics, such as the uncertainty estimation of frequency measurements, the extrapolation of time deviations by a quadratic model, etc.

REFERENCES

[1] J. E. Deeter and P. E. Boynton, "Techniques for the estimation of red power spectra. i. context and methodology," The Astrophysical Journal, vol. 261, pp. 337–350, October 1982.

[2] F. Vernotte, J. Delporte, M. Brunet, and T. Tournier, "Uncertainties of drift coefficients and extrapolation errors: Application to clock error prediction," Metrologia, vol. 38, no. 4, 2001, accepted for publication.

[3] F. Vernotte, G. Zalamansky, M. McHugh, and E. Lantz, "Cut-off frequencies and noise power law model of spectral density : adaptation of the multi-variance method for irregularly spaced timing data using the lowest mode estimator approach.," IEEE Transactions on Ultrasonics, Ferroelectrics, and Frequency Control, vol. 43, no. 3, pp. 403–409, 1996.

[4] W. C. Lindsey and C. M. Chie, "Theory of oscillator instability based upon structure function," Proceedings of the IEEE, vol. 64, pp. 1652–1666, December 1976.

[5] J. Rutman, "Characterization of phase and frequency instabilities in precision frequency sources: fifteen years of progress," Proceedings of the IEEE, vol. 66, pp. 1048–1075, 1978.

[6] F. Vernotte and D. A. Howe, "Generalization of the total variance approach to the different classes of structure functions," in Proc. of the 14th European Frequency and Time Forum, 2000, pp. 375–379.

GALILEO AND ACES

Chairwoman: Patrizia Tavella

MODELISATION AND EXTRAPOLATION OF TIME DEVIATION : APPLICATION TO THE ESTIMATION OF THE DATATION STABILITY OF A NAVIGATION PAYLOAD

Jérôme DELPORTE*, François Vernotte**, Thierry TOURNIER*, Michel BRUNET*

* Centre National d'Etudes Spatiales
18 avenue Edouard Belin - 31401 TOULOUSE Cedex 4 - FRANCE
Phone : 33+5.61.27.44.36 - Fax : 33+5.61.28.26.13 - E-mail : jerome.delporte@cnes.fr

** Observatoire de Besancon - UPRESA CNRS 6091
41 bis avenue de l'Observatoire - BP 1615 - 25010 BESANCON Cedex - FRANCE
Phone : 33+3.81.66.69.22 - Fax : 33+3.81.66.69.44 - E-mail : francois@obs-besancon.fr

ABSTRACT

In Global Navigation Satellite Systems, the on-board time has to be adjusted and extrapolated in order to broadcast the time parameters to final users. The needs of synchronisation for a GNSS are specified as the maximum error of the time prediction from the extrapolated model. As a consequence, the key parameter for the navigation payload is the time prediction performance.

Our previous work about the estimation of uncertainties in time deviation extrapolation has allowed us to establish a link between the noise levels of a clock and its time prediction performance.

In this paper, we will take into account the temperature sensitivity of the clock and the measurement noise in order to know their impact on the datation performance. We will also show that there is an optimum adjustment duration according to the dominating noise type.

Finally, experimental results on a navigation payload demonstrator developed by CNES will be presented. These experiments allowed us to compare simultaneously the datation performance of the clock and the datation performance of the whole payload.

1. INTRODUCTION

In Global Navigation Satellite Systems, each satellite has to broadcast a certain number of time parameters so that the user can determine the satellite code phase offset (referenced to the phase center of the satellite antenna) with respect to the system time. Generally, the time parameters are a polynomial of first or second degree, which corresponds to a time linear or quadratic model. The coefficients of this polynomial shall describe the offset for the interval of time in which the parameters are transmitted [Ref. 1]. So, as far as timing is concerned, the system-level specification for the navigation payload is its time prediction performance.

For GALILEO, the coefficients of this polynomial can be computed as follows : the raw data of the OD&TS (Orbit Determination and Time Synchronisation) process are collected with a τ_0 period, they are adjusted by a least mean square model over a time interval called T_m. This model is extrapolated during a time interval called T_p that follows T_m. We consider the maximum extrapolation error over T_p ; on average, this maximum is obtained at the end of T_p. So, the specification deals with S_{ext} that is the one-sigma extrapolation error at the end of T_p.

The figure below illustrates the adjustment and extrapolation process in case of a time quadratic model :

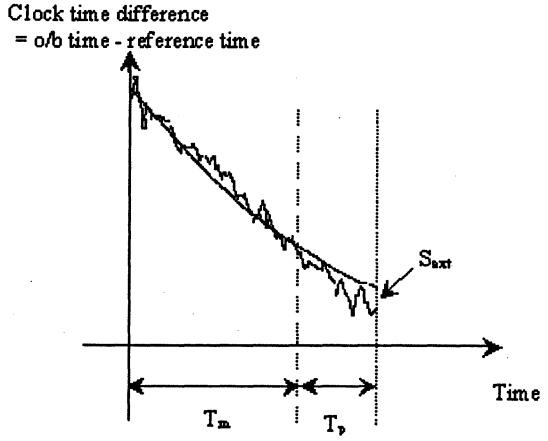

Figure 1 : Adjustment and extrapolation process

The specification deals with the datation provided by the navigation payload, taking into account every source of error : the intrinsic noise of the on-board clock, the sensitivities of the on-board clock to environment variations, the variations of the propagation delays within the equipments of the rest of the payload.

In previous papers [Ref. 2-3], we have described the relationships between the noise levels of a clock and its time prediction performance. These relationships are valid for a clock in a stable environment.

In this paper, we will first recall these relationships, then we will show that there is an optimum adjustment duration for a given extrapolation duration, for each type

of noise. Then, we will look into the environmental conditions impact on the datation stability of the on-board clock and the measurement noise. Last, we will present the tests and measurements performed on a navigation payload demonstrator developed by CNES.

2. DATATION STABILITY OF A CLOCK IN STABLE ENVIRONMENT

2.1. Adjustment principle

In this part, we will recall the adjustment principle and the extrapolation error determination method for a quadratic model. The equations for a linear model can be derived from these ones very easily.

Let us consider a sequence of N time deviation data x(t) regularly spaced with a sampling period τ_0 : $\{x(t_0), x(t_1),\ldots,x(t_{N-1})\}$, with $t_k = k.\tau_0$. The adjustment using the 3 first Tchebychev polynomials can be written :

$$x(t) = P_0.\varphi_0(t)+P_1.\varphi_1(t)+P_2.\varphi_2(t)+e(t) \qquad (1)$$

with :

$$\varphi_0(t) = \frac{1}{\sqrt{N}}$$

$$\varphi_1(t) = \sqrt{\frac{3}{(N-1)N(N+1)}}\left[2\frac{t}{\tau_0}-(N-1)\right]$$

$$\varphi_2(t) = \sqrt{\frac{5}{\prod_{k=-2}^{2}(N+k)}}\left[6\left(\frac{t}{\tau_0}\right)^2-6(N-1)\frac{t}{\tau_0}+(N-2)(N-1)\right]$$

Let us note the vector $\varphi_i = (\varphi_i(t_0) \ldots \varphi_i(t_{N-1}))^T$ and the matrix $[\varphi] = (\varphi_0\ \varphi_1\ \varphi_2)$. We also note the vectors $X = (x(t_0)\ldots\ x(t_{N-1}))^T$, $E = (e(t_0)\ldots\ e(t_{N-1}))^T$ and $P = (P_0\ P_1\ P_2)^T$.

The relationship (1) can be written vectorially :

$$X = [\varphi].P + E \qquad (2)$$

It is easy to show that the most probable estimator of P in the sense of the least mean square [Ref. 2,3] :

$$\hat{P} = [\varphi]^T.X \quad that\ is \quad \hat{P}_j = \sum_{i=0}^{N-1}\varphi_j(t_i).x(t_i) \qquad (3)$$

We define the "Time Interval Error" (TIE) as the difference between the true time deviation x(t) and the extrapolation of the model previously estimated from t_0 to t_{N-1}, that is (for $t > t_{N-1}$) :

$$TIE(t) = x(t)- P_0.\varphi_0(t)-P_1.\varphi_1(t)-P_2.\varphi_2(t) \qquad (4)$$

with $t = T_m + T_p$.

The TIE is the combination of 2 effects : the error in the determination of the P model parameters and the error due to the noise of the clock. These 2 errors for random clock noises can be positive or negative and the ensemble average of the TIE is equal to zero. Moreover, simulations have clearly shown that the statistics of TIE is Gaussian and centered [Ref. 2]. Consequently, we only need to estimate its variance to define it completely. Using (4), the variance of TIE can be estimated by :

$$\hat{\sigma}_{TIE}^2 = \sigma_X^2 + \sigma_{P_0}^2.\varphi_0^2(t) + \sigma_{P_1}^2.\varphi_1^2(t) + \sigma_{P_2}^2.\varphi_2^2(t)$$
$$-2.\sum_{j=0}^{2}\left[Cov(x(t),P_j).\varphi_j(t)\right] + 2\sum_{\substack{i,j=0\\ i\neq j}}^{2}\left[Cov(P_i,P_j).\varphi_i(t).\varphi_j(t)\right]$$

We will use the power law model of the relative frequency (or phase) spectral densities. We note the time deviation spectral density $S_x = k_\alpha f^\alpha$ for $\alpha = -4$ to 0. This is equivalent to note the relative frequency spectral density $S_y = h_{\alpha+2} f^{\alpha+2}$ with $k_\alpha = h_{\alpha+2} / (4\pi^2)$. The 3 types of noise that are of interest are the white frequency noise, the Flicker frequency noise and the random walk.

2.2. Results for a quadratic model

We note $u = T_p / T_m$.

- White frequency :

$$\sigma_{TIE}^2 = \frac{6\pi^2}{35}k_{-2}T_m\left(50u^4+100u^3+69u^2+19u+1\right)$$

- Flicker frequency :

$$\sigma_{TIE}^2 = \frac{\pi^2}{8}k_{-3}T_m^2\left(\begin{array}{l}192u^6+576u^5+692u^4\\+424u^3+136u^2+20u+1\\+96u^3\ln\left(\frac{u}{1+u}\right)\left(2u^4+7u^3+9u^2+5u+1\right)\end{array}\right)$$

- Random walk :

$$\sigma_{TIE}^2 = \frac{2\pi^4}{315}k_{-4}T_m^3\left(450u^4+690u^3+303u^2+42u+2\right)$$

2.3. Results for a linear model

- White frequency :

$$\sigma_{TIE}^2 = \frac{4\pi^2}{15}k_{-2}T_m\left(9u^2+9u+1\right)$$

- Flicker frequency :

$$\sigma_{TIE}^2 = \frac{\pi^2}{3}k_{-3}T_m^2\left(\begin{array}{l}12u^4+24u^3+20u^2+8u+1\\+2\ln(1+u)\left(6u^2+6u+1\right)\\+2u^3\ln\left(\frac{u}{1+u}\right)\left(6u^2+15u+8\right)\end{array}\right)$$

- Random walk :

$$\sigma_{TIE}^2 = \frac{8\pi^4}{105}k_{-4}T_m^3\left(35u^3+39u^2+11u+1\right)$$

3. OPTIMIZATION OF T_M

3.1. Optimisation of the adjustment duration

It is easy to show that for each type of noise and for a given extrapolation duration T_p, there is an optimal adjustment duration T_m.

The table below summarises the optimal T_m :

	Quadratic model	Linear model
White frequency	$\left(4+\sqrt{31}\right)T_p$ $\cong 9.57T_p$	$3T_p$
Flicker frequency	$\cong 3.13T_p$	$\cong 0.5T_p$
Random walk	$\left(-3+\sqrt{66}/2\right)T_p$ $\cong 1.06T_p$	0

Table 1 : Optimal T_m

It shall be noticed that the optimal adjustment duration for a given type of noise is higher for a quadratic model than for a linear one. Besides, the higher the frequency noise, the higher the optimal T_m.

3.2. Linear vs. quadratic model at the optimum T_m

The table below allows to compare the standard deviation of TIE obtained at this optimum :

	Quadratic model	Linear model
White frequency	$\cong \sqrt{62.4\,k_{-2}T_p}$	$\cong \sqrt{39.5\,k_{-2}T_p}$
Flicker frequency	$\cong \sqrt{334.9k_{-3}T_p^2}$	$\cong \sqrt{131.6\,k_{-3}T_p^2}$
Random walk	$\cong \sqrt{918.6\,k_{-4}T_p^3}$	$\cong \sqrt{259.7\,k_{-4}T_p^3}$

Table 2 : Optimal extrapolation error

We deduce from this table that without frequency drift the linear model is always potentially better than the quadratic model.

Nevertheless, it needs to be added that the linear model does not adjust a frequency drift. In other words, the frequency drift has a contribution in the extrapolation error that is to be taken into account in order to carry out a fair comparison. If this contribution is dominating, the quadratic model may become more interesting.

3.3. Contribution of the frequency drift in case of a linear model

Let us consider that we have $x(t) = a_2t^2$. According to (3), we can write :

$$\hat{P}_0 = \frac{a_2\tau_0^2}{\sqrt{N}}\frac{N}{6}(N-1)(2N-1))$$

$$\hat{P}_1 = \sqrt{\frac{3}{N(N^2-1)}}a_2\tau_0^2\,\frac{N}{6}(N+1)(N-1)^2$$

We can deduce that :

$$TIE(t) = a_2t^2 - \hat{P}_0.\varphi_0(t) - \hat{P}_1.\varphi_1(t)$$

$$= \frac{a_2}{6}\left(6t^2 - 6\tau_0^2(N-1)t + \tau_0^2(N-1)(N-2)\right)$$

Noticing that $t = T_m + T_p$ and $T_m = N\tau_0$, and under the assumption that $N >> 1$, we get :

$$\boxed{TIE(T_m, T_p) = \frac{d}{12}T_m^2\left(6u^2+6u+1\right)} \qquad (5)$$

where $d = a_2/2$ is the frequency drift per second.

Contrary to the previous formula, this error is deterministic. When using a linear model, the TIE will be centered on the value given by (5).

Example : the following figure represents the comparison between the mean of TIE obtained experimentally and the value predicted by (5), for a quartz crystal oscillator which relative frequency drift has been estimated over the whole measurement sequence to $1{,}1.10^{-11}$/day. This comparison is performed for T_m = 3 h and T_p varying from 0.5 to 5 h :

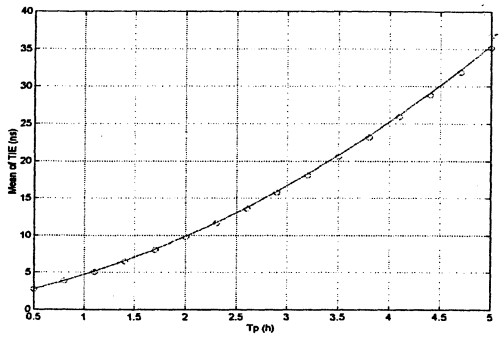

Figure 2 : Theoretical (o) and experimental (-) mean of TIE (ns)

4. IMPACT OF ENVIRONMENTAL CONDITIONS ON THE DATATION STABILITY OF THE O/B CLOCK

4.1. Assumptions and theoretical approach

For a MEO (Medium Earth Orbit) constellation like GPS or GLONASS, the Earth magnetic field is very low (± 1 μT) and can be neglected.

As for radiation, the MEO environment is very severe. For a 4 mm equivalent Al shielding, the average radiation dose received is about 50 krad / year, without taking into account the solar eruptions. The effect of radiation has not been studied in detail here, but shall not be overlooked.

As for temperature, we have assumed that the temperature variations will follow a sinusoidal pattern which period is the orbital period (T = 12 hours) :

$$Tmp(t) = A*\sin(wt + \phi)$$

where A is the magnitude and $w = 2\pi/T$.

If we note TS the frequency thermal sensitivity of the clock, y the relative frequency at stable temperature, and $y^{\#}$ the relative frequency with the sinusoidal variations of temperature, we obviously have :

$$y^{\#}(t) = y(t) + A*TS*\sin(wt + \phi)$$

And then :

$$x^{\#}(t) = x(t) - A*TS*\cos(wt + \phi) / w$$

As we have also :

$$TIE^{\#}(T_m,T_p) = x^{\#}(t) - P_0^{\#}.\varphi_0(t) - P_1^{\#}.\varphi_1(t) - P_2^{\#}.\varphi_2(t)$$

with $P_j^{\#} = \sum_{i=0}^{N-1} \varphi_j(t_i).x^{\#}(t_i)$

We deduce that :

$$TIE^{\#}(t) = TIE(t) - \frac{A*TS}{w}\cos(wt+\phi) + \sum_{j=0}^{2}\left[\sum_{k=0}^{N-1}\varphi_j(t_k).\frac{A*TS}{w}\cos(wt_k+\phi)\right]*\varphi_j(t)$$

It is the sum of three terms : the TIE at stable temperature, a sinusoidal term which represents the sine variations of temperature and a third term which represents the deformation of the fit due to the variations of temperature.

4.2. Validation

Let us consider the same quartz crystal oscillator as in the last example. We have tested it using a thermal chamber which temperature can be monitored, so that it has underwent sinusoidal variations of temperature of ± 1.3 °C with a 12 hours period. Its thermal sensitivity was estimated by a least square method to TS = $-5{,}1.10^{-13}$/°C. The figure below compares the experimental standard deviation of TIE (continuous line) to the theoretical one (o). This theoretical values are obtained by the quadratic sum of the experimental standard deviation of TIE without variations of temperature (dash line) and the contribution of the sinusoidal variations of temperature (x). This has been carried out for a quadratic model :

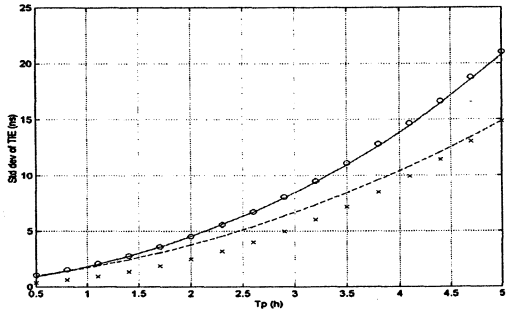

Figure 3 : Theoretical (o) and experimental (continuous line) standard deviation of TIE (ns)

5. MEASUREMENT NOISE

5.1. Assumption and theoretical approach

In order to take into account the measurement noise, we assume that this noise can be considered as white phase noise. This white phase noise affects the adjustment period only. The measurement noise during the extrapolation isn't taken into account since it doesn't depend on the system but on the user's receiver.

Let us note $m(t_k)$ the measurement noise which affects $x(t_k)$ for k = 0 to N-1, and TIE^* the Time Interval Error when the measurement noise is taken into account and TIE the Time Interval Error without measurement noise. We will carry out here the computation of TIE^* for a quadratic model.

$$TIE^* = TIE - \hat{P}_0.\varphi_0(t) - \hat{P}_1.\varphi_1(t) - \hat{P}_2.\varphi_2(t)$$

with $\hat{P}_j = \sum_{i=0}^{N-1}\varphi_j(t_i).m(t_i)$

Consequently :

$$\sigma^2_{TIE^*} = \sigma^2_{TIE} + \sum_{j=0}^{2}\sigma^2_{P_j}\varphi_j^2(t) - 2.\sum_{j=0}^{2}\left[Cov(m(t),P_j).\varphi_j(t)\right] + 2\sum_{\substack{i,j=0\\ i\neq j}}^{2}\left[Cov(P_i,P_j).\varphi_i(t).\varphi_j(t)\right]$$

It has been shown [Ref. 4] that $\sigma^2_{P_j} = k_0 f_h = \sigma^2_m$ for j = 0 to 2 and that all the covariances Cov(m,P_j) and Cov(P_i,P_j) were equal to zero for a white phase noise.

$$\sigma^2_{TIE^*} = \sigma^2_{TIE} + \sigma^2_m\left(\varphi_0^2(t) + \varphi_1^2(t) + \varphi_2^2(t)\right)$$

This gives for a quadratic model :

$$\sigma^2_{TIE^*} = \sigma^2_{TIE} + \frac{9\tau_0}{T_m}\sigma^2_m\left(20u^4 + 40u^3 + 28u^2 + 8u + 1\right)$$

and for a linear model :

$$\sigma^2_{TIE^*} = \sigma^2_{TIE} + \frac{4\tau_0}{T_m}\sigma^2_m\left(3u^2 + 3u + 1\right)$$

One can notice immediately that the measurement noise has a smaller impact on the extrapolation error for a linear model than for a quadratic model, whatever T_m and T_p.

5.2. Validation

To validate the above formula, we simulated 10,000 white frequency noise sequences ($h_0 = 10^{-21}$ s, N = 8640, τ_0 = 10 s). We added white phase noise ($h_2 = 6.10^{-13}$ s^3, f_h = 0.5 Hz) in the adjustment duration and compared the theoretical and experimental TIE as a function of T_p :

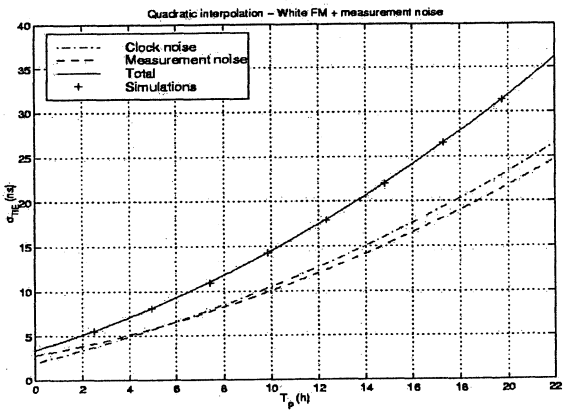

Figure 4 : Theoretical (continuous line) and experimental (+) standard deviation of TIE (ns)

This has also been performed for a linear model and we have in both cases an excellent agreement between theory and simulations.

6. DATATION STABILITY OF THE REST OF THE PAYLOAD

The variations of the propagation delays within the equipments of the rest of the payload (code generator, frequency synthesis, modulators, amplifiers, filters,...) can degrade the datation stability provided by the on-board clock.

At CNES, in the frame of the DE Navigation, a mock-up of a navigation payload has been developed and tested [Ref. 5]. In order to measure the datation stability provided by this payload, we used a fixed receiver. This experiment allowed us to measure simultaneously the datation stability of the on-board clock and of the whole payload :

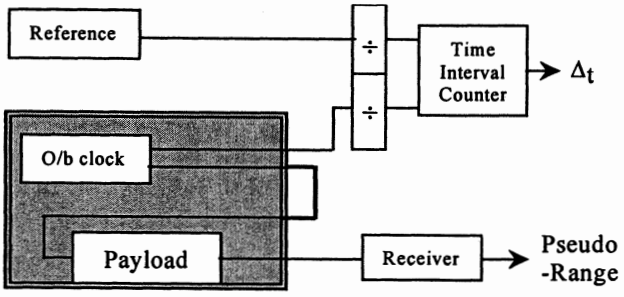

Figure 5 : Navigation payload test

The time interval counter and the receiver are synchronised by the reference clock. The whole payload is stabilised at a constant temperature.

The following figure allows to compare the extrapolation error of the on-board clock and the extrapolation error of the whole payload (that is of the pseudo-range divided by the speed of light) :

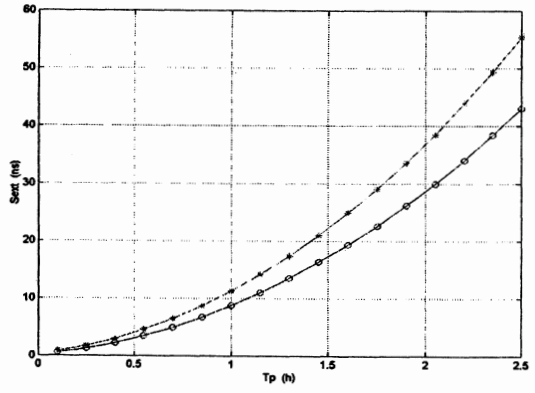

Figure 6 : Standard deviation of TIE for the on-board clock (o) and for the whole payload (*) (ns)

This figure was obtained with T_m = 0.5 h and T_p varying from 0.1 to 2.5 h.

The extrapolation error of the whole payload should be the quadratic sum of the extrapolation error of the on-board clock and of the rest of the payload plus or minus a correlation term. This figure shows that the contribution of the rest of the payload is to be taken into account. Moreover, if the payload undergoes variations of temperature, the propagation delays are likely to be modified a great deal, which will degrade all the more the datation stability of the payload.

7. CONCLUSION

The datation stability broadcast by a navigation payload is the sum of several contributions : the intrinsic noise of the on-board clock, the effect of environment on this clock, the measurement noise, the variations of the propagation delays within the rest of the payload, ...

In this paper, we have studied the impact of all these effects in terms of extrapolation error. With a simple Allan deviation curve and a figure of sensitivity to temperature, we can deduce the time prediction performance of the on-board clock. The formula we obtained allow to :

- show that there is an optimum adjustment duration for a given extrapolation duration
- carry out a thorough synchronisation error budget
- perform a sensitivity analysis
- carry out a complete comparison between linear and quadratic models
- choose adjustment and extrapolation durations which minimize the extrapolation error

8. REFERENCES

[Ref. 1] "Standardization Agreement - Navstar GPS system characteristics" - NATO - Military Agency for Standardization.

[Ref. 2] "Estimation of uncertainties in time error extrapolation" - F. Vernotte, J. Delporte, M. Brunet, T. Tournier - Proceedings of 31st PTTI, p. 305-316, Dana Point, December 1999.

[Ref. 3] "Modelisation and extrapolation of time deviation of USO and atomic clocks in GNSS-2 context" - J. Delporte, F. Vernotte, T. Tournier, M. Brunet - Proceedings of 32nd PTTI, Reston, November 2000.

[Ref. 4] "Uncertainties of drift coefficients and extrapolation errors" - F. Vernotte, J. Delporte, M. Brunet, T. Tournier - submitted to Metrologia, 2000.

[Ref. 5] "Development and Test of a Galileo OAS Navigation Payload Demonstrator" - L. Lestarquit, J.L. Issler, J. Delporte, J. Dantepal, L. Ries - ION-GPS 2000, Salt Lake City, Utah, 19-22 September 2000.

Scientific objectives of ACES project

Ch. SALOMON , *Laboratoire Kastler-Brossel [ENS-LKB]*
N. DIMARCQ , *Laboratoire de l'Horloge Atomique [LHA]*
M. ABGRALL, A. CLAIRON, P. LAURENT, P. LEMONDE, G. SANTARELLI, P. UHRICH , *Laboratoire Primaire du Temps et des Fréquences [BNM-LPTF]*
L.G. BERNIER, G. BUSCA, A. JORNOD, P. THOMANN , *Observatoire Cantonal de Neuchâtel [ON]*
E. SAMAIN , *Observatoire de la Côte d'Azur [OCA – CERGA]*
P. WOLF , *Bureau International des Poids et Mesures [BIPM]*
F. GONZALEZ, Ph. GUILLEMOT, S. LEON, F. NOUEL, Ch. SIRMAIN, *Centre National d'Etudes Spatiales [CNES]*
S. FELTHAM , *European Space Agency - ESTEC*

ENS-LKB, 24 rue Lhomond, 75231 Paris cedex 5, France
LHA, Observatoire de Paris, 61 avenue de l'Observatoire 75014 Paris, France
BNM-LPTF, Observatoire de Paris, 61 avenue de l'Observatoire 75014 Paris, France
ON, rue de l'Observatoire 58, 2000 Neuchâtel, Switzerland
OCA-CERGA, 2130 route de l'Observatoire 06460 Caussols, France
BIPM, Pavillon de Breteuil, 92312 Sèvres cedex, France
CNES, 18 Avenue Edouard Belin, 31402 Toulouse, France
ESA / ESTEC, Keplerlaan, 2200 AG Noordwijk, The Netherlands
Corresponding author : noel.dimarcq@obspm.fr

I. Introduction

ACES is a space mission which aims at operating ultrastable clocks on board the International Space Station (ISS). The ACES payload is scheduled to be launched in june 2005 on the UF6 shuttle flight. ACES Principal Investigator (PI) is Christophe Salomon (ENS-LKB) and the chairman of the ACES International User Community is Pierre Thomann (Neuchâtel Observatory). In this article, we describe briefly ACES instruments and equipment (Section II) and point out expected performance of clocks and Time and Frequency links. In section III, the main science objectives in fundamental physics are detailed. As a conclusion, Section IV gives the present status of the ACES mission.

II. ACES system description

The ACES payload (Figure 1) includes two clocks :

- **PHARAO**
  PHARAO is a cold cesium atom clock designed by BNM-LPTF, ENS-LKB, LHA with the technical and financial support of the french space agency CNES.
- **SHM**
  SHM is an active hydrogen maser designed by ON with a financial support of the european space agency ESA

These two clocks can be intercompared on board in the **FCDP** (Frequency Comparison and Distribution Package). They can also be compared to Earth based clocks using either the optical link T2L2 (Time Transfer by Laser Link) or the microwave link MWL.

ACES operation requires standard equipment (payload computer, power distribution unit) and specific equipment which is supported by ESA :

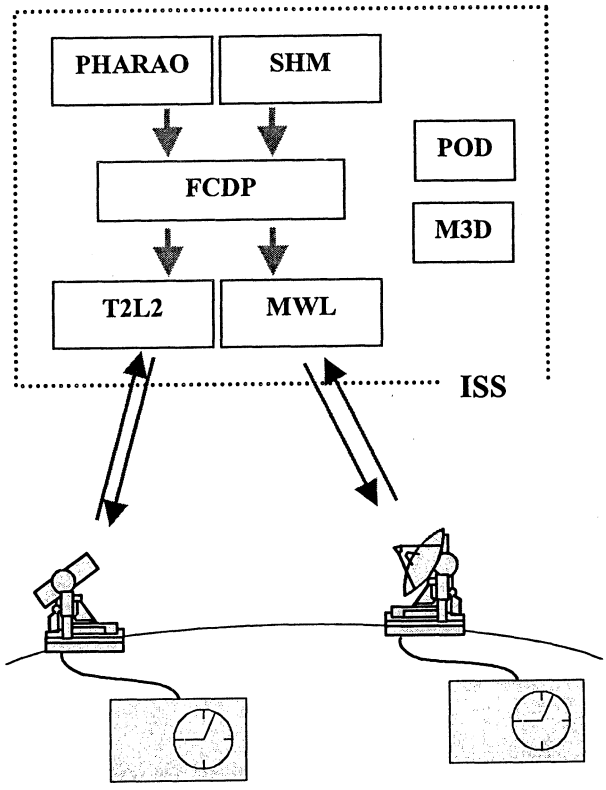

Fig. 1 The ACES system

- **M3D** which is the Microvibrations and Magnetic Measurement Device
- **POD** (Precise Orbit Determination) which determines the orbit of ACES payload.

The ACES payload will be installed on a nadir oriented Express Pallet on board the International Space Station. This pallet will be located either on ISS main truss or on the European pressurized module COLOMBUS.

The allocated resources for the complete ACES payload are about 1 m^3 for the volume, 220 kg for the mass and 450 W for the electrical power.

II.1. Clocks

➢ *PHARAO*

PHARAO relative **frequency stability** is expected to be better than $\sigma_y(\tau) = 10^{-13}.\tau^{-1/2}$ for an integration time τ (Figure 2). It corresponds to a frequency stability below 3.10^{-16} for a one-day integration time and below $1.\ 10^{-16}$ for ten days. PHARAO **frequency accuracy** target is at 10^{-16} level.

➢ *SHM*

SHM relative **frequency stability** is expected to be (Figure 2) :

$\sigma_y(\tau = 1\ s) \leq 1.5 \times 10^{-13}$
$\sigma_y(\tau = 10\ s) \leq 2.1 \times 10^{-14}$
$\sigma_y(\tau = 100\ s) \leq 5.1 \times 10^{-15}$
$\sigma_y(\tau = 1\ 000\ s) \leq 2.1 \times 10^{-15}$
$\sigma_y(\tau = 10\ 000\ s) \leq 1.5 \times 10^{-15}$

Thanks to its better medium term stability, SHM will be used for the evaluation of some frequency shifts affecting PHARAO accuracy and as a high spectral purity local oscillator for PHARAO.

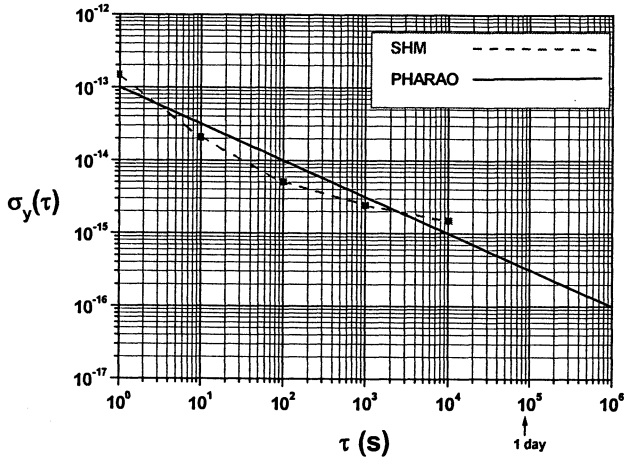

Fig. 2 Expected Allan standard deviation for PHARAO and SHM

II.2. Time and Frequency (T&F) links

a) Required T&F link performance

In order to perform space-ground clock comparisons with a reduced degradation (less than 20 %), ACES T&F links must exhibit a very low phase noise compatible with the clock stability of 10^{-16}. The variations of the time deviation expected for T2L2 and MWL as a function of the integration time τ are depicted on Figure 3. Two characteristical times are taken into account in ACES :

- 300 s, which is the mean duration of an ISS pass over a given point. It will be the mean duration of a comparison session between ground and space clocks. The T&F link must exhibit rms time fluctuations below 0.3 ps over 300 s.
- 90 min which is the orbit period. The minimal dead time between two successive comparison sessions will be 90 min. Larger dead times (as large as 1 day) may occur. This requires a T&F link with a very good long term time stability, typically better than 6 ps over 1 day.

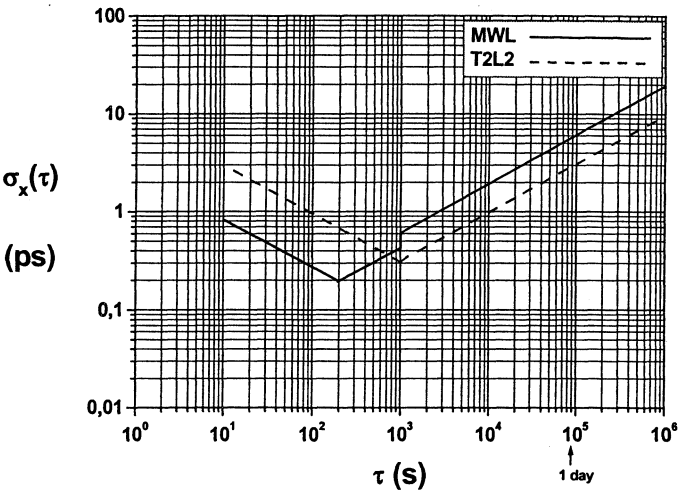

Fig. 3 Expected time deviation for T2L2 and MWL

All primary scientific objectives of ACES require only stability for the T&F link. No accuracy is needed. Nevertheless, an absolute calibration of ground instrument delays will be performed with a resolution of 50 ps for T2L2 and a few hundreds of ps for MWL.

b) The optical link : T2L2

T2L2 is designed by the Observatoire de la Côte d'Azur (OCA-CERGA) with the technical and financial support of CNES.

The operation principle of T2L2 is simple. A ground laser station emits light pulses towards ISS. On the ACES payload, the laser pulse is both detected and partially reflected towards the ground station with a corner cube reflector. For each pulse, three datations are performed :

- date T_0 of pulse emission from the ground station (date in ground clock time scale)
- date T_1' of pulse detection on the ACES payload (date in space clock time scale)
- date T_2 of reflected pulse detection in the ground station (date in ground time scale).

The comparison of ground and space clock time scales relies on the knowledge of the ensemble of date triplets (T_1, T_2', T_3) corresponding to a large number of detected laser pulses. The « Two-way » (up and down link) operation of T2L2 rejects a lot of common mode noise sources, especially the tropospheric delay. The ionospheric delay is extremely small at optical frequencies and is also cancelled by the Two-Way scheme.

Instrumental delays are the main noise sources in T2L2. Preliminary experiments have been already carried out and have demonstrated instrumental delay fluctuations whose time deviation is at the required picosecond level (Figure 4).

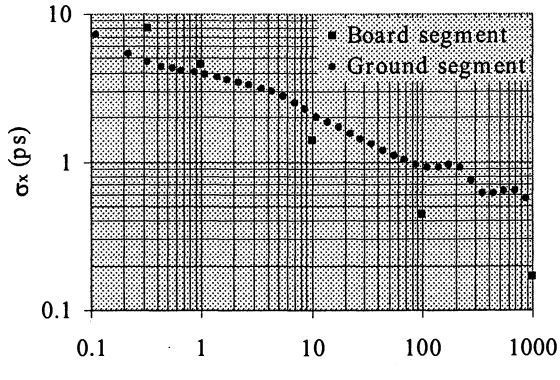

Fig. 4 Instrumental delay fluctuations measured on T2L2 demonstrator breadboard

c) The microwave link : MWL

No existing microwave link (GPS, TWSTFT) can reach today the required performance for ACES. With ESA support, a new microwave link technique will be developed. Two different concepts have been proposed by two compagnies which have already a long experience in T&F transfer techniques : Timetech, in Germany (designer of PRARE and SATRE systems) and Thalès, in France (designer of T2L2 datation device). Proposed MWL concepts are ugraded versions of the Vessot Two-Way technique used for the GP-A experiment in 1976 [1-2]. In this experiment, a two-way link with 3 frequencies in S band (one signal up, two signals down) allowed the frequency comparison between two H-masers (one on ground and one in a rocket) at the level of 8. 10^{-15} at 1000 seconds. This Two-Way / 3 frequencies method allowed :

- the complete rejection of tropospheric delay, 1st order Doppler effect
- a partial rejection of ionospheric delay ; the up and down frequency are not equal to avoid interference effects and they do not lead to equal ionospheric delays. The evaluation of this residual ionospheric delay required the knowledge of the ionosphere Total Electronic Content (TEC) which was evaluated using the second down link at different frequency.
- a partial independence on the positions of antennas phase centers.

Nevertheless, Vessot's technique was a frequency comparison technique : it required the clocks to be in permanent visibility during the comparison. Moreover, it did not offer multi-user capability which is mandatory for ACES mission to allow common view comparisons of ground clocks.

The two MWL concepts proposed for ACES are improved Vessot's technique and their main characteristics are (see Table 1) :

- the carrier frequency f_c is increased to Ku band (about 15 GHz) ; this leads to a noticeable reduction of the inospheric delay which varies as $1/(f_c)^2$. Timetech technique uses a third frequency in S band to determine ionosphere TEC. In Thalès technique, up and down links have the same frequency : the ionospheric delay is thus completely rejected by the two-way scheme.
- the operation of Timetech system is continuous whereas Thalès one is pulsed to avoid interference effects (equal up and down link frequencies)
- a PN-code is used to remove 2π phase ambiguity between two successive comparisons sessions separated by large dead times. This code modulation is applied on the phase (Timetech) or the amplitude (Thalès) of the carrier.
- both systems allow multi-users capability : different ground users are distinguished by different PN-codes and different Doppler shifts.

	Timetech Technique	Thalès Technique
Concept	- Two-Way (up and down link) - 3 frequencies	- Two-Way (up and down link) - 1 frequency
Carrier frequency	- Ku band (one up and one down link) - S band (one down link) for TEC determination	- Ku band
Operation mode	Continuous	Pulsed
PN-code	on carrier phase of Ku and S signals	on carrier amplitude
Code rate	- 100 Mchip/s for Ku signals - 1 Mchip/s for S signal	- 100 MHz
Multi-users capability	YES (4 simultaneous users)	YES (2 simultaneous users)

Table 1 Main characteristics of proposed MWL concepts

Relativistics effects affecting time or frequency transfer (gravitational shift, 2nd order Doppler effect, Sagnac effect, ...) will be corrected using the orbitography data (see Section II.4).

Preliminary studies have already benn performed on these two MWL concepts and they bring a sufficient confidence in the feasability of the high stability microwave T&F link for ACES.

II.4. Orbitography requirements

Science objectives described in Section III rely on comparisons between space and ground clocks. A precise knowledge of space clocks orbit is required because both altitude and velocity are involved in the

relativistics effects which affect both clocks and T&F links.

Relativistics effects affecting clock frequency

Due to relativistics effect, the clock proper frequency differs by an amount Δf compared to its coordinate value f it would have in a geocentric isotropic inertial reference frame (GRS) :

$$\frac{\Delta f}{f} = -\frac{1}{c^2}\left(U + \frac{v^2}{2}\right) \qquad \text{Eq(1)}$$

where v is the GRS coordinate velocity of the clock and U is the gravitational potential at clock location (with $U \geq O$ following the International Astronomical Union convention). The gravitational shift is as large as $-6.9\ 10^{-10}$ for a ground clock and $-6.5\ 10^{-10}$ for a clock onboard ISS at the altitude of 400 km. The 2nd order Doppler effect frequency shift is equal to $-1.3\ 10^{-12}$ for a ground clock and $-3.3\ 10^{-10}$ for a clock onboard ISS with a velocity about 7 $km.s^{-1}$.

In order to evaluate these relativistics frequency shifts with a precision compatible with clock stability and accuracy, the whole orbit of both ground and space clocks must be known with uncertainties lower than :

- 1.7 m (averaged over 1 day) for the altitude
- 1.9 $mm.s^{-1}$ (averaged over 1 day) for the velocity

Relativistics effects affecting T&F links

The space-ground clock comparisons will be performed using a two–way time or frequency transfer in order to cancel the effect of atmospheric fluctuations and first order Doppler. The frequency shift induced by relativistics effects in the frequency transfer is given by :

$$\frac{\Delta f}{f} = \frac{1}{c^2}\left[-U_E(\vec{w}_S) + U_E(\vec{w}_E) - \frac{|\vec{v}_E - \vec{v}_S|^2}{2} - \vec{r}_{SE}\cdot\vec{a}_E\right] + o\left(\frac{1}{c^3}\right) \qquad \text{Eq. (2)}$$

In Equation 2, $U_E(w_S)$ is the Earth gravitational potential applied to the clock on-board the ISS located at the co-ordinate position $\vec{w}_S$ in the GRS. $U_E(\vec{w}_E)$ is the Earth gravitational potential applied to the clock on the ground located at the co-ordinate position $\vec{w}_E$ in the GRS. c is the velocity of the light, $\vec{v}_E$ is the GRS co-ordinate velocity of the clock on ground, $\vec{v}_S$ is the GRS co-ordinate velocity of the ISS clock. $\vec{r}_{SE}$ is the range between a ground reference point and an ISS reference point expressed in the GRS, $\vec{a}_E$ is the acceleration of the Earth in the GRS.

All terms of equation (2) are expressed in the same geocentric inertial reference frame, which is chosen here as the GRS. The first term of equation (2) $\left[-U_E(\vec{w}_S) + U_E(\vec{w}_E)\right]/c^2$ describes the influence of the Earth gravitational potential. As the ISS is a low orbiting satellite, the influence of other bodies (e.g. the Moon) is negligible at the expected 10^{-17} level. For an ISS orbit of 400 km, this term is $+4.6\ 10^{-11}$.

The second term $|\vec{v}_E - \vec{v}_S|^2/2c^2$ describes the second order Doppler effect between two moving clocks and has a value of $-3.3\ 10^{-10}$.

The third term $(\vec{r}_{SE}.\vec{a}_E)/c^2$ includes the effect of the rotation of the Earth (Sagnac $1/c^2$ effect). It is maximal for a ground station on the equator and is lower than $7\ 10^{-13}$.

In order to evaluate these relativistics frequency shifts with a precision compatile with clock stability, both ground and space clocks orbits during an ISS pass (300 s duration) must be known with an uncertainty lower than :

- 24 m for the altitude
- 26 $mm.s^{-1}$ for the velocity

Equation (2) is valid up to second order (c^{-2}). Nevertheless, for time transfer between clocks at a level of 10^{-16}, the contribution of third order terms (c^{-3}) must be included in equation (2) [3-4]. The three terms of (3) must then be multiplied by $\left[1 + c^{-1}.\vec{r}_{SE}.(\vec{v}_S - \vec{v}_E)/r_{SE}\right]$. This c^{-1} term can be interpreted as a Doppler correction to the three relativistic terms in equation (2). During the frequency comparison, this correction is maximum at low elevation and unsymmetrical around zenith. Its absolute value is less than $2.7\ 10^{-5}$ or $1.2\ 10^{-15}$ in relative frequency. It is thus sufficient to calculate this correction at the 5 % level for frequency comparisons at 10^{-16}.

ACES orbitography requirements can be fulfilled with DORIS. Nevertheless, it is generally the orbit of a specific ISS point (center of gravity COG) which is determined. As a consequence, the knowledge of ISS attitude and structural deformations could be needed to deduce the orbit of ACES payload if it is not on a location close to ISS COG.

III. ACES science objectives

The first part of ACES mission will be a 6 months characterization phase (evaluation of clocks and T&F links performance). Then, the utilization phase (12 to 30 months duration) will take place. ACES user groups have identified experiments in the following domains :

- physics of cold atoms
- relativistic effects
- precise orbit determination
- laser time transfer
- microwave link
- T&F metrology
- geodesy
- earth observation

ACES has obvious objectives in T&F metrology (primary standards, clock comparisons, time scales,). ACES tests in Fundamental Physics are of outstanding importance and will be further detailed.

III.1. Measurement of the gravitational frequency shift

A direct consequence of the equivalence principle, which is a pillar of Einstein's General Relativity, is that a source of radiation in a gravitational potential U_s appears to an observer in a different gravitational potential U_o shifted in frequency by an amount $\Delta f/f = -\Delta U/c^2$ where $\Delta U = U_s - U_o$ is the gravitational potential difference between the source « s » and the observer « o » positions. Pound and Rebka made a direct determination of this effect in 1960 using the Mossbauer effect. The result confirmed the prediction of the theory to within +/-1%. The most precise measurement of this gravitational shift is presently the Gravitational Probe A experiment performed in 1978 by Vessot, Levine and colleagues [2].

The ACES red shift measurement will use a different technique. Instead of modulating the red shift by changing the altitude of satellite, ACES will utilise the high accuracy of the PHARAO clock (10^{-16}) and ground clocks (10^{-16} or better) to make an ***absolute*** measurement. Knowing precisely the orbital parameters of the space station (position and velocity), the frequency difference between the ground clocks and the PHARAO clock will be calculated and compared to theory. As the ISS orbit changes as a function of the time, the gravitational redshift will also be modulated but only by about 10% of its magnitude.

If both the ground and space clocks used in the frequency comparison possess an accuracy of 10^{-16} and if the link does not degrade clock performance, the Einstein effect can be determined with a relative uncertainty of $3\ 10^{-6}$. This represents a factor 25 improvement over the GPA experiment.

III.2. Search for a possible time variation of the fine structure constant

The fine structure constant $\alpha = e^2/4\pi\varepsilon_0\hbar c$ {equal to 1/137.0359895(61)} characterises the strength of the electromagnetic interaction in an atom or a molecule and is called the fine structure constant.

In 1937 Dirac suggested that it was interesting to check if these fundamental constants were indeed constant in time and a great deal of effort has been devoted to this goal with increasing precision. In General Relativity as in other metric theories of gravitation, a change in time of non-gravitational constants is forbidden. This is a consequence of the equivalence principle. However a number of modern theories predict the existence of new interactions which violates Einstein's equivalence principle. Damour and Polyakov for instance predict a time variation of the fine structure constant [5].

Among the numerous experiments designed to check the equivalence principle, methods utilising space (STEP, MICROSCOPE), and stable clocks have a long history. The high stability and accuracy of the ACES clocks and of the cold atom ground clocks make the search for a drift in α a very attractive proposition.

The principle involves the comparison of the frequencies given by clocks using different elements as a function of time. Any change of the frequency difference between two clocks might be attributed to a change of fundamental constant or to imperfections in long term behaviour of the clocks. Therefore to make a convincing test, it is mandatory to involve a large number of clocks and to make cross-correlation between the measurements. ACES will provide access to a large number of laboratories world-wide. This will involve clocks operating with many different atoms, e.g. cesium, rubidium, hydrogen, mercury ion, ytterbium ion, etc, etc. These frequency standards operate either in the microwave domain (caesium and rubidium fountains, H, Hg^+, Yb^+, Cd^+,...) or in the visible part of the spectrum.

In the case of an alkali atom with atomic number Z and having a hyperfine transition in the microwave domain, Prestage et al [6] calculated the effect of a possible drift of α upon the hyperfine energy as a function of Z. The calculation showed a very rapid variation of $(d\alpha/dt)/\alpha$ as a function of Z (more than quadratic). If one then makes the ratio between the hyperfine energies of two (or more) atoms having very different Z numbers, one finds the sensitivity of the test of the constancy of α. For instance, if $(d\alpha/dt)/\alpha = 1.\ 10^{-14}$/year, then a frequency drift of $1.4\ 10^{-14}$/year would occur between a cesium clock (Z=55) and a mercury ion clock (Z=80). For cesium and rubidium (Z=35) this figure is $0.45\ 10^{-14}$/year. The best experiments to date established an upper limit for $(d\alpha/dt)/\alpha < 2\text{–}3\ 10^{-14}$/year [6,13]. Since both the ACES cesium clock and ground rubidium clocks will have 10^{-16} accuracy, the frequency drift can be determined with a resolution as low as $\sqrt{2}.10^{-16}$ / year giving an improvement of a factor 100 / year. For a 3 year mission the gain is larger than 300. The Z dependence means that the signature of a drift of α, if found, will be unambiguous. Such a discovery would be a major breakthrough and have profound implications on our understanding of the laws of physics.

III.3. Test of special relativity

A number of alternative theories that allow for violations of special relativity have been developed (see [7] for a review). Such theories all postulate some "universal rest frame" Σ in which the basic postulates of special relativity are valid : in particular, the slow clock transport and Einstein synchronization ([12] pp. 38-40) procedures for distant clocks are equivalent. In special relativity this is also valid in any inertial frame S moving at constant velocity **v** in Σ but this is not the case in the alternative theories. This implies, for example, that for a light signal transmitted one-way between two distant points its speed, as measured by clocks that were synchronised using slow clock transport, is a constant in Σ (i.e. independent of the direction of signal transmission), but not in S.

For a certain type of experiments, those that measure one way signal transmissions, a simple test

theory based on a parameter $\delta c/c$ is often used. In this interpretation distant clocks are synchronised in S using slow clock transport. Then c is the round trip speed of light (independent of the chosen synchronization convention) and δc the deviation from c of the speed of light in S (measured by the transport synchronised clocks) for a signal propagating one-way along a particular direction. Then the experiments look for a variation of $\delta c/c$ as a function of the direction of signal transmission in S. In special relativity $\delta c/c = 0$ which, of course, reflects the fact that the two synchronization conventions are equivalent.

A number of experiments testing for a non zero value of $\delta c/c$ have been carried out either by direct measurements of the variation of one way transmission times of light signals between distant clocks or by indirect measurements searching for the variation of the first order Doppler shift. The former used the clocks and time links in the JPL deep space tracking network [8] and the GPS system [9], the latter the first order Doppler effect in Two Photon Absorption [10], the Mössbauer effect [11], and the frequency links of the GP-A experiment [1-2]. A violation of special relativity is, in this model, linked to a particular spatial direction (velocity $\vec{v}$ of S in Σ) and the experiments search for the modulation of the effect as the direction of signal transmission is changed. Consequently those experiments that rely on the rotation of the Earth for a change of direction are only sensitive to the component of $\delta c/c$ that lies in the equatorial plane.

The ACES experiment is expected to improve previous limits on $\delta c/c$ by about one order of magnitude. The experiment will compare the space clocks to the ground clocks continuously during the passage of ISS. The time transfer link will consist of laser and/or microwave signals that are exchanged in both directions between the clocks. All emission and reception times and frequencies are measured on the local space and ground clocks respectively. The difference of the measured reception and emission times provides the one-way travel time of the signal plus some unknown but constant offset Δ_s due to the fact that the clocks are not synchronized (by slow clock transport). Then the difference of the up and down travel times is sensitive to a non zero value of $\delta c/c$ along a preferred direction

$$T_{up} - T_{down} = \Delta_s + \Delta_m + 2\frac{\delta c}{c} T \cos\theta \qquad \text{Eq ()}$$

where T is half the return travel time, θ is the angle between the link and the preferred direction, and Δ_m are known small corrections due to path asymmetries, atmospheric delays, etc... Δ_s is unknown (desynchronization) but remains constant, so adjusting the cosine to the data over the passage allows the measurement of $\delta c/c$.

The sensitivity of the experiment is determined by the instabilities over one passage of both the clocks and T&F links phase. The value of T varies during the passage (min. $\approx$ 1.5 ms, max. $\approx$ 8 ms) With an overall time instability over one ISS pass as low as 1 ps, the expected sensitivity to $\delta c/c$ should be in the low 10^{-10} region which is an improvement by a factor 10 or more over previous measurements. Such a performance seems even more likely when considering that several systematic error sources (atmospheric delay, orbit accuracy, clock stability) that were likely sources of uncertainty for the GPS experiment [9] will be negligible for ACES because of the two way systems used (cancellations between the up and down links) and the high stability of the ACES clocks.

IV. Conclusion - Present status of ACES mission

Due to mass excess, some ACES instruments and pieces of equipment have be descoped. The new baseline proposed for ACES payload includes PHARAO, SHM, MWL and FCDP. Both the optical link T2L2, the Magnetic and Microvibration Measurement Device M3D and the DORIS receiver for the orbit determination have been removed.

Nevertheless almost all the science objectives of ACES are expected to be fulfilled with this new baseline assuming the ACES payload orbit will be determined at the required precision level by an external device.

This new baseline should be approved in April 2001 and phase C/D for ACES instruments and equipment should start before at the end of 2001.

REFERENCES

[1] R.F.C. Vessot and M.W. Levine, Journ.of General Relativity and Gravitation, 10, 181 (1979) .

[2] R.F.C. Vessot al., Phys. Rev. Lett. 45, 2081 (1980).

[3] L. Blanchet et al., ACES relativity meeting, Paris February 1999 and to be published

[4] N. Ashby, in Proc. of the 1998 IEEE Frequency Control Symposium, p. 320 (1998).

[5] T. Damour and A. Polyakov, Nucl. Phys. B, 423, 532 (1994)

[6] J. Prestage, R. Tjoelker and L. Maleki, Phys. Rev. Lett. 74, 3511 (1995)

[7] Will C.M., *Theory and Experiment in Gravitational Physics revised edition*, (Cambridge University Press, Cambridge) 1993.

[8] Krisher T.P. et al., Phys. Rev. D 42, 731 (1990).

[9] Wolf P., Petit G., Physical Review A 56, 4405 (1997).

[10] Riis E. et al., Phys. Rev. Lett. 60, 81 (1988).

[11] Turner K.C. and Hill H.A., Phys. Rev. 134, B252 (1964).

[12] Lorentz H.A., Einstein A., Minkowski H., Weyl H., *The Principle of Relativity*, (Dover, New York) 1923

[13] Sortais Y. et al., IEEE Trans. on UFFC 47, 1093 (2000)

GALILEOSAT SYSTEM TEST BED: A UNIQUE OPPORTUNITY TO TEST SYNCHRONISATION TECHNIQUES

Monica Gotta
Alenia Spazio S.p.A.
Via Saccomuro, 24 - 00131 Roma, Italy
Tel: +39 06 4151 4157, Fax: +39 06 4129 4035, m.gotta@roma.alespazio.it

Franco Gottifredi
Alenia Spazio S.p.A.
Via Saccomuro, 24 - 00131 Roma, Italy
Tel: +39 06 4151 2064, Fax: +39 06 4129 4035, f.gottifredi@roma.alespazio.it

Mauro Leonardi
Alenia Spazio S.p.A.
Via Saccomuro, 24 - 00131 Roma, Italy
Tel: +39 06 4151 2587, Fax: +39 06 4129 4035, m.leonardi@roma.alespazio.it

ABSTRACT

Galileo is a space-based navigation system under contract of European Union (EU) and European Space Agency (ESA), which would enable users to determine their three-dimensional position, velocity and time with a high degree of performance in terms of accuracy, availability, integrity and continuity.

The GalileoSat System Test Bed (GSTB) aims to investigate and to make early experimentation on those elements of the Galileo System which are considered critical. The GSTB is then a great added value to the final Galileo, in terms of design consolidation, key technology qualification and gained confidence and experience.

This paper presents the current baseline regarding the Test Bed approach towards validation of timing topics such as Galileo System Time realisation, Galileo System synchronisation, time transfer links performance, UTC (Universal Time Co-ordinated) steering and Galileo Timing Service Demonstration.

The critical aspects of the system related to timing issues are exploited during this program and the conclusions in terms of analyses and results will be used to review the relevant design of the GalileoSat System. In this way, the GSTB may be seen as a Verification Tool for Time Synchronisation aspects.

INTRODUCTION

The GalileoSat System Test Bed is an ESA program oriented to verify specific topics of the Galileo System using one GalileoSat-like Navigation payload which will be flown as piggy-back on a GLONASS-M SV starting from mid 2003 for 1 year operations. The Definition Phase (A/B) of the GSTB, in fact, has been concluded in February 2001 and the Development Phase (C/D) will start in the second half of the same year.

Such test-bed will adopt a reduced ground segment with respect to the overall Galileo System. Constituted by 12 world-wide Orbitography and Synchronisation Stations and 8 European Integrity Monitoring Stations, it will evaluate Orbit Determination (OD) algorithm, Time Synchronisation (TS) issues (see [1] for details about GalileoSat OD&TS), Navigation and Integrity functions, together with the qualification of some space hardware such as atomic clocks like Rubidium Atomic Frequency standard (RAFS) and Passive Hydrogen Maser (PHM).

In particular the performance of atomic clocks under qualification shall be evaluated together with a test of the clock switching mechanism in case of failure. Phase comparison data of the clocks shall be collected and stored on-board to be transmitted to ground through telemetry; the data shall than be post-processed and analysed with a suitable software in order to assess stability characteristics.

In order to accomplish the previous objectives it is necessary a detailed evaluation of the impairments caused by the same mentioned functions, due to the reduced Ground Segment and to the very exotic configuration, in which one GLONASS SV (on its orbit) transmits the GalileoSat signals.

In addition, since it is foreseen to use a reduced Space Segment constituted by only 1 Space Vehicle, signals from existing constellations (GPS and GLONASS) will also be used, in order to solve the orbits and perform the navigation solution. As described in [2], GSTB program consists of the following incremental scenarios:

1. *Navigation Payload Verification*, which objective is to validate the GalileoSat Hardware on-board (the performance of final

Galileo clocks together with the navigation signal generation will be tested);

2. *OD&TS Verification*, in which the OD&TS algorithm (see [1]) will be tested using, as inputs, pseudorange from the experimental payload together with GPS/GLONASS pseudorange, and calculated orbits will be compared with IGS/IGEX ones;
3. *Navigation Service Demonstration,* in which a verification of the UERE budget will be carried out, together with an end-to-end demonstration of the services to the user (navigation & timing);
4. *Integrity Service Demonstration,* in which an end-to-end demonstration of the Integrity Service will be performed.

In the frame of these complex verification procedures, timing aspects are twice involved. This paper is oriented to face with both of these two different timing aspects.

The former one refers to the synchronisation of the whole system. This is the fundamental condition in order to perform a navigation service (the accuracy of the positioning solution strictly depends on the synchronisation accuracy).

The latter refers to the Timing Service, which is offered to the users together with the Navigation Service, in order to deliver the system time (E-GST, Experimental Galileo System Time) and the official UTC time to the user.

With regard to the first aspect, since synchronisation of the system is a task of the OD&TS algorithm, its related issues will be experimented and tested in the OD&TS Scenario (as described in §1).

For what concern the second aspect, an "ad-hoc" experiment will be performed in the frame of the Navigation Service Demonstration in order to test the functionality of the user receiver to recover the system (and UTC) time from the generated navigation message. The experiment is described in details in §2.

In the frame of this early experimentation of time transfer related issues, ESA and industry welcome recommendations and proposal from the Timing community in order to take advantage of the expertise in this field and to establish a fruitful co-operation between the industry and the scientific world. Such recommendations (see [3]) have already been considered in outlining the GSTB experimentation as described in the following.

1. EVALUATION OF SYNCHRONISATION TECNIQUES ACCURACY EXPERIMENT

The following items need to be considered when talking about synchronisation in the Galileo context:

a) determination of the system clocks offset (space and ground) versus the common E-GST, which allows system synchronisation;

b) steering of E-GST towards UTC in order to allow the recovering of UTC from E-GST information together with the calculated offset of this last versus UTC).

Both the topics are output of the OD&TS batch algorithm running at the E-OSPF (Experimental Orbitography & Synchronisation Processing Facility) [1] and therefore will be tested in the frame of the OD&TS Verification Scenario shown in Figure 1.

This scenario will follow a stepwise approach (see [4] for more details):

step 0) *performance assessment by simulation*

step 1) *processing of GPS/GLONASS data*

step 2) *processing of E-GPL (Experimental Galileo Payload) +GLONASS data*

step 3) *update of performance assessment by simulation*

step 4) *real-time implementation (demonstration)*

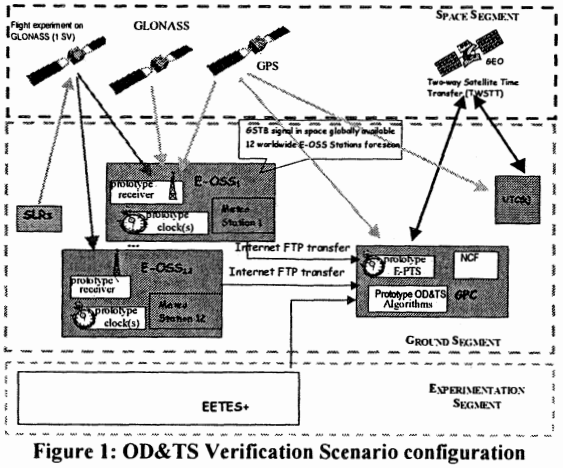

Figure 1: OD&TS Verification Scenario configuration

For what concern item *a)*, the GalileoSat baseline [1] consists in a Common View (CV) synchronisation approach in which one-way pseudorange from all satellites are collected at Orbitography and Synchronisation Stations (OSS). These data are processed in a batch algorithm running at the E-OSPF, which outputs are orbit parameters and clock corrections. The application of the described stepwise approach to this aspect (item *a*) leads to the following:

step 0) *review of previous work and of GalileoSat baseline, identification of algorithm major characteristics and adaptation to GSTB context*

step 1&2) *assess OD&TS algorithm with GPS/GLONASS/E-GPL data and GSTB E-OSS network:*

- preliminary characterisation of station measurement (noise, measurement

quality)
- measurement campaign (E-OSS), using GPS/GLONASS/E-GPL signal
- data processing at E-OSPF and analysis of results (estimation of OD&TS performance, analysis of errors, comparison with other products as IGS/IGEX)

step 3) *update GalileoSat OD&TS performance and upgrade of models used in step 0 using the steps 1 and 2 results*

step 4) *implement OD&TS end-to-end demonstration:*
- implement real-time links between E-OSS and E-NCF (Experimental Navigation Control Facility)
- measurement campaign (E-OSS) with GLONASS and E-GPL signal
- data processing at E-OSPF
- output of ephemeris/clock correction/raw data to E-NCF
- monitoring of data transmission of ephemeris/clock correction to experimental receiver via GSM

For what concern topic *b)*, steering of E-GST towards UTC(k) will be performed through either CV or TWSTFT approach as recommended in [3]. In this context the time transfer accuracy will be tested in order to investigate the limits achievable in performance with state of art techniques.

In order to perform steering through CV inside OD&TS algorithm processing, two E-OSSs will be co-located inside the E-PTS (where E-GST is calculated) and the UTC(k) laboratory, in order to receive signals from satellites and send the measured pseudorange to the E-OSPF where the steering software runs as well.

In the TWSTFT approach ([5]-[6]), a traditional two-way link will be established between the E-PTS and the UTC(k) laboratory in order to measure the offset between the two time scales.

The application of the described stepwise approach to this second time aspect (item *b*) leads to the following:

step 1.a) assess steering performance of E-GST by CV method (GPS):
- measurement campaign (E-PTS), using GPS signal (performed according to CV standard /CGGTTS schedule)
- collection of GPS measurements performed at UTC(k) sites (CGGTTS schedule)
- data processing at E-OSPF and analysis of performance of E-GST steering

step 1.b) assess steering performance of E-GST by Two-Way method:
- measurement campaign using Two-Way signal between E-PTS and UTC(k)
- data processing at E-OSPF and analysis of performance of E-GST steering

step 3) *update performance of E-GST synchronisation to UTC(k):*
- analyse results from steps 1.a), 1.b)
- derive error budgets for both methods CV and Two-Way and estimate synchronisation performances

2. TIMING SERVICE DEMONSTRATION EXPERIMENT

Time transfer of Galileo System Time is a service, which can be demonstrated (as described in [7]) with only one Galileo SV, supposed that the user position as well as the satellite position is known. With this experiment, the time scale deduced from pseudorange measurements including corrections is compared with the true E-GST.

The time accuracy investigation experiment has to be performed at E-NCF (where is located the E-PTS, Experimental-Precision Timing Station, which collects AFS contributing to E-GST), for the comparison of the user (test) receiver reference time with E-GST.

The time accuracy will be evaluated for a stationary test receiver with known position at E-NCF, receiving ranging signals from only one E-GPL SV. The measured pseudorange (PR) can be divided in the following contributions:

$$PR_{measured} = (R_{true} + \Delta R_{propagation}) + \Delta R_{orbit} + \Delta R_{clock's} + \Delta R_{noise} + \Delta R_{multipath}$$

where R_{true} is the true distance between the antenna phase centres of E-GPL SV and receiver, and all other terms are statistical and systematic error contributions due to the indicated effects, respectively. In principle, after correcting the measured pseudorange for propagation delays and subtracting the true range, results in the receiver time offset $\Delta t_{RX\text{-}GST}$ relative to E-GST. By this, the receiver time is related to E-GST.

To investigate the accuracy of this kind of time transfer, the receiver time has to be compared also directly to E-GST (to get $\Delta t'_{RX\text{-}GST}$), transferred via direct link from E-PTS. This time offset $\Delta t'_{RX\text{-}GST}$ then acts as a reference for time service accuracy investigation. This accuracy is then described through the statistic of the parameter $\Delta t_{accuracy} = \Delta t_{RX\text{-}GST} - \Delta t'_{RX\text{-}GST}$. Of course, $\Delta t_{accuracy}$ is dependent on the accuracies of the used corrections.

With respect to SV position errors and receiver

time errors, a two step approach for validation of timing service is proposed for each signal option.

First, for maximum accuracy, all error contributions to the measured pseudoranges should be minimised or corrected to an optimum degree. This implies the following methods:
Propagation delays $\Delta R_{propagation}$ can be obtained with the following methods:

- *Ionospheric delay: compensation by two-frequency evaluation.*
- *Tropospheric delay: compensation with existing models, taking into account measured meteorological quantities of temperature, humidity and pressure. For improved tropospheric correction, the humidity profile, measured with a scanning radiometer could be considered, additionally. Tropospheric corrections by use of redundant GPS signals also would be possible.*

By using a directive antenna together with an environment of low masking angle for the test receiver, multipath can be avoided and the contributions ΔR_{noise} will get negligible due to maximum C/N_0. To minimise orbit errors ΔR_{orbit}, the test receiver should get SV positions with optimum precision (e.g. from SLR), perhaps even offline. Finally, a high precision atomic frequency standard as reference for the test receiver time gives the lowest error contribution due to the receiver clock.

Secondly, for standard accuracy, the test receiver should use nominal Galileo methods for orbit determination (usage of ephemeris data), standard propagation error corrections and a standard omni-directional receiver antenna. Additionally, the test receiver will be referenced to a commercial GPS locked reference oscillator. The time service accuracy will be evaluated for a stationary user with different elevations, from 90° down to 10°.

A functional diagram of the GSTB test receiver system adapted to the time accuracy experiment is shown in Figure 2.

Alternatively to Figure 2, also a system with two GSTB test receivers according to Figure 3 could be reasonable to evaluate both steps (maximum and standard accuracy) simultaneously.

As reported in both these figures, the reference oscillators (AFS and standard oscillator) should be compared to E-GST system time as a reference.

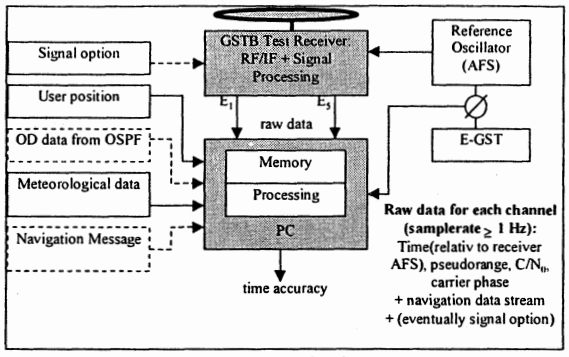

Figure 2: Functional diagram of GSTB test receiver system for time accuracy demonstration

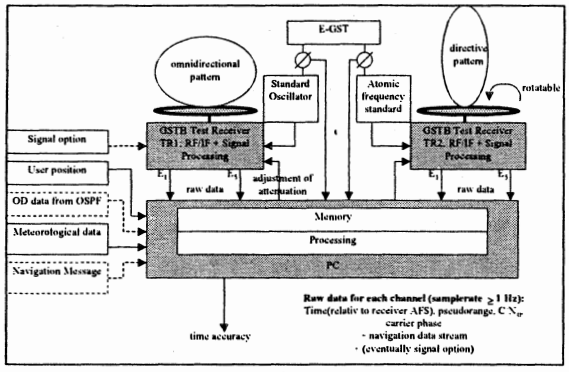

Figure 3: Alternative functional diagram of GSTB test receiver system for time accuracy demonstration

CONCLUSIONS

This paper has presented the current baseline of the Test Bed program as defined in the Phase A/B of GSTB, focusing on Verification of time transfer techniques and demonstration of Timing Service. A stepwise approach has been described and the main topics to be verified have been highlighted.

The GalileoSat System Test Bed represents a unique opportunity to gain confidence in establishing and maintaining an European time scale and in improving and exercising the newest time transfer techniques. In this context a fruitful co-operation of industry with the scientific community could be a great added value in term of expertise and know-how.

ACKNOWLEDGEMENTS

The authors are thankful to the Working Group on Galileo Time Interface that provides a valuable support in GSTB definition and to the colleagues of Alcatel Space Industries and Astrium for their work on experimentation issues in the frame of GSTB.

REFERENCES

[1] J. Hahn, G. Graglia, G. Salgado, P. Tavella, G. Busca, "Timekeeping for GalileoSat", Proceedings of ION-GPS 2000

[2] M. Gotta, GSTB Mission Requirements Document, Issue 3, RQS/GAL/0146/ALS, 18/12/2000

[3] J. Laverty, P. Tavella, G. Petit, A. Bauch, P. Uhrich, J. Clarke, G. de Jong, W. Schaefer, G. Dudle , J. Johannsen , J. Davis, M. Brunet, GalileoSat - Report and Recommendations of the Working Group on the Galileo Time Interface, GWGGTI_01, Issue 2, 21/02/2001

[4] Ch. Bourga, GalileoSat System Test Bed - System Experimentation, Issue 2, GAL-ASPI-TN-310, 11/12/2000

[5] D. Kirchner, "Two-Way Time Transfer via Communication Satellites", Proc. IEEE 79, vol.7, pp.983

[6] W. Schaefer et al., "New Trends in Two-Way Time and Frequency Transfer via Satellite", Proc. PTTI 99, vol.31, pp.505

[7] M. Söllner, GSTB -Application Experimentation, Issue Draft, GSTB-ASDM-TN-6300-0001, 11/12/2000

UTC AND GALILEO TIME SERVICES: A REPORT FROM THE GALILEOSAT WORKING GROUP ON THE GALILEO TIME INTERFACE

John Laverty[1], Patrizia Tavella[2] and Jörg Hahn[3] on behalf of the Working Group

(1) National Physical Laboratory, Queens Road, Teddington, Middlesex, TW11 0LW, UK
(2) Istituto Elettrotecnico Nazionale G. Ferraris, Strada delle Cacce 91, 10135 Torino, Italy
(3) European Space Agency, Galileo Project Office, European Space Agency - ESTEC, Keplerlaan 1, Postbus 299, 2200 AG Noordwijk, The Netherlands

ABSTRACT

This paper describes the work of a group of 13 European timing specialists who reviewed the baseline design for Galileo's timing system between July 2000 and February 2001.

1. INTRODUCTION

1.1 Background

Galileo is a Global Satellite Navigation System to be designed, built and operated by European industry and institutions. The Galileo Programme completed its Definition Phase during 2000 and early 2001, during which a number of studies were undertaken to investigate user requirements and design issues in detail. One of the main studies, organised by the European Space Agency (ESA), was the GalileoSat Programme for the design, development and in-orbit validation of the Galileo space and related ground segment. With the GalileoSat Definition Phase study underway, ESA invited the leading European organisations involved in time-keeping to participate in a new Working Group to review particular timing aspects of the GalileoSat design. Nearly fifty representatives attended a meeting at ESTEC on 29 June 2000, with a core of thirteen representatives agreeing to actively participate in the new GalileoSat Working Group on the Galileo Time Interface (abbreviated to "WG" for short).

1.2 The Working Group

The baseline for the timing aspects of GalileoSat design had already been fixed at the time the WG was formed on 29 June 2000 [Ref. 1]. In this context, the objectives set for the WG were to review the baseline definition, and to make recommendations to the GalileoSat Programme, through ESA, on the timing aspects of the system. The WG members are listed in the Box below. Most of the work was carried out by correspondence, with some additional meetings at ESTEC to allow participants to debate the issues more freely. Those meetings enabled ESA and the relevant experts from the Galileo Industries to provide news and comments from the GalileoSat developments. The WG presented its initial observations and recommendations to ESA on 14 September 2000. The Working Group activities were then extended to the end of February 2001, and this paper presents a summary of the WG's findings [Ref.2].

Members of the Working Group

John Laverty (NPL/Chair), Patrizia Tavella (IEN/Co-Chair), Jörg Hahn (ESA), Jon Clarke (NPL), John Davis (NPL), Gregor Dudle (METAS), Jan Johannsen (SP), Pierre Uhrich (BNM-LPTF), Gerard Petit (BIPM), Andreas Bauch (PTB), Gerrit de Jong (VSL), Wolfgang Schäfer (Timetech) and Michel Brunet (CNES).

1.3 GalileoSat Baseline Design

The brief description of the GalileoSat Baseline Design given here is based on information provided to the WG during the GalileoSat Definition Phase. However, it should be noted that the GalileoSat design was evolving during the lifetime of this WG, and hence this description is intended as a guide to the main timing elements anticipated in the system. It is not a definitive statement on GalileoSat's architecture.

The Orbit Determination and Time Synchronisation (OD&TS) architecture is expected to consist of:

- 30 x Galileo Space Vehicles, each with 2 passive hydrogen masers (PHM) and 2 rubidium atomic frequency standards (RAFS)
- 12 Orbitography and Synchronisation Stations (OSS) (+3 for redundancy, 1 at each PTS, 1 at UTC(k))
- 2 Orbitography and Synchronisation Processing Facilities (OSPF)
- 2 Precise Timing Stations (PTS)
- UTC(k) interface

The Precise Timing Stations (PTS) each include two active hydrogen masers and twelve high-performance caesium clocks. The Orbitography and Synchronisation Stations (OSS) are based on rubidium clocks, measure one-way pseudo-ranges and transmit that data to the Orbitography and Synchronisation Processing Facility (OSPF). An OSS is co-located in each PTS and in at least one UTC(k) laboratory. The Orbitography and Synchronisation Processing Facilities collect pseudo-range measurements from the OSS and calculate orbits and synchronisation parameters. The OSPF calculates Galileo System Time as part of the OD&TS process. In addition to the Baseline Design, it is clear that many of these ideas will be tested as part of a Galileo System Test Bed (GSTB) during the next Development Phase.

2. BENCHMARKS FOR GALILEO TIMING SERVICES

2.1 The Benchmarks Set by GPS

GPS occupies a dominant position in the timing market because of its global coverage, high accuracy and the relatively low cost and availability of GPS timing receivers. If Galileo is to succeed in this environment, it will have to complement GPS both in terms of technical performance and in terms of price. The most likely route to market success is probably through joint GPS/Galileo timing products in applications that value redundancy such as telecommunications networks, power generation/distribution, and digital broadcasting. The dependence on the world's economy on the reliable delivery of these services is enormous. Such receivers are then likely to be taken up in other applications such as frequency calibration and time-tagging.

The most demanding commercial applications at present are probably Primary Reference Clocks (PRC) for telecommunications networks (10^{-11} normalised frequency offset relative to UTC [Ref.3]) and time-stamping for fault location in power networks (1 microsecond accuracy required to locate faults to the nearest 300m [Ref.4]). While the accuracy requirements for time-tagging are, in general, not severe (1 ms for network time protocol servers in computer networks to about 1 s for a wide range of every day activities) the demands for frequency calibration do approach 10^{-13}.

The argument for joint GPS/Galileo timing products assumes that:

- Galileo will operate independently of GPS
- Galileo will be inter-operable with GPS
- Galileo's timing performance will be comparable with GPS

Independence is required for the redundancy. Inter-operability is needed to reduce costs in the user segment, as is the timing performance.

In considering the relationship between Galileo and GPS is vital to recognise that GPS will improve during Galileo's lifetime [Ref.5]. If Galileo aims at parity with GPS today, it will almost certainly be behind GPS when it reaches its operational state. The removal of Selective Availability from GPS at the beginning of May 2000 was just a first step in the modernisation process. Further improvements in GPS are anticipated such as new down-link frequencies for improved ionosphere delay corrections and cycle ambiguity resolution.

2.2 Galileo: Some Target Specifications

In order to gain acceptance, Galileo needs to provide the key outputs needed by timing users at the right performance levels, and to help those users by specify its performance in a clear and user-friendly format. In terms of *what* to provide, Galileo should provide the user with both the civil time standard Coordinated Universal Time (UTC) and International Atomic Time (TAI) for those applications where a continuous time scale is required (i.e. avoiding leap seconds in UTC).

The Working Group identified the parameters listed in Table 1 as targets for the Galileo's timing services. An initial target accuracy of 33 ns (2σ) in the GST – TAI time offset is recommended in order to approach the GPS performance (see next section). The figure of 50 ns for the offset from of GST from TAI is based partly on the CCDS recommendations for UTC(k) performance [Ref.6] and partly on what is observed for GPS: in other words, it is a guide for Galileo as to the performance of comparable time systems. **Note that table 1 identifies target specifications that are appropriate for Galileo today, but that further improvement is expected from GPS in the next decade.** Galileo should identify a way of updating its specifications in the light of actual system performance. We would expect the performance of Galileo to improve with operating experience, and it would be easier to "sell" Galileo solutions if the published specifications are as stringent as can be safely achieved.

GST-TAI	Specification
Uncertainty, Time Offset	33 ns (2σ)
Uncertainty, Normalised Frequency Offset *(one day averaging time)*	5.5×10^{-14} (2σ)
Limits, Time Offset *(95% of time over any yearly time interval)*	50 ns

TABLE 1
The Working Group's recommended target specifications for the Galileo timing services.

Source	Uncertainty budgets: time transfer against UTC over 24 hours using stand-alone GPS, 2σ (ns)		
	GPS today with receiver calibration limitations.	GPS today: improved receiver calibrations	Estimate for GPS in 5-10 years
Signal-in-space (SIS)			
Ephemeris	8	8	4
Ionosphere	16	16	2
Troposphere	2	2	2
Multipath, random	6	6	2
Satellite clock	7	7	7
Broadcast UTC(USNO) offset	2	2	2
Stability of UTC(USNO)	14	14	14
Total for SIS	25	25	17
User segment			
Antenna co-ordinates	4	4	2
Receiver noise	2	2	2
Receiver calibration	60	12	6
Total for SIS & user segment	65	28	18

TABLE 2
Uncertainty budgets for stand-alone GPS time transfer [see Ref.2 for more explanation].

In addition, the WG believes that the specifications for Galileo should be written in a user friendly format, using the metrics adopted in the major time markets, and over averaging times that reflect the interests of the main user groups. In practice, this would mean the main metrological parameters (ADEV, MDEV, TDEV, etc.) and those for telecommunications (TIE, MTIE, etc.), as well as time and frequency uncertainties. Standard statistical reference should be used in specifying uncertainties (e.g. 95% confidence intervals). The specifications should be explicit about the operating modes under which these specifications can be met (e.g. elevation angles, etc.) and choose conditions that are meaningful to the main user groups. Given that the averaging time is a key parameter, it would be extremely helpful to manufacturers and users if Galileo could quantify the stability of the timing signals at averaging times from 1 s to 1 month, at increasing decade intervals. Note that these more detailed specifications would have to be developed as part of further studies based on user requirements.

2.3 GPS Example: Stand-alone Use

Uncertainty budgets for the timing output of a stand-alone GPS receiver against UTC, with 24 hour averaging are shown in Table 2. This example was chosen because inexpensive receivers (costing ~€300) measuring only the C/A-code on a single frequency with a patch antenna are widely used. The best accuracy is achieved with the receiver using fixed co-ordinates and only calculating the time, as opposed to doing a combined time and position solution at each epoch. The table gives results for three scenarios:

(1) Estimates based on the current GPS constellation and with current knowledge of the receiver calibration uncertainties;
(2) Estimates based on the current GPS constellation following improvements in receiver calibration procedures;
(3) Estimates of the uncertainty that may be obtained in 5-10 years following GPS modernisation.

The improvements in receiver calibrations assumes that better data will be available for delay variations in UTC time transfer links, while the most significant of many improvements promised by the GPS modernisation process will be dual frequencies for civilian use enabling more accurate ionosphere corrections.

3. THE GST-UTC INTERFACE

3.1 Generation of Galileo System Time

The WG's view of Galileo System Time (GST) and the Galileo - UTC interface takes account of the need for the Galileo system operators to develop their knowledge and skills in running a state-of-the-art time scale, and the mutual benefit of sharing clocks between the two time scales. Also it recognises the potential for improving the stability of the Galileo time scale by using measurements of the most stable clocks from UTC(k) laboratories including, if appropriate, primary frequency standards and cold atom clocks (anticipating similar developments underway at USNO which would benefit GPS). The WG see the GST generation happening in three stages, as illustrated in figure 1.

(1) A free-running time scale, GSTR, is generated from the PTS clocks and GST is generated from GSTR by applying a rate correction. A physical realization of GST called GSTH (hardware) is provided at one PTS, with a second realization at the other PTS which acts as a hot spare;

(2) The rate difference between GST and GSTR is updated at regular intervals (e.g. daily) so that GST is steered to a *prediction* of TAI (denoted here "TAIp") in the medium-term. A maximum correction step not to degrade GSTR stability has to be fixed;

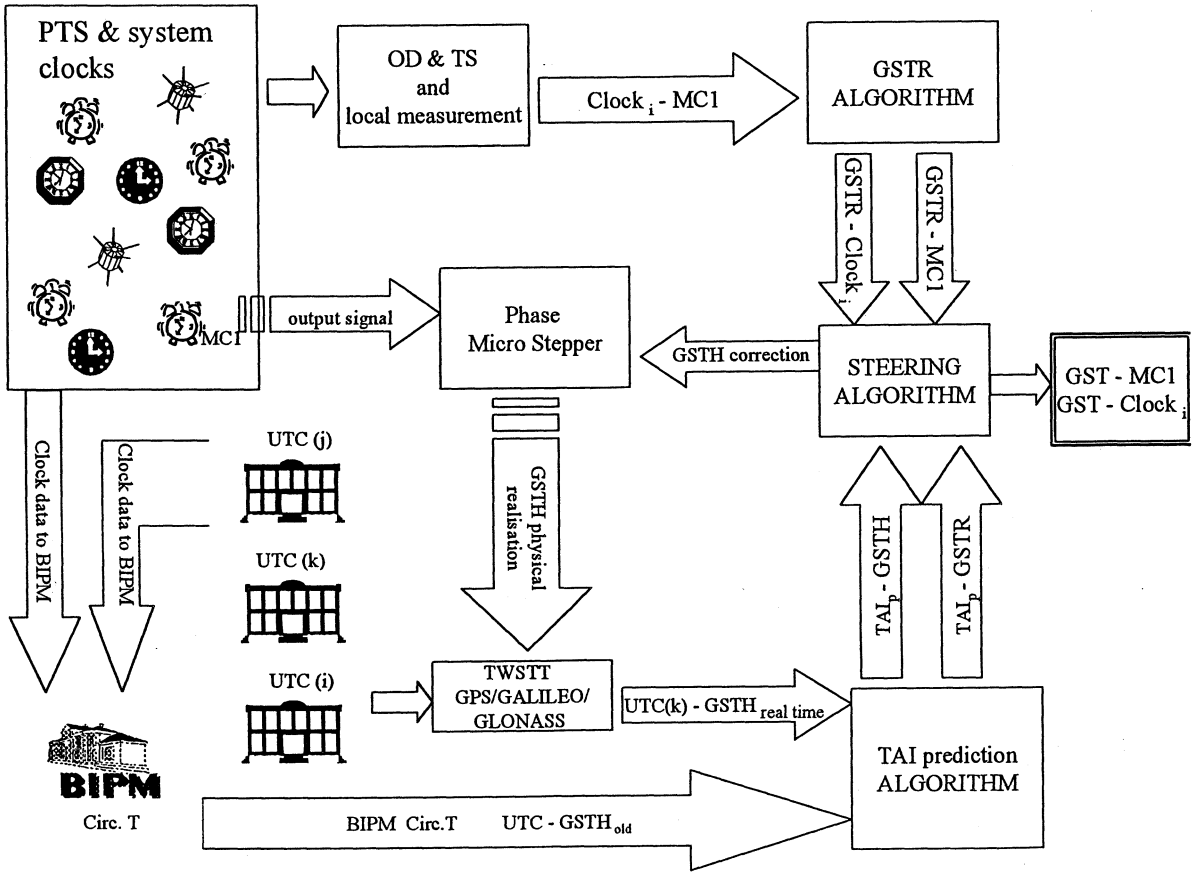

(3) Through TAIp, GST is designed to track TAI in the long-term (month).

We emphasise the need for a physical reference point providing the realization of GST. This is required for two main purposes: validation of the equipment calibration through delay measurements with respect to any other system; and determination of the differences GST-TAI through UTC(k) and GST-GPS time, based on measurements at the PTS.

One dedicated atomic clock [MC1] will be the master clock in PTS#1 and its output signal (standard frequency and 1 PPS) will be shifted by a phase micro stepper PMS to be a realization of GST, here named GSTH. The group of clocks operated in the PTS#1 are compared to one physical output (MC1 as in the example shown in Figure 1) and these measurements are processed in an algorithm to generate GSTR [Here an up-date interval has to be defined, e.g. one hour or it may be the same of the OD&TS update rate]. According to two independent inputs, the results of GSTR-MC1 and that on GSTR-TAIp, the relation between MC1 and PMS output (GSTH) is updated. For security, a redundant master clock and PMS are envisaged.

A similar strategy is followed for the PTS#2. Here the redundantly generated time scale GSTX serves as the reference for the local clocks as well as for comparison with GST. The WG identify TWSTFT as a strong candidate for linking PTS#1 to PTS#2, as the difference between the two physically separated sources of the operational time should be known in real time with an accuracy and a precision of 1 ns. In contrast, every one-way time transfer method would need longer averaging times, while every geodetic method would need at least several hours of data for processing. However, note that the PTS#1 to PTS#2 link would have to be operated nearly continuously to be consistent with the update rate of GSTR, which has cost implications for a TWSTFT link.

If such a close link between the two PTS, operating with the update rate of GSTR, comes to existence, one can treat the clocks in both PTS as a common ensemble, and one can envisage an algorithm of combining the clocks to yield an optimum GST (the latest information from the Galileo developers indicates that GST will be calculated using all the clocks from both PTS sites). The PMS in PTS#2 is to be adjusted so that GSTH and GSTX agree with each other. In due course, it could also be possible to add more clocks, and hence stability, for the GSTR ensemble if Galileo could incorporate clocks from some of the national time laboratories, provided that links operating with the required accuracy and continuity are available.

3.2 Linking and steering GST to TAI/UTC

In order to fulfil the goal of steering GST to TAI and, by that means, to broadcast GST-UTC to the required uncertainty, GST should be steered in the medium term (e.g. daily) to TAIp, a prediction of TAI. To be able to make such a prediction, GST would need an explicit link to one or more UTC(k)s by an appropriate and redundant link (GPS/Galileo

FIGURE 1

Schematic diagram of showing the proposed GST –UTC interface

common-view or TWSTFT link). In fact any UTC(k) is a real time prediction of UTC and therefore also of TAI (apart from the integer number of seconds difference between UTC and TAI). However, at this time, the uncertainty of the UTC prediction from each UTC(k) is not precisely specified in general. The advantage of developing TAIp is that it would be dedicated to predicting TAI as accurately as possible in real-time. The exact mechanism for making the TAIp prediction depends on the relative stability and accuracy of the GST and UTC(k) time scales, the time transfer links used to compare those time scales, the need for redundant UTC links to aid reliability, and the actual accuracy target for |GST-TAI|. In the present situation, the WG considered three broad scenarios for the Galileo-UTC interface:

(i) Galileo self-sufficient
Each of Galileo's PTSs has the necessary clocks, equipment and expertise to manage the GST steering and UTC dissemination alone;

(ii) Galileo dependent on UTC(k)
UTC(k) laboratories provide the GST steering recommendations on the basis of GSTH-UTC(k) time transfer links;

(iii) A Mixed Solution
A solution combining (i) and (ii), in which Galileo PTS independently maintains clocks, generates GST and manage TAI steering but a strict collaboration with UTC(k) labs is established.

The WG prefers option (iii) because it allows skills and clocks to be shared by Galileo and the European UTC(k) for mutual benefit, and enables Galileo to move up its learning curve more quickly. All three options involve

- TWSTFT and/or Galileo common-view, Galileo carrier-phase and GalileoSat time transfer equipment to link the PTS to UTC through UTC(k);
- PTS consisting of a number of clocks, the exact number depending on the accuracy target (see table 1 for the current recommendations);
- A time scale algorithm generating GSTR;
- A procedure to compute TAIp, a real-time prediction of TAI.

The specific advantages of option (iii) are

- The total number of clocks is higher than the number of clocks available in the PTS itself which can help improve the stability and accuracy of GST;
- Existing laboratories can provide UTC(k) in real time and therefore can provide the means for evaluating TAIp, even if the necessary GST steering is calculated at the PTS itself;
- Redundancy in the TAIp provision;
- Caesium fountain frequency standards developed in UTC(k) laboratories could be introduced into TAIp computation;
- A wider pool of expertise from UTC(k) laboratories would be available to Galileo, in particular concerning the calibration of the time transfer equipment.

Contracts would be needed to standardise outputs and service agreements, in addition to the resources needed to develop these systems.

Note that the "redundancy" principle should apply to the number of UTC(k) comparisons, the number of time transfer methods on individual UTC(k)-UTC(j) or UTC(k)-PTS links and the number of clocks at a given UTC(k). Ideally, triple redundancy is needed to isolate performance deficiencies as quickly and unambiguously as possible. Fortunately, Galileo can gain from the investments already made by the UTC(k) laboratories where a high level of redundancy already exists in many cases.

3.3 Linking GST to GPS system time

In long term (monthly) TAIp and hence GST would track TAI and UTC as calculated by the BIPM. Because UTC(USNO) is steered to UTC (i.e. TAI), and GPS time is steered relative to UTC(USNO), GPS time also tracks TAI in the long term so that both GST and GPS time will maintain close agreement. However, this would only be realized to the combined level of uncertainty to which both time scales are expected to match TAI/UTC, i.e. of order several tens of ns. We recommend that, in addition, Galileo directly monitors the difference GST-GPS time by using GPS receivers in the Galileo ground segment, at the physical realization of GST, in order to estimate, predict and broadcast this difference with a better accuracy (some nanoseconds) than GST – UTC. Calibration of the receivers is pre-requisite for this process. The reason for recommending this approach is for Galileo to be interoperable with GPS in timing applications. It is possible that such data could be provided to Galileo by an independent service provider, rather than being measured directly in the Galileo ground-segment.

3.4 Galileo contributions to UTC

The WG highlights that the PTS could contribute directly to TAI and UTC through the BIPM, and that GSTH becomes a UTC(k) in its own right (with the addition of the necessary number of leap seconds), here denoted UTC(PTS). The advantage of having a UTC(PTS) is the demonstration of GST traceability to UTC. This could be a Galileo high quality service for those users that ask for traceability to international standards. The realisation of UTC by BIPM would benefit from having more high-stability clocks, while Galileo would at the same time have more control over a key parameter needed for its timing services. In principle this is not a difficult task, as detailed below, but one that requires careful planning to avoid making unnecessary mistakes.

As an aside, it is worth noting that since GST and other satellite navigation systems' time scales are steered on TAI, the long term stability of TAI is a guarantee of long term stability of the GNSS time scale also. Therefore it would always be beneficial for GalileoSat to make its PTS clocks available to the BIPM for the computation of TAI. The marginal cost of collecting and forwarding the relevant data to BIPM would not be significant in terms of the long-term benefits of being able to access a more stable TAI.

The BIPM would report UTC-UTC(PTS) in the same way as for the other UTC(k)s, currently at five-day intervals in the monthly Circular T. When a Galileo signal-in-space (SIS) is

available, the BIPM would report UTC-GST in a similar way as is done for GPS time and GLONASS time, currently at one-day intervals in the monthly Circular T.

4. CONCLUSIONS

The WG has been able to take a brief look at the GalileoSat Baseline Design and to make comments and top-level recommendations on the Galileo timing systems. Some of the key recommendations are that:

- Galileo should be designed to be competitive with GPS, both now and in the future;
- Galileo should specify its performance in an accurate and user friendly manner;
- Galileo should predict and broadcast the difference TAI-GST in real time along with TAI-UTC (i.e. leap seconds), and the difference GST-GPS time;
- Galileo's PTS should become UTC(k) laboratories and its clocks should be made available to the BIPM for the computation of TAI and UTC;
- In the frame of Galileo System Test Bed (GSTB), the Galileo-UTC Time Interface should be formed from a network of at least three UTC(k) laboratories and the two PTS stations to test the Galileo timing infrastructure;
- Also, the WG strongly recommends the Two-Way Time Transfer Method as an independent means of validating Galileo's time transfer performance in the GSTB.

Looking forward, there is much detailed design work to be completed. However, there is also a need for a more general interface between the global time community and Galileo, one that is open to all timing users. We hope that the mechanisms for such an interface will be established in the future.

5. ACKNOWLEDGEMENTS

This paper reflects the contributions of all its members: Jon Clarke (NPL), John Davis (NPL), Gregor Dudle (METAS), Jan Johannsen (SP), Pierre Uhrich (BNM-LPTF), Gerard Petit (BIPM), Andreas Bauch (PTB), Gerrit de Jong (VSL), Wolfgang Schäfer (Timetech), Michel Brunet (CNES) as well as the authors. In addition, the open dialogue with colleagues both from Industry (Alenia Spazio, Astrium GmbH, Astrium Ltd., and Alcatel Industries) and individuals in the Galileo Project Office at ESA-ESTEC (Javier Benedicto, , Manfred Lugert, Rafael Lucas, Marco Falcone) helped enormously.

6. REFERENCES

[1] "*Note on System Time and Ephemeris Determination*" ESA reference TNO/GAL/28/ASP, 28 May 2000.
[2] *"Report and Recommendations of the GalileoSat Working Group on the Galileo Time Interface"*, March 2001.
[3] ITU-T Recommendation G.811
[4] ITU Handbook on the *'Selection and Use of Precise Frequency and Time Systems'*, 1997.
[5] Sandhoo, Turner and Shaw, *'Modernization of the Global Positioning System'*, Proc. IoN GPS-2000.
[6] CCDS Recommendation S5 (1993).

THE ARCHITECTURE AND EXPECTED PERFORMANCE OF THE GALILEO SATELLITE TIMING SUBSYSTEM

Thomas Vogler, Stefan Berberich, Michael Scheuble

EADS, Astrium GmbH, 88039 Friedrichshafen, Germany

1. ABSTRACT

This paper presents one of the core elements of the future Galileo satellite navigation system, the on-board Timing Subsystem (TSS).

The basic function of the TSS is to provide a highly stable on-board time reference which is used for coherent navigation signal synthesis. The navigation system measurement accuracy for position and time depends on the precision of the TSS.

2. OVERVIEW

The schematic of the TSS is shown in Figure 3.

It comprises a clock ensemble of four Atomic Frequency Standards (AFS), combining Space Rubidium Atomic Frequency Standards (S-RAFS) and Space Passive H-Masers (S-PHM), which is operated in a hot redundant configuration.

Apart from the AFS ensemble, the TSS consists of a Clock Monitoring and Control Unit (CMCU) which performs clock selection and control, the frequency conversion from the AFS output frequency of about 10 MHz to 10.23 MHz and the supply of power to the S-RAFS.

Initially, one S-PHM and one S-RAFS are switched on. A 10.23 MHz signal is generated out of both AFS output signals, but only the primary AFS signal is directed to the CMCU output after conversion. This primary AFS signal normally comes from a S-PHM, but can be, if both S-PHM have failed, a S-RAFS as well.

A phase meter compares the primary and the secondary 10.23 MHz signals. The phase meter output is made available to the Galileo ground segment via telemetry which ensures that clock model parameters can be calculated continuously for the secondary AFS as well. Thus periods of non-availability of Galileo satellites are minimised increasing the integrity of the system.

3. S-RAFS

The S-RAFS to be foreseen for Galileo is manufactured by TEMEX Time Neuchâtel. It is shown in Figure 1.

It is a box of 113.5 mm height, 124 mm width and 117.5 mm depth. Its mass including a thermally controlled base plate is less than 2200 gr. Total power consumption is maximum 35 W during nominal operation and never exceeds 55 W, even within the extended qualification temperature range (operational temperature range ± 10°C) and during switch-on.

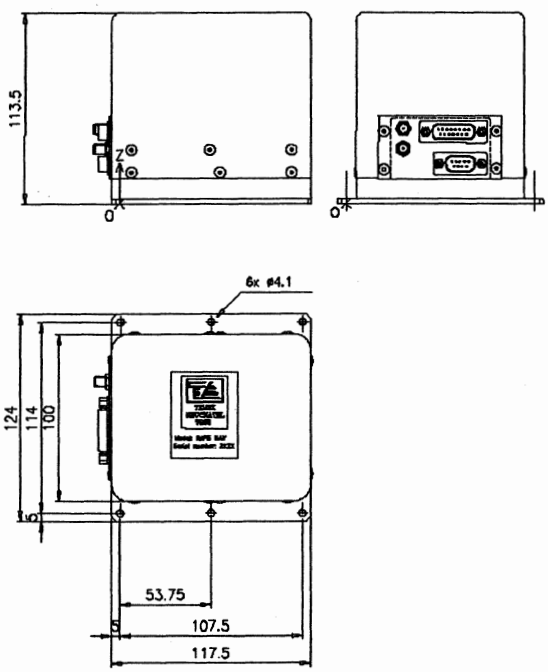

Figure 1: The S-RAFS interfaces

The atomic frequency of Rubidium (Rb) is converted within the S-RAFS by a PLL circuit to result in a 10 MHz output frequency which is provided through decoupled output ports.

Telemetry signals are available for PLL lock indication (bilevel), Rb signal (analogous), Rb light (analogous) and the base plate temperature (analogous). Telemetry is provided directly to the on-board data handling system (OBDH).

The short term stability and the phase noise characteristics of the S-RAFS are shown in Figure 4 and Figure 5.

The S-RAFS is completely developed. A lifetime verification test of 5 models is running since June 2000. The qualification programme will be completed by end of 2001.

4. S-PHM

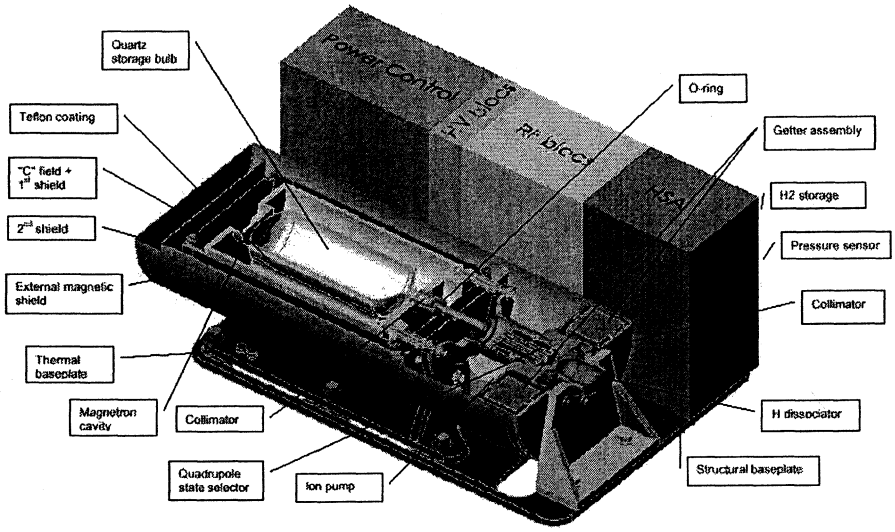

Figure 2: The S-PHM overall design

The S-PHM is developed at the Observatoire Cantonal Neuchâtel (ON) and Officine Galileo Milano (OG). ON is responsible for the physics package (storage bulb and microwave cavity, hydrogen storage, distribution and dissociaton, state selection, vacuum maintenance), whereas OG works on the electronics package (atomic interrogation loop, automatic cavity tuning loop, power supplies, controllers). Figure 2 shows the S-PHM overall design.

Qualification and industrialisation of the S-PHM instrument will be led by TEMEX Time Neuchâtel.

Substantial parts of the physics package are adopted from an existing industrial PHM design, the VCH-1006 model, developed by VREMYA-CH in Russia. These parts include the magnetron microwave cavity, ion pumps, the hydrogen purifier and the hydrogen dissociator. Parts which have been identified to be sensitive to mechanical stress have been already successfully subjected to a vibration environment similar to Galileo during launch.

The S-PHM is specified to have a mass of maximum 17 kg. The total power consumption is specified to be maximum 80 W during nominal operation and to never exceed 100 W, even within the extended qualification temperature range and during warm-up.

The S-PHM is equipped with two control circuits, both realised as PLL (phase locked loops). Besides the atomic interrogation circuit which locks to the excitation of resonance within the microwave cavity, the S-PHM is equipped with an automatic cavity tuning (ACT) control circuit. The latter fine-tunes the microwave cavity to the atomic frequency of Hydrogen via an varactor, thus providing optimised cavity resonance characteristics. This enhances the quality of the atomic signal to be detected regarding its stability and phase noise properties.

The output frequency of the S-PHM is 10.00285741 MHz provided by decoupled output ports.

There is a multitude of telemetry signals provided by the S-PHM (about 20). In order to simplify the telemetry interface and to achieve robustness against EMC, the interface is a serial RS422 type.

Telemetry signals are delivered in a digital data stream with a resolution of 8 bit. They are provided directly to the OBDH.

Telecommands are supplied by the OBDH in the format of the telemetry signals. Besides temperature settings they comprise commands for pre-adjustment of the atomic interrogation PLL and the ACT facility.

The short term stability and the phase noise characteristics of the S-RAFS are shown in Figure 4 and Figure 5.

The S-PHM design and development phase is running since July 2000. This phase will be finished with a fully operational EM (engineering model) by end of 2001. The EM has to prove full functionality, but does not have to withstand the qualification process for Galileo.

Qualification will start in July 2001. Completely qualified EQM (engineering qualification model) and PFM (prototype flight model) are expected to be available by end of 2002.

The lifetime verification test of 5 models will start in June 2003 and will take 27 months.

5. CMCU

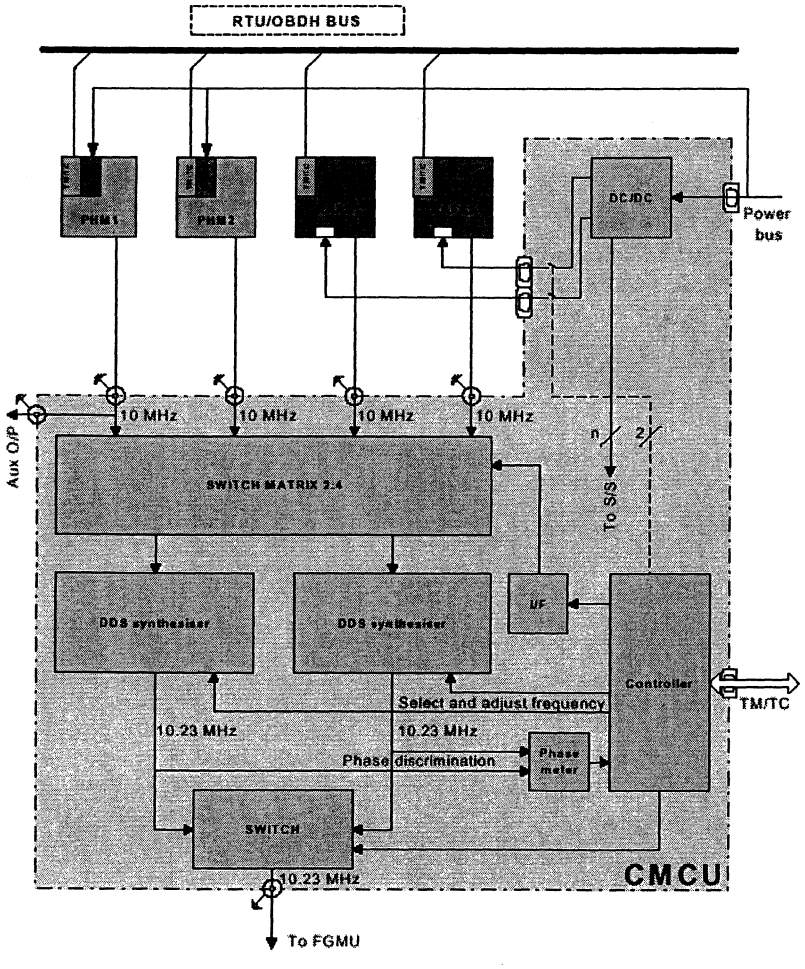

Figure 3: The TSS architecture

A schematic of the CMCU is shown in Figure 3. It has to fulfill the following tasks:

- Provision of a S-RAFS power supply
- Generation of the reference frequency to be used by the frequency generation unit (FGMU)
- Phase comparison system for the control of the primary operative AFS (normally a S-PHM) versus the secondary, hot redundant AFS (S-RAFS)
- Telemetry/telecommand interface with the on-board data handling system

5.1 Frequency generation

The on-board reference frequency of 10.23 MHz is generated from the 10 MHz AFS output signals by using a DDS (direct digital synthesis) synthesiser technique.

The core element of the DDS synthesiser is the programmable NCO (numerically controlled oscillator). Due to the non-availability of space qualified and radiation hardened NCOs in Europe, Astrium GmbH will develop a specific design. It will be optimised with respect to numerical rounding and truncation effects, thus reducing phase noise.

The purpose of the NCO is to provide a signal derived from the AFS output frequency which shall be adjusted in a range of $\Delta f/f = \pm 2 \times 10^{-9}$ with a resolution of $\Delta f/f = \pm 4 \times 10^{-12}$. This frequency adjustment capability is necessary to account for deterministic frequency drift effects of the AFS.

The NCO output frequency is fed into a PLL (phase locked loop) circuit consisting of a phase comparator, a low pass filter and a VCXO (voltage controlled quartz oscillator). The purpose of the PLL is to form a noise bandpass filter with a very low bandwidth, which is not possible to be achieved by other filtering techniques. The frequency of 10.23 MHz is provided at the VCXO output.

The chosen configuration is excellent in suppressing phase noise generated by noisy elements like the AFS, the NCO, the phase comparator and semiconductor switches. Only phase noise within the small PLL filter bandwidth may propagate to the VCXO output. Outside the filter bandwidth only the VCXO contributes to the

phase noise of the 10.23 MHz on-board reference signal (see Figure 5).

In the time domain, the Allan variance of the output signal is determined by the VCXO for integration times lower than the PLL time constant and the AFS for those higher (see Figure 4). The influence of the NCO and the phase comparator is negligible, based on the characteristics of existing equipment.

The Allan variance of the AFS is typically $\sim\sqrt{t}$, thus corresponding to a white noise power spectrum density. The Allan variance of the VCXO is typically constant for low integration times, corresponding to a 1/f noise power spectrum density

5.2 Phase discrimination

As described before, the phase meter provides to the ground segment the exact frequency of the secondary 10.23 MHz signal via the phase delta information The architecture of the phase meter is similar to a dual mixer with offset oscillator. It is planned to integrate the complete circuit into a single FPGA. This technique ensures thermal equilibrium within the symmetric internal signal paths, thus eliminating thermally driven phase changes.

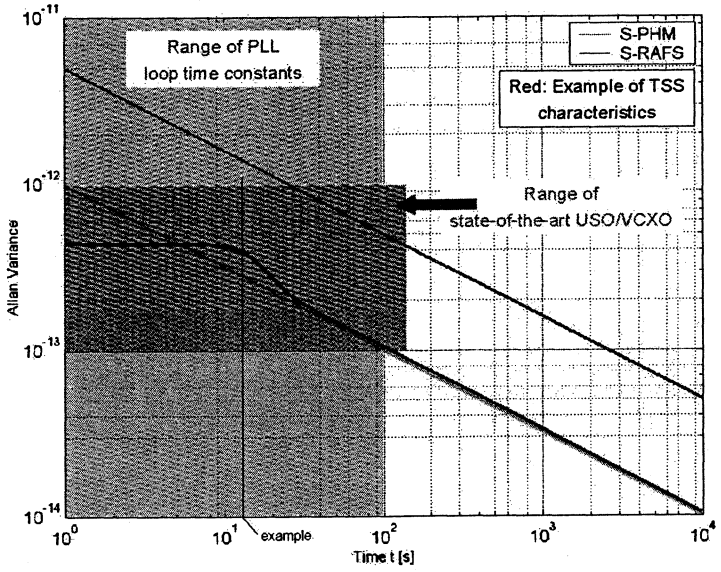

Figure 4: The expected TSS Allan variance performance

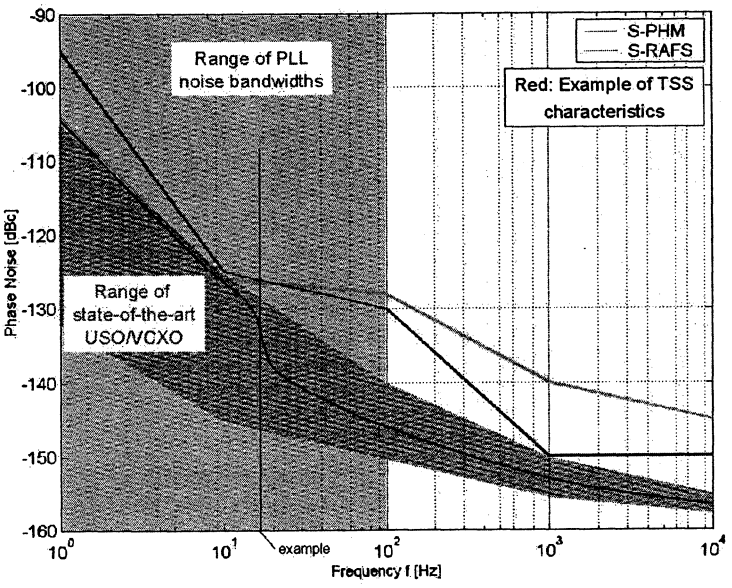

Figure 5: The expected TSS phase noise performance

6. INTERFACES

6.1 Thermal interfaces

The AFS are critical in terms of operational and non-operational (cold redundant stand-by, storage) temperature. The situation is more complex in case of the S-PHM, where a too high ambient temperature directly leads to lifetime loss of critical elements (e.g. hydrogen dissociator). Both instruments, S-PHM and S-RAFS suffer from mechanical stress problems for too low ambient temperature.

Furthermore, the susceptibility of the performance of both instruments to ambient temperature variation is significant:

- S-RAFS: $\Delta f/f = 1 \times 10^{-13}$/ °C specified
- S-PHM: $\Delta f/f = 1 \times 10^{-14}$/ °C specified

In order to avoid performance degradations due to temperature effects, different counter-measures are taken:

- The spacecraft platform provides a thermally controlled interface to the AFS. This interface ensures that the temperature at the TRP (thermal reference point) of operative AFS is set to be within [-12°C, 3°C]. Non-operative AFS in cold redundant stand-by may be subjected to a TRP temperature of [-10°C, 30°C]. In order to ensure full S-PHM performance, its TRP temperature must be timely very stable (± 1.8 m°C/min).
- The S-RAFS is equipped with a thermally controlled base-plate, comprising heating elements and an active control circuit.

6.2. Magnetic environment

Both AFS are sensitive to local and timely variations of the ambient magnetic field:

- S-RAFS: $\Delta f/f = 1 \times 10^{-12}$/ Gauss spec.
- S-PHM: $\Delta f/f = 1 \times 10^{-14}$/ Gauss spec.

The actual Galileo spacecraft architecture does however not impose a significant negative impact on the on-board reference signal integrity by magnetic fields.

6.3. Mechanical environment

Structural elements sensitive to mechanical stress are identified in the S-PHM and S-RAFS.

The S-RAFS has been completely subjected to a vibration test similar to the Galileo launch environment and passed the test successfully.

The S-PHM is not yet available as a complete instrument. However, sensitive parts have been already successfully tested as described earlier.

The CMCU will consist of rack mounted PCBs. This is a standard method in space engineering, which has proven its mechanical robustness throughout many previous programs.

6.4 Radiation

All electronics circuits of the TSS are designed with components radiation hardened up to 100krad. Wherever it is necessary, additional shielding is applied via the units walls.

7. CONCLUSION

The architecture and expected performance of the Galileo on-board reference frequency generation instance, the Timing Subsystem, has been presented.

It has been described how atomic frequency standards of different technology are operated as to optimise the system accuracy, availability and integrity.

The Timing Subsystem uses a space passive H-maser technology for the first time. Benefits of this ambitious project are an excellent frequency stability characteristics.

In order to further optimise the on-board reference signal quality, it is derived by using a state-of-the-art DDS synthesiser technique with a small bandwidth PLL filter. The NCO, responsible for frequency conversion within the DDS synthesiser, will be a dedicated design, optimised for the respective task.

Although the Galileo program is in an early stage of development, the identified critical items of the TSS make good progress. The S-RAFS will be completely qualified by end of 2001. The S-PHM will be available as an EM by end of 2001.

8. ACKNOWLEDGEMENT

The work described in this paper has been performed under different contracts of the European Space Agency ESA.

POSTERS A

MATERIALS

Chairman: Sergei Kulakov

OBSERVATION OF SSBW TO PSAW CONVERSION ON (YXl)/36° $LiTaO_3$ CUT

Y. Fusero, J. Desbois*, S. Ballandras, S. Magnaval*
LPMO-CNRS associé à l'Université de Franche-Comté, 32 Ave. de l'observatoire, 25044 Besançon Cedex
**THALES MICROSONICS (TMX),399 Rte des Crêtes,06904 Sophia Antipolis Cedex*

Abstract : The need for more and more efficient SAW devices requires the development of electrode grating to Acoustic Waves (PSAW) on standard (YXl)/36° $LiTaO_3$ cut versus Aluminum strip height. It is shown that the Surface Skimming Bulk Wave (SSBW) which accompanies the PSAW on such crystal orientations may be trapped by the grating, exhibiting a PSAW-like behavior when close to the Bragg condition. Experiments are performed to confirm the theoretical prediction and to underline the capability of heavy mechanical loading to favor such mode conversion.

I. Introduction

Radio-Frequency (RF) filtering for cellular phone applications requires the use of largely coupled surface waves to answer the demand of wide band low Insertion Loss (IL) High reducing the influence of acoustic leakage on PSAW based filter responses [1-3]. The development of efficient computation tools using Boundary Integral Methods (BIM) mixed with Finite Element Analysis (FEA) has allowed to point out the influence of mass loading on the PSAW characteristics. Hashimoto *& al* [2] and also Koskela *& al* [3] have shown the possibility to reduce leakage effects on $LiTaO_3$ and $LiNbO_3$ by a proper choice of metal thickness for various simply rotated cuts.

Nevertheless, the use of heavy mechanical loading to improve surface guiding may also induce unexpected phenomena yielding spurious response on PSAW resonators built on $LiTaO_3$. It has been shown theoretically that the SSBW close to the PSAW on the (YXl)/36° $LiTaO_3$ cut can be strongly affected by heavy mass loading using a FEA/BIM calculation[4]. In the proposed paper, particular configurations of IDT identified as very sensitive to this phenomenon have been studied. It consists in synchronous devices exhibiting an electrical excitation pattern allowing the identified mode to contribute to the admittance at the end of the frequency stop band. The corresponding response is due to a conversion of the SSBW in a PSAW like wave. Predictions of the electrical admittance of these IDT are performed using an non periodic FEA/BIM computation [5]. Results are compared to experiments demonstrating the existence of the predicted phenomena. As a conclusion, the correct use of advanced computation tools to optimize IDT structures for SAW applications are discussed.

II. Fundamentals of the model

The structure is composed of a semi-infinite substrate expanding along $x_2 > 0$ whose surface supports a periodic metal strip grating. The grating electrodes are parallel to x_3, centered at $x_1 = np$ (n : number of the electrode, p : grating period) and of width a (see fig.1).

improve trapping and guiding. In this work, theoretical models are used to analyze the evolution of Pseudo Surface frequency filters. Quasi-shear waves propagating a singly rotated Lithium Tantalate or Lithium Niobate substrate are particularly well suited in that matter, exhibiting electromechanical coupling coefficients ranging from 5 to 10 % together with propagation velocities form 4100 to 4700 ms^{-1}. However, these waves are only partially guided by the surface of the substrate, a part of its electromechanical energy being radiated toward the bulk. As a consequence, these waves are identified as pseudo or Leaky Surface Acoustic Waves (P or LSAW).

Many effects have been performed to precisely simulate these PSAW in order to define the best Interdigital Transducer (IDT) configurations

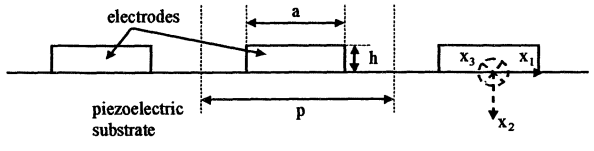

Fig. 1. Definition of the axes and of the geometric parameters of the addressed problem

All the considered fields exhibit a time dependence given by $e^{j\omega t}$. All the developments are conform to already published material [1,5]. The addressed problem is treated using a method based on an integral representation of the propagation domain (the so-called BIM part) mixed with a discrete formulation of the diffraction element of the structure, i.e. the electrodes (the FEA part).

Considering an harmonic excitation, only one period of the grating is considered for the BIM:

$$u_i(x_1) = \int_{-p/2}^{p/2} G_{ij}^{(\gamma)}(x_1 - x')\, t_{j2}(x')\, dx' \qquad (1)$$

$G_{ij}^{(\gamma)}(x_1)$ is the periodic Green's function. For an harmonic excitation, the electrode currents and voltages exhibit the same dependence :

$$I_n(\gamma) = I_0 e^{-j2\pi n\gamma} \qquad (2)$$

The ratio $I_n(\gamma)/V_n(\gamma)$ which does not depend on n is the "strip admittance" or "harmonic admittance" (HA) :

$$\tilde{Y}(\gamma)=\frac{I_n(\gamma)}{V_n(\gamma)} \qquad (3)$$

The determination of the grating HA is described in ref. [1,5]. The results are used to derive the excitation and propagation parameters of any SAW. On the other hand, eq. (1) can be used under its non periodic form to compute finite length transducer responses [5]. In this approach, the periodic Green's function is replaced by the Fourier transform of the spectral Green's function, and the global admittance is computed as the sum of the charge under the active electrodes times the angular frequency.

III. Computation results

The analysis of SAW devices is mainly based on numerical techniques (FEA/BIM) and heuristic models such as COM [2,3] or Mixed or P-Matrix [1,5]. These models only consider some acoustical modes which are generally called "coupled modes" (COM) or "pseudo modes" (Mixed Matrix). They only use a few parameters characterizing the surface coupled modes (slowness, attenuation, coupling strength, reflection coefficient, directivity factor) deduced from a particular form of the SAW contribution to the HA :

$$\tilde{Y}(\gamma)=R(\gamma)+jY_p\frac{1-\eta}{\hat{\eta}-\eta} \qquad (4)$$

where η is equal to $cos^2(\pi\gamma)$ and $R(\gamma)$ represents the residual behavior of the HA (differing from the SAW). An iterative 3 point calculation process is applied to compute Yp and $\hat{\eta}$. They are chosen close enough to the singularity to assume $R(\gamma)=R(\hat{\gamma})$. $\hat{\gamma}$ is then deduced from $\hat{\eta}$.

Applying the above-described method, some convergence problems have been met when trying to extract PSAW parameters on LiTaO3 (YX*l*)/36° cut considering propagation under very thick electrodes (h ≥ 6% of 2p). It was found that the iterative procedure might converge toward another unexpected singularity of the HA. Actually, since the SSBW is assumed not affected by the mass loading, the observed phenomenon could not correspond to the SSBW singularity given by $\hat{\gamma}_{BULK}=f.p.s_{BULK}$. No other known mode on (YX*l*)/36° Tantalate verifies the equation $\hat{\gamma}_{NEW\ PHENOMENON}=f.p.s_{KNOWN\ MODE}$. As a consequence, this new contribution should be generated by a not yet identified guided propagation, arising only for thick strip gratings. To identify the physical reason of the problem, the HA has been computed and plotted for different h/2p on $LiTaO_3$ (YXl)/36° in the vicinity of the end of the PSAW stop band. The results for h/2p=4% for different values of *2fp* are reported in fig. 3. For frequencies smaller that the one for which the phenomenon is observed, the PSAW enters normally it's stop band with $Re(\hat{\gamma}_{PSAW})=0.5$. The SSBW"+" contribution gets closer to $\gamma = 0.5$ and starts to be "disturbed" (the shape of the SSBW contribution becomes sharp).

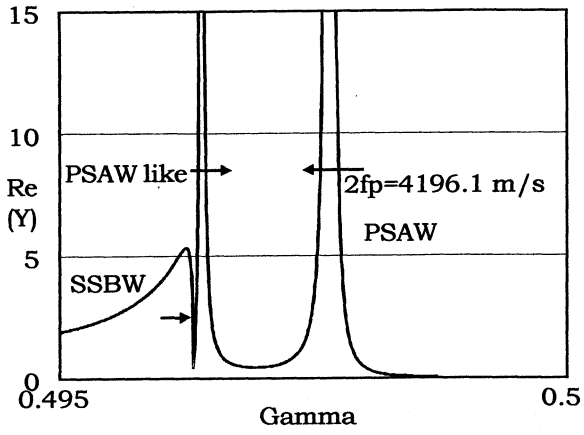

Fig. 3a.

Figure (3a) shows the PSAW"-" getting out of its stop-band and the SSBW"+" contribution separated into a PSAW"+"-like contribution and the classical SSBW"+" contribution. These two contributions are going towards γ=0.5 indicating "+" modes. The classical PSAW"-" is going toward the new PSAW "+"-like.

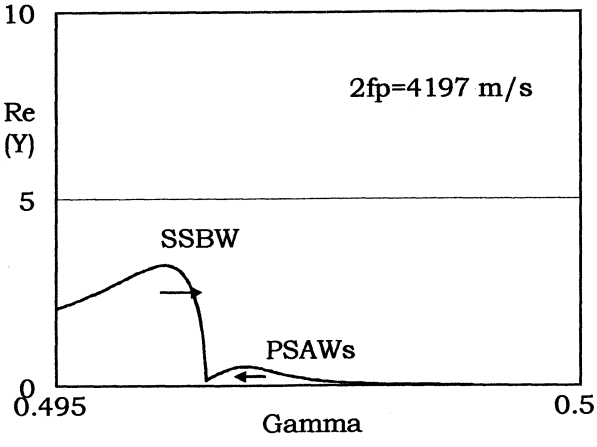

Fig. 3b.

In fig. (3b), the two PSAW are interacting and presenting a classical stop band shape (the two contributions cancel each other). For higher frequencies, the classical PSAW"-" contribution goes out of its interaction zone with the new PSAW"+"-like wave but crosses the SSBW contribution in the same time, thus presenting a large leakage (its peak is smaller but larger).

IV. Experimental Verification

As mentioned in ref. [4], spurious contributions may arise due to the PSAW-like phenomenon in standard synchronous resonators built on (YX*l*)/36° $LiTaO_3$ substrates. However, to highlight the existence of the SSBW to PSAW-like conversion, a special device had to be designed and fabricated along the following approach described below and compared to a standard synchronous resonator.

The idea consists in building an IDT structure allowing the observation of the phenomenon. For instance, a phase excitation corresponding to γ=0.4975 covers a region where the PSAW like wave is assumed to exist for h/λ=6%. From a mechanical point of view, the device has to be synchronous,

but the excitation pattern must be shifted twice by simply changing the alternation +V/-V. One port modified SAW synchronous resonator have been then built with an excitation distribution conform to the one previously define. Two shifts are introduced in the synchronous excitation pattern in order to approach γ=0.4975 at best. The mechanical period has been fixed to 2 µm with a ratio *a/p* of 0.5 and a metal thickness of 240 nm (h/2p=6%). This configuration promotes the magnitude of the expected electrical response due to the PSAW-like wave. A standard synchronous resonator was also built with the same mechanical parameters to compare the electrical responses.

The test devices have been manufactured on a 4 inches $LiTaO_3$ wafer using a photolithography stepper and dry aluminum reactive ion etching. The measurement of the admittance of the device has been performed via a network analyzer. Experiment results are reported in fig. 4 corresponding respectively to the modified and standard test devices. A very small contribution is pointed out on the standard resonator response at the frequency for which the PSAW-like is assumed to exist. However, larger variations of the admittance (resonance) are measured for the modified device, for which the only possible explanation is the trapping of the PSAW-like wave under the electrode array. Thus, one can consider these results as a trustful evidence of the existence of the PSAW-like phenomenon, providing the best illustration of its influence on different IDTs configurations. Moreover, simulation of the finite length structures reported in fig. 5 provides results in good agreement with the experimental measurement, allowing a clear identification of each modes.

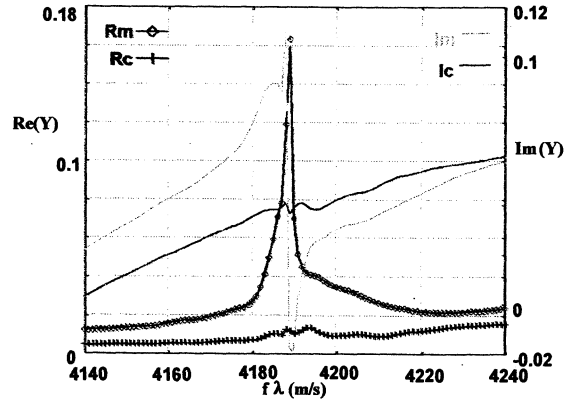

Fig. 4 Experimental results for the classical and modified resonators

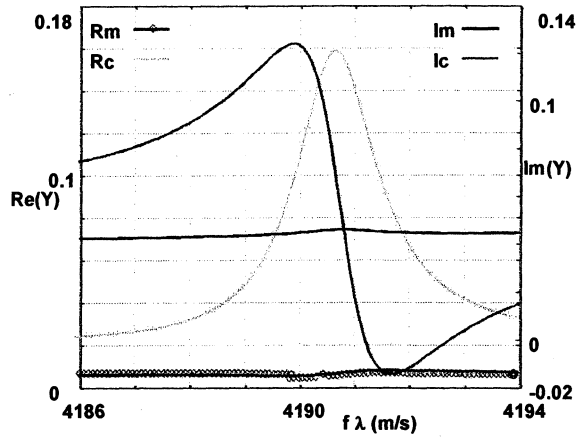

Fig.5 Theoretical predictions for the tested devices

V. Conclusion

The existence of a SSBW-to-PSAW conversion on (YX*l*)/36° $LiTaO_3$ cut has been found theoretically and experimentally for large electrode thickness. The influence of this phenomenon on the electrical response of classical and modified SAW resonators has been shown. One can expect the existence of such effects on other PSAW substrates.

Acknowledgements : This work was partly founded by the DGA under grant # 987.667.87.575.757.57

References :

[1] P. Ventura, JM. Hodé, M. Solal, "A new efficient combined FEM and periodic Green's function formalism for the analysis of Periodic SAW structures", Proc. of the IEEE Ultrasonics Symp. IEEE cat #95CH35844, Seattle, pp. 263-268, 1995.

[2] O. Kawachi, ,G. Endoh, M. Ueda, O. Ikata, K. Hashimoto and M. Yamaguchi, "Optimum cut of $LiTaO_3$ for high performance leaky surface acoustic wave filters", Proc. of the IEEE Ultrasonics Symp. IEEE cat #96CH35993, 1996, pp. 71-76.

[3] J. Koskela *& al*, "Suppression of the leaky SAW attenuation with heavy mechanical loading", IEEE Trans. on UFFC, Vol 45, n°2, pp.439-449, 1998.

[4] Y. Fusero *& al* "SSBW to PSAW conversion in SAW devices using heavy mechanical loading", Proc. of the IEEE Ultrasonics Symp. 2000 (to be published)

[5] P. Ventura *& al*, "Numerical methods for SAW propagation characterization", Proc. of the IEEE Ultrasonics Symp. IEEE, cat #98CH36118, Sendaï, pp. 175-186, 1998.

THEORETICAL AND EXPERIMENTAL STUDIES OF THE FORCE-FREQUENCY EFFECT IN BAW LGS AND LGT RESONATORS

J.J. BOY, E. BIGLER, R. BOURQUIN, B. DULMET

ENSMM / LCEP - 26, chemin de l'Epitaphe - 25000 BESANÇON – France

Tel : 33 381 40 28 23 – Fax : 33 381 88 57 14 - E-mail : jjboy@ens2m.fr

ABSTRACT

It is well known that, for quartz crystal, mechanical and / or thermal stress sensitivities prevent the achievement of ultimate performances of bulk acoustic wave piezoelectric resonators. It is important to check these effects in newly developed Langasite (LGS) and Langatate (LGT) resonators. A theoretical and experimental study of the force-frequency effect (denoted by the K_f coefficient) in Y-cut LGS thickness-shear resonators, working at various overtone modes, is presented. Theoretical predictions are based on Tiersten theory of wave propagation in a pre-stressed medium. For LGS crystals, 3rd order non linear elastic constants have been published and used here for modeling the behavior of thickness-shear resonators submitted to diametrical compression. A comparison between theoretical predictions and experimental measurements is presented. In the case of LGT crystal, numerical data of the third order elastic coefficients are not available at this time. Only experimental measurements of K_f coefficient are presented in order to compare behaviors of LGS and LGT Y-cut resonators.

INTRODUCTION

Langasite and Langatate are materials having very attractive piezoelectric properties (more intense piezoelectric properties than quartz, temperature compensation for several cuts, low acoustic losses, ...). In addition to very interesting properties for dielectric applications, LGS or LGT are also used for SAW and BAW applications.

Generally, to design devices for high performances oscillators, it is necessary to know the influence of stresses generated by the mounting structure. With the knowledge of the third order elastic coefficients of the LGS [1], an analytical approach [2] is presented to calculate the force frequency effect of a plano-convex resonator using Y-cut Langasite.

RESONATORS PARAMETERS

To analyze the force-frequency effect in BAW LGS or LGT resonators, we have fabricated two types of Y-cut resonators to which we applied the model of H.F. Tiersten and co-authors [3], [4] to study the energy trapping. We show below calculations of the radius of curvature for comparable energy trapping in the 10 MHz 3rd Overtone resonance and in the 5th Overtone at the same frequency. The external diameter is 13.2 mm and the electrodes are 6 mm.

In fact, even if the calculation gives different values for the optimal curvatures for those 2 sets of resonators (see table below), for technological reasons, we have chosen the same radius, equal to 500 mm for both.

Table 1 : Dispersion constants (see ref. [4]) and Radius of curvature (in mm) for LGS resonators providing residual amplitude (10^{-6} x U_{max}) at the edge

In Gpa	Mn	Rc	Pn	Rc
C 300	23	3500	49	1300
C500	100	1700	49	2500

The following table gives the main parameters for our LGS and LGT resonators, compared to the same parameters of the well-known SC-cut 10 MHz 3rd Overtone built in quartz and measured under vacuum.

Table 2 : Main parameters of studied LGS, LGT and quartz resonators

	Y-cut LGS / LGT 10MHz 3rd.	Y-cut LGS / LGT 10MHz 5th	SC-cut Quartz 10MHz 3rd
Rc (mm)	500 / 500	500 / 500	230
Thickness (mm)	0.411 / 0.394	0.687 / 0.597	0.558
Rm (Ohms)	10 / 6	20 / 24	85
Q (10^6)	0.25 / 0.43	0.30 / 0.22	1.30
Self (H)	0.04 / 0.04	0.096 / 0.08	1.76

Interestingly enough, the 7th Overtone of the second type of LGS resonator, located at about 13.990 MHz, is slightly better than the 5th Ov., the Q-factor being : $0.295 * 10^6$.

As previously reported in [6], we have observed a much larger number of anharmonic modes in these resonators than in a quartz resonator with similar design. This accounts stronger trapping. As an example, we give below the 9 first anharmonic modes of the LGS 10 MHz 5th Ov. (which is located exactly at 9.996 MHz) :

10.046 MHz – 10.068 MHz
10.095 MHz – 10.114 MHz – 10.138 MHz
10.145 MHz – 10.162 MHz – 10.183 MHz
10.208 MHz

We have drawn the frequency temperature characteristics for each vibrating mode at 10 MHz. Our experiments have been realized in the range [10, 120 °C], the resonator being inserted in the "PI" bridge recommended by IEC 444 norms.

The following table gathers the usual coefficients of the cubic equation which best fits the experimental data. For comparison, we also provide here the coefficients of the frequency temperature curve of the "classical" SC-cut quartz resonator.

Table 3 : frequency temperature characteristics of Y-cut LGS and LGT

	a (10^{-6}/°C)	b (10^{-9}/°C^2)	c (10^{-12}/°C^3)	T.O.P. (°C)
Y-cut LGS 10MHz 3rd	5.73	-59.4	14.1	74.1
Y-cut LGS 10MHz 5th	6.72	-61.4	34.5	82.5
Y-cut LGT 10MHz 3rd	6.94	-76	52	73.1
Y-cut LGT 10MHz 5th	6.5	-76	60	70.2
SC-cut Q. 10MHz 3rd	0.91	-13.1	56	80

FORCE FREQUENCY EFFECT

The above mentioned resonators have been tested in a force frequency apparatus (Fig. 1b) built on purpose and previously used [5]. A vertical load, namely 1 Kg, is repeatedly applied on the edge, along a diameter of the resonator. The direction of the force, with respect to the crystallographic X-axis, is defined on Fig. 1a by the azimuthal angle ψ.

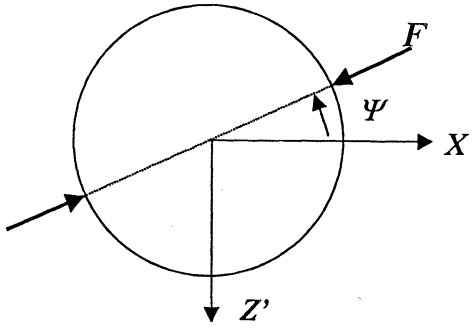

Fig. 1a : Definition of the ψ-angle

An example of the recorded frequency shift versus time for one azimuthal angle is shown on Fig.2. Typical order of magnitude of this effect is +/- 20 to 50 Hz at 10 MHz for 1 Kg load.

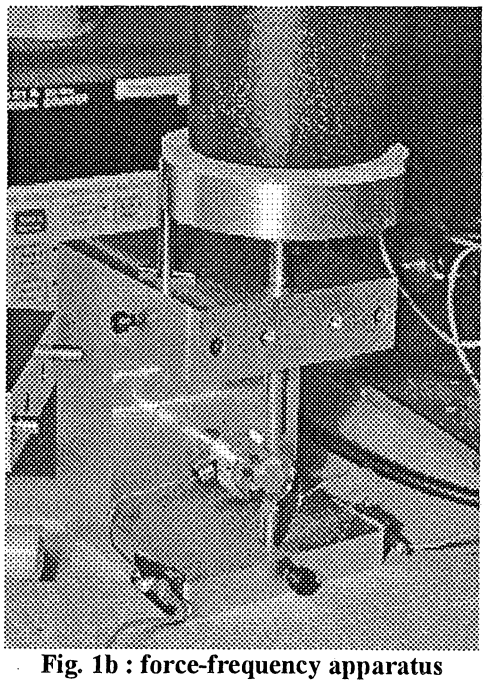

Fig. 1b : force-frequency apparatus

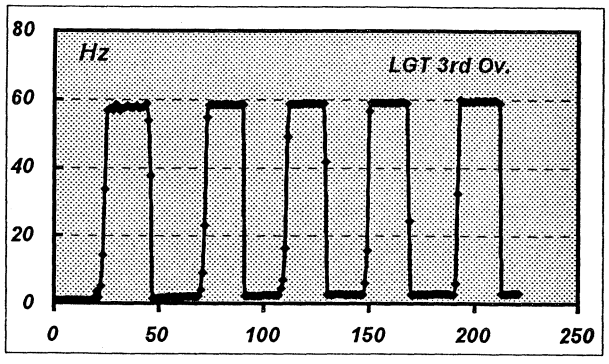

Fig. 2 :recorded frequency shift versus time

Plots of the force frequency effect versus ψ angle are represented on Fig. 3a (thickness 0.394 mm) and Fig. 3b (thickness 0.542 mm for 11MHz 5th overtone) for the LGT resonators. The overall shape of the curve is sinusoidal, as is well known for quartz [7] where is defined an intrinsic coefficient which it is called K_f :

$$K_f = \frac{\Delta f}{f}\frac{D\,t}{F}$$

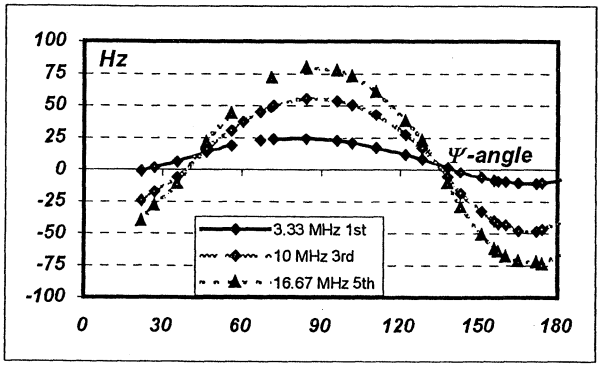

Fig. 3a : LGT resonators (0.394 mm thick)

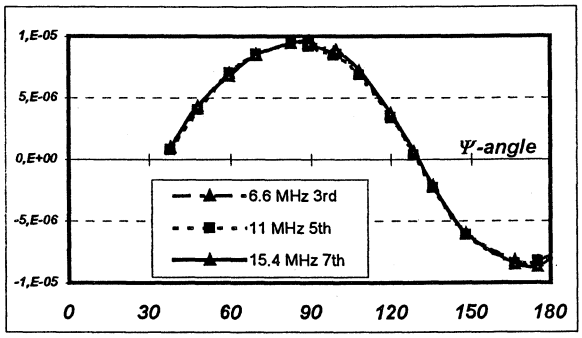

Fig. 3b : LGT resonators (0.542 mm thick) : Δf/f

The previous experimental data can be compared with those obtained with quartz resonators. For an AT-cut quartz resonator, the maximum value of the force frequency effect is obtained with the azimuthal angle Ψ = 0 and, in this X-direction, the relative frequency shift due to 1 Kg load applied on a 11MHz 5th overtone is : 3.7 x 10^{-5}. A similar resonator in Langatate exhibits a maximum relative frequency shift close to 10^{-5} at Ψ = 90° (Fig. 3b). And the maximum relative frequency shift for a 1 Kg load on the edge of a SC-cut 10MHz 3rd overtone is close to 3 x 10^{-5}.

Finally, in the next figure (Fig. 4), we present the force-frequency effect of the Y-cut 10MHz 3rd overtone built in Langasite. The theoretical model, previously developed for quartz [5], has been used to compare the theoretical prediction with experimental data. The model is based on previously published material constants by Sakharov et al. [1] and Alexandrov et al. [8]. In the case of quartz, the agreement between calculated and measured values for K_f is good. But, we observe that, in our case, for LGS crystal, only general shape and anisotropy dependence is correctly modeled. As can be seen on this Fig. 4, the existence of "neutral points" of zero force sensitivity is found. However, a major discrepancy is found for the sign and magnitude of this effect.

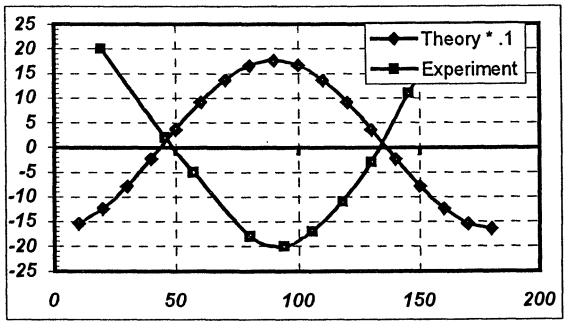

Fig. 4 : LGS resonator – comparison between theory and experiment (Δf versus azimuthal angle)

The situation is really puzzling because the apparatus and the model were both extensively used for quartz with good results [5]. The only change in the computing model was entering material constants. It is for this reason that we present the following figure in order to show the influence of the accuracy of constants on K_f behavior (Fig. 5). Indeed, if we apply a scaling factor to the set of the third order elastic coefficients used in the K_f calculation, we can observe significant changes in the force-frequency effect showing that the effect of the third order coefficients can be balanced by the effect of the second ones.

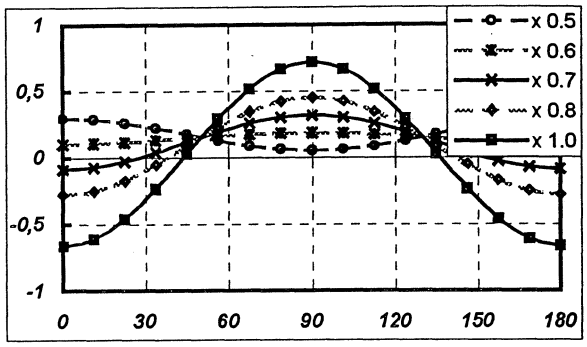

Fig. 5 : Influence of the predicted values of the third order elastic coefficients on the force-frequency effect on Langasite resonator (normalized values)

CONCLUSION

Plano-convex LGS and LGT resonators have been fabricated, their electrical parameters measured and the force frequency experimentally studied. Even if the second order temperature coefficient of Y-cut is higher than AT or SC-cuts quartz, this LGS / LGT Y-cut exhibits interesting properties in terms of stress sensitivity.

The theoretically predicted magnitude of K_f is about half the value of K_f for AT-cut quartz, the experimental results being even smaller by at least a factor 3. The anisotropy dependence of the effect is very symmetrical, somewhat similar to the SC-cut of quartz : the interesting perspective is that resonators built from LGS cuts in the vicinity of the Y-cut will exhibit, like SC-cut quartz resonators, a reduced sensitivity to planar homogeneous stresses.

REFERENCES

[1]. S. SAKHAROV et al. – IEEE Inter. Freq. Cont. Symp., pp. 647, 652 (1995)

[2]. BAUMHAUER, H.F. TIERSTEN – J. Acoust. Soc. Am. N°54, pp. 1017, 1034 (1973)

[3]. H. F. TIERSTEN – J. Acoust. Soc. Am. Vol. 64, N°3, pp. 832, 837 (1978)

[4]. D.S. STEVENS, H.F. TIERSTEN - J. Acoust. Soc. Am. VOL. 79, N°6, pp. 1811, 1826 (1986).

[5]. R. BOURQUIN, B. DULMET – Proc. 41st, A.F.C.S. 1987.

[6]. J. DETAINT et al. – Proc. of 9th E.F.T.F., pp. 289, 296.

[7]. J. M. RATAJSKI – Proc. of 20th A.F.C.S., pp. 39, 46 (1966).

[8]. K.S. ALEXANDROV et al. – IEEE Ultrasonics Symp., pp. 409, 412 (1995).

CZOCHRALSKI GROWTH, STRUCTURE AND PROPERTIES OF LANGASITE ($La_3Ga_5SiO_{14}$) PIEZOELECTRIC SINGLE CRYSTALS

S. Georgescu*, L. Gheorghe*, M. Popescu**, F. Sava**, H. Bradaczek***

*National Institute for Lasers, Plasma and Radiation Physics, RO-76900 Bucharest, P.O. Box MG. 36, ROMANIA
**National Institute of Materials Physics, Bucharest-Magurele, P.O. Box MG.7, ROMANIA
***EFG International Berlin, Research Center, Dueppelstr. 13, D-14163 Berlin, GERMANY

ABSTRACT

The growth of langasite crystals of approximately 10 mm diameter using the Czochralsky method is reported. Details of the synthesis and growth procedures that ensure satisfactory piezoelectric properties of the crystals are described. The crystals were proved to be single phase. The lattice parameters were accurately determined by X-ray diffractometry on langasite powder obtained by milling a crystal. The microhardness of the crystals on the main growth faces was measured.

Langasite, crystal growth, Czochralski technique, X-ray diffractometry, microhardness.

1. INTRODUCTION

In recent years, considerable efforts were invested to develop new piezoelectric crystals with the purpose to improve the quality of the electronic devices. Digital communication systems demand new materials suitable for the production of wider band pass filters than ST quartz.

Lanthanum gallium silicate, $La_3Ga_5SiO_{14}$ (langasite or LGS) and its homologous compounds $La_3Nb_{0.5}Ga_{5.5}O_{14}$ (langanite or LNG) and $La_3Ta_{0.5}Ga_{5.5}O_{14}$ (langatite or LTG) have been pointed out as promising materials for piezoelectric devices (Ref. 1-2). Langasite is an appropriate material for bulk acoustic wave (BAW) and surface acoustic wave (SAW) devices. LGS crystals exhibit excellent thermal stability and high electro-mechanical coupling coefficients for both BAW and SAW (Ref. 3-4). Langasite is very well suited for miniaturized band pass filters with low insertion losses for satellite microwaves and mobile terrestrial communication. LNG and LTG exhibit larger electromechanical coupling coefficients and improved band pass filter behavior than LGS (Ref. 5).

In this work we report the growth of single crystals of langasite belonging to the enantiomorphic class 32 by means of the Czochralski technique. The quality of the crystals and several structural and mechanical properties will be also reported.

2. LANGASITE CRYSTAL GROWTH

The starting materials were prepared from silicon, lanthanum and gallium oxides (SiO_2, La_2O_3, Ga_2O_3) of 99.99 % purity. According to the phase diagram of the system La_2O_3-Ga_2O_3-SiO_2 at 1450° C (Ref. 6-8), the synthesis was performed in two stages.

In the first stage the corresponding powders taken in stochiometric ratios were dried and thoroughly mixed in an agate mortar. Then, the powder mixture was pressed in pellets, heated at 1200° C and maintained at that temperature for 5 hours. The following compounds compose the resulting polyphasic mixture: $La_3Ga_5SiO_{14}$, $LaGaO_3$, Ga_2O_3 and SiO_2 (high temperature form).

In the second stage the material resulting from the first stage was milled in a ball mill and a new pellet was obtained by pressing the corresponding powder in a special device. The final thermal treatment was performed at 1450° C. This temperature is very near to the melting temperature of langasite (1490° C). The sample was maintained three hours at that temperature. The crystal growth atmosphere was technical argon gas. Using a platinum wire as support the first crystal was grown.

3. THE CRYSTALS

The langasite crystals obtained by us using the Czochralski method are transparent and exhibit pink color. Crystals of 8-10 mm in diameter and larger in length were obtained.

Optical microscopy observations and X-ray diffraction measurements were carried out. Careful optical studies did not evidence any cracks or inclusions. All the crystals were homogeneous with uniform coloring.

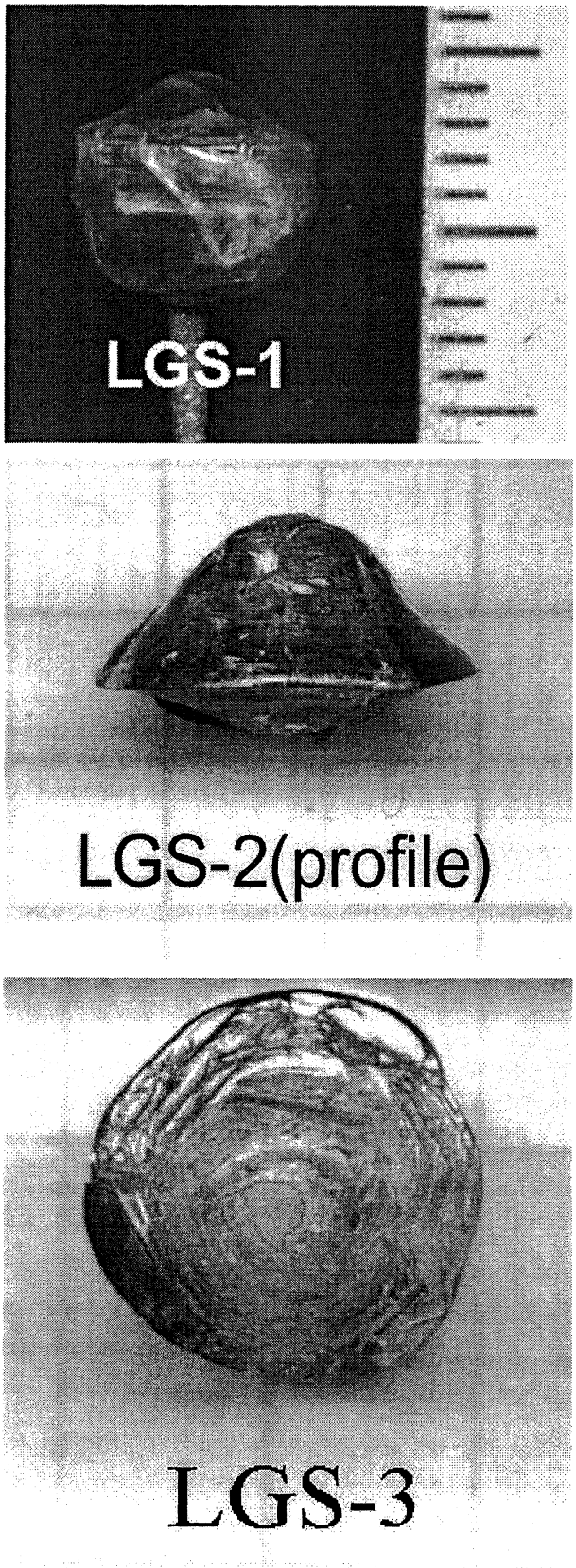

Fig.1. Photographs showing the general features of three LGS crystals grown by the Czochralski method.

A regular shape consistent with the crystal symmetry belonging to the enantiomorphous class 32 was assessed. On the cylindrical parts of the crystals six {1010} facets were observed.

Typical single crystals grown by us applying the technique described above are shown in Figure 1.

4. CRYSTAL PROPERTIES

Phase identification of the grown crystals was carried out by X-ray diffractometry. A powder diffractometer equipped with a copper target tube and proportional counter was used for the measurements. The LGS powder obtained by milling small pieces of a single crystal was pressed in a special support and the sample was then mounted on the diffractometer. The X-ray powder diffraction diagram is shown in Figure 2. Indexing the diffraction lines has identified the unique langasite phase with trigonal symmetry (quartz-type).

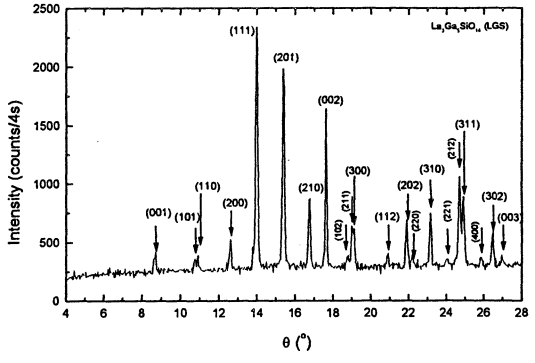

Fig. 2. X-ray diffraction pattern of the powder sample of a langasite crystal grown by the Czochralski technique (Θ: diffraction angle).

The lattice parameters of the langasite crystal were determined at room temperature (22° C) by the least squares method. The highest possible number of peak positions was used. Each peak profile was recorded in angular steps of the diffraction angle of 0.002° with a measuring time per angular position of 10 s. The unit cell parameters of LGS determined in this way are a = 0.8159 nm and c = 0.5095 nm with an accuracy of ± 0.0005 nm. The c/a ratio (0.6245) is a little larger than that reported in the literature (c/a = 0.6233).

A study of microhardness of a langasite crystal was performed. We have used a PMT-3 tester provided with a diamond indenter. The Vickers hardness was measured. Using medium indentation loads (P = 100 g) we calculated the microhardness for various facets of

the single crystal. A typical value is 8.03 GPa, with no significant deviations from one facet to another. This value is larger than the microhardness values, for example, of SiO_2 (6.3 Gpa, Ref. 9) as well as of many other covalent compounds (Ref. 10).

5. CONCLUSIONS

The optimal conditions for the growth of LGS crystals have been determined. The pink color of the crystals is probably related to the effect of minor impurities present in the raw oxides used for crystal growth. The accurate lattice parameters were measured. A value of the microhardness on the growth facets is reported for the first time.

REFERENCES

[1] S. A. Sakharov, I.M. Larionov, A.V. Medvedev, "Application of langasite crystals in monolithic filters operating in shear modes", Proceedings of IEEE Frequency Control Symposium , 713-718, 1992.

[2] H. Kawanaka, H. Takeda, K. Shimamura, T. Fukuda, "Growth and characterization of $La_3Ta_{0.5}Ga_{5.5}O_{14}$ single crystals", Journal of Crystal Growth **183**, 274-277, 1998.

[3] A. Gotalskaya, D.I. Drezin, V. V. Bezdelkin, V. N. Stassevich, "Peculiarities of technology, physical properties and applications of new piezoelectric material langasite ($La_3Ga_5SiO_{14}$)", Proceedings of IEEE Frequency Control Symposium, 339-344, 1993.

[4] J. Detaint, J. Schwartzel, A. Zarka, B. Capelle, J. P. Denis, E. Philippot, "Bulk wave propagation and energy trapping in the new thermally compensated materials with trigonal symmetry", Proceedings of the IEEE International Frequency Control Symposium, 58-71, 1994.

[5] J. Bohm, R. B. Heimann, M. Hengst, R. Roewer, J. Schindler, "Czochralski growth and characterization of piezoelectric single crystals with langasite structure: $La_3Ga_5SiO_{14}$ (LGS), $La_3Ga_{5.5}Nb_{0.5}O_{14}$ (LGN) and $La_3Ga_{5.5}$ $Ta_{5.5}O_{14}$ (LGT)", Journal of Crystal Growth. **204**, 128-136, 1999.

[6] K. Shimamura, H. Takeda, Y. Kohno, T. Fukuda, "Growth and characterization of lanthanum gallium silicate $La_3Ga_5SiO_{14}$ single crystals for piezoelectric applications", Journal of Crystal Growth **163**, 388-392, 1996.

[7] J. Sato, H. Takeda, H. Morikoshi, K. Shimamura, P. Rudolph, T. Fukuda, "Czochralski growth of $RE_3Ga_5SiO_{14}$ (RE= La, Pr, Nd) single crystals for the analysis of the influence of rare earth substitution on piezoelectricity", Journal of Crystal Growth **A91**, 746-753, 1998.

[8] H. Takeda, K. Shimamura, V. I. Chani, T. Fukuda, "Effect of starting melt composition on crystal growth of $La_3Ga_5SiO_{14}$", Journal of Crystal Growth **197**, 204-209, 1999.

[9] M. Yamane, J. D. Mackenzie, "Vickers hardness of glass", Journal of Non-Crystalline Solids **15**, 153-164, 1974.

[10] L. Garbato, A. Rucci, "Microhardness of ternary chalcopyrite semiconductors", Philos. Mag. **35**, 1685-1688, 1977.

DIAGNOSTIC SYNCHROTRON X-RAY TOPOGRAPHIC IMAGING OF STRIATIONS AND OTHER DEFECTS IN LANGATATE AND LANGANITE SINGLE CRYSTALS AND ASSESSMENT OF THEIR INFLUENCE ON RESONATOR PERFORMANCE

M. DUDLEY,[1] B. RAGHOTHAMACHAR,[1] H. CHEN,[1] W. JOHNSON,[2] S. TIDROW,[3] A. KHAN,[3] AND C. FAZI[3]
[1] Department of Materials Science and Engineering, State University of New York at Stony Brook, Stony Brook NY 11794-2275, USA
[2] National Institute of Standards and Technology, Materials Reliability Division, MS 853, 325 Broadway, Boulder, CO 80305, USA
[3] Army Research Laboratory, 2800 Powder Mill Road, Adelphi, MD 20783-1145, USA

Synchrotron White Beam X-ray Topography (SWBXT) has been used to characterize defect and strain configurations in Langatate single crystals, grown using the Czochralski technique. Both as-grown boules and wafers sliced parallel and perpendicular to the [001] growth axis have been examined. Defects observed include growth striations, precipitates, and dislocations. The striation contrast is indicative of either a slight local non-stoichiometry or impurities in the crystals, produced by periodic variations experienced during growth. Topographs recorded from boules reveal striations and inclusions located close to the boule surface. Striations observed on topographs recorded from crystal sections cut parallel to the growth axis reveal a cross-sectional view of the melt-solid interface shape. Typically this is observed to be convex. On topographs recorded from sections cut perpendicular to the growth axis, the growth striation structures appear as roughly concentric rings, the spacing of which reveals the periodicity of the striations, and the symmetry of which reveals the symmetry of the thermal field inside the growth chamber. Topographs recorded from wafers cut from the same boule revealed an asymmetry to the thermal field, which is present throughout the growth process. Clear images of precipitates are also routinely observed, providing further evidence of inhomogeneous constituent element or impurity segregation. Investigation of the chemical nature of the inhomogeneities is being carried out using a combination of techniques including Scanning Electron Microscopy, and Infrared Spectroscopy. Once identified, strategies for elimination of the inhomogeneities will be developed. Preliminary studies of the influence of microstructure on Q.f in Langanate resonators was also carried out.

Introduction

Langatate (LGT; $La_3Ga_{5.5}Ta_{0.5}O_{14}$), similar to its isomorphs langasite (LGS; $La_3Ga_5SiO_{14}$) and langanite (LGN; $La_3Ga_{5.5}Nb_{0.5}O_{14}$) is currently attracting a lot of attention due to its potential for application as a bulk wave resonator for precision oscillators. Like its isomorphs, LGT exhibits high piezoelectric coupling, low acoustic loss (high Q) and temperature compensation. However, the influence of crystal quality on piezoelectric properties, for example, on mode shapes (see work of Capelle et al.[1] and Zarka et al.[2]) dictates that high quality crystals are required for this technology to reach full potential. This requires collaboration between crystal growers and characterizers to gain an understanding of the defect content of the crystals and to enable optimization of growth parameters. In a previous paper we provided a preliminary survey of the quality of langanite and langatate crystals carried out using Synchrotron White Beam X-ray Topography (SWBXT). In this paper we report on the results of a more systematic study of the defect content of langatate boules carried out using Synchrotron White Beam X-ray Topography (SWBXT). This was achieved by examining as-grown boules in reflection geometry, and then by examining numerous wafers cut from adjacent locations in the boule in transmission geometry. This enables some insight to be gained as to the evolution of the three-dimensional defect microstructure, including the interface shape, during growth. We also report some preliminary results on the influence of microstructure on Q factors in langanite resonators.

Results and Discussion

Topography of Langatate Boule

The curved surface of the langatate boule was examined using SWBXT in reflection geometry. Topographs were recorded covering the entire length of the boule in longitudinal strips of approximately 5 mm in width. Following the recording of one image, the crystal was rotated by a few degrees in a clockwise direction (looking at the tail-end) and the subsequent topograph recorded. A schematic of the diffraction geometry is shown in figure 1(a) with an optical micrograph of the tail-end of the boule with the angular reference scale superimposed being shown in figure 1(b). Figure 2(a)-(h) shows a series of images recorded in the 0-90° quadrant, with an optical micrograph showing this aspect of the crystals being shown as figure 2(i). Figure 3(a) shows an enlargement from one of these images. Figure 3(b) shows a similar enlargement taken from one of the images recorded in the 180-270° quadrant. Growth striations, K, can be clearly observed on figures 3(a) and (b), as are precipitates, P. The precipitates appear to be concentrated towards the tail end of the boule corresponding to the last regions to crystallize. Optical microscopy was used to distinguish the precipitates from pinhole-like surface features that gave similar

contrast. Some additional surface artifacts are also present, such as the wavy lines shown at A. These correspond to channel-like indentations on the surface and do not appear to be crystallographic in nature. The vertical white bands shown on figure 3(b) are due to the existence of facets on the boule surface. These facets prevent the X-ray beam from reaching those regions, hence the local absence of diffracted intensity.

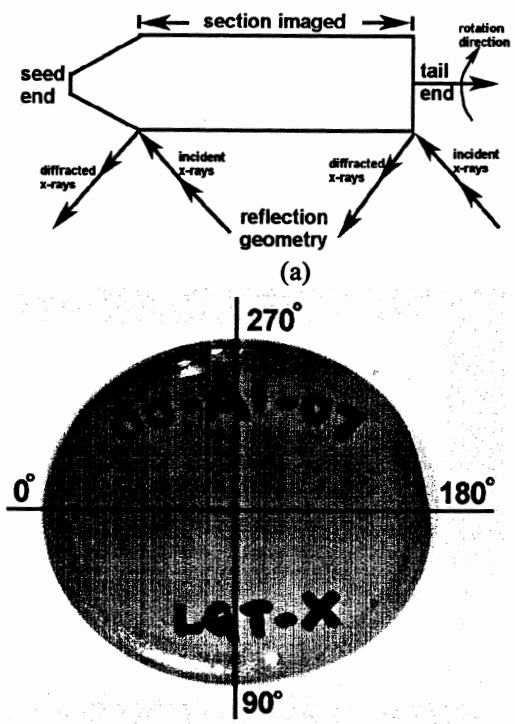

Figure 1 (a) schematic of diffraction geometry adopted for imaging of boule; (b) angular reference scale shown in reference to boule tail-end.

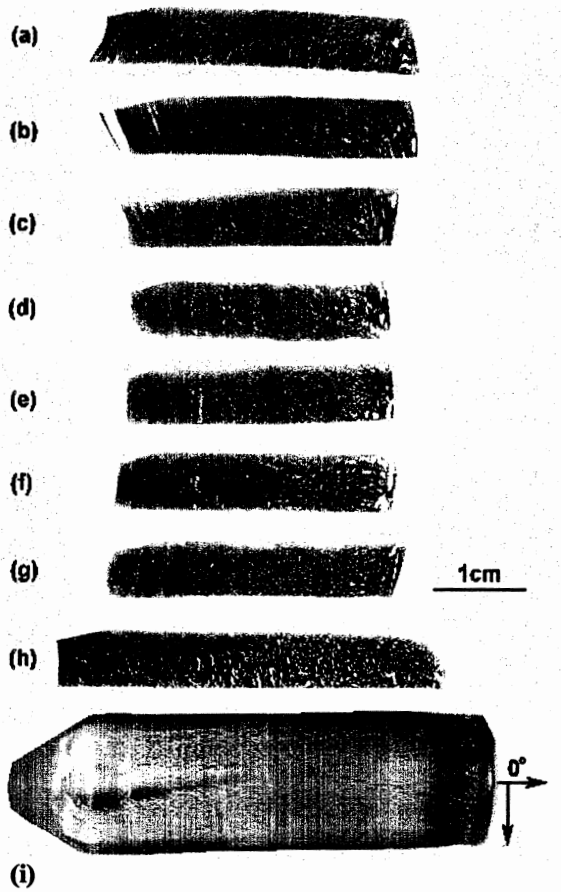

Figure 2. (a)-(h) SWBXT images recorded in the 0-90° range; (i) optical image of this aspect of the boule.

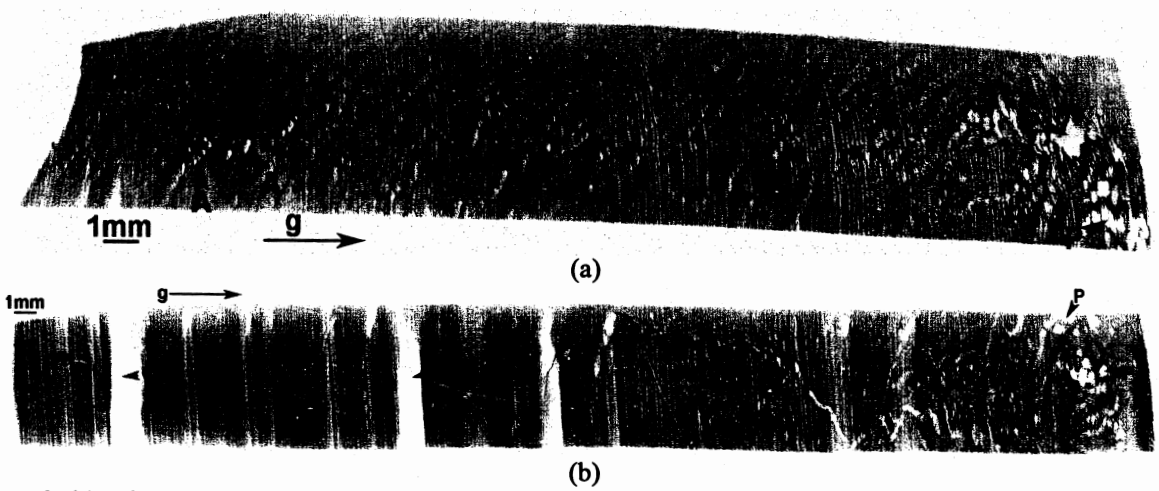

Figure 3. (a) enlargement of figure 1(a) showing striations, K, precipitates, P, and surface artifacts A; (b) similar images recorded from the 180-270° series. In this case the vertical features, C, are due to facets preventing the X-ray beam from hitting part of the crystal surface.

Topography of Langatate Wafers

Figure 4 shows a transmission topograph recorded from a wafer cut parallel to the [001] growth axis. This is one image from a series comprising five such images recorded from parallel wafers. Each of these images showed similar features. Note the striation images, which give an indication of how the interface shape evolved during growth. Figure 5 shows a transmission topograph, again one from a series (in this case comprising eleven wafers), recorded from a wafer cut perpendicular to the growth axis. This image gives a "snapshot" of the local interface shape in the wafer volume. Slight modifications were observed from wafer to wafer, reflecting the evolution of interface shape during growth. Note the irregular shape of the interface in the central region of the wafer, along with the attendant inhomogeneous distortion. Features similar to this were found in all such wafers. Dislocation slip bands that appear to originate from the inhomogeneous distortion generated by the irregular interface shape can be observed at B on figure 5. Figure 6 shows an enlargement of this region showing the slip bands more clearly.

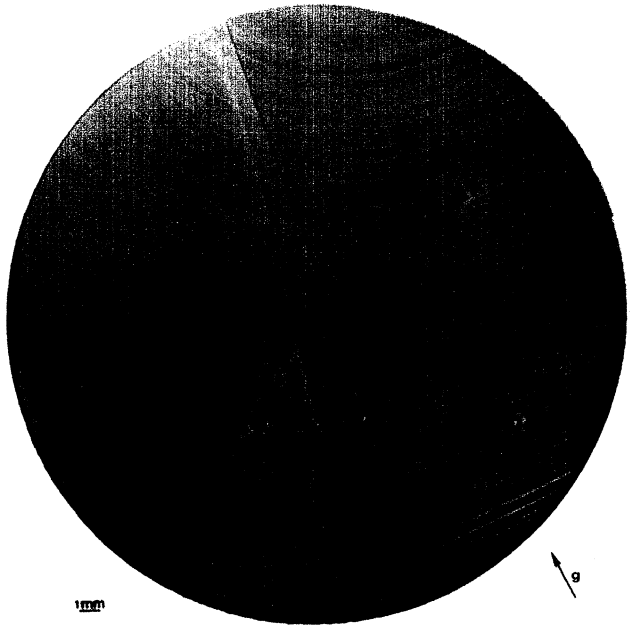

Figure 4. Transmission topograph recorded from a LGT wafer cut parallel to the growth axis. K indicates growth striations, while D indicates dislocations. Note the irregular interface shape at the various stages of the growth process.

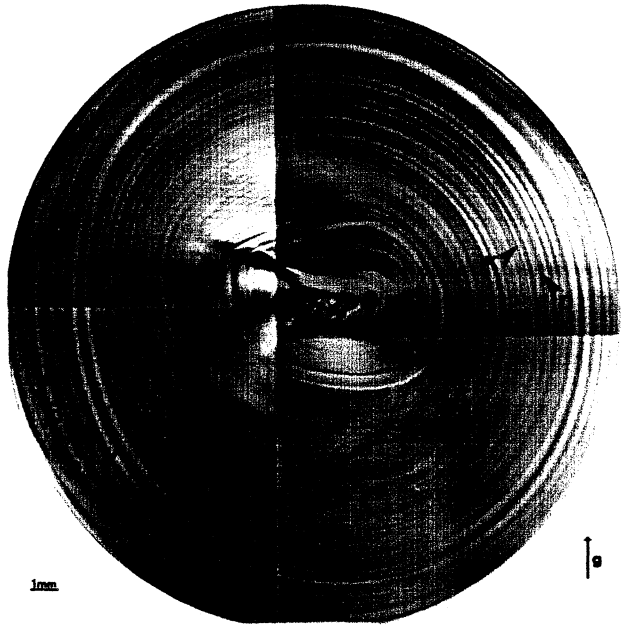

Figure 5 Transmission topograph recorded from a LGT wafer cut perpendicular to the growth axis. K indicates growth striations, D indicates dislocations, and B indicates slip bands.

Investigations into the exact origins of the striations are underway with a combination of different techniques. It is most likely that the striations reflect slight deviations in stoichiometry which appear during the growth process. These can result from the small size or even the complete absence of the field of congruent melting (where the melt composition is the same as the solid) due to the complexity of these ternary component systems.[3] The small but finite evaporation of G_2O_3 from the melt can also lead to stoichiometry fluctuations.[3] Energy dispersive X-ray analysis carried out in a Scanning Electron Microscope revealed no differences at various positions inside and around the striations. Further studies using Auger electron spectroscopy and infrared microscopy are also underway. Detailed SWBXT and High Resolution Triple-Axis X-ray Diffraction (HRTXD) studies are being carried out to determine the exact nature of the distortion associated with the striations. The HRTXD is being applied in view of its ability to distinguish between lattice rotations and strains. This will enable a model for the distortions associated with the striations to be developed similar to that which was recently developed for the case of growth striations in sulfur doped indium phosphide crystals.[4] Once the detailed nature of the striations has been determined, strategies

for their elimination during the growth process can be postulated in order to improve both crystal quality and resonator performance.

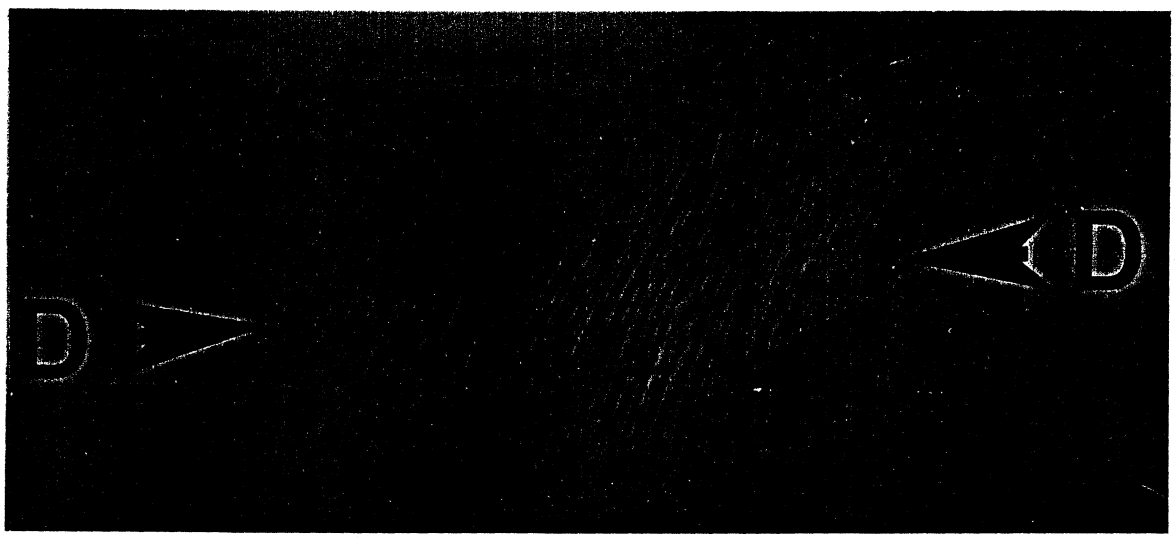

Figure 6. Enlargement of the lower central region of figure 5 showing slip bands.Note the numerous precipitates observed throughout the region (variously sized white spots).

Microstructure versus Q.f in Langanite Wafers

Q.f was measured for langanite resonators fabricated on wafers cut from two different langanate boules. Striations were visible in both sets of wafers, although the striation contrast observable from one of the sets was much weaker than the other. This can be clearly seen in figure 7, where much sharper striation images are visible in figure 7(a) compared to figure 7(b). This is potentially attributable to one or both of the following factors: an improved quality of surface polish for wafers from boule 4 or a superior inherent crystal quality. The highly irregular interface shape evolution observable in figure 7(b) would lend credence to the latter of these possibilities. Table 1 shows values of Q.f obtained for wafers from the two boules.

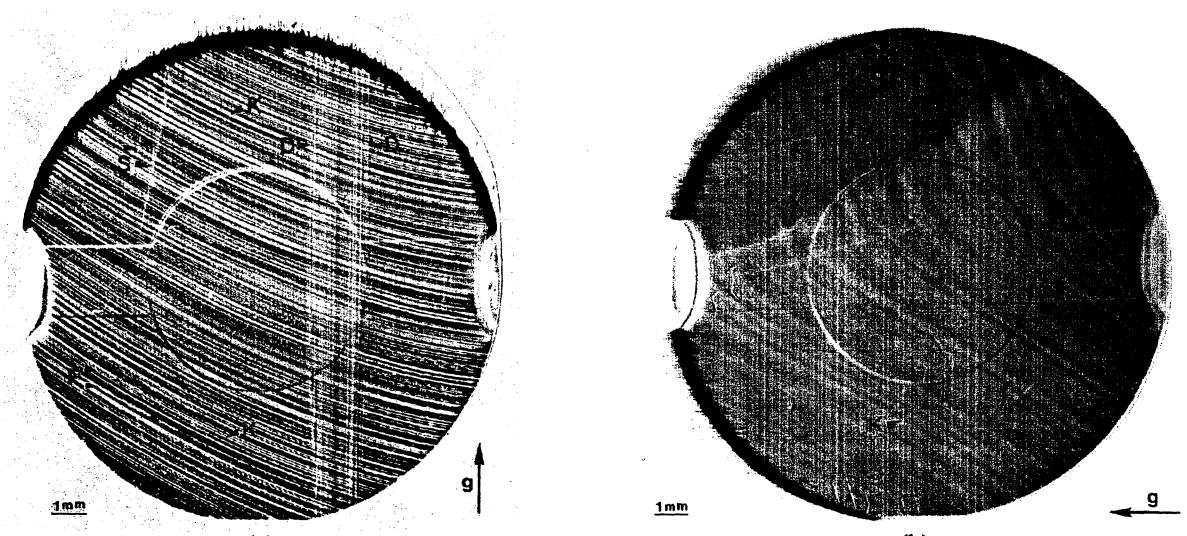

(a) (b)

Figure 7. SWBXT images recorded in transmission geometry from wafers with resonators fabricated upon them (a) sample number 2 from LGN boule 4; (b) sample number 10 from LGN boule 8.

There appears to be a systematic difference in Q.f values for resonators obtained from the two boules. Like the differences in striation contrast, at this point it is not clear whether the differences in Q.f may be attributable to differences in surface finish or inherent crystal quality. Further studies are underway. Similarly, the influence of growth striations on Q.f is not clear since both sets of wafers had observable striations. Further studies investigating the influence of the defect microstructure on the temperature independence of the resonators are also envisaged.

Boule	Sample Number	Q.f/1E06 MHz	
		5^{th} OT	7^{th} OT
LGN-4	2	16.0	18.2
	3	17.3	19.0
	5a	18.8	20.7
LGN-8	6	7.4	
	7	6.8	
	8	7.4	
	9	7.9	
	10	7.0	

Table 1. Q.f values measured for resonators fabricated on wafers cut from two different langanite boules.

Conclusions

Systematic SWBXT studies have been carried out of langatate boules, and wafers cut either parallel or perpendicular to the growth axis. This enables the overall three-dimensional distribution of defects and strains to be determined. The boule images revealed growth striations and precipitates. Wafers cut parallel to the growth axis enable insight into the evolution of the interface shape during growth. Significant irregularities were observed. Imaging of wafers cut perpendicular to the growth axis confirmed the irregularities in interface shape, and provided clear views of the highly irregular interface shape in the central region of crystal. This regions was found to be highly strained to the point where dislocation generation was visible. The detailed origins of the striations have not yet been determined, i.e., the exact nature of the deviations from stoichiometry. Further studies are underway. Measurements were made of Q.f factors for resonators made from crystal cut from two different boules. SWBXT images recorded from these two kinds of resonator revealed differences in striation contrast that could either be attributable to differences in either surface polish or inherent crystal quality. In a similar way, Q.f values for the two kinds of resonator shows systematic differences but again whether these differences were attributable to surface finish or inherent crystal quality was not clear. Further studies are underway.

Acknowledgements

Support is acknowledged from the U.S. Army Research Office under contract number DAAG55-98-1-0392 (contract monitor Dr. John Prater). Topography carried out at the NSLS, at BNL, which is supported by the U.S. Department of Energy Division of Materials Sciences and Division of Chemical Sciences.

References

[1] B. Capelle, A. Zarka, J. Detaint, J. Schwartzel, A. Ibanez, E. Philippot and J.P. Denis, "Study of Gallium Phosphate and Langasite Crystals and Resonators by X-ray Topography", Proceedings of 1994 IEEE International Frequency Control Symposium, IEEE, (1994), pp.48-57.

[2] A. Zarka, B. Capelle, J. Detaint, and D. Cochet-Muchy, "New Results on High Perfection Langasite Crystals: Studies of Crystalline Defects and Mode Shapes", Proceedings of 1995 IEEE International Frequency Control Symposium, IEEE, (1995), pp.629-637.

[3] B. Chai, J.L. Lefaucheur, Y.Y. Ji, and H. Qui, "Growth and Evaluation of LGS ($La_3Ga_5SiO_{14}$), LGN ($La_3Ga_{5.5}Nb_{0.5}O_{14}$) and LGT ($La_3Ga_{5.5}Ta_{0.5}O_{14}$) Single Crystals", Proceedings of 1998 IEEE International Frequency Control Symposium, IEEE, (1998), pp.748-760.

[4] H. Chung, Ph.D. Thesis, SUNY Stony Brook, (1997).

MEASUREMENT OF THERMAL CONDUCTANCE OF INTERFACES USING MICROWAVE RESONANT COMPOSITE DIELECTRIC STRUCTURES

Ling Hao and John Gallop
National Physical Laboratory,
Teddington TW11 0LW, UK

1. ABSTRACT

We show that the high Q composite dielectric resonator structure which we are developing –Refs 1-3 as a secondary microwave frequency standard also has the ability to provide straightforward accurate measurement of the thermal conductance of the interface between components of the composite resonator. This is potentially applicable to widely varying thermal conductance values over a broad range of temperature.

Thermal conductivity, interface, dielectric microwave resonator

2. INTRODUCTION

We have pioneered the use of composite dielectric resonators to provide high Q temperature compensated microwave oscillators as stable secondary frequency standards with low phase noise –Refs 1-3. These composite dielectric resonators employ a small number (n) of low loss single crystal dielectric components, each element i of the composite, possessing a temperature dependent permittivity $S_i=d\varepsilon_i/dT$, with some of the elements possessing S_i values with opposite sign, to provide temperature compensation of the resonant frequency of a selected mode. In the resonator structure these materials are joined either by a thin layer of adhesive, are mechanically clamped or joined by a more rigid bond such as fusion bonding.

The time independent temperature variation of the resonant frequency of the composite structure is determined by the microwave filling factors Γ_i for each element and the compensation temperature T^* at which $f(T)$ demonstrates a turning point where $df(T^*)/dT=0$ is given by

$$\sum_i \Gamma_i S_i(T^*)=0 \qquad (1)$$

The time dependent response of the resonant frequency for small temperature changes around T^* is governed by the thermal conductance K_i of the i components and of the interfaces between them, together with their thermal capacities C_i. If, for example, the stored microwave energy in the resonator is changed in a step-wise fashion at time $t = 0$ the time evolution of the frequency may be measured and, if the C_i are known, together with the R_i, then the thermal conductance K_i may be deduced from a simple multi component one dimensional thermal model of the resonator.

We develop this method in more detail below and present measurements of the thermal conductance of a polymer layer separating sapphire and rutile elements which we have used in the composite dielectric resonators.

3. THERMAL MODEL

We interpret the thermal properties of the puck according to a simplified 'lumped circuit' model shown schematically in Fig. 1, for which there are only two puck components. Since each component of the composite puck is made of single crystal dielectrics and these materials all possess rather high thermal conductivities in the temperature range of operation (~10K to 100K) it is valid to treat each component as if at any instant it is at a uniform temperature $T_i(t)$. Temperature differences will exist between the puck components which will be due to the thermal conductance between components and these differences are assumed to be much greater than any gradients within each component.

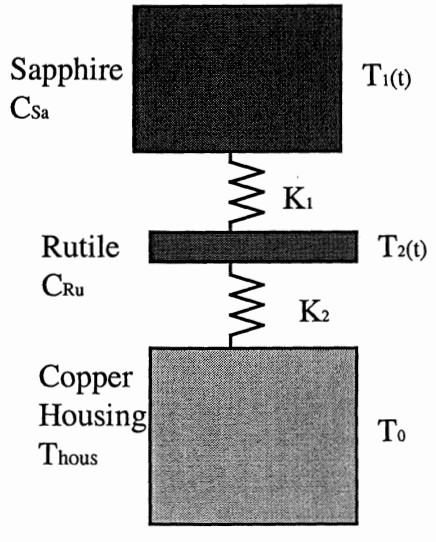

Fig. 1 Schematic of the thermal heat links between the two components of the composite puck and the heat bath, maintained at copper housing temperature T_{hous}.

To calculate the time dependence of the temperatures $\{T_i(t)\}$ we need to know both the thermal conductance K_1 (the thermal conductance between the sapphire and rutile puck components) and K_2 (between the heat bath, assumed to be maintained at T_{hous}, and the second element of the composite puck, in this case a rutile disc). In the case of the experiments reported below these conductances arise predominantly from the thin polymer adhesive layer which holds the components in contact.

In addition the heat capacity $\{C_i(T)\}$ of each puck component is required. For insulating single crystal samples these can be derived rather accurately from puck dimensions and the Debye expression for the specific heat, provided the Debye temperatures $\{\Theta_i\}$ of the components are known.

$$C_i = 9R\left(\frac{\pi^4}{15}\right)\left(\frac{T_i}{\Theta_i}\right)^3\left(\pi a_i^2 h_i\right)\frac{D_i}{M_i} \quad (2)$$

where a_i, h_i are the radius and height of the *ith* cylindrical component, whose density is D_i and molecular weight M_i.

To solve the time dependent problem a set of n coupled first order ordinary differential equations must be solved:

$$\frac{dT_1}{dt} = \frac{P_1(t) - K_1(T_2 - T_1)}{C_1}$$

$$\ldots\ldots \quad (3)$$

$$\frac{dT_i}{dt} = \frac{P_i(t) - K_i(T_{i+1} - T_i) + K_{i-1}(T_i - T_{i-1})}{C_i}$$

Here $P_i(t)$ is the (time dependent) power dissipated in the *ith* component which in general may arise from any form of heat but for our discussion represents the microwave power dissipation. The unknowns in these equations are in general the $\{K_i\}$. By solving the coupled differential equations numerically for guessed values of $\{K_i\}$ the optimum set of *values* may be deduced. Fig. 2 shows the calculated temperature dependence of the two components of a composite puck, based on the properties of the real puck described below. This shows how the temperatures would change for a large (~12 mW) change in input power to the resonator.

4. TIME DEPENDENT FREQUENCY OF THE RESONATOR

Having considered how the temperatures of the puck components vary with time under the influence of a change in the microwave power applied to the resonator we must now consider how these temperature changes

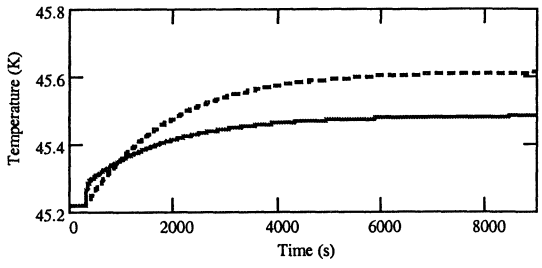

Fig. 2. Time dependent temperature changes for the two components of a composite puck. The solid line represents the rutile component and the dashed line the sapphire. Note the very different thermal time constants.

feed in to the observed time dependent oscillation frequency of the resonator. The frequency versus temperature relationship for a sapphire/rutile composite resonator may be calculated from equation (4) where Γ is the *rutile filling factor* (fractional electromagnetic energy stored in the rutile) and $\varepsilon_s(T)$ and $\varepsilon_r(T)$ are the temperature dependent relative permittivities for sapphire and rutile, respectively.

$$f(T) = f(0)\left[(1-\Gamma)\sqrt{\frac{\varepsilon_s(0)}{\varepsilon_s(T)}} + \Gamma\sqrt{\frac{\varepsilon_r(0)}{\varepsilon_r(T)}}\right] \quad (4)$$

Polynomial fits to experimentally determined temperature dependences of the permittivity $\varepsilon(T)$ of sapphire and rutile are used in equation (4). There exists a maximum in the $f(T)$ curve for all values of Γ. By choosing Γ appropriately the turning point temperature can be adjusted to be close to the value where Γ is desired to be known. Operating close to the turning point temperature makes the temperature stabilisation problem in these thermal conductivity measurements much less difficult.

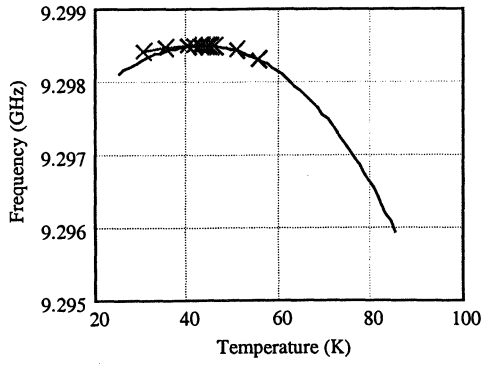

Fig. 3 Plot of the measured frequency versus temperature data for a rutile-sapphire composite puck resonator. The solid line represents a fit to equation (4).

From the T-derivative of equation (4) the relative frequency deviation for a 1 mK temperature deviation from this turning point has also been calculated for a range of Γ values –Ref. 3. Fig. 3 shows an experimentally measured $f(T)$ curve where the full line represents a fit to equation (4), treating Γ as a fitting parameter.

5. EXPERIMENTAL RESULTS

We have measured the frequency response of a high Q composite sapphire-rutile resonator based oscillator (of the type described above) as a function of time following a sudden change in the microwave power dissipated in the composite dielectric puck. The puck is made of a single crystal sapphire component bonded to a single crystal rutile disc using a thin layer (< 10 μm thickness) of a polymer adhesive –Ref. 4. The masses, dimensions and densities of the puck components are known and the starting temperatures are measured with calibrated resistive temperature sensors (Pt or Cernox). The entire time dependence of this two components system can then be fitted using the thermal model (equations (2) and (3)) and equation (4) of the frequency versus temperature relationship for a sapphire/rutile composite resonator described above.

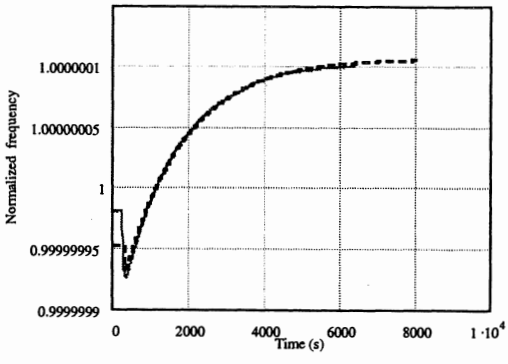

(a)

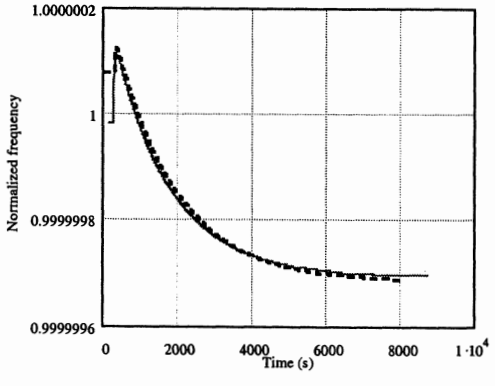

(b)

Fig. 4 experimental data (solid line) is fitted to two-component puck resonant frequency as a function of time (dash line), following a step change in microwave input power: (a) 5.3 mW, (b) 12 mW.

The data for two such runs and the fit to these data are shown in Fig. 4. The value of thermal conductivity k for the polymer adhesive deduced from these measurements is 1.21×10^{-6} W/mK at 45.22 K. This compares with values of 1×10^{-6} W/mK measured for a similar material, polystyrol -Ref 5.

6. SPEED OF MEASUREMENT

Note that frequency measurements of the loop oscillator may be made rapidly with high accuracy. Thus an Allan variance of 4 parts in 10^9 after a measurement time of only 20 μs has been demonstrated elsewhere –Ref. 6 with the composite sapphire-rutile puck system described in this paper. Since a change of microwave power level can easily induce a fractional frequency shift of parts in 10^6 (~10 kHz) it is clear that highly sensitive measurements of k may be made, even when the thermal time constants of the system are well below 1 ms. This is another feature which makes the method potentially attractive for a range of applications.

7. CONCLUSIONS AND FURTHER WORK

The proposed method has a number of advantages over conventional methods for measuring thermal conductivities. First the heat is introduced by a means (microwave irradiation) which does not require physical contact to the heated elements, thus reducing the influence of unwanted heat leaks through connected wires or supports. Second the dielectric puck components also act as the thermometers in the system, through the known temperature dependence of their permittivities and hence through the measured frequency versus time behaviour.

The method is particularly suitable for thin thermal barriers made from electrically insulating materials with poor thermal conductivity where conventional methods of applying well-defined temperature gradients are not suitable. We believe it will be possible to demonstrate that it is not restricted to such systems. Thus as long as the components on either side of the thin layer of material whose thermal conductivity is required have reasonably low (and known) losses at microwave frequencies, have considerably higher thermal conductance than does the thin layer, and possess relative permittivity temperature coefficients with opposite signs from one another then measurements are possible in any temperature range where these conditions are satisfied. It is not even essential to arrange the composite puck geometries to provide a turning point in $f(T)$ close to the operating temperature, although if this can be done the need for accurate temperature control is considerably relaxed.

REFERENCES

[1] F Abbas, J. C. Gallop and L.Hao, 'Microwave dielectric composite puck resonators' Applied Superconductivity (IOP Conference Publication 158) pp.315-8, 1997.

[2] J. C. Gallop, C. D. Langham, L. Hao and F. Abbas, "Dielectric loaded HTS resonators as frequency standards and low phase noise oscillators," *IEEE Trans. Instrum. Meas.*, vol. 46, pp. 122-125, April, 1997.

[3] L Hao, N Klein, J C Gallop, W J Radcliffe and I S Ghosh, "Temperature compensated cryogenic whispering gallery mode resonator for microwave frequency standard applications," *IEEE Trans. Instrum. Meas.*, vol. 48, pp. 524-527, April, 1999.

[4] "Opticlean", produced by Caliope Ltd. CB2 5LD, UK.

[5] F. Pobell, "Matter and methods at low temperatures", Springer (Berlin), p57, 1996.

[6] J. Gallop and L. Hao, "Further developments of a sapphire/rutile compensated dielectric resonator frequency standard" presented at 15th EFTF, March, 2001.

ACKNOWLEDGMENT

This work was supported under the UK Department of Trade Industry NMS Foundation Programme (project PF9834) and under the European Commission Framework 5 CSG Programme (FOAMS project).

FREQUENCY-TEMPERATURE CHARACTERISTICS OF THE PLAN-PARALLEL LANGASITE RESONATORS

I.Mateescu, J.Nosek*, L.Kretchmerova*, E.Tsoi**, A.Manea

National Institute of Materials Physics,
PO-Box MG-7, 76900 Bucharest-Magurele, Romania
*Technical University in Liberec,
Halkova 6, CZ-461217 Liberec 1, Czech Republic
**National Center for Scientific Research "Demokritos",
153 10 Ag. Paraskevi, Athens, Greece

1. ABSTRACT

This paper studies the mass-loading effect on the frequency-temperature characteristics of the plan-parallel Y-cut langasite resonators measured on 5MHz fundamental frequency, third and fifth overtones for various electrode thickness. Circular Sawyer Y-cut langasite blanks with 14mm diameter, Au electrodes with 7mm diameter and 100, 200, 300nm thickness were used in experiments. The resonant frequencies were measured in the temperature range - 35^0 C and $+100^0$ C. First, second and third order of the resonance frequency-temperature coefficients were computed for fundamental, third and fifth overtones. From measured fundamental and third harmonic resonance frequency were computed the electromechanical coupling factors. The results revealed that the fractional frequency variation with temperature approximates a parabolic function and that the influence of mass-loading on these characteristics is significantly lower than in the case of the AT-cut resonators.

2. INTRODUCTION

Langasite and its isomorphs have been recognized for a number of years as promising piezoelectric crystals which have the quite unique property of temperature compensation similar to that of quartz. Materials in the langasite family are of current interest for both bulk-wave and surface-wave devices. For frequency control applications it is necessary to have the weakest possible dependence of the resonator parameters on temperature.

Our study presents the results for plan-parallel Y-cut bulk-wave resonators because the thickness-shear vibration of Y-cut langasite resonators provides the minimum frequency variation with temperature in a large temperature range.

The temperature dependence of the resonant frequency of the bulk piezoelectric resonators is a function of the material constants which are temperature dependents, on thermal expansion coefficients, on coupling between the vibration modes and on the nature and thickness of the electrodes [Ref.1].

The temperature characteristics of the material constants and the thermal expansion coefficients depend on the orientation of the quartz plate [Ref.2]. The coupling between the vibrations modes is conditioned by the shape and size of the plate. The electrodes cause the mass-loading of the plate, they define the electrical conditions of the vibrations and determine small changes in the elastic properties of the plate [Ref. 3]

Some authors [Refs.4-7] revealed that the frequency-temperature characteristics are dependent on mass-loading caused by the metallic electrodes deposited on piezoelectric substrate. The electrodes define the electrical conditions of the vibration and change a little the effective elastic properties of the plate by means of which is modified the variation of the frequency with the temperature.

An experimental and theoretical study of the influence of the mass-loading (material and thickness of the electrodes) on the frequency-temperature characteristics of AT-cut quartz resonators was performed in the paper [Ref.8]. The results obtained in this investigation allow to conclude that the quartz plate and electrode parameters have a major influence on the frequency-temperature characteristics of the resonators.

Recently the measurements of the frequency-temperature characteristics of Y-cut plan-convex langasite resonators on fundamental frequency and on overtones were performed by Smythe [Ref.9]. One found that these characteristics are parabolic and that the turn-over temperature could be adjusted to a desired value by small changes in the Y-Y' angle.

In this paper the results of the experimental investigation of the frequency-temperature dependence of the plan-parallel Y-cut langasite resonators on fundamental, third and fifth harmonics are presented and the influence of the mass-loading (electrode thickness) on this dependence is considered.

The analysis of the measured frequency-temperature characteristics of the Y-cut langasite resonators revealed that the fractional frequency variation with temperature closely approximates a parabolic function and that the influence of mass-loading on these characteristics is significantly lower than in the case of the AT-cut quartz resonators. This result is similar with that obtain previously [Refs. 10,11] which found that the electrodes influence on the electrical parameters of the Y-cut langasite resonators is much smaller than that on AT-cut quartz resonators characteristics.

3. EXPERIMENTAL

For experiments Sawyer Y-cut plan-parallel polished langasite plates with 14mm diameter and 5MHz resonant frequency were used.

As-cut langasite wafers were lapped with 3μm alumina powder. Between lapping and polishing steps, langasite wafers were chemically etched in a $2HNO_3$:CH_3COOH solution for removal of disturbed layer due to mechanical treatment. Polishing process used slurry of colloidal alkaline suspension of silica gel (QUSO) on a Politex pad material [Ref.12].

On the resonators, whose characteristics are given in this paper, have been deposited by thermal evaporation in vacuum Au electrodes with diameter of 7mm and electrode thickness of 100nm, 200nm and 300nm. The frequency-temperature dependence in the temperature range -35^0 C and $+100^0$ C was measured for all three types of resonators (100, 200, 300nm electrode thickness). The frequencies of fundamental, third and fifth overtones were been measured in Saunders Temperature Test System by changing the temperature in steps of 5^0 C.

4. RESULTS

The frequency-temperature characteristic of the piezoelectric resonators is usually expressed by the relation:

$$f = f_0 [\, 1 + Tf_n^{(1)} (T-T_0) + Tf_n^{(2)} (T-T_0)^2 + Tf_n^{(3)} (T-T_0)^3 \,]$$

where f and f_0 are the resonant frequency at the temperature T and T_0 respectively and Tf_n^m are m-th order of temperature coefficient of frequency, n is overtone order.

For Y-cut langasite resonators the fractional frequency variation with temperature closely approximates a parabolic function.

The measurements show that on fundamental, third and fifth overtones the frequency-temperature characteristics are parabolic functions.

The frequency-temperature characteristic of resonator 7 measured on fundamental, third and fifth overtones frequencies is presented in figure 1. Similar dependences have been obtained for all resonators.

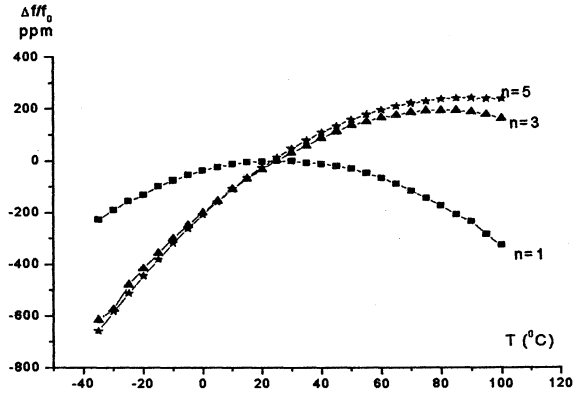

Fig. 1. Frequency - temperature characteristic of res. 7

The turnover temperature points of all measured resonators with different electrode thickness for fundamental, third and fifth overtones are presented in Table 1.

Table 1. Turnover temperature points

Res. number	Electrode thickness (nm)	Turnover temperature (^{0} C)		
		n=1	n=3	n=5
5	100	25	65	90
7	100	25	70	90
8	200	25	70	90
9	200	25	80	90
10	200	25	80	90
11	300	25	80	90
12	300	25	85	95

The first, second and third order of the resonance frequency-temperature coefficients and the turnover points of the curves were computed for fundamental, third and fifth overtones. The results are presented in Table 2.

We observe that the parabolic constants on fundamental and harmonics are close to 60.10^{-9}, value obtained for Y-cut langasite resonators in [Ref. 13].

Table 2. Temperature coefficients for n=1, 3, 5

Resonator number	$Tf_1^{(1)}$ x10^{-6}	$Tf_1^{(2)}$ x10^{-9}	$Tf_1^{(3)}$ x10^{-12}
5	-0.2832	-63.29	67.2
7	0.1246	-60.71	10.4
8	-0.8246	-60.13	58.4
9	-0.4261	-61.10	100.0
10			
11	-0.2423	-64.00	68.0
12	-0.0480	-68.00	4.0

Resonator number	$Tf_3^{(1)}$ x10^{-6}	$Tf_3^{(2)}$ x10^{-9}	$Tf_3^{(3)}$ x10^{-12}
5	6.216	-62.78	76.0
7	6.737	-59.10	-16.8
8	6.308	-62.50	36.0
9	6.698	-61.00	34.4
10	6.669	-62.02	36.8
11	6.599	-61.99	42.4
12	6.550	-58.10	16.8

Resonator number	$Tf_5^{(1)}$ x10^{-6}	$Tf_5^{(2)}$ x10^{-9}	$Tf_5^{(3)}$ x10^{-12}
5	7.216	-61.88	44.0
7	7.344	-61.40	39.2
8	7.314	-62.16	47.2
9	7.370	-62.18	46.4
10	7.392	-61.99	28.8
11	7.296	-62.10	50.4
12	7.420	-56.00	68.0

The electromechanical coupling factor k_{26} of the Y-cut langasite resonators were computed from the measured fundamental and third harmonic resonance frequency of the thickness-shear vibrations.

The temperature dependence of coupling coefficient k_{26} with temperature of resonators 7 and 11 is presented in figure 2. The difference between values of coupling factors of resonators 7 (100nm) and 11 (300nm) could be ascribed to the mass-loading effect.

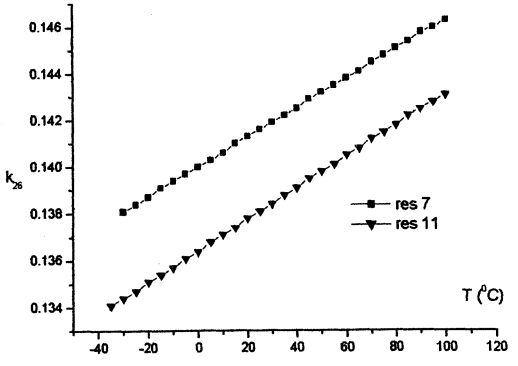

Fig. 2. Coupling coefficients vs. temperature

To study the mass-loading effect on frequency-temperature.characteristics of Y-cut langasite resonators the analysis of these characteristics on fundamental, third and fifth overtones frequencies for resonators with different electrode thickness was performed. The frequency-temperature dependence of resonators 7, 11 with minimum (100nm) respectively maximum electrode thickness (300nm) working on fundamental frequency is given in figure3.

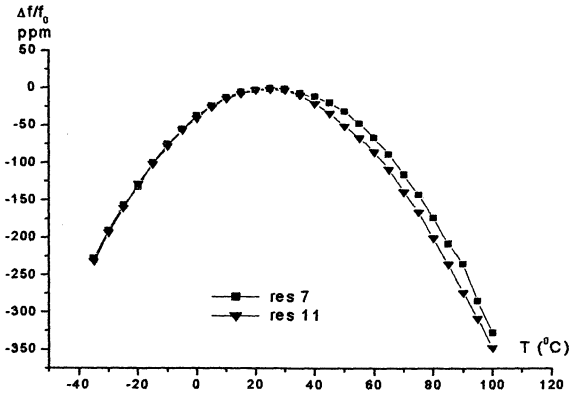

Fig. 3. Frequency-temperature characteristics of res. 7, 11 for n = 1

Figure 4 shows the frequency-temperature characteristics of the same resonators on third overtone and figure 5 on fifth overtone.

Analysing these figures we can conclude that the change of the frequency-temperature characteristics of Y-cut langasite resonators due to the electrode thickness variation is enough small for fundamental and third harmonic (16ppm respectively 12ppm) and higher for fifth overtone (29ppm).

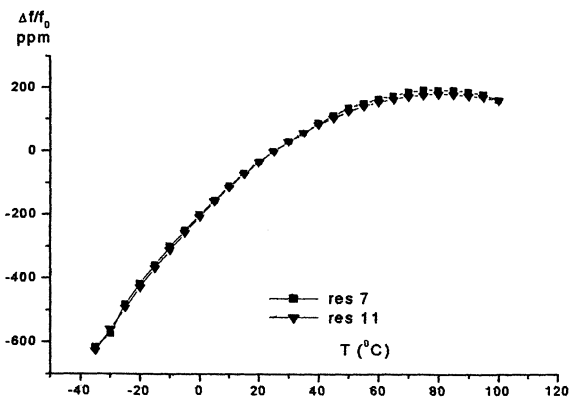

Fig. 4. Frequency-temperature characteristics of res.7, 11 for n=3

Comparing these results with the previous ones, obtained for AT-cut quartz resonators [Ref. 8] we can conclude that the mass-loading effect on frequency-temperature characteristics of Y-cut langasite resonators is smaller than that on AT-cut quartz resonators.

This result is similar with of our previous papers [Refs. 10,11] which found that the electrode influence on electrical parameters of Y-cut langasite resonators is much smaller than that on AT-cut quartz resonator characteristics

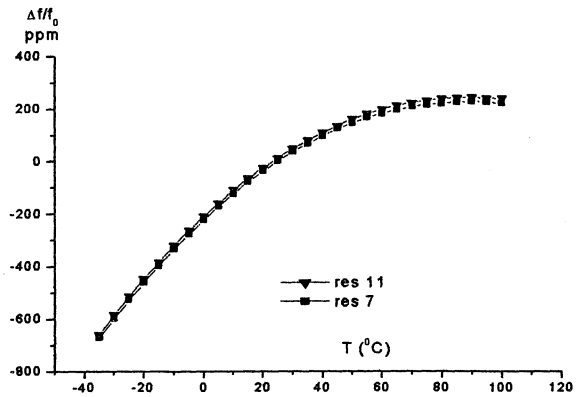

Fig. 5. Frequency-temperature characteristics of res.7, 11 for n = 5

4. CONCLUSIONS

The investigated Y-cut langasite resonators with various electrode thickness present an essentially parabolic frequency-temperature characteristic on fundamental, third and fifth overtone frequencies.

The turnover point temperature is almost constant for fundamental and fifth overtone and increases for third overtone may be due to the mass-loading effect. This conclusion have to be verify by new investigations.

The parabolic constants for all frequencies are similar with values obtained by others authors.

We suppose that the variation with temperature of the coupling coefficient is possible to bo related with mass-loadind change.

The mass-loading effect on frequency-temperature characteristics of langasite resonators is smaller than that on AT-cut quartz resonators.

5. ACKNOWLEDGMENTS

The authors would like to thank Dr. Gary Johnson for langasite blanks used in these experiments.

6. REFERENCES

1. J.Zelenka, The calculation of the resonant frequency temperature dependence of quartz bulk resonators, Proc.of 8th Piezoelectric Conference PIEZO' 94, Poland, 1994, pp. 49-60.

2. R.Bechmann, Frequency-temperature angle characteristics of AT and BT type quartz oscillators in an extended temperature range, Proc. IRE, No 48, 1960.

3. J.Zelenka, Piezoelectric resonators and their applications, Academia Prague, 1986

4. J.Zelenka, The influence of electrode on the resonance frequency of AT-cut quartz plates, Int. J. Solids Structures, Vol.11, 1975.

5. J.Nosek, J.Zelenka, Quartz strip resonator as a temperature sensor for mechatronics, To be published in Trans. on Ultrasonics, Ferroelectrics and Frequency Control.

6. A.D.Ballato, T.Lukaczek, Higher order temperature coefficients of frequency of mass-loaded piezoelectric crystal plates, Proc.29th Annual Symposium of Control Frequency, 1978, USA.
7. J.Pavlovec, J.Suchanek, J.Zelenka, The influence of the thickness of electrodes on the temperature - frequency dependence of AT-cut quartz resonators, 8th Piezoelectric Conference PIEZO' 94, Zakopane, Poland.
8. I.Mateescu, J.Zelenka, I.V.Mateescu, The effect of mass-loading on the frequency-temperature characteristics of fundamental AT-cut quartz resonators, Proc. European Frequency and Time Forum 1995, Besancon, France, pp. 443-446.
9. R.Smythe, R.Helmbold, E.Hague, K.Snow, Langasite, Langanite and Langatite bulk-wave Y-cut resonators, IEEE Trans. on Ultrasonics, Ferroelectrics and Frequency Control, Vol.47, No.2, March 2000, pp.355-360.
10. I.Mateescu, G.Johnson, M.Hatzakis, E.Tsoi, D.Tsoukalas, Mass-loading effect on quartz resonator parameters: recent results, Proc.3rd European Workshop on Piezoelectric Materials 2000, Montpellier, France, in print.
11. I.Mateescu, G.Johnson, A.Manea, I.Boerasu, The mass-loading influence on the electrical parameters of langasite resonators, Proc. European Frequency and Time Forum 2000, Torino, Italy, pp.234-238.
12. S.Laffey, M.Hendrickson, J.R.Vig, Polished and etching langasite and quartz crystals, Proc. of the IEEE Int. Frequency Control Symposium, USA, 1994, pp.245-250
13. J.Detaint, J.Schwartzel, A.Zarka, B.Capelle, J.P.Denis, E.Philippot, Bulk wave propagation and energy trapping in the new thermally compensated materials with trigonal symmetry, Proc. of the IEEE Int. Frequency Control Symposium, 1994, pp.58-71.

THE ANALYSIS OF NON-HOMOGENEITY OF SAW VELOCITY IN LANGASITE.

S.A.Sakharov, O.A. Buzanov, A.V.Medvedev,
"Fomos-Technology", Buzheninova St.16, Moscow, Russia

S.N.Kondratiev, E.Girardet,"Temex S.A.W." Puits-Godet 8, CH-2000 Neuchâtel, Switzerland

T.Thorvaldsson, "Thoronics" GmbH, Pré-Pond 6, CH-2022, Bevaix, Switzerland.

1. ABSTRACT

The researches results of the influence of different technology parameters of crystal growing and device manufacturing process on SAW velocity variation on langasite (LGS) wafers Ø 3'' are presented. The wafers were made from crystals grown by Czochralsky method along <00.1> and <01.1> directions. The paper also gives a technology process description of langasite crystal growing along <01.1> direction and of making Ø 3'' wafers. SAW velocity measurements were performed utilizing specially developed test structures. The test structures were also used to estimate the device sensitivity due to electrode-thickness and electrode-width variations of the manufacturing process.

Advantages of LGS wafers for possible SAW device applications are discussed. Due to good temperature stability and moderately high electromechanical coupling coefficient, langasite is known as a promising material for SAW devices. The filters on LGS have exhibited better electrical parameters than their analogues on quartz and lithium tantalate.

In order to demonstrate a practical filter application on LGS, a SAW filter at the center frequency of 114.99MHz was designed and realized. The chip fits into a 3.8x3.8 mm^2 SMD package. Measured performance is in excellent agreement with the predicted response and the chip size was dramatically reduced compared to the state-of-the-art for this kind of filters.

2. Single Crystal Growth

The procedure of initial charge preparation and langasite crystal growth is described in detail in our paper [1]. However, principal aspects have been revealed, which required a more detailed investigation.

The initial charge synthesis has been made by the method of self-propagating high temperature synthesis (SHS). Lanthanum oxide (99,99%), silicon oxide (99,99%), gallium oxide (99,99%) and metal gallium (99,999%) have been used as initial components. Substitution of gallium oxide for a part of metal gallium during the SHS process compared with that described in [1], made it possible to significantly increase the part of melted phase (up to 85%) and, consequently to decrease losses of easily volatile components caused by evaporation at the stage of melt homogenization. The total impurity contents in the charge did not exceed their level in the initial components (not over $5*10^{-3}$ mass. %).

Langasite crystals have been grown by using Czochralski method in "Kristall-3m" pulling machine along <00.1> and <01.1> directions. The usual "as grown" crystals had the inscribed circumference diameter of the cylindrical part equal to 82 mm and the total length over 150 mm. The crystal mass exceeded 4,0 – 5,5 kg. The growth process of langasite crystals having such dimensions is connected with many difficulties. It has been found, in particular, that the material of the crucible and its geometrical dimensions are very critical for obtaining high quality langasite crystals. Besides of this, thermal gradients in the crystallization chamber, the geometrical shape of the conical part of the crystal and cinematic process parameters exert especially strong influence on the quality of the grown crystal. Crystal grown proceeded with the availability of the close to flat crystallization front, which made it possible to avoid defects described in [2]. The problem consisted in the fact, that the growth of whole cylindrical part occurred with the close to flat interface boundary.

The "as grown" single crystals were subjected to high temperature annealing after growth on the air.

3. The Synchronous SAW Resonator Analysis

We have analysed the admittance performance of a synchronous one-port resonator structure realized on two different cuts of langasite crystals: yxlt/48.5°/26.6° and yxlt/50°/25°. Fig.1 shows a schematic drawing of the synchronous surface acoustic wave (SAW) resonator used.

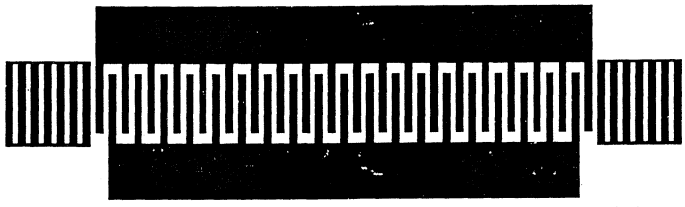

Fig.1 A schematic drawing of the synchronous SAW resonator.

The number of electrodes for the interdigital transducer (IDT) and gratings are equal to 299 and 100, respectively. The pitch is equal to 18μm, the aperture of the IDT is equal to 8λ (where λ is a wavelength of the IDT at the center frequency).
The wafer parameters are presented in the Table 1

Table 1

Wafer number	Crystal orientation	Requested Al thickness, μm
1	yxlt/48.5°/26.6°	0.1
8	yxlt/50°/25°	0.1
15	yxlt/50°/25°	0.52
23	yxlt/48.5°/26.6°	0.52

Both crystal orientations have a coupling coefficient in the range 0.34-0.37% (which is 3-3.5 times higher than for quartz), the TCF=0 and the diffraction coefficient is about –1.0 [3].

The goal of the experiment was:
1) The estimation of the COM-parameters of langasite crystals,
2) The estimation of the velocity variation on the wafers,
3) The simulation and realization of a SAW device with a unique performance, on langasite crystal.

4) The estimation of the sensitivity of SAW devices to process parameters
5) The estimation of bulk acoustic wave radiation.

The Figure 2 presents the measured and fitted curves of the admittance of a synchronous SAW resonator realized on yxlt/48.5°/26.6° cut (wafer 23, Table 1).

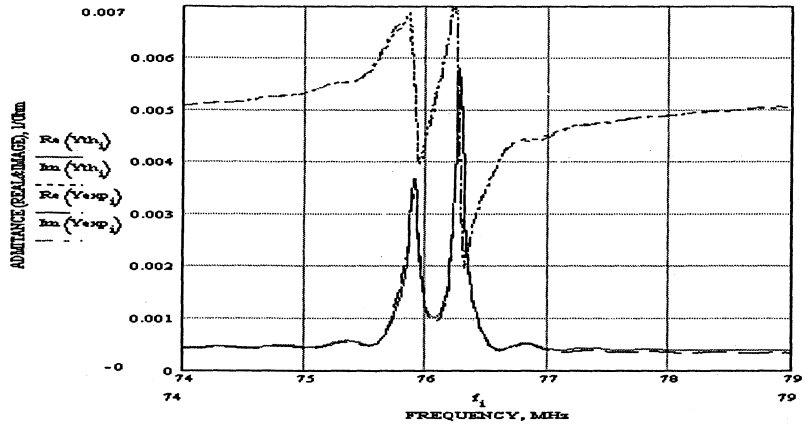

Fig.2 The measured and fitted curves of the admittance of SAW resonator (real and imaginary part)

The dual admittance performance shows that both cuts have a "natural" unidirectional directivity behavior. The bulk acoustic wave radiation is very low because in the admittance performance we observe no additional peaks in a wide frequency range. The measurements of wafers 1 and 8 were used for phase velocity estimation across the wafer. For the Al thickness of about 1.44% of a wavelength and m/p in the range 0.5-0.6 we have estimated the sensitivity of SAW devices to thickness and electrode width variation as :

4.9±1.9 ppm/nm for sensitivity of SAW devices to thickness control,

13±5 ppm/0.01m/p for sensitivity of SAW devices to electrode width control,

m/p=(electrode width)/pitch is the mark to period ratio

Both values are positive. It means that high Al thickness and m/p corresponds to highest velocity.

On the contrary, for Quartz, Lithium Niobate and Lithium Tantalate devices the sign of both coefficients is negative.

The 3-dimensional plot of the center frequency variation over a wafer is shown in Fig.3-Fig.4. The SAW resonators are shown on the surface of the wafer in 4 columns.

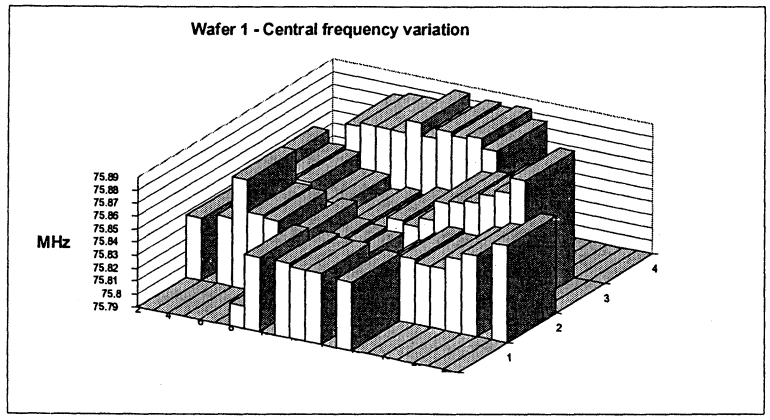

Fig.3 A 3-dimensional plot of the center frequency variation on wafer 1.

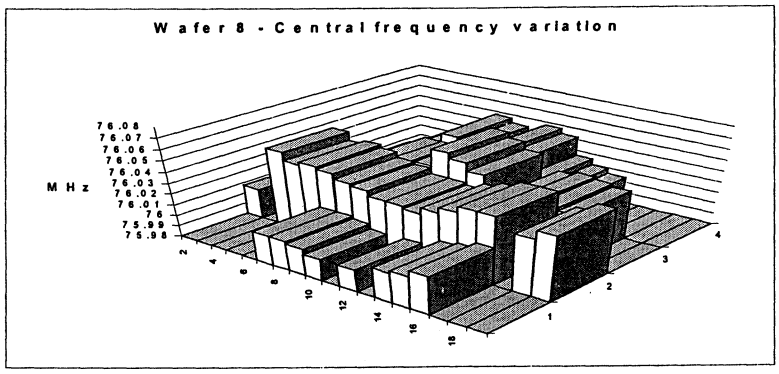

Fig.4 A 3-dimensional plot of the center frequency variation on wafer 8.

We have measured the thickness variation on the wafers 1 and 8. For both wafers the thickness variation due to manufacturing process is in the range 738 –1096 Å. As a result the frequency shift due to thickness variation is about 175.5 ppm. Additional 20 ppm shift is estimated to be due due electrode width variation.
According to the statistical analysis of the centre frequency on the wafers 1 and 8 the standard deviation is in the range 216.2-255.2 ppm. It means that the real phase velocity variation on wafer is about 50-70 ppm across the wafer.
We have modelled and realized a SAW filter for a CDMA application on the frequency 114.99 MHz. The chip fits into a 3.8x3.8 mm^2 SMD package, but for the specific experiment we used 5x5 mm^2 package. Usually standard CDMA filters are realised in 13.3x6.5mm^2 SMD packages. The Fig.5- Fig.6 show the measurement of the SAW filter on top of the simulated response. The 0.5 dB bandwidth of the SAW filter is about 1.5 MHz, the minimum insertion loss is measured to be 7.9 dB and the group delay variation is less than 50 ns. A simple parallel inductor matching circuit was used for impedance matching purposes.

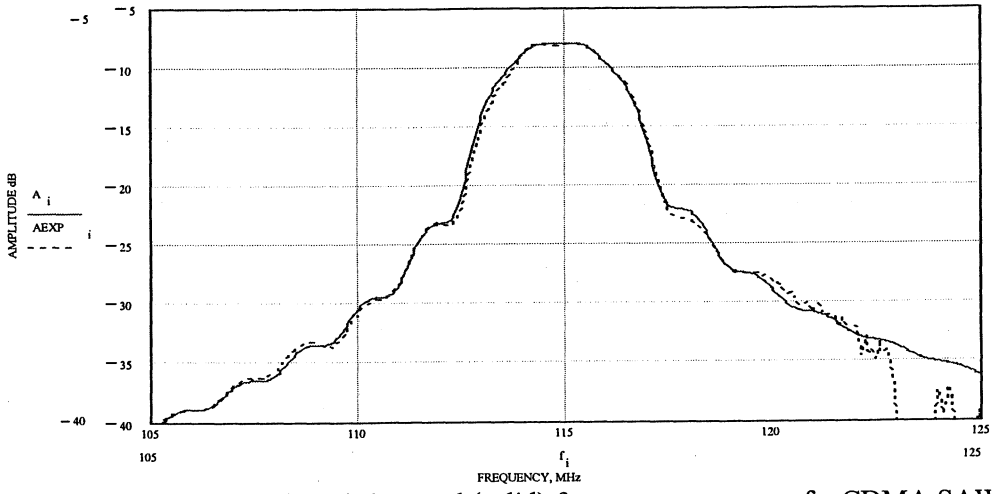

Fig 5 Measured (dotted) and simuated (solid) frequency response of a CDMA SAW filter.

Fig.6 shows a wider frequency range demonstrating the bulk wave activity for frequencies at the higher frequency wing (125-140MHz). The simulations do not include the modeling of the bulk wave activity. Looking still wider up in frequency we observe a clean response (see Fig.7) and rejection up to 60dB. The requested Al thickness of this device is about 800 Å. As a result the frequency shift in the temperature range ±50 °C is about 20 kHz (180ppm) for this specific filter. The frequency shift due to 5% thickness variation and 0.01 m/p is 2.3 kHz (20 ppm) and 1.5 kHz (13 ppm) respectively. The frequency shift due the phase velocity variation across the wafer is about 70 ppm. The total frequency shift is less than 283 ppm (32.5 kHz).

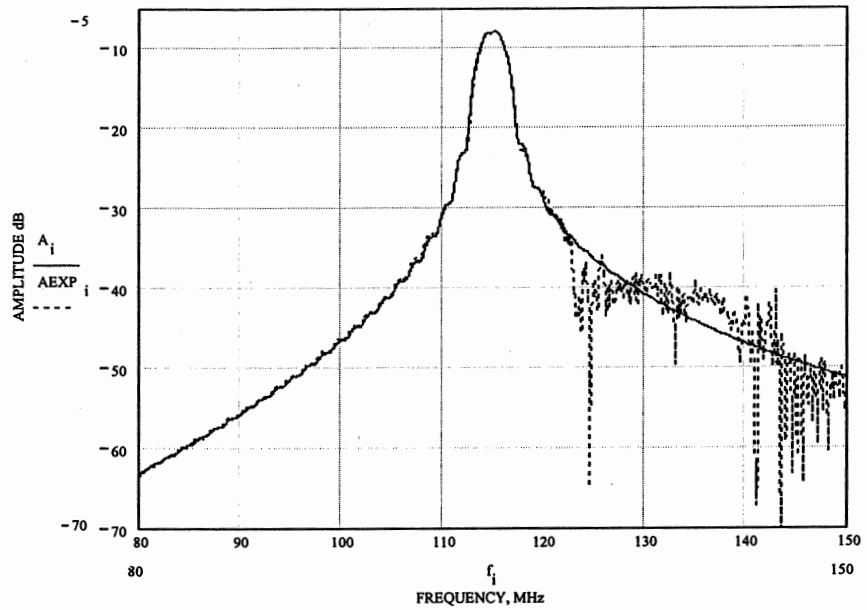

Fig.6 Measured (dotted) and simulated (solid) frequency response of a CDMA SAW filter for wide frequency range.

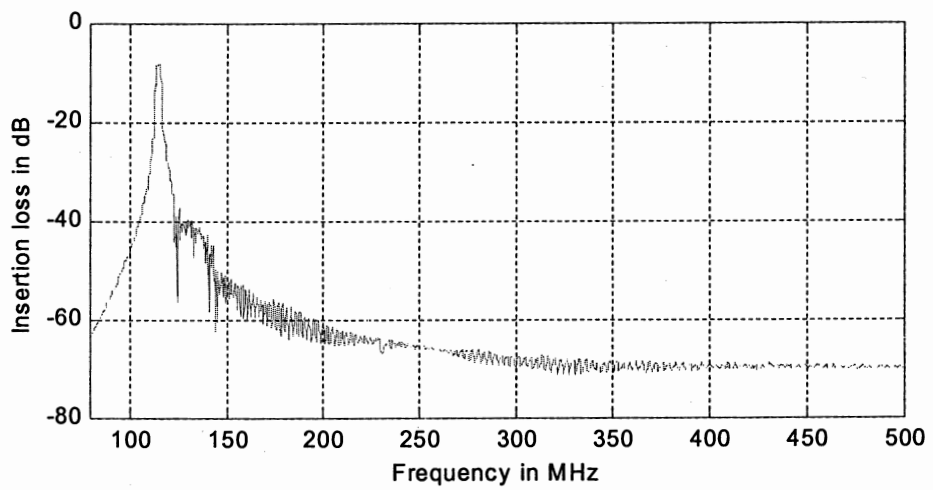

Fig.7 Measured (dotted) and simulated (solid) frequency response for wide frequency range

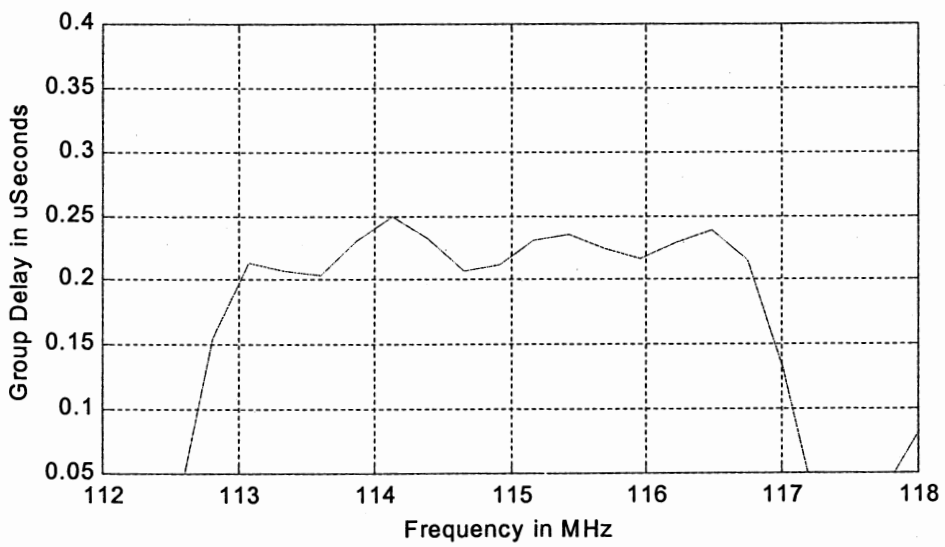

Fig.8 The group Delay of CDMA SAW filter in a narrow frequency range.

4. The Bulk Wave Activity

On the cut of Langasite investigated in the present paper, the situation for bulk wave activity is quite different to what we experience on other substrate materials e.g. $LiTaO_3$. One advantage of Langasite is in low bulk wave excitation. In reference [4] experimental results were presented concerning bulk wave activity on 42°-$LiTaO_3$ [5] and 36°-cut of $LiTaO_3$. It was found that the bulk wave activity is higher on the 36-degree cut compared to the 42-degree cut and as a result the insertion loss is higher on the 36-degrees cut. Additionally, the interaction between the surface acoustic wave and the reflected bulk wave from the substrate backside causes increased ripple on the 36-degree cut. Especially for impedance element filters when the length of an impedance element is much longer than the thickness of the substrate material additional attenuation due to interaction between surface acoustic wave and bulk wave is measured. The results shown in Fig.3 of reference [4] which were obtained by fitting experimental data to theory clearly confirms the above statements.

Utilizing rotation angles between 42°- and 60° of rotated Y-cut $LiTaO_3$ will also give us improved insertion loss performance because the bulk wave activity is reduced. Actually for each metal film thickness and mark-to-period ratio used for design, there is a different optimum of cut in terms of minimizing bulk wave activity.
For the Langasite-cut investigated in this paper, bulk wave activity does not depend as much on the thickness used and the interaction of bulk waves and acoustic waves is less compared to the rotated cuts of $LiTaO_3$.

5. Conclusions

The langasite crystal is an excellent material for many SAW applications. The main advantages of langasite are:

1) Higher coupling coefficient compared to quartz,
2) Low phase velocity (small size),
3) Low diffraction,
4) Temperature coefficent TCF=0,
5) Low sensitivity to process parameters. This is mainly due to the fact that there is a kind of "self-stabilizing" effect taking place. Variations of velocity and reflectivity due to mass loading have a different sign compared to the electrical loading terms and for a certain range of Al film thickness this helps lowering the sensitivity to process parameters on the investigated crystal cut.
6) Low level of excitation of bulk acoustic waves.
7) A non-pyroelectric substrate.

References

[1] O.A.Buzanov, A.V.Naumov, V.V. Nechaev, S.N. Knyazev. New approach to the growth of langasite crystals. Proc. 1996 IEEE Int. Frequency Control Symp., p. 131
[2] O.A.Buzanov, A.V.Naumov, V.V. Nechaev, S.N. Knyazev. New approach to the growth of langasite crystals. Proc. 1996 IEEE Int. Frequency Control Symp., pp. 131-136
[3] N. F. Naumenko, L. P. Solie, "*Optimal Cut of Langasite for High Performance SAW Devices*", Proc. IEEE International Ultrasonics Symp., pp. 243-248, 1999.
[4] S. N. Kondratiev and T. Thorvaldsson, "Influence of Bulk Wave Excitation on Performance of Impedance Element SAW Filters Realised on 36° and 42°- $LiTaO_3$ Substrates", *IEEE Ultrasonics Symposium Proceedings*,1999, pp.317-320.
[5] K.Hashimoto,M.Yamaguchi,S.Mineyoshi,O.Kawach,M.Ueda,G.Endoh,O.Ikata,"Optimum Leaky SAW Cut of LiTaO3 for Minimised Insertion Loss Devices", *1997 IEEE Ultrasonics Symposium Proc.*, pp.245-254.

POSTERS A

SENSORS

Young's Modulus Tester Using a Quartz-Crystal Tuning-Fork Tactile Sensor

Hideaki Itoh and Goro Kanbe

Shinshu University, 4-17-1 Wakasato, Nagano 380-0922, Japan

Abstract- Sample materials of five kinds of metals (slide glass, aluminum, brass, stainless steel, and copper) were used in this contact experiment. The frequency of quartz-crystal tuning-fork tactile sensor increased in the order listed above when the sensor's base got brought into contact with flat surface of materials in such a way that the base of the tuning fork was pressed by a strong lateral force induced in acrylic resin case. These results have been found to correspond with Young's modulus of these materials. This sensor functions as a Young's modulus tester by only observing its frequency.

1. Introduction

The piezoelectric tactile sensors so far proposed are classified, according to their adopted vibrating modes, into two types; longitudinal[1-2] and flexural vibration-mode sensors[3]. Both of them make use of the change in frequency induced when their vibrating sections get brought into contact with an object. On the other hand, the sensing mechanism of the quartz-crystal tuning-fork tactile sensor[4-5] used in this study comprises two principles as follows: one is that, when the sensor's base gets brought into contact with an object, the difference in acoustic impedance between the quartz resonator and the object will cause the longitudinal vibration energy to leak from the sensor's base to the object, which leak will then cause the quartz-crystal tuning-fork impedance at resonant vibration; the other is that the impedance change depends on the energy leaking from contact area corresponding to the roughness of the object. This sensor is capable of distinguishing a lot of materials from one to hard ones like metals, and is also another, ranging from soft ones like silicone rubber capable of distinguishing materials from one another in quality and surface roughness, besides softness and hardness[4-5]. This sensor was capable of sensing the paper quality[6] based on the later principle described above. These results mentioned above shows the experimental facts in the case of an application of a week lateral clamping force onto the base of a sensor with acrylic resin case. On the other hand, for an application of a strong lateral clamping force onto its base, no impedance change is observed but the frequency change yields in the order of about 100 mHz according to Young's modulus of an object before and after the sensor's base to an object in contact.

Two methods have existed in the field of measuring Young's modulus of materials; one is to measure the velocity of elastic wave traveling in a material cut in a rectangular rod's form and another is to measure strain induced in an application of stress on a material cut in a rectangular rod's form. In this paper, quartz-crystal tuning-fork tactile sensor was tested in view of its frequency for its ability to measure Young's modulus except two methods mentioned above when the base is brought into contact with an object.

2. Experiments and Discussion

The tactile sensor and measurement system used in this study are identical to those previously described[4-5].

Figure 1 shows the structure of the tactile sensor fabricated. The quartz crystal blank was held in acrylic resin case. The section, in the base of the quartz-crystal tuning fork, corresponding to the nodal point of the flexural vibration, was clamped by an acrylic resin case. For this experiment, the base of a sensor was fitted into narrower slit of the clamping portion of the case to produce a stronger lateral clamping force in its base than usual one.

Contact experiments with the tactile sensor require a fixed stand capable of keeping the condition of contact unchanged with repetitive contact examinations. A fixed stand as shown in Fig. 2 was used in this experiment. A weight of the set of the sensor, clip, and bar shown in Fig. 2 is 50 g. In the case of an application of a load onto the sensor, weights are added on the plate fixed on the top of bar as shown in Fig. 2.

Figure 3 shows the measurement system used in this experiment. The frequency of the sensor was obtained with an impedance analyzer (HP-414A), to which the lead wires of the quartz-crystal tuning-fork tactile sensor was connected, and which used a built-in program to calculate equivalent circuit constants from

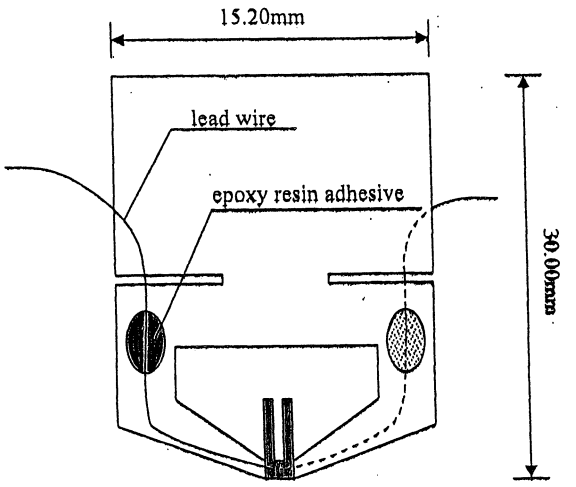

Fig.1 Structure of the tactile sensor

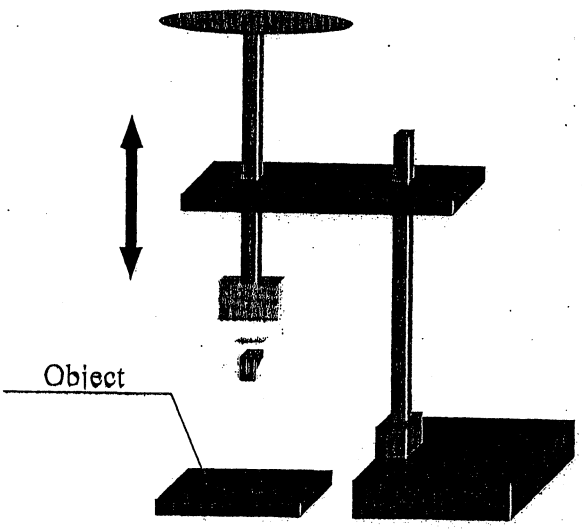

Fig.2 Fixing stand

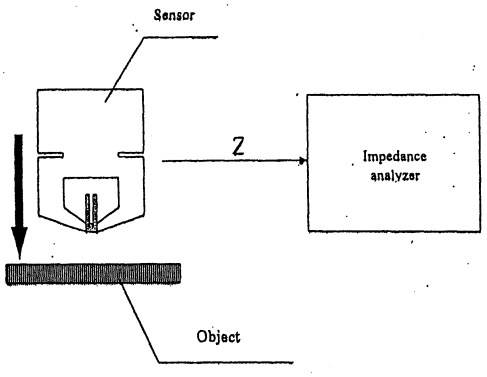

Fig.3 Measurement system

measured impedance characteristics for executed frequency variations. The frequency of the sensor, as measured with the impedance analyzer, is caused to increase several hundreds mHz for the 32.768 kHz quartz resonator by contact operation.

For frequency measurements, the quartz-crystal tuning-fork tactile sensor was applied on the following samples: slide glass (76.0×26.0 ×1.2 mm), aluminum (30.0×20.0×12.0 mm), brass (41.0×39.0×5.3 mm), stainless steel (58.0 ×58.0×5.0 mm), and copper (16.0 ϕ ×14.0 mm) under application of 50gG, 75gG, and 125gG load onto the sensor. The measured values are shown in Fig. 4, with Young's modulus of an object on the X-axis and the frequency of the sensor on the Y-axis. As seen from Fig. 4, the frequency changes exponentially according to Young's modulus of materials in the order listed above. No impedance change is observed with repetition of contact examinations. The frequency of the sensor depends on a load, as shown in Fig. 4. Based on the later principle described above, it may be concluded that the sensor's base closely gets brought into contact with the surface of an object on an application of a load onto the sensor so clearance decreases gradually.

The contact experiment has revealed that there is a high correlation between the frequency change of this sensor and Young's modulus of materials.

3. Conclusion

The authors have developed a tactile sensor capable of measuring Young's modulus of materials, which makes use of the increase in quartz-crystal tuning fork frequency at resonant vibration while the base of its quartz-crystal tuning-fork for wrist watch application is in contact with flat surface of materials. Experimental findings are as follows. (1) The contact experiment with slide glass, aluminum, brass, copper, and stainless steal, has revealed that the frequency increases exponentially according to Young's modulus of the object brought into contact with the base of the tuning fork. (2) The contact experiment with five kinds of metals,

under application of a load onto the sensor, has revealed that the frequency increases slightly with a load. (3) The contact experiment has revealed that with the sensor's base weekly held in an acrylic resin case the impedance increases but the frequency does not change, while for its base strongly held the frequency increases according to Young's modulus of an object but the impedance does not change.

It may be concluded from the above findings that this tactile sensor may enable us to read Young's modulus of materials directly by only observing its frequency, which has been beyond the power of the conventional Young's modulus testers.

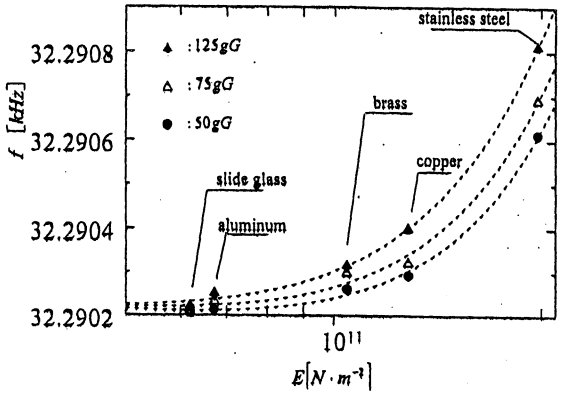

Fig.4 Frequencies measured with various materials brought into contact with the base vs. Young's modulus as a function of a load applied on the sensor.

References

1) S. Omata: Sensor Technol. **10** (1990) **27** [in Japanese].

2) H. Itoh, N. Horiuchi and M. Nakazawa: *Proc. 1996 Frequency Control Symp.* (IEEE Inc., Pistcataway, 1996) p. 572.

3) T. Kosawada: Ultrason. Technol. **9** (1997) **25** [in Japanese].

4) H. Itoh, M. Nomura and M. Nakazawa: *Proc. 12th European Frequency and Time Forum, 1998*(Tele & Radio Research Institute, Warszawa, 1998) p. 430.

5) H. Itoh, M. Nomura and N. Katakura: Jpn. J. Appl. Phys. **35** (1999) 3225.

6) H. Itoh, M. Nomura and N. Katakura: *Proc. 1998 Ultrason. Symp.* (IEEE Inc., Pistcataway, 1998) p.559.

POSTERS A

SAW

GENERALIZATION OF FREQUENCY ELEMENT FACTOR CONSIDERING THE SAW VELOCITY DISPERSION EFFECT

Yuri Abramov

Soliton, Har Hatzofim 24/4, Holon 58492 Israel, email: yuri_a@netvision.net.il

1. ABSTRACT

The frequency element factor is modified for the assumption the SAW wave propagates with different wave-numbers within an electrode and within an inter-electrode gap. This generalization explains the SAW spectrum behavior for high harmonics and especially for the SAW devices made up on piezo-film.

Modified frequency spectrum

2. INTRODUCTION

The quasi-static approach simplifies the analysis of generalized SAW transducers [– Refs 1, 2]. This approach is based on the assumption the charge density is dominated by an electrostatic term, defined as a charge density obtained when an acoustic wave excitation is ignored. Considering the SAW wave propagation with wave-number κ, that does not depend on coordinate x along the direction of the SAW wave propagation, the frequency spectrum of the SAW acoustic potential is expressed through the Fourier transform of the charge distribution density. However the simplest approximation of the SAW wave-number with κ_e within electrode and κ_g within inter-electrode gap generalizes the definition of the acoustic potential frequency spectrum.

3. QUASI-STATIC APPROACH

The quasi-static approach is based on the assumption the charge density is dominated by an electrostatic term, defined as a charge density obtained when acoustic wave excitation is ignored. The frequency spectrum of the SAW acoustic potential $\varphi_a(\omega)$ on the left port of the radiating transducer is expressed through the Fourier transform $R(\kappa)$ of the charge distribution density $\rho(x)$:

$$\varphi_a(\omega) = j\,\Gamma_s\,R(\kappa) \qquad (1)$$

where

Γ_s is a constant, that depends on the piezoelectric material and cut; this factor is a measure of the piezoelectric coupling of the substrate material;

j is an imaginary unit;

ω is a cycle frequency;

κ is a wave-number, $\kappa = \omega / v$;

v is an effective SAW velocity;

$R(\kappa)$ is the Fourier transform of the charge distribution density $\rho(x)$.

The quasi-static approach assumes the $\rho(x)$ is the electrostatic charge distribution density.

The superposition method for the function $\rho(x)$ definition may be used for an infinite periodical electrode grating, i.e.

$$\rho(x) = \sum_n A(n)\,\rho_o(x - np) \qquad (2)$$

where $\rho_o(x)$ is a basic function and $A(n)$ is the n-th weight, associated with the n-th period of the grating, p is a grating period. So the function $R(\kappa)$ is written as:

$$R(\kappa) = R_o(\kappa) \sum_n A(n)\exp(-j\kappa np) \qquad (3)$$

where $R_o(\kappa)$ is a frequency element factor, defined as the Fourier transform of the basic function $\rho_o(x)$. Herein we assume that the wave-number of the SAW excited by the oscillated charges, distributed as the basic function $\rho_o(x)$, is the same as the wave-number of the SAW excited by the oscillated sum charges, distributed as the result function $\rho(x)$.

4. GENERALIZATION

Till now it was assumed that the SAW wave propagates with the wave-number κ independent on coordinate x. However the electrode grating assumes that the electrical and mechanical boundary conditions depend on the coordinate x along the direction of the SAW propagation and thus the SAW velocity dispersion effect has place around the electrode-gap boundaries. The simplest approximation of the SAW wave-number with κ_e within electrode and κ_g within inter-electrode gap suggests itself [– Ref. 9]. Let then κ be an effective wave-number and r be a ratio $r = \kappa_e / \kappa_g$. In this case the SAW potential $\varphi_a(\omega)$ is described by the modified spectrum function $R_o(\kappa,r)$ instead of $R_o(\kappa)$. The physical meaning of the function $R_o(\kappa,r)$ is a modified frequency spectrum of the SAW excited by oscillated basic distributed charge $\rho_o(x)$, therewith the SAW propagates with the wave-number κ_e within electrodes and κ_g within gaps. Such a generalization of the element factor

becomes essential for high harmonics, when the difference between κ_g and κ_e is expected to be significant, especially for devices working on piezo-films.

5. MODIFIED FREQUENCY ELEMENT FACTOR

Let us consider the classic electrostatic basic charge distribution $\rho_o(x)$, where the zeroth finger in the periodical electrode grating has the voltage equal to **1** and all other fingers are grounded. We admit the following assumptions.

- The infinite periodical sequence of the parallel electrodes is placed in *(X, Z)* - plane. The intervals occupied by the electrodes along the *X*-axis are (a_n,b_n). The *X*-axis' s zero point is chosen at the center of the zeroth electrode, so $a_0 = -b_0$. An electrode width equals w, $w = b_n - a_n$, and the grating period equals p, $p=b_n - b_{n-1}$ **(Figure. 1).**
- The upper half-plane is the vacuum with the dielectric permittivity ε_o and the lower half-plane is a piezo-electric material with the effective dielectric permittivity ε_p.
- The electrodes are infinitely long in *Z*-direction, so the electrostatic problem becomes two-dimensional in *(X, Y)* - plane.
- The electrodes have zero thickness and zero electrical resistance.
- The electrodes are enumerated from $-\infty$ to $+\infty$.

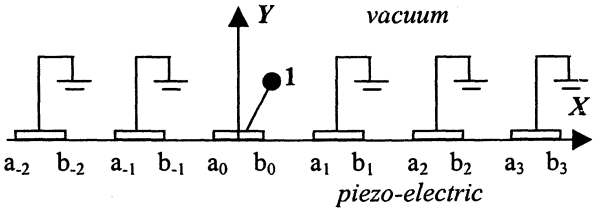

Figure 1.
The intervals (a_n,b_n) along *X*-axis are occupied by electrodes. The electrode's width equals w, $w = b_n - a_n$, and the grating period equals p, $p = b_n - b_{n-1}$. The zeroth electrode is hot and others are grounded.

Such a basic function $\rho_o(x)$ is expressed as [– Refs 1-8]:

$$\rho_o(x) = 0, \quad x \in (b_m, a_{m+1}) \qquad (4a)$$

$$\rho_o(x) = \frac{(-1)^m}{p} \frac{(\varepsilon_o + \varepsilon_p)\sqrt{2}\ G(x,\theta)}{\sqrt{Cos\frac{2\pi x}{p} - Cos\theta}}, \quad x \in (a_m, b_m) \qquad (4b)$$

where:

m – is an electrode number,

$\theta = \pi\eta$,

η is a metallization ratio, $\eta = w/p$,

w is an electrode width,

p is a grating period,

$$G(x,\theta) = \int_{-1}^{+1} \frac{Cos\frac{\pi\tau}{2}\, Cos\frac{\pi x\,\tau}{p}}{P_{\frac{\tau-1}{2}}(-Cos\theta)}\, d\tau$$

$P_s(x)$ is the Legendre function.

In the assumption that the SAW wave-number does not depend on coordinate x along the direction of the SAW wave propagation, the basis element factor $R_o(\kappa)$, defined as the Fourier transform of the charge distribution density $\rho_o(x)$, is equal to [– Refs 1-8]:

$$R_o(\kappa) = (\varepsilon_o + \varepsilon_p)\frac{2Sin(\pi s)}{P_{-s}(-Cos\theta)} P_n(Cos\theta)$$

$$\text{for} \quad n \le \frac{\kappa p}{2\pi} \le n+1, \qquad (5)$$

where

$$s = \frac{\kappa p}{2\pi} - n, \quad 0 \le s \le 1$$

Let us now define the modified frequency spectrum function $R_o(\kappa,r)$ having physical meaning of the amplitude of the SAW wave excited at the cycle frequency ω by the oscillated charges distributed as $\rho_o(x)$, wherein now κ be an effective wave-number and r be a ratio $r = \kappa_e / \kappa_g$. Thereby, the modified function $R_o(\kappa,r)$ is defined as the following integral [– Ref. 9]:

$$R_0(\kappa, r) = \int_{-\infty}^{+\infty} \rho_o(x)\ \exp(-j\omega t(x))dx \quad (6)$$

where $t(x)$ is a respective delay between SAW beams excited from the central zero point and from the point with coordinate x. The function $t(x)$ is defined as:

$$t(x) = \int_0^x \frac{\kappa(x)}{\omega} dx \qquad (7)$$

where $\kappa(x)$ is a wave-number function, wherein the function $\kappa(x)$ is approximated by SAW wave-number κ_e within electrodes and SAW wave-number κ_g within inter-electrode gaps, thus, $\kappa(x)$ is a periodical function and the effective wave-number κ is used for the interval $[0, mp]$. Therefore, the interval of integrating in (7) may be divided in two intervals: $[0, mp]$ and $[mp, x]$, **i.e.**

$$t(x) = \frac{\kappa}{\omega} mp + \int_{mp}^{x} \frac{\kappa(x)}{\omega} dx \qquad (8)$$

and consequently,

$$t(x)=\frac{\kappa}{\omega}mp+\frac{\kappa_e}{\omega}(x-mp),\ x\in[a_m,b_m] \quad (8a)$$

$$t(x)=\frac{\kappa}{\omega}mp+\frac{\kappa_e}{\omega}(w/2)+\frac{\kappa_g}{\omega}(x-mp-w/2),\ x\in[b_m,a_{m+1}] \quad (8b)$$

Substituting functions $\rho_o(x)$ and $t(x)$ in (6) with their expressions (4a,b) and (8a,b) respectively , we obtain:

$$R_0(\kappa,r)=\sum_{m=-\infty}^{+\infty}\int_{-a_m}^{+b_m}\frac{(-1)^m}{p}\frac{(\varepsilon_o+\varepsilon_p)\sqrt{2}}{\sqrt{Cos\frac{2\pi x}{p}-Cos\,\theta}}\times\int_{-1}^{+1}\frac{Cos\frac{\pi\tau}{2}\,Cos\frac{\pi x\tau}{p}}{P_{\frac{\tau-1}{2}}(-Cos\theta)}d\tau\times\exp(-j[\kappa mp+\kappa_e x-\kappa_e mp])\,dx \quad (9)$$

Further, by taking into account the following functional equation:

$$\sum_{m=-\infty}^{+\infty}\exp(-j\pi mz)=2\sum_{n=-\infty}^{+\infty}\delta(z+2n)$$

where $\delta(z)$ is the Dirac Delta function,

and the Mehler-Dirichlet formula:

$$P_\nu(Cos\theta)=\frac{1}{\pi\sqrt{2}}\int_{-\theta}^{+\theta}\frac{Cos[u(\nu+0.5)]\,du}{\sqrt{Cos(u)-Cos(\theta)}}$$

the equation (9) is transformed to:

$$\frac{R_0(\kappa,r)}{(\varepsilon_o+\varepsilon_p)}=\frac{2Sin(\pi s)}{P_{-s}(-Cos\theta)}P_{n+\gamma}(Cos\theta)$$

$$\text{for}\quad n\le\frac{\kappa p}{2\pi}\le n+1, \quad (12)$$

where $\kappa=\eta\kappa_e+(1-\eta)\kappa_g$

$$\gamma=\frac{\kappa p}{2\pi}\frac{(r\text{-}1)(1\text{-}\eta)}{1+\eta(r\text{-}1)},\quad r=\frac{\kappa_e}{\kappa_g}$$

$$s=\frac{\kappa p}{2\pi}-n,\quad 0\le s\le 1$$

In the particular case, when we may ignore the difference between SAW wave-number κ_e within electrodes and SAW wave-number κ_g within inter-electrode gaps, i.e. if $r=1$, the function $R_o(\kappa, r=1)$ turns to $R_o(\kappa)$:

$$R_o(\kappa, r=1) \equiv R_o(\kappa) \quad (13)$$

Figure 2. shows the difference between the element factor $R_o(\kappa)$, defined as Fourier-transform of the basic electrostatic charge distribution, and the modified frequency spectrum $R_o(\kappa,r)$ of SAW with assumption the ratio $r = 1.1$.

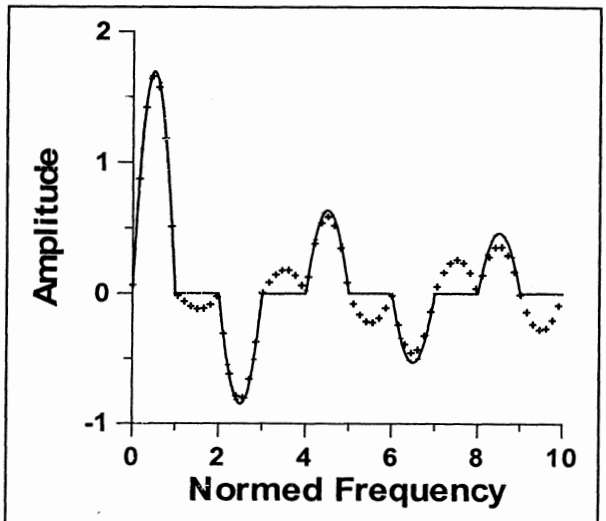

Figure 2. Basis element factor for metallization ratio $\eta = 0.5$.
——— Fourier-transform $R_o(\kappa)$ of the basic charge distribution $\rho_o(x)$.
++++ Modified spectrum $R_o(\kappa, r)$ of SAW with assumption the ratio $r = 1.1$

6. CONCLUSIONS

A generalization of frequency element factor considering the SAW velocity dispersion effect is presented. The generalization remains in the quasi-static approach that is based on the assumption the charge density is dominated by an electrostatic term, defined as the charge density obtained when acoustic wave excitation is ignored. The velocity dispersion effect is simulated by the simplest approximation of the SAW wave number κ_e within electrodes and κ_g within inter-electrode gaps. The splitting of the effective wave number κ on the two κ_e and κ_g generalizes the definition of the acoustic potential frequency spectrum. Such a generalization of the element factor becomes essential for high harmonics, when the difference between κ_g and κ_e is expected to be significant. The modified frequency element factor's behavior implies the SAW waves are excited on all the high harmonics. Especially, this effect is expected for devices working on piezo-films.

7. ACKNOWLEDGES

The author is grateful to V.Duntzov for the helpful cooperation, during the work in the Tajik Polytechnic University in 1991.

8. REFERENCES

1. **D.P.Morgan,** *Surface-wave devices for signal processing, Chapter-4*, Elsevier, Amsterdam, 1985.

2. **D.P.Morgan,** *Quasi-static analysis of generalized SAW transducers using the Green's function method,* – IEEE Trans. SU-27, 111-123 (1980)

3. **B.Lewis, P.M.Jordan, R.F. Milsom and D.P. Morgan,** *Charge and field superposition methods for analysis of generalized SAW interdigital transducers,* – IEEE Ultrasonics Symp., 1978, pp.709-714.

4. **D.P.Morgan, B.Lewis and J.G.Metcalfe,** *Fundamental charge distributions for surface-wave interdigital transducer analysis,* – Electronics Lett. 15, 583-585 (1979).

5. **S.Datta, B.J.Hunsinger, and D.C.Malocha,** *A generalized model for periodic transducers with arbitrary voltages* – IEEE Trans. Sonics and Ultrason., vol. SU-26, No.3, pp.235-242, (1979).

6. **S.Datta and B.J.Hunsinger,** *Element factor for periodic transducers* – IEEE Trans. **SU-27**, 42-44 (1980)

7. **R.C.Peach,** *A general approach to the electrostatic problem of the SAW IDT* – IEEE Trans. **SU-28**, 96-105 (1981)

8. **A.Rukhlenko,** *Charge Distribution and Capacitance Calculation for Generalized Periodic SAW Transducers Using Floquet's Technique* – IEEE Ultrason. Symp., 1994, pp.325-329

9. **Yu.M.Abramov, V.P.Dunzov and V.S.Orlov,** *Frequency Spectrum of SAW with Account of Difference of Its Transmission Velocity on a Free Surface from that under the IDT Electrodes* – Theses of the Report of the IV School-Seminar "Acoustic Electronic Devices". USSR Ministry of Communication, Moscow-1991, p.5.

SLOWNESS CURVES FOR SURFACE WAVES PROPAGATING IN ELECTRODE GRATINGS

V. Laude†, S. Ballandras† and J. Desbois‡

†LPMO/CNRS, UPR 3203, associé à l'Université de Franche-Comté,
32 avenue de l'Observatoire, F-25044 Besançon cedex, France

‡Thales Microsonics
399, route des Crêtes, 06904 Sophia-Antipolis cedex, France

Abstract: *The characteristics of surface acoustic waves propagating obliquely in electrode gratings are investigated, with the mass-loading effect taken into account. The slowness of the surface waves, as well as the attenuation, piezoelectric coupling and beam-steering are obtained as a function of the propagation angle with respect to the grating axis. A modification of classical finite element analysis is derived for this purpose. Examples are presented for 36°YX quartz, X-112°Y lithium tantalate and 36°YX lithium tantalate.*

Key-words: *Surface acoustic waves (SAW), pseudo surface acoustic waves (PSAW), finite element analysis for SAW, slowness curves.*

1. INTRODUCTION

During the last decade, much work has been devoted to the modeling and the numerical simulation of surface acoustic waves (SAW) propagating under interdigital transducers (IDT), including the mass-loading effect that is due to acoustic propagation inside the aluminum electrodes [1-5]. Such tools are especially useful to understand the wave propagation characteristics in actual SAW filters, and hence are used routinely to obtain the basic parameters required for filter design. The approach we use is based on a mixed finite element analysis (FEA) / boundary integral method (BIM) [2], in which the wave in the electrodes and in the substrate are respectively described by FEA and a Green's function, and the two domains are linked using a BIM to obtain the harmonic admittance.

One limitation of the FEA/BIM method is that for computation reasons the problem is restricted to two dimensions, with the electrodes assumed infinite in the transverse direction. However, real SAW devices are of finite width, and transverse effects occur that can not be taken into account using a 2D model. Though an exact 3D model is probably still beyond reach, useful information can be gained by examining the propagation of slanted acoustic waves in gratings. Defining the phase angle θ as the angle of propagation with respect to the electrodes axis, we show how the phase velocity can be obtained as a function of θ, including the mass-loading effect, which allows us to determine the slowness curves of SAW under periodic gratings. Along with the phase velocity, we discuss how other useful information can be obtained as well, i.e. the attenuation, the piezoelectric coupling and the beam-steering angle.

Numerical simulation results are presented for three standard piezoelectric substrates used for SAW devices, 36°YX quartz, X-112°Y tantalate and 36°YX lithium tantalate.

2. LOCATING SURFACE WAVES

In the process of computing slowness curves for surface waves, it is necessary to locate the slowness as a function of the propagation angle θ in the surface plane. Fig. 1 illustrates the notations employed. The actual algorithm employed will depend on the nature of the propagation problem. On a free or shorted surface, the wave characteristics are functions of the material constants only, and are not dispersive. In a metallic grating however, the wave characteristics are dispersive, i.e. they depend on the frequency period product fp, but in addition they also depend on the electrodes shape, which for a rectangular electrode is scaled by the form factor $h/2p$, where h is the electrode height.

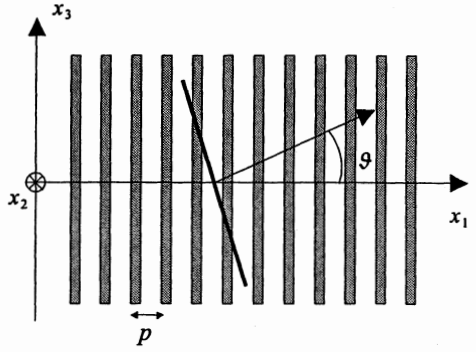

Fig. 1: Geometry for slanted SAW propagation in a periodic metallic grating.

In the case of an homogeneous surface with either free or shorted boundary conditions, it is well-known that the slowness is given respectively by a pole or a zero of the

so-called effective permittivity. Such an approach has been used routinely to obtain maps of surface waves parameters [6]. The effective permittivity is a restriction of the Green's function of the semi-infinite substrate to its electrical components [7]. The computation of the surface Green's function in the spectral domain has for instance been described in Ref. [8].

In the case of periodic electrode gratings, two additional phenomena have to be accounted for, namely the frequency dependence arising from the periodic perturbation of the surface and the periodic electrical excitation of waves, and the so-called mass-loading effect of the electrodes. The first phenomenon is adequately described (at least as regards the electrical part of the problem) using the notion of the strip admittance [9], extended to the notion of harmonic admittance (HA) in Ref. [7]. The occurrence of a piezoelectrically coupled surface wave is then given by a pole of the HA. There have been many approaches to the computation of the mass-loading effect, with most of them relying on a finite element analysis (FEA) of the acoustical propagation in the electrodes [1-4]. In this work, we have used the approach described in [3], which is a combination of a FEA for the electrodes with a boundary integral method (BIM) for the substrate. This BIM relies upon the Green's function of the semi-infinite substrate. We describe in Section 3 how the classical finite element approach can be modified to accommodate for slanted propagation.

3. FINITE ELEMENT FOR SLANTED PROPAGATION

The finite element that we use was derived from a classical two-dimensional triangle with 3 degrees of freedom, originally intended for isotropic acoustic problems. More precisely, for an infinitely long electrode, the displacements and constraints are usually assumed not to depend on the transverse coordinate x_3 (hence the two-dimensional element), but the 3 components of the displacement must be taken into account (hence the 3 degrees of freedom). Another possible representation of the finite element is an infinitely long volume with a triangular section. To take into account slanted propagation inside the electrodes, we assume in addition a sinusoidal dependence of the displacements in the transverse coordinate with a given wave-vector k_3 according to

$$\boldsymbol{u}=\sin(k_3 x_3+\varphi)[P(x_1,x_2)]\{\boldsymbol{u}\}_T \tag{1}$$

where φ is an arbitrary phase. T stands for the finite element considered, P is the polynomial interpolation inside the element, and $\{\boldsymbol{u}\}_T$ is the vector of coordinates of the nodes. Following the usual procedure of FEA, a variational problem is constructed, which can be cast in a linear form

$$([K]-\omega^2[M])\{\boldsymbol{u}\}=\{\boldsymbol{B}\} \tag{2}$$

where $[K]$ is the stiffness matrix, $[M]$ is the mass matrix, ω is the angular frequency and $\{\boldsymbol{B}\}$ represents the excitation forces applied to the electrode. Using the notations $[P]$ for the polynomial interpolation matrix, $[DP]$ for the matrix of the polynomial derivatives, $[C]$ for the stiffness tensor in contracted notation, ρ for the mass density, and the constant matrices

$$[D]=\begin{pmatrix}1&0&0&0&0&0\\0&0&0&1&0&0\\0&0&0&0&0&0\\0&1&1&0&0&0\\0&0&0&0&0&1\\0&0&0&0&1&0\end{pmatrix} \tag{3}$$

and

$$[D_3]=\begin{pmatrix}0&0&0\\0&0&0\\0&0&1\\0&0&0\\0&1&0\\1&0&0\end{pmatrix} \tag{4}$$

the elementary stiffness and mass matrices can be written respectively as

$$[M_T]=\int_T {}^t[P]\rho[P]\,dx \tag{5}$$

and

$$\begin{aligned}[K_T]=&\int_T {}^t([D][DP])[C]([D][DP])\,dx\\&+\int_T k_3^2\,{}^t([D_3][P])[C]([D_3][P])\,dx\end{aligned} \tag{6}$$

In the derivation, the sinusoidal dependence has dropped by integration along the x_3 axis. By comparison with the usual case of normal propagation $(k_3=0)$ it is seen that only the stiffness matrix is affected, and that a positive matrix has to be added to it, weighted by the square of the transverse wave-vector.

4. EXAMPLES OF SLOWNESS CURVES

All results presented in this section are obtained for an infinite periodic electrode grating on a semi-infinite piezoelectric substrate. The zero phase angle refers to propagation along the grating axis. All parameters given are those obtained for a pole or pseudo-pole of the harmonic admittance, i.e. for the resonance condition, with the frequency period product fp set to 1000 m/s, i.e. far from the stop-band in all cases.

4.1. 36°YX quartz

The denomination for the considered AT cut of quartz is (YXl)/36 in the IEEE 1949 piezoelectric standard. The

dependence of the slowness, beam-steering and piezoelectric coupling for the SAW of 36°YX quartz are depicted in Figs. 2, 3 and 4 respectively, for three values of the electrode aspect ratio $h/2p$ (0, 5 and 10 %). The slowness is seen to be rather strongly affected by the mass loading effect, as is well-known for 36°YX quartz, and to assume a symmetrical and mostly parabolic shape. The beam-steering remains limited, while the coupling increases with the phase angle. It should be noted that no attenuation was found to occur at any angle.

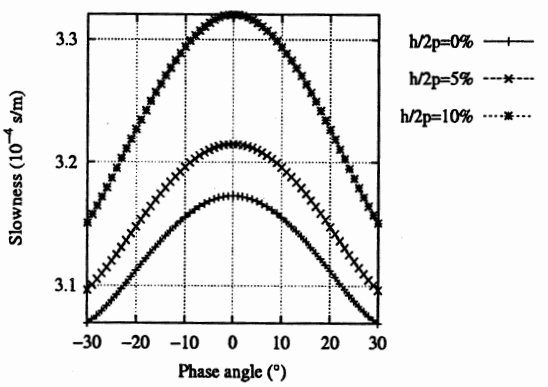

Fig. 2: Slowness of the SAW of 36°YX quartz (fp=1000 m/s).

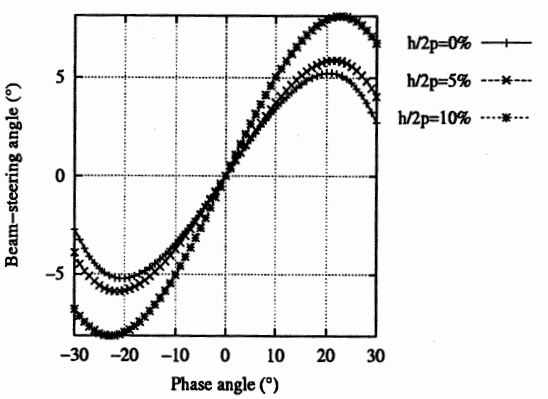

Fig. 3: Beam-steering of the SAW of 36°YX quartz (fp=1000 m/s).

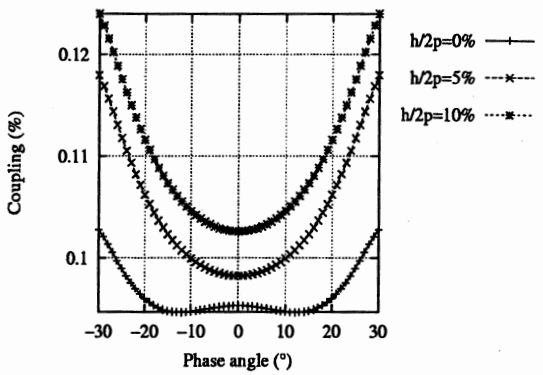

Fig. 4: Piezoelectric coupling of the SAW of 36°YX quartz (fp=1000 m/s).

4.2. X-112°Y tantalate

The denomination for the considered cut of lithium tantalate is (XYt)/112.2 in the IEEE 1949 piezoelectric standard. The dependence of the slowness, beam-steering and piezoelectric coupling for the SAW are depicted in Figs. 5, 6 and 7 respectively, for three values of the electrode aspect ratio $h/2p$ (0, 5 and 10 %). The slowness is seen to be less affected by the mass loading effect than is that of the SAW of 36°YX quartz, and to assume a very uneven shape. The beam-steering remains limited, while the coupling decreases with the phase angle. As for 36°YX quartz, no attenuation was found to occur at any angle.

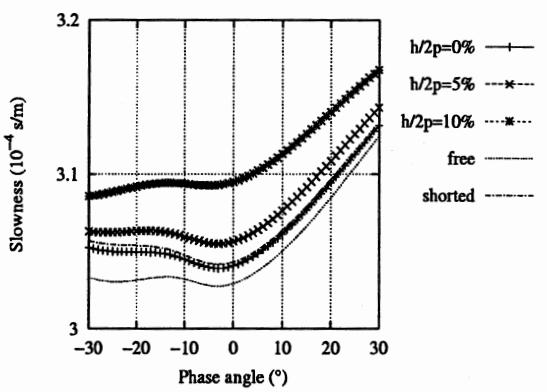

Fig. 5: Slowness of the SAW of X-112°Y tantalate (fp=1000 m/s).

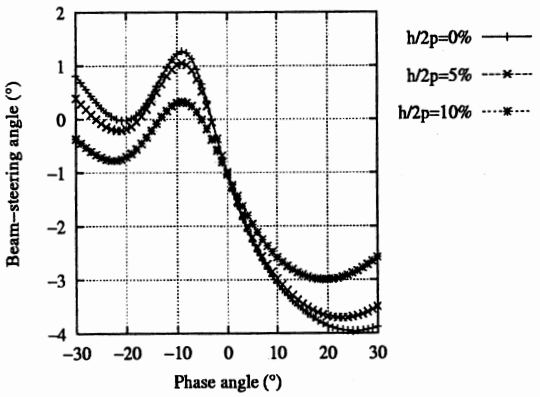

Fig. 6: Beam-steering of the SAW of X-112°Y tantalate (*fp*=1000 m/s).

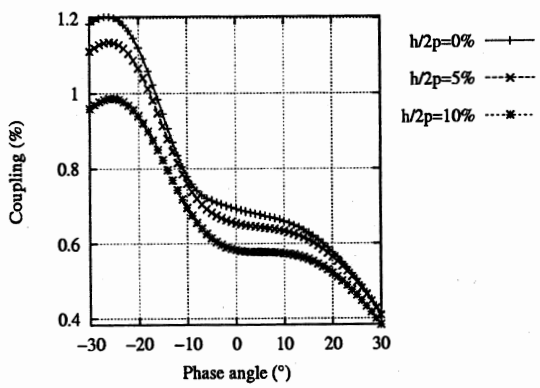

Fig. 7: Piezoelectric coupling of the SAW of X-112°Y tantalate (*fp*=1000 m/s).

4.3. 36°YX tantalate

The denomination for the considered cut of lithium tantalate is (YXl)/36 in the IEEE 1949 piezoelectric standard. This cut is famous for its leaky SAW, or pseudo SAW (PSAW). The dependence of the slowness, attenuation, beam-steering and piezoelectric coupling for the PSAW are depicted in Figs. 8, 9, 10 and 11 respectively, for three values of the electrode aspect ratio *h/2p* (0, 5 and 10 %). The slowness is seen to be much less affected by the mass loading effect than are that of the SAW of 36°YX quartz and X-112°Y tantalate, and to assume a parabolic shape. The beam-steering varies rather largely with the phase angle. The coupling is maximum along the grating axis, while at the same time the attenuation is at a minimum.

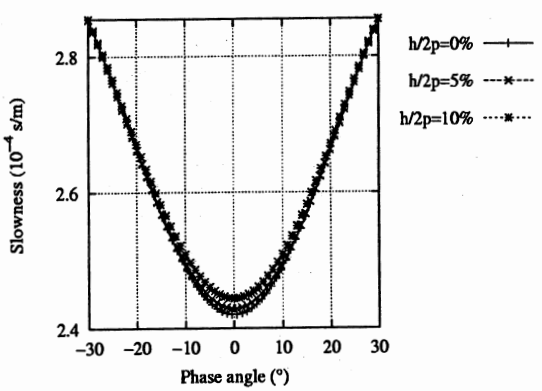

Fig. 8: Slowness of the PSAW of 36°YX tantalate (*fp*=1000 m/s).

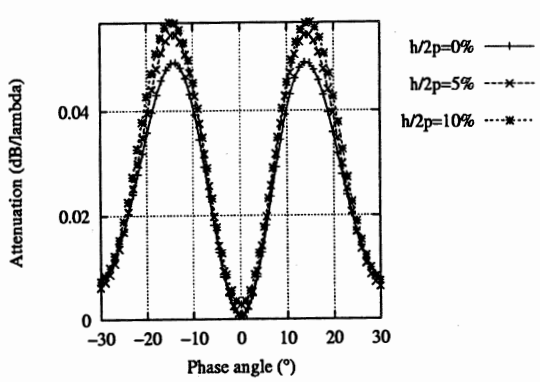

Fig. 9: Attenuation of the PSAW of 36°YX tantalate (*fp*=1000 m/s).

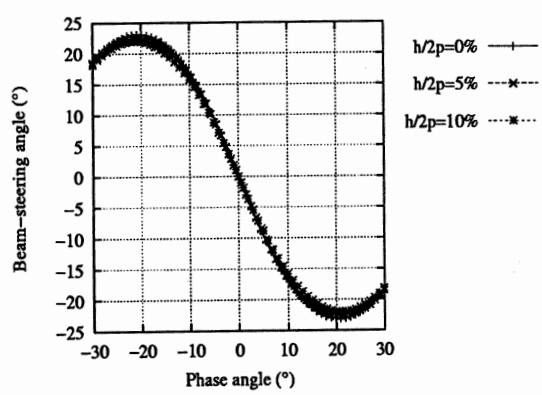

Fig. 10: Beam-steering of the PSAW of 36°YX tantalate (*fp*=1000 m/s).

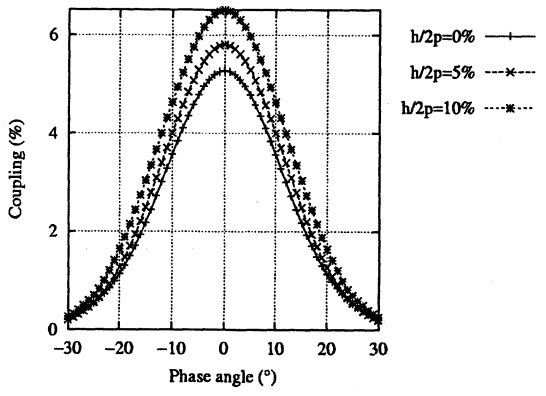

Fig. 11: Piezoelectric coupling of the PSAW of 36°YX tantalate (fp=1000 m/s).

5. CONCLUSION

The characteristics of surface acoustic waves propagating obliquely in electrode gratings have been investigated, with the mass-loading effect taken into account. The slowness of the surface waves, as well as the attenuation, piezoelectric coupling and beam-steering have been obtained as a function of the propagation angle with respect to the grating axis. The method is based on the monitoring of poles in the harmonic admittance, which is computed using a FEA/BIM approach. A modification of classical finite element analysis was derived to account for slanted propagation. Examples have been presented for 36°YX quartz, X-112°Y tantalate and 36°YX lithium tantalate. Efforts are still required to obtain slowness curves in the stop-band of the grating.

6. REFERENCES

[1] M. Buchner, W. Ruile, A. Dietz and R. Dill, "FEM analysis of the reflection coefficient of SAWs in an infinite periodic array," IEEE Ultrason. Symp. Proc., 371-375 (1991).

[2] H. P. Reichinger and A. R. Baghai-Wadji, "Dynamic 2D analysis of SAW devices including mass-loading," IEEE Ultrason. Symp. Proc., 7-10 (1992).

[3] P. Ventura, J.-M. Hodé and J. Desbois, "A new efficient combined FEM and periodic Green's function formalism for the analysis of periodic SAW structures," IEEE Ultrason. Symp. Proc., 263-266 (1995).

[4] G. Endoh, K. Hashimoto and M. Yamaguchi, "Surface acoustic wave propagation characterization by finite element method and spectral domain analysis," Jpn. J. Appl. Phys. **34**, 2638-2641 (1995).

[5] K. Hashimoto, G. Endoh, M. Ohmaru and M. Yamaguchi, "Analysis of SAWs obliquely propagating under metallic gratings with finite thickness," Jpn. J. Appl. Phys. **35**, 3006-3009 (1996).

[6] A. L. Slobodnik, E. D. Conway and R. T. Delmonico, Eds., Microwave acoustic handbook, Volume 1A (1973).

[7] Y. Zhang, J. Desbois and L. Boyer, "Characteristic parameters of surface acoustic waves in a periodic metal grating on a piezoelectric substrate," IEEE Trans. on Ultrason. Ferroelec. Freq. Control **UFFC-40**, 183-192 (1993).

[8] R. C. Peach, "A general Green function analysis for SAW devices," IEEE Ultrason. Symp. Proc., 221-225 (1995).

[9] K. Blotekjaer, K. A. Ingebrigtsen and H. Skeie, "A method for analysing waves in structures consisting of metal strips on dispersive media," IEEE Trans. Ultrason. Devices **ED-20**, 1133-1138 (1973).

SAW REFLECTION FIELD PEAK SHIFT OF SLANTED GRATING

K.I. Volianski, Yu.G. Smirnov, S.V. Kulakov, L.P. Konovalova

Saint-Petersburg State University of Aerospace Instrumentation
Bolshaya Morskaya, 67, St.Petersburg, 190000, Russia
e-mail: weconf@spb.cityline.ru

Beam shift of surface acoustic wave (SAW), reflected from slanted grating, regarding the center of acoustic synchronism area is considered. This shift increases at increasing grooves depth and caused by multi-reflections inside the grating. This factor is studied by numerical modeling using algorithm taking into account the SAW multi-reflections between grating's elements. Chevron-type gratings are under consideration in this paper. Calculation results and diagrams of amplitude distribution acoustic field inside grating are presented.

1. INTRODUCTION

The traditional method of building dispersive filters with large group time delay difference consists in using two gratings of chevron-type topology. Ref.1 Every grating is a system of parallel grooves of h depth, which are etched in the surface of substrate symmetrically regarding the longitudinal axis of device (fig.1). The main demerit of such a topology is rather high level of attenuation (30 – 35 dB Ref.2) caused by the necessity of using grooves of small depth ($h/\lambda<0.1$) and

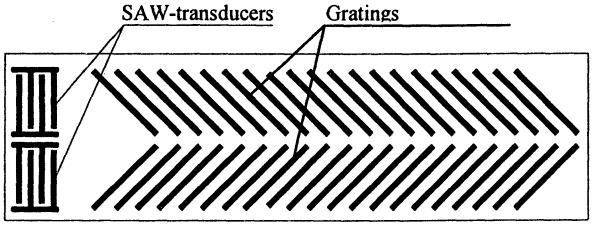

Fig. 1

therefore with small reflectance. Unfortunately it is not succeeded to decrease the attenuation by simply increasing the grooves depth as the SAW-device characteristics are more and more determined by uncontrollable effects conditioned by multi-reflections of waves between grating's elements while increasing grooves depth. Among such effects, the effect of reflected acoustic beam shift regarding the acoustic synchronism area of grating has the noticeable influence Ref.2. While increasing grooves depth, the reflected beam intensity increases but the phase structure of incident wave inside the first grating changes because of reflected waves accumulation. As a result the area of maximum reflection doesn't coincide with synchronism area of grating. Therefore instead of beam center, its border having noticeably less intensity strikes the synchronism area of the second grating. It prevents increasing the intensity of the wave reflected by the second grating and can result its decreasing.

2. CALCULATION RESULTS AND ANALISYS

The effect of shifting the reflected beam described in this paper is investigated through mathematical modeling of acoustic fields inside every grating of dispersive filter. The amplitudes of oscillations of reflected waves acoustic fields are calculated with using recursive algorithm with taking into account the secondary reflections described in Ref. 3.
The results of the modeling are presented as the diagrams on fig. 2-5. The relative value of oscillations amplitude is represented on diagrams as gray scale: the larger amplitude the darker color. The center and borders of grating synchronism area containing Ne=100 reflectors are represented by white lines.
The spread of reflected field amplitudes inside the first grating area at small depth of reflecting grooves (h/λ=0,003), when the secondary reflections are negligible, is shown on fig.2. The grating with aperture greater than the optimal one /Ref.4/ is intentionally presented. As it is follows from the diagram, it is necessary to select grating aperture so that the field maximum

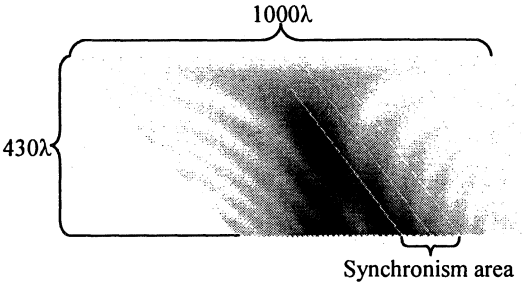

Fig. 2

is on the lower border of grating.

When the grating aperture is optimal, the reflected beam has the minimal width and maximum intencity in its center. The amplitude spread in the cross section of beam corresponds to a function of sin(x)/x type.
Diagrams of acoustic fields inside the both gratings at aperture close to optimal are presented on fig.3a and effective reflection (synchronism) areas are indicated. It is obviously that the reflected field inside the second grating has its maximum in the center of the grating aperture. For clearness, the spread of SAW field amplitude at the output of the second grating (the section, in which this spread was calculated, is indicated by white line) is shown on fig.3b.

When increasing the grooves depth, the secondary reflections influence increases and the main lobe of reflected field of the first grating starts to shift toward the left side that causes the shift of reflected field of the second grating toward its lower border (fig. 4a and 4b). In this case as a result of incomplete synchronism, the part of refracted SAW energy going through the second grating and not incidenting on the output transducer increases.
Diagrams show that the maximum of reflected field in the second grating is shifted to the center of its aperture and the part of the SAW energy which is coming to a output transducer grows.

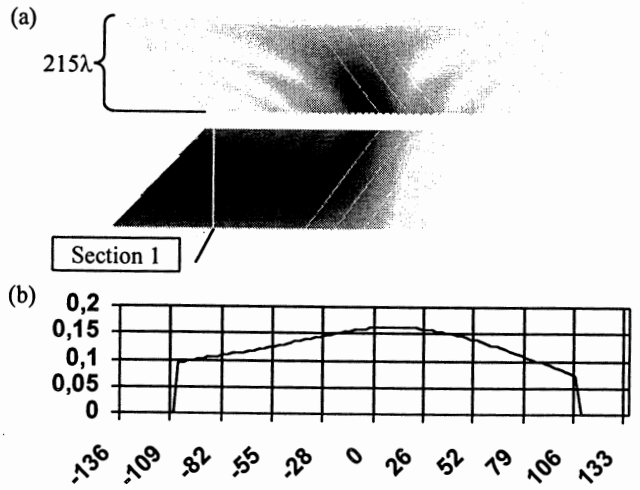

The distance from aperture center, wavelenght

Fig.3

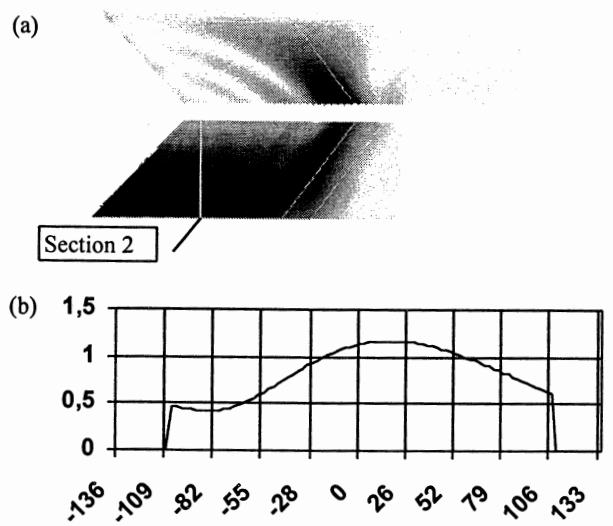

The distance from aperture center, wavelength

Fig. 4

3. CONCLUSION

The fulfilled investigation shows that it is possible to decrease in some degree the insertion loss of a SAW filter with chevron-type grating by shifting the second grating with taking into account the shift of the acoustic beam reflected from the first grating. The modeling of acoustic fields allows to select an optimal value for such a shift for determined set of characteristics. A disadvantage here is the dependence of the shift value on grating depth.

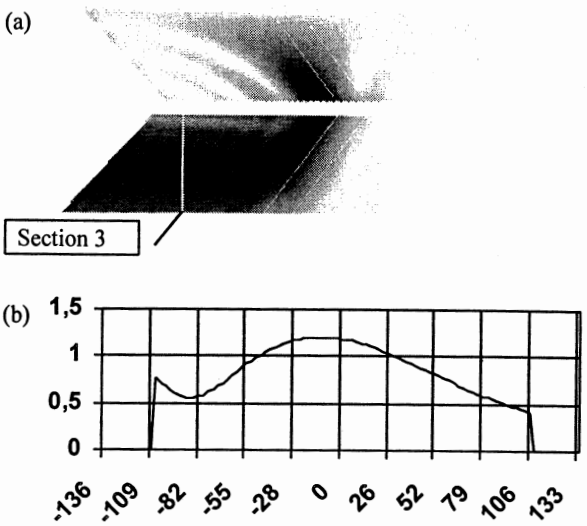

The distance from aperture center, wavelenght

Fig.5

4. LITERATURE

1. Surface Wave Filters (design, construction and use)/H.Matthews, Editor // John Wiley &Sons, New York, London, Sydney, Toronto, 1977.
2. Балышева О.Л., Коновалова Л.П., Кулаков С.В., Смирнов Ю.Г. Дисперсионные линии задержки с отражательными структурами.// Зарубежная радиоэлектроника: Успехи современной радиоэлектроники.1997, №6. С.52-61.
7. K.I.Volyansky, A.R.Zhezherin, J.G.Smirnov. Acoustic fields in dispersive SAW filters with reflective arrays. // Proc. 4 International Symp. on Surface Waves in Solid and Layered Structures. 1998, St.-Petersburg, Russia, p.226-230.
4. Report on research work ГБ № 53-00-291-2. № state registration. 01.950003040.

POSTERS A

QUARTZ OSCILLATORS & RESONATORS

RECENT PROGRESS IN ULTRA STABLE OSCILLATORS FOR SPACE ON BOARD AND GROUND APPLICATIONS

Vincent CANDELIER, Jacques LAMBOLEY, Gérard MAROTEL, Patrice CANZIAN, Pierre POULAIN

C-MAC Frequency Products, 44, Avenue de la Glacière 95100 ARGENTEUIL – FRANCE
Tel : 33 (0) 1 39 98 36 00 Fax : 33 (0) 1 39 98 36 90 e-mail : cfp@france.cfpwww.com
ISO 9001 Certified/DNV/99FRQ-10063 ESA/SCC/3501 qualified / quartz crystal resonators

ABSTRACT

For new space applications in accurate orbitography, and positioning, and time-keeping systems, ultra stable oscillator performance must be constantly improved :

- irradiation sensitivity below 5.10^{-13}/rad for a board device,
- ageing below 1.10^{-11}/day,
- magnetic field sensitivity below 5.10^{-13}/gauss,
- short-term and medium term frequency stability below 7.10^{-14}

This paper presents the state-of-the-art of these characteristics, obtained from C-MAC improved ultra stable oscillators.

1. INTRODUCTION

Accurate systems such as navigation, telecommunication and measurement schemes require more and more demanding performances from ultra stable oscillators (USO) in each type of application (Space, Avionics and Commercial) [1] [2] [4] [5].

Some tens of first generation USO flight model are actually on board [3]. The new generation of USO : OUS NG was qualified in 1998 and first flight models have been delivered [6].

In the new DORIS precise orbit determination and localization and in navigation applications such as GALILEO, a better stability is required including short, medium and long-term stability, magnetic field sensitivity, and irradiation sensitivity. In the aim of improving these characteristics, specific research and development has been contracted by C-MAC with the french MOD (DGA - Délégation Générale de L'armement) and the French Space Agency (CNES - Centre National d'Etudes Spatiales). The findings and conclusions of this project are presented here.

2. OSCILLATORS REQUIREMENTS

The main requirements :

- Short-term stability in Allan or Picinbono standard deviation $\sigma y(\tau)$ or $\sigma yp(\tau)$, with a time interval, τ, of 10 s, [11], [15].

- The medium term stability between τ = 900 s (DORIS configuration [4]) and τ = 100000 s (time-keeping application [6]). The frequency standard deviation $\Delta F/P(\tau)$ from the mean slope or the phase standard deviation MTIE (τ) from the extrapolated slope [16].

These stabilities must be obtained under environment conditions (temperature, magnetic field, irradiation).

Tables 1 and 2 show the On-board (0B) and Ground base station (GB) specifications and requirements for the new generation of USO.

	OB USO	GB USO
σyp (10s)	$7x10^{-14}$	$7x10^{-14}$
$\sigma\Delta F/P$ (900 s)	$2x10^{-13}$	$2x10^{-13}$
MTIE (100000 s)	10 ns	10 ns

Table 1 : USO specification

	OB USO	GB USO
Frequency temperature stability	$2.5x10^{-13}$/°C	$2.5x10^{-13}$/°C
Irradiation sensitivity	$5x10^{-13}$/rad	-
Magnetic field sensitivity	$5x10^{-13}$/gauβ	$5x10^{-13}$/gauβ
Ageing	$1x10^{-11}$/day	$1x10^{-11}$/day

Table 2 : Required USO environment sensitivity

3. PRODUCTS IMPROVEMENTS

The On-board and Ground base USOs have been described in the articles [8] and [9].

The improvements consist in two new C-MAC developments in the quartz crystal resonator and a new electronic design :

- A new quartz material
- A new mechanical and amagnetic structure
- Amagnetic electronics with very low noise

A new type of resonator with these improvements was developed and qualified in accordance with ESA rules for the space model.

The short-term measurement process was also improved.

4. IRRADIATION SENSITIVITY

In irradiation sensitivity the material quality is essential. Until now, we used a swept, high quality quartz (IR absorption lower than 0.02 cm^{-1}). An analysis of the irradiation sensitivity of 10 MHz QAS resonators constructed with this material was carried out.

Only the quartz resonator was irradiated. We measure the frequency, before and after irradiation, in an ovenised oscillator. The result is presented in figure 1. We observe a saturation after 20 Krad. The irradiation sensitivity at different doses is summarized in table 3.

We have developed and made a new autoclave capable of producing a new material (material N) with less impurities without sweeping. We have performed the same analysis with this material in the same type of resonator as with the swept material. The improvement is significant (see figure 2 and table 3) : a gain of about ten.

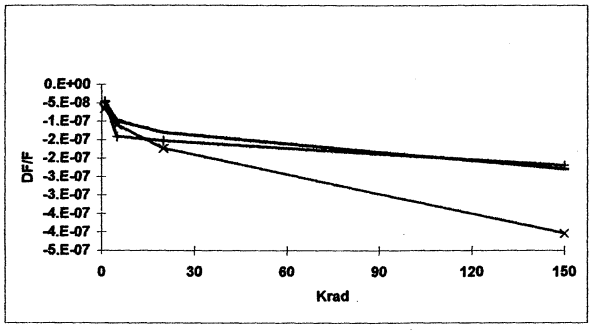

Figure 1 : QAS 10 MHz SWEPT material : frequency deviation versus accumulated irradiation dose

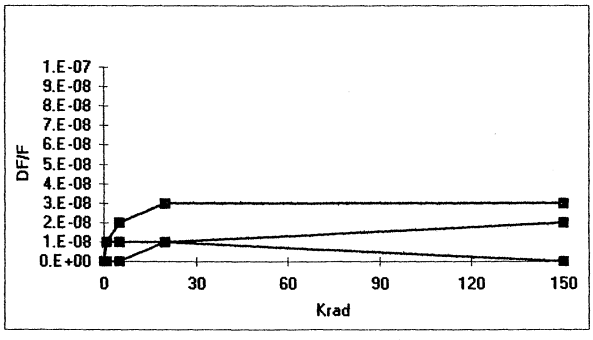

Figure 2 : QAS 10 MHz material N : frequency deviation versus accumulated irradiation dose

Dose/ Material	5 Krad	10 Krad	150 Krad
Swept	3.10^{-11}/rad	1.10^{-11}/rad	3.10^{-12}/rad
N	4.10^{-12}/rad	1.10^{-12}/rad	3.10^{-13}/rad

Table 3 : 10 MHz QAS irradiation sensitivity versus material at different accumulated dose

The irradiation sensitivity at low level (1rad/hour) is a critical characteristic for the medium term stability. Figure 3 shows the frequency deviation due to a low level of irradiation dose for a production batch.

In this batch, the irradiation sensitivity distribution is as shown in figure 4. If we want a very low sensitivity we have two solutions : either by sorting after a low irradiation or by a pre-irradiation at a higher dose. The improved characteristics of the new material alone covers the requirements of general space applications. For time-keeping and navigation, sorting may be the solution.

The other parameters (short-term, ageing, electrical parameters) of the resonator after irradiation were tested and no degradation was observed.

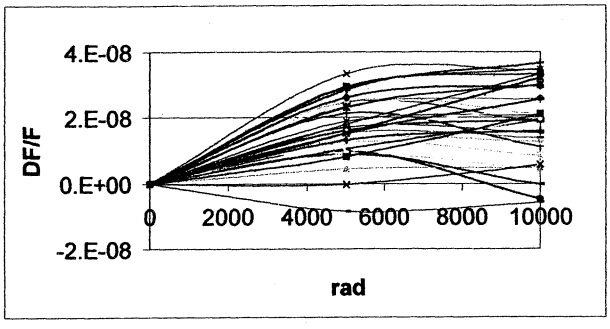

Figure 3 : 10 MHz QAS material N : frequency deviation versus irradiation dose

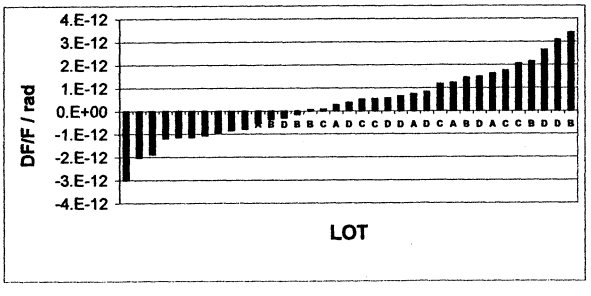

Figure 4 : 10 MHz QAS material N : irradiation sensitivity distribution between 5 and 10Krad for 40 resonators in 4 lots A, B, C , D.

5. MAGNETIC FIELD SENSITIVITY

The use of appropriate components and the redesign of the quartz crystal mounting allow us to reduce the frequency sensitivity of the USOs to below the 1.10^{-12}/gauβ limit.

As a result, in satellite applications, the influence on frequency due to magnetic fields generated by the actuators is reduced on the OB USO. This eliminates the need for extra shielding.

Figures 6 and 7 show the magnetic field sensitivity for four batches of 10 MHz QAS resonators. The lots A and B are with magnetic mounting and the lots C and D are with amagnetic mounting. The difference is clearly demonstrated.

The magnetic field sensitivity measurement had to be modified. We applied a ten gauβ magnetic field in three perpendicular axes, in each direction. As shown in figure 5 the effects of the magnetic field are barely visible against the frequency noise of the test oscillator. The new resonator now has the improved mounting.

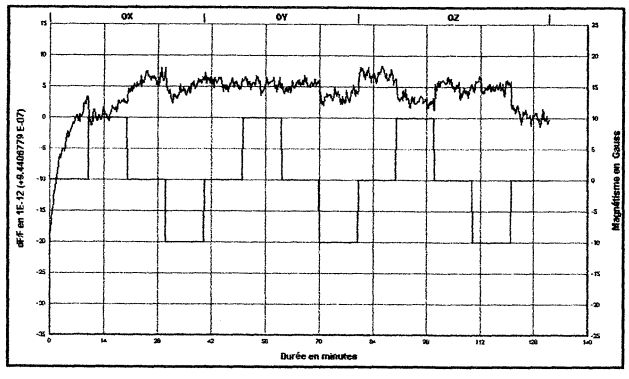

Figure 5 : magnetic field frequency sensibility measurement (± 10 Gauβ field applied in each axis)

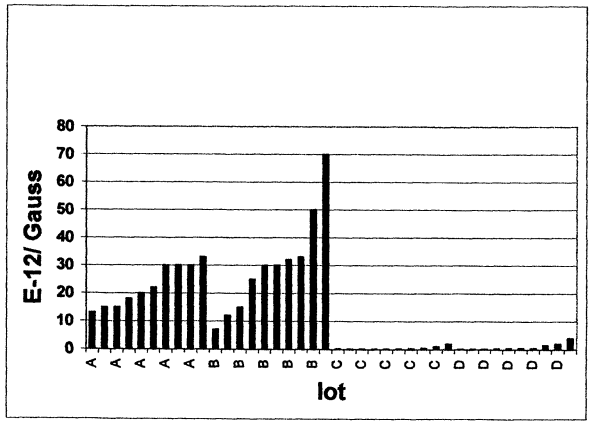

Figure 6 : 10 MHz QAS worse case axis magnetic field sensibility : lots A and B magnetic structure, lots C and D amagnetic structure

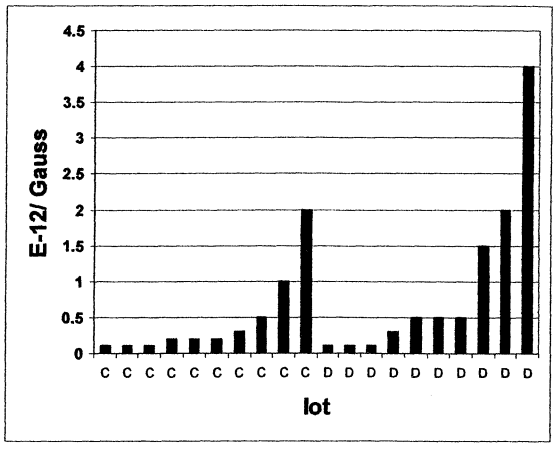

Figure 7 : 10MHz QAS worse case axis magnetic field sensibility : lots C and D amagnetic structure

6. SHORT-TERM STABILITY

We have shown in [8] and [9] that we obtain better results in short-term stability with a 5 MHz QHS resonator than with a 10 MHz QAS resonator. With new 5 MHz QHS resonators, and with sorting electronic components with respect to their noise characteristics, we have improved the short-term stability for integration time τ between 1 to 10 seconds. Figures 8 and 9 give the result of a measurement of some parts in 10^{+14} in Allan variance and Picinbono variance (Three sample variance or suppressed frequency drift variance). The measurement (figure 10) has been possible by the use of a saphir frequency reference which has a short-term stability floor below 1.10^{-14} between 1 to 100 seconds. These measurements were done at the LPTF(Laboratoire Primaire du Temps et des Fréquences - FRANCE).

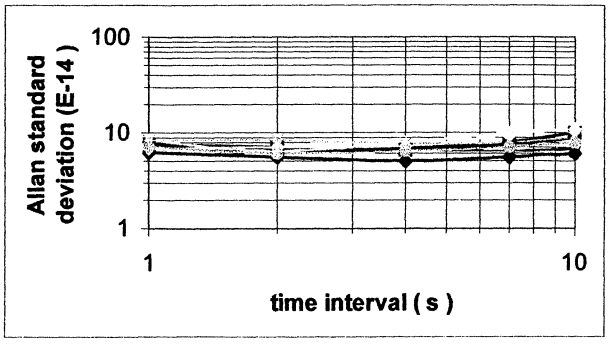

Figure 8 : 5 MHz GB QHS USO Allan standard deviation versus integration time between 1s to 10s for 10 parts

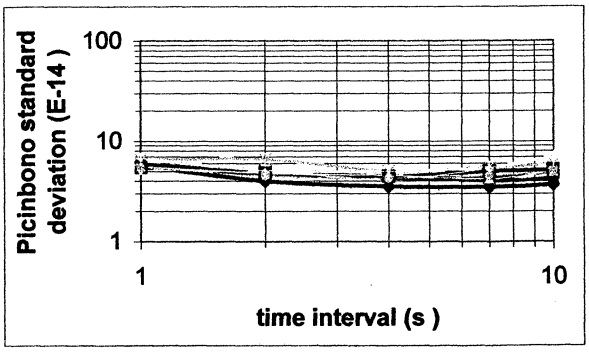

Figure 9 : 5 MHz QHS GB USO Picinbono standard deviation versus integration time between 1s to 10s for 10 parts

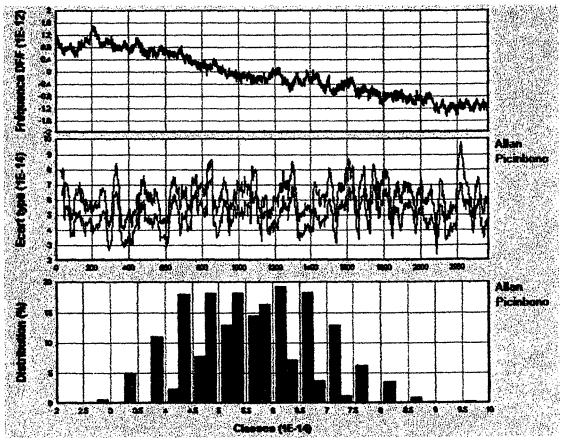

Figure 10 : 5 MHz QHS GB USO short-term measurement with LPTF saphir frequency reference

In short-term stability, the contribution of the quartz resonator and the electronics were estimated and measured.

Three 5 MHz QHS parts were measured at the LPMO (Laboratoire Primaire de Métrologie des Oscillateurs) with the interferometric method [7]. The results are given in figure 11. The contribution of the electronics was estimated by non linear simulation [15] and is presented in figure 13.

The measurements of 5 MHz USO short-term stability is summarized in figure 12. It can be seen that we are near the limit of the quartz crystal contribution.

For new space requirements (see table 1), it is clear that with 5 MHz QHS quartz resonator it is possible to meet the specification but not with the 10 MHz QAS quartz resonator. We are currently qualifying a 5 MHz QHS quartz resonator in accordance with ESA rules and with the support of the CNES.

N°QUARTZ	FO	Q	Sy(1Hz) measured	2 parts σy(1s)	σy (1s)	Lf (1Hz)
	MHz	K	E-28	E-14	E-14	dBc/Hz
9949/P/818/20	5	2647	25	5.89	4.16	-138.06
9949/P/891/17	5	2650	25	5.89	4.16	-138.06
9949/P/880/19	5	2701	25	5.89	4.16	-138.06

Figure 11 : Quartz resonator contribution to Allan standard deviation and to frequency spectral density, measured by interferometric method at the LPMO

N°QUARTZ	FO	Q	LPTF picinbono(4s)	LPTF Allan (4s)
	MHz	K	E-14	E-14
9949/P/818/20	5	2647	5.00	7.50
9949/P/891/17	5	2650	4.50	6.70
9949/P/880/19	5	2701	5.00	6.50

Figure 12 : 5 MHz QHS USO short-term standard deviation, measured with saphir frequency reference at the LPTF

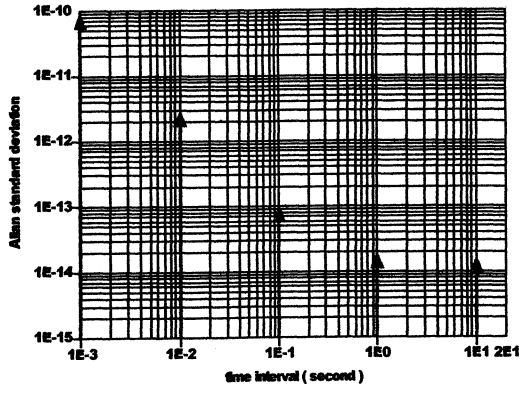

Figure 13 : 5 MHz USO electronics contribution to short-term stability obtained by non linear simulation

7. MEDIUM-TERM STABILITY

For a 10 MHz QAS On-board USO, the medium-term stability is shown in figures 14 and 15. It is expressed, in frequency, by the Allan standard deviation $\sigma y(\tau)$ and the Allan standard deviation with drift removed $\sigma yc(\tau)$. In phase measurement, it may be quantified by the mean time interval error (MTIE) (τ) [12], [11].

In time-keeping and navigation applications, it is necessary to know the time during a prediction period.

We can calculate the phase for quartz oscillator with a quadratic curve interpolated during a period of time, tm, and we can extrapolate the phase at time Tp, after this period. Then, the mean time interval error between the phase and the interpolated curve is given by the MTIE (Tm, Tp) [13]. Some results of this approach are given by CNES [14] with one of our 10 MHz QAS OB USOs. We can see that the limit of MTIE (Tm, Tp) for our oscillators is the frequency short-term stability floor (frequency flicker-noise), in stable conditions [6].

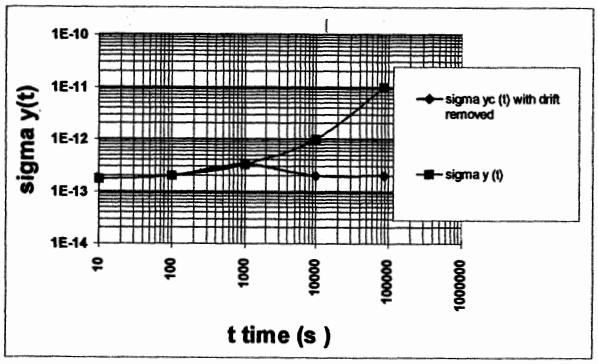

Figure 14 : 10 MHz QAS ON BOARD USO :Allan standard deviation versus integration time

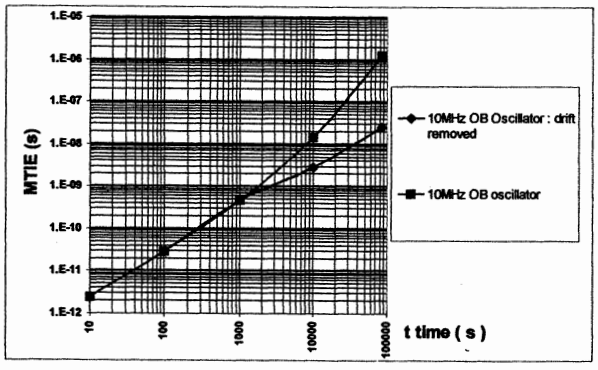

Figure 15 : 10 MHz QAS ON BOARD USO mean time interval error versus integration time

Figure 16 shows the calculated MTIE (24h, Tp) for the 10 MHz QAS OB USO with its stability given by figure 14. The measurement gives :

$$MTIE\ (24h\ ;\ 3{,}5h) \cong 7{,}0\ ns$$

In good compliance with the calculation point. Under environment stress, only the irradiation degraded the phase stability.

With the new material 5 MHz QHS resonator which has the following characteristics :

- $\sigma y\ (10s) = 7.10^{-14}$
- irradiation sensitivity : 5.10^{-13}/rad
- magnetic field sensitivity : $1{,}5.10^{-13}$/gauβ

The USO could maintain, with the orbital environment (an irradiation dose of 1.6 rad/h),

$$MTIE\ (24h,\ 3{,}5h) \leq 5\ ns$$

as shown in figure 17 and with calculation of [14].

A qualification program of this new on board USO is under way with the CNES.

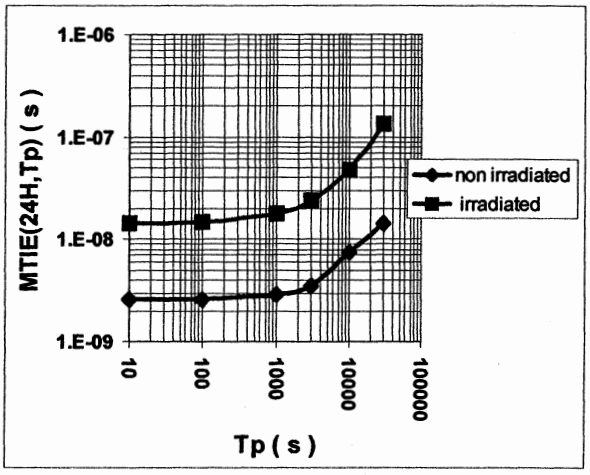

Figure 16 : 10 MHz QAS On-board USO : MTIE (24H, Tp) with or without 38.4 rad/day irradiation level

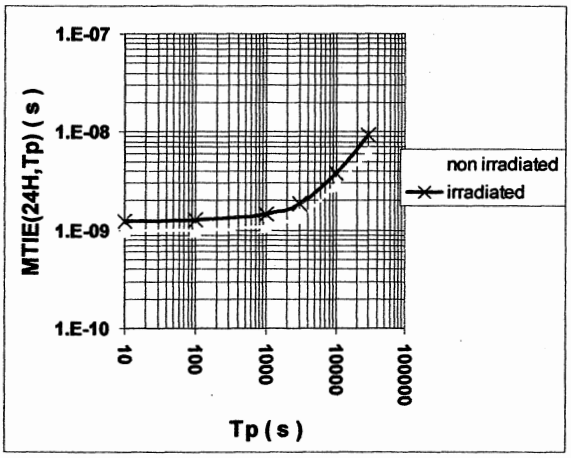

Figure 17 : 5 MHz QHS On-board USO : MTIE (24H, Tp) with or without 38.4 rad/day irradiation level

8. LONG TERM STABILITY

In the article [8], we have described the long term performances production batch of 10 MHz QAS oscillators (figure 18 and 19). Their ageing follows the well known law as described in MIL-0-55310. Because the average time period before launching is 5 years, we can calculate, according to the law, for a production batch, an ageing per month at five years better than 3.10^{-10}/month. That is confirmed by a sample batch preserved for 5 years under operation, and by measurements taken by the CNES for the models in the DORIS orbit.

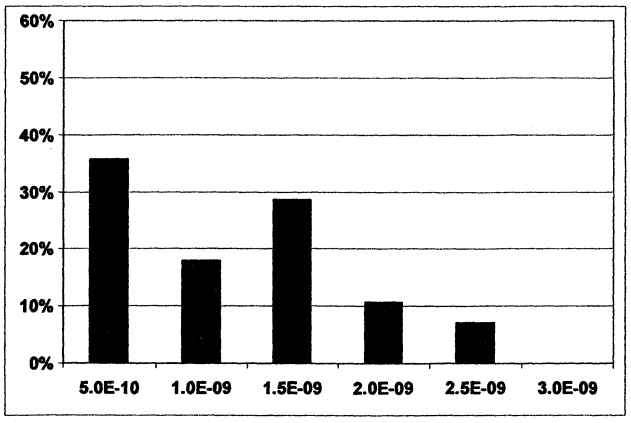

Figure 18 : 10 MHz QAS GB USO fifth month ageing distribution

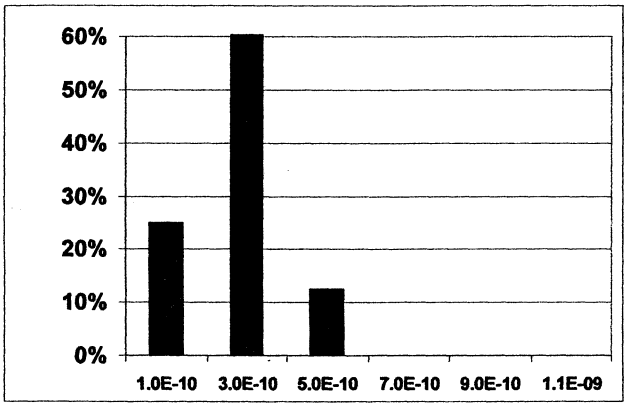

Figure 19 : 10 MHz QAS GB USO month ageing distribution after 5 years

The improvement of long-term stability may be achieved by using a quartz resonator 5 MHz QHS, third overtone, SC Cut. The ageing distribution of a production batch, ovenised in a GB USO, is presented in figures 20 and 21, at different times. An improvement of a factor of two may be obtained in comparison to the 10 MHz solution.

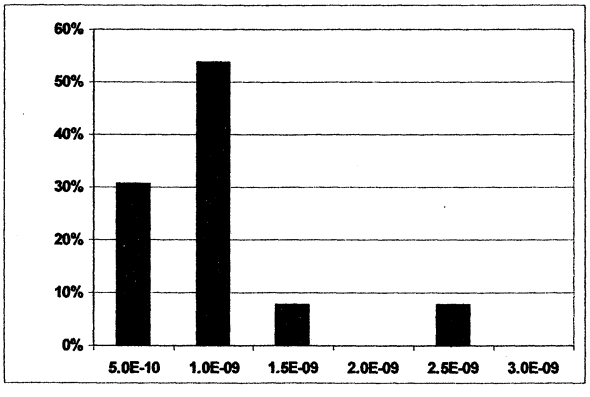

Figure 20 : 5 MHz QHS GB USO fifth month ageing distribution

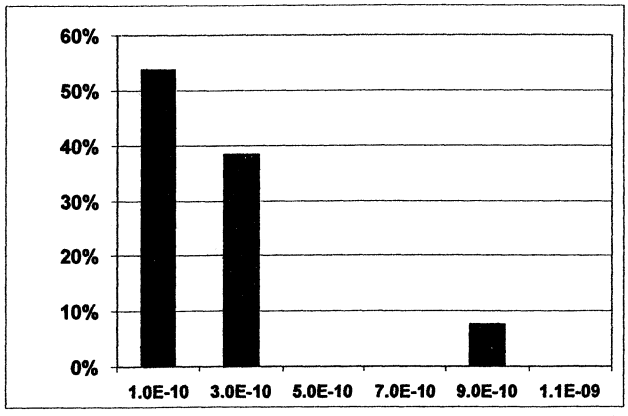

Figure 21 : 5 MHz QHS GB USO month ageing distribution after five years

9. CONCLUSION

With the new material, with the use of the new 5 MHz QHS quartz resonator and by sorting the electronic components, we have obtained a significant improvement with our USO in :

- short-term stability
- magnetic field sensitivity
- irradiation sensitivity
- ageing

and we are aim to fulfill the GALILEO requirements.

A qualification program of the new On-board USO is under way with the CNES. For the Ground base USO, the new 5 MHz QHS resonator is already in production : CFPO-US 1 model.

We would like to thank :

- M. BRUNET from the CNES (Toulouse),
- M. GROSLAMBERT from the L.P.M.O (Besançon),
- M. SANTARELLI from the LPTF (Paris),

for their help and support in the frequency short-term measurement of C-MAC resonators and USOs.

[1] Jari Mannermaa, Kalevi Kallioniäki, Tapio Mansten, "Long Term Stability of high quality OCXOs", Proceedings of the 12th EFTF, March 1998.

[2] W. Weidemann, "Oscillator selection to support CDMA holdover requirements" Proceedings of the 12th EFTF, March 1998.

[3] E. Gerard and R. Molle, "Design and Qualification of an Ultra Stable Oscillator for Space Applications, Proceedings of the 5th EFTF., Besancon 1991, pp 347.

[4] M. Brunet, A. Auriol, J.P. Berthias, M. Costes, J.K. Issler, P. Sengenes, "DORIS precise orbit determination and localization - Performances in orbit and preliminary studies of DORIS-NG", 11th European Frequency and Time Forum Neuchâtel - March 1997.

[5] G. Santarelli, C. Audoin, A. Makdissi, Ph. Laurent G. J. Dick, and A. Clairon, "Frequency stability degradation of an oscillator slaver to a periodically interrogated atomic resonator", IEEE Trans Ultra. Ferro. Elec Freq. Contr., vol. 54, pp. 887-894, 1998.

[6] V. Candelier, G. Marotel, D. Thorax, C. Trialoup, "Cost Effective Time and Frequency Reference", Proceedings of the 31st Annual PTTI - December 1999.

[7] Enrico Rubiola, Jacques Groslambert, Michel Brunet, and Vincent Giordano "Flicker Noise Measurement of HF Quartz Resonators" IEEE Transactions on UFFC, June 27, 1999.

[8] Vincent Candelier, Gérard Marotel, Didier Thorax, Claude Trialoup, "New miniature ultra – stable oscillators" Proceedings of the 13th EFTF, March 1999.

[9] V. Candelier, J. Chauvin, C. Gellé, G. Marotel, M. Brunet, R. Petit, "Ultra Stable Oscillators " Proceedings of the 12th EFTF, March 1998.

[10] J. Rutman, "Characterization of Phase and Frequency instabilities in precision frequency Sources : fifteen years of progress", Proceedings IEEE 66, 1048-1075, 1978.

[11] C. Audoin, Reprint from "Metrology and Fundamental Constants", 1980 LXVIII Corso Soc. Italia di Fisica, Bologna (Italia).

[12] J.A. Barnes, A.R. Chi, L.S. Cutler, D.J. Healey, D.B. Leeson, T.E. Mc Gunigal, J.A. Mullen, W.L. Smith, R.L. Sydnor, R.F.C. Vessot and G.M.R. Winkler – IEEE Trans. Instr. Meas. IM 20, 105 (1971).

[13] F Vernotte, J. Delporte, M. Brunet and T. Tournier, "Uncertainties of Drift Coefficients and Extrapolation Errors : Application to Clock Error Prediction" Metrologia - February 1, 2001.

[14] J. Delporte, F. Vernotte, M. Brunet, T. Tournier "Modelisation ans Extrapolation of Time Deviation of USO and Atomic Clocks in GNSS-2 Context" Proceedings of 32th Annual - PTTI 2000.

[15] Ph. Cathelin, B. Nasreddine, P. Canzian, V. Candelier, "Short Lead Time for the Design of High Performance Airborne Oscillators", Proceedings of 8th EFTF, 1994.

MINIATURE DOUBLE OCXO WITH LOW POWER CONSUMPTION

Igor Abramzon
Roman Boroditsky
VF Technologies, 75 South Street, Hopkinton, MA 01748, USA

1. ABSTRACT

Essentially novel design of a double ovenized crystal oscillator (DOCXO) has been developed recently to satisfy high frequency stability, low power consumption and small size requirements. Based on the newest design of TO-8 packaged OCXO the DOCXO provides (1-3) E-9 temperature stability at 500 mW power consumption while packaged in about 5 cm^3 volume.

The paper describes design, operation and most important characteristics of the DOCXO.

2. INTRODUCTION

Recent developments in the area of telecommunication, navigation, and data transmission systems require crystal oscillators with high frequency stability, small size, and low power consumption. For instance, Stratum 3E standard requires a total frequency excursion of the local oscillator in "holdover mode" not to exceed 10 ppb over 24 hour period [Ref. 1]. That includes stability over temperature (usually -40°C to +85°C), aging, and initial offset. This in turn require better than ± 4 ppb temperature stability. Accompanied by less than 800 mW power consumption and 1/2 inch package height requirements, such performance is hardly achievable using conventional OCXO designs. Single oven approach would not yield temperature stability requirements, while double oven being prohibitively expensive in some cases, would not satisfy power consumption and size requirements. We suggested essentially novel approach in designing a high stability oscillator based on fully integrated OCXO packaged in TO-8 vacuum holder. Additional stabilization of the TO-8 unit with a simple external heater allows significant improvement in temperature stability at minimal expenses in power consumption and volume. The paper discusses construction and operation of the DOCXO as well as describes its most important characteristics.

3. DESIGN AND OPERATION

As mentioned above, design of the double OCXO is based on fully integrated OCXO packaged in a TO-8 evacuated holder. The TO-8 OCXO includes SC-cut crystal blank plated with electrodes and heater, as well as all electronic circuitry - sustaining stage, buffer amplifier, thermocontroller, and voltage regulator. Hybrid thick-film ceramic circuit is assembled on the TO-8 header (fig. 1).

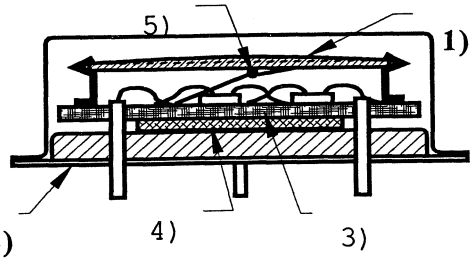

Fig.1

1) – SC-cut crystal
2) – TO-8 header
3) – Hybrid circuit
4) – Insulation
5) – Thermosensor

Due to the excellent thermal insulation of the heated parts via high vacuum level and low thermal conductivity of the mounting structure very low power consumption (about 60 mW at room temperature) is achieved. In

conjunction with thermal stabilization of the oscillator circuitry high frequency stability (10-30 ppb) and fast warm-up time (15-30 s) is also attained [Ref. 2].

To further improve temperature stability of the OCXO, a second stage of temperature stabilization is added into new design. The second stage is implemented on a ceramic substrate and includes thermocontroller circuit, thick-film heater, and thermosensor. The substrate is attached to the bottom of the TO-8 header with thermoconductive adhesive. The whole assembly is mounted on a printed circuit board and sealed in 20x20x12.5 mm^3 package (Fig.2.).

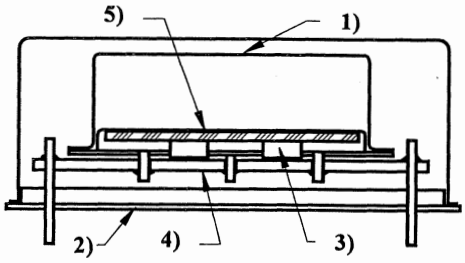

Fig.2.

1) - TO-8 OCXO
2) - Package
3) -Second stage substrate with components
4) – Printed circuit board
5) – Adhesive

The external stage of temperature stabilization is tuned to temperature close to the highest specified operating temperature. Stabilization coefficient of this stage is about 10 and limited by thermal gradients over the TO-8 holder. It does not noticeably depend on whether air or other insulation matter is used between the heated assembly and the enclosure cover. Power consumption of the DOCXO is mostly determined by the consumption of the external stage, which in turn is a function of the surface area dissipating power. Confinement of the heated surface by the TO-8 package results in low power consumption of the DOCXO.

4. PERFORMANCE OF THE DOCXO

This chapter describes some of the most important performance parameters of the developed oscillator.

4.1. Temperature stability.

Typical frequency versus temperature curves of the DOCXO is depicted in fig. 3 (curve 1). Combined stabilization coefficient of the both stages of about 1000 results in frequency stability over 120°C range of no more than ±3 ppb.

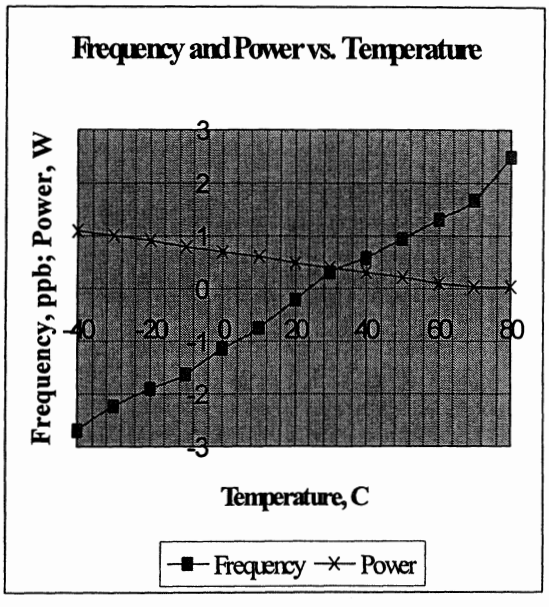

Fig.3.

Power consumption.

Power consumption of the DOCXO versus ambient temperature is shown on Fig. 3. It's about 500 mW at 20°C for air gap insulation and remains almost the same when foam insulation

material is used. The presence of such insulation, however, is appeared to be important for short-term stability of the DOCXO as correlated to the SSB phase-noise power density close to the carrier. Tests showed –90 dBc/Hz at 1 Hz offset, and about –160 dBc/Hz at 10 KHz offset with the foam insulation. About 15 to 20 dB degradation of the phase noise in close-to-the carrier region was observed with the air-gap insulation. We explain this phenomenon as a combination of small time constant of the insulation layer and small thermal inertia of the TO-8 enclosure.

Warm-up time.

Transient processes determine warm-up time of the DOCXO in both the internal and external stages. Fig.4. displays transient process of the oscillator in terms of heating current at 5V input voltage. As one can see start current 250 mA falls to 100 mA after 100 s. Shown data represents device behavior at room temperature ambient.

Frequency settling curve (Fig.5.) has smooth character due to relatively weak influence of the external heating on the frequency. The frequency reaches 1E-7 accuracy after 45s from powering-up as with the single TO-8 OCXO while 10 ppb accuracy is attained in 90 s after stabilization of the second stage.

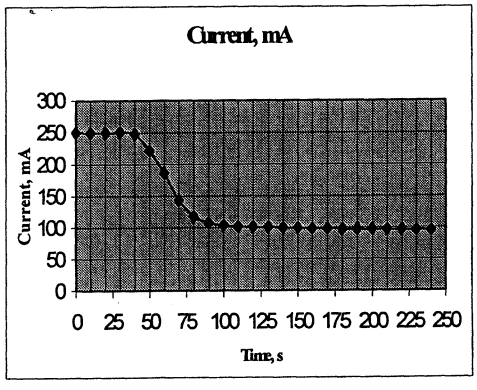

Fig.4.

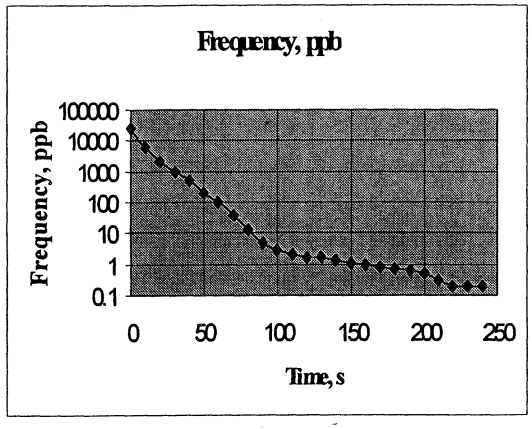

Fig.5.

Aging.

Aging rate of the DOCXO is determined entirely by aging of the TO-8 OCXO because of the negligible influence of the second stage circuit on frequency of the oscillator. The TO-8 OCXO aging is of special interest as a number of electronic components and materials are involved in the design.

Over the period of more than a year we tested 25 units of 10 MHz SC-cut OCXO packaged in TO-8 holder. The units were fabricated using specially developed procedures of wet cleaning, vacuum-bake, and "cold-welding" to attain high level of vacuum and minimal absorption activity after the packaging. All, but one unit exhibited less than 0.1 ppm drift over the first year of operation without pre-aging. About 70% of the units drifted less 50 ppb over that period.

The results are comparable to the aging of conventional OCXO using individually sealed crystals. Carried out research allows to conclude that the hybrid integration of the whole OCXO does not affect the long-term stability provided that proper cleaning and evacuation processing are used.

5. CONCLUSION.

Due to the use of the integrated micro-size OCXO as the basis for a developed device, the miniature DOCXO has excellent frequency stability over a wide temperature range surpassing that of single oven OCXO at similar size and lower power consumption. It proved to be the best option to satisfy stringent requirements of modern communication standards, when a combination of high frequency stability, low power consumption, and small size requirements can not be realized using conventional techniques.

6. REFERENCES

1. Bellcore, GR-1244-CORE. Clocks for the Synchronized Network: Common Generic Criteria.
2. I. Abramzon, R. Boroditsky, D. Cocuzzi. Proceedings of 1997 IEEE IFCS, pp. 943 – 945, 1997

THE ANHARMONIC MODE VIBRATING SC-cut RESONATORS EXCITED BY LATERAL FIELD. APPLICATION IN OSCILLATORS

Krzysztof Weiss*, Wiesław Szulc*, Barbara Gniewińska*, Jacques Groslambert**

*Tele and Radio Research Institute, ul. Ratuszowa 11, 03-450 Warsaw, Poland
**Laboratorie de Physique et Metrologie des Oscillateurs, 32 Avenue de L'Observatoire, F25044 Besançon Cedex, France
e-mail. kweiss@itr.org.pl

1. ABSTRACT

Different versions of SC 301 and 310 mode resonators have been presented over past several years on EFTF's, but only the main parameters of these resonators were measured and optimized. The main mode lateral field excited resonators exhibit high value of motional resistance and very low value of motional capacitance. One undesirable property of these resonators is difficult frequency calibration and oscillator frequency adjustment. The anharmonic mode resonators exhibit lower motional resistance and few times higher motional capacitance. Because of that frequency calibration and frequency adjustment in oscillator is significantly easier. In Tele and Radio Research Institute lateral field excited resonators working on the main mode 300 and working on anharmonic modes 301 and 311 were manufactured. The resonators noise were measured in LPMO in Besançon using the interferometric method described in [Ref. 1]. For lateral field excited resonators the double oven OCXO oscillator was designed. The resonators were mounted in oscillators. Next the short term stability, long term stability and thermal stability of oscillators were measured, using conventional methods of measurement. All resonators used in oscillators were manufactured from the same swept quartz material in the same technological process. The long term frequency stability measurements were carried out in laboratory with ambient temperature stabilization in the range 20 ±1°C. The long term frequency stability was corrected for atmospheric pressure and air humidity. In the paper the results of chosen anharmonic mode lateral field excited resonators noise parameters are presented. The parameters such as short term, long term and thermal frequency stability of oscillators utilizing lateral field anharmonic mode resonators are compared with those of oscillators utilizing classical lateral field excited SC cut resonators.

quartz oscillator, lateral field anharmonic mode resonator

2. INTRODUCTION

The lateral field excited resonators working on anharmonic modes have been presented on EFTF's since 1998 [Refs 1-3]. The construction of these resonators and problems concerned with their manufacturing have been described [Ref. 4]. In the year 2000 the first anharmonic mode working resonators were mounted in oscillators and parameters of oscillators were measured. Parameters of oscillators with anharmonic mode resonators were compared with parameters of the same construction oscillator with classical lateral field excited resonator. For full comparison of obtained results the classical lateral field resonators and anharmonic mode resonators were made of the same material and in the same technological conditions. For lateral field resonators excitation the special oscillator was designed.

3. RESONATORS CONSTRUCTION AND PARAMETERS

All resonators were made of synthetic swept quartz produced by russian company Morion. Vibrators were of diameter 14 mm and crystallographic orientation, thickness and curvature radius depending on utilized mode of vibration. Parameters of vibrators are presented in table 1.

Table 1. Orientation and dimensions of quartz plates

Vibration mode	Frequency [kHz]	Crystallographic orientation		Diameter [mm]	Thickness [mm]	Curvature radius [mm]	Frequency constant [kHz×mm]
		ϕ	θ				
300	10 000	22°10'±1'	34°06'30"±30	14	0,542	750	5420
301	10 000	-"-	34°07'30"±15	-"-	0,545	1000	5449
	8 192	-"-	34°07'30"±15	-"-	0,668	500	5472
311	10 000	-"-	34°06'30"±	-"-	0,548	750	5475
	8 192	-"-	34°06'30"±	-"-	0,671	500	5497

The typical technology for vibrators manufacturing was used. The electrodes of 50nm gold on chromium were deposited on one side of quartz plate. The electrodes shape is presented in fig. 1. The resonators parameters are presented in table 2.

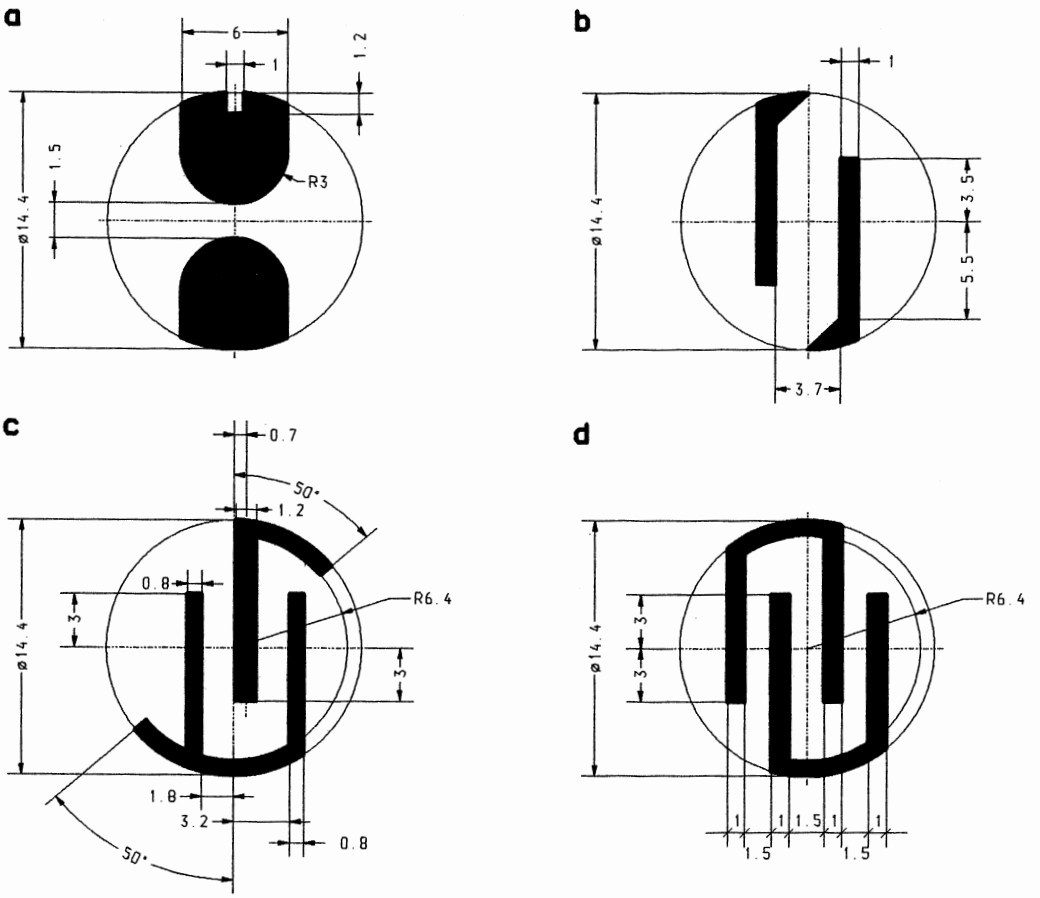

Fig. 1. Electrodes configuration and dimensions used in lateral field resonators

Table 2. Parameters of resonators

Resonator symbol	No	T_e [°C]	f_{sT_e} [Hz]	R_1 [Ω]	C_1 [aF]	C_0 [pF]	$\tilde{a}$ [S/K]E-7	Q [E6]	Electrode Fig.1
LF_{300}	P65	82	9 999 995,5	660	18,96	0,6	1,2	1,28	a
	101	75	10 000 000,9	1004	11,68	0,13	-0,5	1,36	b
	102	80	9 999 998,7	1133	10,86	0,14	1,3	1,30	b
LF_{301}	301	68	9 999 998,4	405	36,59	0,3	-8	1,07	c
	302	60	9 999 996,0	403	36,37	0,3	-3,8	1,08	c
	303	70	9 999 997,5	338	40,72	0,3	-6,8	1,16	c
	304	70	10 000 002,5	384	40,38	0,3	-4,8	1,03	c
	305	70	10 000 005,0	409	37,39	0,3	-4,8	1,04	c
	401	64	8 192 000,4	291	48,33	0,3	-1,6	1,38	c
	404	64	8 191 996,5	311	44,71	0,3	-1,9	1,40	c
LF_{311}	501	62	9 999 997,4	323	44,92	0,48	3,8	1,10	d
	502	65	9 999 998,2	360	39,21	0,48	5,1	1,13	d
	503	68	10 000 005,0	297	53,41	0,48	2,4	1,00	d
	505	65	10 000 001,0	297	48,76	0,48	1	1,10	d
	506	75	10 000 008,5	284	50,24	0,48	0,8	1,11	d
	507	75	10 000 006,8	309	45,10	0,48	0,8	1,14	d
	602	62	8 191 992,6	263	44,71	0,51	5,0	1,32	d

Spectral density of relative frequency fluctuations $S_y(f)$ of two 311 mode resonators was measured in LPMO in Besançon using interferometric method [Ref. 5]. Both resonators exhibit this parameter lower than $5,7\times10^{-13}$ for 1Hz. It corresponds to Allan variance $7,3\times10^{-13}$ for τ=1s. The dynamic coefficient of thermal frequency dependence was measured using the method of resonator response to step temperature change [Ref. 6]. The values of dynamic coefficient presented in table 2 show that direction of quartz plate mounting of 301 mode and 311 mode resonators is not optimal and needs optimization and better repeatability. The high value of this coefficient may influence short term stability of resonator frequency.

4. OSCILLATOR CONSTRUCTION AND PARAMETERS

The modified Butler oscillator was designed for lateral field excited resonators. The same oscillator design was used for all types of resonators. The oscillator was optimized for very low frequency noise level and low temperature frequency coefficient. The resonator excitation power was in the range of 8÷15μW depending on resonator motional resistance. The electric circuit influence on short term frequency stability and noise level was determined on the basis of noise measurement in the open loop of oscillator and temperature characteristics was determined with equivalent resistor, assuming Q value of 1×10^6. The results are presented in table 3.

Table 3. Parameters of exciting circuit

No.	Parameter	Value
1.	Phase power fluctuation density spectrum S_a(1Hz)	-120 dB
2.	Allan variance	$1,2\times10^{-13}$
3.	Frequency vs. temperature coefficient[K^{-1}]	$(5\div10)\times10^{-10}$

The resonator and exciting circuit were located in thermostat with parameters presented in table 4.

Table 4. The oscillator oven parameters

No.	Parameter	Value
1.	Thermal quality in resonator surrounding zone	1000
2.	Thermal quality in oscillator circuit surrounding zone	800
3.	Temperature fluctuation measured in resonator[K]	
	$\sigma_{at(1s)}$	2×10^{-6}
	$\sigma_{at(10s)}$	$2,5\times10^{-5}$
	$\sigma_{at(100s)}$	$2,5\times10^{-4}$
4.	Long term temperature stability [1/24 h]	$1,5\times10^{-4}$

5. THE OSCILLATORS TESTING RESULTS

The frequency vs. temperature characteristics of oscillators were measured in the range 0÷50°C.

Typical characteristic of oscillator frequency vs. temperature (with LF_{301} resonator no. 305) is presented in fig. 2.

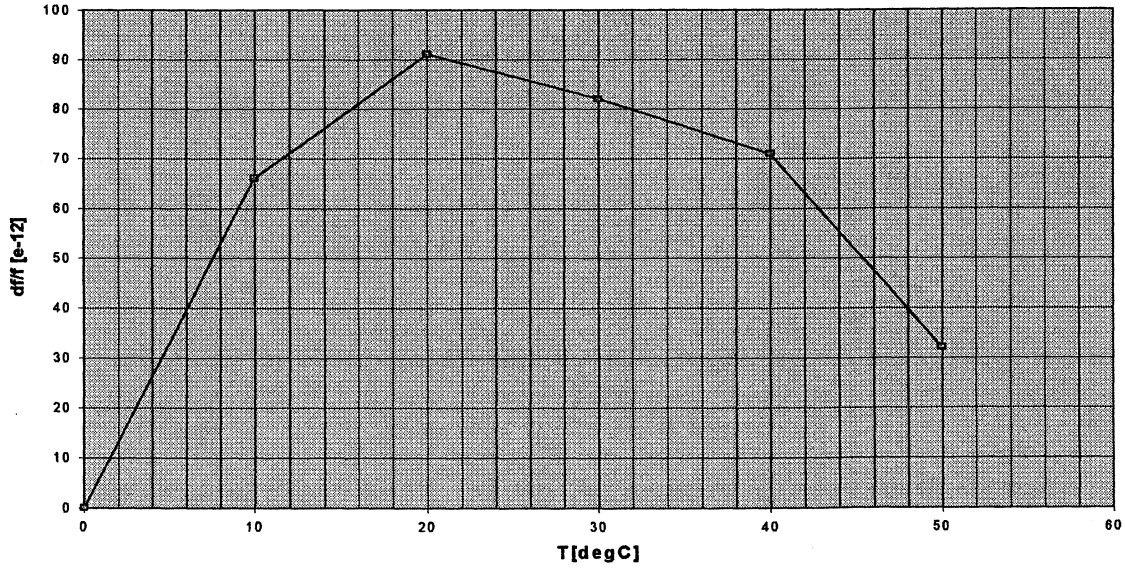

Fig. 2. Characteristic of oscillator frequency vs. temperature (with LF_{301} resonator no. 305)

The short term frequency stability of oscillators with resonators presented in table 2 was measured. The insignificant differences between short term stability of oscillators with different types of resonators were observed. The oscillators with 300 mode lateral field excited resonators exhibited lower noise level. Extreme values of this parameter are presented in fig. 3.

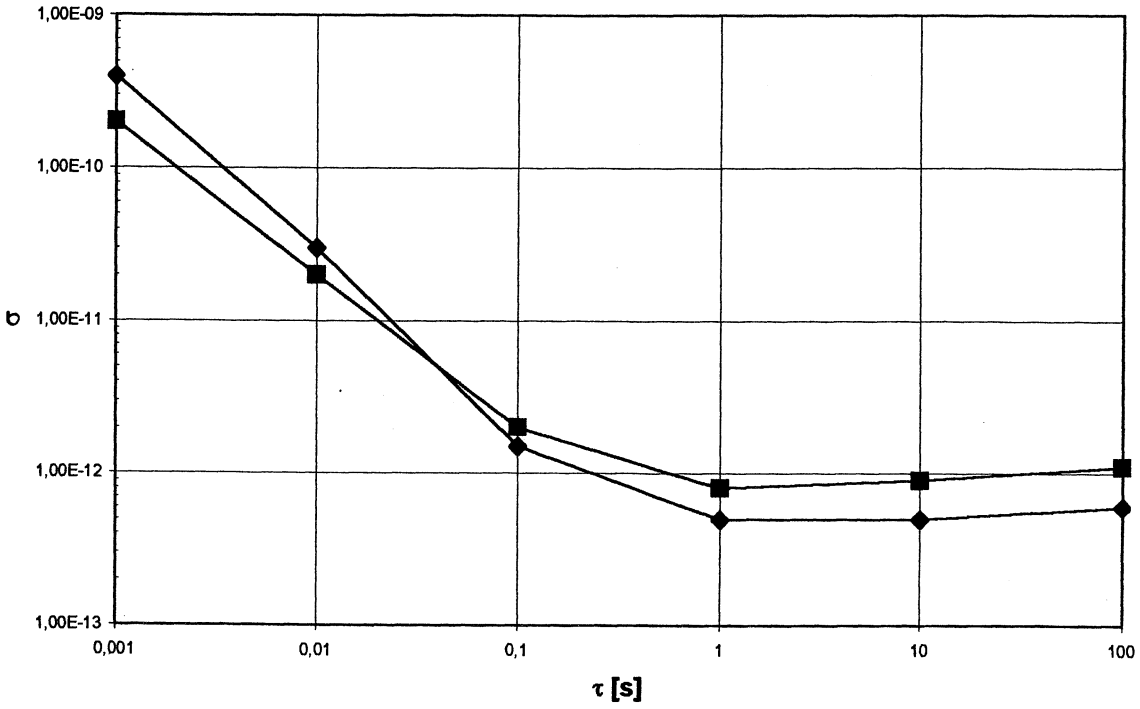

Fig. 3. The short term frequency stability of oscillators, the best and the worst results

The better short term frequency stability of oscillators with 300 mode resonators probably is result of higher Q value and lower dynamic frequency vs. temperature coefficient. On the basis of these results it is very difficult to evaluate which resonators construction have better or worse noise parameters.

The long term frequency stability of oscillators was measured in two months period. At the beginning three oscillators with resonators, admitted for mounting in oscillators optionally because of little scratches observed by microscopic examination on vibrator surface out of vibrating region, were removed. These oscillators exhibited significant worse preliminary aging. The long term frequency stability measurements were carried out in laboratory with ambient temperature stabilization in the range 20 ±1°C. The long term frequency stability was corrected for atmospheric pressure and air humidity. The pressure coefficient was in the range $-(2\div9)\times10^{-12}$/hPa. The air humidity coefficient was in the range $-(4\div13)\times10^{-12}$/%. The aging results are presented in table 5.

Table 5. The oscillators aging results

Resonator type	Number of oscillators with aging in range			Total
	$(5\div10)\times10^{-11}$/24 h	$(10\div15)\times10^{-11}$/24 h	$(15\div20)\times10^{-11}$/24 h	
LF_{300}	3	-	-	3
LF_{301}	3	2	-	5
LF_{311}	-	3	3	6

6. CONCLUSIONS

The thermal parameters of oscillator are very good. It came out that the short term frequency stability of oscillators with lateral field excited resonators were independent of the type of resonator used. Probably better results are possible to obtain as dynamic frequency vs. temperature coefficient will be improved by vibrator mounting in holder direction correction. Long term frequency stability exhibit significant difference for different kinds of

resonators. The best are oscillators utilizing 300 mode resonators, but also oscillators with 301 mode resonators achieve long term instability lower than 10^{-10}. The oscillators were tested over two month period only. The oscillators aging prediction shows for all measured oscillators the possibility to achieve long term stability better than 10^{-10} in time period 4 ÷ 5 months. It's necessary to make the oscillator case hermetic for atmospheric pressure and humidity influence on frequency long term stability reduction. These investigations confirmed that any perceptible defects of quartz plate surface are inadmissible if such parameters are to be achieved.

7. REFERENCES

1. K. Weiss, W. Szulc, The SC-cut lateral field quartz resonator working on anharmonic antisymmetric mode, Proc. of the 12th EFTF, Warszawa, 1998
2. K. Weiss, W. Szulc, B. Dulmet, R. Bourquin, The 311 anharmonic mode vibration SC-cut resonator excited by lateral field, Proc. of the joint meeting 13th EFTF and 1999 IEEE/IFCS, Besançon, 1999
3. K. Weiss, W. Szulc, B. Gniewinska, A. Masiukiewicz, B. Kalinowska, Parameters comparison of different resonators excited by lateral field, Proc. of the joint meeting 13th EFTF and 1999 IEEE/IFCS, Besançon, 1999
4. K. Weiss, W. Szulc, The anharmonic mode vibrating SC-cut resonators excited by lateral field – recent results, Proc. of the 14th EFTF, Torino, 2000
5. E.Rubiola, V.Giordano, J.Groslambert, VHF and microwave interferometric PM and AM noise measurement, Proc. of the 12th EFTF, Warszawa, 1998
6. B.Gniewińska, B.Kalinowska. Termiczne własności dynamiczne rezonatorów kwarcowych, Prace ITR, zeszyt 84/1980, s.5-17

INFLUENCE OF THE ELECTRODE BOUNDARY ON THE FREQUENCY SPECTRUM OF SC-CUT CONVEX CRYSTAL PLATE

STANISLAV NEDOREZOV[×]*, OLEKSANDR SHMALIY*, YURIY SHMALIY**, KRZYSZTOF WEISS*°

[×] Ukrainian Engineering-Pedagogical Academy, Ukraine, docents@vl.kharkov.ua
* "Sichron" Center, 4 Skrypnyka Str., Kharkiv, 310057, Ukraine, sich@kharkov.ua
** Guanajuato University, Salamanca, Mexico
*° Tele-Radio Research Institute, Warsaw, Poland

The recently proposed modulation method [1] allows getting progress in self-contained frequency stabilization of crystal oscillators owing to use of resonator anharmonic modes as sensors of environment. The approach requires accurate determination of the resonator frequency spectrum and sensor frequencies to avoid the problems with modes interaction. Modulation may cause, in principle, the nonlinear products that fall within bandwidth of the sensor, and, as a result, both unwanted splashes in the phase spectrum of oscillator and distortions of a sensitivity curve of a sensor may appear. Both phenomenons can be easily prevented at the early stage if the electrodes shape and a piezoelectric plate geometry are slightly changed based on a correspondent mathematical model of a resonator.

In the report we show the influence of the electrode boundary on the frequency spectrum of a convex crystal plate of SC-cut aiming to satisfy the conditions for the frequencies replacement. We show that to get effect it is necessary to account in the formula for the frequencies calculation both the additional term produced by a nonequidistance of ω^2 [2] and the electrode bound influence. We present the analysis results of the frequencies of the vibration modes of SC-cut convex quartz crystal plates. Those had been carried out with respect to the units with lateral excitation field [3]. It is shown that for the closely replaced anharmonic modes, just as in the considered case, the perturbation theory [2] cannot be efficiently applied. For this case we present the modified approach, in which case the influence of the electrode bound is accounted for an arbitrary shape and size of an electrode. The comparison is given between calculated values of the frequencies and those obtained by experimentally, and we show that prediction fills the experimental data well.

References

1. Yu. S. Shmaliy, "The modulational method of quartz crystal oscillator frequency stabilization", *IEEE Trans. UFFC,* vol. 45, no. 6, pp. 1476-1484, Nov. 1998.
2. S. S. Nedorezov and E. A. Ganenko, "Frequency spectrum of the piezoelectric resonators", *Proc. Int. Symp. on AFSG,* St. Peterburg, Russia, pp. 89-92, 1998.
3. K. Weiss and W. Szulc. "The SC-cut lateral field quartz resonator working in anharmonic antisymmetric mode", *Proc. 12th EFTF,* 1998.

RAPID X-RAY QUARTZ ANGLE SORTING BASED ON THE LAUE METHOD - AN ALTERNATIVE ?

H. Berger, H. Bradaczek, G. Hildebrandt

EFG International Berlin, Research Center, Dueppelstr. 13,
14163 Berlin, Germany

ABSTRACT

The conditions for a rapid orientation determination of quartz blanks by means of white X-ray diffraction (Laue method) in comparison with the well-established Ω-scan method are estimated. The unambiguous indexing of the reflections of a Laue pattern and the influences of statistic as well as of systematic errors are considered using simulation calculations. To gain the reproducibility (a few arcsec) and the cycle time (a few sec) of the Ω-scan, the positions of about 50 reflections would have to be measured with a precision of smaller than 0.01 mm. This cannot be realized with conventional laboratory X-ray sources and detectors available at present.

X-ray Laue method, quartz, orientation determination, simulation calculations.

1. INTRODUCTION

The exact determination of the orientation, i.e., of the angular coordinates of the blank surface related to the crystal lattice and the sorting according to it, is one important step in the production of quartz resonators. It is performed up to now by means of X-ray diffraction methods utilizing characteristic X radiation. These methods need the precise rotation of the specimen through the reflection maximum, either around an axis positioned in the blank surface (so-called "Θ-scan") or around an axis perpendicular to the surface (so-called "Ω-scan"). The last mentioned method developed ten years ago (Ref 1) and improved after that in some ways (Refs 2-4) allows the rapid automatic orientation measurement and sorting of AT-cut blanks with standard deviations of the cutting angle of a few arcsec taking cycle times of three sec. With the machine designed for doubly rotated blanks (Ref 5), a reproducibility of better than two arcsec is reached with cycle times of 8 to 15 sec.

On the other hand, X-ray diffraction using white radiation, the well-known Laue method, is widely used for the orientation determination of various materials. It has the advantage that a stationary measuring arrangement can be used, without any need to rotate the specimen. Therefore, the question arises whether the Laue method could be an alternative to the Ω-scan method for the orientation determination of quartz blanks. In this case, all the properties characterizing the quartz-blank sorting machines based on the Ω-scan should be approximated also by the alternative method. The following points have to be considered:

1. The reproducibility for the main angular coordinate (Θ or the cutting angle) should not exceed a few arcseconds.
2. The total measuring time resulting from the time for X-ray signal accumulation including the evaluation time should be in the order of a few seconds.
3. The measurement must be possible in any azimuthal angular position of the blank.
4. Systematic errors should be smaller than or comparable to the statistic errors and correctable in a simple way.

In the following, it will be discussed whether these demands have chances to be fulfilled. For this purpose, the results of simulation calculations will be considered.

2. PRINCIPLE OF THE LAUE METHOD

The Laue method can be realized in back-reflection as well as in transmission geometry. Both possibilities have to be taken into account. However, the back-reflection geometry is preferred because it is to a wide extent independent of the specimen shape and thickness and opens up more opportunities of the specimen holding and of additional simultaneous measurements.

A sketch of a back-reflection Laue arrangement is shown in Fig. 1. Only perpendicular incidence of the X-ray beam will be considered.

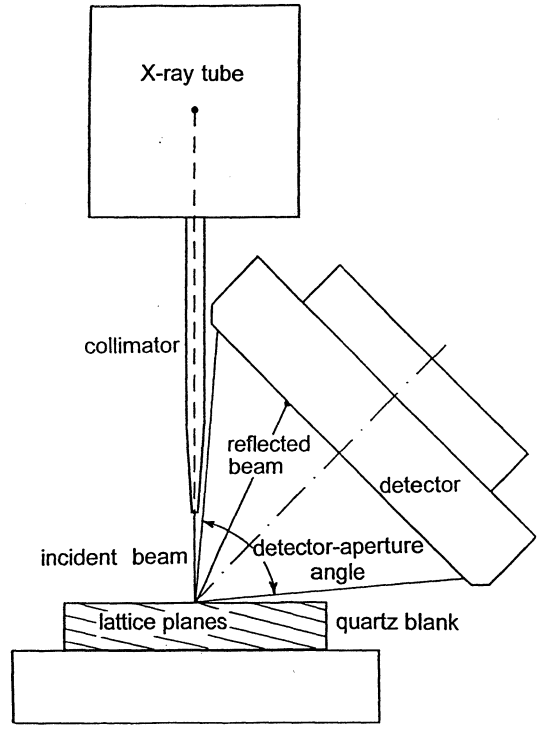

Fig. 1. Scheme of a back-reflection Laue arrangement. Geometry as used for the simulation calculations; one arbitrary set of lattice planes and the corresponding reflected beam are shown.

A position-sensitive detector with suitable resolution and a real-time output must be used. At the present state of technology, only a CCD camera with image intensifier is applicable. It should cover a space angle as large as possible. Further, it must be sensitive for a larger energy range of the white radiation and detect low-intensity reflections. The positions of all reflections exceeding a defined intensity level have to be measured using a suitable integration procedure.

According to the usual procedure (see, e.g., Refs 6-8) the reflections are identified by comparison of the interplanar angles calculated from the reflection positions with those principally possible, calculated before for the given crystal. In general, this is a very complex problem requiring high-sophisticated algorithms and relatively large computing time (Ref 7). Sometimes, semi-automatic procedures have been used (Ref 8). In our case, the problem is simpler because we are concerned with relatively small orientation ranges only, in the order of magnitude of a few degrees (each for AT, SC, and so on).

After indexing the reflections, all their measured positions are used to calculate the angular coordinates of the surface by means of a least-square procedure.

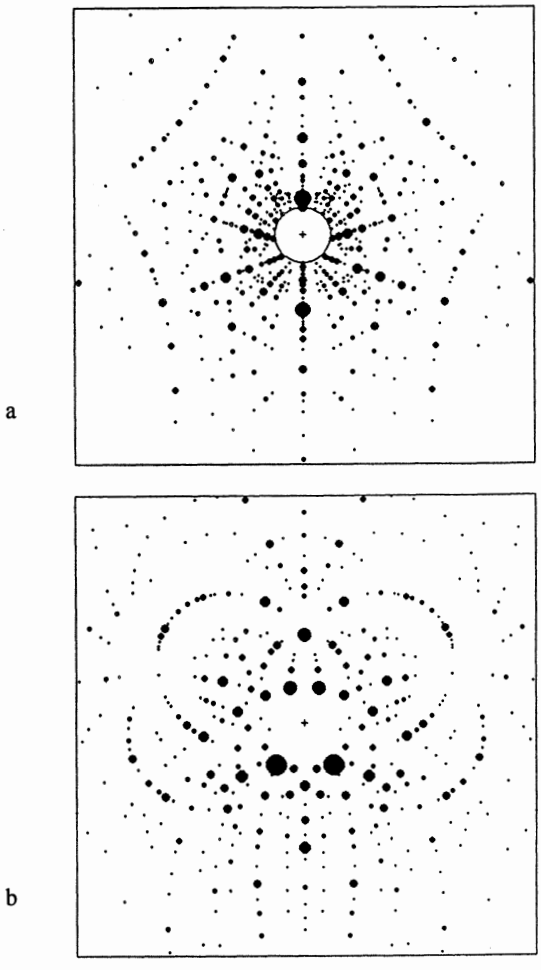

Fig. 2. Calculated Laue patterns of AT-cut quartz. Reflections in a plane perpendicular to the incident beam and parallel to the crystal surface; proportion of the width of the array to the distance from the crystal: 10 : 3; minimum wavelength 0.03 nm (corresponding to X-ray tube voltage 40 kV); reflection areas proportional to intensities; without lower-intensity reflections. a) Back-reflection geometry, b) transmission geometry (crystal thickness 0.5 mm).

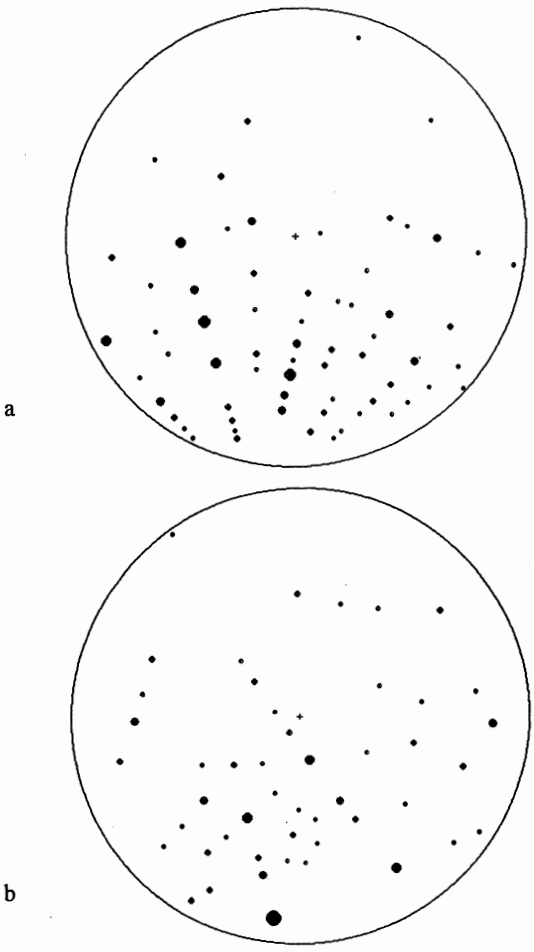

Fig. 3. Examples of simulated Laue-pattern reflection distributions at the detector entrance surface at arbitary azimuths of the blank position. Back-reflection case, detector axis 45° inclined to the incident beam; minimum wavelength 0.04 nm; distance crystal - detector 35 mm, detector radius 30 mm; reflection areas proportional to intensities; without lower-intensity reflections. a) AT-cut blank, b) SC-cut blank.

3. SIMULATION OF LAUE PATTERN EVALUATION

In order to estimate whether a given set of reflection positions taken from a Laue pattern can be evaluated with a sufficient precision in a sufficiently small time using a usual PC, the Laue patterns have been calculated for given quartz orientations.

The intensities were estimated using simple models for the spectrum distribution (Ref 9) and the crystal reflectivity (kinematic for transmission, dynamic for back-reflection, Ref 10). Intensity thresholds have been defined empirically so that the number of reflections corresponds nearly to that of Laue photographs. Calculated Laue patterns are shown in Fig. 2.

Using a round detector, a maximum reflector cone with an aperture angle of about 80° can be detected containing, e.g., 50 reflections. Some examples of resulting reflection distributions in the detector surface are given in Fig. 3.

The reflection positions were assumed to be modified stochastically as well as systematically. Reflections over-

Table 1. Simulation and evaluation of back-reflection Laue patterns of AT-cut quartz with stochastically changing azimuthal positions. Detector axis 45° inclined to the incident beam; minimum wavelength 0.04 nm; distance crystal - detector 35 mm, round detector; radius 30 mm; 50 to 69 reflections (50 evaluated); standard deviations of the reflection positions: 0.005 mm.

Systematic error/mm	Searching toler. angle/°	Evaluation time/sec	Std. dev. of cutt. angle/arcsec
0	0.015	0.25	2.7
0	0.05	0.95	2.7
0	0.1	6.2	2.7
0.005	0.1	6.2	12

laying partially one another were omitted. The time-consuming calculation of interplanar-angle tables can be performed before for a certain orientation and geometry (AT, SC; back-reflection, transmission; direction of the reflection cone).

According to the statistic errors, a tolerance angle for the searching procedure must be defined. The time for the identification depends strongly on this tolerance angle (see Table 1). Up to a tolerance angle of 0.1°, nearly all reflections can be identified unambigously in any geometry (proportion of non-identified reflections: <1%).

In order to gain a precision of the main angular coordinate (Θ or cutting angle, resp.) of three arcsec, the reflection positions must be measured with a precision of about 0.01° (for 50 reflections) corresponding to about 0.005 mm at a detector distance of 35 mm. If constant systematic errors of the reflection positions (e.g., caused by a zeropoint error of the detector) are assumed, the standard deviation of the angular coordinates increases drastically (Table 1).

4. DISCUSSION AND CONCLUSIONS

As demonstrated by the results of the simulation calculations, a rapid reflection indexing and a sufficiently exact orientation determination from a given set of reflection positions is possible if the errors (statistic as well as systematic) of these positions are sufficiently small. Special efforts have to be undertaken to make the systematic errors nearly negligible. This can be done by special procedures minimizing the statistic errors when the assumed systematic errors are changed.

The precision of the reflection position measurement must be rather high, too, in order to become comparable to the Ω-scan. In principle, the reproducibility can be improved by registration and evaluation of a larger number of reflections, e.g., by decreasing the minimum wavelength. However, the resulting increase of the computing time and the memory limits of the present PC's have to be taken into account. Besides that, for the considered detector distances the number of reflection overlays will also increase compensating or overcompensating the larger number of reflections. This could be overcome, again, by positioning a larger detector at a larger distance.

The essential limiting factor, however, is the detector sensitivity in connection with the limited power of conventional laboratory X-ray sources. At present, it is not possible to accumulate in a few seconds a sufficient number of photons per reflection to fulfill the conditions for detectability and reproducibility of the reflection positions. High-brilliance sources and expensive detector systems are not an alternative to the well-established sorting machines based on the Ω-scan.

REFERENCES

[1] Nestler, B., Kuhr, H.-J., Hildebrandt, G., Bradaczek, H.: "Novel Use of a Commercial Goniometer for Sorting Round Quartz Blanks", Meas. Sci. Technol. **2**, 528-531, 1991.

[2] Morys, B., Bradaczek, H., Hildebrandt, G.: "Improved Ω-Scan for Separate Measurement of True AT-Cutting Angles and X-Miscutting Angles for Round Quartz Blanks", Proc. Intern. Frequ. Contr. Symp. 237-240, 1994.

[3] Berger, H., Bradaczek, H., Hildebrandt, G.: "Improvements of the Ω-Scan Method by Eliminating Systematic Errors", Proc. 19th Piezoelectr. Dev. Conf., 15/1-15/15, 1997.

[4] Bradaczek, H.-A., Lim, T., Pianowski, H.: "Optical Surface Scan by Laser Device, an Improvement in the Cutting Angle Determination of Round Quartz Blanks", Proc. 19th Piezoelectr. Dev. Conf., 12/1-12/8, 1997.

[5] Berger, H., Bradaczek, H., Bradaczek, H.-A., Hildebrandt, G.: "Application of the Ω-Scan to the Sorting of Doubly Rotated Quartz Blanks", Proc. Intern. Frequ. Contr. Symp. 412-415, 1996.

[6] Ohba, R., Yamada; H., Watanabe, H.: "Automated Indexing of X-Ray Laue Spots for Arbitrary Lattices, Japan. J. Appl. Phys. **23**, 652-655, 1984.

[7] N.N.: "Rapid Measurement System for Single Crystal Orientation RASCO-L", Rigaku J. **9**, 55-58, 1992.

[8] Sheremet'ev, I.A., Izergin, D.B., Ignatov, D.A.: "Method of Model Rotations for Indexing Laue Patterns", Crystallgr. Reports **44**, 392-397, 1999.

[9] Blochin, M.A.: "Physik der Röntgenstrahlen", Berlin 1957.

[10] Hirsch, P.B., Ramachandran, G.N.: "Intensity of X-Ray Reflexion from Perfect and Mosaic Absorbing Crystals", Acta Cryst. **3**, 187-194, 1950.

THE FORCED VIBRATIONS OF ELECTRODED PIEZOELECTRIC BARS

Jiri Zelenka
Technical University in Liberec
Hálkova 6, 461 17 Liberec, Czech Republic
jiri.zelenka@vslib.cz

ABSTRACT

Bars with material properties of the hexagonal crystals, class 6mm and with the rectangular cross section and the length in the *c*-axis direction are supposed. The forced vibrations excited by the electric field parallel with the length of the bar are considered. The bar vibrations are described by means of the length-extensional, symmetric with-shear and width-stretch coupled vibration modes. The influence of the bar cross section dimensions on its resonant frequency spectrum is discuss.

1. INTRODUCTION

By the design of piezoelectric resonators it is asked to eliminate the resonance frequency of all modes of vibrations what can be excited in the neibourhood the desirable mode. For the quartz X+5° cut resonators in the shape of bars or thin plate of rectangular cross section it was derived by Lee (Ref.1) that the exploited length-extensional vibration is elastically coupled with the width-length flexural and width-shear modes. The situation is the same for all bars cut from trigonal crystals, class 32. The elastic coupling is usually completed with the piezoelectric excitation of undesirable modes.

Another situation is for the bars and thin plates of rectangular cross section prepared from structure of hexagonal symmetry, class 6mm (also for instance polarized PZT type piezoceramics). For this resonators there is no the elastic coupling of the extensional mode with the width-length flexure and width-shear ones. The voltage applied on the electrodes does not excite the width-shear mode.

Two arrangements of the bars or thin plates with hexagonal symmetry, class 6mm are used in applications. The first type has the *c* axis (or the direction of the PZT type ceramic polarization) parallel to the thickness of the plate. The electrodes are deposited on the surfaces perpendicular to the thickness of the bar. In the second type of the bars the *c* axis is parallel with its length. The bar is isotropic in the plane of the cross section. The electrodes are deposited on the surfaces perpendicular to the length of the bar.

In the present paper the second type of the excitation of the bars vibrations are considered. It is supposed that the length of the bar is much greater than the other two dimensions. The results of the study of the bar cross section dimensions on its resonance frequency spectrum of the forced vibrations is given. A system of 1-D equations derived by Lee and Wang (Ref.2) for the AT-cut quartz plates are modified for the description of the bar vibrations

2. RESULTS OF MEASUREMENT

The resonance frequency of the thin narrow plate prepared from the PZT type ceramic polarized in the length of the plate was measured by Burianova (Ref. 3) in the frequency range prom 10 to 1400 kHz. At the first the plate of the dimension 14×7×1 mm was measured. Then the width of the plate was cut to 3.1 mm and the frequency spectrum was measured again. The results of the measurement are given in Table 1.

Table 1. Resonance f_s and antirezonance f_p frequencies of the PZT type ceramic plate measured by Burianova (Ref. 3) for two different width of the plate.

Vibration mode	Width 7 mm		Width 3.1 mm	
	Reson. frequency [kHz]		Reson. frequency [kHz]	
	f_s	f_p	f_s	f_p
E1	95.9	125.0	97.0	122.3
	188.4	194.5		
	217.3	220.3		
E3	387.2	397.2	358.9	371.5
			451.9	462.4
			495.5	507.9
E5	653.1	665.2	653.1	668.3
E7	907.8	920.4	891.3	912.0
E9	1119.4	1140.2	1109.2	1135.0
E11	1297.1	1318.2	1303.2	1318.3

It follows from the comparison of the both measured results that the resonance frequencies of the fundamental and harmonic modes of the length-extensional vibrations differs for both width dimensions very small. The greatest difference is for the E-3 (approximately 8 %). They are also interesting resonance frequencies measured between the length-extensional vibrations E-1 and E-3 for the width 7 mm and between E-3 and E-5 for the width 3.1 mm

3. PLATE EQUATIONS

Consider a rectangular finite bar of the thickness $2b$, width $2c$, and length $2a$ in the rectangular coordinate system x_i as shown in Fig. 1. The bar has the material properties of hexagonal crystal, class 6mm and its dimensions b and c are smaller then the half length a ($b<c<a$). The faces of the bar $x_3 = \pm a$ are covered with conducting metal electrodes. The ratio of the mass of the platings per unite area to the mass of the bar per unite area is R.

The alternating voltage applied across electrodes excites in the bar coupled length-extensional, width-stretch and symmetric width-shear vibrations described in general by Lee and Wang (Ref. 2). The one-dimensional equations of motion and charge equations of electrostatic corresponding to the coupled vibrations are

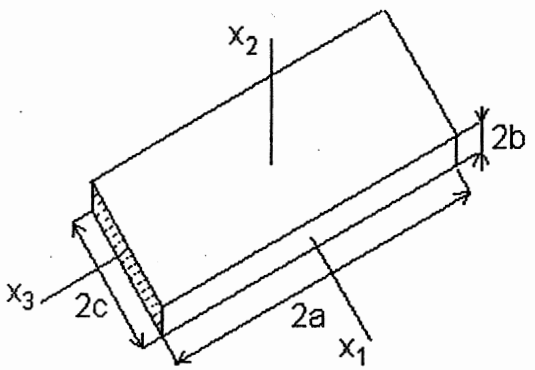

Fig. 1. Finite bar with rectangular cross section in orthogonal system of axis.

$$\bar{c}_{33}u^{(00)}_{3,33}+\frac{\alpha_1}{c}\bar{c}_{13}u^{(01)}_{1,3}+\bar{e}_{33}\varphi^{(00)}_{,33}=\rho(1+R)\ddot{u}^{(00)}_3,$$

$$c_{55}u^{(01)}_{1,33}-\left(\frac{\pi}{2c}\right)^2\bar{c}_{11}u^{(01)}_1-\frac{2\alpha_1}{c}\bar{c}_{13}u^{(00)}_{3,3}$$

$$+\frac{2}{3c}(\bar{c}_{13}+4c_{55})u^{(02)}_{3,3}+\frac{2}{3c}\bar{e}_{31}\varphi^{(02)}_{,3}=\rho(1+R)\ddot{u}^{(01)}_1,$$

$$\bar{c}_{33}u^{(02)}_{3,33}-\left(\frac{\pi}{c}\right)^2c_{55}u^{(02)}_3-\frac{2}{3c}(\bar{c}_{13}+4c_{55})u^{(01)}_{1,3}$$

$$+\bar{e}_{33}\varphi^{(02)}_{,33}=\rho(1+R)\ddot{u}^{(02)}_3,$$

$$\bar{e}_{33}u^{(00)}_{3,33}+\frac{\alpha_1}{c}\bar{e}_{31}u^{(01)}_{1,3}-\varepsilon_{33}\varphi^{(00)}_{,33}=0,$$

$$2(\bar{e}_{33}u^{(02)}_{3,33}-\varepsilon_{33}\varphi^{(02)}_{,33})+\left(\frac{\pi}{c}\right)^2\varepsilon_{11}\varphi^{(02)}$$

$$-\frac{2}{3c}\bar{e}_{31}u^{(01)}_{1,3}=0, \qquad (1)$$

where

$$\bar{c}_{pq}=c_{pq}-\frac{c_{p2}c_{2q}}{c_{22}}, \qquad p,q=1,3$$

$$\bar{e}_{3p}=e_{3p}-\frac{e_{32}c_{32}}{c_{22}}, \qquad p=1,3$$

$$\alpha_1=\frac{\pi}{\sqrt{8}}. \qquad (2)$$

When $\varphi^{(00)}_{,33}$ is obtained from $(1)_4$ and substitute to $(1)_1$ then we receive

$$c^*_{33}u^{(00)}_{3,33}+\frac{\alpha_1}{c}c^*_{13}u^{(01)}_{1,3}=\rho(1+R)\ddot{u}^{(00)}_3, \qquad (3)$$

where $c^*_{33}=\bar{c}_{33}+\frac{\bar{e}^2_{33}}{\varepsilon_{33}}$, $\quad c^*_{13}=\bar{c}_{13}+\frac{\bar{e}_{31}\bar{e}_{33}}{\varepsilon_{33}}$,

and the system of equations (1) reduced to four.

This four governing equation describing the bars free vibrations can be studied by choosing

$$u^{(00)}_3=\sum_{r=1}^{4}A_{1r}\sin\xi_r x_3e^{i\omega t},$$

$$u^{(01)}_1=\sum_{r=1}^{4}A_{2r}\cos\xi_r x_3e^{i\omega t},$$

$$u^{(02)}_3=\sum_{r=1}^{4}A_{3r}\cos\xi_r x_3e^{i\omega t}$$

$$\varphi^{(02)}=\sqrt{\frac{c_{44}}{\varepsilon_{33}}}\sum_{r=1}^{4}A_{4r}\sin\xi_r x_3e^{i\omega t}, \qquad (4)$$

By substituting (4) into $(1)_{2\text{-}3}$, $(1)_5$ and (3) we have

$$[d]\{A\}=0, \qquad (5)$$

where d_{ij} are the elements of the coefficient matrix.

$$d_{11}=\tilde{c}_{33}\bar{\xi}^2_r-(1+R)\Omega^2, \qquad d_{12}=\frac{1}{\sqrt{2}}\frac{b}{c}\tilde{c}_{13}\bar{\xi}_r,$$

$$d_{13}=d_{14}=0, \qquad d_{21}=\sqrt{2}\frac{b}{c}\hat{c}_{13}\bar{\xi}_r,$$

$$d_{22}=\hat{c}_{55}\bar{\xi}^2_r+\hat{c}_{11}\left(\frac{b}{c}\right)^2-(1+R)\Omega^2,$$

$$d_{23}=d_{32}=-\frac{4}{3\pi}\frac{b}{c}(\hat{c}_{13}+4\hat{c}_{55})\bar{\xi}_r,$$

$$d_{24}=2d_{42}=-\frac{4}{3\pi}\frac{b}{c}\hat{e}_{31}\bar{\xi}_r, \qquad d_{31}=d_{41}=0,$$

$$d_{33}=\hat{c}_{33}\bar{\xi}^2_r+4\hat{c}_{55}\left(\frac{b}{c}\right)^2-(1+R)\Omega^2,$$

$$d_{34}=d_{43}=\hat{e}_{33}\bar{\xi}^2_r,$$

$$d_{44}=-(\bar{\xi}^2_r+2\left(\frac{b}{c}\right)^2\hat{\varepsilon}_{11}),$$

where

$$\tilde{c}_{p3}=\frac{c^*_{p3}}{c_{44}}, \qquad \hat{c}_{p3}=\frac{\bar{c}_{p3}}{c_{44}}, \qquad \hat{c}_{55}=\frac{c_{55}}{c_{44}},$$

$$\hat{e}_{3p}=\frac{\bar{e}_{3p}}{\sqrt{c_{44}\varepsilon_{33}}}, \qquad \hat{\varepsilon}_{11}=\frac{\varepsilon_{11}}{\varepsilon_{33}},$$

The vanishing of the determinant of the coefficients matrix $[d] = 0$ gives the dispersion relation which yield four frequency branches.

For the traction-free and charge-free edges at $x_3 = \pm a$ we required

$$T_3^{(00)} = T_5^{(01)} = T_2^{(02)} = D_3^{(02)} = 0, \qquad (6)$$

where

$$T_3^{(00)} = 4(c_{33}^{*} u_{3,3}^{(00)} + \frac{\alpha_1}{\acute{c}} \bar{c}_{13} u_1^{(01)}),$$

$$T_5^{(01)} = 2c_{55}(u_{1,3}^{(01)} + \frac{8}{3c} u_3^{(02)}),$$

$$T_1^{(02)} = 2(\bar{c}_{33} u_{1,1}^{(02)} - \frac{2}{3c} \bar{c}_{13} u_1^{(01)} + \bar{e}_{33} \varphi_{,3}^{(02)}),$$

$$D_3^{(02)} = 4(\bar{e}_{33} u_{3,3}^{(02)} - \frac{1}{3c} \bar{e}_{31} u_1^{(01)} - \varepsilon_{33} \varphi_{,3}^{(02)}). \qquad (7)$$

The normalized frequency Ω, the normalized wave number $\bar{\xi}_r$ and the ratio of amplitudes γ_{sr} let be defined by the relations

$$\Omega = \omega \frac{2b}{\pi} \sqrt{\frac{\rho}{c_{44}}}, \qquad \bar{\xi}_r = \xi_r \frac{2b}{\pi},$$

$$\gamma_{sr} = \frac{A_{sr}}{A_{3r}}, \qquad s = 1, 2, 4. \qquad (8)$$

Inserting (4) into (7) and then the result into (6), Ω vs. dimensions ratio *a/c* curves can be computed for given *a/b*.

4. CONCLUSION

From computed curves expressing the dependence of the normalized frequency on the dimension ratio of the bar follows that the coupling of the length extensional vibrations with the other two modes is very week. The more important is coupling between length extensional and symmetric with-shear modes namely for the overtones of length extensional vibrations. The week resonant frequencies find between the E-1 and E-3, and also between E-3 and E-5 modes belong to the width-stretch vibrations. The fundamental length-extensional mode of vibration (E-1) is not disturbing with the symmetric width-shear mode as the resonance frequency of the symmetric width-shear mode is for all considered ratio of bar dimensions higher then the fundamental resonance frequency of the length-extensional mode.

ACNOWLEDGMENT

This project was supplied with the subscription from Ministry of Education, Youth and Sports of the Czech Republic, project MSM 242200002.

REFERENCES

[1] P.C.Y. Lee, "Extensional, flexural, and width-shear vibrations of thin rectangular crystal plates", J. Appl. Phys., vol. 42 (11), pp. 4139-4144, (1971).

[2] P.C.Y. Lee and Ji. Wang, "Vibrations of AT-cut quartz strips of narrow width and finite length", J. Appl. Phys., vol. 75 (12), pp. 7681-7695, (1994).

[3] L. Burianova, private communication.

Quartz Resonator Treatment by Rapid Thermal Annealing

V. Georgieva, Ts. Angelov, L Vergov, L. Spassov, G Beshkov
Institute of Solid State Physics, Bulgarian Academy of Sciences
72, Tzarigradsko Chaussee Blvd., 1784 Sofia - Bulgaria
E-mail: lazarova@issp.bas.bg

Abstract

We have already shown in earlier work that the parameters of the quartz resonators could be improved by applying of Rapid Thermal Annealing (RTA). Temperature of the heater has been taken as estimation of the temperature of the treated resonators.

This paper deals with farther improvement of the RTA conditions. It is achieved by using Thermosensitive Quartz Resonators (TSQRs) as temperature sensors for measurement of the actual temperature of the resonators during the treatment. RTA conditions have been improved by using TSQRs as temperature sensors for calibration of the equipment and estimation of the actual temperature of the resonators during the treatment.

1. Introduction

Thermal treatment of the resonator structures influences on the structure, morphology, electro-physical parameters of the metal electrodes as well as on the function of the devices itself.

The rapid thermal annealing (RTA) is one of the possible methods for treatment of such structures [1,2]. Our earlier investigations [3] have shown, that different changes emerge within electrodes, depending on initial state of the layers and on the RTA parameters - temperature and time of duration. Morphological investigations have shown densification of the layer and smoothing of their surface. On the dependence of the sheet resistance of Al-electrodes as a function of the RTA parameters a maximum has been obtained [4]. A layer of constant hardness has been detected beneath the initial interface by measuring of microhardness depth profiles of annealed quartz –Al film structures [5].

All mentioned investigations has been performed at temperatures of the heater (Th) corresponding to 700°C, 800°C and 900°C for duration in the range of 5s to 180s. The aim of the present work is to improve the RTA conditions by using Thermosensitive Quartz Resonators (TSQRs) as a temperature sensors for calibration of the equipment for RTA and to measurement of the actual temperature of the resonators during the treatment.

2.Experiments

In order to determine of the real temperature of the resonator structure TSQRs have been used, calibrated as quartz temperature sensors at eight points within the temperature interval from minus 35°C to 235°C. The stabilized temperature with accuracy of ± 0,01° C could be supported by thermostat ULABO, by cooling system and a suitable electronic unit of the heaters. A precise Hewlett Packard quartz thermometer HP 2804A measured the established temperature. The frequency measurements of the calibrated thermosensitive resonators were carried out at temperatures respectively: minus 30,362°C;

minus 9,590°C; 10,108°C; 90,475°C; 130,681°C; 170,086°C; 210,474°C and 235,514°C.

On the base of the measured data the linear temperature – frequency characteristics (TFC) of the investigated samples were determined. A typical TFC is shone on Figure1.

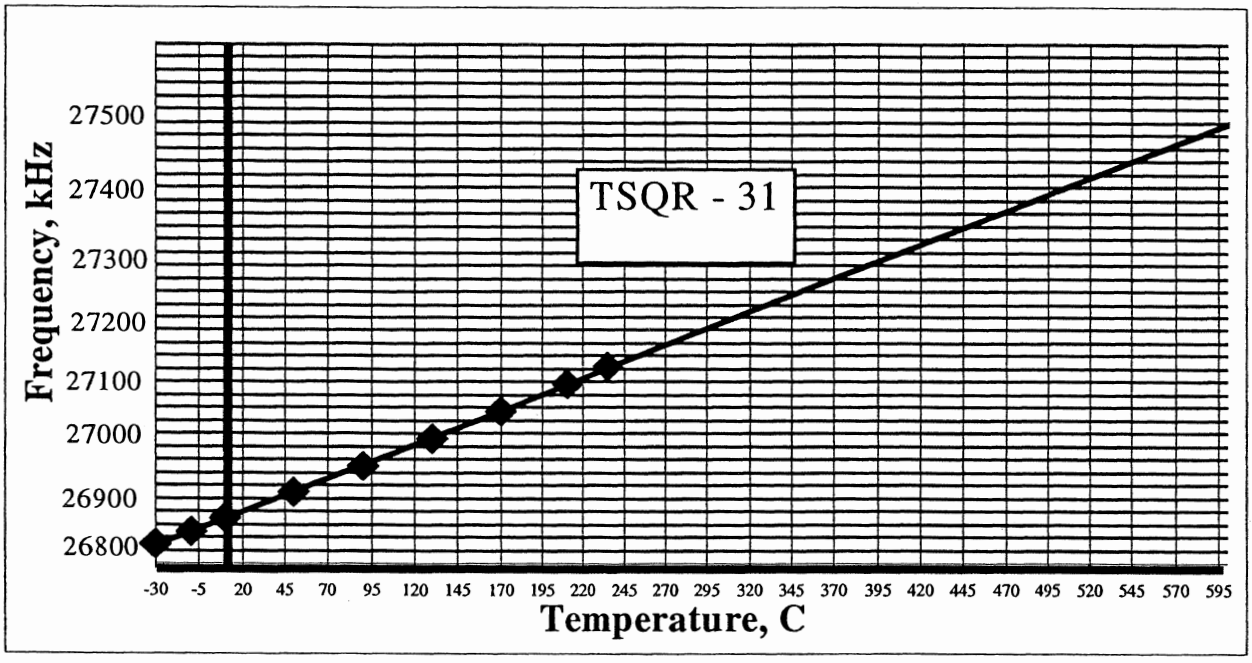

Fig. 1 Temperature – frequency characteristic

The linear change of the frequency with the temperature allows to extrapolate the TFC toward the 500°C. A scheme of the experimental set-up used for determination of the samples temperature during the RTA process is shown in Figure 2.

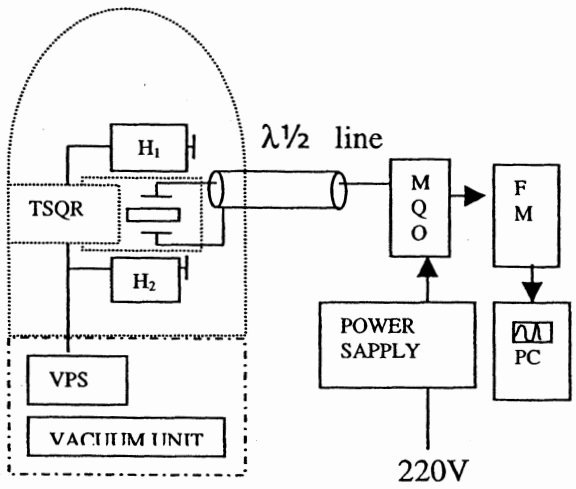

Fig.2 Block scheme of the experimental unit

Preliminary calibrated TSQRs were used as a temperature influenced and the same time temperature sensitive subject. They were directly connected with a measuring quartz oscillator (MQO) by coaxial ½λ line. A frequency meter CH3-64 is used for measurement of the resonance frequency of the TSQRs. An adjusting device for exact positioning of the quartz resonator between both heaters was made use of. Horizontally situated tungsten bands were located as a both heaters themselves (H_1,H_2). The heaters are supplied by a variable power supply allowing the necessary temperature to be reached.

After positioning TSQR, the vacuum chamber was pumped out and the heating was switched on.

In this way the TSQR frequencies were measured by a step of 1 s and the results were registered on the PC memory. This allowed a fast and exact control of the whole temperature process.

After calibration, each sample underwent rapid thermal annealed at the heaters temperatures 700°C, 800°C and 900°C with a duration time of 15s, 30s, 60s and 180s.

3. Results

A typical frequency – time characteristic of a TSQR is presented at the Figure 3.

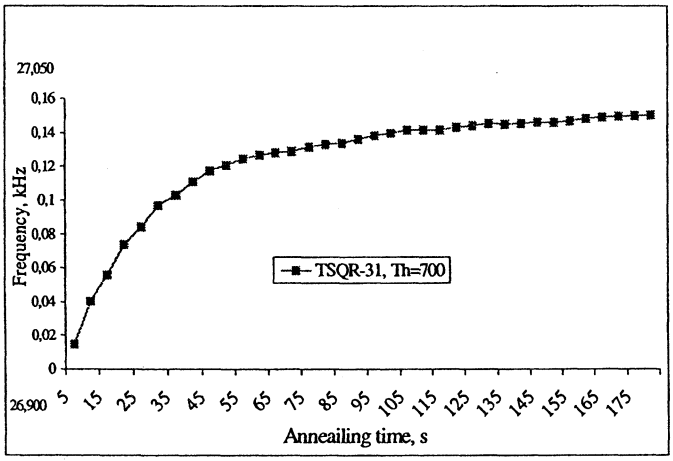

Fig3 Frequency – time characteristic

By interpolation of temperature – frequency characteristics, the measured frequencies of each sample during the RTA were transformed as temperatures and temperature – time characteristics were been obtained.

On Figure 4 temperature – time dependencies are represented for the samples TSQR-31, TSQR-73 and TSQR-74 at the heater temperature 700°C.

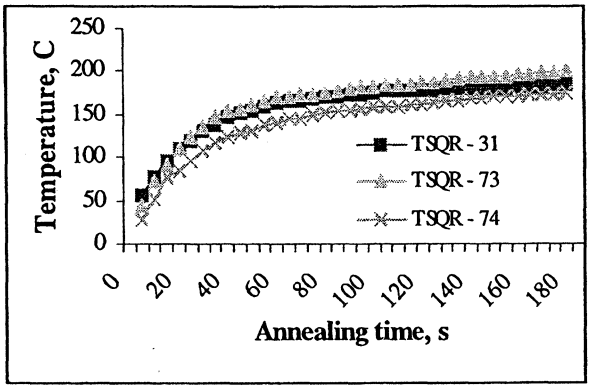

Fig 4. Temperature – time dependencies

The obtained results shown that with increasing RTA processing time the samples temperature increases and for a duration of 180 s it reaches 200 °C.

The maximum registrated difference between the samples undergone RTA treating is less than 26°C.

Figure 5 illustrates the temperature – time dependencies of TSQR – 31 at three different heater's temperatures – 700 °C, 800 °C and 900 °C. For the same duration of the RTA treatment, the temperatures reached by the samples are function of the given heater'stemperature.

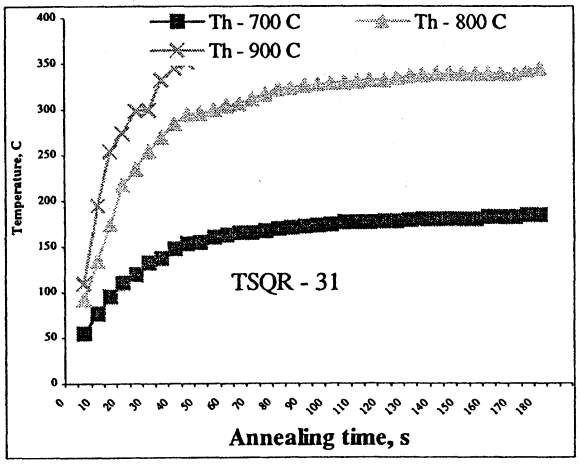

Fig. 5 Temperature – time dependencies

By a duration of RTA treatment of 30 s the temperatures of the samples are 132 °C, 255 °C and 300 °C for the heater's temperatures of 700 °C, 800 °C and 900 °C respectively. While for duration of 100 s the temperature of the treated samples became 175 °C, 329 °C for heater's temperature 700 °C and 800 °C respectively. At heater's temperature 900 °C the measurements of the samples are successful for a duration up to 60 s. The longer duration of the RTA treatment leads to its destruction because of the thermal stresses.

4. Conclusion

RTA conditions were improved by using TSQRs as temperature sensors for calibration of the equipment and estimation of the actual temperature of the resonators during the treatment.

These results are very important for further investigations, related to RTA influence on the equivalent dynamic resonator's parameters and the quality factor of the quartz resonators.

Acknowledgments

This work is partly supported by the Bulgarian Ministry of Science and Education in the framework of Project F-902.

5. References

[1]. L.Spassov, V.Lazarova, M.Marinov, "Behavior of Al-Quartz System After Rapid Thermal Annealing" *Proc. of the 4-th International Symposium on Surface Waves in Solid and Layered Structures (ISSWAS-4), 7-12 June, 1998, St.Petersburg, pp.163-173.*

[2]. L.Spassov, V.Lazarova, G.Beshkov, L.Vergov, Ts.Angelov, "Influence of Vacuum Rapid Thermal Annealing on Some Properties of Quartz Resonators ", *Vacuum, Vol. 51, pp.173-175, 1998.*

[3].L.Spassov, V.Georgieva, M.Marinov, "Structure and Morphology of Thin Al-Layers in Resonator's Systems After Rapid Thermal Annealing", *Proc. of IEEE, vol. 1 ,pp.481-484,1999.*

[4]. V.Georgieva, D,B.Dimitrov, G.Beshkov, L.Spassov, "Influence of Vacuum Rapid Thermal Annealing on the Sheet Resistance of Thin Al Films Deposited on Quartz Crystal", *Proc. of 14-th EFTF, European Frequency and Time Forum, pp. 225-228, 2000.*

[5]. E.P.Trifonova, V.Lazarova, L.Spassov, N.Efremova, "Composite Microhardness of Quartz-Alstructures", *Cryst.Res.Technol.,34,Vol.3, pp.391-395,1999.*

SWEEPING AND ANNEALING APPLIED TO QUARTZ RESONATORS EXPOSED TO LOW DOSE RADIATION

M. A. PASQUALI

ENSMM /LCEP - 26, Chemin de L'Epitaphe - 25000 BESANÇON - FRANCE

ABSTRACT

The aim of this work is to verify the effect of ionizing radiations on low doses quartz resonators. The quartz treatment is based on electrodiffusion (sweeping) and annealing processes. The applied electrical field is high (1500 - 3000 V/cm) and the sweeping process is realized in consecutive steps, being inserted by annealings. Two kinds of atmosphere conditions are applied : sweeping in nitrogen (inert conditions) and sweeping in air (hydrogen supply). The objective of this treatment is to modify the hydrogen defects and to promote its diffusion and reorganization in the quartz or its diffusion out of the material. In order to control these treatments, the evaluation of (OH) concentration ([OH]) and the $[AlO_4]^0$ centers are determined.

From the variation of the turnover point of the frequency - temperature curves as function of irradiations and also to the frequency sensitivity (Hz/rad), it has been concluded that the most radiation stable resonators are those which for the treatment has been made in hydrogen atmosphere.

Key-words : hydrogen centers, aluminum centers, sweeping, annealing, quartz crystals, infrarouge (IR).

1 - INTRODUCTION

The sweeeping process is a post-synthesis treatment that results in the selective ion changes as similar as electrolysis process [1]. It is applied in order to reduce the foreign atoms of SiO_4 lattice. Usually, these elements are monovalent alkalis as Li^+, Na^+ and K^+ and also Hydrogen. They are bonded to other foreign atoms, as substitutional species Al^{3+}, Ti^{4+}, Ge^{4+} or also, the OH^- radicals. The direct bonding with $[SiO_2]^0$ requests a higher energy [2].

Sweeping and irradiation produce a similar effect in some kinds of stuctural defects as the Aluminum centers. It can be represented as follow :

$$[AlO_4/M^+]^0 \rightarrow x\,[AlO_4/M^+]^0 + (1\text{-}x)\{y\,[AlO_4/H^+]^0 + (1\text{-}y)\,[AlO_4]^0\}$$

(1) (2) (3)

M = Li, Na, K ,...

(1) Al-M centers (Al-Li, Al-Na,...), in the synthetic original quartz crystals, and **x** is the remaining proportion after irradiation or sweeping ;
(2) Al-OH centers and **y** is its proportion of formation ;
(3) "Al-hole" center and **(1-y)** is the formation ratio of these electronic charged centers.

Usually, the $[AlO_4/M^+]^0$ dissociation follows the sequence above. It means that paramagnetic Aluminum defects are produced when the Hydrogen supply is stopped in this process. The Hydrogen source is coming from [H] content of samples as the HOH groups or other hydrogen related defects [3]. In the case of sweeping, the H_2 can be supplied by the atmosphere of the reaction chamber.

The dissociation of diamagnetic $[AlO_4/M^+]^0$ centers request less energy than the Hydrogen center, $[AlO_4/H^+]^0$. By the reaction energies listed in Table 1, it is possible to compare the relative stability of the Aluminum and Hydrogen centers [2].

Table 1 - Reaction energies of aluminum centers in α-quartz.

CENTER	E_r (eV)
(1) $[AlO_4]^0 + e^- \Rightarrow [AlO_4]^-$	-1.97
(2) $[AlO_4/H^+]^+ + e^- \Rightarrow [AlO_4/H^+]^0$	-3.22
(3) $[AlO_4/Li^+]^+ + e^- \Rightarrow [AlO_4/Li^+]^0$	-3.67
(4) $[AlO_4]^+ + e^- \Rightarrow [AlO_4]^0$	-3.92

(4) $[AlO_4]^+$: Two-hole aluminum paramagnetic center.

The alkalis diffusion in quartz by irradiation occurs above 200 K. Otherwise, the Hydrogen atoms can diffuse just below 77 K when the oscillation of O-H vibrations are slow [4]. Usually, above 200 K, the potential barrier energy to dissociate alkalis is lower than this of Hydrogen centers. Therefore, the sweeping process requests a lower energy for alkalis dissociation, as 30 to 40 V/cm in spite of 1500 to 3000 V/cm for Hydrogen [5].

In cultured quartz for electronic applications, usually the impurity content is ranged from 10 to about 200 µg/g for Hydrogen and lower than 50 µg/g for Aluminum. As it was shown above, the changes in Aluminum centers by hardening process, like sweeping and irradiation, are well established and presented in many papers [4]. Otherwise, the reaction mechanisms that involve hydrogen species are understood. Up to now, the changes of hydrogen centers are evaluated by some specific bands of IR spectrum.

If we consider that this spectrum is composed also by a broad band and its size is correlated to (OH) content, [OH], it will be reasonable to understand the nature of these defects and also the possibilities in measuring it. Some of these are hydrogenic diamagnetic species, as $[H_4O_4]^0$ or clusters of H_2O molecules, and others [3].

In this work is proposed also the evaluation of (OH) content of quartz samples submitted to different treatments, in addition to the conventional methods of caracterization. These treatments are applied in order to promote increasing or reduction of [OH] and, by this manner, to monitor changes of quartz and resonators parameters.

2 - SAMPLES IDENTIFICATION

Two kinds of samples were employed for these experiments : cultured quartz, SP and natural quartz NB (from Brazil). The resonators identification is the same as the quartz crystals. For each sample a total of eight plates were prepared, being four employed to characterization monitoring and the others for the resonators manufacture.

Quartz Samples and Resonators Identification :

XTy

X = sample name, **SP** (synthetic) or **NB** (natural).
T = treatment. Index **1** (sweeping in air) and **2** (in N_2).

Treatment :
1S , 2S and 3S : first, second and third electrodiffusion steps.
1T, 2T : first and second annealing steps.

Also, some samples were kept in the as-received condition and others, submitted only to one electrodiffusion in inert conditions (N_2). They are identified respectively by SP and NB for the as-received samples, and SPS and NBS.

3 - ANALYTICAL CONDITIONS

3.1 - Samples Treatments :

Electrodiffusion (sweeping) was carried out by applying an electric field of 1500 V/cm and 3000 V/cm along the c-axis of the crystal, when the temperature of 500 °C was reached. Two conditions were employed : air and inert (N_2) atmospheres. The sweeping was realized in 3 consecutives steps, being inserted by annealings. For the first electrodiffusion, the applied electric field was 1500 V/cm. In the second step it was increased to 3000 V/cm and kept in this condition for the last one. As example, the following table shows the changes in the current density ($\mu A/cm^2$) from the first to the last electrodiffusion, in both conditions, air and inert atmospheres.

Table 2 - Current Density.

	SW	J ($\mu A/cm^2$)
NBT_1 sweeping in air	1st	1.84
	2 nd	0.42
	3 rd	0.07
NBT_2 sweeping in N_2	1st	1.70
	2 nd	0.02
	3 rd	0.05

(SW) : Sweeping Step

The heating treatment was carried out on inert conditions by inserting dry nitrogen in the chamber after promoting the vacuum supply. The heating slope was 350°C that corresponds to the annealing temperature of $[AlO_4]^0$ center.

After the treatments above, the quartz samples and resonators were exposed to γ-irradiation from a CO^{60} source. Gamma-ray irradiation was adjust to give a total absorbed dose of 7.5 krad in the rates of 25 rad/min. Five exposures were applied in the same conditions for the samples and the resonators to achieve a total dose of 37.5 Krad.

3.2 - Analytical Methods :

The analytical methods employed to evaluate the changes as function of the treatments above were the infrared spectroscopy and the optical laser absorption at 632.8 nm.

The infrared results were obtained by using a single beam NICOLET Magna 750 FT-IR spectrometer. The measurements were obtained at the nitrogen liquid temperature and the spectra were recorded at 0.125 cm^{-1} resolution. The absorption coefficients of each sharp band were normalized by the fondamental Si–O vibration at 3200 cm^{-1}. The hydrogen content was determined by the method of the "calibration curves" described in a previous publication [3].

In order to estimate the "Al-hole" centers formation, the laser absorption at 632.8 nm (He-Ne source) was applied. This method is also described in a previous work [6]. The absorption coefficients are evaluated by Beer - Lambert's equations. By this technique we can determine qualitatively the "Al-hole" formation. The quantitative results are obtained only by comparison with EPR measurements.

3.3 - Resonators Parameters :

The resonators were submitted to the same treatment as the caracterization plates. They are AT-cut crystals in a standard assembly and working at 10 MHz or 14 MHz. The following parameters were determined :

■ **PI (°C)** : the turnover point of the frequency - temperature curves ;

■ the $\Delta f/f_0$ variation reported to the frequency at 25°C and represented by the third degree polynomia as :

$$\frac{\Delta f}{f_0} = a(\Delta T) + b(\Delta T)^2 + c(\Delta T)^3$$

$\Delta T=(T-T_0)$
T_0 = reference temperature. Usually, 25 °C
f_0 = frequency at T_0 (Hz).

The **a**, **b** and **c** are, respectively, the first, second and third order temperature coefficients. These measurements in the rank [10, 100°C], are important in order to calculate the turnover point that is the working point of the controled temperature oscillators.

■ the motional -resistance, **Rm**.

■ **Q-factor** : The quality factor is given by :

$$Q = \frac{\omega L_1}{R_1}$$ where,

$\omega = 2.\pi.f$ and $L_1.C_1.\omega^2 = 1$

R_1 (Rm), L_1 and C_1 = motional parameters of the equivalent circuit.

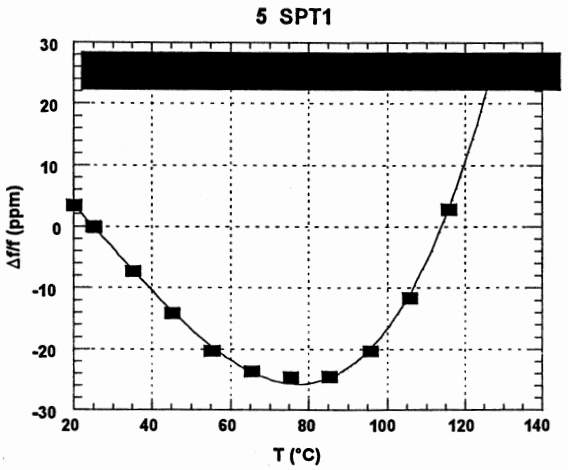

Fig.1(a)

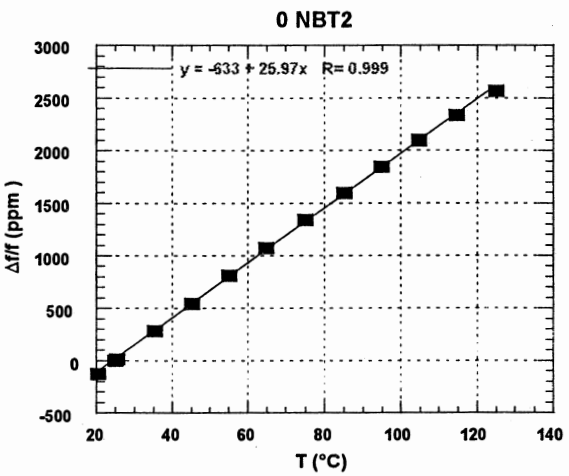

Fig.1(b)

FIGURE 1 - Frequency (ppm Hz) x Temperature (°C) curves. (a) temperature compensate resonator ; (b) linear variation.

4 - RESULTS

The applied treatments, sweeping and annealing in consecutive steps, produce similar changes in the point defects configuration for both crystals, synthetic and natural. As consequence, the irradiation effects in the pre-treated samples are similar also, independently of sample origin. The figures 2 and 3 show the [OH] (ppma), determined by IR measurements. At first, it can be seen that the samples submitted to air treatments, SPT_1 and NBT_1, show a higher level of hydrogen content in comparison with the samples treated under inert conditions, SPT_2 and NBT_2. These samples keep the same [OH] level as function of irradiation. Otherwise, the untreated samples, SP and NB and the samples submitted only to one electrodiffusion, SPS and NBS, show a higher variation. In the case of SP and NB, the [OH] reduction can indicate the formation of hydrogen paramagnetic centers or the dissociation of some species as HOH. For SPS and NBS the changes as function of irradiations are variable.

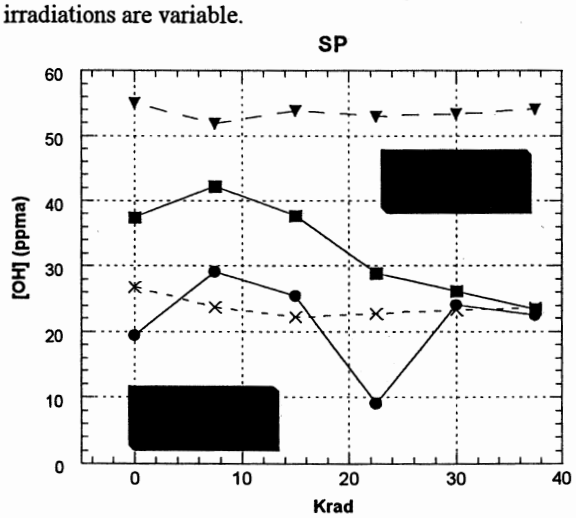

Figure **2** - [OH] changes after γ-irradiation. Synthetic SP Quartz.

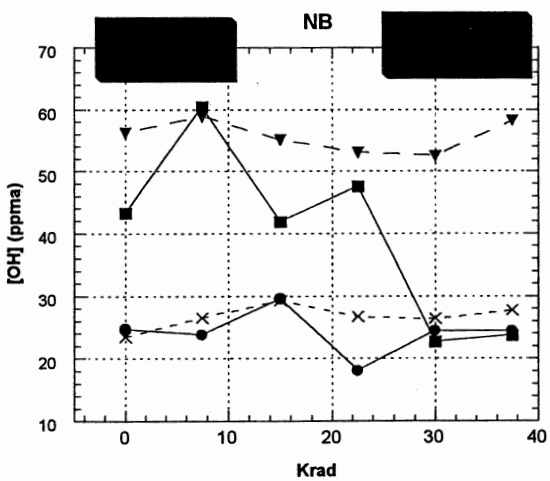

Figure **3** - [OH] changes after γ-irradiation. NB quartz.

The $[AlO_4]^0$ centers formation is intense for the SPS and NBS samples (figure 4). Then, one step electrodiffusion applied in inert conditions increases these paramagnetic centers as for the as-received SP sample. The most stable results concerning the variation of "Al-hole" centers are seen for the pre-treated naturel quartz, NBT_1 and NBT_2. Almost samples present an opposite variation of [OH] and $[AlO_4]^0$ centers as can be seen in figure 5 for the synthetic sample treated at inert conditions, SPT_2. There is not a mechanism for the compensation between these defects, but this relation means that an increasing of [OH] will inhibit the formation of $[AlO_4]^0$ centers.

The $[AlO_4/H]^0$ centers follow typical changes for the SP as-received sample, figure 6. It means that for untreated synthetic samples there is a prioritary compensation between the "s" (as-grown OH^- defects) and the "e" bands (Al-OH). Except for SP, all others samples show an equivalent variation between "Al-OH" and others "OH^-" defects, including natural quartz also (example, figure 7).

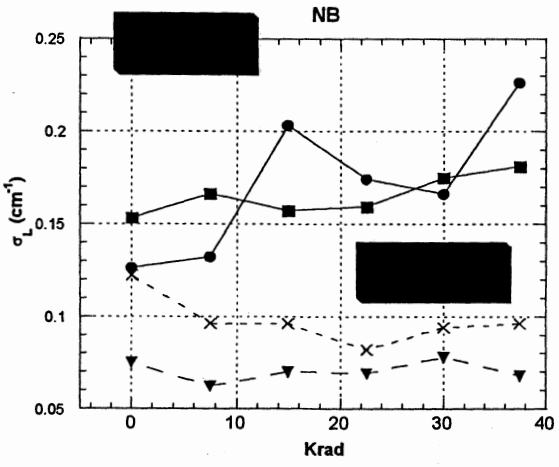

Figure 4 - "Al-hole" changes after γ-irradiation - Natural NB Quartz.

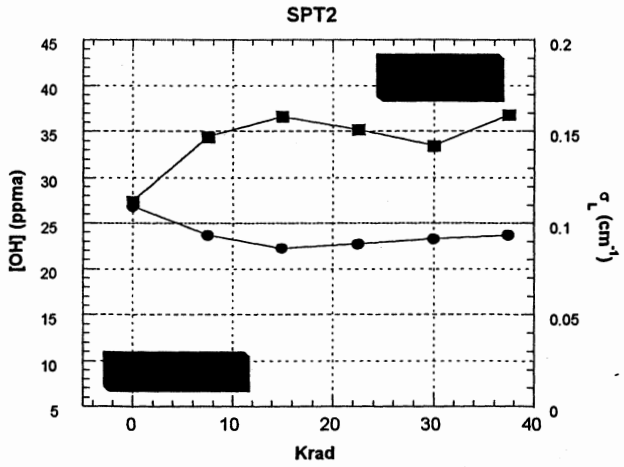

Figure 5 -[OH] (ppma) and $[AlO_4]^0$ center as function of γ- irradiation.

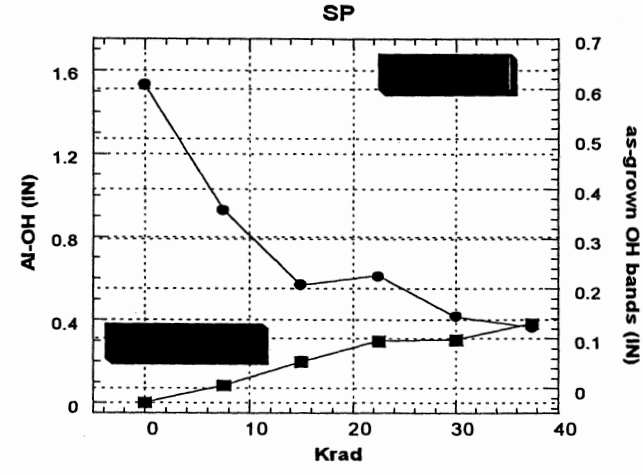

Figure 6 - As-grown OH and Al-OH defects. Synthetic SP quartz..

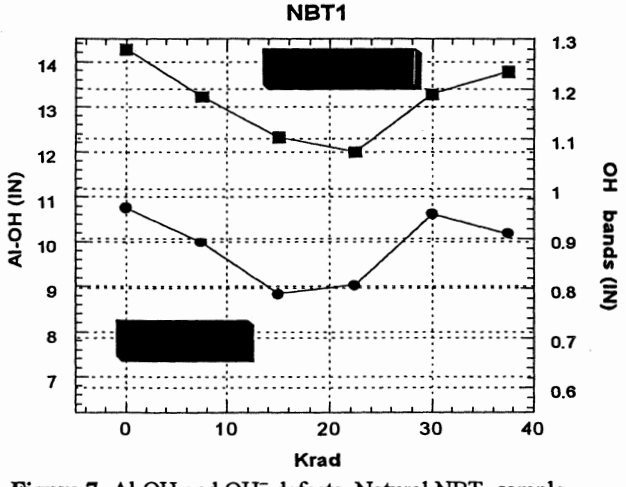

Figure 7- Al-OH and OH^- defects. Natural NBT_1 sample.

In Table 3 are compared the values of Q factor as function of the treatment and after submitting the resonators to 37.5 Krad γ-irradiation. It can be noted that the treatment applied before induced, approximatively, to the same transformations in quartz resonators, indenpendently of sample origin. In fact, as it was commented above, the characterization of quartz plates gave the same results for a specific traitement applied. The electrodiffusion realized in one step in N_2 conditions has a deleterious effect on quality factor of these resonators. In spite of this, three sweepings, in the same conditions (N_2), provides an increasing of this factor, as can be seen for samples SPT_2 and NBT_2. These results are in agreement with the motional resistance values. In relation to the resonators mounted in air swept quartz plates (SPT_1 and NBT_1) the quality factor is close to 1×10^6, i.e. slightly bigger than for as-received quartz resonators, SP and NB (mean value 0.72×10^6).

The results of sensitivity (Hz/rad) for these resonators are given in Table 4. They are evaluated after each dose of 7.5 Krad and the mean values are related to five exposures. As conclusion, the most stable resonators are those for which the sweeping was realized in consecutive steps in Hydrogen supply (SPT_1 and NBT_1).

Then, this treatment provides a hardness to irradiation effects. In other condition, SPT_2 and NBT_2, the treatment can induce an increasing of resonators sensitivity. In spite of this, these resonators show a good Q-factor. In the figures 8 and 9 is compared the variation of turnover point for these groups of resonators. The conclusion is the same as above, or else, the quartz treated in air conditions gave the most stable resonators. Another feature of synthetic quartz group is that SPT_1 and SP resonators show comparable results relating to the stability. Otherwise, the Q-values are different. In the case of natural quartz resonators, NBT_2 and NBS, instead of turnover point is shown the fractional $\Delta f/f_0$, related to 125 and 25 °C (figure 9). For these resonators the freqency-temperature curves give a linear relation, as can be seen at figure 1(b). Some results of quartz plates characterization reproduce the resonators characteristics. As example, the weak variations of "Al-hole" centers for the air-treated samples, SPT_1 and NBT_1, can indicate a probable stability of resonators to radiation effects, contrary to N_2 treated samples. In this case the instability of resonators are related, maybe, to the formation of $[AlO_4]^+$ centers (two "Al-hole") that can not be detected at 632.8 nm laser absorption spectroscopy.

Table 3 - Q factor and motional parameters of quartz resonators.

RESONATOR	F (Hz)	Q (x 10^6)	Rm (Ω)
SP	9 986 386	0.67	36
SPS	9 985 073	0.49	48
SPT1	9 986 391	0.96	30
SPT2	9 991 053	1.03	24
NB	9 985 971	0.77	31
NBS	14 740 349	0.56	45
NBT1	9 986 787	1.04	26
NBT2	14 697 625	1.75	15

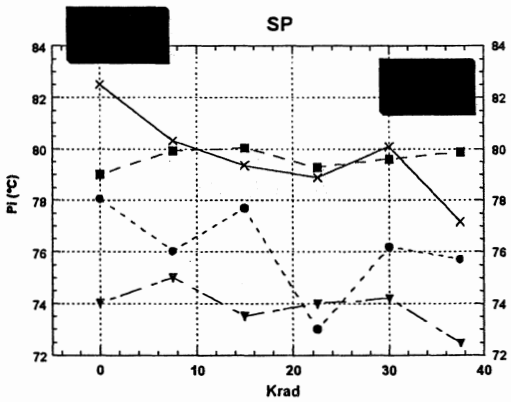

Figure 8 - Turnover point variation as function of irradiation SP Quartz.

Tableau 4 - Mean Sensitivity of quartz resonators on five exposures of 7.5 Krad γ-irradiation.

RESONATORS	MEAN SENSITIVITY x 10^{-11} (Hz / rad)
SP	2.0
SPT_1	3.4
SPT_2	4.3
SPS	7.8
NB	3.0
NBT_1	1.8
NBT_2	52.3
NBS	69.3

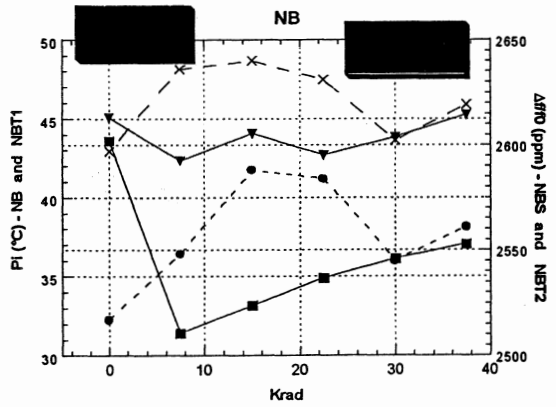

Figure 9 - Turnover point variation as function of irradiation. NB Quartz.

5 - CONCLUSION

The feature of the treatment applied is that it can change the material characteristics and promote the similar transformations in quartz crystals independently of sample origin. The monitoring parameters of quartz plates and quartz resonators gave similar variations.

The mainly reactions that can be occur related to Aluminum centers are :

– sweeping in air (H_2 supply) :

$$\tfrac{1}{2}\,H_2 + (AlM)O_2 \leftrightharpoons (AlH)O_2 + M\uparrow$$

(M = alkalin ions, as Li^+, Na^+ ,...)

– sweeping in inert conditions (vacuum and N_2 supplies) :

$$(AlM)O_2 \leftrightharpoons (AlH)O_2 + (Al)^+O_2 + M\uparrow$$

In the case of sweeping in air, the H_2 supply comes from the air atmosphere, but for inert conditions the source of protons is given by Hydrogen content of crystal. Thus, for air electrodiffusion, the treatment will be favorable to an increasing of H^+ , as can be seen on the curves in figures 2 and 3. The improvement in stability for these resoantors can be justify, maybe, by the [OH] increasing. It was just seen that [OH] can inhibit the $[AlO_4]^0$ centers formation (figure 5). Thus, it can supply a protection to irradiation effects.

In spite of the instability of resonators mounted on quartz treated in inert conditions, they give a higher Q-values if compared to other ones. Other feature of this treatment is that it can promote the formation of other paramagnetic centers, as $[AlO_4]^+$, after the oxydation reaction of precursor center $[AlO_4]^0$. In this case the electronic properties of this material will change also. In near future other results concerning only the electrodiffusion will be published, as the current density variations, conductivity curves, time constants, activation energies and the pre-exponentiel factor of Ahrrenius equation [7].

ACKNOWLEDGEMENTS

The IR analyses were performed at LCCM, Besançon. Thanks to Profs. P. Zecchini and H. Merigoux. I express also my gratitude to Dr. Jose Isturiz of "Centre Radiothérapie du Parc" - Dijon,. where the irradiations were realized. Thanks to CAPES (Brazil) for financial support.

REFERENCES

[1] King J.C. (1962). "Electrolysis of synthetic quartz. Effect upon resonator performance . " Proc. IEE (London), vol. B 109, Suppl 22, 295-301.

[2] Mombourquette M. J., Weil J.A. (1985). "Ab initio self-consistent-field molecular-orbital calculations on AlO_4 centres in alpha-quartz. II". Can. J. Phys. 63, 1282-1293.

[3] Pasquali M.A. ; Boy J.J. (2000). "A practical method to determine the OH concentration in quartz crystals". 14 th EFTF, 216-220.

[4] Halliburton L.E. , Chen C.Y., Tapp S.D. (1985). "Radiation effects in quartz : Low doses and defect production mechanisms". Proc. 40th Annual Freq. Control Symposium, 259-265.

[5] Martin J.J. (1988). " Electrodiffusion (Sweeping) of Ions in Quartz - A Review." IEEE Trans. on Ultras., Ferroelec. and Freq. Control, 35(3), 288-296.

[6] Boy J.J., Pasquali M.A., Viard B., Yamni K. (1995), "Defects characterization in synthetic and natural quartz : The role of ionizing radiations. Part II of "Non-destructive study of Al-hole concentration and frequency change of quartz resonators". 9th EFTF, 255-260.

[7] Pasquali M.A. (2001). "Modification des centres hydrogene et aluminium dans le cristal de quartz". Thesis to be published. ENSMM - Besançon.

100 MHz LOW NOISE XTAL OSCILLATOR FOR SPACE APPLICATION

O. FRANQUET, A.R.ELECTRONIQUE F-25047 BESANÇON
B. WOLCOFF, A.R.ELECTRONIQUE F-78500 SARTROUVILLE
P. GUILLEMOT, CNES F-31401 TOULOUSE

Espace Valentin Nord – B.P. 3113 – F 25047 BESANCON CEDEX
Tél. : (00.33.3) 81.88.66.77 – Fax : (00.33.3) 81.88.33.55
Email : are@ar-e.com

1- Abstract

A.R.Electronique, in collaboration with the CNES has investigated for a new kind of 100 MHz oscillator used for frequency synthesis.
This original oscillator's design is dedicated for the specific environemental requirements in space applications, like PHARAO program.
Usually, we are tempted to develope an ovenized oscillator (OCXO) with the highest level of performances for phase noise and temperature behavior. But, on the other side, the ovenized solution leads to more complexity, and to mass, consumption, and resonator's aging increasement.
In this paper we describe our solution without any oven, based on the use of an optimized crystal resonator cut dedicated to a narrow operating temperature range [+10, +50]°C.
The design, including our specific XTAL, will be discussed with an analysis on the global requirement for space application.
A detailed comparison between OCXO and free oven XO will justify our solution.
A presentation of experimental results obtained with the new structure will pointed out the enhanced parameters.
A final discussion of potential other applications of this basic structure will conclude this paper.

2- Specificities of this oscillator's requirements

Thermal aspect

In this space application, the thermal operating profile is very particular. The external temperature variation is < 1°C near a middle value T_M, and there is a slow evolution of T_M during the mission. The middle temperature evolution is about few degrees for a five years mission. According to this small temperature operating range, we don't really need a high level of thermal regulation for this application.

Mechanical aspect

We need a hardened oscillator's enclosure in order to resist at the high vibration and shock level during launch step. However, in operating mode there're no specific requirements on g sensitivity.Volume and mass have to be minimized as much as possible.

Electrical aspect

100 MHz oscillator used in synthesis chain gives a good compromize between reference and final output frequency to reach a high level of phase noise performance.
This one allows a good S/N ratio either with a high multiplication level of the frequency.
However, the relatively poor intrinsec long term stability leads to lock this UHF oscillator on a ultra stable frequency reference USO).
In order to be compatible with the PLL locking bandwith, during the mission, we have to mimize all the frequency deviation effects, like thermal and aging behavior (we can neglect frequency pulling and pushing).
The more the frequency deviation due to these effects is important, the more we have to increase the tuning sensitivity. But it has a direct degradation effect on the phase noise behavior up to 1 KHz of the carrier.
A.R.Electronique has investigated on different oscillators concept in order to find the best compromize : phase noise / tuning sensitivity / complexity / reliability. The free oven XO seems to be a good alternative in small operating temperature range.

3- Oscillator description and comparaison with OCXO

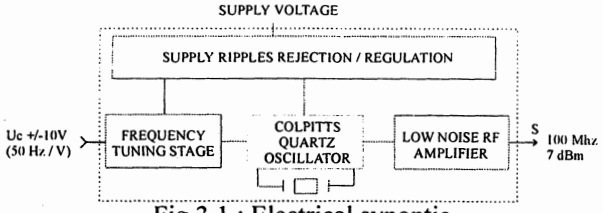

Fig.3.1 : Electrical synoptic

Actually, the best way to reduce phase noise a small as possible is to integrate a SC cut crystal in the oscillator. On the other hand, we need an ovenized structure in order to maintain the quartz temperature at the turn over point.(TOP). When operating, the quartz temperature is few degrees upper than the upper range temperature point.
It induces an aging performance degradation, but with a such ovenized oscillator, ΔF/F can reach ~1.10^{-8} for an external temperature range of about 50°C.

A.R.Electronique has developed an original quartz resonator designed with a particular cut (SC_D) able to preserve SC cut properties (stress behavior, phase noise...) with a turning point in the middle of the operating temperature range. In this case the quartz frequency deviation is limited to ~5ppm instead of ~100ppm for standard angle SC cut.
For thermal aspect, in comparaison with AT cut we obtain a comparable frequency deviation. But for PHARAO application the reel temperature excursion is < 10°C, the temperature dependance is reduced around the TOP (~30°C) with this SC_D quartz.

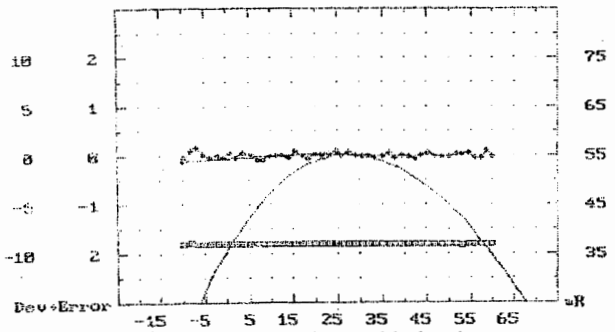

Fig.3.2 : quartz thermal behavior

Mechanical behavior

The resonator is mounted on a 4 points hardened structure in a T05 enclosure. It's naturally able to resist to schock and vibration space profiles (mechanical resonances are beyond 6 KHz).

We have tested different batches of resonators under vibration in order to determine an average g sensitivity of this kind of XTAL resonators. Results are presented below.

We have measured the degradation level of phase noise under vibration profile (idealized) shown fig. 3.3. The total acceleration level for this profile is about 5 grms.

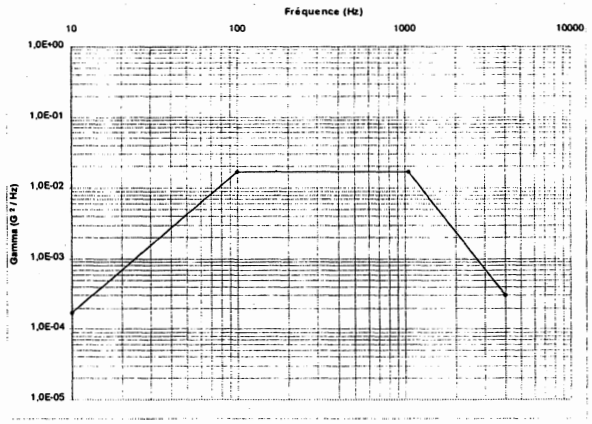

Fig.3.3 : excitation profile "A.R.E." 5 grms

The experimental set up and the oscillator under test is shown fig.3.4 :

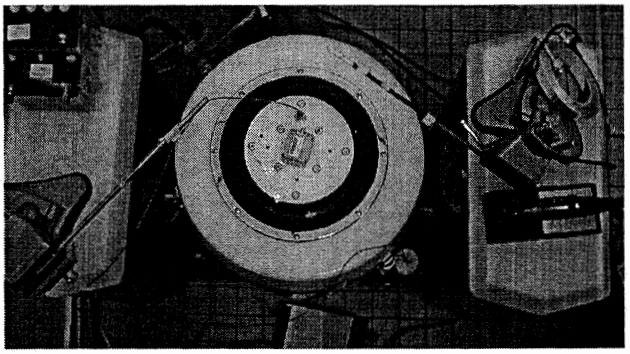
Fig.3.4 : experimental set up

The vibration profile effect on phase noise behavior can be calculated by :

$$L(F)=20LOG\frac{\gamma_{rms}.k.F_o}{\sqrt{2}.F_v} \quad (1)$$

We obtain the g sensitivity K :

$$K=\frac{\sqrt{2}.F_v}{\gamma_{rms}F_o}10\frac{L(F)}{20} \quad (2)$$

Where :

K = g sensitivity (g^{-1})

F_v = vibration frequency (Hz)

F_o = oscillator frequency (Hz)

L(F) = phase noise(dBc / Hz)

γ_{rms} = acceleration (g)

We can notice that the measured phase noise under vibration (Fig 3.5) is very close to the calculated phase noise degradation profile by formula (1) : white noise in the range [60 Hz – 100 Hz], F^{-2} noise in the [100 Hz – 1 kHz] decade.

Spurious from 2 KHz and up to 100 kHz are induced by excitator resonance frequencies and electrical spurious from vibrating set up.

The experimental result obtained fig.3.5 leads to a g sensitivity in the tested axis (perpendicular to the plate) about 5.10^{-11}/g. For the integrality of the batches we have found a 3 axes g sensitivity < 1.10^{-10}/g.

This level of performance is very close to typical SC cut results. The enhanced ratio in comparison with AT cut is about 5 to 10.

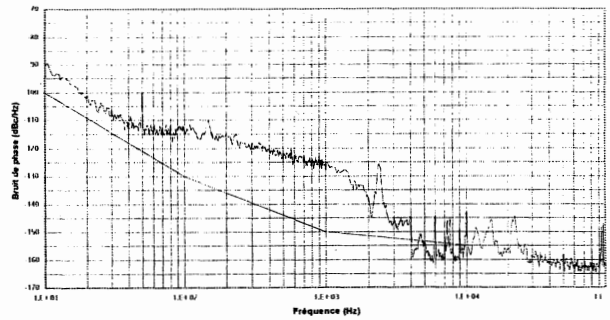

Fig.3.5 : phase noise under profile "A.R.E" 5 grms

Thermal behavior

The thermal behavior of our XO is led only by quartz frequency vs temperature response. Because of the relatively low consumption (~10mA), the internal dissipated power effect can be neglect. Vacuum and atmospheric test results are shown below.

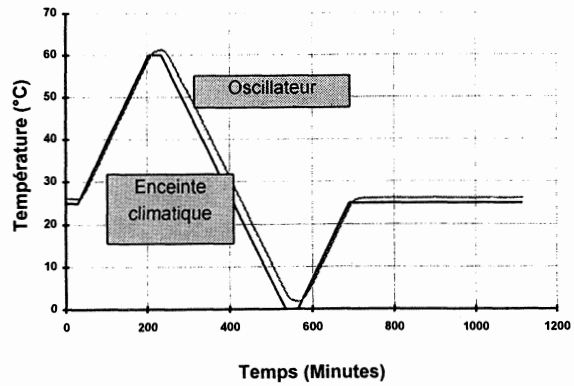

Fig.3.6 : temperature vs time profile in the temperature chambers

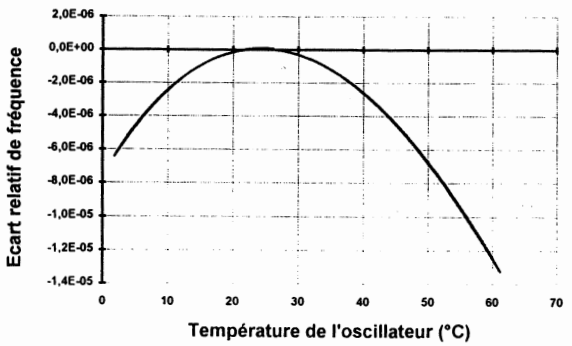

Fig.3.7-A : F = f(T) at P_{ATM}

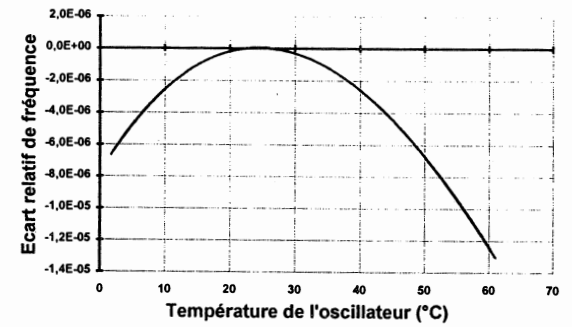

Fig.3.7-B : F = f(T) under 10^{-4} torr

There is not signifiant difference in thermal response under vacuum or atmospheric pressure (P_{ATM}). The temperature slope sign does no affect the result, the thermal hysteresis is reduced.
The frequency jump induced by vacuum (10^{-4} torr) to atmospheric pressure (fig.3.8),does not exceed 3.10^{-8}.

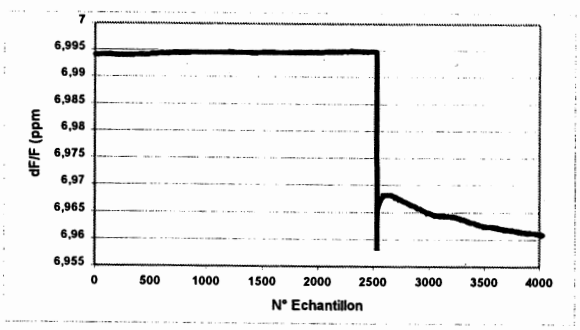

Fig.3.8 : frequency jump vaccum to P_{ATM}

For OCXO, thermal structure design is more difficult in order to keep P_{ATM} performances in vacuum condition. If convective exchange is important in thermal regulation at P_{ATM}, the vacuum behavior will completely change : the upper limit of the operating temperature can be reduced. To avoid this problem of heat evacuation, it involves a design based on conductive exchange and a minimization of internal dissipated power.
For instance, we have tested a standard 100 MHz OCXO with an upper operating temperature under vacuum limited at +30°C instead of +70°C at P_{ATM}.

Aging behavior

Two main parameters are involved in the quartz aging behavior :
- quartz cut (SC, AT...),
- average operating temperature.

Our specific cut enables the typical SC-cut level of aging performances. At 100 MHz, the aging slope ratio is about 5 between our solution and a AT cut crystal. Moreover, the essential improvement is achieved by the relatively low operating temperature. For SC cut in OCXO, the average quartz temperature is nearly 70 to 80°C during the whole oscillator's life and independently of environmental temperature conditions. In our case, it leads to a ~50°C drift in the quartz average operating temperature (T_M ~30°C).
We obtain an aging slope divided by two in comparaison with hundreds of 100 MHz SC cut OCXO results.
Fig. 3.9 presents, for instance, an aging curve of a such free oven XO.

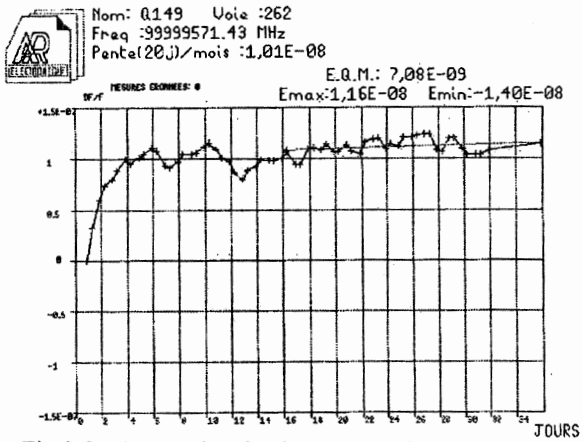

Fig.3.9. : Example of aging curve of free oven XO

Résult fig.3.9 shows an aging slope ~1.10^{-8}/month only after 36 days of continuous operating time. For the other samples, the slope is about 1.10^{-8}/month to 5.10^{-8}/month.

Phase noise in inert conditions

Experimental results are shown fig. 3.10.

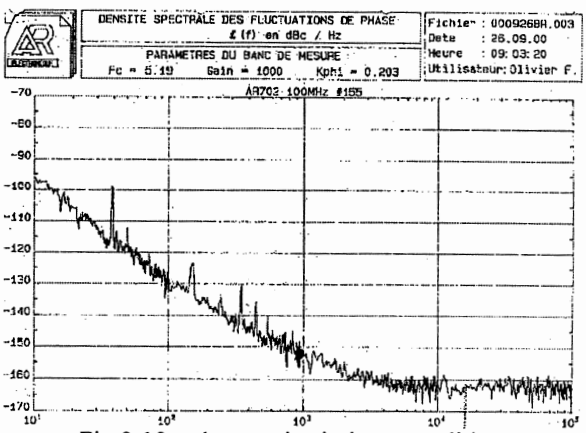

Fig.3.10 : phase noise in inert condition

This phase noise curve was obtained with a tuning sensitivity adjusted to compensate ΔF/F induced by thermal and aging effects.
The total frequency excursion around the carrier is about +/- 7 ppm for a –10V < Uc < +10V tuning voltage range.

Results obtained with this free oven structure are not fully at our best classical SC cut phase noise level. In comparaison the table below shows typical performances for A.R.Electronique product in AT, SC and SC_D cut.

Product	XTAL cut	Phase noise (dBc / Hz)			
		10 Hz	100 Hz	1 kHz	Floor
VCSI 100 AR465	AT	- 95	- 125	- 155	- 165
Free oven XO AR702	SC_D	- 97	- 130	- 153	- 165
PULSAR-H 100 AR360	SC	- 105	- 135	- 162	- 168

Free oven XO results are between VCXO (AT cut) and OCXO (SC cut) performance. However, the structure was tested with a SC cut crystal and has given same results, like in OCXO structure. That mean that we have to investigate the origin of phase degradation in our SC_D quartz batches. A new SC_D quartz manufacturing process is in development in order to stabilized phase noise behavior.

Other characteristics

Electrical characteristics

- Output level : SINE, +7 dBm
- Harmonics : < - 40 dBc
- Spurious : < - 70 dBc
- Output load : 50 Ω WSR < 1,1
- Tuning range : > +/- 5.10^{-6} for –10V<Uc<+10V
- Power consumption : 0,18W

Case

The oscillator is enclosed in a milled aluminium case. The total mass is < 25 grams.

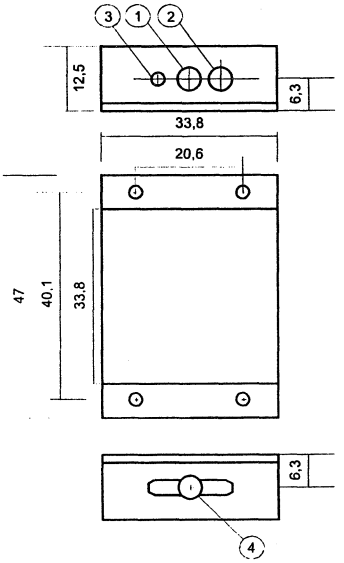

Fig.2.10 Aluminium case

4-Conclusion

A.R.Electronique has developed an alternative to 100MHz ovenized oscillator. This structure is well adapted for space environmental requirements. Using a SC_D cut crystal at ambient temperature enables an aging behavior enhancement. The frequency tuning range is comparable to sensitivity used in OCXO structure. Actually, phase noise results have to be improved by an adjustement of quartz process manufacturing. However, this structure gives a natural high reliability combined with low cost.
Applications who need very low g sentivity at high frequency are other kind of use of this oscillator.
For instance, in radar or other tactical application, it will be able to suppress mechanical damping structure with its natural very low g sensitivity.

This work was supported by "Région de Franche Comté" and "Centre National d'Etudes Spatiales".
Particular acknowledgment to Mr G. MARIANNEAU from "Laboratoire de Physique et Métrologie des Oscillateurs" for vacuum experimentations help.

References

1- E.GIRARDET and B. WOLCOFF
High stability miniature OCXO's for severe environmental conditions.
Joint meeting european frequency and time forum – IEEE – IFCS (1999)

2- FILLER R.L. and VIG J.R.
The acceleration sensitivity of quartz crystal oscillators
Review proc. 41ST ASFC (1987), pp 398-408

3- TULADHAR K.K.
High frequency quartz crystal oscillators for avionic systems.

Visualization of Mode Shapes in Piezoelectric Resonators using Image Processing

Yasuaki WATANABE, Yuji SHIKAMA, Shigeyoshi GOKA, Takayuki SATO and Hitoshi SEKIMOTO
Graduate School of Engineering, Tokyo Metropolitan University, 192-0397, Tokyo, JAPAN
watanabe@sknext.eei.metro-u.ac.jp

Abstract: - An image processing technique for measuring the mode shapes of piezoelectric resonators is described. In this method the whole surface of the resonator is irradiated by a semiconductor laser, and a field of speckles is generated above the resonator. The resonator driving current is pulse-modulated with a low frequency oscillator (LFO). A CCD camera, which is connected to a PC, captures the speckle patterns in synchronization with, and at double the frequency of the LFO output. The speckle patterns for the driven and resting states are thus obtained alternately. The vibrational patterns are obtained as the difference between the images for driving and resting phases.
The experiments were performed using a rectangular AT-cut quartz plate with a resonant frequency of 1 MHz. The shapes of the fundamental thickness-shear mode and of a spurious mode were measured. We calculated the shapes of these modes by using finite element analysis (FEA), to verify the reliability of the proposed system. Finally, we applied this technique to measuring the shapes.

KEYWORDS: piezoelectric resonator, mode shape, image processing, laser speckle, CCD camera

1. Introduction

Piezoelectric resonators, in particular quartz resonators, are widely used in such electronic devices as mobile phones. Recent advances in computer technology have enabled the application of finite element analysis (FEA) to the design of piezoelectric resonators. In the design of resonators, confirming the reliability of calculated results is very important. Comparison of the mode shape as predicted by analysis as obtained by experiments is the best way to obtain positive proof.

For the above reason, number of methods for plotting the vibrational patterns of piezoelectric resonators have been developed and reported on 1-8. Almost all of the methods involve dividing the resonator surface in to a large number of small regions or pixels in which vibrational displacement is measured. This can be repeated for each of the pixels and the resulting vibrational displacement data can then be merged to create a composite displacement image. However, measurement with high-resolution images takes a long time when this procedure is applied, because the spatial resolution of the composite image is proportional to the number of the pixels.

In the method described here both laser speckle interferometry and image processing techniques are used. This method has two advantages: a scanning system and procedure for making the composite image are not required, and measurement time is thus much shorter than with previous techniques; and the method requirements in terms of mechanical isolation from external vibration is not severe. The principle of the method and the setup for measurement are described in section 2. We used a 1 MHz rectangular AT-cut quartz resonator and circular AT-cut resonators operating in the VHF and UHF bands to verify the reliability of the proposed system. The experimental results are presented in section 3 and show that this method can correctly measure the in-plane mode shapes of the resonator, and that it is applicable to piezoelectric devices with resonant frequencies higher than the VHF range.

2. Principle and System Configuration

2.1 Principle

The principle of measurement system is illustrated in Fig. 1[8]. A laser beam irradiates a roughly finished resonator surface, and a speckled pattern is generated above the resonator by interference between scattered-light components. When the resonator is driven by an external voltage source that generates the resonant frequency, the speckle pattern is amplitude modulated by the resonant frequency if the vibration in the irradiated area is parallel to the laser beam direction. The in-plane modal patterns are obtained by mapping the intensities of speckle modulation. The difficulties with this method are that the optical detector used must have a gain bandwidth that corresponds to the resonant frequency of the device under test, and that a process for scanning the whole of the area under measurement is required.

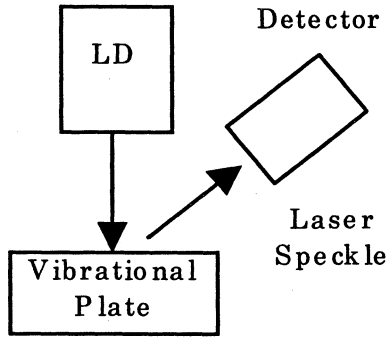

Fig.1 Block diagram of the laser speckle method[8]

2.2 Measurement system

To overcome the difficulties outlined above, we made the measurement system shown in Fig. 2. The whole surface of the resonator is irradiated by visible-range light from a semiconductor laser, and a field of speckles is generated above the resonator. The resonator driving current is tuned to the resonant frequency and pulse-modulated by the output of a low-frequency oscillator (LFO). We have already reported that correct mode shapes can be obtained by mapping the modulation component in synchronization with the LFO output. By using this technique, we can measure the mode shapes of high-frequency resonators without having to use a high-speed optical detector. A charge coupled device (CCD) camera, which is connected to a PC, captures the patterns of speckles in synchronization with, and at double the frequency of, the LFO output. Speckle patterns for driven and resting states are thus alternately obtained. The vibrational patterns are obtained as the difference between the images for the driven and resting phases. However, the difference image is noisy because the vibrational displacements are generally very small. To reduce the amount of noise in the image, we obtained the sum of data from many images then normalized the resulting summed image.

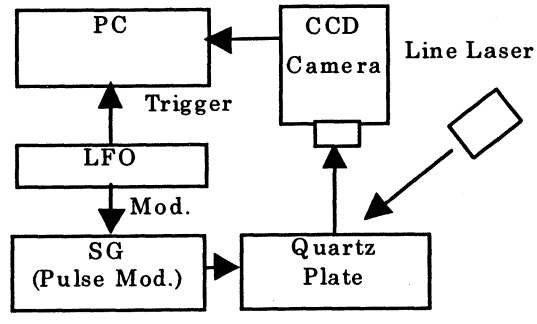

Fig. 2 Measurement system

3. Experimental Results

To test the reliability of the present method we applied the method to a rectangular 1 MHz AT-cut quartz plate. We measured the shapes of its fundamental thickness-shear mode and nearby inharmonic mode at room temperature. We also used a finite element analysis (FEA) method10) to calculate the mode shapes and obtain a standard against which we could verify the reliability of the

proposed system. The dimensions of the plate we used were x1(x) = 13.964 mm, x2(y') = 1.737 mm, and x3(z') = 13.0 mm. The resonator surface was roughly finished (#3000) and fully plated. The results of the FEA are completely reliable for a rectangular plate of such dimensions.

Figure 3 shows the experimental and FEA results for the fundamental thickness-shear and inharmonic modes. The FEA results show the dominant displacement, u1, in each mode. In this experiment a red semiconductor line laser (λ= 630 nm and P_{opt} = 10 mW) was used to irradiate the resonator surface. Pairs of images were captured two thousand times and processed in 6 minutes. The spatial resolution of the images was 320 x 240 pixels.

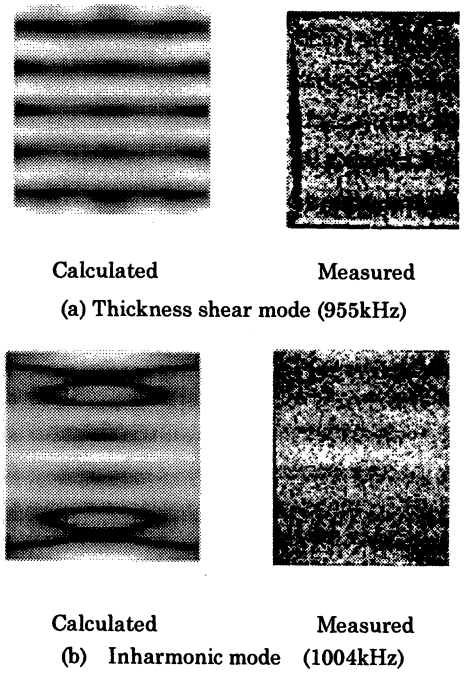

Fig. 3 Results for 1 MHz AT-cut quartz plate with the dimensions x1(x) = 13.964 mm, x2(y') = 1.737 mm, and x3(z') = 13.0 mm.

In each image in the figure, the magnitude of vibration is expressed in terms of an absolute value; that is, the white regions indicate high-amplitude vibration while the black regions indicate nodes or nodal lines. All the experimental images are normalized by a maximum value in each image. Figure 3 shows the good correspondence of these patterns with the calculated images.

To test the frequency range of the method, we went on to measure vibration in two circular AT-cut quartz resonators, operating at 23 MHz (resonator A) and 200 MHz (resonator B). Our intention was to measure the shapes of the thickness-shear modes for both resonators and of nearby spurious modes for resonator A. Resonator A is designed in such a way as to operate at the third overtone (70 MHz), and its surface was roughly finished (#4000). Resonator B operates at the seventh overtone and its surface was polished. To enhance the scattered-light components, a dilute water-soluble glue was applied to the surface of resonator B. In this experiment a red semiconductor spot laser (λ = 630 nm and P_{opt} = 10 mW) was used. The number of images captured and spatial resolution were the same as for the first experiment.

Figure 4,(a),(b), and (c), show the measured results for the fundamental thickness-shear mode and the nearby inharmonic modes of resonator A. It is obvious from these figures that our method provides very clear patterns. Figure 4(d) is an image of the resonator itself.

Figure 5,(a) and (b), show the measured results for the 7th overtone (200 MHz) and the 15th overtone (428 MHz) of the thickness-shear mode of resonator B, respectively. These images are normalized by a maximum value in each image. Figure 5(c) is an image of the resonator itself.

Figure 5(a) exhibits a low contrast image as compared with Fig. 5(b). The difference of the contrast explains that the vibrational displacement spreads hole surface of the resonator at the 7th overtone mode and converges on the electrode area at the 15th overtone mode.

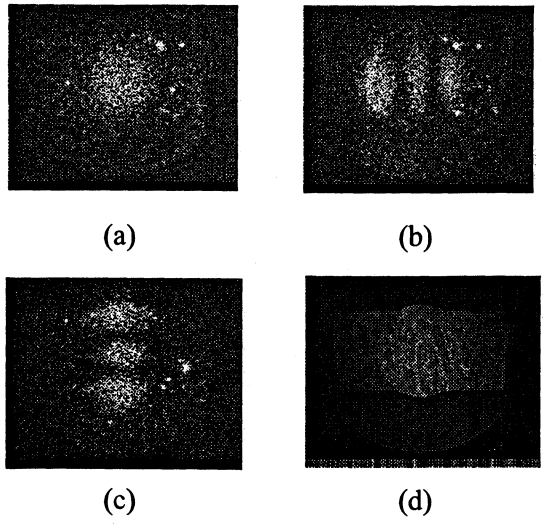

Fig. 4 Experimental results for 23 MHz AT-cut quartz resonator unit; (a) fundamental thickness-shear, (b) and (c) inharmonic modes, (d) actual image.

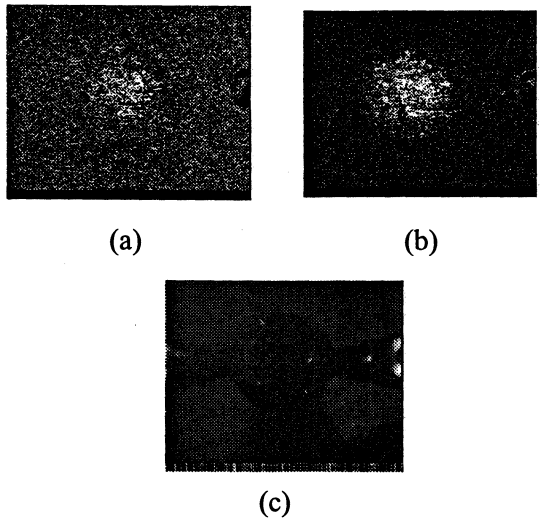

Fig. 5 Experimental results for 200 MHz AT-cut resonator unit; (a) 200 MHz (7th overtone), (b) 428 MHz(15th overtone), (c) actual image

It is generally known that the vibrational displacement of a thickness-shear resonator concentrates at a small area in the electrode region. However, the experimental results obtained here represent spread vibrational patterns. The reason of the results is ascribable to the glue that was applied to the resonator surface to enhance the scattered-light components. Although the experimental results do not indicate crude vibrational patterns, they are enough to demonstrate that this method is applicable to frequencies higher than the VHF range.

4. Conclusions

The method described in this paper allows the in-plane component of the mode shapes of piezoelectric resonators to be plotted. The experimental results for two circular AT-cut resonators have demonstrated that the system is capable of mode-shape measurements at frequencies higher than the VHF range. The basic principle of the method is applicable to piezoelectric devices operating at any frequency. With increased laser power, it will be possible to measure devices with polished surfaces without having to proof the resonator surface. This is being tried and results will be reported on in the future.

References

1) R. J. Williamson: *Proc. 44th Annu. Symp. Freq. Control* (1990) p.436.

2) W. J. Spencer: Physical Acoustics (Academic Press, New York, 1968) Vol.5, Chap.3.

3) I. Koga and H. Fukuyo: J. Inst. Electr. Commun. Eng. Jpn. **36** (1953) 59 [in Japanese].

4) T. Adachi, M. Okazaki and Y. Tsuzuki: *Proc.43th Annu. Symp. Freq. Control* (1983)p.187.

5) Y.Hirose and Y.Tsuzuki: *Proc.43th Annu. Symp. Freq. Control* (1989) p.360.

6) Y. Watanabe, H. Sekimoto, Y. Kitada and Y. Ohmura: Trans. IEICE Jpn. **77-A** (1994) 285 [in Japanese].

7) Y. Watanabe, M. Koyama. H. Sekimoto and Y. Ohmura: Jpn. J. Appl. Phys. **34** (1995) 2617.

8) Y. Watanabe, K. Niikura, G. Yuan, S. Goka and H. Sekimoto: Jpn. J. Appl. Phys. **38** (1999) 938.

9) S. Hertl, E. Benes, L. Wimmer, M. Schmid: *Proc. 39th Annual Freq. Control Symp.(*1985) p.535.

10) A. Ishizaki, H. Sekimoto and Y. Watanabe: *Proc. 1996 IEEE Int. Freq. Control Symp.*(1996) p.518.

DIRECT IMPEDANCE METHOD FOR LOAD RESONANT MEASUREMENT OF CRYSTAL

Arthur Lee and Kenneth Chan
Kolinker Industrial Equipments Limited

ABSTRACT

With today's hardware (Network Analyzers), the Direct Impedance Method provides better accuracy, convenience and at lower cost over other methods such as the Physical Load Capacitor method. However, a lot of crystal engineers still ask frequently, "Where is the Physical Load Capacitor?"

This paper addresses how and why the Direct Impedance Method is better than the other measurement methods.

1. HISTORICAL BACKGROUND OF DIFFERENT MEASUREMENT METHODS

Due to the relatively low impedance of Fs and Fr, Fs/Fr measurements have never been difficult with both the IEC 444 and EIA 512 configurations. The challenge lies in FL measurement, especially at low CL.

This paper focuses in Load Resonant (FL) measurement.

The impedance of a crystal at FL is relatively high, and to measure high impedance with a 50-Ohm network analyzer requires both high stability and good accuracy of the measuring equipment. Traditionally, these requirements were either impractical or too costly. Hence, several methods for FL measurement were derived, such as Calculated Method, and Physical Load Capacitor Method. These methods are designed to measure a crystal at lower impedance level, thus hopefully, allowing equipment with lower accuracy to be used. This paper will discuss in detail the merits and drawbacks of these methods.

2. VARIOUS FL MEASUREMENT METHODS

2.1. Calculated Method

As described in the IEC 444 publications, the DUT (Device Under Test) is measured at about ±45 degree for its motional parameters, and then the FL is "Calculated" based on this ±45 degree data.

The advantage of this method is that the DUT is measured at relatively low impedance, close to 25 Ohm. Hence, the requirement of software compensation for stray components in the test head is relatively simple.

The drawback of this method is that the DUT is not tested at its destined condition: i.e. not at the phase shift equal to the specified CL / FL. If the crystal behaves strictly according to its four-component model, this method is acceptable. However, if the crystal is NON-Linear (not behaving as per the four component model [2], see Figure 1, and Figure 2) then, the FL measurement will not be accurate.

If you know already your DUT is a linear crystal, you may use this method to test it. However, in most case, you need a test method to tell you how good the DUT is, so this method is quite useless, unless you know the crystal is linear before testing.

2.1.1. Linearity of a crystal

- Circuit Application standpoint :
  As long as the crystal has a stable (repeatable), sharp impedance –frequency curve, and it functions properly in an oscillator, then it is a good crystal; whether it is linear, or not, is not a question. Non-linear crystal does not imply a bad crystal.
- Crystal Designer standpoint :
  The market trend is toward smaller crystals, such as the AT-strip crystal and SMD crystal. Unlike larger crystals with circular geometry, rectangular blanks are inherently more difficult to model using the four-components method. However, the problem with measurement should not imply a bad crystal. Instead, we need some test method or system that can measure the crystal more accurately in spite of non-linearity, and provide more information, such as how serious a spurious mode is affecting the crystal performance over temperature.
- Crystal Measurement standpoint :
  The Calculated Method is not suitable for testing a non-linear crystal, because the degree of measurement accuracy depends on the crystal characteristics, which may vary significantly[2]. If there are other practical means of measurement, we should simply abandon the use of this method.

2.2. Physical Load Capacitor Method

As described in the IEC 444 standard, the basic concept of this method is to measure the crystal at its specified CL condition, by inserting an actual capacitor in series with the crystal and measuring both simultaneously (see Figure 3). This is a good improvement over the Calculated Method, as no more estimation is done, while the Network Analyzer measures FL at relatively low impedance.

2.2.1. This method has been widely used and it seems to have the following advantages:

- Good "Repeatability" in FL, as compared to the Calculated Method;
- Correlation between different machines can be done easily by trimming the physical load capacitor. No need to change any software parameters: Simply keep a look up table between different customers / suppliers / machines / frequency / and test head configurations for the differences in CL;
- Measurement speed is good.

2.2.2. The well known disadvantage is:

- The Fr/Rr/Co values cannot be measured accurately in a one-pass test. The same DUT must be tested twice: With and without the physical load capacitor so as to get all parameters with reasonable accuracy. These measurements become more difficult when DLD and Spurious Mode measurements are made. ([1] IEC 444-6 : Both DLD measurements and Spurious

measurements: are based on series measurements instead of load measurements).

2.2.3. The problem with Physical Load Capacitor Method:
If we look into the "Advantages" more closely, we may well ask: If this method is good enough for accurate measurement, then why are we still correlating with a look up table of CL ?

.The answer is crystal clear, the method is not good enough, but we accept the habit because it seems that there is no other better choice.

The difficulty in getting accuracy in this method is :

- The impact of stray components (CX and CY in [2]) on accuracy is significant and difficult to compensate (as described in [2]).
- The IEC standard [1] defines an "ideal" test jig with minimal stray component (CX and CY). However, the "ideal" test jig is often impractical in mass volume / automation applications, and so "minimal stray" may be difficult to achieve. Also, a variable CL in the "ideal" test jig jeopardizes the "ideal" behavior of that jig due to excessive stray components.
- Many engineers have tried very hard to compensate for CX and CY to obtain an acceptable level, however in vain.
- To look into the issue in greater detail, the stray components may not be limited to CX and CY, it could have been a lumped circuit with LX and LY ... That is why the correlation table that we use also involves frequency as a variable.

2.2.4. Major technical difficulties:
Both calibrating the Physical Load Capacitor and compensating for the stray capacitance and inductance at the junction of the crystal and the capacitor remain largely unresolved.

2.3. Direct Impedance Method

From the circuit application standpoint, a circuit requiring FL at CL means that the crystal must behave, at the specified FL, as an inductor :

Impedance of DUT = - Impedance of CL

This is the basic requirement, and whenever possible the crystal should be tested at exactly this condition without any estimation. The Direct Impedance Method is based on this basic principle.

2.3.1. Test Set up and Method
The test set up of the Direct Impedance Method is simple (see Figure 4 and Figure 5) :

- The DUT is placed into a π-network test head.
- With the same hardware configuration according to IEC444 [1], measure Co, Fr, and Rr.
- The frequency of the frequency synthesizer is iterated to search for :
  Impedance of DUT = - Impedance of CL.
- The other motional parameters L1 and C1 are then calculated based on the FL, Fr and Co.

2.3.2. Major Advantage

- Measure the crystal at its destined CL condition. No more estimation is done, so that even if the crystal is non-linear, it does not matter.
- Does not have to calibrate CX, CY (or LX, LY, etc.) in the presence of an unknown physical CL. This would allow accuracy and reproducibility, instead of only repeatability.
- Fr/Fs/FL/Rr/Rs all measured at one time, making DLD and spurious response measurement much easier and more accurate.

The following discussion [Section 3] will present the test data of Repeatability, Reproducibility and Accuracy in detail.

2.3.3. Other considerations

a) Software calibration and stray component compensation:

The IEC 444 standard does not require explicitly stray component compensation and calibration with software techniques but rather relies on a perfect test head. Without proper software compensation, the IEC 444 standard is limited to measuring at low impedance with the ideal test head. However, such a test head with minimal stray components is impractical in mass volume operations. That is why most practical measurement systems are already implemented to some extent with software techniques to compensate stray reactive components.

The Direct Impedance Measurement Method requires a more comprehensive model of the π-head and more extensive mathematical computations, which fortunately, are practical with the speed and cost of today's computers / network analyzers. This must be done properly, otherwise the system will not be able to measure high impedance with good Repeatability, Reproducibility and Accuracy.

b) Drive level:

When measuring FL, the voltage amplitude required in the Direct Impedance Method is much larger compared to the other methods using the same hardware set up.

- Luckily, when measuring Fr/Fs, the same drive level range can be achieved compared with other methods. Hence, DLD (Drive Level Dependence) and Spurious Ratio tests can be done accurately, providing a safe guard on extremely poor crystals.
- With the addition of a commercially available power amplifier, costing in the range of a few hundreds USD to over a thousand, the practical drive level of this method can go up to >400 micro-Watt at say CL=20 pF, 20MHz.
- The accuracy of the Drive Level with the passive measurement (both IEC444 and EIA512 standards) has always been subject to question: Within a typical one-second test, most of the iteration search is not applying the target drive power to the DUT. Until the last few readings, it may be possible to exert the target drive power, but these readings take just a few milliseconds or fractions of a millisecond. This is the same for all the above mentioned test methods.

3. COMPARISON TEST DATA WITH DIFFERENT HARDWARE CONFIGURATIONS

Test data using the same Direct Impedance Measurement Method using different network analyzers, different test heads, different frequencies and different CL are presented to verify the result of a proper implementation of the test method.

3.1. *Experiment Matrix*

For repeatability and reproducibility test, we use the Direct Impedance Measurement Method equipped with:

- 2 different Network Analyzers: Hewlett Packard E5100A, and Kolinker KH1200. Both are equipped with internal frequency reference, warmed up, and calibrated.
- 4 different kind of Test Jigs #1 to #4 as per Figure 6, including an IEC compatible Jig and three other jigs suitable for volumn production;
- One crystal of 11.150MHz HC49US, tested 1400 times on each of the above combinations of Network Analyzers and test jigs, for Fs and FL at CL=10, 20 and 30 pF.

For accuracy test, the above test data are used with the addition of:

- Using the Physical Load Capacitor Method, and a Fixed Physical CL at 8.725pF. No software compensation on head parameters was used.
- Using the Physical Load Capacitor Method, and a Variable Physical CL tuned to 10pF. No software compensation on head parameters was used.

3.2. *Raw Data*

As the data volumn is very large, the mean and standard deviation of each group of data is presented in Figure 7 to Figure 9.

For repeatability and reproducibility, Figure 7 and Figure 8 show that the repeatability and reproducibility of the Direct Impedance Method is good : well within |0.2pF| for crystal with Ts as large as 30 to 40 ppm/pF.

For accuracy, Figure 10 shows that the method yields good accuracy (well within |0.2pF|) when compared with an ideal test jig (small stray component). But the physical load capacitor method with an non-ideal test jig (variable load capacitor, large stray component) is not comparable.

3.3. *Comment on the Experiment*

The above data shows that the Direct Impedance Method worth more attention and effort to be focused because of its repeatability, reproducibility and accuracy with different hardware configurations.

However, more experiment should be done to verify:

- Error due to different frequency standards;
- Error due to different crystal samples : overtones, deliberately chosen non-linear crystals etc.

4. CONCLUSION

Based on the above conceptual and experimental data, we propose that more effort should be spent on the Direct Impedance Measurement Method with the goal of possibly further enhancing the IEC444 and EIA512 measurement standards.

The above discussion focuses on the accuracy of FL measurement because this is the greatest headache in the crystal industry. We also have to be reminded that the method also gives accurate results for Fs, Fr, Co and ESR. This means that in a one-pass test, we can test all crystal parameters including DLD, spurious mode, Q, etc. without the need to insert or change any load capacitor. Equipment utilizing this method is now commercially available providing accurate measurement of all crystal parameters with super user friendliness and at low cost.

5. REFERENCES

[1] IEC Publication 444-1 to 444-6 : Measurement of quartz crystal unit parameters by zero phase technique in a π-network.

[2] Dwane Rose, Saunders and Associates, Inc., Load Resonant Measurements of Quartz Crystals, http://www.saunders-assoc.com/paper/paper.html.

6. ACKNOWELDGEMENT

Thanks to Mr. James Socki of Pletronics Inc. for his input and for proof reading the paper.

Figure 1 : The Four component model

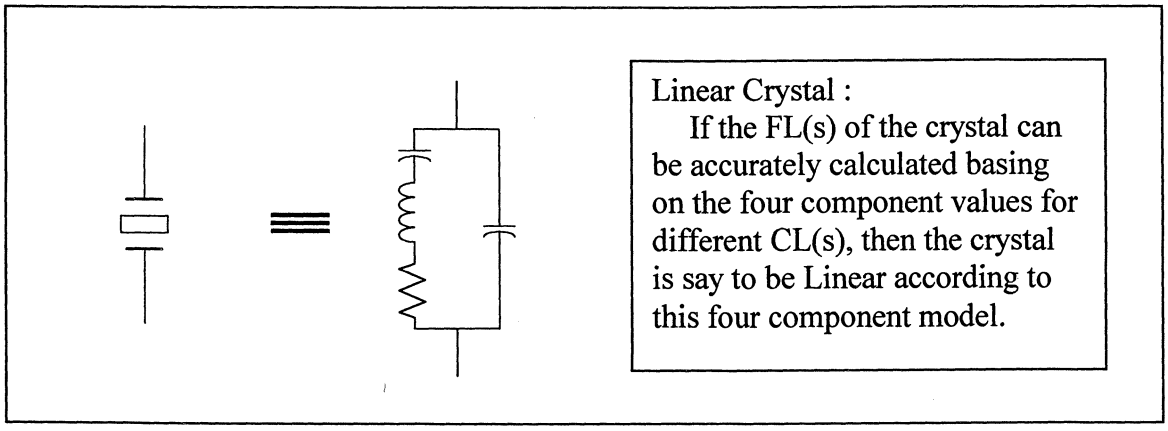

Figure 2 : Impedance of Linear and Non-Linear Crystals

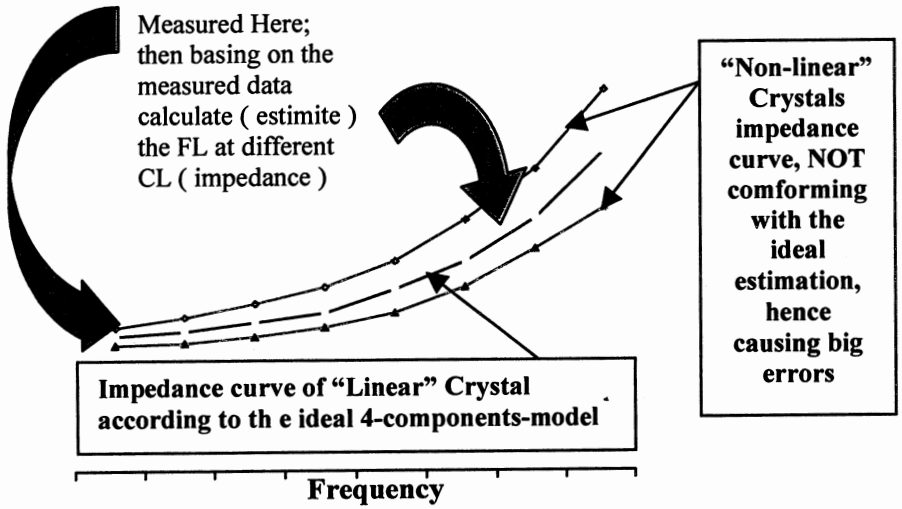

Figure 3: Physical Load Capacitor Method

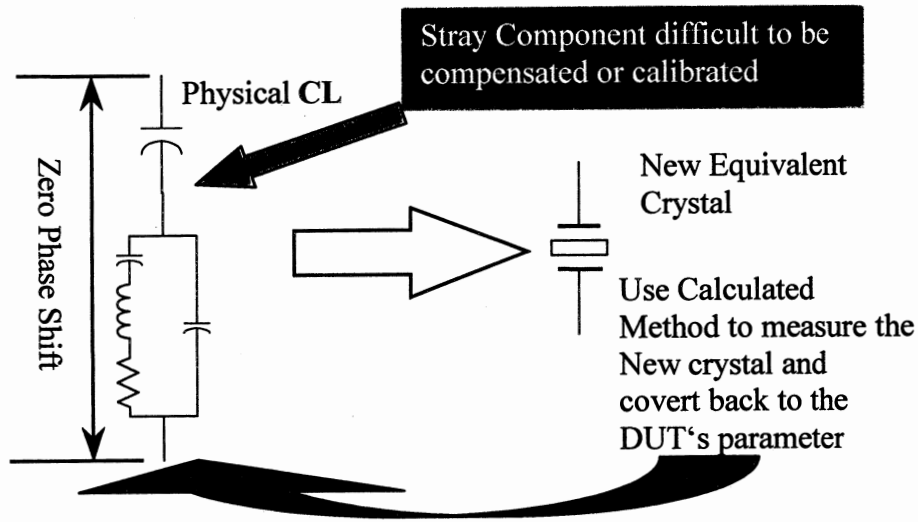

Figure 4 : Direct Impedance Measurement Method

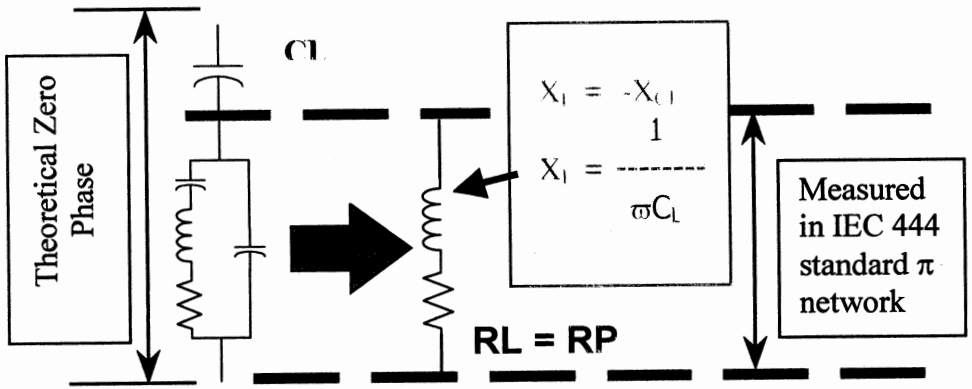

Figure 5 : Direct Impedance Measurement Impedance Map

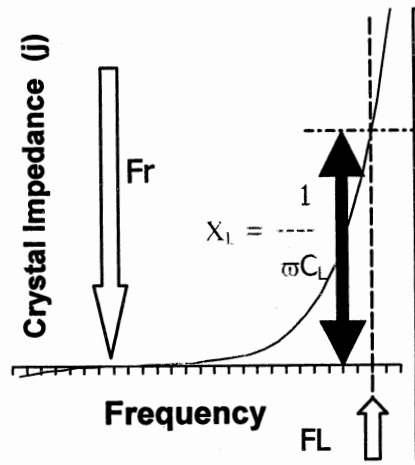

- The DUT is placed into a π-network test head, measure Co, Fr, and Rr.
- The frequency of the frequency synthesiser is iterated to search for :
  j of DUT = - j of CL.
- Other motional parameters are then calculated based on the FL, Fr and Co.

Figure 6 : Test Jigs with different stray components

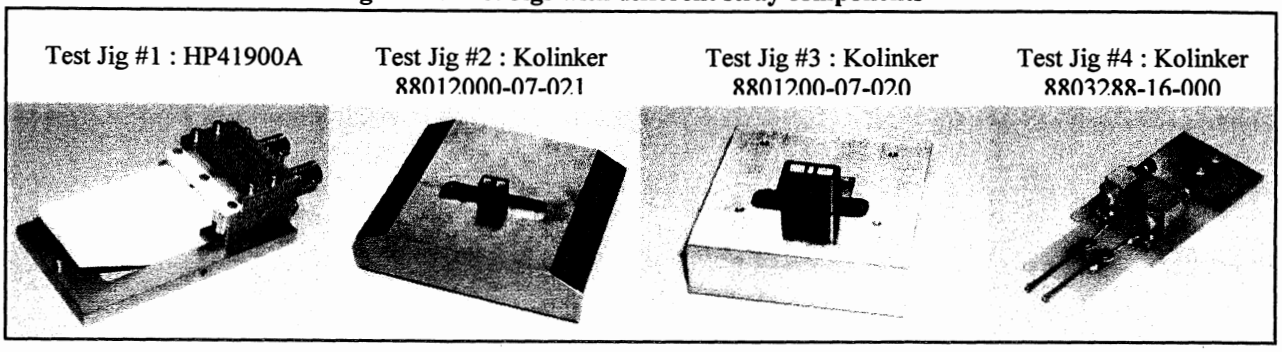

Figure 7 : Error between different Hardware Configurations

Mean of 1400 readings [ppm]	Network Analyser	Different Test Jig				Max error [ppm]	Max error in CL [pF]
		#1 Jig	#2 Jig	#3 Jig	#4 Jig		
Fs	E5100A	-310.78	-310.72	-310.62	-310.66	0.90	N/A
	KH1200	-310.70	-311.38	-311.37	-311.52		
FL at CL=8.725pF	E5100A	130.73	130.52	131.43	131.22	0.91	0.02
Ts = 40ppm/pF)	KH1200	131.22	131.17	131.41	131.36		
FL at CL=10pF	E5100A	86.98	86.11	87.39	87.39	1.28	0.04
(Ts = 30ppm/pF)	KH1200	87.11	87.07	86.94	87.14		
FL at CL=20pF	E5100A	-87.44	-87.71	-86.99	-87.30	0.77	0.07
(Ts = 10ppm/pF)	KH1200	-86.94	-87.61	-87.52	-87.80		
FL at CL=30pF	E5100A	-155.59	-155.70	-155.19	-155.49	0.93	0.18
(Ts = 5ppm/pF)	KH1200	-155.67	-155.91	-155.21	-156.12		

Figure 8 : Repeatability (spread) between different Hardware Configurations

Standard Deviation of 1400 readings	Network Analyser	Different Test Jigs			
		#1 Jig	#2 Jig	#3 Jig	#4 Jig
Fs	E5100A	0.037	0.027	0.025	0.021
	KH1200	0.028	0.018	0.022	0.029
FL at CL=10pF	E5100A	0.174	0.167	0.166	0.170
	KH1200	0.340	0.333	0.323	0.333
FL at CL=20pF	E5100A	0.018	0.014	0.014	0.010
	KH1200	0.173	0.186	0.182	0.189
FL at CL=30pF	E5100A	0.021	0.017	0.016	0.012
	KH1200	0.130	0.140	0.139	0.136

Figure 9 : Error between Physical Load Capacitor Method

Mean of 1400 readings [ppm]	Network Analyser	Different Test Jig				Note A	Note B
		#1 Jig	#2 Jig	#3 Jig	#4 Jig		
Fs	E5100A	-310.78	-310.72	-310.62	-310.66		
	KH1200	-310.70	-311.38	-311.37	-311.52		
FL at CL=8.725pF	E5100A	130.73	130.52	131.43	131.22		123.98
(Ts = 40ppm/pF)	KH1200	131.22	131.17	131.41	131.36		125.50
FL at CL=10pF	E5100A	86.98	86.11	87.39	87.39	64.02	
(Ts = 30ppm/pF)	KH1200	87.11	87.07	86.94	87.14	65.58	

Note A : CL=10pF : obtained by a variable capacitor (significant stray components), tuned and checked according to IEC444 procedures, but without any further software compensation on stray components. Error is large (13 / 30 = 0.5 pF) due to uncompensated stray components.

Note B : CL=8.725pF : obtained by fixed capacitor (small / insignificant stray components), tuned and checked according to ICE444 procedures, without any further software compensation on stray components. Error is small (7 / 40 = < 0.2 pF) due to less uncompensated stray components.

POSTERS B

ATOMIC, OPTICAL & FOUNTAIN FREQUENCY STANDARDS

Chairman: Léon Prost

LASER FREQUENCY STANDARDS - A CHANGING PERSPECTIVE

D. J. E. Knight

DK Research,
110 Strawberry Vale, Twickenham, Middx., TW1 4SH, UK
E-mail: djek@cix.co.uk

1. ABSTRACT

A list of laser frequency standards is presented and discussed. Improvements since 1997 (Ref.1) include a simplifying shift in the technique of frequency measurement to an octave-width optical-comb method which gives direct access between the VHF and optical regions. This, together with the Cs fountain standard, has allowed new measurements in the visible/uv region ten times more accurately than four years ago, and on new cooled systems. The high resolution of optical frequency standards, combined with the simplified technique of frequency transfer across the spectrum promises rapid progress in high-resolution physics and metrology.

Keywords: lasers, frequency standards, accurate, list

2. INTRODUCTION

This paper updates a list of laser frequency standards made four years ago (Ref.1) and goes beyond the surveys made for realising the metre (Ref.2) in extending over a wider spectrum and taking note of basic-physics experiments. The frequency range now extends to 5000 THz and the accuracy now extends to 1 part in 10^{14} (single sigma) in the ultraviolet region, a factor 10 better than before. Frequency measurements on laser-cooled atoms and ions are now being made at accuracies which exploit the advantages of near-stationary systems for frequency standards: measurements are now concerned with cm/s velocities of atoms or ions in the laboratory frame. The potential accuracy of such systems now exceeds the accuracy of conventional primary caesium-beam standards, about 1 part in 10^{14}, and their measurement depends on the application of laser cooling and fountain geometry to the caesium microwave standard. This produces an accuracy of 1 part in 10^{15} with a prospect for improvement (Ref.3), and for the Rb fountain microwave standard the improvement may extend towards 1 part in 10^{17} (Ref.3). Highly accurate measurements have also been made on the more calculable atomic and sub-atomic systems, and these are concentrated at the higher frequencies, extending now as far as 60 nm wavelength (Ei97). (References begining with letters are Table References.)

The discovery, somewhat unexpected but immensely promising, that the frequencies of the comb of sidebands from the Ti-sapphire femtosecond mode-locked laser are useful for accurate frequency measurement is a great advance. The comb spacing is the pulse repetition rate, and when correctly set up, the sidebands are equally and accurately spaced in frequency and stable, see for example, Ud99. This, together with the ability to broaden such combs in optical fibres over the 1000-500 nm octave, has very recently provided a compact and inexpensive "bridge" from the VHF to the optical region. Already this has facilitated high-accuracy measurements on cooled hydrogen and trapped-ion systems in the uv region (Re00, St01a,b, Ud01).

Table 1 lists the more-accurate optical frequency measurements, or those which are potentially more accurate, and is mainly concerned with frequency measurement at frequencies above about 100 THz, 3 μm wavelength. A schematic diagram of the main routes of frequency measurement from the caesium standard to these frequencies is shown in Figure 1. Note the new fs-laser route.

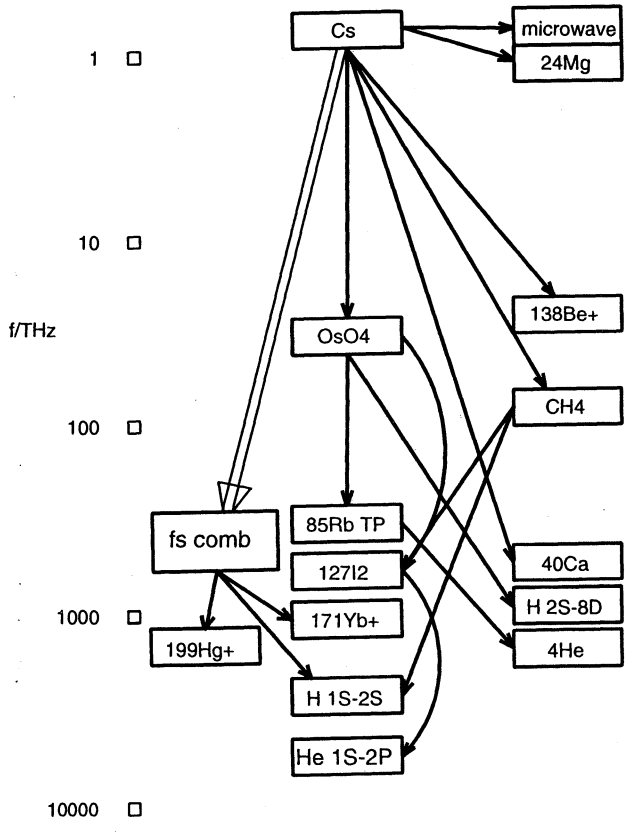

Figure 1: Frequency standard links

Cooled-atom or -ion frequency standards at lower frequencies are also included, together with high-accuracy transfer standards such as OsO_4 near 30 THz, that remain outside the "mise en pratique" for the metre. Also some transitions of interest for atomic frequency standards are covered (Ref.4).

TABLE 1: FREQUENCY STANDARDS FOR LASERS

system	app*	reference(s)	label	frequency/Hz	uncert.	notes (line;)std used; etc
He	B	Ei97		5130.495083	+12 8.8 -09	1S-2P;I2
H	**B**	**Ud97Re00Ni00**		**2466.061413187103**	**+12 1.8 -14**	**1S-2S TP;Cs fountain**
muonium	~B	Sch95Me00		2455.5289410	+12 4.0 -09	1S-2S TP;I2
115In+	**T**	**Pe99Za00**		**1267.40245289992**	**+12 1.8 -13**	**5:^1S-^3P0coldion;CH4**
Ps#	~B	Ch84Da89		1233.6072189	+12 8.7 -09	1S-2STP;D beta viaTe2
199Hg+	**T**	**Ud01**		**1064.721609899143**	**+12 9.4 -15**	**cold ion;Cs fountain**
H	B	Sc99		799.1917274028	+12 8.4 -12	2S-12D5/2TP;Cs/778Rb
D	B	Sc99		799.4091849676	+12 8.1 -12	2S-12D5/2TP;Cs/778Rb
D	B	deB97Sc99		770.8592528483	+12 7.1 -12	2S-8D5/2TP;Cs/778Rb
4He	G	Pav94		770.732839058	+12 2.4 -10	2\3S1-3\3P0;778Rb
H	B	deB97Sc99		770.6495615811	+12 7.6 -12	2S-8D5/2TP;Cs/778Rb
172Yb+	T	Gi95Tay97		729.4688689	+12 5.5 -10	633I2 via 1m FP
171Yb+	**T**	**St01b**		**688.358979309312**	**+12 1. -14**	**cold ion;Cs fountain**
172Yb+	T	Gi95Ro97		642.1167853	+12 1.1 -09	octopole;633I2/467Te2
130Te2	G	Ro97	467Te2	642.1165136	+12 9.3 -10	633I2
130Te2	G	Ba85	486Te2	616.6788575	+12 4.0 -10	b1;633I2; also b2
130Te2	G	Ba91	488Te2	613.8811491	+12 7.6 -10	d4;633I2;+b2,b1,e3,i3
127I2	G	Ed96	637I2	470.76645546	+12 2.2 -10	a4;633I2
40Ca	**T**	**Ri99St01a**	**657Ca**	**455.98624049413**	**+12 2.5 -13**	**cooled; Cs**
40Ca	**T**	**Ud01**	**657Ca**	**455.986240494158**	**+12 5.7 -14**	**cooled; Cs fountain**
88Sr+	**T**	**Be99**		**444.7790440954**	**+12 4.5 -13**	**S-D, cold ion; Cs**
85Rb	G	To97	778Rb	385.28514237828	+12 5.2 -12	5S-5D F=3-5 TP; OsO4
87Rb	G	Ye96	780Rb	384.2279818773	+12 1.4 -11	D2,d/f; 778'Rb
85Rb	G	Ba93	795Rb	377.10627149	+12 1.5 -10	D1,c'; 633I2
Cs	B	Av86	852Cs	351.7257682	+12 3.5 -08	D2;633I2;l-m,hyp.res.
Cs	G	Ud99	895Cs	335.116048807	+12 1.2 -10	D1;CH4
C2HD	G	Ye296		281.635363961	+12 1.2 -10	532I2; 1.3Pa
20Ne	L	Po83		260.10324926	+12 3.1 -10	CH4 F
12C2H2	G	Nak96		197.75046656	+12 7.6 -10	v1+v3 R(18)high;778Rb
13C2H2	G	Nak96		196.92974592	+12 7.6 -10	v1+v3 R(23)high;778Rb
12C2H2	G	Nak96		194.91619955	+12 7.7 -10	v1+v3 P(21)low;778Rb
13C2H2	G	Nak95Nak96		193.22000472	+12 5.7 -10	v1+v3 P(30)low;778Rb
HCN	G	Nak95		192.6224469	+12 5. -10	2v1 P(27); 778Rb
CO	G	Po283		129.019381761	+12 5.4 -10	R12; CH4 F
CO	G	Po283		128.360848969	+12 5.5 -10	R05; CH4 F
CO	G	Po283		127.598179703	+12 6.3 -10	P01; CH4 F
CO	G	Po283		126.990495584	+12 6.3 -10	P06; CH4 F
CH4 E	G	Er98		88.373149028553	+12 2.3 -12	Cs; <1.4Pa
172Yb+	T	Be92		87.360087	+12 5. -08	515I2, 633I2
OsO4	G	Ac93		29.37081407841	+12 2.7 -12	CO2 R26; OsO4 R10
OsO4	**G**	**Ac93Du99**		**29.054057446579**	**+12 3.5 -13**	**CO2 R10; Cs**
192OsO4	G	Do87		28.464676938787	+12 3.3 -12	CO2 P14; Cs
138Ba+	T	Mad96		24.01204831717	+12 1.8 -11	Cs
26Mg	B	Go93		601.278870352	+09 5. -12	
24Mg	**B**	**Go87Go93**		**601.2771578691**	**+09 1. -12**	**Ramsey; Cs**
199Hg+	**T**	**Poi96Ber98**		**40.50734799684159**	**+09 1.1 -14**	**cold ions; Cs**
113Cd+	T	Tan96		15.199562858	+09 1.3 -10	rf trap; Cs
171Yb+	**T**	**Bau96**		**12.642812118471**	**+09 7. -13**	**Cs**
171Yb+	**T**	**Se95Fi96**		**12.642812118468**	**+09 1.3 -13**	**Cs**
87Rb	**F**	**Bi99Le01**		**6.834682610904333**	**+09 2.5 -15**	**fountain;Cs fountain**
9Be+	**T**	**Bo85Bo91**		**303.016377265070**	**+06 1.9 -13**	**Cs**
Some CIPM Recommendations**						
H	**B**	**Bip98Qu99**	**243H**	**1233.0307065937**	**+12 8.5 -13**	**1S-2S TP CIPM1997;Cs**
127I2	G	Bip98Qu99	532I2	563.26022348	+12 7. -11	(a10)2fYAG CIPM1997
127I2	G	Bip98Qu99	633I2	473.612214705	+12 2.5 -11	(i),HeNe,CIPM1997;Cs
40Ca	**T,B**	**bip98Qu99**	**657Ca**	**455.98624049415**	**+12 6. -13**	**station.y atomCIPM1997**
88Sr+	T	bip98Qu99	674Sr+	444.77904404	+12 1.3 -10	centreZee.mult.tCIPM97
85Rb	G	bip98Qu99	778Rb	385.285142378	+12 1.3 -11	F=3-5TPdiode CIPM1997
CH4 F	G,B	Bip98Qu99		88.3761816005	+12 2.3 -11	hyp.unres.CIPM1997;Cs
CH4 F	G,B	Bip98Qu99		88.37618160018	+12 3.0 -12	hyp.res. CIPM1997;Cs
OsO4	G	Bip98Qu99		29.09627495234	+12 6. -12	<0.2Pa CIPM1997;Cs

Notes
(i) All uncertainties are 1-sigma.
(ii) Labels of I2 and Te2 lines have 3-digit wavelength in nm: e.g. 633I2.
**: omitting here 515/543,612,640 nm Ar+/HeNe stabilised lasers
*: app: apparatus
#: positronium (Ps)
1m FP: 1 metre Fabry Perot (resonator)
B: in beam
F: fountain, after laser cooling
F-t: Fourier transform (spectroscopy)
G: in gas
hyp.res.: hyperfine resolved
L: in gas-laser Lamb dip
l-m: lambda meter
T: in trap
TP: two photon;f/2 for 778Rb,CIPM97

Some stabilised lasers listed in the 1997 revision of the "mise en pratique" of the definition of the metre (Ref.2) are listed at the foot of Table 1, with their recommended frequencies and their uncertainties when operated as prescribed. All uncertainties in this table are single-sigma, but those of the recommended standards are more conservative than those in the measurements table, which each reflect one particular measurement. It is notable that a number of measurements and standards have uncertainties smaller than 1 part in 10^{12}, and these are shown in bold type. Apart from the entries in this Table, many additional laser frequency standards exist, such as have been listed up to 130 THz, 2.3 μm for spectroscopic calibration (Ref.5) and in the 190-240 THz, 1.6-1.25 μm region for optical communications etc. (Refs.6,7).

3. THE LIST FORMAT

The list in Table 1 is intended for transmission as a text file, or for use as a computer data file, with space to accommodate the frequency to 16 or more significant figures, together with its uncertainty. Exponential notation is used. There is space for up to 3 references, also a brief note on the frequency measurement route used. There is not room however for the wavelengths in addition, except that for multiple gas reference lines, such as in I_2 or Te_2, the lines are given a wavelength-based label placed in the `reference' column, and which is used to identify it in the `notes' column. Apart from the `system' column at the left, for which transition information can appear as the first item in the `notes' column at the right, there is a single-letter column `app.', for `apparatus' which indicates how the system was interrogated: B: beam; G: gas; L: gas laser Lamb dip; or T: trap. (`~B' is entered for thermal evaporation from a nearby surface into vacuum.) This broadly correlates with increasing potential accuracy in the order L, G, B and T. All standards listed, except those using traps, use a method such as saturated absorption or two-photon excitation (TP) to eliminate the Doppler effect to first order. The Table references have codes in the form of two or three letters for the start of the first author's name plus two digits for the year, and are listed in Section 5.

4. DISCUSSION OF THE MEASUREMENTS

4.1 The entries

The uncertainty range of the measurements in Table 1 lies between about 1 part in10^8 and 1 part in 10^{14}. It is notable that the higher-accuracy measurements include the H 1S-2S two-photon transition at 2466 THz and the $199Hg^+$ transition at 1065 THz. Measurements made primarily to test the theories of physics, such as to compare with quantum electrodynamic calculations for such systems as Ps, muonium, H, D and He contribute to the recent high-accuracy data. The trapped-ion or cooled-atom measurements do not yet fully exploit the possibilities of the method, e.g. for the octopole Yb^+ transition at 642 THz, which has an exceedingly narrow natural width, having a measured lifetime of 3700 days (see Ro97). In the latter case technical trade-offs exist, e.g. between signal/noise ratio and minimising the state perturbation. Progress with cooled-atom or ion measurements is of special interest, so that more than one measurement can be listed.

4.2 Technological advances

The main technological advance is first the femtosecond-laser comb method. This new technique has been directly proved to be accurate at a few parts in 10^{17} (Ref. 8) and is increasingly viewed as revolutionary, although only a few papers quoted here will have used it. The real benefits are still to come, since building apparatus and doing experiments takes time. Second, broadening of the comb to a full octave in low-dispersion fibre greatly simplifies calibration of the comb, see e.g. Ref. 9, and has a demonstrated accuracy of a few parts in 10^{16} (Ref.10). A review of prior techniques has been edited by Luiten (Ref.11).

4.3 Dissemination/transportation of frequency standards

The new list extends to yet higher frequency, into regions where continuous-wave measurement is replaced by pulsed, owing to shortness of upper-state lifetimes. Not shown however, because it is the primary standard, is the laser-cooled Cs fountain at 9.2 GHz, which now reaches 1 part in 10^{15} in accuracy, and is more widely installed in metrology laboratories (Ref.12), to improve realisation of the SI hertz and second. A transportable version has also been directly used to measure the H 1S-2S transition (Ni00). The "Mise en pratique" for the metre of 1997 (Qu99) included for the first time the laser locked to the H 1S-2S transition, and begins to include solid-state laser standards which are capable of replacing the older gas-laser standards.

4.4 Conclusion

Quite unexpectedly, a new accurate optical frequency measurement system, comparable in simplicity with the ubiquitous lambda meter for comparing wavelengths, has appeared on the scene. The interest in basic physics, which is driving development into the uv, for example, can now be pursued at considerably less expense. (Both increased optical accuracy and increased numbers of measurements of optical reference resonances can be expected). The situation is in general no longer one of realising the metre, as laser stabilisation heads for reproducibilities in the 10^{-16} and smaller regions. These values are needed rather for basic-physics purposes, including searching for cosmological effects such as time variation of the fine structure constant and gravitational waves. Broadly, the new simplified and inexpensive frequency measurement route provides a good tool for basic physics experiments, and we may expect the latter to bring pressure for yet better realisation of the SI hertz and second. Given the high resolution in the optical region and the existence of long-lived solid state devices for stabilised-laser systems and now also for frequency division to the VHF region, we can expect to see demonstrations towards useful optical clocks.

5. TABLE 1 REFERENCES

Ac93: (OsO4) O. Acef, J. J. Zondy, M. Abed, D. G. Rovera, A. H. Gérard, A. Clairon, Ph. Laurent, Y. Millerioux and P. Juncar, "A CO2 to visible optical frequency synthesis chain: accurate measurement of the 473 THz HeNe/I2 laser", Optics Commun. 97, 1993, 29-34.

Av86: (Cs D2) G. Avila, P. Gain, E. de Clercq and P. Cerez, "New absolute wavenumber measurement of the D2 line of caesium", Metrologia 22, 1986, 111-114.

Ba85: (130Te2) J. R. M. Barr, J. M. Girkin, A. I. Ferguson, G. P. Barwood, P. Gill, W. R. C. Rowley and R. C. Thompson, "Interferometric frequency measurements of 130Te2 transitions at 486 nm", Optics Commun. 54 (4), 15 June 1985, 217-221.

Ba91: (130Te2) G. P. Barwood, W. R. C. Rowley, P. Gill, J. L. Flowers and B. W. Petley, "Interferometric measurements of 130Te2 reference frequencies for 1S-2S transitions in hydrogen-like systems", Phys. Rev. A, 43, 1991, 4783-4790.

Ba93: (85Rb, 87Rb) G. P. Barwood, P. Gill and W. R. C. Rowley, "Optically narrowed Rb-stabilized laser GaAlAs diode laser frequency standards with 1.5 x 10-10 absolute accuracy", Proc. SPIE - Int. Soc. Opt. Eng. 1837, 1993, 262-270.

Bau96: (171Yb+) A. Bauch, D. Schnier and Chr. Tamm, "Microwave spectroscopy of 171Yb+ stored in a Paul trap", Proc. 5th Symp. on Frequency Standards and Metrology, Ed. J. C. Bergquist (Singapore: World Scientific) 1996, 387-388.

Be92: (172Yb+) A. S. Bell, P. Gill, H. A. Klein, A. P. Levick and W. R. C. Rowley, "Precision measurement of the 2F7/2-2D5/2 3.43 μm interval in trapped 172Yb+", J. Mod. Opt. 39 (2), 1992, 381-387.

Be99: (88Sr+) J. E. Bernard, A. A. Madej, L. Marmet, B. G. Whitford, K. J. Siemsen and S. Cundy "Cs-based frequency measurement of a single, trapped ion transition in the visible region of the spectrum", Phys. Rev. Lett. 82 (16), 1999, 3228-3231.

Ber98: (199Hg+) D. J. Berkeland, J. D. Miller, J. C. Bergquist, W. M. Itano and D.J. Wineland, "Laser-cooled mercury ion frequency standard", Phys. Rev. Lett. 80 (10), 1998, 2089-2092.

Bi99: (87Rb) S. Bize, Y. Sortais, M. S. Santos, C. Mandache, A. Clairon and C. Salomon "High-accuracy measurement of the ^87Rb ground-state hyperfine splitting in an atomic fountain", Europhys. Lett. 45 (5), 1999, 554-564.

Bip98: BIPM, Le Systeme international d'unites (SI) (Paris: Organisation intergouvermentale de la Convention du metre, 7e edition 1998)

Bo85: (9Be+) J. J. Bollinger, J. D. Prestage, W. M. Itano and D. J. Wineland, "Laser-cooled atomic frequency standard", Phys. Rev. Lett. 54 (10), 11 March 1985, 1000-1003.

Bo91: (9Be+) J. J. Bollinger, D. J. Heinzen, W. M. Itano, S. L. Gilbert and D. J. Wineland, "A 303-MHz frequency standard based on trapped Be+ ions", IEEE Trans. Instrum. Meas. 40 (2), April 1991, 126-128.

Ch84: (positronium (Ps), e+e-) S. Chu, A. P. Mills Jr. and J. L. Hall, "Measurements of the positronium 13S1-23S1 interval by Doppler-free two-photon spectroscopy", Phys. Rev. Lett. 52 (19), 7 May 1984, 1689-1692.

deB97: (H and D) B. de Beauvoir, F. Nez, L. Julien, B. Cagnac, F. Biraben, D. Touahri, L. Hilico, O. Acef, A, Clairon and J. J. Zondy, "Absolute frequency measurement of the 2S-8S/D transitions in hydrogen and deuterium: new determination of the Rydberg constant", Phys. Rev. Lett. 78 (3), 20 January 1997, 440-443.

Do87: (OsO4) Yu. S. Domnin, N. B. Koshelyaevskii, A. N. Malimon, V. M. Tatarenkov and P. S. Shumyatskii, "Infrared frequency standards based on osmium tetroxide", Sov. J. Quant. Electron. 17 (6), June 1987, 801-803; also Kvantovaya Elektron. (Moscow) 14, June 1987, 1260-1263.

Du99: (OsO4) F. Ducos, G. D. Rovera, C. Daussy and O. Acef "Performance of OsO4 stabilized CO2 lasers as optical standards near 29 THz", Proc. 1999 Joint Meeting EFTF-IEEE IFCS, 13-16 April 1999, Besançon, France,(IEEE Cat. No. 99CH36313), pp714-717.

Ed96: (127I2) C. S. Edwards, G. P. Barwood, P. Gill, F. Rodríguez-Llorente and W. R. C. Rowley, "Frequency stabilised diode lasers in the visible region using Doppler-free iodine spectra", Optics Commun. 132, 1996, 94-100.

Ei97: (He) K S Eikema, W Ubachs, W Vassen and W Hogervorst "Lamb shift measurement in the 1^1S ground state of helium", Phys. Rev. A 55 (3), 1997, 1866-1884.

Er98: (CH4 E line) P. S. Ering, D. A. Tyurikov, G. Kramer and B. Lipphardt "Measurement of the absolute frequency of the methane E-line at 88 THz", Optics Commun. 151, 1998, 229-234.

Fi96: (171Yb+) P. T. H. Fisk, M. J. Sellars, M. A. Lawn and C. Coles, "A microwave frequency standard based on trapped, buffer gas-cooled 171Yb+ ions - some accuracy issues", Proc. European Frequency Time Forum 5-7 March 1996, (London:IEE) Conf. Publ. 418, 1996, 212-217.

Gi95:(172Yb+) P. Gill, H. A. Klein, A. P. Levick, M. Roberts, W. R. C. Rowley and P. Taylor, "Measurement of the 2S1/2-2D5/2 411-nm interval in laser-cooled trapped 172Yb+ ions", Phys. Rev. A 52 (2), August 1995, R909-R912.

Go87: (24Mg) A. Godone, E. Bava and C. Novera, "High-resolution frequency measurement of the 3P1-3P0 24Mg transition", Metrologia 24, 1987, 133-138.

Go93: (26Mg) A. Godone, C. Novero "The magnesium frequency standard", Metrologia 30(3), 1993 163-181.

Le01: (87Rb fountain): see text ref. 3

Mad96: (Ba+, Sr+) A. A. Madej, K. J. Siemsen, B. G. Whitford, J. E. Bernard and L. Marmet, "Precision absolute frequency measurements with single atoms of Ba+ and Sr+", Proc. 5th Symp. on Frequency Standards and Metrology, Ed. J. Bergquist (Singapore: World Scientific) 1996, 165-170, and A. A. Madej and K. J. Siemsen, "Absolute heterodyne frequency measurement of the 88Sr+ 455-THz S-D single ion transition", Optics Lett. 21 (11), 1 June 1996, 824-826.

Me00: (Muonium μ+e-) V Meyer + 28, "Measurement of the 1s-2s energy interval in muonium", Phys. Rev. Lett. 84 (60), 2000, 1136-1139.

Nak95: (HCN, C2H2, 13C2H2) K. Nakagawa, M. de Labachelerie, Y. Awaji and M. Kourogi, "Precise optical frequency atlas of acetylene lines in the 1.5 μm region", Proc. Laser Spectoscopy XII, Isle of Capri, Italy, 11-16 June 1995, Ed. M. Inguscio, M. Allegrini and A. Sasso (Singapore: World Scientific) 1996, 228-229.

Nak96: (C2H2, 13C2H2) K. Nakagawa, M. de Labachelerie, Y. Awaji and M. Kourogi, "Accurate optical frequency atlas of the 1.5 μm bands of acetylene", J. Opt. Soc. Am. B 13 (12), December 1996, 2708-2714. Note: 36 lines in 12C2H2 and 54 lines in 13C2H2 are listed: the high and low extremes are given.

Ni00: (H 1S-2S) M Niering, R Holzwarth, J Reichert, P Pokasov, Th Udem, M Weitz, T W Hänsch, P Lemonde, G Santarelli, M Abgrall, P Laurent, C Salomon and A Clairon "Measurement of the hydrogen 1S-2S transition frequency by phase coherent comparison with a microwave cesium fountain clock", Phys. Rev. Lett. 84 (24) 12 June 2000, 5496-5499.

Pav94: (4He) F. S. Pavone, F. Marin, P. De Natale, M. Inguscio and F. Biraben, "First pure frequency measurement of an optical transition in helium: Lamb shift of the 23S1 metastable level", Phys. Rev. Lett. 73 (1) 4 July 1994, 42-45.

Pe99: (155In+) E. Peik, J. Abel, Th. Becker, M. Fries, J. von Zanthier and H. Walther "Towards an indium single-ion optical clock", Proc. 1999 Joint Meeting EFTF-IEEE IFCS, 13-16 April 1999, Besançon, France,(IEEE Cat. No. 99CH36313), pp682-685.

Po83: (20Ne) C. R. Pollock, D. A. Jennings, F. R. Petersen, J. S. Wells, R. E. Drullinger, E. C. Beaty and K. M. Evenson, "Direct frequency measurements of transitions at 520 THz (576 nm) in iodine and 260 THz (1.15 μm) in neon", Optics Lett. 8 (3), March 1983, 133-135.

Po283: (CO) C. R. Pollock, F. R. Petersen, D. A. Jennings and J. S. Wells, "Absolute frequency measurements on the 2-0 band of CO at 2.3 μm; calibration standard frequencies from high resolution color center laser spectroscopy", J. Mol. Spectrosc. 99, 1983, 357-368.

Poi96: (199Hg+) M. E. Poitzsch, J. C. Bergquist, W. M. Itano and D. J. Wineland, "Cryogenic linear ion trap for accurate spectroscopy", Rev. Sci. Instrum. 67 (1), January 1996, 129-134.

Qu99: (CIPM 1997 revision of "Mise en pratique" of the definition of the metre) T. J. Quinn, "Practical realisation of the definition of the metre (1997), Metrologia 36, 1999, 211-244.

Re00: (H 1s-2s) J Reichert, M Niering, R Holzwarth, M Weitz, Th Udem and T W Hänsch "Phase coherent vacuum-ultraviolet to radio frequency comparison with a mode-locked laser", Phys. Rev. Lett. 84 (15), 2000, 3232-3235.

Ri99: (Ca) F. Riehle, H. Schnatz, B. Lipphardt, G. Zinner, T. Trebst and J. Helmcke "The optical calcium frequency standard", IEEE Trans. Instr. Meas. 48 (2), 1999, 613-617.

Ro97: (172Yb+) M. Roberts, P. Taylor, G. P. Barwood, P. Gill, H. A. Klein and W. R. C. Rowley, "Observation of an electric octupole transition in a single ion", Phys. Rev. Lett. 78, 1997, 1876-1879.

Sc99: (H,D 2S-12D) C Schwob, L Jozefowski, B de Beauvoir, L Hilico, F Nez, L Julien and F Biraben, O Acef and A Clairon "Optical frequency measurement of the 2S-12D transitions in hydrogen and deuterium: Rydberg constant and Lamb shift determinations", Phys. Rev. Lett. 83 (25), 1999, 4960-4963.

Sch95: (muonium, μ+e-) W. Schwarz + 24, "Spectroscopy of the 1S-2S energy splitting in muonium", IEEE Trans. Instrum. Meas. 44 (2), April 1995, 505-509.

Se95: (171Yb+) M. J. Sellars, P. T. H. Fisk, M. A. Lawn and C. Coles, "Further investigation of a prototype microwave frequency standard based on trapped 171Yb+ ions", in Proc. 1995 IEEE International Symposium on Frequency Control (49th Annual Symposium) (New York: IEEE) 1995, 66-73.

St01a: (Ca) J. Stenger, T. Binnewies, G. Wilpers, F. Riehle, H. R. Telle, J. K. Ranka, R. S. Windeler and A. J. Stentz, "Phase-coherent frequency measurement of the Ca intercombinatioon line at 657 nm with a Kerr-lens mode-locked femtosecond laser", Phys. Rev. A 63, 17 January 2001, 021802 (R).

St01b: (171Yb+) J. Stenger, Chr. Tamm, N. Haverkamp, S. Weyers and H. R. Telle, Absolute frequency measurement of the 435.5 nm 171Yb+ clcck transition with a Kerr-lens mode-locked femtosecond laser", preprint, 19 March 2001.

Tan96: (113Cd+) U. Tanaka, H. Imajo, K. Hayasaka, R. Ohmukai, M. Watanabe and S. Urabe, "Laser microwave double-resonance experiment on trapped 113Cd+ ions", CPEM96 Digest, TH1B-4, 515-6; see also Phys. Rev. A, 53(6), June 1996, 3982-3985.

Tay97: (172Yb+) P. Taylor, M. Roberts, S. V. Gateva-Kostova, R. B. M. Clarke, G. P. Barwood, W. R. C. Rowley and P. Gill, Investigation of the ^2S1/2-^2D5/2 clock transition in a single ytterbium ion", Phys. Rev. A, 1997, 56, pp.2699-2704.

To97: (85Rb two-photon) D. Touahri, O. Acef, A. Clairon, J.-J. Zondy, R. Felder, L. Hilico, B. de Beauvoir, F. Biraben and F. Nez, "Frequency measurement of the 5S1/2(F=3)-5D5/2(F=5) two-photon transition in rubidium", Optics Commun. 133, 1 January 1997, 471-478.

Ud97: (H) Th. Udem, A Huber, M. Weitz, D. Leibfried, W. König, M. Prevedelli, S. Dimitriev, H. Geiger and T. W. Hänsch, "Phase-coherent measurement of the hydrogen 1S-2S frequency with an optical frequency interval divider chain", IEEE Trans. Instrum. Meas. 46(2) April 1997, 166-168; also Phys. Rev. Lett. 79(14), 6 October 1997, 2646-2649.

Ud99: (Cs D) Th. Udem, J. Reichert, R. Holzwarth and T. W. Hänsch, "Absolute optical frequency measurement of the cesium D1 line with a mode-locked laser" Phys. Rev. Lett., 82(18), 3 May 1999, 3568-3571.

Ud01: (199Hg+, 40Ca) Th. Udem, S. A. Diddams, K. R. Vogel, C. W. Oates, E. A. Curtis, W. D. Lee, W. M. Itano, R. E. Drullinger, J. C. Bergquist and L. Hollberg, "Absolute frequency measurements of the Hg+ and Ca optical clock transitions with a femtosecond laser", electronic preprint (arXiv:physics/0101029) 4 January 2001.

Ye96: (87Rb) J. Ye, S. Swartz, P. Jungner and J. L. Hall, "Hyperfine structure and absolute frequency of the 87Rb 5P3/2 state", Optics Lett., 21 (16), 15 August 1996, 1280-1282.

Ye296: (C2HD) J. Ye, L-S. Ma and J. L. Hall, "Ultra-stable optical frequency reference at 1.064 μm using a C2HD molecular overtone transition", CPEM96 Digest, WE2A-6, Braunschweig, Germany, 17-20 June 1996, Supplement, 19-20.

Za00: (115In+) J. von Zanthier, Th. Becker, M. Eichenseer, A. Yu. Nevsky, Ch. Schwedes, E. Peik, H. Walther, R. Holzwarth, J. Reichert, Th. Udem and T. W. Hänsch, "Absolute frequency measurement of the In+ clock transition with a mode-locked laser", Optics Lett., 25 (23), 1 December 2000, 1729-1731.

6. TEXT REFERENCES

1. D. J. E. Knight, "Present frequency standards for lasers", Proc. EFTF'97, Neuchâtel, Switzerland, 4-6 March, 1997, pp 623-627.

2. T. J. Quinn, "Practical realisation of the definition of the metre(1997), Metrologia **36**, 1999, 211-244.

3. P. Lemonde, Ph. Laurent, G. Santarelli, M. Abgrall, Y. Sortais, S. Bize, C.Nicolas, S. Zhang, A. Clairon, N. Dimarcq, P. Petit, A. G. Mann, A. N. Luiten, S. Chang and C. Salomon "Cold-atom clocks on earth and in space", in A. N. Luiten, (Ed.): *Frequency measurement and control*, Topics Appl. Phys. **79**, 131-152 (2001)

4. J. Vanier and C. Audoin, *The quantum physics of atomic frequency standards* (Bristol: Adam Hilger) 1989, Chapter 1.

5. A. G. Maki and J. S. Wells, *Wavenumber calibration tables from heterodyne frequency measurement.* (Washington D.C.: US Government Printing Office, NIST Special Publication 821) 1991.

6. A. G. Maki, "Infrared and far-infrared absorption frequency standards", in D. R. Lide and H. P. R. Frederikse, Eds., *CRC Handbook of Chemistry and Physics*, 75th Edition (Boca-Raton: CRC Press) 1994, pp **10**-319 - **10**-323.

7. D. J. E. Knight, "Requirements and practical possibilities for frequency standards for optical fiber communication bands", in M. Ohtsu, Ed., *Frequency control of semiconductor lasers* (New York: John Wiley and Sons) 1996, 173-206.

8. Th. Udem, J. Reichert, R. Holzwarth and T. W. Hänsch, Opt. Lett. **24**, 1999, 881.

9. J. L. Hall and J. Ye, "Merging the ultrasensitive, the ultrastable and the ultrafast: a new era of frequency standards and optical frequency measurement", Optics & Photonics News, **12** (2) February 2001, 44-50.

10. R. Holzwarth , Th. Udem, T. W. Hänsch, J. C. Knight, W. J. Wadsworth and P. St.J. Russell, "Optical frequency synthesiser for precision spectroscopy", Phys. Rev. Lett. **85** (11), 11 September 2000, 2264-2267.

11. A. N. Luiten, (Ed.) *Frequency measurement and control: advanced techniques and future trends*, Topics Appl. Phys. **79**, 394pp (2001).

12. See reports from 8 or more laboratories at this Conference.

FEMTOSECOND LASER COMBS FOR OPTICAL FREQUENCY MEASUREMENT AT NPL

S.N. Lea, G. Huang, H.S. Margolis, and P. Gill

National Physical Laboratory, Teddington, Middlesex TW11 0LW, UK

1. INTRODUCTION

The use of Kerr-effect mode-locked Ti:sapphire lasers, together with spectral broadening in photonic crystal fibres, to generate octave-span optical frequency combs is effecting a revolution in the fields of absolute optical frequency metrology and optical frequency standards [1-4], at last making it feasible to operate an optical frequency standard as an optical clock. Candidates for such highly-stable optical clocks include laser-cooled trapped single ions such as Sr^+ and Yb^+, both of which are being studied at NPL [5].

This paper presents some preliminary data on the femtosecond laser comb at NPL. We also discuss some approaches to checking the accuracy of our femtosecond comb, using a frequency chain to measure the frequency of the Sr^+ ion trap relative to a methane-stabilised He-Ne laser system (HeNe/CH_4 standard) at 3.39 μm which we are currently completing [6]. This chain will enable us to evaluate the performance of the femtosecond laser comb at the 5 parts in 10^{13} level.

2. FEMTOSECOND LASERS

The femtosecond laser repetition rate is a key parameter in the design of an octave-span frequency comb using photonic crystal fibre. As the repetition rate is increased, the average power per comb mode is increased. This is beneficial from the point of view of observing a beat with another (reference) laser and has the added advantage that as the comb modes are more widely spaced in frequency, it will be easier to identify with which mode the reference laser is beating. However, a higher repetition rate results in lower peak pulse power which will reduce the efficiency of comb broadening by self-phase modulation in the fibre. A further consideration, as pointed out by Holzwarth *et al.* [4], is that at lower repetition rate, with less power per comb mode, the broadened comb may be swamped by incoherent mixing processes in the fibre.

Two femtosecond Ti:sapphire lasers are in use in our laboratory. One is a GigaOptics [7] ring cavity design using mirrors with negative group velocity dispersion coatings. The absence of intra-cavity elements in this design permits lasers to be constructed with repetition rate of several gigahertz [8] but for our application a compromise has to be made between the benefit of increased average power per comb mode and lower pulse energy. We have chosen to work with a repetition rate of 800 MHz.

The other laser is built from a KMLabs kit [9] and has a linear cavity with dispersion compensation by means of intra-cavity prisms. We have operated it at repetition rates from 80 MHz up to 100 MHz. With this laser we have obtained pulses with a spectral FWHM of 50 nm centred at 800 nm (fig. 1) and 600 mW average power with a pump power of 4.5 W at 532 nm. With the GigaOptics laser we have obtained 40 nm FWHM pulses and 600 mW average power with 6.5 W pump power. Both lasers have one piezo-mounted mirror, which can be used for repetition rate stabilisation to a suitable microwave oscillator [10]. Control of the absolute carrier phase, to provide frequency stabilisation of the comb modes to a reference laser or optical frequency standard, can be achieved for the KMLabs laser by the scheme first demonstrated by Udem *et al.* [1] whilst for the GigaOptics laser we propose to use pump power modulation as demonstrated by Holzwarth *et al.* [4].

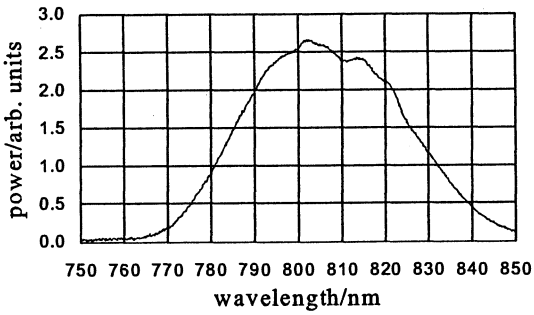

Figure 1. wavelength spectrum of the pulses obtained from the KMLabs laser observed using an HP70951A optical spectrum analyser. The 45 mW FWHM of this particular spectrum corresponds to a pulse length of 15 fs (HWHM).

We expect the GigaOptics laser to be the better choice in the long term. However, for our initial experiments we have used the KMLabs laser and the work described in the remainder of this paper has been carried out using this laser at 88 MHz repetition rate. We have made some initial tests to characterise the servo requirements for repetition rate locking at around 10 GHz but the beats spectra presented below are taken with the free-running laser.

3. OCTAVE COMB GENERATION

We have observed spectral broadening of the output pulses from the KMLabs laser using a piece of photonic crystal fibre obtained from the group of J. Knight at the University of Bath. Using a 35 cm long piece of this fibre we have generated a white-light spectrum spanning more than one optical octave (fig. 2). When the fibre output is dispersed by a 1200 lines/mm diffraction grating it can be seen to extend from the violet through to the infrared. Although the spectrum appears to be of uniform intensity in the visible, it is clear that there is a large non-uniformity in intensity in the infrared. With 140 mW average power incident on the fibre, we obtain 45 mW in the output spectrum. Increasing the average power results in excessive feedback to the laser.

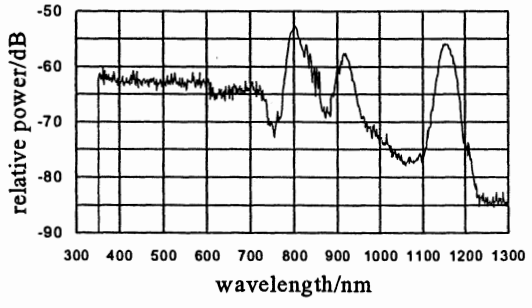

Figure 2. Wavelength spectrum after broadening in the photonic crystal fibre. The cut-off at 350 nm is an artefact of the optical spectrum analyser. Note the logarithmic vertical scale.

4. BEATS SPECTRA

Fig. 3 illustrates the rf beat spectrum observed when light from a single frequency extended cavity diode laser (ECDL) is mixed with the femtosecond comb. The comb is dispersed using a 1200 lines/mm diffraction grating and the beats spectra are observed on an avalanche photodiode. Light from about 20,000 comb modes is detected. The rf spectrum consists of strong intermode beat signals at $f_{laser} = n \times 88$ MHz and weaker beats of the 841 nm ECDL with the nearest comb modes at $f_{ECDL} = n \times 88$ MHz $\pm \Delta f$. Here Δf is the offset frequency of the ECDL laser from the nearest comb mode and is of ambiguous sign. These beats have around 20 dB signal-to-noise in 1 MHz bandwidth. The upper trace in fig. 3 shows the beats obtained with the femtosecond laser pulse only while the lower trace shows beats obtained after broadening in the photonic crystal fibre. The rf spectrum observed after the fibre shows no degradation in signal-to-noise at this wavelength.

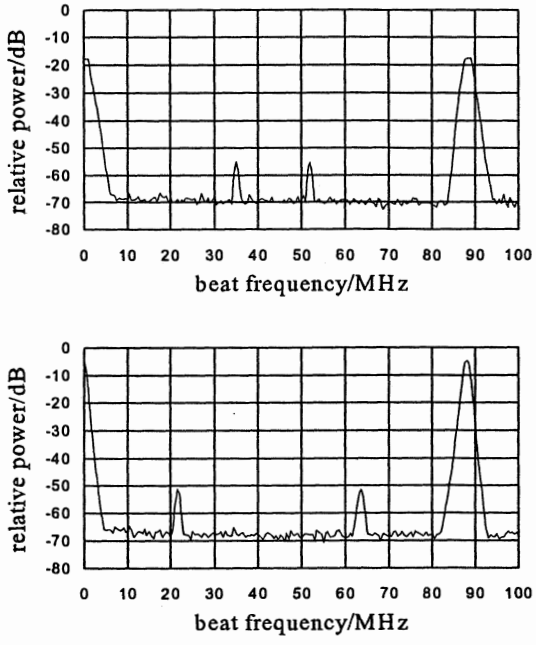

Figure 3. The rf beat spectra of the comb with an ECDL at 841 nm. Top: without fibre. Bottom: with fibre. Resolution bandwidth: 1 MHz.

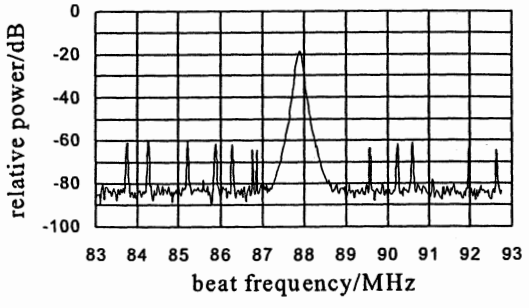

Figure 4. The rf beat spectra of the fs comb with an ECDL at 841 nm showing frequency jitter of the absolute frequency of the comb modes. Resolution bandwidth: 100 kHz; sweep time: 20 ms.

The intermode beat frequency of the free-running laser has a high degree of common-mode noise rejection and is consequently very stable. The beat

between modes spaced by 114 times the repetition rate (about 10 GHz) has been observed. This beat frequency has been mixed with the output of a 10 GHz synthesiser and the downconverted frequency, adjusted to about 1 kHz, observed on an oscilloscope. From a measurement of the jitter of the 1 kHz signal, we estimate the relative stability of the absolute frequency of the modes to be 2×10^{-8}. This is in rough agreement with the observed jitter of the beat with the 841 nm ECDL, which is about 10 MHz (figure 4).

5. TESTS OF THE FEMTOSECOND COMB

There are unresolved questions relating to the accuracy of femtosecond laser combs. One feature of the output spectrum of the photonic crystal fibre which we have observed is its non-uniform intensity, both spectrally and temporally. Ideally, the frequency accuracy of the femtosecond comb should be evaluated by comparison with frequency measurements made using traditional harmonic frequency chains. We have the possibility to perform such tests at the few parts in 10^{13} level using our methane-stabilised He-Ne laser (HeNe/CH_4 standard) at 3.39 μm (88.4 THz). This laser system was constructed by the group of M. Gubin at the P.N. Lebedev Physical Laboratory. The absolute frequency of this laser has been measured using the rf-to-optical frequency chains at PTB and LPTF at various times over a three-year period with relative standard uncertainty 4×10^{-13} and reproducibility over an interval of one year between successive measurements at PTB of 1.2×10^{-13} [11].

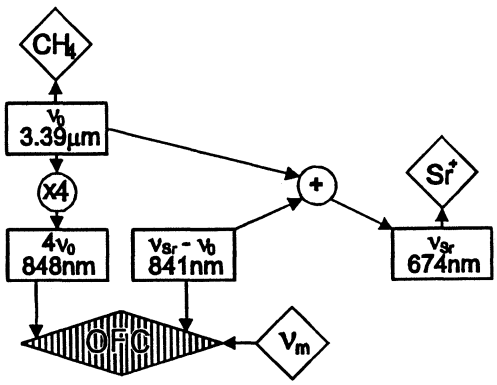

Figure 5. The frequency chain linking the Sr^+ ion standard at 674 nm (ν_{Sr}) to the methane-stabilised HeNe laser at 3.39 μm (ν_0). OFC: Optical frequency comb with mode spacing $\nu_m \approx 9.68$ GHz.

The femtosecond comb can be tested using our methane-to-strontium frequency chain illustrated in fig. 5. In this chain, four times the HeNe/CH_4 frequency (848 nm) is synthesised by frequency doubling of two intermediate sources: a singly-resonant OPO at 3.39 μm and a DFB diode laser at 1.7 μm. The Sr^+ frequency is synthesised by sum-frequency mixing of the 3.39 μm OPO idler output and a laser at 841 nm, creating a frequency interval in the near infrared equal to the HeNe/CH_4 frequency. The residual 2.9 THz interval is bridged by a passive optical frequency comb generator. This provides four possible tests of the accuracy of the femtosecond comb:

- Comparison of the femtosecond comb with the passive optical frequency comb. This can provide a very accurate test over an interval of a few THz near the centre wavelength of the femtosecond comb.

- Measurement of the interval 674 nm – 841 nm, which is equal to the methane frequency. This provides a test of the fs comb over a span of 88.4 THz.

- Direct measurement of the fourth harmonic of the methane frequency at 848 nm.

- Comparison of measurements of the strontium ion frequency at 674 nm using the femtosecond comb and the methane-to-strontium chain.

Only the last two tests, being absolute frequency measurements relative to the laser repetition rate, require a full octave comb span.

Measurements made using the methane-strontium frequency chain only test the fs comb in the near infrared part of the spectrum. The HeNe/CH_4 standard can be used to test the femtosecond comb over the its full range by transposing the 88.4 THz frequency interval to different parts of the optical spectrum. This can be done in the visible region by making use of frequency mixings which we have already demonstrated in preparation for frequency measurements of working optical frequency standards:

- Nd:YAG/I_2 at 532 nm – ECDL at 631 nm.
  We have demonstrated the required mixing with single-pass conversion efficiency of 4×10^{-4} W^{-1} in a 19 mm long PPLN crystal with room-temperature poling period Λ_{RT} = 10.4 μm at phase-matching temperature T_{pm} = 133 °C.

- HeNe/I_2 at 633 nm – Rb 2-photon at 778 nm.
  We have demonstrated the required mixing with single pass efficiency 7×10^{-4} W^{-1} in a similar PPLN crystal with Λ_{RT} = 14.6 μm; T_{pm} = 152 °C.

The OPO mentioned above could provide a further test at the infrared end of the comb. The OPO is pumped at 1053 nm by a single-frequency Nd:YLF

laser. In order to generate OPO idler output at the $HeNe/CH_4$ frequency the signal output is at 1528 nm. The frequency difference between the pump and signal can be measured using the femtosecond comb if it can be extended out to the 1.5 μm telecomms band.

6. CONCLUSIONS

We have presented some of our preliminary work towards the construction of a femtosecond laser comb at NPL. Using our $HeNe/CH_4$ standard and our existing strontium-to-methane frequency chain, we can test the accuracy of the femtosecond comb at the 5 parts in 10^{13} level. By referencing the repetition rate of the comb to a maser and hence ultimately to the caesium fountain primary standard also under construction at NPL, this new chain technology will enable us to make absolute optical frequency measurements of our Sr^+ and Yb^+ ion trap optical frequency standards. The accuracy of these measurements relative to the caesium standard have the potential to be at an level of limited only by the systematic uncertainties of the ion trap standards. The combination of ion trap optical frequency standard and femtosecond comb should make it feasible for us to realise an optical clock, which can input directly to the atomic timescale based on microwave clocks.

ACKNOWLEDGEMENTS

The authors thank Th. Udem, D. Rovera, H. Telle, and D. Henderson for sharing their experience of femtosecond laser stabilisation. This work is supported by the UK National Measurement System Length Programme under contract LE99/A01.

REFERENCES

[1] Th. Udem *et al., Phys. Rev. Lett.* **82**, 3568 (1999).
[2] D. Jones *et al., Science* **288**, 635 (2000).
[3] S.A. Diddams *et al., Phys.Rev.Lett.* **84**, 5102 (2000).
[4] R. Holzwarth *et al., Phys.Rev.Lett.* **85**, 2264 (2000).
[5] G.P. Barwood *et al., Phys.Rev. A* **59**, R3178 (1999); M. Roberts *et al., Phys.Rev.A***62**, 020501(R), (2000).
[6] H.S. Margolis *et al.,* in *Proc. 14th EFTF*, Torino, Italy, p194 (2001).
[7] GigaOptics GmbH, Louis-Raverat Str. 23, D-63165 Muehlheim am Main, Germany.
[8] A. Bartels *et al., Opt. Lett.* **24**, 996 (1999).
[9] Kapteyn-Murnane Laboratories L.L.C., 3509 Kirkwood Pl., Boulder, CO 80304, USA.
[10] M.J.W. Rodwell *et al, IEEE J. Quant. Electron.* **25**, 817 (1989).
[11] O. Acef *et al.*, in *Proc. 1999 Joint Meeting EFTF – IEEE IFCS*, Besançon, France, p742 (1999).

THE NEW BNM-LPTF OPTICAL FREQUENCY MEASUREMENT CHAIN

G. D. Rovera † J. J. Zondy † O. Acef † F. Ducos †
J. C. Knight ‡ P. St. J. Russel ‡
†BNM-LPTF Observatoire de Paris, France
‡Optoelectronic Group, School of Physics University of Bath, UK

A new optical frequency standard based on cold strontium atoms is under development at the BNM-LPTF. To link this standard to the primary microwave standard we are realizing a new frequency chain based on a femtosecond laser. In its ultimate version the chain will serve to measure the absolute frequency of the Sr frequency standard operating on the 671 nm line, with an uncertainty only limited by the atom spectroscopy. As intermediate results we plan to measure the Sr standard stabilized on the 689 nm intercombination line, and some other optical frequency standards that were previously measured with the traditional harmonic chain.

A mode-locked Ti:Sa laser with a repetition rate of about 880 MHz is used to produce a frequency comb centered at about 800 nm and extending over more than 40 nm. The spacing of the lines of the frequency comb is imposed by phase locking the repetition rate of the fs laser to the signal from an Hydrogen maser [1]. To obtain good phase noise performance the 10^{th} harmonic of the repetition rate is mixed with the signal from a microwave synthesizer [2]. The resulting beat-note is phase compared with the signal from a low noise commercial radio frequency synthesizer to generate the error signal, that controls the position of the flat chirped mirror via a piezodriver.

The light is passed through a photonic crystal fiber (PCF) [3] with a coupling efficiency of about 50 % by using two microscope objectives. The spectrum of the "white" light emerging from the fibers extends over more than one octave, from wavelengths longer than 1200 nm up to 530 nm. To use this broad frequency comb for absolute frequency measurement we are investigating two different solutions; both without locking the absolute position of the comb lines. At first glance we can expect that the comb lines are at integer multiple of the repetition frequency f_{rep} but in practice this is not true [4], and we must consider that the comb has some frequency offset, therefore the frequency of the n^{th} line of the comb is $f_n = nf_{rep} + \delta$.

Several methods can be employed to measure or eventually annihilate this offset, and we are testing two different possibilities. In the first envisaged setup (fig2), we will take advantage from the availability of a Nd:YAG laser and of its frequency doubling setup developed for the realization of an I_2 stabilized 532 nm frequency standard. In this case we don't consider the offset of the comb and we determine the absolute frequency of the Nd:YAG laser by measuring the frequency gap between the laser signal and its second harmonics.

Referring to figure 1, b_1 is the beat note between the Nd:YAG signal and the upper nearest comb's line, b_2 the beat between the second harmonics of the Nd:YAG signal and the lower nearest comb's line, while f_{rep} is the repetition frequency, i.e the spacing of the comb. The frequency of the Nd:YAG laser is given by:

$$\begin{aligned} \nu_{YAG} &= b_1 + (2n - 1 - n)f_{rep} + b_2 \\ &= b_1 + b_2 + (n-1)f_{rep} \end{aligned}$$

Obviously n can only be inferred by *a priori* knowledge of the Nd:YAG frequency, with an uncertainty lower than $f_{rep}/2$, but this can be obtained with a commercial lambda-meter. Once known the frequency of the Nd:YAG laser we can measure any frequency standard operating in the range covered by the comb. Referring again to fig. 1 and calling b_x the beat-note of the unknown frequency with the nearby line of the comb the following relationship is evident:

$$\nu_X - \nu_{YAG} = b_1 + (m-n)f_{rep} + b_x$$

By substitution:

$$\nu_X = 2b_1 + b_2 + b_x + (m-1)f_{rep}$$

In this equation the absolute frequency of the Nd:YAG disappears, as well as the absolute frequency of the comb's lines.

A simplified diagram of this setup is reported in fig. 2. A beam, formed by superimposing the signal of a Nd:YAG laser with its second harmonics

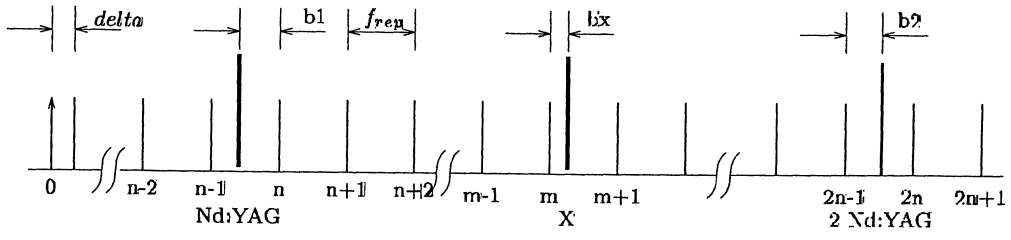

Figure 1: Representation of the beat-note used in the measurement

and with the the signal of the frequency standard to be measured is made collinear with the white light beam.

A 1200 grooves diffractive grating spatially separates the three CW beams, by keeping the superposition of each laser line with the surrounding lines of the comb. This guarantees that the signal of the comb's lines not contributing to the useful signal doesn't introduce additional shot noise in the three beat notes obtained by the three photodiodes. Considering that the jitter of the comb absolute position can be of a few MHz we have chosen of implementing the frequency arithmetics with an electronic box containing the necessary doubly balanced mixers, tunable filters and RF-amplifiers. This to avoid the conversion of noise that arose in synchronous frequency counting with dead time [5].

As an alternative to the first setup, we will test the self-referencing technique previously introduced by the JILA group [4]. This technique don't use auxiliary laser and probably gives better results in terms of signal to noise ratio. Let the frequency of the comb line n, which is on the red side of the spectrum have a frequency $f_n = nf_{rep} + \delta$. The comb line corresponding to 2n, which is in the blue side of the spectrum will have a frequency $f_{2n} = 2nf_{rep} + \delta$. We obtain δ by frequency doubling the n^{th} line and tacking the difference: $2f_n - f_{2n} = \delta$.

Instead of using this signal to lock the absolute position of the comb we will only use the information of the offset to evaluate the absolute frequency of the measured standard, given by the equation.

$$\nu_x = \delta + nf_{rep} + b_x$$

Where b_x is again the beat between the frequency standard to be measured and the upper nearest comb's line and n an integer. Also in this case the frequency of the standard must be known with an uncertainty lower than the half the spacing of the comb's lines.

References

[1] T. Udem, J. Reichert, T. W. Hänsch, and M. Kourogi, "Accuracy of optical frequency comb generators and optical frequency interval divider chains," *Optics Letters*, vol. 23, pp. 1387–1389, Sept. 1998.

[2] G. D. Rovera, G. Santarelli, and A. Clairon, "Frequency synthesis chain for the atomic fountain primary frequency standard," *IEEE Trans. Ultrason., Ferroelec., Freq. Contr.*, vol. 43, pp. 354–358, May 1996.

[3] T. A. Birks, J. C. Knight, and P. St. J. Russel, "Endlessy single-mode photonic crystal fiber," *Optics Letters*, vol. 22, no. 13, pp. 961–963, 1997.

[4] D. J. Jones, S. A. Diddams, J. K. Ranka, A. Stentz, R. S. Windeler, J. L. Hall, and S. T. Cundiff, "Carrier-envelope phase control of femtosecond mode-locked lasers and direct optical frequency synthesis," *Science*, pp. 635–639, April 28 2000.

[5] G. D. Rovera and O. Acef, "Optical frequency measurements relying on a mid infrared frequency standard," in *Frequency measurement and control* (A. Luiten, ed.), vol. 79 of *Topics in Applied Physics*, Springer-Verlag, 2000.

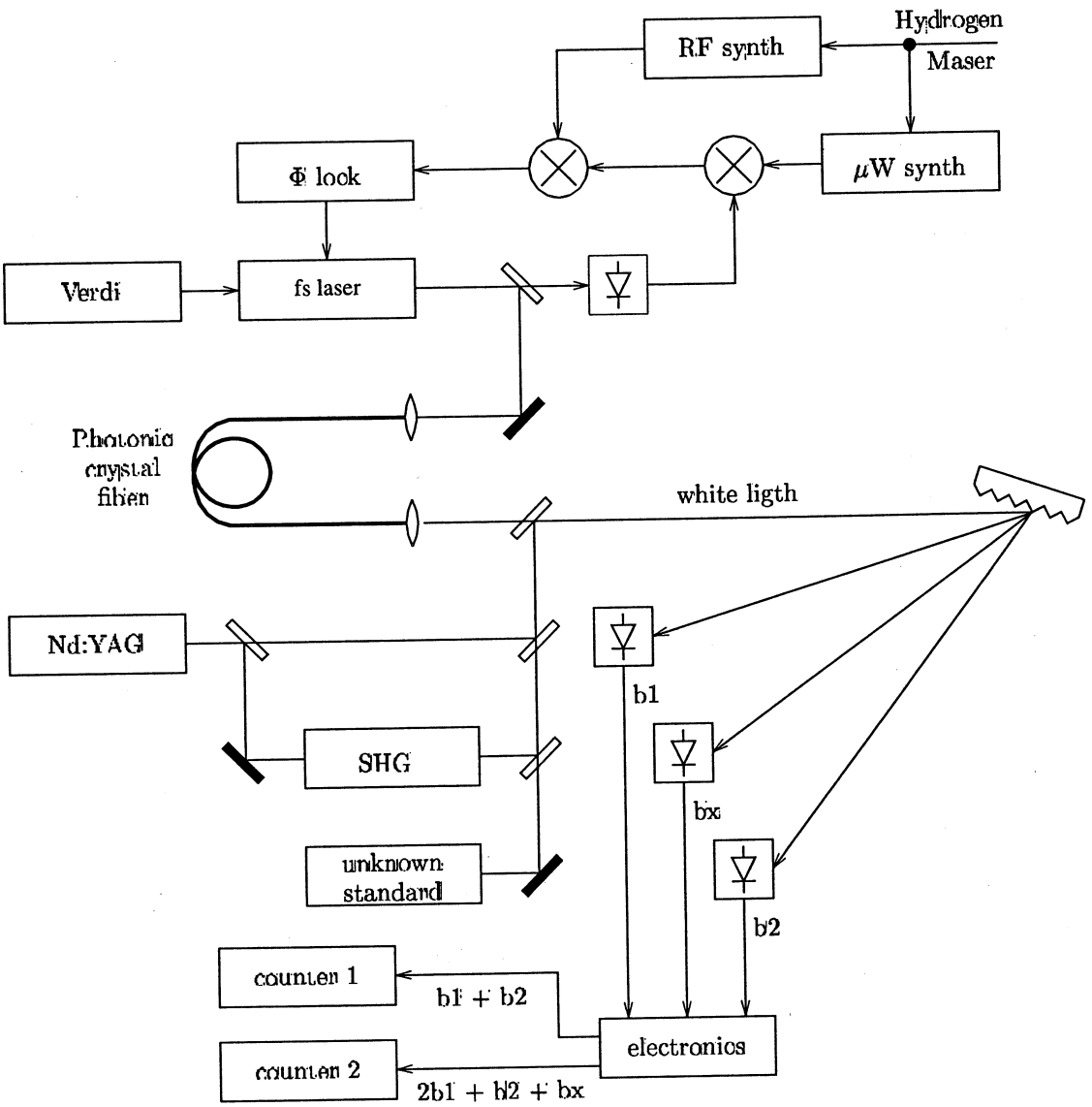

Figure 2: Simplified schematic of the first proposed setup

EFFECT OF SUB-DOPPLER GREEDY ABSORPTION IN Cs VAPOURS

Yu. S. Domnin, V.M.Tatarenkov, A.V.Novoselov and V.G.Pal'chikov

Institute of Metrology for Time and Space at National Research Institute for Physical-Technical and Radiotechnical Measurements, Mendeleevo, Moscow Region, 141570 Russia. Phone: 007095 5359151, Fax: 007095 5340609, E-mail: ydomnin@imvp.aspnet.ru,

ABSTRACT

The cesium D_2 resonance lines have been studied in saturated absorption for various intensities of the counter-propagating waves. Experiment was realized with two orthogonally polarized laser beams in the case of linear polarization. All principal and cross-over highly contrasting resonances are obtained for the $6s_{1/2}$ (F=3) - $6p_{3/2}$ (F'=2,3,4) transitions in Cs. Enhanced absorption for the transitions having common excited level (F'=2) is observed. Theoretical interpretation and some potential applications are given. We have calculated the positions and magnitudes for 6 principal and cross-over resonances. These theoretical results are compared with measurements. Preliminary results with transition (F=4)-(F'=5) are shown.

1. INTRODUCTION

Cs atom is used in a number of important applications in metrology including atomic clocks, laser cooling, parity violation experiments, the search for a permanent electron dipole moment, atom interferometry, etc. In particular, a saturation absorption spectroscopy with its recent developments Ref.1-2, is a powerful technique widely used in high resolution spectroscopy as well as in the laser frequency stabilization. A number of theoretical and experimental works on saturation absorption have been published at present time (see, for example Ref. 3-6).

In this work we studied the saturation absorption spectrum of the cesium D_2 lines in some details both experimentally and theoretically. We have investigated the sub-Doppler resonances of saturated absorption in the particular case of two counter-running coaxial laser beams with orthohonal linear polarizations. We analysed also, the influence of a power of laser radiation source on the magnitude of the principal and cross-over saturated sub-Doppler resonances , and found, that this quantity is a slowly varying function of the laser power.

The plan of this paper is as follows. In Section 2 we given a description of the experimental set-up used. Section 3 tabulates experimental results and compares part of them with the theoretical calculation.

2. EXPERIMENTAL SET-UP

The aim of the experimental setup was to find optimum conditions for having narrow and a powerful peak for laser frequency stabilization. We have done the preliminary experiments with a standard setup configuration. In this configuration the laser simulated the transitions in Cs atom from its ground state (F=3). The emission was passed through a cell and was reflected back by a mirror to a detector. It was noted that the most powerful absorption saturation peaks were observed when the saturating and probing laser beams had one and the same circular polarization. In case of opposite circular polarization for the transition (F=3)-(F'=2) we had the enhanced absorption instead of the saturated one. This phenomenon was firstly observed and analyzed in the works Ref.1-2. Apart this we observed the enhanced absorption for the transitions, having common excited state (F'=2). In particular, we investigated the peak behavior for mutually perpendicular linear polarization. For making more careful investigation the experimental setup was assembled as shown in fig.1.

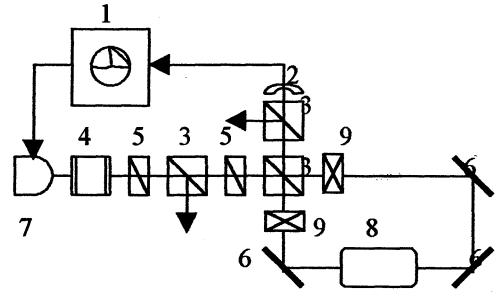

Fig 1.

1 – oscilloscope, 2 – photodiode, 3 – PBS,
4 –Faraday isolator, 5 – λ/2 plate, 6 –mirror,
7 – laser diode, 8 – Cs-cell, 9 - λ/4 plate

The idea of the experiment is as the following: The ramp voltage from an oscilloscope 1 is used to sweep the frequency of a laser diode 7. To prevent the feedback the laser emission is passed through the Faraday optical isolator 4. A first set of a half wave plate 5and PBS 3 is used to vary a total power, delivered to a Cs cell 8. The second set of the λ/2 and PBS is used to redistribute the power between saturating and a probing beams. And the third PBS is used to prevent passing the saturation beam on to a photodiode 2, while the probing beam is passed through it to the photodiode. The polarization of the both beams can be adjusted by the quarter wave plates.

The signal from the photodiode is synchronized and monitored by the oscilloscope.

To get one mode operation of the laser we used a feedback from an external grating. The grating was put on a PZT driver. A fast frequency modulation was performed through the laser diode current. It is used to have a first derivative from the signal. The laser beam diameter is about 2 mm.

The Cs sell has the length near 60 mm and the diameter near 40 mm. It was put into a permalloy screen to isolate it from the Earth magnetic field. We evaluated that the resulting magnetic field in the cell is a few tens times less than the Earth's.

3. RESULTS AND DISCUSSIONS

The first and the most important result is the following. For the transitions F3-F'2 and F3-F'2/F'3 for some beams polarization we observe not a saturation in absorption but in contrast enhanced or "greedy" absorption as shown in Fig 2.

The explanation of such behavior looks very simple in case of mutually perpendicular (opposite) circular polarization. While an atom is placed in a laser beam it scattered the photons manifold. The photons have a projection of own momentum m=1 to the axis of their propagation. But scattered photons have momentum m=1, m=0, and m=-1 That means, that atom in the process of interaction with the photons turns to go into the state with the highest momentum projection to the beam axis. In case of F3-F2' transition atom moves into position F3, m=3 (and m=2). But as soon as it reaches this state it stops interact with the beam according to the quantum selection rules. So atoms with m=-3, -2, etc. Move to m=3 and m=2 states. The atoms cannot scatter more light. If we pass the opposite beam with the same circular polarization it won't interact with the atoms. The result is the saturation. But if the opposite beam will have the opposite circular polarization it "sees" the atoms in the state m=-3 and m=-2 and interact with them intensively. The atoms move to the state m=3 for this beam, but for the opposite beam it will be again the state with m=-3, m=-2. So one beam prepare population for other and vice versa. The more power in one beam the faster population is prepared for another. As a result we have the 'greedy' absorption.

According to our experimental results we have also the greedy absorption in the mutually perpendicular linear polarised beams. It is evident that the explanation, presented above cannot be applied in this case. We cannot use the beam propagation direction as the quantum axis due to rotational symmetry. There is no rotational symmetry for linear per linear polarization.

In case of linear polarisation it looks like atom intencively interact with the photon if it has m=0 projection on to the plane of polarisation. After many scatterings the atom moves into the state with m=±3 projection on the polarisation plane. But again for opposite beam atom has the projection m=0 and interact intencively with the photons. We have the same situation as in the previous case. One beam prepares population for another and vice versa.

Fig. 2 shows a saturation spectrum of the cesium D_2 lines. The zero point of the frequency scale and of the saturation spectrum are arbitrary. In the present work a relatively simple theoretical model for the saturation absorption resonances can be given in the limiting case $I_s << Ip$, where I_s and Ip are intensities for the saturation and for the probe laser beams, respectively [3]. In the framework of this condition, the saturation spectrum can be expressed in the form of linear combination of the scalar (C_0), magnetic-dipole (C_1) and quadrupole scattering terms from Ref.3:

$$C_\kappa = 2\gamma G_\tau \sum_{m,n,m_1,n_1} (-1)^{F_m - F_{m_1}} \frac{N^{(n_1)}}{2F_{n_1}+1} |d_{mn}|^2$$

$$\times |d_{m_1 n_1}|^2 \begin{Bmatrix} 1 & 1 & \kappa \\ F_n & F_n & F_m \end{Bmatrix} \left[\delta_{nn_1} \begin{Bmatrix} 1 & 1 & \kappa \\ F_n & F_n & F_{m_1} \end{Bmatrix} \right.$$

$$+ (-1)^{F_{m_1}+F_{n_1}} (2J_1+1) |d_{mn_1}|^2 \begin{Bmatrix} F_{m_1} & F_{m_1} & \kappa \\ F_n & F_n & F_m \end{Bmatrix}$$

$$\left. \times \begin{Bmatrix} 1 & 1 & \kappa \\ F_{m_1} & F_{m_1} & F_n \end{Bmatrix} \right] \exp\left\{ -\pi^2 \left[\frac{(\nu_{mn} - \nu_{mn})}{k\nu_0} \right]^2 \right\}$$

$$\times \left[1 - i\frac{2\pi}{\gamma} \left(2\nu - \left| \nu_{mn} - \nu_{m_1 n_1} \right| \right) \right]^{-1},$$

where $\begin{Bmatrix} a & b & c \\ d & e & f \end{Bmatrix}$ is the 6-j Wigner symbol. Here numbers n,m correspond to the hyperfine sublevels of the ground states, n_1, m_1 - to the excited state. d_{mn} is normalized matrix element:

$$|d_{mn}|^2 = (2F_m+1)(2F_n+1) \begin{Bmatrix} J_1 & I_n & F_m \\ F_n & 1 & J_0 \end{Bmatrix}^2,$$

where J_1 and J_0 are the total angular momentum of the exited and the ground states, I_n in the nuclear spin. The constant γ is a radiation constant of excited states, G_τ is a saturation parameter. The quantity $2kv_0$ is the Doppler width of the line, and $N^{(n)}$ is

$$N^{(n)} = \frac{(2F_n+1)}{\sum_{n'} (2F_{n'}+1)}.$$

The magnitudes of saturation sub-Doppler resonances for the $6s_{1/2}$ (F=3) - $6p_{3/2}$ (F'=2,3,4) transitions in Cs are

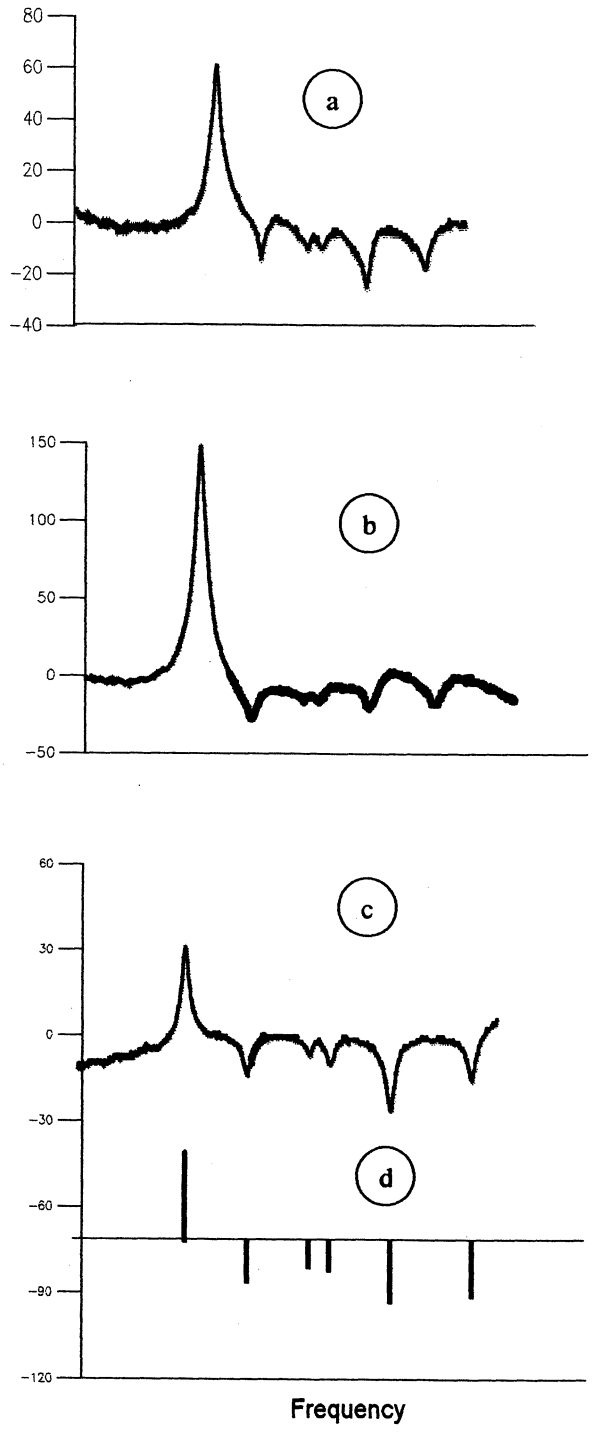

Fig.2
Saturation absorption resonances for the $6s_{1/2}$ (F=3) - $6p_{3/2}$ (F'=2,3,4) transitions in Cs with various I_s :

a – I_p=100 μW, I_s=600 μW
b – I_p=600 μW, I_s=1.2 mW
c – I_p=16 μW, I_s=160 μW
d – theory fort the case (c)

shown in Fig. 2 respectively with theoretically calculated data. Note, that these magnitudes correspond to the law

$$(Is + Ip)^{\alpha},$$

where $\alpha > 1$ in the general case Ref.3. The agreement between experimental results and calculated values is reasonably good. An alternative theoretical approach to saturation absorption signals has been proposed in Ref.5.

4. CONCLUSIONS

In the present experiments a laser saturation spectroscopy is applied to study of the principal and cross-over highly contrasting resonances for D_2 lines in cesium.

Measured data shown that:

- there is a inverse sharp-crested peak in the absorption spectrum at coincidence of the laser frequency with the frequency, which corresponds to the line $6s_{1/2}$ (F=3) - $6p_{3/2}$ (F'=2) in Cs;
- note, that such a peak observed cannot be considered as an saturation absorption peak because we have enhanced or greedy absorption ;
- the absorption peak contrast reaches about 50%;
- the absorption line width is a slowly varying function of the power laser radiation source
- observed effect ultimately limited within the absorption line widths (~ 5 MHz) and can be illustrated by its application to the frequency stability of the laser radiation source

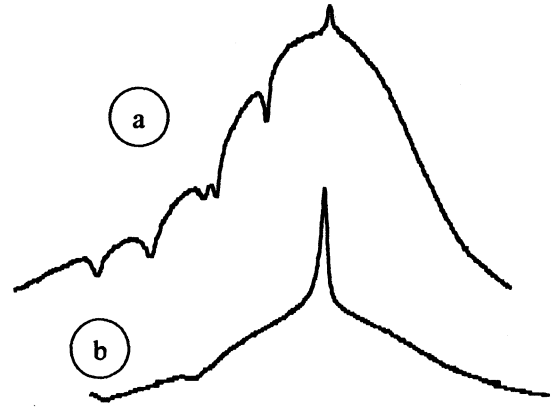

Fig. 3. Observed peaks for the $6s_{1/2}$ (F=4) - $6p_{3/2}$ (F'=3,4,5) in Cs; Peak $6s_{1/2}$ (F=4) - $6p_{3/2}$ (F'=5) with I_s = Ip =380 μW.

More detailed investigations with the present experimental technique can yield the corresponding

results for the other transitions in Cs atoms. For example, the intensive signals for $6s_{1/2}(F=4)$-$6p_{3/3}(F'=5)$ transition with an elliptically mixed polarization are shown in Fig.3 a, b.

The greedy absorption peak $6s_{1/2}(F=3)$-$6p_{3/3}(F'=2)$ looks very attractive for laser frequency stabilization due to its high contrast, good signal to noise ratio and low sensitivity to the power broadening.

The peak $6s_{1/2}(F=4)$-$6p_{3/3}(F'=5)$ is good enough for having short-term stability but it is fairly sensitive to the variations in polarization and magnetic field.

6. REFERENCES

[1] A. M. Akul'shin, V.L. Velichansky, R.G. Gamidov, A.Ch. Izmailov, V.V. Popovich and V.A. Sautenkov, Sov. Phys. JETP, Vol. 72, pp. 58-62, 1991.

[2] R. Gamidov, M.Cetintas, A.Ch. Izmailov, IEEE Transaction, pp.114-117, 1999.

[3] A. M. Akul'shin, V.L. Velichansky, M.V. Krasheninnikov, V.A. Sautenkov , V.S.Smirnov, A.M. Tumaikon and V. I. Yudin. Sov.Phys. JETP, Vol. 69, pp. 456-461, 1989.

[4] M.Himbert, S.Reynaud, J.Dupont-Roc and C. Cohen-Tannoudji, Optics Comm. Vol. 30, pp. 184-188, 1979.

[5] D.-Hai Yang, Yi-Q. Wang, Optics Comm. Vol. 74, pp. 54-58, 1989.

[6] S.G. Rautian and A.M.Shalagin, Kinetic Problems of Nonlinear Spectroscopy, Amsterdam: Elsevier, 1990

NEW CAVITIES FOR MINIATURE COLD ATOMS CLOCK

P.-E. Pottie, C. Valentin, P. Petit, and N. Dimarcq
Laboratoire de l'Horloge Atomique,
Laboratoire des repères spatiaux-temporels, UMR 8630 CNRS,
61, avenue de l'Observatoire,
75014 PARIS
E-mail: paul-eric.pottie@obspm.fr

Abstract— **This paper reports on the last development on HORACE, a very compact atomic clock using isotropic cooling light. Cooling, preparation, interrogation and detection of the clock signal take place inside the microwave cavity itself. New cavities with a capsule shape, that shall improve the isotropic laser field, were designed and successfully excited in a TE_{011}-like mode. Their linewidth is narrow since we measure Q in the 16.000-18.000 range. Since HORACE follows a temporal scheme, numerical simulation demonstrates that the performances of the clock may be improved playing with the time of interrogation of each Ramsey-pulse. It appears from results that multi-pulse interrogation scheme allows us to map the phase gradient of the microwave cavity *in situ*.**

I. Introduction

We aim at building a very compact atomic clock thanks to the use of the last techniques in laser cooling of neutral atoms. In order to satisfy our goal of compacity, we intend to cool the caesium atoms and to detect the clock signal inside the microwave cavity itself following a temporal scheme (HORACE project [1]). Isotropic cooling techniques must then be implemented [2]. The efficiency of such a method was first proved by Ketterle and al. [3], and was successfully implemented in several 3D-configurations at the Laboratoire de l'Horloge Atomique. Temperatures below 7 μK were reached in a square cylinder of polished copper fed in by $852 - nm$ laser light through multimode fibers. With this configuration, the maximum number of cold atoms measured in the Time Of Flight (TOF) signal is 3.7×10^7 and is reached when the detuning between the laser frequency and the atomic transition frequency is $\delta = -1.6\Gamma$, where Γ is the natural width of the atomic transition [4], [5]. Thus, with a resonator as small as a few ten millimeters (typically 43 mm for a TE_{011} square cylinder cavity), the expected stability for our atomic clock is evaluated to a few $10^{-13}\tau^{-1/2}$ [4].

Here we report on the last developments improving the performances of the future HORACE clock. The first part of our work was dedicated to improve the cold atom source for HORACE. A more accurate analysis tool has been built for a more precise knowledge of the temperature, the density, and the shape of the atomic cloud. Moreover we have designed new microwave cavity with a capsule shape. These cavities should improve the isotropy of the laser radiation inside the cavity. The second part of our work was dealing with the improvement of the interrogation scheme. Thanks to the temporal scheme of HORACE we can adjust the times of interrogation and the shape of the pulses. We studied in particular multi-pulses configuration since it will allow us to map the phase gradient of the microwave cavity set up in the clock.

II. Study and improvement of the cold atom source

A. *experimental set-up*

Caesium atoms have been cooled by isotropic cooling techniques for five years at the Laboratoire de l'Horloge Atomique [6]. Successful tests were essentially done with cylinders and spheres made of diffusive and reflective materials. However our previous apparatus offered only a single-TOF probe beam, and no image of the atomic cloud was available. Our set-up has then been modified to study more deeply the features of the cold atomic cloud. The main modification is the implementation of a pushing laser beam 6 centimeters below the center of the cavity, that allows us to slice the atomic cloud. By this way, we will be able to measure accurately the temperature and the density of the atomic cloud.

As several configurations (cylinder and sphere) had to be studied, we built multi-part cavities that can be placed around a quartz bulb, where caesium atoms are confined under ultra-vacuum. Thus ultra-vaccuum is not broken between two tests. The experimental results should be given this spring.

B. *capsule shape cavities*

In order to achieve the most isotropic laser radiation inside the microwave cavity, we designed new capsule-shape cavities. The first one is a capsule made up of a central cylindrical part and of two half-sphere parts. This is a non-concentric capsule. The second one is made up of a central cylindrical part and of two half-sphere parts, that are truncated so that the center of curvature of the two half-spheres are merged. Their size is 60 mm long for the non-concentric capsule, and 55 mm long for the concentric one. A resonnant TE_{011}-like mode close to the frequency of the hyperfine transition of the ground states of the caesium atom was observed by reflection in these two cavities (see figure 2 and figure 3). The coupling is done by means of a 1×9 mm rectangular slit. The tuning of the resonant frequency is achievable by playing with the length of the central cylindrical part of the cavity. The tuning is linear

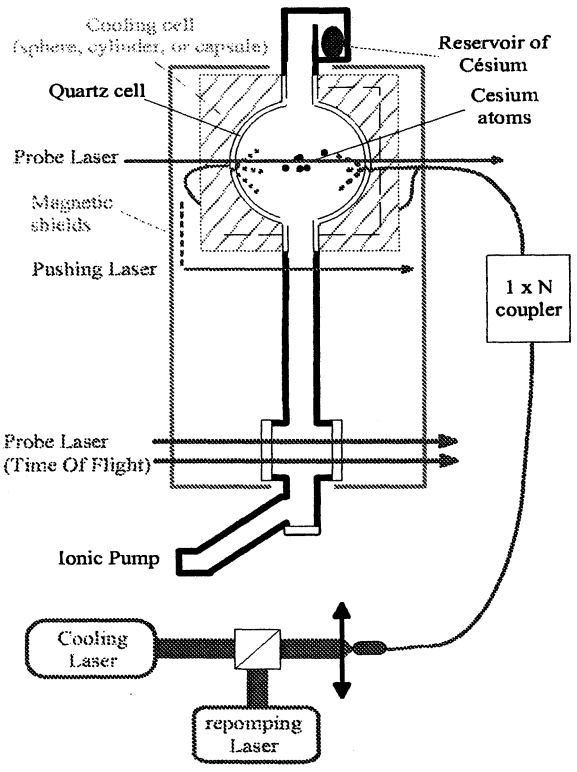

Fig. 1. *Scheme of the experiment.*

with a slope of 65.7 kHz/μm. The concentric capsule is 58 Mhz detuned below the hyperfine transition frequency of caesium. It has not been tuned closer because we were limited by the size of the coupling slit.

III. Improvement of the interrogation scheme

In order to estimate the frequency stability and the frequency accuracy of the clock, we have performed numerical simulations based on the calculation of the transition probability of an atom in interaction with a microwave magnetic field [8]. The evaluation of the first-order Doppler shift and the stability limitation by Dick effect for a Rabi-like and for a Ramsey-like interrogation was reported in [4], [6]. The first-order Doppler shift was evaluated as small as 1.0×10^{-15}. The frequency stability limited by Dick effect is $3 \times 10^{-13}\tau^{-1/2}$. These numerical calculations were also used for improving the accuracy and the stability of HORACE. We perform calculations for several interrogation schemes, playing with the time and the amplitude of each Ramsey-pulse, the shape of the pulses, and even the number of pulses.

A. *Improvement of the sensibility function*

Due to the acceleration of gravity, the atoms are falling down through the microwave cavity. The TE_{011} mode of the cavity is no longer seen as a sinusoid by the atoms falling along the z-axis (see figure 4). For long interrogation time, the velocity of the atom increase strongly between the

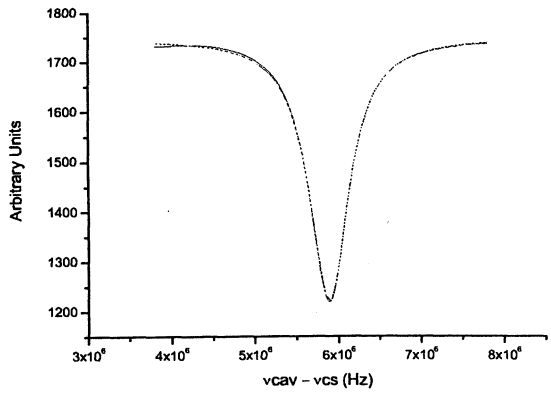

Fig. 2. *resonant curve of the microwave field for the non-concentric capsule shape cavity. The measurements give Q=16270 and the resonant frequency* $\nu_{cav} = \nu_{Cs} + 5.8$ *MHz.*

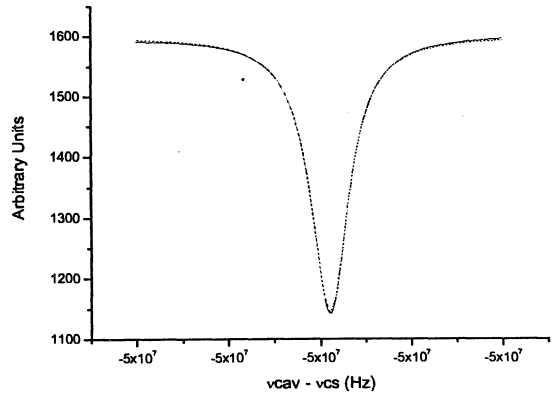

Fig. 3. *resonant curve of the microwave field for the concentric capsule shape cavity. The measurements give Q=18594 and the resonant frequency* $\nu_{cav} = \nu_{Cs} - 52$ *MHz.*

two Ramsey-pulses. when an atom interact with the two Ramsey-pulses of two strongly different velocities. The calculus shows thus that the sensibility function is degraded. For interrogation time longer than 30 ms, we observed that the contrast of the Ramsey-fringes decreases.

As HORACE is operated with a temporal sequence we can vary the interaction durations τ_1 and τ_2 and the dead time T in the interrogation sequence. We can thus counterbalance the two interactions by setting the second pulse longer than the first one. The best contrast obtained is for $\tau_1 = 3$ ms, $\tau_2 = 7$ ms, and $T = 50$ ms. The sensibility function increases and the contrast is close to one. Moreover, we can also play with the amplitude of each pulse. We obtain the best result for the second pulse 2.467 times more powerful than the first one. The sensibility function is optimized and the contrast of the Ramsey fringe is one. It appears from the figure 5 that the best result is for an amplitude correction.

The pulse shape affects also the performances of the

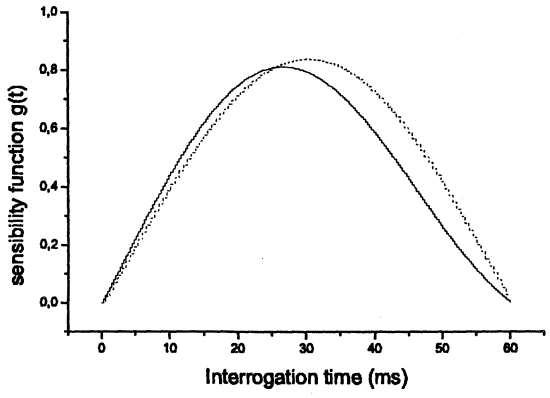

Fig. 4. *Sensibility function calculated for an atom accelerated or not in the gravity field that undergoes a sinusoidal amplitude field along the vertical axis. The dot line is for the non-accelerated atom, and the plain line for the accelerated one.*

HORACE clock. We compute the width of the central fringe, the residual first-order Doppler shift and the frequency stability for several pulse shapes: uniform, triangle, sinus, gaussian, exponential, Blackman, and Hamming shape. The numerical simulations performed demonstrate that, as expected, the narrowest linewidth is obtained for a uniform shape pulse. Regarding to the relative frequency shift due to residual first-order Doppler shift, we find that the frequency shift is the same whatever the pulse shape is in the case of a Ramsey-like interrogation. Only in the case of a Rabi-like interrogation, the frequency shift is minimized by a gaussian shape.

The limitation of the frequency stability of the clock by Dick effect [7] is weakly affected by the shape of the pulse and decreases with the increasing duty cycle. For a Ramsey-like interrogation, the effect is negligible for duty cycles greater than 0.3. On the contrary, in the case of a Rabi-like interrogation, we point out a 2.6 maximum factor between the frequency stabilities calculated for a uniform shape and the one calculated for a gaussian shape.

B. *multi-pulse running*

In addition we studied multi-pulse interrogation schemes. We were particularly interested in a three-pulses scheme. When we set the three pulse durations equal, and the two dead times equal (see figure 6), the residual first-order Doppler shift is the same for the Ramsey-like and for the three-pulse interrogations. If the second dead time is twice longer than the first one, then the sensibility function is modified and the first-order Doppler shift increases (see figure 7). By this way, playing with the dead-time and the interrogation duration, we will be able to map the phase gradient of the clock cavity.

IV. Conclusion

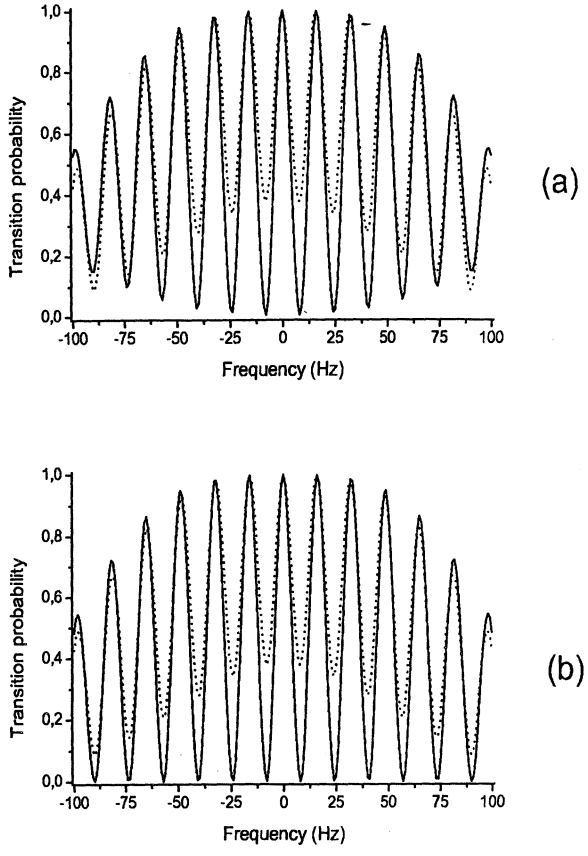

Fig. 5. *Calculated fringes for HORACE. The dot line is for a regular Ramsey-like interrogation. The plain line is for the corrected Ramsey-like interrogation. Figure a: amplitude correction* $\tau_1 = \tau_2 = 5.5$ *ms and* $T = 55$ *ms,* $b_{opt} = 286$ $rad.s^{-1}$. *Figure b: Time correction* $\tau_1 = 3.5ms$, $\tau_2 = 7.5ms$, $T = 55ms$, $b_{opt} = 405$ $rad.s^{-1}$

In order to fulfill the complete evaluation of the HORACE clock, our set-up has been modified. The gain will be more precise measurements related to the temperature, the number of atoms, the shape of the atomic cloud and its homogeneity. New capsule cavities have been designed. A resonant TE_{011}-like mode close to the frequency of the hyperfine transition of the ground states of the caesium atom was observed in these two capsule-shape cavities. A modelisation of the amplitude and phase of these capsules should be achieved very soon. We then will be able to calculate the phase gradient inside these cavities and the related shift. Numerical calculations have been done for several interrogation schemes to improve the accuracy and the stability of HORACE. A Ramsey-like interrogation with two uniform pulses and with two pulses of different times seems to be the best choice. In addition, it appears that multi-pulses interrogation schemes will allow us to map the phase gradient inside the microwave cavity.

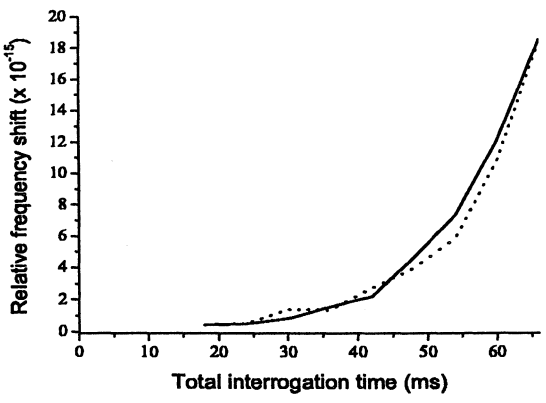

Fig. 6. *Calculated residual first-order Doppler shift for a Ramsey-like interrogation and for a three-pulses interrogation. The plain line is for the three-pulses interrogation, where* $\tau_1 = \tau_2 = \tau_2 = 2.8$ *ms and* $T_1 = T_2 = 28$ *ms. The dot line is for the Ramsey-like interrogation, where* $\tau_1 = \tau_2 = 5.5$ *ms and* $T = 55$ *ms.*

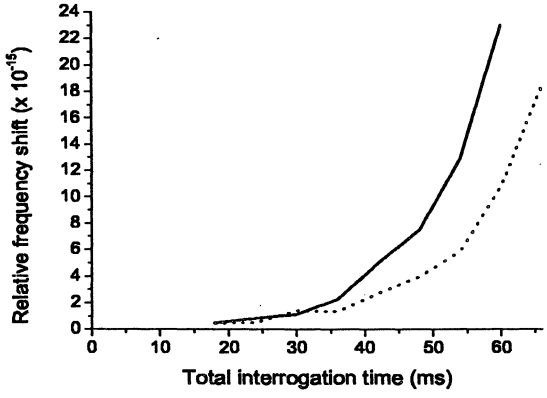

Fig. 7. *Calculated residual first-order Doppler shift for a Ramsey-like interrogation and for a Three-pulses interrogation. The plain line is for the three-pulses interrogation, where* $\tau_1 = \tau_2 = \tau_2 = 2.8$ *ms and* $T_1 = 19$ *ms and* $T_2 = 38$ *ms. The dot line is for the Ramsey-like interrogation, where* $\tau_1 = \tau_2 = 5.5$ *ms and* $T = 55$ *ms.*

ACKNOWLEDGEMENTS

The authors gratefully acknowledge CNES (Centre National d'Etudes Spatiales) and DGA (Délégation Générale pour l'Armement) that support this work. We are very grateful to Daniel Guitard for his technical support.

REFERENCES

[1] E. Guillot, P. Petit, C. Valentin, and N. Dimarcq, *HORACE: a new advance for compact clocks with cold atoms*, in Proc. of 12^{th} European Frequency and Time Forum, Warsaw, Poland, 1998.

[2] E. Guillot, P.-E. Pottie, C. Valentin, P. Petit, and N. Dimarcq, *HORACE : Atomic clock with cooled atoms in a cell*, in Proc. of 13^{th} Joint Meeting EFTF - IEEE IFCS, Besançon, France, pp 81-84, 1999.

[3] W. Ketterle, A. Martin, M. Joffe, and D. Pritchard, *Slowing and cooling of atoms in isotropic light*, in Physical Review Letter, 69 (17), 2483-2486, October 1992.

[4] C. Valentin, Ch. Guillemot, E. Guillot, P.-E. Pottie, E. Fretel, P. Petit, and N. Dimarcq, *Isotropic cooling of cesium atoms for a compact atomic clock: first results and expected performances*, in Proc. of 14^{th} European Frequency and Time Forum, Torino, Italia, pp 489-493, 2000.

[5] E. Guillot, P.-E. Pottie, and N. Dimarcq, *3D-cooling of cesium atoms in a reflecting copper cylinder*, submitted.

[6] Emmanuel Guillot, *Nouveau concept d'horloge atomique : HORACE, HOrloge à Refroidissement d'Atomes en CEllule*, Thesis from the Université Paris-Sud, Orsay, 2000.

[7] Giorgio Santarelli, Claude Audoin, Ala'a Makdissi, Philippe Laurent, G. John Dick, and André Clairon, *Frequency stability degradation of an oscillator slaved to a periodically interrogated atomic resonator*, IEEE Trans. Ultra., Ferro. and Freq. Control, vol. 45, pp 887-894, 1998.

[8] C. Valentin, N. Dimarcq, E. Fretel, G. Dudle, A. Joyet, and P. Thomann *Numerical simulations of atomic behaviour for several configurations of cold cesium atomic clocks*, in Proc. of 13^{th} Joint Meeting EFTF - IEEE IFCS, Besançon, France, pp 100-103, 1999.

CPT MICROWAVE FREQUENCY STANDARDS: THE ROLE OF THE ELECTRAMAGNETICALLY INDUCED TRANSPARENCY

F. Levi[1], A. Godone[1], S. Micalizio[2], J. Vanier[3]
[1]IEN G. Ferraris, Torino, Italy
[2]Politecnico di Torino, Torino, Italy
[3]Université de Montreal, Montreal, Canada

1 ABSTRACT

In this work, we report a theoretical and experimental analysis of some phenomena observed in an optically thick atomic ensemble of ^{87}Rb prepared in a CPT (Coherent Population Trapping) state in buffer gas. In particular, for an increase of the atomic density, it is possible to show that the dark line may look inverted appearing as a bright line, while in the transmission signal a narrowing of the resonance line width is observed. A significant time group delay has also been measured.
These effects are related to the Electromagnetically Induced Transparency (EIT) phenomenon. The experimental results here reported are in excellent agreement with the theory developed.

Keywords: CPT, EIT, inverted dark line, subnatural line width, group delay.

2 INTRODUCTION

Recently a particular attention has been devoted to quantum coherence and interference phenomena. These studies have led to the observation of new effects and to the development of new techniques in quantum optics, such as lasing without inversion, laser cooling, refractive index enhancement and non absorption dark resonances. In particular, dark resonances are observed when two laser radiation fields are applied to a three level atomic system in a Λ excitation scheme. When the frequency difference of the two radiation fields is equal to the hyperfine splitting of the ground state levels, an interference quantum phenomenon occurs and the atoms are driven in a non absorbing coherent state (Coherent Population Trapping) [1, 2]. Then, a dark line appears in the fluorescence spectrum. Moreover, the same CPT phenomenon creates a strong coherence in the atom ground state and a coherent microwave emission is readily observed when the atomic ensemble is placed in a microwave cavity tuned to the ground state hyperfine frequency. It is well known that both these phenomena, dark resonances and CPT microwave emission, may be used in the practical implementation of a highly stable atomic frequency reference [3, 4]. This paper will be essentially devoted to the analysis of some phenomena observed in optically thick atomic vapors with buffer gas which may be of particular importance in the implementation of a frequency standard. Due to the Electromagnetically Induced Transparency effect in the optical domain, inverted dark lines in the fluorescence spectrum and line width narrowing versus atomic density are predicted in the case of optically thick samples. The experimental results obtained with ^{87}Rb or ^{133}Cs are in good agreement with the theoretical predictions.
Recently it has been pointed out that due to extremely efficient non linear interactions taking place in an EIT medium, it is possible to measure very large group delays for laser fields propagating in the medium [14, 15]. We observed analogous time delay phenomena in CPT maser emission signal.
The impact of these new effects on the practical realization of atomic frequency references is also discussed.

3 THEORY

A detailed analisys of CPT and EIT phenomena and their applications in the atomic frequency standards field can be found in many papers [5-11] . We will only remind here the main results useful for our discussion.
The dynamical evolution of a three-level atomic system submitted to a Λ excitation scheme is described by the Liouville's equation for the density matrix $\hat{\rho}$:

$$\frac{\partial \hat{\rho}}{\partial t} = \frac{1}{i\hbar}[\hat{H}, \hat{\rho}] \qquad (1)$$

where $\hat{H}$ is the interaction Hamiltonian.

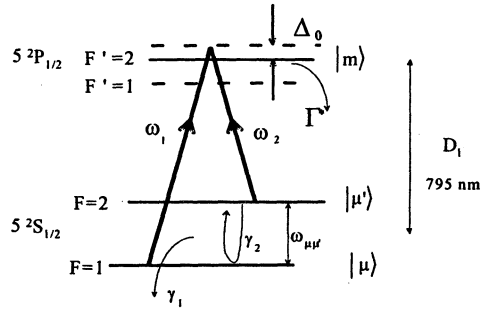

Fig. 1 Energy levels in ^{87}Rb.

In the Fig. 1 the decay rate of the excited state Γ^* takes into account the spontaneous emission and the collisions between the buffer gas and the alkali metal atoms. When N_2 is used as buffer gas the emission profile line width is reduced by Dicke effect and radiation trapping effects are avoided. The relaxation rates γ_1 and γ_2 of the ground state hyperfine levels population difference and coherence take into account spin exchange and buffer gas collisions. Δ_0 is the laser detuning from the optical resonance.
An applied static magnetic field $\vec{B}_0$ provides a quantization axis and resolves the Zeeman levels in the ground state.
We consider two laser beams collinear and we suppose that the laser polarization remains unchanged while the laser is moving into the atomic medium. In order to describe the laser fields propagation, we consider the Maxwell's equations in the slowly varying approximation for amplitudes and phases; we write the fields in the form:

$$E_j(z,t) = \frac{1}{2}\mathcal{E}_j(z,t)e^{i[\omega_j t - k_j z + \phi_j(z,t)]} + c.c. \quad (j=1,2) \qquad (2)$$

where ω_j and k_j are the angular frequency and the wavevectors of the laser fields respectively; $\mathcal{E}_j(z, t)$ and $\phi_j(z, t)$ are slowly-variable functions of z and t.
The electric-dipole interaction of the laser radiation fields with the atomic ensemble is described by [12]:

$$\frac{\partial^2 E_j(z,t)}{\partial z^2} - \frac{1}{c^2}\frac{\partial^2 E_j(z,t)}{\partial t^2} = \mu_0 \frac{\partial^2 P_j(z,t)}{\partial t^2} \qquad (3)$$

which is derived from Maxwell's equations for a homogeneous and isotropic medium. On the other hand, analyzing the atomic system in the ensemble-averaged density matrix formalism [12], the polarization $P_j(z, t)$ in (3) may be expressed as:

$$P_j(z, t) = n\, Tr\left(\hat{\rho}\, \hat{P}_j\right) \qquad (4)$$

where n is the atomic density and $\hat{P}_j$ the polarization quantum operator.
Assuming a linear response of the atomic vapor, and elaborating the previous relations we obtain the following system of first order partial differential equations:

$$\begin{cases} \dfrac{\partial \rho_{mm}}{\partial t} + \Gamma^* \rho_{mm} = \dfrac{\omega_{R1}^2 + \omega_{R2}^2 - (\omega_{R1}^2 - \omega_{R2}^2)\Delta + 4\omega_{R1}\omega_{R2}\,\mathrm{Re}\,\delta_{\mu\mu'}}{2\Gamma^*} \\ \dfrac{\partial \Delta}{\partial t} + \left(\gamma_1 + \dfrac{\omega_{R1}^2 + \omega_{R2}^2}{2\Gamma^*}\right)\Delta = \dfrac{\omega_{R1}^2 - \omega_{R2}^2}{2\Gamma^*} \\ \dfrac{\partial \delta_{\mu\mu'}}{\partial t} + \left[\gamma_2 + \dfrac{\omega_{R1}^2 + \omega_{R2}^2}{2\Gamma^*} + i\left(\Omega_\mu + \dfrac{\partial(\phi_1 - \phi_2)}{\partial t}\right)\right]\delta_{\mu\mu'} = -\dfrac{\omega_{R1}\omega_{R2}}{2\Gamma^*} \\ \dfrac{\partial \omega_{R1}}{\partial z} + \dfrac{1}{c}\dfrac{\partial \omega_{R1}}{\partial t} = -\dfrac{\alpha}{2\Gamma^*}\left[\omega_{R1}(1-\Delta) + 2\omega_{R2}\,\mathrm{Re}\,\delta_{\mu\mu'}\right] \\ \dfrac{\partial \omega_{R2}}{\partial z} + \dfrac{1}{c}\dfrac{\partial \omega_{R2}}{\partial t} = -\dfrac{\alpha}{2\Gamma^*}\left[\omega_{R2}(1+\Delta) + 2\omega_{R1}\,\mathrm{Re}\,\delta_{\mu\mu'}\right] \\ \dfrac{\partial(\phi_1 - \phi_2)}{\partial z} + \dfrac{1}{c}\dfrac{\partial(\phi_1 - \phi_2)}{\partial t} = -\dfrac{\alpha}{\Gamma^*}\left(\dfrac{\omega_{R2}}{\omega_{R1}} + \dfrac{\omega_{R1}}{\omega_{R2}}\right)\mathrm{Im}\,\delta_{\mu\mu'} \end{cases} \qquad (5)$$

where we have introduced the Rabi angular frequencies:

$$\begin{cases} \omega_{R1} = \mathcal{E}_1 \langle \mu | e\, \hat{r}\cdot\hat{e}_\lambda | m \rangle / \hbar \\ \omega_{R2} = \mathcal{E}_2 \langle \mu' | e\, \hat{r}\cdot\hat{e}_\lambda | m \rangle / \hbar \end{cases} \qquad (6)$$

and the density parameter:

$$\alpha = \frac{\omega_1 \langle \mu | e\, \hat{r}\cdot\hat{e}_\lambda | m \rangle^2}{\varepsilon_0 \hbar c} n \qquad (7)$$

Besides, $\Delta = \rho_{\mu'\mu'} - \rho_{\mu\mu}$ is the population difference of the ground state hyperfine levels, $\Omega_\mu = (\omega_1 - \omega_2) - \omega_{\mu'\mu} \ll \Gamma^*$ is the "microwave detuning", that is the detuning of the difference between the two beams angular frequency and the ground state hyperfine angular frequency.
To obtain system (5), we made the adiabatic approximation for optical coherences and we considered $\omega_{Rj} \ll \Gamma^*$, $\forall$ z, t (j=1, 2), i.e. the population of the excited state is small in comparison to that of the ground state. All the hypotheses done in developing the theory are widely satisfied in the usual frequency standard applications.

The set of equations (5) describes well an optically thick atomic sample under optical excitation in a Λ scheme and it contains all the physical behaviors exposed in the following sections.

4 INVERTED DARK LINE AND LINE WIDTH REDUCTION

In this section we consider the steady-state solution ($\partial/\partial t \to 0$) of system (5); then we take into account only the spatial dependence of density matrix elements and of Rabi frequencies.
Numerical results of the steady-state set of equations (5) are shown in Fig. 2a and in Fig. 2b. Fig.2a represents the fluorescence intensity emitted by the atomic system, proportional to ρ_{mm}, while Fig. 2b represents the intensity of the light transmitted through the cell, proportional to ω_R^2; the numerical values of the parameters correspond to typical experimental conditions.

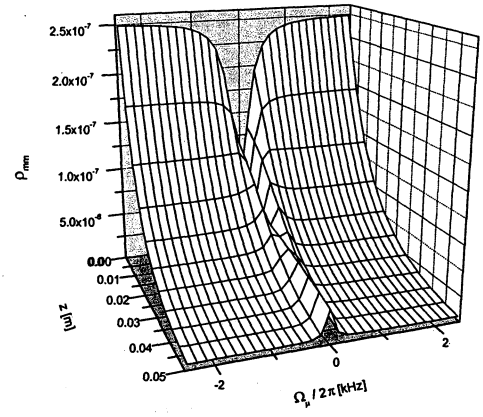

(a)

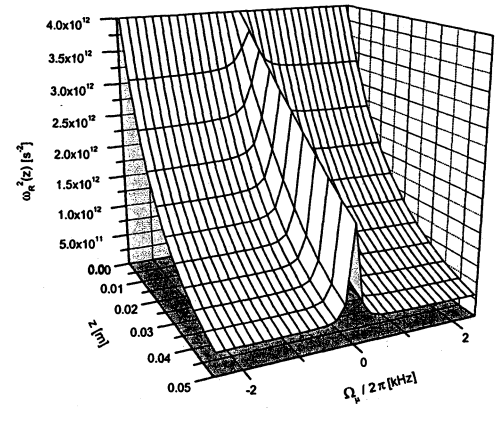

(b)

Fig. 2. 3D representation (a) of ρ_{mm} (z) (fluorescence) and (b) of $\omega_R^2(z)$ (transmission) as a function of distance within the cell versus the microwave detuning $\Omega_\mu/2\pi$, for $\Gamma = 4\text{x}10^9$ s^{-1}, $\gamma_2 = 350$ s^{-1}, $\alpha = 3\text{x}10^{11}$ m^{-1}s^{-1}, $\omega_R(0) = 2\text{x}10^6$ s^{-1}. In all calculations we assumed for the electric-dipole moment a value of $2\text{x}10^{-29}$ C/m.

These 3D behaviors make evident that at high densities, after a few *cm* of propagation in the atomic vapor, the fluorescence on resonance appears larger than the fluorescence off resonance. The dark line appears to be inverted looking like a

bright line. This effect may be understood taking into account that outside resonance the laser fields follow the classical Bouguer-Lambert-Beer attenuation law (exponential), while near resonance the attenuation law is linear due to EIT. The inverted dark line predicted in our computations is then an EIT effect which may be observed in the fluorescence spectrum. On the other hand, the atomic system is in a non absorbing state due to the coherent population trapping and the transmission is then always maximum at exact resonance ($\Omega_\mu = 0$). The EIT effect is evident on the transmission signal with a resonance profile line width reduction and with an increment of the signal to background ratio. The experimental results reported in the following figures are in very good agreement with the previous analysis. The experiments have been made at 30 °C and 50 °C. With the total buffer gas pressure [16] of 25 Torr, we have $\Gamma^* \approx 4\text{x}10^9\ s^{-1}$, $\gamma_1 \approx \gamma_2$, $\gamma_2 \approx 280\ s^{-1}$ at 30 °C and $\gamma_2 \approx 350\ s^{-1}$ at 50 °C; the pumping rate $\omega_R^2(z=0)/\Gamma^*$ is of the order of $2000\ s^{-1}$.

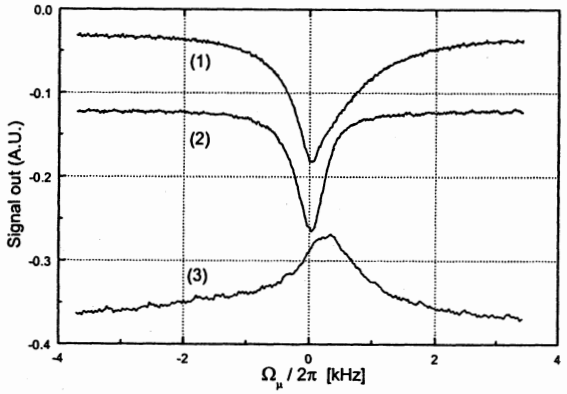

(a)

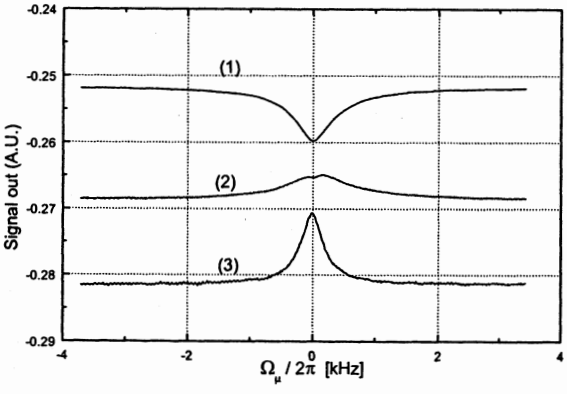

(b)

Fig. 3. Experimental behaviors of fluorescence and transmission signals for a pumping rate of 2000 s^{-1}; (a) 30°C and (b) 50°C. (1) fluorescence at L = 0.5 *cm*; (2) fluorescence at L = 5 *cm*; transmission signal at L= 5 *cm*.

Moreover, our calculations show that, in a pure three-level atomic system, this line width reduction can achieve "sub-natural" level when the atomic density is increased above a certain value, as demonstrated in Fig. 4 where we have also reported the ground state relaxation rate of Rb atoms in buffer gas [16].

The corresponding high Q factor, together with a high signal to background ratio, could be of great interest for atomic frequency standard applications. In particular, it should be possible to achieve the shot noise limit, leading to a high short term frequency stability. At a temperature of 60°C, with a Q of the order of 10^8 and with a number of atoms of $N_a \approx 9\text{x}10^{12}$, we obtain the following estimate for the Allan's variance:

$$\sigma_y(\tau) \approx \frac{1}{Q\left(\frac{S}{N}\right)_{1Hz}} \approx 1\cdot 10^{-14}\,\tau^{-1/2} \qquad (8)$$

where the signal to noise ratio (S/N) in the shot noise limit is:

$$\left(\frac{S}{N}\right)_{1Hz} \approx \sqrt{N_a} \qquad (9)$$

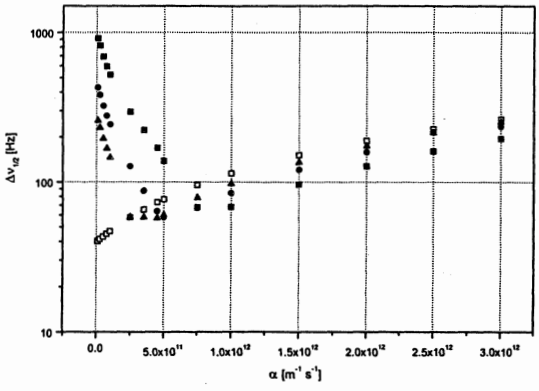

Fig. 4. Full width at half maximum of the light transmitted profile and ground state relaxation rate versus the atomic density represented by α: ■ $\omega_R(0) = 3\text{x}10^6\ s^{-1}$; ● $\omega_R(0) = 2\text{x}10^6\ s^{-1}$; ▲ $\omega_R(0) = 1.5\text{x}10^6\ s^{-1}$; □ γ_2/π.

However, our real atomic ensemble is not a pure three-level system but shows a Zeeman structure resolved by an applied static magnetic field. We take into account that the atoms involved in the EIT phenomenon are those in $m_F = 0$-$m_F = 0$, that is about ¼ of the total atoms in the ground state for ^{87}Rb; we solved the system (5) introducing a density parameter $\alpha' = \alpha/4$ for the ground state atoms really excited by the coherent process. Figure 5 shows that even if the linewidth is greatly reduced, it stays always above the transmission profile natural line width.

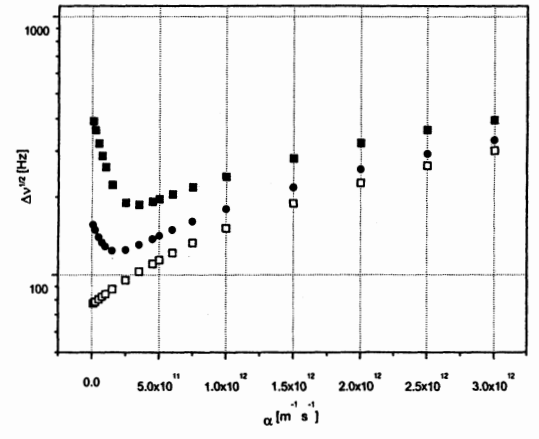

Fig. 5. . Same as Fig. 3 but now taking into account the real number of atoms in the ground state involving in the EIT process, as explained in the text:■ $\omega_R(0) = 2\text{x}10^6\ s^{-1}$;● $\omega_R(0) = 1\text{x}10^6\ s^{-1}$; □ γ_2/π.

We have also measured the linewidth reduction in ^{87}Rb as atomic density function; the results, shown in Fig. 6, are in good quantitative agreement with theoretical prediction of Fig. 5. This phenomenon is very important in the realization of a frequency standard because allows to work at higher signal with a narrower line.

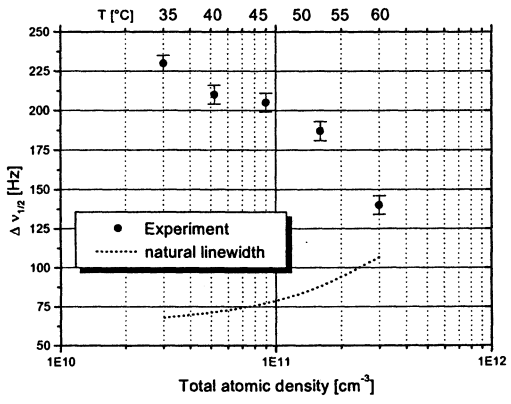

Fig.6. Experimental measurements of the line width reduction in ^{87}Rb versus atomic density. The natural line width is also drawn; $\omega_R(0)$ is of the order of $1.5x10^6$ s^{-1}.

6 GROUP DELAY MEASUREMENTS

It is well know that in a coherently driven hot atomic vapor, very large group delays of light (low group velocity) can be observed [14, 15]. In particular, it is possible to measure a time delay of the information carried by the light; this information may be represented, for example, by an amplitude or phase modulation. We observed this effect in the dark line transmission signal, but here we report measurements of this remarkable phenomenon for CPT microwave emission output. The experimental set-up is illustrated in Fig. 7.

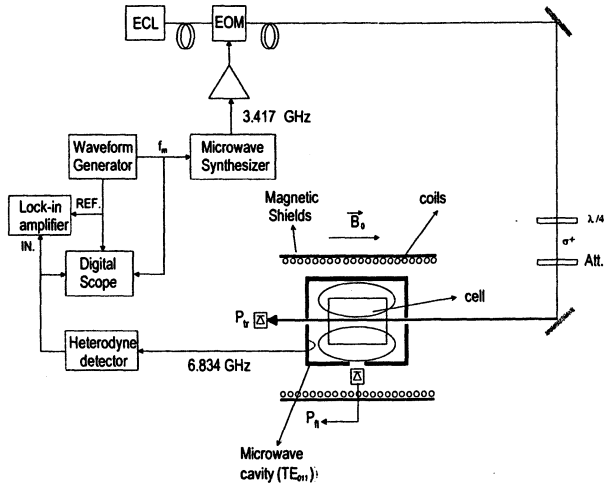

Fig. 7 Schematic of our experimental set-up for group delay measurment.

A laser field tuned to the D_1 line of ^{87}Rb is modulated by an EOM at one half of the hyperfine frequency transition. The two first sidebands created in this way are in resonance with the two optical transitions and generate the coherence in the ground state. Moreover, in order to study time group delay phenomena, the two first sidebands are also amplitude modulated. The laser beam, circularly polarized, is then sent to the physical package constituted by a quartz cell containing the rubidium vapor and a mixture of buffer gas; the cell is placed in a microwave cavity tuned at 6.8 GHz resonating on the TE_{011} mode. The CPT maser emission is detected by means of a heterodyne receiver.

We measured the time delay between the input laser amplitude modulation signal and the CPT maser signal. In particular, the lock-in amplifier measures the phase difference between the two signals, as illustrated in figure 7. We also investigated a possible presence of unwanted phase shifts in our experimental set-up: we found that the time delay introduced by the electronic servo system is < 50 μs.

We made measurements varying modulation frequency from 5 Hz to about 200 Hz. A typical measure for a fixed frequency modulation f_m is represented in Fig. 8.

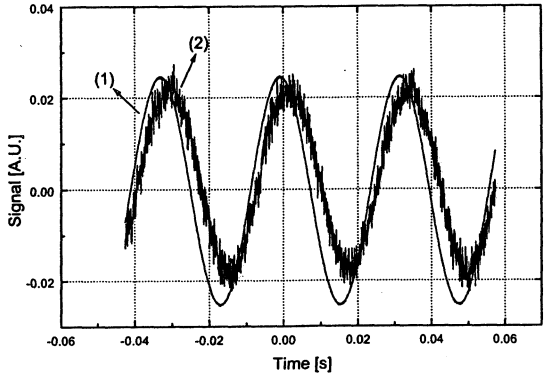

Fig. 8. Time delay measurement between laser input signal (1) and CPT maser signal (2). f_m = 31 Hz. T= 69°C, $\Gamma^* \approx 4x10^9$ s^{-1}, $\gamma_2 \approx 500$ s^{-1}, $\omega_{R1}(0) = \omega_{R2}(0) = \omega_R(0) \approx 1x10^6$ s^{-1}, $\alpha \approx 1.2x10^{12}$ m^{-1} s^{-1}, L = 4 cm. Time delay $\tau \approx 2.5$ ms.

There is a range of frequencies modulation where this group delay is nearly constant. In this range the values measured are of the order of 2.5 ms, that is the information carried by the light propagates at a group velocity of about 20 m/s. Figure 9 shows that these results are in very good agreement with our theoretical computations made for values of the parameters similar to the experimental ones.

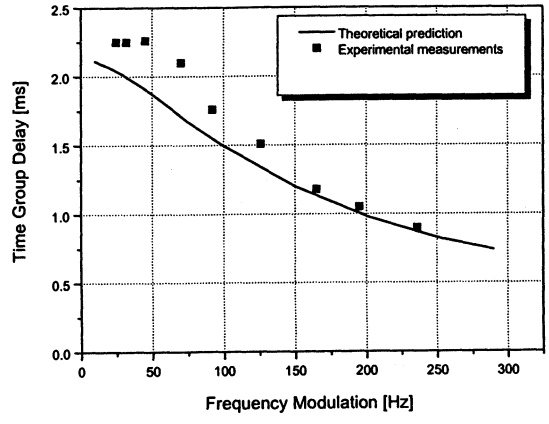

Fig. 9 Theoretical and observed group delay in CPT maser as a function of the frequency modulation. T = 69°C, $\Gamma^* \approx 4x10^9 s^{-1}$, $\gamma_2 \approx 500$ s^{-1}, $\omega_{R1}(0) = \omega_{R2}(0) = 1x10^6$ s^{-1}, $\alpha \approx 1.2x10^{12}$ m^{-1} s^{-1}. L = 4 *cm*.

We made also a theoretical comparison between the dark line transmission signal and the CPT maser signal as a laser power function. At low laser power, the group delay is higher in the CPT maser which contains only the information about the coherence excited by the CPT phenomenon.

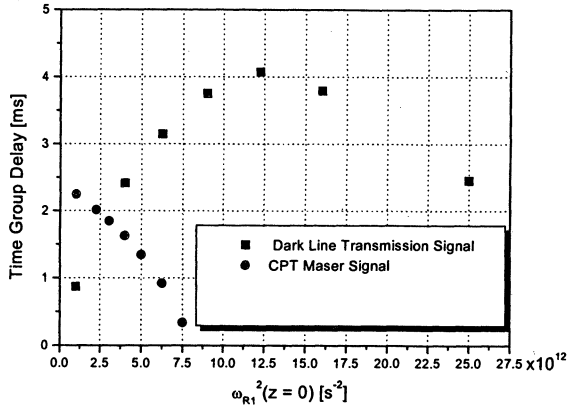

Fig.10. Time group delay for dark line and CPT maser.
$\alpha \approx 5x10^{11} m^{-1}s^{-1}$, $\Gamma' \approx 3x10^9 s^{-1}$, $\gamma_2 \approx 400 s^{-1}$, $\omega_{R1}(0) = \omega_{R2}(0) = 1x10^6 s^{-1}$
L = 5 *cm*.

7 CONCLUSIONS

In this paper we analyzed some phenomena observed in optically thick atomic vapors prepared in a CPT state of ^{87}Rb in buffer gas. In particular, we discussed three main points:
1) when the atomic density is increased, the dark line may look inverted appearing as a bright line;
2) in the transmission signal a narrowing of the resonance line width is observed. In a pure three levels system, this line width reduction achieves sub natural levels when the atomic density is increased above a certain value;
3) we measured time delay in CPT maser emission signal of the order of milliseconds. It means that, in a coherently driven hot atomic vapor, the information carried by light propagates in the medium at very low group velocity. This may have a consequence in the implementation of an atomic frequency standard, because the time group delay phenomenon can affect the bandwidth of the frequency control servo-system.
Then, besides being very interesting from a physical point of view, all these effects related to EIT may play a very important role in the atomic frequency standard field.

8 REFERENCES

[1]. G. Alzetta, A. Gozzini, L. Moi and G. Orriols, Nuovo Cimento, **B 36**, 5 (1976).
[2]. G. Orriols, Nuovo Cimento **53**, 1 (1979).
[3]. A. Godone, F. Levi and J. Vanier, Phys. Rev **A 59**, R12 (1999).
[4]. J. Vanier, A. Godone and F. Levi, Phys. Rev **A 58**, 2345 (1998).
[5]. N. Cyr, M. Têtu and M. Breton, IEEE Trans. IM, **42**, 640 (1993).
[6]. A. Aspect, E. Arimondo, R. Kaiser, N. Vansteenkiste and C. Cohen-Tannoudji, JOSA B **11**, 2112 (1989).
[7]. A. Godone, F. Levi and J. Vanier, IEEE Trans. UFFC, **46**, 609 (1999).
[8]. F. Levi, A. Godone and J. Vanier, IEEE Trans. UFFC, **47**, 466 (2000).
[9]. E. Arimondo, Progr. Opt. **XXXV**, 257 (1996).
[10]. H. Lee, M. Fleischauer and M. O. Scully, Phys. Rev. A. **58**, 2587 (1998).
[11]. M.D.Lukin, M. Fleischauer, A. S. Zibrov, H. G. Robinson, V. L. Velichansky, L. Hollberg and M. O. Scully, Phys. Rev. Lett. **79**, 2959 (1997)
[12]. M O. Scully and M. S. Zubairy, *Quantum Optics*, (Cambridge University Press, Cambridge, England, 1999).
[13]. C: L. Bentley Jr, J. Liu and Y. Liao, Phys. Rev. **A 61**, 023811 (2000);
[14]. M: M. Kash, V. Suatenkov, A. S. Zibrov, L. Hollberg, G. R. Welch, M. D Lukin, Y. Rostovtev, E. S. Fry and M.O. Scully, Phys. Rev. Lett. **82**, 5229 (1999).
[15]. O. Kocharovskaya, Y. Rostovstev and M. O. Scully, Phys. Rev. Lett. **86**, 628 (2001).
[16]. J. Vanier and C. Audoin, *The Quantum Physics of Atomic Frequency Standards*, (Adam Hilger, Bristol, England,1989).

TOWARDS A CAESIUM FOUNTAIN FREQUENCY STANDARD AT THE NPL

D. Henderson, S. N. Lea, K. Szymaniec, P. Whibberley

National Physical Laboratory, Teddington, TW11 0LW, U.K.

ABSTRACT

We report on progress made at the NPL towards a Cs fountain primary frequency standard. We present an evaluation of the short-term and long-term stability of our experimental device. The short-term stability (Allan deviation) is $5 \times 10^{-13}\tau^{-1/2}$. The long-term stability is compromised by an effect similar to Ramsey pulling due to insufficient magnetic screening.

1. INTRODUCTION

In an atomic fountain a cloud of cooled atoms is launched up and then falls back under gravity. The atoms pass twice through a single microwave (μW) cavity, once on their way up and again on their way down. Such an implementation of Ramsey's method of *separated oscillatory fields* was first suggested in the 1950s, but the successful realisation was only achieved in the early 1990s, once the technique of *laser cooling* and trapping had been demonstrated [1].

In the fountain the time interval between the μW interactions can be of the order of a second, which gives a width for the central *Ramsey fringe* of 1 Hz or less. (The quality factor of the atomic resonance is $Q_{at} \sim 10^{10}$.)

Fountain frequency standards usually operate in a pulsed mode*). A single pulse (or cycle) consists of three phases:

1) cooling and launching – thermal Cs atoms are collected from a vapour by a *magneto-optical trap* (MOT) or *optical molasses* and cooled down to a few μK (v_{rms}=1-2 cm/s). Next the frequencies of the cooling beams are shifted and the atoms are accelerated (launched) upwards. After the launch the atoms are cooled further in the *moving molasses*. The cooling process prepares the atoms in one of the two ground state hyperfine sublevels (F=4).

2) ballistic flight & interaction with μW field – the upward- moving atomic cloud is falling freely under gravity. The atoms have a chance to be transferred to F=3 by interaction with the μW field either on their way up or down. Those two 'paths' from F=4 to F=3 interfere giving rise to observation of the so-called Ramsey fringes.

3) detection is done by laser-induced fluorescence. Atomic populations in F=4 and F=3 are detected separately and usually a normalized ratio of the two populations $P_3/(P_3+P_4)$ is given as the 'fountain signal'.

*) A continuous fountain has also been demonstrated and is being developed by the group in the Observatoire de Neuchâtel.

2. THE NPL EXPERIMENTAL FOUNTAIN

The design of the NPL fountain has been shown previously [2]. The cooling region forms a central part of the vacuum system with the flight tube (the C-field region) above and detection region below.

Three pairs of laser beams (one vertical and two horizontal) create an optical molasses, which is loaded for 500 ms, collecting about 10^6 atoms (we do not use the MOT). The atoms are launched upwards by changing the frequencies of the upward- and downward-going vertical beams by + 4 MHz and – 4 MHz, respectively. During the last 2 ms of the *moving molasses* phase the laser is decreased in intensity and detuned to the red, reducing the cloud's temperature to 2 μK (v_{rms}=1 cm/s).

The atoms are launched up to 60 cm above the cooling region. The peak of the atomic trajectory is about 30 cm above the microwave cavity. The atoms travel in a weak (100-200 nT) magnetic field (C-field) produced by an 80 cm long and 15 cm diameter solenoid. This field should be uniform and stable. Hence the flight tube is screened by three layers of μ-metal shields.

The atoms experience a *π/2 pulse* each time they traverse the microwave cavity. Their final state is detected by measuring fluorescence induced by two laser beams (6×12 mm^2 cross-section, separated vertically by an 8 mm gap). The upper beam is used to detect the atoms in F=4, which are then removed by radiation pressure. The atoms in F=3 reach the lower beam, are optically pumped to F=4 and detected. The detection signal is time resolved, allowing the temperature of the atomic cloud to be measured by the time-of-flight technique in addition to measuring the number of atoms in each of the atomic states.

2. SHORT-TERM STABILITY

A requirement for any fountain performance evaluation is its capability to produce Ramsey fringes with a good signal-to-noise ratio. Fig. 1. shows an example of the Ramsey fringes obtained in our fountain for typical parameters:

Fountain height:	31 cm,
Atomic temperature:	< 2 μK (v_{rms}=1 cm/s),
Number of atoms detected:	7×10^5,
Number contributing to the 'clock' transition:	5×10^4.

(no pre-selection of the (4,0) state)
Note that the fringe contrast at the centre is less than the potential maximum by about 20%.

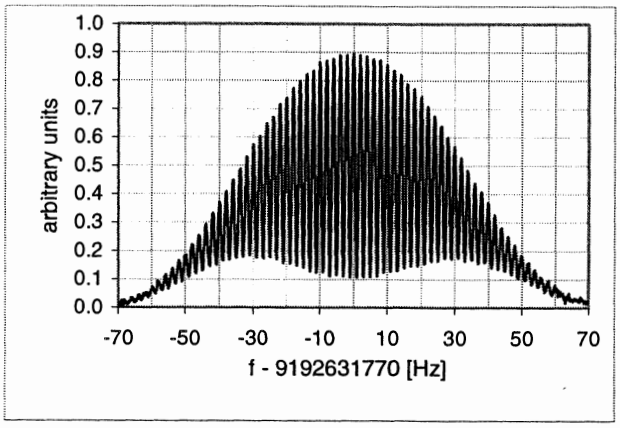

Fig. 1. A Ramsey fringe record. Shown is a normalized ratio of populations $P_3/(P_3+P_4)$. Data were taken with no averaging.

The narrow central Ramsey fringe is used to lock the local oscillator (LO) to the Cs resonant frequency. Every fountain cycle the LO frequency is toggled between f+Δν/2 and f-Δν/2 (where Δν is the full width at half maximum of the fringe). The fountain signal is measured and the difference between the LO frequency and the Cs frequency is calculated every two cycles. This frequency correction is then fed back to the LO. (This approach is called fringe 'tracking'.) The correction values for a measurement session are recorded, enabling statistical analysis.

We measured the time constant of the servo loop locking the LO to the frequency of the Cs hyperfine transition. This was done by setting the starting value for f to 0.5 Hz offset from the Cs resonant frequency. This is the maximum offset we could use, resulting in an excitation frequency on one side of the central fringe being near to the fringe minimum. Beyond three pairs of cycles, the corrections were distributed symmetrically about the caesium resonance, giving a time constant of about 10 s. The LO frequency was updated with 1 mHz resolution.

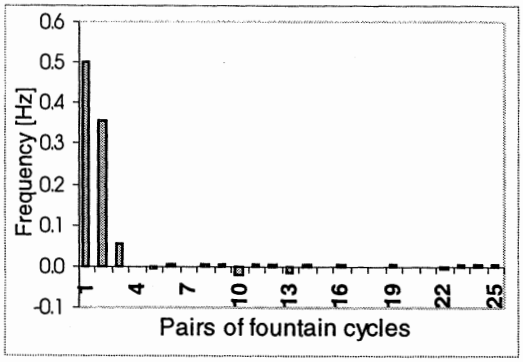

Fig. 2. The frequency correction applied to f, starting with an offset of 0.5 Hz.

The frequency of the Cs resonance can only be determined with a finite resolution due to the noise processes in the measurement. The main contributions to the noise are:

1) detection (technical) noise (S/N);
2) local oscillator noise (γ);
3) quantum projection and partition noise ($\propto \sqrt{N_{at}}$).

The Allan deviation of the measured Cs frequency $\sigma_y(\tau)$ can be expressed as [3]:

$$\sigma_y(\tau) = \frac{\Delta\nu}{\pi \cdot \nu_{Cs}} \sqrt{\frac{T_c}{\tau}\left(\left(\frac{N}{S}\right)^2 + \gamma + \frac{1}{N_{at}}\right)}^{1/2}$$

or

$$\sigma_y^2(\tau) = \left(\sigma_y^{(1)}(\tau)\right)^2 + \left(\sigma_y^{(2)}(\tau)\right)^2 + \left(\sigma_y^{(3)}(\tau)\right)^2$$

For our fountain we found:

$\sigma_y^{(1)}(\tau) = 2.6\times10^{-13}\tau^{-1/2}$ (for S/N=150),

$\sigma_y^{(2)}(\tau) = 2\times10^{-13}\tau^{-1/2}$ (for LO stability 4×10^{-13} at 1 s[4]),

$\sigma_y^{(3)}(\tau) = 1.8\times10^{-13}\tau^{-1/2}$ (for 5×10^4 atoms contributing to the 'clock' signal),

Hence the expected value of the Allan deviation is:

$$\sigma_y^{TH}(\tau) = 4\times10^{-13}\tau^{-1/2},$$

which can be compared with the measured value of

$$\sigma_y^{EXP}(\tau) = 5\times10^{-13}\tau^{-1/2}$$ (see below).

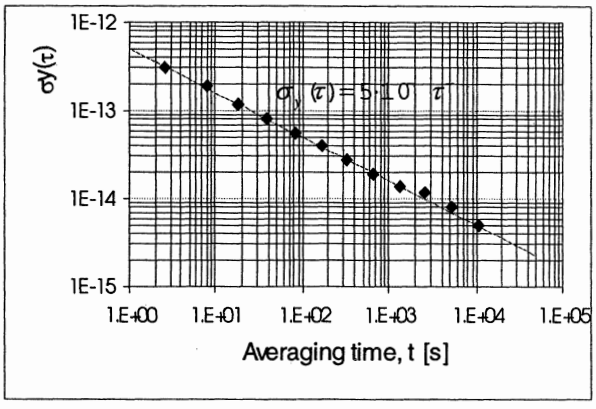

Fig. 3. The frequency stability of the fountain relative to an H-maser.

3. LONG-TERM STABILITY – FREQUENCY OFFSETS

3.1. Reduced fringe contrast

The reduced contrast of the Ramsey fringes suggests that magnetic sublevels F=3, $m_F \neq 0$ are populated during the Ramsey interaction. To confirm this, we selected the atoms in m_F=0 and transferred them to F=3 during the first passage through the microwave cavity. (We removed those remaining in F=4 by radiation pressure.) During the second passage through the cavity we probed

all the sublevels of the F=3 state by changing the microwave frequency so as to be resonant with the other transitions. A normalized signal of F=4 atoms was measured ($P_4/(P_3+P_4)$) (see fig. 4). A single peak at the "clock" frequency ($m_F=0 \leftrightarrow m_F'=0$) should be observed if there is no population transfer between Zeeman sublevels. However, in our case we see other peaks spaced by the Larmor frequency. The spectra depend strongly on the applied static magnetic field. For certain values of the C-field, a small change of the field results in a strong suppression of the $m_F=0$ and an increase of $m_F \neq 0$ populations. (Compare the grey and black lines in fig. 4.)

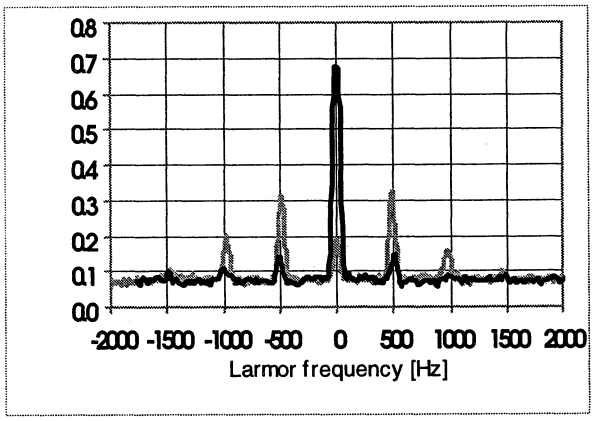

Fig. 4. The population of the magnetic sublevels during the second μW interaction. (The first interaction selects the $m_F=0$ atoms.) The grey and the black lines correspond to data taken for 37 and 40 nT respectively.

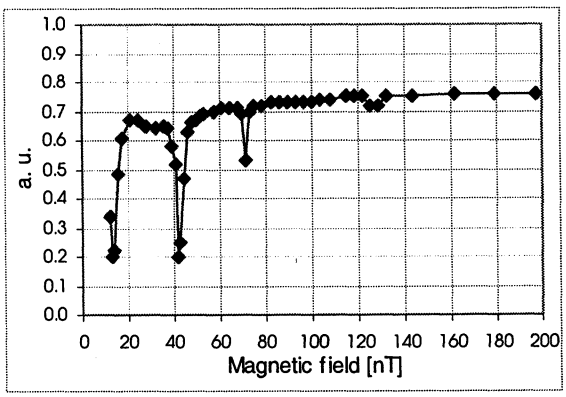

Fig. 5. The height of the central peak ($m_F=0$ population) as a function of the C-field. The sharp dips correspond to Larmor frequencies of 50, 150, 250,...Hz.

3.2. Shielding factor

We believe that the populating of the $m_F \neq 0$ states is due to an AC field in the C-field region. As shown in fig. 6, the shielding factor, S, of our magnetic screens is better than 1000 only between 10 cm and 38 cm above the μW cavity. At the cavity level the shielding factor has dropped to 170. We measured the shielding factor by applying a known magnetic field with alternating polarity and using atoms as a probe. We launched the atoms to different heights and applied a microwave pulse of 100 ms duration at the top of their trajectory. The μW frequency was scanned over the magnetic field-sensitive resonance ($3,+1 \leftrightarrow 4,+1$) and the Larmor frequency was measured. The uniformity of the applied C-field was mapped in the same way (fig. 7).

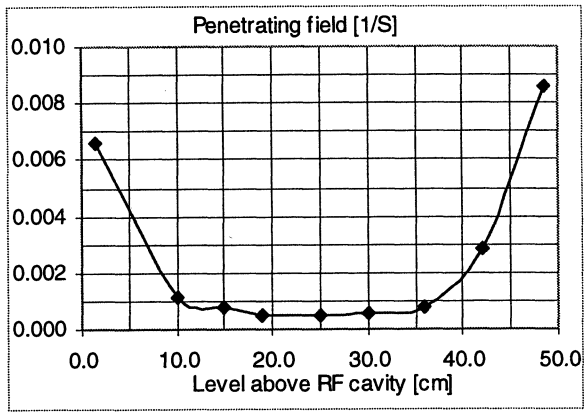

Fig. 6. A map of the magnetic field "leaking" into the C-field region, expressed as a reciprocal of the shielding factor.

3.3. C-field map

The spectral and spatial accuracy of the pulsed microwave method was sufficient to determine the quadratic Zeeman shift of the ($3,0 \leftrightarrow 4,0$) transition with uncertainties of better than 2 parts in 10^{-15} for a C-field in the range of 100-200 nT. An example of a C-field map (DC component) is shown in fig.7. The DC component of the "leaking" field can be compensated for by trim coils. The AC component, however, cannot be readily eliminated.

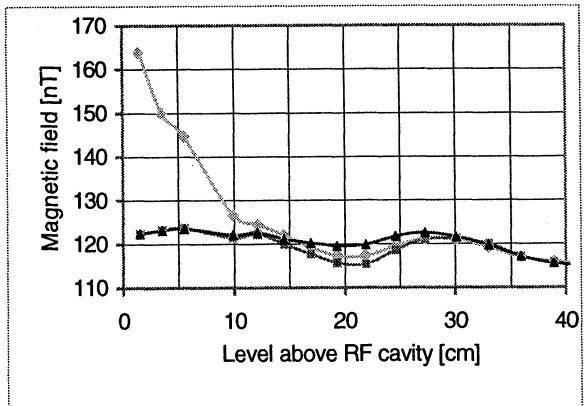

Fig. 7. A map of the static magnetic field in the C-field region. To improve the uniformity two trim coils were used, at the cavity level (1) and one 20 cm above (2). Light grey line - no correction applied, dark grey - coil (1) only, black - both coils (1) and (2) used.

3.4 Ramsey pulling

The excitation of the $\Delta m_F=1$ ($\Delta F=0$) transitions during the Ramsey interaction may lead to a large error in the measured frequency of the hyperfine transition. The cause is similar to that of the Ramsey pulling effect [5]. The frequency shift will appear only if there is an asymmetry in the probability of $m_F=-1$ and $m_F=+1$ excitation. An asymmetry of a few percent may result in a relative frequency shift of the order of 10^{-12}. As the level of asymmetry may vary in the long term, so may the measured frequency of the Cs resonance.

We measured frequency offsets ranging from -1.5×10^{-13} to $+1.5 \times 10^{-13}$ over a period of two weeks by comparing the fountain with a stable H-maser (see fig. 8). The fountain was run in sessions lasting from 5 to 15 hours. The statistical uncertainty of the frequency measurement in each session was less then 10^{-14}. The measured frequencies were corrected for the quadratic Zeeman shift and the black body radiation shift. The cold-collisional-shift is negligible on the 10^{-14} scale for the atomic densities we used. Similarly, other known systematic frequency shifts were estimated to be negligible.

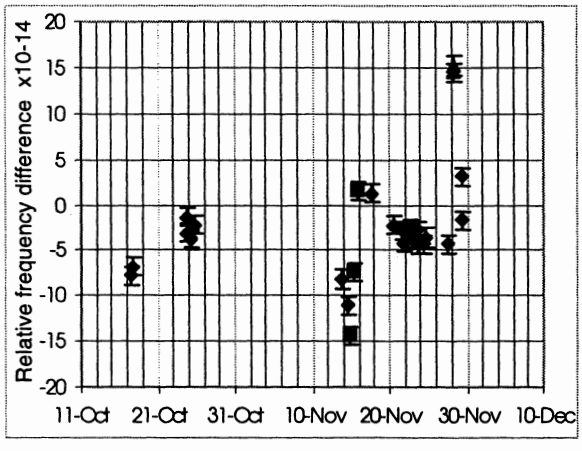

Fig. 8. The Cs hyperfine frequency measured against an H-maser, stable to 3×10^{-15} over the period.

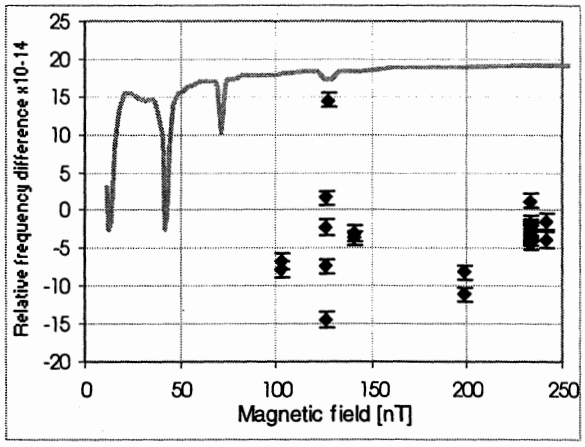

Fig. 9. The same data as in fig. 8, plotted as a function of the applied C-field. Fringe contrast data from fig. 5 are also shown as a reference. Note the excessive scatter of the frequency data for the C-field of 129 nT, corresponding to Larmor frequency of 9×50 Hz.

4. CONCLUSIONS

We have demonstrated an experimental Cs fountain frequency standard with a short-term stability (Allan deviation) of $5 \times 10^{-13}\tau^{-1/2}$.

We have also found a variable frequency offset, or instability of parts in 10^{13} due to an effect similar to Ramsey pulling. We have established that the frequency offset is due to inadequate magnetic shielding.

A second fountain (F2) is under construction with improved magnetic shielding. F2 will use an MOT, and the larger number of atoms, together with a BVA-based local oscillator, is expected to improve both the short-term and the long-term stability.

***

This work is supported by the UK National Measurement System in the Foundation Programme.

REFERENCES

[1] M.Kasevich, E. Riis, S. Chu and R. DeVoe, Phys. Rev. Lett. 63, 612 (1989); A. Clairon, C. Salomon, S. Guellati and W. D. Phillips, Europhys. Lett. 16, 165 (1991).

[2] P.B. Whibberley, D. Henderson, S.N. Lea, in Proc. Joint Meeting EFTF-IEEE IFCS, 1999.

[3] G. Santarelli, Ph. Laurent, P. Lemonde, A. Clairon, A.G. Mann, S. Chang, A.N. Luiten, C. Salomon, Phys. Rev. Lett. 82, 4619 (1999).

[4] G. Santarelli, C. Audoin, A. Makdissi, Ph. Laurent, G.J. Dick, and A. Clairon, IEEE Trans. Ultra. Ferr. Elec. Freq. Contr, 45, 887 (1998).

[5] C. Audoin, Metrologia, 29, 113-134 (1992).

MEASUREMENT OF THE SPATIAL PHASE VARIATION IN A RING CAVITY OF AN ATOMIC BEAM FREQUENCY STANDARD

R. Augustin, A. Bauch, R. Schröder

Physikalisch-Technische Bundesanstalt,
POB 3345, D-38023 Braunschweig, GERMANY

The microwave cavity in PTB's primary clocks CS1 consists of the central waveguide, 28 half-wavelengths in length and two terminal parts of ring-shaped design, as proposed by De Marchi et al. [1]. The main purpose of the ring structure is to sustain a microwave field with a maximum magnetic field and a zero Poynting vector at the midpoint of the irradiation section. The rings are strongly coupled to the straight part of the cavity.

The spatial dependence of the phase in the X-direction around the phase minimum of a ring cavity should be quadratic, and it should remain within 4 μrad over the 3 mm diameter of the CS1 atomic beam [1]. Some years ago, measurements at the PTB had yielded less optimistic results, but they may have been corrupted by frequency shifts caused by microwave leakage, possibly present in the experimental apparatus that was used [2]. A worst case estimate of those results was taken as the basis for the current CS1 uncertainty estimate [3], where we assumed that the phase variations might be as large as 20 μrad/mm, much more than one would predict for a ring cavity.

In a new series of experiments the spatial phase dependence in the ring cavity is currently been studied. The experimental atomic beam frequency standard CSX is used for that purpose. First results indicate that the phase dependence is within a factor of two in agreement with the theoretical prediction. As the conductivity of real materials with machined surfaces is known to deviate from tabulated values for perfect materials, such a discrepancy is not astonishing.

Data collection will continue up to early year 2001, and statistically safe material should be available at the date of the conference.

[1] De Marchi A., Shirley J., Glaze D.J., Drullinger R., *IEEE Trans. Instrum. Meas.*, **IM-37**, 1988, 185-190.

[2] de Boer H., Fischer B., Heindorff T., Schröder R., *Proc. 4th European Frequency and Time Forum*, 1990, 523-526.

[3] Bauch, A., Fischer, B., Heindorff, T., Schröder, R., *Metrologia*, 1998, **35**, 829– 845.

OSCILLATION OF THE CENTRE OF THE RABI PEDESTAL IN AN OPTICALLY PUMPED Cs BEAM STANDARD

E. de Clercq and A. Makdissi

Bureau National de Métrologie - Laboratoire Primaire du Temps et des Fréquences
Observatoire de Paris
61 Avenue de l'Observatoire, 75014, Paris, France

ABSTRACT

This paper is devoted to the study of the symmetry of the Rabi pedestal of the clock transition in an optically pumped Cs beam frequency standard. The frequency of the microwave oscillator is locked on the center of the Rabi pedestal using a square wave frequency modulation. We observe a modulation of the center frequency as a function of the modulation depth. Experimental investigations on this unexpected effect are reported.

Keywords:Frequency standard, optical pumping, Cs, Rabi pedestal.

1. INTRODUCTION

In Cs beam standards using the Ramsey interrogation method, the Ramsey fringes are located at the top of a broader curve, the Rabi pedestal. Shirley et al. -Ref. 1- have shown that useful information could be deduced from the difference between the center of the Ramsey fringes and the center of the Rabi pedestal. In particular, the cavity pulling on the clock transition can be deduced from this difference. We have measured the center frequency of the Rabi pedestal , f_c, as a function of the modulation depth f_m. When the cavity is tuned to the atomic resonance frequency (no cavity pulling), and when there is no Rabi pulling by the neighboring transitions, the plot of f_c versus f_m should be a horizontal line. Surprisingly we have observed some oscillations of f_c around this line.

2. EXPERIMENTAL SET-UP

A scheme of the experimental set-up is shown on Fig. 1. The Cs beam issued from the oven is first optically pumped by a laser beam locked on the (F = 4 – F' = 4) polarized sigma transition of the D_2 line, see Fig. 2. Then the beam travels across the Ramsey cavity. The drift length between the two interaction regions is 1m. The static magnetic field (C field) is perpendicular to the figure plane. The static magnetic field area covers the cavity length and the optical zones. After the fluorescence signal is detected using the (F = 4 - F' = 5) transition. The polarization of the detection beam can be changed with a retardation plate. The polarization can be circular or linear, pi or sigma.

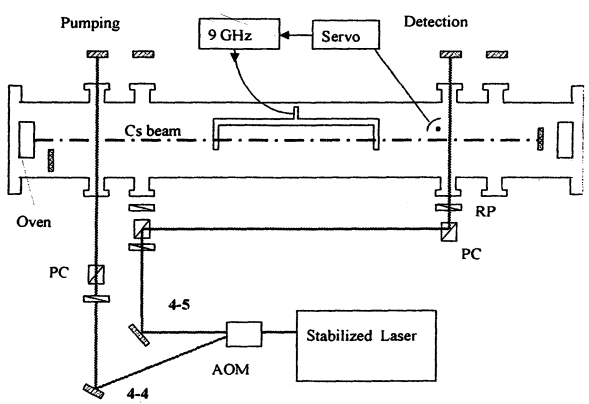

Fig. 1. Experimental set-up. AOM: acousto-optic modulator, PC: polarizing cube, RP retardation plate.

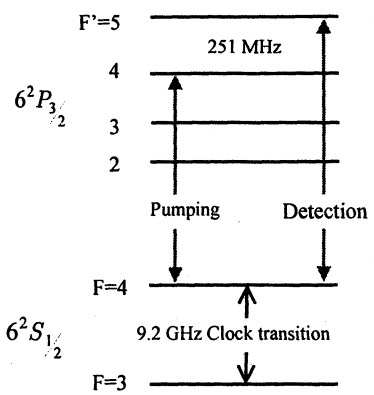

Fig. 2. Involved Cs energy levels.

Fig. 3 shows the record of the signal when the microwave frequency is scanned around the clock transition. The linewidth of the central Ramsey fringe is 100 Hz, The linewidth of the Rabi pedestal is about 20 kHz.

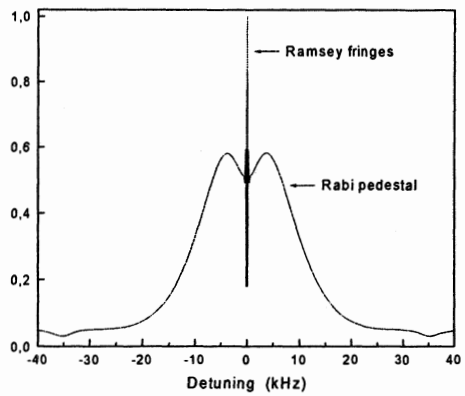

Fig. 3. The Rabi pedestal.

In order to measure the center of the Rabi pedestal, we lock the frequency of the microwave signal on the center of the Rabi pedestal, using a square wave frequency modulation. We use the same loop that for locking the microwave oscillator on the central Ramsey fringe, when the standard is operated as a clock, but with a larger modulation depth (several kHz).

3. EXPERIMENTAL RESULTS

The plot of the measured center frequency , f_c, of the Rabi pedestal as a function of the modulation depth, fm, is shown on Fig. 4.

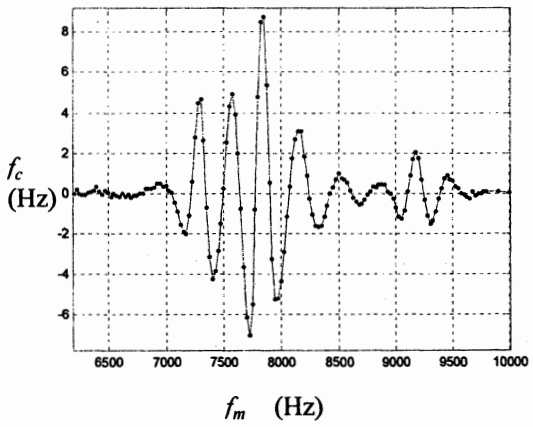

Fig. 4. Middle frequency of the Rabi pedestal versus the modulation depth.

The oscillations are caused by very tin amplitude modulations on the Rabi pedestal. The amplitude modulation is estimated to be a few 10^{-4} times the maximum of the Rabi pedestal.

The strength of the static magnetic field is measured by the Zeeman frequency, F_z, the frequency difference between the microwave transitions (F = 3, m –F = 4, m) and (F = 3, m+1 – F = 4, m+1), where m is the Zeeman sublevel number. When the Zeeman frequency increases, the oscillation patterns move towards higher frequencies, about like one tenth of the Zeeman frequency increase. And the amplitude of the oscillations decreases, see Fig. 5.

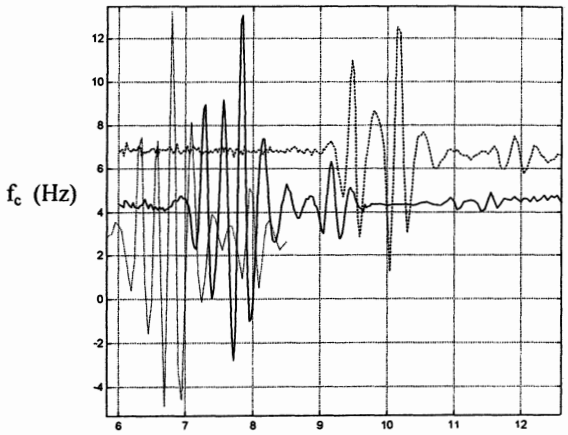

Fig. 5. Same as Fig. 4. Dotted line: F_z = 61 kHz, solid line: F_z = 71 kHz, dashed line: F_z = 91 kHz.

The oscillations are not shifted when the microwave power is changed. But the oscillations amplitude increases with the microwave power. The increase is about linear with the power. We have also changed the optical power. There is no change with the power of the pumping beam. But the oscillations amplitude increases, without frequency shift, when the power of the detection beam decreases.

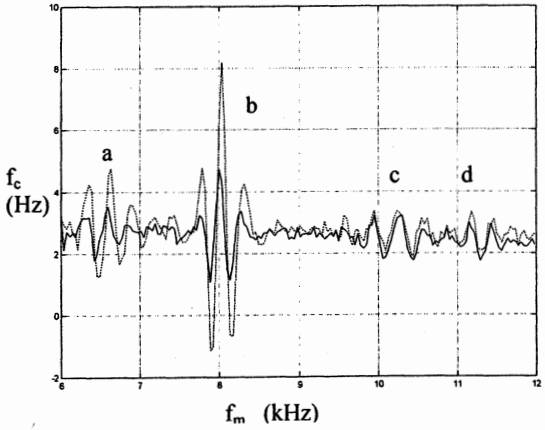

Fig. 6. f_c versus f_m. Solid line: p = 200 μW, dashed line: p = 50 μW.

Fig. 6 shows the experimental records for two powers of the detection beam: 200 μW, and 50 μW, the beam diameter is 7 mm. One can distinguish on Fig. 6 four oscillation patterns, labeled a, b, c, d. The amplitudes of the first two patterns vary with the power. The two last are smaller and independent of the optical power.

All these records have been obtained with a circular polarization of the detection beam. When the circular polarization is reversed, the oscillations of the two first patterns, a and b, are also reversed. The c and d patterns are unchanged, see Fig. 7.When the polarization of the detection beam is linear, pi or sigma, the two first patterns, a and b, disappear. The two last patterns, c and d, are unchanged. Fig. 8 shows a record with a pi polarization superposed to a record with the sigma polarization.

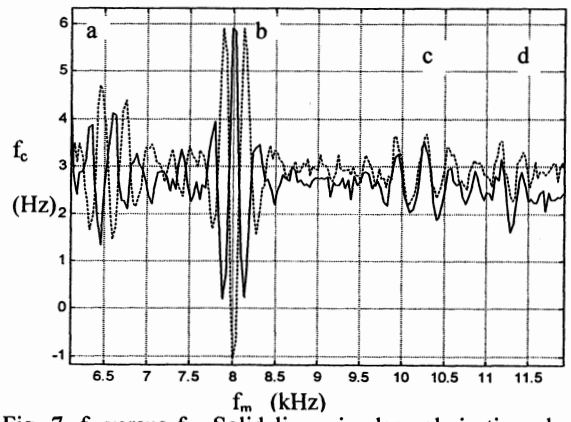

Fig. 7. f_c versus f_m. Solid line: circular polarization, dashed line: reversed circular polarization.

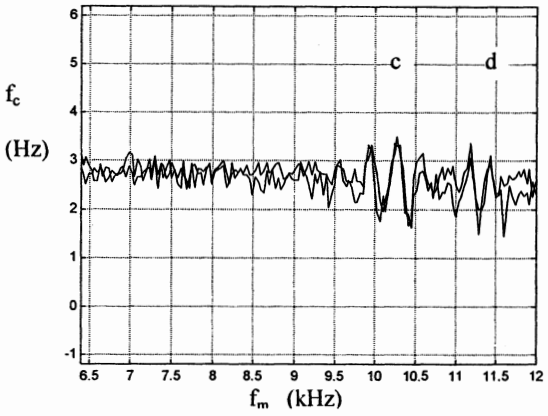

Fig. 8. f_c versus f_m for a linear polarization of the detection beam: pi and sigma polarization.

4. SUMMARY

The full velocity distribution, not filtered by selecting magnets, is used in our standard. The velocity distribution is then broad. In this case the Rabi pedestal is expected to be smooth, without ripples. However, when we lock the frequency of the microwave oscillator on the center of the Rabi pedestal, we observe oscillations of the middle frequency as a function of the modulation depth. These oscillations are due to tin ripples on the Rabi pedestal. The oscillation move with the Zeeman frequency, and their amplitude decreases. The amplitude of the main oscillation patterns increases with the microwave power, and decreases when the optical power of the detection beam increases. These oscillations are reversed when the circular polarization of the detection beam is reversed, and disappear for a linear polarization. Another group of oscillations does not change with the optical power and the polarization.
We have no explanation on the origin of this phenomenon.

REFERENCE

[1] J. H. Shirley, W. D. Lee, G. D. Rovera, and R. E. Drullinger, "Rabi pedestal shifts as a diagnostic toll in primary frequency standards", IEE Trans. Instrum. Meas., 44, 136-139, 1995.

HYDROGEN MASER WITH IMPROVED SHORT-TERM FREQUENCY STABILITY

A.Boyko,G.Yolkin,N.Gestkova,G.Kurnikov,V.Paramzin.

IMVP,GP VNIIFTRI Mendeleevo,Moskow region,Russia

Abstract. A hydrogen maser with improved short-term frequency stability is proposed as a highly stable locale oscillator (LO) for fountain type cesium frequency standards. A hydrogen maser has been designed and constructed for that purpose. Its design and preliminary experimental results are reported. The signal-to-noise ratio of maser receiver output signal is $2{,}5\cdot10^{6}$ in 100 Hz bandwidth. The cavity pulling factor (Q_c/Q_l) is $5\cdot10^{-5}$

1.Introduction

The main specific feature of cesium fountain frequency standard [1] is its pulsed mode of operation. Atom package twice passes through the cavity where it undergo a microwave interaction during time τ = 0,02 sec through the interval T = 0,5 sec. The complete cycle is 1,5 sec.

So mistake shift on every cycle of frequency measurement LO is:

$$\frac{\Delta f}{f_0}=\frac{1}{2\pi T f_0}\left\{\frac{1}{\tau}\int_{t}^{t-\tau}\varphi(\xi)d\xi-\frac{1}{\tau}\int_{t-T}^{t-T-\tau}\varphi(\xi)d\xi\right\} \qquad (1)$$

where τ - microwave interaction time, T – Ramsey drift time, $\varphi(\xi)$ and f_0 – noise phase and midle frequency of a LO's signal.

Assuming LO white phase noise, Allan's variance for chosen T and τ (50 Hz filter bandwidth) should not exceed $2\cdot10^{-13}$ in order to achieve masers frequency instability $1\cdot10^{-15}$ per day.

Therefore the hydrogen maser as a LO with high short-term stability must have a considerably increased output signal power. The unavoidable deterioration of long-term stability for τ > 100 sec is not a problem in the case as LO will be regularly tuned to the atomic spectral line.

2.Short-term frequency stability and maser output signal power. Maser parameters.

The maser frequency stability for τ up to 100 sec is mainly due to the additive noise at the receiver input , and frequency deviation, results from thermal noises within linewidth. In this case Allan's variance can be written as [2]:

$$\sigma^2(\tau)=\frac{\kappa T\cdot FB}{\omega^2\tau^2}\cdot\frac{1}{mP}+\frac{\kappa T}{2\tau}\cdot\frac{1}{PQ^2} \qquad (2)$$

where F- is the noise factor of the maser receiver; k- is Boltzmann constant; T- is the absolute temperature of the maser storage bulb; B - is the equivalent noise bandwidth of the receiver; P - is the total power radiated by the hydrogen atoms in the storage bulb; m - is the coupling factor to the cavity; Q - is the atomic line Q-factor.

For typical value of parameters: $P=1\cdot10^{-12}$W, m=0,2, F=2, $Q=1\cdot10^{9}$, $B=2\pi\cdot50=3\cdot10^{2}$ and for τ = 0.5 sec additive phase noise component is equal to $6\cdot10^{-13}$ and 10 times second component (2).

Thus, considerably increased maser output power is needed in order to get $mP= 2\cdot10^{-12}$W. The total power P taking into consideration spin exchange relaxation of the radiating atoms and average life time of atom within the bulb can be written as [3]:

$$P=A\cdot\frac{V_e}{\alpha}q\left(-2\Delta^2+\frac{1+q}{q}\Delta_0\Delta-\frac{1}{q}\Delta_0^2\right) \qquad (3)$$

where $\alpha=\dfrac{N_{tot}}{N_1-N_0}$

N_{tot} is the number of all atoms entering the bulb; N_1 and N_0 – the numbers of atoms in states (F =1, m=1) and (F=0, m=0) respectively.

$$q=B\frac{V_c}{V_e}\cdot\frac{\alpha}{Q_c}\cdot\frac{1}{\eta};\qquad \eta=\frac{\langle H_x\rangle^2 e}{\langle H^2\rangle c}$$

V_c and Q_c- cavity volume and Q-factor respectively, A и B are some constants independent on the maser design $\Delta_0=Q_0^{-1}=\dfrac{2}{\omega_0\tau_0}$ is inverted atomic Q-factor due to escape of atom from the bulb, $\Delta=Q^{-1}$ is inverted Q- factor.From (3) the initial optimum Q_0 can be found in order to get maximum power for chosen Q

$$\overline{Q_0}=Q\frac{2}{1+q} \qquad (4)$$

Which gives :

$$P_{max} = A\frac{V_c}{\alpha}\frac{1}{Q^2}\left(1-6q+q^2\right) \qquad (5)$$

The masing is impossible for $q=q^*\cong 0.172$ and $P=0$.

It is seen from (5) that it is necessary:

- to decrease the atomic line Q-factor;
- to choose optimal relation between bulb and cavity sizes (q – parameter);
- to increase the storage bulb volume;
- to avoid the flux of atoms which are in undesirable state ($\alpha \to 1$).

If atomic line Q-factor is reduced to $0{,}5\cdot 10^9$ value the second phase noise component in (2) doesn't exceed $1\cdot 10^{-13}$ for 0,5 sec.

For cylindrical shapes of the maser cavity and bulb q has minimum value when [4]:

$$D_B=0{,}48D_c \; ; \qquad L_B=0{,}74L_c \qquad (6)$$

where D_B, D_c, L_B, L_c – the diameters and length of bulb and cavity respectively.

These bulb dimensions corresponds to the minimum threshold intensity of the atomic beam.

According to (5) the optimum dimensions of the bulb are 10% larger due to the first factor in (5), which is proportional to the bulb volume.

Usually the diameter and the length of the cavity are about 27cm, That gives the optimum cavity volume of 3,4 l.

Further increasing the storage bulb volume is possible by reducing of its diameter and increasing its high.

The elimination of undesirable atoms flux could raise the maser power by factor 2÷4.

3. The design

The design of the maser reported here (fig. 1) is similar to "Sphera" maser design [5].

The main modifications:

- the dimensions of the cavity made of fused quartz are $D_c\cong 260$ мм, $L_c=400$ мм.
- the storage bulb volume is $V_B=3\cdot 10^3$ sm^3 ($D_c\cong 260$ mm, $L_c=400$ mm.)
- life time of atoms within the bulb is $\tau_o = 0{,}45$sec.

The cavity is controled by two-stage thermostat. Three layer permalloy magnetic shield system has $5\cdot 10^3$ shielding factor.

The cavity with the storage bulb, thermostat and magnetic shield system is situated in the upper vacuum chamber. The bottom vacuum chamber 'of the hydrogen maser is fixed to the bottom, where there is a magnetic selection system, a getter pump, an atomic hydrogen source.

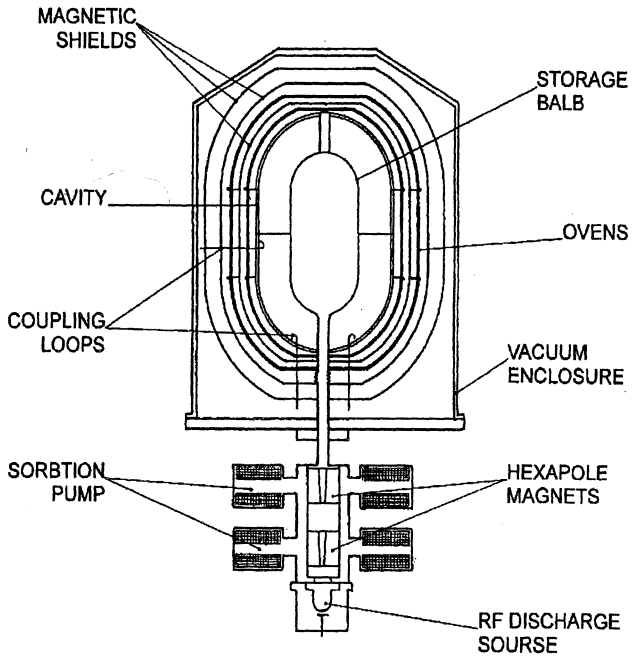

Fig.1 The structure of hydrogen maser.

The magnetic selection consists of hexapol focus magnets. Residual gases are pumped in both vacuum chambers by ion pump.

4. Results

The main coupling loop has been chosen such that the loaded Qc –factor is about $26\cdot 10^3$ while unloaded Qc – factor is $48\cdot 10^3$. The signal power at the receiver input is 46% of total power P.

The cavity Qc –factor regeneration loop allows to vary Qc –factor from initial value $26\cdot 10^3$ up to $38\cdot 10^3$

The measurements of the ratio P/Pn where P is output signal power, Pn is noise power have been carried out in 9kHz bandwidth. The P/Pn dependence (recount on 100Hz) on inverted line Qc – factor for three Qc value are shown in Fig 2.

From (3) the parameter q can be expressed by inverted Q-factor values

$$q \approx \frac{\Delta_1}{4\Delta_{max}} \qquad (7)$$

where Δ_1 is Q-factor at the moment when the masing starts, Δmax corresponds to the maximum power. From Fig.2 and (7) we have: $q_1=0.12$; $q_2=0.10$; $q_3=0.08$ for Qc –factor $26\cdot 10^3$,$29\cdot 10^3$, $38\cdot 10^3$ respectively.

The using of large cavity coupling, Q-regeneration with low-noise amplifier gives increased signal/noise ratio at the receiver input about two time.

Allan variance for averaging interval τ=0.5 sec is equal to $2 \cdot 10^{-13}$ for $P/P = 4 \cdot 10^{6}$

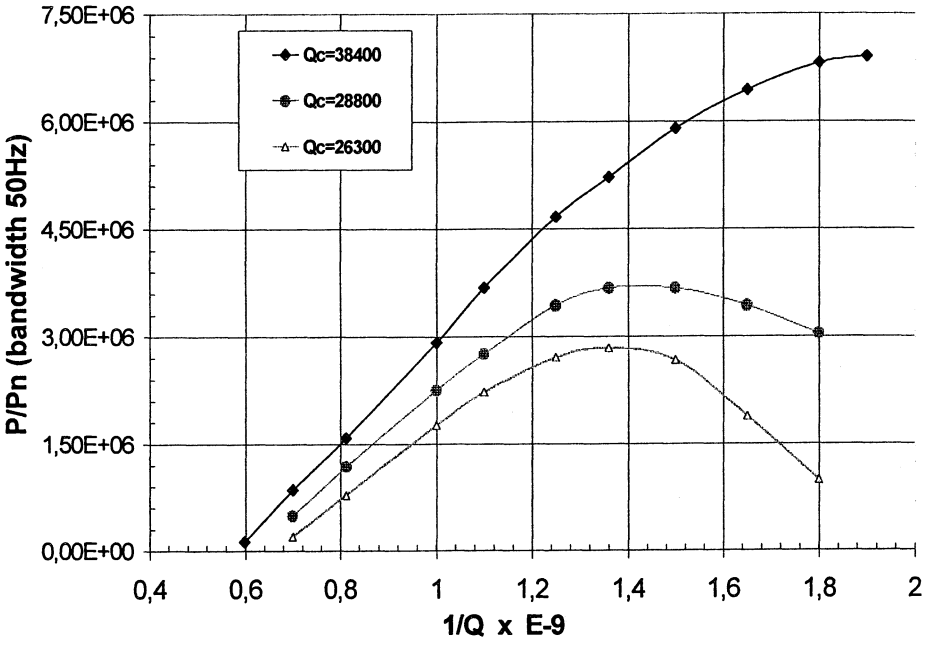

Fig2. The ratio of output maser'spawer (P) et nois pawer(P_n) versus inverse lain Q for different of the values loaded cavity Qc in the bandwidth

References

[1] G.Santarelli, et al."Resent Results of the LPTF Cesium Fountain Primary Frequency Standard" IEEE Internetionel Frequency Control Simposium.1993

[2] L.S.Cutler, et al. "Some Aspects of Theory and Measurement of Frequency Fluctuations in Frequency Standard"

[3] E. M. Mattison, R. F. C. Vessot, end Wei Shen. "Single- Stite Selection Sistem for Hydrogen Masers",IEEE Trans. On ultrasonics,..vol. UFFC-34,NO.6,1987

[4] D.Kleppner et al.," Hydrogen masers principles and techniques."Phis. Rev.,vol.138, 1965.

[5] A. I. Boiko, B. A. Gaygerov, G. Yolkin, N. Gestkova, G. Kurnikov, V. Sysoev. "Hydrogen Time and Frequecy Standard SPHERE". Proc.4-th EFTF 91,pp. 296,299

A HIGH-ISOLATION POWER DIVIDER FOR H-MASERS

Pekka Eskelinen[1] and Harri Eskelinen[2]
[1]Helsinki University of Technology, FINLAND
[2]Lappeenranta University of Technology, FINLAND

1. ABSTRACT

Through careful dimensioning, avoidance of transition discontinuities and by using a special conductive cylinder which blocks the internal airgap, a conventional ring hybrid can be an attractive RF power divider for hydrogen masers, where a high isolation is desired between the 1.42 GHz cavity output arrangement and the feed-back electronics. When typical commercial units hardly exceed 40 dB, an improved isolation up to 90 dB and more is demonstrated here while maintaining the wanted coupling better than 3.15 dB. The milling and mounting uncertainty required for a succesful and repeatable result in a combined metallic / PTFE stripline form was found to be 0.01 mm.

Keywords: power divider, ring hybrid, RF isolation

2. INTRODUCTION

A conventional ring hybrid, as demonstrated e.g. in [1] and [2], is attractive as an RF power divider also for hydrogen masers [3], where naturally a high degree of internal isolation is desired between the 1.42 GHz cavity output arrangement and the feed-back electronics. In the basic four-port hybrid, see Fig. 1, port 4 is normally terminated into 50 ohms and port 2 operates as the sum channel. The ring itself is of 75 ohms characteristic impedance.

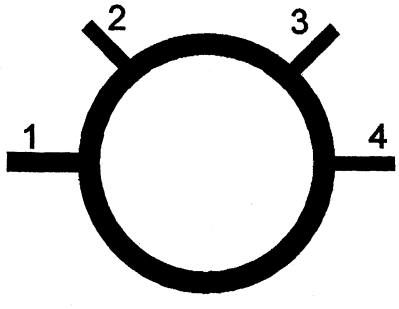

Fig. 1. The basic geometry of a classical RF ring hybrid showing the numbering convention of ports.

It is desirable to have the coupling between ports 1 and 3 as small as possible in order to reduce any external effects against the primary maser frequency to a minimum but the attenuation between the adjacent ones (1-2 or 2-3) is to be low so that we don't spoil the noise figure. The construction allows naturally a mirror configuration starting from port 4.

3. PROTOTYPE CONSTRUCTION

An combined metallic / PTFE stripline construction was chosen. The center conductor has been milled on the two-sided board with an uncertainty below 0.02 mm. Initially, some prototypes were constructed and their performance was carefully evaluated. It turned out that a lengthwise manufacturing error, that means either a slightly too short or too long path between ports, will cause a shift in the best-performance center frequency only. A 5 per cent impedance error in the 3/4 branch will change both the isolation value by about 20 dB and the center frequency by 0.5 per cent where as a similar error in the 1/4 branch will mainly affect the isolation performance by up to 30 dB. The most important observation was that the best available isolation value with the classical design was hardly to exceed 40 dB which is typical for commercial OEM units as well, see e.g. [4], although the attenuation between adjacent ports was less than 3.2 dB or 0.2 dB above theoretical.

4. THE USE OF A CENTER BLOCK

An idea was born to test if there exists a coupling directly across the ring which might limit the obtainable isolation. For this experiment thin aluminium sheets of circular cross-section were added in the middle of the hybrid thus completely closing the airgap and when this turned out to be of benefit, a completely new platform was milled . This is illustrated in Fig. 2 which is a mechanical drawing of the hybrid enclosure and in Fig. 3 where the complete assembled hybrid is seen from its rear thus revealing the removal of excess external metal.

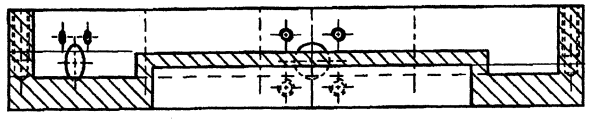

Fig. 2. The cross-section of the proposed construction shows the blocking cylinder's relative dimension as compared to the coaxail SMA-type connectors.

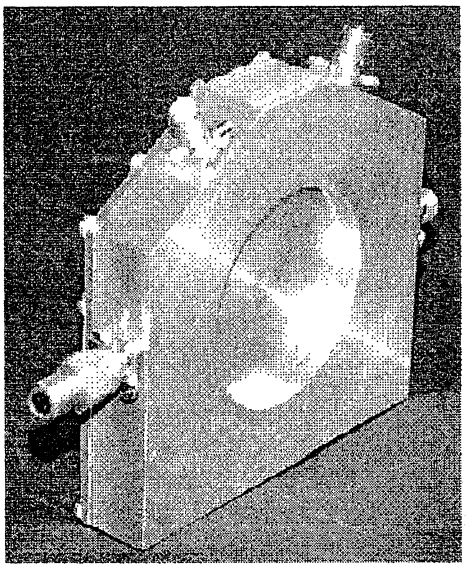

Fig. 3. A fully assembled prototype hybrid as seen from the back. In order to reduce overall weight the interior of the blocking cylinder was drilled open.

Further on, the coaxial stripline launchers were not soldered to the center conductor but are kept in place by the mechanical pressure caused by the cover fastening screws. Thus the discontinuity at the transition is kept as small as possible. The case milling uncertainty required for a succesful and repeatable connection was found to be 0.01 mm. The internal lay-out of one of the prototypes is shown in Fig. 4. Note that different blocking cylinder diameters were tried in order to find out the limit where the vertical cylinder skirt starts to intervene with the propagating wave in the ring. In our experiments a guard space of twice the ring's line width was found very sufficient which is considerably less than the traditional recommendation of a factor of five, stated e.g. in [5].

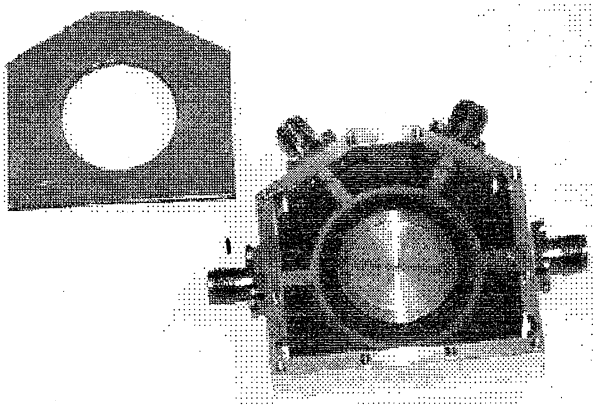

Fig. 4. Our practical construction is assembled from a sturdy milled aluminium housing and two teflon-based circuit boards, the upper of which is removed to show the ring geometry inside which the blocking cylinder is mounted. An extension which adjusts the outer radius of the cylinder for some trials is just visible.

The suggested principle looks promising as is shown in Fig. 5. Without affecting the wanted coupling or port impedances at all we are able to add about 20 - 30 dB of isolation thus ending with 70 dB, depending on the overall accuracy of the mechanical lay-out.

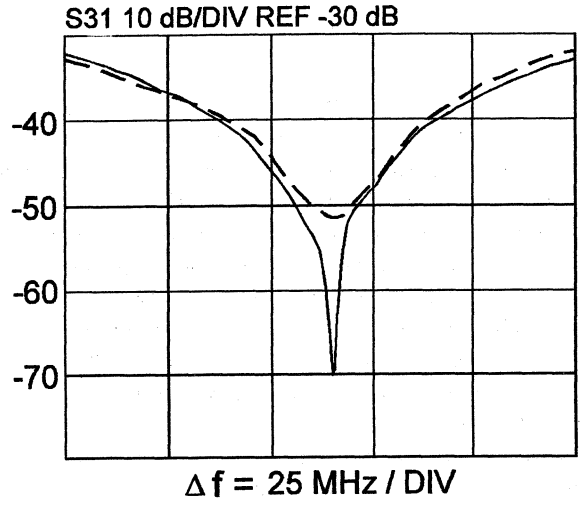

Fig. 5. The best obtainable isolation with a conventional, carefully assembled hybrid (dashed line) and the improvement which came through the introduction of the blocking cylinder inside the ring.

5. FINE-TUNING PORT IMPEDANCE

When striving for extreme performance we made an experiment - inspired by the classical but frequently cited work of [5] - with a tuning screw positioned just above the coaxial launcher of port four as demonstrated in Fig. 6. The 2 mm screw goes through the upper circuit board and approaches the ring geometry from above. As is seen from the drawing, the electrical connection is maintained across the entire length of the screw thus minimizing inductance.

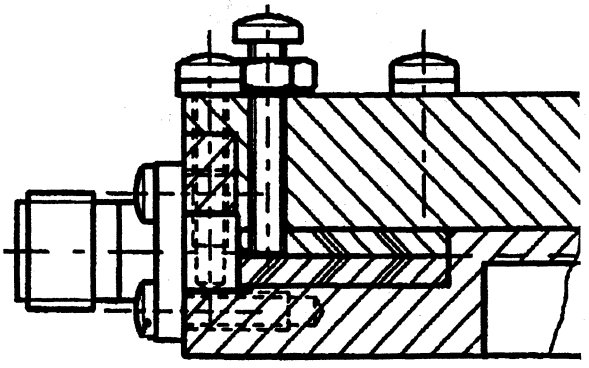

Fig. 6. A tuning screw was mounted next to the coaxial input for the fourth hybrid arm to further improve isolation by adjusting the port impedance.

It seems that the trial was succesful indeed. The plot in Fig. 7 certifies the obtained isolation of 97 dB, actually

a result which approached the limits of the vector network analyzer if no averaging over time were used. Note that the x-axis scaling has been changed from the previous plot in order to be able to visualize the whole rejection performance. Again here the wanted coupling between ports 1-2 and 2-3 stays stable.The measured values were demonstrated to be typically 3.15 dB (3.08 dB best case) and had a data spread, as is seen in Fig. 8, of about 0.1 dB over the entire frequency band. The physical nature of the ring hybrid with its transmission lines dictates the phase behaviour where nothing surprising came up. Fig. 9 illustrates the obtained response for the wanted coupling from which a group delay estimate of 185 ps can be calculated.

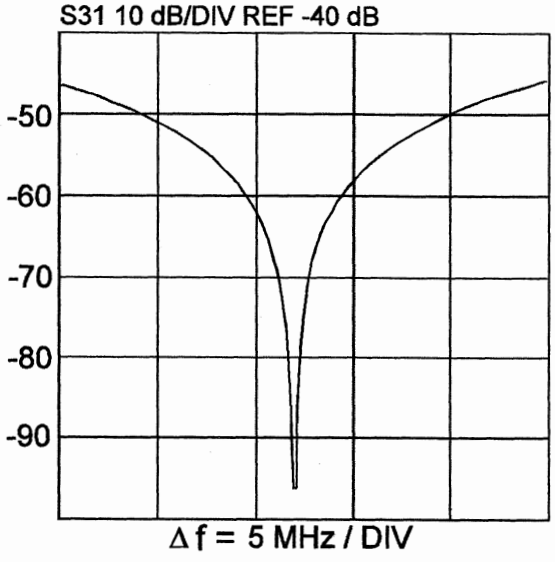

Fig. 7. After optimizing the tuning screw depth we get about 97 dB of isolation between hybrid ports 1 and 3 and at the same time maintain the wanted coupling at 3.1 dB.

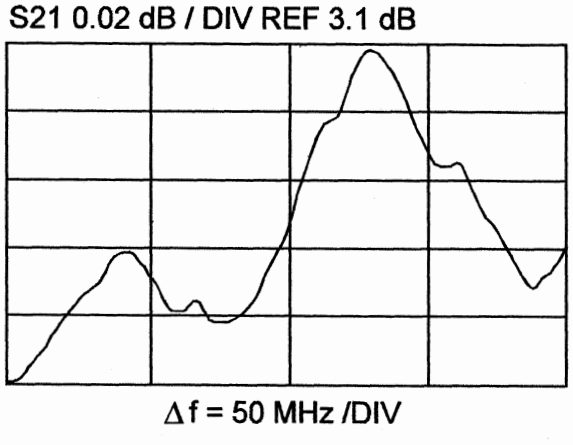

Fig. 8. A careful construction also pays for itself in the wanted coupling (from port 1 to port 2) where we have a maximum variation of 0.1 dB peak-to-peak and an intrinsic attenuation of 3.1 dB.

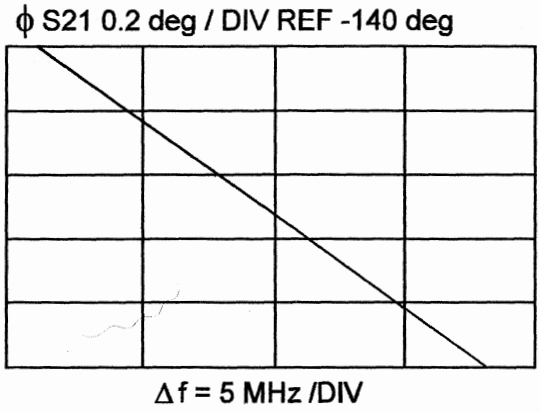

Fig. 9. As the physical nature of the coupling implies we have a linear phase shift or a constant group delay as a function of frequency offset near the band center for the wanted coupling.

6. CONCLUSIONS

Based on our experimental research, it looks highly possible to design and construct a ring hybrid which is suitable as a high isolation power divider e.g. in a hydrogen maser environment. The typical rejection between de-coupled branches can be brought to 90 dB and more if a very precise mechanical lay-out is followed - respecting an uncertainty requirement of 10 μm - and a conducting center block is used to limit the stray coupling across the ring. Additionally, a fine tuning for the unused port impedance is necessary. This is easily accomplished e.g. by a 2 mm machine screw mounted next to the coaxial-to-stripline launcher.

7. REFERENCES

[1] Collin R. : Foundations for microwave engineering, McGraw Hill 1992, 2nd edition

[2] Collin R.: Theory of guided waves, McGraw Hill 1990

[3] Kusters J. : Precision Time and Frequency Sources, McGraw-Hill 1994, 2nd edition

[4] Ludwig R. and Bretchko P.:RF Circuit Design, Prentice Hall, 2000

[5] Matthaei G., Young L. and Jones E.: Microwave Filters, Impedance Matching Networks and Coupling Structures, Artech House (reprint) 1990

A SYNCHRONOUS MULTIPLE FREQUENCY SYNTHESIZER FOR ATOMIC FOUNTAIN FREQUENCY STANDARDS

Claudio Calosso, Giovanni A. Costanzo, Andrea De Marchi
Politecnico di Torino, C.so Duca Degli Abruzzi 24
I-10129 Torino, Italy

Abstract

In this paper a Direct Digital Synthesizer (DDS) and Programmable Logic Device (PLD) based application for cesium atomic fountain handling is presented. The Politecnico di Torino is realizing a cesium fountain frequency standard in collaboration with N.I.S.T (U.S.A) and I.E.N. (Italy). A multiple frequency synthesis system in the 60-80 MHz band is required. These frequencies are necessary to drive acousto-optic modulators, in order to properly control laser beams involved in cooling, launching, post-cooling and detecting operations. For adequate management of cesium atoms, specifications must be met for amplitude (50 dB of dynamic), frequency (1 Hz resolution, 60-80 MHz range, -40 dBc spurs) and timing (less than 10 ms settling time, 0.1 ms resolution, less than 0.1 ms jitter between channels). Commercial synthesizers meet frequency and amplitude conditions, but problems arise about their synchronization. For this reason a dedicated system was realized. The latter consists of six identical channels driven by a PLD which implements a highly parallel architecture. This guarantees speed (up to 2 millions new frequencies per second) and low jitter between channels (less than 5 ns) as well as amplitude and frequency sweep and PC interfacing capabilities. The core of each channel is a fast 32 bit DDS which makes possible a baseband synthesis. A 80 MHz low pass filter attenuates the alias spectral lines and its analog transient is in charge of the settling time (less than 100 ns). Amplitude changes are possible thanks to a 8 bit digital to analog converter combined with a digital attenuator. A monolithic amplifier gives the appropriate power level to the synthesized signal.

1. INTRODUCTION

Laser frequencies involved in cesium atoms manipulation are obtained using AOM. Three different lasers (Z_{down}, Z_{up}, $X+Y$) with fixed amplitude and fixed frequency are mixed with RF signals which realize amplitude and frequency specifications. A proper fountain operation can be achieved with a multiple RF synthesis system able to perform a sequence of steps each yielding a signal of the type

$$(A_i + \alpha_i t)\sin\left(2\pi(f_i + \beta_i t)\, t\right) \quad t_{n-1} < t < t_n \qquad (1)$$

where $(A_i + \alpha_i t)$ is the amplitude and $(f_i + \beta_i t)$ is the frequency of the signal generated by the channel i during the step n. This is a generalization of the signals required by the atoms. Only one step (the post-cooling and launching step) requires different frequency and amplitude sweeps ($A_i \neq A_j$, $f_i \neq f_j$, $\alpha_i \neq 0$, $\beta_i \neq 0$); other steps require only fixed amplitude and frequency synthesis or no synthesis and this is easily achievable by setting one or more coefficients equal to zero. On the other hand more complex synthesis realization (i.e. arbitrary amplitude and frequency sweeps) can be approximated by a sub-sequence of linear sweeps.

Conceptually and phisically the synthesis system is divided in an analog and in a digital part. The first one basically realizes frequency and amplitude specifications whereas the second one satisfies timing requirements.

2. ANALOG PART

The analog part corresponds to a set of six identical synthesis channels and realizes sinusoids like

$$A\sin(2\pi f_0 t) \qquad (2)$$

where the amplitude A and the frequency f_0, which meet fountain specifications, are imposed by the control unit. (Each channel has no intrinsic sweep capabilities).

The core of each channel is a 180 MHz Direct Digital Synthesizer. It makes possible a baseband synthesis, realizing some advantages about complexity, speed and space. The system is sympler, because frequency up-conversion is avoided, and faster, because of the larger band of the analog part. On the other hand particular care is required by the low-pass filter: it has to have a very narrow transition band, in order to attenuate the first alias spectral line which is at 100 MHz for the maximum output frequency (80MHz). A 7th order elliptic filter is used and care was spent in components disposition in order to minimize parasitic effects. Our DDS use accentuates spectral spurs, but fortunately, the biggest

of them are located below frequency range of interest. High pass filter is able to attenuate them and spurs specifications are met.

The DDS used can not change amplitude digitally, so external circuitry was added. The current flowing through an external resistor is proportional to the sinusoid amplitude. This resistor was replaced by a Digital to Analog Converter with current output.This allows digital amplitude changes in a 6 dB range. Higher variations are possible, but not convenient, because they would reduce the signal to noise ratio. So a digital attenuator was added after the filters. It's used at 6dB steps and it provides high amplitude variations. The amplitude A of the output sinusoid can be expressed in the form

$$A = k\,D\,2^E \qquad (3)$$

where D is the DAC data, E is the Digital Attenuator data and k is a multiplicative constant. The amplitude is physically expressed in floating point, where DAC provides the mantissa and the digital attenuator provides the exponent. In this manner the relative resolution is kept constant. Unfortunately, the DDS amplitude control loop has longer settling time ($2.5\,\mu s$) than the digital attenuator and glitches are present when the exponent changes, but experimental results show how this problem doesn not affect the fountain operation.

A space saving monolithic amplifier guarantees the appropriate output power level. Low gain is required, because the baseband synthesis scheme, in comparison with frequency up-conversion schemes, slightly attenuates the signal. Particular care was spent in de-coupling the power supply in order to minimize crosstalk between channels that may be a problem when channel frequencies are different (i.e. during the launching step).

Overall, a channel is comparable with a commercial synthesizer for amplitude and frequency features, but it presents better timing control characteristics.

3. DIGITAL PART

The control unit principally satisfies time requirements: its principal goal is to drive channels and provide synchronous signals at the same time. Furthermore, the control unit has to quickly compute arithmetical progressions necessary for amplitude and frequency sweep.

The digital part takes advantage of the last years' remarkable improvements of PLD. The great number of gates, the efficient memory and specialized logic functions as well as more and more powerful development tools allowed a profitable use of this technology for fountain purposes. In this manner, instead of microcontrollers and Digital Signal Processors, equivalent functional blocks are implemented:

Time resolution	$1\,\mu s$
Jitter between channels	$< 5\,ns$
Settling time	$< 100\,ns$
Step lenght	$1\,\mu s \div 1\,hour$
Max step number	$19 \div 42$
Frequency resolution	$50\,mHz$
Spurious spectral lines	$< -40\,dBc$
Crosstalk	$< -90\,dBc$
Amplitude range	$> 50\,dB$
Size	$11\,cm$ x $18\,cm$ x $7\,cm$
Power consumption	$20\,W$

Table 1: Synthesis system ratings

Finite State Machines for data flow management and adders for arithmetical sequences computations. Instead of software, hardware is direcly implemented. Development time was little longer, but advantages are many. They come from the intrinsic parallel nature of the system: six identical channels that execute at the same time the same operations aren not well driven by a microcontroller which has basically a sequential operation. On the contrary a good parallel architecture is allowed by the remarkable PLD capacity which made possible, for the single channel structure (one data memory, one 16 bit adder for amplitude sweep, one 40 bit adder for frequency sweep together wity several data transfert registers), a times six physical multiplication. In this manner six identical channels driven by the same control signals in a structure with definite propagation delays make up a system in which sinchronization of outputs is a natural consequence. Further speed increase is derived by a three levels pipelined data flowing: while data is transferred to channels, new amplitudes and frequencies are computed and data for the following step are loaded from memories. Finally, high number of programmable pins makes possible to preserve the parallel nature outside the PLD: each device (DAC, DDS, digital attenuator) of each channel has a dedicated data bus, with beneficial effects on speed, simplicity and data transfer syncronization.

4. RESULTS

The main characteristics are reported in tab.1 and are confirmed by the following figures.

Small physical dimension of the system and shared timing signals allow small jitter between channel signals (less than $5ns$). The lenght of each step is limited on the lower side by the speed of data transfer from memories and on the upper side by the 32 bits of the timer. For simplicity, time resolution was limited to the minimum step lenght ($1\mu s$). Settling time is due to filters or DACs transients. In fact it's possible to swicth off sinusoids setting to zero both the

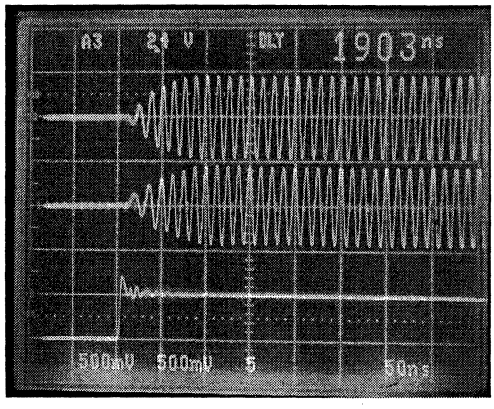

Figure 1: Timing of two synthesized signals and a digital output. Vertical scale: 500 mV/div for the sinusoids, horizontal scale: 50 ns/div.

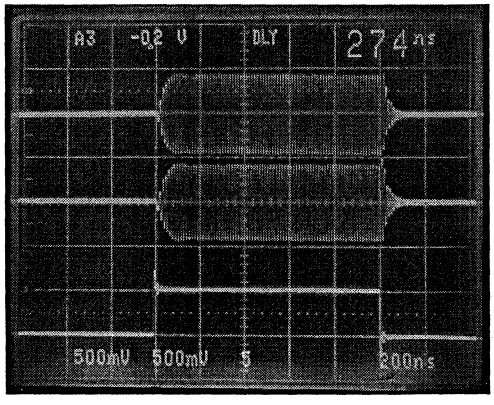

Figure 2: Example for the minimun step lenght ($1\mu s$). Vertical scale: 500 mV/div for the sinusoids, horizontal scale: 200 ns/div.

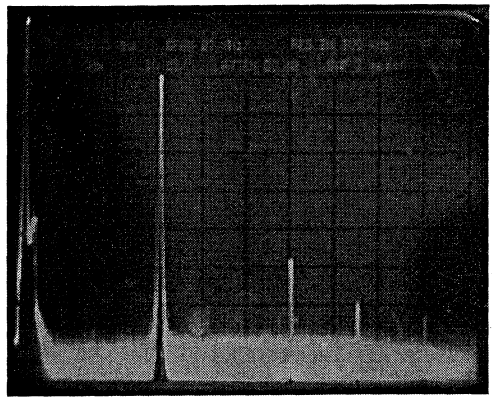

Figure 3: Power spectrum for 60 MHz synthesis. Vertical scale: 10dB/div, horizontal scale: 20 MHz/div, central frequency 100 MHz.

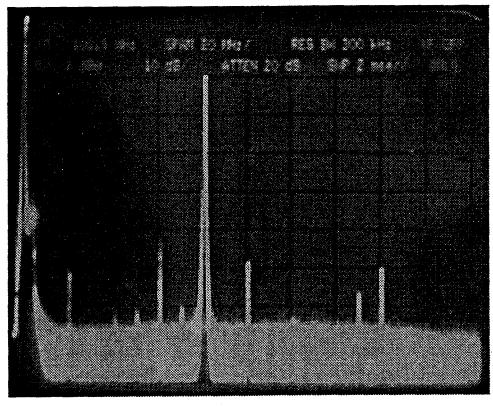

Figure 4: Power spectrum for 80 MHz synthesis. Vertical scale: 10dB/div, horizontal scale: 20 MHz/div, central frequency 100 MHz.

frequency and the amplitude of the sinusoid.

Fig.1 and fig.2 show 80 MHz outputs of two channels togheter with a digital syncronization output signal in the case of maximun output frequency and the minimun step lenght. The first one is focused on the initial part and it shows synchronization and settling time.

Fig.3 and fig.4 show power spectrum for 60 and 80 MHz synthesis. The first one looks better than the second one, but it's a particulare case, because the output frequency is one third of the clock frequency. So the second harmonic of the first alias spectral line coincides with the output frequency and the second harmonic coincides with the first alias spectral line (120 MHz).

5. IMPROVEMENTS

The presented system derives qualities (i.e. baseband synthesis) and restrictions (i.e. external amplitude circuitry) form the utilized DDS. Fast development in telecommunication area produced improvements also in DDS devices. By using more modern and faster DDS (i.e. AD9854) it's possible to relax filters specifications, to eliminate the external circuitry for amplitude variations, to set digital part free from frequency sweep computation and to reduce spurs and phase noise thanks to faster onboard DACs with increased bit number.

References

[1] S.R. Jefferts, D. Meekhof, L.W. Hollberg, D.Lee, F.L. Walls, R.E. Drullinger, , C. Nelson, F. Levi, T.E. Parker, "NIST Cs fountain frequency standard: preliminary results", IEEE IFCS, pp.2-5, May 1998, Pasadena

[2] S.R. Jefferts, D. Meekhof, J.H. Shirley, T.E. Parker, F.Levi, "Preliminary accuracy evaluation

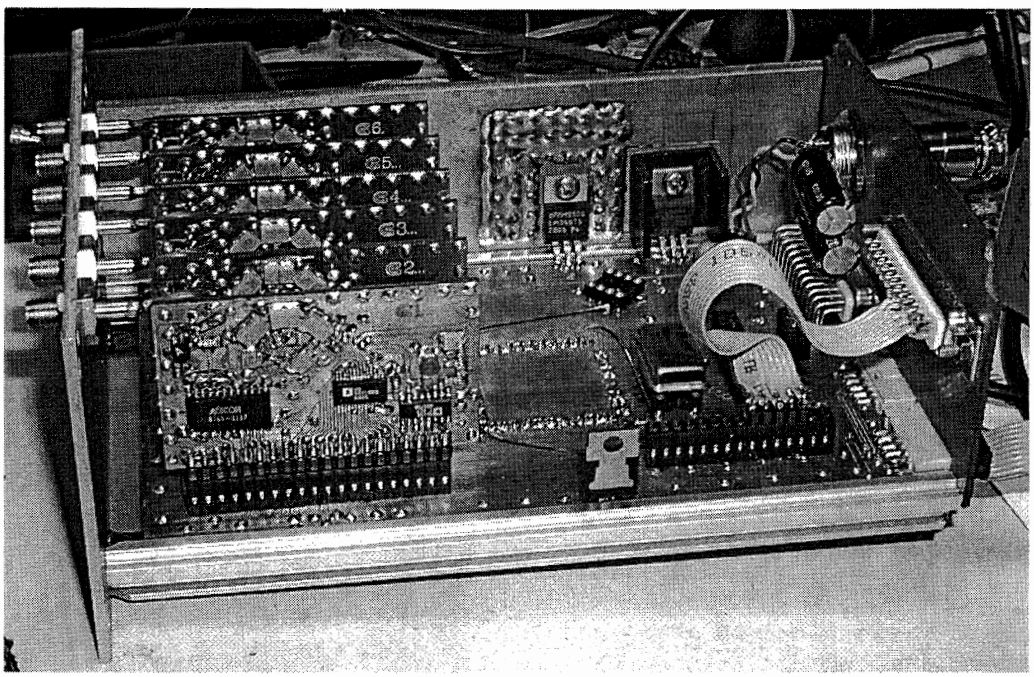

Figure 5: The synchronous multiple frequency synthesizer

of a Cs fountain primary frequency standard at NIST", Proc. 1999 Joint Meeting EFTF-IFCS, pp.12-15, April 1999, Besanon

[3] F. Levi, A. Godone, L. Lorini, D. Calonico, "Progress toward the realization of a cesium fountain frequency standard at IEN", Proceeding of the 14th EFTF (2000)

PROGRESS REPORT ON THE CS FOUNTAIN FREQUENCY STANDARD AT THE POLITECNICO DI TORINO

Giovanni A. Costanzo, Claudio E. Calosso, Andrea De Marchi

Dipartimento di Elettronica, Politecnico di Torino
Corso Duca degli Abruzzi 24
I 10129 – Torino – Italy

1. ABSTRACT

The Politecnico of Torino, within a joint collaboration with NIST (Boulder, USA) and IEN (Turin, Italy), is currently developing an atomic frequency standard based on the fountain scheme. The physical package is developed at NIST and was reproduced in 3 copies, one for each laboratory involved in this joint research program. A complete experimental apparatus was realized, useful to perform basic experiments on cooling, launching and microwave excitation of Cs atoms.
The whole set-up and some preliminary results concerning this frequency standard are here reported.

2. INTRODUCTION

A few years ago the technique of laser-cooling was presented to the scientific community as a possible solution to overcome the limits of Cs frequency standards based on thermal beams. Presently Cs atoms can be cooled down to a few microkelvin thanks to sub-Doppler cooling mechanisms which allow velocities of the order of cm/s and long interaction times with the microwave interrogating signal. As a matter of fact, neutral atoms manipulation opened a new way to reach accuracies in the low 10^{-15} range.
A full analysis of the fountain experiment can be found in several papers [1,2] with a schematic diagram of the main subcomponents. The fountain apparatus uses a (0,0,1) geometry with four laser beams in the x-y plane and two vertical along the z axis. Two identical copper cavities are used to perform state selection and Ramsey type interaction. In order to improve laser beam quality and MOT characteristics an optical setup, using polarization maintaining optical fibers, is used.
All parameter affecting the cold sample are optimized by a PC which controls a synchronous multiple frequency synthesizer [3], in order to get the best TOF signal. In this manner a temperature of a few microkelvin and long TOF duration have been achieved for the atomic sample.

3. THE EXPERIMENTAL SET-UP

3.1 The physical package

Four main regions constitue the physical structure of the fountain: the trapping zone, upper and lower detection zone, drift region (see Fig. 1). The trapping zone is filled with a low pressure Cs vapor through a simple oven. This relatively high Cs pressure region is separated from the neighboring vacuum regions by graphite getters allowing a differential Cs pressure between the trapping zone and the drift zone where the long time of flight for the atomic samples need a very low pressure.

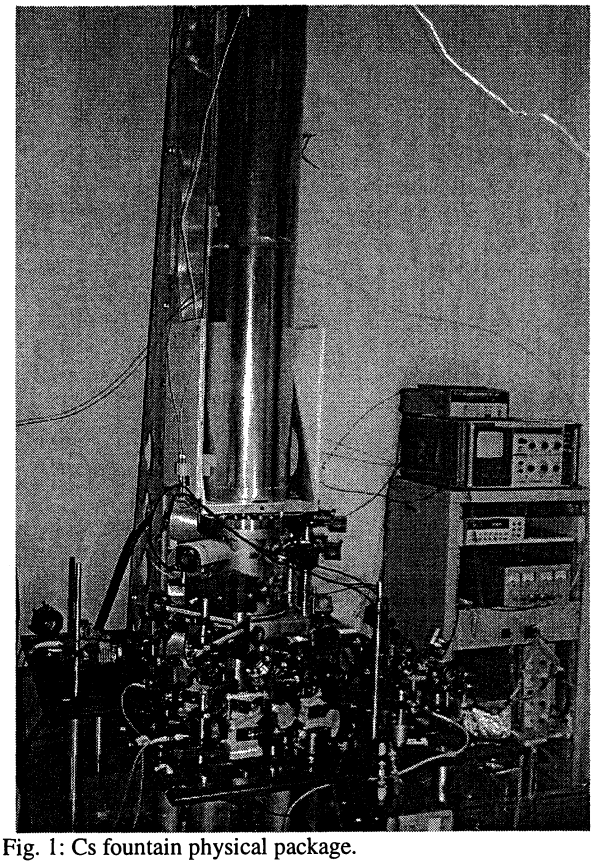

Fig. 1: Cs fountain physical package.

Two cylindrical cavities are set along the drift path in order to perform atomic state selection and Ramsey interaction process. These cavities [4] are finely tuned by temperature: twisted wires, directly wound around the cavities and the drift tube, act as heater. The latter is switched off, during the atoms to microwave interaction time, to prevent residual magnetic field which can affect C-field value, reducing at the same time magnetic uniformity.
The 1m tall drift zone is surrounded by four cylindrical moly-Permalloy magnetic shields. Inside the innermost shield a cylindrical solenoid generates the C-field necessary to separate the Zeeman sublevels.
No magnetic shields are used for the loading zone. A set of three mutually orthogonal compensation coils are placed close to the trapping region. A digitally controlled current supply is then used for static magnetic field optimization across the loading volume. Since optimizing the magnetic field null at the center of the trap is important for postcooling efficiency, it is performed by optimizing the cloud return signal. Furthermore, anti Helmholtz coils are used to generate the static quadrupole magnetic field necessary to build the magneto-optical trap (MOT).

Two pairs of mutually orthogonal coils are wound close to the drift tube. These will permit an easy check of the field uniformity by low frequency transition excitation method as described in Ref. 2.

3.2 The laser set-up

In this experiment the optical set-up is rather complex. In order to perform basic cooling and tossing experiments the laser system must be conceived maintaining a number of degrees of freedom.
Nowadays semiconductor lasers in the near infrared region are a useful tool in Cs spectroscopy. Extended cavity laser diodes are commonly used. In our system a DBR diode laser is offset locked to the (F=4-F'=5) transition using the saturated feature absorption of a Cs cell which is surrounded by a magnetic shield to prevent the frequency instabilities due to the variations of the magnetic field in the laboratory environment. A few percent of the total power of the laser beam are inserted in an electro-optical modulator driven by a 15MHz synthesizer.
In this manner the common FM sideband method is applied without the modulation of the diode laser current which would introduce detrimental sidebands in the main beam. The saturated absorption signal is then detected by a fast photodiode and subsequently demodulated in order to get the error signal which is used to control the laser current and the PZT voltage through the loop filter. From the analysis of the Fourier Transform of the error signal in closed loop conditions it is possible to assume a value of several tens of kHz for the loop bandwidth.
A master-laser configuration is then used. This method transfers the spectral purity of the low power stabilized master laser (ML) to the higher power of the slave injected laser (SL). For this purpose only several microwatt of the ML are necessary and, moreover, no servo electronics.
The laser beams of the slave lasers are then modulated by acousto-optical devices to get appropriate frequency detuning and power level. Polarization maintaining fibers are used to spatially filter the beams and also to allow convenient distribution of each laser beam from the optical table to the physical apparatus. Finally a fourth laser is used to repump the atoms from F=3 to F=4 level. A schematic drawing of the laser set-up is depicted in Fig.2.
In this scheme, the main problems are the long term instabilities of the laser power and the poor fiber coupling efficiency (about 40%). The former is mainly ascribed to the beam drift when the temperature variations slightly change the relative positions of the optical paths. A useful laser power of $4mW/cm^2$ is obtained in a nice gaussian beam of the order of 15mm ($1/e^2$ points).
In order to properly drive the AOMs, which control the laser beams involved in cooling, launching, post-cooling and detecting procedures, a multiple frequency synthesis system in the 60-80MHz range was realized. For adequate management of Cs atoms, specifications must be met for amplitude (50 dB of dynamic range), frequency (1Hz resolution, 60-80MHz range, spurs at -40dBc) and timing (less than 10μs settling time, 0.1μs resolution). Commercial synthesizers meet frequency and amplitude conditions, but problems arise about their synchronization. For this reason a dedicated system was realized [3]. The latter consists of six identical channels driven by a programmable logic device which implements a highly parallel architecture. This guarantees speed (up to 2 millions new frequencies per second) and low jitter between channels (less than 5ns) as well as amplitude and frequency sweep and PC interfacing capabilities.

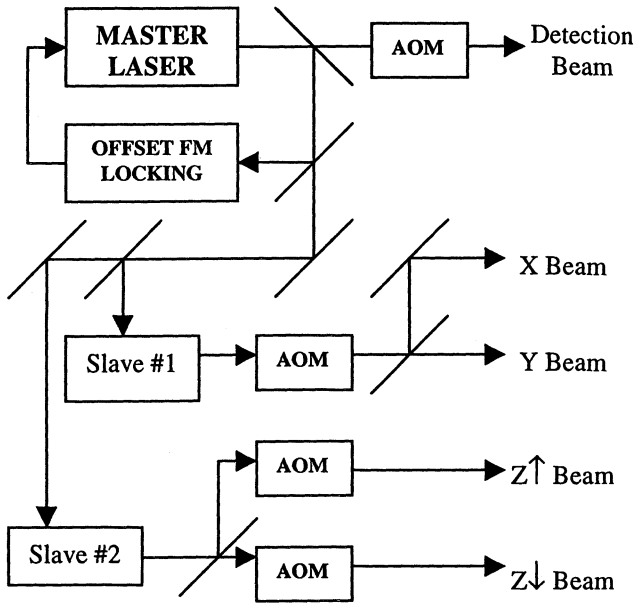

Fig.2: schematic drawing of the master-slave lasers configuration.

3.3 Fountain operation sequence

A magneto-optical trap with post-cooling is used to capture and cool atoms to a few μK. Atoms are then accelerated upwards by detuning the vertical beams symmetrically by Δν: a moving frame is created in order to toss the atoms at velocity $v=\lambda\,\Delta\nu$ in the laboratory frame.
The intensity and frequency of the lasers are controlled by acousto-optical modulators performing a postcooling process. The latter is accomplished by power reduction and frequency detuning of each trapping laser. After the loading-launching sequence atoms enter the shielded region where a first microwave cavity is used as state selection. A π-pulse at 9.192GHz moves the atoms in the $|F=4,m_F=0\rangle$ to the $|3,0\rangle$ state. All the remaining atoms in $|F=4, m_F\neq0\rangle$ are then pushed away applying an optical pulse.
Only atoms in $|3,0\rangle$ state move to the second cylindrical cavity where the Ramsey interrogation process is accomplished thanks to the parabolic flight of the atomic sample.
Atoms detection and normalization is finally achieved after the detection of the $|F=4\rangle$ and $|F=3\rangle$ populations in a scheme similar to that used in the NIST fountain. The population of both the hyperfine levels is measured and Ramsey pattern is given after normalization which reduces signal variations due to shot-to-shot atom number fluctuation.

4. TRAP CHARACTERIZATION

Optical molasses characteristics were investigated in order to understand if the whole set-up works properly. Among the possible measurements, loading time and molasses temperature are common tests which can give prominence to some possible problems connected to the laser set-up and timing sequence.

When loading time is increased atomic fluorescence is improved because the collected atoms increase. The cycle time in operation is necessarily decided as result of a compromise between Dick effect and signal amplitude considerations. It is therefore important to determine how the signal varies with loading time. A typical curve can be found in Fig.3.

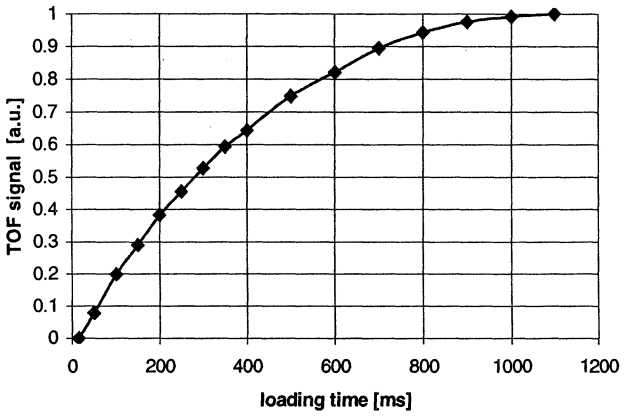

Fig.3: TOF signal vs. loading time (oven temperature is 35°C).

When the MOT is released the final temperature attained can be evaluated from the width of the TOF signal. Because the temperature is correlated to the cooling and postcooling process it is strongly recommended to investigate into the achieved molasses temperature. The latter must be minimized when long time of flight of the sample is the primary goal. In fact typical temperature of a few microkelvin is necessary when transversal velocity of about 2cm/s must be met in order to improve resonance signal minimizing the lost atoms. Fig. 4 shows a record of the molasses temperature obtained when post-cooling process is increased.

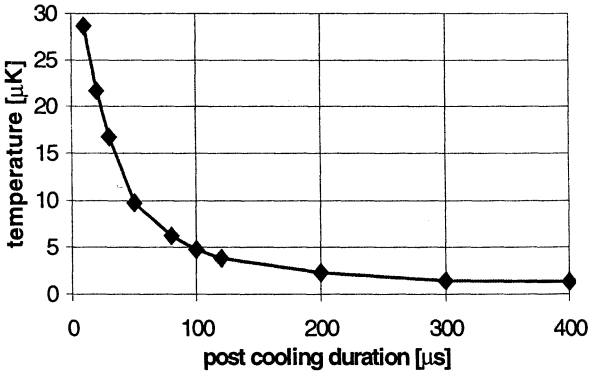

Fig. 4: molasses temperature vs. post cooling time measured via the TOF technique.

Time of flight technique is used because it gives primary information on the temperature of the molasses. Furthermore the sub-Doppler friction coefficient α can be evaluated from the previous curve. A value of the order of $6 \cdot 10^{-21}$kg/s was measured in good agreement with the results found in the scientific literature. Fig.5 reports the different behavior of the TOF signal when post cooling time duration is increased from a few μs to 300μs.

The time of flight distribution is obtained for atoms collected through MOT, released from an optical molasses after post cooling process and, finally, detected 25cm below the loading zone. As it can be seen in the figure, when post cooling duration is increased it follows that the signal to noise ratio is improved because molasses temperature decreases.

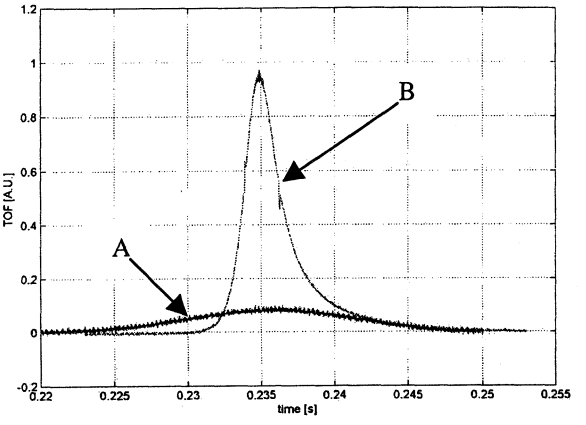

Fig.5: typical TOF signals measured after molasses release. The two curves are reported for comparizons when postcooling is changed from a few μs (curve A) to 300μs (curve B). Curve B corresponds to a typical 2μK molasses temperature.

5. ATOMS TOSS AND DETECTION

The usual moving frame technique is used to toss the atoms above the cylindrical cavity where the Ramsey interaction process would be accomplished. A high reduction of the TOF signal was observed when atoms performed long parabolic flight. Fig.6 reports the detected atom number as a function of the time of flight: TOF signals are recorded for different toss height corresponding to different toss velocities.

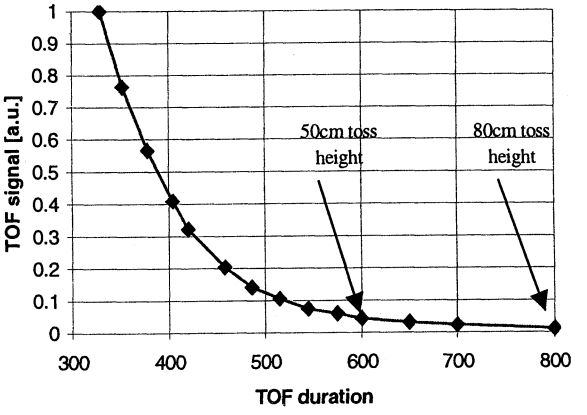

Fig.6: TOF signal corresponding to incresing TOF duration. The measurement at 800ms of TOF corresponds to a toss height of 20cm above the cylindrical Ramsey cavity.

Only 1% of the initial number of atoms is detected when apogee is about 80cm above the loading zone. This is mainly attributed to the inaccurate alignment of the laser beams with the gravitational force vector. Moreover, some misalignements arise from the fact that the atoms are trapped some mm's outside the cylindrical symmetry axis.

Finally, even if the atomic samples reached the cylindrical cavity where microwave excitation of the atomic sample can be performed (Ramsey cavity is crossed after 0.7s of TOF duration), the signal detected was not sufficient to record a first Ramsey pattern.

CONCLUSIONS

In this paper we reported the activity research related to the development of a Cs fountain at the Politecnico di Torino. A description of the whole apparatus usefull to perform basic Ramsey interaction experiment was shown with results concerning trap characterization. First atomic launch and detection were also here reported.

ACKNOWLEDGEMENTS

Authors would like to thank S.R. Jefferts (NIST, USA) and F.Levi (IEN, Italy) for their invaluable help in the realization of the fountain and for scientific discussions.

REFERENCES

[1]S.R. Jefferts, D. Meekhof, L.W. Hollberg, D.Lee, F.L. Walls, R.E. Drullinger, , C. Nelson, F. Levi, T.E. Parker, "NIST Cs fountain frequency standard: preliminary results", IEEE IFCS, pp.2-5, May 1998, Pasadena; and also in
S.R. Jefferts, D. Meekhof, J.H. Shirley, T.E. Parker, F.Levi, "Preliminary accuracy evaluation of a Cs fountain primary frequency standard at NIST", Proc. 1999 Joint Meeting EFTF-IFCS, pp.12-15, April 1999, Besançon
[2]G.A.Costanzo, D.Meekhof, S.R.Jefferts, A.De Marchi, "An old method for magnetic field mapping applied in a new way in a Cs fountain frequency standard", Proc. 14th European Frequency and Time Forum, pp.494-497, March 2000, Turin
[3]C. Calosso, G.A.Costanzo, A.De Marchi, "A synchronous multiple frequency synthesizer for atomic fountain frequency standards", in these Proceedings
[4]S. Jefferts, R.E. Drullinger, A. De Marchi, "NIST Cs fountain microwave cavities", Proc. IFCS, pp.6-8, May 1998, Pasadena

THE DUAL MIXER TIME DIFFERENCE AT NIMB

Anca Niculescu
National Institute of Metrology, Sos. Vitan – Barzesti 11, Bucharest, Romania
Liviu Giurgiu, Octav Gheorghiu
National Institute of Laser, Plasma and Radiation Physics, PO Box MG 36,Bucharest, Romania

ABSTRACT

In order to upgrade the short-term frequency stability measurement capabilities of the National Institute of Metrology, for time intervals between 1 and 1000 s, we have developed the measurement system based on the well known Dual-Mixer Time-Difference (DMTD) scheme.

We report the results obtained with this frequency system working at 10 MHz with a 1 Hz beat note

1. INTRODUCTION

The measurements of the frequency stability could be done as well in the frequency domain as in the time domain. Time domain in contrast to frequency domain deals with the effects of averaging over different values of time,τ. Time domain characterization conventionally uses statistics computed from a discrete time series of average frequency samples obtained from a digital counter. This one is used to measure the beat note between the oscillator under test and a reference oscillator or the time difference between zero crossing of these beat supply by two identically channel.

The conventional method used in time domain characterization is to heterodyne the original signal down to an arbitrary low beat frequency by mixing a reference signal with one or two other test signals. The low frequency beat signal reproduces faithfully the original frequency fluctuations of the test signals, which is typically measured with a digital counter.

The commercial counter devices have "dead time" which destroys the opportunity to get to "true" time fluctuations. Also, when making measurements between a pair of frequency standards or clocks is desirable to have less noise in the measurement system than the composite noise in the pair of standards being measured.

The measurement system proposed in this paper have the advantage that satisfied these requirements.

2. DUAL MIXER TIME DIFFERENCE SYSTEM

The DMTD (Dual Mixer Time Difference) system proposed by D.W.Allan and H.Daams [Ref.1] is a system very convenient when we want to measure the frequency stability of the quasi-synchrone signals. The measurement of frequency stability according to the DMTD method is not performed directly against another frequency reference source, at the same nominal frequency, but indirectly, by means of a third source, usually called common oscillator, having a little frequency offset $\delta\nu$, (typically 1 Hz), from the nominal frequency of the reference and source under test. This system open the door to make measurements of frequency stability for sample times as short as a few milliseconds as well as for longer sample times and all without dead time.

Unlike the system proposed by D.W.Allan and H. Daams we are made some modifications to our DMTD system:

- We use two phase shifters with complementary action on the beat signals instead the high frequency phase shifter which could be o source of medium and long term drift ;
- We interposed a second order filter, with cut frequency f_c = 12 Hz, between the phase shifter and the zero crossing detector on each channel;
- We used a frequency deviation multiplier (x 100).

A block diagram of the Dual - Mixer Time -Difference system is shown in Fig.1. The signal from the common oscillator is compared to the reference and also to the under test signals by means of a pair of double–balanced mixers. The signals from the Oscillators 1 and 2 go to the ports of a pair of double balanced mixers MX1 and MX2 (DBM166). The signal from the common oscillator goes to a power splitter and two identically signals obtained are fed to the remaining other two ports of the pair of double balanced mixers. This common oscillator's frequency is offset by a desired amount, from the frequency of the other two oscillators, producing the same beat frequency with Oscillators 1 and 2. These beats will be out of phase by an amount proportional to the time difference between Oscillators 1 and 2, when running as clocks, and will differ in frequency, by an amount equal to the frequency difference between Oscillators 1 and 2.

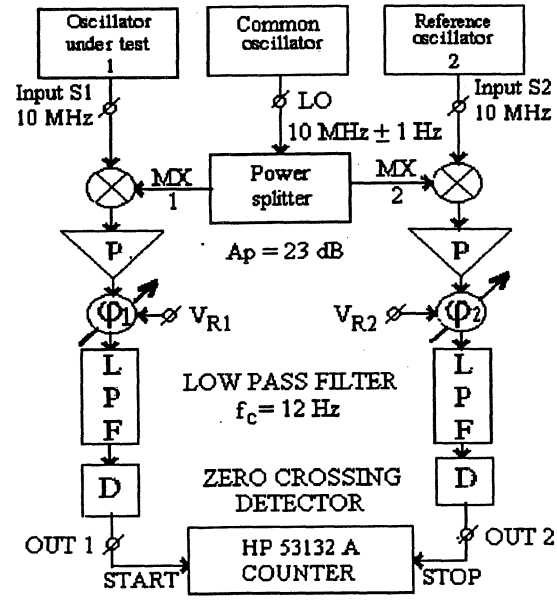

Figure 1. The block diagram of our dual mixer time system

Two phase shifters was inserted, as illustrated in Fig.1, to adjust the phase in order to obtain small time interval readings on the counter. This adjustment sets up the condition that the noise of the common oscillator tends to cancel when

the time difference is determined – depending on the level and the type of noise as well as the sample time involved as described below. Nevertheless in a real measurement situation we must pay attention to the common oscillator contribution because an however small frequency deviation between the two clocks produces a progressive evolution of the time interval between the two low frequency beat notes from zero up to $1/\delta_\nu$, to restart again from zero and so on. This problem is particularly serious for long-term frequency measurement. Another way to face the problems is the use a frequency synthesis of a dedicated common oscillator with a precise frequency offset from the reference oscillator, and a low phase noise contribution [3].

The DMTD system has two identically channels, but for simplicity, the explanation will be given only for one channel.

The beat signal go to the input of a preamplifier P (OP27) with a gain A_p =23 dB. The amplified signal is fed to a phase shifter which adjust the phase by using a reference voltage V_{R1} (V_{R2}). By construction the reference voltage V_{R2} = -V_{R1} which leads to φ_2 = - φ_1. After that, the output signal goes to a low pass filter and to zero crossing detector. The time interval between the two beat signals is measured with a time interval counter. The start port of a time interval counter is triggered with the zero crossing of one beat and the stop port with the zero crossing of the other beat. If the phase fluctuations of the reference oscillator are small during this time interval as compared to the phase fluctuations between Oscillators 1 and 2 over a full period of the nominal beat frequencies, the noise of the reference oscillator is insignificant in the measurement noise error budget [Ref. 2]. This means that the noise of this oscillator can be worse than either Oscillators 1 and 2 and still not contribute significantly. The experimental verification confirms the noise rejection of the local oscillator. For short measure times (τ~ few seconds) this supposition is confirmed, but not in the case of long measurement time.

In a real measurement situation we must pay attention to the common oscillator contribution because an however small frequency deviation between the two oscillators produces a progressive evolution of the time interval between the two low frequency beat notes from zero up to $1/\delta t$, to restart again from zero and so on.

This problem is particularly serious for long-term frequency stability measurement because the noise floor of the system fluctuates along the time while, for short-term measurement, an initial adjustment of the phase shifter, to reduce near zero the time interval between beat notes, may be sufficient to reject the common oscillator noise. A way to face the problems is the realization by frequency synthesis of a dedicated common oscillator with a precise frequency offset with respect to the reference oscillator, and a low phase noise contribution [Ref.3]

3. EXPERIMENTAL RESULTS

The noise floor of the DMTD system has been evaluated supplying the same quartz oscillator signal in place of the reference and in measurement oscillators. As common oscillator we used a 10 MHz signal from an atomic frequency standard HP 5071A which was multiply by 100 (using a laboratory frequency deviation multiplier) before being apply to the ports S1 and S2.

The time interval between the two beat signals was measured with a time interval counter HP 53132A, synchronized with 10 MHz signal generated by the same atomic frequency standard HP 5071A. The data acquisition was made by using a personal computer with an RS-232 interface and a dedicated program write for this purpose. The formula used to calculate the stability floor of the measurement system, in Allan variance terms, is:

$$\sigma_y(\tau) = \frac{1}{2\tau\, T_B\, \nu_0}\sqrt{<\Delta_2^2(\delta t)>} \qquad (1)$$

where T_B is the beat period, τ (= nT_B) measure time, ν_0 the frequency of the oscillators under test and $\sqrt{<\Delta_2^2(\delta t)>}$ is the r.m.s. value of the second difference on δt.

The two samples Allan deviation reported in Fig. 2 summarizes the measurement results obtained in these conditions.

The curve *a* reports the results of a time series data set taken one second apart. The plot clearly shows a white phase noise behavior, inversely proportional to the integration time τ, determined from the dominant additive amplitude white noise of the zero-crossing detectors. The trend for the curve *a* is:

$$\sigma_y(\tau) = 3.8\times10^{-14}\cdot\tau^{-1} \qquad (2)$$

Our prototype was not thermal isolated or temperature controlled. A measured temperature sensitivity of some picoseconds per Celsius it is to be expected [Ref. 6]. The short-term frequency stability of a couple of commercial cesium frequency standards HP 5071A (with high performance beam tube) has been measured using this DMTD system. The curve *b* in Fig.2 shows the results of this measurement. The value reported is the sum of the frequency instabilities of the phase-input signals. In this case, the common oscillator was the quartz oscillator used above to supply the ports S1 and S2. Before starting the data logging, the variable phase shifter has been adjusted to have nearly in phase input signals. The initial time deviation between the two clocks was 38 ns. Along the measurement the two clocks walk away each other reach a time deviation of about 43 ns after 10000 s. In this situation the common oscillator instability gives negligible contribution along the measurement and the noise floor of the DMTD system is low that of clocks. Frequency stability for averaging time between 1s and 1000 s clearly shows a behavior (white frequency noise) typical for passive standards. The trend for the curve *b* is:

$$\sigma_y(\tau) = 2\times10^{-13}\cdot\tau^{-1/2} \qquad (3)$$

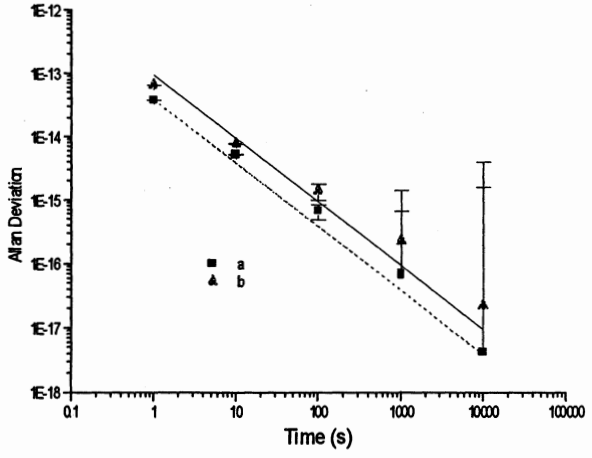

Fig.2 Dual-Mixer Time-Difference noise floor

4. CONCLUSIONS

This work reports the results obtained at National Institute of Metrology with the improved DTMD system.

The additive noise contributions from DMTD electronic place a limit on the system measurement capability. The development of an high resolution frequency measurement system requires, from this point of view, a low noise electronic design of the zero-crossing detector and the selection of a pair of low noise mixers [Refs. 4,5].

Attention must also be paid to cross-talk and ground loop problem [Ref.5]. Temperature sensitivity of the measurement system may also significantly reduce its effectiveness.

5. REFERENCES

[1] *D.W. Allan* and *H.Daams*, "Picosecond time difference measurement system", Proc. 29th Annual Frequency Control Symp., pp. 404 – 411, May 1975

[2] *L.Sze-Ming*, "Influence of noise of common oscillator in dual-mixer time-difference Measurement System", in Transactions on Instrumentation and Measurement, vol. IM-35, n°4, pp.648-651, December 1986.

[3] *R.L.Hamell, P.F. Kuhnle, R.L. Sydnor*, "An improved offset generator developed for Allan Deviation measurement of ultra stable frequency standards", in Proc. 23 th Precision Time and Time Interval 1991, pp. 209-218

[4] *R.Barillet*, "Comparateur de phase ultra faible bruit pour les futures étalons de frequence", in Proc. of the 3rd European Forum on Time and Frequency, pp.249-254,1989.

[5] *G.J.Dick, P.F.Kuhnle, R.L.Sydnor*, "Zero-crossing detector with sub-microsecond jitter and crosstalk", in Proc. 22th Precision Time and Time Interval, pp. 269-282, 1990

[6] *G.Brida*, "The Dual Mixer Time Difference at IEN", CPEM 2000 special issue of IEEE Trans. I&M, 2000

TOTAL HADAMARD VARIANCE: APPLICATION TO CLOCK STEERING BY KALMAN FILTERING

Dave Howe[†], Ron Beard[‡], Chuck Greenhall[§], François Vernotte[*] and Bill Riley[¶]

[†] Time and Frequency Division, NIST, 325 Broadway, Boulder, CO 80305, USA; E-mail: dhowe@nist.gov

[‡] US NRL, 4555 Overlook Ave. SW, Washington, DC 20375-5354, USA; E-mail: beard@juno.nrl.navy.mil

[§] JPL, 4800 Oak Grove Dr., 298-100, Pasadena, CA 91109 USA; E-mail: charles.greenhall@jpl.nasa.gov

[*] LAOB (UMR 6091), 41 bis avenue de l'observatoire, BP 1615, 25010 Besançon Cedex, France; E-mail: francois@obs-besancon.fr

[¶] Datum Inc., 34 Tozer Road, Beverly, MA 01915-5510, USA; E-mail: wrile@datum.com

Abstract—**The Total variance approach has been developed for increasing the confidence of the estimation of the classical Allan variance, particularly for large integration times. This method is based on a procedure involving extension of the original data. Recently, we showed how this approach may be applied to all classes of structure functions (i. e. variances) relevant to the time and frequency community.**

In particular, we obtained an improvement in the confidence of the estimation of the Hadamard variance. The utility of this variance is its insensitivity to linear frequency drifts and its convergence for very low frequency noises (f^{-4} FM). As a consequence, the Hadamard variance is often used for estimating low frequency noises without significant influence from drift.

As an example, this variance has a primary use in GPS and its master control operations. Parameters of the Hadamard function are used to estimate q coefficients in the GPS Kalman algorithm. In this paper, we propose applying this method to clock steering in a more general context. The total approach increases the equivalent degrees of freedom (edf) of the q estimates. We give simple formulae for computing the edf and removing the bias induced by the total approach.

1. INTRODUCTION

Using a type of Hadamard variance, the goal of this paper is to reduce the uncertainty of long-term estimates of frequency stability without increasing the length of a data run. For measurements of frequency stability, the two-sample frequency variance known as the Allan variance was generalized to an N-sample variance weighted with binomial coefficients by R. A. Baugh (Ref. 1). The case of the three-sample frequency variance that is used here is the Picinbono variance (Ref. 2) times $\frac{3}{2}$. However, in this paper, it will be called a Hadamard variance (following Baugh's work) that is defined as follows. Given a finite sequence of frequency deviates $\{y_n, n = 1, \ldots, N_{ymax}\}$, presumed to be the measured part of a longer noise sequence and with a sampling period between adjacent observations given by τ_0, define the $\tau = m\tau_0$-average frequency deviate as

$$\overline{y}_n(m) \equiv \frac{1}{m} \sum_{j=0}^{m-1} y_{n+j}. \qquad (1)$$

Let $H_n(m) = \overline{y}_n(m) - 2\overline{y}_{n+m}(m) + \overline{y}_{n+2m}(m)$ be the second difference of the time-averaged frequencies over three successive and adjacent time intervals of length τ. Define the Hadamard variance as

$${}_{\mathrm{H}}\sigma_y{}^2(\tau) = \frac{1}{6} \left\langle H_n^2(m) \right\rangle, \qquad (2)$$

where $< \cdot >$ denotes an infinite time average over n, and ${}_{\mathrm{H}}\sigma_y{}^2$ depends on m.

The GPS program office uses this particular time-series statistic for estimating Kalman algorithm coefficients according to (Ref. 3), which coefficients will be discussed in a later section. The Hadamard deviation ${}_{\mathrm{H}}\sigma_y(\tau)$ is a function that can be interpreted like the more efficient Allan deviation as a frequency instability *vs.* averaging time τ for a range of frequency noises that cause different slopes on ${}_{\mathrm{H}}\sigma_y(\tau)$. This is shown in figure 1. For estimating Kalman drift noise coefficients, ${}_{\mathrm{H}}\sigma_y(\tau)$ is inherently insensitive to linear frequency drift and reports a residual "noise on drift" as a $\tau^{\frac{3}{2}}$ slope, or what is commonly called random run FM (RRFM). This is in contrast to the Allan deviation, which is sensitive to drift and causes a τ^{+1} slope. If the level of drift is relatively high, it masks the underlying random noise. It is customary to estimate and remove overall frequency drift. Depending on the method of drift removal, this procedure can significantly alter the Allan deviation in the longest term τ region of interest, so estimating underlying noise can be a formidable task for any given data span. On the other hand, the Hadamard deviation is unaffected by removing overall frequency drift. For this reason, it is the preferred statistic in situations in which the frequency drift may be above the random noise effects, which is the case with the use of Rb clocks in the GPS Block II satellite program. We do not imply that systematics such as frequency drift can be ignored. Indeed, satellite clocks are changed and these systematics must be learned as quickly as possible to ensure a smooth changeover.

Throughout this writing, we will make comparisons using the traditional best statistical estimators, denoted by "Hvar" and "Avar" referring to the maximum-overlap estimators of the Hadamard and Allan variances. Section 2 reviews the "total" approach to improving statistical estimation. Sections 3 and 4 give two methods of computing total Hadamard variance, designated as TotHvar, using measurements first of fractional frequency deviations

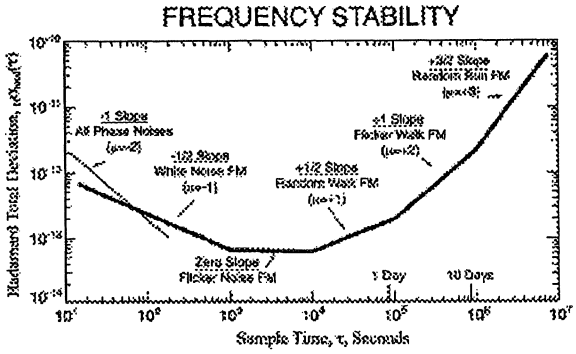

Fig. 1. The Hadamard deviation (root Hvar) shows FM power-law noises as straight lines in addition to PM sources of noise for τ-domain power-law exponent μ (that is, ${}_{\mathrm{H}}\sigma_y^2(\tau) \propto \tau^{\mu}$) range of $-2 \le \mu \le 3$. We define a new estimator that can be interpreted identically called Hadamard-total deviation (root TotHvar) and that has significantly improved confidence at long term. The Hadamard-total deviation is insensitive to linear frequency drift that can mask characteristic random noise typically encountered here in the region where τ = one-week and longer. The goal is to identify μ even-integer power-law noises and accurately estimate their levels in order to set system parameters associated with the GPS Kalman filter.

and then of time deviations. Then we quantify the advantage of TotHvar over Hvar in Section 5, giving formulae for computing bias and equivalent degrees of freedom (edf) of TotHvar. Section 6 reviews how an estimate of τ-domain frequency stability is used to set Kalman filter parameters (or q's) used in GPS operations. Finally, Section 7 discusses the application of the total Hadamard variance in the more general context of clock steering.

2. The "Total" Approach

The total estimator approach has been developed to improve confidence of major statistical tools used in analyzing and characterizing instabilities in phase and frequency of oscillators and synchronization systems (Refs 4, 5, 6, 7, 8, 9, 10). Making a "total" estimator of eqn. (2) involves joining each real data subsequence, namely the subsequence of y_i that goes into each $H_n(m)$ term, at both its endpoints by the same original data subsequence so that it repeats. This creates a new extended version of each y_i subsequence that may be extended by a forward or backward repetition, with or without sign inversion, thus with four possible ways to extend. From numerous simulation studies, we have determined that an extension by even (uninverted) mirror reflection of linear-frequency-detrended $H_n(m)$ subsequences yields the largest edf gain and least bias for the range of noise types identified by standard Hvar. This is described in the next section.

3. Computation using y_n-series

$H_n(m)$ is computed from a $3m$-point data segment or *subsequence* $\{y_i\}_n = \{y_i, i = n, \ldots, n+3m-1\}$. Before applying any data extensions, we must remove a linear frequency trend (drift) from each subsequence by making

$$ {}^{\circ}y_i = y_i - c_1 i, $$

where c_1 is a frequency offset that is removed to minimize $\sum_{i=n}^{n+3m-1} ({}^{\circ}y_i - \overline{{}^{\circ}y_i})^2$, to satisfy a least-squared-error criterion for the subsequence. In practice, it is sufficient to compute this background linear frequency slope by averaging the first and last halves of the subsequence divided by half the interval and subsequently subtracting the value. Now extend the "drift-removed" subsequence $\{{}^{\circ}y_i\}_n$ at both ends by an uninverted, even reflection. Utility index l serves to construct the extensions as follows. For $1 \le l \le 3m$, let

$$ {}^{\circ}y^{\#}_{n-l} = {}^{\circ}y_{n+l-1}; \quad {}^{\circ}y^{\#}_{n+3m+l-1} = {}^{\circ}y_{n+3m-l}; \qquad (3) $$

to form a new data subsequence denoted as $\{{}^{\circ}y_i^{\#}\}_n$ consisting of the drift-removed data in its center portion, plus the two extensions, and thus having a tripled range of $n-3m \le i \le n+6m-1$ with $9m$ points. To be clear, we now have *extended subsequence* $\{{}^{\circ}y_i^{\#}\}_n = \{{}^{\circ}y_i^{\#}, i = n-3m, \ldots, n+6m-1\}$. Define

$$ \mathrm{Total}_{\mathrm{H}}\sigma_y^2(m, \tau_0, N_{ymax}) = \frac{1}{6\,(N_{ymax} - 3m + 1)} \times \sum_{n=1}^{N_{ymax}-3m+1} \left(\frac{1}{6m} \sum_{i=n-3m}^{n+3m-1} \left({}^{\circ}H_i^{\#}(m) \right)^2 \right), \qquad (4) $$

for $1 \le m \le \left\lfloor \frac{N_{ymax}}{3} \right\rfloor$, where $\lfloor c \rfloor$ means the integer part of c and notation ${}^{\circ}H_i^{\#}(m)$ means that $H_n(m)$ above is derived from the new triply-extended subsequence $\{{}^{\circ}y_i^{\#}\}$. The symmetries of the extension and the Hvar filter allow the computational effort to be halved as follows. Let $k = \lfloor 3m/2 \rfloor$. We need to calculate ${}^{\#}y_i^{\circ}$ only for $n-k \le i \le n+k+3m-1$, and ${}^{\#}H_i^{\circ}(m)$ only for $n-k \le i \le n+k$. Then

$$ \begin{aligned} \sum_{i=n-3m}^{n+3m-1} \left({}^{\#}H_i^{\circ}(m) \right)^2 &= 2 \sum_{i=n-k+1}^{n+k-1} \left({}^{\#}H_i^{\circ}(m) \right)^2 \\ &\quad + \left({}^{\#}H_{n-k}^{\circ}(m) \right)^2 \qquad (5) \\ &\quad + \left({}^{\#}H_{n+k}^{\circ}(m) \right)^2, m \text{ even}, \\ &= 2 \sum_{i=n-k}^{n+k} \left({}^{\#}H_i^{\circ}(m) \right)^2, m \text{ odd}. \end{aligned} $$

4. Computation using x_n-series

The methodology described above can be written in terms of calculations on residual time differences between clocks, namely an x_i-series (to adhere to usual notation), recalling that

$$ y_i(m) = (x_{i+m} - x_i) / (m\tau_0). $$

Thus in the total approach applied to x_i-series, the data extensions on subsequences of x_i will be constructed in such a way that

$$^{\circ}y_i^{\#} = \left(^{\circ}x_{i+1}^{\#} - {}^{\circ}x_i^{\#}\right)/\tau_0,$$

in agreement with section 3 above. This has the effect of requiring an odd mirror extension and a third-difference operator when considering subsequences of x_i. The Hadamard variance discussed in section 3 as a second-difference operator on τ-averaged y_n values can now be re-expressed in terms of a third-difference operator on time-error x_i-values. The sample variance (or mean square) of these third differences falls neatly into a class of structure functions, namely the variance produced by a difference operator of order three (Ref. 10). The modified Allan variance can also be treated as a third-difference variance (Ref. 11).

The x_i-subsequence that corresponds to the y_i-subsequence starting at n is $\{x_i;\ n \le i \le n+3m\}$, which has $3m+1$ terms. Compute the detrended subsequence $^{\circ}x_i$ according to

$$k = \left\lfloor \frac{3m}{2} \right\rfloor, \quad c_2 = \frac{x_n - x_{n+k} - x_{n+3m-k} + x_{n+3m}}{k\,(3m-k)},$$

$$^{\circ}x_i = x_i - \tfrac{1}{2}c_2\,(i-n)\,(i-n-3m), \quad n \le i \le n+3m.$$

Define the extended subsequence $\left\{^{\circ}x_i^{\#};\ n-3m \le i \le n+6m\right\}$ by

$$\begin{aligned} ^{\circ}x_i^{\#} &= {}^{\circ}x_i, \quad n \le i \le n+3m, \\ ^{\circ}x_{n-l}^{\#} &= 2\,(^{\circ}x_n) - {}^{\circ}x_{n+l}, \quad 1 \le l \le 3m, \\ ^{\circ}x_{n+3m+l}^{\#} &= 2\,(^{\circ}x_{n+3m}) - {}^{\circ}x_{n+3m-l}, \quad 1 \le l \le 3m. \end{aligned}$$

Then

$$\begin{aligned} m\tau_0\left(^{\circ}H_i^{\#}(m)\right) = & -{}^{\circ}x_i^{\#} + 3\left(^{\circ}x_{i+m}^{\#}\right) \\ & -3\left(^{\circ}x_{i+2m}^{\#}\right) + {}^{\circ}x_{i+3m}^{\#}, \end{aligned}$$

$$n - 3m \le i \le n + 3m - 1,$$

where $^{\circ}H_i^{\#}(m)$ has the same meaning as in Section 3. Now the Hadamard-total variance is computed from (4) as before with $N_{ymax} = N_{xmax} - 1$. Because of symmetry we need $^{\#}x_i^{\circ}$ only for $n - k \le i \le n + k + 3m$, and (5) applies.

5. Bias and Equivalent Degrees of Freedom

We consider the random frequency-modulation (FM) noises since these dominate at long-term averaging times where we can capitalize on the improved confidence of using the total approach. To analyze phase-modulation (PM) noises, one would usually use Total TDEV(Ref. 6) rather than the Hadamard deviation. For brevity, let $\mathrm{Total}_{\mathrm{H}}\sigma_y^2(m, \tau_0, N_{ymax})$ be TotHvar (τ, T), where $\tau = m\tau_0, T = N_{ymax}\tau_0$. The normalized bias and edf for TotHvar are given by

TABLE I

Coefficients for computing (6) and (7), normalized bias and edf of TotHvar.

Noise	Abbrev.	α	a	b_0	b_1
White FM	WHFM	0	-0.005	0.559	1.004
Flicker FM	FLFM	-1	-0.149	0.868	1.140
Random Walk FM	RWFM	-2	-0.229	0.938	1.696
Flicker Walk FM	FWFM	-3	-0.283	0.974	2.554
Random Run FM	RRFM	-4	-0.321	1.276	3.149

$$\mathrm{nbias}(\tau) = \left[\frac{E\{\mathrm{TotHvar}(\tau, T)\}}{E\{\mathrm{Hvar}(\tau, T)\}} - 1\right] = a, \qquad (6)$$

$$\mathrm{edf}(\tau) = \mathrm{edf}[\mathrm{TotIIvar}(\tau, T)] = \frac{T/\tau}{b_0 + b_1\tau/T}, \qquad (7)$$

where $E\{\cdot\}$ is expectation of $\{\cdot\}$, $0 < \tau \le \frac{T}{3}$, $\tau \ge 16\tau_0$ (to be explained), and a, b_0, and b_1 are given in Table I for the five FM noise types considered by the Hadamard variance. α is the corresponding power-law exponent of the fractional-frequency noise spectrum $S_y(f) \propto f^{\alpha}$. In the context here, its valid range is $-4 \le \alpha \le 2$. $E\{\mathrm{TotHvar}(\tau, T)\}$ relative to $E\{\mathrm{Hvar}(\tau, T)\}$ in (6) is independent of τ and T, dependent on noise type, and biased low, giving a the negative sign in Table I. The edf formula (7) is a convenient, empirical or "fitted" approximation with an observed error below 10% of numerically computed exact values derived from Monte-Carlo simulation method using the b_0 and b_1 coefficients of Table I and with the error decreasing with averaging factor $m = \tau/\tau_0$ increasing.

To show the improvement in estimating the Hadamard function, Table II lists the exact values of edf from theory for computations using TotHvar *vs.* plain Hvar for the longest averaging factor in which $\tau = T/3$. This point is the last point in the estimate, and the improvement in confidence using TotIIvar is substantial, particularly for the general case of WHFM noise. TotIIvar is a significantly improved estimator that offsets much of the criticized inefficiency in using the sample Hadamard deviation as opposed to the sample Allan deviation in the presence of common WHFM noise in frequency standards.

6. The Kalman Noise Model and the GPS Operations Problem

The time update of clock states in the Master Control Station (MCS) Kalman prediction algorithm is based on an average of the the most recent measurement of these states for each individual clock, modeled simply by random noise acting on phase $x(t)$, frequency $y(t)$, and frequency drift $z(t)$. With this model, the measured power-

TABLE II
EXACT $\frac{edf\{\text{TotHvar}(T/3,T)\}}{edf\{\text{Hvar}(T/3,T)\}}$ GAIN FOR $\tau_{max} = T/3$.

Noise	edf gain of TotHvar $(T/3,T)$
WHFM	3.447
FLFM	2.448
RWFM	2.044
FWFM	1.676
RRFM	1.313

law α exponents of the frequency-fluctuation noise spectrum take on only the values 0,-2, and -4, corresponding to WHFM, RWFM, and RRFM, or μ = -1, 1, and 3 in the τ-domain. Hence, we want to precisely extract the level of these noises for each clock using the most efficient method possible, which heretofore has been the sample Allan variance with drift removed from the data run, and more recently the sample Hadamard variance, because of its logical link to the model. If white PM (WHPM) is a significant noise component, and for completeness, the $\alpha = 2, \mu = -2$ case corresponding to WHPM is included as a separate error.

The parameters used by the MCS within GPS system operations are denoted as Kalman filter q's. By convention, each filter parameter $q_i, i = 0, 1, 2, 3$ corresponds respectively to τ-domain power law exponents $\mu = -2, -1, 1, 3$. For the Hadamard variance, the relationship is (Ref. 3)

$$\mathrm{H}\sigma_y^2(\tau) = \sigma^2_{WHPM} + \sigma^2_{WHFM} + \sigma^2_{RWFM} + \sigma^2_{RRFM}$$
$$= \tfrac{10}{3} q_0 \tau^{-2} + q_1 \tau^{-1} + \tfrac{1}{6} q_2 \tau + \tfrac{11}{120} q_3 \tau^3. \quad (8)$$

Tuning the Kalman filter depends on the ability to "q" each individual clock according to estimates of its noise. The GPS Block IIR satellite program incorporates Rb atomic oscillators that are characterized by a mix of various levels and types of random noise and with frequency drift that may be significantly above noise. Using "frequency-drift insensitive" Hvar and using (8), the confidence becomes a factor of about $\frac{1}{3}$ less than using Avar near the last and crucial long-term $\tau_{max} = T/3$ value. This is because the plain sample Hadamard's edf is one less than Allan's edf. For the proper perspective, note that we are in the one-week averaging τ-region with a last real-time data run of about one month, thus edf $\approx$ 1–2; so estimating filter q's is somewhat subjective. Figure 2 illustrates a summary of estimates of frequency stability for each GPS satellite clock as published in reports issued by the Naval Research Laboratory (Ref. 13).

Table II shows that the new TotHvar $(T/3,T)$ edf is multiplied by a factor of 1.3 to 3.4 over plain Hvar $(T/3,T)$. TotHvar can be applied directly and reliably, while retaining the efficiency of the sample Allan variance without the difficulty associated with real-time drift removal.

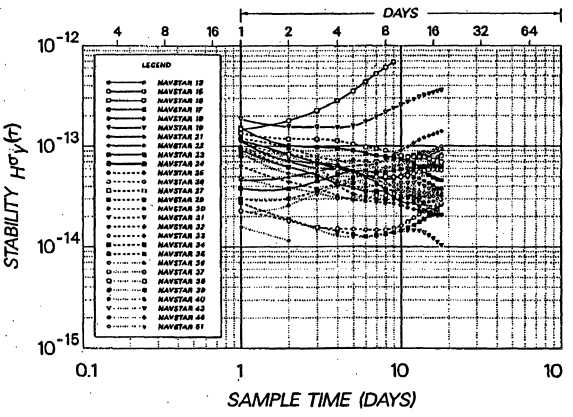

Fig. 2. Hadamard-deviation frequency stability of individual GPS satellite clocks *vs*. USNO Master Clock for the period 1 January to 1 July, 2000 (Ref. 18).

The work of this paper has impact on two GPS operational issues. The first is that the time needed to estimate the Hadamard variance is substantially reduced. For example, to obtain a τ = one-week estimate of the Hadamard variance with, say, the last 40 days of measured data, the Total approach using TotHvar obtains a one-week estimate with the same or better confidence in about 26 to 34 days of measured data (see figure 3). The second issue is that satellite data are obtained by the linked common-view method (Ref. 14), and the delay in receiving the monitor station tracking data is currently at 2 to 3 days. Thus, it is important to extract maximum information from data at hand.

7. APPLICATION TO CLOCK STEERING

In many applications, the time given by an oscillator must be modeled and predicted. As a consequence, the time prediction performance of this clock has to be characterized.

In order to estimate the time uncertainty given by an oscillator, a linear or parabolic fit may be performed over a sequence of observed time deviations and extrapolated during a prediction period. Thus, the requirements of synchronization are specified by the maximum error of the time deviation prediction from the extrapolated fit.

The question is then, "How is this maximum error related to the noise levels of the clock ?" Let us call Time Interval Error (TIE) the differences between the extrapolated parabola and the real time deviation. The TIE is due to two effects: (1) the error of determination of the parabolic parameters and (2) the error due the noise of the clock. Obviously, both of these errors may be positive or negative, and the ensemble average of the TIE is equal to zero. Moreover, it can be easily shown that the distribution in TIE is Gaussian. Consequently, we only need to estimate the variance of the TIE in order to define its statistical characteristics.

The theoretical variance of the TIE versus the noise

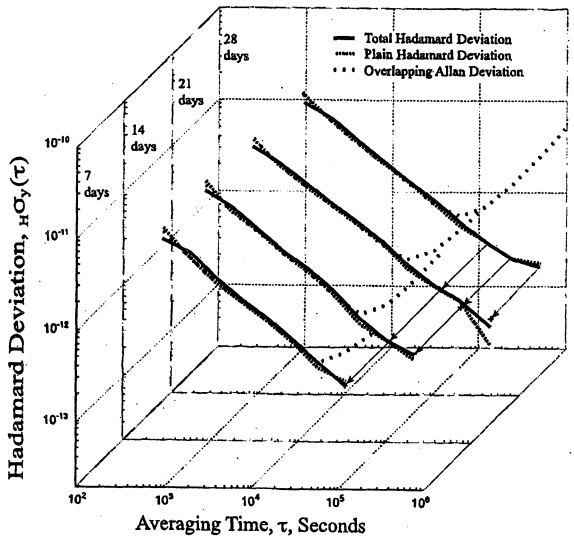

Fig. 3. Total Hadamard deviation, plain Hadamard deviation, and Allan deviation for SV24 satellite clock data as the data run increases from 7 days (front plot) to 28 days (rear plot). The last (rightmost) values of TotHdev for shorter data runs anticipates the underlying noise level of longer runs compared to plain Hdev (arrowed lines are projected off 28-day data run). The Allan deviation's response to frequency drift masks the long-term noise level.

levels has been calculated in Ref. 15 which shows that the time prediction performance is directly linked to the accuracy of the noise level estimation. The estimates of the TIE standard deviation are distributed following a Student law, and the edf of these estimates are the same as the edf of the dominating noise level. If the time deviation sequence contains a parabola with an amplitude that is much higher than the random fluctuations, one must use a noise level estimator which is insensitive to quadratic drift while still sensitive to low frequency random noise. The Total Hadamard variance described in this paper is the most reliable estimator for such applications.

8. Conclusion

We have developed a significantly improved estimator of the three-sample Hadamard frequency variance based on the so-called "total" approach and denoted as TotHvar, for use in GPS operations and analysis. Practically speaking, we have reduced the long-term estimation uncertainty in terms of edf by a factor of 1.3 to 3.4, depending on the noise type. Having confidence greater than plain Hvar and even equal to or greater than Avar, TotHvar is a statistic that permits tuning of the MCS Kalman filter with more accurately chosen clock-estimation parameters (or q's) that are linked to the most recent measurements of frequency stability of each clock. The increased confidence from TotHvar and shorter data processing delays will play significant roles in adequately managing future GPS system events. More generally, the Total Hadamard variance may be used in any application needing an accurate estimation of the low frequency noise levels when a high level of frequency drift is present in the signal.

9. Acknowledgements

We thank Capt. Curtis Hay of the GPS Joint Program Office and Steven Hutsell for valuable discussions leading to this work.

References

[1] R. A. Baugh, "Frequency modulation analysis with the Hadamard variance," *Proc. 25th Annual Frequency Control Symposium*, Ft. Monmouth, NJ., June 1971, pp. 222–225.

[2] E. Boileau and B. Picinbono, "Statistical study of phase fluctuations and oscillator stability," *IEEE Trans. Instrum. Meas.*, **IM-25**, no. 1, pp. 66–75, March 1976.

[3] S. T. Hutsell, "Relating the Hadamard variance to MCS Kalman filter clock estimation," *Proc. 27th Annual PTTI Systems and Applications Meeting*, San Diego, CA., Nov. 29–Dec. 1, 1995, pp. 291–301.

[4] D. A. Howe and C. A. Greenhall, "Total variance: a progress report on a new frequency stability characterization," *Proc. 29th Ann. PTTI Systems and Applications Meeting*, pp. 39–48, 1997.

[5] D. B. Percival and D. A. Howe, "Total variance as an exact analysis of the sample variance," *Proc. 29th Ann. PTTI Systems and Applications Meeting*, pp. 97–105, 1997.

[6] M. A. Weiss and D. A. Howe, "Total TDEV," *Proc. IEEE International Frequency Control Symposium*, pp. 192–198, 1998. Total TDEV has subsequently been redefined by using (Ref. 8) below to be published in D. A. Howe and T. K. Peppler, "Definitions of total estimators of common time-domain variances" *Proc. IEEE Int. Freq. Cont. Symp.*, Seattle, WA, June, 2001.

[7] C. A. Greenhall, D. A. Howe and D. B. Percival, "Total Variance, an Estimator of Long-Term Frequency Stability," *IEEE Trans. Ultrasonics, Ferroelectrics, and Freq. Control*, **UFFC-46**, no. 5, 1183–1191, Sept, 1999.

[8] D. A. Howe and F. Vernotte, "Generalization of the Total variance approach to the modified Allan variance," *Proc. 31st Ann. PTTI Systems and Applications Meeting*, Dana Point, CA., Dec. 7–9, 1999.

[9] D. A. Howe, "The Total Deviation Approach to Long-Term Characterization of Frequency Stability," *IEEE Trans. Ultrasonics, Ferroelectrics, and Freq. Control*, **UFFC-47**, no. 5, 1102–1110, Sept, 2000.

[10] F. Vernotte and D. A. Howe, "Generalization of the Total variance approach to the different classes of structure functions," *Proc. 14th European Frequency and Time Forum*, Torino, It, March 2000.

[11] C. A. Greenhall, "The third-difference approach to modified Allan variance," *IEEE Trans. Instrum. Meas.*, **IM-46**, no. 3, pp. 696–703, June 1997.

[12] D.B. Sullivan, D.W. Allan, D.A. Howe, and F.L. Walls (Editors), *Characterization of Clocks and Oscillators*, Natl. Inst. Stand. Technol. Technical Note 1337, Section A-6, March 1990.

[13] Navstar Quarterly Report 00-3, Space Application Branch, NRL, Wash D.C. 20 July 2000.

[14] W. G. Reid, "Continuous Observation of Navstar Clock Offset from the DoD Master Clock Using Linked Common View-Time Transfer," *Proc. 28th Annual PTTI Systems and Applications Meeting*, Dec. 3–5, 1996, Reston, Virginia, USA, pp. 397-408.

[15] F. Vernotte, J. Delporte, M. Brunet, and T. Tournier, "Uncertainties of drift coefficients and extrapolation errors: Application to clock error prediction," *Metrologia*, vol. 38, no. 4, 2001, accepted for publication.

IMPROVED COUPLING OF A MICROWAVE RAMSEY CAVITY: THEORETICAL STUDIES AND EXPERIMENTAL VERIFICATION

Roland Schröder, Rolf Augustin, and Andreas Bauch

Physikalisch-Technische Bundesanstalt, Bundesallee 100, D-38116 Braunschweig, Germany

ABSTRACT

Based on theoretical and experimental studies, an improved design for coupling of the microwave field to the Ramsey type cavity for use in atomic beam frequency standards was developed. A concept was worked out, for minimizing the temperature sensitivity of the end-to-end phase difference by using the improved coupling design and proper dimensions of the cavity itself.

1. INTRODUCTION

Previous experiments made in connection with the blackbody frequency shift experiments in the experimental caesium atomic beam frequency standard CSX of the Physikalisch-Technische Bundesanstalt (PTB) [1] had revealed that the end-to-end phase difference φ of the Ramsey-type microwave cavity is more sensitive to the cavity temperature than intuitively assumed. A sensitivity of the relative CSX frequency on the cavity temperature of $7 \cdot 10^{-15}$/°C was obtained which was attributed to a change of φ. De Marchi *et al.* [2] indicated the potential cause of this phenomenon: In fact, the phase difference φ depends not only on the electrical asymmetry of the two cavity arms but also on the overall cavity dimensions, affected by temperature changes. To minimise this dependence of φ overall dimensions have to be chosen appropriately. This choice can roughly be controlled by microwave amplitude measurements. The dependence of the microwave field amplitude in the cavity on the excitation frequency f_e is shown in Fig. 1 for the type of cavities employed in PTB's atomic clocks CS1 - CS4, and hitherto also in CSX. The middle resonance represents the normal point of operation, $f_e \approx f_0$, where f_0 is the caesium hyperfine transition frequency of 9 192 MHz. Sharp dispersion-shaped resonances lie between adjacent broad cavity resonances. The sharp resonances vanish in case of perfect symmetry of the Ramsey cavity as will be explained below. If the operating frequency $f_e \approx f_0$ lies midway between two neighbouring sharp resonances, φ should be rather insensitive to the overall cavity dimensions. The cavities of PTB's clocks were apparently not manufactured to ideal dimensions in this respect.

In Section 2, a new cavity concept will be contrasted to the old one. Substantial changes were made to the coupling between the feed waveguide and the straight waveguide of the cavity. A relatively simple expression for the phase difference φ is derived in Section 3, which gives a detailed physical insight to the decisive parameters influencing φ and its temperature dependence. From that the dimensioning rules used in the new cavity concept have been deduced. Experimental studies were made to verify the theoretical expressions, using cavities

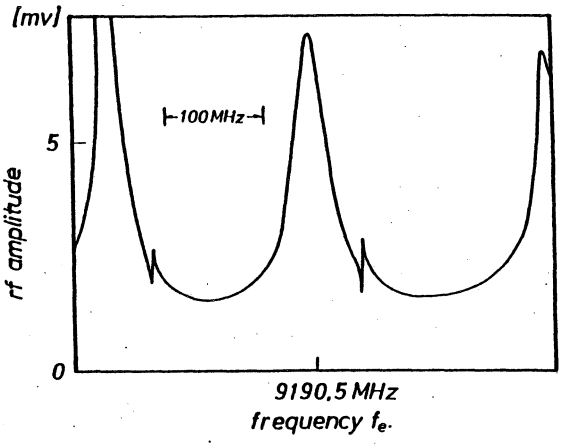

Fig.1 Amplitude of the microwave field, measured at the beam intersection (interaction region) of a Ramsey cavity of the design used currently in PTB's primary clocks, in dependence on the excitation frequency f_e.

of the old and the new style in PTB's CSX, during which the length asymmetry between the cavity arms was artificially increased. Results are presented in Section 4. The temperature sensitivity of φ for the new cavity type was found reduced by more than a factor of 10 compared to the old results mentioned above. In the most recent experiments, the standard corner-shaped end sections of the cavity were replaced by De Marchi-type ring ends [3]. The then observed phase difference φ and its temperature sensitivity could also be explained using the results of Section 3.

2. CAVITY CONCEPT

The cavity used in PTB's clocks is schematically depicted in Fig. 2, showing a photograph and a schematic drawing, including labels and denominations used in the subsequent discussions. The dimension of the standard corner end parts, denoted *a* and *b* in Fig. 2, were chosen in such a way that the standing wave pattern in the straight part of the cavity (of Type H_{10}) does not suffer distortions in the end parts. The feed waveguide lies on top of the straight guide. The dimensions of the vacuum tube of the clocks called for such a compact construction instead of a more standard H-plane T as feed.

To ease understanding of the paper it is at first necessary to recall the construction of the old version of the straight cavity part. Design of the feed guide had been motivated by the same considerations as used for the end sections, namely the transition of the standing wave pattern between the feed guide, as shown in Fig. 3, and

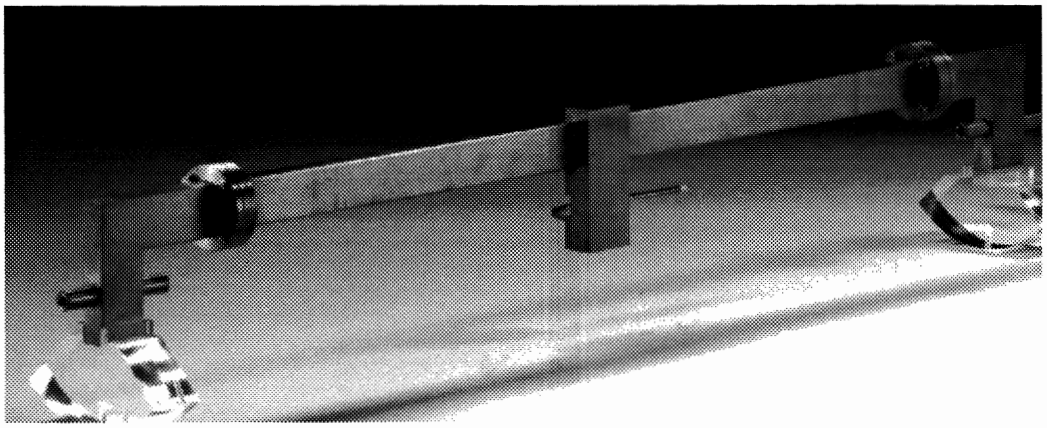

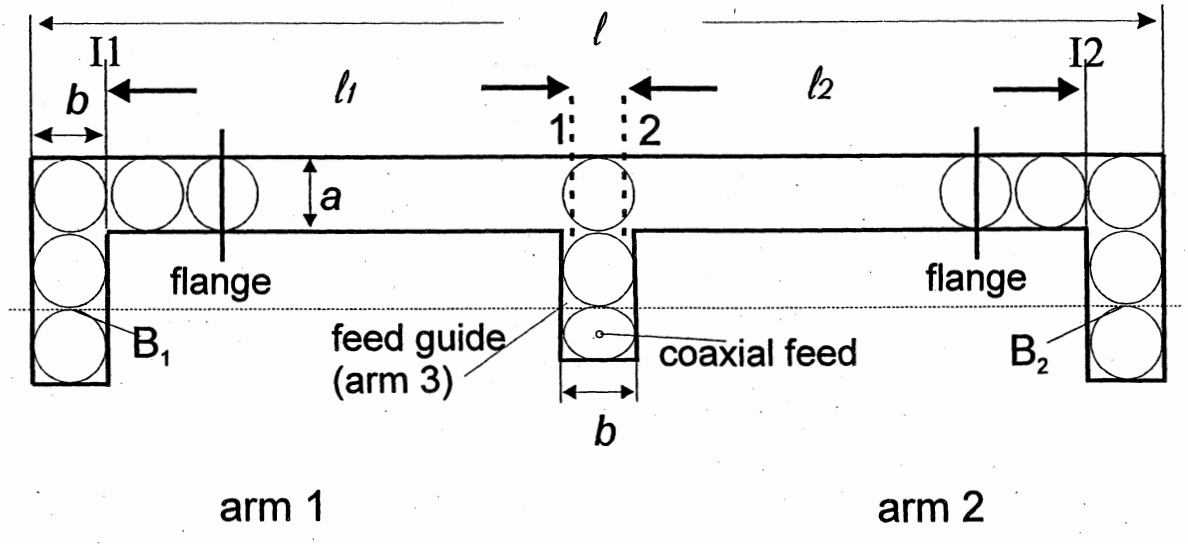

Fig.2 Photograph and schematic drawing of the Ramsey cavity currently used in PTB's primary clocks. Parameters: $\ell = 35 \cdot \lambda_g/2$, a = 22,86 mm, $b = \lambda_g/2$, λ_g = waveguide wave length at 9,2 GHz, 46,52 mm. The planes 1 and 2, and I1, I2, are explained in the text. B1 and B2 represent the location of the interaction of the atomic beam with the microwave field.

the straight cavity part should happen without field distortions. This was realised by opening the straight guide completely to the feed guide and by choosing appropriate dimensions for the feed guide as depicted in Fig. 2. The signal is fed to the feed guide via a coaxial cable and a probe. The depth of penetration of the probe into the feed guide of about 5 mm determines the bandwidth of the broad coupling resonance (≈ 25 MHz) whose centre frequency is tuned by the position of the short in the feed guide. The distance between probe and the gap to the straight waveguide was chosen in such a way that higher modes excited by the probe vanish. In consequence, small deviations of the lateral symmetry of the probe position do not influence the symmetry of the field excited in the straight part and thus the phase shift φ. The position of the short in the feed guide determines the centre frequency of the broad coupling resonance but not the dispersion-shaped asymmetry resonances. These are determined by the dimensions of the coupling T and by those of the straight part of the cavity. The latter had to be chosen to $(2n+1)\lambda_g/2$, with n an integer and λ_g the waveguide wavelength (n = 17 in our particular case) following the prescription not to distort the standing wave pattern. But then the sharp dispersion-shaped asymmetry resonances do not lie symmetrical with respect to f_0.

As a symmetrical position appeared more desirable, we had to give up the concept of a transition without distortion. Finally we ended in a coupling design as depicted in Fig. 4 from which technical details and dimensions can be deduced. In contrast to the previous design, coupling between the three arms has been improved so that a record of the field amplitude in the cavity as a function of f_e exhibits a periodic succession of broad coupling resonances and small asymmetry resonances over a wide frequency range. The position of the latter on the frequency axis have to be adjusted by proper tuning of the length of the cavity arm, as will be explained subsequently.

3. ANALYTICAL DERIVATION OF THE PHASE DIFFERENCE φ

In our cavity, the signal is coupled through arm 3 into the two arms 1 and 2 as illustrated in Figure 2. As for each H plane T, one can find (after some calculations not shown here) two planes 1 and 2, indicated in Figure 2, in which

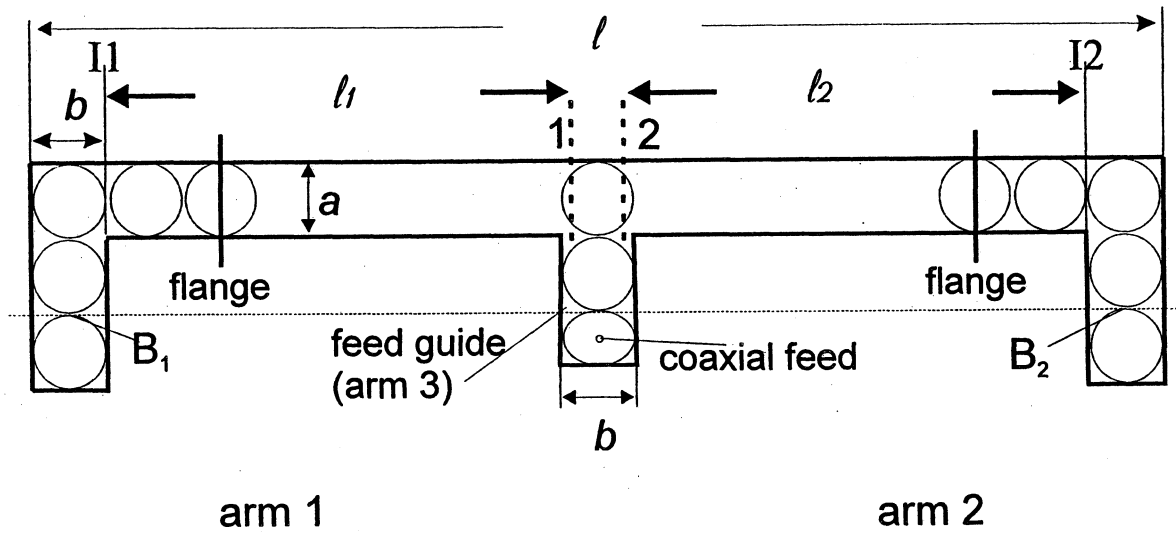

Fig.2 Photograph and schematic drawing of the Ramsey cavity currently used in PTB's primary clocks. Parameters: $\ell = 35 \cdot \lambda_g/2$, a = 22,86 mm, $b = \lambda_g/2$, λ_g = waveguide wave length at 9,2 GHz, 46,52 mm. The planes 1 and 2, and I1, I2, are explained in the text. B1 and B2 represent the location of the interaction of the atomic beam with the microwave field.

the straight cavity part should happen without field distortions. This was realised by opening the straight guide completely to the feed guide and by choosing appropriate dimensions for the feed guide as depicted in Fig. 2. The signal is fed to the feed guide via a coaxial cable and a probe. The depth of penetration of the probe into the feed guide of about 5 mm determines the bandwidth of the broad coupling resonance (≈ 25 MHz) whose centre frequency is tuned by the position of the short in the feed guide. The distance between probe and the gap to the straight waveguide was chosen in such a way that higher modes excited by the probe vanish. In consequence, small deviations of the lateral symmetry of the probe position do not influence the symmetry of the field excited in the straight part and thus the phase shift φ. The position of the short in the feed guide determines the centre frequency of the broad coupling resonance but not the dispersion-shaped asymmetry resonances. These are determined by the dimensions of the coupling T and by those of the straight part of the cavity. The latter had to be chosen to $(2n+1)\lambda_g/2$, with n an integer and λ_g the waveguide wavelength (n = 17 in our particular case) following the prescription not to distort the standing wave pattern. But then the sharp dispersion-shaped asymmetry resonances do not lie symmetrical with respect to f_0.

As a symmetrical position appeared more desirable, we had to give up the concept of a transition without distortion. Finally we ended in a coupling design as depicted in Fig. 4 from which technical details and dimensions can be deduced. In contrast to the previous design, coupling between the three arms has been improved so that a record of the field amplitude in the cavity as a function of f_e exhibits a periodic succession of broad coupling resonances and small asymmetry resonances over a wide frequency range. The position of the latter on the frequency axis have to be adjusted by proper tuning of the length of the cavity arm, as will be explained subsequently.

3. ANALYTICAL DERIVATION OF THE PHASE DIFFERENCE φ

In our cavity, the signal is coupled through arm 3 into the two arms 1 and 2 as illustrated in Figure 2. As for each H plane T, one can find (after some calculations not shown here) two planes 1 and 2, indicated in Figure 2, in which

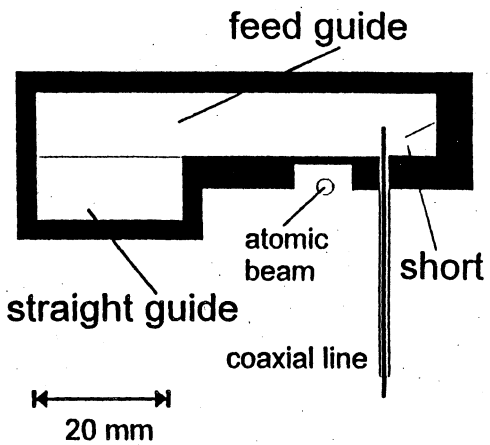

Fig.3 Section view of the coupling between feed waveguide and straight waveguide of the Ramsey cavity of the design used currently in PTB's primary clocks.

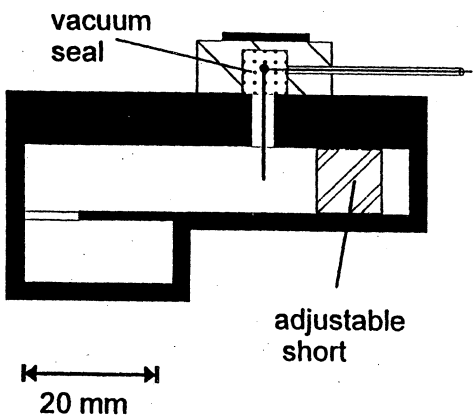

Fig.4 Section view of the coupling between feed waveguide and straight waveguide of the Ramsey cavity of the new design, developed in course of studies presented in this paper.

the transversal magnetic field components, H_1 and H_2, are equal but have opposite sign,

$$H_1 = -H_2 . \qquad (1)$$

No assumption about the terminations of the arms have to be made when deriving (1). Only the coupling T has to be presupposed as lossless.

Relation (1) allows to calculate the course of the phase of the standing wave field (transversal magnetic component) for both arms of the cavity separately. Both arms can be divided into a straight part and an end part. The planes I1 and I2 define the input planes for the end parts. Each of them is located at a maximum of the transversal magnetic field component at a position as shown in Fig. 2. Then the phase difference of the straight part for example of arm 1 between the fields in plane 1 and plane I1 can be calculated to

$$\phi_{S1} \approx A_1 \mathrm{tg}(\xi_1). \qquad (2)$$

A_1 and ξ_1 can be found from the reflection coefficient Γ_1 in plane 1

$$\Gamma_1 = |\Gamma_1| \exp\{-2i\,\xi_1\}. \qquad (3)$$

$A_1 = (1-|\Gamma_1|)/(1+|\Gamma_1|) \approx (1-|\Gamma_1|)/2$ indicates the losses of arm 1 and the angle ξ_1 is defined by $\xi_1 = \beta\ell_1 + \gamma_1$ and $\beta = 2\pi/\lambda_g$, where ℓ_1 is the distance between plane 1 and the plane I1. γ_1 is defined by the reflection factor of the end part $\Gamma_{11} = |\Gamma_{11}| \cdot \exp\{-2\,i\,\gamma_1\}$. With ϕ_{E1} the phase difference between the fields in the input plane I1 and the location B1 of the atomic beam passage through the cavity as indicated in Fig. 2, one finds the phase difference φ_1 between the fields in plane 1 and location B1 to

$$\varphi_1 = \phi_{S1} + \phi_{E1} = A_1 \mathrm{tg}(\xi_1) + \phi_{E1}. \qquad (4)$$

Having repeated the same procedure for arm 2 one finds with (1) the end to end phase difference $\varphi = \varphi_1 - \varphi_2$

$$\varphi = A_2 \cdot \mathrm{tg}(\xi_2) - A_1 \cdot \mathrm{tg}(\xi_1) + (\phi_{E1} - \phi_{E2}). \qquad (5)$$

For further discussions it is advantageous to introduce average and difference values, according to

$$A = (A_1 + A_2)/2 \qquad \xi = (\xi_1 + \xi_2)/2 \qquad (6a)$$

$$\tilde{A} = (A_1 - A_2)/2 \qquad \tilde{\xi} = (\xi_1 - \xi_2)/2 . \qquad (6b)$$

This allows (5) to be written as

$$\varphi = A\tilde{\xi}/\cos^2(\xi) + \tilde{A}\mathrm{tg}(\xi) + (\phi_{E1} - \phi_{E2}) , \qquad (7)$$

where the physical meaning of the terms is rather obvious now: The first term is due to the geometrical asymmetry, $\sim \tilde{\xi}$, between arm 1 and arm 2 (including the end parts). Usually only this term was discussed in the literature as being responsible for a phase difference φ. So eq. (5.6.105) in [4] is equivalent to $\varphi = A \cdot \tilde{\xi}$ here. The second term in (7) is due to an asymmetry of the losses, $\sim \tilde{A}$, and the last term has been already described above.

The overall cavity dimensions come into play in (7) by the average value ξ. A choice of $\xi = n \cdot \pi$ (n = 0,1...) minimises in (7) the first term and makes the second term in (7) vanish. In the case of a change of temperature it is obvious that the angle ξ, representing the geometrical dimensions of one arm (including the end part), will be influenced particularly. Again the choice $\xi = n \cdot \pi$ is advantageous because the first term in (7) ($\sim 1/\cos^2\xi$) is an even function and thus cannot contribute. Condition $\xi = n \cdot \pi$ imposes that the planes 1 and 2 coincide with planes of maximum field amplitude. The junction between the realised end parts and the central straight section (see Fig. 2) have to be done in planes of zero transversal magnetic field. Thus, the distance between the two flanges and planes 1 or 2, respectively, have to be machined to exactly $(m+1/2) \cdot \lambda_g/2$ which can in practise be controlled in the following way: If, for example, the distance in arm 1 is machined to the correct length, a short circuit at its flange will produce a standing wave field in arm 1 with a node of the transversal magnetic

field in plane 1. Thus with $H_2 = -H_1 = 0$ in plane 2, as follows from (1), no rf power will be detected using a probe at the flange of arm 2. With the probe attached to the flange of arm 1 the length of arm 2 can be controlled. Tuning of both arms will never be perfect, and the remaining small differences entail the weak, dispersion shaped asymmetry resonances, seen e.g. in Fig. 1, which occur at $\xi = (n\pm1/2)\cdot\pi$. Assume that arm 1 is slightly longer than arm 2 and that the probe is located at position B2 of arm 2. Sweeping the frequency f_e, at some point the condition $\xi_1 = (n\pm1/2)\cdot\pi$ is fulfilled, the standing wave field has a node in plane 1 and no field is transmitted to arm 2, explaining the sharp minimum in the recorded signal. At a slightly higher frequency f_e, the resonance condition $\xi_2 = (n\pm1/2)\cdot\pi$ is fulfilled in arm 2, no field is transmitted to arm 1, and the probe in arm 2 records a sharp increase in signal.

The two sharp resonances at f_e above and below f_0 will thus be recorded at frequencies corresponding to $\xi = (n\pm1/2)\cdot\pi$, approximately shifted by equal amounts with respect to f_0, with deviations due to the frequency dependence of the wavelength λ_g, of the S-parameters of the T, and of the reflections from the end parts. As the frequency separation between them corresponds to $\Delta\xi = \pi$ one can estimate from Fig. 1 that $\xi = n\cdot180° + 45°$ prevails in case of our cavities. The measured value is 48,8° (instead of 45°), meaning that plane 1 or 2 is shifted by 6,3 mm from the ideal position.

4. EXPERIMENTAL STUDIES

Cavities were built into PTB's atomic beam frequency standard CSX, which in this context is characterised by its line Q of $3\cdot10^7$ (252 Hz clock transition line width) and a short-term relative frequency instability of $< 4\cdot10^{-14}$ $(\tau / \mathrm{h})^{-1/2}$. Details of CSX have been previously described [1,5,6]. Frequency measurements were carried out with respect to PTB's primary clocks CS1 and CS2. The CSX frequency is corrected for all known systematic shifts except that one due to the phase difference φ which is, in turn, derived from the observed relative frequency differences $F_X = (f_{CSX} - f_{prim})/f_{prim}$ with respect to the primary clocks, using the relation $\varphi = -F_X\cdot\pi\cdot Q$.

4.1 Experiments with strongly asymmetrical cavities

To verify the validity of expressions (7) we exaggerated the asymmetry of the cavity by artificially lengthening one arm. A 2-mm disc was mounted between the straight part and one end section. Then only the first term in (7) should be significant. We studied both types of cavities, the old one with $\xi_{old} = (1+6,3)\ \mathrm{mm}/\lambda_g \cdot 360° = 56,48°$, and the new one with $\xi_{new} = 1\ \mathrm{mm}/\lambda_g \cdot 360° = 7,74°$, but the same difference value for both, $\tilde{\xi} = 360°\cdot1\ \mathrm{mm} / \lambda_g = 7,74°$. Using the same corner-shaped cavity end parts in the same orientation, we deduced $\varphi_{old} = 5,89\cdot10^{-3}$ for the old cavity and $\varphi_{new} = 1,61\cdot10^{-3}$ for the new one, i.e. $\varphi_{old}/\varphi_{new} = 3,66$. The first term in (7) instead predicts $\cos^2(\xi_{new})/\cos^2(\xi_{old}) = 3,35$. With the two values for φ one can calculate the A factors. One finds $A_{old} = 0,0133$ and $A_{new} = 0,0127$, two values which are compatible with tabulated loss figures of copper. A=0,013 corresponds to a damping constant $\alpha = 1,43\cdot10^{-5}$/mm. This value is slightly larger than the theoretical of $\alpha = 1,35\cdot10^{-5}$/mm.

The temperature dependence of φ follows from the total differential of the first term in (7),

$$\varphi = A\cdot\tilde{\xi}\cdot\mathrm{d}\left(\frac{1}{\cos^2(\xi)}\right) = \frac{2A\tilde{\xi}tg(\xi)}{\cos^2(\xi)}\,\mathrm{d}\xi \qquad (8)$$

For standard X-band wave guide at $f_e \approx 9,2$ GHz one can show that $\mathrm{d}\xi \approx 2\cdot\beta\cdot\ell_a\,(\mathrm{d}\ell_a/\ell_a)$, and we get $\mathrm{d}\xi = 2,45\cdot10^{-3}$ ($\ell_a \approx 19.5\cdot\lambda_g/2$, total length of one arm) and with $(\mathrm{d}\ell_a/\ell_a) = 2\cdot10^{-5}$ and $A = 0,013$, from (8) $\mathrm{d}\varphi_{old} = 4,26\cdot10^{-5}$ and $\mathrm{d}\varphi_{new} = 1,19\cdot10^{-6}$ are predicted for a 1°C temperature change. We found experimentally $\mathrm{d}\varphi_{old,ex} = 4,45\cdot10^{-5}$ and $\mathrm{d}\varphi_{new,ex} = 3,89\cdot10^{-6}$, in good agreement for the old cavity, but not really for the new cavity. One could try to explain the discrepancy as due to the neglect of the second term in (7). But this is not the case as the losses in the two cavity arms would have to differ by as much as $\tilde{A}/A \approx 0,05$, which could not be verified in experiments described in the next section.

4.2 Experiments with symmetrical cavities

We repeated the same kind of experiments with the two cavities as symmetrical as possible, i.e. without the additional disk. From the frequency measurements we derived the following results which clearly show the superiority of the new cavity design with respect to the old one

old cavity ($\xi_{old} = 48,74°$)	new cavity ($\xi_{new}=0°$)
$\varphi_{old} = 7,11\cdot10^{-5}$	$\varphi_{new}=1,94\cdot10^{-5}$
$(-6,4\cdot10^{-13})$	$(-1,75\cdot10^{-13})$
$\mathrm{d}\varphi_{old} = 7,67\cdot10^{-7}$	$\mathrm{d}\varphi_{new}=4,44\cdot10^{-8}$
$(-6,9\cdot10^{-15}\pm10^{-15})$	$(-4\cdot10^{-16}\pm10^{-15})$

values for $\mathrm{d}\varphi$ as before, for a one degree temperature change. The values in parentheses indicate the observed relative frequency differences F_X and their temperature sensitivity. The total measurement time for the temperature coefficients was about 15 days for each individual temperature value. Minimum and maximum cavity temperatures differed by about 9 °C.

The first two terms in (7) will be used for the discussion of these results. For the temperature dependence they predict

$$\mathrm{d}\varphi = 2\tilde{\xi}\frac{tg(\xi)}{\cos^2(\xi)}A\mathrm{d}\xi + \frac{\tilde{A}}{A}\frac{A\mathrm{d}\xi}{\cos^2(\xi)} \quad . \qquad (9)$$

Thus a temperature dependence can be expected for the new cavity ($tg(\xi_{new}) = 0$!) only if an asymmetry in the losses of the two arms ($\tilde{A}\neq0$) is present. From the experimental result for $\mathrm{d}\varphi$ one deduces $\tilde{A}/A = 1,4\cdot10^{-3}$ (corresponding to $\mathrm{d}F_X = 4\cdot10^{-16}$).

Assuming for the old cavity similar values for $\tilde{A}/A$, one can neglect in (9) the second term and one would expect a ratio $d\varphi_{old}/\varphi_{old} = 2 \cdot tg(\xi) \cdot d\xi = 2 \cdot 1{,}14 \cdot 2{,}45 \cdot 10^{-3} = 5{,}6 \cdot 10^{-3}$, whereas $11 \cdot 10^{-3}$ was found in the experiments.

4.3 Experiments with ring-end parts

Instead of the standard corner end parts, seen in Fig. 2, we mounted ring-shaped end parts, as proposed by de Marchi et al. [3] on the new central cavity part ($\xi_{new} = 0$). We obtained the following results for φ_R and $d\varphi_R$, respectively: $\varphi_R = 1{,}67 \cdot 10^{-4}$ $(-1{,}5 \cdot 10^{-12})$ and $d\varphi_R = 3{,}89 \cdot 10^{-7}$ $(-3{,}5 \cdot 10^{-15} \pm 10^{-15})$.

The rather large value of φ_R compared to φ_{new} can be explained only if the summand $(\phi_{E1} - \phi_{E2})$ of (7) is no longer negligible, whereas the second term is still zero due to $tg(\xi)=0$. In contrary to the corner end parts which are broadband devices, the ring end parts have the characteristic of a strongly coupled cavity with a distinctive frequency sensitivity. Thus, differences in the dimension of the the two ring endparts may have a stronger impact on amplitude and phase of the fields in B1 and B2 than this can be anticipated to be the case in the corner end parts. We calculated the wave propagation in the end sections with a simplified model (E-Plane-T coupled to the ring which is considered as simple waveguide) assuming certain dimensional asymmetries between the two rings which may exist in the coupling to the rings, and the losses and the length of the rings. As an example Fig. 5 shows $(\phi_{E1} - \phi_{E2})$ plotted as a function of the ring circumference ℓ_r when an asymmetry of 0,1 mm in the circumference of the ring was assumed. The losses of the ring were supposed twice of those of a standard X-band waveguide and the circumference of the ring was varied between $4\lambda_g/2$ and $6\lambda_g/2$. The ring is in resonance at $4\lambda_g/2$ or $6\lambda_g/2$ where $(\phi_{E1} - \phi_{E2})$ is quite large. At that time following the proposed design of De Marchi we have almost realised $4\lambda_g/2$, and our measurement results apparently agree with the predicted magnitude of $(\phi_{E1} - \phi_{E2})$ in this case. Similar results can be found if asymmetries in coupling or losses are introduced.

To explain the temperature dependence of φ_R one has to form the total differential of all three terms in (7). One finds an expression with many terms. In contrast to the cavity with corner end parts not only the variation of the overall dimensions has to be taken into account but due to the resonant behaviour of the ring also the change of the differential magnitudes $(d\tilde{\xi}, d\tilde{A}, d(\phi_{E1} - \phi_{E2}))$. If the ring is working at resonant conditions (as in our case, $\approx 4\lambda_g/2$) several terms can reach values which correspond to relative frequency shifts of the order $1 \cdot 10^{-15}$. Also the temperature dependence of the second term of (7) may be significant at resonant conditions: Forming from this term the total differential one obtain with $\xi=0$, $d\varphi = \tilde{A}\, d\xi$. A relative difference of only 2% in the losses of the two rings on each arm, but also in the coupling between the straight part and the rings would alone be sufficient to explain the magnitude of the experimental findings. Such differences in the ring properties would be insignificant if the rings were designed to be non-resonant.

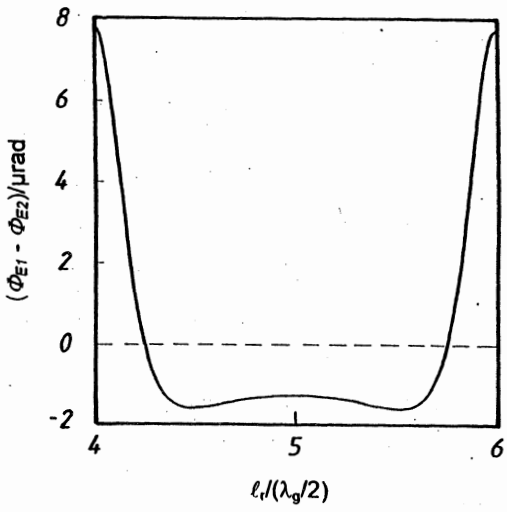

Fig. 5 Contribution to the end-to end phase difference φ (third summand in (6)), $(\Phi_{E1} - \Phi_{E2},)$ as a function of the circumference ℓ_r of the De Marchi type ring cavities [3] mounted as end parts. Between the two rings, an asymmetry in ring circumference of 0,1 mm was assumed.

5. CONCLUSION

Stimulated by previously unexplained experimental results we have re-examined the coupling of the microwave field to a Ramsey type cavity, and studied, in particular, the impact of the coupling and of other cavity parameters on the resulting end-to-end phase difference φ. We have derived an analytical expression for φ which shows how φ and its temperature dependence can be minimised choosing special dimensions for the cavity. Based on these findings, the temperature sensitivity of the end-to-end phase difference of the previous cavity design could be explained and an improved design for coupling of the microwave field to the Ramsey type cavity could be realised with the temperature sensitivity reduced by an order of magnitude.

6. REFERENCES

1. Bauch A., Schröder R., *Phys. Rev. Lett.*, 1997, **78**, 622 - 625.

2. De Marchi A., Francescangeli O., Bava G.P., *IEEE Trans. Instr.Meas.*, 1993, **IM- 42**, 434-438.

3. De Marchi A., Shirley J., Glaze D.J., Drullinger R., *IEEE Trans. Instr. Meas.*, **IM-37**, 1988, 185-190.

4. Vanier J., Audoin, C., *The Quantum Physics of Atomic Frequency Standards*, Bristol and Philadelphia, Adam Hilger, 1989.

5. Bauch A., Heindorff T., Schröder R., *IEEE Trans. Instr. Meas.*, **IM-34**, 1985, 136-138.

6.Bauch, A. Heindorff, T. *Proc. 5th European Frequency and Time Forum*, 1991, 243-248.

DEVELOPMENT OF A FREQUENCY SYNTHESIS CHAIN FOR THE ABSOLUTE FREQUENCY MEASUREMENT OF A $^{127}I_2$-STABILIZED Nd:YAG LASER AT 563.2 THz/532 nm

F. Ducos, Y. Hadjar, G.D. Rovera, J-J. Zondy and O. Acef

BNM-LPTF/CNRS-UMR 8630/Observatoire de Paris
61 Avenue de l'Observatoire, F-75014 Paris (France)
e-mail : Franck.Ducos@obspm.fr

ABSTRACT

We have developed a frequency chain to measure the absolute frequency of a $^{127}I_2$-stabilized Nd:YAG laser at 563.2 THz/532 nm. The measurement is achieved with respect to two secondary optical frequency standards (OFS) operating at 29.1 THz/10.3 μm and 385.4 THz/778 nm respectively. These two OFS have been previously measured against primary cesium clock at the BNM-LPTF.

Keywords: frequency chain, non-linear mixing, femtosecond laser, optical frequency standard, stabilized laser

1. INTRODUCTION

The a_{10} hyperfine component of the R(56) 32-0 iodine transition line is one of recommended radiations by the Comité International des Poids et Mesures (CIPM) for the practical realization of the definition of the meter with a relative standard uncertainty of 40 kHz (Ref. 1). Recently, several measurements for the determination of the absolute frequency of iodine transition lines have been achieved with reduced uncertainties ranging 1 to 5 kHz (Refs. 2-3) using a femtosecond laser.

In this paper, we propose an independent measurement of the absolute frequency of iodine stabilized frequency doubled Nd:YAG lasers at 532 nm with a uncertainty of 1 kHz using the LPTF frequency chain based on the use of two optical frequency standards (OFS).

The first OFS, operating at 29.1 THz/10.3 μm, is a sealed CO_2 laser frequency locked to an OsO_4 saturated absorption line, which is achieved in an external Fabry-Perot cavity. This OFS is known with 4 Hz uncertainty (Ref. 4) and exhibits a very good stability as:

$$\sigma_y(\tau) \sim 1.4 \times 10^{-14}\, \tau^{-1/2}$$

with a minimum value of 6×10^{-16} for an integration time τ=300-400 s (Ref. 5).

The second OFS is based on the use of a low power laser diode, frequency locked on the $5S_{1/2}$, F_g=3 – $5D_{5/2}$, F_e=5 Doppler free two-photon transition of the rubidium atom at 385.4 THz/778 nm. It is known with 1 kHz uncertainty and exhibits a stability as:

$$\sigma_y(\tau) \sim 4 \times 10^{-13}\, \tau^{-1/2}$$

with a minimum value of 2×10^{-14} for an integration time τ=200-5000 s (Ref. 6).

This last uncertainty will determine the ultimate accuracy of the measurement of the OFS at 563.2 THz.

2. EXPERIMENTAL SET-UP

The frequency synthesis chain set-up is shown in Fig. 1. We employ two compact laser diode sources. The first one (LD1) is an α-DFB (angled-grating distributed feedback) laser diode (tunable from 1.063 to 1.067 μm) operating in this case at 1.064 μm. It delivers up to 500 mW cw output power. The second (LD2) is a laser diode operating at 1.551 μm with an output power of 20 mW. This later is frequency doubled using a Periodically Poled Lithium Niobate (PPLN) crystal in order to phase lock its frequency on a transfer laser diode (LD3) operating at 775.5 nm.

On the other hand, the LD1 laser is phase locked on the $^{127}I_2$-stabilized Nd:YAG laser standard (1.06421 μm). The twice value of 611 GHz frequency gap between LD3 and the LD/Rb OFS, is bridged in the visible domain using a femtosecond laser itself phase-locked against H-maser. The difference frequency generation (DFG) between LD1 and LD2 is realized in a 15 mm long type-II cut $AgGaS_2$ crystal. The issued radiation from this nonlinear mixing at 3.39 μm is compared to the one delivered by a 2 m long He-Ne transfer laser. This laser is linked to the third harmonic of OsO_4 standard using a MIM diode. Finally, the frequency in the green will be determined as

$$\nu_{I2} = \nu_{Rb} + 6 \times \nu_{OsO4} + 2 \times 611\ \text{GHz} + \Delta$$

where Δ is the algebraic sum of all frequency beat notes involved in our chain.

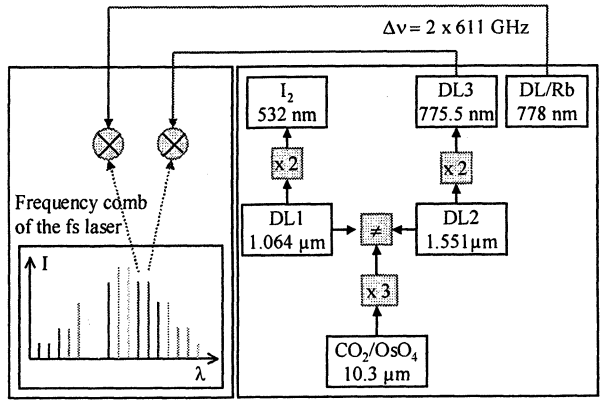

Fig. 1 Chain principle measurement

3. RESULTS

3.1 Bridging the 611 GHz frequency gap

Several methods have been considered to measure this 611 GHz frequency gap. The first one consisted to use an harmonic mixing in a Schottky diode with a far infrared laser phase locked against H-maser (Ref.7). The second one is to generate an optical frequency comb (Ref. 8) in the 1.5 μm range in order to bridge the 611 GHz frequency gap. This last technique is at present under development.

But since the recent coming of femtosecond laser in our laboratory, we have preferred to use it to measure the twice value of frequency gap in the visible domain. The fs laser is a Kerr-lens mode-locked Ti:sapphire laser which operates at a ~880 MHz repetition rate. The optical spectrum covers the 780-820 nm range. For the frequency gap measurement purpose, we use an intermediate laser diode operating in the visible at 775.5 μm (LD3) and the laser diode frequency locked on the two photon transition at 778 nm (LD/Rb).We measure the frequency difference by comparing to the appropriate components of fentosecond laser spectrum separated by 1.2 THz.

As a preliminary result, we have been able to observe beat notes with the fs laser corresponding to two laser diodes with SNR of ~25 dB in a resolution bandwidth of 300 kHz.

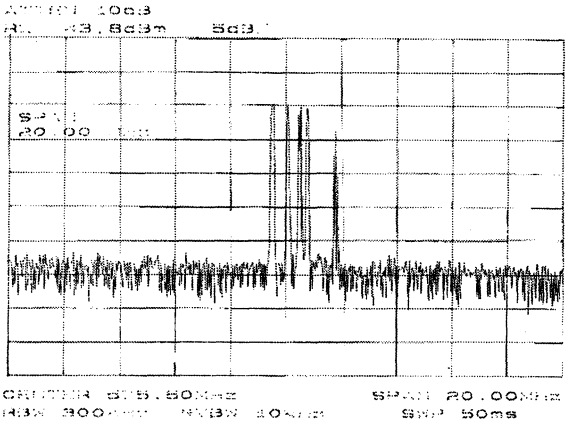

Fig. 2 Beat note at 775.5 nm between the free running fs laser and the LD3.

3.2 SHG at 1.551 μm in a PPLN crystal

To frequency lock the laser diode 2 (LD2) on the intermediate laser diode, we frequency double LD2 in a 19 mm long PPLN crystal of grating period 19 μm. The SHG experimental set-up is shown in figure 3.

The sample is heated at 33 °C to achieve the optimum second harmonic conversion at 1.551 μm. In these conditions, we have detected up to 6.5 μW power at 775.5 nm using 20 mW fundamental power on the crystal. The second harmonic radiation is mixed with 450 μW of LD3 power. We have obtained a beat note at 775.5 nm of SNR~45 dB in a resolution bandwidth of 300 kHz.

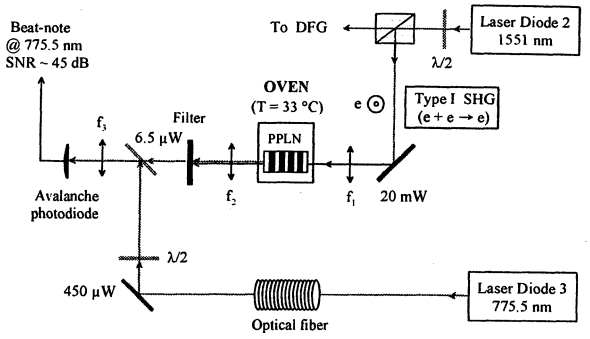

Fig.3 SHG experimental set-up at 1.551 μm in a PPLN crystal

The 6.5 μW of second harmonic power corresponds at 0.85%/Wcm single-pass conversion efficiency. This result is in good agreement with the theoretical value :

$$\eta_{th} = \frac{2\omega_1^3 d_{eff}^2 \hbar(0,\zeta)}{\pi n_1 n_2 \varepsilon_0 c^4} \sim 0.4 - 0.9\%/\mathrm{Wcm} \quad [1]$$

using the effective nonlinear coefficient $d_{eff} = (2/\pi)d_{33} \sim 17$ pm/V ± 20%. ω_1 is the frequency of the fundamental beam, $\hbar(0,\zeta)$ is the Boyd-Kleinman focusing factor (Ref. 10) for the assumed geometry, n_1 and n_2 are refractive index at the fundamental and second harmonic wavelengths, ε_0 is the permittivity of vacuum and c is the speed of light.

The SHG power as a function of the wavelength and of the temperature are shown in figure 4(a) and 4(b). We have determined the acceptance bandwidths for the wavelength at 1.551 μm and the temperature respectively. We have obtained $\Delta\nu$=1.1 nm and ΔT=10°C. This is in good agreement with the calculated values which are $\Delta\nu$= 1.2 nm and ΔT=8°C.

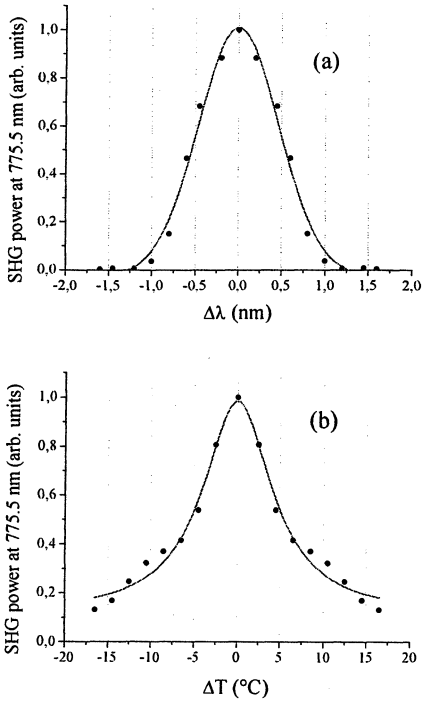

Fig. 4 Acceptance bandwidths for the wavelength at 1.551 μm (a) and the temperature (b)

3.4 DFG in a type II cut $AgGaS_2$ crystal

The DFG experimental setup is presented in figure 5. We generate the frequency difference between LD1 and LD2 using a (2 x 2 x 15) mm type-IIA $AgGaS_2$ (AGS) crystal (θ=68°, φ=0°). The two beams are combined collinearly using a dichroic beamsplitter and focused into the AGS crystal. The type-II A ($e_p - o_s \rightarrow e_i$) interaction gives the largest coefficient in AGS, d_{36}=13 ± 2 pm/V (Ref. 11). Therefore, the pump (1.064 μm) and signal (1.551 μm) beams must be polarized perpendicularly with respect to the crystal axis. The two faces of crystal were not antireflection coated. In this situation, only 70% of the input powers are coupled into the crystal, corresponding to 87 mW pump power at 1064.21 nm and 14 mW of signal power at 1551 nm. A spectral filter is placed in front of the detector to block the pump and signal beams. Taking into account the transmission of the CaF_2 lens and spectral filter, a maximum idler power of 128 nW was achieved, then linked to the intermediate He-Ne laser. We have realized the beat note at 88.4 THz with 300 μW of intermediate He-Ne laser power. We have obtained a SNR of 40 dB in a resolution bandwidth of 300 kHz.

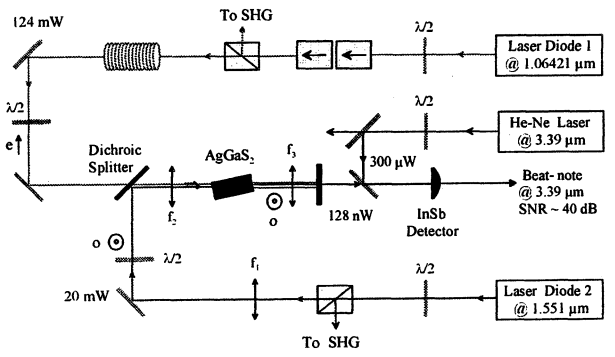

Fig. 5 DFG experimental set-up at 3.39 μm in a $AgGaS_2$ non-linear crystal.

The measured infrared power corresponds to a normalized conversion efficiency of 7.1 x 10^{-3} %/Wcm and gives an effective nonlinear coefficient ~ 9 pm/V.
The theoretical expression for an optimum DFG conversion efficiency for the case of two Gaussian beams with a joint waist location at the middle of the crystal is (Ref. 12) :

$$\eta_m = \frac{P_i}{P_p P_s l} = \frac{8\omega_i^2 d_{eff}^2 \exp(-\alpha_i l) h_m(B,\mu)}{\pi \varepsilon_0 c^3 n_p n_s n_i (k_s^{-1} - k_i^{-1})} \quad [2]$$

where ω_i is the idler frequency, d_{eff} is the effective nonlinear coefficient, α_i is the idler linear absorption coefficient, $h_m(B,\mu)$ is the optimum focusing parameter (Ref. 12) which is a function of the walk-off parameter

$$B = \rho \left[(k_p - k_s) l \right]^{1/2} / 2$$

with ρ the walk-off angle and degeneracy parameter $\mu = k_s / k_p$, ε_0 and c are the permittivity and the speed of light in vacuum respectively, n_p, n_s, n_i are the refractive indices for the pump, signal and idler wavelengths respectively, k_s, k_i are the signal and idler wave-vectors.
For the lasers used in this experiment, $\mu \approx 0.69$ and the walk-off angle is about 0.87°, indicating a walk-off parameter B of 1.9 inside the crystal. We estimate an optimum focusing parameter value of $h_m(B,\mu) \approx 1.2 \times 10^{-2}$. The calculated internal efficiency according to the equation [2] is 7.8 x 10^{-3} % /Wcm when absorption is neglected. The measured efficiency is comparable with the calculated efficiency in our crystal. The experimental values of the DFG power are plotted as a function of the product of pump and signal input powers in figure 7.

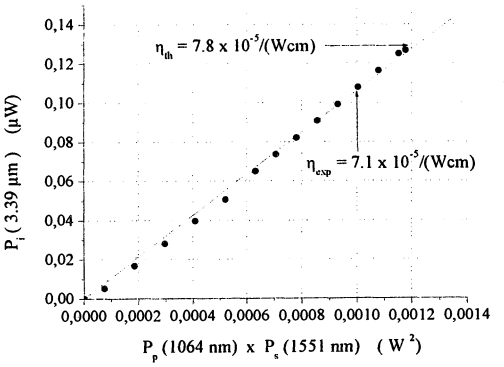

Fig. 7 DFG power P_i (3.39 μm) as a function power product P_p (1064 nm) x P_s (1551 nm). The pump power was fixed at P_p=87 mW.

We have varied the signal input power at 1.551 μm while was fixed the pump power as P_p=87 mW. A maximum of P_i=128 nW was so obtained. The DFG power versus of the product P_p x P_s (Fig. 7) is linear with a length normalized slope efficiency of η=7.1 x 10^{-3} %/Wcm. This is in good agreement with the value calculated by use of Eq. [2].
The DFG power as a function of the signal and pump wavelengths are shown in Fig. 7(a) and 7(b). The theoretical curves are obtained by deriving the phase-mismatch $\Delta k = k_p - k_s - k_i$ with respect to λ_s, λ_p and plotting the $\text{sinc}^2(\Delta kl/2)$.

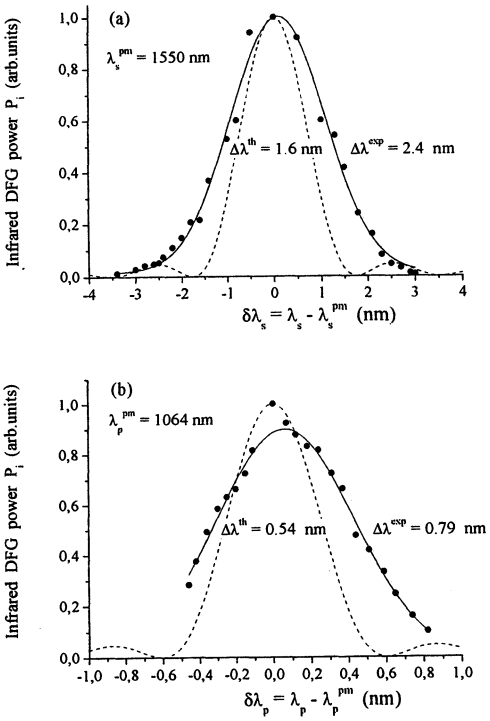

Fig. 7 Wavelength acceptance bandwidths for the signal (a) and pump (b) beams.

The wavelength acceptance bandwidths for the both beams are respectively 2.4 nm and 0.79 nm. The calculated values give $\Delta\lambda_s$=1.6 nm and $\Delta\lambda_p$=0.54 nm, using a plane-wave analysis. This discrepancy is due to the combined effect of walk-off and focusing. Using a Gaussian-wave DFG analysis (Ref. 12), it is possible to show these broadenings and to predict the slight asymmetry of the curves due to the aperture effect (Ref. 13). We have also measured the DFG power as a function of the crystal angle (Fig. 8). The theoretical curve is obtained by deriving the phase-mismatch $\Delta k = k_p - k_s - k_i$ with respect to θ and plotting the $\text{sinc}^2(\Delta kl/2)$. The calculated value gives $\Delta\theta$ =0.15° using plane-wave analysis. Experimentally, we find an angular acceptance bandwidth of about 0.24°.

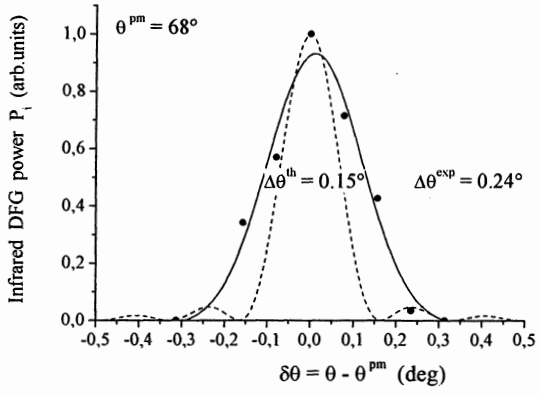

Fig. 8 Internal angular acceptance bandwidth was accomplished by rotating the mixing crystal for pump and signal wavelengths fixed.

4. CONCLUSION

We have realized all the frequency mixings necessary for the frequency synthesis chain. We have achieved SHG from 1551 to 775.5 nm in a PPLN crystal with 6.5 μW of output power, corresponding to a single-pass conversion efficiency of 0.85%/Wcm. We have generated the frequency difference (DFG) in a $AgGaS_2$ crystal with a maximum idler power of 128 nW. Then, we have compared its frequency with the transfer He-Ne laser frequency at 88.4 THz.
The next step of this work is to link the intermediate He-Ne laser to the third harmonic of our 29.1 THz OsO_4 standard. We expect to measure the absolute frequency of iodine stabilized frequency doubled Nd:YAG laser at 563.2 THz/532 nm with an uncertainty of 1 kHz (~2 x 10^{-12}).

5. ACKNOWLEDGEMENTS

This work is a part of the scientific developments of the Bureau National de Métrologie (BNM-France). We gratefully thank P. Yelisseyev and L.I. Isaenko from DTIM (Novossibirsk) for providing the first AGS crystal used in early stage. Great thanks are due to the electronic staff and to A.H. Gerard for their help in the course of this work. I wish doing homage at Y. Millérioux, deceased the last year, for his useful discussions on the development of the frequency chain.

REFERENCES

[1] T. J. Quinn, "Practical realization of the definition of the meter (1997)", Metrologia, Vol. 36, pp. 211-244, 1998

[2] S. A. Diddams, D. J. Jones, Jun Ye, S.T. Cundiff, J.L. Hall, J.K. Ranka, R.S. Windeler, R. Holzwarth, Th. Udem, T.W. Hänsch, Phys. Rev. Lett., No. 84, pp. 5102, 2000.

[3] H. Schnatz, private communication.

[4] F. Ducos, G.D. Rovera, C. Daussy and O. Acef, " Performances of OsO4 stabilized CO2 lasers as optical frequency standards near 29 THz", in Proceedings of the 1999 Joint Meeting of the European Frequency and Time Forum and the IEEE International Frequency Control Symposium, Vol.2, 1999, pp.714-717.

[5] F. Ducos, Y. Hadjar, G.D. Rovera, J-J. Zondy and O. Acef, "Progress toward absolute frequency measurements of the 127-I2-stabilized Nd:YAG laser at 563.2 THz/532 nm", IEEE Transactions on Instrumentation and Measurement, Vol. 50, No. 2, 2001.

[6] D. Touahri, O. Acef, A. Clairon, J.J. Zondy, R. Felder, L. Hilico, B. Beauvoir, F. Nez and F. Biraben, "Frequency measurement of the $5S_{1/2}$-$5D_{1/2}$ two photon transition in rubidium", Optics Comm., Vol. 133, p. 471, 1997.

[7] O. Acef, L. Hilico, M. Bahoura, F. Nez and P. de Natale, "Comparison between MIM diodes as harmonic mixers for visible lasers and microwave sources", Optics Comm., Vol. 109, pp.428-434, 1994.

[8] M. Kourogi, K. Nakagawa and M. Ohtsu, "A highly accurate frequency counting system for 1.5 μm wavelength semiconductor lasers", SPIE, Vol. 1837, pp. 205-215, 1992.

[9] G.D. Rovera, J-J. Zondy, O. Acef, F. Ducos, "The new BNM-LPTF optical frequency measurement chain", this issue.

[10] G. D. Boyd and D. A. Kleinman, "Parametric interaction of focused gaussian light beams", J. Appl. Phys, Vol. 39, pp. 3597-3639, 1968.

[11] V. G. Dmitriev, G.G. Gurzadyan, D.N. Nikogosyan, Handbook of nonlinear optical crystals, 3rd Edition, Springer Series in Optical Sciences, Vol. 64, pp. 132, 1999.

[12] J. J. Zondy,"the effects of focusing in type-I and type-II difference-frequency generations", Opt. Com., No. 149, pp. 181-206, 1998.

[13] J.J. Zondy, D. Touahri, O. Acef, J. Opt. Soc. Am. B, No. 14, pp. 2481, 1997.

Electrostatic Trapping of Linear Polar Molecules

Masatoshi Kajita[1], Takayuki Suzuki[1, 2], Hitoshi Odashima[3], Yoshiki Moriwaki[4], and Maki Tachikawa[2]

1) Communications Research Laboratory, Koganei, Tokyo 184-8795, Japan
2) Department of Physics, Meiji University, Tama-ku, Kawasaki 214-8571, Japan
3) Department of Physics, Toyama University, Gofuku, Toyama 930-8555, Japan
4) Institute for Molecular Science, Myodaiji, Okazaki 444-8585, Japan

Abstract: We theoretically demonstrate possibility of trapping linear polar molecules in static quadrupole electric fields. Classical analysis shows that molecules rotating in a specific direction experience a restoring force toward the center of the field distribution. The potential depth is quantum-mechanically evaluated for alkali-halide molecules to be in the order of hundred mK.

Key words: molecule, trapping, Mojorana effect, Stark effect

1. Introduction

Molecular spectrum has been used for optical frequency standards [1]. To improve the accuracy of the measured frequency, it is preferable to observe Doppler free spectrum from cold molecules trapped in space.

Just recently, several groups developed effective methods to prepare ultra-cold gases and confine them in three-dimensional traps. Harvard group used static magnetic fields to trap paramagnetic CaH molecules pre-cooled through buffer gas collisions [2,3]. Cesium dimers produced by the photo-association of laser-cooled Cs atoms were trapped in focused CO_2 laser beam [4].

The idea of trapping molecules with static electric fields was first proposed by Wing [5]. Bethlem et al. decelerated ND_3 molecular beams by time-varying inhomogeneous electric fields and loaded them into an electrostatic trap [6]. In the quadrupole electric fields, three-dimensional restoring force is exerted on molecules that show second-order Stark energy shift.

In this paper, we theoretically investigate motion of a linear polar molecule, another molecular species that has the second-order Stark effect, in static quadrupole electric fields. The depth of the trap potential is quantum mechanically estimated from the Stark energy shift. Numerical simulation based on classical equations of motion shows that a linear molecule is stably trapped when its plane of rotation is parallel to the electric field. The stability of the trap is discussed in relation to the Majorana effect.

2. Electrostatic Quadrupole Trap

In our analysis, we consider a quadrupole trap composed of two end-cap electrodes and a ring electrode, as is shown in Fig. 1. The end-cap electrodes are biased with respect to the ring electrode by a static voltage V_0. The inner surfaces of these electrodes form hyperboloids of revolution with inner radius r_0 and end-cap-to-end-cap distance $2z_0$. In Cartesian coordinate system with its origin at the trap center, the electric field distribution is expressed as,

$$\vec{E}(x,y,z) = a\,(x,y,-2z)\,, \qquad (1)$$

where $a = \dfrac{2V_0}{r_0^2 + 2z_0^2}$.

The electric field is zero at the trap center and becomes stronger in any direction as the distance from the center increases.

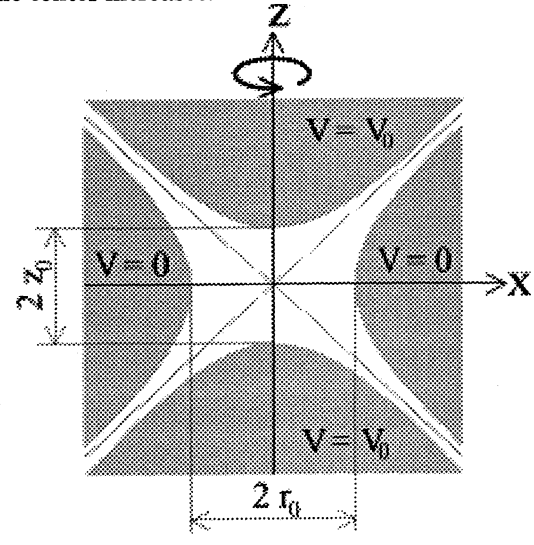

Fig. 1 Cross section of the quadrupole electrodes. The inner surfaces of the electrodes are hyperboloids of revolution symmetric around the z-axis. The end-cap electrodes are biased with respect to the ring electrode by a static voltage V_0.

To make a three-dimensional potential well with

the quadrupole field distribution, it is necessary that the molecular species have the second-order Stark effect so that the energy increases with increasing magnitude of E. For a linear polar molecule, the Stark energy shift for reasonably weak electric field is written as,

$$\Delta W = \frac{\mu^2 E^2}{2hBJ(J+1)} \frac{J(J+1)-3M^2}{(2J-1)(2J+3)}, \qquad (2)$$

where μ is the dipole moment, h Plank's constant, and B the rotational constant of the linear molecule. The quantum numbers J and M represent the total angular momentum and its projection on the electric field, respectively.

Molecules in a quantum state with $J(J+1)>3M^2$ have higher energy where the electric field is stronger. The field gradient exerts a restoring force on these molecules that is directed to the trap center; the molecule is in the low-field searching state. Molecules in a state with $J(J+1)<3M^2$ are driven by an opposite force and are expelled from the trap; the molecule is in the high-field searching state. In a classical picture, which is valid in the limit of $J\to\infty$, the condition for being trapped is $\cos^2\Theta < 1/3$, where Θ is the angle of the molecular angular momentum with respect to the electric field.

Figure 2 shows the Stark energy shift of the $|J, M> = |1, 0>$ state of NaCl more rigorously calculated from diagonalization of the Hamiltonian matrix. It is noted that the energy first increases and then decreases with an increase in the field strength. The potential depth of 200 mK is achieved at the electric field of 7 kV/cm.

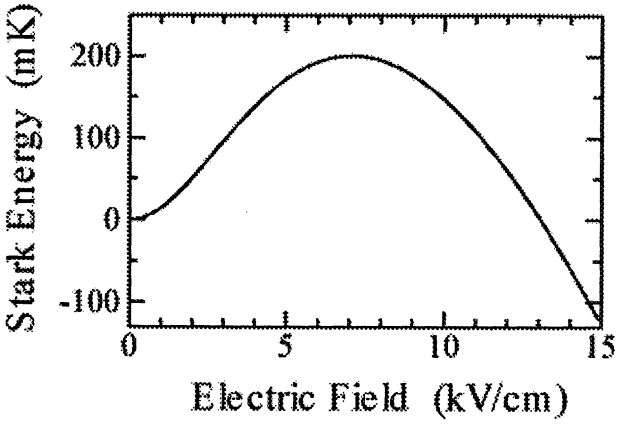

Fig.2 Stark energy of NaCl in the $|J,M> = |1,0>$ state as a function of the electric field.

3. Equations of Motion and Numerical Results

As a molecule travels in the inhomogeneous fields, the direction of electric field at its position changes. If a molecule is initially in the low-field searching state, and its angular momentum keeps a constant angle with the electric field, the molecule remains in the same $|J, M>$ state and is stably trapped. On the other hand, when a molecule moves too fast, so-called Majorana effect takes place in which the angular momentum does not follow the change in the field direction, and its angle with the field changes in time.

We investigate motion of a linear polar molecule numerically on the basis of classical equations of motion, and clarify whether or not the Majorana effect is dominant.

In our classical model, we assume that the linear molecule is a rigid rotor with the mass m and the moment of inertia about axes perpendicular to the internuclear axis I. Motion of the polar molecule in the electric fields (1) is described by the following equations:

$$m\frac{d^2x}{dt^2} = \mu a \sin\theta\cos\varphi, \qquad (3)$$

$$m\frac{d^2y}{dt^2} = \mu a \sin\theta\sin\varphi, \qquad (4)$$

$$m\frac{d^2z}{dt^2} = -2\mu a \cos\theta, \qquad (5)$$

$$I\frac{d^2\theta}{dt^2} = I\sin\theta\cos\theta\left(\frac{d\varphi}{dt}\right)^2 + \mu a\left(x\cos\theta\cos\varphi + y\cos\theta\sin\varphi + 2z\sin\theta\right), \qquad (6)$$

$$I\sin^2\theta\frac{d^2\varphi}{dt^2} = -2I\sin\theta\cos\theta\left(\frac{d\theta}{dt}\right)\left(\frac{d\varphi}{dt}\right) + \mu a\left(-x\sin\theta\sin\varphi + y\sin\theta\cos\varphi\right). \qquad (7)$$

Here (x, y, z) is the position of center of gravity of the molecule, and its orientation in space is specified by the spherical polar coordinates θ and φ.

Equations (3)-(7) are numerically integrated by the Adams method with parameter values for NaCl molecule (m=58 a.u., I=1.28 x 10^{-45} kgm^2, μ =8.5 debyes). The field parameter a is fixed to 20 kV/mm^2. The total energy of the system is monitored to check the accuracy of the calculation. Figures 3 (a) and (b) show projection of a calculated molecular orbit on the x-y plane and the x-z plane. Initially the molecule is placed on the x axis 1 μm away from the trap center, and rotates in the x-y plane with an angular frequency

of 2π x 1.1 x 10^{10} Hz, which corresponds to the rotational energy of the $J = 1$ state. The molecule is initially in the low-field searching state since its angular momentum is perpendicular to the electric field. Initial translational velocity is (0 m/s, 0.2 m/s, 3 m/s).

The fact that the orbit is a closed loop implies that the static fields are working as a confining force to the rotating molecule. The center-of-mass motion in each degree of freedom is well described by harmonic oscillation.

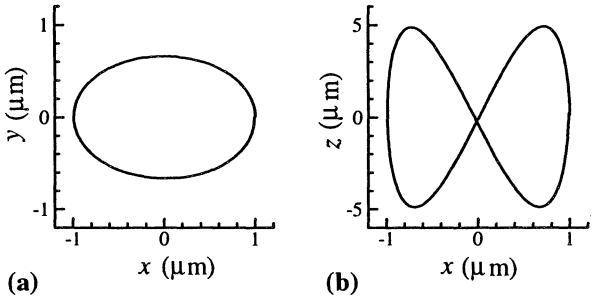

Fig. 3 The center-of-mass orbit of a NaCl molecule numerically calculated with the condition described in the text. (a) and (b) show the trajectory in the x-y and x-z planes, respectively.

The angle of the angular momentum to the electric field always falls around 90°. The molecule remains in the low-field searching state while orbiting around the trap region.

Numerical analysis suggests that the Majorana effect is negligibly small under the present condition. The center-of-mass drift is much slower than the internal rotation, and the plane of rotation almost keeps a constant angle to the field direction.

4. Conclusion

We have theoretically demonstrated that a linear polar molecule is stably trapped in static quadrupole electric fields, if it initially rotates in a plane parallel to the electric field. It has been shown that a potential well is as deep as several hundred mK for alkali halide molecules. Laser ablation and successive buffer-gas cooling can prepare such low-temperature gases.

References

1. P. E. Durand *et al.*, Europhys. Lett. **73**, 103 (1997).
2. J. D. Weinstein *et al.*, Nature **395**, 148-150 (1998).
3. J. M. Doyle *et al.*, Nature **401**, 749-751 (2000).
4. T. Takekoshi et al., Phys. Rev. Lett. **81**, 5105-5108 (1998).
5. W. H. Wing, Phys. Rev. Lett. **45**, 631-634 (1980).
6. H. L. Bethlem et al., Nature **406**, 491-494 (2000).

ALL OPTICAL ATOMIC CLOCKS BASED ON A SINGLE MERCURY ION AND CALCIUM ATOMS

R.E. Drullinger, Th. Udem*, S.A. Diddams, K.R. Vogel**, C.W. Oates,
E.A. Curtis, W.D. Lee†, W.M. Itano, L. Hollberg, and J.C. Bergquist
National Institute of Standards and Technology, Boulder Colorado, USA
*Max-Planck-Institut fur Quantenoptik, Hans-Kopfermann-Str.1, Garching Germany
**Precision Photonics, Boulder, Colorado, USA
† Research Electro Optics, Boulder Colorado, USA

ABSTRACT

The frequency comb created by a femtosecond mode-locked laser and a microstructure fiber is used to phase-coherently measure the frequencies of both the Hg^+ and Ca optical frequency standards with respect to the SI second as realized at NIST. We find the transition frequencies to be f_{Hg} = 1 064 721 609 899 143(10) Hz and f_{Ca} = 455 986 240 494 158(26) Hz, respectively. This work begins to reveal the high stability and accuracy potential of optical atomic clocks based on the Hg^+ and Ca standards. Furthermore, when combined with previous measurements, we find no time variations of these atomic frequencies within the uncertainties of $|(\partial f_{Hg}/\partial t)/f_{Hg}| < 2 \times 10^{-14}$ yr^{-1} and $|(\partial f_{Ca}/\partial t)/f_{Ca}| < 8 \times 10^{-14}$ yr^{-1}.

Keywords: Optical, Atomic Clock, femtosecond, comb

INTRODUCTION

Optical frequency standards based on laser-cooled atoms and ions promise superior stability and accuracy over existing microwave standards [1–5]. However, because of their high frequencies (~ 10^{15} Hz or PHz), it has proven difficult to count cycles as required for building functioning clocks. Only recently, a reliable and convenient clockwork fast enough to count optical oscillations has been realized [6–9]. Here, we report on work toward an all-optical- clock based on a femtosecond laser that phase-coherently divides down the frequency of the visible radiation from either a Hg^+ or Ca optical-frequency standard to a countable radio frequency. We have measured the absolute frequencies of these optical transitions in terms of the SI second as realized at NIST [10]. Indeed, for the Hg^+ standard, the uncertainty in the measurement is essentially limited by our knowledge of the SI second at ~2 × 10^{-15}. Additionally, the comparison of atomic frequencies over time provides constraints on the possible time variation of fundamental constants. We now have measurements of the absolute Hg^+ frequency taken over a six month interval that differ by less than their statistical uncertainty and much less than their systematic uncertainty.

THE OPTICAL STANDARDS

The Hg^+ and Ca systems have recently been described elsewhere [1,4, 11-13], so we summarize only their basic features. The mercury optical frequency standard is based on a single, laser-cooled $^{199}Hg^+$ ion that is stored in a cryogenic, radio-frequency, spherical Paul trap. The ion is cooled and detected by driving the $^2S_{1/2}$ - $^2P_{1/2}$ cycling transition at 194 nm. The $^2S_{1/2}$ (F =0, M_F = 0) - $^2D_{5/2}$ (F =2 , M_F = 0) electric-quadrupole transition at 282 nm [Fig.1] provides the reference for the optical standard [1]. We lock the frequency-doubled output of a 563 nm dye laser with sub-hertz linewidth[12] to the quadrupole resonance. Transitions to the metastable $^2D_{5/2}$ state are detected with near unit efficiency since the absorption of a single 282 nm photon suppresses the scattering of many 194 nm photons on the strongly allowed $^2S_{1/2}$ - $^2P_{1/2}$ transition [14, 15]. In figure 2 we show an example of a normalized spectrum that was obtained from multiple, bidirectional scans through the resonance, where the probe time was 20 ms. Most often, the frequency was locked to resonance with a 10 ms interrogation period, which yielded a fractional frequency stability of 2 ×10^{-15} $\tau^{-1/2}$ for an averaging time τ measured in seconds [16].

The calcium standard starts with a collection of ~10^7 laser-cooled ^{40}Ca atoms held in a magneto-optic trap. The 423 nm^1 S_0 - $^1P_1$ transition is used for trapping and Doppler-cooling the atoms to a residual temperature of ~2 mK. The $^1S_0$ (M_J = 0) - $^3P_1$ (M_J = 0) weakly allowed electric-dipole transition (400 Hz natural linewidth) at 657 nm is the "clock" transition for this frequency standard [Fig. 3]. We excite the transition with a four-pulse Bordé-Ramsey sequence (pulse duration =1.5 μs) with light from a continuous-wave (CW), frequency-stabilized diode laser. Using a shelving detection technique similar to that employed in the Hg^+ system, near-resonant 423 nm pulses (5 μs duration) are used before and after the 657 nm excitation to determine the fraction of atoms transferred from the ground state. Figure 4 shows the Bordé-Ramsey fringes taken at a resolution of 960 Hz. This system has demonstrated a fractional frequency stability of 4 × 10^{-15} $\tau^{-1/2}$ when probing sub-kilohertz linewidths[4]. For the measurements presented here the Ca spectrometer was operated with linewidths ranging from 0.96 to 11.55 kHz, which are integer submultiples of the recoil splitting.

THE OPTICAL COMB

The recent introduction of mode-locked lasers to optical frequency metrology greatly simplifies the task of optical-frequency measurements [6 –8, 17 –19]. The spectrum emitted by a mode-locked laser consists of a comb of regularly spaced continuous waves that are separated by the pulse repetition rate f_r. The frequency of the nth mode of the comb is given by $f_n = nf_r + f_0$ [20, 21], where f_0 is the frequency offset common to all modes. This offset is caused by the difference between the group- and the phase-velocity inside the laser cavity. f_r can be measured by direct detection of the laser's output with a photodiode. f_o is measured by heterodyning the 2nd harmonic of mode $f_n = nf_r + f_0$ from the infrared wing of the comb with mode $f_{2n} = 2nf_r + f_0$ from the blue side of the comb [7, 8]. This self-referenced technique requires that the optical comb span at least an octave in frequency space. While an octave-spanning comb can be produced directly from a mode-locked laser [22], launching the longer pulses from a

commercially-available femtosecond laser into an air-silica microstructure fiber [23, 24] also produces a frequency comb that spans an octave. Nonlinear processes in the fiber produce the additional equally spaced and phase-coherent modes to the transmitted light. It has been demonstrated that this process of spectral broadening preserves the uniformity of spacing and spectral fidelity of the comb to at least a few parts in 10^{16} [8].

We couple approximately 200 mW average power from a femtosecond, Ti:sapphire ring laser ($f_r \approx 1$ Ghz) through a 15 cm piece of microstructure fiber that has a 1.7 μm core and group-velocity dispersion that vanishes near 770 nm [23]. This power density is sufficient to increase the spectral width of the laser from 13 THz to more than 300 THz, spanning from ~520 nm to ~1170 nm. The infrared part of the comb from the fiber ($\lambda \approx 1060$ nm) is split off by a dichroic mirror and frequency-doubled into the green portion of the visible spectrum by means of a $KNbO_3$ crystal 2 mm long. Following an adjustable delay line that matches the optical path lengths, the frequency-doubled light is spatially combined with the green part of the original comb to produce a beat note at f_0. We phase-lock both f_0 and f_r to synthesized frequencies derived from a cavity-tuned hydrogen maser that acts as the transfer standard to the NIST realization of the SI second [10]. Control of f_r is achieved with a piezo transducer driving a cavity mirror, while f_0 is controlled by adjusting the 532 nm pump beam's intensity with an electro-optic modulator [8]. When both f_0 and f_r are phase-locked, the frequency of every mode in the comb is known with the same accuracy as that of the reference maser.

The CW light from the Hg^+ (563 nm) and Ca (657 nm) standards is transferred to the mode-locked laser system via two single-mode optical fibers that are 130 m and 10 m long, respectively. Approximately 2 mW of CW light from each fiber is mode-matched with the appropriate spectral region of the frequency comb to generate a beat signal f_b with a nearby mode. This beat note is amplified and measured with a counter. The optical frequency is then expressed as $f_{opt} = mf_r + f_0 + f_b$, where m is a large integer uniquely determined for each system from previous coarse measurements of f_{opt}.

RESULTS

Figure 5 summarizes the frequency measurements of Hg^+ made between August 2000 and February 2001, while figure 6 summarizes the Ca measurements made from October 26 to November 17, 2000. The frequency of the maser is calibrated by comparing to the local NIST time scale (5 hydrogen masers and 3 commercial cesium clocks), which in turn is calibrated by the local cesium fountain standard (NIST-F1 [10]). The fractional uncertainty in the frequency of the reference maser relative to the SI second was about 1.8×10^{-15} for these measurements.

The weighted mean of our measurements of the Hg^+ clock transition is f_{Hg} =1 064 721 609 899 143 Hz. The statistical uncertainty ($\approx 4 \times 10^{-15}$) of our limited duration measurements is essentially the result of the reference-maser's short-term stability ($\sim 2 \times 10^{-13}\tau^{-1/2}$). Because we have not made a full experimental evaluation of the Hg^+ standard, we assign a very conservative value of 10 Hz for the total systematic uncertainty. The dominant contribution to the uncertainty of the *S-D* transition frequency is the electric-quadrupole shift of the $^2D_{5/2}$ state arising from coupling with the static potentials of the trap. In our spherical Paul trap, where the confinement of the ion uses no static applied fields, the maximum quadrupole shift should be less than 1 Hz (or fractional frequency shift $<10^{-15}$) [25]. In principle, it is possible to eliminate the quadrupole shift by averaging the *S-D* transition frequencies for three mutually orthogonal orientations of quantizing magnetic field of constant magnitude. In the present experiment, we have measured the *S-D* frequency for various field values, but we have made no attempt to eliminate the quadrupole shift by using three orthogonal fields of constant magnitude. No shift of the resonance frequency is observed within the precision of these measurements even under strongly varying conditions of magnetic field. We anticipate that the uncertainties of all systematic shifts in the Hg^+ system can be reduced to values approaching 1×10^{-18} [1, 25].

For the Ca data shown [Fig. 6], an additional correction is applied each day to account for frequency shift caused by residual phase chirping on the optical Ramsey pulses produced by amplitude modulating an acoustooptic modulator (AOM). The phase chirping produced resolution-dependent frequency shifts on the order of 100 Hz for fringes 11.5 kHz wide but of only 10 Hz for fringes 0.96 kHz wide. On each day, the Ca frequency was measured for ~30 minutes at each of several fringe resolutions, and the zero-intercept of a linear fit to the data was used as the corrected frequency. On the last 3 days of measurements, we were able to reduce this shift by a factor of ~3 with improvements to the RF pulses that drive the AOMs. The statistical uncertainty (typically 8 Hz) for each day's measurement is smaller than the uncontrolled systematic uncertainties in the Ca frequency. The largest systematic uncertainty stems from incomplete knowledge of the angular overlap of the counter-propagating beams in the Ca spectrometer, combined with transverse drift velocity of the cold Ca ensemble. This leads to residual first-order Doppler shift with magnitude < 15 Hz (except on November 16, where a large drift velocity led to an uncertainty of ~52 Hz). Other significant uncertainties include our lack of knowledge or control of electronic offsets and baseline symmetries (< 12 Hz), wavefront curvature (< 10 Hz), and cold-atom collisional shifts (< 10 Hz). Taking all known systematic uncertainties in quadrature gives a confidence level of ~26 Hz for the measured mean values indicated by the dashed lines in figure 6.

Figure 6 also shows the good agreement between our measurement and the most recent value measured with a harmonic frequency chain [26], which provides a degree of confidence in the reproducibility of the Ca standards. It is also in reasonable agreement with the very recent PTB measurements made with a femtosecond comb [27]. An additional measure of the Ca frequency can be made by using the present absolute measurement of Hg^+ and our earlier measurement of the 76 374 564 455 429(40) Hz gap between f_{Hg} and the Ca standard [28]. This yields a value of f_{Ca} =455 986 240 494 143(40) Hz in good agreement with the value from the present direct measurement.

Finally, these results also provide data on the relative time variability of atomic frequencies. S. Karshenboim has recently reviewed the implications of such comparisons and their

contribution toward constraining the possible time variation of fundamental constants [29]. In this regard Hg^+ and Ca are two of the most interesting cases to study. Comparing our present measurement of f_{Ca} to measurements made by PTB in 1997 [26] gives $(\partial f_{Ca}/\partial t)/f_{Ca} < 8 \times 10^{-14}$ yr^{-1}. Similarly, our August 2000 to February 2001 measurements on f_{Hg} provides an initial baseline constraint on the time variation of $(\partial f_{Hg}/\partial t)/f_{Hg} \leq 2 \times 10^{-15}$ yr^{-1}. Here we use the defined unit of time based on the frequency of the Cs hyperfine interval and assume that any time dependence is slow and dominantly linear over the relevant time scale. We believe this represents the tightest laboratory test yet of the time variability of these disparate transitions.

ACKNOWLEDGMENTS

We acknowledge the support of the Office of Naval Research. This work was also supported through a Cooperative Research and Development Agreement with Timing Solutions, Corp., Boulder, Colorado. This work is a contribution of the National Institute of Standards and Technology, and is therefore not subject to United States copyright.

REFERENCES

[1] R.Rafac, B.C. Young, J.A. Beall, W.M. Itano, D.J. Wineland and J.C. Bergquist, Phys. Rev. Lett. 85, 2462 (2000).
[2] J.E.Bernard, A. A. Madej, L. Marmet, B. G. Whitford, K. J. Siemsen, and S. Cundy , Phys. Rev. Lett. 82, 3228 (1999).
[3] H.Schnatz, B. Lipphardt, J. Helmcke, F. Riehle, and G. Zinner, Phys. Rev. Lett. 76, 18 (1996).
[4] C.W.Oates, E. A. Curtis, L. Hollberg, Opt. Lett. 25, 1603 (2000).
[5] J.von Zanthier, Th. Becker, M. Eichenseer, A. Yu. Nevsky, Ch. Schwedes, E. Peik, H. Walther, R. Holzwarth, J. Reichert, Th. Udem, T. W. Hänsch, P. V. Pokasov, M. N. Skvortsov, S. N. Bagayev, Opt. Lett. 25, 1729 (2000).
[6] S.A.Diddams, David J. Jones, Jun Ye, Steven T. Cundiff, and John L. Hall, Phys. Rev. Lett. 84, 5102 (2000).
[7] D.J.Jones, S.A. Diddams, J.K. Ranka,A. Stentz, R.S. Windeler J.L. Hall and S.T. Cundiff, Science, 288, 635 (2000).
[8] R.Holzwarth, Th. Udem, and T. W. Hänsch, Phys. Rev. Lett. 85, 2264 (2000).
[9] S.A. Diddams, Th.Udem, K.R. Vogel, C.W. Oates, E.A. Curtis, R.S. Windeler, A. Bartels, J.C. Bergquist and L. Hollberg, Proc SPIE Conf. on Laser Frequency Stabilization, Standards, Measurement, and Applications, San Jose, CA January 2001.
[10] S.R.Jefferts, *et al.*, submitted to Metrologia; S.R.Jefferts, *et al.*, IEEE International Freq.Control Symp., 714 (2000).
[11] C.W.Oates, F. Bondu, R.W. Fox and L. Hollberg, J.Phys.D, 7, 449 (1999).
[12] B.Young, F. C. Cruz, W. M. Itano, and J. C. Bergquist, Phys. Rev. Lett. 82, 3799 (1999).
[13] J.C. Bergquist, R.J. Rafac, B.C. Young, J.A. Beall, W.M. Itano, and D.J. Wineland, Proc SPIE Conf. on Laser Frequency Stabilization, Standards, Measurement, and Applications, San Jose, CA January 2001.
[14] H.Dehmelt, Bull. Am. Phys. Soc. 20, 60 (1975).
[15] J.C.Bergquist, Wayne M. Itano and D. J. Wineland, Phys. Rev. A, 36, 428 (1987).
[16] D.J.Wineland, *et al.*, *The Hydrogen Atom* ed. by T.W.Hänsch (Springer,Berlin,Heidelberg 1989) pp.123-133.
[17] Th.Udem, J. Reichert, R. Holzwarth, and T. W. Hänsch, Phys. Rev. Lett. 82, 3568 (1999).
[18] J.Reicher, M. Niering, R. Holzwarth, M. Weitz, Th. Udem, and T. W. Hänsch, Phys. Rev. Lett. 84, 3232 (2000).
[19] M.Niering, R. Holzwarth, J. Reichert, P. Pokasov, Th. Udem, M. Weitz, and T. W. Hänsch , Phys. Rev. Lett. 84, 5496 (2000).
[20] A.I.Ferguson, J.N. Echstein, T. W. Hänsch, Appl. Phys. 18, 257 (1979).
[21] J.Reicher, R. Holzwarth, Th. Udem and T. W. Hänsch, Opt. Comm. 172, 59 (1999).
[22] F.X.Kärtner, *et al.*, Opt.Lett. (in press).
[23] J.K.Rank, R. S. Windeler, A. J. Stentz , Opt. Lett. 25, 25 (2000).
[24] W.J.Wadsworth, J.C. Knight, A. Ortigosa-Blanch, J. Arriaga, E. Silvestre, P.St.J. Russell, Electron.Lett. 36, 53 (2000).
[25] W.M.Itano, J.Res.NIST (in press).
[26] F.Riehle, H. Schanatz, B.Lipphardt, G. Zinner, T. Trebst, T. Binnewies, G. Wilpers, J. Helmcke, Proceedings of EFTF-IEEE IFCS, 700 (1999).
[27] J. Stenger,T. Binnewies, G. Wilpers, F. Riehle, H.R. Telle, J.K. Ranka, R.S. Windeler, and A.J. Stentz, Phys Rev A 63 021802 (2001).
[28] K.R.Vogel, S. A. Diddams, C. W. Oates, E. A. Curtis, R. J. Rafac, W. M. Itano, J. C. Bergquist, R. W. Fox, W. D. Lee, J. S. Wells, L. Hollberg , Opt. Lett., 26, 102 (2001).
[29] S. Karshenboim, Can.J.Phys. 78, 639 (2000).

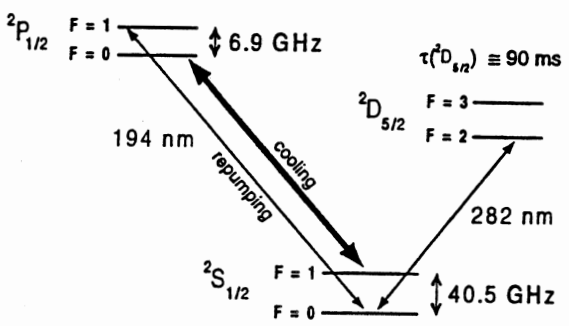

Fig. 1: Partial level scheme for $^{199}Hg^+$. The 194 nm radiation is used for Doppler cooling, state preparation and detection. The 282 nm transition from the ground state $^2S_{1/2}$ ($F=0, M_F=0$) to the metastable $^2D_{5/2}$ ($F=2, M_F=0$) state is the "clock" transition.

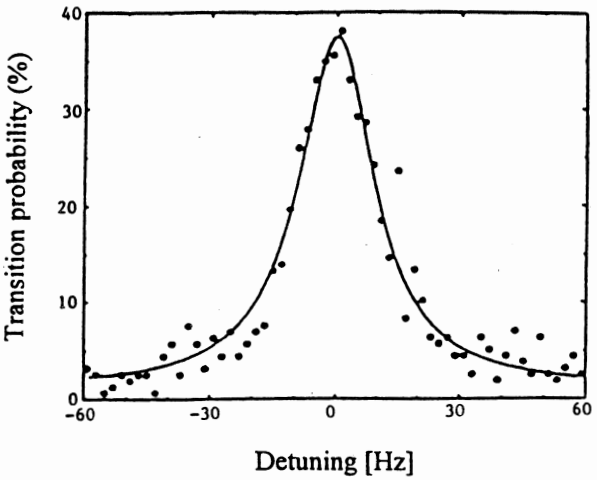

Fig. 2: A typical spectrum of the 282 nm transition . Here, the excitation pulse length was 20 ms and the measured linewidth is Fourier transform limited at about 20 Hz.

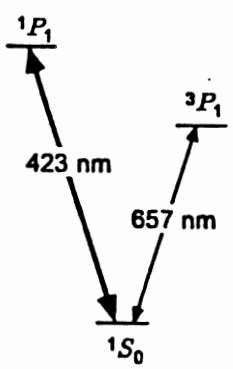

Fig. 3: Simplified diagram of the relevant energy levels in the Ca standard.

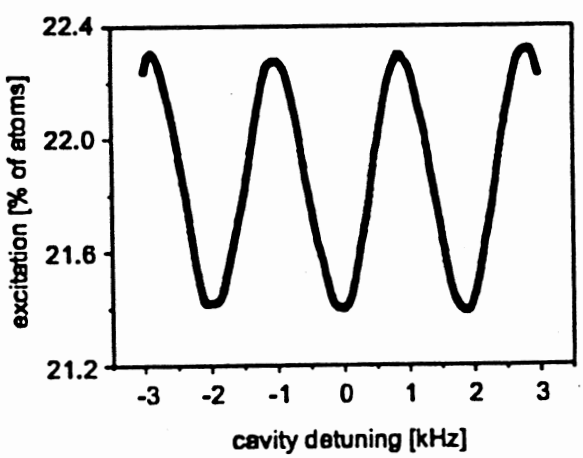

Fig. 4: Optical Bordé-Ramsey fringes with a 960 Hz (FWHM) resolution. The total averaging time to generate this figure was 20 s.

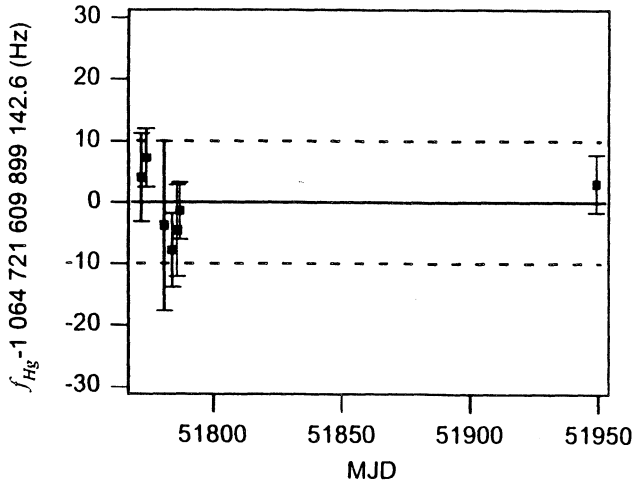

Fig. 5: A chronological record of the average daily frequency of the $^{199}Hg^{+}$ clock transition measured in August 2000 and February 2001. The error bars represent the statistical fluctuations. The dashed lines represent our assigned 10 Hz uncertainty in systematic effects.

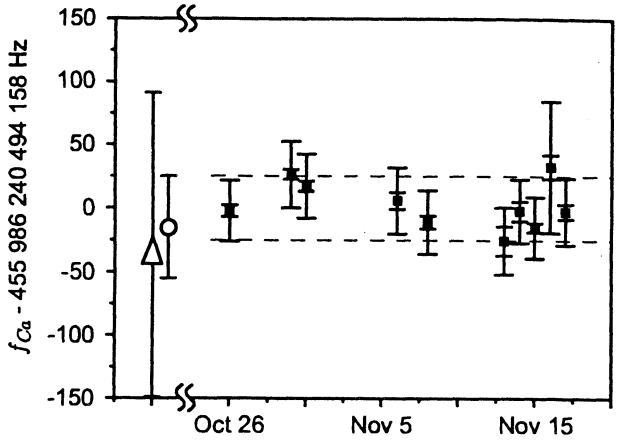

Fig. 6: The filled squares are the measured Ca frequencies on ten days over a 23-day period representing 38 787 s of total measurement time. The inner and outer error bars for each day represent the statistical and total uncertainty, respectively. The dashed lines show the 26 Hz systematic uncertainty assigned to the mean. The open triangle is the PTB measurement [26] while the open circle is the Ca frequency calculated from the present Hg^{+} result and our previous measurement of the 76 THz gap between Ca and Hg^{+} [28].

AMPLITUDE NOISE RESPONSE OF FABRY-PEROT FREQUENCY DISCRIMINATORS BASED ON THE POUND DREVER TECHNIQUE

E. Bava, G. Galzerano, M. Zabatta and C. Svelto

Dipartimento di Elettronica e Informazione – Politecnico di Milano, INFM, and CNR - CSTS
Piazza Leonardo da Vinci 32, 20133 Milano, Italy
E-mail: Elio.Bava@PoliMI.IT Phone: +39 02 2399 3609 Fax: +39 02 2399 3413

ABSTRACT

The response of optical frequency discriminators, based on the Pound-Drever-Hall technique, to frequency and amplitude noise is discussed by studying the demodulated transients to phase or amplitude steps impressed on the incident frequency-modulated light. Small detunings between the laser frequency and the Fabry-Perot resonance are allowed to simulate real operations.

1. INTRODUCTION

The characterization of frequency noise of cw laser oscillators is of importance both in basic metrology and in many scientific applications as well. For this purpose a few frequency-domain measurement methods have been developed and used, with different sensitivities to frequency noise. However they show widespread characteristics of amplitude noise immunity.

The use of the Michelson interferometer with balanced detection as a frequency discriminator has been thoroughly studied in [1]; in ideal operation conditions it shows no sensitivity to amplitude noise. This structure turns out to be very agile, however to achieve an adequate discrimination sensitivity to measure the low frequency noise in a narrow bandwidth around the carrier, as occurs in diode-pumped solid-state lasers, large unbalances between the two arms of the Michelson interferometer are necessaries, which could make unsuitable the use of this scheme. On the other hand, Fabry-Perot resonators with an adequate linewidth compared to the oscillator noise bandwidth are suitable devices to carry out such measurements.

A former scheme which exploits the slope of a resonance fringe side is very similar to the traditional radio frequency discriminator. Partial amplitude noise rejection is obtained by using either a reference optical path or transmitted and reflected beams, which improves frequency sensitivity as well. Fringe-side slope transients have been analyzed in [2] and [3], whereas the discriminator properties have been discussed in [4]. The amplitude noise immunity has been studied in [5] by using the transient analysis.

An alternative method is the use of the discrimination properties of Fabry-Perot cavities with the Pound-Drever-Hall (PDH) method [6]. The performance of the method have been carefully analyzed in [7-9] by means of a frequency domain approach, moreover in [9] some investigation was carried out on the amplitude–noise sensitivity as well. The use of this set-up for laser frequency noise measurements is reported in [10].

In this work transient analysis in the PDH method is used for studying the system response to both frequency and amplitude-noise. A phase step $\Delta\varphi\, U(t)$ is supposed to originate in the laser under test; this is equivalent to a frequency perturbation $(\Delta\varphi/2\pi)\,\delta(t)$ and the overall system can be linearized supposing a low amount of noise: therefore the spectrum of the output signal is the spectral response to a white frequency noise at the input. In nearly the same way, an amplitude step $\Delta E\, U(t)$ originating inside the laser yields a transient at the output of the overall system whose time derivative produces the spectral response to a white amplitude noise at the input. As expected for a laser angular frequency ω_l coincident with a Fabry-Perot resonance ω_c the PDH discriminator is completely immune to amplitude noise, therefore a small detuning is introduced to evaluate the system sensitivity in real conditions. Diagrams of the frequency responses to both types of noise are reported for symmetric and asymmetric resonators.

2. THE PDH FREQUENCY DISCRIMINATOR

The set-up to measure the frequency fluctuations of a laser oscillator through the PDH technique is shown in Fig.1. The use of the reflection mode of operation of the cavity has been chosen because of its much higher discrimination efficiency, however most of the formal development here given is common also to the transmission mode [9].

Let the laser field, phase modulated at ω_m with index m, incident into the Fabry-Perot and undergoing a phase step $\Delta\varphi\, U(t)$, be described by

$$E_i = E_0\, e^{j\varphi_0} \left\{ 1 + U(t)\left[e^{j\Delta\varphi} - 1 \right] \right\} \times \sum_{n=-\infty}^{+\infty} J_n(m) \exp\left[j(\omega_l + n\omega_m)t \right] \quad (1)$$

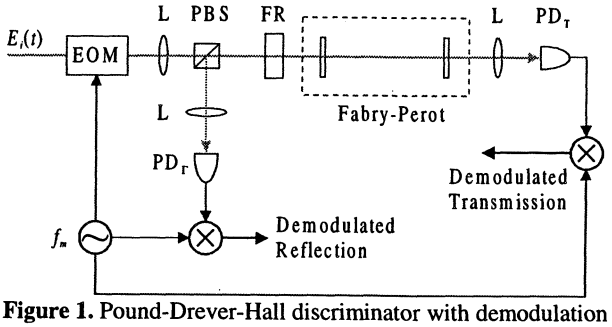

Figure 1. Pound-Drever-Hall discriminator with demodulation of the reflected and transmitted field. EOM electro-optic modulator, PD photodetector, FR Faraday rotator, PBS polarizing beam splitter, L lens.

where φ_0 is a phase constant, $U(t)$ the unit step function and $J_n(m)$ the Bessel function of the first kind of n-th order. If $\Gamma(j\omega)$ stands for the Fabry-Perot reflection coefficient, the field E_R in front of the detector is expressed by a series of steps, due to multiple reflections inside the cavity, labeled with the index k (k=0,1,2,..) and of time duration equal to the resonator round trip time τ

$$E_R(k\tau) = E_0 e^{j\varphi_0} \sum_{n=-\infty}^{+\infty} J_n(m)\exp[j(\omega_l + n\omega_m)t] \times \Gamma[j(\Delta\omega + n\omega_m)] \left\{ 1 + U(t)\left[e^{j\Delta\varphi} - 1 \right] [1 - \gamma_{n,k}] \right\} \quad (2)$$

where for a lossless resonator

$$\Gamma(j\omega) = \frac{r_1 - r_2 e^{-j\omega\tau}}{1 - r_1 r_2 e^{-j\omega\tau}} = \Gamma' + j\,\Gamma'' \quad (3)$$

and

$$\gamma_{n,k} = (r_1 r_2)^k \frac{t_1^2 r_2 e^{-j(k+1)(\Delta\omega + n\omega_m)\tau}}{r_1 - r_2 e^{-j(\Delta\omega + n\omega_m)\tau}} = \gamma'_{n,k} + j\,\gamma''_{n,k} \quad (4)$$

where $r_{1,2}$ and $t_{1,2}$ are the amplitude reflection and transmission coefficients of mirrors 1 an 2 respectively and $\Delta\omega = \omega_l - \omega_c$ is the detuning between laser and cavity frequencies. Because we are dealing with noise, we suppose $\Delta\varphi << 1$, and therefore we can approximate $(e^{j\Delta\varphi} - 1) \cong j\Delta\varphi$ and retain only the linear terms of $\Delta\varphi$ in the subsequent expressions.

A radiation field with electric component as in expression (2) incident on a photodetector with efficiency η yields a photocurrent

$$i(t) = \eta S \left(\frac{c\varepsilon_0 e}{2h\nu_0} \right) E_R E_R^* = \frac{1}{2} k_i E_R E_R^* \quad (5)$$

where S represents an equivalent detector area and k_i is a factor which transforms the incident light intensity into a detected photo-current. We need then the expression of $E_R E_R^*$ evaluated in particular at ω_m. After some mathematical developments we obtain

$$(E_R E_R^*)_{\omega_m} = 2 E_0^2 \sum_{0}^{+\infty}{}_n J_n(m) J_{n+1}(m) \operatorname{Re}\left\{ [M_{n,k} - M_{-(n+1),k}] \exp[j\omega_m t] \right\} \quad (6)$$

where

$$M_{n,k} = \Gamma[j(\Delta\omega + (n+1)\omega_m)]\Gamma^*[j(\Delta\omega + n\omega_m)] \times \{1 + j\Delta\varphi U(t)\left[\gamma^*_{n,k} - \gamma_{n+1,k} \right]\} \quad (7)$$

and the expression (6) with (7) is different from zero for $\Delta\varphi \neq 0$, with a maximum slope for $\Delta\omega = 0$.

If we suppose the laser under test locked to the cavity, then $\Delta\omega = 0$ and the following simple expression is obtained for the output transient, which goes to 0 as $k \to \infty$

$$(E_R E_R^*)_{\omega_m} = -\,U(t)\, 4\,\Delta\varphi\, E_0^2 \sum_{n=0}^{+\infty} J_n(m) J_{n+1}(m)\ \mathrm{Im} \{ \Gamma[j(n+1)\omega_m]\, \Gamma^*[jn\omega_m] \left[\gamma^*_{n,k} - \gamma_{n+1,k} \right] \exp(j\omega_m t) \} \quad (8)$$

A simpler but satisfactory insight in the performance of the PDH discriminator is obtained by taking only the first term in the series, an approximation already discussed elsewhere [7-9]. The following expression then holds

$$(E_R E_R^*)_{\omega_m} \cong -U(t)\, 4\,\Delta\varphi\, E_0^2\, J_0(m) J_1(m)\ \mathrm{Im} \{ \Gamma(j\omega_m)\, \Gamma^*(0) \left[\gamma^*_{0,k} - \gamma_{1,k} \right] \exp(j\omega_m t) \}$$

$$\cong -U(t)\, 4\,\Delta\varphi\, E_0^2\, J_0(m) J_1(m)\, \Gamma'(0)\ \{ [\Gamma''(\omega_m)\gamma''_{1,k} + \Gamma'(\omega_m)\,(\gamma'_{0,k} - \gamma'_{1,k})] \sin\omega_m t + [\Gamma''(\omega_m)\gamma''_{1,k} + \Gamma'(\omega_m)\,(\gamma'_{0,k} - \gamma'_{1,k})] \cos\omega_m t \} \quad (9)$$

The detected photo-current at ω_m multiplied by a transimpedence gain k_v yields the voltage at the input of a double-balanced mixer pumped by a local oscillator at ω_m with a variable phase adjusted to obtain the maximum output voltage. The following demodulated voltage signal is obtained:

$$S_{R,\varphi} = 2 E_0^2\, k_i k_v k_c\, \Delta\varphi J_0(m) J_1(m) U(t) \left| \Gamma(j\omega_m) \right| \frac{r_1 - r_2}{1 - r_1 r_2} \left\{ \gamma'_{1,k} - \gamma'_{0,k} \right\} \quad (10)$$

where k_c accounts for the mixer conversion loss.

After evaluating the Laplace transform $F_R(s) = L\left[\frac{2\pi}{\Delta\varphi} S_{R,\varphi}\right]$, and substituting $j\omega = s$, the discriminator frequency response is obtained

$$F_R(j\omega) = CE_0^2 f_R(j\omega) \qquad (11)$$

where

$$f_R(j\omega) = \Gamma'(0)|\Gamma(j\omega_m)|t_1^2 r_2 a \frac{(j\omega-\alpha)^2 - \frac{b}{a}(j\omega-\alpha) - \frac{c}{a}}{(j\omega-\alpha)\left[(j\omega-\alpha)^2+\omega_m^2\right]}$$

$$C = 4\pi k_i k_v k_c J_0(m) J_1(m)$$

$$a = \frac{r_1(r_1+r_2)(\cos\omega_m\tau - 1)}{\rho_1^2(r_1-r_2)}; \qquad b = \frac{\omega_m r_1 \sin\omega_m\tau}{\rho_1^2};$$

$$c = \frac{\omega_m^2}{r_1-r_2}; \qquad \rho_1^2 = r_1^2 + r_2^2 - 2r_1r_2\cos\omega_m\tau;$$

$$\alpha = \frac{1}{\tau}\log r_1 r_2 \cong -\pi\Delta\nu_c;$$

The PDH frequency discriminator response in reflection is reported in Fig. 2, in the case of symmetric and asymmetric resonators, by keeping constant the input intensity. By exploiting asymmetries it appears feasible to increase the discriminator sensitivity, however, as we shall see, the amplitude noise immunity decreases.

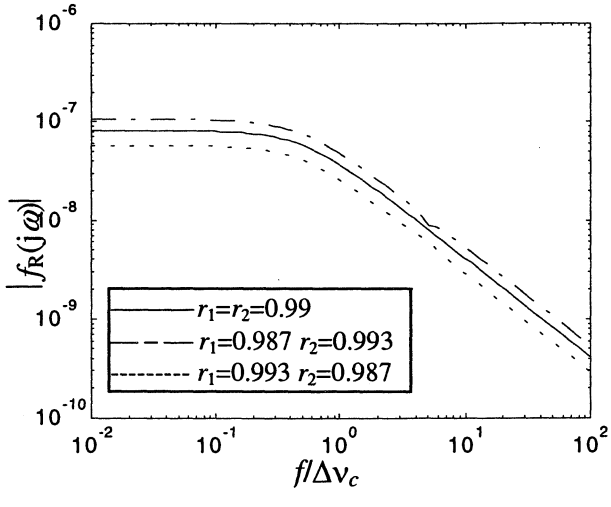

Figure 2. Frequency discriminator response versus the normalized frequency: $f_m = 10\Delta\nu_c/2 = 19.2$ MHz, $\tau = 1.667$ ns.

3. AMPLITUDE NOISE IMMUNITY

To evaluate the discriminator amplitude-noise immunity let us consider the transient produced at the synchronous discriminator output by an amplitude step $\Delta EU(t)$. The field incident into the Fabry-Perot is then described by

$$E_i = (E_0 + \Delta EU(t)) \sum_{-\infty}^{+\infty}{}_n J_n(m)\exp[j(\omega_l + n\omega_m)t] \qquad (12)$$

and the reflected field impinging on the detector is

$$E_R(k\tau) = \sum_{-\infty}^{+\infty}{}_n J_n(m)\exp[j(\omega_l+n\omega_m)t]\Gamma[j(\Delta\omega+n\omega_m)]$$

$$\{E_0 + \Delta EU(t)[1-\gamma_{n,k}]\} \qquad (13)$$

therefore after some analytical developments the following expression is obtained

$$(E_R E_R^*)_{\omega_m} = 2E_0^2 \sum_{0}^{+\infty}{}_n J_n(m) J_{n+1}(m)$$

$$\mathrm{Re}\left\{[N_{n,k} - N_{-(n+1),k}]\exp[j\omega_m t]\right\} \qquad (14)$$

where

$$N_{n,k} = \Gamma[j(\Delta\omega+(n+1)\omega_m)]\Gamma^*[j(\Delta\omega+n\omega_m)]\times$$

$$\{1 + \frac{\Delta E}{E_0} U(t)\left[2 - \gamma^*_{n,k} - \gamma_{n+1,k}\right]\} \qquad (15)$$

In the ideal case $\Delta\omega = \omega_l - \omega_c = 0$, the synchronous detector output is zero because $N_{n,k} - N_{-(n+1),k} = 0$. Therefore the PDH discriminator exhibits a total immunity to amplitude noise under perfect locking of the laser frequency to the cavity resonance. However in real operation an optoelectronic loop with a finite gain and a narrow bandwidth is used. As a consequence during the time interval necessary to perform the frequency-noise measurement a small offset $\Delta\nu \neq 0$ is assumed with the condition $\Delta\nu << \Delta\nu_c << \nu_m$, where $\Delta\nu_c$ is the Fabry-Perot full width at half maximumm. In general an approximate, but still valuable, expression is obtained for the demodulated output taking into account that only the term with $n = 0$ in (14) and in (15) is rapidly varying with ω in the expressions of Γ and γ, whereas in the others, which, on the contrary, are varying slowly we can substitute $\Delta\omega = 0$. After some cumbersome and time consuming developments the two quadratures of $(E_R E_R^*)_{\omega_m}$ are obtained and, by keeping in the synchronous detector the same phase value used for the frequency discriminator, the demodulated output is

$$S_{R,E}(k\tau) = -4\frac{1}{2} k_i k_v k_c J_0(m) J_1(m) E_0 \Delta EU(t) |\Gamma(\omega_m)|$$

$$\left\{ \Gamma'(j\Delta\omega)\gamma''_{0,k} + \Gamma''(j\Delta\omega)(\gamma'_{1,k}+\gamma'_{0.k}) \right\} \qquad (16)$$

After the application of the Laplace transform, the multiplication by the s variable and the substitution $j\omega = s$, the frequency responses corresponding to output voltages $S_{R,E}(\omega)$ excited by $\Delta E(\omega)$ are obtained. The

result for $r_1 = r_2$, with $R = r_1 r_2$ and $T = -t_1 t_2$, is:

$$H_{R,E}(j\omega) = -C' E_0^2 h_{R,E}(j\omega) \qquad (17)$$

where

$$h_{R,E}(j\omega) = j\omega \frac{(1+T)\sqrt{R}}{(1-R)} \Delta\omega\tau |\Gamma(\omega_m)| \times$$

$$\frac{(j\omega-\alpha)^3 + b'(j\omega-\alpha)^2 + c'(j\omega-\alpha) + d'}{\left[(j\omega-\alpha)^2 + \Delta\omega^2\right]\left[(j\omega-\alpha)^2 + \omega_m^2\right]}$$

$$C' = -\frac{2}{E_0} k_i k_v k_c J_0(m) J_1(m);$$

$$b' = \left[\frac{T}{\tau} - \frac{1}{2}\Delta\omega^2\tau + \frac{1}{4}\rho T\omega_m\right]\frac{1}{1+T};$$

$$c' = \left[\frac{1}{2}T(\omega_m^2 + \Delta\omega^2) + \omega_m^2\right]\frac{\tau}{1+T};$$

$$d' = \left[\omega_m^2\left(\frac{T}{\tau} - \frac{1}{2}\Delta\omega^2\tau\right) - \frac{1}{4}\rho T\Delta\omega^2\omega_m\right]\frac{1}{1+T};$$

$$\rho = \frac{\sin\omega_m\tau}{\sin^2\left(\frac{\omega_m\tau}{2}\right)}.$$

By using the same parameter values of the previous section, the normalized amplitude-noise response in the case $\Delta\nu = 0.001\Delta\nu_c/2$ is reported in Fig. 3. The direct proportionality of the output signal with $\Delta\nu$ allows an easy extrapolation for different values of $\Delta\nu$. As already

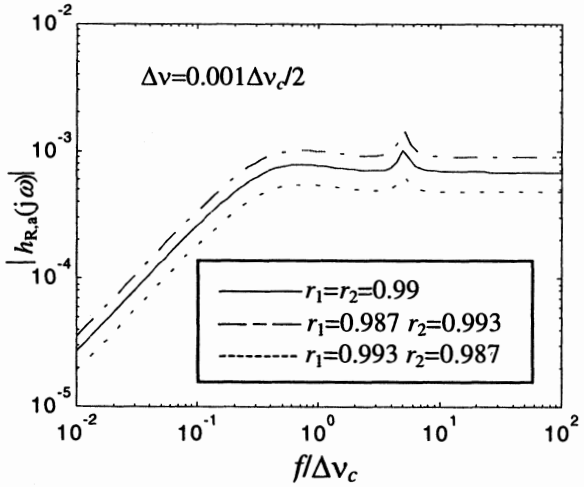

Figure 3 Example of amplitude noise frequency response of a PDH frequency discriminator.

anticipated it turns out that resonator asymmetry increases sensitivity both to frequency noise and to amplitude noise. By comparing this rejection with that attainable in compensated fringe-side Fabry-Perot frequency discriminators evaluated in [5], it turns out that the amplitude noise immunity in the PDH technique is increased in the order of $\Delta\nu_c/\Delta\nu$.

4. CONCLUSIONS

The PDH technique when applied to the measurement of laser frequency noise exhibits not only interesting discrimination properties due to the high frequency modulation with synchronous detection, but also a very high rejection of amplitude noise level. In the ideal case this rejection is infinite, as also occurs with the discriminator based on the Michelson interferometer, which however is more difficult to be used, for the requested large arm unbalance, when a high sensitivity to frequency noise is required.

REFERENCES

[1] E. Goobar, "A Michelson interferometer with balanced detection for the characterization of modulation and noise properties of semiconductor lasers," *IEEE J. Quantum Electron.*, vol. QE-29, pp. 1116-1130, Apr. 1993.

[2]. J. Helmcke, S.A. Lee and J.L. Hall, "Dye laser spectrometer for ultrahigh spectral resolution: design and performance," *Appl. Optics,* vol. 21, pp. 1686-1694, 1 May 1982.

[3] M. Houssin, M. Jardino and M. Desaintfuscien, "Comparison of the calculated transient responses of a Fabry-Perot used in reflection and in transmission", *Rev. Sci. Instrum.*, vol. 61, pp. 3348-3352, Nov. 1990.

[4] P. Tremblay and R. Ouellet, "Frequency response of a Fabry-Perot interferometer used as a frequency discriminator," *IEEE Trans. Instrum. and Meas.*, vol. IM-40, pp. 204-207, Apr. 1991.

[5] E.Bava, G.Galzerano and C. Svelto, "Amplitude response of Fabry-Perot frequency discriminators", *IEEE Trans. Ultrasonics, Ferroelectrics and Freq. Control,* vol.47, pp.1115-21, Sept. 2000.

[6] R. W. P. Drever, J. L. Hall, F. V. Kowalsky, J. Hough, G. M. Ford, A. J. Munley, and H. Ward, "Laser phase and frequency stabilization using an optical resonator", *Appl. Phys. B*, vol. 31, pp. 97-105, 1983

[7] D. Hils and J. L. Hall, "Response of a Fabry-Perot cavity to phase modulated light", *Rev. Sci. Instrum.*, vol. 58, pp. 1406-14, August 1987.

[8] E. Bava and F. Massari, "Phase sensitive detection of light reflected from a Fabry-Perot interferometer", *Rev. Sci. Instrum.*, vol. 67, pp. 1714-1720, May 1996.

[9] E. Bava and F. Massari, "Comparison of calculated phase-sensitive recoverable signals using a Fabry-Perot cavity in reflection and in transmission", *Rev. Sci. Instrum.*, vol. 68, pp. 1927-1934, May 1997.

[10] Y. J. Cheng and P. L. Mussche, "Measurement of laser quantum frequency fluctuations using a Pound-Drever stabilization system", *IEEE J. Quantum Electron.*, vol. QE-30, pp. 1498-1504, June 1994.

HIGH-STABILITY FIBER-PUMPED ROOM-TEMPERATURE TEMPERATURE Tm-Ho:YAG LASER AT 2.097 μm AND SPECTROSCOPY OF HBr

C. Svelto, G. Galzerano, and E. Bava

Dipartimento di Elettronica e Informazione – Politecnico di Milano, INFM, and CNR - CSTS
Piazza Leonardo da Vinci 32, 20133 Milano, Italy
E-mail: Cesare.Svelto@PoliMI.IT Phone: +39 02 2399 3610 Fax: +39 02 2399 3413

ABSTRACT

A single-frequency diode-pumped Tm-Ho:YAG laser with continuous wave emission around 2.097 μm is developed. The laser is based on a compact hemispheric resonator longitudinally pumped by a fiber-coupled laser diode and operates near room temperature. Single frequency operation is achieved by inserting in the laser cavity two uncoated etalons and output powers in excess of 20 mW with a slope efficiency of ~7 % are obtained. A wavelength tunability of 4.6 nm is obtained, ranging from 2.0938 nm to 2.0984 nm. Linear spectroscopy of the HBr P(12) resonance at 2.097 μm is performed both in single- and multi-pass absorption cells.

1. INTRODUCTION

High-resolution spectroscopy and frequency metrology in the 2 μm region of the electromagnetic spectrum are assuming an important scientific interest in order to realize high-accuracy optical frequency standards and frequency connections between standards at different wavelength [1]. Lasers with emission at a wavelength of 2 μm are also useful sources for applications that require eye-safe propagation through the atmosphere. Such applications include coherent Doppler-LIDAR, DIAL measurements of CO_2 and H_2O, and Doppler velocimetry (wind shear detection, global wind speed measurement from satellite) [2, 3]. Moreover these sources may be useful in medical applications because the water molecule and hence human tissues present strong absorption in this wavelength region [4]. All these applications require significant power and often single frequency operation, and wide frequency tuning range.

In this work, we describe a single-frequency diode-pumped Tm-Ho:YAG laser with continuous wave emission at around 2 μm wavelength at around room temperature. Spectroscopy of HBr by means of this tunable and narrow-linewidth laser source is reported.

2. THE Tm-Ho:YAG ACTIVE MEDIUM

The Tm-Ho:YAG crystals used in our experiments, have a nominal dopant concentration of 5.7 % with Tm^{3+} ions and 0.36 % with Ho^{3+} ions, respectively. A schematic diagram of the relevant energy levels of both the Tm^{3+} and Ho^{3+} ions in a YAG host is reported in Fig. 1. The upper and lower laser levels are $^5I_7$ a $^5I_8$ in the Ho^{3+} ions. For each absorbed pumping photon from the $^3H_6 \rightarrow {}^3H_4$ levels, two Tm^{3+} ions are raised in the upper laser level by means of a cross-relaxation process between the Tm^{3+} levels $^3H_4 \rightarrow {}^3F_4$ and $^3H_6 \rightarrow {}^3F_4$. The population inversion in the Ho system is obtained by means of an energy transfer process between $^3F_4 \rightarrow {}^3H_6$ and $^5I_8 \rightarrow {}^5I_7$.

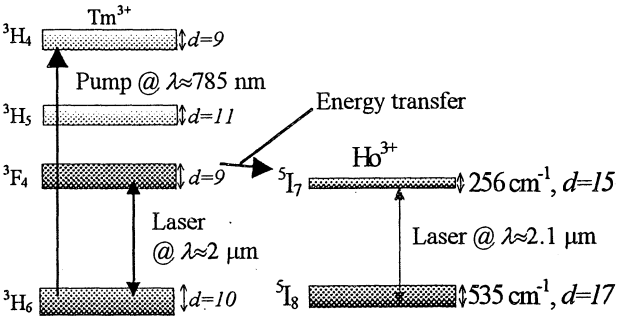

Figure 1. Energy levels of Tm^{3+} and Ho^{3+} ions in YAG.

Typical lasing wavelengths are in the 2080–2100 nm spectral region as can be observed from the emission and absorption cross sections of Fig. 2. Anyway, a very interesting possibility of achieving laser operation near 2128 nm is under investigation. This longer wavelength

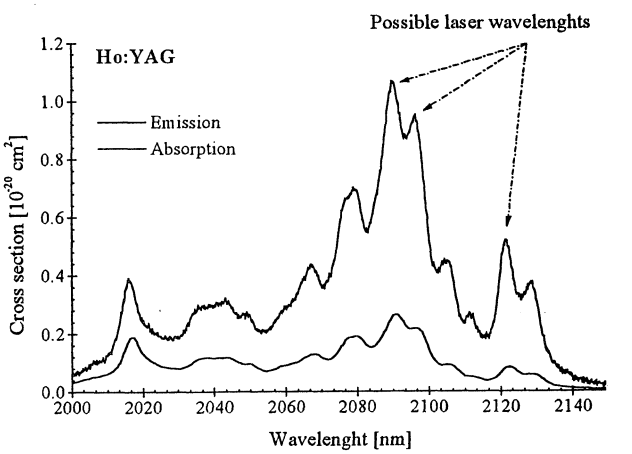

Figure 2. Ho:YAG emission and absorption cross sections.

is in fact twice the wavelength of the Nd:YAG laser so that by frequency doubling a properly designed Tm-Ho:YAG laser one could lock this 2 μm emission directly to the 532 nm I_2-based wavelength standard [5]. This would allow interesting wavelength calibration capabilities in the 2 μm optical region (*e.g.* see Fig. 3).

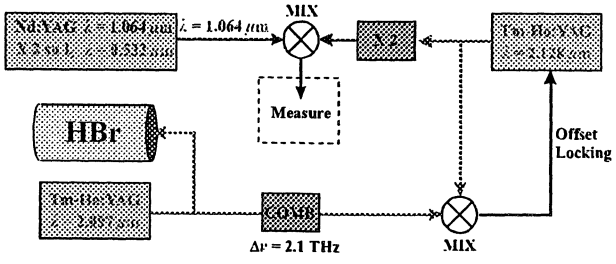

Figure 3. Proposed optical frequency measurement chain from 2 μm wavelength to 532 nm.

3. LASER CAVITY

To build the laser cavity, we used an end-pumped hemispherical resonator as shown in Fig. 4. The end facets of the active material are flat polished and covered with dicroic multidielectric coatings. The first facet of the laser crystal is coated for high reflectivity (HR>99.99 %) at 2 μm laser wavelength and for high transmission (HT>96 %) at the pump wavelength 781 nm. The second facet is antireflection coated at the laser wavelength (AR<0.2 %) and for a high reflectivity at pump wavelength (R>95%). Using this double-pass pumping configuration, more than 65% of the available pump power can be usefully absorbed within the Tm-Ho:YAG active medium. A spherical output coupling mirror (T=1%), with radius of curvature of -80 mm, is placed at a distance L_{cavity}~40 mm from the first facet (pump entrance) of the crystal.

An high-brightness fiber-coupled pump diode was used in the end-pumping configuration with the indicated output coupler of –80 mm radius. The pump source has a 100 μm fiber core (diameter) with a numerical aperture of 0.22 and a maximum output power of 3 W at 781 nm. An optical imaging system with two spherical lenses of focal lengths f_1=20 mm and f_2=30 mm, respectively, was adopted. With this quite intense pump beam the population inversion within the active medium reaches a much higher value than the ones obtained in previous versions of this oscillator. This turns out in a lower pump threshold and higher laser efficiency. The pump wavelength is tuned to the Tm^{3+} absorption peak, near 781 nm [6], using a thermoelectric cooler (TEC) to control the temperature of the laser diode at ~20.5 °C. The YAG crystal is held in a copper structure and then mounted on a Peltier cooler used to remove pump-generated heat and to actively control the crystal temperature.

4. OUTPUT POWER AND WAVELENGTH TUNABILITY

The optimized laser configuration allowed to achieve a rather low threshold value P_{th}≅470 mW for the Tm-Ho:YAG laser operating at a quasi-room temperature of 14 °C. The corresponding slope efficiency turned out to be η≅7 % with a maximum single-frequency output power of more than 20 mW. Stable single-frequency operation is observed when using two band selective etalons: a first thin etalon (~100 μm) selects the operating wavelength range whereas a second thick etalon (~0.5 mm) is used to select a single longitudinal mode within the transmission bandwidth of the first etalon. By the use of a birefringent plate (Lyot filter) instead of the first etalon even larger wavelength tunability was achieved. In this case, the measured wavelength tunability is shown in Fig. 6 where a tuning interval of ~5 nm around 2097 nm wavelength is demonstrated.

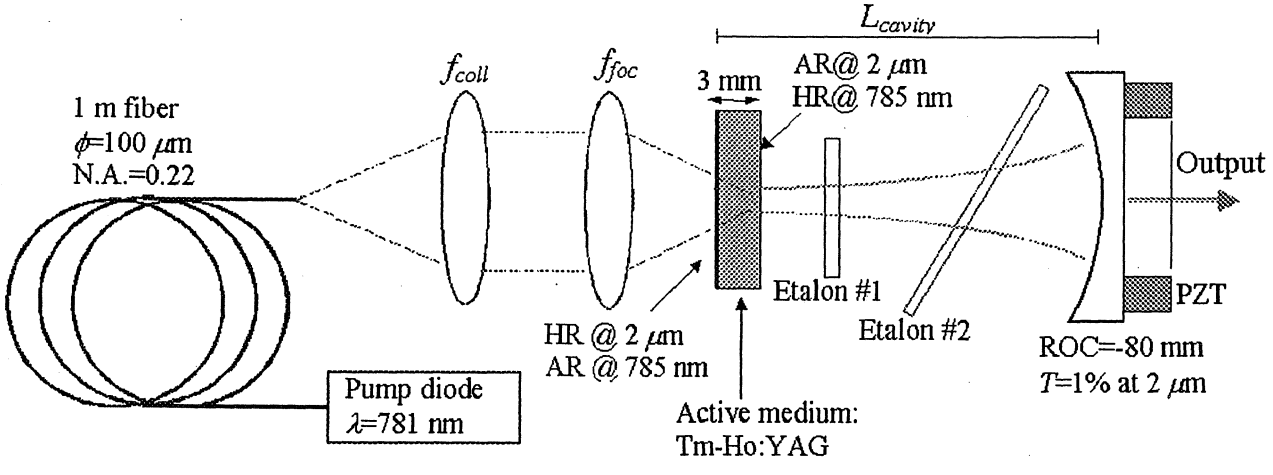

Figure 4. Schematic diagram of the Tm-Ho:YAG end-pumped laser cavity.

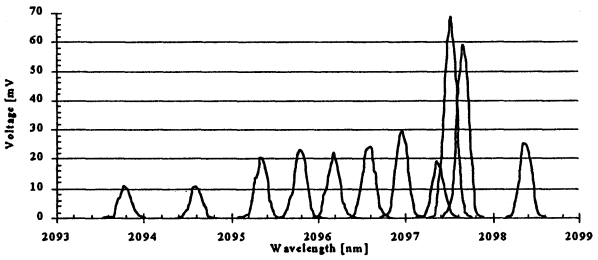

Figure 5. Wavelength tuning interval around 2097 nm for the Tm-Ho:YAG laser.

5. HBr SPECTROSCOPY

By means of our tunable Tm-Ho:YAG laser preliminary spectroscopic measurements of HBr at these wavelengths were performed. In particular, we used gas samples containing the natural mixture of $H^{81}Br$ and $H^{79}Br$, which is approximately 50 % each, and we adopted gas pressure values of ~10 kPa. The interesting absorption line in this spectral region corresponds to the rovibrational transition P(12) of the HBr molecule located at 2097.508 nm and 2097.222 nm for the heavier and lighter isotopes, respectively.

In a first set of experiments linear spectroscopy of $H^{81}Br$ P(12) line was performed using a 1 m long gas cell in a single-pass configuration. The recorded absorption spectrum is shown in Fig. 6. A full width of the absorption profile is ~500 MHz (both Doppler and collision broadened) whereas the peak absorption is 8 %. The gas pressure was 11 kPa. The oscilloscope trace of Fig. 6, however, is rather noisy but we have not repeated the experiment since a better idea is to go on with these measurements using a multi-pass gas cell.

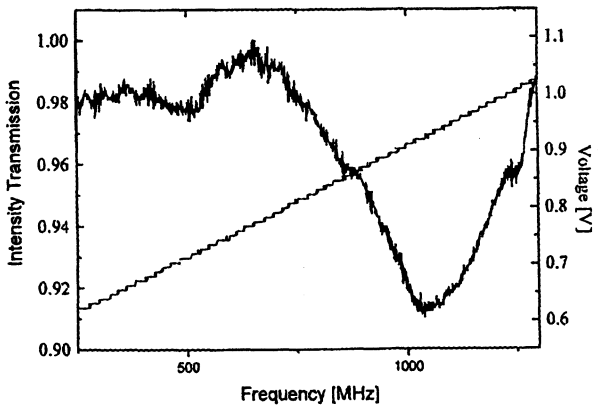

Figure 6. Absorption spectrum of $H^{81}Br$ P(12) line at 2097.508 nm wavelength. The ramp voltage used to scan the cavity length and hence the laser frequency is also shown in the digital scope recording.

In the meanwhile in our neighboring Department of Physics, our colleagues received the ordered multi-pass gass cell and they performed, with a very similar Tm-Ho:YAG laser, better spectroscopic recordings. The adopted multi-path is a 37-times folded 20 cm length for a whole absorption path of 7.54 m. Again with a gas pressure of ~10 kPa, the absorption spectrum was precisely recorded. The result is shown in Fig. 7 from where a full linewidth of 500 MHz and peak absorption of 44 % result.

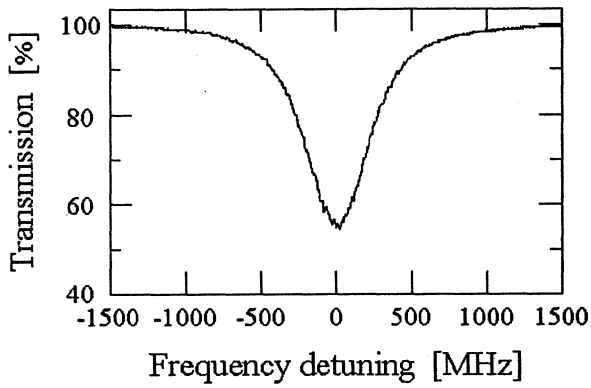

Figure 7. Absorption spectrum of $H^{79}Br$ P(12) line at 2097.222 nm wavelength using the multi-path absorption cell.

4. CONCLUSIONS AND DEVELOPMENTS

A novel optical frequency chain from 2 μm spectral region to the I_2 transitions at 532 nm was proposed. A single-frequency widely-tunable Tm-Ho:YAG laser operating at around 2.097 μm wavelength at room temperature was developed. Linear spectroscopy of the HBr molecule was performed by this narrow linewidth 2 μm lasers measuring the expected transition widths in the order of 0.5 GHz. This suggests, to perform accurate frequency locking in this spectral region, to move further into saturation spectroscopy and to lock to Doppler-free absorption lines of this molecule.

The described optical oscillator is an interesting source for high-resolution spectroscopy, metrology, and high-sensitivity optical sensors. In all of these applications it is very important to achieve both amplitude and frequency stability.

REFERENCES

[1] J. E. Bernard, B. G. Whitford, and A. A. Madej, «A Tm:YAG laser for optical measurements: mixing 148 THz with CO_2 laser radiation», *Optics Comm.*, vol. **140**, pp. 45–48 (1997).

[2] S. M. Henderson, C. P. H. Hale, J. R. Magee, M. J. Kavaya and A. V. Huffaker, «Eye-safe coherent radar system at 2.1 μm using Tm,Ho:YAG lasers», *Opt. Lett.* vol. **16** (10), pp. 773–775 (1991).

[3] M. E. Storm, «Coherent 2 μm sources burst into wind shear detection», *Laser Focus World*, pp. 117-122 (April 1991).
[4] J. A. Curcio and C. C. Petty, *J. Opt. Soc. Am.*, vol. **41**, p. 302 (1951).
[5] P. Cordiale, G. Galzerano, and H. Schnatz, "International comparison of two iodine-stabilised frequency-doubled Nd:YAG lasers at λ=532 nm", *Metrologia* 37, 177-182, 2000.
[6] M. G. Jani, R. J. Reeves, R. C. Powell, G. J. Quarles, L. Esterowitz, «Alexandrite-laser excitation of Tm-Ho:$Y_3Al_5O_{12}$ laser», *J. Opt. Soc. Am. B*, vol. **8**, pp. 741-746 (1991).

Notes

See page 457 for Posters B, Instrumentation & Telecommunications

Notes

POSTERS B

INSTRUMENTATION & TELECOMMUNICATIONS

EFFECTS OF CLOCK INSTABILITIES ON SIGNAL CORRELATION OF CDMA RECEIVERS

R. Ylinen[1], J.Mannermaa [2], K.Kalliomäki [1]

[1)]Univ. of Oulu, Faculty of Technology, FIN-90014 University of Oulu, Finland
[2)] Nokia Mobile Phones, FIN-33100, Tampere, Finland

ABSTRACT

Effects of clock instabilities on tracking loops of cdma receivers have been studied, especially on signal correlation processes. This research has been carried out by the RTA unit of Nokia Mobile Phones in co-operation with the Systems Engineering Laboratory of the University of Oulu. The theoretical consideration indicates that the short term instability (δf/f in 1ms) for proper operation should be less than 10^{-7} .This result has been supported by practical tests by which, on the hand, momentary instabilities of 10^{-4} have been observed, in the worst case. Thus this phenomenon is a real practical problem which must be taken seriously into account in the design of tracking loops.

1.INTRODUCTION

CDMA receivers have been under intensive study all over the world during the last years because of the scientific and economic possibilities hidden into the functions of mobile phones, and positioning and navigation receivers. Due to the expanding range of CDMA receiver applications with e.g. more stringent positional accuracy demands manufacturers have to concentrate more and more on the performance of internal clocks of the receivers. The RTA unit of Nokia Mobile Phones has also made these studies in co-operation with the Systems Engineering Laboratory of the University of Oulu. The study started in spring 2000, and aims to achieve comparable information and results of the performance of different CDMA technologies.

A typical signal tracking loop consists of a NCO (Numerically Controlled Oscillator), one or two signal generators and two correlators for detecting the phase of the input signal and a loop filter for controlling the NCO frequency. Obviously the difference between the frequency of NCO and of the input signal affect the correlation function and further the discriminator function used for phase detection. This difference is influenced both by the changes in the control signal as well as by the instability in clock frequency of NCO. Both effects will be analysed in the paper.

2.METHODS

The system to be studied in the paper is a GPS C/A code tracking loop based an early-late discriminator.

The difference between the frequencies of NCO and the input signal as well as the errors in clock frequency affect the correlation function and further the discriminator function. This will be analysed in what follows.

Let f_o the code frequency in the input, $\hat{f}$ the NCO frequency and

$$f = f_o - \hat{f}$$

Let further x be the code in the input signal and $\hat{x}$ the reference code with frequency $\hat{f}$. Then

$$\hat{x}(t) = x(\frac{\hat{f}}{f_o}t) = x(\hat{t})$$

where

$$\hat{t} = \frac{\hat{f}}{f_o}t .$$

Suppose now that the clock frequency $\hat{f}$ is time-varying and of the form /1/

$$\hat{f}(t) = \hat{f}_o + \hat{f}_1 t$$

Then

$$\hat{t}(t) = \frac{\hat{f}(t)}{f_o}t = \frac{\hat{f}_o}{f_o}t + \frac{\hat{f}_1}{f_o}t^2$$

Correspondingly

$$t(\hat{t}) = \frac{-\hat{f}_o + \sqrt{\hat{f}_o^2 + 4 f_o \hat{f}_1 \hat{t}}}{2\hat{f}_1}$$

The correlation function can be written as

$$R_{\hat{x}x}(\tau) = \frac{1}{T}\int_0^T \hat{x}(t)x(t+\tau)dt = \frac{1}{T}\int_0^T x(\hat{t})x(t+\tau)dt$$

$$= \frac{1}{T}\int_0^{\hat{t}(T)} x(\hat{t})x(\hat{t}+t(\hat{t})-\hat{t}+\tau)\frac{dt(\hat{t})}{d\hat{t}}d\hat{t}$$

$$= \frac{1}{T}\int_0^{\hat{t}(T)} x(\hat{t})x(\hat{t}+\hat{\tau}(\tau,\hat{t})\frac{dt(\hat{t})}{d\hat{t}}d\hat{t}$$

where

$$\hat{\tau}(\tau,\hat{t}) = t(\hat{t}) - \hat{t} + \tau$$

and

$$\frac{dt(\hat{t})}{d\hat{t}} = \frac{f_o}{\sqrt{\hat{f}_o^2 + 4 f_o \hat{f}_1 \hat{t}}}$$

This integral can be approximated by a sum by dividing the interval $[0,\hat{t}(T)]$ into N intervals of equal length.

$$R_{\hat{x}x}(\tau) = \frac{1}{T}\sum_{i=1}^{N}\int_{(i-1)\Delta\hat{t}}^{i\Delta\hat{t}} x(\hat{t})x(\hat{t}+\hat{\tau}(\tau,\hat{t}))\frac{dt(\hat{t})}{d\hat{t}}d\hat{t}$$

$$\approx \frac{1}{T}\sum_{i=1}^{N}\frac{dt(i\Delta\hat{t})}{d\hat{t}}\Delta\hat{t}R_x(\hat{\tau}(\tau,i\Delta\hat{t}))$$

where

$$\Delta\hat{t} = \frac{\hat{t}(T)}{N}$$

The experimental tests were realized by the measurement set-up which can be used both in PPS and Fast Allan Variance studies. This set-up has been presented in /2/.

3.RESULTS

3.1. Simulation Results

Suppose that the signal to be correlated is a C/A-code in a GPS signal with 1023 chips/ms frequency. The ideal correlation function is triangular with width $2T_c$=2/1023 ms. For different values of $\hat{f}_o$, $\hat{f}_1$ and T the correlation function is depicted by Figs. 1-4.

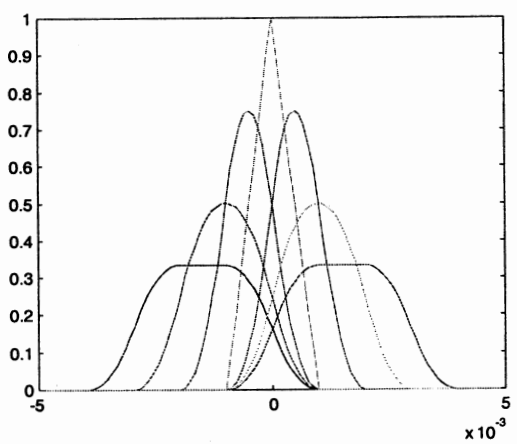

Figure 1. The correlation functions with parameter values $\hat{f}_1 = 0$ and

$\hat{f}_o - f_o = -0.3,-0.2,-0.1,0,0.1,0.2,0.3$ % of f_o

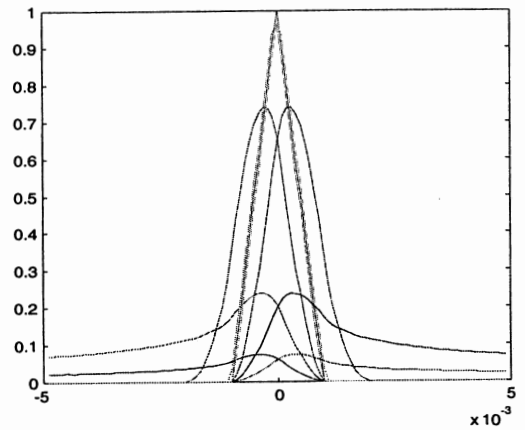

Figure 2. The correlation functions with parameter values $\hat{f}_o = f_o$ and

$\frac{\hat{f}_1}{f_o} = -10^{-1},-10^{-2},-10^{-3},-10^{-4},0,10^{-4},10^{-3},10^{-2},10^{-1}$ s^{-1}

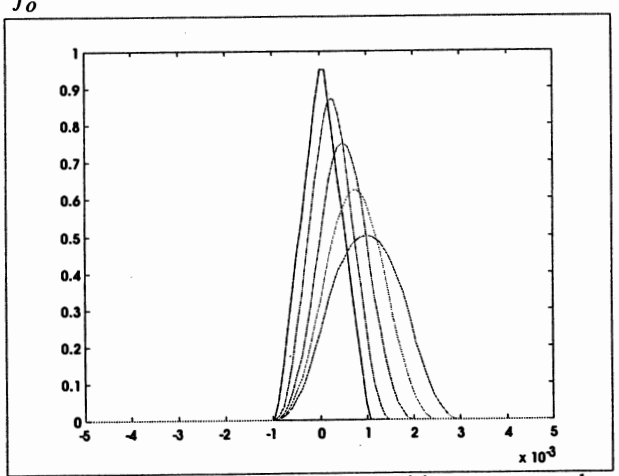

Figure 3. The correlation functions with parameter values $\hat{f}_1 = 0$, $\hat{f}_o - f_o = 0.01\%$ of f_o, T=1,5,10,15,20 ms.

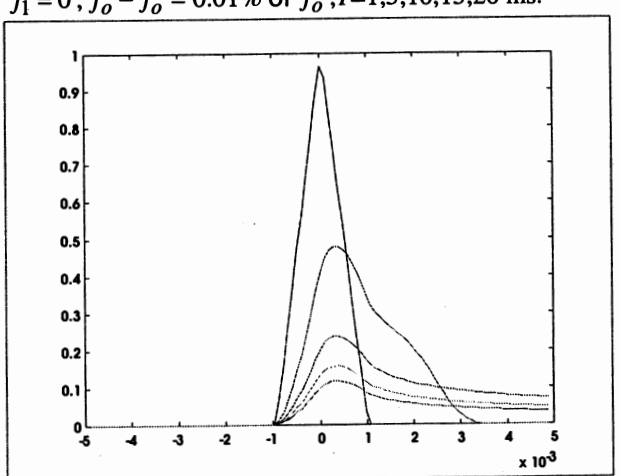

Figure 4. The correlation functions with parameter values $\hat{f}_o = f_o$, $\frac{\hat{f}_1}{f_0} = 10^{-4}$s^{-1}, T=1,5,10,15,20 ms.

The corresponding early-late-discriminator functions with $\Delta=T_c/2$ are depicted by Figs. 5-8.

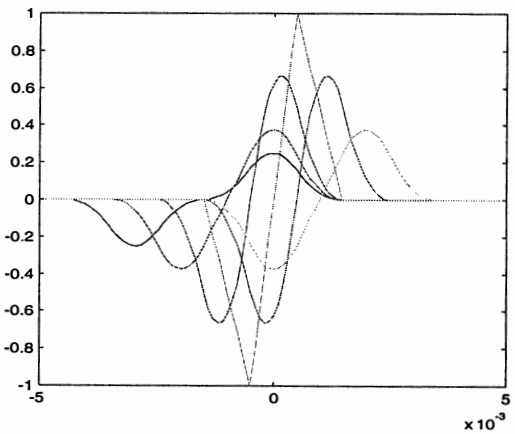

Figure 5. The discriminator functions with parameter values $\hat{f}_1 = 0$ and

$\hat{f}_o - f_o = -0.3,-0.2,-0.1,0,0.1,0.2,0.3$ % of f_o.

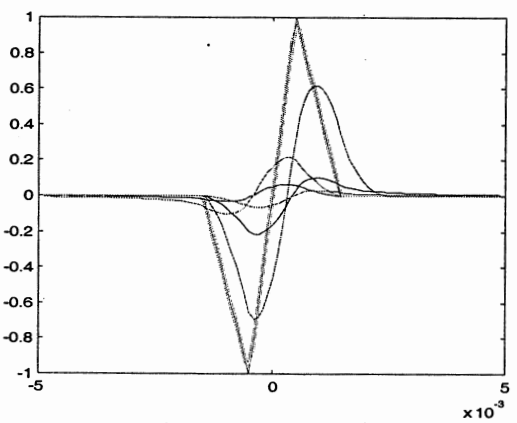

Figure 6. The discriminator functions with parameter values $\hat{f}_o = f_o$ and

$\frac{\hat{f}_1}{f_o} = -10^{-1},-10^{-2},-10^{-3},-10^{-4},0,10^{-4},10^{-3},10^{-2},10^{-1}\,\mathrm{s}^{-1}$

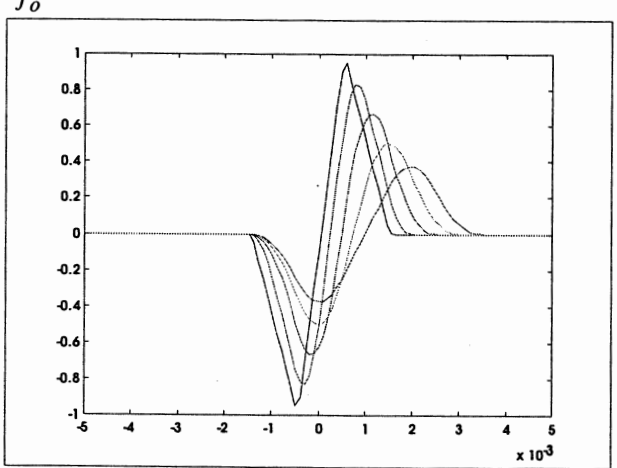

Figure 7. The discriminator functions with parameter values $\hat{f}_1 = 0$, $\hat{f}_o - f_o = 0.01\%$ of f_o, T=1,5,10,15,20 ms.

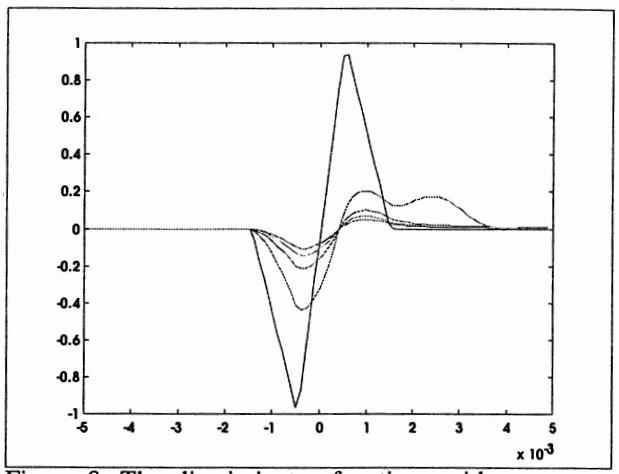

Figure 8. The discriminator functions with parameter values $\hat{f}_o = f_o$, $\frac{\hat{f}_1}{f_0} = 10^{-4}\mathrm{s}^{-1}$, T=1,5,10,15,20 ms.

Thus the theoretical results point out that a limit of short term instability (δf/f in 1ms) for proper operation is about 10^{-7}. Due to the other disturbances is practice, the required instability should be better than 10^{-8}.

3.2. Experimental Tests

The parameter values used in theoretical studies have been studied by practical experiments.

In the very beginning, the lowest achievable (bottom) levels of the measurement system was determined to find out the performance of the set-up, Fig. 9.

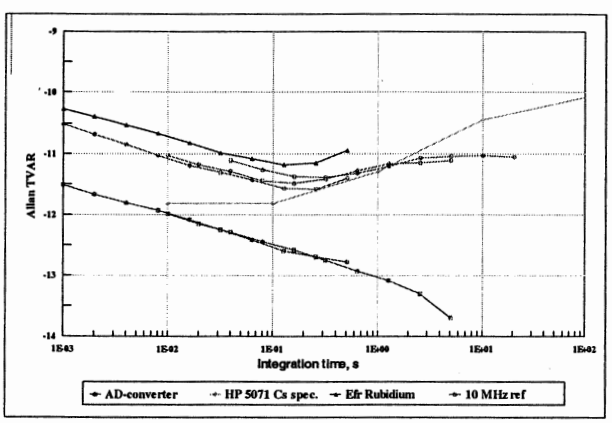

Figure 9. Lowest achievable (bottom) levels for fast Allan variance measurement set-up.

A GPS receiver was tested with abrupt (step-like) temperature changes. These changes were produced by blowing air at room temperature to the oscillator. At first only the PPS output of the receiver was measured. Later, simultaneous measurements with a probe and spectrum analyzer at 25 ms intervals were done along

with the PPS measurement to see the behaviour of the crystal oscillator during cooling.

The first tests consisted of four temperature steps. The first blow was relatively strong, followed by a very light blow, which caused no oscillations. The strength of the third blow was something in between. The last blow was very strong and caused vigorous oscillations for 2.5 minute period.

Examples of the measurements results are presented in Figs. 10 and 11 comprising the light and very strong blow, respectively. The instabilities in these examples are about 10^{-5}...10^{-6}.

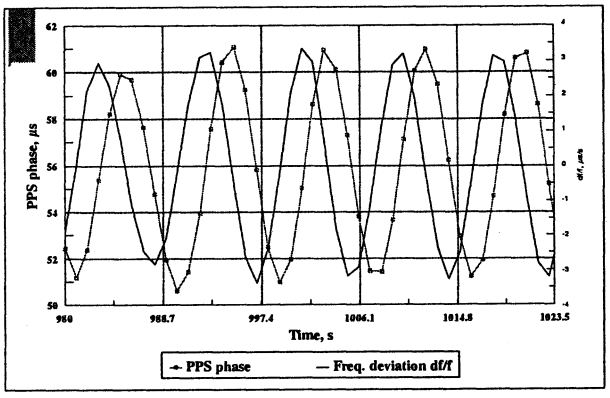

Figure 10. Crystal Oscillator cooling experiments; strong cooling with air.

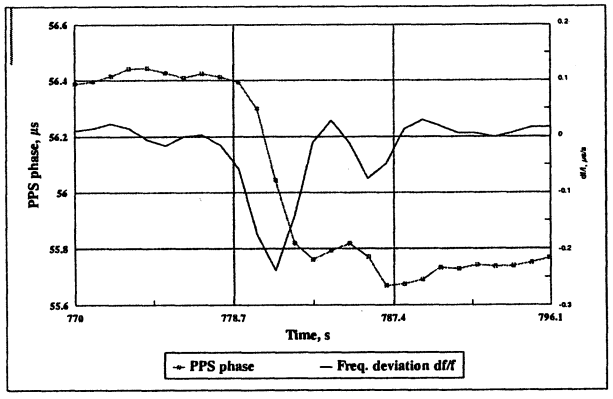

Figure 11. Crystal oscillator cooling experiments; light cooling with air.

In addition the sequential significance of temperature steps were studied to find out e.g. the needed delay to avoid cross effect between them, Fig. 12. A rather ideal situation is presented in Fig. 12 where the former phase signal seems to be settled but as seen from pictures the rise time of the response of latter case is somewhat shorter.

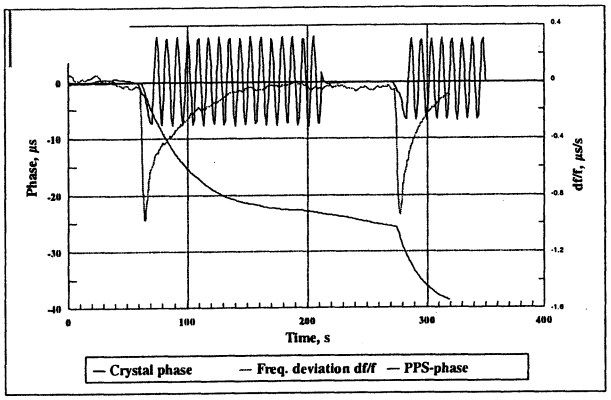

Figure 12. Crystal oscillator cooling experiments; two sequential coolings with air; crystal oscillator phase is also measured.

4.CONCLUSION

The theoretical results point out that a limit of short term instability ($\delta f/f$) for proper operation is about 10^{-7}. Due to the other disturbances, in practice, the required instability should be better than 10^{-8} and e.g. it is observed over time that for a GPS C/A-code receiver this value should be 10^{-9} or better. Practical experiments show that the instabilities of 10^{-3} ... 10^{-4} is possible to achieve even by real thermal changes or, especially, by thermal shocks. Moreover, these experimental results supported the theoretical ones.

5.REFERENCES

/1/ H. Meyr, G. Asheid, " Synchronization in Digital Communications, Vol. 1 Phase-, Frequency-Locked Loops and amplitude Control" Wiley, New York, USA, 1990.

/2/ J.Mannermaa, K.Kalliomäki, T. Mansten, S.Turunen, "Short-term Stability of Crystal Oscillators in Commercial GPS Receivers". Proceedings of the 14th European Frequency and Time Forum, pp. 424-428, Turin, Italy, 2000.

IMPACT OF TIME ERROR DATA PREPROCESSING FOR TDEV ASSESSMENT

Andrzej Dobrogowski, Michal Kasznia

Institute of Electronics and Telecommunications
Poznan University of Technology
ul. Piotrowo 3A, 60-965 Poznan, Poland
dobrog@et.put.poznan.pl, mkasznia@et.put.poznan.pl

ABSTRACT

In the paper the influence of time error preprocessing on the quality of the time deviation (TDEV) estimate is analyzed. The preprocessing of the time error consists in the reduction of the data amount used for TDEV calculation. The data reduction based on the time error samples averaging offers short time of TDEV estimate calculation. In the paper the results of TDEV estimate calculation for several time error series are presented. The time of calculation and the quality of the obtained estimates are analyzed.

Keywords: timing signal, time error, time deviation

1. INTRODUCTION

Time deviation TDEV is one of the parameters, which describe the quality of the synchronization signals in the telecommunication network. Frequently verification of the values of the parameters is an important process in the service and maintenance of the network. The sequence of time error samples measured at some network interface is used for the assessment of the TDEV estimate. The amount of the samples entails rather long time of the estimate calculation. In order to achieve rather short time of calculation linked with good quality of the parameter's estimate some methods of TDEV calculation were proposed and described in the paper presented at the 14th EFTF in 2000 (Ref. 3). The methods consist in the reduction of the amount of data used for the calculation for long observation intervals. One of the methods basing on the averaging of the time error subsets is developed in the paper.

The reduction is not a simple short cut of the time error sequence obtained from the measurement (or short cut of the measurement time), because some important information characterizing timing signal may be lost. The telecommunications standards (Ref. 1) require the duration of the measurement time twelve times greater than the longest observation interval taken into consideration. The methods of the data amount reduction consist in the creation of a new sequence that represents the old sequence taken from the measurement. The detailed description of the time error preprocessing is presented in the Section 2 of the paper.

The new sequence is created if the estimate is calculated for observation interval greater than specified threshold value (starting interval). Changing the starting interval and the dimension of the time error subsets we can affect the quality of the TDEV estimate. The influence of the preprocessing depends on the statistical behavior of the time error values. In the Section 3 the results of TDEV calculation made on the several time error sequences are presented. The results of calculation performed on the modified data are compared with the results of calculations made on the raw data. The influence of subset dimension and starting interval is discussed in the Section 4.

2. TDEV ESTIMATION WITH TIME ERROR PREPROCESSING

The time error (TE) samples measured at some network interface are used for the TDEV estimate calculation. The results of the time error measurement are taken with the sampling interval τ_0 and stored in the data file. In the telecommunication standards (Ref. 1) some conditions for the measurement of time error are specified. Time error should be measured using an anti-aliasing filter with the cut-off frequency f_0. The minimum observation interval τ_{min} must be three times greater then maximum sampling time τ_0 and the anti-aliasing filter cut-off frequency f_0 must be equal $f_0=1/\tau_{min}$. The minimum measurement period T for time deviation calculation should be twelve times longer then the observation interval τ.

In telecommunication standards the formula for the estimator of the time deviation TDEV is given:

$$TDEV(\tau)=\sqrt{\frac{1}{6n^2(N-3n+1)}\sum_{j=1}^{N-3n+1}\left[\sum_{i=j}^{j+n-1}(x_{i+2n}-2x_{i+n}+x_i)\right]^2} \quad (1)$$

where:

$\{x_i\}$ - sequence of N samples of time error function $x(t)$ taken with interval τ_0;

$\tau=n\tau_0$ - observation interval.

In order to reduce the calculation time of TDEV estimate for long observation intervals the preprocessing of the time error samples is proposed. In the paper (Ref. 3) three methods of data modification were described. One of the methods based on the averaging is further developed in the paper.

The time error sequence taken with sampling interval τ_0 is stored in the memory of the equipment. The row of the TDEV estimates should be calculate for the observation intervals τ from the range for $\tau_{min}=3\tau_0$ till τ_{max}. The TDEV estimate calculation for small observation intervals without data preprocessing is performed. The reduction of the amount of the data for long observation intervals τ taken into consideration is performed. The first step of the preprocessing is made when the observation interval is greater than specified threshold interval τ_S. The time error sequence is divided into the subsets of m samples. The new data set contains the average values of each subset. In this case the amount of data is m times smaller than the amount of samples in the raw data set. The second step of the preprocessing is performed when the observation interval is greater than $10\tau_S$. The item in the new data sequence is the average value of the subsets containing m^2 raw TE samples each. The length of the new sequence is m^2 times smaller than the length of the original TE sequence. The operation can be performed in the next steps of data reduction for the observation intervals greater than

$100\tau_S$ and $1000\tau_S$ until the observation interval τ reach the value of τ_{max}. The dimension of the time error subset for the next reduction steps is the successive power of m.
Setting the factors τ_S and m we can affect the time and accuracy of the TDEV estimate calculation. In the experiment described in the next section we assumed the starting interval τ_S as 1 s, 3 s, 5 s, and 10 s and the subset dimension m as 5 samples and 10 samples for each starting interval. Thus we consider 8 cases of data preprocessing method (Table I). In the experiment the 81 values of TDEV estimate were computed. The observation interval varied from τ=0.1 s to 1000 s. The time error samples were taken with the sampling interval τ_0=1/30 s.

Table 1. Starting intervals and subset dimensions in the data preprocessing method

case (τ_s, m)	starting interval τ_s [s]	subset dimension m	threshold intervals for next steps [s]	subset dimensions for next steps
(1,10)	1	10	10 100	100 1000
(3,10)	3	10	30 300	100 1000
(5,10)	5	10	50 500	100 1000
(10,10)	10	10	100	100
(1,5)	1	5	10 100	25 125
(3,5)	3	5	30 300	25 125
(5,5)	5	5	50 500	25 125
(10,5)	10	5	100	25

Another method of the reducing of the time error sequence length is to increase the sampling interval τ_0 in the time error measurement process. In this case we cannot evaluate the timing signal for small observation interval (smaller than $3\tau_0$) if it is needed. This is because it is not permitted to calculate the TDEV estimate for observation interval smaller than $3\tau_0$. The method with averaging is helpful, if the time error sequences were measured with small sampling interval and the parameter's estimate should be calculate for the several values of observation interval τ.

3. EXPERIMENT

The time of calculation and the accuracy of calculated TDEV estimates were analyzed in the experiment. Several time error sequences with different types were used for the calculations. Five sequences representing the typical noises for the timing signals were artificially generated: white phase modulation (WPM), flicker phase modulation (FPM), white frequency modulation (FPM), flicker frequency modulation (FFM) and random walk frequency modulation (RWFM). Three sequences were obtained from the measurement process (Ref. 3). The first time error sequence (denoted as MSG, Fig. 1) was obtained from the measurement of the oscillator being the part of the timing signal measurement system. The GPS disciplined oscillator served as a reference. The second sequence (denoted as GPS, Fig. 2) resulted from the comparison of two different oscillators controlled by the GPS signals. The third sequence (denoted as DCF, Fig. 3) was obtained from the measurement of the oscillator controlled by the DCF-77 signal with the GPS disciplined oscillator as a reference.

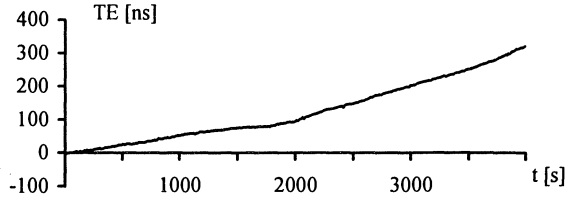

Fig. 1. Time error of the MSG signal measurement

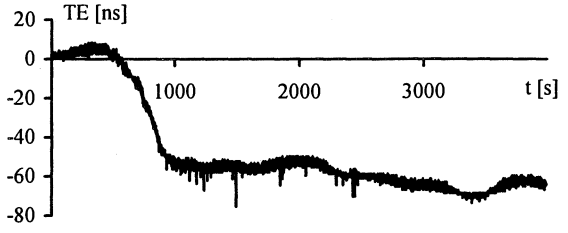

Fig. 2. Time error of the GPS signal measurement

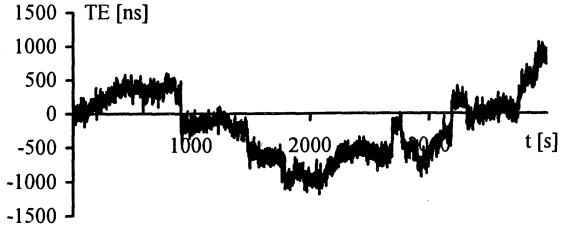

Fig. 3. Time error of the DCF signal measurement

In the Table 2 the time of calculation for the whole range of 81 observation intervals and for the decade subranges of the whole range is presented. In the Table 3 the time of calculation for some chosen observation interval is given. The format of the time data is as follows: minutes:seconds. All calculations were performed using the PC computer with Pentium II 450 MHz processor.

Table 2. Time of TDEV calculation for the range of observation intervals

method	the range of observation interval				
	[0.1-1000]	[0.1-1]	(1-10]	(10-100]	(100-1000]
direct	36:19.72	9:14.92	9:00.30	9:20.13	8:44.37
(10,10)	19:15.80	-	-	55.36	5.22
(5,10)	15:59.76	-	6:05.09	36.24	3.51
(3,10)	14:12.62	-	4:28.42	26.69	2.59
(1,10)	10:11.58	-	52.89	5.27	0.50
(10,5)	20:22.70	-	-	1:47.21	20.27
(5,5)	17:37.15	-	6:43.97	1:23.27	14.99
(3,5)	15:23.41	-	4:57.42	59.48	11.59
(1,5)	11:25.47	-	1:45.51	21.03	4.01

Table 3. Time of TDEV calculation for some chosen observation intervals

method	observation interval τ [s]				
	0.1	1	10	100	1000
direct	26.37	26.48	27.52	27.85	23.39
(10,10)	-	-	-	2.80	0.27
(5,10)	-	-	2.64	0.27	0.02
(3,10)	-	-	2.64	0.27	0.02
(1,10)	-	-	2.64	0.27	0.02
(10,5)	-	-	-	5.44	0.94
(5,5)	-	-	5.33	1.04	0.16
(3,5)	-	-	5.33	1.04	0.16
(1,5)	-	-	5.33	1.04	0.16

The time of calculation with data modification for particular observation intervals is from five to thousand times smaller than the time of calculation using direct method. Using data preprocessing we get the calculation time of the whole range of the TDEV estimate more than three times shorter than the calculation time using direct method. The averaging of the time error data causes the error in the calculation results. The relative error of the TDEV calculation using the methods described for the typical phase noises is presented in Fig. 4-8.

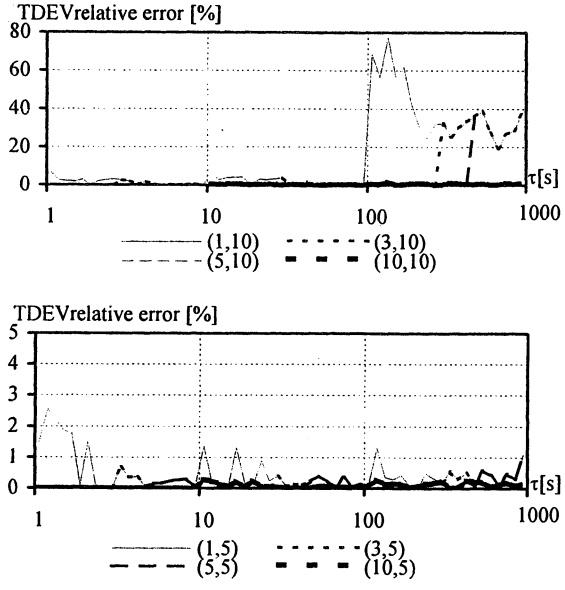

Fig. 4. TDEV relative error for the WPM sequence

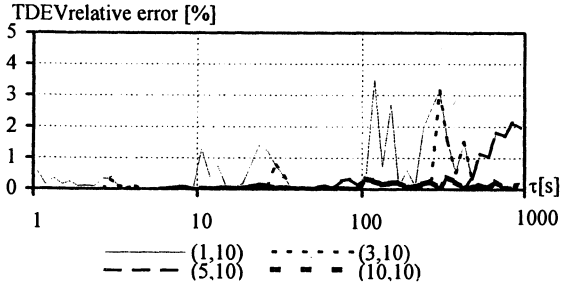

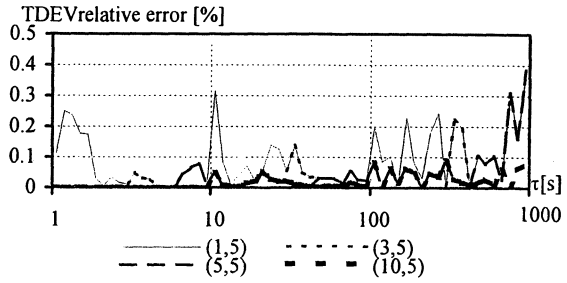

Fig. 5. TDEV relative error for the FPM sequence

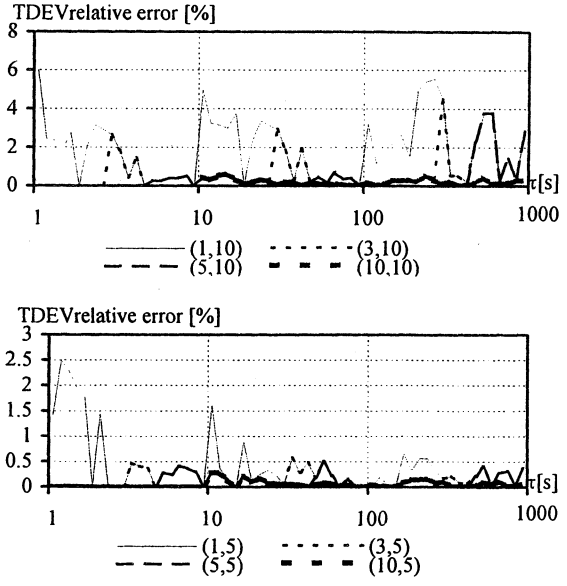

Fig. 6. TDEV relative error for the WFM sequence

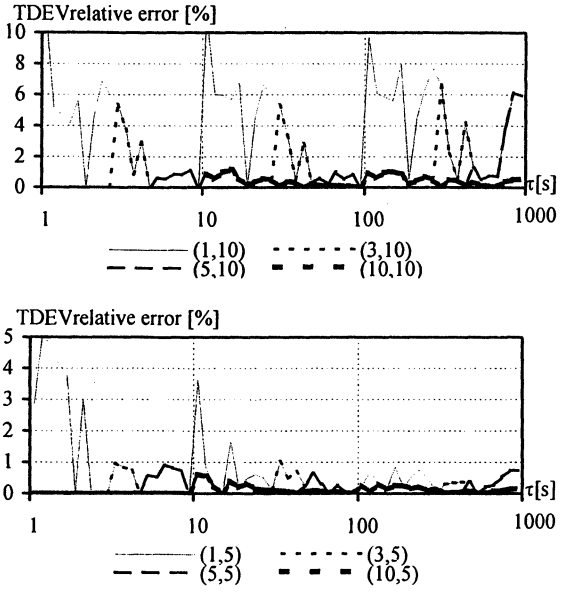

Fig. 7. TDEV relative error for the FFM sequence

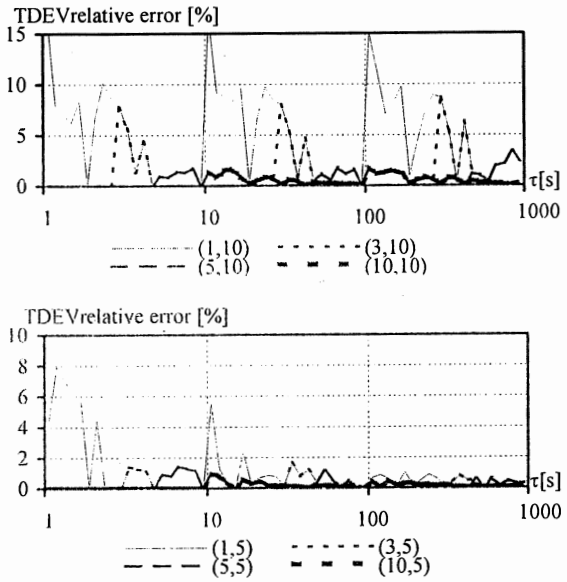

Fig. 8. TDEV relative error for the RWFM sequence

Time deviation for the MSG time error sequence is presented in Fig. 9. The relative error of the TDEV estimate calculation for the MSG sequence is presented in Fig. 10.

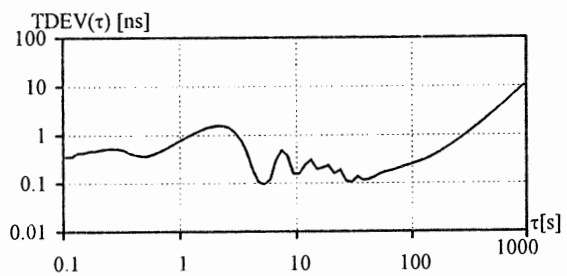

Fig. 9. TDEV for the MSG sequence

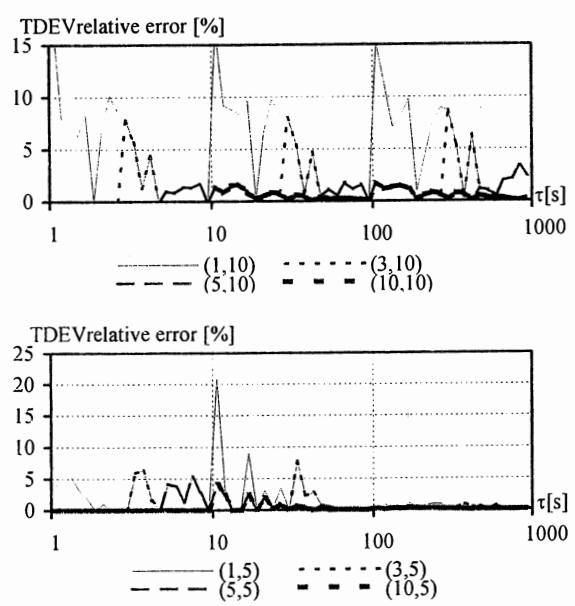

Fig. 10. TDEV relative error for the MSG sequence

Time deviation for the GPS time error sequence is presented in Fig. 11. The relative error of the TDEV estimate calculation for the sequence is presented in Fig. 12.

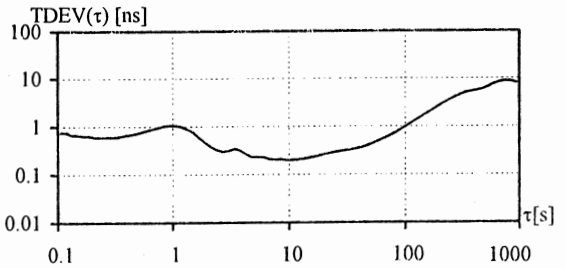

Fig. 11. TDEV for the GPS sequence

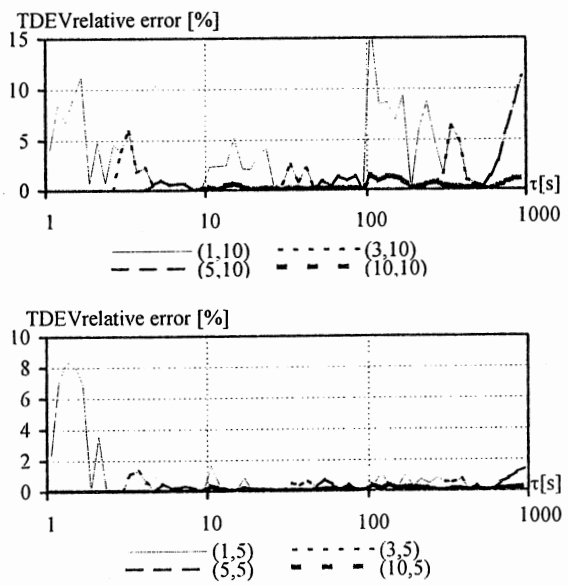

Fig. 12. TDEV relative error for the GPS sequence

Time deviation for the DCF time error sequence is presented in Fig. 13. The relative error of the TDEV estimate calculation for the sequence is presented in Fig. 14.

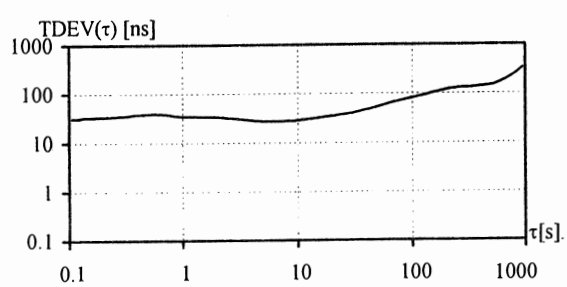

Fig. 13. TDEV for the DCF sequence

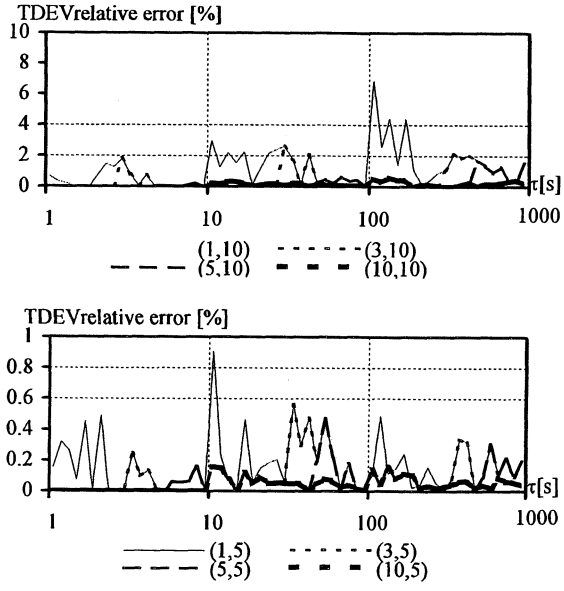

Fig. 14. TDEV relative error for the DCF sequence

4. COMMENTS ON THE EXPERIMENT RESULTS

Application of the time error data preprocessing in the TDEV estimate calculation process causes indisputable reduction of the calculation time. In some cases the time of the calculation with data preprocessing is thousand times smaller than the time of calculation using direct method. The shortening of the calculation time is linked with the deterioration of the estimate quality. The problem of low quality is visible for the method with averaging of 10 (and power of 10) samples. The relative error for the averaging starting for the interval τ_S=1 s exceeds 15% for the RWFM, MSG, and GPS time error sequences and exceeds 60% for the WPM sequence. The error for the averaging starting with 3 s and 5 s is acceptable and does not exceed 10% except of the WPM sequence, when it exceeds 20%. The acceptable results were obtained for the averaging starting with 10 s. The relative error for the case does not exceed 2%. Better results were obtained for the preprocessing with the subset dimension of 5 (and power of 5) samples. The calculation using the faster method with starting interval τ_S=1 s produces the relative error smaller than 8%. The relative error for the cases with starting interval of 3 s, 5 s, and 10 s does not exceed 2%.

In general, the best results were obtained for the preprocessing with small subset dimension (5 and the successive power of 5) and for staring interval longer than 3 s. The averaging of 10 samples (and power of 10) is suggested for the starting interval greater than 5 s. In the experiment the time error sequences taken with sampling interval τ_0=1/30 s were considered. For longer sampling intervals the relatively greater starting intervals τ_S should be applied.

The TDEV calculation with preprocessing is suggested, if the row estimate values should be computed for several values of observation interval. The advantage of the method is visible for the calculation for long observation interval τ made on the time error sequence taken with small sampling interval τ_0. In the Table 4 the time of the TDEV estimate calculation for variable ranges of observation interval is given. The results in the column 4 and 5 of the table indicate the advantage of the proposed method.

Table 4. Time of TDEV calculation for the variable ranges of observation interval

method	the range of observation interval			
	[0.1-1000]	[1-1000]	[10-1000]	[100-1000]
direct	36:19.72	27:31.28	18:32.02	9:12.22
(10,10)	19:15.80	10:27.36	1:28.40	8.02
(5,10)	15:59.76	7:11.32	42.39	3.78
(3,10)	14:12.62	5:24.18	31.92	2.86
(1,10)	10:11.58	1:25.15	8.41	0.77
(10,5)	20:22.70	11:34.26	2:35.00	25.71
(5,5)	17:37.15	8:49.71	2:05.59	16.03
(3,5)	15:23.41	6:35.57	1:16.40	12.63
(1,5)	11:25.47	2:37.03	30.37	5.05

5. CONCLUSIONS

Application of the averaging of time error samples for the TDEV estimate assessment results in short time of the estimate's calculation. Great dimension of the averaged data subset offers short time of the calculation but poor quality of the estimate, when the calculation with preprocessing for small observation intervals is performed. In order to avoid the deterioration of the estimate quality two possible procedures are suggested. The first is the calculation with great subset dimension (e.g. 10 and power of 10) started for long observation intervals. The second solution is the calculation with preprocessing started for small observation intervals but with small subset dimension (e.g. 5 and power of 5).

The methods proposed can be used for the TDEV estimation, when the series of the parameter's values for the different observation intervals is to be calculated. The time engaged for the data modification and single parameter value calculation can exceed the calculation time using direct method.

This work is supported by State Committee For Scientific Research under grant 8 T11D 007 18.

REFERENCES

1. ETSI ETS 300 462-1-1, "Generic requirements for synchronization networks. Definitions and terminology for synchronization networks"

2. M. Kasznia, "Some Approach to Computation of ADEV, TDEV and MTIE", Proc. of the 11th European Time and Frequency Forum, pp.544-548, Neuchatel, 4-6 March 1997.

3. A. Dobrogowski, M. Kasznia, "Modification of the Raw Data Set for Time Efficient ADEV and TDEV Assessment", Proc. of the 14th European Time and Frequency Forum, pp.338-342, Torino, 14-16 March 2000.

EC CRAFT Award Contract # "Alpha One" Primary Reference Clock For Telecoms & Metrology Including space qualified Passive Hydrogen Maser Element

Clive Green

The results of research to date on five of the 10 elements in the EC CRAFT Award. Passive Hydrogen Maser, Temperature Controlled Quartz Oscillator, High Resolution Frequency and Phase measurement System, GPS Common View Time Transfer Receiver results and Rubidium Oscillator for Space Vehicle Redundancy/Holdover use are reported.

Passive Hydrogen Maser

A major challenge to reduce size and weight by 50% approximately and improve stability whilst adding telemetry features of and to the existing unique CH1-76 Passive Hydrogen Maser has been modeled to the extent that hardware design for the maser electronics and reduced size physics Package has commenced. The microprocessor choice and software for this 21st Century project has to consider a harsh radiation environment, low budget development and reliability implications. The entirely new electronics philosophy replaces 25kg of existing modules(that exhibit a stability of 7 x better than high performance cesium) with only three Eurocards! The new circuit blocks are described.

New OCXO considerations include a very low phase noise under vibration curve, fast warm time (down to 15 seconds) 150mW consumption, small size whilst immunity to radiation with good EMC characteristics are also essential. Acceleration stability is reported.

The problem of High Resolution in a Frequency Measurement System with short gate times in a compact package is considered. Phase comparators at this level of low noise floor are both large and heavy for the projects requirement. Weight reduction of 80% is envisaged. A $1x10^{-15}$ resolution in only 100s measurement time is needed in maximum height of 40mm with phase stability vs temperature change of 1 ps / °C.

In Metrology use at Commercial calibration laboratories in many countries, the Passive Hydrogen Maser will be more stable than the National Laboratory reference. With peripheral carrier phase tracking GPS RX, the PHM can maintain offset to the GPS noise floor level of $5x10^{-14}$. The need for independent (if not national reference) traceable confirmation of the limits of uncertainty may be obtained by the use of GPS Common View Time Transfer. A joint UK/NPL project with Quartzlock to trial a feasible GPS CVTT RX has shown the results reported. These may satisfy the needs of a national accreditation authority(who may be unfamiliar with Hydrogen Masers(Passive if not Active) and the user or users customer in a due diligence exercise, increasingly important where multinational-corporate QA requirements are not met by ISO 9001 accreditation.

In power saving or redundant oscillator mode a disciplined Rubidium frequency Standard may be required to holdover for telecoms G801 specifications to$<1x10^{-11}$.

A High Stability Rubidium Oscillator may achieve x 10^{-13}/day. (in the case of PHM use offsite upgrade or standby power mode in SV use). Severe environmental tests completed on near production and production test bed examples for stock and vibration and EMC testing of the Rubidium Oscillator element not only show 100% survival but maintained specification during test. Results are displayed. Quartzlock used its defense production test facility (Bosnia Nato Project) Rubidium and NIST Traceable measurement facility to confirm characteristics reported. A new phase noise measurement standard for GSM2000 Rubidium definition phase confirmed the low noise specification required and spurii elimination target compliance.
Quartzlock are grateful to its CRAFT Project partners and technology transfer colleagues space engineering electronics J.V. & advisors at Astrium. (ONIIP& IEM KVARZ have a seven year heritage with Quartzlock).

SIMPLE MOVING AVERAGE, WIENER, AND KALMAN ESTIMATES OF TIME ERRORS: A COMPARATIVE STUDY

yuriy shmaliy, anatoliy marienko*, oscar ibarra-manzano, roberto rojas-laguna, miguel torres-cisneros,

guanajuato university, fimee, salamanca, 36730, mexico, shmaliy@salamanca.ugto.mx
* "sichron" center, 4 skrypnyka str., kharkiv, 310057, ukraine

1. ABSTRACT

In this report we show that the following digital filter is best for a time error estimate of the clock with known fractional frequency offset y_0 (time error rate), namely: a simple moving average (MA) is for $|y_0| < r_1$, the Wiener filter is for $r_1 \le |y_0| \le r_2$, and the three-state Kalman filter is for $r_2 < |y_0|$, where r_1 and r_2 depends on the required accuracy. We prove this by simulation and give an example of the GPS-based time error estimate of the rubidium clock employing the Motorola GPS UT+ Oncore Timing receiver.

Time error process, optimal filtering, estimating

2. INTRODUCTION

GPS timing plays a critical role in modern practice of the time error "on-line" estimate and synchronization. Major difficulties here are caused mainly by both big variance of the measured data inherently produced by GPS receiver and the non-stationary nature of a time error. Statistically, once a discrete time random process is a stationary one then the Wiener filter (Ref. 1) is efficient through convolution and, if not, the Kalman filter (Ref. 2) is proved as the best for the non-stationary process. Even though both approaches evidentially cover all cases, test and measurement still uses a moving average (MA) filter (Ref. 3) owing to its transparency and small noise, and despite an estimate bias inevitably caused by the non-stationary process.

Modern timekeeping employs all three filters (Refs 4-8). Of course, there are different clocks in timekeeping, however, it seems important to note that for the same quality master clocks the different estimators used yield different errors. In this connection, while attempting to obtain precise filtering and control, it is helpful to be aware that each filter yields the smallest processing error only under the certain conditions, obeying certain rules. Then, what type of the filters should be used to provide the most accuracy for the fixed time constant and known rate of a time error caused by the crystal oscillator, rubidium and cesium standard, or even hydrogen maser?

In this paper we answer the question in the following way. We focus attention on all three above-mentioned filters, namely: simple MA, Wiener and Kalman, fixing in each case the same transient time θ as that of a simple MA. We show that for the same θ the following filter seems like the best for the known y_0, namely, a simple MA is best for the range of $|y_0| < r_1$, the Wiener is best for $r_1 \le |y_0| \le r_2$, and the three-state Kalman's is best for $r_2 < |y_0|$, where r_1 and r_2 are symbolized for the total error as r_{1t} and r_{2t}, and for the maximal error as r_{1m} and r_{2m}, respectively. Because processing time influences the error strongly we then study the errors for various θ, presenting correspondent dependencies $r_{1,2}(\theta)$ and their approximations $r_i = a_i\theta^{-1.5}$, where a_i is a constant, and $i \equiv 1t,\ 2t,\ 1m,\ 2m$. Employing the Motorola UT+ Oncore receiver, we finally investigate the example of the filter selection for the rubidium-based clock with known y_0.

2. SIGNALS MODEL

2.1 Oscillator Time Error Model

A model of the total instantaneous phase $\Phi(t)$ of oscillator is truly justified in (Ref. 9) as

$$\Phi(t) = \Phi_0 + 2\pi\nu_{nom}(1+y_0)t + \pi D\nu_{nom}t^2 + \varphi(t), \quad (1)$$

where: Φ_0 is initial phase offset; y_0 is the fractional frequency offset from the nominal frequency ν_{nom} (mainly due to finite frequency setability of the clock) so that y_0 [in ns/hour] equals $3.6{\cdot}y_0$ [in parts of 10^{-12}]; D is a linear fractional frequency drift rate (basically representing oscillator temperature and aging effects), and $\varphi(t)$ is a random phase deviation component.

Subtracting from (1) the same type phase model of a reference source and then dividing the result by $2\pi\nu_{nom}$, one comes to the time error model of local oscillator

$$x(t) = x_0 + (y_0 - y_{0ref})t + \frac{D - D_{ref}}{2}t^2 + \frac{\varphi(t) - \varphi_{ref}(t)}{2\pi\nu_{nom}}, \quad (2)$$

where x_0 is initial time error. In (2) we can also assume that all the degradation sources y_{0ref}, D_{ref}, and $\varphi_{ref}(t)$ of the reference source are negligible as compared to those of the clock under test. As a result, the $x(t)$ model reduces to the practical form of

$$x(t) = x_0 + y_0 t + \frac{D}{2}t^2 + \frac{\varphi(t)}{2\pi\nu_{nom}}. \quad (3)$$

5.2 Model of a Noisy Time Error

Basically, we measure a time error $x(t)$ in discrete time, providing values of x_v for discrete time points t_v for the constant time interval $\Delta = t_v - t_{v-1}$, where $v = 0, 1, 2, \ldots$. The GPS receiver unavoidably adds noise to the measurement, which is normally distributed in practice, thus, it may be modeled as Gaussian noise. Both time error and noise are summed (3) allowing the presentation of a measured noisy time error (observation ξ_v) and the clock states (time error x_v, frequency offset y_v, and frequency aging D_v) in the matrix form as follows

$$\xi_v = \mathbf{H}_v\lambda_v + n_{0v}, \quad (4)$$

$$\lambda_v = \mathbf{A}_{v-1}\lambda_{v-1} + \mathbf{n}_{\lambda v}, \quad (5)$$

where λ_v is a 3×1 dimensional clock state vector, $\mathbf{H}_v$ is a 1×3 dimensional measurement matrix, $\mathbf{A}_v$ is a 3×3 dimensional clock state transition matrix, n_{0v} and $\mathbf{n}_{\lambda v}$ are jointly independent white noises with zero expectations and covariances V_v and Ψ_v of 3×3 dimension, respectively,

$$V_v = E\{n_{0v} n_{0v}^T\}, \quad (6)$$

$$\Psi_v = E\{\mathbf{n}_{\lambda v} \mathbf{n}_{\lambda v}^T\}. \quad (7)$$

In discrete time the model (3) transfers to the form of

$$x_v = x_{v-1} + y_{v-1}\Delta + \frac{D_{v-1}}{2}\Delta^2 + n_{xv}, \quad (8)$$

where $y_v = y_{v-1} + D_{v-1}\Delta + n_{yv}$; $D_v = D_{v-1} + n_{Dv}$; n_{xv}, n_{yv}, and n_{Dv} are correspondent discrete noises, and all the matrixes necessary for (4) and (5) are presented via (8) as

$$\lambda_v = \begin{bmatrix} x_v \\ y_v \\ D_v \end{bmatrix}, \quad \mathbf{A}_v = \begin{bmatrix} 1 & \Delta & \Delta^2/2 \\ 0 & 1 & \Delta \\ 0 & 0 & 1 \end{bmatrix}, \quad \mathbf{n}_{\lambda v} = \begin{bmatrix} n_{xv} \\ n_{yv} \\ n_{Dv} \end{bmatrix}, \text{ and}$$

$$\mathbf{H}_v = [1 \;\; 0 \;\; 0]. \quad (9)$$

Observation (4) is also presented in the more simple form of

$$\xi_v = x_v + n_{0v}, \quad (10)$$

and the noise matrix (7) simplifies to

$$\Psi_v = E\{\mathbf{n}_{\lambda v} \mathbf{n}_{\lambda v}^T\} \cong S_{Dv}\Delta \begin{bmatrix} 0 & 0 & 0 \\ 0 & 0 & 0 \\ 0 & 0 & 1 \end{bmatrix}, \quad (11)$$

where S_{Dv} is the two-side spectral density of a continuous white noise of aging that depends on Δ (Ref. 10) and expressed through the time error noise straightforward.

3. ESTIMATING OF A TIME ERROR

We consider here the simple MA, Wiener, and Kalman filters. To simplify, we assume that aging is negligible and present deterministic part of a time error for (10) as

$$x_v = x_0 + y_0 \Delta v, \quad (12)$$

instead of the recursive form of (8). For the filtering error

$$\varepsilon_v = \hat{x}_v - x_v, \quad (13)$$

where $\hat{x}_v$ is an estimate of a time error, the four particular estimates are of our special interest: error mean or estimate bias $\bar{\varepsilon}_v = \langle \varepsilon_v \rangle \equiv E\{\varepsilon_v\}$, error variance $\sigma_{\varepsilon v}^2 = \langle (\varepsilon_v - \bar{\varepsilon}_v)^2 \rangle$, total error $\varepsilon_{tv} = |\bar{\varepsilon}_v| + \sigma_{\varepsilon v}$, and maximal error $\varepsilon_{\max} = |\max(\varepsilon_v)|$.

3.1 Simple Moving Average Filter

Simple average filtering allows getting a non-optimal estimate $\hat{x}_v$ of a time error x_v (in the sense of a minimal RMS error) based on an observation ξ_v (10) straightforward. The algorithm does not require any a priori knowledge about the oscillator state model, time error, and even the observation, yielding an estimate as follows

$$\hat{x}_v = \frac{1}{N}\sum_{i=0}^{N-1} \xi_{v-i}, \quad (14)$$

where we assume $\xi_v = 0$ if $v < 0$, N is the number of average points. Here, once the first estimate appears with delay on N points, the filter transient time equals

$$\theta = \Delta(N-1), \quad (15)$$

where $\Delta = t_v - t_{v-1}$ is a time step. Substitute (12) into (10) and (10) into (14) transforms (14) into the form of

$$\hat{x}_v = \frac{1}{2} x_v + n_{0Nv}, \quad (16)$$

where n_{0Nv} is a new discrete noise with variance $\sigma_{nN} = \sigma_n^2 / N$. Then, based on (16) estimate the bias, variance, and total error straightforward as:

$$\bar{\varepsilon}_v = -\frac{1}{2} x_v = -\frac{1}{2}(x_0 + \Delta y_0 v), \quad (17)$$

$$\sigma_{\varepsilon v}^2 = \frac{\sigma_n^2}{N}, \quad (18)$$

$$\varepsilon_{tv}^{AS} = \frac{1}{2}|x_v| + \frac{\sigma_n}{\sqrt{N}}. \quad (19)$$

It follows that a mean error (17) for the assumed linear case (12) is 50% and that the estimated variance (18) reduces proportionally to N.

3.2 Wiener Filter

In discrete time the Wiener filter provides an estimate via a convolution of its impulse response h_v and an observation (10)

$$\hat{x}_v = \sum_{i=0}^{M-1} h_i \xi_{v-i} = \sum_{i=v-M+1}^{v} \xi_i h_{v-i}, \quad (20)$$

where we assume $\xi_v = 0$ if $v < 0$, M determines the length of h_v that is taken to be equal to zero apart from the time interval 0, …, $(M\text{-}1)\Delta$.

To get a minimal RMS error for the estimate, first, in the tradition of Wiener define an optimal unrealizable response

$$H_{0k} = \frac{S_{xk}}{S_{xk} + S_{n0}}, \quad (21)$$

where S_{xk} is discrete power spectral density of a time error (oscillator phase) that in the view of Leeson (Ref. 11) is taken here as $S_{xk} = af_k^{-2}$, where f_k is Fourier frequency; a is a constant; S_{n0} is the constant power spectral density of white noise; $k = 0, \ldots, K\text{-}1$, and K limits the length of the time error sequence taken at the early stage to estimate the spectral densities with enough accuracy. Van Trees has shown in his now classic work (Ref. 12) that the optimal continuous transfer function (21) taken for our particular case of S_{xk} as $H_0 = \dfrac{a^2}{a^2 + S_{n0} f^2}$ is easily inverted to the optimal impulse response $h_0 = 0.5Ae^{-A|t|}$, where $A = \sqrt{a/S_{n0}}$, which for the positive discrete time yields

$$h_{0v} = A\Delta e^{-A\Delta v}, \quad (22)$$

To obtain the same time constant for the simple MA and Wiener filters, we restrict the unlimited response (22) by the level of γ, which normally is taken as 0.1, and solve the equation $\gamma A\Delta = A\Delta e^{-A\Delta(N-1)}$ with respect to $A\Delta$, noting that the trivial solution $A\Delta = 0$ does not satisfy the physical idea, so the only solution is

$$A\Delta = -\frac{\ln \gamma}{N-1}. \quad (23)$$

Let us obtain convolution-based estimate (20) for a time error based on the non-optimal restricted impulse response (22) formed with account of (23)

$$\hat{x}_v = \sum_{i=0}^{v} \xi_i h_{v-i} = \sum_{i=0}^{v} x_i h_{v-i} + \sum_{i=0}^{v} n_{0v} h_{v-i}, \quad (24)$$

Considering the first sum in (24), get

$\hat{x}_{dv} = A\Delta\sum_{i=0}^{v} x_i e^{-A\Delta(v-i)} = A\Delta\sum_{i=0}^{I-1}(x_0 + y_0\Delta i)q^i$ that for $q = e^{A\Delta} \neq 1$ and $I = v+1$ represents arithmetic-geometric progression. Then obtain

$$\hat{x}_{dv} = \frac{A\Delta}{1-e^{-A\Delta}}\left\{x_0[1-e^{-A\Delta(v+1)}] + y_0\Delta v - \frac{y_0\Delta e^{-A\Delta}(1-e^{-A\Delta v})}{1-e^{-A\Delta}}\right\}. \quad (25)$$

The second sum in (24) cannot be transformed because n_{0i} and we present it at this stage in a common form

$$\hat{x}_{rv} = A\Delta\sum_{i=0}^{v} n_{0i}e^{-A\Delta(v-i)}. \quad (26)$$

Define a filtering error (13) for this case as $\varepsilon_v = \hat{x}_{dv} + \hat{x}_{rv} - x_v = \bar{\varepsilon}_{xv} - \tilde{\varepsilon}_{xv}$, come to the estimate bias $\bar{\varepsilon}_v = \langle\bar{\varepsilon}_{xv} - \tilde{\varepsilon}_{xv}\rangle = \hat{x}_v - x_{dv}$, observing that $\langle\tilde{\varepsilon}_{xv}\rangle = 0$, then account (25), and get

$$\bar{\varepsilon}_v = \frac{A\Delta}{1-e^{-A\Delta}}\left\{y_0\Delta v - \frac{y_0\Delta e^{-A\Delta}(1-e^{-A\Delta v})}{1-e^{-A\Delta}}\right\} - y_0\Delta v. \quad (27)$$

Then recall the aim is to estimate the error at the and of the transient, take $v = N$ for (27), and write

$$\bar{\varepsilon}_N = -y_0\theta[1-W(\theta,\gamma)], \quad (28)$$

where, once $\gamma = 0.1$ and $100 < N$, function

$$W(\theta,\gamma) = \frac{\Delta\ln\gamma}{\theta(\gamma^{\Delta/\theta}-1)^2}\left[1-\gamma^{\frac{\Delta}{\theta}}\frac{\theta+\Delta(1-\gamma)}{\theta}\right] \cong 0.61 \quad (29)$$

Thus, we can write $\bar{\varepsilon}_N \cong 0.39y_0\theta$ for (29) instead of (28), allowing an error of 10% and 5% for $9 \le N$ and $15 \le N$, respectively. It is important to observe that, normally, to get an accurate estimate of the time error, one processes a database for several hours. That means that for the step Δ = 100s and say 5 hours of averaging one deals with N = 180 samples, so, practically, the above approximate formula is accurate enough.

Consider that the error variance $\sigma^2_{\varepsilon v} = \langle(\varepsilon_v - \bar{\varepsilon}_v)^2\rangle$ at the end of the transient is just the variance of a random function (26)

$$\sigma^2_{\varepsilon N} \stackrel{\bullet}{=} \left\langle A^2\Delta^2\sum_{i=0}^{N-1}\sum_{j=0}^{N-1} n_{0i}n_{0j}e^{-A\Delta(N-1-i)}e^{-A\Delta(N-1-j)}\right\rangle, \quad (30)$$

$$= A^2\Delta^2\sum_{i=0}^{N-1}\sum_{j=0}^{N-1}\langle n_{0i}n_{0j}\rangle e^{-A\Delta(N-1-i)}e^{-A\Delta(N-1-j)}$$

$$= A^2\Delta^2\sigma_n^2\sum_{i=0}^{N-1}\sum_{j=0}^{N-1}\delta_{ij}e^{-A\Delta(N-1-i)}e^{-A\Delta(N-1-j)}$$

where $\delta_{ij} = \begin{cases}1 & i=j\\ 0 & i\neq j\end{cases}$ is the Kroneker symbol, which transforms (30) to

$$\sigma^2_{\varepsilon N} = A^2\Delta^2\sigma_n^2\sum_{i=0}^{N-1} e^{-2A\Delta(N-1-i)}. \quad (31)$$

Now note that $\sum_{i=0}^{N-1} e^{-2A\Delta(N-1-i)} = \sum_{i=0}^{N-1} e^{-2A\Delta i}$ and, once the transient is over with $N < i$, then forward tend the upper limit in (3) to infinity, and come through the known limited sum $\sum_{k=0}^{\infty} a^{kx} = \frac{1}{1-a^x}$ to the desired result $\sigma^2_{\varepsilon N} = A^2\Delta^2\sigma_n^2\frac{1}{1-e^{-2A\Delta}}$.

Taking into account (23), we get

$$\sigma^2_{\varepsilon N} = \sigma_n^2\frac{\Delta}{\theta}G^2(\theta,\gamma), \quad (32)$$

where for the above-assumed value $\gamma = 0.1$, the function $G^2(\theta,\gamma) = \frac{\Delta\ln^2\gamma}{\theta(1-\gamma^{2\Delta/\theta})} \cong 1.151$, once $100 < N$. For the same error as in the case of (28), we may take $\sigma^2_{\varepsilon N} \cong 1.151\sigma_n^2\frac{\Delta}{\theta}$.

Finally, based on (28) and (32), define the total error (13) for the Wiener filter as follows

$$\varepsilon^W_{rv} = |y_0|\theta[1-W(\theta,\gamma)] + \sigma_n\sqrt{\frac{\Delta}{\theta}}G(\theta,\gamma). \quad (33)$$

3.3 Three-State Kalman Filter

The three-state Kalman filter is matched with a clock model (3), allowing the following algorithm for (4) and (5) and taking account of (9)—(11) to get estimates (Ref. 13)

$$\hat{\lambda}_v = \mathbf{A}_{v-1}\hat{\lambda}_{v-1} + \mathbf{K}_v(\xi_v - \mathbf{H}_v\mathbf{A}_{v-1}\hat{\lambda}_{v-1}), \quad (34)$$

where the filter gain is

$$\mathbf{K}_v = \tilde{\mathbf{R}}_v\mathbf{H}_v^T(\mathbf{H}_v\tilde{\mathbf{R}}_v\mathbf{H}_v^T + V_v)^{-1}, \quad (35)$$

where $\tilde{\mathbf{R}}_v = \mathbf{A}_{v-1}\mathbf{R}_{v-1}\mathbf{A}_{v-1}^T + \Psi_v$ is a matrix of predicted errors, V_v is defined by (6), and the filtering errors matrix is

$$\mathbf{R}_v = (\mathbf{I} - \mathbf{K}_v\mathbf{H}_v)\tilde{\mathbf{R}}_v, \quad (36)$$

where $\mathbf{I}$ is a unit matrix. For "on-line" operating Kalman filters the transient depends on the time of an error (17) calculation. The procedure inevitable requires solution of the Riccati equation in discrete time (36) that for the three-state model seems like a non-simple task (Ref. 14). This is the reason why we limit here the analysis by a numerical study of the Kalman filter transient time, controlling it by changing the spectral density S_{Dv} in (11), so that since S_{Dv} rises then the transient tends to be shorter, and versa visa.

4. NUMERICAL STUDIES AND ANALYSIS

With equal transient times (15) all three estimates, namely the simple MA (14), Wiener (20), and Kalman (34)—(36) are examined here for the same time error process. First, to demonstrate the filtering effect, we simulate a noisy process (3) with variance σ = 40 ns and for both the stationary part of a deterministic time error ($0 \le t < 25$ hours), in which case $x_0 = y_0 = D = 0$, and non-stationary part ($25 \le t$ hours) with $y_0 = -2\cdot10^{-12} = -7.2$ ns/hour and $D = 0$. Because the time constant is a principle performance factor for a filter, then, to know the trade-off while estimating a time error, we obtain θ = 10 hours for an average filter and take it the same (level $\gamma = 0.1$) for the Wiener and Kalman filters. Figure 1 shows the simulated process with the extracted estimates, and Figure 2 gives correspondent filtering errors (13).

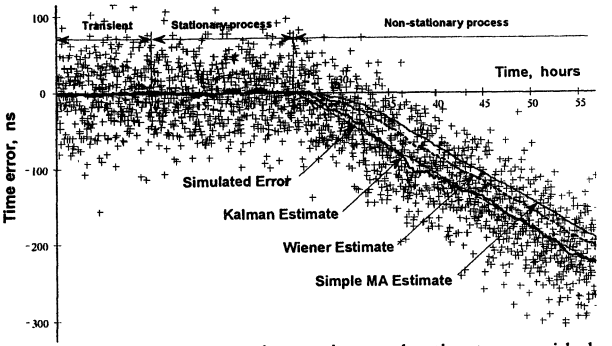

Figure 1. Simulated error, observation, and estimates provided by the simple MA, Wiener, and three-state Kalman filters

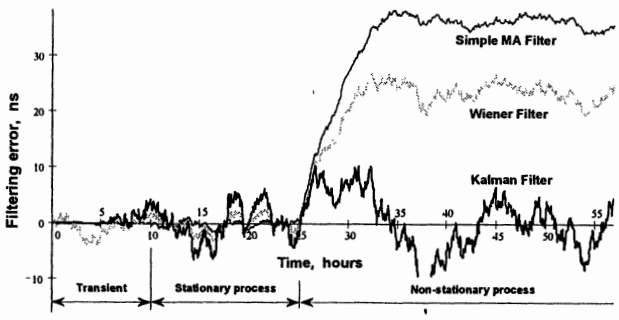

Figure 2. Errors of the simple MA, Wiener, and three-state Kalman filters related to the Figure 1

It follows that for the dynamic range (25 hours $< t$), the Kalman approach yields the smallest error, the Wiener is less accurate, and a simple MA is the worst due to its bias. In contrast, for the stationary range ($t < 25$ hours), a simple MA is the best, the Wiener exhibits a much bigger error, and the Kalman seems to be the worst.

Because of the different filtering errors for the stationary and non-stationary processes with the same θ, we performed another experiment. It follows (Fig. 1 and 2) that a simple MA filter yields the smallest total error for $y_0 < r_{1t} = 1.57\times10^{-13}$, Wiener relation is the most accurate for $r_{1t} = 1.57\times10^{-13} < y_0 < r_{2t} = 4.035\times10^{-13}$, and Kalman is accurate for $r_{2t} = 4.035\times10^{-13} < y_0$. The same filters provide the smallest maximal error for the ranges of $y_0 < r_{1m} = 7.59\times10^{-13}$, $r_{1m} = 7.59\times10^{-13} < y_0 < r_{2m} = 9.22\times10^{-13}$, and $r_{2m} = 9.22\times10^{-13} < y_0$, respectively.

Because of the visible separation in the range, we then estimate coordinates r_{1t}, r_{2t}, r_{1m}, and r_{1m} for various θ and reflect the result in Fig. 3. We also observe that r_{1t} may be found by analytically through an equality of the total errors (19) and (33). This yields

$$r_{1t}^{a} = \sigma_n \frac{\sqrt{\frac{\Delta}{\theta}}G(\theta,\gamma) - \sqrt{\frac{\Delta}{\theta+\Delta}}}{\theta[W(\theta,\gamma)-0.5]}. \qquad (37)$$

Assuming $1 << N$ and $\Delta << \theta$, and based on the above-proved asymptotics $W(\theta,\gamma) \cong 0.61$ and $G^2(\theta,\gamma) \cong 1.151$, we come from (37) to the solution $r_{1t}^{a}\left[\frac{\text{ns}}{\text{s}}\right] \cong 0.673\sigma_n[\text{ns}]\sqrt{\frac{\Delta[\text{s}]}{\theta[\text{s}]^3}}$, which in terms of frequency offset gives

$$r_{1t}^{a}[\times10^{-12}] \cong 3.116\cdot10^{-3}\sigma_n[\text{ns}]\sqrt{\frac{\Delta[\text{s}]}{\theta[\text{hour}]^3}}. \qquad (38)$$

Function (38) separates the field for a simple MA and Wiener filters for an arbitrary σ_n and Δ being dependent on θ so that for the particular case of $\sigma_n = 40$ns and $\Delta = 100s$ we get

$$r_{1t}^{a}[\times10^{-12}] \cong 1.246\cdot\theta[hour]^{-3/2}. \qquad (39)$$

This analytic law $r \sim \theta^{-3/2}$ (38) fills the simulated curves (Fig. 4), allowing the following approximations in each case

$$r_{1t} \cong 2.3\times\theta^{-3/2},\ r_{2t} \cong 6.0\times\theta^{-3/2},$$
$$r_{1m} \cong 11\times\theta^{-3/2},\ r_{1m} \cong 15\times\theta^{-3/2}, \qquad (40)$$

and demonstrating that the curves (Fig. 3) are nothing more then the noisy dependencies $r_i = a_i\theta^{-3/2}$ (40), where $a_i = A_i\sigma_n\sqrt{\Delta}$, A_i is a constant, and $i \equiv 1t,\ 2t,\ 1m,\ 2m$, obtained for the particular case of $\sigma_n = 40$ ns and $\Delta = 100$ s. Based on (38) we easily determine the new coefficients a_i' for (39) for an arbitrary σ_n' and Δ' as follows

$$a_i' = a_i\frac{\sigma_n'\sqrt{\Delta'}}{400}. \qquad (41)$$

Despite the good qualitative correspondence, we examine the Fig. 3 for the visible discrepancy between r_{1t} and r_{1t}^{a}.

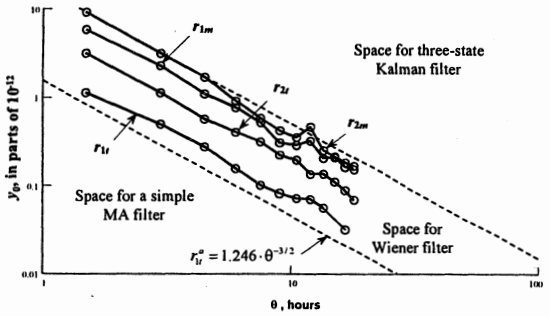

Figure 3. Simulated values of r_{1t}, r_{2t}, r_{1m}, and r_{2m}, their approximating functions, and analytic line r_{1t}^{a} as functions of θ

This is because in our considerations we assumed zero mean for the time error, since a numerical simulation yields its real value coupled with the random sequence length. Properly, Fig. 4 separates the space for all three filters, however, we must observe that this separation is conditional in a sense. Indeed, while interested in the total error, one must be based on an average filter for the space lying lower on the curve r_{1t} or r_{1t}^{a} and on the Kalman filter for the space occurring in upper curve r_{2t}. Yet, since one intends to provide filtering with smallest maximal error, the correspondent ranges for the simple MA and Kalman filters occur lower on the curve r_{1m} and higher on the curve r_{2m}, respectively.

4.1 Example: Time Error of the Rubidium Standard

Measurement of the time error of the rubidium standard had been carried out employing the Motorola GPS timing Oncore UT+ receiver for $\Delta = 100$s during about 30 hours with the initial error of $x_0 \cong 2.1$ ns and offset $y_0 \cong -4.7$ ns/hour $= -1.3\times10^{-12}$ (Ref. 15). To separate the ranges for the filters, substitute y_0 for (39) instead of each r_i and arrive at the following prediction:

- The minimal total error should be obtained by simple MA, the Wiener's and three-state Kalman's filters for θ < 1.455 hours, 1.455 hours < θ < 2.757 hours, and 2.757 hours < θ, respectively.
- The smallest maximal error should be provided by the same filters for θ < 4.129 hours, 4.129 hours < θ < 5.078 hours, and 5.078 hours < θ, respectively.

Then, tune the filters for the θ taken inside the above-determined ranges and estimate the total and maximal errors. Table 1 presents the results and proves that just as it had been forecasted the three-state Kalman filter yields both the smallest total error for 3.0 hours ≤ θ, and maximal error for 4.5 hours ≤ θ. The Wiener filter allows the smallest errors for θ = 2.2 hours and θ = 3.0 hours, respectively, and a simple MA

filter is the most accurate for $\theta \leq 1.0$ hours and $\theta \leq 2.2$ hours, respectively.

Table 1

θ, hours	Total error, ns			Maximal error, ns		
	Simple MA	Wiener	Kalman	Simple MA	Wiener	Kalman
1.0	8.367	8.210	10.83	17.20	16.63	36.36
2.2	9.429	8.225	9.446	14.45	14.84	18.09
3.0	10.45	8.677	8.279	15.54	14.76	16.85
4.5	13.36	10.25	6.622	19.02	14.49	13.81
6.0	16.94	12.38	5.306	26.10	16.20	12.76

In the range of $\theta \leq 1.0$ hours we also looked for the small error of the Wiener filter. This is because of the limited processing sequence available with small average time. Thus, we have proved in this way the above-given methodology generalized by the Fig. 4, except for the case of $\theta = 1.0$ hour.

5. CONCLUSIONS

We have examined the errors of the three filtering approaches, namely a simple MA, Wiener, and Kalman since they are employed to get "on-line" time error estimate in modern time-keeping systems. As a major result we present Fig. 3, which, first, practically answer the question "What are "stationary" and "non-stationary" time error processes?" separating space for those left and right, respectively, by corresponding curves and, most important, allowing the filter selection for the desired θ since y_0, σ_n, and Δ are known.

It seems also important to observe that for the cesium standard and hydrogen maser based clocks the aging effect may be taken as negligible inherently at least for the processing while θ, hence, the time model (3) simplifies for the two states that inevitably require the two-state matched Kalman filter. Such a filter inherently exhibits less filtering variance so that coordinates r_{1m} and r_{2m} tend to be closer to r_{1t} and r_{2t} (Fig. 3), and, as a result, the Wiener filter occupies a narrower range. Thus, it is most appropriate in this case to speak about space separation for a simple MA and the Kalman filter only, taking r_{1t} and r_{2t} as the proper bounds.

Finally, for the maximal error, we conclude that the following filter is proved as the most accurate for the aforementioned case of $\sigma_n = 40ns$ and $\Delta = 100s$, depending on y_0 and θ, namely (Ref. 16),

- The three-state Kalman filter is best for $y_0 \cong 10^{-11}$ (crystal oscillator) with $\theta >$ 1hour,
- A simple MA filter is best for $\theta <$ 5 hours, the Wiener filter is for 5 hours $< \theta <$ 6 hours, and the three-state Kalman filter is for 6 hours $< \theta$, since $y_0 \cong 10^{-12}$ (crystal or rubidium),
- A simple MA filter is best with $\theta <$ 24 hours for $y_0 \leq 10^{-13}$ (cesium or hydrogen).

And, since the other particular cases of σ_n and Δ are of interest, the above-given values of θ are easily recalculated being based on (41). Moreover, the methodology is readily extended to the general case of the model (3), including aging. Evaluate the possible maximal frequency offset of your oscillator for the given θ and follow the example.

6. REFERENCES

1. N. Wiener. Extrapolation, Interpolation, and Smoothing of Stationary Time Series, *John Wiley & Sons*, New York, 1949.
2. R. E. Kalman, "A New Approach to Linear Filtering and Prediction Problems," *Trans. ASME, Ser.D., J. Basic Engineering*, vol.82, pp.35-45, 1960.
3. Handbook for Digital Signal Processing/ Edited by S.K. Mitra and J.F. Kaiser, *John Wiley & Sons*, 1993, 1268p.
4. Y. C. Chan, J. C. Camparo, and R. P. Frueholz, "Space-segment Timekeeping for Next Generation Milsatcom", *Proc. of 31st Precise Time and Time Interval Syst. And Appl. Meeting*, pp.121-132, 1999.
5. C. Griffith, S. Peck, and P. Diamond, "WAAS Network Time Performance Using WRS Data", *Proc. of 31st Precise Time and Time Interval Syst. And Appl. Meeting*, pp.161-172, 1999.
6. P. A. Koppang and D. N. Matsakis, "New Steering Strategies for the USNO Master Clocks", *Proc. of 31st Precise Time and Time Interval Syst. And Appl. Meeting*, pp.277-284, 1999.
7. M. S. Grewal, W. Brown, *et. al.*, "Geo Uplink Subsystem (GUS) Clock Steering Algorithms Performance, Validation, and Test Results", *Proc. of 31st Precise Time and Time Interval Syst. And Appl. Meeting*, pp.173-180, 1999.
8. P. Fenton, E. Powers, *et. al.*, "Time Transfer Using WAAS: An Initial Attepmt", *Proc. of 31st Precise Time and Time Interval Syst. And Appl. Meeting*, pp.191-202, 1999.
9. G.810. Definitions and terminology for synchronization networks, ITU-T, Geneva, Aug 1996.
10. O. E. Rudnev, Yu. S. Shmaliy, *et al.* "Kalman filtering of a frequency instability based on Motorola Oncore UT GPS Timing signals," *Proc. of 13th Eur. Freq. Time Forum and IEEE 1999 Freq. Contr. Symp.*, pp.251-254, 1999.
11. D.B. Leeson, "A Simple Model of Feedback Oscillator Noise Spectrum," *Proc. IEEE*, vol.54, no.2, pp.329-330, 1966.
12. H.L. Van Trees. Detection, Estimation and Modulation Theory, Part I, *Wiley*, New York, 1968.
13. Yu.S. Shmaliy, A.V. Marienko, and O.V. Savchuk. "GPS-based optimal Kalman estimation of time error, frequency, and aging", *Proc. of 31st Precise Time and Time Interval Syst. And Appl. Meeting*, pp.431-440, 1999.
14. R.G. Brown, P.Y.C. Hwang. Introduction to Random Signals and Applied Kalman Filtering, *John Wiley & Sons*, 1997, 484p.
15. Yu. Shmaliy, A. Marienko, *et. al.*, "GPS-based time error estimates provided by smoothing, Wiener, and Kalman filters: A comparative study," *Proc. of 32st Precise Time and Time Interval Syst. And Appl. Meeting*, 2000, (to be published).
16. Yu. Shmaliy, A. Marienko, *et. al.*, "Average, Wiener, and Kalman Estimates of a Time Error: A Comparative Study," *IEEE Trans. on UFFC* (under revision).

A PERFORMANCE COMPARISON BETWEEN COMMERCIAL CAESIUM AND H-MASER CLOCKS FOR VLBI MEASUREMENTS

Pekka Eskelinen and Pekka Sjöman
Helsinki University of Technology, FINLAND

1. ABSTRACT

An ensemble of three GPS receivers, one hydrogen maser and one high stability caesium unit has been evaluated in terms of mutual timing discrepancies for 2200 hours. The H-maser had a relative frequency drift of 6.7E-15/d and 30 ns fluctuations composed of several non-periodic and periodic terms the clearest showing time constants of 24 and 140 hours. Voltages, humidity or barometric presssure did not correlate with the H-maser behaviour, the most notable weaknesses of which were the drift and the random timing errors. Discrepancies traced down to e.g. room temperature were around 1-2 ns. In the Cs unit indications of non-repeatable poor synthesizer performance were seen. After a frequency steering of -55E-15 the synthesizer showed an overshoot of 60 ns which settled down by itself in 600 hours but left an average bias of 20 ns.

Keywords: atomic clocks, time&frequency measurements, hydrogen masers

2. INTRODUCTION

Due to the importance of timing for the astronomical measurements at Helsinki University of Technology, many attempts have been made to define the uncertainty of the installed hydrogen maser clock, see eg. [1] and [2]. As VLBI astronomy requires repeated synchronizing actions, e.g. once per week, between globally separated sites, the clocks are in less favourable use than in conventional T&F centers and the internal control loops etc. work near their extremes and we thus might get valuable information for other users as well. When a transportable high performance Cs clock came available and as the laboratory's maser was refurbished, a new test was considered relevant. The arrangement included the three local GPS receivers as well. As a background [3], [4] and particularly [5] were used. About 1000 hours were allowed for the caesium clock to stabilize itself into the new environment.

3. KEY OBSERVATIONS

During the total 2200 hours of comparison, the H-maser had a relative frequency drift of 6.7E-15/d which exceeds by one decade the reported value for similar units [5]. This is illustrated in Fig. 1 where the intentional corrective adjustment on the hydrogen maser is also marked at 1420 hours.

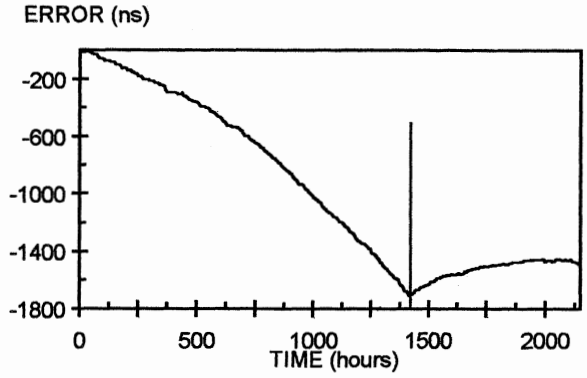

Fig. 1. The difference between the caesium clock and the H-maser shows a relative frequency drift of 6.7E-15 / d. A corrective adjustment to the maser was attempted at 1420 hours.

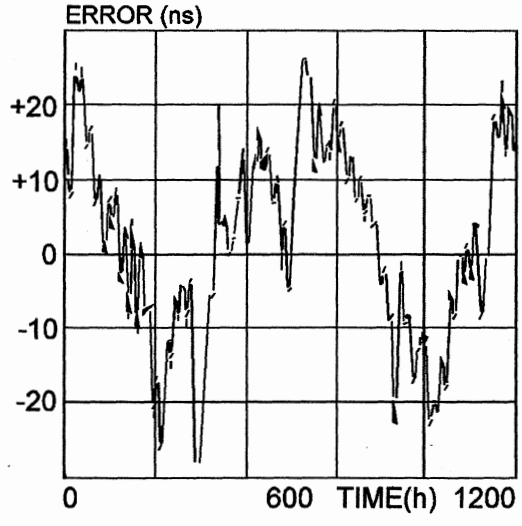

Fig. 2. After removing the linear frequency drift we see the fluctuations in the comparison between the hydrogen maser and the caesium clock to be about 30 ns peak-to-peak. The longest time constant seems to be 140 hours.

The action included a removal of the accumulated timing offset plus a frequency tuning of 1 mHz. As was anticipated, the tuning was not succesful. Instead, after about 700 hours, the maser had gained the same

relative frequency offset. For a closer look, Fig. 2 shows the same recording but without timing bias and drift. Here we notice a roughly 30 ns fluctuation composed of several periodic and non-periodic terms.

From 500 hours on the GPS data and caesium agree indicating a timing error in the hydrogen maser output. This can be seen in Fig. 3 where one of the available GPS clocks (averaged over 1000 seconds) is compared with the hydrogen maser 1 PPS output.

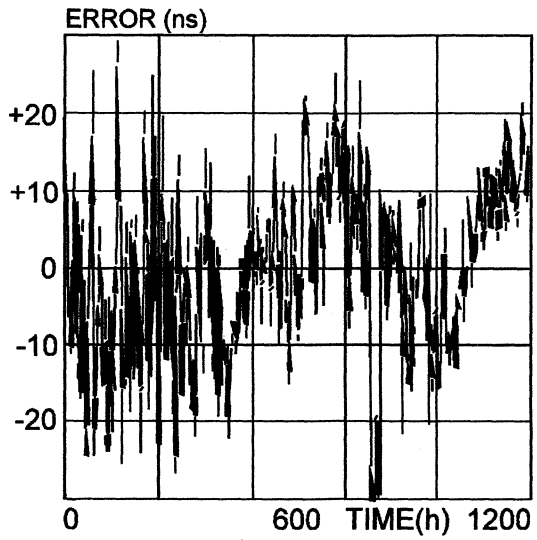

Fig. 3. Although very noisy, this comparison of GPS receiver output to the hydrogen maser 1 PPS signal verifies the fault to be in the maser - see especially the bend around 600 hours.

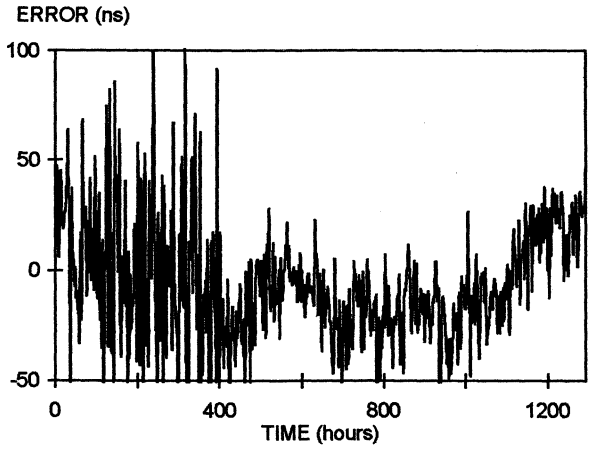

Fig. 4. The simultaneous GPS measurement shows the noise in the receiver 1 PPS output. S/A was turned of by the US DoD at 400 hours.

Commercial GPS receivers are still, without S/A, hardly suitable for judgements below 100 ns unless several hundreds of hours of measuring time is available, which was our case this time. Fig. 4. illustrates how the three local GPS receivers (without averaging) felt the removal of the S/A degradation on the 1st of May 2000.The clearest periodic terms of the hydrogen maser 1 PPS output have time constants of 24 and 140 hours. Two FFT results are shown in Fig. 5 and Fig. 6. When the short term noise is missing, which is the case when comparing the two local atomic clocks in Fig. 5, we clearly see the dominating role of th 24 hour cycle. However, the time functions of temperature, voltages, humidity or barometric presssure, opposed to [6], do not correlate with the H-maser behaviour, the most notable weaknesses of which are the drift and the random timing errors. In Fig. 6 we use GPS outptu as the reference just to show that the 24 hour term still is there, but we also notice a lot of spurious effects, part of which were found to come from the GPS antenna cabling.

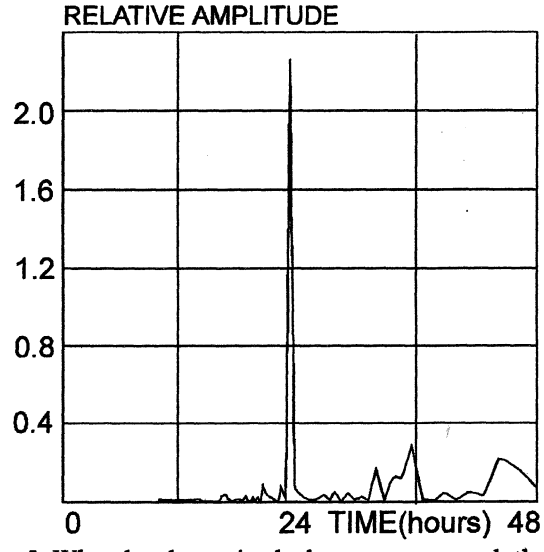

Fig. 5. When local atomic clocks were compared, the FFT reveals only the 24 hour cycle.

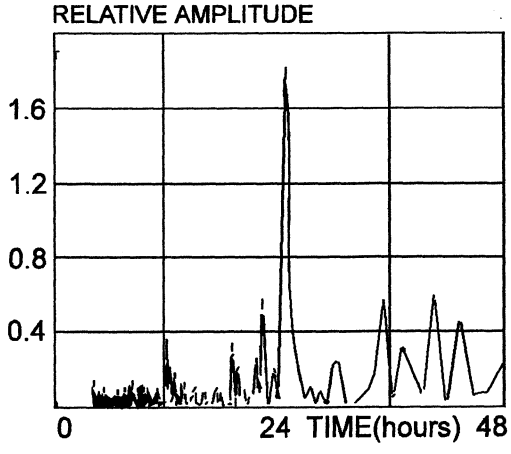

Fig. 6. The short term noise content of the GPS output is naturally visible in this FFT result between GPS and the local hydrogen maser, but we clearly observe also the same 24 hour term as in Fig. 5 plus a number of long term spurious signals, part of which were caused by the GPS antenna cabling.

The discrepancies within the clock system under test traced down to e.g. room temperature are an order of magnitude smaller, around 1-2 ns, than the remaining ones. The possible contribution of the H-maser 1 pps distribution electronics to the time fluctuations remains to be verified. At 400 hours a 1.2 °C transient caused a momentary 40 ns deviation - but in the Cs unit which also gave indications of non-repeatable poor synthesizer performance. For about 500 hours, after a frequency offset of -55E-15 was introduced as an intentional tuning action, the synthesizer showed a control system overshoot of 60 ns which settled down by itself but left an average bias of 20 ns for the rest of a second 7000 hour test. This is shown in Fig. 7.

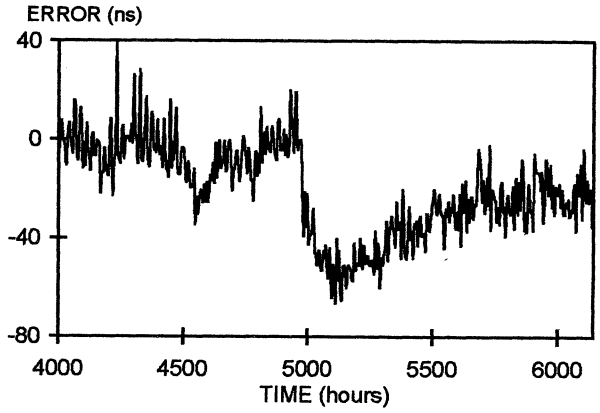

Fig. 7. It seems that the internal synthesizer which is intended for frequency steering does have an overshoot problem at 4950 hours, when a frequency correction was attempted.

4. CONCLUSIONS

Based on our measurements, it looks very probable that the local hydrogen maser is not working within its specifications concerning frequency drift. The 24 hour cycle in its 1 PPS output, having a maximum excursion of about 30 ns, could be a problem in the internal servo system, but a certain contribution may come from the associated distribution amplifier itself. Some concerns have risen also against the hydrogen supply valve. However, the 140 hour period stays totally unexplained.

The well-known high performance caesium clock did not behave without remarks either. First of all, the required warm-up time to metrology-grade comparisons is at least 1000 hours, possibly 1500 hours. An annoying feature is in the frequency steering synthesizer, which seems to produce an overshoot to timing as well when a frequency correction is applied. Finally, according to general experience with electronic instrumentation, we consider the surface temperature of the caesium unit to be relatively high if a long lifetime for its interior is anticipated.

Although highly desired, the improvement of the transmitted GPS signal did not solve the case of short term timing comparisons if the choice of receiver is arbitrary. Straight-forward measurements must still be follow the ca. 100 ns limit, if a high level of confidence is to be maintained.

5. REFERENCES

[1] Eskelinen P.: Comparison of cesium, H-maser and GPS-based timescales, *Proc. 11th European Frequency and Time Forum*, Neuchatel 1997, 477-480

[2] Eskelinen P. and Sjoman P.: A short performance evaluation of the Metsähovi clock arrangement for VLBI measurements, Proc. URSI XXV Convention on Radio Science, Helsinki 2000, 60-61

[3] Weiss M. and Parker T.: Effects of Antenna Cables on GPS Timing Receivers, *Proc. 1999 Joint Meeting of The European Frequency and Time Forum*, Besancon, 259-262

[4] Eskelinen P.: Observations on Stability Measurements of Atomic Clocks, *Proc. 1999 Joint Meeting of The European Frequency and Time Forum*, Besancon, 186-189

[5] Parker T.: Hydrogen Maser Ensemble Performance and Characterization of Frequency Standards, *Proc. 1999 Joint Meeting of EFTF and FCS*, Besancon, 173-177

[6] Dragonette R.: Barometric pressure-induced frequency offsets in hydrogen masers, *Proc. 45th Annual Symposium on Frequency Control*, New York 1991, 586-590

A DSP BASED RADIO SYNCHRONIZED CLOCK

A.Busso**, V. Pettiti*, F. Cordara*, and M. Mascarello*,
* Istituto Elettrotecnico Nazionale "Galileo Ferraris"
Strada delle Cacce, 91 – 10135 Torino, Italy
Tel +39 011 39191, Fax +39 011 346384, E-mail: vpettiti@ien.it
** Politecnico di Torino

1. ABSTRACT

The work presented is an application of a Digital Signal Processor (DSP) used as a precise source of time and frequency synchronized to a national standard by an FM radio tuner receiving a radio coded time signal.

Keywords: coded time signals, digital signal processing, traceability

2. INTRODUCTION

In the USA and in some European countries, are continuously available radio broadcasted time signals like the WWVB by NIST or the DCF77 by PTB (Germany). In Italy, a radio time signal, generated by the Italian primary laboratory IEN, is also provided and transmitted, along with the regular programs, many times a day by the national broadcasting company RAI. This time information is coded using a FSK modulation during the normal AM and FM radio transmissions and, using some suitable decoders, it is possible to have a clock synchronized within one millisecond to UTC (Universal Time Coordinated).

For this feature, it is used by many industrial laboratories to establish a traceability to the Italian national time and frequency standard as required by the ISO9000 quality assurance policies.

Using the computational power of a DSP, it has been implemented a small sized (about one tenth of the actual size) radio clock receiver with the Radio Data System (RDS) feature for searching the best signal available at the receiving site. This device could be used as a local reference for the calibration activities of secondary laboratories.

The description of this system and some experimental results are presented in the followings.

3. THE ITALIAN RADIO TIME CODE (SRC)

The Coded RAI Signal (SRC) is one of the Italian time reference signals generated by the IEN, and transmitted all over Italy by the RAI radio networks. Usually it is transmitted about every hour, for a duration of 8

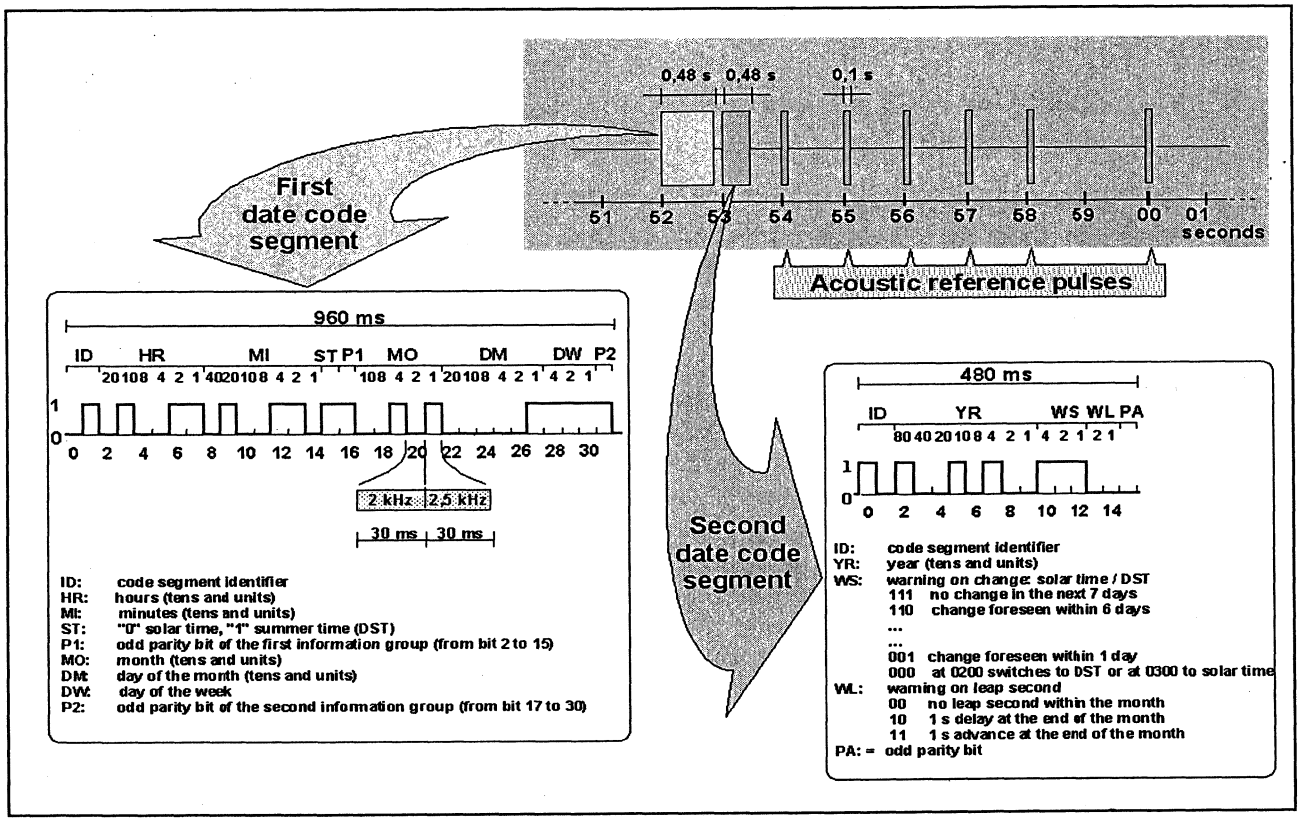

Fig. 1 - SRC format.

seconds, on the 'Radio RAI Uno' channel, and less frequently on the other two channels ('Radio RAI Due' and 'Radio RAI Tre').

The time code, as visible in Fig. 1, starts at second 52 by a coded signal splitted into two segments; the first lasts 960 ms and consists of 32 bits, modulated with a frequency shift keying (FSK), using two tones: a 2kHz for bit 0 and 2,5kHz for bit 1. This signal supplies the month, the day of the month and the week, the hour and the minute and specifies whether the legal or solar time is intended. The second segment, beginning at second 53, lasts 480 ms and consists of 16 bits, having the same specification of above; this signal gives the calendar year and the warning about the introduction of legal/solar time and of a leap second in the UTC time scales. At seconds 54, 55, 56, 57, 58, 00 it follows a sequence 1kHz modulated pips lasting 0,1 second.

The SRC signals are generated by a redundant system of three clocks that are continuously compared through a phase comparator (see Fig. 2) and are connected to a switching unit that checks for any anomaly in the coded signals, and selects those to be sent to the RAI studios in Rome for the broadcasting. The SRC generators are kept synchronized to UTC(IEN) within few microseconds.

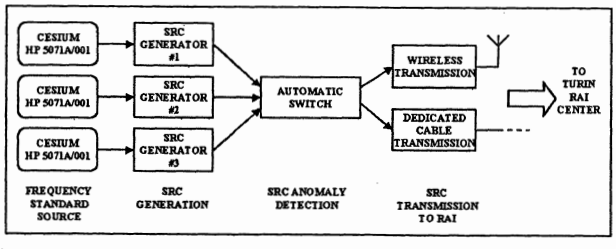

Fig. 2 - Block diagram of the equipments generating the SRC.

These signals are widely used in industries to synchronize remote clocks with a precision of the order of 0,1ms and for disciplining the frequency of a local quartz oscillators at the 10^{-9} level [1], thanks to the availability on the market of dedicated receivers.

4. THE DIGITAL SRC DECODER

The core of the clock is a Texas Instruments DSP TMS320C21. Its main function is to decode the SRC, but also to control the external circuits needed by the device. The DSP is mounted on an evaluation board which includes an analog to digital (A/D) and digital to analog (D/A) 14 bit converter, a parallel interface used to load the program into the RAM of the DSP and a programmable array logic (PAL) device, used as address bus decoder. All the signals generated by this board are also available on four connectors, to allow the connection of an extension board.

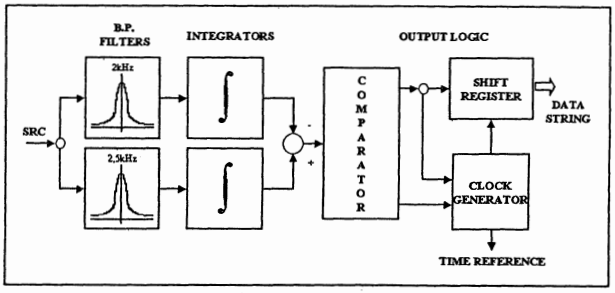

Fig. 3 - SRC demodulator block diagram.

The SRC decoding is obtained using the computation capabilities of the DSP board. The SRC is first sampled and digitized by the A/D converter at a 10kHz frequency, and then processed by the DSP. The block diagram of the decoder can be seen in Fig. 3. It is based on two band-pass filters, the first 2kHz centered, and the second one at 2.5kHz, that are the modulation frequencies used in the SRC to represent a 0 or a 1 respectively. The two filters are followed by two integrators that compute the absolute average value of the filters outputs. These last two signals are independent from the instantaneous amplitude value of the SRC received, and they depend only from the value of the bit received: if the first filter output is bigger than that of the second one, the received bit is a '0', otherwise it is a '1'. This check is performed by the next block (comparator) of the SRC decoder, that also verifies if the bit received is a valid one. This confirmation is obtained by checking if the difference between the amplitudes of the two signals described above, is bigger than a fixed threshold. This means that one and only one of the two modulation signals is present at the decoder input, and that the signal is a FSK modulated one.

The FSK demodulation is completed by a clock generator and a shift-register. The first determines when the bit received can be stored in the shift register, according to the SRC repetition. It also generates the reference pulse used to set the clock time; it is represented by the end of the second data segment of the SRC and corresponds to the second 53,480, so the clock must be set at the date and time received using this value for the second and millisecond synchronization.

5. THE SYNCRONIZED CLOCK

The radio synchronized clock is implemented using the DSP board described above and an extension board, that contains all the peripherals not included in the previous one. This board includes:

- a 16x2 display with standard interface;
- a PLL FM radio tuner programmable by a standard I^2C interface;

- 3 function keys, to allow the user to program the clock and select some parameters;
- all the logic circuits necessary to connect it to the DSP board;
- an analog band-pass filter in the range 1KHZ – 3kHz.

A 10MHz integrated voltage controlled crystal oscillator (VCXO), is mounted on a third board that also includes an output buffer and a voltage regulator, to provide a fixed voltage independent to the main power supply. The control voltage input of the VCXO is driven by the D/A converter through an RC low-pass filter.

The whole system block diagram is shown in Fig. 4.

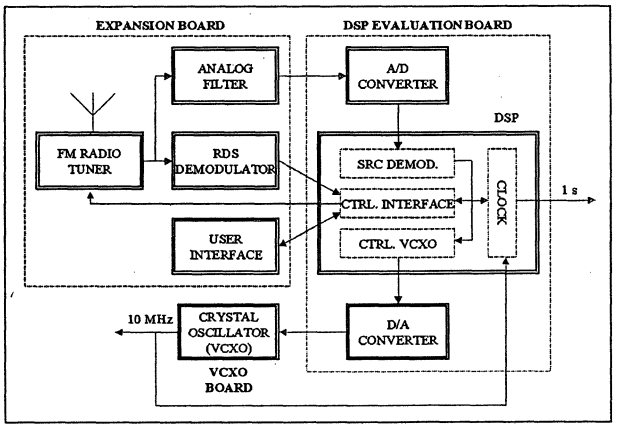

Fig. 4 - Block diagram of the synchronized clock.

The radio signal received by the FM tuner, is first filtered and then digitally converted using a 10kHz sample frequency by the A/D converter, then is processed by the SRC demodulator described above. It is also applied to an embedded RDS demodulator whose output is a bit stream that corresponds to the RDS signal received and it is decoded using the DSP. This RDS capability is useful to tune automatically the receiver on the best locally available FM RAI channel, without the necessity of knowing its broadcasted frequency.

The FM tuner and the user interface (display and keys) are directly driven by the DSP using its data and address buses, through bi-directional buffers for the data bits and through a decoder for the address bits.

The clock is also realized using the capabilities of the DSP. It is controlled by the 10MHz output frequency of the VCXO that is divided to obtain the 1s reference signal and gives seconds, minutes, hours, day, month and year. When the DSP receives and decodes a SRC it is automatically resynchronized. At the same time the DSP measures the difference between the time of the local clock before and after the synchronization, that represent the time offset accumulated, starting from the last synchronization, versus UTC(IEN). This offset is proportional to the frequency deviation of the local VCXO versus UTC (IEN), and it is used compute the correction that must be applied to discipline the VCXO frequency through the D/A converter. The frequency correction is applied every 5 hours: in this way the measurement uncertainties and the syncronization errors, can be reduced to a level that is negligible compared to the time difference accumulated. The available reference output signals of 1s and 10MHz controlled by the system can be used as a reference traceable to UTC(IEN) that can be used for time and frequency measurements purposes.

6. EXPERIMENTAL RESULTS

The scope of this experimental sessions is the determination of the reliability and synchronization capabilities of the SRC decoder, and the uncertainty level traceability of the device to the Italian national time scale UTC(IEN). The block diagram of the used measurement set-up is shown in Fig. 5.

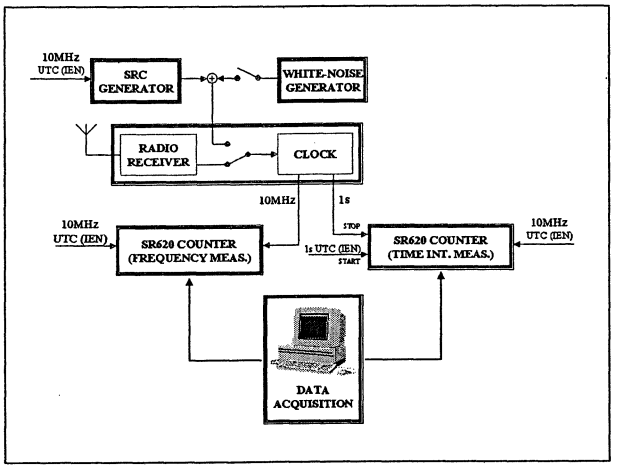

Fig. 5 - Measurement set-up block diagram.

The first set of measurements have been done using a SRC and a white-noise generators to simulate a real received SRC signal with different signal to noise ratios. In this way, it has been determined the minimum S/N ratio allowing a correct recognition of the totality of the SRC signal. It has also been determined the standard uncertainty of the synchronization signal with different S/N ratios.

In Fig. 6 is reported, as a sample, the histogram of the time dispersion of two S/N experimental receiving conditions (>40 dB and 7 dB). It can be seen that the time dispersion, in the case of the best S/N, is very concentrated compared to the other case. It is important to underline that a 20 - 40 dB S/N ratio is very close to the real FM receiving condition, while a 7 dB S/N ratio corresponds to a very bad case.

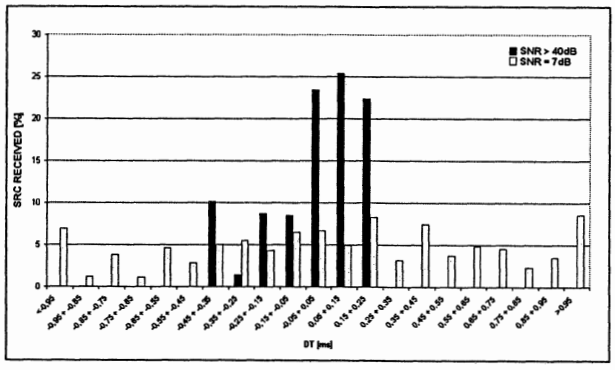

Fig. 6 - SRC synchronization dispersion with different S/N ratios.

The most significant experimental results, obtained simulating different S/N ratios, are resumed in the table below. From the table it can be seen that, with a very bad S/N ratio of 0 dB, the decoder is yet capable of recognize the totality of the signal with an acceptable standard uncertainty.

Table 1

S/N RATIO	% OF SRC DECODED	STANDARD UNCERTAINTY
> 40 dB	100	0,21 ms
7 dB	100	0,66 ms
0 dB	100	1,1 ms
-3.5 dB	90	-

As last check, the device has been tested under normal working conditions, using the radio signals received in the IEN Time and Frequency Laboratory by the FM tuner of the device under test. In this case it has been measured the behavior of both the time difference of the 1s reference output of the clock versus UTC(IEN) and the 10 MHz output frequency supplied by the disciplined VCXO. In Fig. 7 is reported, for the period 17 – 22 January 2001, the time difference between UTC(IEN) and the 1s signal of the disciplined clock, while in Fig. 8 is reported, for the same period, the behavior of the normalized frequency departure of the 10 MHz output. Looking at the results obtained it is possible to evaluate the traceability level obtainable using the reference signals generated by the clock.

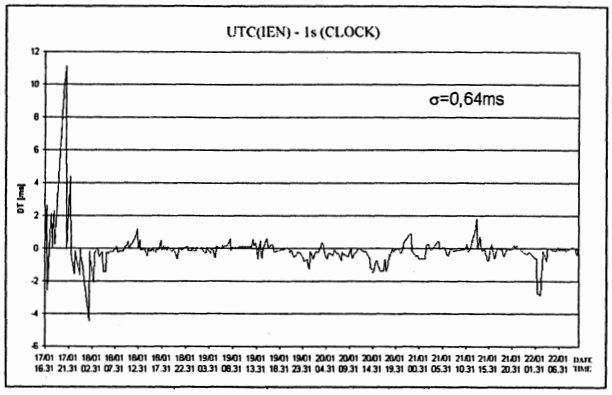

Fig. 7 - Difference of UTC(IEN) vs. 1s clock output.

The experimental data reported in Fig. 7 an in Fig. 8 have been collected starting the measurement immediately after having powered the clock; so the first part of the graphs shows the behavior of the system that needs at least 5 hours before applying the first time and frequency correction. Consequently the first results are affected, for about half a day, by the influence of the initial transient before reaching the steady-state. It can be seen, from Fig. 8, that the initial frequency departure is about $1{,}5 \cdot 10^{-6}$ and lowers to a smallest level, after some correction cycles, to reach a steady level with a standard uncertainty of $1{,}9 \cdot 10^{-7}$. Concerning the time offset of Fig. 7, it can be also noticed the effect of the initial transition: the standard uncertainty of the measured delays reaches the level of 0,6 ms after half a day from the beginning of the measurements.

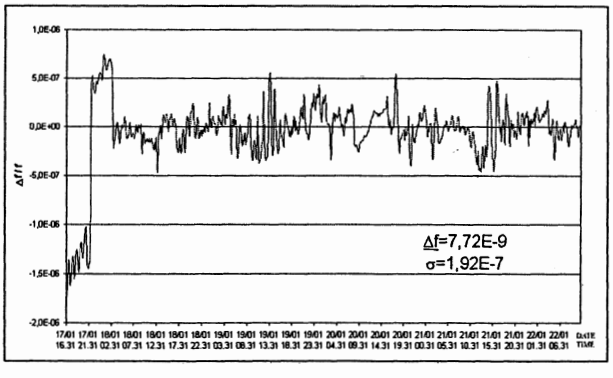

Fig. 8 – Normalized frequency departure of the 10 MHz output.

7. DESCRIPTION OF THE PROTOTYPE

In Fig. 9 is represented the real prototype of the synchronized clock. From the picture it is clearly visible the top extension board over the bottom DSP evaluation board. It is also possible to see the reduced size achievable with the integration of all the main functions in the DSP.

Future improvements will provide a complete digital radio receiver using a more powerful DSP device, the choice of a Temperature Compensated Crystal

Oscillator (TCXO) for better short term behavior, the possibility to increase the number of output functions, such as the possibility to generate programmable time intervals and parallel output of the complete information of time and date. It will also be developed a new frequency correction algorithm to reduce the short and medium term instabilities.

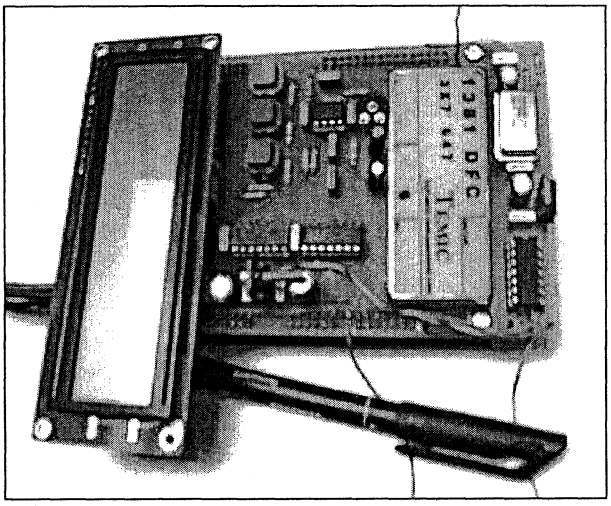

Fig. 9 – Picture of the realized prototype.

8. CONCLUSIONS

The suitability of the use of a DSP to decode the SRC standard time signals, disseminated by IEN as a national reference of time for Italy has been demonstrated.

A synchronized clock based on this principle has been set-up and tested in the IEN Time and Frequency Laboratory versus the reference time scale UTC(IEN) especially as regards to its capabilities in providing a reliable traceability to the national time and frequency standard.

The experimental results has demonstrated that such a device can give a traceability to UTC(IEN) at a level below one millisecond for time and of the order of 10^{-7} for frequency.

Finally, it can be noticed that this device, characterized also by its small size, reduced price and goods general behavior, allows the realization of a time and frequency traceability system, utilizable by secondary laboratory in Italy

9 REFERENCES

[1] F.Cordara, V.Pettiti and P. De Giorgi "Time and Frequency traceability sources in the Italian Calibration Service" Proceedings of the 8th EFTF, 9-11 March 1994, Weihenstefan, Germany.

[2] F.Cordara, V.Pettiti and P.Tavella "IEN Time and Frequency metrological activity and support to user needs" 28th annual precise time Interval application and planning meeting, 3-5 December 1996, Reston, USA.

[3] Texas Instruments "TMS320C3X User's Guide" Texas Instruments Incorporated, USA, 1997.

[4] Texas Instruments "TMS320C3X DSP Starter Kit User's Guide" Texas Instruments Incorporated, USA, 1996.

[5] CENELEC "Specification of the radio data system (RDS)" Comité Européen de Normalisation Electrotechnique, Belgique, 1992.

ESTABLISHMENT OF INTERNET TIME SERVERS IN SWEDEN

Kenneth Jaldehag[1], Jan Johansson[1], Göran Lundqvist[1], Carsten Rieck[1], Håkan Nilsson[1], Peter Löthberg[2], and Hans Nästèn[3]

[1]SP Swedish National Testing and Research Institute, Box 857, S-501 15 Borås, Sweden
[2]Stupi AB, Box 9129, S-102 72, Stockholm, Sweden
[3]Everyware Mikrodata AB, Pålsundsgatan 3B, S-117 31, Stockholm, Sweden

ABSTRACT

Several servers for time synchronisation via the Internet using the Network Time Protocol (NTP) have been established in Sweden. The time servers are traceable to the Swedish national time scale UTC(SP) which is based on caesium clocks. This paper describes the establishment of the servers at the time and frequency laboratory of SP, and at present and future Internet exchange points in Sweden. The time servers at SP are directly synchronised to UTC(SP), via serial ports or a specially designed ISA PPS-card. The time servers at Internet exchange points are synchronised to a set of four rubidium frequency standards, which are traceable to UTC(SP) via GPS common view observations. We present typical synchronisation stabilities and estimate the time accuracy by comparing the time servers relative to each other. The results show synchronisation stabilities in the order of microseconds or less, and time accuracies of about 100 μs.

KEYWORDS: Internet time synchronisation, Network Time Protocol, NTP, Atomic clocks, GPS common view

1. INTRODUCTION

SP Swedish National Testing and Research Institute, Borås, Sweden is the national reference laboratory for time and frequency in Sweden. This implies the assurance of measurement units in Sweden and their traceability or connection to the SI system. The objectives of the laboratory are to keep competence and resources for the measurement units of time, time interval, and frequency in Sweden, to maintain a national time scale, UTC(SP), traceable to the international agreed-upon official time scale UTC (Coordinated Universal Time), and to support and supply the Swedish industry and general public with accurate references of time and frequency.

Using the facilities of the time and frequency laboratory, the Swedish government has given SP the objectives of developing a system of Internet time servers to be established at Swedish Internet exchange points, and, during operation, monitor and maintain the accuracy and functionality of the time servers. Included in this is the important objective that the time servers should be traceable to UTC(SP).

The establishment of the national nodes for exchange of Internet traffic has been planned by Netnod Internet exchange i Sverige AB together with Swedish Internet Service Providers organisation, and Swedish network user's society. The purpose of the national exchange points is to obtain high reliability in the central and common parts of Internet in Sweden. The Internet exchange points are maintained by Netnod AB, and used for exchange traffic between different Internet Service Providers in Sweden. Exchange points are last resort for traffic exchange between providers, but a primary location for common recourses, such as domain name servers, time servers, whois-servers and index-servers (for more information about the Internet exchange points in Sweden, see http://www.netnod.se). Presently (March 2001), three exchange points are established and at least one more is planned.

This paper describes the establishment of national time servers at SP and at the Internet exchange points in Sweden. The paper includes a technical overview of different synchronisation methods and their typical performance characteristics. First, we describe the time servers located at time laboratory of SP, which have a direct connection to UTC(SP). Further, the time servers at the Internet exchange points are described, including the rubidium atomic clock system used as synchronisation source.

2. TIME KEEPING VIA THE INTERNET

The most established technique to obtain computer time synchronisation via the Internet, is the use of the Network Time Protocol (NTP) (Ref 1, see also http://www.ntp.org). The synchronisation accuracy range from about 1 ms within local area networks to several tens of milliseconds on a global scale. NTP is designed to work in a large, diverse Internet system. The best accuracy is normally obtained when the time server is located as close as possible, in terms of network delay and latency, to the inquiring clients. The main issues for good stability are, however, low network jitter and symmetric paths.

Today, there exist more than 200 primary time servers synchronised to UTC in the world, and several thousand hosts and gateways that directly or indirectly synchronise their clocks via NTP. The most common source of UTC is the Global Positioning System (GPS), see e.g. Ref 2, which gives time to within 1 μs relative to UTC. Other common UTC sources are long-wave radio transmitters with varying accuracy and stability. One disadvantage with these radio transmitters, as well as with GPS, are that they are out of control by the users, and may be subject to changes without previous notice to the users. Other time sources are of course local time scales based on one or several atomic frequency standards.

Primary time servers are given the stratum number 1. Servers or clients synchronised to stratum 1 servers become stratum 2 servers, and so on. A server and a client can operate in three different NTP modes: procedure-call, multicast, and symmetric mode. In the procedure-call mode, the server announces its willingness to provide synchronisation, but not to be synchronised itself. Such a server is a primary server that synchronises its clock to a UTC source. The client on the other hand announces its willingness to be synchronised, but usually not to provide synchronisation. The active communication between the client and the server makes it possible to estimate the time- and frequency offset between their clocks and also to estimate and correct for the network path delay.

In the multicast mode, the server sends periodic NTP broadcasts. The client receives these and determines the time offset on the basis of an assumed delay. The major difference between this mode and the procedure-call mode is that the path delay cannot be estimated momentarily. Instead, the path delay has to be estimated, if needed, in advance. The multicast

mode is mainly intended for synchronisation within local area networks, which implies short distances, constant and predictable delays, and symmetric paths.

In the symmetric mode, a server announces its willingness to provide synchronisation, but also its willingness to be synchronised itself, if necessary. This mode is normally used when primary servers need a back-up if the UTC source fails.

The NTP software distribution supports the use of redundant time servers. This means that a client has the possibility to, after outlier detection and different combining techniques, choose the most trustable server or combination of servers among those inquired. Redundant time servers are especially important for time sensitive applications involving economic transactions or legal issues. These applications would also gain in reliability if a set of primary time servers were available in the close vicinity (say within a country or region).

3. INTERNET TIME SERVERS AT SP

Presently, there are six time servers established in the time and frequency laboratory of SP, see Table 1. The servers called Fur1 and Fur2 are used for the national speaking clock system, but use the NTP software distribution for the time synchronisation. They are included here for comparison purposes only. All servers are synchronised to UTC(SP) in two different ways: (1) via a time code generator (TCG) and (2) via 1-second-pulses (1-pps). The output from the TCGs is a stream of ASCII-characters every second containing date information. These characters are read by the time servers via a serial port. To synchronise the server clock to the TCG, a reference clock driver in the NTP software distribution called "PTBACTS" is used. The stability of this synchronisation is abouts 10 ms. As soon as the time server has synchronised to the TCG (within 128 ms), the 1-pps input is used to furnish the stability of the synchronisation down to a few microseconds or less. The 1-pps synchronisation is kept as long as the time server is synchronised to the TCG as well.

The 1-pps synchronisation has been done in two different ways. For the two servers running xntp3.5-93 (Spntp1 and Spntp2) and for the two servers Fur1 and Fur2, a gadget box is used. The gadget box, which is a slightly modified version of the one available via http://www.ntp.org, converts the 1-pps TTL-level pulses to RS232-level pulses. These pulses are then read by the time servers via a serial port. The NTP software distribution supports this through the reference clock driver called "ATOM".

Figures 1 and 2 show, for a typical day, the time- and frequency offsets of Spntp1 and Spntp2 relative to the external 1-pps clock, i.e., UTC(SP). This information is extracted from log-files that the NTP software distribution creates. The data sample rate is 64 s. As seen in the figures, the stability of the time offset is similar for the two servers, and within a few microseconds. In the long term, the frequency offset is much more stable for Spntp1, shown in Figure 1, than for Spntp2, shown in Figure 2. (Even if it is not an optimum estimate for frequency stability, the standard deviation (std) for the frequency offset is given in these and following figures for comparison purposes.) It is apparent that the quartz crystal in the Linux 486-processor PC has a larger frequency- offset and drift than the one in the Digital Alpha server. On the other hand, as mentioned above, the stability of the time offset is similar, which implies that the NTP software distribution handles the large frequency offset very well.

Figure 3 shows, for a typical day, the time- and frequency offset of the Fur1 server (the Fur2 server has similar characteristics). This server is using the ntp4 distribution, which supports kernel modification for nanosecond resolution, and, accordingly, the standard deviation of the time offset is

Table 1: Summary of time servers at SP

Server name	Spntp1	Spntp2	Fur1* and Fur 2*	Ntp1 and Ntp2
Type	Digital Alpha Server 800	PC 486-processor	IBM Netfinity 5000	PC Pentium III
OP	Digital Unix 4.0B	SUSE Linux 2.0.35	Redhat Linux 2.2.12-20	FreeBSD 3.4
NTP version	xntp3.5-93	xntp3.5-93	ntp4.0.99	ntp4.0.90
Date info.	TCG	TCG	TCG	TCG
1-pps	Gadget box	Gadget box	Gadget box	PPS-card

* These servers are used for the national speaking clock system and are not available via the Internet. They are included here for comparison purposes only

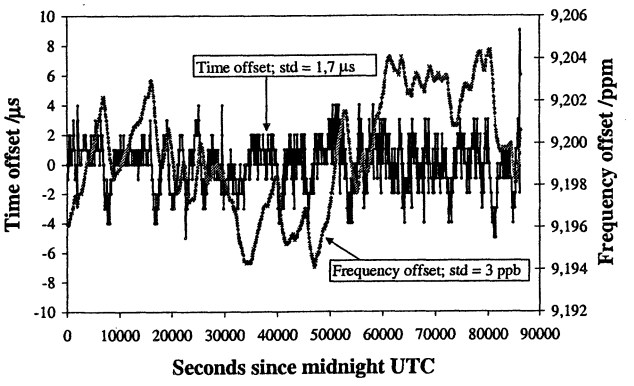

Figure 1: Time- and frequency offset of time server Spntp1 relative to UTC(SP) as estimated by the NTP software

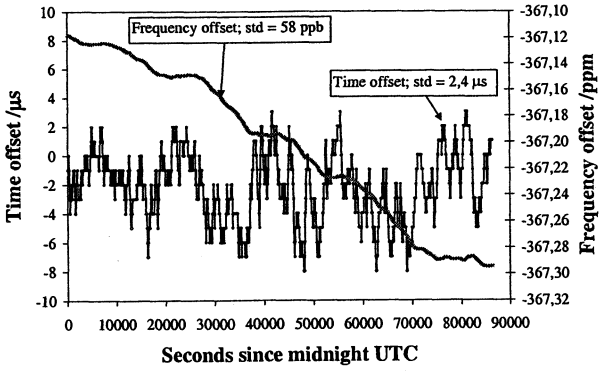

Figure 2: Time- and frequency offset of time server Spntp2 relative to UTC(SP) as estimated by the NTP software

much less, about 25 ns. A constant time offset of about 100 ns, of presently unknown origin, is apparent. The frequency offset is large but relatively stable.

For the servers Ntp1 and Ntp2 we have used a different method for the 1-pps synchronisation. Instead of using the serial port we have designed an ISA PPS-card, see Figure 4, and a reference clock driver for the card. The 1-pps is read by the NTP software distribution in which the reference clock driver has been compiled. The card also contains a quartz crystal and an input for an external 10 MHz reference. By removing the quartz crystal from the server's motherboard and by connecting a cable between the motherboard and the PPS-card, the quartz crystal on the PPS-card is used. One additional option is to connect an external 10 MHz that

automatically replaces the quartz crystal on the PPS-card. The advantage of using an external 10 MHz reference is that frequency changes due to temperature variations can be minimised. For the two servers Ntp1 and Ntp2, the 10 MHz comes from SP caesium clocks.

Figure 5 shows, for a typical day, the time- and frequency offset of the Ntp1 server (the Ntp2 server has similar characteristics). The time offset for these servers has a different character compared to the servers using the gadget box and serial port solution. Instead of a random jitter as in Figure 3, we see a spike-like pattern with several spikes within a couple of hundred nanoseconds and a few of nearly 1 µs. We do not fully understand this behaviour at present time. The frequency offset is much more stable than we have seen for the other servers. This is expected since the server clock frequency is based on a caesium clock.

4. INTERNET TIME SERVERS AT SWEDISH INTERNET EXCHANGE POINTS

Presently (March 2001), three Internet exchange points are established at different locations in the south of Sweden, in Stockholm, Göteborg, and Malmö. One more is planned in the north of Sweden, in Sundsvall. As mentioned in the Introduction, the Swedish government has given SP the objectives of developing a system of time servers to be established at these exchange points. One system has already been installed in Göteborg. The time servers are synchronised to a local clock system of four rubidium frequency standards, which are monitored relative to GPS time, see Figure 6 and Ref 3. The traceability to UTC(SP) is obtained from GPS common-view observations (Ref 4) using single-frequency multi-channel receivers, with an identical GPS receiver at SP. The complete system contains the clock system, two time servers, a control PC, and measurement hardware. The time servers use the PPS-card shown in Figure 4 and are configured in the same way as the time servers Ntp1 and Ntp2, see Table 1, except for the TCG. Instead, to set the date in the time servers to within ±0.5 s, the time servers need to be synchronised at start-up from another time server. The NTP daemon is also configured to inquire time from other servers. This is also needed in order to handle leap seconds. The control PC is a Pentium III machine running Linux.

Following Figure 6, two outputs are available from each rubidium standard, one 10 MHz sinus signal and one 1-pps TTL level signal, the latter via a frequency divider. The 1-pps signals are sequentially (every 6th minute for each rubidium standard) monitored relative to a 1-pps signal from the GPS receiver, using a switch matrix and a time interval counter. This measurement process is controlled from software installed in the local control PC. The software also estimates, using the latest week of data, the time- and frequency offset, the frequency drift, and the stability of each rubidium standard relative to GPS time. The rubidium standard with the presently best stability, estimated as the Allan deviation for τ equals approximately one day, is then selected as the reference "clock" for the time servers, and its 1-pps signal is directed to the PPS-card in the time servers via the switch matrix.

Since the rubidium standards by no means are synchronised to GPS time, other than in software, the 1-pps from the selected rubidium standard will be out of synch. This is handled by a daemon running on the time servers that receives corrections from the control PC. Using these corrections, including time- and frequency offset and frequency drift for the selected rubidium standard relative to GPS time, the daemon updates a microstepper on the PPS-

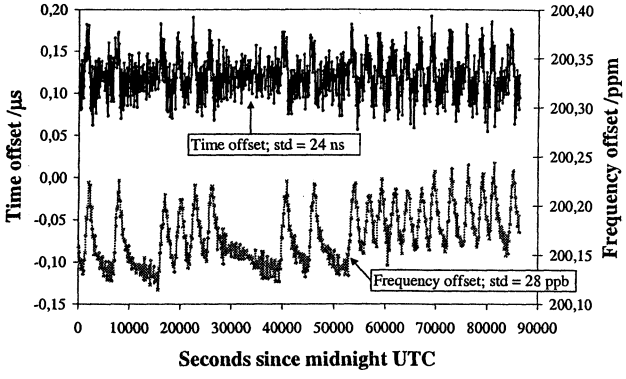

Figure 3:Time- and frequency offset of time server Fur1 relative to UTC(SP) as estimated by the NTP software

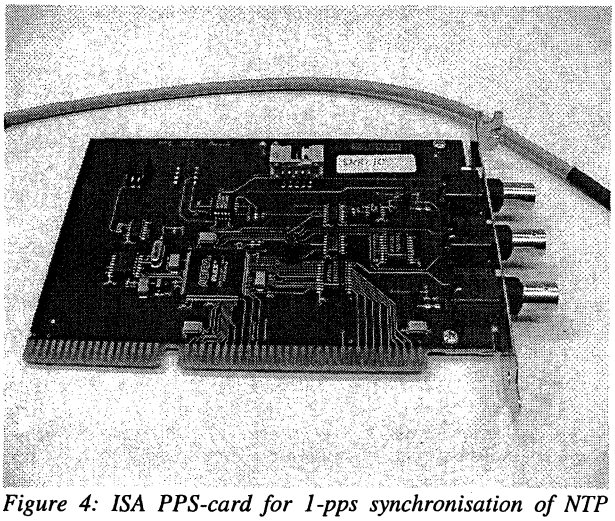

Figure 4: ISA PPS-card for 1-pps synchronisation of NTP time servers. The cable is used to replace the internal quartz crystal with an external 10 MHz reference

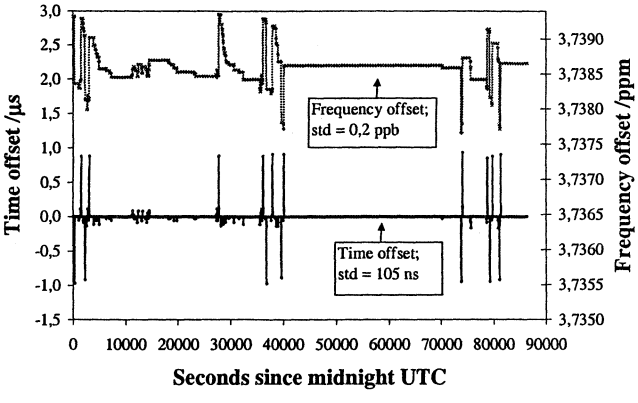

Figure 5: Time- and frequency offset of server Ntp1 relative to UTC(SP) as estimated by the NTP software

card. The corrected signal is then read by the NTP daemon. The microstepper daemon updates the corrected signal based on the frequency offset and drift at specified time intervals. New corrections are sent from the control PC if the reference standard is changed or if the present corrections need to be updated. The communication between the control PC and the time servers uses a SSL (Secure Socket layer) TCP connection via a specified TCP port.

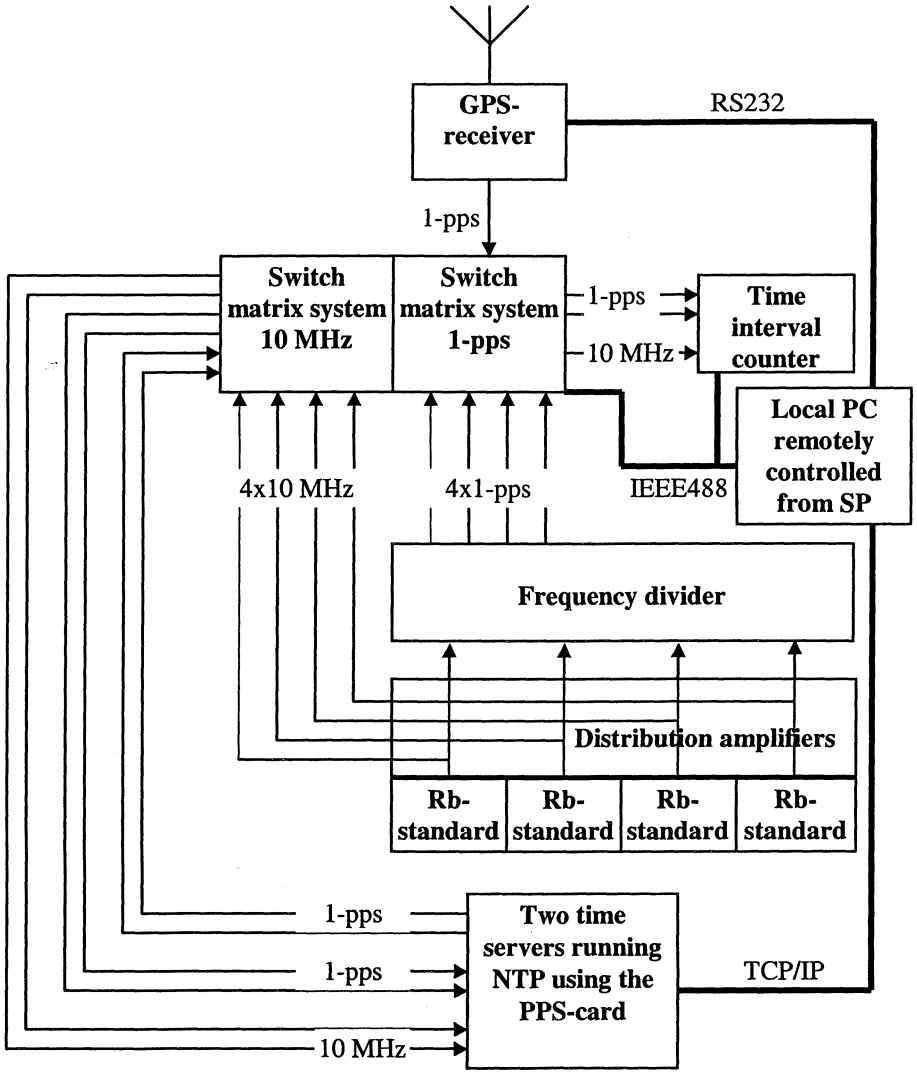

Figure 6: System design of an ensemble of rubidium frequency standards used for the synchronisation of NTP time servers at present and future Internet exchange points in Sweden

The switch matrix for the 10 MHz signal is used to direct the 10 MHz signals to the time interval counter and to the time servers. As mentioned in the previous section, the 10 MHz input to the PPS-card is replacing the internal quartz crystal. Besides, the 10 MHz signal does not need to come from the same rubidium standard as is selected for the 1-pps reference.

Another feature of the time servers is the possibility to reject NTP queries depending on the present NTP synchronisation time offset and dispersion. Presently, the time servers reject NTP queries if the NTP time offset is larger than ±50 μs or if the dispersion is larger than 1 ms. Yet Another feature is a 1-pps output from the PPS-card. This output is an estimate of the time offset in microseconds between the 1-pps input after the microstepper and the time server system time.

Figure 7 shows, for a typical day, the time- and frequency offset for an Internet exchange point time server, herein called Ntp1-node. In comparison with Figure 5, it is apparent that the stability of Ntp1-node is comparable to what is obtained by the use of UTC(SP), i.e., synchronised caesium clocks. The accuracy and traceability of this system relative to UTC and UTC(SP), are dependent on the availability of the GPS signal. However, if the rubidium standards have been characterised long enough time, and by stepping the signal using the microstepper in the PPS-card, the system should be able to keep accurate time well within the general performance of NTP for several weeks, even with the lack of GPS observations. A picture of the system installed at the Internet exchange point in Göteborg is shown in Figure 8.

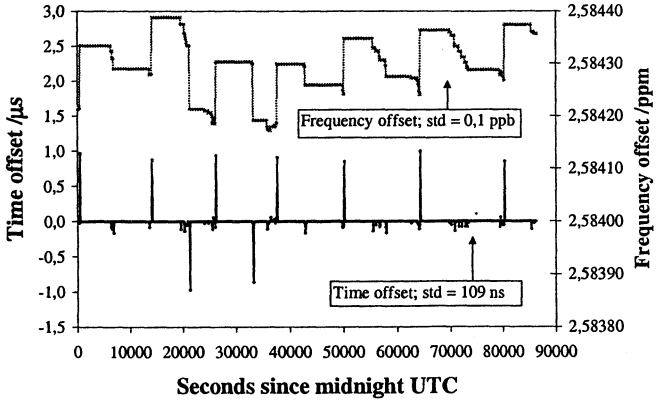

Figure 7: Time- and frequency offset, as estimated by the NTP software, of an Internet exchange point time server, herein called Ntp1-node, relative to the selected rubidium standard after microstepper corrections

6. ACCURACY OF TIME SERVERS IN SWEDEN

We have so far mainly discussed the stability of the time synchronisation of a time server to an external UTC source. To determine the accuracy, or at least the conformity between time servers in Sweden, one has to estimate cable delays, and computer hardware and software delays. Cable delays are normally easy to estimate, but hardware and software delays are difficult. One way to estimate the accuracy of a time server is to compare it with other time servers synchronised to the

same time source. This is possible by configuring one server to inquire time from other servers. In order to do this accurately, it is required that the estimate of the network path delay between the servers is accurate and stable. This in turn requires that the servers must be connected to the same local subnet.

To estimate the accuracy of the servers we have presented in this paper, we configured a test set-up: Ntp1-node was configured (1) to synchronise to the 1-pps and use this as the primary source, and (2) to query time from the time servers Spntp1, Spntp2, Ntp1, Ntp2, and Ntp2-node. The last server is a second Internet exchange point time server. These servers were temporarily connected to the same local subnet during the test, in order to prevent network jitter and asymmetric delays.

Figure 9 shows the result based on 24 hours of data. Each point in the figure represents the median of the total NTP time-offset estimations during the 24 hours. The error bars represent the standard deviation of the data. The offset for Ntp2-node, which is synchronised to the same rubidium standard as Ntp1-node, is less than 2 μs. The offsets for Ntp1 and Ntp2, which are configured in the same way as Ntp1-node, except that they are synchronised directly to UTC(SP), are less than 4 μs. The offsets for Spntp1 and Spntp2 are about -340 and 50 μs, respectively. The different synchronisation methods, 1-pps via a serial port instead of via the PPS-card, may explain these larger offsets. All offsets, excluding the offset for Spntp1, are, however, within the error bars. In addition to the operating systems, the difference between Spntp1 and Spntp2 is the detection of the 1-pps signal via the serial port. On Spntp1, the 1-pps signal is read via the serial data leads, while it is read via the serial data-carrier detect lead on Spntp2. These differences may explain the larger time offset for Spntp1.

To summarise, we claim that our servers are accurate to the millisecond level, and most likely somewhat better. By a careful calibration using the results in Figure 9, an accuracy and conformity of about 100 μs should be possible.

5. CONCLUSIONS AND FUTURE WORK

We have presented and discussed different methods for the synchronisation of server clocks used for time synchronisation via the Internet. The synchronisation stability is in the order of a few microseconds or less. The accuracy of the servers after estimated corrections is believed to be within 100 μs. We have in detail described a system of time servers synchronised to a set of four rubidium frequency standards using a specially designed ISA PPS-card. This system has been installed at the Internet exchange point in Göteborg and will be installed at other Internet exchange points in Sweden.

Future work in this area will include studies of different authentication techniques, multicast distribution of network time, and time server data available from a dedicated homepage. These projects are important for the integrity and traceability of the time servers. We will also continue to work with improvements of the PPS-card.

Acknowledgements

This research was funded by Stiftelsen för Kunskaps- och Kompetensutveckling, Sweden. The time servers at Internet exchange points are funded by Netnod Internet Exchange i Sverige AB.

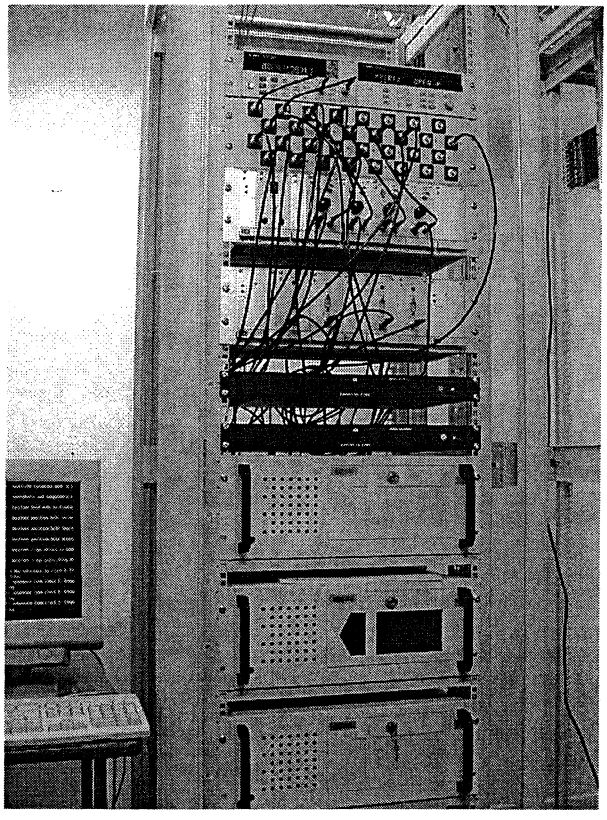

Figure 8: The time server system at the Internet exchange point in Göteborg. This system is located some 60 meters below ground and fibre optics are needed for the data flow and 1-pps from the GPS receiver, which is located above ground close to the antenna

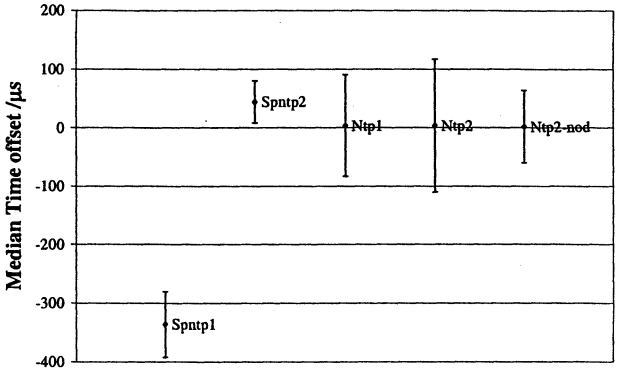

Figure 9: Time offset, based on 24 hours of data, between the time server Ntp1-node and other time servers

References

[1] D. L. Mills, Internet Time Synchronization: The Network Time Protocol. IEEE Trans. on Comm., **vol. 39,** No. 10, pp. 1482-1493, October 1991.

[2] G. Seeber, Satellite Geodesy. Walter de Gruyter & Co., Berlin New York, 1993.

[3] K. Jaldehag and H. Nästèn, A Network Time Protocol (NTP) server synchronised to rubidium atomic clocks: Documentation, 2000. (Available from the author upon request.)

[4] W. Lewandowski and C. Thomas, GPS Time Transfer. Proc. of the IEEE, **vol. 79,** No. 7, pp. 991-1000, July, 1991.

MULTI-FREQUENCIES PRECISE PHASE TIME COMPARATOR

X.Stehlin, P. Rochat
Temex Neuchâtel Time (CH)

Abstract

By means of the conventional instruments, it is difficult, even impossible to measure the frequency and the phase time with a precision of the pico-second in a continuous frequency band of 1 to 35MHz.

Within the Galileo project, TNT has to make an evaluation of the embarked Rubidium atomic clocks as well as the Hydrogen Maser. With this intention, a system was developed making it possible to measure the frequency and the phase time with a precision of the pico-second.

The development is based on a heterodyne system with a double frequency conversion using direct digital synthetizer technology to allow measurements in the range of up to 35MHz.
The measurement bandwidth is limited by a separated crystal oscillator based PLL. Two outputs are available : One with ~100KHz bandwidth and a second channel with 1Hz measurement bandwidth only.

The paper includes a description of the system using a block-diagram. The measurement principle is explained and the results are discussed.

1. INTRODUCTION

The role of the time interval comparator in time and frequency metrology is very important as it is perhaps the only measuring instrument in the field. It measures in a direct way, the duration of time interval between two signals. This way, it allows one to determine the stability of one device against a reference.

Time interval comparators are very important components for the most sophisticated time and frequency systems such a GPS, Glonass, etc.
Within the Galileo project, the European Space Agency has undertaken a development program in which the Rubidium atomic clocks and the Space Hydrogen Maser need to be evaluated. That becomes possible by using a phase time comparator which has reported resolution down to pico-second level.

2. SYSTEM DESCRIPTION

The system is designed to make a direct frequency measurement and a time interval measurement to plot the stability of the device using the Allan Deviation.
The system allows one to measure device with a frequency range of 1 to 35MHz. An external reference of 10MHz divided by 1000 is used to make time interval measurement.

Direct frequency measurement is used for programming DDS which divides the device frequency around 10KHz by using two mixers. As the following block-diagram shows, the whole system is based on a heterodyne architecture with a double frequency conversion. The branch of the first DDS is more sensitive to spurious than the second because in the second one, the frequency is divided by 32.

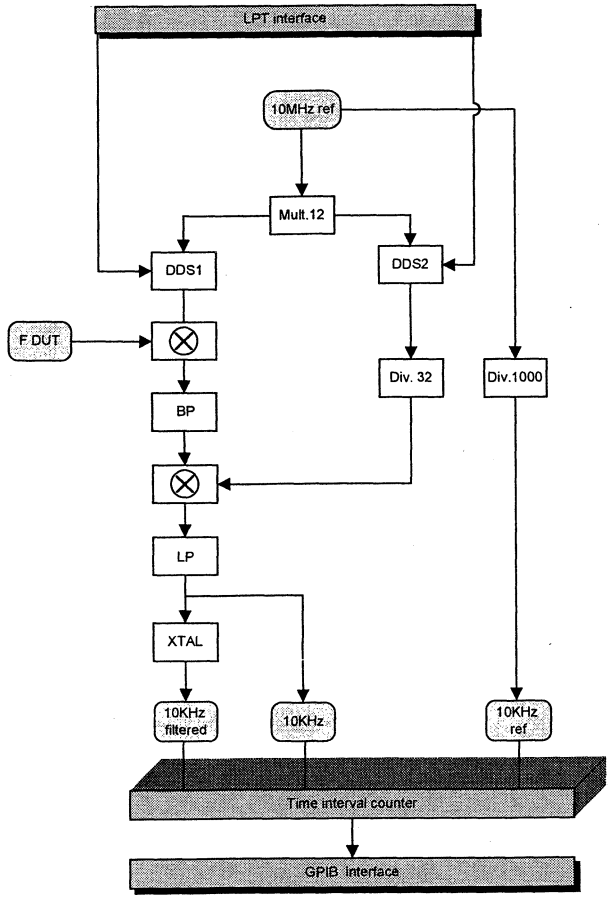

Figure 1: Block-diagram

Two outputs are available: one where a crystal filter based PLL is used to restrict the bandwidth to only 1Hz and a second channel with about several 100KHz bandwidth.

The external counter is controled with an GPIB interface and all the system is piloted with the LPT interface to a software conceived in Visual Basic. Power supply is reached by an external converter (230V~/50Hz to +12V-) through a jack connector.

The whole system is placed into a box which has the Euro dimensions (168x103x42 mm) and is thermally regulated

3. SPECIFICATIONS

The specifications for the phase-time comparator system are the following:

Parameters	Specifications
Input frequency	1 to 35 MHz
Freq. Stability long term @10MHz	$1x10^{-15}$
Freq. Stability short term @10MHz	$1x10^{-12}$ (1/τ)
Operating temperature	10°C-30°C
Mass (without counter and power supply)	~730g

The Frequency Stability Measurement System is able to measure a Passive Hydrogen Maser. After 100s the FSMS is 10 times better than the specifications of the Maser.

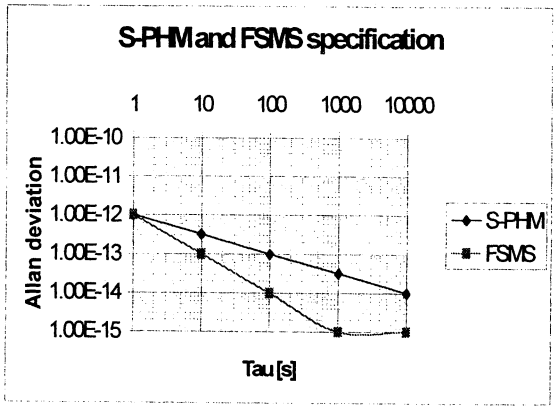

Figure 2: FSMS and S-PHM Specifications

The precise phase-time comparator named FSMS (Frequency Stability Measurement System) is a small package which is compatible with Agilent counters like 53131A or 53132A. Its light weight and its small volume allows the FSMS to be easily transportable.

An another solution is to replace the conventional counter by a PC-card counter to obtain a very comfortable station for stability measurements.

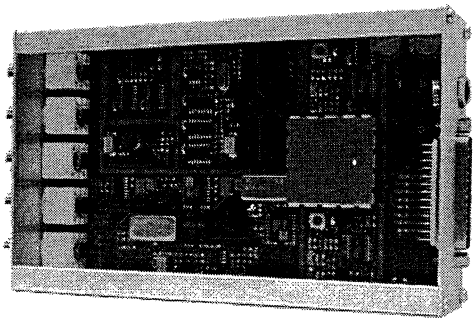

Figure 3: FSMS Engineering model

4. PINCIPLE OF MEASUREMENT AND RESULTS

A clock of 120MHz is used to pilot the DDS. The 10MHz reference is multiplied by 12 through a PLL based on a VCO of 120MHz. The stability of the whole system depends on the characteristics of this VCO. Its phase noise is the following :

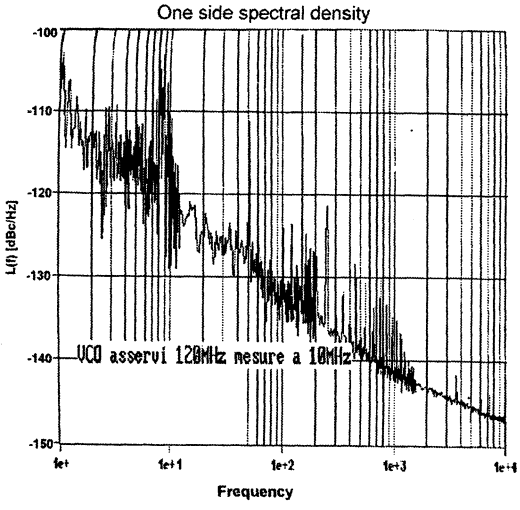

Figure 4: Phase noise VCO-120MHz@10MHz

There are two quantities which completely specify $S_y(f)$ for a particular power low-noise process:

- The slope on a log-log plot for a given range of f;
- The amplitude;

The phase noise diagram of the VCO gives two different slopes:

- Flicker PM (1/f) noise is related to the flicker noise floor of the phase comparator.
- White PM (f^0) noise is broadband phase noise and has little to do with the phase comparator. This noise floor is dependant of the VCO related phase noise level.

It is possible to do the translation from frequency domain to time domain stability

One can pick (arbitrarily) a convenient Fourier freqency f and determine the corresponding values of $S_\Phi(f)$ given by the plot.

$$S_\phi(f) = \frac{\upsilon_0^2}{f^2} S_y(f)$$

$$\upsilon_0 = 10MHz$$

If, f = 10, thus $S_\Phi(10) = 10^{-12}$.

The equation designating flicker PM noise yields:

$$\sigma_y^2(\tau) = \frac{[1.038 + 3\ln(\omega_h \tau)]f}{(2\pi)^2 \tau^2 \upsilon_0^2} S_\phi(f)$$

Thus we can solve the different tau, assuming:

$$f_h = 10^5$$

$$\sigma_y(1) = \sqrt{\frac{[1.038 + 3\ln(2\pi \cdot 10^5)]10}{(2\pi)^2 1^2 (10^7)^2} 1 \cdot 10^{-12}} = 3.2 \cdot 10^{-13}$$

$$\sigma_y(10) = \sqrt{\frac{[1.038 + 3\ln(2\pi \cdot 10^{15} \cdot 10)]10}{(2\pi)^2 10^2 (10^7)^2} 1 \cdot 10^{-12}} = 3.5 \cdot 10^{-14}$$

$$\sigma_y(100) = \sqrt{\frac{[1.038 + 3\ln(2\pi \cdot 10^{15} \cdot 100)]10}{(2\pi)^2 100^2 (10^7)^2} 1 \cdot 10^{-12}} = 3.8 \cdot 10^{-15}$$

$$\sigma_y(1000) = \sqrt{\frac{[1.038 + 3\ln(2\pi \cdot 10^{15} \cdot 1000)]10}{(2\pi)^2 1000^2 (10^7)^2} 1 \cdot 10^{-12}} = 4 \cdot 10^{-16}$$

The slope is equivalent to ~1/τ.

Again, after a Fourier frequency of 10^4, if f = 10^5, thus $S_\Phi(10^5) = 10^{-15}$.

This time the equation designating white PM yields:

$$\sigma_y^2(\tau) = \frac{3 f_h}{(2\pi)^2 \tau^2 \upsilon_0^2} S_\phi(f)$$

We obtain:

$$\sigma_y(\tau) = \sqrt{\frac{3 \cdot 10^5}{(2\pi)^2 \tau^2 (10^7)^2} 10^{-15}} = 2.75 \cdot 10^{-13} 1/\tau$$

The flicker FM can be estimated less than 10^{-15}. This kind of noise is representated in time domain by a constant (see next figure).

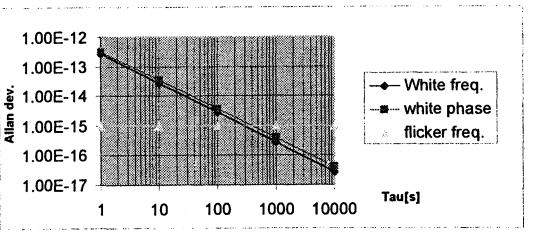

Figure 5: Different noises in time domain

The result time domain characterization is the following:

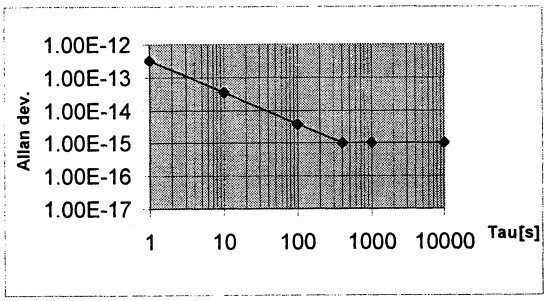

Figure 6: Result of time domain stability

We are able to specify that the results must follow figure 6 if no dead time is introduced. These results are verified with a mesurement. To avoid dead time and the lose of the concordance of phase the method of time interval (of T) between two signals is used

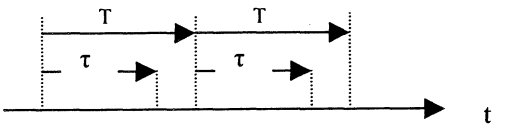

Figure 7: Dead time

If the method of frequency measurement (with an averaging time of τ) is applied, the concordance of phase is not ensured. Statistically a factor of the square root of sample (N) will be introduced and the slope of τ^{-1} is transformed in $\tau^{-½}$.

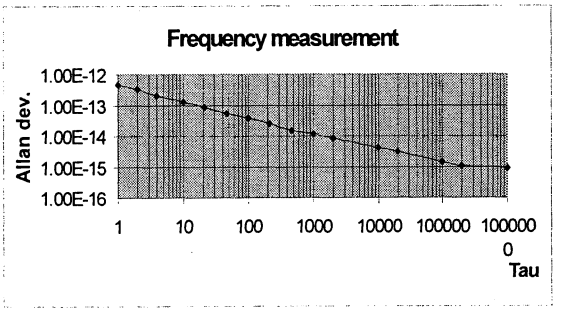

Figure 8: Results with frequency measurement

5. CONCLUSION

This system proposes a solution by using DDS which have sufficient phase noise characteristics. Problems of spurious are eliminated by rejecting them through a narrow band-pass filter.

The advantages with this system are the possibility to measure any frequencies between 1 to 35MHz in a very small package.

The method of time intervalls is more interesting than the frequency measurement method because the slope of $1/\tau$ is obtained, so the noise floor of 10^{-15} is achieved more quickly.

However, the system is still under development in order to obtain the best performances and to achieve an easy software for utilisization.

6. REFERENCES

[1] Characterization of Clocks and Oscillators. NIST Technical Note 1337, D.B. Sulivan, D.W. Allan, D.A. Howe, F.L. Walls.

[2] Frequency Control Symposium. Proc of IEEE International 1997.

[3] Frequency Control Symposium. Proc of IEEE International 1995.

A FAST COMPUTATION APPROACH FOR MAXIMUM TIME INTERVAL ERROR IN TELECOMMUNICATIONS MEASUREMENT

Mingfu Li, Chia-Shu Liao

National Standard Time and Frequency Lab.
Telecommunication Labs., Chunghwa Telecom Co., Ltd.
12, Lane 551, Min-Tsu Road Sec. 5, Yang-Mei, Taoyuan, Taiwan 326, R.O.C.
Tel: +886-3-4245181 Fax:+886-3-4245474
E-Mail: mfli@cht.com.tw

ABSTRACT— **In telecommunications standards, Maximum Time Interval Error (MTIE) is one of the main time domain quantities for characterizing clock stability. However, the direct computation of MTIE, defined in ITU-T Recommendation G.810, tends to be unmanageable when the number of samples becomes large. The aim of this paper is to propose a fast computation approach for MTIE. The approach is based on the recursive algorithm and the computation exactly conforms to the ITU-T G.810 MTIE definition. As compared with the direct computation approach, the time complexity of the proposed approach is reduced by a factor of N, the number of samples. It reveals that the real-time MTIE measurement or monitoring will be feasible by employing the proposed computation approach.**

KEYWORDS—**Maximum Time Interval Error, Clock stability, Jitter, Wander, Network synchronization, Telecommunications measurement.**

1 INTRODUCTION

NETWORK synchronization has played a central role in telecommunications networks since the introduction of digital exchanges [1], [2]. The early digital transport standard is called Plesiochronous Digital Hierarchy (PDH) [3]. Recently, Synchronous Digital Hierarchy (SDH) [4] has been widely deployed and acknowledged as a transmission standard replacing the existing PDH. For the introduction of SDH standard, network synchronization and timing becomes more apparent and challenge.

In digital communication systems, the variations of the significant instants of a digital signal from their ideal position in time are called jitter or wander [5]. Short-term variations which are of frequency larger than or equal to 10 Hz are defined as jitter, while long-term variations which are of frequency less than 10 Hz are defined as wander. Jitter is usually induced in the regenerators or multiplexiers where bit stuffing or pointer justification events can occur, and may increase the bit error rate in the receiving end. Thus, in order to reduce the jitter, many schemes have been proposed, including Stuff Threshold Modulation (STM) [6], jitter attenuator [7], Phase-Lock Loop (PLL) [8] and bit leaking [9] schemes, etc. As to the wander, it usually results from the frequency offset or changes in cable delay due to temperature variation, and can lead to data slips. The data slips can be a severe problem for data services. Hence, the digital switching equipment requires network synchronization to avoid slips in the input elastic store. For guarantee of network synchronization quality, ITU-T has enacted the jitter and wander specifications in [10], [11], [12], [13] for equipment testing and telecommunications measurement.

In telecommunications synchronization standards and measurements, clock stability characterization, jitter and wander are the main concerns. In order to evaluate the synchronization quality, some parameters such as Time Interval Error (TIE), Maximum Time Interval Error (MTIE), Time Deviation (TDEV), Allan Deviation (ADEV), Modified Allan Deviation and Root Mean Square Time Interval Error (TIErms) are defined [5]. In this paper, we will focus our discussion on the MTIE, which is an important parameter for characterizing the wander. In addition, MTIE can characterize frequency offsets and phase transients of a Clock Under Test (CUT). When MTIE is used to characterize high frequency noise, it should be computed from the data collected at the highest possible sampling rate. Consequently, the number of data samples becomes large and direct computation of MTIE will be a troublesome problem. Therefore, efficient alternative computation algorithms or suitable apporaches are required to simplify the computation. In [14], the MTIE measurement using disjointed intervals is suggested. The computational effort is significantly reduced by employing this approach. However, this approach is an approximate estimation of MTIE. The results can be reliable only under certain of measurement conditions and the approach should be carefully employed. Moreover, in [15] a binary decomposition algorithm which calculates MTIE only at observation times $(2^i - 1)\tau_0$ was proposed. In this paper, we will present an exact and fast computation approach for MTIE estimation. The proposed computation technique is more general than the approach in [15]. In other words, the binary decomposition scheme is just a special case of the novel technique presented in this paper. In the following, we will first introduce the formal definition of MTIE, and then suggest an efficient approach for MTIE computation.

The rest of this paper organizes as follows. In Section II, the definition of MTIE will be described. Next, a fast computation approach for MTIE is proposed in Section III. In Section IV, the superiority of the proposed approach is demonstrated in terms of time complexity. Finally, in Section V we make a concise remark.

2 MAXIMUM TIME INTERVAL ERROR (MTIE)

In general, the sine-wave voltage output of a precision oscillator can be modeled as follows.

$$V(t) = V_0 \sin(2\pi f_0 t + \phi(t)), \qquad (1)$$

where $\phi(t)$ denotes the phase deviation and f_0 is a constant nominal frequency. The amplitude fluctuations of the voltage

output is usually assumed to be negligible around V_0. Then the normalized frequency deviation $y(t)$ is defined as

$$y(t) = \frac{1}{2\pi f_0}\frac{d\phi(t)}{dt}. \tag{2}$$

Integrating $y(t)$ yields the time error function $x(t)$, which has the dimensions of time and is given by

$$x(t) = \int_0^t y(t')dt' = \frac{\phi(t)}{2\pi f_0}. \tag{3}$$

From (3), one can observe that the time error function can be written as a function of the phase deviation $\phi(t)$.

Time domain signal characterization of an oscillator can be done by a Time Interval Counter (TIC). Let the sampling interval of the TIC be τ_0, then the discrete set of samples $x_i = x(t_0 + i\tau_0)$ is defined as the Time Error (TE), where t_0 represents the starting time of the measurement. Subsequently, the Time Interval Error (TIE) is defined as

$$TIE(n\tau_0) = x_n - x_0\,, \tag{4}$$

where $\tau = n\tau_0$ is usually called observation interval.

The maximum peak-to-peak delay variation of a given timing signal with respect to an ideal timing signal within an observation interval $\tau = n\tau_0$ for all observation times of that length within the measurement period $T = N\tau_0$ is called the Maximum Time Interval Error (MTIE) [5]. By definition, it can be estimated by the following formula:

$$MTIE(n\tau_0) = \max_{j=1}^{N-n}\left\{\max_{i=j}^{n+j} x_i - \min_{i=j}^{n+j} x_i\right\}, \tag{5}$$

where $n = 1, 2, \cdots, N-1$. The behaviour of $MTIE(n\tau_0)$ is substantially independent of the sampling interval τ_0. MTIE is suitable for characterizing the buffer size. Its observation interval τ (= $n\tau_0$), specified in ITU-T standards, spans from 0.1 s to 10^3 s, or even wider from milliseconds up to 10^5 s.

3 Fast Computation Approach for MTIE

In this section, we will present the fast computation technique for MTIE. The scheme is based on the recursive approach. We will first derive the recursive formula for $MTIE(n\tau_0)$ and then give the corresponding recursive algorithms.

3.1 Recursive Formula for MTIE

According to (5), one can denote $X(n,j)$ and $Y(n,j)$ as follows.

$$X(n,j) = \max_{i=j}^{n+j} x_i \tag{6}$$

$$Y(n,j) = \min_{i=j}^{n+j} x_i \tag{7}$$

Therefore, the expression of $MTIE(n\tau_0)$ can be rewritten as

$$MTIE(n\tau_0) = \max_{j=1}^{N-n}\left\{X(n,j) - Y(n,j)\right\}. \tag{8}$$

Following the definition of $X(n,j)$, we have

$$\begin{aligned} X(n,j) &= \max\{x_j, x_{j+1}, x_{j+2}, \cdots, x_{n+j-1}, x_{n+j}\} \\ &= \max\left\{\max\left\{x_j, x_{j+1}, x_{j+2}, \cdots, x_{n+j-1}\right\}, \right. \\ &\qquad \left. \max\left\{x_{j+1}, x_{j+2}, \cdots, x_{n+j-1}, x_{n+j}\right\}\right\} \\ &= \max\left\{X(n-1,j),\ X(n-1,j+1)\right\}. \end{aligned} \tag{9}$$

That is, $X(n,j)$ can be computed recursively with respect to n. By using (9), it requires only one operation but not n operations to obtain $X(n,j)$ for any n. This reduces the computation complexity significantly. Similarly, by using the same procedure as in (9), one can derive the recursive formula for $Y(n,j)$ which is given by

$$Y(n,j) = \min\left\{Y(n-1,j),\ Y(n-1,j+1)\right\}. \tag{10}$$

Combining (8), (9) and (10), $MTIE(n\tau_0)$ can be expressed as follows.

$$\begin{aligned} &MTIE(n\tau_0) \\ &= \max_{j=1}^{N-n}\left\{\max\left\{X(n-1,j),\ X(n-1,j+1)\right\}\right. \\ &\qquad \left. -\min\left\{Y(n-1,j),\ Y(n-1,j+1)\right\}\right\} \end{aligned} \tag{11}$$

Based on (11), the computation of $MTIE(n\tau_0)$ is simplified and it can be done recursively, with the initial condition $X(0,j) = Y(0,j) = x_j$ for $1 \le j \le N$.

Sometimes, it is unnecessary to compute $MTIE(n\tau_0)$ for all n. For example, if the MTIE changes smoothly or slowly, one can calculate $MTIE(n\tau_0)$ only at some observation times instead of all. As an example, we can compute $MTIE(n\tau_0)$ only at $n = 2^i$, $i = 1, 2, 3, \cdots$, for decade plot realization. In general, if we only want to compute $MTIE(n\tau_0)$ at observation time $n\tau_0$ with $n = f(i)$, where $f(i)$ is a positive integer function of i, then a more general recursive formula can be derived. The result is described in Theorem 1.

Theorem 1: Let a be a constant integer not less than 2 and $f(i)$ be a positive integer function, if $f(i) \le af(i-1) + (a-1)$, then

$$X(f(i),j) = \max_{k=0}^{a-1}\left\{X(f(i-1),\ j+k\Delta f_i)\right\}, \tag{12}$$

$$Y(f(i),j) = \min_{k=0}^{a-1}\left\{Y(f(i-1),\ j+k\Delta f_i)\right\}, \tag{13}$$

where Δf_i is an integer and is defined as

$$\Delta f_i = \frac{f(i) - f(i-1)}{a-1}. \tag{14}$$

Proof: If $f(i) \le af(i-1)+(a-1)$, then the inequality $f(i)-f(i-1) \le (a-1)(f(i-1)+1)$ holds. It follows that $\Delta f_i \le f(i-1)+1$. Thus, all the terms in the data sequence $\{x_{j+k\Delta f_i}, x_{j+k\Delta f_i+1}, \cdots, x_{j+(k+1)\Delta f_i+f(i-1)}\}$ will be included in the two sequences $\{x_{j+k\Delta f_i}, x_{j+k\Delta f_i+1}, \cdots, x_{j+k\Delta f_i+f(i-1)}\}$ or $\{x_{j+(k+1)\Delta f_i}, x_{j+(k+1)\Delta f_i+1}, \cdots, x_{j+(k+1)\Delta f_i+f(i-1)}\}$. Consequently,

$$\begin{aligned} &\max\left\{\max_{l=j+k\Delta f_i}^{j+k\Delta f_i+f(i-1)} x_l\,,\ \max_{l=j+(k+1)\Delta f_i}^{j+(k+1)\Delta f_i+f(i-1)} x_l\right\} \\ &= \max_{l=j+k\Delta f_i}^{j+(k+1)\Delta f_i+f(i-1)} x_l\,. \end{aligned} \tag{15}$$

always holds for $0 \le k \le a-1$. Hence, from definition of $X(n,j)$ and (15) one has

$$\max_{k=0}^{a-1}\left\{X(f(i-1),j+k\Delta f_i)\right\}$$

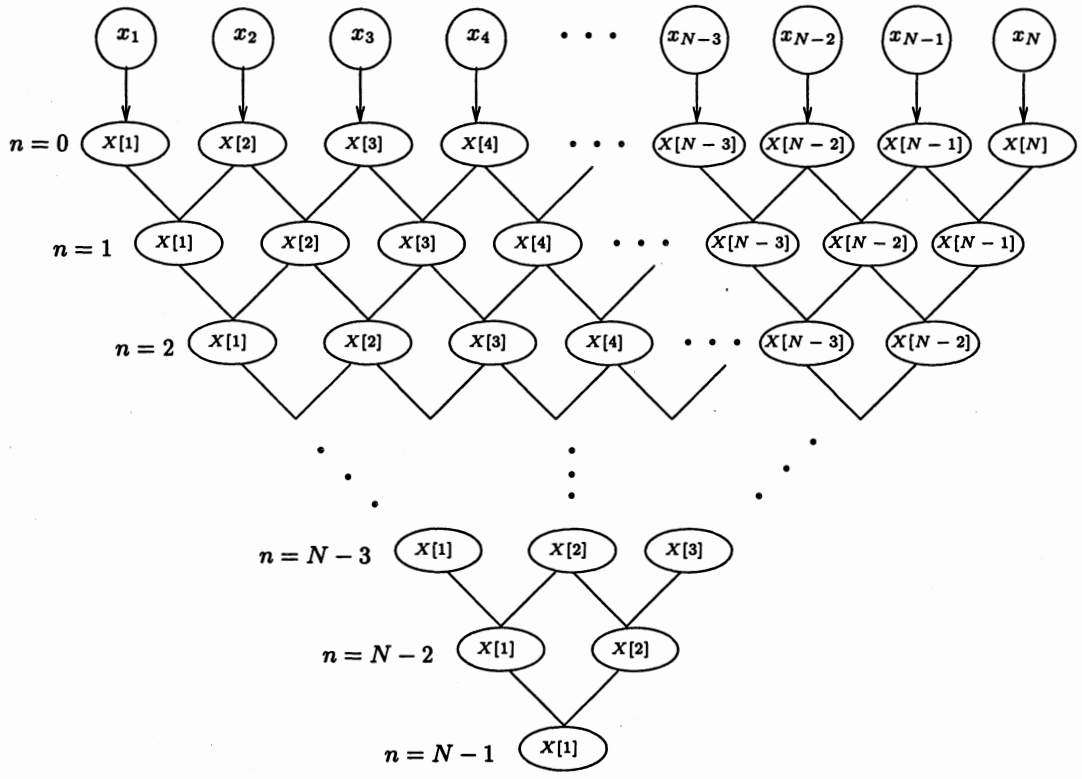

Fig. 1. The recursive process tree for computing $X[j]$. (Each merging process is taken by the *max* operation to obtain $X[j]$)

$$
\begin{aligned}
&= \max\Big\{ \max\{x_j, x_{j+1}, \cdots, x_{j+f(i-1)}\}, \\
&\qquad \max\{x_{j+\Delta f_i}, x_{j+\Delta f_i+1}, \cdots, x_{j+\Delta f_i+f(i-1)}\}, \\
&\qquad \max\{x_{j+2\Delta f_i}, x_{j+2\Delta f_i+1}, \cdots, x_{j+2\Delta f_i+f(i-1)}\}, \\
&\qquad \vdots \\
&\qquad \max\{x_{j+(a-1)\Delta f_i}, x_{j+(a-1)\Delta f_i+1}, \cdots, x_{j+f(i)}\}\Big\} \\
&= \max\{x_j, x_{j+1}, \cdots, x_{j+f(i)}\} \\
&= X(f(i), j) \qquad (16)
\end{aligned}
$$

We thus have proved (12). Similar approach can be used to prove (13), so we omit it here. ■

Example 1: (*MTIE computation at equally spaced points, $n = bi$*) Assume $n = f(i) = bi$, where b is a natural number and $i = 1, 2, \cdots$. One can easily show that the condition of Theorem 1 with $a = 2$, i.e., $f(i) \leq 2f(i-1) + 1$, is always satisfied for $i \geq 2$. Hence, the recursive formulas of Theorem 1 can be reduced to

$$
\begin{aligned}
&X(bi, j) \\
&\quad = \max\Big\{X(b(i-1), j),\ X(b(i-1), j+b)\Big\}, \qquad (17) \\
&Y(bi, j) \\
&\quad = \min\Big\{Y(b(i-1), j),\ Y(b(i-1), j+b)\Big\}, \qquad (18)
\end{aligned}
$$

with initial conditions $X(b, j) = \max_{i=j}^{b+j}\{x_i\}$ and $Y(b, j) = \min_{i=j}^{b+j}\{x_i\}$. If $b = 1$, then (17) and (18) always hold for $i \geq 1$, and the initial conditions are changed into $X(0, j) = Y(0, j) = x_j$. This case coincides with (11). ■

Example 2: (*MTIE computation at exponentially distributed points, $n = a^i$*) Consider the case $n = f(i) = a^i$, where $i = 1, 2, \cdots$, and $a \geq 2$. One can verify that the condition of Theorem 1, $f(i) \leq af(i-1) + (a-1)$, is always satisfied for $i \geq 1$. Thus, the recursive formulas (12) and (13) lead to

$$
\begin{aligned}
X(a^i, j) &= \max_{k=0}^{a-1}\Big\{X(a^{i-1}, j + ka^{i-1})\Big\}, \qquad (19) \\
Y(a^i, j) &= \min_{k=0}^{a-1}\Big\{Y(a^{i-1}, j + ka^{i-1})\Big\}, \qquad (20)
\end{aligned}
$$

with initial conditions $X(1, j) = \max\{x_j, x_{j+1}\}$ and $Y(1, j) = \min\{x_j, x_{j+1}\}$. By the way, one can show that the binary decomposition algorithm in [15] is equivalent to the case $n = f(i) = 2^i - 1$ with initial condition $X(0, j) = Y(0, j) = x_j$. ■

3.2 Recursive Algorithms for MTIE Computation

When one employs the recursive formulas to compute $MTIE(n\tau_0)$, additional memory space should be allocated to store the parameter $X(n, j)$ and $Y(n, j)$. The values $X(n, j)$ and $Y(n, j)$, for $j = 1, \cdots, N$ and all n, can be stored in the two arrays $X(X[1], X[2], \cdots, X[N])$ and $Y(Y[1], Y[2], \cdots, Y[N])$, respectively. According to (9) and (10), the values of $X[j]$ and $Y[j]$ for the case $n = f(i) = i$ can be calculated recursively as shown in Fig. 1, where only $X[j]$ is indicated for simplicity. Each merging process is taken by the *max* operation for $X[j]$ and *min* for $Y[j]$. From Fig. 1, one can observe that the computational effort is linearly decreased.

Subsequently, some popular sequential recursive algorithms for computing $MTIE(n\tau_0)$ are given. In these algorithms, $MTIE(n\tau_0)$ is stored in the variable $M[n]$. The first algorithm is given to implement the case in Example 1, where $MTIE(n\tau_0)$ is calculated only at the points $n = f(i) = bi$, $i = 1, 2, 3, \cdots$. When $b = 1$, $MTIE(n\tau_0)$ will be calculated for all n. The second algorithm which realizes the case $n = f(i) = a^i$ in Example 2 is given by Algorithm 2.

If the function $f(i)$ does not satisfy the condition of Theorem 1, then the recursive formulas (12) and (13) can not be used directly. However, in this case MTIE can still be calculated recursively by slightly modifying Algorithm 2. Thus, we give the Algorithm 3 as an example for this case. In Algorithm 3, $f(0)$ is assumed to be zero.

In the telecommunications measurement, the computation of MTIE can be done simultaneously with the TIC data acquisition. This can really save much time to accomplish the MTIE measurement. By using the fast computation approach proposed in this paper, it is possible to fulfill the real time MTIE measurement or monitoring. An example of the real time computation algorithm is given in Algorithm 4. Here, *new_N* is the number of data samples observed up to the present, and *old_N* is the number of data samples observed at the previous computation cycle.

Algorithm 1: (*Recursive MTIE Computation Algorithm for $n = bi$*)

```
for (1 ≤ j ≤ N − b)
    { for (1 ≤ k ≤ b)
          { X[j] = max{x_j, x_{j+k}};
            Y[j] = min{x_j, x_{j+k}};
          }
      M[b] = max{ M[b], X[j] − Y[j] };
    }
i = 2;
while (bi ≤ N − 1)
    { for (1 ≤ j ≤ N − bi)
          { X[j] = max{ X[j], X[j + b] };
            Y[j] = min{ Y[j], Y[j + b] };
            M[bi] = max{ M[bi], X[j] − Y[j] };
          }
      i = i + 1;
    }
```

4 Complexity Analysis

In this section, we will briefly analyze the time complexity for different MTIE computation algorithms, including the direct computation of equation (5) and the proposed recursive computation algorithms. For simplicity, in the following complexity analysis, we will only consider the number of comparison tests.

4.1 Complexity of Direct Computation

At first, we will consider the complexity of direct computing $MTIE(n\tau_0)$ only at $n = bi$ according to (5). Here, we assume that $\frac{N-1}{b}$ is an integer. For direct computing MTIE, it is obvious that the number of comparison tests to obtain a specific $MTIE(n\tau_0)$ is $\sum_{j=1}^{N-n}(2n+1)$, which is equivalent

Algorithm 2: (*Recursive MTIE Computation Algorithm for $n = a^i$*)

```
for (1 ≤ j ≤ N − 1)
    { X[j] = max{x_j, x_{j+1}};
      Y[j] = min{x_j, x_{j+1}};
      M[1] = max{ M[1], X[j] − Y[j] };
    }
i = 1;
while (a^i ≤ N − 1)
    { for (1 ≤ j ≤ N − a^i)
          { for (1 ≤ k ≤ a − 1)
                { X[j] = max{ X[j], X[j + a^{i−1}k] };
                  Y[j] = min{ Y[j], Y[j + a^{i−1}k] };
                }
            M[a^i] = max{ M[a^i], X[j] − Y[j] };
          }
      i = i + 1;
    }
```

Algorithm 3: (*Recursive MTIE Computation Algorithm for $n = f(i)$*)

```
for (1 ≤ j ≤ N)
    { X[j] = x_j;
      Y[j] = x_j;
    }
i = 1;
while (f(i) ≤ N − 1)
    { for (1 ≤ j ≤ N − f(i))
          { for (1 ≤ k ≤ f(i) − f(i − 1))
                { X[j] = max{ X[j], X[j + k] };
                  Y[j] = min{ Y[j], Y[j + k] };
                }
            M[f(i)] = max{ M[f(i)], X[j] − Y[j] };
          }
      i = i + 1;
    }
```

to $(N-n)(2n+1)$. Therefore, for calculating $MTIE(n\tau_0)$ at all $n = bi$, where $i = 1, 2, \cdots, \frac{N-1}{b}$, the total number of comparison tests should be

$$\sum_{i=1}^{\frac{N-1}{b}}(N-bi)(2bi+1)$$
$$= \frac{1}{3b}N^3 + \frac{1}{2b}N^2 - \frac{2b^2-3b+6}{6b}N + \frac{(b-1)(2b-1)}{6b}.$$

If we limit MTIE computation to those observation times $n\tau_0$ with $n = a^i$ and assume $a^k = N - 1$, then the number of comparison tests is

$$\sum_{i=1}^{k}(N-a^i)(2a^i+1)$$

Algorithm 4: *(Real-Time Recursive MTIE Computation Algorithm for $n = f(i)$)*

```
while (new_N ≤ N)
  { for (old_N < j ≤ new_N)
      { X[j] = x_j;
        Y[j] = x_j;
      }
    i = 1;
    while (f(i) ≤ new_N − 1)
      { m = max{1, old_N − f(i) + 1};
        for (m ≤ j ≤ new_N − f(i))
          { for (1 ≤ k ≤ f(i) − f(i − 1))
              { X[j] = max{X[j], X[j + k]};
                Y[j] = min{Y[j], Y[j + k]};
              }
            M[f(i)] = max{M[f(i)], X[j] − Y[j]};
          }
        i = i + 1;
      }                    // ends a computation cycle here
    old_N = new_N;
    update new_N;
  }
```

$$= \frac{2a}{a^2-1}N^2 + N\log_a(N-1) - \frac{a^2+5a}{a^2-1}N + \frac{2a}{a-1}.$$

Thus, the complexity of direct computation equals $O(N^3)$ for all $n = bi$, and equals $O(N^2)$ for all $n = a^i$.

4.2 Complexity of Recursive Computation

First, we consider the time complexity of Algorithm 1. According to Algorithm 1, the number of comparison tests to obtain $MTIE(b\tau_0)$ is equal to $(2b+1)(N-b)$. For $i \geq 2$, the number of comparisons to determine a certain $MTIE(bi\tau_0)$ is $\sum_{j=1}^{N-bi} 3$, which is equivalent to $3(N-bi)$. Similarly, one can assume that $\frac{N-1}{b}$ is an integer for convenience. Then for computing all $MTIE(bi\tau_0)$, $i = 2, \cdots, \frac{N-1}{b}$, the total number of comparison tests should be $\sum_{i=2}^{\frac{N-1}{b}} 3(N-bi)$. It follows that the number of comparison operations to compute all $MTIE(bi\tau_0)$ for $i = 1, 2, \cdots, \frac{N-1}{b}$ is equal to

$$(2b+1)(N-b) + \sum_{i=2}^{\frac{N-1}{b}} 3(N-bi)$$

$$= \frac{3}{2b}N^2 + (2b - \frac{7}{2})N + \frac{3(b-1)}{2b} - 2b^2 + 2b\,.$$

Next, we will evaluate the complexity of Algorithm 2 in which the MTIE computation is only required at $n = a^i$. Let's assume that $a^k = N-1$ holds, then the number of comparison tests for calculating a specific $MTIE(n\tau_0)$ equals $\sum_{j=1}^{N-n}(2a-1)$. And the total number of comparison tests to acquire all $MTIE(a^i\tau_0)$ for $i = 1, \cdots, k$, is

$$\sum_{i=1}^{k}(N-a^i)(2a-1)$$

Complexity	$n = f(i) = a^i$	$n = f(i) = bi$
Direct Computation	$O(N^2)$	$O(N^3)$
Recursive Computation	$O(N\log_a N)$	$O(N^2)$

TABLE I
COMPARISON OF TIME COMPLEXITY FOR DIFFERENT COMPUTATION APPROACHES.

$$= (2a-1)N\log_a(N-1) - \frac{(2a^2-a)(N-2)}{a-1}\,.$$

Therefore, the complexity is $O(N^2)$ for the case $n = bi$ in Algorithm 1 , and equals $O(N\log_a N)$ for the case $n = a^i$ in Algorithm 2. It is obvious that the complexity of the direct computation approach can be improved by a factor up to N when the new recursive technique is employed. All the above results are summarized in Table 1.

5 Conclusions

MTIE is one of the key parameters for clock stability characterization in telecommunications measurement. The important features and computation issues of MTIE have been pointed out. For resolving the troublesome computation, we have presented an efficient and fast approach to compute MTIE in this paper. The superiority of the proposed approach has been demonstrated in terms of time complexity. The new approach is found to be the best one at present from the time complexity criterion. In addition, it provides fast speed to compute the MTIE without violating the MTIE definition in (5). For these merits, we believe that it would improve the performance of some commercial timing testing equipment which includes MTIE measurement.

References

[1] M. J. Klein and R. Urbansky, " Network Synchronization — A Challenge for SDH/SONET? ", *IEEE Commun. Mag.*, pp. 42-50, Sept. 1993.

[2] J. C. Bellamy, " Digital Network Synchronization, " *IEEE Commun. Mag.*, Vol. 33, pp. 70-83, April, 1995.

[3] ITU-T Rec. G.702, " Digital Hierarchy Bit Rates, " 1988.

[4] ITU-T Rec. G.707, " Synchronous Digital Hierarchy Bit Rates, " 1993.

[5] ITU-T Rec. G.810, " Definition and Terminology for Synchronization Networks, " Aug. 1996.

[6] W. D. Grover, T. E. Moore, and J. A. McEachern, " Waiting Time Jitter Reduction by Synchronizer Stuff Threshold Modulation, " *IEEE GLOBECOM'87*, pp. 514-518, 1987.

[7] R. F. Bridge, S. Bily, J. Klass, and R. Taylor, " Jitter Attenuation in T1 Networks, " *IEEE ICC'90*, pp. 685-689, 1990.

[8] Y. Matsuura, " Reducing Jitter in PDH and ATM, " *IEEE GLOBECOM'95*, pp. 1323-1326, 1995.

[9] H. Sari and G. Karam, " Cancelation of Pointer Adjustment Jitter in SDH Networks, " *IEEE Trans. Commun.*, Vol. 42, No. 12, pp. 3200-3207, Dec. 1994.

[10] ITU-T Rec. G.823, " The Control of Jitter and Wander Within Digital Networks Which are Based on the 2048 kbit/s Hierarchy, " March 1993.

[11] ITU-T Rec. G.824, " The Control of Jitter and Wander Within Digital Networks Which are Based on the 1544 kbit/s Hierarchy, " March 1993.

[12] ITU-T Rec. O.171, " Timing Jitter and Wander Measuring Equipment for Digital Systems Which are Based on the Plesiochronous Digital Hierarchy (PDH) , " April 1997.

[13] ITU-T Rec. O.172, " Timing Jitter and Wander Measuring Equipment for Digital Systems Which are Based on the SDH , " June 1999.

[14] S. Bregni, " Measurement of Maximum Time Interval Error for Telecommunications Clock Stability Characterization, " *IEEE Trans. Instrum. Meas.*, Vol. 45, No. 5, pp. 900-906, Oct. 1996.

[15] S. Bregni and S. Maccabruni, " Fast Computation of Maximum Time Interval Error by Binary Decomposition, " *IEEE ICC'99*, pp. 1741-1745, 1999.

POSTERS B

GPS, GALILEO & CARRIER PHASE

RUBIDIUM ATOMIC CLOCK FOR GALILEO

F. Droz©, P. Rochat©, F. Emma♦
©Temex Neuchâtel Time (CH)
♦European Space Technology Centre (NL)

Abstract

The overall performance of navigation payloads is dependent on the performance of the on-board clocks. Better stability leads directly to improved space segment autonomy and simplified ground segment operation. The European Space Agency supports the development of advanced atomic clocks in the frame of the GNSS-2 program. Two major activities are currently running with the aim of fully space qualifying a Rubidium Atomic Frequency Standard (RAFS) and a Space Hydrogen Maser (SHM). The development activity for the Rubidium clocks is driven by the following major design goals:

- ***Mass < 2.3 Kg***
- ***Short term Stability (100s) < $5x10^{-13}$, flicker floor < $5x10^{-14}$***
- ***Volume < 2 ltr***

As the configuration of the Galileo satellite constellation is now better defined, special emphasis has been placed on thermal regulation constraints, on radiation shielding and on reliability for a 15-year mission. This article presents the status of the rubidium development program and focuses on the significant design goals and results obtained to date.

1. INTRODUCTION

The European Space Agency has continuously supported the development of better clocks for scientific applications in the frame of its Technology Demonstration Program and more recently, for navigation, in the GNSS-2 (Global Navigation Satellite System) program. The requirement for improved, space-qualified clocks became evident once the need for a European independent navigation system was established and materialized in the "Galileo" program. Galileo is an initiative of the European Union and the European Space Agency for the development and implementation of a global navigation satellite system. The high level of ranging accuracy (below 1 meter) specified in the Galileo system for some critical applications, requires the development of suitable ultra stable frequency standards. Atomic clocks, with their unsurpassed performance in terms of frequency stability, are the best solution to fulfil these system requirements. Atomic clocks are used on-board of GPS and Glonass, the two currently operational satellite navigation systems. There is a continuous improvement of performance of these clocks, especially in the GPS constellation. GPS block IIR spacecraft will rely exclusively on an improved Rubidium Atomic Frequency Standard designed to fulfil the lifetime requirements of 10 years for block IIR satellites. Cesium clocks on Glonass satellites have a frequency stability of $1x10^{-13}$ for an averaging time of 1 day. The frequency stability of on-board clocks has a direct impact on the complexity and amount of work that has to be carried out by the ground segment as this latter must take care of corrections of satellite clock data.

For a given ranging accuracy, the stability of on-board clocks determines the frequency of up-loads of correction data. To keep a goal accuracy of 0.3 meter an up-load every 2 hours would be required for the ESA specified Rubidium clock and every 8 hours in case of the ESA specified Passive Maser. In this calculation the assumption is made that the specified frequency drift (≤ $1x10^{-13}$/day for the Rubidium and < $1x10^{-14}$/day for the Passive Maser) is removed through modelling of clocks behaviour. At system level the trade-off performed in the GalieloSat definition phase led to the definition of an onboard timing sub-system constituted by two Rubidium Clocks and two Passive Hydrogen Maser. The European Space Agency is currently funding a development program that will lead to the space qualification of a Rubidium Atomic Frequency Standards. This work is performed by Temex Neuchâtel Time (TNT) as a follow on of prevoius development activities. The development of the a Space Passive Hydrogen Maser is currently performed by the Observatory of Neuchâtel.

2. RUBIDIUM ATOMIC FREQUENCY STANDARD

An initial development of a Rubidium Ultra Stable Oscillator (RUSO) for space applications, was funded by ESA under its Technology Demonstration Program (TDP-II) in 1993. The objective of such development was to manufacture and qualify a compact spaceborne RUSO for the Russian Radioastron mission (Radioastron is a Russian lead international mission to deploy a space-based radiotelescope for a Very Long Baseline Interferometry (VLBI) radiotelescope). The oscillator was supposed to be used for calibration purposes and as back-up of the main clock to be used on board (a maser or a quartz oscillator locked to ground masers via microwave links).

The development activity for the RUSO was completed in 1995 leading to the manufacturing of 3 flight models and one EQM. The EQM unit successfully underwent a series of qualification tests. These included random vibration, low frequency vibration, temperature, thermal vacuum radiation and EMC.

All the RUSO units manufactured under this development activity have shown short-term stability better than $5x10^{-12}\ \tau^{-1/2}$ when measured against a ground hydrogen maser. The units also underwent a long-term

performance test lasting 5 months. Their long term drift which is typically below $4x10^{-11}$ per month , was measured against a cesium standard. Following this initial development for a space qualified Rubidium clock, the Agency placed, in January 1997, a contract on TNT for the development of an improved Rubidium Clock which was suited for navigation applications. The two initial contracts for the RAFS development and the manufacturing of initial models were completed in 2000 by a third one to execute a complete qualification program in view of GALILEO. The actual main RAFS specifications for navigation are the following:

Parameters	Specifications
Frequency	10 MHz
Freq. Stability Long Term (goal)	$5x10^{-14}$ (per 24 hr.)
Freq. stability short term 1 sec	5×10^{-12}
10 sec	1.6×10^{-12}
100 sec	5×10^{-13}
1000 sec	1.6×10^{-13}
10000 sec	7×10^{-14}
100000 sec	5×10^{-14}
Power consumption at 5°C	< 18W
In the operating temp. range	< 35W

Parameters	Specifications
Temperature sensitivity	$< 5 \times 10^{-14}$ / °C
Operating temperature	-10 to +5 °C
Phase Noise	
1 Hz	-90 dBc
10 Hz	-110 dBc
100 Hz	-130 dBc
1000 Hz	-150 dBc
10000 Hz	-150 dBc
Mass	<2.3 kg
Volume	<2 ltr

The design of the RAFS for navigation was completed in 2000. The unit is designed to withstand more than ten years of cosmic radiation in MEO orbit. A double oven concept is utilized to provide a good thermal behaviour. In addition, a dedicated thermally regulated base-plate was integrated on the bottom of the clock. Before the final configuration of the RAFS, several tests were conducted by TNT on industrial units and on engineering models in order to determine what were the limiting parameters.

3. SHORT TERM STABILITY

A short term stability measurement was made at the beginning of the project in order to assess the performance of a dedicated industrial MCFRS unit (integrated filter cell). With some modifications, it has been possible to reach $4x10^{-14}$ level . Furthermore, it was then demonstrated that the original use of integrated filter cell surrounded by the patented magnetron microwave resonator had the capability to reach the specified stability level of less than $5 \times 10^{-12} \times \tau^{-1/2}$.

Based in these results, engineering models were developed on the base of the existing physics package adapted to operation under vacuum. A double oven concept was integrated in order to provide the good thermal behavior. The Figure 1 shows the test result of the engineering model operated under vacuum in summer 2000. The reference clock was an EFOS Maser of the Observatory of Neuchâtel.

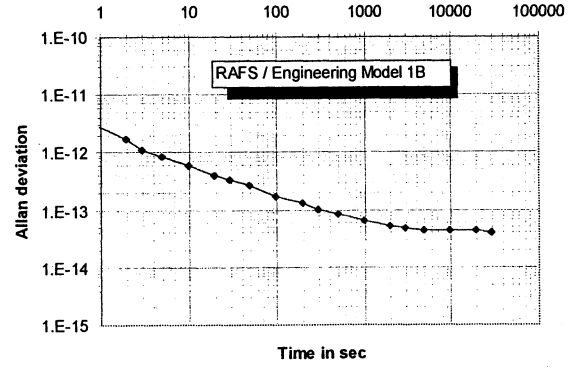

Figure 1 : Engineering Model Allan deviation

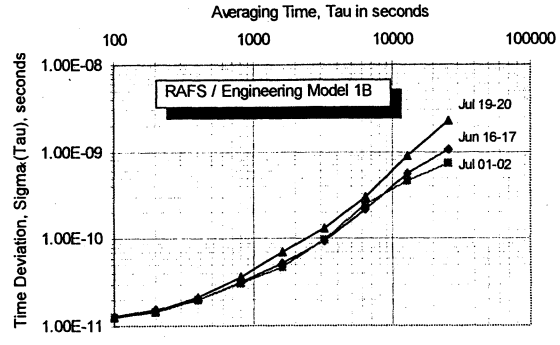

Figure 2 : Engineering Model Time Deviation (summer 2000)

4. LONG TERM STABILITY

The long term stability is systematically measured before delivery on all the Rubidium clock produced by TNT (several thousands of units) . This parameter is time dependent and decreases versus time.
However, industrial units are equipped with a natural Rubidium lamp working at high temperature (~140°C). The systematic measurement has shown unit with a long term stability of few 10^{-13}/day. The high lamp temperature is probably one of the main cause of the RAFS drift. Improvement are expected in the future by using a lamp filled with Rb^{87} isotope. Initial measurement demonstrates the good operation with Rb^{87} isotope lamp working 10°C below natural Rb.

5. RADIATION TOLERANCE

The digital loop synthesizer is built using standard rad-hard available components which have been chosen according to radiation data bases available from the manufacturers. The analog electronic functions are also designed with rad-hard available components. A 4-point mount SC cut 10MHz resonator for the local oscillator has been used. With a lower radiation shielding configuration, radiation sensitivity of such a crystal, produced by Temex, has been measured at less than $7x10^{-12}$/Rad(Si) [8]. Such low sensitivity ensures the correct operation of the RAFS over the 10 year Galileo mission.

6. RELIABILITY AND LIFETIME

The RAFS electronic package reliability computation was performed according to MIL-HDBK-217F-1 part stress. The reliability figure is 94% for a mission duration of 10 years in space environment.

The only consumable in the RAFS design is the Rubidium filled the lamp bulb. The life time of the lamp bulb has been evaluated by a measurement of the rubidium absorption rate (see www.temex.ch) by a microcalorimetric system measurement. Since the RAFS is using the same lamp as in the industrial rubidium, with the same bulb operating temperature, the life time is also expected longer than 20 years (50 years by design).

7. FLICKER FLOOR REQUIREMENT ($< 5 \times 10^{-14}$)

RAFS is equipped with a direct synchronous digital synthesizer which only generates spurious at known frequencies and does not degrade the signal purity. The very high accuracy local oscillator gives the capability to increase the overall Rb signal amplification factor before synchronous detection and therefore reduce the influence of loop integrator flicker noise by a very large amount. An efficient offset and noise cancellation scheme has also been implemented at the loop integrator level. The flicker floor of the heater controllers have also been verified to be compatible with noise floor requirements. Figure 2 shows the result obtain on engineering model.

8. TEMPERATURE SENSITIVITY UNDER VACUUM

A double oven technique has been used to minimize thermal effects on the stability of the clock. by a factor of 1000. The use of a double oven configuration is very effective in stabilizing the inner temperature of the lamp oscillator, the crystal oscillator and frequency multiplier. A very good thermal stabilization is already achieved through the first oven. The final performance are ensured by the presence of the second oven.

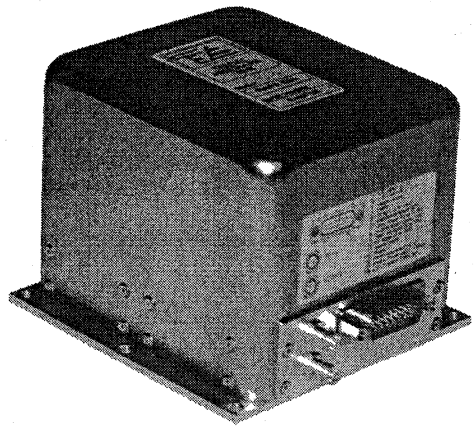

Figure 3 : RAFS Engineering model once closed

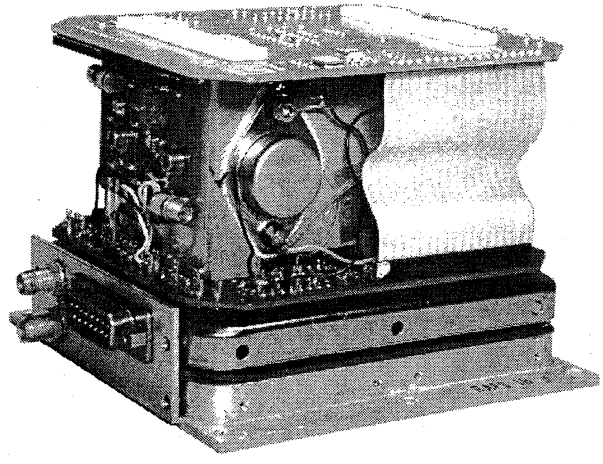

Fig 4: RAFS Engineering model without cover

The RAFS physics package enclosure is non hermetic to avoid any leakage problem. This forced us to find a solution for evacuating the RF power dissipated into the discharge lamp by conductivity only.

9. PROGRAMME STATUS

At the end of the initial contracts, the engineering model unit underwent successfully a series of pre-qualification tests. These include random vibration, low frequency vibration, temperature, thermal vacuum and EMC. Nevertheless, three categories of problems remind:

- The electronic of the initial RAFS design was too sensitive to the environment (EMC and Thermal).
- Some performances were not reproducible enough (i.e. long term stability).
- The environmental conditions of GALILEO satellite diverge of the pre-qualification test constraints.

The main objectives achieve during this preliminary phase were:

- The demonstration of the RAFS capability to stay below $5 \times 10^{-12} \times \tau^{1/2}$
- The demonstration of the RAFS capability to stay below 1ns for 2 hours period (see figure 5)
- The good RAFS operation for several months under vacuum.
- The robustness of the design under vibration and thermal cycles.

Based on these intermediate results, a new activity has been initiated under ESA funding in June 2000 for the design optimization and the lifetime test of 5 RAFS. . The objectives of the design phase are the reduction of the electronic sensitivity to the environment and the optimization of the physic package operation to obtain a better stability performance In addition, in order to minimize the thermal stability constraints on the satellite platform, the design and implementation of a dedicated thermally regulated base-plate integrated on the bottom of the clock has been foreseen.

For the optimization of the physic package, mainly a redesign of the lamp was initiated. First step was to increase the light density inside the cell in order to obtain a cell characteristic versus temperature with a extrema (see figure 5). Second step was to avoid gluing process for lamp bulb assembly. Any glue chemical aging (optical, mechanical or thermal) being able to disturb the lamp long term stability.

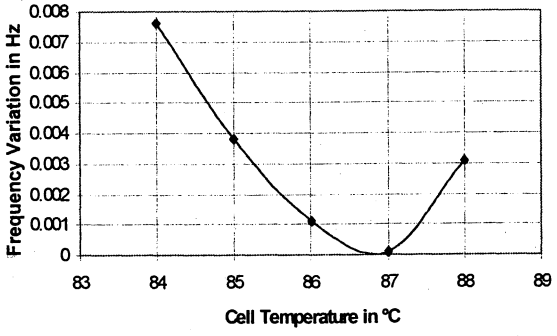

Figure 5 : Cell temperature optimum (86.8°C)

To solve the problem of electronic sensitivity to environment, two changes have been implemented. The first one concerns the addition of a cover which improve the protection again EMC perturbation and thermal variation. The second was the redesign of the frequency multiplier electronic function which was the most sensitive function.

The implementation of the modification will be completed for May 2001. A complete qualification program will start on the a qualification model available at that time and lifetime test will start on six other models for a two years period. The lifetime program will be concentrated on measurement on key parameters like lamp efficiency, VCXO control or temperature stability.

10. CONCLUSION

The current results and analysis of the RAFS show that the most important RAFS specifications for GALILEO satellites have been achieved. These specifications have been obtained operating under vacuum conditions. Engineering models have been submitted to vibration, thermal cycles and EMC at qualification level without any damages. A dedicated discharge lamp assembly has been successfully designed proving that it is not necessary to place the physics package into a hermetic enclosure for proper operations. The thermal configuration is satisfactory for stabilizing the various ovens, the mechanical design has been frozen and a set of RAFS will be assembled to prove the repeatability of the processes and to demonstrate the lifetime capability. The RAFS, with its more than 20 years of life expectancy and sub-nanosecond stability for more than two hours, will be a perfect candidate for being an on-board frequency reference of the Galileo satellite system.

11. REFERENCES

[1] "Rubidium Atomic Clocks for Galileo", F. Emma, A. Jeanmaire, P. Rochat, PTTI 1999

[2] Study of potential applications for atomic clocks. (ESTEC contract No. 9099/90)

[3] Rubidium Ultra-Stable Oscillator. (ESTEC contract 9099/90)

[4] Miniaturized Rubidium Ultra Stable Oscillator (ESTEC contract 12220/96)

[5] Industrialisation of High Performance rubidium Atomic Clocks (ESTEC contract 12884/98)

[6] Steven C. Fisher and Kamran Ghassemi " GPS IIF-The next Generation" . Proc of IEEE vol. 87 No. 1, Jan. 1999.

[7] "Scanning the Issue/technology" Special Issue on GPS, Proc. of IEEE, vol. 87 No. 1

[8] "Dérive de fréquence des oscillateurs TNT sous irradiation à faible débit de dose", DT-96-31 DGA/T/AE/TTL/TF, Ph. Guillemot & M. Brunet, CNES (F), 20.11.1996

IMPROVING THE ACCURACY OF GPS TIME TRANSFER BY THERMAL STABILIZATION OF GPS ANTENNA AND RECEIVER

Andrzej Smolarski[1], Aleksander Lisowiec[1], Jerzy Nawrocki[2]

[1]Tele and Radio Research Institute, Warsaw, Poland
[2]Astrogeodynamical Observatory, Space Research Center, Polish Academy of Sciences, Kórnik, Poland

1. ABSTRACT

In GPS time transfer system, the temperature dependence of signal delay in GPS receiver and antenna significantly lowers the transfer accuracy.

In the paper thermal stabilization systems of Motorola VP Oncore GPS receiver and antenna have been presented. The achieved temperature stability of the receiver is ±0.14 °C over +15÷+30 °C ambient range and stability of the antenna is ±1.0 °C over -20÷50 °C ambient air temperature range plus additional heating due to solar radiation to +80 °C of outer antenna enclosure. The temperature chamber of the antenna practically doesn't modify its gain and radiation pattern.

Diurnal and seasonal signal delay variations due to changes in outdoor temperature have thus been brought down to less than 0.5 ns.

time transfer, GPS, temperature stabilization

2. INTRODUCTION

The accuracy of time transfer by GPS is limited by the GPS system and also by the instrumentation used. The main factor increasing the uncertainty of the transfer on the instrument side is temperature dependence of signal delay in GPS antenna and receiver. The GPS receiver is subjected to temperature changes of not more than 15 °C and 1 °C if placed in temperature controlled room, whereas the antenna is subjected to up to 100 °C temperature changes.

To reduce the temperature dependence of signal delay by an order of magnitude, the receiver should be stabilized to at most few tens of degree and antenna to at most one or two °C.

3. THERMAL STABILIZATION OF THE RECEIVER

The Motorola VP Oncore receiver generates about 1 W of heat power. The permissible operating temperature range is –40 °C÷+85 °C. The receiver has been placed in a copper block (fig. 1) with the walls 8 mm thick. The block is insulated from ambient air by a foam layer. The thickness of the foam layer must be high enough to ensure proper temperature stability of the receiver and at the same time low enough to let dissipate the heat generated by the receiver.

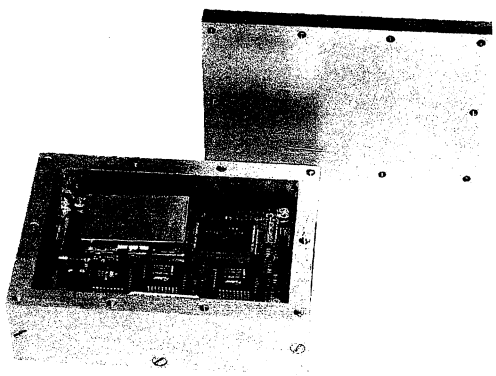

Fig.1. A view of the receiver inside the copper block

The proportional high sensitivity thermoregulator has been mounted at the outer surface of the copper enclosure. As a sensor a high stability thermistor has been used.

A thermal cutoff has been placed inside the oven in series with power supply that cuts off the heating current if the temperature inside the oven goes above 70 °C. When the oven cools, the cutoff connects the current again, so this is some sort of regulation at 70 °C.

The characteristics of the receiver oven have been presented in table 1.

Table 1.

Parameter	Value
Temperature T_T stabilized inside the copper block	50 °C
Setting time (from 20 °C ambient temperature)	50 min
Ambient temperature T_A influence	$\frac{\delta T_T}{\delta T_A} = 13.7 \cdot 10^{-3}$ [°C/°C]
Voltage supply U influence	$\frac{\delta T_T}{\frac{\delta U}{U} \cdot 100} = 3.3 \cdot 10^{-3}$ [°C/%]
Ambient temperature T_A range	+15°C ÷ +35°C
Power supply	12 V DC±5%/800 mA_{max}

4. THERMAL STABILIZATION OF THE ANTENNA

The antenna oven must stabilize inner temperature in spite of thermal energy generated by the antenna, large ambient temperature fluctuations and periodical high solar irradiation. Additionally the oven must not modify the gain pattern of the antenna or attenuate the GPS signal at 1.5 GHz.

The previous solutions like 3S Navigation TSA-100 antenna used a thermal pump made of Peltier cells carrying away excessive heat generated by the active antenna block. Using thermal pump has disadvantages, namely large dimensions, lower reliability and high dissipated power that is particularly unfavorable in battery operated setups.

The developed thermal stabilization system of the antenna (patent pending) consists of two different thermal insulation parts (fig. 2). The first part shields the antenna from above and on both sides. It has high thermal resistance R_1 and its cover reflects the solar energy. Practically no thermal energy flows through this insulating part to and from the antenna.

The second insulation part that shields the antenna block from below has thermal resistance R_2 that is much lower than R_1. Thermal energy generated in the antenna can flow away through R_2 to the environment because from that side the ambient temperature is lower than above the antenna because there is no solar irradiation. Nevertheless the thermal resistance R_2 must be high enough to prevent excessive losses of thermal energy of the antenna.

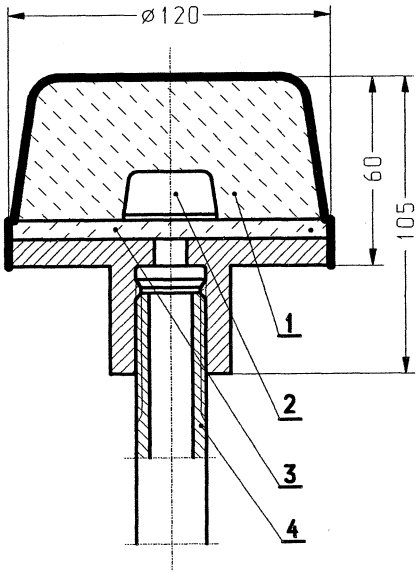

1) insulation part with thermal resistance R_1
2) antenna
3) insulation part with thermal resistance R_2
4) mounting

Fig. 2. GPS antenna inside the oven.

Basic characteristics of the antenna oven have been presented in table 2.

Table 2

Parameter	Value
Temperature T_T stabilized inside the oven	60 °C
Setting time (from 20 °C ambient temperature)	50 min
Ambient temperature T_A influence	$\frac{\delta T_T}{\delta T_A} = 25 \cdot 10^{-3}$ [°C/°C]
Voltage supply U influence	$\frac{\delta T_T}{\frac{\delta U}{U} \cdot 100} = 3.3 \cdot 10^{-3}$ [°C/%]
Ambient temperature T_A range	-20°C ÷ +80°C
Power supply	12 V DC±5%/800 mA_{max}

Indication of the temperature settling in the antenna oven as well as in the receiver oven is done by sensing the current drawn from the power supply. The circuit sensing the power supply current is shown in fig. 3. This circuit also indicates if there is a break in the power supply to the heater. Separate circuit must be used for antenna and receiver oven.

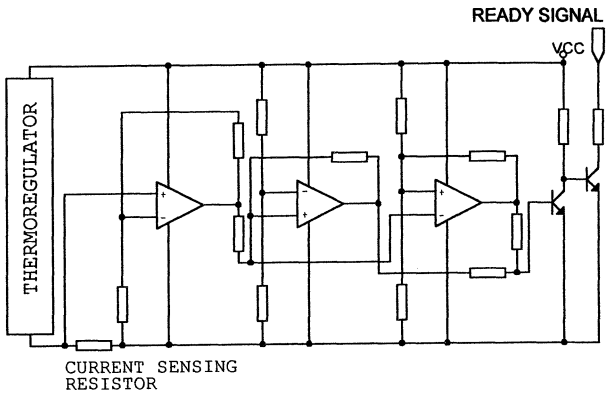

Fig. 3. Diagram of oven power supply current sensing circuit

The attenuation of GPS signal at 1.5 GHz by the antenna oven has been evaluated by observing the SS number transmitted by the VP receiver. This number is a measure of signal strength and signal to noise ratio and is in the range 0÷255. Higher SS number means higher signal strength and higher signal to noise ratio. Figure 4 shows SS number for satellite with PRN=5 against observation time. Fig. 5 corresponds to the case when the power to the antenna was cut off and the temperature inside it was equal to the ambient temperature about 0 °C and the fig. 6 corresponds to the case when the temperature inside the oven was 60 °C. As can be seen the SS number reached its upper bound. An interesting thing was observed. The gain of the antenna is evidently temperature dependent and is higher at low than at high temperatures.

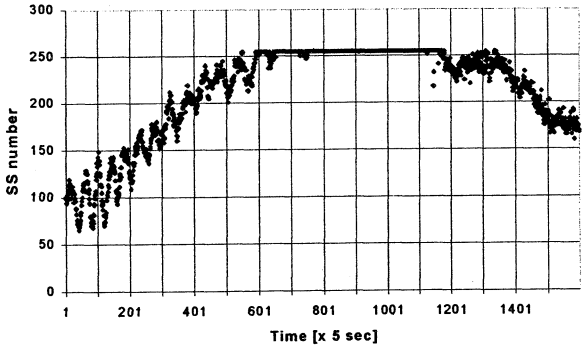

Fig. 4. SS number of the antenna inside the oven at 0 °C.

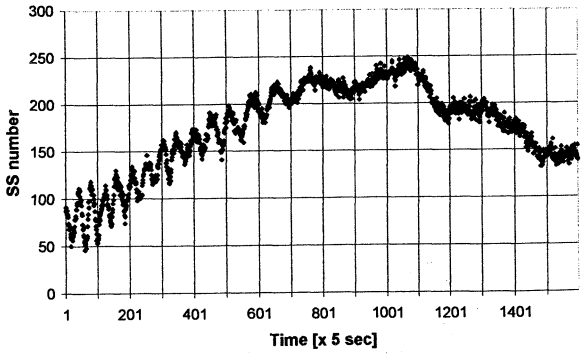

Fig. 5. SS number of the antenna inside the oven at 60 °C.

The SS number as a function of elevation angle for satellite with PRN=5 is presented in fig. 6 in the case when the temperature of the oven was 0 °C and in fig. 7 in the case when the temperature of the oven was 60 °C.

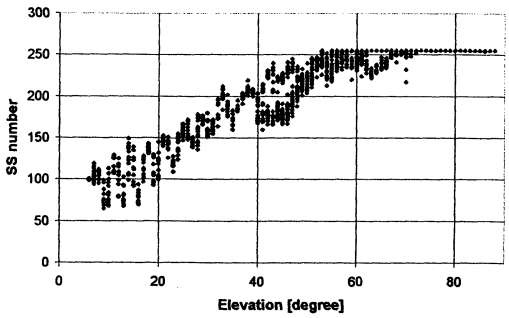

Fig. 6. SS number for satellite with PRN=5 with oven temperature equal to 0 °C.

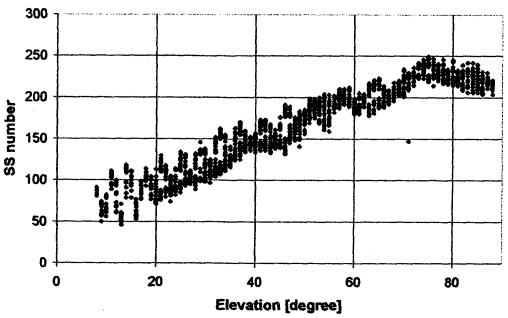

Fig. 7. SS number for satellite with PRN=5 with oven temperature equal to 60 °C.

As can be seen from the above figures, thermal stabilization of the receiver and antenna stabilizes also their gain and that additionally improves the accuracy of time transfer.

5. MEASUREMENT RESULTS

The temperature dependence of signal delay in GPS VP Oncore receiver and antenna has been measured in a setup presented in fig. 8. It consisted essentially of two independent time transfer systems, REF 1, REF 4, working in Common View mode running special test software. Each of the time transfer systems measured the time interval between 1pps from GPS receiver and 1pps from local atomic clock. These time intervals corresponding to the same observation time and the same satellite were then subtracted from each other and what was observed was the difference. The use of two systems eliminated most ionospheric, tropospheric and stratospheric errors, errors in the ephemeris of the satellites and local clock inaccuracies.

5.1. Measurements of temperature coefficient of signal delay in the antenna

The temperature of one of the antennae was switched during the experiment several times between 0 °C (outdoor temperature) and 60 °C by turning on and off the power supply of the oven. Denoting the time intervals difference between two systems for observation time τ and satellite with PRN=η as a function of temperature T by $\Delta D_{\tau,\eta}(T)$, and denoting by $\Delta D(T)$ the $\Delta D_{\tau,\eta}(T)$ averaged over τ and η, it was observed that

$$|\Delta D(0\ °C) - \Delta D(60\ °C)| \cong 6\ ns.$$

The average change of signal delay per 1 °C for the antenna is about 0.1 ns.

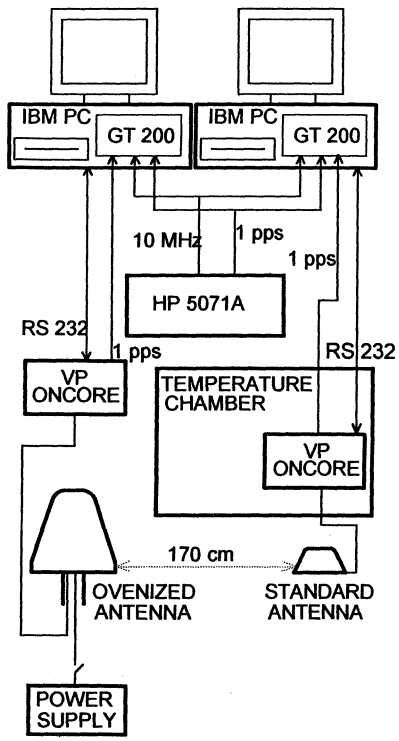

Fig. 8. Signal delay measurement setup

5.2. Measurements of temperature coefficient of signal delay in the receiver

The ambient temperature of one of the receivers was switched during the experiment between 30 °C and 70 °C in a temperature chamber. Keeping the notation of paragraph 5.1, the difference of ΔD at 30 °C and 70 °C for the receiver was

$$|\Delta D(0\ °C) - \Delta D(60\ °C)| \cong 6\ ns.$$

so the average change of signal delay per 1 °C for this receiver was about 0.1 ns.

6. CONCLUSION

The temperature influence upon the accuracy of time transfer by GPS can be reduced to 0.5 ns by thermal stabilization of Motorola VP Oncore receiver and antenna. The copies of receiver and antenna that have been tested exhibit about 0.1 ns change of signal delay per 1 °C. It is thus more effective to stabilize the temperature of the antenna as it is subjected to far greater temperature changes than the receiver.

7. REFERENCES

1. J. Nawrocki, M. Mirianian, E. Powers, J. Azoubib, W. Lewandowski, Some tests of GPS Multi Channel Time Transfer Units TTS-2 Based on a Motorola Receiver and Using CCTF Standards, Proc. of The 14th EFTF, 2000, Turin
2. W. Lewandowski, J. Azoubib, W.J. Klepczynski, GPS: Primary Tool for Time Transfer, Proceedings of the IEEE, Vol. 87, No. 1, January 1999, pp. 163-172
3. J. Levine, GPS and the Legal Traceability of Time, GPS World, January 2001
4. J. Nawrocki, W. Lewandowski, J. Azoubib, GPS Multi-Channel Time Transfer Unit Based on a Motorola Receiver and Using CCTF Standards, Metrologia, Paris, 2001, in print

GPS TIME ACCURACY AFTER THE SELECTIVE AVAILABILITY (SA) SWITCH OFF

Rainer Krämer, Ulrich Grunert

German Aerospace Center (DLR), Institute of Communications and Navigation,
P.O. Box 1116, D-82230 Wessling, Germany, E-mail: rainer.kraemer@dlr.de, ulrich.grunert@dlr.de

1. ABSTRACT

Since May 1st 2000 the United States have stopped the intentional degradation of the Global Positioning System (GPS) signals available to the public, by dithering the time and ephemeris data provided in the navigation message. This degradation feature was called Selective Availability (SA). Now the civilian users of GPS can use the full positioning and timing accuracy of the so called Standard Positioning Service (SPS).
The paper compares the current GPS capabilities (without SA) to those in the past (with SA) for time dissemination and time transfer applications. For that the paper will present results from the DLR time monitoring station in Oberpfaffenhofen (Germany). Furthermore the basic GPS based methods for time dissemination and time transfer will be outlined and their accuracy discussed.

Keywords: GPS Accuracy, Time Dissemination, Selective Availability

2. INTRODUCTION

Satellite navigation systems like GPS, GLONASS or the planned new European Galileo system are all based on the same basic concept of measuring the signal propagation time from satellites to a receiver. Therefore these systems must ensure that their satellites have a common high stable time base. Thus each satellite is equipped with atomic clocks, which are precisely synchronised among each another. With that all satellite navigation systems distribute a high stable system time over the whole world, which can be used for synchronisation in different fields of applications. In the following figure 2.1 an overview of some of these time applications are shown.

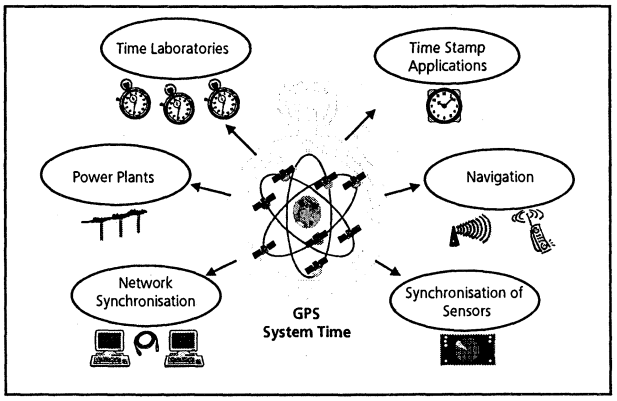

Fig. 2.1: Time applications

Especially the time laboratories, where the national time scales are generated, have high requirements on the time synchronisation accuracy. These national time scales are synchronised to the world time called UTC.

Another application is the satellite navigation. To navigate with GPS the satellite clocks must be synchronised to the system time in the range of nanoseconds. Also for the new generation of digital telecommunication networks and for power plants, synchronisation plays an important role. Furthermore a lot of applications need the synchronisation of sensors, which are located in different places (e.g. VLBI). Commercial transactions like at the stock exchange are synchronised with a time stamp.

Time User	Time Accuracy Requirement in the range of:
Time Laboratories	ns
Navigation	ns
Synchronisation of Sensors	up to ns
Network Synchronisation	up to µs
Power Plants	ms
Time Stamp Applications	ms

Tab 2.1: Time Accuracy Requirements

3. DIRECT GPS TIME RECEPTION

3.1 Basic concept

One method which is used by time applications is the direct system time reception, where the user directly receives the system time from the satellites. With this information he is e.g. able to synchronise applications world wide to this global time.

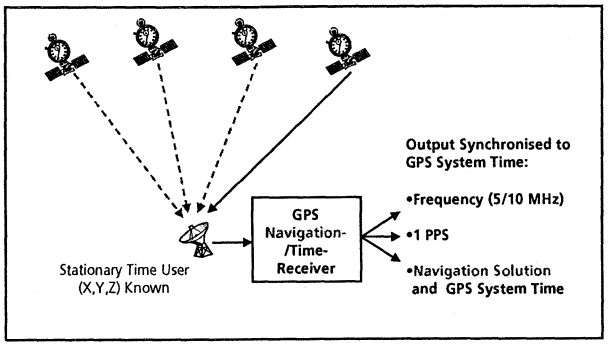

Fig. 3.1: Basic concept of direct time reception

As depicted in figure 3.1, the receiver provides a frequency and a 1pps output synchronised to the GPS system time. For the case of a stationary receiver with well known own antenna co-ordinates, the reception of only one GPS satellite is necessary. In the other case four satellites must be visible to determine both, the position and the system time.

3.2 Results

The following figures show the results of the direct GPS system time reception with and without the Selective Availability (SA) monitored at the DLR in Oberpfaffenhofen (Germany). For the measurements a R100-40T (3S Navigation) time receiver connected to the DLR master clock (passive H-Maser) was used, which makes each 16 minutes one smoothed measurement per each visible satellite. The figure 3.2 shows the results for the time span between 27th March 2000 and 22nd April 2000. In this time span the SA was switched on.

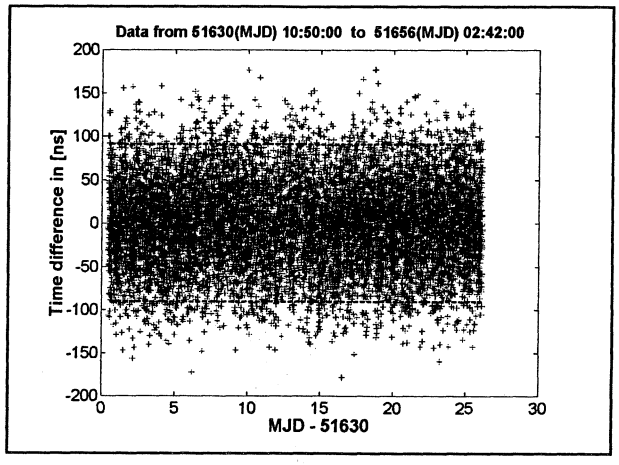

Fig. 3.2: Direct GPS time reception with SA

The dotted line in the picture shows the limit of the range of values within 95% of all measurements can be found. In the above example with activated SA this is about 90.8 ns. The next figure 3.3 shows the measurements between 22nd December 2000 and 19th January 2001, where no SA existed.

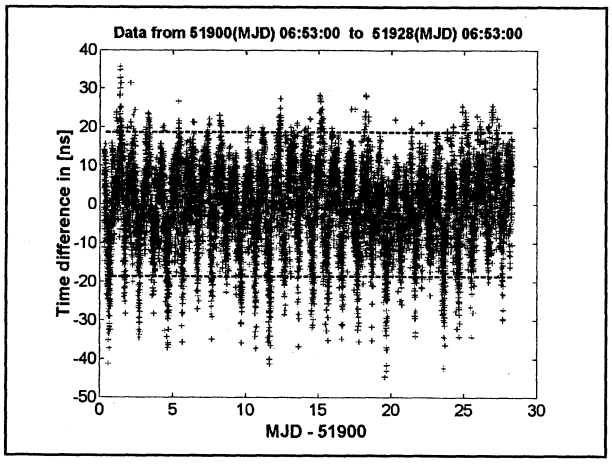

Fig. 3.3: Direct GPS time reception without SA

Now in the case of no SA the 95% accuracy is 18.6 ns, thus the switch off of the SA has improved the accuracy of the direct GPS time reception with a factor of 5.

4. "COMMON VIEW" TIME TRANSFER

4.1 Basic concept

Another kind of time application, which uses the signals of navigation satellite systems like GPS is the time transfer. The purpose of this application is to compare two atomic ground clocks, which can be e.g. located in two different continents on earth. The following figure 4.1 depicts the basic principle of the so called common view (CV) method.

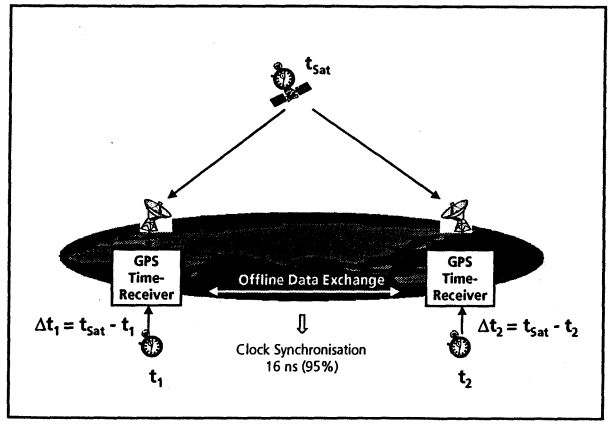

Fig. 4.1: Basic concept of the common view method

Both ground stations, which each contain a GPS time receiver connected to an atomic clock, measure nearly simultaneously the time offsets

$$\Delta t_1 = t_{Sat} - t_1$$
$$\Delta t_2 = t_{Sat} - t_2$$

between their local clock (t_1,t_2) and the clock of a GPS satellite (t_{sat}), which is visible on both stations at the same time. After the measurements, the stations exchange their data (Δt_1,Δt_2) for example by using the internet. The searched difference between the two ground clocks can then simply be calculated as:

$$t_1 - t_2 = \Delta t_2 - \Delta t_1$$

As it can be seen, the satellite clock does not impact in the solution of the comparison of the two ground clocks. Thus the switch off of the SA has no effect to the reachable accuracy of the time transfer with the CV method.

4.2 Results

The accuracy of the comparison of two clocks by using the common view method depends on the distance between the locations of the clocks.

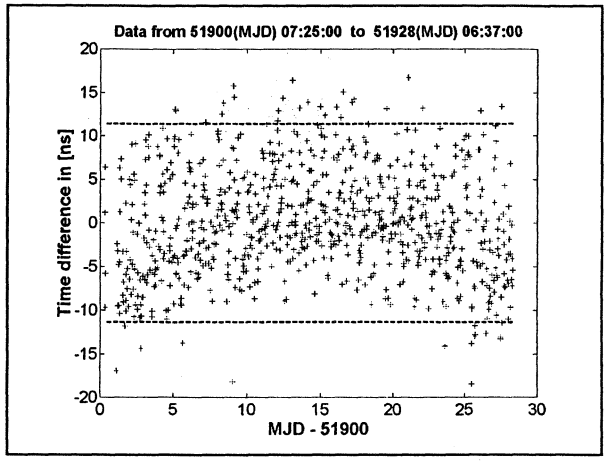

Fig. 4.2: Common view between DLR (Germany) and NPL (Great Britain)

An example of the common view results for a short and a long distance is given in the figures 4.2 and 4.3. In the first case (figure 4.2) a common view is performed between Germany (DLR) and Great Britain (NPL). As it can be seen the 95% accuracy is 11.4 ns. The result over a much longer distance like between Germany (DLR) and United States (USNO) is not as good and has an accuracy of 14.6 ns. The measurements are shown in the figure 4.3.

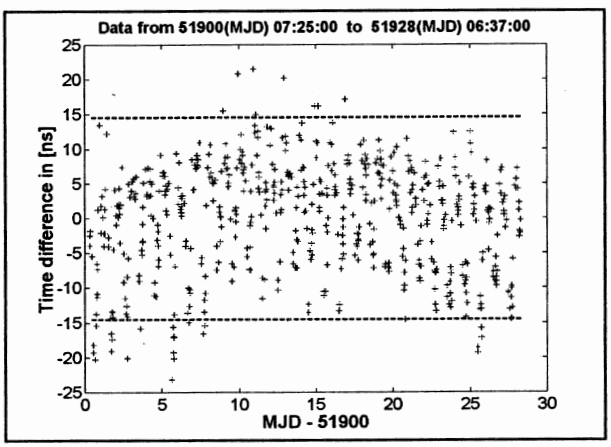

Fig. 4.3: Common view between DLR (Germany) and USNO (United States)

5. POSITIONING ACCURACY

In this chapter the positioning accuracy of GPS with and without the Selective Availability will be compared by using the measurements from the DLR monitoring station in Oberpfaffenhofen (Germany). In the following figures 5.1, 5.2, 5.3 and 5.4 the horizontal and vertical position errors will be shown. After that some histograms of the position errors in east, which are very similar to the errors in north, and height direction are depicted in the figures 5.5, 5.6, 5.7 and 5.8. Current position and time errors are also available at the DLR internet page http://www.dlr.de/KN/KN-NL.

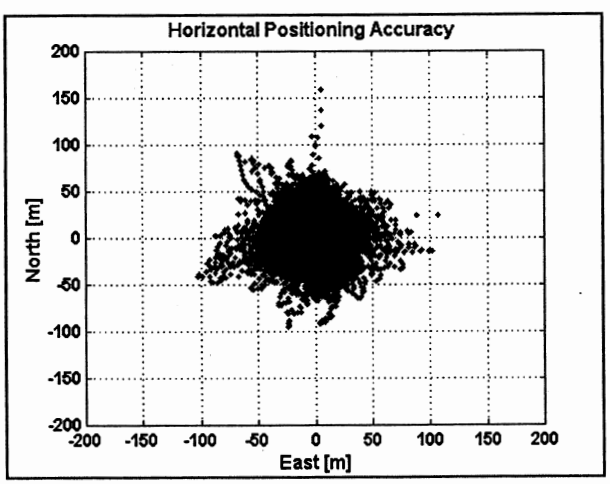

Fig. 5.1: Horizontal Positioning Accuracy with SA

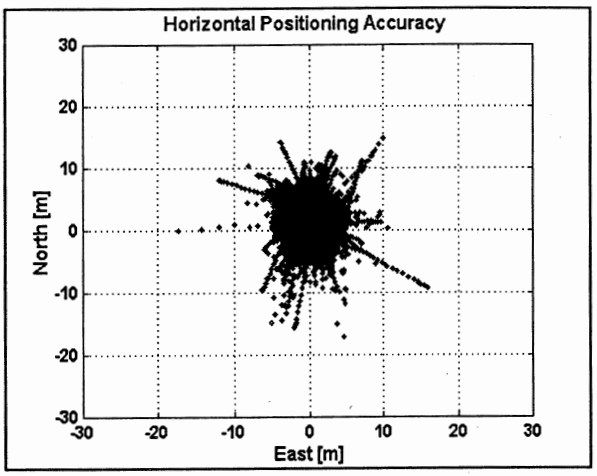

Fig. 5.2: Horizontal Positioning Accuracy without SA

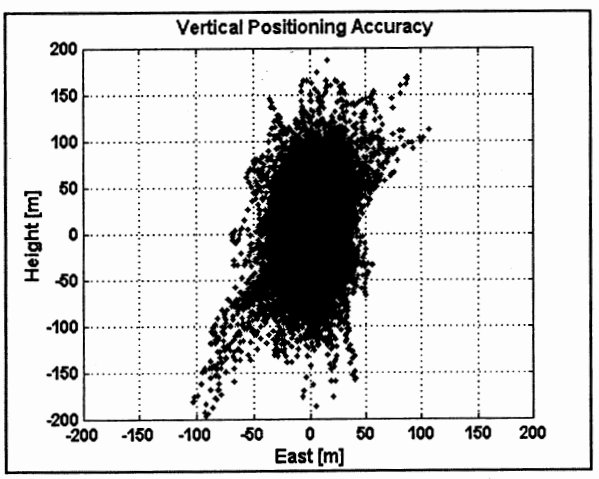

Fig. 5.3: Vertical Positioning Accuracy with SA

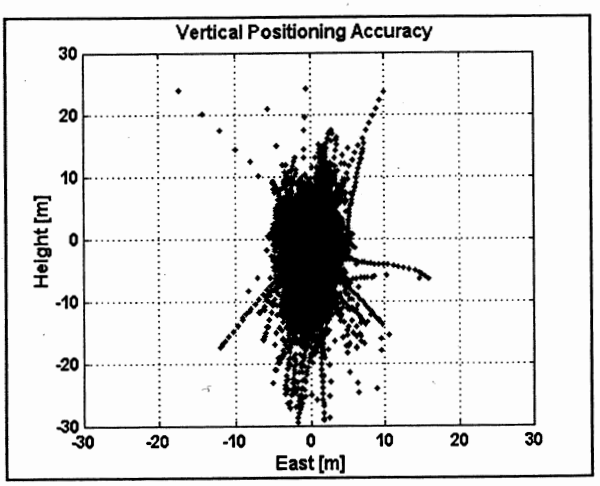

Fig. 5.4: Vertical Positioning Accuracy without SA

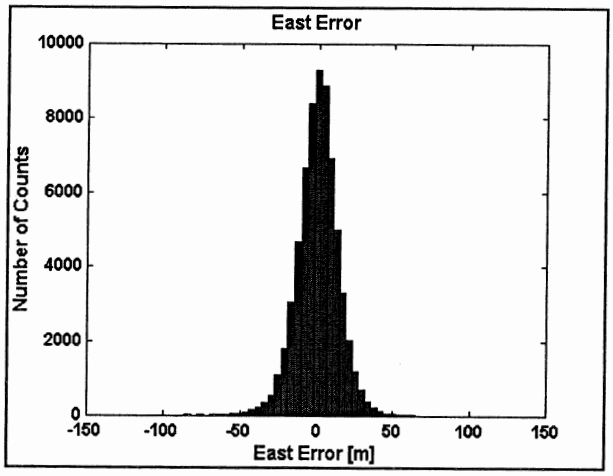

Fig. 5.5: Histogram of the East Error with SA

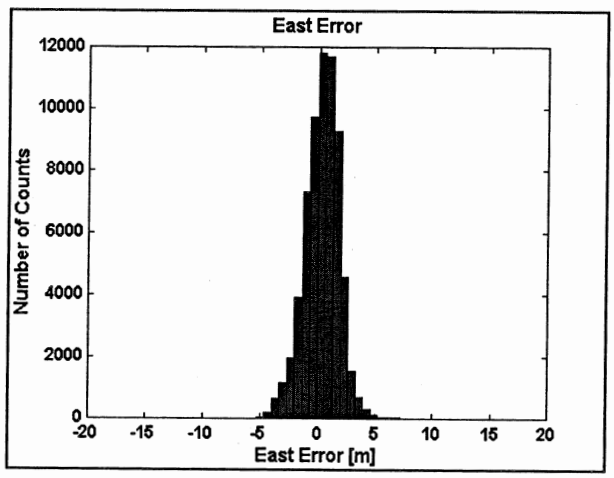

Fig. 5.6: Histogram of the East Error without SA

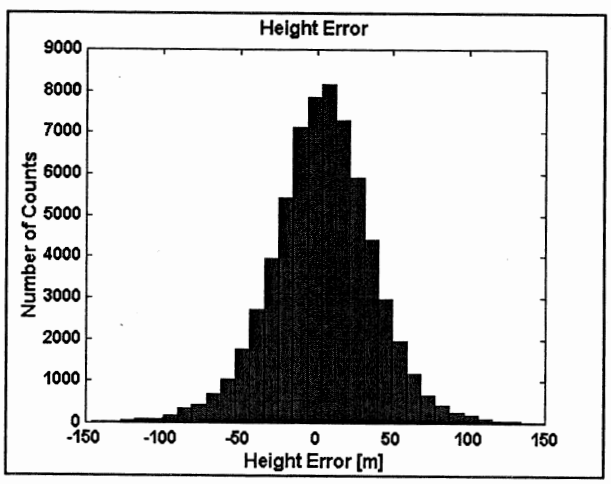

Fig. 5.7: Histogram of the Height Error with SA

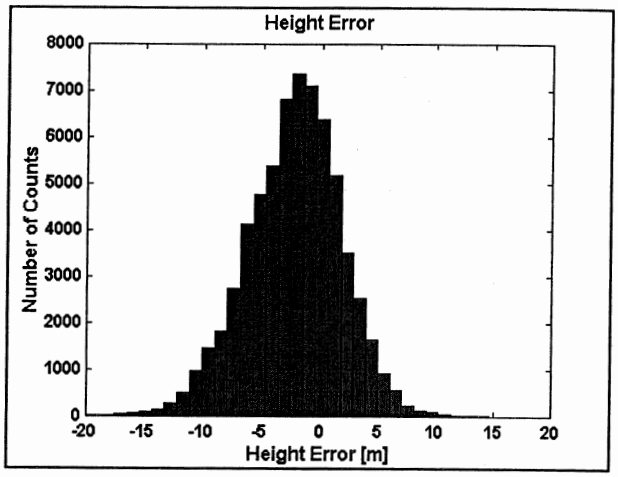

Fig. 5.8: Histogram of the Height Error without SA

6. CONCLUSION

It has been shown that the Selective Availability switch off has improved the position accuracy of GPS up to a factor of 10 and the time accuracy up to a factor of 5. For the time transfer with the common view method no changes have occurred. The main advantage for the time users are now the ability to directly receive the GPS time with an accuracy of about 18.6 ns (95%), which can be used for synchronisation purposes.

7. ACKNOWLEDGEMENTS

The authors would like to thank the National Physical Laboratory (NPL) in Great Britain and the United States Naval Observatory (USNO) for providing their common view data in the internet, which we have used together with our data from the German Aerospace Center (DLR) monitoring station for preparing the common view measurements.

ANALOG VS DIGITAL BROADCAST OF TIME/FREQUENCY INFORMATION

K.Kalliomäki [1], T.Mansten [2]

[1)] University of Oulu, Department of Electrical Eng., FIN-90570 Oulu, Finland
[2)] MIKES, Electricity and Time Metrology, Otakaari 7B, FIN-02150 Espoo, Finland

ABSTRACT

Phase and frequency stability of old analog broadcast time signals and new time signals produced by digital technique has been compared. Both conventional time signals ("peeps") and TV-frame synch. phase has been registered in the National laboratory for more than 20 years. The new digital technique ruins the short term stability but long term (>1 day) stability seems to be good. The results point out the importance of local time signal/frequency transmitters.

1. INTRODUCTION

The National Broadcasting Company of Finland (YLE) has a long tradition in disseminating accurate time signals ("peeps"). During sixties and up to 1972 time signal was traced to GBR. In 1972 it was traced to LORAN-C clocks situated in National Standards Laboratory, and finally in 1989 GPS-clock replaced the Loran receiver.

TV-synchronisation pulse frequency of YLE has been locked to the same above-mentioned clocks since 1985. The intention was to serve calibration laboratories utilising a TV-set and "TV frequency standard", a simple phase locked crystal oscillator which was locked to line frequency of a TV-set.

Digital voice and picture coding started to replace earlier analog systems during the nineties. The use of digital memories to store signals like "peeps" for indeterminate times causes problems. Typical phase plots from both analog and digital epochs of transmission techniques are presented and analysed.

2. TIME SIGNAL OF YLE, THE NATIONAL BROADCASTING COMPANY

Repeatability of the time signal up to 1996 was good, typically 1 μs and its daily SD (standard deviation) less than 1 μs. Naturally phase jumps due to varying link connections occurred frequently.

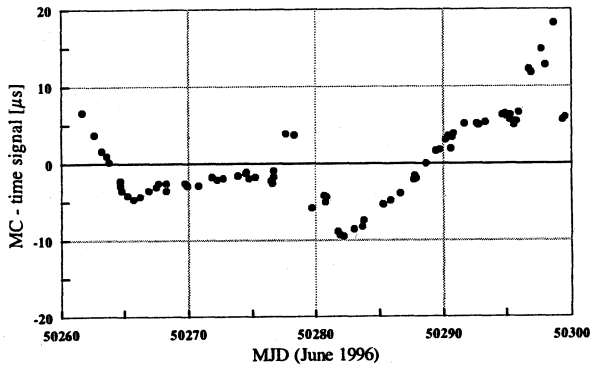

Fig. 1: The quality of analog time signals during one month of 1996. Typical daily SD is 0.5 μs

New digital techniques used for sampling, coding, decoding and storing voice signals impaired the short term stability. One-day repeatability of time signal has degraded to about 10 μs (SD). Probably time signal is stored into hard disc and forwarded to transmission when master clock interrupts the program.

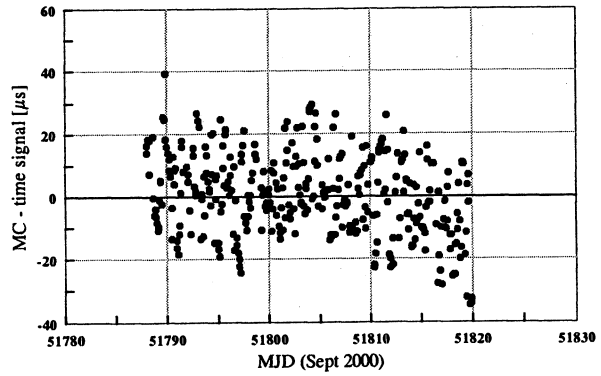

Fig. 2: The increased time signal scatter due to digital studio techniques. Typical daily SD is 12 μs

3. TV FRAME AND LINE FREQUENCIES

TV-method allowed frequency comparison accuracy down to $1 \cdot 10^{-11}$ level in 30 minutes, which is a convenient time to follow high quality crystal oscillators. Calibration laboratories all over in Finland and in Scandinavia utilise TV-signal as a frequency reference.
The uncertainty of TV-line frequency has increased 10-fold due to the new techniques. To obtain a comparison inaccuracy of $1 \cdot 10^{-11}$, one day integration time is needed, see Fig. 4.

New digital links contain memories up to five frames (100 ms). Therefore each link causes a permanent delay to the picture. Crystal oscillators ("PC-clocks") controlling memory read/write operations are probably cheap OCXO:s which are sensitive e.g. to temperature fluctuations. The frequency of those clocks must be locked into frame (or line) frequency using some kind of phase comparator.

Fig. 3 presents what happened on 16th of March 1999 (MJD 51252) when new digital link replaced the old analog TV-link. The phase of frame synchronisation pulse became unstable indicating diurnal variation of nearly 1 μs_{pp}, probably due to changes in temperature. Due to this variation the quality of the frequency is much worse than earlier.

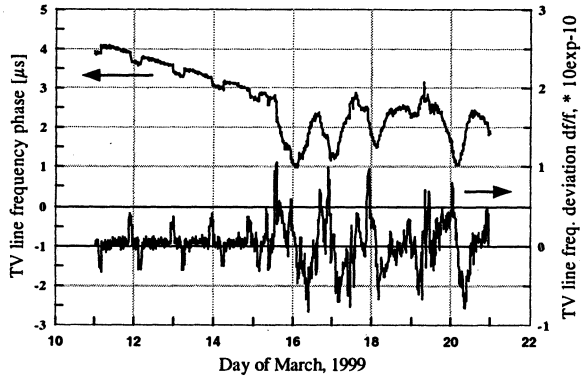

Fig. 3: Effect of a new digital TV-link to the phase of frame synch. pulse. The residual SD of daily frequency deviation changed from $0.44 \cdot 10^{-11}$ to $3.4 \cdot 10^{-11}$ on 15th of March in 1999.

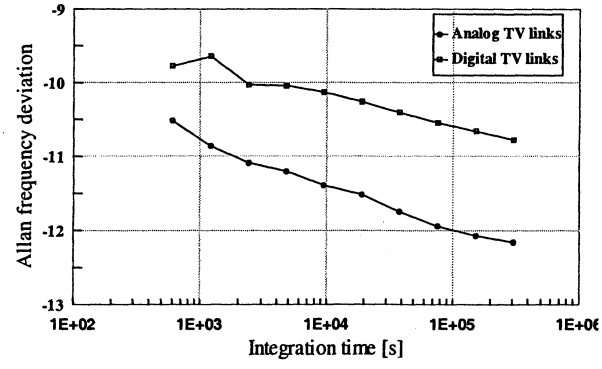

Fig. 4: Allan variance of TV-frame frequency, old and new

4. CONCLUSION

As a conclusion, the significance of classical time signal transmitters has increased in the maintenance and dissemination of accurate national time/frequency information.

5. REFERENCES

/1/ A Computerized Time and Frequency Standards Monitoring System, Kalliomäki, Kalevi; Mansten, Tapio, Proceedings of **4th** Eur. Frequency and Time Forum/EFTF 90. Neuchatel, Switzerland, 13 -15 March 1990. Scientific Communities of Neuchatel and Besançon, Neuchatel. (1990), pp. 177 - 179

/2/ TV-frequency Standard as a Traceability Source in Accredited Calibration Laboratories, Kalliomäki, Kalevi; Mansten, Tapio, Proceedings of **7 th** European Frequency and Time Forum Neuchatel, 16 - 18 March 1993, Switzerland, (1993) , pp. 383-385

/3/ TV Network Signal as a Temporary Source for Navigation, Kalliomäki, Kalevi, Mannermaa, Jari, Proceedings of **11 th** European Frequency and Time Forum, Neuchatel, Switzerland, (1997), pp. 486-490

ULTRA PRECISE TIME DISSEMINATION SYSTEM

C.LOPES, P.HOURS, B.RIONDET

IN-SNEC a company of INTERTECHNIQUE GROUP

INTRODUCTION

During the last two meetings : the Joint Meeting of the 13th European Frequency and Time Forum and the IEEE International Frequency Control Symposium in Besançon (FRANCE) 12-16 April, 1999 and the 14th European Frequency and Time Forum in Torino (ITALY) 14-16 March 2000, we presented an Ultra Precise Time Dissemination System reporting the possibility of performing time transfer between two areas separated by few kilometers with an accuracy of a few picoseconds. We demonstrated the ability to synchronize remote systems within 10 to 30 picoseconds over a temperature variation of 4°C. In Torino we also demonstrated improved temperature corrections in order to accommodate drift in electronic transit time with temperature operating range extended from 15°C to 35°C.

The path variation range can be as high as several nanoseconds and the synchronisation process is maintained in the picosecond range.

In the present time we are getting similar results from production equipements that confirm the reliability of the measurements presented at Besançon and Torino.

The architecture of the system is based on a master equipment broadcasting a digital message to remote slave equipment linked to the master by optical fiber. The system continuously monitors and compensates the transit time variations between the master and slaves. The transit time stability between the master and slaves is maintained in the 10 picoseconds range even if the time variation of the optical path is on the order of one nanosecond or more. The operating range can be extended from 10 °C to 40 °C with slight performance degradation. The system can address from 1 to 400 slaves.

SYSTEM PERFORMANCE

Figure 1 describes the system. Due to the low propagation loss along the fiber, we can feed slaves separated from the master and each other by kilometers. The propagation delay along the fiber change with temperature, the coefficient is 100 ps/°C/km and 200 ps/°C/km depending the fiber used [5].

The system is not only able to measure transit time transfer but he has the capability to compensate the transit time variations. The transit time is compensated between the master and each slave then it is possible to create an accurate time interval between two slaves [3,4,5,6].

The accuracy of the time propagation measurement

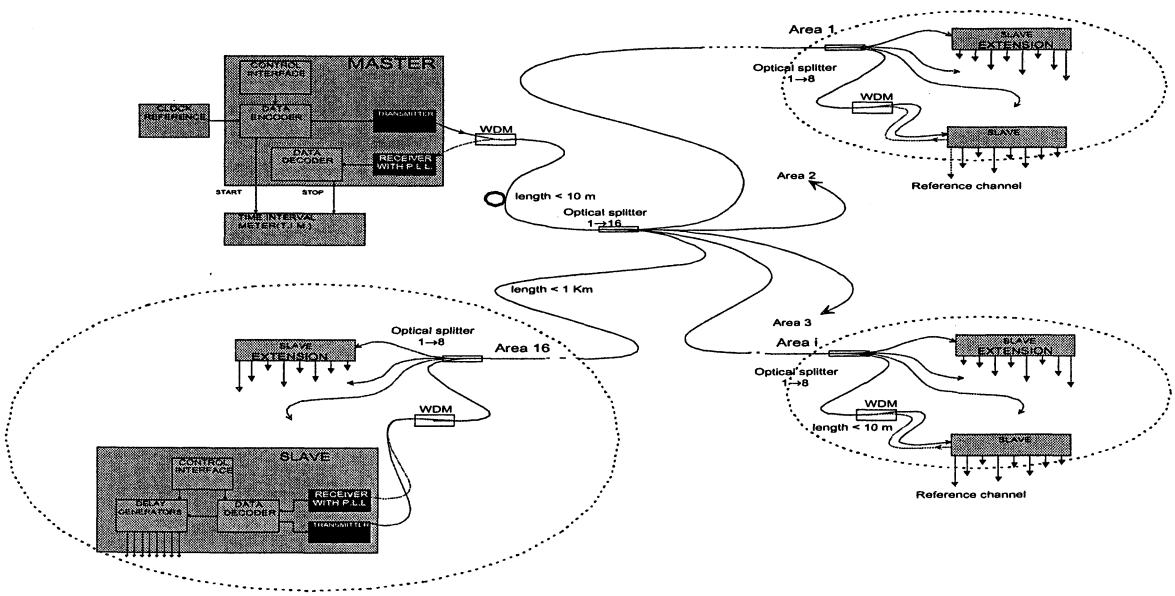

Figure 1 : System Architecture

depends of the fiber length.

The accuracy is on the order of a few picoseconds for a fiber length of few kilometers.

As the delay generated by the equipment is formed by the intrinsic minimum delay of the equipement and a programmable delay we should carrefully study the behavior of the minimum delay and the programmable delay.

The study of the programmable delay generator has already been carried out [6] and those of the production equipment work like the prototype.

First we will show the minimum delay variation and the effect of appropriate corrections of the minimum delay for these equipment and then as the purpose of this system is to allow the synchronisation of equipment located in different areas we will show the accuracy and stability of the synchronisation process obtained with the production equipment.

Before entering in the measurements description we will despict the test setup used.

Test setup :

Figure 2 shows the setup used to measure these performances. We can see a master and two slaves equipment linked to the master through an optical splitter and the necessary optical fiber. One of the two slaves shown is the device under test and the other one is the reference slave of the test setup. An electrical swiching matrix is used to bring the signals to the interval meter. A computer is controlling all the system using TCP/IP protocols for master and slaves and IEEE488 for instrumentation devices.

With this setup we can characterize all the transit times involved in the synchonisation process. We use climatic chambers to vary the temperature on the master, the slaves or the optical fiber.

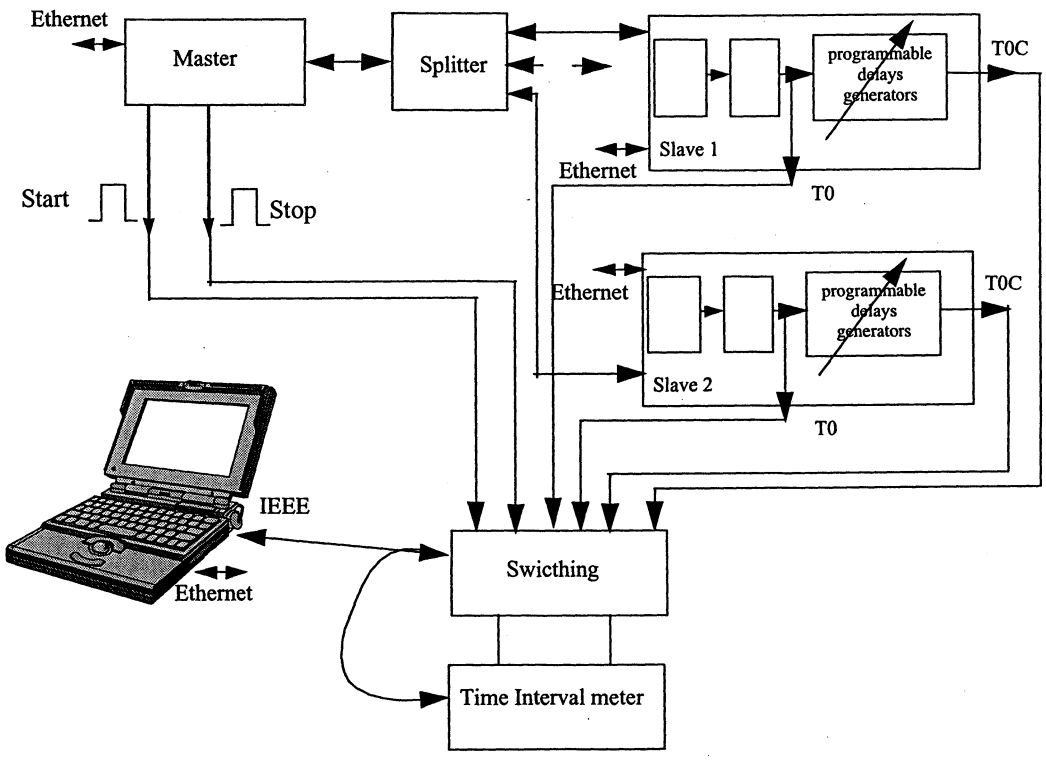

Figure 2 : System Architecture

Minimum Delay variation :

Figure 3 shows the uncorrected Minimum Delay variation against temperature variation of five differents production slaves yet delivered to our customer.

The ambient temperature is varied from +/- 10 °C around 25 °C this is why the temperature axis is graduated from -10 °C to 10 °C it is a temperature relative to 25 °C.

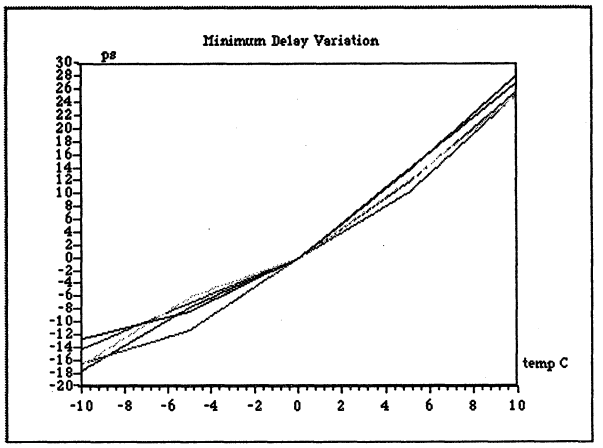

Figure 3 : Uncorrected Minimum Delay variation

The programmable delay generators [6] are set to 0 and the minimum delay is recorded when temperature is varied.

We can see on these curves that the variation of the minimum delay is nearly the same for these five different production equipment.

Figure 4 shows the effect of the correction on the minimum delay. The blue curve shows one of the minimum delay of the figure 3 and the red curve (flat) shows the corresponding corrected minimum delay over the temperature range from 15 °C to 35 °C expressed relatively to 25 °C on the temperature axis of the figure.

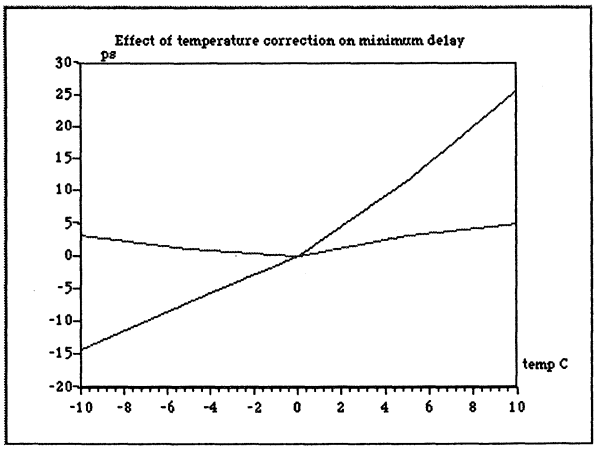

Figure 4 : Corrected Minimum Delay variation

The residual minimum delay variation with correction is in the order of 3 to 4 picoseconds peak to peak.

Figure 5 shows the corrected Minimum Delay variation for 4 equipements over a temperature variation from 20 °C to 30 °C. The temperature scale of the graphic is relative to 25 °C.

The blue and red curves are confounded between 20 °C and 25 °C.

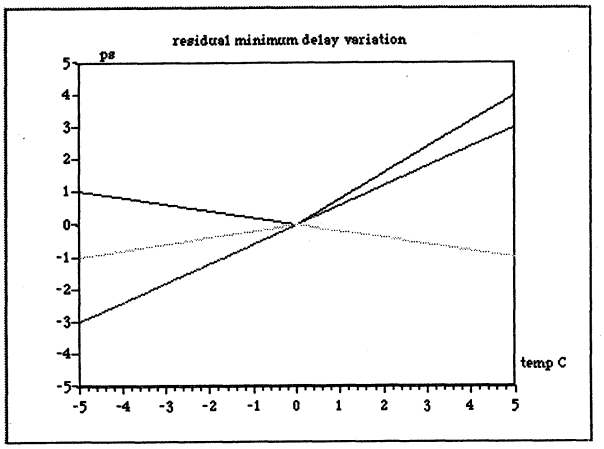

Figure 5 : Corrected Minimum Delay variation

The green and yellow curves are confounded between 20 °C and 25 °C. This is showing that for all the equipements the residual minimum delay over temperature is on the order of 3 to 4 picoseconds peak to peak. These residual variations are very weak and are in the "noise floor" of the experiment.

Figure 6 shows the jitter of the experiment, the jitter is of **6,2 ps** rms.

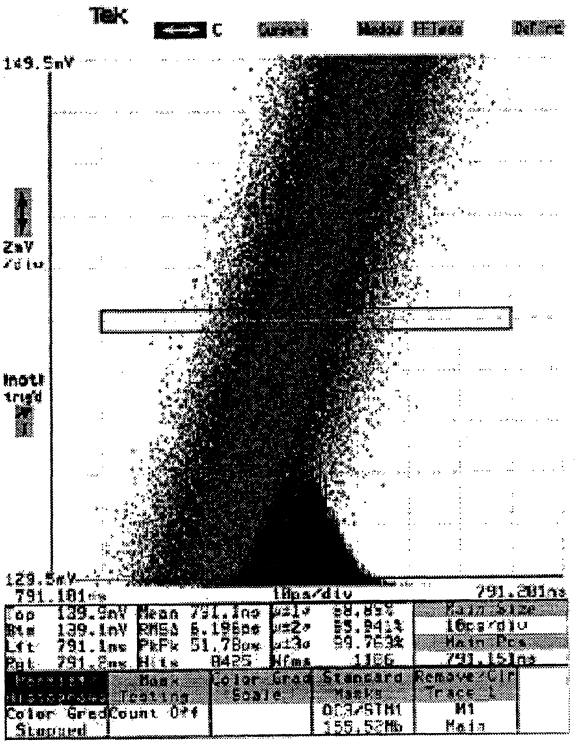

Figure 6 : Jitter of the experiment : 6,2 ps

The jitter of the time interval meter is about 3 to 4 ps rms then we can estimate that the jitter of the equipement is less than **5 ps** rms.

Synchronisation :

This system has been designed to perform synchronisation process between remote equipment. We should be able even if the equipment are not in "visibility" to define an accurate interval between them as described in figure 7.

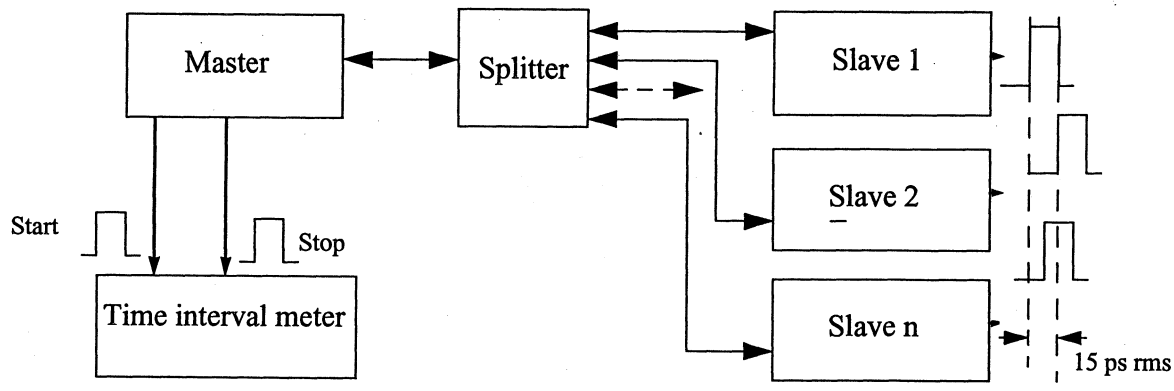

Figure 7 : Synchronisation process

In our laboratory using the test set up shown in figure 2 we demonstrate that this goal is achievable[5,6]. Now with the results obtained with the production equipment we are demonstrating that these results remains stable and reliable giving confidence in the method used to achieve this performance.

Figure 8 shows for four different equipment the difference between the programmed and the measured value of an interval between two slaves. An interval of 50 µs is programmed between the two slaves, the test setup is maintained at constant temperature when the temperature of the equipment under test is varied from +/- 5 °C around 25 °C.

The variations of the measured interval are recorded at different temperatures and compared to the value at 25 °C.

The peak to peak deviation is of few picoseconds and these results are also very similar to those obtained with the prototypes.

Now we will demonstrate the ability of the system to compensate a variable path length between master and slaves. We still monitoring the interval between the two slaves while we modify the path transit time between the master and the slave under test.

To perform this test all the equipment and apparatus are at constant temperature, one of the slaves is linked to the master by a 1 km long optical fiber. This fiber is placed into a climatic chamber and the temperature inside the climatic chamber is varied from 20 °C to 30 °C. We program a 50 µs interval between the two slaves and we compare the interval measured at different temperatures to the interval we have when the fiber is at 25 °C.

Figure 9 shows these measurements for four different

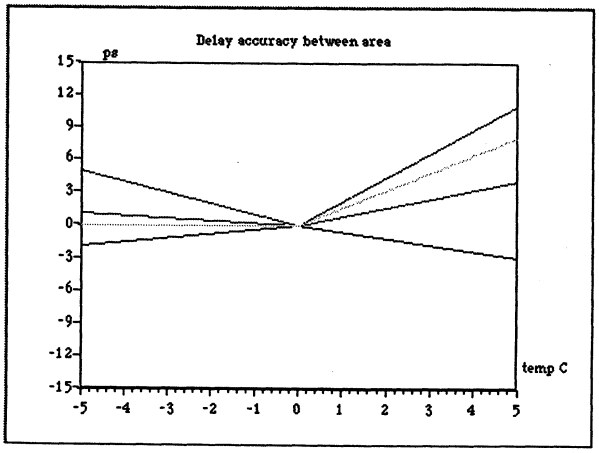

Figure 8 : Synchronisation process versus temperature

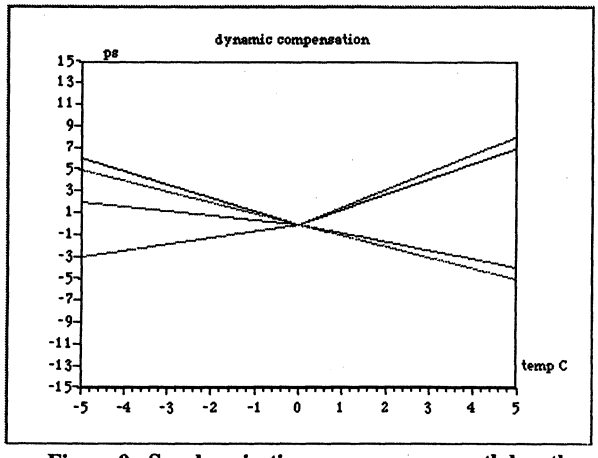

Figure 9 : Synchronisation process versus path length

equipment.

The coefficient of path length variation is about 200ps/ km/°C. The path length varies of about 2 ns when the temperature of the fiber changes from 20 °C to 30 °C.

This path length variation is compensated by our equipment within an accuracy better than **10 ps** peak to peak.

Figure 10 shows the path length variation in nanoseconds when the temperature of 1 km long of optical fiber varies of +/- 5 ° C around 25 °C.

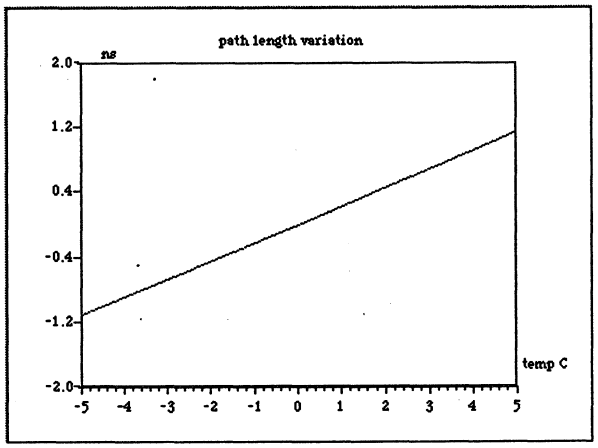

Figure 10 : Path length variation

The accuracy and stability shown by figure 9 is to be compared to this obtained with the prototypes which can be observed on figure 11. On the prototypes testing, the path length was of several hundred of picoseconds but not two nanoseconds and the peak to peak deviations is about **20 ps** (6,8 rms).

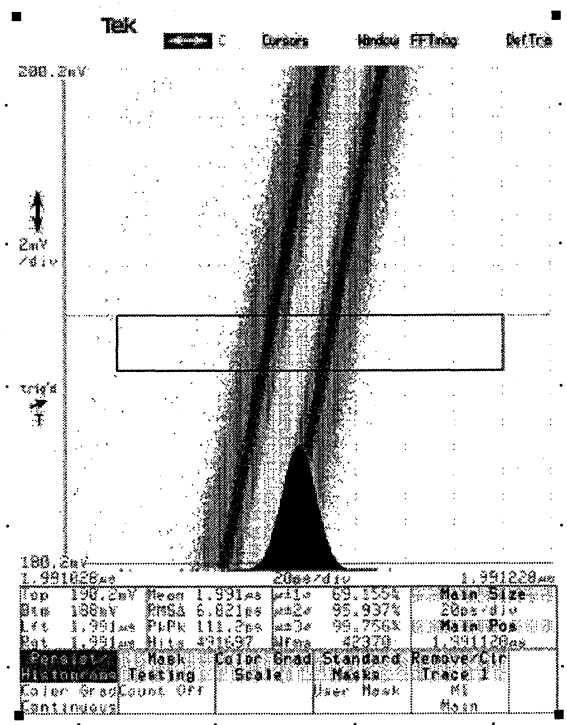

Figure 11 : Synchronisation process : prototypes

CONCLUSION

The performances of our synchronisation system demonstrated in the last two meetings are confirmed with the production equipment. The behaviour of the production equipement is very homogeneous.

The production equipment are even better than the prototypes.

Now we are working in an improved model for minimum delay corrections.

We would like to perform synchronisation process using this method with equipment separated by larger distancies than one kilometer.

We hope this system has the potential to perform synchronisation overseas or over country accepting some degradation of the performances.

REFERENCES

[1] L. Primas R. Logan, G. Lutes, "Application of ultra-stable fiber optic distribution system ," 43rd Annual Symposium on frequency control 1989 pp 202,211 June 89 IEEE.

[2] S.R. Jefferts, M Weiss, S. Dilla and T. Parkeer, «Two-way time and frequency transfer using optical fibers» Conference on precision electromagnetic measurements 17-21 June 96 Braunschweig, Germany pp. 520, 521 IEEE, ISBN 0 7803 3376 A.

[3] C. Lopes «Maquettage et validation d'une liaison optique numérique bidirectionnelle faible gigue» June 1998 private communication.

[4] C. Lopes «Cahier de Résultats d'Essais de la maquette de liaison bidirectionnelle». November 1998 private communication

[5] C. Lopes, B. Riondet «Ultra Precise Time Dissemination System». Joint Meeting of the Frequency Control Symposium and the European Frequency and Time Forum April 1999, Besançon, France.

[6] C. Lopes, B. Riondet «Ultra Precise Time Dissemination System». 14th European Frequency and Time Forum March 2000, Torino, Italy.

B.RIONDET/ C.LOPES/ P.HOURS
IN-SNEC
5 Av. des Andes
91943 Les Ulis Cedex
FRANCE
tel: 33 1 69 82 79 70 / 78 53 / 78 16
fax: 33 1 69 07 39 50
e-mail : briondet@wanadoo.fr
e-mail : christian.lopes@free.fr

TIME TRANSFER TO TAI USING GEODETIC RECEIVERS

P. Defraigne[1], C. Bruyninx[1], J. Clarke[2], J. Ray[3], K. Senior[3]

[1] Royal Observatory of Belgium, Brussels, Belgium
[2] National Physical Laboratory, London, UK
[3] US Naval Observatory, Washington, US

ABSTRACT

We present a procedure to contribute to TAI without a time receiver, but using any geodetic GPS receiver driven by an external frequency. The CCTF files are generated from the RINEX observation files (1-second or 30-second sampling rate). We apply this procedure succesfully on different types of geodetic receivers. The validity of the method is demonstrated from the comparison of the results with colocated time receivers. The clock resets which commonly occur in geodetic receivers are accounted for by monitoring with a time interval counter the 1pps out signal of the receiver.

1. INTRODUCTION

The International Atomic Time scale (TAI) is computed by the Bureau International des Poids et Mesures (BIPM) from a set of atomic clocks distributed in about 40 time laboratories over the world. In order to perform the link between the different clocks, the time labs are equipped with time receivers, which observe the GPS satellites following the international tracking schedules distributed by the BIPM. The time receivers are connected to the 1 pps (pulse per second) signal delivered by UTC(k) (local realization of UTC in the laboratory 'k', to which all the clocks of the laboratory are reported). An internal software analyses the C/A-code data during each 13-min track and computes (UTC(k)-GPS time) at the midpoint of the track, following a given procedure [1]. These clock offsets are collected in a well-determined format, called CCTF (defined by the Consultative Committee for Time and Frequency). For the computation of TAI, the BIPM computes the differences between the CCTF files (the so-called 'common-view' method) in order to get the time comparisons between the different UTC(k)'s. For that reason, the realization of TAI is only valid if all the time receivers involved apply exactly the same observing and analysis procedure for generating the CCTF files.

One of the goals of the IGS-BIPM pilot project [2] is to establish a link between the IGS clock combinations (satellite and receiver clock offsets [3]) and TAI. In a recent study [4], we have shown that it is possible to generate CCTF files from geodetic receivers using the RINEX observation and broadcast navigation files. In this previous paper, we used data from the Ashtech ZXII-T receiver installed at the Royal Observatory of Belgium (ORB). This receiver has the advantage of allowing continuous time transfer: the internal oscillator has been disconnected and an external clock frequency is used to steer the receiver. Moreover, the receiver synchronizes its internal 1pps on the 1pps signal provided by the external clock, so that its internal timing is directly a mirror of the external clock which can be chosen as UTC(k). When comparing the RINEX-based CCTF results obtained from the ZXII-T receiver with the CCTF results generated by a colocated time receiver (R100-30T from 3S-Navigation), we obtained satellite-dependent residuals for which the origin was unclear. We test here the procedure using two other geodetic receivers colocated with time receivers: a Javad Legacy at NPL (National Physical Laboratory, London) and an AOA TTR12 in USNO (US Naval Observatory, Washington). Contrary to the Ashtech ZXII-T, these receivers do not accept a 1 pps in, so that a Time Interval Counter (TIC) is necessary to compute the clock offsets between the receiver clock (1 pps out) and the external clock corresponding to UTC(k). These time interval measurements are necessary to correct for the occasional clock jumps, and as shown in this paper, must also be used to correct the data for the temperature-dependent effects on the receiver clock.

2. 30-SECOND VERSUS 1-SECOND RINEX FILES

The values of 'UTC(k)-GPS time' given in the CCTF files result from a well-defined analysis procedure [1] based on the use of raw single frequency GPS C/A-code data taken at a 1-second sampling rate. However, within the IGS, the standard sampling interval is 30 second. If these geodetic receivers would be used to contribute to TAI, we need to define a procedure, similar to the CCTF convention, but using the 30-second data.
In the CCTF conventions the 780 pseudo-range data of each staellite track are separated into 52 blocks of 15 data points. In each of the blocks the 1-second data are smoothed using a quadratic polynomial. The rest of the procedure (corrections for geometric distance, ionospheric effects, tropospheric effects, satellite clock offsets etc.) is applied on the 52 points corresponding to the values of the quadratic fits at the midpoints of the blocks. The final results correspond to the value at the midpoint of the 13-minute track using a linear fit applied to the 52 corrected points.
In order to use the 30-second RINEX files, we chose to apply a linear fit directly to the 26 points corresponding to the 13-min track (after having corrected for the effects mentioned here above and given in the CCTF conventions). Figure 1 shows the comparison between the pseudo-CCTF results so obtained and those obtained from the 1-second RINEX files following strictly the CCTF conventions. The data used are 1-second RINEX files generated by the receiver Ashtech ZXII-T of Brussels, on which we performed a decimation in order to get the corresponding 30-second RINEX files.

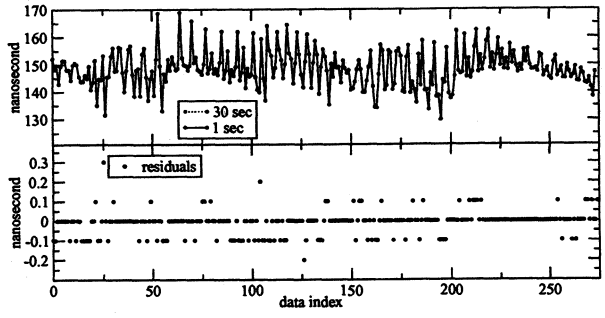

Figure 1. Comparison between the CCTF results 'UTC(ORB)-GPS time' obtained with the use of 1-second and 30-second RINEX files from the receiver Ashtech ZXII-T from Brussels.

The residuals between both approaches are smaller than 0.3 ns, well below the precision of the time transfer by common view with the C/A code (4 ns, [5]). This result indicates that the 30-second data from IGS receivers can be used as is, certainly now that SA has been removed.

3. IONOSPHERIC CORRECTIONS

When comparing the CCTF results provided by a time receiver and those obtained from the RINEX-CCTF procedure, some large differences (up to 20 ns) can appear. This is due to the ionospheric corrections. The ionospheric parameters (α_i, β_i) used in the Klobuchar model and broadcast with the navigation message are modified during the day, and the time receivers use them in real time as they are broadcast. The RINEX navigation files, on the other hand, are produced once per day, and hence the ionospheric model is computed with the same set of parameters for the whole day. So, occasionally these parameters are different from the ones which are broadcast and used by the time receiver. Furthermore, the ionospheric model parameters in RINEX navigation file headers translated from several receiver-dependent formats are bogus (TEQC bug report, http://www.unavco.ucar.edu/software/teqc/bugs.html) and can then give rise to unrealistic results, as shown in Figure 5 where the two boxes indicate periods of bad ionospheric parameters in the RINEX navigation files of BKG (European Regional IGS Data Center).
For these reasons, when comparing the CCTF results provided by a time receiver and those obtained from RINEX-CCTF procedure, the same ionospheric corrections are used in both data sets. Note also that if the ionospheric corrections are replaced by an IGS ionosphere model, this no-coincidence of the Klobuchar parameters will not affect the TAI computation.

4. TESTS WITH DIFFERENT GEODETIC RECEIVERS

The RINEX-CCTF procedure has firstly been applied to the 30-second RINEX files from a Javad Legacy receiver installed at NPL and compared to those generated by two time receivers in NPL: an AOA TTR5A and an NPL-TFS. Figure 2 shows the residuals between the RINEX-based CCTF results and the time receiver CCTF results. The noise level (rms of 3.6 ns for the comparison between the Javad and the multi-channel time receiver NPL-TFS) of these residuals is the same as the noise level of the residuals between the CCTF data generated by the

two time receivers. This demonstrates that the use of geodetic receivers for time transfer to TAI, using the RINEX-CCTF procedure, is totally justified. Furthermore, as shown in Figure 3, there are no satellite-dependent biases as it was the case when comparing the RINEX-based CCTF results of an Ashtech ZXII-T with a R100-30T from 3S-Navigation [4]. So, as already suspected in [4], these biases were probably due to some satellite-dependent corrections which are applied in the R100-30T software and which differ from the CCTF conventions.

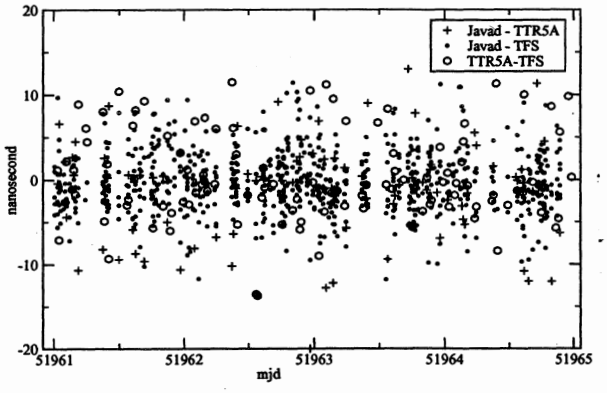

Figure 2. Residuals between the RINEX-based CCTF results of the receiver Javad Legacy and the NPL time receivers CCTF results.

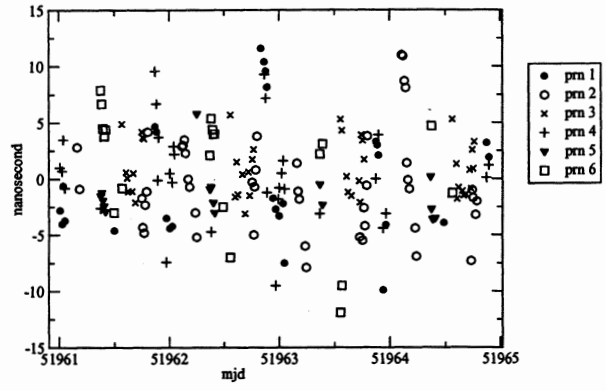

Figure 3. Same as Figure 2 but plotted for several satellites separately.

A second test has been performed with an AOA TTR12 receiver installed in USNO. This receiver provides both RINEX files and 'pseudo-CCTF' files, i.e. clock offsets between the external clock and GPS time, computed for the satellites and epochs appearing in the BIPM tracking schedules, but not exactly in the same way as indicated in the CCTF conventions. We took two days of data and compared the RINEX-based CCTF files with the results provided by the receiver. As the TTR12 receiver uses measured ionosphere instead of modelled, we corrected for this difference in the comparison. As shown in Figure 4, the noise level of the residuals has the expected amplitude (RMS of 2.5 ns) but there are satellite-dependent biases mainly due to the fact that the TTR12 computes the time offsets using the P1 code rather than the C/A code.

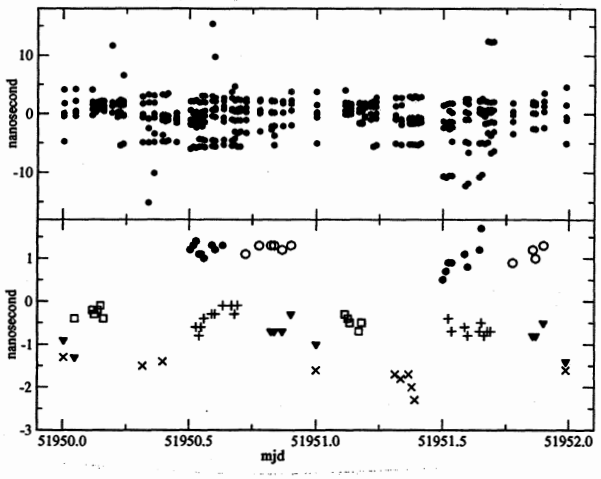

Figure 4. Residuals between the RINEX-based CCTF results of the receiver AOA TTR12 and the 'pseudo-CCTF' results generated by the receiver, after correcting for the differences in ionospheric models.

An important point to consider when using geodetic receivers for time transfer to TAI is the correction for clock jumps which can occur in geodetic receivers. The recurrence of such jumps depends on the receiver type. As an example, we applied the RINEX-CCTF procedure to one month of data collected by different kinds of receivers involved in the IGS and driven with hydrogen masers. As shown in Figure 5, some receivers reset their internal clock frequently so that a strict monitoring of their 1pps out is needed to allow a continuous time transfer within the frame of TAI.

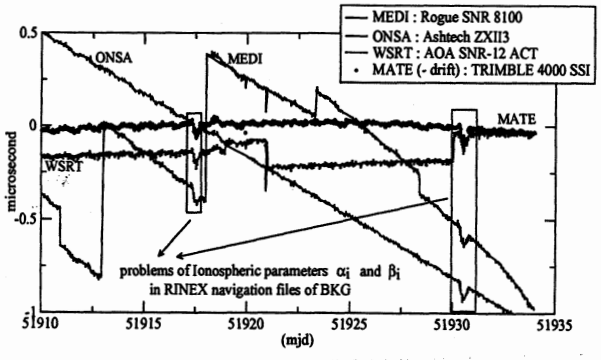

Figure 5. CCTF results 'receiver clock - GPS time' for several receivers involved in IGS.

There are several possible methods to determine the jumps: a first one consists in using the CCTF results and computing the difference between the clock offset before and after the jump, but the precision of this method is limited by the noise of the C/A code (4 ns) and the small number of data (due to the limited number of 13-minute tracks). A second procedure consists in monitoring the receiver 1pps out by a comparison with the 1pps signal provided by the atomic clock used to drive the receiver. This monitoring must be done with a Time Interval Counter (TIC). We tested this method on data of a receiver Rogue SNR12 installed in Brussels, driven by the frequency of UTC(ORB), and for which we artificially generated a clock jump by resetting the receiver. The receiver 1pps out was connected to a TIC (Stanford SR-620) and monitored with respect to the reference clock UTC(ORB). The jump was determined with an estimated error of +/- 24 ps, well inside the precision of the time transfer to TAI. This correction can then be applied to the CCTF results. The receiver clock jumps can also be determined using a global analysis of GPS codes and phases using the IGS precise ephemerides. Our analysis estimated the precision of the clock jump determination as about 15 ps.

As a last remark, note that in order to know the absolute values for the time transfer, we have to measure the receiver clock offset at an initial epoch, accounting for all cable delays receiver hardware delay (which can be determined by a differential calibration using a calibrated time receiver, as proposed in [6]). Then the receiver 1pps must be monitored in order to correct for any subsequent jumps.

5. RECEIVER CLOCK VERSUS EXTERNAL CLOCK

Figure 6 shows the clock offsets between the Brussels' Rogue SNR12 receiver clock 1pps out and UTC(ORB). While the receiver is driven by the 5 Mhz frequency of UTC(ORB), the signal does not scatter randomly around a constant, but presents some variations. These variations are weakly correlated with the temperature variations in the lab. It can be seen that the large temperature variation of about 5 degree leads to a receiver clock variation of about 2 ns, i.e. nearly at the level of the precision of the time transfer to TAI. However, some other variations in the 1 pps out signal cannot be explained by temperature sensitivity, and their origin is still unclear. This variability of receiver clock is not a problem for the time receivers because their internal software corrects for the clock offsets between the receiver clock and the 1pps signal coming from the external clock. For geodetic receivers, since we want to have the exact value of the offset between the external clock and the GPS time, it is thus necessary to correct the RINEX-based CCTF results for the clock offsets between the receiver clock and the external clock as measured by the TIC.

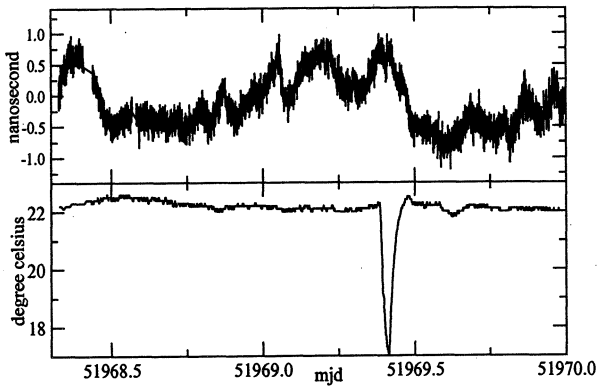

Figure 6. (top) Time interval measurements of 1pps out - UTC(ORB) for the receiver Rogue SNR12 of Brussels driven by UTC(ORB); (bottom) temperature variations in the time lab.

6. CONCLUSIONS

We have demonstrated that the software developed in [4] to generate the CCTF files can be applied to any geodetic receiver driven by an external frequency and having an output signal of the internal clock 1pps. The exact procedure corresponding to the CCTF conventions requires the use of 1-second RINEX files. We modified this procedure in order to use the standard 30 second-RINEX file, and showed that the differences between the CCTF results of both approaches are below 0.3 ns, well inside the precision of the common-view time transfer used for TAI (4 ns). So, the 30-second data from IGS receivers can be used as is for time transfer to TAI.

We also pointed out the necessity to monitor this 1pps out in order to correct for the clock jumps and for the variations with respect to the external clock used to drive the receiver. These variations are certainly receiver-dependent, but their origin of is not yet fully explained. This will be the subject of a further study.

7. REFERENCES

[1] Allan, D.W., and C. Thomas, "Technical directives for standardization of GPS time receiver software", Metrologia 31, PP. 69-79, 1994.

[2] Ray, J.R., "IGS/BIPM time transfer project", GPS Solutions, 2(3), pp. 37-40, 1999.

[3] Kouba, J., and T. Springer, " New IGS Station and Satellite Clock Combination", GPS Solutions, issue 4(4), in press, 2001.

[4] Defraigne, P., and C. Bruyninx, 2001, " Time Transfer for TAI using a geodetic receiver, An Example with the Ashtech ZXII-T", GPS Solutions, in press.

[5] Levine, J., "Time transfer using multi-channel GPS receivers", IEEE Trans., UFFC, 46(2), pp. 392-398, 1999.

[6] Petit, G., Z. Jiang, P. Uhrich, F. Taris, "Differential calibration of Ashtech ZXII-T receivers for accurate time comparisons", Proc. 14th EFTF, in press, 2000.

Award of the «2001 Prix Européen Temps-Fréquence»

delivered by the Société Française des Microtechniques et de Chronométrie (SFMC)

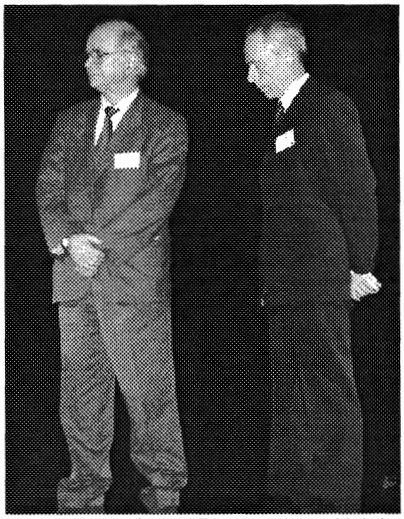

Pierre Cerez (left) and Dieter Kirchner (right)

This evening is for me an exceptional opportunity. For the fifth time, I am going to publically introduce to you the winners of the «2001 Prix Européen Temps-Fréquence». As the President of the Société Chronométrique de France, I believe this kind of event is extremely important for our scientific community, because it triggers competition and recognizes exceptional contributions. Like the previous winners, the winners this evening deserve worldwide recognition.

Again this year the choice of our committee was a hard task since many extremely good candidates were nominated. It is for me a great pleasure to announce that, in its session of February 21, 2001, the committee has attributed the Award simultaneously to :

Dr Pierre CEREZ
for his outstanding contribution to the study and development of optically pumped cesium beam frequency standards,

and to

Dr Dieter KIRCHNER
for outstanding contributions in development of satellite synchronisation techniques, in particular the two ways satellite time and frequency transfer, and for realization of the first telephone time code generators now largely used in the dissemination fields.

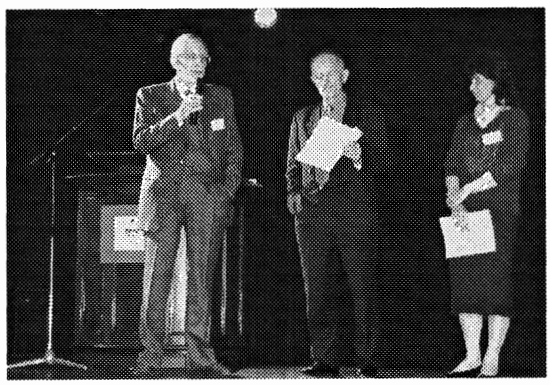

From the left: Claude Audoin, Raymond Besson and Patrizia Tavella

Claude Audoin will now present the work of Pierre Cerez whereas Patrizia Tavella will present the work of Dieter Kirchner. Then they will help me to deliver the award certicate and check...this is probably needed because of my real emotion in front of you.

Prof. Raymond J. Besson
President of SFMC

Meeting report

Event	15th European Frequency and Time Forum
Date	6-8 March '01
Organizer	FSRM - Swiss Foundation for Research in Microtechnology, Neuchâtel, Switzerland
Location	University of Neuchâtel, Switzerland
Number of participants	308
Countries represented	25 (for details see next page)
Number of papers	
- invited	4
- orals	52
- posters	58
Sessions	19 (opening + 10 led in parallel + one plenary + 7 posters sessions)
Number of exhibitors' booths	18

An ACES workshop was held on Monday, March 5, giving the latest information to potential users of this project.

Support

The organizers wish to thank :

- The Republic and Canton of Neuchâtel
- The City of Neuchâtel
- The Swiss Academy of Engineering Sciences (SATW/ASST), Zurich
- The Federal Office of Metrology and Accreditation, Berne
- The Federal Office of Science and Education, Berne

...for their financial support

The organizers and participants express their gratitude for the gifts and assistance provided by :

- L'imprimerie Krattiger, Corcelles
- The Tourism Office, Neuchâtel
- L'Office des Vins et Produits du Terroir, Neuchâtel
- Silicon Graphics, Cortaillod
- EICN / L'Ecole d'Ingénieurs du Canton de Neuchâtel, Le Locle

PARTICIPANTS BY COUNTRY

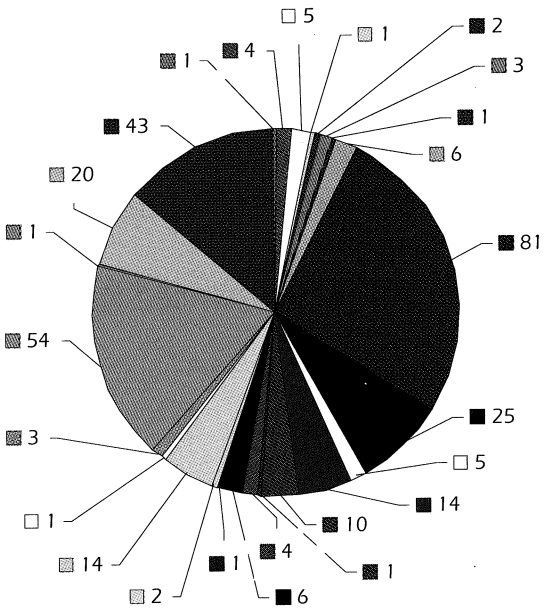

- Australia (1)
- Austria (4)
- Belgium (5)
- Canada (1)
- China (2)
- Czech Republic (3)
- Danemark (1)
- Finland (6)
- France (81)
- Germany (25)
- Israel (5)
- Italy (14)
- Japan (10)
- Mexico (1)
- The Netherlands (4)
- Poland (6)
- Portugal (1)
- Romania (2)
- Russia (14)
- Spain (1)
- Sweden (3)
- Switzerland (54)
- Taiwan (1)
- United Kingdom (20)
- USA (43)

CONTRIBUTED PAPERS (ORALS + POSTERS)

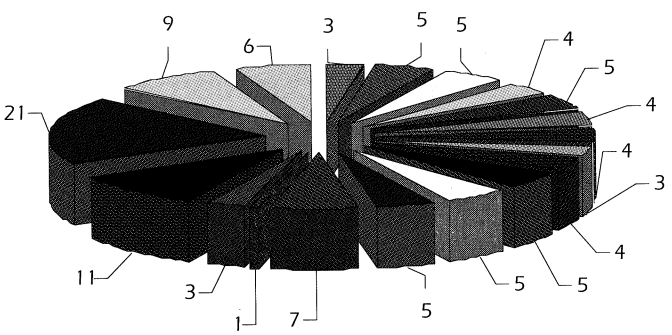

- Opening Session (3)
- Atomic Fountains (5)
- Atomic Frequency Standards (5)
- Optical Frequency Standards (4)
- Cryo Frequency Generation (4)
- Instrumentation & Telecommunications (5)
- Posters Materials (7)
- Posters SAW (3)
- Posters Atomic, Optical & Fountain Frequency Standards (21)
- Posters GPS, Galileo & Carrier-Phase (6)
- Materials (5)
- Sensors (4)
- Quartz Oscillators (4)
- GPS Carrier-Phase (3)
- SAW (5)
- Galileo & Aces (5)
- Posters Sensors (1)
- Posters Quartz Oscillators & Resonators (11)
- Posters Instrumentation & Telecommunications (9)

1. Programme

The future main developments and challenges in the field of Time and Frequency are stringent requirements for clocks used in future satellite systems (ISS, GALILEO) deserving accurate time-keeping and distribution and global transmission services. A second field deals with the generation and measurement of highly stable optical frequency signals with ultrashort laserpulses. These aspects were treated in the opening session and in several dedicated sessions. Atomic fountains are now routinely used or in a final development stage in several labs, stressing out the needs for highly accurate intercomparison methods usually over large baselines. Both aspects were handled during the forum in two sessions. Progress in classical atomic standards were reported in one session. Four sessions were devoted to materials, sensors, SAW and quartz oscillators and the low temperature technology was treated in one session.
Two poster sessions were devoted to the same subjects, but treated more specific problems and thus permitted discussions among the participants.

2. Facilities

The Aula of the University of Neuchâtel is still a good choice for the Forum. Due to the shift of interest of participants, the atomic and optical frequency generation sessions attracted more participants than the materials and classical frequency generation sessions and this should be accounted for in the future when dealing with the rooms. Also enough surface should be foreseen for the poster sessions. The computer corner offered by Silicon Graphics was especially appreciated by the participants.

3. Exhibition

The premises allocated for the exhibitors are too small and more room must be foreseen as this sector is further developed. We had 18 exhibitors, 7 from the USA, 3 from Germany, 3 from the United Kingdom, 2 from Russia, 2 from Switzerland and 1 from China. Most exhibitors are in the frequencies generating business, but 4 of them produce manufacturing and measuring/testing equipments. The absence of french exhibitors was noted.

4. Conclusions

The Forum has now gained a certain maturity and is well accepted also in Eastern Europe. It can however not be denied that there is a certain stagnation and it is important to attract young scientists working in the field. We have noted that apparently R & D activities in the field have almost completely left private industry and are now concentrated in universities and state laboratories. The extraordinary possibilities of synchronisation by the internet or similar means permits perhaps to attract the interest of computer industry and their applications to the field of Time and Frequency.

Léon Prost
Scientific Chairman EFTF '01

List of participants - March 6-8, 2001 - Neuchâtel, Switzerland

NAME		AFFILIATION	ADDRESS			COUNTRY
Abgrall	Michel	BNM - LPTF	61, av. de l'Observatoire	75014	Paris	FRANCE
Abramov	Yuri	Soliton	Har Hatzofim 24/4	58492	Holon	ISRAEL
Adamowicz	Waldemar	Telekomunikacja Polska SA	Nowy Swiat 6/12	00-400	Warsaw	POLAND
Addouche	Mahmoud	CNRS - LPMO	32, av. de l'Observatoire	25044	Besançon	FRANCE
Alenkov	Vladimir	FOMOS	Buzheninova st. 16	105023	Moscow	RUSSIA
Amy-Klein	Anne	Lab. de Physique des Lasers	Av. J.-B. Clément 99	93430	Villetaneuse	FRANCE
Arias	Elisa Felicitas	BIPM	Pavillon de Breteuil	92310	Sèvres	FRANCE
Arkhipov	Mikhail	SPC Goodwill	1, Institutskay Street	601600	Alexandrov, Vladimir	RUSSIA
Aubril	Jean-Claude	Oscilloquartz SA	Rue des Brévards 16	2002	Neuchâtel	SWITZERLAND
Aubry	Jean - Pierre	Oscilloquartz SA	Rue des Brévards 16	2002	Neuchâtel	SWITZERLAND
Audoin	Claude		2, rue des Vallées	92290	Châtenay-Malabry	FRANCE
Auterlot	Jules	Tekelec Temex C.Q.E	2, Rue Robert Keller, Z.I.	10150	Pont Sainte Marie	FRANCE
Babino	Massimiliano	Fordahl SA	Erlenstrasse 31	2503	Bienne	SWITZERLAND
Baldy	Michel	Temex Telecom	29, Av. de la Baltique	91953	Les Ulis	FRANCE
Ballandras	Sylvain	CNRS - LPMO	32, av. de l'Observatoire	25044	Besançon Cedex	FRANCE
Barillet	Roland	CNRS / LHA	Bâtiment 221, Université de	91405	Orsay Cedex	FRANCE
Bartholome	Thomas	TASC	6767 North Wickham Road	32940	Melbourne, FL	USA
Bauch	Andreas	Physikalisch-Technische Bundesanstalt	Bundesallee 100	38116	Braunschweig	GERMANY
Baumont	Françoise	OCA / CERGA	Av. Nicolas Copernicus	06130	Grasse	FRANCE
Bava	Elio	Politecnico di Milano	Piazza Leonardo da Vinci 32	20133	Milano	ITALY
Bavière	Philippe	CNES - Université Paris XIII	2, Place Maurice Quentin	75035	Paris	FRANCE
Beard	Ronald L.	U.S. Naval Research Laboratory	4555 Overlook Avenue, SW.	20375	Washington, D.C.	USA
Becker	Jürgen	Physikalisch-Technische Bundesanstalt	Bundesallee 100	38116	Braunschweig	GERMANY
Begni	Mala	Temex Neuchâtel Time SA	Rue de Vauseyon 29	2000	Neuchâtel	SWITZERLAND
Beliaev	Alexander	VREMYA-CH	67, Osahrskaya St.	603105	Nizhny Novgorod	RUSSIA
Beliaev	Alexander	Observatoire Cantonal	Rue de l'Observatoire 58	2000	Neuchâtel	SWITZERLAND
Berberian	John	Agilent Technologies	5301 Stevens Creek Blvd	95152	Santa Clara, CA	USA
Berger	Hans	EFG International	Düppelstrasse 13	14163	Berlin	GERMANY
Bernier	Laurent G.	METAS	Lindenweg 50	3003	Berne - Wabern	SWITZERLAND
Besson	Raymond J.	ENSMM / LCEP	26, ch. de l'Epitaphe	25030	Besancon Cedex	FRANCE
Bichsel	René	Vibro-meter SA	Route de Moncor 4, P.O. Box	1701	Fribourg	SWITZERLAND
Bigler	Emmanuel	ENSMM / LCEP	26, ch. de l'Epitaphe	25044	Besançon Cedex	FRANCE
Bize	Sébastien	BNM - LPTF	61, av. de l'Observatoire	75014	Paris	FRANCE
Bloch	Martin	Frequency Electronics Inc.	55 Charles Lindberg Blvd	11553	Mitchel Field, NY	USA
Boroditsky	Roman	VF Technologies	75 South Street	01748	Hopkinton, MA	USA
Bourquin	Roger	ENSMM / LCEP	26, ch. de l'Epitaphe	25030	Besançon Cedex	FRANCE
Boy	Jean-Jacques	ENSMM / LCEP	26, ch. de l'Epitaphe	25030	Besançon Cedex	FRANCE
Boyko	Alexandr	Inst. of Metrology for Time and Space		141570	Mendeleevo, Moscow	Russia
Brendel	Jürgen	Roditi International Corp. Ltd.	130 Regent Street	W1R 6B	London	UNITED KINGDOM
Brendel	Rémi	CNRS - LPMO	32, av. de l'Observatoire	25044	Besançon Cedex	FRANCE
Brod	Konrad	Quintenz Hybridtechnik	Eichenstrasse 15	82061	Neuried	GERMANY

NAME		AFFILIATION	ADDRESS			COUNTRY
Brunet	Michel	CNES	18, av. Edouard Belin	31401	Toulouse Cedex 4	FRANCE
Bühler	Steeve	Ecole d'Ingénieurs de Bienne	Grand'Rue 2	2603	Péry	SWITZERLAND
Burt	Eric	U. S. Naval Observatory	3450 Massachusetts Ave N	20392-	Washington, DC	USA
Busca	Giovanni	Observatoire Cantonal	Rue de l'Observatoire 58	2000	Neuchâtel	SWITZERLAND
Calonico	Davide	Politecnico di Torino	Corso Duca Degli Abruzzi 24	10129	Torino	ITALY
Calosso	Claudio E.	Politecnico di Torino	Corso Duca Degli Abruzzi 24	10129	Torino	ITALY
Camou	Serge	CNRS - LPMO	32, av. de l'Observatoire	25044	Besançon Cedex	FRANCE
Candelier	Vincent	C-MAC	44, av. de la Glacière, B.P. 16	95105	Argenteuil Cedex	FRANCE
Cao	Cuong	Micro Crystal	Mühlestrasse 14	2540	Grenchen	SWITZERLAND
Capelle	Bernard	LMCP / CNRS	4, Place Jussieu	75252	Paris Cedex 05	FRANCE
Casey	Kenneth E.	Hoffman Materials, Inc.	321, Cherry Street, P.O. Box	17013	Carlisle, PA	USA
Cerez	Pierre	CNRS - LHA	Bâtiment 221 - Université de	91405	Orsay Cedex	FRANCE
Chambon	Maguelonne	BNM	1, rue Gaston Boissier	75015	Paris	FRANCE
Chapman	David	Saunders & Associates, Inc.	7440 E. Karen Drive	85260	Scottsdale, Arizona	USA
Clairon	André	BNM - LPTF	61, av. de l'Observatoire	75014	Paris	FRANCE
Cordara	Franco	IEN Galileo Ferraris	Strada delle Cacce 91	10135	Torino	ITALY
Courtillot	Irène	BNM - LPTF	61, av. de l'Observatoire	75014	Paris	FRANCE
Dach	Rolf	University of Berne	Sidlerstrasse 5	3012	Berne	SWITZERLAND
Dalla Piazza	Silvio	Micro Crystal	Mühlestrasse 14	2540	Grenchen	SWITZERLAND
Davis	John A.	National Physical Laboratory	Queens Road	TW11 O	Teddington, Middlese	UNITED KINGDOM
De Clercq	Emeric	BNM - LPTF	61, av. de l'Observatoire	75014	Paris	FRANCE
De Jong	Gerrit	NMi Van Swinden Laboratory	P.O. Box 654	2600 A	Delft	THE NETHERLANDS
De Larquier	Pierre-Claude	Temex Telecom	29, avenue de la Baltique	91953	Les Ulis	FRANCE
De Marchi	Andrea	Politecnico di Torino	Corso Duca Degli Abruzzi 24	10129	Torino	ITALY
Defraigne	Pascale	Royal Observatory of Belgium	Av. Circulaire 3	1180	Brussels	BELGIUM
Delporte	Jérôme	CNES	18, av. Edouard Belin	31401	Toulouse Cedex 4	FRANCE
Deng	Jinguan	Datum Inc. Irvine	9975 Toledo	92656	CA - Irvine	USA
Deyzac	François	ONERA	29, av. de la division Leclerc	92320	Châtillon	FRANCE
Di Domenico	Gianni	Observatoire Cantonal	Rue de l'Observatoire 58	2000	Neuchâtel	SWITZERLAND
Dick	John	Jet Propulsion Laboratory	4800 Oak Grove Drive	91109	Pasadena, CA	USA
Dimarcq	Noël	Observatoire de Paris	61, avenue de l'Observatoire	75014	Paris	FRANCE
Domnin	Yury	Inst. of Metrology for Time and Space	Mendeleevo	141570	Moscow Region	RUSSIA
Droz	Fabien	Temex Neuchâtel Time SA	Vauseyon 29	2000	Neuchâtel	SWITZERLAND
Drullinger	Robert	NIST	325 Broadway	80303-	Boulder, CO	USA
Ducos	Franck	BNM - LPTF	61, av. de l'Observatoire	75014	Paris	FRANCE
Dudle	Gregor	METAS	Lindenweg 50	3003	Berne - Wabern	SWITZERLAND
Dulmet	Bernard	ENSMM / LCEP	26, ch. de l'Epitaphe	25030	Besançon Cedex	FRANCE
Durrant	Phil	Temex SAW	Puits-Godet 8	2000	Neuchâtel	SWITZERLAND
Ecabert	Marcel	FSRM	Rue Jaquet-Droz 1 / CP20	2007	Neuchâtel	SWITZERLAND
Eichel	Gabriele	TSS Technical Software Service	Maria-Theresia-Strasse 10	89264	Weissenhorn	GERMANY
Eichel	Klaus	TSS Technical Software Service	Maria-Theresia-Strasse 10	89264	Weissenhorn	GERMANY
Ejov	Evgueni	Observatoire Cantonal	Rue de l'Observatoire 58	2000	Neuchâtel	SWITZERLAND

NAME		AFFILIATION	ADDRESS			COUNTRY
Ekstrom	Christopher	U.S. Naval Observatory	3450 Massachusette Ave, N	20392	Washington, DC	USA
Elies	David	Direction des Constructions Navales	P.O. Box 26	29240	Brest Naval	FRANCE
Emmons	Donald A.	Datum	34 Tozer Road	01915	Beverly, MA	USA
Engdahl	Nils	Fordahl S.A.	Erlenstrasse 31	2503	Bienne	SWITZERLAND
Erhard	Philippe	Alcatel Space Industries	Av. J.-F. Champollion 26, BP 1	31037	Toulouse Cedex	FRANCE
Eskelinen	Pekka	Helsinki University of Technology	Otakaari 5A	02015	Hut, Espoo	FINLAND
Faillet	Frédéric	C-MAC Frequency Products	44, av. de la Glacière - BP 16	95105	Argenteuil	FRANCE
Fatiyanov	Nikita	Gosstandart	Leninsky pr-t, 9, B-49, GSP 1	119991	Moscow	RUSSIA
Fazi	Christian	US Army Research Laboratory	2800 Powder Mill Road	20783	Adelphi, MD	USA
Featonby	Paul	Sagem SA	72, Rue de la Tour Billy	95101	Argenteuil	FRANCE
Feltham	Steve	ESA - European Space Agency ESTEC	Keplerlaan 1	2200 A	Noordwijk	THE NETHERLANDS
Ferrand	Dominique	Agilent Technologies France	1, rue Galvani	91745	Massy Cedex	FRANCE
Fick	Franz	Quarz-Technik	Kiefernberg 19	21075	Hamburg	GERMANY
Firouzi	Elham	Université de Neuchâtel	Rue A.-L. Breguet 2	2000	Neuchâtel	SWITZERLAND
Foret	Bertrand	Gillam-Fei SA	Mont St. Martin 58	4000	Liège	BELGIUM
Fouilleul	Bernard	Aura International SA	1, Place du Serpentaire, SILI	94513	Rungis	FRANCE
Franquet	Olivier	AR Electronique	Espace Valentin-Nord, BP 311	25004	Besançon Cedex	FRANCE
Friedt	Jean-Michel	IMEC	Kapeldreef 75	3001	Leuven	BELGIUM
Fromm	Hans-Hermann	ESA-ESTEC	P.O. Box 299	2200 A	Noordwijk	THE NETHERLANDS
Galliou	Serge	ENSMM / LCEP	26, ch. de l'Epitaphe	25030	Besançon Cedex	FRANCE
Gallop	John	National Physical Laboratory	Queens Road	TW11 O	Teddington, Middlese	UNITED KINGDOM
Garvey	Michael	Datum	34 Tozer Road	01915-5	Beverly, MA	USA
Gifford	Al	NIST	325 Broadway	80303	Boulder, CO	USA
Gillard	Michel	Gillam-Fei SA	Mont St. Martin 58	4000	Liège	BELGIUM
Gillet	Daniel	CNRS - LPMO	32, av. l'Observatoire	25044	Besançon Cedex	FRANCE
Giordano	Vincent	CNRS - LPMO	32, av. l'Observatoire	25044	Besançon Cedex	FRANCE
Girardet	Emmanuel	AR Electronique	Espace Valentin-Nord, BP 311	25048	Besançon Cedex	FRANCE
Gisiger	Arnaud	Alcatel Space Switzerland SA	Neuenburgstrasse 7	2076	Gals	SWITZERLAND
Goka	Shigeyoshi	Tokyo Metropolitan University	1-1 Minamiosawa		Hachioji, Tokoy	JAPAN
Gotta	Monica	Alenia Spazio S.p.A	Via Saccomuro 24	00131	Roma	ITALY
Graf	Erhard		Chemin de Cuard 31	2022	Bevaix	SWITZERLAND
Granier	Jean-Pierre	CNES	18, av. Edouard Belin	31401	Toulouse Cedex 4	FRANCE
Green	Clive	Quartzlock UK Limited	Gothic, Plymouth Road	TQ9 5L	Devon	UNITED KINGDOM
Grigorievski	Valeri	Russian Academy of Sciences	Vvedensky Square 1	141120	Fryazino	RUSSIA
Grunert	Ulrich	German Aerospace Center	P.O. Box 1116	82230	Wessling	GERMANY
Gufflet	Nicolas	Vectron International GmbH	Waibstadter Strasse 2-4	74924	Neckarbischofsheim	GERMANY
Guillemot	Philippe	CNES	18, av. Edouard Belin	31401	Toulouse Cedex	FRANCE
Guillot	Emmanuel	Inst. for National Measurements Standar	M36 Montreal Road	K1A OR	Ottawa, ON	CANADA
Hald	Jan	DFM - Danish Institute of Fundamental M	Matematiktorvet, Bldg. 307	2800	Lyngby	DANEMARK
Hänsch	Theodor	Max-Planck Institut für Quantenoptik	Hans-Kopfermann-Strasse 1	85748	Garching	GERMANY
Hao	Ling	National Physical Laboratory	Queens Road	TW11 O	Teddington, Middlese	UNITED KINGDOM
Hartnett	John	University of Western Australia	35, Stirlong Hwy	6009	Crawley	AUSTRALIA

NAME		AFFILIATION	ADDRESS			COUNTRY
Hauden	Daniel	CNRS - LPMO	32, av. de l'Observatoire	25044	Besançon Cedex	FRANCE
Henderson	Dale	National Physical Laboratory	Queens Road	TW11 0	Teddington, Middelse	UNITED KINGDOM
Hermann	Virgile	CNRS - LHA	61, av. de l'Observatoire	75014	Paris	FRANCE
Herwe	Jan	Pendulum Instruments AB	Box 541	162 15	Vallingby	SWEDEN
Hillel	Armon	Nofech Electronics Ltd	11, Beith Hadfus Street	95483	Jerusalem	ISRAEL
Hilty	Kurt	METAS	Lindenweg 50	3003	Bern-Wabern	SWITZERLAND
Huber	Felix	Steinbeis Transferzentrum Raumfahrt	Rötestrasse 15	71126	Gäufelden	GERMANY
Ikegami	Takeshi	National Research Laboratory of Metrolog	1-1-4, Umezono	305-85	Tsukabi-Shi, Ibaraki-	JAPAN
Imae	Michito	Communications Research Laboratory	4-2-1 Nukuikita-machi, Konag	184-87	Tokyo	JAPAN
Itoh	Hideaki	Shinshu University	Wakasato 4-17-1	380-09	Nagano	JAPAN
Jaldehag	Kenneth	Swedish Natio. Testing and Research Inst.	Box 857	5-50115	Boras	SWEDEN
Jefferts	Steve	NIST	325 Broadway	80305-	Boulder, CO	USA
Jornod	Alain	Observatoire Cantonal	Rue de l'Observatoire 58	2000	Neuchâtel	SWITZERLAND
Joyet	Alain	Observatoire Cantonal	Rue de l'Observatoire 58	2000	Neuchâtel	SWITZERLAND
Kajita	Masatoshi	Communications Research Laboratory	4-2-1, Nukui-Kitamachi, Koga	184-87	Tokyo	JAPAN
Kalliomäki	Kalevi	University of Oulu	P.O. Box 400	098570	Oulu	FINLAND
Kasznia	Michal	Poznan University of Techology	Piotrowo 3 A	60 965	Poznan	POLAND
Kersalé	Yann	CNRS - LPMO	32, av. de l'Observatoire	25044	Besançon Cedex	FRANCE
Kihara	Masami	NTT Network Innovation Laboratories	Hikari-no-oka 1-1	239 08	Yokosuka	JAPAN
Kimberley	Robin	Zyfer Europe Limited	530-535 Eskdale Road, Winn	RG41 5	Wokingham, Winners	UNITED KINGDOM
Kirchner	Dieter	Technische Universität Graz	Inffeldgasse 12	8010	Graz	AUSTRIA
Klemenz	Christine	EPFL	IMO-DP	1015	Lausanne	SWITZERLAND
Klepczynski	William	Innovative Solutions International	3530 South River Terrace	21037	Edgewater, Maryland	USA
Knight	David J.E.	DK Research	110 Strawberry Vale	TW1 4S	Twickenham, Middles	UNITED KINGDOM
Kondratiev	Serguei	TEMEX SAW	Puits-Godet 8	2000	Neuchâtel	SWITZERLAND
Koshelyaevs	Nicholas	Inst. of Metrology for Time and Space	Mendeleevo	141570	Moscow Region	RUSSIA
Kraemer	Rainer	German Aerospace Center	P.O. Box 1116	82230	Wessling	GERMANY
Krempl	Peter W.	AVL List GmbH	Hans-List-Platz 1	8020	Graz	AUSTRIA
Kretschmer	Lenka	ENSMM / LCEP	26, ch. de l'Epitaphe	25044	Besançon Cedex	FRANCE
Kulakov	Sergei	St Petersburg State University	Bolshaya Morskaya 67	190000	St Petersburg	RUSSIA
Lalandre	Philippe	Oscilloquartz SA	Rue des Brévards 16	2002	Neuchâtel	SWITZERLAND
Lambert	Christian	Unaxis SPTec	Chapon-des-Prés 11	2022	Bevaix	SWITZERLAND
Lange	Werner R.	Lange Electronic GmbH	Ganghoferstrasse 29	82216	Gernlinden	GERMANY
Lange	Oliver	Lange Electronic GmbH	Ganghoferstrasse 29	82216	Gernlinden	GERMANY
Laude	Vincent	CNRS - LPMO	32, av. de l'Observatoire	25044	Besançon Cedex	FRANCE
Laverty	John	National Physical Laboratory	Queens Road	TW11 0	Teddington, Middlese	UNITED KINGDOM
Lawery	John	Zyfer Europe Limited	530-535 Eskdale Road, Winn	RG41 5	Wokingham	UNITED KINGDOM
Lea	Stephen Nichol	National Physical Laboratory	Queens Road	TW11 O	Teddington, Middlese	UNITED KINGDOM
Lefevres	Stéphane	Temex Neuchâtel Time SA	Rue de Vauseyon 29	2000	Neuchâtel	SWITZERLAND
Lehtonen	Saku	Helsinki University of Technology	P.O. Box 2200	02015	Hut	FINLAND
Leonardi	Mauro	Alenia Spazio S.p.A.	Via Saccomuro 24	00131	Roma	ITALY
Levi	Filippo	IEN Galileo Ferraris	Strada delle Cacce 91	10135	Torino	ITALY

NAME		AFFILIATION	ADDRESS			COUNTRY
Li	Mingfu	Chunghwa Telecommunications Labs	12, Lane 551, Min-Tsu Road S	326	Yang-Mei, Taoyuan	TAIWAN
Lienard	Laurent	Temex Neuchâtel Time SA	Rue de Vauseyon 29	2000	Neuchâtel	SWITZERLAND
Lisowiec	Aleksander	Tele and Radio Research Institute	Ratuszowa 11	03-450	Warsaw	POLAND
Lopes	Christian	IN-SNEC	5, av. des Andes	91943	Les Ulis Cedex	FRANCE
Lorini	Luca	IEN Galileo Ferraris	Strada delle Cacce 91	10135	Torino	ITALY
Mancini	Oleandro	Frequency Electronics Inc.	55 Charles Lindbergh Blvd.	11553	Mitchel Field, NY	USA
Mandache	Cipriana	INFLPR	P.O Box MG-36	76900	Bucharest, Magurele	ROMANIA
Mannermaa	Jari	Nokia Mobile Phones	Sinitaival 5	33721	Tre	FINLAND
Mansten	Tapio	Centre for Metrology and Accreditation	Otakaari 7B	02150	Espoo	FINLAND
Marques	Fatima Silverio	IPQ Instituto Português da Qualidade	Rua Antonio Giao 2	282951	Caparica	PORTUGAL
Martin	David	Datum	34 Tozer Road	01915	Beverly, MA	USA
Marty	Oliver	Saunders & Associates, Inc.	7440 E. Karen Drive	85260	Scottsdale, Arizona	USA
Massay	Jacques	CNES	18, av. Edouard Belin	31401	Toulouse Cedex 4	FRANCE
Mateescu	Irina	National Institute of Materials Physics	P.O. Box MG 7	76900	Bucarest Magurele	ROMANIA
Matsakis	Demetrios	U.S. Naval Observatory	3450 Massachusetts Avenue,	20392	Washington DC	USA
Meirs	Marvin	Frequency Electronics Inc.	55 Charles Lindbergh Blvd.	11553	Mitchel Field, NY	USA
Messina	Filippo	Cagliari Astronomical Observatory	Str. 54 loc. Poggio dei Pini	09012	Capoterra	ITALY
Meyer	François	Observatoire de Besançon	41 bis, av. de l'Observatoire	25010	Besançon Cedex	FRANCE
Micalizio	Salvatore	Politecnico di Torino	Strada delle Cacce 91	10135	Torino	ITALY
Mileti	Gaetano	Observatoire Cantonal	Rue de l'Observatoire 58	2000	Neuchâtel	SWITZERLAND
Minguy	Yves	DCN / SC	SC / BREST / MOSN	29240	Brest Naval	FRANCE
Mochizuki	Ken	Anritsu Corporation	1800 Onna, Atsugi-shi	243-85	Kanagawa-Pfr.	JAPAN
Moser	Vincent	Université de Neuchâtel	Rue A.-L. Breguet 2	2000	Neuchâtel	SWITZERLAND
Mountfield	Mike	Zyfer Europe Limited	530-535 Eskdale Road, Winn	RG41 5	Wokingham	UNITED KINGDOM
Nawrocki	Jerzy	Astrogeodynamical Observatory	Borowiec	62-035	Kornik	POLAND
Neubig	Bernd W.	Corning Frequency Control	Landstrasse 2	74924	Neckarbischofsheim	GERMANY
Nosek	Jaroslav	Technical University of Liberec	Halkova 6	46117	Liberec	CZECH REPUBLIC
Nouel	François	CNES	18, Avenue Edouard Belin	31401	Toulouse Cedex 4	FRANCE
Overhoff	Stéphanie		Wallstrasse 10	46535	Dinslaken	GERMANY
Ozaki	Kiyoharu	Tokyo Metropolitan University	1-1 Minamiosawa		Hachioji, Tokoy	JAPAN
Pal'chikov	Vitaly	Inst. of Metrology for Time and Space		141570	Mendeleevo, Moscow	RUSSIA
Palacio	Juan	Real Observatorio de la Armada	Cecilio Pojazon S/N	11100	San Fernando	SPAIN
Parker	Thomas E.	NIST	325 Broadway	80305	Boulder, CO	USA
Pasche	Marc-Yvain	Fordahl SA	Erlenstrasse 31	2503	Bienne	SWITZERLAND
Pavlenko	Iouri	Observatoire Cantonal	Rue de l'Observatoire 58	2000	Neuchâtel	SWITZERLAND
Pawlitzki	Alexander	TimeTech GmbH	Curiestrasse 2	70563	Stuttgart	GERMANY
Peier	Ulrich R.	Peier Engineering SA	Endlikerstrasse 60	8400	Winterthur	SWITZERLAND
Pellegrini	Angelo	Fordahl SA	Erlenstrasse 31	2503	Bienne	SWITZERLAND
Petit	Roger	DGA / CELAR	BP 7419	35174	Bruz	FRANCE
Petit	Gérard	BIPM	Pavillon de Breteuil	92312	Sèvres Cedex	FRANCE
Philippot	Etienne	CNRS - LPMC	Place E. Bataillon, cc 003	34095	Montpellier Cedex 5	FRANCE
Pianowski	H.D.	EFG GmbH	Düppelstrasse 13	14163	Berlin	GERMANY

NAME		AFFILIATION	ADDRESS			COUNTRY
Pietropaoli	Tomaso	ISCTI - Ministero delle Commnicazioni	Viale America 201	00144	Roma	ITALY
Piwowarczyk	Zdzislaw	Central Office of Measures	2, Elektoralna Str.	00-950	Warsaw	POLAND
Planat	Michel	CNRS - LPMO	32, av. de l'Observatoire	25044	Besançon Cedex	FRANCE
Plessky	Victor	Thales	Fahys 9	2000	Neuchâtel	SWITZERLAND
Poetzsch	Reinhard	Vectron International GmbH	Waibstadter 2-4	74924	Neckarbischofsheim	GERMANY
Pottie	Paul-Eric	CNRS - LHA	61, av. de l'Observatoire	75014	Paris	FRANCE
Prost	Léon		Rue des Préels 26	2036	Cormondrèche	SWITZERLAND
Ratier	Nicolas	CNRS - LPMO	32, av. de l'Observatoire	25044	Besançon	FRANCE
Riley	William J.	Datum	34 Tozer Road	01915	Beverly, MA	USA
Riondet	Bernard	IN-SNEC	5, av. des Andes	91943	Les Ulis Cedex	FRANCE
Rochat	Pascal	Temex Neuchâtel Time SA	Rue de Vauseyon 29	2000	Neuchâtel	SWITZERLAND
Rovera	Daniele	BNM - LPTF	61, av. de l'Observatoire	75014	Paris	FRANCE
Rubado	Neil	Perkin Elmer Optoelectronics	35 Congress Street	01970	Salem, MA	USA
Rubiola	Enrico	CNRS - LPMO	2, rue Jean Lamour	54519	Vandoeuvre	FRANCE
Safonova	Ekaterina	Kazan State Technical University	Kul-Gali 7a apt 15	420141	Kazan	RUSSIA
Sakharov	Boris	VREMYA-CH	67, Osahrskaya St.	603105	Nizhny Novgorod	RUSSIA
Sakharov	Sergey	FOMOS	16 Buzheiniova street	105023	Moscow	RUSSIA
Salomon	Christophe	Laboratoire Kastler Brossel / ENS	24, rue L'Homond	75005	Paris	FRANCE
Salzenstein	Patrice	CNRS - LPMO	32, av. de l'Observatoire	25044	Besançon Cedex	FRANCE
Sandfeld	Ken	Zyfer Europe Limited	530-535 Eskdale Road, Winn	RG41 5	Wokingham	UNITED KINGDOM
Santarelli	Giorgio	BNM - LPTF	61, av. de l'Observatoire	75014	Paris	FRANCE
Saunders	Steve	Roditi International Corp. Ltd.	130 Regent Street	W1B 5S	London	UNITED KINGDOM
Schadegg	Gabriel	Fordahl SA	Erlenstrasse 31	2503	Bienne	SWITZERLAND
Schaefer	Wolfgang	TimeTech GmbH	Curiestrasse 2	70563	Stuttgart	GERMANY
Schlueter	Bernard		7, rue des Mésanges	25130	Villers-Le-Lac	FRANCE
Schröder	Roland	Physikalisch-Technische Bundesanstalt	Bundesallee 100	38116	Branuschweig	GERMANY
Schweda	Hartmut	Observatoire Cantonal	Rue de l'Observatoire 58	2000	Neuchâtel	SWITZERLAND
Senior	Ken	US Naval Observatory	3450 Massachusetts Avenue	20392	Washington, D.C	USA
Sevely	Laure	ESIEE	Cité Descartes, BP 99	93162	Noisy-le-Grand Cedex	FRANCE
Seydel	Eberhard	Quartz Pro	Box 6062	17506	Järfälla	SWEDEN
Shemar	Setnam	National Physical Laboratory	Queens Road	TW11 O	Teddington, Middlese	UNITED KINGDOM
Shmaliy	Yuriy	Guanajuato University	P. O. Box 215-A, Prol.Tampic	36730	Salamanca, Gto	MEXICO
Siccardi	Marco	Datum	9975 Toledo	92618	Irvine, CA	USA
Sikama	Yuji	Tokyo Metropolitan University	1-1 Minamiosawa		Hachioji, Tokoy	JAPAN
Silverman	Phil	XECO Inc.	1651 North Bulldog Rd	84720	Cedar City, Utah	USA
Sommer	Roland	Kistler Instrumente AG	Eulachstr. 22	8408	Winterthur	SWITZERLAND
Sortais	Yvan	BNM - LPTF	61, av. de l'Observatoire	75014	Paris	FRANCE
Soufyane	Abdelaziz	CNRS - LPMO	32, av. de l'Observatoire	25044	Besançon Cedex	FRANCE
Sramar	Jaroslav	Krystaly H.K, a.s.	Okruzni 1144	50003	Hradec Kralove	CZECH REPUBLIC
Staudte	Marci	XECO Inc.	1651 North Bulldog Rd	84720	Cedar City, Utah	USA
Stehlin	Xavier	Temex Neuchâtel Time SA	Vauseyon 29	2000	Neuchâtel	SWITZERLAND
Stenger	Jörn	Physikalisch-Technische Bundesanstalt	Bundesallee 100	38116	Branuschweig	GERMANY

NAME		AFFILIATION	ADDRESS			COUNTRY
Stern	Avinoam	AccuBeat Ltd	5, Hamarpeh Street, P.O. Bo	91450	Jerusalem	ISRAEL
Stevenart	Baudoin	Gillam-Fei SA	Mont St. Martin 58	4000	Liège	BELGIUM
Stevens	Ron	Femtosecond Systems	4894 Van Gordon Street	CO-800	Wheat Ridge, CO	USA
Studer	Bruno	Micro Crystal	Mühlestrasse 14	2540	Grenchen	SWITZERLAND
Syme	Richard	Astrium Ltd	Gunnels Wood Road	SG1 2A	Stevenage	UNITED KINGDOM
Szymaniec	Krzysztof	National Physical Laboratory	Queens Road	TW11 O	Teddington	UNITED KINGDOM
Takahei	Kenichiro	Anritsu Corporation	1800 Onna, Atsugi-shi	243-85	Kanagawa-Ken	JAPAN
Tavella	Patrizia	IEN Galileo Ferraris	Strada delle Cacce 91	10135	Torino	ITALY
Teodoridis	Viron	Observatoire Cantonal	Rue de l'Observatoire 58	2000	Neuchâtel	SWITZERLAND
Teytaud	Olivier	Institut des Sciences Cognitives	67, boulevard Pinel	69675	Bron Cedex	FRANCE
Thanner	Herbert	AVL List GmbH	Hans-List-Platz 1	8020	Graz	AUSTRIA
Théobald	Geneviève	CNRS - LHA	Bâtiment 221, Université Pari	91405	Orsay Cedex	FRANCE
Thomann	Pierre	Observatoire Cantonal	Rue de l'Observatoire 58	2000	Neuchâtel	SWITZERLAND
Thurner	Marc	Ecole d'Ingénieurs de Bienne	Les Pingeons 5	2075	Wavre	SWITZERLAND
Tignanelli	Gaetano	ISCTI - Ministero delle Commincazioni	Viale America 201	00144	Roma	ITALY
Tribes	Robert	CNES	18, av. Edouard Belin	31401	Toulouse Cedex 4	FRANCE
Uhrich	Pierre	BNM - LPTF	61, av. de l'Observatoire	75014	Paris	FRANCE
Underhill	Michael	University of Surrey		GU2 5X	Guildford	UNITED KINGDOM
Unverdross	Rainer	Unverdross - Technik	Am Pfeifenberg 5	82237	Wörthsee	GERMANY
Vaccaro	John A.	Perkin Elmer Optoelectronics	35 Congress Street	01970	Salem, MA	USA
Valat	David	BNM - LPTF	61, av. de l'Observatoire	75014	Paris	FRANCE
Valbin	Laurie	ESIEE	Cité Descartes, BP 99	93162	Noisy-le-Grand Cedex	FRANCE
Vernotte	François	Observatoire de Besançon	41 bis, av. de l'Observatoire,	25010	Besançon Cedex	FRANCE
Vidoni	Pierino	Fordahl SA	Erlenstrasse 31	2503	Bienne	SWITZERLAND
Vig	J.R.	U.S. Army Electronics Technology		07703	Fort Monmouth, N.J.	USA
Vogler	Thomas	Astrium GmbH		88039	Friedrichshafen	GERMANY
Voisard	Damien	Fordahl SA	Erlenstrasse 31	2503	Bienne	SWITZERLAND
Wagner	Gérard	Thales-Microelectronics	Z.I. de Bellevue	35221	Chateaubourg	FRANCE
Walls	Heidi E.	Femtosecond Systems	4894 Van Gordon Street	CO-800	Wheat Ridge, CO	USA
Walls	Warren	Femtosecond Systems	4894 Van Gordon Street	CO-800	Wheat Ridge, CO	USA
Wang	Qinghua	Observatoire Cantonal	Rue de l'Observatoire 58	2000	Neuchâtel	SWITZERLAND
Wasserman	Israel	AccuBeat Ltd	5, Hamarpeh Street, P.O. Bo	91450	Jerusalem	ISRAEL
Weiss	Marc	NIST	325 Broadway	80303	Boulder, CO	USA
Weiss	Krzysztof	Tele and Radio Research Institute	Ratuszowa 11	03-450	Warsaw	POLAND
Weyers	Stefan	Physikalisch-Technische Bundesanstalt	Bundesallee 100	38116	Braunschweig	GERMANY
Whatmough	Steve	Astrium Ltd	Gunnels Wood Road	SG1 2A	Stevenage	UNITED KINGDOM
White	Joe	US Naval Research Laboratory	4555 Overlook Ave SW	20375	Washington, DC	USA
Wickard	Timothy	Bliley Technologies, Inc.	2545 West Grandview Blvd	16506	Erie, PA	USA
Wiedermann	Werner	Zyfer Europe Limited	530-535 Eskdale Road, Winn	RG41 5	Wokingham	UNITED KINGDOM
Worsch	Peter	AVL List GmbH	Hans-List-Platz 1	8020	Graz	AUSTRIA
Wuthrich	Christian	Asulab SA	Rue des Sors 3	2074	Marin	SWITZERLAND
Yerna	Jo	YeTech Applications b.v.	PO Box 674	7000 A	Doetinchem	THE NETHERLANDS

NAME		AFFILIATION	ADDRESS			COUNTRY
Ylinen	**Raimo**	University of Oulu	Linnanmaa	90014	Oulu	*FINLAND*
Zelenka	**Jiri**	Technical University of Liberec	Hálkova Str. 6	461 17	Liberec 1	*CZECH REPUBLIC*
Zhang	**Shougang**	BNM - LPTF	61, av. de l'Observatoire	75014	Paris	*FRANCE*
Zingg	**Walter**	Montres Rolex SA	Rue François-Dussault 3-7	1211	Genève 24	*SWITZERLAND*
Zomet	**Simon**	Time Squared	PO Box 268		Or Akiva	*ISRAEL*

List of exhibitors - March 6-8, 2001 - Neuchâtel, Switzerland

COMPANY	ADDRESS			COUNTRY
Datum	34 Tozer Rd	01915	Beverly	*USA*
Femtosecond Systems	4894 Van Gordon Street	CO-8003	Wheat Ridge, CO	*USA*
Frequency Electronics Inc.	55 Charles Lindberg Blvd	11553	Mitchel Field, NY	*USA*
Kolinker Industrial Equipments	84-92 Chai Wan Kok Street, Shi		Hong Kong	*CHINA*
Lange Electronic GmbH	Ganghoferstrasse 29	82216	Gernlinden	*GERMANY*
Oscilloquartz SA	Rue des Brévards 16	2002	Neuchâtel	*SWITZERLAND*
Perkin Elmer Optoelectronics	35 Congress Street	01970	Salem, MA	*USA*
Quartzlock UK Limited	Gothic, Plymouth Road	TQ9 5LH	Devon	*UNITED KINGDOM*
Roditi International Corp. Ltd.	130 Regent Street	W1R 6BR	London	*UNITED KINGDOM*
Saunders & Associates, Inc.	7440 E. Karen Drive	85260	Scottsdale, Arizona	*USA*
SPC Goodwill	1, Institutskay Street	601600	Alexandrov	*RUSSIA*
Temex Neuchâtel Time SA	Rue de Vauseyon 29	2000	Neuchâtel	*SWITZERLAND*
TimeTech GmbH	Curiestrasse 2	70563	Stuttgart	*GERMANY*
Transat Corporation	31000 Bainbridge Road	44139-2	Solo, Ohio	*USA*
True Time Inc	3750 Westwind Blvd	95403	Santa Rosa, California	*USA*
TSS Technical Software Service	Maria-Theresia-Strasse 10	89264	Weissenhorn	*GERMANY*
VREMYA-CH	67, Osahrskaya St.	603105	Nizhny Novgorod	*RUSSIA*
Zyfer Europe Limited	530-535 Eskdale Road	RG41 5T	Wokingham	*UNITED KINGDOM*

Index of the authors

T

U

V

W

Y

Z